frontiers | Research Topics

Optical radiometry and satellite validation

Edited by
Agnieszka Bialek, David Doxaran, Vittorio Ernesto Brando, Clemence Goyens, Kevin Ruddick and Ana Ines Dogliotti

Published in
Frontiers in Remote Sensing



FRONTIERS EBOOK COPYRIGHT STATEMENT

The copyright in the text of individual articles in this ebook is the property of their respective authors or their respective institutions or funders. The copyright in graphics and images within each article may be subject to copyright of other parties. In both cases this is subject to a license granted to Frontiers.

The compilation of articles constituting this ebook is the property of Frontiers.

Each article within this ebook, and the ebook itself, are published under the most recent version of the Creative Commons CC-BY licence. The version current at the date of publication of this ebook is CC-BY 4.0. If the CC-BY licence is updated, the licence granted by Frontiers is automatically updated to the new version.

When exercising any right under the CC-BY licence, Frontiers must be attributed as the original publisher of the article or ebook, as applicable.

Authors have the responsibility of ensuring that any graphics or other materials which are the property of others may be included in the CC-BY licence, but this should be checked before relying on the CC-BY licence to reproduce those materials. Any copyright notices relating to those materials must be complied with.

Copyright and source acknowledgement notices may not be removed and must be displayed in any copy, derivative work or partial copy which includes the elements in question.

All copyright, and all rights therein, are protected by national and international copyright laws. The above represents a summary only. For further information please read Frontiers' Conditions for Website Use and Copyright Statement, and the applicable CC-BY licence.

ISSN 1664-8714
ISBN 978-2-8325-5653-5
DOI 10.3389/978-2-8325-5653-5

Generative AI statement
Any alternative text (Alt text) provided alongside figures in the articles in this ebook has been generated by Frontiers with the support of artificial intelligence and reasonable efforts have been made to ensure accuracy, including review by the authors wherever possible. If you identify any issues, please contact us.

About Frontiers

Frontiers is more than just an open access publisher of scholarly articles: it is a pioneering approach to the world of academia, radically improving the way scholarly research is managed. The grand vision of Frontiers is a world where all people have an equal opportunity to seek, share and generate knowledge. Frontiers provides immediate and permanent online open access to all its publications, but this alone is not enough to realize our grand goals.

Frontiers journal series

The Frontiers journal series is a multi-tier and interdisciplinary set of open-access, online journals, promising a paradigm shift from the current review, selection and dissemination processes in academic publishing. All Frontiers journals are driven by researchers for researchers; therefore, they constitute a service to the scholarly community. At the same time, the *Frontiers journal series* operates on a revolutionary invention, the tiered publishing system, initially addressing specific communities of scholars, and gradually climbing up to broader public understanding, thus serving the interests of the lay society, too.

Dedication to quality

Each Frontiers article is a landmark of the highest quality, thanks to genuinely collaborative interactions between authors and review editors, who include some of the world's best academicians. Research must be certified by peers before entering a stream of knowledge that may eventually reach the public - and shape society; therefore, Frontiers only applies the most rigorous and unbiased reviews. Frontiers revolutionizes research publishing by freely delivering the most outstanding research, evaluated with no bias from both the academic and social point of view. By applying the most advanced information technologies, Frontiers is catapulting scholarly publishing into a new generation.

What are Frontiers Research Topics?

Frontiers Research Topics are very popular trademarks of the *Frontiers journals series*: they are collections of at least ten articles, all centered on a particular subject. With their unique mix of varied contributions from Original Research to Review Articles, Frontiers Research Topics unify the most influential researchers, the latest key findings and historical advances in a hot research area.

Find out more on how to host your own Frontiers Research Topic or contribute to one as an author by contacting the Frontiers editorial office: frontiersin.org/about/contact

Optical radiometry and satellite validation

Topic editors

Agnieszka Bialek — National Physical Laboratory, United Kingdom

David Doxaran — UMR7093 Laboratoire d'océanographie de Villefranche (LOV), France

Vittorio Ernesto Brando — Institute of Marine Science, Department of Earth System Sciences and Technologies for the Environment, National Research Council (CNR), Italy

Clemence Goyens — Ghent University, Belgium

Kevin Ruddick — Royal Belgian Institute of Natural Sciences, Belgium

Ana Ines Dogliotti — Universidad de Buenos Aires, Argentina

Citation

Bialek, A., Doxaran, D., Brando, V. E., Goyens, C., Ruddick, K., Dogliotti, A. I., eds. (2025). *Optical radiometry and satellite validation*. Lausanne: Frontiers Media SA. doi: 10.3389/978-2-8325-5653-5

Table of contents

06 Editorial: Optical radiometry and satellite validation
Kevin George Ruddick, Agnieszka Bialek, Vittorio Ernesto Brando, Ana Ines Dogliotti, David Doxaran and Clemence Goyens

11 Spatial structure of *in situ* reflectance in coastal and inland waters: implications for satellite validation
Thomas M. Jordan, Stefan G. H. Simis, Nick Selmes, Giulia Sent, Federico Ienna and Victor Martinez-Vicente

28 Retrieving BRDFs from UAV-based radiometers for fiducial reference measurements: caveats and recommendations
Sebastian Schunke, Vincent Leroy and Yves Govaerts

41 Apparent surface-to-sky radiance ratio of natural waters including polarization and aerosol effects: implications for above-water radiometry
Tristan Harmel

61 Erratum: Apparent surface-to-sky radiance ratio of natural waters including polarization and aerosol effects: implications for above-water radiometry
Frontiers Production Office

62 Verification of uncertainty estimates of autonomous field measurements of marine reflectance using simultaneous observations
Frédéric Mélin, Ilaria Cazzaniga and Pietro Sciuto

80 Superyachts could support satellite ocean colour validation
Robert J. W. Brewin, Xuerong Sun, Dirk A. Aurin, Johannes J. Viljoen, Christopher Walsh and Shubha Sathyendranath

87 Validation of satellite-derived water-leaving reflectance in contrasted French coastal waters based on HYPERNETS field measurements
David Doxaran, Boubaker ElKilani, Alexandre Corizzi and Clémence Goyens

112 Optical water characterization and atmospheric correction assessment of estuarine and coastal waters around the AERONET-OC Bahia Blanca
Maximiliano Arena, Paula Pratolongo, Hubert Loisel, Manh Duy Tran, Daniel Schaffer Ferreira Jorge and Ana Laura Delgado

129 Reconstructing hyper-spectral downwelling irradiance from multi-spectral measurements
Jing Tan, Robert Frouin, Nils Häentjens, Andrew Barnard, Emmanuel Boss, Paul Chamberlain, Matt Mazloff and Cristina Orrico

144 Validation of satellite water products based on HYPERNETS *in situ* data using a Match-up Database (MDB) file structure
Luis González Vilas, Vittorio E. Brando, Javier A. Concha, Clèmence Goyens, Ana I. Dogliotti, David Doxaran, Antoine Dille and Dimitry Van der Zande

167 Using the automated HYPERNETS hyperspectral system for multi-mission satellite ocean colour validation in the Río de la Plata, accounting for different spatial resolutions
Ana I. Dogliotti, Estefanía Piegari, Lucas Rubinstein, Pablo Perna and Kevin G. Ruddick

183 HYPERNETS: a network of automated hyperspectral radiometers to validate water and land surface reflectance (380–1680 nm) from all satellite missions
Kevin G. Ruddick, Agnieszka Bialek, Vittorio E. Brando, Pieter De Vis, Ana I. Dogliotti, David Doxaran, Philippe Goryl, Clémence Goyens, Joel Kuusk, Daniel Spengler, Kevin R. Turpie and Quinten Vanhellemont

191 Complete characterization of ocean color radiometers
Viktor Vabson, Ilmar Ansko, Kim Duong, Riho Vendt, Joel Kuusk, Kevin Ruddick, Agnieszka Bialek, Gavin H. Tilstone, Juan Ignacio Gossn and Ewa Kwiatkowska

206 Utilising LANDHYPERNET data products over a deciduous broadleaf forest to validate Sentinel-2 and Landsat surface reflectance products
Harry Morris, Morven Sinclair, Pieter De Vis and Agnieszka Bialek

219 Generating hyperspectral reference measurements for surface reflectance from the LANDHYPERNET and WATERHYPERNET networks
Pieter De Vis, Clemence Goyens, Samuel Hunt, Quinten Vanhellemont, Kevin Ruddick and Agnieszka Bialek

245 Design and verification of a highly accurate *in-situ* hyperspectral radiometric measurement system (HyperNav)
Andrew Barnard, Emmanuel Boss, Nils Haëntjens, Cristina Orrico, Robert Frouin, Jing Tan, Justin Klumpp, Michael Dewey, David Walter, Matthew Mazloff and Paul Chamberlain

257 Validation of full resolution remote sensing reflectance from Sentinel-3 OLCI across optical gradients in moderately turbid transitional waters
Gaia Gleratti, Victor Martinez-Vicente, Elizabeth C. Atwood, Stefan G. H. Simis and Thomas Jackson

275 HYPSTAR: a hyperspectral pointable system for terrestrial and aquatic radiometry
Joel Kuusk, Alexandre Corizzi, David Doxaran, Kim Duong, Kenneth Flight, Joosep Kivastik, Kaspars Laizans, Edouard Leymarie, Silvar Muru, Christophe Penkerc'h and Kevin Ruddick

294 Selecting HyperNav deployment sites for calibrating and validating PACE ocean color observations
Paul Chamberlain, Robert J. Frouin, Jing Tan, Matthew Mazloff, Andrew Barnard, Emmanuel Boss, Nils Haëntjens and Cristina Orrico

308 A float-based Ocean color vicarious calibration program
Andrew Barnard, Emmanuel Boss, Nils Haëntjens, Cristina Orrico, Paul Chamberlain, Robert Frouin, Matthew Mazloff and Jing Tan

316 WATERHYPERNET: a prototype network of automated *in situ* measurements of hyperspectral water reflectance for satellite validation and water quality monitoring
Kevin G. Ruddick, Vittorio E. Brando, Alexandre Corizzi, Ana I. Dogliotti, David Doxaran, Clémence Goyens, Joel Kuusk, Quinten Vanhellemont, Dieter Vansteenwegen, Agnieszka Bialek, Pieter De Vis, Héloise Lavigne, Matthew Beck, Kenneth Flight, Anabel Gammaru, Luis González Vilas, Kaspars Laizans, Francesca Ortenzio, Pablo Perna, Estefania Piegari, Lucas Rubinstein, Morven Sinclair and Dimitry Van der Zande

343 Feasibility of satellite vicarious calibration using HYPERNETS surface reflectances from Gobabeb and Princess Elisabeth Antarctica sites
Pieter De Vis, Adam Howes, Quinten Vanhellemont, Agnieszka Bialek, Harry Morris, Morven Sinclair and Kevin Ruddick

frontiers | Frontiers in Remote Sensing

TYPE Editorial
PUBLISHED 09 July 2025
DOI 10.3389/frsen.2025.1585494

Check for updates

OPEN ACCESS

EDITED AND REVIEWED BY
Robert J. Frouin,
University of California, San Diego,
United States

*CORRESPONDENCE
Kevin George Ruddick,
kruddick@naturalsciences.be

RECEIVED 28 February 2025
ACCEPTED 25 April 2025
PUBLISHED 09 July 2025

CITATION
Ruddick KG, Bialek A, Brando VE, Dogliotti AI, Doxaran D and Goyens C (2025) Editorial: Optical radiometry and satellite validation. *Front. Remote Sens.* 6:1585494. doi: 10.3389/frsen.2025.1585494

COPYRIGHT
© 2025 Ruddick, Bialek, Brando, Dogliotti, Doxaran and Goyens. This is an open-access article distributed under the terms of the Creative Commons Attribution License (CC BY). The use, distribution or reproduction in other forums is permitted, provided the original author(s) and the copyright owner(s) are credited and that the original publication in this journal is cited, in accordance with accepted academic practice. No use, distribution or reproduction is permitted which does not comply with these terms.

Editorial: Optical radiometry and satellite validation

Kevin George Ruddick[1]*, Agnieszka Bialek[2], Vittorio Ernesto Brando[3], Ana Ines Dogliotti[4], David Doxaran[5] and Clemence Goyens[6]

[1]Royal Belgian Institute of Natural Sciences (RBINS), Brussels, Belgium, [2]National Physical Laboratory (NPL), Teddington, United Kingdom, [3]Consiglio Nazionale delle Ricerche (CNR-ISMAR), Rome, Italy, [4]Instituto de Astronomía y Física del Espacio, Consejo Nacional de Investigaciones Científicas y Técnicas, University of Buenos Aires (IAFE, CONICET/UBA), Buenos Aires, Argentina, [5]Laboratoire Océanographique de Villefranche, Sorbonne Université (SU/LOV/CNRS), Villefranche-sur-Mer, France, [6]Department of Biology, Marine Optics and Remote Sensing (MarSens), Ghent University, Ghent, Belgium

KEYWORDS

optical radiometry, satellite validation, measurement networks, reflectance, hyperspectral

Editorial on the Research Topic
Optical radiometry and satellite validation

Introduction

This Research Topic gathers 21 state of the art papers on the Research Topic of Optical Radiometry and Satellite Validation.

This Editorial and all included papers are focussed on water and land surface reflectance measurements. Validation of other measurands, including end-user products derived from satellite reflectance, e.g. chlorophyll *a* concentration in water or vegetation indices on land, are outside the scope of this Research Topic.

Motivation

Strict quality control is essential to ensure that the satellite data products routinely used for environmental monitoring of water and land surfaces are fit for purpose. A crucial step in this process is the validation of the water and land surface reflectance, from which the final end-user products are derived. The topic of radiometric validation is growing rapidly in importance both because of the advent of operational satellite missions for routine environmental monitoring and because of the rapid expansion in the number of satellite missions, including CubeSat constellations with limited calibration/validation resources. This enhanced need for radiometric validation data covering a wide VIS/NIR/SWIR range (e.g., 380–2,400 nm), preferably with a hyperspectral resolution, must be met by new techniques and hardware, particularly ground-based automated radiometry.

Summary

The following subtopics are covered in papers from this Research Topic and are summarised in the following sections:

- Measurement networks and validation strategy
- Radiometer design, calibration, characterisation and comparison
- Data processing, quality control and measurement uncertainty
- Differences in angular and spatial characteristics of satellite and *in situ* measurements
- Examples of use of *in situ* measurement water and land surface reflectance measurements for satellite calibration and validation

A few other single-paper subtopics are addressed and some "missing" subtopics, not covered by this Research Topic, are highlighted for future work.

Measurement networks and validation strategy

Measurement networks with a common data portal for users have proven to be most effective as a source of data for satellite validation. Until now, the main source of *in situ* measurements for satellite radiometric validation over water and satellite calibration have been the AERONET-OC (Zibordi et al., 2009; Zibordi et al., 2021) and RadCalNet (Bouvet et al., 2019) networks.

The AERONET-OC network is based on deployment of a multispectral instrument system at a federated network of sites, typically on offshore platforms in coastal waters. The instruments have common hardware, calibration, data processing and quality control. This network has grown from a single prototype site in 2002 to 14 active sites (and 31 currently inactive sites) at the time of writing and is the main source of *in situ* measurements for radiometric validation of operational ocean colour missions such as VIIRS and Sentinel-3/OLCI as well as many other satellite missions.

The RadCalNet network federates various instrument systems, typically mounted on masts and deployed at land sites with optimal conditions for vicarious calibration, including low spatial variability. Instrumentation may be multispectral or hyperspectral and processing to surface reflectance may be performed in different ways. Data is unified by traceability to the SI units with corresponding measurement uncertainties. Acceptance of a site in the network is subject to approval of documents describing the measurement method and uncertainty analysis. This network has grown to 5 active sites at the time of writing and is used as one of the calibration methods for optical missions including Sentinel-2.

This Research Topic gathers papers from 2 new emerging networks, HYPERNETS and HYPERNAV.

The HYPERNETS network has been designed similarly to the AERONET-OC federated model and is based on the newly-developed HYPSTAR® radiometer system (Kuusk et al.), and the PANTHYR radiometer system (Vansteenwegen et al., 2019) based on the mature TRIOS/RAMSES instrument. Both systems are hyperspectral with common radiometer calibration and characterisation, data processing, quality control and (future) data distribution portals. An overview of the HYPERNETS network is given by (Ruddick et al.), covering user needs, measurement method, instrumentation and validation site considerations and some first results. HYPERNETS is composed of subnetworks for water (WATERHYPERNET) and land surface reflectance (LANDHYPERNET). The WATERHYPERNET is described in detail by (Ruddick et al.), including demonstrations of validation for Sentinel-2 and Sentinel-3/OLCI and use of data for phytoplankton monitoring.

The strategy of the HYPERNAV network is outlined in (Barnard et al.) for the purposes of satellite system vicarious calibration (SVC). A newly designed radiometric system is integrated with an autonomous profiling float to be deployed from ships at multiple locations. The overview of the data portal and network logistics are complemented by discussion of governance and funding considerations. The selection of HYPERNAV sites is described by (Chamberlain et al.) with an approach estimating the cost per validation matchup, taking account of logistics and the need to reposition floats which have drifted far from the initial location using simulations of deployments.

Brewin et al. proposes to reach out to wealthy citizen scientists with superyachts and an active interest in environmental monitoring. A pilot study is described where the Archimedes superyacht was used to mount radiometers with data processing using the open source HyperInSPACE software (https://github.com/nasa/HyperCP). This approach may help fill gaps in remote ocean areas not routinely covered by research vessels or ships-of-opportunity.

Radiometer design, calibration, characterisation and comparison

Kuusk et al. describe the design of a HYperspectral Pointable System for Terrestrial and Aquatic Radiometry (HYPSTAR®) to provide automated, *in situ* multiangular reflectance measurements of land and water targets. The radiometer covers 380–1,020 nm spectral range at 3 nm spectral resolution for water targets with an extension of the spectral range to 1,680 nm at 10 nm spectral resolution for land targets. The radiometer is mounted on a two-axis pointing system with 360° range of free movement in both axes and incorporates a stable light emitting diode as a light source, used for monitoring the stability of the radiometric calibration during the long-term unattended field deployment. This radiometer has been tested and used in the HYPERNETS network at 10 water and 11 land sites.

Vabson et al. describes laboratory calibrations and characterizations on a set of 37 hyperspectral field radiometers representative of those most used by the ocean colour community. The study covers radiometric responsivity, long-term stability, the accuracy of the spectral scale, non-linearity and accuracy of integration times, spectral stray light, angular response of irradiance sensors in air, dark signal, thermal sensitivity, polarization sensitivity, and signal-to-noise ratio. This work contributes to establishing consistent correction of biases and procedures for uncertainty analysis of *in situ* data obtained from different instruments and measurement models.

Barnard et al. describe the design and field verification results of an *in situ* radiometric system, called HyperNav, integrating dual upwelling radiance heads coupled to individual spectrometers, with spectral resolution of ~2.2 nm (full width, half-maximum) across 320–900 nm, integrated shutter systems for dark measurements, and integrated tilt and

pressure sensors. This radiometric system is mounted on an autonomous float for surface and under water profiling measurements and is used for system vicarious calibration of satellites (Barnard et al.).

Melin et al. compare water remote sensing reflectance and aerosol optical thickness data from a 5.5 years time series of two autonomous pointable photometers deployed together at the Acqua Alta Oceanographic Tower. Uncertainty tree diagrams are used to illustrate all error sources and uncertainty cone diagrams are used to compare uncertainty estimates with matchup comparison statistics across their range of values. The mathematical theory developed here showed that the centred root-mean-square difference between data collected by two systems is a conservative estimate of the uncertainty associated with these data (excluding systematic contributions) if these data show a good agreement and if their uncertainties can be assumed similar with errors moderately correlated.

Data processing, quality control and measurement uncertainty

De Vis et al. describes the processing algorithm and software for the HYPSTAR® *in-situ* hyperspectral data products from both land and water sites of the HYPERNETS network. Radiance and irradiance data are acquired at the measurement sites following standardised measurement protocols, and are calibrated, processed and quality controlled to give reflectance data products for distribution to users, annotated by anomaly and quality flags, where appropriate. In order to achieve fiducial reference measurement quality, uncertainties are propagated through each step of the processing chain, taking into account temporal and spectral error-covariance. Examples of measurements from HYPERNETS sites are provided to illustrate the processing.

Differences in angular and spatial characteristics of satellite and *in situ* measurements

In situ measurements are generally acquired and distributed for the specific acquisition viewing and solar geometry, time instant and spatial field of view, and ideally include an estimate of the uncertainty of the *in situ* measurement. When *in situ* measurements are compared with satellite measurements in a matchup validation context, there will be additional uncertainties associated with the different viewing and solar geometry, time instant and spatial field of view. This is addressed in 3 papers from this Research Topic.

The difference in spatial coverage between an *in situ* radiometer footprint (typically 0.1–5 m) and a satellite instantaneous field of view (typically 1–1,000 m) can generate high validation uncertainties for targets with high spatial variability at intermediate length scales. Dogliotti et al. used spatial averaging of higher spatial resolution satellite data to quantify the spatial variability between a small footprint and larger satellite data pixels and estimate the matchup validation uncertainty associated with spatial variability for a range of satellite pixel sizes, from Planet SuperDoves (3 m) to MODIS (1,000 m). A different reference pixel is defined for each satellite pixel size to minimise the difference caused by spatial variability between *in situ* measurement at a HYPERNETS site and satellite measurement and to avoid mixed water/land near the coast.

Jordan et al. analysed high-frequency shipborne autonomous water remote sensing reflectance data using variograms to partition variability into spatial and intrinsic (non-spatial) components and to quantify the validation uncertainty due to spatial discrepancy between *in situ* and satellite measurements. The spatial decorrelation length scale serves as a guideline for selection of spatially independent *in situ* measurements when matching with a satellite image.

As regards angular variability, Schunke et al. studied the relationship between surface Bidirectional reflectance factor (BRF), an intrinsic optical property of the observed target, and the hemispherical conical reflectance factor (HCRF), which can be measured in the field but is affected by factors such as the angular variability of illumination. Simulations were performed on a 3D vegetation scene to analyse the impact of four parameters (atmospheric scattering, measurement device field of view cropping, acquisition duration, non-Lambertian reference panels) for typical Unmanned Airborne Vehicle measurements. It was found that the dominant source of difference between HCRF and BRF is the atmospheric scattering, which can cause a relative root-mean-square difference of more than 10%. Recommendations are provided for field measurements to minimise uncertainty in BRF estimation from HCRF.

Examples of use of *in situ* water and land surface reflectance measurements for satellite calibration and validation

The use of *in situ* measurements for validation of satellite measurements is demonstrated by case studies over water in the following papers:

- Doxaran et al. compared *in situ* measurements from two HYPERNETS sites in French waters, one in a coastal lagoon and one at the mouth of a highly turbid estuary, with high (Sentinel2-MSI and Landsat8/9-OLI) and medium (Sentinel3-OLCI and Aqua-MODIS) spatial resolution satellite data to assess the performance of 8 different atmospheric correction algorithms. The matchup results highlight the failure and limits of several atmospheric correction algorithms in complex/turbid coastal waters. The importance of accurate sun glint corrections in low to moderately-turbid waters is demonstrated while the use of dark targets and spectral fitting to estimate the aerosol contributions is shown to be the most effective approach in turbid waters.
- Gleratti et al. evaluated the performance of the POLYMER atmospheric correction algorithm for the Ocean and Land Colour Instrument (OLCI) onboard Sentinel-3 (S3) for the retrieval of remote sensing reflectance in the transitional waters near Plymouth. The impact of different satellite-*in situ* time windows, spatial averages and quality control flags on matchup statistics were studied.
- Ruddick et al. used *in situ* measurements from two WATERHYPERNET sites with very different turbidity to analyse the performance of different atmospheric correction algorithms for Sentinel-2 data using statistical metrics

calculated on many matchups. A Validation Diagnostic Sheet was automatically generated for each matchup and was subjectively analysed by experts for the outlier cases, approximately the worst 1/3 of matchups. This analysis concluded with hypotheses on the causes of poor performance. For example, a positive bias (mean difference) was found for ACOLITE_DSF processing of Sentinel-2 in clear waters (Acqua Alta) and clues were provided on how to improve the ACOLITE_DSF processing.

- Dogliotti et al. used *in situ* measurements from a HYPERNETS site in the La Plata estuary to evaluate the quality of satellite water reflectance products from multispectral and hyperspectral satellite missions including Landsat 8&9/OLI, Sentinel-2/MSI and Sentinel-3/OLCI, PlanetScope SuperDoves, Aqua/MODIS, SNPP&JPSS1/VIIRS and PRISMA. If sun glint contamination is avoided, the matchups show generally good results for high spatial resolution satellite sensors when using an atmospheric correction approach designed for land targets (e.g., LANDSAT-8 standard product and SEN2COR) and thus avoiding the errors of many atmospheric corrections approaches designed for clearer waters. An example is also provided where *in situ* measurements are used for validation of 8 satellite sensors on a single day, thus demonstrating the multi-mission economy of scale of automated high frequency measurements such as those provided by HYPERNETS.
- Gonzalez Vilas et al. demonstrated use of a Match-up Database (MDB) file structure and tools to facilitate the validation analysis of satellite water products from different sites, satellites and atmospheric correction processors. An MDB file is a NetCDF file containing all the potential match-ups between satellite and *in situ* data on a specific site and within a given time window. These files are generated and manipulated with three modules to implement the validation protocols: extract satellite data, associate each extract with co-located *in situ* radiometry data, and then perform the validation analysis. The approach is demonstrated by a multi-site matchup comparison between satellite data from the Sentinel-2 MSI and Sentinel-3 OLCI sensors, and HYPSTAR® *in situ* data acquired over six water sites from February 2021 to March 2023. Results showed that the performance of the processors depends on the optical regime of the sites. The open-source MDB-based approach is recommended to implement validation protocols and generate automated matchup analyses for different missions, processors and sites.

The use of *in situ* measurements for calibration and validation of satellite measurements over land is demonstrated by case studies in the following papers:

- De Vis et al. demonstrated the feasibility of using surface reflectance data for vicarious calibration of multispectral (Sentinel-2 and Landsat 8/9) and hyperspectral (PRISMA) satellites over two LANDHYPERNET sites: Gobabeb in Namibia and the Princess Elizabeth Base in Antarctica. *In situ* surface reflectance data are spectrally binned and propagated to the top of atmosphere reflectance and compared to the satellite measurements, quantifying mean differences over multiple matchups. The study confirms that data from radiometrically stable HYPERNETS sites with sufficient spatial and angular homogeneity can be used for satellite vicarious calibration purposes.
- Morris et al. compared *in situ* measurements from a forest LANDHYPERNET site with multispectral satellite data from Sentinel-2, Landsat 8 and Landsat 9. No systematic bias was found between the *in situ* and the satellite data, although relative differences varied widely with differences as large as 100% for spectral bands with low reflectance. Hypotheses for the differences included spatial and temporal mismatch between the *in situ* and satellite measurement, or shadowing caused by the flux tower. Recommendations included the incorporation of a Bidirectional Reflectance Distribution Function model into the processing chain for the forest canopy.

Other studies

In addition to the subtopics covered in the preceding sections, this subtopics includes individual papers on specific subtopics with relevance to Optical Radiometry and Satellite validation as follows:

Harmel considered the important issue of modelling the light reflected by the air-water interface for the above water reflectance measurement method, using a newly proposed terminology of surface-to-sky radiance ratio, Rss. Vector radiative transfer computations were performed over the spectral range 350–1,000 nm to provide angular values of Rss for a comprehensive set of aerosol loads and types and water surface roughness expressed in wave slope variances or in equivalent Cox-Munk wind speeds. After separating direct and diffuse light components, it was shown that the spectral shape and amplitude of Rss are very sensitive to aerosol load and type. It was concluded that the viewing geometry should be adapted as function of sun zenith angle and that aerosol measurements should be made concurrently with above water radiometric measurements.

Arena et al. used *in situ* remote sensing reflectance derived from an AERONET-OC site and *in situ* hyperspectral radiometric data to classify optical water types (OWTs) in the turbid waters of the Bahía Blanca Estuary. The OWTs were linked to the concentrations of chlorophyll-*a* and suspended particulate matter and to the absorption coefficients of phytoplankton, non-algal particles, and dissolved organic matter measured on water samples. After a matchup validation analysis to select the best-performing atmospheric correction algorithm for Sentinel-3 OLCI satellite data, the latter was used to describe spatial and temporal variability of the different OWTs in the region.

Tan et al. described a method for constructing hyperspectral downwelling irradiance at 0.5 nm resolution from 315 to 900 nm from multispectral measurements at 4 spectral bands (412, 489, 555, and 705 nm) using a multi-linear regression model. Radiative transfer simulations are made for Sun zenith angles from 0 to 75° and a wide range of atmospheric, surface, and water conditions. The regression model allows estimation of hyperspectral downwelling irradiance with a bias of less than 0.4% in magnitude and an RMS error (RMSE) ranging from 0% to 2.5%, depending on wavelength, for noise-free input data. The impact of noisy input data and of adding extra spectral bands in the ultraviolet, e.g., centred on 325, 340, and 380 nm, is

analysed. The results indicate that it is sufficient for many scientific applications, including measurement of hyperspectral reflectance by the HyperNav system (Barnard et al.), to measure downwelling irradiance in a few coarse spectral bands in the ultraviolet to near infrared and reconstruct the hyperspectral signal using the proposed multivariate linear modelling.

Conclusion and perspectives

Spaceborne optical satellites are used routinely for environmental monitoring of water and land surfaces, and spaceborne data is often used to aid management of environmental challenges, such as coastal water quality and the impacts of climate change. The spaceborne data must therefore be of sufficient quality for these purposes and "matchup" validation with simultaneous ground-based measurements is used to determine whether the spaceborne data is sufficiently accurate and to identify any weaknesses that need to be remedied. While fitness for purpose depends on the purpose and the end-user measurand, e.g., aquatic chlorophyll a concentation or a land vegetation index, validation of water and land surface reflectance conveniently indicates overall data quality and poor results for such radiometric validation indicate where data quality needs to be improved, often in the atmospheric correction step of data processing. The works in this Research Topic thus contribute to the understanding and improvement of the quality of spaceborne data used for managing environmental challenges.

While this Research Topic gathers papers describing various aspects of the state-of-the-art of Optical Radiometry and Satellite Validation, it is clear both that some important subtopics have not been covered here and that this field will evolve further in the coming years. The following developments are expected in the future:

- The estimation of measurement uncertainty remains very challenging for these measurements and will undoubtedly improve in the next few years.
- Although within the stated scope for the Research Topic and badly needed for satellite validation, only a few papers address the measurement of land surface reflectance, which is less mature than the measurement of water-leaving radiance reflectance. The lack of such measurements is a clear gap in knowledge.
- The issues of spatial and angular variability of land surface reflectance and how these can be represented when comparing *in situ* and satellite measurements clearly need more attention. This issue has been raised often in recent workshops relating to radiometry and satellite validation and clearly represents a gap in research, only partly addressed here (see above).
- Most of the papers in this Research Topic focus on measurement of only water and land surface reflectance. As automated reflectance data becomes more easily available, it is likely that measurements from additional instruments such as imaging cameras, sun photometers, polarimeters and profiling lidar or other optical measurements of atmospheric properties will be used in synergy with the reflectance measurements to enhance the validation of optical satellites and help identify the cause of atmospheric correction and satellite calibration errors. The potential for synergy with atmospheric data is strong and can be explored with existing data, e.g., from co-located AERONET and HYPERNETS sites.

Author contributions

KR: Writing – original draft, Writing – review and editing. AB: Writing – review and editing. VB: Writing – review and editing. AD: Writing – review and editing. DD: Writing – review and editing. CG: Writing – review and editing.

Funding

The author(s) declare that no financial support was received for the research and/or publication of this article.

Conflict of interest

The authors declare that the research was conducted in the absence of any commercial or financial relationships that could be construed as a potential conflict of interest.

The author(s) declared that they were an editorial board member of Frontiers, at the time of submission. This had no impact on the peer review process and the final decision.

Generative AI statement

The author(s) declare that no Generative AI was used in the creation of this manuscript.

Publisher's note

All claims expressed in this article are solely those of the authors and do not necessarily represent those of their affiliated organizations, or those of the publisher, the editors and the reviewers. Any product that may be evaluated in this article, or claim that may be made by its manufacturer, is not guaranteed or endorsed by the publisher.

References

Bouvet, M., Thome, K., Berthelot, B., Bialek, A., Czapla-Myers, J., Fox, N. P., et al. (2019). RadCalNet: a radiometric calibration network for Earth observing imagers operating in the Visible to Shortwave infrared spectral range. *Remote Sens.* 11 (20), 2401. doi:10.3390/rs11202401

Vansteenwegen, D., Ruddick, K., Cattrijsse, A., Vanhellemont, Q., and Beck, M. (2019). The Pan-and-tilt hyperspectral radiometer system (PANTHYR) for autonomous satellite validation measurements-prototype design and testing. *Remote Sens.* 11 (June), 1360. doi:10.3390/rs11111360

Zibordi, G., Holben, B., Slutsker, I., Giles, D., D'Alimonte, D., Mélin, F., et al. (2009). AERONET-OC: a network for the validation of ocean color Primary product. *J. Atmos. Ocean. Technol.* 26, 1634–1651.

Zibordi, G., Holben, B. N., Talone, M., D'Alimonte, D., Slutsker, I., Giles, D. M., et al. (2021). Advances in the Ocean color component of the aerosol Robotic network (AERONET-OC). *J. Atmos. Ocean. Technol.* 38 (4), 725–746. doi:10.1175/2009JTECHO654.1

frontiers | Frontiers in Remote Sensing

TYPE Original Research
PUBLISHED 09 November 2023
DOI 10.3389/frsen.2023.1249521

Check for updates

OPEN ACCESS

EDITED BY
Kevin Ruddick,
Royal Belgian Institute of Natural Sciences, Belgium

REVIEWED BY
Juan Ignacio Gossn,
European Organisation for the Exploitation of Meteorological Satellites, Germany
Tim J. Malthus,
Oceans and Atmosphere (CSIRO), Australia
Susanne Elizabeth Craig,
National Aeronautics and Space Administration, United States

*CORRESPONDENCE
Thomas M. Jordan,
tjor@pml.ac.uk

RECEIVED 28 June 2023
ACCEPTED 20 October 2023
PUBLISHED 09 November 2023

CITATION
Jordan TM, Simis SGH, Selmes N, Sent G, Ienna F and Martinez-Vicente V (2023), Spatial structure of *in situ* reflectance in coastal and inland waters: implications for satellite validation.
Front. Remote Sens. 4:1249521.
doi: 10.3389/frsen.2023.1249521

COPYRIGHT
© 2023 Jordan, Simis, Selmes, Sent, Ienna and Martinez-Vicente. This is an open-access article distributed under the terms of the Creative Commons Attribution License (CC BY). The use, distribution or reproduction in other forums is permitted, provided the original author(s) and the copyright owner(s) are credited and that the original publication in this journal is cited, in accordance with accepted academic practice. No use, distribution or reproduction is permitted which does not comply with these terms.

Spatial structure of *in situ* reflectance in coastal and inland waters: implications for satellite validation

Thomas M. Jordan[1]*, Stefan G. H. Simis[1], Nick Selmes[1], Giulia Sent[2], Federico Ienna[2] and Victor Martinez-Vicente[1]

[1]Plymouth Marine Laboratory, Plymouth, United Kingdom, [2]Marine and Environmental Science Centre, Faculdade de Ciências da Universidade de Lisboa, Lisboa, Portugal

Validation of satellite-derived aquatic reflectance involves relating meter-scale *in situ* observations to satellite pixels with typical spatial resolution ~ 10–100 m within a temporal "match-up window" of an overpass. Due to sub-pixel variation these discrepancies in measurement scale are a source of uncertainty in the validation result. Additionally, validation protocols and statistics do not normally account for spatial autocorrelation when pairing *in situ* data from moving platforms with satellite pixels. Here, using high-frequency autonomous mobile radiometers deployed on ships, we characterize the spatial structure of *in situ* R_{rs} in inland and coastal waters (Lake Balaton, Western English Channel, Tagus Estuary). Using variogram analysis, we partition R_{rs} variability into spatial and intrinsic (non-spatial) components. We then demonstrate the capacity of mobile radiometers to spatially sample *in situ* R_{rs} within a temporal window broadly representative of satellite validation and provide spatial statistics to aid satellite validation practice. At a length scale typical of a medium resolution sensor (300 m) between 5% and 35% (median values across spectral bands and deployments) of the variation in *in situ* R_{rs} was due to spatial separation. This result illustrates the extent to which mobile radiometers can reduce validation uncertainty due to spatial discrepancy via sub-pixel sampling. The length scale at which *in situ* R_{rs} became spatially decorrelated ranged from ~ 100–1,000 m. This information serves as a guideline for selection of spatially independent *in situ* R_{rs} when matching with a satellite image, emphasizing the need for either downsampling or using modified statistics when selecting data to validate high resolution sensors (sub 100 m pixel size).

KEYWORDS

satellite validation, optical radiometry, above-water reflectance, autonomous monitoring, variogram, spatial structure, water quality

1 Introduction

Satellite observations of aquatic reflectance are used to derive water quality parameters such as photosynthetic pigment concentration, light availability, and infer the transport of suspended solids. These are used to delineate aquatic habitats and to investigate biogeochemical processes in aquatic ecosystems. Satellite radiance recorded at the top of the atmosphere requires correction for atmospheric scattering and absorption to provide consistent observation of water colour. Accurate derivation of the

water-leaving radiance is challenging as the aquatic signal component is often < 10% of the top-of-atmospheric radiance budget (Wang et al., 2009). To calibrate and validate the atmospheric correction, networks of stations measuring above-water *in situ* remote-sensing reflectance (R_{rs}) have been increasingly used to complement observations in the water column which are relatively demanding on ship time and maintenance. Validation of satellite-derived reflectance accuracy is achieved by quantifying the statistical differences with coincident *in situ* observations, where the latter are assumed to represent truth values within specified uncertainty bounds (Loew et al., 2017).

The atmospheric correction of satellite radiometry is particularly challenging in coastal and inland waters, due to their optical complexity relative to ocean waters where optical properties are closely coupled to the phytoplankton component. Inland and coastal waters also have pronounced diversity in their particulate constituents, and therefore the shape of reflectance spectra (Spyrakos et al., 2018; Lehmann et al., 2023). A wide turbidity range, particularly at rivers and in relatively shallow areas with soft substrate, can cause near-infrared (NIR) reflectance to depart significantly from zero, making the atmospheric correction harder to constrain than in the open ocean (Siegel et al., 2000). Near land, the top-of atmosphere radiance is further perturbed by light reflected from neighbouring land pixels and scattered into the field of view of the sensor, also known as the adjacency effect (Otterman and Fraser, 1979; Bulgarelli et al., 2014). Additionally, near the coast, there are complex aerosol mixtures that make selection of an appropriate aerosol model very challenging (e.g., Montes et al., 2022). Current satellite radiometer systems used for inland and coastal waters include those designed for ocean colour observation with a spatial resolution up to 300 m and daily revisit time, as well as land imagers with fewer and broader spectral bands but higher spatial resolution (up to 10 m) and longer revisit times up to 5 days at the equator. There are several atmospheric correction processors developed for these systems that are undergoing validation with *in situ* R_{rs} (e.g., Barnes et al., 2019; Warren et al., 2019; Pahlevan et al., 2021). Due to dependencies between water type and satellite R_{rs} accuracy (Pahlevan et al., 2021), it is desirable to perform satellite validation across a range of sites representing optical variability in water and atmospheric composition.

In addition to the atmospheric correction, the differing spatial scales of satellite and *in situ* reflectance are sources of uncertainty within a validation analysis (Salama and Su, 2011; Lee et al., 2012; Salama et al., 2022). Historically, pixel sizes for satellite aquatic remote sensing sensors were ~ 100–1,000 m^2 (Groom et al., 2019), which is far greater than the meter-scale footprint of *in situ* R_{rs}. For example, ESA Sentinel-3 OLCI (Ocean Land Color Instrument) has a pixel size 300 m. More recently, higher resolution sensors such as ESA Sentinel-2 Multi Spectral Imager (MSI), which has pixel size 10–60 m, have been used for remote sensing of coastal and inland waters (Warren et al., 2019). Mobile (typically shipborne) and fixed radiometric platforms are both used to collect *in situ* R_{rs}, and the different sampling strategies impact on how spatial discrepancy with the satellite pixel can be accounted for. Validation from fixed platforms, for example, the Aeronet-OC network (Zibordi et al., 2009; 2022), is reliant on selecting spatially homogeneous sites and applying filters for spatial homogeneity (Concha et al., 2021). Mobile radiometers deployed for along-track sampling on research vessels and ships-of-opportunity have the benefit that sub-pixel averaging can quantify sub-pixel variability in the presence of horizontal heterogeneity (Brewin et al., 2016), depending on vessel speed and instrument frequency. Deploying mobile radiometers on ships-of-opportunity is a particularly attractive solution to obtaining extensive spatial sampling of inland and coastal water bodies at a low operational cost.

In addition to repeat spatial sampling within an individual pixel, mobile radiometers are also more likely to sample data within multiple satellite pixels within a match-up time window. In principle, this capacity allows for many different match-up pairs to be identified from a single satellite scene. However, validation metrics are typically based on an assumption of statistically independent observation pairs (Loew et al., 2017). Consequently, it is desirable to test for spatial autocorrelation - the statistical dependence of *in situ* R_{rs} within neighbouring pixels - prior to performing the match-up analysis. Spatial autocorrelation (in the context of match-up analysis) has received surprisingly little attention within the ocean colour research community, in part due to the relative scarcity of R_{rs} transects. Research into the scale-dependence of variability and spatial autocorrelation through variography is, however, relatively common in other areas of satellite validation; for example, forest (Román et al., 2009) and glacier (Ryan et al., 2017) albedo. Variography has also successfully been applied to optical water properties in different scientific contexts; for example, spatially resolving sediment plumes (Aurin et al., 2013) and investigation of the spatial structure of planktonic marine ecosystems at the mesoscale (~10–100 km) (Glover et al., 2018).

In this study we quantify the spatial structure of *in situ* R_{rs} from mobile radiometric deployments in coastal and inland waters (Lake Balaton, Western English Channel, Tagus Estuary) over repeat transects which range from ~ 1 km - ~ 35 km in length. The overall goal is to provide insight on how spatial structure of *in situ* R_{rs} impacts on satellite validation and provide recommendations on how data from mobile radiometers can best be used in the future. We do not perform an explicit match-up analysis with satellite data, but instead apply variogram analysis to *in situ* data selected within a time interval broadly representative of a match-up window. We partition variation of *in situ* R_{rs} into spatial and intrinsic (non-spatial) components, and provide statistics across different spectral bands and deployments. We assess the variation in *in situ* R_{rs} at a length scale representative of a medium-resolution satellite sensor such as OLCI (300 m), which enables us to assess how the mobile radiometer is able to reduce *in situ* R_{rs} variability via sub-pixel sampling. We then assess the autocorrelation length of *in situ* R_{rs}; a quantity which serves as a criterion for selecting independent pixel match-ups for validation from a single scene. This study informs the process of working towards fully automated satellite validation services, specifically highlighting the role of spatial statistics when using data from mobile autonomous radiometric systems.

2 Satellite validation of remote-sensing reflectance

To motivate the study, we first present a brief review of R_{rs} satellite validation practice, focusing on spatial and temporal collocation. Satellite validation is defined as the process of evaluating, by independent means, the accuracy of satellite-derived data products and quantifying their uncertainties by comparison with *in situ* reference data (Justice et al., 2000; Loew et al., 2017). In aquatic remote sensing *in situ* measurements of R_{rs} (defined as the ratio of water-leaving radiance to downwelling planar irradiance just above the water surface), or the related variable of normalized-water leaving radiance, provide reference data for validation of satellite products (Bailey and Werdell, 2006; Zibordi et al., 2009; Qin et al., 2017; Warren et al., 2019; Pahlevan et al., 2021). R_{rs} from satellite sensors is normally multi-spectral, consisting of measurements in discrete spectral bands. R_{rs} from *in situ* sensors is typically hyperspectral and convolved with the spectral response function of the satellite sensor when performing validation. For convenience, we generally do not explicitly notate the wavelength-dependence of R_{rs} and other radiometric quantities.

2.1 Match-up criteria and validation metrics

The ocean colour community has applied a range of criteria to match-up analysis which differ primarily in quality control thresholds and spatiotemporal collocation criteria (Bailey and Werdell, 2006; Zibordi et al., 2009; Concha et al., 2021). Prior to matching with *in situ* data, satellite R_{rs} are often locally averaged (e.g., using a moving 3 × 3 average of neighbouring pixels). This spatial window, the 'satellite extract', is also used to test for spatial homogeneity in R_{rs} via the local coefficient of variation and to filter out noisy or heterogeneous regions (Bailey and Werdell, 2006). The time window is kept sufficiently short to limit spatiotemporal discrepancies between the *in situ* and remote sample population, or long to produce sufficient data to allow statistical analysis. The length of the temporal window about a satellite overpass that is used to select *in situ* R_{rs} has varied from ±0.5 h (Ilori et al., 2019) (highly dynamic environments) to ±1 day or greater (Kutser, 2012; Warren et al., 2019) (inland waters). Match-up windows for coastal environments typically range from ±1 h to ±3 h (refer to Table 3 in Concha et al. (2021)). Recent IOCCG recommendations for dynamic regions are ±1 h (IOCCG, 2019). If there are repeated *in situ* R_{rs} measurements within a pixel within the match-up window, these are typically averaged before being defined as a match-up pair. In addition, a sequence of quality control filters are applied to both *in situ* R_{rs} (e.g., restrictions on viewing angles, wind speed, and levels of sunglint), and the satellite-derived reflectance (e.g., restrictions on the pixel classification).

Following data selection and filtering, a range of statistical metrics are then used to assess the uncertainties of the system of remote sensor and atmospheric correction against *in situ* R_{rs} (Bailey and Werdell, 2006; Zibordi et al., 2009; Concha et al., 2021). Common validation metrics are, for each sensor waveband, the root-mean-square error (RMSE), mean bias (δ), percentage bias (ψ), defined by:

$$RMSE = \sqrt{\frac{1}{N}\sum_{i=1}^{N}(x_i - y_i)^2}, \tag{1}$$

$$\delta = \frac{1}{N}\sum_{i=1}^{N}(y_i - x_i), \tag{2}$$

$$\psi = \frac{100}{N}\sum_{i=1}^{N}\frac{(y_i - x_i)}{x_i}, \tag{3}$$

where y_i notates the remote observation (a pixel or local average of pixels), x_i notates an *in situ* match-up (one or many observations averaged over a pixel), and N the number of match-up pairs. The bias metrics can also be defined for absolute differences and/or median averages. Regression methods including ordinary least-squares, Type 2 (Qin et al., 2017) and Deming regression (Warren et al., 2019)) are also used in match-up statistics, in each case, generating correlation, slope and intercept parameters.

In applying validation metrics, Eqs 1–3, underlying statistical assumptions (e.g., requirements on stationary, Gaussianity, linearity, independence of residuals) should be considered (Loew et al., 2017). The assumption of independence of residuals (which applies to all of the metrics above) is particularly relevant to this study, which considers spatial autocorrelation of R_{rs}. Specifically, the presence of spatial autocorrelation leads to correlation in the residuals, which results in negative/positive residuals tending to occur together. In turn, this leads to an overestimation of the number of independent match-up pairs (i.e., the value of N), therefore impacting on the validity of the statistics.

2.2 Decomposition of sources of uncertainty

To isolate either spatial or temporal sources of uncertainty, previous studies (Salama and Stein, 2009; Salama et al., 2022) have used the following error decomposition

$$\Delta_{tot} \approx \sqrt{\Delta_d^2 + \Delta_s^2 + \Delta_t^2}, \tag{4}$$

where Δ_{tot} is the total retrieval uncertainty, Δ_d is the 'derivation uncertainty', Δ_s is the spatial discrepancy uncertainty, and Δ_t is the temporal discrepancy uncertainty. Δ_{tot} could be expressed, for example, by δ or ψ in Eqs 2 and 3. Δ_d represents all non spatiotemporal sources of uncertainty, including sensor calibration, algorithmic uncertainty in atmospheric correction, and normalisation of observation geometry. Δ_s represents uncertainty due to differences in spatial representation; i.e., uncertainty associated with relating meter-scale *in situ* measurements with a satellite pixel. Δ_t represents uncertainty due to differences in the temporal representation; i.e., uncertainty associated with the time difference between the satellite overpass and the *in situ* measurement. Eq. 4 is approximate, in the sense that the three sources of uncertainty are modelled as independent.

Most R_{rs} validation studies do not consider Δ_s and Δ_t explicitly, and instead aim to minimize their impact via selecting spatially homongenous sample sites and sufficiently short time windows about the satellite overpass (Concha et al., 2021). This is generally done so that the validation accuracy metrics can be used to compare different atmospheric correction schemes (i.e., the assumed dominant sub-component of Δ_d). In this study, we instead focus on spatial statistics which relate to the Δ_s term in Eq. 4. Specifically, via characterization of

the scale-dependence of R_{rs} variability, we consider how mobile radiometers can reduce Δ_s via sub-pixel sampling. Additionally, via characterization of the autocorrelation length, we provide pixel separation distances for selection of spatially independent *in situ* R_{rs}.

3 Data

3.1 Radiometric measurement system

In situ R_{rs} were obtained using the autonomous Solar-tracking Radiometry platform (So-Rad), developed at Plymouth Marine Laboratory (Wright and Simis, 2021; Jordan et al., 2022), and based on the earlier system described by Simis and Olsson (2013). So-Rad obtains R_{rs} via three synchronised individual spectroradiometer measurements of downwelling irradiance (E_d), sky radiance (L_s) and total upwelling radiance (L_t). A key feature of So-Rad is that the L_s and L_t sensors are mounted to an azimuthally rotating motor which enables optimization of the azimuthal viewing angles with respect to solar azimuth and ship heading. The L_s sensor is at viewing zenith of 40°, with the L_t sensor in the corresponding specular direction. To ensure an unobstructed field of view, the E_d sensor is ideally mounted in an elevated position with unobstructed view of the sky.

The E_d, L_t, and L_s instruments used in So-Rad were TriOS RAMSES ARC (radiance) and ACC (irradiance), calibrated annually at Tartu Observatory (Estonia). The calibrated spectral range of all sensors was 320–950 nm, the spectral resolution was ~ 10 nm, and the spectral sample spacing was 3.3 nm. The temporal sample spacing between sets of E_d, L_t, and L_s measurements was nominally 15 s. So-Rad was automatically set to record data for solar zenith angles $< 60°$. The field of view of the TriOS RAMSES ARC sensors is 7°. For a typical platform height of ~ 5 m this translates to measuring a spot size of ~ 1 m in diameter and we therefore refer to *in situ* observations as being "meter-scale".

3.2 Reflectance processing

The retrieval of *in situ* R_{rs} used the 3C (3 glint component) algorithm (Groetsch et al., 2017), following the parameterization in Jordan et al. (2022). 3C reconstructs R_{rs} by inputting a set of E_d, L_t, and L_s spectra into a spectral optimization procedure that incorporates models for solar irradiance (Gregg and Carder, 1990) and the inherent optical properties of water (Albert and Mobley, 2003). The 3C R_{rs} equation is of the form

$$R_{rs}(\lambda) = \frac{L_t(\lambda)}{E_d(\lambda)} - \rho_s \frac{L_s(\lambda)}{E_d(\lambda)} - \Delta(\lambda), \quad (5)$$

where the air-water reflectance factor (ρ_s) and spectral offset ($\Delta(\lambda)$) are both solved for within the spectral optimization. 3C is particularly useful in automated, stand-alone deployments, as it bounds how physically realistic a solution is via an optimization residual parameter (Pitarch et al., 2020). It is also effective in non-ideal conditions; e.g., glint affected data or higher wind speeds (Groetsch et al., 2020).

The quality control for R_{rs} follows the previous steps for the 3C algorithm (Groetsch et al., 2017) as described in Jordan et al. (2022) and provided through the *monda* (MONocle Data Analysis) Python package (Simis et al., 2022). The key steps are as follows. First, a set of radiometric filters were applied to measured $E_d(\lambda)$, $L_s(\lambda)$, and $L_t(\lambda)$; for example, setting a minimum value on the spectral maximum of $E_d(\lambda)$ (500 mW m^{-2}nm^{-1}). Second, we removed glint affected spectra when $L_t(\lambda)/E_d(\lambda)$ exceeded an empirical threshold of 0.025 sr^{-1} on the interval 850–900 nm. Third, filtering was applied based on the convergence and residuals of the 3C algorithm optimization.

3.3 Field deployments

The study consists of deployments at three different water bodies. In each case, a So-Rad system was mounted onboard a ship-of-opportunity undergoing operational tasks:

1. Lake Balaton (Hungary) between 28 May and 5 July 2019 onboard the car ferry connecting Tihany and Szántód. The coverage consists of an approximately 1 km transect between the North and South shores of the lake, with the round trip taking approximately 40 min and with minor variation in the exact route over the course of the day.
2. The Western (English) Channel, United Kingdom, between 25 April and 13 October 2021 onboard the Plymouth Marine Laboratory research vessel *Quest*. The coverage typically consists of weekly transects from the harbour in Plymouth to the L4 buoy and once per month extending to the E1 buoy, approximately 16 km and 37 km from the shore respectively. Radiometric data from *Quest*, with similar spatial sampling to this study, is presented by Martinez-Vicente et al. (2013).
3. The Tagus Estuary in Lisbon (Portugal) between 29 June and 27 November 2021 onboard the *Lisboat* sight-seeing ferry. The coverage consists of counter-clockwise circuits of the estuary inlet channel that are approximately 20 km in total transect length.

Example reflectance spectra and coverage maps from each deployment are shown in Figure 1. All three deployments have reflectance peaks between 550 and 600 nm which is typical of inland and nearshore marine water. Lake Balaton (Figures 1A,B) has the highest absolute reflectance values, whilst the Western Channel (Figures 1C,D) has the lowest. The Western Channel dataset spans a larger geographical area and has larger distance between observations due to ship speed. It has the greatest apparent variation in spectral shape and amplitude, and the spectral shape is less constrained towards shorter wavelengths compared to the other sites. All transects correspond to data collected from a 4 h time window (Tagus Estuary) or 6 h time window (Lake Balaton and the Western Channel) centred at 12 noon (approximate solar maximum) in the local time zone as used in the variograms.

3.4 Data gridding and selection from time window

Prior to the variogram analsyis (Section 4), the hyperspectral *in situ* R_{rs} spectra were downsampled to discrete spectral bands centred on 443, 560, 665, and 783 nm using a Gaussian weighting based on the full width at half maximum of the MSI spectral response function. The band

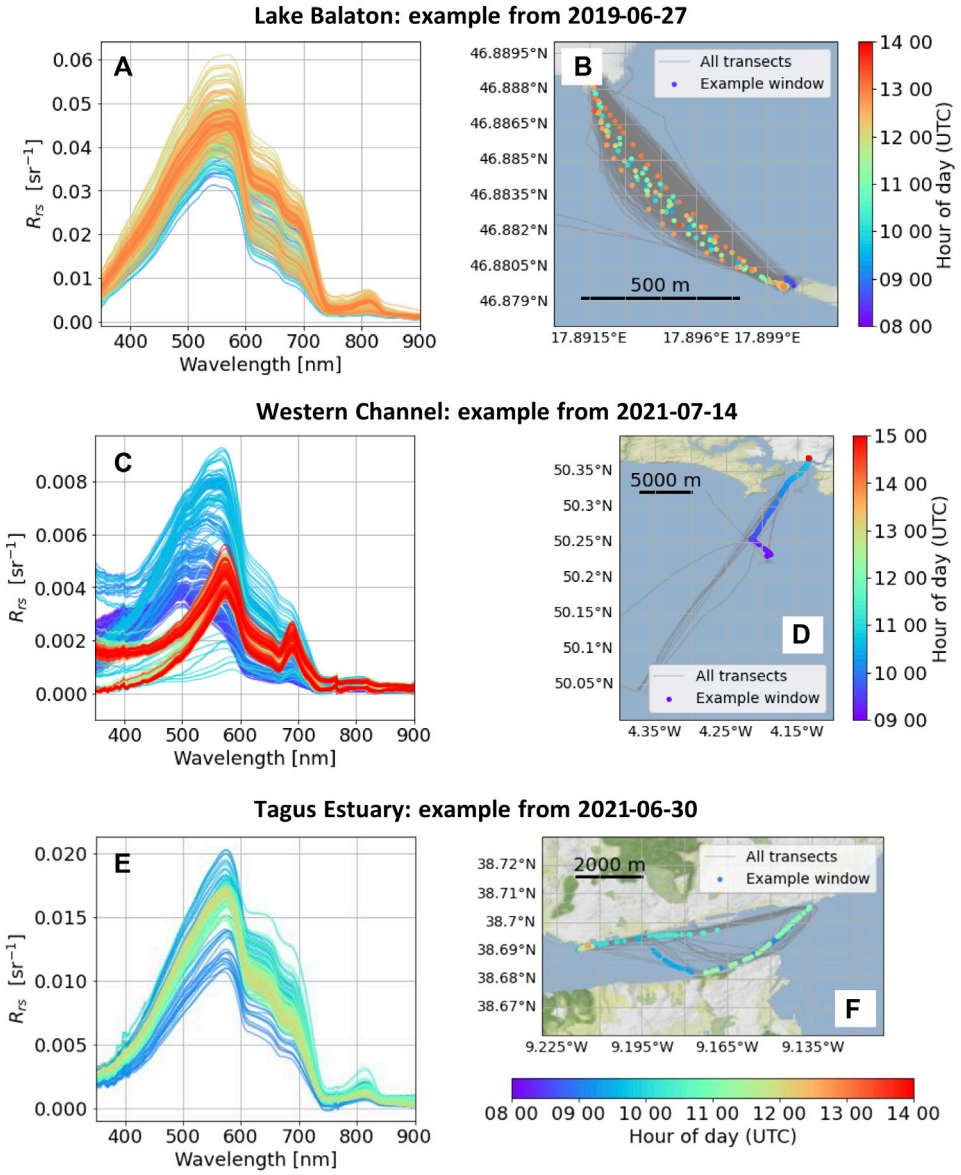


FIGURE 1
Example reflectance (R_{rs}) spectra and ship transects from each deployment. Top row **(A, B)** Lake Balaton. Centre row **(C, D)** Western Channel. Bottom row **(E, F)** Tagus Estuary. The R_{rs} spectra correspond to a time window of data as used in the variogram analysis (6 h for Lake Balaton and the Western Channel and 4 h for the Tagus Estuary) centred around noon in the local time zone. The R_{rs} spectra are referenced to the points and colour bar in the coverage maps.

centres correspond to the chlorophyll-*a* absorption maximum (443 nm), the chlorophyll-*a* reference/absorption minimum (560 nm), the second chlorophyll-*a* absorption maximum/suspended sediment band (665 nm) and an NIR band used for atmospheric correction (783 nm). OLCI has similar band centres at 443 nm, 560 nm, 665 nm. R_{rs} within each spectral band was then resampled to a regular 20 m grid, taking the mean R_{rs} when there were multiple measurements within each grid cell. The gridding represents a practical lower bound on the length scale for comparisons to be made between *in situ* and satellite R_{rs}, and follows how *in situ* R_{rs} has been gridded for MSI validation (Warren et al., 2019). The gridding also regularizes the sampling for the variograms as longer time series when the ship is stationary are averaged to a single measurement.

Our variogram analysis considers the spatial dependence of R_{rs} variability, but neglects (explicit) temporal variation. For each variogram computation, *in situ* R_{rs} were selected on a daily basis from a time window centred about 12 noon in the local time zone, allowing ±3 h from noon for the Lake Balaton and Western Channel deployments, and ±2 h for the more dynamic Tagus Estuary. The time window lengths are a trade-off so that data can be adequately sampled to generate the variograms, whilst being sufficiently short to be (broadly) comparable to a satellite match-up window (Section 2.1). The variograms are computed from multiple pairwise *in situ* measurements, so the associated timescale differs from the single

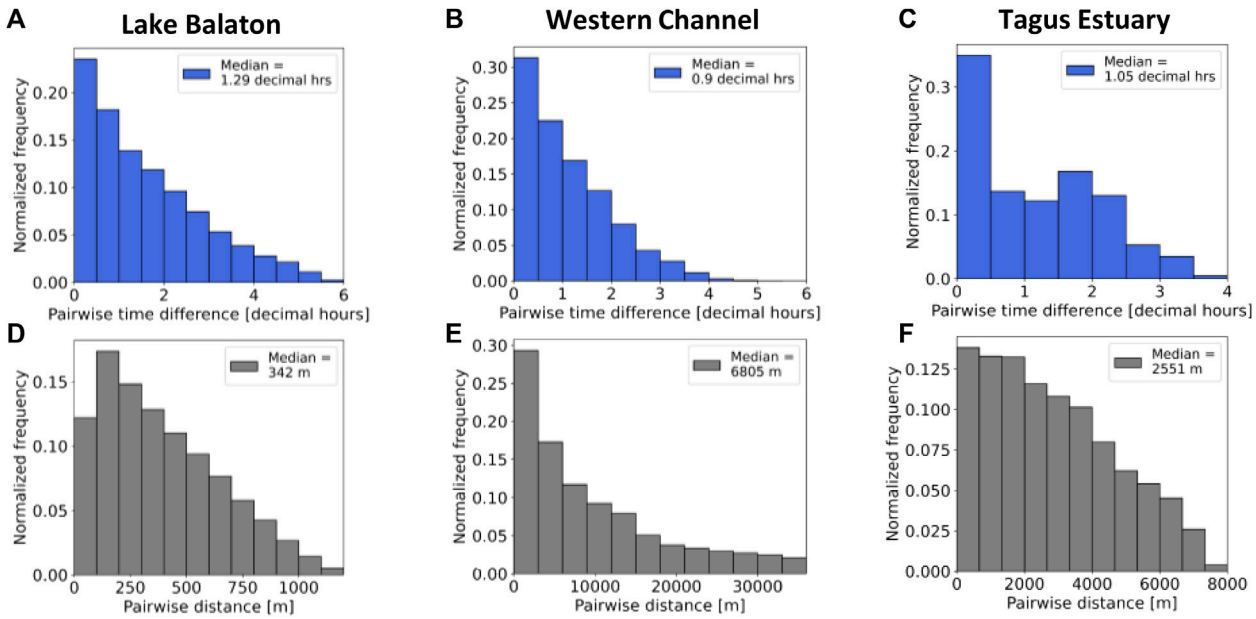


FIGURE 2
Top row **(A–C)**: Normalized frequency distributions of pairwise time separation for each deployment. Bottom row **(D–F)**: Normalized frequency distributions of pairwise point-separation distance for each deployment.

match-up pairs that are used in satellite validation. The distribution of pairwise time separation therefore gives an alternative quantification of the time difference between R_{rs} measurements within the variogram (Figures 2A–C). The distributions have a strong positive skew and median time separations of 1.29 decimal hours (Lake Balaton), 0.90 decimal hours (Western Channel), 1.05 decimal hours (Tagus Estuary). The Western Channel has the lowest pairwise time separation, as the transects are typically collected over a fraction of the allowed time window (e.g., Figure 1D).

Additionally, the distribution of pairwise point separations, which are an input to the variogram analysis, are shown for each deployment in Figures 2D–F. The maximum point separations are ~ 1,200 m for Lake Balaton, ~ 35,000 m for the Western Channel, and ~ 8,000 m for the Tagus Estuary.

4 Materials and methods

4.1 Overview of variogram analysis

The variogram is a commonly used graphical method to characterize variation in a geographic quantity as a function of the separation distance between measurements, and is described in geostatistics textbooks (e.g., Cressie, 1993) aswell as ocean colour studies (e.g., Glover et al., 2018). The variogram enables partitioning of variance into a structural component that is associated with spatial separation and an intrinsic component not associated with spatial separation. The variogram also enables characterization of the autocorrelation length, which is the characteristic length scale at which a quantity ceases to be spatially correlated with neighbouring observations.

Variogram analysis expresses the semivariance (γ) as a function of separation distance (h), which is also referred to as the lag or ground-sample distance (GSD). For *in situ* R_{rs}, computation of the semivariance uses an equation of the form

$$\gamma(h) = \frac{1}{2N(h)} \sum_{i=1}^{N(h)} [R_{rs}(x_i) - R_{rs}(x_i + h)]^2, \quad (6)$$

where $R_{rs}(x_i)$ is an *in situ* reflectance observation at geographic location x_i and, $N(h)$ is the total number of measurement pairs at distance h (Glover et al., 2018). $\gamma(h)$ is computed separately for each spectral band. The summation in Eq. 6 applies across the set of all pairwise point separations, and pivots about each data point in turn, sampling from a circular annulus with thickness δh (the lag bin width). The radial sampling method can be applied to both distributed data (as occurs for the variable paths of the Lake Balaton car ferry, Figure 1A) and purely transect-like data (as is the case for the Western Channel deployment). Eq. 6 assumes that $\gamma(h)$ depends only on h but not on the spatial location. In other words, $\gamma(h)$ represents an average quantity computed over the extent of the geographic survey, unless spatial windowing is applied. As it graphs the semivariance, the variogram is sometimes referred to as a semivariogram (Bachmaier and Backes, 2011). Eq. 6 is applied after quality control of R_{rs} (see Section 3.2). Numerical details on the computation of $\gamma(h)$ and fitting procedure are provided in Section 4.3.

$\gamma(h)$ in Eq. 6 can be interpreted as representing the variance in R_{rs} at separation distance h (refer to Bachmaier and Backes (2011) for an explanation how the formula relates to a conventional expression for the variance). In the context of *in situ* R_{rs}, $\gamma(h)$ has units sr^{-2}. In satellite validation of R_{rs} it is preferable to express uncertainty in units of sr^{-1} (i.e., expressed as a standard deviation of R_{rs}). We therefore consider graphs of $\sqrt{\gamma(h)}$ which we refer to as the "root-variogram".

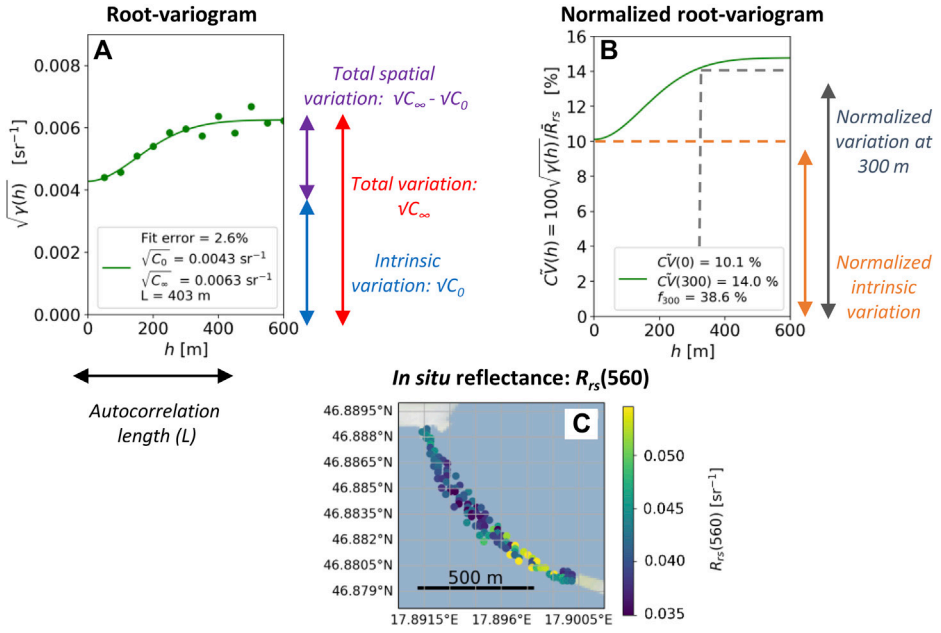


FIGURE 3
Annotated examples of **(A)** root-variogram, $\sqrt{\gamma(h)}$, **(B)** normalized root-variogram $\widetilde{CV}(h) = 100\sqrt{\gamma(h)}/\bar{R}_{rs}$, **(C)** corresponding reflectance map for R_{rs}(560). Panel **A** shows the three fitted parameters: $\sqrt{C_0}$ (variogram nugget, representing variation in R_{rs} as h tends to zero), $\sqrt{C_\infty}$ (variogram sill, representing variation in R_{rs} as h tends to infinity), and L (autocorrelation length; the distance R_{rs} ceases to be spatially autocorrelated), along with the curve fit (mean percentage) error. Panel B shows measures of normalized variation at h = 0 m and h = 300 m that are used in the computation of f_{300}, using Eq. 8. The example is from 2019-06-27 and corresponds to the same data as Figures 1A,B.

4.2 Interpreting the root-variogram and spatial structure of *in situ* R_{rs}

This section describes the features of the root-variogram and how these relate to spatial properties of R_{rs}. A schematic example from Lake Balaton is shown in Figure 3 for R_{rs}(560). The root-variogram (Figure 3A) shows empirical computations (points) and fitted curves (solid lines), with the computations and fitting procedure described in Section 4.3. The root-variogram has three fitted parameters: $\sqrt{C_0}$ is the value of $\sqrt{\gamma(h)}$ when $h = 0$ (with C_0 often referred to as the variogram nugget), $\sqrt{C_\infty}$ is the value of $\sqrt{\gamma(h)}$ as h tends to infinity (with C_∞ often referred to as the variogram sill) and L is the autocorrelation length (often referred to as the variogram range). The model fits (Section 4.3) assume a Gaussian semivariance function of the form

$$\sqrt{\gamma(h)} = \sqrt{C_0 + (C_\infty - C_0)\left(1 - \exp\left(-kh^2/L^2\right)\right)}, \qquad (7)$$

where k is a constant. In the data analysis we also consider the root-variogram normalized by the survey mean ($\bar{R}_{rs}$) which we define as $\widetilde{CV}(h) = 100\sqrt{\gamma(h)}/\bar{R}_{rs}$ due to the analogy with the coefficient of variation. This normalization is done to compare relative variation between spectral bands and deployments, as the R_{rs} magnitude can vary substantially (Figure 1). Examples of the normalized variogram curves are shown in Figure 3B.

$\sqrt{C_0}$, $\sqrt{C_\infty}$, L and derived parameters relate to the spatial structure of *in situ* R_{rs} as follows:

Intrinsic variability represents variation in R_{rs} that is not due to measurement point separation. In the root-variogram, intrinsic variation is quantified by $\sqrt{C_0}$ (the $h = 0$ intercept of the fitted curve) and in the normalized root variogram, by $\widetilde{CV}(0) = 100\sqrt{C_0}/\bar{R}_{rs}$. In the data analysis, we focus on $\widetilde{CV}(0)$ as it provides a relative measure of intrinsic variation between spectral bands and deployments. Intrinsic variability arises from a combination of factors including instrument noise, environmental perturbations, and precision of the R_{rs} retrieval method (further discussed in Section 6.3).

Spatial variability represents variation in R_{rs} that occurs due to measurement point separation. The quantity $\sqrt{C_\infty} - \sqrt{C_0}$, the amount by which the root-variogram nugget exceeds the root-variogram sill, quantifies the maximum spatial variation in R_{rs} that occurs due to measurement point separation, and is indicated graphically in Figure 3A. In the data analysis we focus on spatial variability at a length scale representative of a medium resolution sensor pixel (300 m). We do this by quantifying the fraction of variation in R_{rs} associated with spatial separation at 300 m

$$f_{300} = \left(\sqrt{\gamma(300)} - \sqrt{C_0}\right)\Big/\sqrt{\gamma(300)}, \qquad (8)$$

where the numerator, $\sqrt{\gamma(300)} - \sqrt{C_0}$, represents the spatial component of variability at 300 m and the denominator, $\sqrt{\gamma(300)}$, represents the total variation. A way to interpret f_{300} is that it relates to a reduction in spatial discrepancy uncertainty (i.e., reduction of the Δ_s term in Eq. 4) due to sampling across the satellite pixel. Specifically, $\sqrt{\gamma(300)} - \sqrt{C_0}$ represents the additional variation across the pixel that the mobile radiometer samples relative to a fixed platform which samples a single fixed location and $\sqrt{\gamma(300)}$ represents the total variation that measurements from a fixed platform would be subject to. Therefore $f_{300} = (\sqrt{\gamma(300)} - \sqrt{C_0})/\sqrt{\gamma(300)}$ serves as a relative

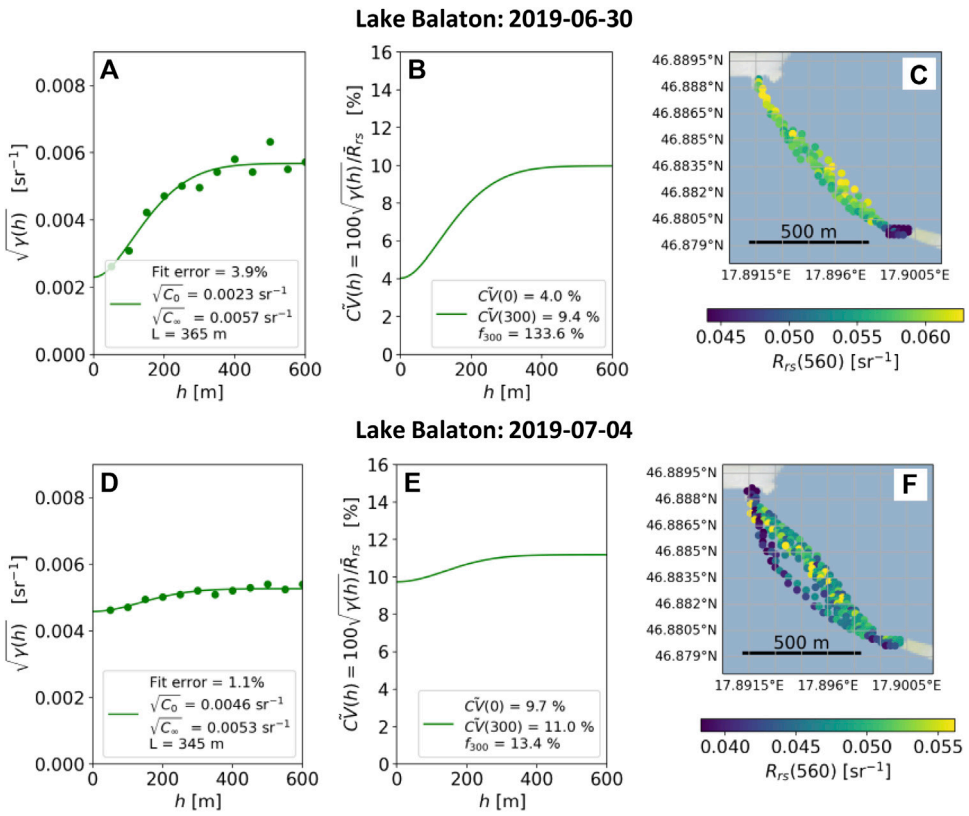


FIGURE 4
Illustrative examples of root-variograms $\sqrt{(\gamma(h))}$ (panels **A and D**), normalized root-variograms $\widetilde{CV}(h) = 100\sqrt{\gamma(h)}/\bar{R}_{rs}$ (panels **B and E**), and corresponding reflectance maps (panels **C and F**) from the Lake Balaton deployment for $R_{rs}(560)$. The examples illustrate difference degrees of spatial structure.

measure of the capacity of the mobile radiometers to sample sub-pixel variability. f_{300} is illustrated graphically in Figure 3B, taking into account that the f_{300} ratio is the same in the normalized plot; i.e., $(\sqrt{CV(300)} - \sqrt{CV(0)})/\sqrt{CV(300)} \equiv (\sqrt{\gamma(300)} - \sqrt{C_0})/\sqrt{\gamma(300)}$.

Spatial autocorrelation. The autocorrelation length L quantifies the separation distance at which R_{rs} measurements cease to be spatially correlated with the original location. This is also the distance at which further increasing measurement point separation does not increase the variation in R_{rs}. In general, the definition of L can vary between variogram models and correspondingly the decay constant k in Eq. 7 can also take different definitions (Mälicke, 2022). Here we set $k = 3$ which corresponds to the fitted curve reaching ~ 98% of the difference between the sill value ($\sqrt{C_\infty}$) and the nugget value ($\sqrt{C_0}$).

4.3 Computation and fitting of the variograms

Prior to the variogram analysis, geographic coordinates were converted to Universal Transverse Mercator coordinates using the WGS 84 ellipsoid. The variogram computations were performed using the Python geostatistics module (Mälicke 2022) using the inbuilt variogram function to compute $\gamma(h)$ via Eq. 6. The computations select R_{rs} data from 12 discretized lag (h) bins. Following recommendations that the maximum lag must be order half the maximum point separation or less (Mälicke, 2022), the maximum possible lag of 600 m was used for Lake Balaton, corresponding to a bin width of δh = 50 m. For the other deployments a maximum lag of 1,500 m was used, corresponding to a bin width of δh = 125 m.

The fitting of Eq. 7 to the empirical variogram, which determines $\sqrt{C_0}$, $\sqrt{C_\infty}$ and L, used the Levenberg-Marquardt (non-linear least squares) algorithm. The absolute mean percentage error between empirical and fitted variogram curves was used to measure the goodness-of-fit. It was then used as a quality control parameter to filter out poor fits to the Gaussian model, with 10% used as maximum allowed value. In our study the Gaussian model was used as it gave the best overall fit to the data from the conventional choices of variogram model (spherical, Gaussian, exponential). Future studies on different data sets should experiment with different choices of parametric model, or non-parametric approach to extract the variogram parameters. Additionally, we required that at least 60 (Lake Balaton) or 100 (Western Channel, Tagus Estuary) data points were present to generate the variograms. (The number of data points available fluctuates due to the variable ship paths, variable time intervals when the ship is stationary, and R_{rs} quality control (Section 3.2)).

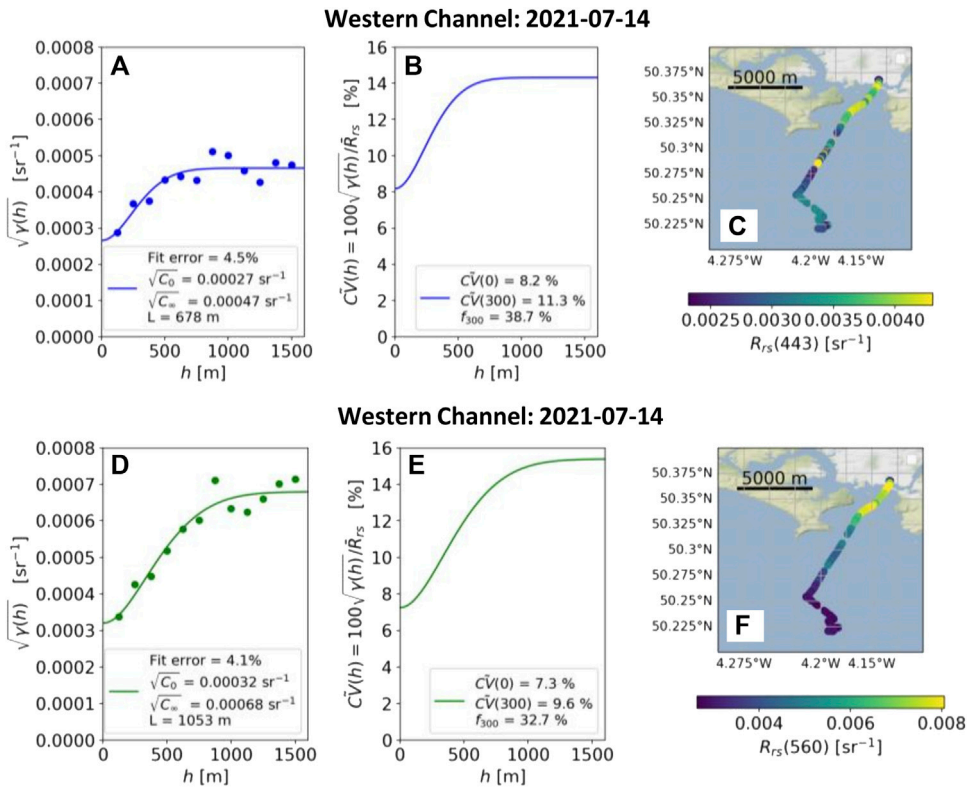


FIGURE 5
Illustrative examples of root-variograms $\sqrt{(\gamma(h))}$ (panels **A and D**), normalized root-variograms $\widetilde{CV}(h) = 100\sqrt{\gamma(h)}/\bar{R}_{rs}$ (panels **B and E**), and corresponding reflectance maps (panels **C and F**) from the Western Channel deployment for R_{rs}(443) (top row) and R_{rs}(560) (bottom row). The examples illustrate subtle differences in the variogram shapes and autocorrelation length between the 443 nm and 560 nm bands. The data in both rows is the same as in Figures 1C,D.

5 Results

5.1 Variogram structure of *in situ* R_{rs}

We first illustrate how the spatial distribution of *in situ* R_{rs} relates to variogram structure, and how this can differ for different days within each deployment or between spectral bands. The examples from Lake Balaton (Figure 4) illustrate different degrees of spatial structure within the green band (R_{rs}(560)). The example in the top row (Figures 4A–C) has significantly more spatial variation than the bottom row (Figures 4D–F) indicated by the steeper curve and the greater difference between $\sqrt{C_\infty}$ and $\sqrt{C_0}$ (absolute measure of total spatial variation) and f_{300} (relative measure of spatial variation at 300 m). The differences in variogram structure relate to the R_{rs}(560) map in the top row having greater spatial coherence than the bottom row. The examples from the Western Channel (Figure 5) are chosen to illustrate subtle differences between the variogram structure for different spectral bands within the same match-up window. Notably, R_{rs}(560) in the bottom row has a longer autocorrelation length (1,053 m) than R_{rs}(443) in the bottom row (678 m). The larger autocorrelation length means that spatial variation in R_{rs}(560) occurs over a longer length scale than R_{rs}(443), visually corresponding to a smoother spatial gradient in the R_{rs}(560) map. The examples from the Tagus Estuary (Figure 6) are chosen to illustrate different degrees of intrinsic variation that can occur within each deployment. Specifically, the example in the bottom row has much higher intrinsic variation ($\widetilde{CV}(0)$ = 16.3%) than the top row ($\widetilde{CV}(0)$ = 8.3%).

Figures 7, 8 show summaries of root-variograms ($\sqrt{\gamma}(h)$) and normalized root-variograms ($\widetilde{CV}(h) = 100\sqrt{\gamma(h)}/\bar{R}_{rs}$) across the three deployments in four spectral bands: 443 nm (blue), 560 nm (green), 665 nm (red), 783 nm (NIR). The purpose here is to provide an overall summary, and related variogram statistics are described in Section 5.2. Each individual $\sqrt{\gamma}(h)$ curve represents a theoretical fit to the empirical root variogram. Curves based on the median goodness-of-fit parameters are also shown. The $\sqrt{\gamma}(h)$ curves in Figure 7 illustrate that, for each deployment, the dependence of absolute variation in R_{rs} scales broadly with the spectral shape and magnitude of the R_{rs} spectra in Figure 1. Specifically, across the deployments, the values of $\sqrt{\gamma}(h)$ are highest for the 560 nm band, and lowest for the 783 nm band. The $\widetilde{CV}(h)$ curves in Figure 8 illustrate that relative variation in R_{rs} typically ranges between 5% and 40% for the length scales shown. In reverse of the result in Figure 7 the 665 nm and 783 nm bands have higher relative variability than the shorter wavebands.

The diversity of curves in each panel in Figures 7, 8 show that a range of variogram structure exists for each deployment and spectral band. However, some clear trends are present. Notably,

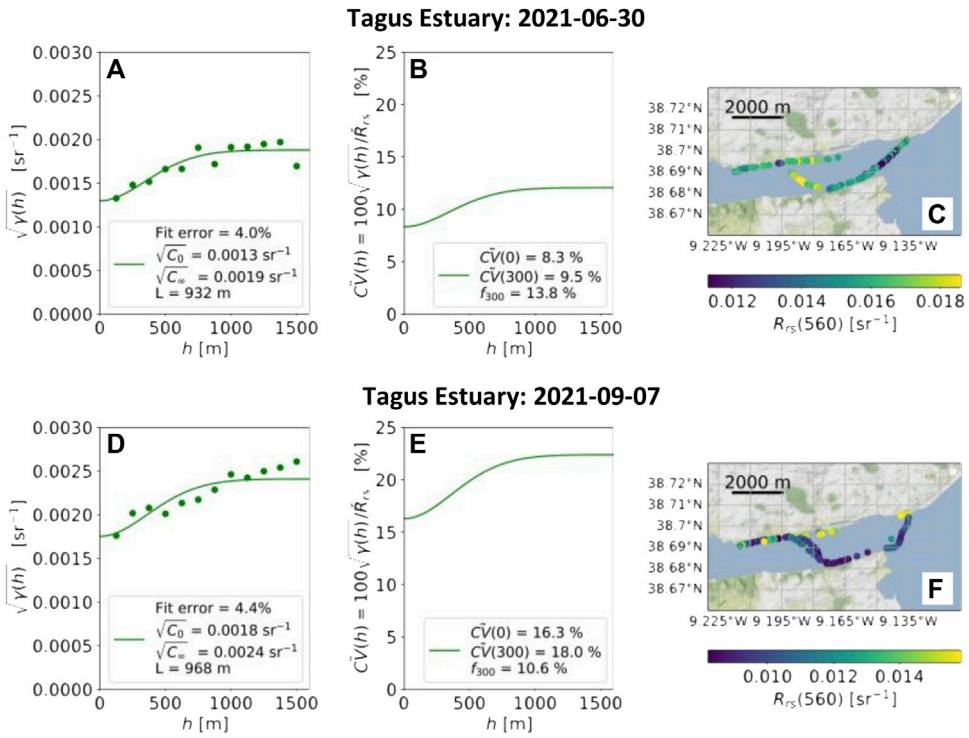


FIGURE 6
Illustrative examples of root-variograms $\sqrt{\gamma(h)}$ (panels **A and D**), normalized root-variograms $\widetilde{CV}(h) = 100\sqrt{\gamma(h)}/\bar{R}_{rs}$ (panels **B and E**), and corresponding reflectance maps (panels **C and F**) from the Tagus Estuary deployment for $R_{rs}(560)$. The examples illustrate differences in intrinsic variation in R_{rs}. The data in the top row is the same as in Figures 1E,F.

the variogram curves from Lake Balaton have a markedly different shape than the other deployments, with the sill being reached at shorter length scales than the other deployments (note the different horizontal axis scale in Figure 7). This difference in variogram structure represents that spatial variation in R_{rs} occurs over a shorter length scale in Lake Balaton than other deployments. Additionally, the Tagus Estuary generally has a greater spread of variogram curves and higher relative variability than the Lake Balaton and Western Channel deployments.

5.2 Variogram statistics for spatial structure of *in situ* R_{rs}

Figure 9 shows frequency distributions for $\widetilde{CV}(h) = 100\sqrt{C_0}/\bar{R}_{rs}$ for each deployment and spectral band. This parameter measures the relative intrinsic variation in R_{rs} (i.e., percentage variation in R_{rs} not due to measurement point separation) and corresponds to the distributions of the $h = 0$ intercepts in Figure 8. Median values of $\widetilde{CV}(0)$ range from 7% to 21% across spectral bands and deployments. Within each deployment, the blue and green bands typically have the lowest variability with the red and NIR bands having the highest variability. Averaged across spectral bands, the Tagus Estuary has significantly higher $\widetilde{CV}(0)$ than the other two deployments (17% compared with 11% and 10% for Lake Balaton and the Western Channel respectively). We note that the results in Figure 9 hold for the normalized variograms. Alternatively, intrinsic variability could be expressed in steradians for absolute values of R_{rs} (the $h = 0$ intercepts in Figure 7).

Figure 10 shows frequency distributions for f_{300}, Eq. 8, for each deployment and spectral band. This parameter represents the fraction of R_{rs} variability due to measurement point separation at 300 m (chosen due to the pixel size of OLCI). The values of f_{300} are significantly higher for Lake Balaton than the other deployments, with median values > 30% in the blue, green and red bands. The Tagus Estuary has lower values of f_{300} than the other deployments with median values < 10% in all bands. The Western Channel has the greatest difference in f_{300} between spectral bands, with median value 21% for the green band and 7% for the NIR band. The f_{300} distributions are broad and values often greatly exceed the median; e.g., the example in the top row of Figure 4 has $f_{300} > 100\%$, indicating that over half of the variation at 300 m is due to measurement point separation.

Figure 11 shows frequency distributions for the autocorrelation length, L. Lake Balaton has lower values of L than the other deployments, with median values between 250 and 300 m. The Western Channel has median values of L between 1,000 and 500 m, with the Tagus Estuary between 1,800 and 2,500 m. In all panels the frequency distributions for L are broad, indicating that the spatial autocorrelation structure of *in situ* R_{rs} is changeable throughout the timescale of the deployment.

We note that the results for f_{300} in Figure 10 and for L in Figure 11 hold for both unnormalized ($\sqrt{\gamma(h)}$) and normalized ($\widetilde{CV}(h)$) root-variograms.

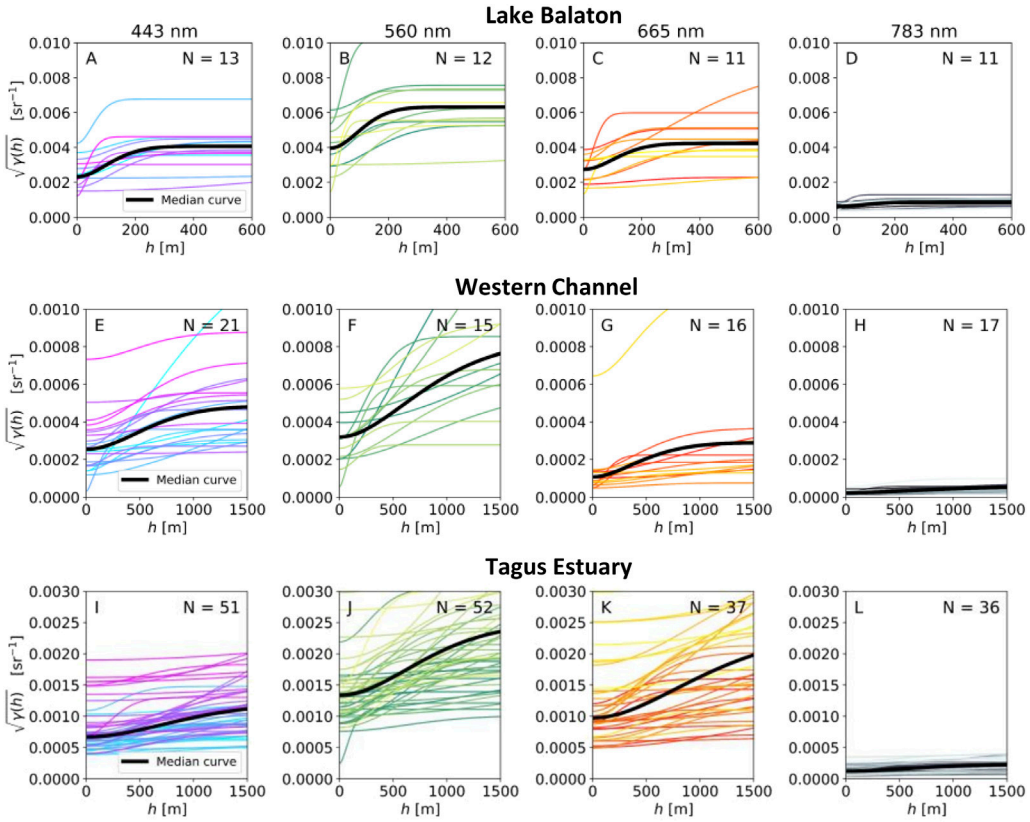


FIGURE 7
Summary of root-variograms ($\sqrt{\gamma}(h)$) in four spectral bands for each window/day of deployment. Top row **(A–D)**: Lake Balaton. Middle row **(E–H)**: Western Channel. Bottom row **(I–L)** Tagus Estuary. The vertical scale is fixed within a deployment, but differs between different deployments. The horizontal data range is smaller for Lake Balaton than the other deployments. Curves based on median fit parameters are shown. The number of curves (*N*) varies slightly between spectral bands within each deployment due to quality-control filtering of the variogram fitting (Section 4.3).

6 Discussion

6.1 Comparison with previous variographic analyses of ocean colour and inland water quality

The spatial structure of R_{rs} (or related ocean colour variables) has been assessed in numerous past studies, based on satellite images (Yoder et al., 1987; Aurin et al., 2013; Glover et al., 2018), airborne (Bissett et al., 2004; Davis et al., 2007; Moses et al., 2016) and shipborne (Moses et al., 2016) radiometric platforms. The key novelty of our study is quantification of the spatial structure of *in situ* R_{rs} from autonomous radiometric systems deployed in the context of satellite validation. In coastal regions, reported autocorrelation lengths range from ~ 1–100 km (Davis et al., 2007; Aurin et al., 2013; Moses et al., 2016), consistent with the Western Channel and Tagus estuary deployments in our study (Figure 11). For example, in near-coastal waters Moses et al. (2016) established that R_{rs} variability can increase rapidly when measured on scales of 10–100 m (up to a ~ three-fold increase in the local coefficient of variation from a point measurement) with typical autocorrelation lengths being kilometer-scale. In Monterey Bay, California, Davis et al. (2007) showed autocorrelation lengths to be > 2 km. Aurin et al. (2013) showed that sediment river plumes have autocorrelation lengths which range from ~ 10–100 km. In the open ocean, spatial autocorrelation can occur over even larger length scales, with Glover et al. (2018) showing autocorrelation lengths to be in the range 50–300 km.

Spatial structure analysis has also been applied to a diversity of chlorophyll measurements (which strongly correlates with R_{rs}) in inland water bodies. Using a chlorophyll index derived from airborne optical data Hedger et al. (2001) investigated spatial correlation in two Scottish Lochs (Loch Ness, and Loch Awe) reporting autocorrelation lengths between 500 and 1,300 m. Using discrete *in situ* Chlorophyll-*a* measurements, Yenilmez et al. (2014) reported autocorrelation length 1,200 m for the Porsuk Dam Reservoir in Turkey, and Anttila et al. (2008) reported autocorrelation lengths of 945 m and 1,357 m in Lake Vesijärvi, Finland. These autocorrelation lengths are slightly higher than the ferry transect we analysed in Lake Balaton (Figures 11A–D) suggesting that ~ 1 km is a typical length scale of autocorrelation in inland waters.

There are examples of ocean colour variogram structure being more complex than the monotonically increasing Gaussian model used in this study. For example, Aurin et al. (2013) revealed the presence of 'sub-sills' (i.e., where the variogram levels out, then rises again), associated with sediment plumes. As we applied a goodness-of-fit filter to the Gaussian model, variograms that deviated significantly from a monotonic increase were filtered out. In comparing variograms between different ocean colour studies, it

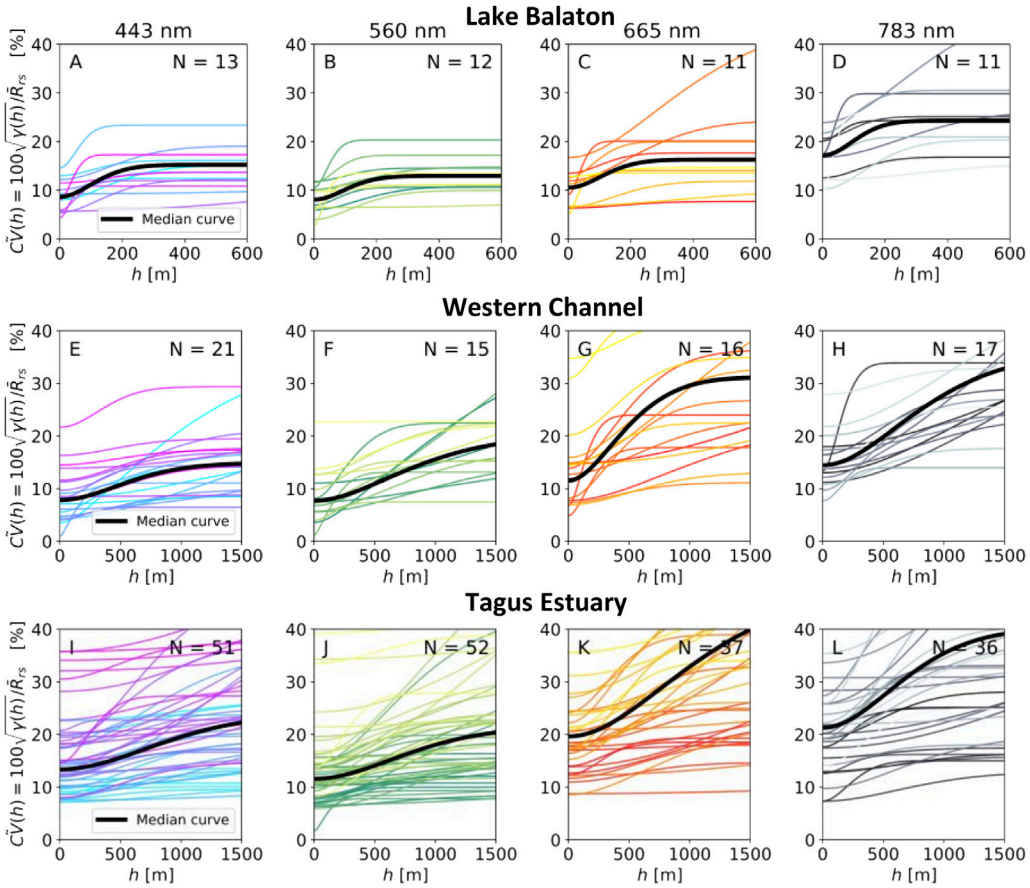


FIGURE 8
Summary of normalized root-variograms ($\widetilde{CV}(h) = 100\sqrt{\gamma(h)}/\bar{R}_{rs}$) in four spectral bands for each window/day of deployment. Top row **(A–D)** Lake Balaton. Middle row **(E–H)** Western Channel. Bottom row **(I–L)** Tagus Estuary. Curves based on median fit parameters are shown. The number of curves (*N*) varies slightly between spectral bands within each deployment due to quality-control filtering of the variogram fitting (Section 4.3).

remains important to note that the transect-like data from shipborne or airborne sampling result in non-uniform spatial sampling, whereas a satellite image will be approximately uniform.

6.2 Opportunities and challenges of using mobile radiometers in satellite validation

Mobile radiometers deployed on ships-of-opportunity enable high-frequency spatial sampling of *in situ* R_{rs} in coastal and inland waters. In the context of satellite validation, the obvious advantage to using a mobile system (*versus* a fixed-platform deployment) is that it enables sampling of variation in *in situ* R_{rs} within a satellite pixel and across optical gradients. Quantifying within-pixel variability is important as nearshore waters are dynamic across short spatiotemporal scales which means that selecting spatially homogeneous sites for satellite validation is not always possible or desirable. Sampling *in situ* R_{rs} across optical gradients is particularly desirable to validate the response of algorithms over a wide biogeochemical concentration range. A specific challenge in improving validation practice from moving platforms is to account for spatial autocorrelation when selecting *in situ* data for match-ups with the same satellite image. In a wider context of data integration, it is also desirable to relate point-like *in situ* reflectance data to optical image data taken at different scales; ranging from drone flight imagery to high and moderate resolution imagery from satellites.

To quantify pixel-scale variation in *in situ* R_{rs} within our 4 or 6 h time windows, we introduced the parameter f_{300} which quantifies the percentage of *in situ* R_{rs} variation due to spatial separation at 300 m (representative of the medium resolution OLCI sensor). The advantage of using a mobile radiometric system to sample sub pixel variation was particularly clear for the Lake Balaton deployment, where f_{300} was greater than 30% across all spectral bands (median values in Figure 10). This was likely because spatial coherence of *in situ* R_{rs} was preserved throughout the time window. On the other hand, the Western Channel and Tagus Estuary deployments are more dynamic systems, which likely results in lower spatial coherence and lower values of f_{300}. In tidal systems, fixed-monitoring stations are also able to sample spatial variation due to the flow of water (Salama et al., 2022), representing an alternative strategy to reduce uncertainty in a validation analysis.

Ultimately, it is the average value of *in situ* R_{rs} sampled within the extent of a satellite pixel that is compared to the satellite observation, and numerically relates to Δ_s in Eq. 4. The spatial sampling of the mobile radiometer will reduce the standard error on the pixel mean by a factor proportional to $(\sqrt{\gamma(300)} - \sqrt{C_0})/\sqrt{N}$

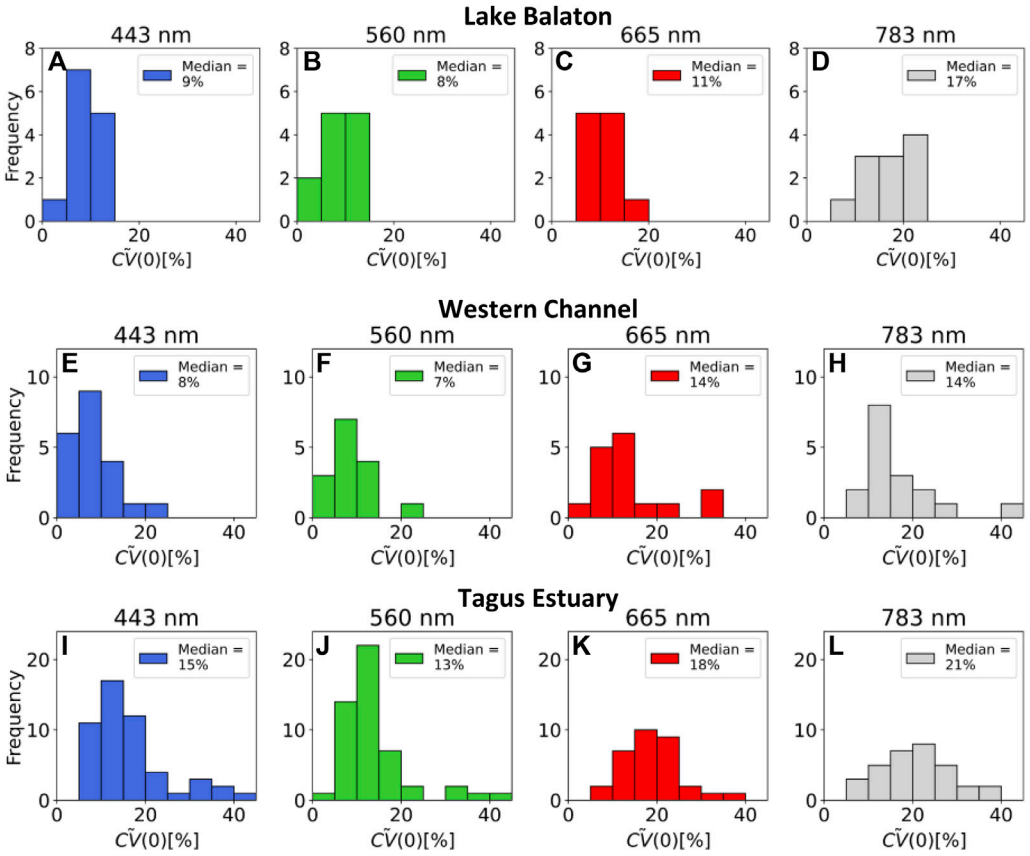


FIGURE 9
Frequency distributions of the intrinsic variation in R_{rs} as measured by $\widetilde{CV}(0) = 100\sqrt{C_0}/\bar{R}_{rs}$ where $\sqrt{C_0} = \sqrt{\gamma(0)}$ is the intercept of the root-variogram. Top row **(A–D)** Lake Balaton. Middle row **(E–H)** Western Channel. Bottom row **(I–L)** Tagus Estuary. This parameter represents all variation in R_{rs} not due to measurement point separation.

where N is the number of spatial locations within the pixel that are sampled, and ultimately determined by platform speed and sensor sampling rate. This means that, for mobile radiometric systems, it is valuable to retain all observations sampled along a transect prior to any data reduction by aggregation or selection, and even on-board analysis of transect observations could be considered. In the context of using *in situ* data for sub-pixel averaging, interpolation across the pixel (e.g., Kriging, based on the variogram structure) could be used to get a more spatially representative average to compare with the satellite image.

In general, accounting for the spatial autocorrelation of *in situ* R_{rs} in validation of remotely-sensed reflectance becomes more important as the resolution of the satellite sensor increases. This is because neighbouring measurements become more likely to be located in adjacent pixels, rather than being averaged within the same pixel. If multiple match-up pairs are used from the same image, a simple approach to account for spatial autocorrelation is to downsample the match-up pairs, based on the autocorrelation length, L. Using Lake Balaton as an example, with a median value of L between 250 and 300 m, match-up pairs for high resolution sensors such as MSI could be downsampled to a 300 m spacing, thus reducing the effect of spatial autocorrelation, and thus providing a suitable number of match-up pairs. As the Lake Balaton autocorrelation lengths were generally comparable to the OLCI pixel scale downsampling is not necessary for OLCI match-up pairs from this area of Lake Balaton. For the other two deployments, downsampling match-up pairs to a separation distance of ~ 2–3 km would be effective to reduce the effects of spatial autocorrelation.

Due to the breadth of the L distributions in Figure 11, and the range of reported water autocorrelation lengths in Section 6.1, it is desirable that downsampling uses the specific variogram on the day of data collection to set the separation distance for the downsampling of *in situ* R_{rs}. However, recognising that coincidence of remote and *in situ* observations is a rarity, as a rule of thumb ~ 1 km is likely to be an appropriate separation distance for inland waters, with 1 km a minimum distance for coastal waters, being aware that sediment features may have much longer scales of autocorrelation (Aurin et al., 2013). Additionally, spatial structure analysis could be applied to climatologically-averaged ocean colour products to produce a map representing a first-order approximation of spatial autocorrrelation. Downsampling represents just one approach to account for spatial autocorrelation in validation statistics. Alternatively, validation statistics could be modified for spatial autocorrelation; for example, spatially-weighted regression methods (Anselinm and Bera, 1998).

As chlorophyll-*a* concentration often controls the majority of the variability in R_{rs}, it typically results in a high degree of co-variance

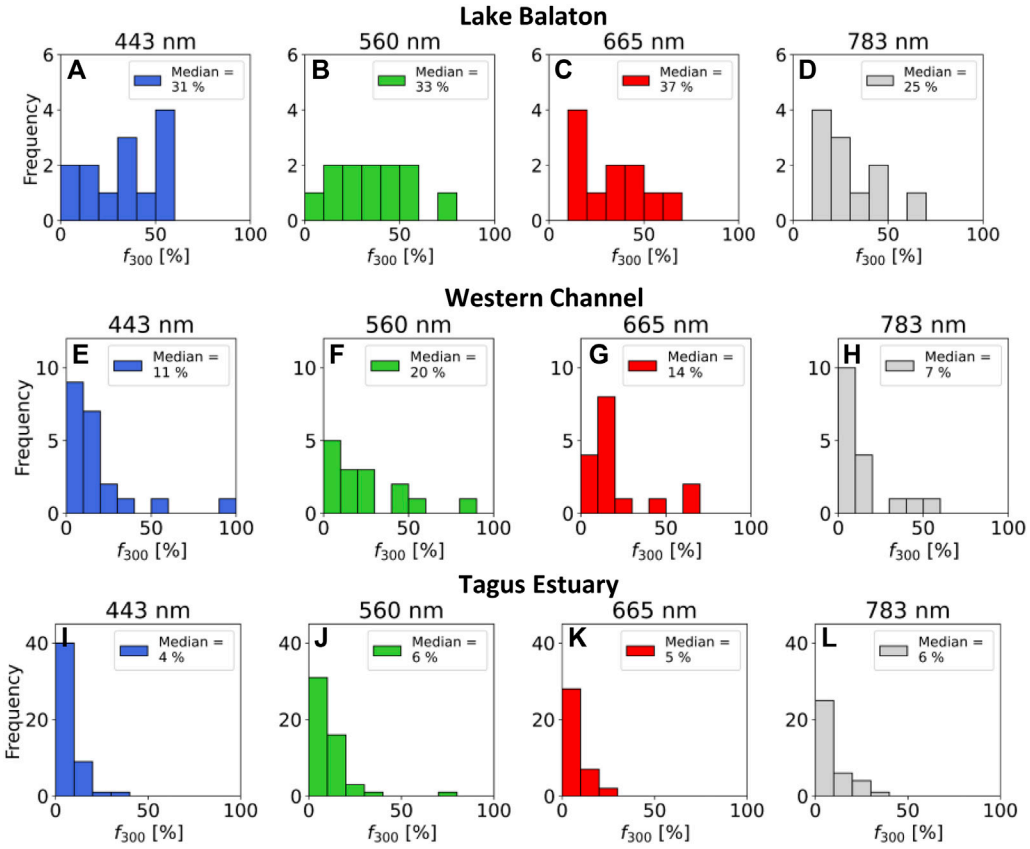


FIGURE 10
Frequency distributions of spatial variation in R_{rs} as measured by $f_{300} = 100\left(\sqrt{\left(\gamma(300)\right)} - \sqrt{C_0}\right)/\sqrt{\gamma(300)}$. Top row **(A–D)** Lake Balaton. Middle row **(E–H)** Western Channel. Bottom row **(I–L)** Tagus Estuary. This parameter represents the percentage of the variation in R_{rs} associated with spatial separation at a length scale of 300 m; typical of a medium resolution sensor such as OLCI. Outliers (f_{300} > 100 %) are not shown.

between spectral bands (e.g., Cael et al., 2023). This is reflected in the variogram statistics in Section 5.2 which show similarity between spectral bands, although band differences can exist (e.g., as shown for the Western Channel in Figures 10, 11) when there is variation in the spectral shape of R_{rs} (Figure 1C). We anticipate that variogram statistics could have the most pronounced differences between spectral bands in optically complex waters, where higher concentrations of suspended sediment and CDOM are present. We therefore recommend continued evaluation of variogram statistics across reflectance bands in coastal and inland waters, until more general conclusions can be drawn on differences between spectral bands.

6.3 Relationship between intrinsic variation and uncertainty of R_{rs}

In this study, we used the metric $\widetilde{CV}(0) = 100\sqrt{C_0}/\bar{R}_{rs}$ to characterize intrinsic variation in *in situ* R_{rs}; i.e., all variation not due to measurement point separation (see Figure 9 for a summary). This quantity has parallels with the variation in *in situ* R_{rs} that would be measured at a fixed-location, e.g., using a coefficient of variation metric applied to time series of R_{rs} in a local time window (Groetsch et al., 2020), with $\widetilde{CV}(0)$ representing a survey-wide average of variability at a fixed location. This interpretation is supported by the values of $\widetilde{CV}(0)$ in Figure 9 being broadly comparable with fixed-location variability from the same radiometric system (Jordan et al., 2022), where typical coefficient of variation values were ~ 5%–20% across different measurement conditions.

Measures of R_{rs} variability provide only a proxy for uncertainty. Formal uncertainty assessment from fiducial reference measurements refers to a component-by-component propagation of sources of uncertainty, traceable to metrology standards (Ruddick et al., 2019; Banks et al., 2020). Individual sources of uncertainty include radiometric calibration, sensor characteristics (e.g., straylight, non-linearity, thermal response), and the uncertainty of the R_{rs} estimation method, which is impacted by environmental conditions: i.e., cloud cover and windspeed (surface roughness). Environmental sources of uncertainty are typically half of the total uncertainty budget (Lin et al., 2022), with higher windspeeds and scattered cloud leading to higher uncertainties. Variable environmental conditions are therefore likely to be a dominant factor influencing the spread of $\widetilde{CV}(0)$ in Figure 9. As co-located wind data were not available to do this in the current study, investigating environmental controls on variogram structure (including strictness of quality control) is an area for future investigation.

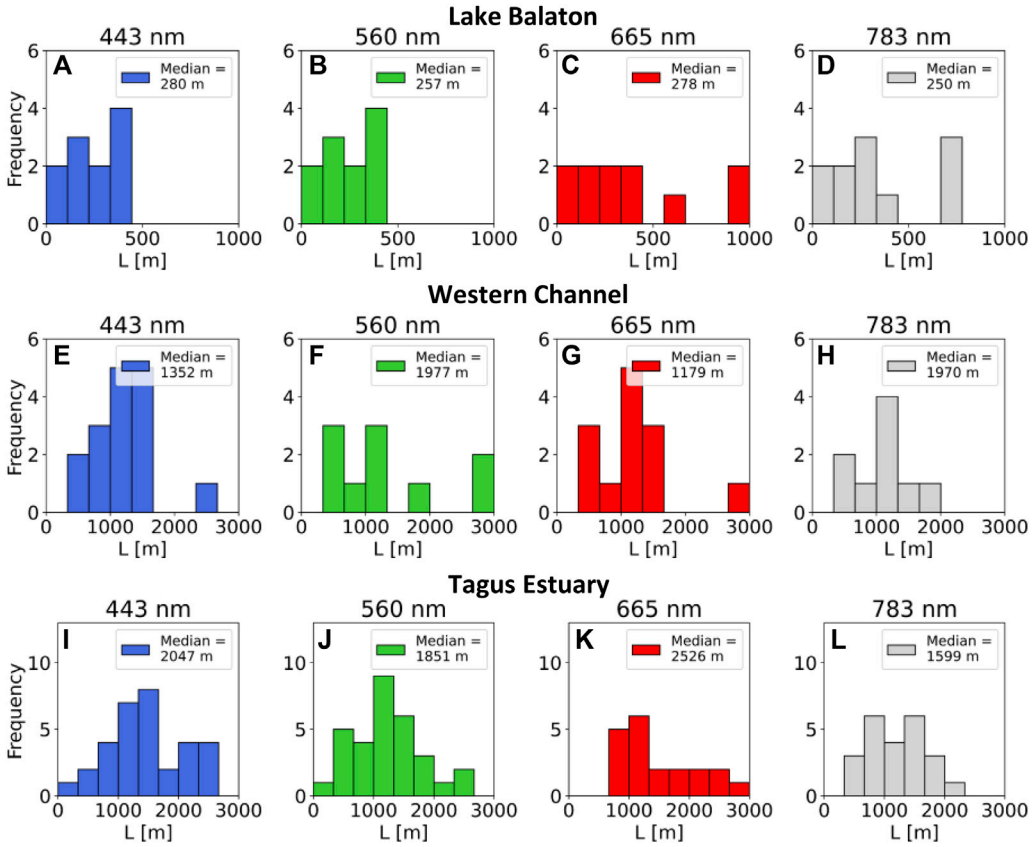


FIGURE 11
Frequency distributions of variogram autocorrelation lengths (*L*). Top row **(A–D)** Lake Balaton. Middle row **(E–H)** Western Channel. Bottom row **(I–L)** Tagus Estuary. This parameter represents the maximum distance at which *in situ* R_{rs} is considered spatially correlated with neighbouring observations. Outliers (L > 1,000 m in the top row and L > 3,000 m in the middle and bottom rows) are not shown.

6.4 Limitations of variogram analysis and future work

Due to computing the variogram over a 4 or 6 h time window, there are temporal sources of variation that are present in the analysis. These include variation in R_{rs} due to changing solar zenith and relative azimuth (Mobley, 1999), as well as natural temporal fluctuations in water constituent concentrations. Casting the analysis in terms of the normalized water leaving radiance, which adjusts for R_{rs} variable zenith angle and atmospheric attenuation (Gordon and Wang, 1994), would give a more accurate picture of how the water properties vary spatially. Additionally, the variogram structure will be impacted by temporal variation. For example, in the Tagus Estuary deployment, the relatively high variation in *in situ* R_{rs} at shorter length scales (Figure 9) is hypothesised to be partially influenced by the ship revisiting a location where R_{rs} changed temporally due to tidal influence (see neighbouring transects collected at different times in Figure 1F). Temporal R_{rs} differences between neighbouring transects is also likely to have an impact on the spatial structure analysis from Lake Balaton.

An important caveat to the variogram analysis is that the ship transects do not uniformly sample across the survey area, or each pixel. Therefore, the variogram structure is anticipated to be specific to the path of the ship within each deployments, and is likely to be very different for alternative ship paths in the same water body. Additionally, due to the quality control of *in situ* R_{rs} (Section 3.2) the effective temporal sampling frequency is also subject to change, because not all observations taken along a transect are suitable to derive estimates of R_{rs}.

A future research direction is to extend the "static" variogram analysis to the temporal dimension, and hence enable spatial and temporal autocorrelation to be considered in a unified way. It is likely this will require the data sampling strategy to be developed around the analysis method; i.e., obtaining repeat *in situ* measurements at a set of fixed locations that can be used to robustly window the variograms. Alternatively, a sequence of images from geostationary satellites which have hourly revisit times (e.g., Choi et al., 2012) could be used to gain insight.

7 Summary and conclusion

This study quantified the spatial structure of *in situ* R_{rs} from mobile radiometers deployed in coastal and inland water bodies. The overarching aim was to inform how spatial statistics can be used to aid in satellite validation practice where ship-transect data is used. A first focus was quantifying how mobile radiometers can reduce variability via sub-pixel sampling and a second focus was

quantifying spatial autocorrelation, and thereby informing *in situ* data selection for match-up analysis.

There were pronounced differences in spatial structure between the deployments, within each deployment, as well as more subtle differences between spectral bands. At a 300 m length scale (typical pixel size of a medium resolution ocean colour satellite sensor) we showed that typically 5%–35% of the total variation in *in situ* R_{rs} was due to the spatial separation of measurements. For validation of medium-resolution sensors, mobile radiometers therefore provide a distinct advantage in generating more spatially representative data than a fixed platform, reducing the contribution of *in situ* variability in the validation process. The autocorrelation length, which informs an ideal minimum separation distance for *in situ* R_{rs} in validation, ranged from ~ 100–1,000 m. Consequently, validation of high-resolution sensors (sub 100 m pixel size) requires either downsampling of *in situ* data to ensure spatial independence or for validation statistics to take spatial autocorrelation into account.

In the future, we anticipate that spatial statistics will become increasingly important for both validation and data integration of aquatic reflectance across multiple sensor systems, including spaceborne, shipborne, airborne, and ground-based platforms.

Data availability statement

The datasets presented in this study can be found in online repositories. The names of the repository/repositories and accession number(s) can be found below: https://pypi.org/project/monda/; https://github.com/tjor/SR_variograms.

Author contributions

TJ, SS, and NS contributed to conception and design of the study. TJ led the data analysis with contributions from SS and NS. SS, VM-V, GS, and FI designed the field deployments and collected data. TJ led the writing of the manuscript with contributions from all authors. SS obtained the primary funding and administered the project. All authors contributed to the article and approved the submitted version.

Funding

This project received primary funding from the European Union's Horizon 2020 research and innovation programme under grant agreement No 776480 (MONOCLE: Multiscale Observation Networks for Optical monitoring of Coastal waters, Lakes and Estuaries), https://monocle-h2020.eu. TJ and VM-V were partially supported by Hyperspectral Bio-Optical Observations Sailing on Tara (HyperBOOST) (ESA contract number: 4000135756/21/I-EF). GS and FI acknowledge funding from from Horizon 2020 grant agreement No 870349 (CERTO: Copernicus Evolution: Research for harmonised and Transitional water Observation). TJ was partially funded by NERC through its Earth Observation Data Acquisition and Analysis Service (NEODAAS), award number NE/S013377/1.

Acknowledgments

We would like to thank our reviewers whose thorough and constructive comments greatly improved our publication.

Conflict of interest

The authors declare that the research was conducted in the absence of any commercial or financial relationships that could be construed as a potential conflict of interest.

Publisher's note

All claims expressed in this article are solely those of the authors and do not necessarily represent those of their affiliated organizations, or those of the publisher, the editors and the reviewers. Any product that may be evaluated in this article, or claim that may be made by its manufacturer, is not guaranteed or endorsed by the publisher.

References

Albert, A., and Mobley, C. (2003). An analytical model for subsurface irradiance and remote sensing reflectance in deep and shallow case-2 waters. *Opt. Express* 11, 2873–2890. doi:10.1364/OE.11.002873

Anselinm, L., and Bera, A. K. (1998). *Spatial dependence in linear regression models with an introduction to spatial econometrics*. CRC Press, 237–290. chap. 7. doi:10.1201/9781482269901-36

Anttila, S., Kairesalo, T., and Pellikka, P. (2008). A feasible method to assess inaccuracy caused by patchiness in water quality monitoring. *Environ. Monit. Assess.* 142, 11–22. doi:10.1007/s10661-007-9904-y

Aurin, D., Mannino, A., and Franz, B. (2013). Spatially resolving ocean color and sediment dispersion in river plumes, coastal systems, and continental shelf waters. *Remote Sens. Environ.* 137, 212–225. doi:10.1016/j.rse.2013.06.018

Bachmaier, M., and Backes, M. (2011). Variogram or semivariogram? Variance or semivariance? Allan variance or introducing a new term? *Math. Geosci.* 43, 735–740. doi:10.1007/s11004-011-9348-3

Bailey, S. W., and Werdell, P. J. (2006). A multi-sensor approach for the on-orbit validation of ocean color satellite data products. *Remote Sens. Environ.* 102, 12–23. doi:10.1016/j.rse.2006.01.015

Banks, A. C., Vendt, R., Alikas, K., Bialek, A., Kuusk, J., Lerebourg, C., et al. (2020). Fiducial reference measurements for satellite ocean colour (FRM4SOC). *Remote Sens.* 12, 1322. doi:10.3390/rs12081322

Barnes, B. B., Cannizzaro, J., English, D., and Hu, C. (2019). Validation of VIIRS and MODIS reflectance data in coastal and oceanic waters: an assessment of methods. *Remote Sens. Environ.* 220, 110–123. doi:10.1016/J.RSE.2018.10.034

Bissett, W. P., Arnone, R. A., Davis, C. O., Dickey, T. D., Dye, D., Kohler, D. D., et al. (2004). From meters to kilometers: a look at ocean-color scales of variability, spatial coherence, and the need for fine-scale remote sensing in coastal ocean optics. *Oceanography* 17 (2), 32–43. doi:10.5670/oceanog.2004.45

Brewin, R. J., Dall'Olmo, G., Pardo, S., van Dongen-Vogels, V., and Boss, E. S. (2016). Underway spectrophotometry along the atlantic meridional transect reveals high performance in satellite chlorophyll retrievals. *Remote Sens. Environ.* 183, 82–97. doi:10.1016/j.rse.2016.05.005

Bulgarelli, B., Kiselev, V., and Zibordi, G. (2014). Simulation and analysis of adjacency effects in coastal waters: a case study. *Appl. Opt.* 53, 1523–1545. doi:10.1364/AO.53.001523

Cael, B. B., Bisson, K., Boss, E., and Erickson, Z. K. (2023). How many independent quantities can be extracted from ocean color? *Limnol. Oceanogr. Lett.* 8, 603–610. doi:10.1002/lol2.10319

Choi, J.-K., Park, Y. J., Ahn, J. H., Lim, H.-S., Eom, J., and Ryu, J.-H. (2012). Goci, the world's first geostationary ocean color observation satellite, for the monitoring of temporal variability in coastal water turbidity. *J. Geophys. Res. Oceans* 117. doi:10.1029/2012JC008046

Concha, J. A., Bracaglia, M., and Brando, V. E. (2021). Assessing the influence of different validation protocols on ocean colour match-up analyses. *Remote Sens. Environ.* 259, 112415. doi:10.1016/j.rse.2021.112415

Cressie, N. A. C. (1993). *Statistics for spatial data*. Revised Edition. John Wiley and Sons, 27–104. chap. 2. doi:10.1002/9781119115151

Davis, C. O., Kavanaugh, M., Letelier, R., Bissett, W. P., and Kohler, D. (2007). "Spatial and spectral resolution considerations for imaging coastal waters," in *Coastal Ocean remote sensing*. Editors R. J. Frouin and Z. Lee (International Society for Optics and Photonics), 6680, 196–207. doi:10.1117/12.734288

Glover, D. M., Doney, S. C., Oestreich, W. K., and Tullo, A. W. (2018). Geostatistical analysis of mesoscale spatial variability and error in seaWiFS and MODIS/aqua global ocean color data. *J. Geophys. Res. Oceans* 123, 22–39. doi:10.1002/2017JC013023

Gordon, H. R., and Wang, M. (1994). Retrieval of water-leaving radiance and aerosol optical thickness over the oceans with seawifs: a preliminary algorithm. *Appl. Opt.* 33, 443–452. doi:10.1364/AO.33.000443

Gregg, W. W., and Carder, K. L. (1990). A simple spectral solar irradiance model for cloudless maritime atmospheres. *Limnol. Oceanogr.* 35, 1657–1675. doi:10.4319/lo.1990.35.8.1657

Groetsch, P. M. M., Foster, R., and Gilerson, A. (2020). Exploring the limits for sky and sun glint correction of hyperspectral above-surface reflectance observations. *Appl. Opt.* 59, 2942–2954. doi:10.1364/AO.385853

Groetsch, P. M. M., Gege, P., Simis, S. G. H., Eleveld, M. A., and Peters, S. W. M. (2017). Validation of a spectral correction procedure for sun and sky reflections in above-water reflectance measurements. *Opt. Express* 25, A742–A761. doi:10.1364/OE.25.00A742

Groom, S., Sathyendranath, S., Ban, Y., Bernard, S., Brewin, R., Brotas, V., et al. (2019). Satellite ocean colour: current status and future perspective. *Front. Mar. Sci.* 6, 1–30. doi:10.3389/fmars.2019.00485

Hedger, R. D., Atkinson, P. M., and Malthus, T. J. (2001). Optimizing sampling strategies for estimating mean water quality in lakes using geostatistical techniques with remote sensing. *Lakes Reservoirs Sci. Policy Manag. Sustain. Use* 6, 279–288. doi:10.1046/j.1440-1770.2001.00159.x

Ilori, C. O., Pahlevan, N., and Knudby, A. (2019). Analyzing performances of different atmospheric correction techniques for landsat 8: application for coastal remote sensing. *Remote Sens.* 11, 469. doi:10.3390/rs11040469

IOCCG (2019). Uncertainties in ocean colour remote sensing. *Int. Ocean. Colour. Coord. Group (IOCCG)* 18. doi:10.25607/OBP-696

Jordan, T. M., Simis, S. G. H., Grötsch, P. M. M., and Wood, J. (2022). Incorporating a hyperspectral direct-diffuse pyranometer in an above-water reflectance algorithm. *Remote Sens.* 14, 2491. doi:10.3390/rs14102491

Justice, C., Belward, A., Morisette, J., Lewis, P., Privette, J., and Baret, F. (2000). Developments in the 'validation' of satellite sensor products for the study of the land surface. *Int. J. Remote Sens.* 21, 3383–3390. doi:10.1080/014311600750020000

Kutser, T. (2012). The possibility of using the landsat image archive for monitoring long time trends in coloured dissolved organic matter concentration in lake waters. *Remote Sens. Environ.* 123, 334–338. doi:10.1016/j.rse.2012.04.004

Lee, Z., Hu, C., Arnone, R., and Liu, Z. (2012). Impact of sub-pixel variations on ocean color remote sensing products. *Opt. Express* 20, 20844–20854. doi:10.1364/OE.20.020844

Lehmann, G., Pahlevan, N., Alikas, K., Conroy, T., and Anstee, J. (2023). Gloria - a globally representative hyperspectral *in situ* dataset for optical sensing of water quality. *Sci. Data* 10, 100. doi:10.1038/s41597-023-01973-y

Lin, J., Dall'Olmo, G., Tilstone, G. H., Brewin, R. J. W., Vabson, V., Ansko, I., et al. (2022). Derivation of uncertainty budgets for continuous above-water radiometric measurements along an atlantic meridional transect. *Opt. Express* 30, 45648–45675. doi:10.1364/OE.470994

Loew, A., Bell, W., Brocca, L., Bulgin, C. E., Burdanowitz, J., Calbet, X., et al. (2017). Validation practices for satellite-based earth observation data across communities. *Rev. Geophys.* 55, 779–817. doi:10.1002/2017RG000562

Mälicke, M. (2022). Scikit-gstat 1.0: a scipy-flavored geostatistical variogram estimation toolbox written in python. *Geosci. Model. Dev.* 15, 2505–2532. doi:10.5194/gmd-15-2505-2022

Martinez-Vicente, V., Simis, S. G. H., Alegre, R., Land, S., and Groom, P. E. (2013). Above-water reflectance for the evaluation of adjacency effects in earth observation data: initial results and methods comparison for near-coastal waters in the western channel, UK. *J. Euro. Opt. Soc.* 8, 13060. doi:10.2971/jeos.2013.13060

Mobley, C. D. (1999). Estimation of the remote-sensing reflectance from above-surface measurements. *Appl. Opt.* 38, 7442–7455. doi:10.1364/AO.38.007442

Montes, M., Pahlevan, N., Giles, D. M., Roger, J.-C., Zhai, P.-w., Smith, B., et al. (2022). Augmenting heritage ocean-color aerosol models for enhanced remote sensing of inland and nearshore coastal waters. *Front. Remote Sens.* 3. doi:10.3389/frsen.2022.860816

Moses, W. J., Ackleson, S. G., Hair, J. W., Hostetler, C. A., and Miller, W. D. (2016). Spatial scales of optical variability in the coastal ocean: implications for remote sensing and *in situ* sampling. *J. Geophys. Res. Oceans* 121, 4194–4208. doi:10.1002/2016JC011767

Otterman, J., and Fraser, R. S. (1979). Adjacency effects on imaging by surface reflection and atmospheric scattering: cross radiance to zenith. *Appl. Opt.* 18, 2852–2860. doi:10.1364/AO.18.002852

Pahlevan, N., Mangin, A., Balasubramanian, S. V., Smith, B., Alikas, K., Arai, K., et al. (2021). Acix-aqua: a global assessment of atmospheric correction methods for landsat-8 and sentinel-2 over lakes, rivers, and coastal waters. *Remote Sens. Environ.* 258, 112366. doi:10.1016/j.rse.2021.112366

Pitarch, J., Talone, M., Zibordi, G., and Groetsch, P. (2020). Determination of the remote-sensing reflectance from above-water measurements with the 3c model: a further assessment. *Opt. Express* 28, 15885–15906. doi:10.1364/OE.388683

Qin, P., Simis, S. G., and Tilstone, G. H. (2017). Radiometric validation of atmospheric correction for meris in the baltic sea based on continuous observations from ships and aeronet-oc. *Remote Sens. Environ.* 200, 263–280. doi:10.1016/j.rse.2017.08.024

Román, M. O., Schaaf, C. B., Woodcock, C. E., Strahler, A. H., Yang, X., Braswell, R. H., et al. (2009). The MODIS (collection V005) BRDF/albedo product: assessment of spatial representativeness over forested landscapes. *Remote Sens. Environ.* 113, 2476–2498. doi:10.1016/j.rse.2009.07.009

Ruddick, K. G., Voss, K., Boss, E., Castagna, A., Frouin, R., Gilerson, A., et al. (2019). A review of protocols for fiducial reference measurements of water-leaving radiance for validation of satellite remote-sensing data over water. *Remote Sens.* 11, 2198. doi:10.3390/rs11192198

Ryan, J. C., Hubbard, A., Irvine-Fynn, T. D., Doyle, S. H., Cook, J. M., Stibal, M., et al. (2017). How robust are *in situ* observations for validating satellite-derived albedo over the dark zone of the Greenland ice sheet? *Geophys. Res. Lett.* 44, 6218–6225. doi:10.1002/2017GL073661

Salama, M. S., Spaias, L., Poser, K., Peters, S., and Laanen, M. (2022). Validation of sentinel-2 (MSI) and sentinel-3 (OLCI) water quality products in turbid estuaries using fixed monitoring stations. *Front. Remote Sens.* 2. doi:10.3389/frsen.2021.808287

Salama, M. S., and Stein, A. (2009). Error decomposition and estimation of inherent optical properties. *Appl. Opt.* 48, 4947–4962. doi:10.1364/AO.48.004947

Salama, M. S., and Su, Z. (2011). Resolving the subscale spatial variability of apparent and inherent optical properties in ocean color match-up sites. *IEEE Trans. Geoscience Remote Sens.* 49, 2612–2622. doi:10.1109/TGRS.2011.2104966

Siegel, D. A., Wang, M., Maritorena, S., and Robinson, W. (2000). Atmospheric correction of satellite ocean color imagery: the black pixel assumption. *Appl. Opt.* 39, 3582–3591. doi:10.1364/AO.39.003582

Simis, S., Jackson, T., Jordan, T., Peters, S., and Ghebrehiwot, S. (2022). *Monda: monocle data analysis python package: so-rad*. Available at: https://github.com/monocle-h2020/MONDA.

Simis, S. G. H., and Olsson, J. (2013). Unattended processing of shipborne hyperspectral reflectance measurements. *Remote Sens. Environ.* 135, 202–212. doi:10.1016/j.rse.2013.04.001

Spyrakos, E., O'Donnell, R., Hunter, P. D., Miller, C., Scott, M., Simis, S. G. H., et al. (2018). Optical types of inland and coastal waters. *Limnol. Oceanogr.* 63, 846–870. doi:10.1002/lno.10674

Wang, M., Son, S., and Shi, W. (2009). Evaluation of MODIS SWIR and NIR-SWIR atmospheric correction algorithms using seabass data. *Remote Sens. Environ.* 113, 635–644. doi:10.1016/j.rse.2008.11.005

Warren, M. A., Simis, S. G. H., Martinez-Vicente, V., Poser, K., Bresciani, M., Alikas, K., et al. (2019). Assessment of atmospheric correction algorithms for the sentinel-2a multispectral imager over coastal and inland waters. *Remote Sens. Environ.* 225, 267–289. doi:10.1016/j.rse.2019.03.018

Wright, A., and Simis, S. G. H. (2021). *Construction of the solar-tracking radiometry platform (so-rad)*. doi:10.5281/zenodo.4485805

Yenilmez, F., Düzgün, S., and Aksoy, A. (2014). An evaluation of potential sampling locations in a reservoir with emphasis on conserved spatial correlation structure. *Environ. Monit. Assess.* 187, 4216. doi:10.1007/s10661-014-4216-5

Yoder, J. A., McClain, C. R., Blanton, J. O., and Oeymay, L.-Y. (1987). Spatial scales in czcs-chlorophyll imagery of the southeastern u.s. continental shelf. *Limnol. Oceanogr.* 32, 929–941. doi:10.4319/lo.1987.32.4.0929

Zibordi, G., Kwiatkowska, E., Mélin, F., Talone, M., Cazzaniga, I., Dessailly, D., et al. (2022). Assessment of OLCI-A and OLCI-B radiometric data products across european seas. *Remote Sens. Environ.* 272, 112911. doi:10.1016/j.rse.2022.112911

Zibordi, G., Mélin, F., Berthon, J.-F., Holben, B., Slutsker, I., Giles, D., et al. (2009). Aeronet-OC: a network for the validation of ocean color primary products. *J. Atmos. Ocean. Technol.* 26, 1634–1651. doi:10.1175/2009JTECHO654.1

frontiers | Frontiers in Remote Sensing

TYPE Original Research
PUBLISHED 20 November 2023
DOI 10.3389/frsen.2023.1285800

Check for updates

OPEN ACCESS

EDITED BY
Agnieszka Bialek,
National Physical Laboratory,
United Kingdom

REVIEWED BY
Dmitry Efremenko,
German Aerospace Center (DLR),
Germany
Raymond Soffer,
National Research Council Canada
(NRC), Canada
Andreas Hueni,
University of Zurich, Switzerland

*CORRESPONDENCE
Sebastian Schunke,
sebastian.schunke@rayference.eu

RECEIVED 30 August 2023
ACCEPTED 30 October 2023
PUBLISHED 20 November 2023

CITATION
Schunke S, Leroy V and Govaerts Y (2023), Retrieving BRDFs from UAV-based radiometers for fiducial reference measurements: caveats and recommendations.
Front. Remote Sens. 4:1285800.
doi: 10.3389/frsen.2023.1285800

COPYRIGHT
© 2023 Schunke, Leroy and Govaerts. This is an open-access article distributed under the terms of the Creative Commons Attribution License (CC BY). The use, distribution or reproduction in other forums is permitted, provided the original author(s) and the copyright owner(s) are credited and that the original publication in this journal is cited, in accordance with accepted academic practice. No use, distribution or reproduction is permitted which does not comply with these terms.

Retrieving BRDFs from UAV-based radiometers for fiducial reference measurements: caveats and recommendations

Sebastian Schunke *, Vincent Leroy and Yves Govaerts

Rayference SRL, Brussels, Belgium

Surface Bidirectional reflectance distribution function (BRDF) is a key intrinsic geophysical variable depending only on the characteristics of the observed medium. It is therefore the most suitable measurand to support the definition of fiducial reference measurements (FRM). Field acquisition of surface reflectance data relies on substantial assumptions and simplifications, often without accounting for their impact. For example, the BRDF is a theoretical concept and can never be measured in the field. In contrast, the hemispherical conical reflectance factor (HCRF), which is the measurand obtained during field campaigns, is impacted by all scene elements and is not intrinsic to the surface. This study analyses the impact of four parameters (atmospheric scattering, measurement device field of view cropping, acquisition duration, non-Lambertian reference panels) on HCRF estimation. Simulations are performed on a 3D vegetation scene, using the new radiative transfer model Eradiate. It is found that among the aforementioned parameters, atmospheric scattering alone leads to a relative root-mean-square error (RRMSE) of more than 10% between HCRF and reference Bidirectional reflectance factor (BRF).

KEYWORDS

fiducial reference measurement, UAV, BRDF, quality control, Earth observation

1 Introduction

Earth Observation (EO) aims at retrieving information about the state of the Earth system, including vegetation, sea, atmosphere, snow and ice covers and other surface types. The validation of the retrieved information requires independent knowledge about the Earth system, which is obtained through fiducial reference measurements (FRM) (Sterckx et al., 2020; Goyens et al., 2021). Dedicated test sites are set up for these various FRMs, including vegetated areas (Bouvet et al., 2019). Among these FRMs, surface reflectance is a key measurand used to characterize the state of the vegetation. Laboratory measurements of vegetation and surface properties, simulation of surrogate vegetative canopies and empirical models can provide useful approximations to real world surface reflectance (Jacquemoud and Baret, 1990). However, *in situ* measurements are the ultimate way to provide surface reflectance FRMs.

A variety of approaches for the acquisition of surface reflectance has been developed and employed over time (Sandmeier et al., 1995; Abdou et al., 2001; Grenzdörffer and Niemeyer, 2012). Surface samples can be measured in a laboratory setting, using photogoniometers, if the surface material allows for this approach. Samples of sand or concrete can be placed in laboratory measurement devices, since their surfaces are homogeneous even on relatively

small scales, and can be relocated without introducing changes to material properties influencing the retrieved reflectance (Viallefont-Robinet et al., 2019). The reflectance of a canopy however, can not easily be retrieved in a laboratory. Vegetated surfaces are usually highly inhomogeneous on the scales which are accessible to photogoniometers. Larger plants like bushes or trees cannot be placed under laboratory based photogoniometers at all.

To solve this, measurement devices have been developed which can be placed on or near the actual surface of interest and estimate surface reflectance *in situ*. Approaches using surface mounted radiometers deliver high precision measurements and dense sampling of the reflecting hemisphere (Painter et al., 2003). Those devices face difficulties of their own, however. Surface mounted devices can be hard to relocate and their proximity to the surface limits the applicability to highly inhomogeneous surfaces. Another approach, which uses radiometers deployed on unmanned aerial vehicles (UAVs) to estimate surface reflectance, has received a lot of attention lately (Grenzdörffer and Niemeyer, 2012; Burkart et al., 2015; Origo et al., 2020; Deng et al., 2021; Latini et al., 2021; Jurado et al., 2022). With the UAV's relatively small size and weight, the measurement setup can easily be relocated to any human accessible location on Earth and their flight elevation, on the order of magnitude of 100 m allows for reflectance retrievals in even the tallest vegetation settings, such as corn fields and mature forests.

Experimental protocols only provide access to the HCRF, while the BRF is a purely theoretical quantity. However, under specific experimental conditions on illumination and sensor, the HCRF can become a proxy to the BRF. Such conditions are only met in a laboratory setup, where the experiment can be restricted to a single collimated light source and a detector with very narrow field of view. In particular, UAV-based field measurements do not satisfy these conditions. Lighting from the sky adds a significant diffuse part to solar illumination and radiometers can employ large fields of view. However, few ground-level reflectance retrieval protocols acknowledge this fact (Origo et al., 2020) and many assume that the measured HCRF is a direct proxy to the BRF.

This study analyses under which conditions the retrieved HCRF deviates the most from the desired BRF. This analysis relies on UAV observations simulated with Eradiate, a state-of-the-art 3D radiative transfer model. Section 2 discusses why BRF should be considered as a measurand for surface reflectance FRM instead of HCRF. For that purpose, a set of parameters is selected and its relevance for this objective is discussed (Section 3). These parameters are combined into a set of experimental scenarios, described in Section 4. Section 5 explains how UAV simulations are performed using Eradiate. Results of the simulation campaign are presented and subsequently discussed in Section 6. Finally, Section 8 features recommendations for future attempts at estimating the BRDF of a surface from *in situ* measurements.

2 Surface reflectance FRM

The acquisition and elaboration of FRM is a key aspect of calibration and validation (Cal/Val) activities. FRMs provide a suite of independent, fully characterized and traceable ground measurements that follow the guidelines outlined by the Quality Assurance framework for Earth Observation defined by the Committee on Earth Observation Satellites (CEOS) (Coll et al., 2019). Surface reflectance is however a loose concept that needs first to be defined following metrological standards (Nicodemus et al., 1977). This requires selecting a measurand that depends only on the state of the surface.

Among all the reflectance quantities defined by Nicodemus et al. (1977), only the bidirectional reflectance distribution function (BRDF), directional hemispherical reflectance (DHR) and bihemispherical reflectance (BHR) are intrinsic to the surface—the DHR and BHR being easily recoverable from the BRDF. However, using the BRDF as the measurand is impracticable for field measurements for two reasons. Firstly, reflected radiance can only be measured within a solid angle of finite size, i.e., a cone. Secondly, it is not possible to discriminate the unscattered (direct) and scattered (diffuse) downwelling surface radiation. Consequently, experimentally accessible reflectance quantities are integrated over illumination directions, i.e., the HCRF and BHR (Schaepman-Strub et al., 2006; Milton et al., 2009).

Using the HCRF as surface reflectance FRM leads to some limitations as this measurand depends on the states of both the surface and atmosphere. Interpreting it might therefore be challenging. This study focuses on the uncertainty resulting from the use of HCRF as a proxy for *in situ* BRDF retrievals. The BRDF is defined as (Nicodemus et al., 1977)

$$f_r\left(\theta_i, \varphi_i, \theta_r \varphi_r\right) = \frac{\mathrm{d}L_r\left(\theta_i, \varphi_i, \theta_r \varphi_r, E_i\right)}{\mathrm{d}E_i\left(\theta_i, \varphi_i\right)} \tag{1}$$

where $\mathrm{d}L_r$ is the reflected radiance, and $\mathrm{d}E_i$ is the incoming irradiance. It depends on the zenith and azimuth angles (θ_i and φ_i) of the incoming irradiance, and on the zenith and azimuth angles (θ_r and φ_r) of the reflected radiance. Closely related to the BRDF, expressed in SR^{-1}, is the dimensionless bidirectional reflectance factor BRF, defined as the ratio for the BRDF by the reference BRDF of a perfectly reflecting Lambertian surface (equal to $1/\pi$):

$$R_{\mathrm{BRF}}\left(\theta_i, \varphi_i, \theta_r \varphi_r\right) = \pi f_r\left(\theta_i, \varphi_i, \theta_r \varphi_r\right). \tag{2}$$

As infinitesimal directional observations are not possible, only the biconical reflectance factor (BCRF)

$$R_{\mathrm{BCRF}}\left(\omega_{ill}, \omega_{obs}\right) = \frac{\pi}{\Omega_{ill}\Omega_{obs}} \int_{\Omega_{ill}} \int_{\Omega_{obs}} f_r\left(\theta_i, \varphi_i, \theta_r \varphi_r\right) \mathrm{d}\Omega_i \mathrm{d}\Omega_r, \tag{3}$$

where Ω_{ill} and Ω_{obs} are the finite solid angles of the cones of illumination and observation, can be measured. The BDRF is integrated over finite solid angles Ω_{ill} and Ω_{obs} for illumination and observation directions and averaged by dividing by those same solid angles. The integration measure Ω is the projected solid angle and is defined as

$$\Omega = \int \mathrm{d}\Omega = \int \cos\theta \mathrm{d}\omega \tag{4}$$

Equation 3 applies for illumination only originating from illumination direction ω_i. In the field, incident irradiance originates from multiple directions, as a result of atmospheric scattering. Consequently, it is not possible to separate the incident irradiance contribution originating from ω_i from all other incident directions. This leads to the definition of the final

quantity used in this study, the hemispherical-conical reflectance factor (HCRF), defined as

$$R_{\mathrm{HCRF}}(2\pi, \omega_{obs}) = \frac{1}{\Omega_{obs}} \int_{2\pi} \int_{\Omega_{obs}} f_r(\theta_i, \varphi_i, \theta_r \varphi_r) \mathrm{d}\Omega_r \mathrm{d}\Omega_i \quad (5)$$

by integrating the BRDF over all incident directions ω_i and over a finite solid angle Ω_{obs} for the outgoing directions.

Importantly, an HCRF (Eq. 5) estimate can, under specific conditions, be used to retrieve the BRF (Eq. 2) of a surface. For this to be possible, the incident radiance field must cover a single direction and the observation geometry must cover a single direction: only then the $\mathrm{d}E_i$ and $\mathrm{d}L_r$ terms of Eq. 1 become experimentally accessible.

3 Review of the parameters affecting HCRF

3.1 Approach

Different types of devices have been developed to acquire HCRF in the field [e.g., (Sandmeier et al., 1995; Abdou et al., 2001; Grenzdörffer and Niemeyer, 2012)]. This study focuses on the acquisition of surface HCRFs using UAV-borne radiometers. The UAV-based approach is seen as the most relevant, as it is highly flexible and can be employed in many places and under a variety of conditions. Acquiring the HCRF of a region of interest with a UAV is, by nature, a process which depends not only on the target surface alone, but is always a combined observation of the surface and the atmosphere. It is therefore of highest importance to identify all surface and atmosphere related parameters as well as those of the measurement apparatus and to quantify their influence on the HCRF acquisition. In the following, we distinguish dependent parameters (which depend on the measurement technique) and independent parameters (which are only determined by the observed scene).

The general approach is to identify the parameters that critically influence the difference between the desired measurand, i.e., the surface BRF as expressed by Eq. 2, and the HCRF, the proxy measurand used in the field defined by Eq. 5. To keep the focus of the study clear, a series of parameters directly related to UAV hardware have been omitted such as the positioning and pointing accuracy of the measurement device, radiometric noise and image post-processing. There is abundant literature, covering different aspects of airborne reflectance retrieval methods (Miura and Huete, 2009; Yusoff et al., 2017; Hutton et al., 2020; Maguire et al., 2021). Since this study is concerned with acquiring reflectance based surface properties, the spectral sensitivity of the sensor was also omitted.

3.2 Measurement dependent parameters

3.2.1 Field of view (FOV)

The definition of the BRF implies an infinitesimal FOV for the recording sensor. Real sensors can only ever approximate this behavior. Typical radiometers or cameras used for field campaigns have a FOV reaching up to 30° (Pan et al., 2020; Li et al., 2021a; Li et al., 2021b). These values are unsuitable to accurately resolve the back scattering reflectance hotspot typical of vegetated surfaces, which is much narrower than that.

3.2.2 UAV flight duration

The multi-directional acquisition of radiometric data by means of a UAV flight requires time, during which the position of the Sun in the sky changes. Similar to atmospheric scattering, the changing celestial position of the Sun during the acquisition process undermines the assumption under which the incoming radiation is unidirectional.

3.2.3 Calibrated radiometric reference panel

According to Eq. 1, reflectance factors are based on the ratio of reflected radiance and incident irradiance. For practical reasons, the irradiance is not measured with an upward pointing irradiance sensor. Instead, a surface with reflectance close to 100% and close to Lambertian scattering properties, referred to as calibrated reference panel (CRP), is placed horizontally, and its reflected radiance is used as a replacement for the irradiance. While CRPs are usually assumed to have a perfectly Lambertian reflectance equal to 100%, the materials used to manufacture them [e.g., Spectralon (Bruegge et al., 1993)] do not have such ideal properties, despite careful selection. Laboratory measurements show a clear directionality of the material's reflectance (Georgiev and Butler, 2008). Especially in conjunction with the celestial movement of the Sun, *in situ* measurements of the CRP will impact the accuracy of the radiometric calibration.

3.3 Measurement independent parameters

3.3.1 Atmospheric scattering

Radiation scattering by the atmosphere makes the incoming radiance field at the bottom of the atmosphere (BOA) more diffuse. This is in fundamental contradiction with the perfect directionality a true BRF retrieval through the proxy of the HCRF would require. In other words, the more the atmosphere scatters radiation at the BOA, the more diffuse the incoming radiance field at ground level, and the more the difference between R_{HCRF} and R_{BRF} increases. A thorough assessment of the impact of molecular (Rayleigh) and aerosol scattering is therefore of prime importance.

3.3.2 Omitted parameters

Since this study aims to illustrate the effects of the aforementioned parameters, other aspects of the simulation design are simplified. The parameters of the surface type and the Leaf area index (LAI) of the 3D vegetation are chosen such that the BRF shows a pronounced hotspot, but no specific type of vegetation is emulated. Finally, only a single type of vegetation is considered, which removes adjacency effects, due to different vegetation types entering the FOV of the sensor and multiple scattering of radiation between the neighboring surface and the atmosphere.

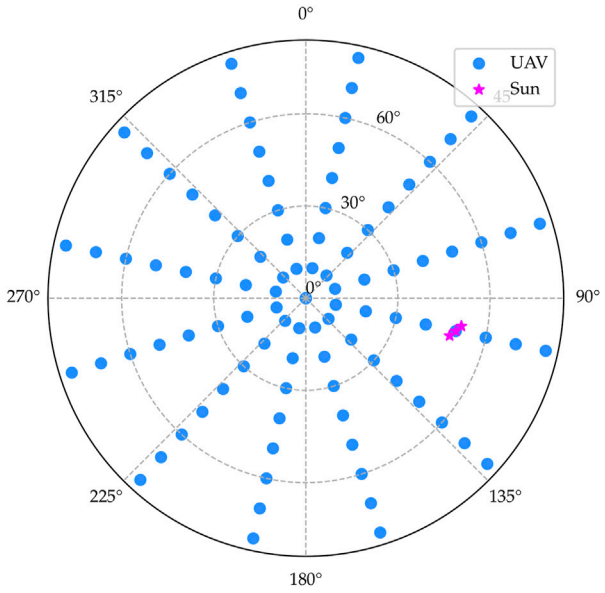


FIGURE 1
Polar plot of observation and illumination geometries.

4 Experimental setup

4.1 General approach

This study relies on simulations of a realistic 3D scene, which was designed to be independent of the radiative transfer model (RTM). To ensure this, a set of simplifying assumptions were made during scene design. The scene is assumed to be translationally invariant and flat. Additionally, the simulated atmosphere is assumed to consist of discrete homogeneous layers of infinite horizontal extent and homogeneous optical properties. The value ranges for the various parameters of the experimental plan are determined in the subsequent sections.

4.2 Choice of parameter values

4.2.1 Field of view

Two values are used for the FOV parameter: in the narrow setting, the FOV is equal to 1°; in the wide setting, the FOV is equal to 30°. The wide setting is chosen based on the total FOV of typically employed sensors, while the narrow setting serves as an upper bound for approaches which treat the pixels in a multi pixel sensor individually (Pan et al., 2020; Latini et al., 2021).

4.2.2 UAV flight duration

The lower value in the range of the flight duration is an instantaneous acquisition with no change in illumination direction. For the upper value, flight patterns of the studies in related literature were investigated and a typical UAV flight duration to cover the hemisphere above a target area was found to take around 20 min (Pan et al., 2020; Latini et al., 2021). On 15 June 2023 10:15 a.m., in Brussels (location of the authors of this study) the Sun is located at around 50° zenith angle. To simulate the celestial movement of the Sun, three points with a temporal spacing of 20 min were chosen around this reference time. These three points are interpolated linearly, to approximate the continuous movement of the Sun. The corresponding illumination directions, given as (zenith, azimuth), are (48.39°, 104.61°), (50.0°, 102.36°), (51.48°, 100.17°). Figure 1 illustrates the observation and illumination geometries.

4.2.3 Atmospheric scattering

Atmospheric scattering is described by two components in this study. First, the molecular atmosphere, modelled using the US Standard atmospheric profile from 1976 (Rodgers, 1976), exhibits Rayleigh scattering. This contributes an aerosol optical thickness (AOT) at 0.55 µm of 0.1. Second, an aerosol layer is added to the atmosphere, which simulates typical aerosol situations in Central Europe. The aerosol distribution was extracted from version 3 of the MAC dataset (Kinne, 2019). The distribution is illustrated in Figure 2. For the AOT at 0.55 µm, the values 0.1 (typical of clear

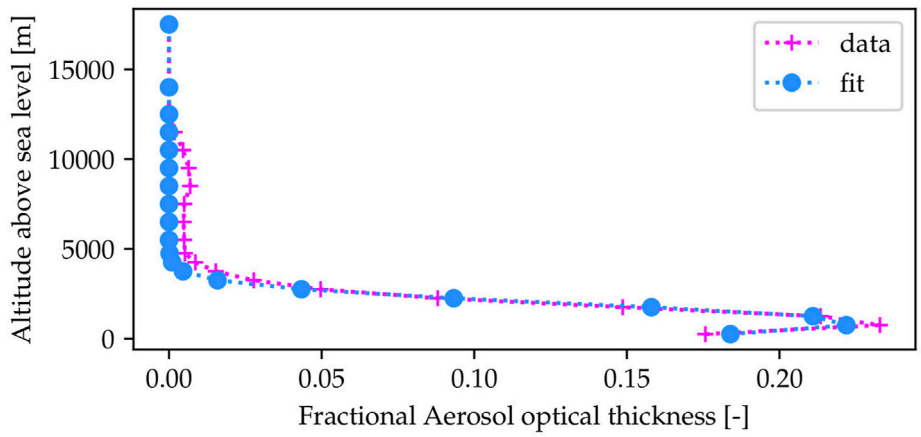


FIGURE 2
Vertical distribution of aerosols, extracted from version 3 of the MAC dataset. The blue line denotes a gaussian fit, with a mean value of 950 m and a standard deviation of 1,030 m.

TABLE 1 MVBP parameters obtained by fitting the model to measured Spectralon reflectance at 0.3 µm. Data in Georgiev and Butler (2008) shows minimal variation in the material BRDF between 0.3 µm and 0.55 µm.

Parameter	Value
ω	0.999
Θ	0.209
$r\Lambda$	4.339
χ_i	−0.060

days) and 0.3 [typical high value in Brussels (Sinyuk et al., 2020)] were chosen. Together with a setting that omits atmospheric scattering, this leads to three simulated cases.

4.2.4 Calibrated radiometric reference panel

Two cases are considered. In the first one the CRP is an ideal Lambertian surface with a BHR of 100%. In the second case, the CRP is a Spectralon panel with 99% BHR (Georgiev and Butler, 2008).

Unfortunately, Georgiev and Butler (2008) provide data only in the principal plane. To overcome this limitation, a fit of the MVBP model (Pinty et al., 1990) to the provided data is performed. The resulting parameters of the model are given in Table 1 and a comparison of the fit to the principal plane data is shown in Figure 3.

At this Sun zenith angle (SZA) value, the BRF of the CRP shows pronounced anisotropy, especially a strong tendency for forward scattering, as well as a slight back-scattering hotspot. Note that the reflectance at the nadir is not 99%. The assumption of 99% reflectance only holds if the total hemispherical reflectance is considered. This is critical, as this study adopts a measurement procedure from related literature (Latini et al., 2021). Here two measurements of the reference panel are taken, from the nadir, at the beginning and end of the 20-min flight duration. The retrieved reflectances are averaged. The actual nadir reflectance for this material is closer to 95%, which means, that unless special care is taken and the actual reflectance value is considered, this measurement approach will overestimate reflectance in the field.

4.3 Illumination

Sun displacement in the sky during the 20-min duration of the UAV flight is simulated by 3 points, shown in Figure 1. To approximate the continuous displacement of the Sun, its position is interpolated linearly between those three fixed points. For all simulations that do not consider the Sun's movement, the central point (50.0, 0.0) is used for the illumination direction.

4.4 Vegetated surface

The surface in this study is designed in two parts, the soil and a layer of vegetation. The soil is modelled using Lambertian scattering, with a reflectance of 0.1 at 0.55 µm. The vegetation layer is created with a procedural model, which approximates grass (Govaerts, 1995). The individual blades of grass are modelled using bilambertian scattering, with a reflectance of 0.14 and a transmittance of 0.09 at 0.55 µm. The vegetated surface extends 40 m in all directions, which ensures, that the entire visible surface is covered in vegetation for all simulated geometries. Figure 4 shows the grass model rendered from both a very short and a very long distance.

4.5 UAV observation

To acquire the surface's reflectance field, the hemisphere of outgoing directions is sampled every 10° for the zenith angles and 30° for the azimuth angles (Pan et al., 2020; Latini et al., 2021). These sampling densities correspond to 9 points along the viewing zenith angle (VZA) dimension and 12 points along the viewing azimuth angle (VAA) dimension. The sensor is pointed at the same location in the vegetated surface for all simulations and the footprint therefore changes with viewing geometry. Figure 1 illustrates the

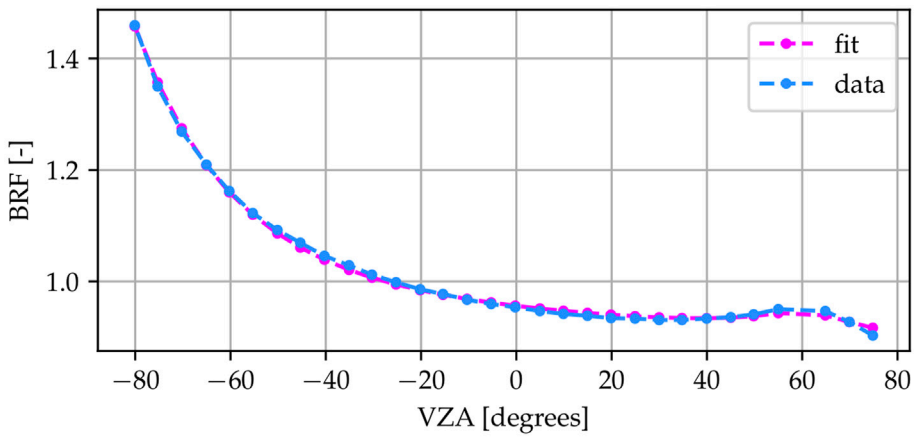


FIGURE 3
The principal plane BRF of the best fit of the MVBP model to the simulated reference panel data for a SZA value of 60°. Negative VZA values correspond to forward scattering. The BRF shows a strong tendency for forward scattering. Note that the BRF at the nadir is not 99%.

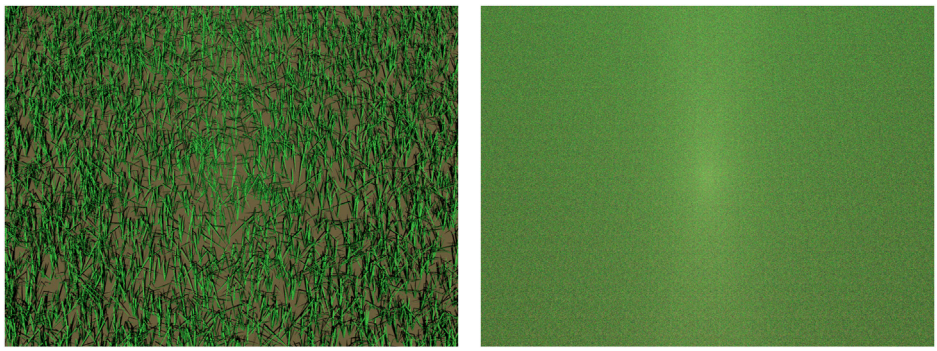


FIGURE 4
The grass surface rendered with a 20° FOV from a (left) 3 m and (right) 120 m distance, without an atmosphere. The solar zenith angle is equal to 50° and the camera points in the back scattering direction. The 120 m-distance view shows the back scattering hotspot, very visible due to the absence of an atmosphere in these simulations. The grass is created procedurally, with parametrizable distributions for the number of segments to each blade and the angle between the segments. Tufts, made up of several blades, are scattered randomly on the surface. Created with eradiate.eu.

measurement geometries as well as the positions of the Sun over the 20-min period mentioned above.

4.6 Reference case

The simulated UAV observations, in which the HCRF is retrieved, are compared to a reference case in which access to the true BRF (Eq. 2) of the vegetated surface describe in Section 4.4 is guaranteed. This reference BRF, denoted REF in the following, is the quantity we want to have a proxy for through the HCRF. It is obtained through a simulation under ideal conditions, that is perfectly directional illumination at 50° zenith and 0° azimuth, in the absence of a participating medium and using a perfectly directional sensor.

4.7 Parameter combinations

The combinations of the four parameters chosen for this study (FOV, UAV flight duration, CRP, atmospheric scattering), lead to a total number of 24 simulated scenarios plus the reference BRF simulation. Since the combination of measured CRP and instantaneous acquisition is omitted, the number of scenarios reduces to 18. To help identify the different scenarios, each parameter's values were assigned letters and each scenario is denoted by a combination of four letters.

Table 2 lists all parameter combinations and their respective shorthand. For further clarification on how the shorthand names are composed, Figure 5 details an example. For example, the scenario in which the parameters are closest to the reference case described in Section 4.6, with Lambertian CRP, static solar position, narrow FOV and no atmosphere would have a shorthand of LINN. The scenario in which the parameters are furthest from the reference case, with a Spectralon measured CRP, moving Sun, a wide FOV and a thick atmosphere would have a shorthand of MRWH. All possible combinations of the parameters were simulated. The only exception is the combination of the non-Lambertian CRP at instantaneous retrieval. The reason for simulating the non-Lambertian CRP is to assess the influence of the variation in reflectance due to the changing illumination across the time of flight of the UAV.

5 Simulation execution

5.1 The eradiate radiative transfer model

Simulations were performed with the Eradiate radiative transfer model (RTM), an open-source 3D Monte Carlo ray-tracing model, which supports explicit 3D geometry and vegetation as well as complex multi-component atmospheric models (Leroy et al., 2022). Its comprehensive Python interface makes it ideally suited to simulate a set of varying scenes with changing parameters such as the campaign described here.

5.2 Reference case simulation

To simulate the reference case, defined in Section 4.6, the reflected radiance is computed with zenith and azimuth angle steps of 1°. The irradiance from the Sun is known for the simulation and can therefore be used to compute the BRF as defined in Eqs 1, 2, as no atmospheric scattering and absorption are accounted for. Eradiate automates this process and outputs the BRF directly.

5.3 UAV observations

As mentioned in Section 3.2.3, reflectance values are computed as the ratio between the observed radiance reflected by the scene and the CRP. The reflectance is defined as

$$R_{\mathrm{HCRF}} = \frac{L_{\mathrm{veg}}}{L_{\mathrm{CRP}}} \tag{6}$$

where L_{veg} is the reflected radiance from the vegetated surface and L_{CRP} is the reflected radiance from the CRP. This approach can be motivated

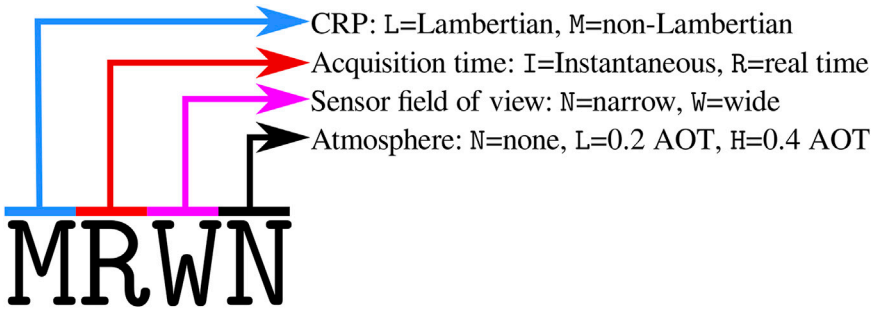


FIGURE 5
Shorthand notations for simulated scenarios. The first position describes the CRP variants, where L denotes the Lambertian CRP and M denotes the non-Lambertian CRP. The second position holds information on the acquisition time. Here, I denotes instantaneous acquisition, while R denotes real-time acquisition. The third position describes the sensor FOV, where N denotes a narrow FOV and W denotes a wide FOV. Finally, the fourth position describes the atmosphere. Here N denotes the absence of atmosphere, L denotes an atmosphere with an AOT of 0.2 and H denotes an atmosphere with an AOT of 0.4.

TABLE 2 Shorthand notations for the 18 simulated scenarios and their parameter combinations. The fist letter denotes the type of reference surface, the second letter denotes the acquisition time, the third letter denotes the measurement device's FOV and the fourth and final letter denotes the type of atmospheric scattering.

Atmosphere	FOV	Lambertian CRP		Spectralon CRP	
		instant	real time	instant	real time
none	1°	LINN	LRNN	—	MRNN
	30°	LIWN	LRWN	—	MRWN
light	1°	LINL	LRNL	—	MRNL
	30°	LIWL	LRWL	—	MRWL
heavy	1°	LINH	LRNH	—	MRNH
	30°	LIWH	LRWH	—	MRWH

from Eq. 1 directly. For individual incident and exitant directions the derivative becomes the ratio. Under the assumption, that the CRP reflects light in a perfectly Lambertian manner, the reflected radiance from the panel can be identified as the incident irradiance in the BRDF definition.

The CRP is represented by a square shape of 1 m squared, with the scattering properties of either the fitted MVBP model (Section 4.2.4) or a Lambertian model.

The UAV observations are simulated using a sensor that emulates a multi-pixel perspective camera, positioned in the scene and pointing towards the ground. Since the FOV is fixed, the surface area which is visible in the rendered image changes with the sensor's position. The multi-pixel images are averaged to produce one radiance value for the chosen observation geometry. This emulates a radiometer with a finite FOV, which records only one value. Two advantages of this approach are that the pixels lead to a stratification of the samples across the sensor plane and that the recorded radiance can be filtered by pixels. The former reduces variance, while the latter allows for cropping of the image to exclude regions of unwanted radiance, such as radiance entering the sensor directly from the sky, which can occur at large values of VZA.

The fixed FOV of the sensor introduces a problem. In oblique observation geometries, radiance from unwanted directions, such as the sky, can enter the sensor. A possible solution to this issue is manual cropping of the images, to exclude contributions from undesired directions. However, in a simulated campaign, cropping can be automated, by creating a mask, which is applied to the images.

The mask for the canopy simulations is created by replacing the vegetated surface with a flat surface with 100% Lambertian reflectance and removing the atmosphere. This will yield an image, which records high radiance values everywhere, where there is vegegation in the original image and zero radiance for the sky. Figure 6 illustrates an oblique observation for the canopy and the corresponding simulated mask.

For the simulations of the CRP, the required cropping region is smaller. In this case, the mask is simulated by setting the reflectance of the soil and the canopy to zero and removing the atmosphere. The simulated image will show non-zero radiance values only for the pixels, which contain the CRP.

The deviation D_r of each scenario from the REF case is defined as the relative difference

$$D_{r,i} = \frac{R_{\mathrm{HCRF}} - R_{\mathrm{BRF}}}{R_{\mathrm{BRF}}} \tag{7}$$

where R_{BRF} and R_{HCRF} are defined by Eqs 2, 6. The overall deviation of the different scenarios from the REF case was quantified by using the relative root mean squared error between each scenario's results and the reference BRF:

$$\Delta_{\mathrm{RRMSE}} = 100 \cdot \sqrt{\frac{\sum_{i=0}^{n} (D_{r,i})^2}{n}} \tag{8}$$

6 Results

6.1 Reference case

The result of the simulations performed for the REF case are presented in Figure 7, which shows the R_{BRF} reference reflectance values defined in Eq. 7. This quantity is the surface FRM defined in Eq. 2.

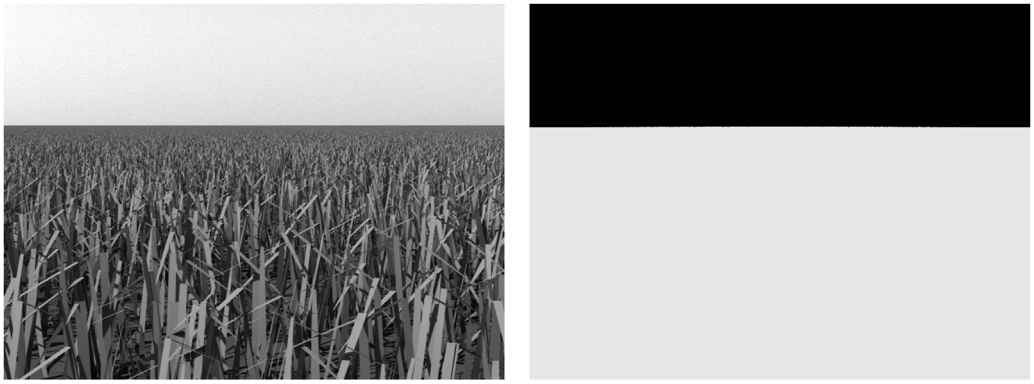


FIGURE 6
Left: A simulated canopy image, recorded at an oblique angle. A significant part of the image records radiance originating from scattering in the atmosphere. Right: A render of a white surface without an atmosphere. Note how the position of the horizon on the left coincides with separating line between the white and black areas on the right. The right image is used to mask the left and crop out unwanted radiance. Created with eradiate.eu

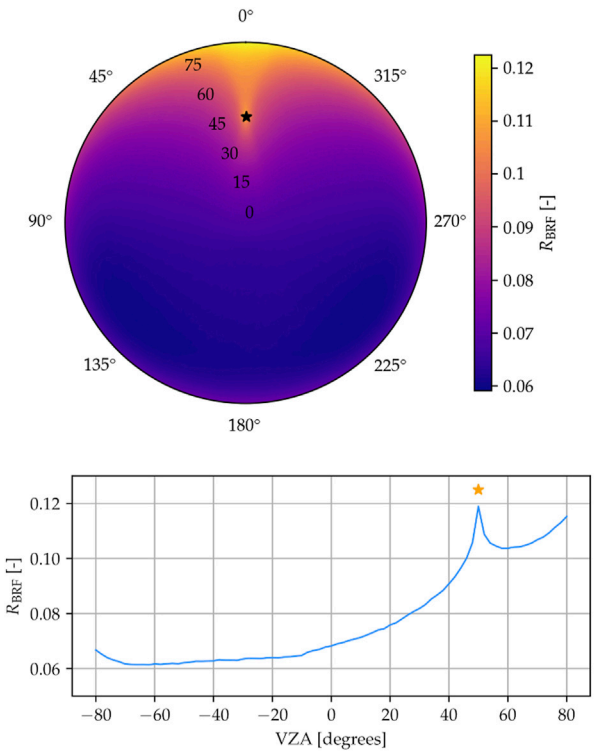


FIGURE 7
Simulated BRF for the REF case. Top: The full hemisphere. Bottom: The principal plane (negative azimuth values correspond to 180° viewing azimuth angle). Stars indicate the direction of illumination. The back scattering hotspot typical of vegetated surfaces is clearly visible.

The overall shape of the reflectance profile is dominated by the back-scattering hotspot (here at 50° zenith angle) typical of vegetated surfaces. The BRF shows high symmetry with respect to the principal plane, which is attributable to the statistical isotropy and uniformity of the vegetated cover.

The lower frame in Figure 7 shows the principal-plane transect of the overall reference BRF. As this typically contains the most distinct features of the BRF, the results of the simulated scenarios provided in the following sections will be similarly provided. However, all statistical quantities and relative differences between the scenarios and the reference are computed across all geometries listed in Section 4.5.

6.2 Narrow FOV (**N* scenarios)

The Lambertian CRP with a narrow FOV and instantaneous acquisition cases (LINN, LINL, LINH in Table 2) are presented first (Figure 8). The LINL and LINH cases illustrate the effects of atmospheric scattering on the HCRF values: increasing levels of atmospheric scattering result in a less intense hotspot in the profile.

The results for the scenarios with Lambertian CRP but non-zero acquisition time (LRN*) are shown in Figure 9. Visually these results differ only by a very small amount from those of the instantaneous acquisition scenarios (LIN*, Figure 8). Figure 10 shows the results for the MRN* scenarios, which include the non-Lambertian CRP. Compared to the LRN* and LIN* scenarios, the observed reflectance values are overall higher.

6.3 Wide FOV (**W* scenarios)

The different atmospheric variants for the wide FOV and otherwise ideal conditions, are shown in Figure 11. The high relative difference values in the back scattering direction suggest that simulations performed with such a wide FOV result in a poorly resolved hotspot. Quantitatively this results in an increased maximum D_r, which is higher than 13% for all cases, whereas it is below 5% for narrow field of view in the **N* scenarios.

Combining the wide FOV with the realistic flight duration yields the LRW* scenarios, which are shown in Figure 12. The changes in Δ_{RRMSE} and maximum D_r, compared to the instantaneous scenarios (LIW*) is small. While Δ_{RRMSE} decreases slightly, the maximum D_r increases.

Finally, the wide FOV scenarios with the non-Lambertian reference panel (MRW*) are shown in Figure 13. Between the

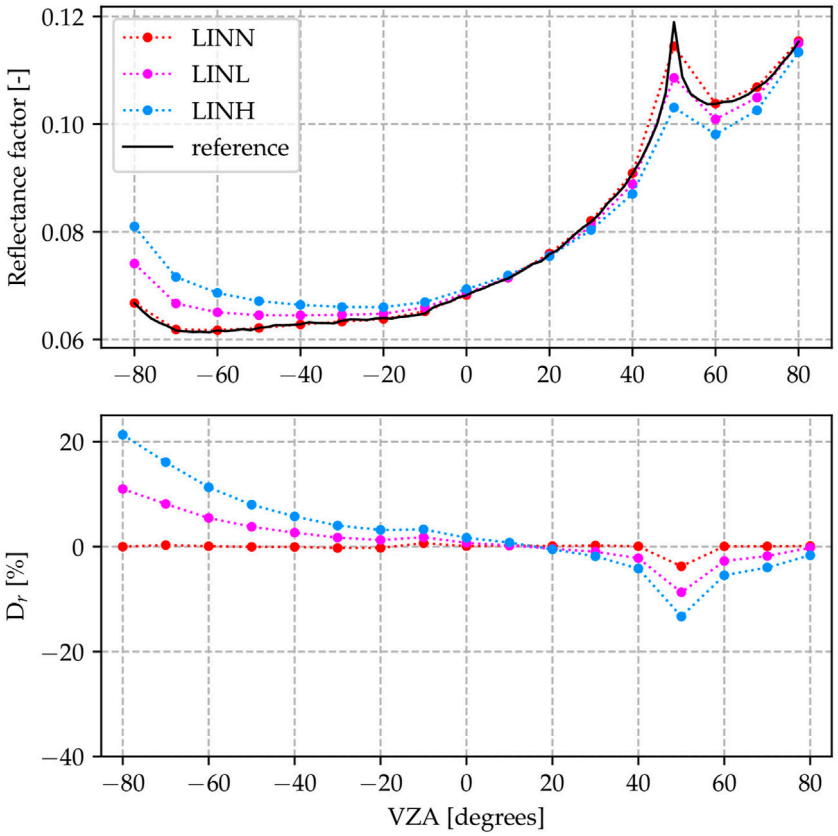


FIGURE 8
Results for the LIN* scenarios (Lambertian CRP, instantaneous acquisition and narrow FOV, varying atmospheric density). The LINN scenario matches the reference well, but the deviation increases with increasing atmospheric density.

LRW* scenarios and these, Δ_{RRMSE} and maximum $D_{r,i}$ increase for the no atmosphere scenario, but decrease significantly for the atmosphere scenarios.

Figures of the reflectances for all scenarios are available as Supplementary Material.

7 Discussion

As expected, the Δ_{RRMSE} is smallest for the LITN scenario (0.4%), because the conditions encountered in this scenario (Lambertian CRP, instantaneous acquisition, tight sensor FOV, no atmosphere) are most similar to the conditions under which the BRF of the REF case is simulated. The largest, appears for the MRWH (non-Lambertian CRP, non-zero time of flight, wide sensor FOV, heavy atmosphere) scenario (8.7%). The influence of various parameters is quantitifed by evaluating the change in mean RRMSE and maximum deviation when changing a single parameter (Table 3). For example, adding light atmosphere means, in terms of scenario abbreviations, ***N → ***L.

The measurement device's FOV is found to have a significant impact. Here the values of 1° and 30° FOV were simulated. While the former might be an overly idealized situation for a real measurement device, the latter is typical for reviewed field measurement campaigns (Li et al., 2021b; Pan et al., 2020; Li et al., 2021a). Although the mean increase in Δ_{RRMSE} when increasing the FOV is rather low at 0.4 percentage points, the maximum deviation increases by a significant amount (4.7 percentage points). In the individual cases it is found that a wide FOV under otherwise idealized conditions, the LIWN scenario, leads to a mean Δ_{RRMSE} of 1.3% with a maximum deviation of around 13%. A close look at Figure 11 reveals that a measurement device with such a large FOV performs poorly at recording the back-scattering hotspot of the surface, even when an idealized case with no atmosphere is considered. Figure 4 can assist in the interpretation of these results: On this image, which shows a wide FOV (20°) render of the surface, the back scattering hotspot is visible. A wide FOV observation is equivalent to averaging all pixels in this image, which results in pixels near the hotspot being blended with the pixels outside the hotspot; in other words, the overall measured value contains the hotspot signal, but is muted due to contributions from adjacent pixels. On the other hand, an observation with a narrow FOV is equivalent to considering only the central portion of the image, which, in practice, means restricting the contributions to the measurement to the near-hotspot pixels.

The largest contribution to bias between HCRF and BRF originates from the scattering of light in the atmosphere. The atmosphere parametrization used for these simulations includes a molecular component featuring Rayleigh scattering (0.1 optical thickness (OT) in the considered spectral band), to which is added an aerosol

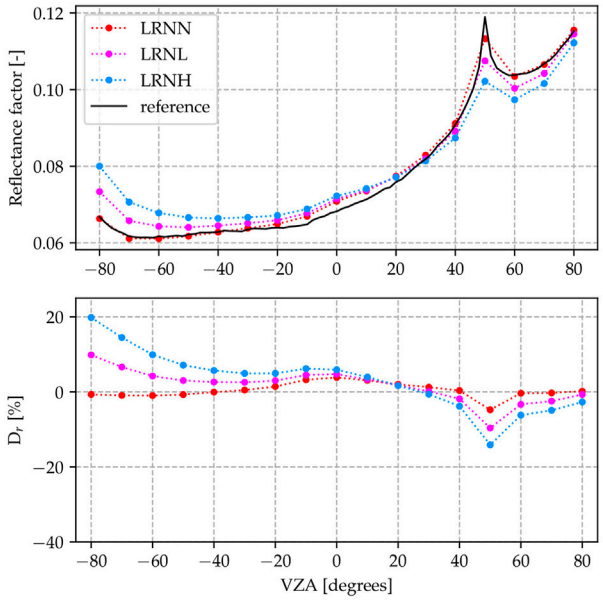


FIGURE 9
Results for the LRN* scenarios (Lambertian CRP, real acquisition time and narrow FOV, varying atmospheric density). The scenario data is lowered near the back-scattering hotspot, compared to the reference result. The difference to the reference increases with increasing atmospheric density.

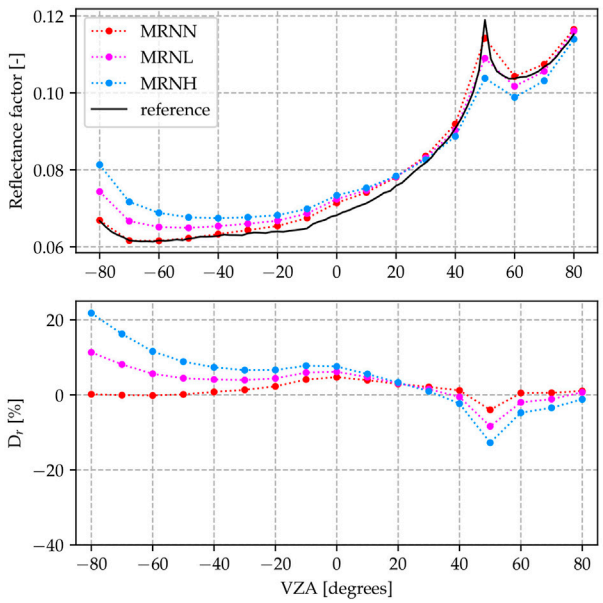


FIGURE 10
Results for the MRN* scenarios (non-Lambertian CRP, real acquisition time and narrow FOV, varying atmospheric density). Note the slight overall increase in values, as compared to the LRN* scenarios.

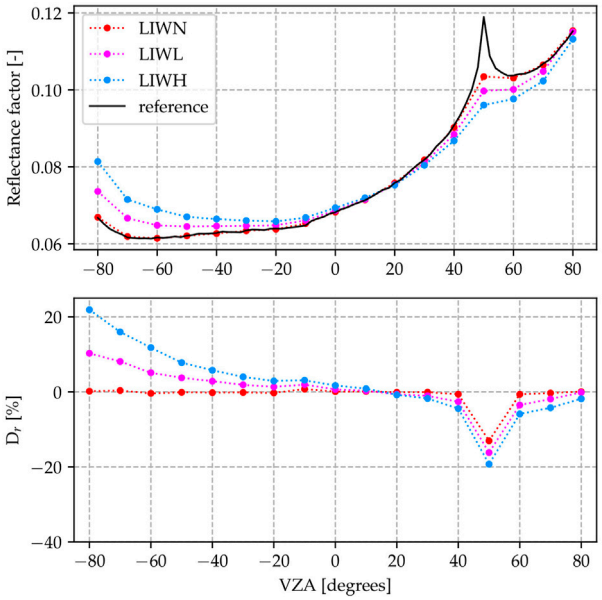


FIGURE 11
Results for the LIW* scenarios (Lambertian CRP, instantaneous acquisition and wide FOV, varying atmospheric density). The back-scattering hotspot is much less resolved, than in the reference result.

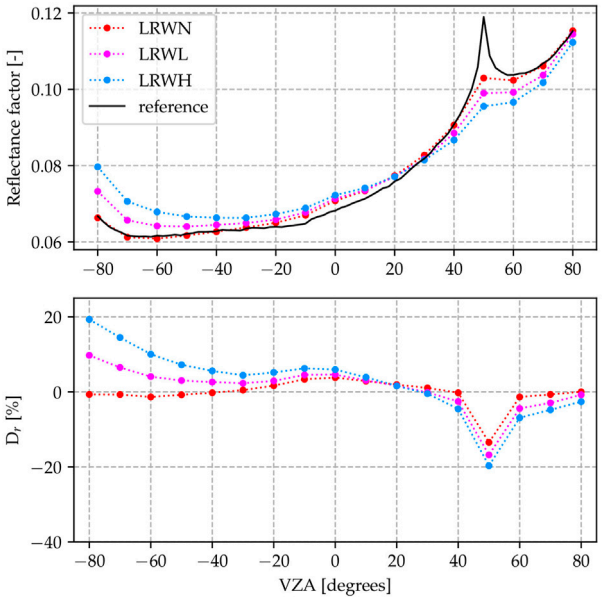


FIGURE 12
Results for the LRW* scenarios (Lambertian CRP, real acquisition time and wide FOV, varying atmospheric density). The back-scattering hotspot is much less resolved, than in the reference result. The difference to the reference result increases with atmospheric density.

component with an OT of 0.1 (***L scenarios) or 0.3 (***H scenarios), thus amounting for a total optical of 0.2 (***L scenarios) or 0.4 (***H scenarios). Already with a total OT of 0.2, typical of clear days, the mean Δ_{RRMSE} increases by 3.5 percentage points. With a total OT of 0.4, typical of more hazy days, the mean Δ_{RRMSE} increases by 7 percentage points. In the LINH scenario (ideal CRP, instantaneous acquisition,

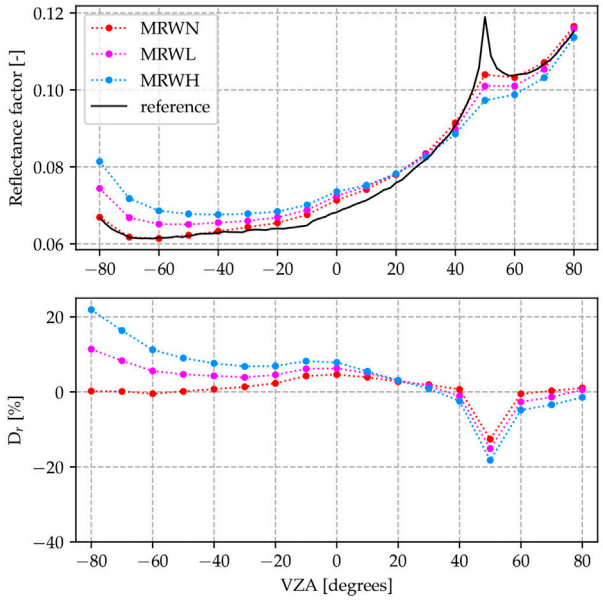


FIGURE 13
Results for the MRW* scenarios (non-Lambertian CRP, real acquisition time and wide FOV, varying atmospheric density). Note the slightly increased reflectance, compared to the LRW* scenarios. The back-scattering hotspot is much less resolved, than in the reference result. The difference to the reference case increases with atmospheric density.

narrow FOV, atmosphere with 0.4 OT), the HCRF significantly deviates from the reference BRF with a RRMSE of 7.6% and a maximum deviation of 21.3% recorded in the back scattering direction. In the LINL scenario (similar with 0.2 OT, typical of clear days), the RRMSE (4.2%) and maximum deviation (11%), recorded in the back scattering direction are still high.

The celestial movement of the Sun is found to have a minor influence on the difference between HCRF and BRF with a mean increase in Δ_{RRMSE} of 0.1 percentage points. Here, a look at the corresponding scenario LRTN, which uses idealized conditions aside from the solar movement, reveals a mean bias of 1.5% with a maximum deviation of 4.8%.

In terms of Δ_{RRMSE}, the biggest deviation of 8.7% appears at the MRWH scenario, which implements the least ideal conditions. The highest maximum deviation at 21.9% occurs in the MRWH and LIWH scenarios, which further emphasizes the importance of atmospheric scattering.

8 Conclusion and outlook

This study illustrates the challenges of surface BRF estimation from UAV-borne observations. As the BRF is a purely theoretical quantity, *in situ* measurements can only approximate it and the HCRF should be chosen as the more appropriate quantity. The analysis relies on simulated UAV observations over a grassland with the open-source 3D radiative transfer model Eradiate.

If bottom of atmosphere measurements are to be used as FRMs, being able to estimate the uncertainty of the retrieved surface reflectance is essential. The variables and parameters of such a measurement approach have been discussed and a subset of four parameters with high expected impact on the HCRF acquisition has been selected. For those four parameters, the atmosphere, the FOV of the measurement device, the celestial movement of the Sun and the non-Lambertian reflectance of reference surfaces, typical and realistic values were chosen based on a literature review.

In the presented experimental plan, the acquisition of the HCRF of a highly realistic scene is recreated under different conditions. The bias for each scenario, determined through comparison with a reference BRF of the scene, is computed and from all scenarios the mean effect of each parameter is extracted (See Table 3). In each row the effect of one parameter is given, with the parameter name in the first column and the corresponding shorthands in the second. Here the two letters in bold print denote the parameters which were fixed, while capital X denotes a placeholder, as all variants were averaged. For example XXXN means LINN, LIWN, LRNN, LRWN, MRNN, and MRWN.

Based on the results of this simulation campaign, we issue recommendations for the preparation of future efforts aiming at retrieving BRF records through *in situ* HCRF retrievals: (*i*) perform the measurements at a date and time when atmospheric conditions are most favorable, i.e., diffuse sky radiation is as low as possible, and (*ii*) crop images acquired by UAVs and used for HCRF estimation to keep the effective FOV as small as possible. Recommendation (*i*) ensures that the illumination is as close as possible to an ideal directional light source, while recommendation (*ii*) ensures that the sensor is as close as possible to a directional radiance meter. Although meeting the ideal conditions of the reference BRF simulation case (perfectly directional illumination and sensor) is impossible, based upon our results this approach will minimize the magnitude of the issues encountered when attempting to use field HCRF estimations as a proxy for surface BRFs.

Future developments could include the design of a protocol to retrieve the intrinsic surface BRF from bottom of atmosphere HCRF measurements, based on available data characterizing the

TABLE 3 Average increase in Δ_{RRMSE} and maximum deviation for all parameters.

Parameter	Abbreviations	Δ_{RRMSE} change	Max D_r change
Light atmosphere	XXX**N** → XXX**L**	1.6% → 4.4%	8.7% → 13.4%
Heavy atmosphere	XXX**N** → XXX**H**	1.6% → 7.9%	1.6% → 21.1%
Field of view	XX**N**X → XX**W**X	4.4% → 4.8%	12.0% → 16.7%
Solar movement	X**I**XX → X**R**XX	3.7% → 3.8%	13.6% → 13.6%
Spectralon reference	**L**XXX → **M**XXX	4.3% → 5.2%	14.1% → 14.6%

atmosphere at the date and time of the acquisition. This should be facilitated if the aforementioned recommendations are applied.

Data availability statement

The raw data supporting the conclusion of this article will be made available by the authors, without undue reservation.

Author contributions

SS: Software, Visualization, Writing–original draft, Data curation, Investigation, Methodology. VL: Supervision, Writing–review and editing. YG: Conceptualization, Funding acquisition, Investigation, Methodology, Project administration, Writing–review and editing, Supervision.

Funding

The author(s) declare financial support was received for the research, authorship, and/or publication of this article. This project has received funding from the European Union's Horizon 2020 research and innovation programme under the grant agreement No. 101004242 (*Copernicus CAL/VAL Solution*).

Conflict of interest

Authors SS, VL, and YG were employed by Rayference SRL.

Publisher's note

All claims expressed in this article are solely those of the authors and do not necessarily represent those of their affiliated organizations, or those of the publisher, the editors and the reviewers. Any product that may be evaluated in this article, or claim that may be made by its manufacturer, is not guaranteed or endorsed by the publisher.

Supplementary material

The Supplementary Material for this article can be found online at: https://www.frontiersin.org/articles/10.3389/frsen.2023.1285800/full#supplementary-material

References

Abdou, W. A., Helmlinger, M. C., Conel, J. E., Bruegge, C. J., Pilorz, S. H., Martonchik, J. V., et al. (2001). Ground measurements of surface BRF and HDRF using PARABOLA III. *J. Geophys. Res. Atmos.* 106, 11967–11976. doi:10.1029/2000JD900654

Bouvet, M., Thome, K., Berthelot, B., Bialek, A., Czapla-Myers, J., Fox, N., et al. (2019). Radcalnet: a radiometric calibration network for earth observing imagers operating in the visible to shortwave infrared spectral range. *Remote Sens.* 11, 2401. doi:10.3390/rs11202401

Bruegge, C. J., Stiegman, A. E., Rainen, R. A., and Springsteen, A. W. (1993). Use of Spectralon as a diffuse reflectance standard for in-flight calibration of earth-orbiting sensors. *Opt. Eng.* 32, 805–814. doi:10.1117/12.132373

Burkart, A., Aasen, H., Alonso, L., Menz, G., Bareth, G., and Rascher, U. (2015). Angular dependency of hyperspectral measurements over wheat characterized by a novel uav based goniometer. *Remote Sens.* 7, 725–746. doi:10.3390/rs70100725

Coll, C., Niclòs, R., Puchades, J., García-Santos, V., Galve, J. M., Pérez-Planells, L., et al. (2019). Laboratory calibration and field measurement of land surface temperature and emissivity using thermal infrared multiband radiometers. *Int. J. Appl. Earth Observation Geoinformation* 78, 227–239. doi:10.1016/j.jag.2019.02.002

Deng, L., Chen, Y., Zhao, Y., Zhu, L., Gong, H.-L., Guo, L.-J., et al. (2021). An approach for reflectance anisotropy retrieval from UAV-based oblique photogrammetry hyperspectral imagery. *Int. J. Appl. Earth Observation Geoinformation* 102, 102442. doi:10.1016/j.jag.2021.102442

Georgiev, G. T., and Butler, J. J. (2008)., 7081. SPIE, 46–54. doi:10.1117/12.795931Brdf study of gray-scale spectralon*Earth Obs. Syst. XIII*

Govaerts, Y. M. (1995). A Model of light Scattering in three-dimensional plant canopies: a Monte Carlo ray tracing approach. *Ph.D. Thesis, université catholique de Louvain*. Ph.D. Thesis.

Goyens, C., De Vis, P., and Hunt, S. E. (2021). "Automated generation of hyperspectral fiducial reference measurements of water and land surface reflectance for the hypernets networks," in *2021 IEEE international geoscience and Remote sensing symposium IGARSS* (Germany: IEEE), 7920.

Grenzdörffer, G. J., and Niemeyer, F. (2012). Uav based brdf-measurements of agricultural surfaces with pfiffikus. In *Int. Archives Photogrammetry, Remote Sens. Spatial Inf. Sci. (Copernicus GmbH),*vol. XXXVIII-1-C22, 229–234. doi:10.5194/isprsarchives-xxxviii-1-c22-229-2011

Hutton, J. J., Lipa, G., Baustian, D., Sulik, J., and Bruce, R. W. (2020). High accuracy direct georeferencing of the altum multi-spectral uav camera and its application to high throughput plant phenotyping. *Int. Archives Photogrammetry, Remote Sens. Spatial Inf. Sci.* XLIII-B1-2020, 451–456. doi:10.5194/isprs-archives-XLIII-B1-2020-451-2020

Jacquemoud, S., and Baret, F. (1990). Prospect: a model of leaf optical properties spectra. *Remote Sens. Environ.* 34, 75–91. doi:10.1016/0034-4257(90)90100-z

Jurado, J. M., Jiménez-Pérez, J. R., Pádua, L., Feito, F. R., and Sousa, J. J. (2022). An efficient method for acquisition of spectral BRDFs in real-world scenarios. *Comput. Graph.* 102, 154–163. doi:10.1016/j.cag.2021.08.021

Kinne, S. (2019). The macv2 aerosol climatology. *Tellus B Chem. Phys. Meteorology* 71, 1623639–1623721. doi:10.1080/16000889.2019.1623639

Latini, D., Petracca, I., Schiavon, G., Niro, F., Casadio, S., and Del Frate, F. (2021). *UAV-based observations for surface BRDF characterization*. 8193–8196. doi:10.1109/IGARSS47720.2021.9554496

Leroy, V., Nollet, Y., Schunke, S., Misk, N., and Govaerts, Y. (2022). *Eradiate radiative transfer model*. doi:10.5281/zenodo.7224315

Li, L., Mu, X., Qi, J., Pisek, J., Roosjen, P., Yan, G., et al. (2021a). Characterizing reflectance anisotropy of background soil in open-canopy plantations using UAV-based multiangular images. *ISPRS J. Photogrammetry Remote Sens.* 177, 263–278. doi:10.1016/j.isprsjprs.2021.05.007

Li, W., Jiang, J., Weiss, M., Madec, S., Tison, F., Philippe, B., et al. (2021b). Impact of the reproductive organs on crop BRDF as observed from a UAV. *Remote Sens. Environ.* 259, 112433. doi:10.1016/j.rse.2021.112433

Maguire, M. S., Neale, C. M. U., and Woldt, W. E. (2021). Improving accuracy of unmanned aerial system thermal infrared remote sensing for use in energy balance models in agriculture applications. *Remote Sens.* 13, 1635. doi:10.3390/rs13091635

Milton, E. J., Schaepman, M. E., Anderson, K., Kneubühler, M., and Fox, N. (2009). Progress in field spectroscopy. *Remote Sens. Environ.* 113, S92–S109. doi:10.1016/j.rse.2007.08.001

Miura, T., and Huete, A. R. (2009). Performance of three reflectance calibration methods for airborne hyperspectral spectrometer data. *Sensors (Basel, Switz.* 9, 794–813. doi:10.3390/s90200794

Nicodemus, F. E., Richmond, J. C., Hsia, J. J., Ginsberg, I. W., and Limperis, T. (1977). *Geometrical considerations and nomenclature for reflectance*, 160. Gaithersburg, MD: NBS MONO. doi:10.6028/NBS.MONO.160

Origo, N., Gorroño, J., Ryder, J., Nightingale, J., and Bialek, A. (2020). Fiducial reference measurements for validation of sentinel-2 and proba-V surface reflectance products. *Remote Sens. Environ.* 241, 111690. doi:10.1016/j.rse.2020

Painter, T. H., Paden, B., and Dozier, J. (2003). Automated spectro-goniometer: a spherical robot for the field measurement of the directional reflectance of snow. *Rev. Sci. Instrum.* 74, 5179–5188. doi:10.1063/1.1626011

Pan, Z., Zhang, H., Min, X., and Xu, Z. (2020). Vicarious calibration correction of large FOV sensor using BRDF model based on UAV angular spectrum measurements. *J. Appl. Remote Sens.* 14, 027501. doi:10.1117/1.JRS.14.027501

Pinty, B., Verstraete, M. M., and Dickinson, R. E. (1990). A physical model of the bidirectional reflectance of vegetation canopies: 2. Inversion and validation. *J. Geoph. Res.* 95, 11767–11775. doi:10.1029/jd095id08p11767

Rodgers, C. D. (1976). Retrieval of atmospheric temperature and composition from remote measurements of thermal radiation. *Rev. Geophys. Space Phys* 14, 609–624. doi:10.1029/rg014i004p00609

Sandmeier, S., Sandmeier, W., Itten, K., Schaepman, M., and Kellenberger, T. (1995). The Swiss field-goniometer system (FIGOS). In *1995 International Geoscience and remote sensing Symposium, IGARSS '95. Quantitative remote Sensing for Science and applications*. vol. 3, 2078–2080. doi:10.1109/IGARSS.1995.524113

Schaepman-Strub, G., Schaepman, M., Painter, T., Dangel, S., and Martonchik, J. (2006). Reflectance quantities in optical remote sensing—definitions and case studies. *Remote Sens. Environ.* 103, 27–42. doi:10.1016/j.rse.2006.03.002

Sinyuk, A., Holben, B. N., Eck, T. F., Giles, D. M., Slutsker, I., Korkin, S., et al. (2020). The AERONET Version 3 aerosol retrieval algorithm, associated uncertainties and comparisons to Version 2. *Atmos. Meas. Tech.* 13, 3375–3411. doi:10.5194/amt-13-3375-2020

Sterckx, S., Brown, I., Kääb, A., Krol, M., Morrow, R., Veefkind, P., et al. (2020). Towards a european cal/val service for earth observation. *Int. J. Remote Sens.* 41, 4496–4511. doi:10.1080/01431161.2020.1718240

Viallefont-Robinet, F., Bacour, C., Bouvet, M., Kheireddine, M., Ouhssain, M., Idoughi, R., et al. (2019). Contribution to sandy site characterization: spectro-directional signature, grain size distribution and mineralogy extracted from sand samples. *Remote Sens.* 11, 2446. doi:10.3390/rs11202446

Yusoff, A. R., Ariff, M. F. M., Idris, K. M., Majid, Z., and Chong, A. K. (2017). Camera calibration accuracy at different uav flying heights. *Int. Archives Photogrammetry, Remote Sens. Spatial Inf. Sci.* XLII-2, 595–600. doi:10.5194/isprs-archives-XLII-2-W3-595-2017

frontiers | Frontiers in Remote Sensing

TYPE Original Research
PUBLISHED 21 December 2023
DOI 10.3389/frsen.2023.1307976

Check for updates

OPEN ACCESS

EDITED BY
Clemence Goyens,
Royal Belgian Institute of Natural Sciences, Belgium

REVIEWED BY
Hui Ying Pak,
Nanyang Technological University, Singapore
Thomas Jordan,
Plymouth Marine Laboratory, United Kingdom

*CORRESPONDENCE
Tristan Harmel,
tristan.harmel@magellium.fr

RECEIVED 05 October 2023
ACCEPTED 28 November 2023
PUBLISHED 21 December 2023

CITATION
Harmel T (2023), Apparent surface-to-sky radiance ratio of natural waters including polarization and aerosol effects: implications for above-water radiometry.
Front. Remote Sens. 4:1307976.
doi: 10.3389/frsen.2023.1307976

COPYRIGHT
© 2023 Harmel. This is an open-access article distributed under the terms of the Creative Commons Attribution License (CC BY). The use, distribution or reproduction in other forums is permitted, provided the original author(s) and the copyright owner(s) are credited and that the original publication in this journal is cited, in accordance with accepted academic practice. No use, distribution or reproduction is permitted which does not comply with these terms.

Apparent surface-to-sky radiance ratio of natural waters including polarization and aerosol effects: implications for above-water radiometry

Tristan Harmel*

Earth Observation Unit, Magellium Artal Group, Toulouse, France

Above-water radiometry (AWR) methods have been developed to provide "ground-truth" (or fiducial) measurements for calibration and validation of the water color satellite missions. AWR is also an important tool for environmental survey from dedicated field missions. Under clear sky, the critical step of AWR is to retrieve the water-leaving radiance from radiometric measurements of the upward radiance that also includes the reflection of the direct sunlight and diffuse skylight reflected by the wind ruffled water surface toward the sensor. In order to correct for the surface reflection, sky radiance measurements are performed and converted into surface radiance through a factor often called "sea surface reflectance factor" or "effective Fresnel reflectance coefficient". Based on theoretical and practical considerations, this factor was renamed *surface-to-sky radiance ratio*, R_{ss}, to avoid misuse of the term *reflectance* as often encountered in the literature. Vector radiative transfer computations were performed over the spectral range 350–1,000 nm to provide angular values of R_{ss} for a comprehensive set of aerosol loads and types (including maritime, continental desert and polluted models) and water surface roughness expressed in wave slope variances or in equivalent Cox-Munk wind speeds, for practical use. After separating direct and diffuse light components, it was shown that the spectral shape and amplitude of R_{ss} are very sensitive to aerosol load and type even for extremely low values of the aerosol optical thickness. Uncertainty attached to R_{ss} was computed based on propagation of errors made in aerosol and surface roughness parameters demonstrating the need to adapt the viewing geometry according to the Sun elevation and to associate concurrent aerosol measurements for optimal AWR protocols.

KEYWORDS

above-water radiometry, aerosol, water-leaving radiance, polarization, cal/val activities

1 Introduction

Optical remote sensing has become a critical tool to monitor oceanic, coastal or inland aquatic environments and their inherent ecosystems thanks to multispectral or hyperspectral measurements of the water-leaving radiance L_w (Werdell et al., 2018; Giardino et al., 2019). L_w is conceptually defined as the radiance exiting a water body in a given upward direction after transmission through the water-air interface (Mueller and Austin, 1995), which strictly does not include the radiance of the air-water interface (i.e., sky and Sun reflection on the water surface). Spectral L_w originates from light interaction with matter within the water

body and is therefore informative on the nature of the optically active water constituents (OAWC). A series of scientific algorithms, in particular the so-called atmospheric correction, must be applied to the raw satellite measurements in order to retrieve the water-leaving radiance which constitutes a small part of the total signal often dominated by the atmosphere and surface-reflected light. The overall process to retrieve the water-leaving radiance from space-sensors is therefore very sensitive to both the radiometric performance of the sensors (calibration) (Hu et al., 2001; Franz et al., 2007) and the optimality of the radiative transfer modeling and inverse problem methods (Gilerson et al., 2023). Since uncertainties accumulate from sensor calibration to retrieval algorithm application, quantitative evaluation of uncertainty and bias is of paramount importance to help minimize them for a beneficial exploitation of the L_w data for scientific or environmental monitoring activities.

For this purpose, field measurements are efficient tools provided that their own data quality is sufficiently high and that their attached uncertainties are metrologically quantified. Two different systems were installed for quality evaluation of the historical "ocean color" satellite sensors (e.g., MERIS, MODIS, SeaWiFS): in-water and above-water radiometric systems (Hooker et al., 2002; Zibordi et al., 2002). Both systems possess their own advantages and weaknesses regarding either the implementation in the field or data processing for retrieval of L_w at the exact water surface level (denoted as 0^+). For instance, retrieval of water-leaving radiance from in-water radiometric methods is very sensitive to extrapolation at 0^+ from the measured underwater profile of the upward radiance (Antoine et al., 2008; Hooker et al., 2013). It is worth noting that for turbid or highly absorbing waters, potentially encountered in coastal or lake environments, in-water methods are impracticable due to rapid loss of light (signal) with depth (e.g., within the first tens of centimeter). As for above-water system, the main issue is to remove the sun and sky light reflected on the water surface. Those inherent difficulties were in part alleviated by the development of dedicated protocols (Mueller and Austin, 1995; Zibordi et al., 2019).

For operational calibration and validation activities of the in-orbit satellite missions, dense time-series are needed to maximize the number of match-up points between reference field measurements and satellite acquisitions. This necessitates the installation of "unattended" radiometric systems with quasi-continuous acquisitions over time. To this end, the AERONET-OC network has been developed since 2002 to provide L_w time-series for open and coastal waters, as well as inland waters, based on an above-water multispectral system (Zibordi et al., 2009). Recently, this network has been complemented by an hyperspectral setup based on the same above-water radiometry procedures (Goyens et al., 2022). In addition to the fixed platforms equipped by those networks, above-water radiometry methods are also deployed on small to big ships including research vessels (Ondrusek et al., 2022), ferries (Nasiha et al., 2022) or even dugout canoes (Marinho et al., 2021) to enable gathering of large amounts of data to document the optical diversity of aquatic environments and consequently help to improve satellite remote sensing capabilities (Pahlevan et al., 2021).

For satellite validation purposes, fiducial measurements are acquired under clear sky conditions, i.e., in absence of clouds in the vicinity. In this case, the water surface is illuminated by the direct sunlight and the diffuse skylight originating from scattering by molecules and aerosols of the overlying atmosphere. Part of this light enters the water body where the radiation is altered through absorption and scattering caused by the water molecules as well as the presence of dissolved and particulate matter. Thus, as already mentioned, the water-leaving radiance carries useful information to estimate parameters related to the OAWC, such as phytoplankton or sediment concentration proxies, and the in-water light regime (e.g., water transparency). The other part is reflected by the wind ruffled air-water interface contributing to the surface component of the upward radiance. The main principle of above-water radiometry (AWR) relies on a couple of measurements: 1) the total radiance coming from the water body and surface measured with an oblique angle (typically 40°), and 2) downward radiance of the direction that would be specularly reflected by a conceptual flat surface toward the sensor used for 1). The second term is converted into the surface radiance to be removed using a factor that should account for the reflection of the air-water interface considering its roughness properties (Mobley, 1999). This factor is usually defined as "a coefficient that represents the fraction of incident skylight that is reflected back towards the water-viewing sensor at the air-water interface and is the Fresnel reflectance coefficient for a flat water surface", see (Ruddick et al., 2019) where the authors argue to name this term "effective Fresnel reflectance coefficient". Note that other terms are also found in the literature with, for instance, *sea surface reflectance factor* (Mobley, 1999) or *radiance reflectance factor* (Mobley, 2015).

In general, the water surface is "crinkled" by gusts of wind modifying its roughness and in turn its reflection properties (Preisendorfer and Mobley, 1986). The main consequence is that the surface-reflected skylight toward the water-viewing sensor originates from many parts of the celestial hemisphere. This can be understood as a superposition of Fresnel reflections integrated over all the hemispherical directions implying that the "effective Fresnel reflectance coefficient" is sensitive to 1) the wave distribution, including gravitary and capillary waves (Mobley, 2015), 2) the radiance distribution within the celestial dome (Mobley, 1999), 3) the polarization state of light (Harmel, Gilerson, Tonizzo, et al., 2012). These three points should be accounted for in the computation of the "effective Fresnel reflectance coefficient". The first tabulated values were calculated based on Monte-Carlo method to the radiative transfer equation under a simplified atmosphere and without accounting for polarization (Mobley, 1999). Further computations included polarization effects but for a pure Rayleigh atmosphere (i.e., no aerosol), (Mobley, 2015). Nevertheless, the two kinds of values were evaluated based on an *in situ* data set showing no significant impact on the L_w retrievals from an AERONET-OC site (Zibordi, 2016). Other studies provided values considering polarization and impact of a few aerosol types (Zhang et al., 2017; Gilerson et al., 2018). The consideration of both polarization and aerosol optical properties enabled the reproduction of the spectral variation of the sky to surface radiance conversion factor observed from the field (Lee et al., 2010; Lin et al., 2023).

It is proposed in this study to expand those computations for all potential viewing geometries for a comprehensive set of air-water interface roughness properties and aerosol types encompassing

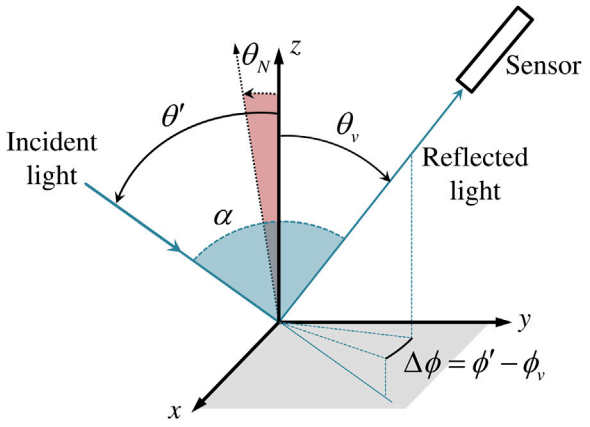


FIGURE 1
Viewing geometry convention: θ_v and ϕ_v are the zenith angle and azimuth of the viewing direction, θ' and ϕ' are the zenith angle and azimuth of a given illumination direction. θ_N is defined as the zenith angle of the vector normal to a given wave facet, and α is the phase angle between the incident and viewing directions.

realistic models for open ocean, coastal, and inland areas (including polluted areas and desert dust). The effects of water surface and aerosol types are taken into account through full vector radiative transfer computations to provide pre-computed tabulated values. The main terms and equations to achieve such computations are detailed in the next section. A specific attention is paid to the nomenclature of the different terms to exemplify possible accordance between theoretical and applicative notations in used in the field of aquatic remote sensing. The uncertainty attached to unknown or partially known input parameters to the modeled values are computed based on Gaussian error propagation. Finally, recommendations to reduce uncertainty in AWR procedures are given based on separate treatment of the diffuse and direct light components, supplementary atmospheric measurements and adaptable viewing geometries.

2 Material and method

2.1 Theoretical background

2.1.1 Radiance components

Above-water radiometry (AWR) methodology mainly relies on (i) radiance measurements performed with a sensor pointed downward to the water, L_t, (ii) measurements of the sky radiance, L_{sky}, with a radiometer pointed to the direction that would be specularly reflected by a conceptual flat surface toward the sensor used for (i), and (iii) correction of the skylight reflected onto the water surface and reaching the downward looking sensor. For the sake of brevity, the impact of the field-of-view of the sensor is not considered in the angular notation below. Assuming the water body and the air-water interface as two different layers, the total radiance measured by the sensor pointing downward can be decomposed as follows:

$$L_t(\theta_s, \theta_v, \Delta\phi, \lambda) = L_w(\theta_s, \theta_v, \Delta\phi, \lambda) + L_{surf}(\theta_s, \theta_v, \Delta\phi, \lambda), \quad (1)$$

where θ_s and θ_v are the sun and viewing zenith angles, $\Delta\phi$ is the relative azimuth between the sun and the direction of the radiometer, the angle convention is given in Figure 1, λ is the wavelength. L_t, L_w and L_{surf} are the total, the water-leaving and the surface (reflected skylight) radiances, respectively. The *remote sensing reflectance* is obtained after dividing L_w by the downwelling irradiance. It is important to note that the three angles (θ_s, θ_v, $\Delta\phi$) must be considered due to the anisotropic nature of the radiation components L_t, L_w and L_{surf}. Note that floating material or foam and white caps are not considered in Eq. 1. A glossary of the main symbols is given in Table 1.

The first AWR protocols were based on the computation of the Fresnel reflection factor to practically compute the surface radiance L_{surf} from the sky radiance L_{sky} (Mueller and Austin, 1995). In a seminal article, Mobley (1999) proposed to further this computation with radiative transfer simulations considering a wind-ruffled air-water interface and provided tabulated values for an *ad hoc* term, hereafter denoted as ρ_{Mobley}, to practically compute the surface radiance from the sky radiance:

$$L_{surf}(\theta_s, \theta_v, \Delta\phi, \lambda) = \rho_{Mobley} L_{sky}(\theta_s, \pi - \theta_v, \Delta\phi, \lambda). \quad (2)$$

The surface component L_{surf} might be further decomposed between the direct and diffuse components, dropping the dependencies for conciseness:

$$L_{surf} = L_{surf}^{diff} + L_{surf}^{dir}. \quad (3)$$

The diffuse part is related to radiation that has undergone at least one scattering event. Conversely, the direct component is defined as the part of the sunlight radiation that has undergone reflection onto the water surface but no scattering interaction within the atmosphere. This latter component was first called *Kumatage* (Spooner, 1822). Thereafter, denominations such as *sheen*, *glint* or *sparkle* were used (Hulburt, 1934) before Cox and Munk popularized the term *glitter* (Cox and Munk, 1954). In the 1960s, with the first satellite pictures of Applications Technology Satellites 1 and 3 (McClain and Strong, 1969) the term *sunglint* has been used until today. All those terms were inspired by the very dynamic nature of the sunglint "flashes" that are controlled by the rapidly propagating waves at the water surface. Based on this erratic modulation of the sunglint intensity, protocols were designed to remove the direct component of light from L_t by taking the minimum values over a sequential series of acquisitions (Hooker et al., 2002; Zibordi et al., 2019). Moreover, recent studies investigated and proposed correction schemes for the sunglint component of the measured signal L_t (Groetsch et al., 2017; Goyens and Ruddick, 2023).

Based on those considerations, it is advocated in this study to separate the diffuse and the direct contributions to further the performances of the AWR correction schemes as already advocated in previous studies (Harmel, Gilerson, Hlaing, et al., 2012; Zhang et al., 2017). On the other hand, several names might be found in the literature for ρ_{Mobley} such as *sea surface reflectance factor* (Mobley, 1999), *radiance reflectance factor* (Mobley, 2015), *effective Fresnel reflectance coefficient* (Ruddick et al., 2019). It is also worth noting that ρ_{Mobley} is not defined as a proper reflectance but simply a ratio of two radiances with specific viewing geometries. The use of the Greek letter ρ, often used to

define reflectance variables, might be misleading. As detailed in the next section, the direct component (i.e., sunglint) was included in Mobley's computations (Mobley, 1999; 2015). Thus, to make a distinction with the Mobley's parameter, a simple notation is proposed standing for *surface-to-sky radiance ratio*, R_{ss}, such as:

$$R_{ss}(\theta_s, \theta_v, \Delta\phi, \lambda) = \frac{L_{surf}^{diff}(\theta_s, \theta_v, \Delta\phi, \lambda)}{L_{sky}(\theta_s, \pi - \theta_v, \Delta\phi, \lambda)}. \quad (4)$$

2.1.2 Polarized nature of light

The electromagnetic radiation of light may be fully defined using the Stokes formalism. According to this formalism, four independent terms are grouped within the so-called Stokes vector that can be written using successively the indicial, Stokes (Stokes, 1852), Perrin (Perrin, 1942), and Chandrasekhar (Chandrasekhar, 1947; Chandrasekhar, 1960) nomenclatures:

$$\mathbf{S} = \begin{pmatrix} S_0 \\ S_1 \\ S_2 \\ S_3 \end{pmatrix} \equiv \begin{pmatrix} A \\ B \\ C \\ D \end{pmatrix} \equiv \begin{pmatrix} I \\ M \\ C \\ S \end{pmatrix} \equiv \begin{pmatrix} I \\ Q \\ U \\ V \end{pmatrix}. \quad (5)$$

Here, the indicial notation is preferred to get more compact equations. Using radiance unit, the term S_0 is equivalent to the radiance L as defined previously. The terms S_1 and S_2 describe the linear polarization and S_3 the circular polarization. S_1 quantifies the linear polarization along the vertical and horizontal planes, and S_2 along the+/−45° planes. It is useful to express the radiance and the other Stokes terms after substitution of the zenith angle by its cosine, $\mu = \cos\theta$. Thanks to this formalism, the radiative transfer equation can be written for an idealized plane-parallel atmosphere as follows:

$$\mu \frac{d\mathbf{S}(\tau, \mu, \phi)}{d\tau} = -\mathbf{S}(\tau, \mu, \phi) + \frac{\omega_0(\tau)}{4\pi} \int_0^{2\pi} d\phi' \int_{-1}^{1} d\mu' \mathbf{P}(\tau, \mu, \phi, \mu', \phi') \mathbf{S}(\tau, \mu', \phi'), \quad (6)$$

with τ the total (absorption + scattering) optical thickness, ω_0 the single scattering albedo, and $\mathbf{P}$ the normalized phase matrix. The reader is referred to (Zhai et al., 2010) and references therein for the complete equations including a coupled atmosphere-water system with a rough air-water interface. This equation must be fully resolved to compute the water, surface and atmosphere (sky) radiation distributions. But, by analogy with the radiative transfer equation, the Stokes vector of the water surface can be retrieved as follows if the sky radiation distribution is known (or measured):

$$\mathbf{S_{surf}}(\mu_v, \phi_v) = \mu_s \mathbf{R_{aw}}(\mu_s, \phi_s; \mu_v, \phi_v) E_0 e^{-\tau/\mu_s} + \frac{1}{\pi} \int_0^{2\pi} d\phi' \int_0^{1} d\mu' \mu' \mathbf{R_{aw}}(\mu', \phi'; \mu_v, \phi_v) \mathbf{S_{sky}}(-\mu', \phi'), \quad (7)$$

with E_0 the extraterrestrial solar irradiance. Note that in this formalism, the minus sign before μ indicates downward direction. In Eq. 7, the $\mathbf{R_{aw}}$ matrix stands for the bidirectional reflectance distribution (BRD) matrix of the air-water interface projected in the reference plane (i.e., meridian plane, see Eqs 7 and 8 in (Harmel et al., 2012)). The first term of the right hand side of Eq. 7 corresponds to the direct "sunglint" contribution. Therefore, the Stokes terms can also be expressed as direct and diffuse component with:

$$S_{surf,i}^{dir}(\mu_v, \phi_v) = \mu_s R_{i0}^{aw}(\mu_s, \phi_s; \mu_v, \phi_v) E_0 e^{-\tau/\mu_s}, \quad (8)$$

$$S_{surf,i}^{diff}(\mu_v, \phi_v) = \frac{1}{\pi} \sum_{j=0}^{3} \int_0^{2\pi} d\phi' \int_0^{1} d\mu' \mu' R_{ij}^{aw}(\mu', \phi'; \mu_v, \phi_v) S_i^{sky}(-\mu', \phi'). \quad (9)$$

Based on those equation, the *surface-to-sky radiance ratio*, R_{ss}, can be rewritten as follows where it is obvious to see that full knowledge of skylight directional distribution and its state of polarization in each celestial direction is needed:

$$R_{ss} = \frac{L_{surf}}{L_{sky}} = \frac{\sum_{j=0}^{3} \int_0^{2\pi} d\phi' \int_0^{1} d\mu' \mu' R_{0j}^{aw}(\mu', \phi'; \mu_v, \phi_v) S_0^{sky}(-\mu', \phi')}{\pi S_0^{sky}(-\mu_v, \phi_v)}. \quad (10)$$

In Mobley's calculations (Mobley, 1999; Mobley, 2015), there is no distinction between diffuse and direct light within the Monte-Carlo resolution of the radiative transfer equation done for a pure Rayleigh atmosphere (i.e., no aerosols included). It is easy to show, in this case, that the direct sunglint component contributes to the spectral dependency of ρ_{Mobley} through the atmosphere optical thickness parameter, $\tau(\lambda)$, that is highly spectrally variable:

$$\rho_{Mobley} = \frac{L_{surf}^{diff}(\mu_v, \phi_v) + \mu_s R_{00}^{aw}(\mu_s, \phi_s; \mu_v, \phi_v) E_0 e^{-\tau(\lambda)/\mu_s}}{L_{sky}(-\mu_v, \phi_v)}. \quad (11)$$

2.1.3 Air-water interface

As seen in Eq. 7, the Stokes vector of the air-water interface stems from the coupling between the sky geometrical distribution of $\mathbf{S_{sky}}$ and the BRD matrix $\mathbf{R_{aw}}$. In the present study, this term is calculated based on the Cox-Munk isotropic wave slope distribution (Cox and Munk, 1956; Munk, 2009). Assuming that the air-water interface can be modeled as a distribution of planar wave facets defined by their orientation μ_N (cosine of θ_N, see Figure 1):

$$\mu_N = \frac{\mu_v + \mu'}{\sqrt{2(1 + \cos\alpha)}}, \quad (12)$$

with α the phase angle between incident and viewing direction:

$$\cos\alpha = \mu_v \mu' - \sqrt{1 - \mu_v^2}\sqrt{1 - \mu'^2}\cos\Delta\phi'. \quad (13)$$

The BRD matrix can be written as:

$$\mathbf{R_{aw}}(\mu', \phi'; \mu_v, \phi_v) = \frac{\pi \mathbf{R_f}(\mu_N, m_w)}{4\mu_v \mu_N^4} p(\mu_N, \sigma), \quad (14)$$

where $\mathbf{R_f}$ is the Fresnel reflection matrix projected in the reference (meridian) plane, $p(\mu_N, \sigma)$ is the statistical proportion of waves having the μ_N orientation, σ is the standard deviation of the wave slope distribution. It is worth highlighting that $\mathbf{R_f}$ directly depends on the water refractive index, m_w, in a non-linear fashion that may induce significant spectral variation of the matrix over the visible to near-infrared part of the spectrum (Harmel et al., 2018). Using the

TABLE 1 Glossary of symbols.

Symbol	Definition
E_0	Extraterrestrial solar irradiance
$\mathbf{S}, S_0, S_1, S_2, S_3$	Stokes vector and its four components. Please note that the Chandrasekhar's nomenclature is also commonly used with the components written as I, Q, U, V
$S^{dir}_{surf,i}, S^{diff}_{surf,i}$	ith component of the Stokes vector for direct and diffuse light reflected on the air-water interface
$L^{dir}_{surf}, L^{diff}_{surf}$	Radiance (or 0^{th} component of the Stokes vector) for direct and diffuse light of the air-water interface
L_t, L_{surf}, L_{sky}, L_w	Total upward, air-water interface, downward sky and water-leaving radiances
$\theta_s, \theta_v, \theta_N, \theta'$	Zenith angles of the Sun, viewing direction, the normal to a wave facet, and incident direction
$\mu_s, \mu_v, \mu_N, \mu'$	Cosines of the zenith angles
$\phi_s, \phi_v, \phi', \Delta\phi$	Azimuth of the Sun, viewing direction, incident direction, and the relative azimuth
α	Phase angle (supplementary of the scattering angle)
λ	Wavelength
τ, τ_a, τ_r	Total, aerosol and Rayleigh components of the atmosphere optical thickness
ω_0	Single scattering albedo of the atmospheric medium
κ, RH	Hygroscopic growth factor and relative humidity
r_{nm}, σ_n	Median radius and standard deviation of the aerosol lognormal distribution in number of particles
$\mathbf{m}_w, \mathbf{m}_{dry}, \mathbf{m}_{wet}$	Complex refractive index of water, dry and wet aerosols
m_R, m_I	Real and imaginary parts of the refractive index
p, σ^2	Wave slope distribution and variance
ws	Equivalent Cox-Munk wind speed
$\mathbf{R}_{aw}$	Bidirectional reflectance distribution matrix of the air-water interface
$\mathbf{R}_f$	Fresnel reflection matrix
$\mathbf{P}$	Normalized scattering phase matrix
CV	Coefficient of variation
ρ_{Mobley}	Tabulated values of the *radiance reflectance factor* including the sunglint contribution
R_{ss}	Apparent *surface-to-sky radiance ratio*

isotropic Cox-Munk model, wave slope statistics can be expressed as:

$$p(\mu_N, \sigma) = \frac{1}{\pi\sigma^2}\exp\left(-\frac{\tan^2\theta_N}{\sigma^2}\right). \quad (15)$$

For practical comparison with other studies, the variance of the slope distribution is also given in wind speed unit through the Cox-Munk parameterization, hereafter denoted as *equivalent Cox-Munk wind speed*:

$$ws = 195.3\sigma^2 - 0.586 \ (\text{in m} \cdot \text{s}^{-1}). \quad (16)$$

2.2 Aerosol models

The aerosols in the atmosphere strongly impact the sky radiance distribution and polarization. To encompass the great variety of aerosol contents of the atmosphere, the radiative transfer simulations (i.e., resolution of Eq. 6) were performed based on the Optical Properties of Aerosols and Clouds (OPAC) models (Hess et al., 1998). The OPAC aerosol models were generated based on a mixture of pure components. Those components are representative of the main aerosol properties retrieved at the global scale. One advantage of those models is to consider non-spherical particles and the spectral variation of the complex refractive index ($\mathrm{m} = m_R + im_I$) of different components of the aerosol pool. Note that the convention of positive imaginary part m_I is used. The optical properties of each component are computed based on a log-normal size distribution of the number concentration of particles, N:

$$\frac{dN(r)}{dr} = \frac{N_0}{\sigma_n r\sqrt{2\pi}}\exp\left(-\frac{(\log(r/r_{nm}))^2}{2\sigma_n^2}\right), \quad (17)$$

where r is the equivalent spherical radius, r_{nm} is the median radius of the distribution, and σ_n its standard deviation. N_0 is the

TABLE 2 Description of the microphysical parameters of the OPAC components for aerosol modeling. The refractive index values are given for the dry part. The abbreviations *acc.*, *coa.* and *nuc.* stand for accumulation, coarse and nucleation, respectively.

Component	Name	σ_n	r_{dry}	Shape	κ	m_R at 500 nm	m_I at 500 nm
Insoluble	INSO	2.51	0.471	sphere	0	1.53	0.008
Water-soluble	WASO	2.24	0.0212	sphere	0.27	1.53	0.005
Soot	SOOT	2	0.0118	sphere	0	1.75	0.45
Sea salt (acc. mode)	SSAM	2.03	0.209	spheroid	1.12	1.50	1.55e-08
Sea salt (coa. mode)	SSCM	2.03	1.75	spheroid	1.12	1.50	1.55e-08
Mineral (nuc. mode)	MINM	1.95	0.07	spheroid	0.1	1.53	0.0078
Mineral (acc. mode)	MIAM	2	0.39	spheroid	0.1	1.53	0.0078
Mineral (coa. mode)	MICM	2.15	1.9	spheroid	0.1	1.53	0.0078

TABLE 3 Mixture of aerosol components used to generate the aerosol models.

Name	Aerosol types	INSO	WASO	SOOT	SSAM	SSCM	MINM	MIAM	MICM
COAV	Continental averaged	0.4	7,000	8,300	0	0	0	0	0
URBA	Urban	1.5	28,000	130,000	0	0	0	0	0
DESE	Desert	0	2000	0	0	0	269.5	30.5	0.142
MACL	Maritime clean	0	1,500	0	20	3.20E-03	0	0	0

total number of particle per unit of volume, here taken as unity for normalization purposes; in the radiative transfer calculations this number is set via the aerosol optical thickness. For each component, the median radius is further modulated by its hygroscopic particle growth parameter, κ, (Zieger et al., 2013):

$$r_{rm} = r_{dry}\left(1 + \kappa\frac{RH}{1-RH}\right)^{1/3}, \tag{18}$$

with RH the relative humidity of the atmosphere. Following the same rule of hygroscopic growth, the complex refractive index of the wet aerosols is given by:

$$\mathrm{m}_{wet} = \frac{\mathrm{m}_{dry} + \left(\kappa\frac{RH}{1-RH}\right)\mathrm{m}_w}{\left(1 + \kappa\frac{RH}{1-RH}\right)}, \tag{19}$$

where m_w is the complex refractive index of pure water taken from Segelstein (1981). The microphysical parameters of the OPAC components used are summarized in Table 2.

The aerosol components listed above are representative of a single "species" whereas in natural conditions aerosols consist of a mixture of those components. The OPAC model provides typical mixtures of those components that are given in Table 3 for the models used in this study. The following codes were used to generate the scattering matrix with Mie theory for homogeneous sphere (Mishchenko et al., 2000), T-matrix for ellipsoidal/spheroidal particles (Mishchenko et al., 2004), those computations were extended for large particle sizes with the "Improved Geometric Optics Method" (Yang et al., 2007). The computations were performed through the MOPSMAP package (Modeled optical properties of ensembles of aerosol particles) coded in FORTRAN and based on pre-computed look-up tables (Gasteiger and Wiegner, 2018).

2.3 Radiative transfer computation

The diffuse component of the Stokes vectors of the air-water interface, $\mathbf{S_{surf}}$, and sky, $\mathbf{S_{sky}}$, were computed at the bottom of the atmosphere level using the *Ordres Successifs Océan Atmosphère Avancé* (OSOAA) code (Chami et al., 2015). This code is based on the successive order method developed for atmosphere application (Deuze et al., 1989; Lenoble et al., 2007) with addition of the coupling with a water layer (Chami et al., 2001). Here, the water layer was set as totally absorbing to compute the contribution of the air-water interface, i.e., the water-leaving radiance is null. Sky and direct sunlight reflections on the water surface are taken into account to solve the radiative transfer Equation 6 but the sunglint contribution to the surface radiation was removed afterward. Angular integrations were based on sixty Gaussian nodes and the maximum order of Fourier expansion in azimuth was set to 1,024 for the scattering matrices and 2048 for the air-water interface BRD matrix. No truncation was applied to the scattering phase functions.

The computations were repeated for a comprehensive series of input parameters which are listed in Table 4. The atmosphere is modeled as a mixture of non-absorbing molecules (i.e., Rayleigh scattering) and aerosols. The Rayleigh optical thickness, τ_r, decreases exponentially with the altitude with the scale height of 8 km, similarly a scale height of 2 km was set for the aerosol optical thickness. The spectral values of τ_r and the depolarization factor were taken from (Bodhaine et al., 1999). As to the aerosol optical properties, the four OPAC models listed in Table 3 were used to implement the scattering matrices and the absorption and extinction cross sections. To limit the number of aerosol models the relative humidity was set to 70%. The BRD matrix of the air-water interface, $\mathbf{R_{aw}}$, was modeled following Eq. 14 with the spectral values of the water refractive index computing as in (Harmel et al., 2018) based on

TABLE 4 Summary of the input parameters used to generate the look-up tables (LUT).

Parameter	Values
Aerosol optical thickness	0., 0.001, 0.01, 0.1, 0.2, 0.35, 0.5, 0.7, 1.0, 1.5
Aerosol model	COAV, DESE, MACL, URBA
Wave slope variance, σ^2	0.0056, 0.0132, 0.0235, 0.044, 0.0849
Cox & Munk equivalent wind speed	0.5, 2, 4, 8, 12, 16 (in m·s^{-1})
Solar zenith angle, θ_s	0°–88° by step of 2°
Viewing zenith angle, θ_v	0°–90° by step of around 1.5°
Relative azimuth, $\Delta\phi$	0°–360° by step of 5°
Wavelengths	350, 400, 500, 600, 700, 800, 1,000 (in nm)

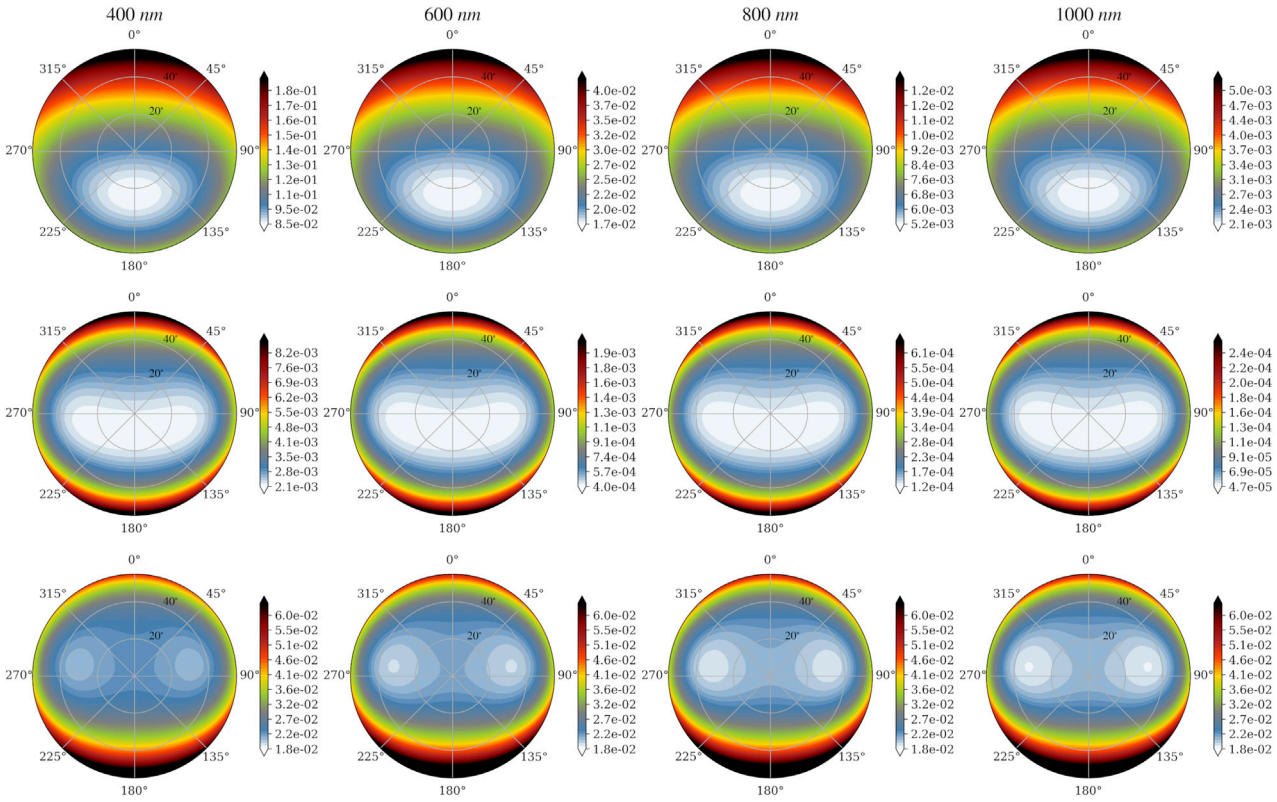


FIGURE 2
Polar view of the downward sky radiance L_{sky}^{diff} (first row), upward surface reflected radiance L_{surf}^{diff} (second row), and the resulting surface-to-sky radiance ratio (bottom row) for a solar zenith angle θ_s = 50°, and a wave slope variance σ^2 = 0.0132 (i.e., *Cox-Munk* wind speed of 2 m s^{-1}). Each column corresponds to the indicated wavelength. Note that the concentric circles correspond to the viewing zenith angles of 20° and 40° and radial angles represent the relative azimuth to the Sun. By convention, the relative azimuth is equal to 0° when the Sun and the sensor are in opposition.

tabulated values (Quan and Fry, 1995; Max and Chapados, 2009; Kedenburg et al., 2012).

2.4 Uncertainty calculus

The surface-to-sky radiance ratios, R_{ss}, were computed by fixing the aerosol and water surface BRD matrix parameters. In practice, those parameters are in the best case scenario known with a given uncertainty or totally unknown if no associated measurements are performed concurrently. In the proposed model, the input parameters, noted x_i below, are the aerosol optical thickness at 550 nm, the aerosol model and the wind speed, or reciprocally the variance of the wave slope distribution. In order to document the impact of unknown or partially known input parameters two different metrics are used. The first one is the coefficient of variation, CV, computed as follows:

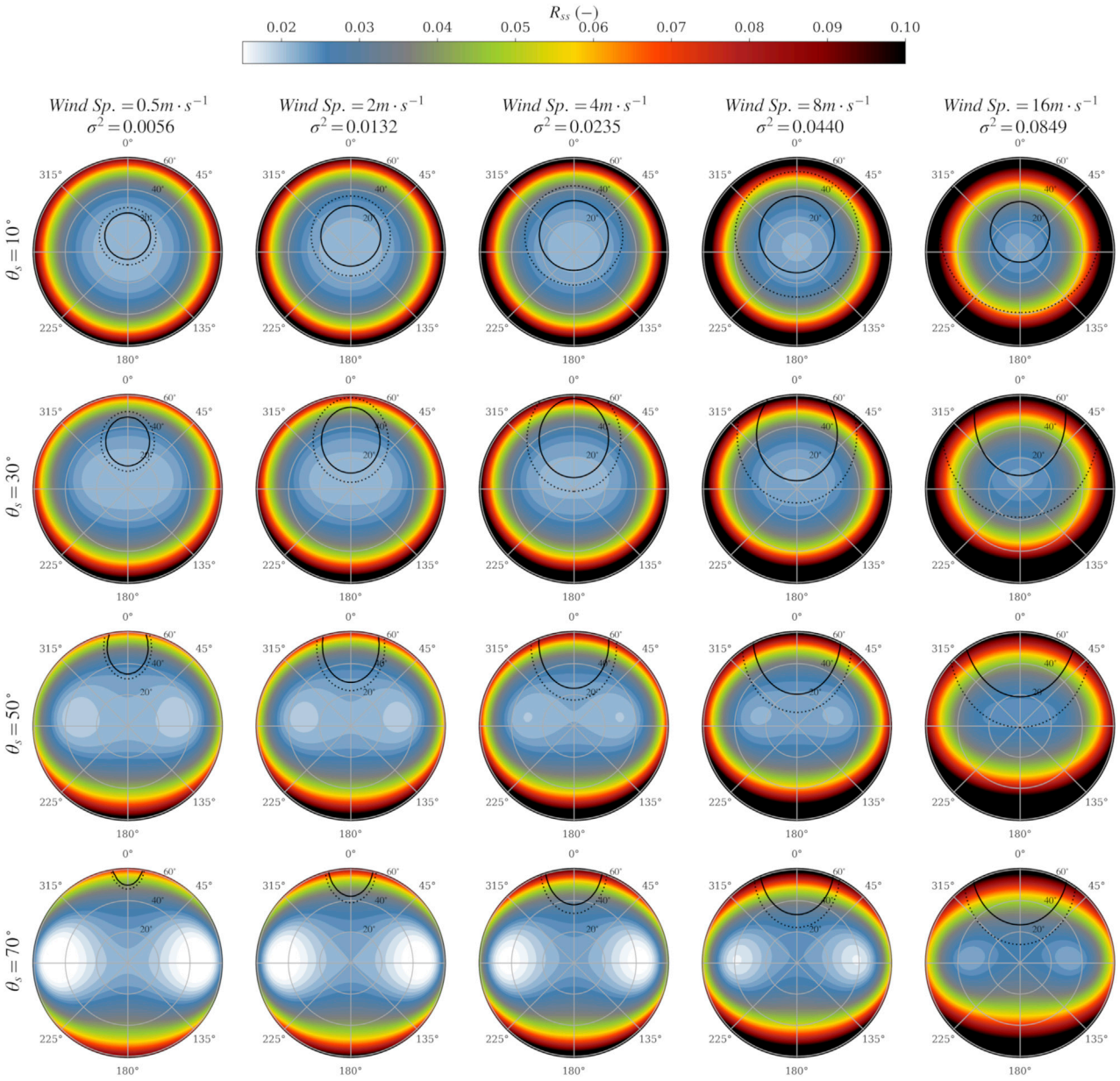


FIGURE 3
Polar diagrams of the surface-to-sky radiance ratios, R_{ss}, at 600 nm for a pure Rayleigh atmosphere and several configurations: each row corresponds to a given solar zenith angle (from 10° to 70°), each column corresponds to a given wave slope distribution expressed through its variance or the equivalent Cox-Munk wind speed. For information, contour lines for sunglint reflectance of 1% (dotted black line) and 5% (continuous line) are superimposed based on the Cox-Munk isotropic model.

$$CV = \frac{\sqrt{\frac{1}{N_x}\sum_{i}^{N_x}\left(R_{ss}(x_i) - \overline{R_{ss}}\right)^2}}{\overline{R_{ss}}}, \tag{20}$$

where N_x is the number of input parameters and $\overline{R_{ss}}$ the average computed over the N_x parameters considered. The second metric is the standard deviation of R_{ss} due to the propagation of errors made in the input parameters. This can be understood as the uncertainty attached to the surface-to-sky radiance ratio assuming uncorrelated Gaussian errors in aerosol optical thickness, τ_a, and wave slope distribution (Eq. 15) set through the wind speed parameter, ws:

$$\Delta R_{ss} = \sqrt{\left(\frac{\partial R_{ss}}{\partial \tau_a}\right)^2 \Delta {\tau_a}^2 + \left(\frac{\partial R_{ss}}{\partial ws}\right)^2 \Delta ws^2}. \tag{21}$$

Following uncertainty estimation based on large scale comparisons (Harmel and Chami, 2012; Levy et al., 2013), the errors were modeled as linear function as follows:

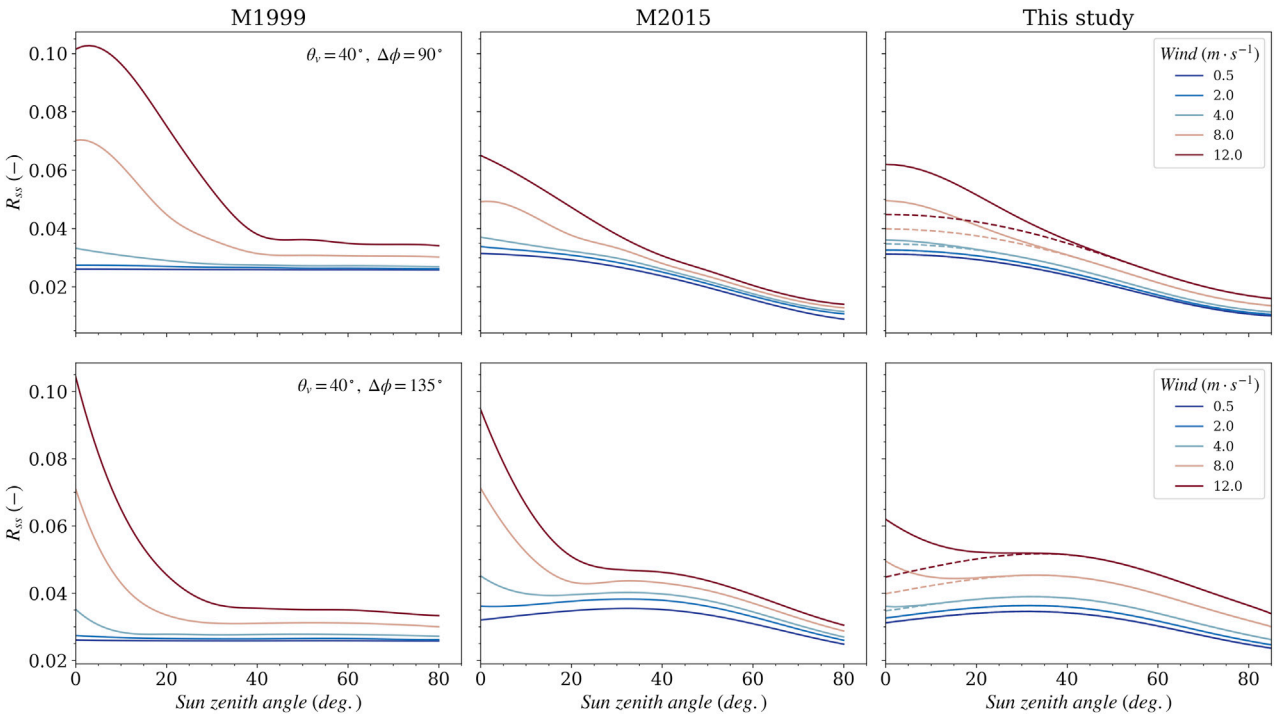


FIGURE 4
Tabulated values of the surface-to-sky ratio computed (first column) without consideration of polarization (Mobley, 1999), (second column) accounting for polarization within a Rayleigh atmosphere (Mobley, 2015) and (third column) this study for pure diffuse light (dashed curves) and with addition of the sunglint component (solid curves). Geometry and equivalent Cox-Munk wind speed are indicated in the insets.

$$\begin{cases} \Delta\tau_a = 0.2\tau_a + 0.05 \\ \Delta ws = 0.2ws + 0.5 \ (\text{in } m \cdot s^{-1}) \end{cases}. \quad (22)$$

3 Results

3.1 Rayleigh atmosphere

The surface-to-sky radiance ratio is first shown for a pure Rayleigh atmosphere (i.e., no aerosol). To illustrate the computation the downward (celestial) and upward (surface) radiance distribution are plotted in Figure 2 given in normalized radiance unit (i.e., actual radiance multiplied by π/E_0). As already mentioned, the direct light component was removed to analyze the diffuse component only. This is why no strong peak is seen for null relative azimuth around the solar zenith angle. For this pure molecular condition, the spectral variation of the sky and surface radiance distribution is very weak. But, a spectral behavior is clearly visible within the R_{ss} angular distribution (see bottom row in Figure 2). In this configuration, the minimum skylight reflection occurs for relative azimuth of 90° (symmetrically 270°) and viewing zenith angles between 30° and 40°. Interestingly, those minima occur in the typical angular region of the neutral points where the degree polarization of the reflected light is null (Fraser, 1968; Adams and Kattawar, 1997). Conversely, the highest reflections appear for relative azimuths close to 180°, that is to say when the Sun is behind the observing system. It is also interesting to note that the value of R_{ss} increases with diminishing wavelengths where the molecular atmosphere is the most scattering, in other terms, when the diffuse light proportion increases.

Beside this spectral dependence, R_{ss} values are mainly driven by the viewing observation and the state of the wavy water surface. Figure 3 shows the R_{ss} values at a fixed wavelength 600 nm for various solar viewing angles and wave slope distributions. The potential impact of the sunglint contribution is also displayed in this figure. Obviously, the angular distribution of R_{ss} is not significantly disturbed within the sunglint area since only diffuse light is considered. For lower wind speed conditions, the minimum values of skylight reflection are outside the sunglint area which is not the case for higher wind speeds or when the Sun is close to zenith. It is also important to note that when the Sun is lower on the horizon, the R_{ss} values are rapidly changing with azimuth that should be accurately known in this case.

Another view of the R_{ss} sensitivity in a Rayleigh atmosphere is given Figure 4 where the ratio calculated at 500 nm is extracted for a relative azimuth of 90° and 135° for a viewing zenith angle of 40°. In this way, the computed values can be compared with previous tabulated calculations performed without polarization (Mobley, 1999) and with polarization for a Rayleigh atmosphere (Mobley, 2015). First, it is readily observable that Mobley's ratios increase sharply with the decreasing solar zenith angle where the direct light from sunglint becomes more pronounced. The corresponding R_{ss} values from this study are displayed with and without considering the sunglint component in the calculations (last column of Figure 4). Clearly, the

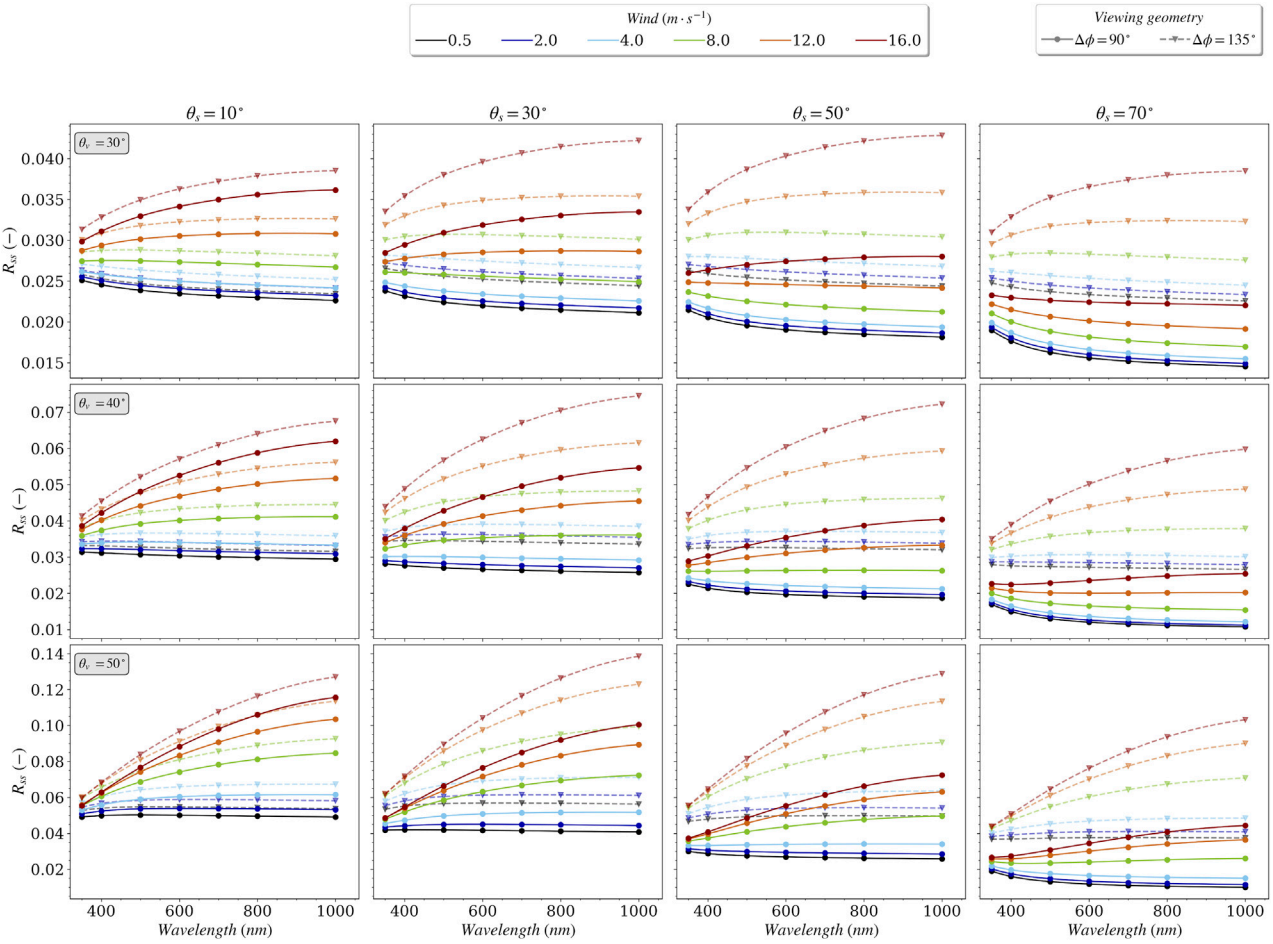


FIGURE 5
Spectral values of the surface-to-sky radiance factor, R_{ss}, for a Rayleigh atmosphere given for three viewing zenith angles of 30°, 40° and 50° (rows) and two relative azimuths of 90° (continuous lines), and 135° (dashed lines).

consideration of sunglint within the ratio calculation produces a significant increase of its value toward low solar zenith angles; the sunglint signal rapidly overwhelms the reflected-skylight signal with increasing wind speeds. For instance, at solar zenith angle 10° and wind speed 12 m s^{-1}, actual R_{ss} computed for diffuse light is around 0.045 and addition of sunglint increases the value up to 0.065 for θ_v = 40° and $\Delta\phi$ = 90°. It is worth remembering that the sunglint signal is strongly wavelength dependent through the action of the direct transmittance of the atmosphere (see Eq. 8). Unspectral consideration of sunglint yields extremely high R_{ss} values for molecular atmosphere which can partly explain the overcorrection and enhanced uncertainty at small solar zenith angles (Harmel et al., 2011), overcorrection is only suppressed when only diffuse light is considered as shown in the Figure 7 of (Harmel et al., 2012). It is shown here that the contribution of sunglint is still significant for solar angles up to 40° where continuous and dashed curves depart from each other in the last column of Figure 4. Notwithstanding the sunglint impact, it is important to highlight that the two calculations including polarization provide quite similar values and shape with varying solar zenith angles (see M2015 and *this study* in Figure 4) when compared to the unpolarized calculation (M1999).

The spectral values of R_{ss} are shown in Figure 5 for a Rayleigh atmosphere for three different viewing zenith angles and two relative azimuths commonly used for AWR acquisitions. These values exhibit conspicuous spectral dependencies with diverse amplitudes depending on both the viewing geometry and the water surface roughness here considered through the equivalent Cox-Munk wind speeds. In general, the ratios decrease with the wavelength for low wind speed conditions up to 4 m s^{-1}. Exceptions might occur for the viewing zenith angle 50° when the Sun is high on the horizon. In all cases, increase in wind speed produces an overall increase of the R_{ss} values with more marked spectral dependencies. In parallel, such modifications of the wave slope variance induce spectral increase of the values toward the near-infrared part of the spectrum. This spectral feature is more pronounced when using 135° for the relative azimuth. As a result of the surface roughness effect, the dependency on wind speed is smaller toward the shorter wavelengths.

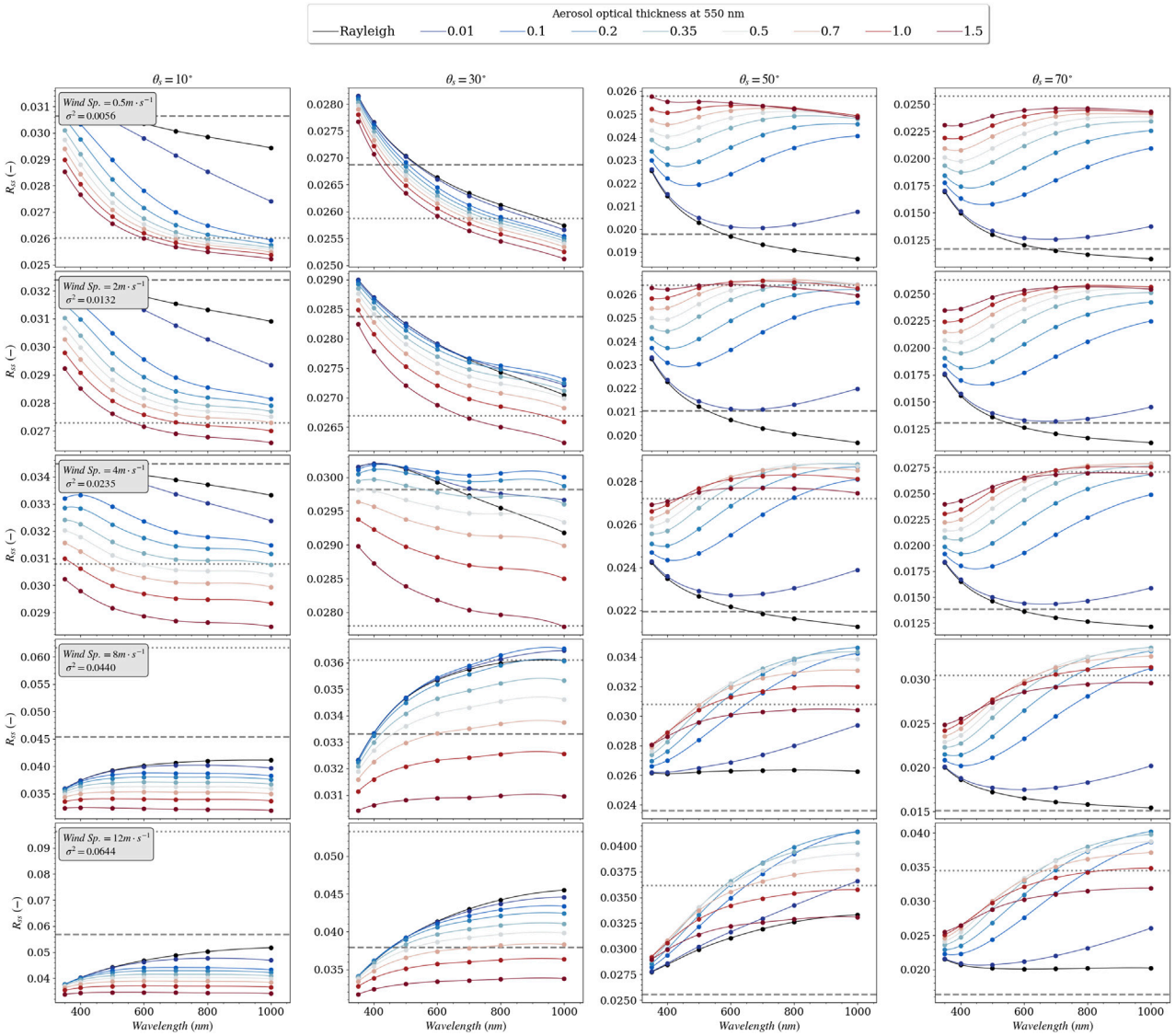


FIGURE 6
Spectral values the surface-to-sky radiance factor, R_{ss}, for several aerosol loads within the atmosphere considering the *maritime clean* (MACL) aerosol model for viewing zenith angle 40° and relative azimuth 90°. Values are shown for several solar zenith angles (columns) and wave slope variance (rows). The unspectral values from previous studies are also displayed with gray lines for M1999 (Mobley, 1999) (dotted lines) and M2015 (Mobley, 2015) (dashed lines).

3.2 Impact of aerosols

3.2.1 Spectral considerations

The presence of aerosols in the atmosphere modifies the downward radiance distribution but also the state of polarization of the celestial hemisphere. The impact of aerosols on the spectral values of R_{ss} is analyzed in this section. The Figures 6, 7 show the spectral dependency of R_{ss} under atmosphere with various loads in *maritime clean* (MACL) aerosols for a viewing angle of 40° and relative azimuths of 90° and 135°, respectively. Similar results obtained for the aerosol models COAV, DESE and URBA are provided in the Supplementary Material. In all the configurations shown, the addition of aerosols in the atmosphere induces a significant modification of the R_{ss} values from the Rayleigh case. It is notable that the departure from the Rayleigh-case values starts for aerosol optical thickness as low as 0.01. In general, the aerosol optical thickness is around 0.1 for clear atmospheres, around 0.4 for moderately turbid and can reach values greater than 1.5 for extremely turbid atmospheres. From the results shown here no specific behavior on R_{ss} can be attributed to changes in the aerosol load: for relative azimuth 90° and according to the sun's zenith angle and surface state the values might be either decreased or increased by addition of aerosol within the atmosphere. As to relative azimuth 135°, increase in aerosol load always produces decrease of the R_{ss} spectral values. Nevertheless, it should be pointed out that the values provided by the polarized values M2015 tabulated (Mobley et al., 2015) are always closer than the unpolarized version M1999 (Mobley, 1999) to the computed R_{ss} for low aerosol optical

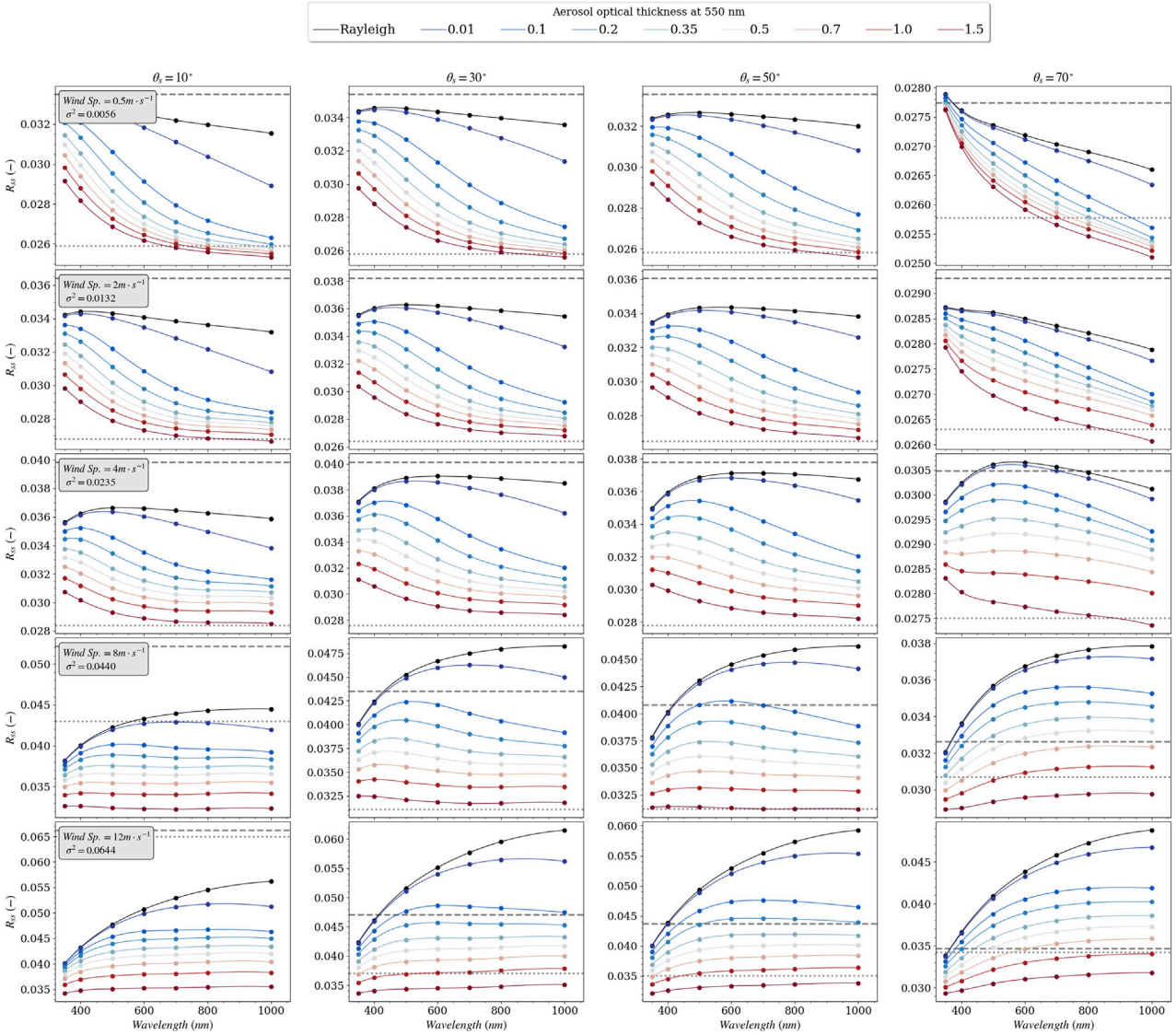


FIGURE 7
Similar to Figure 6 for relative azimuth 135°.

thickness and in particular for the Rayleigh atmosphere. Intersections are even observed between M2015 and the computed spectral values around 550 nm at which M2015 values were computed for a Rayleigh atmosphere. This demonstrates the consistency between the two computations but, in turn, highlights the need to consider the aerosol component for surface light correction in AWR protocols.

3.2.2 Directional considerations

In order to examine the sensitivity of R_{ss} to the viewing geometry, it is of interest to analyze the polar diagrams displayed in Figure 8 for various solar zenith angles and the four aerosol models corresponding to maritime (MACL) or continental (COAV) environments, polluted areas (URBA) and desert dust impacted atmospheres (DESE). Those aerosol models differ between each other by their respective scattering matrix and absorption properties. The models MACL and DESE correspond to coarse size aerosols with a highly peaked scattering function in forward scattering angles. Conversely, COAV and URBA represent smaller particles exhibiting a smoother forward peak of the scattering phase function and more pronounced side and backward scattering. As a result, it is clearly seen from Figure 8 that MACL and DESE induce a narrow pattern of low R_{ss} in the sunglint area (white spots in the figure). This pattern is diminished and more spread in the case of finer aerosols (COAV and URBA). In addition to this geometrical pattern, changes due to the aerosol model can be noticed for other viewing angles and azimuths. This reinforces the need to consider the aerosol load of the atmosphere both with the optical thickness but also the aerosol models defined by their inherent microphysical properties (or optical properties).

Most of the protocols advise to use a viewing zenith angle of 40°. On the other hand, for fixed platforms the sensor can either be rotated to get a constant relative azimuth with respect to the

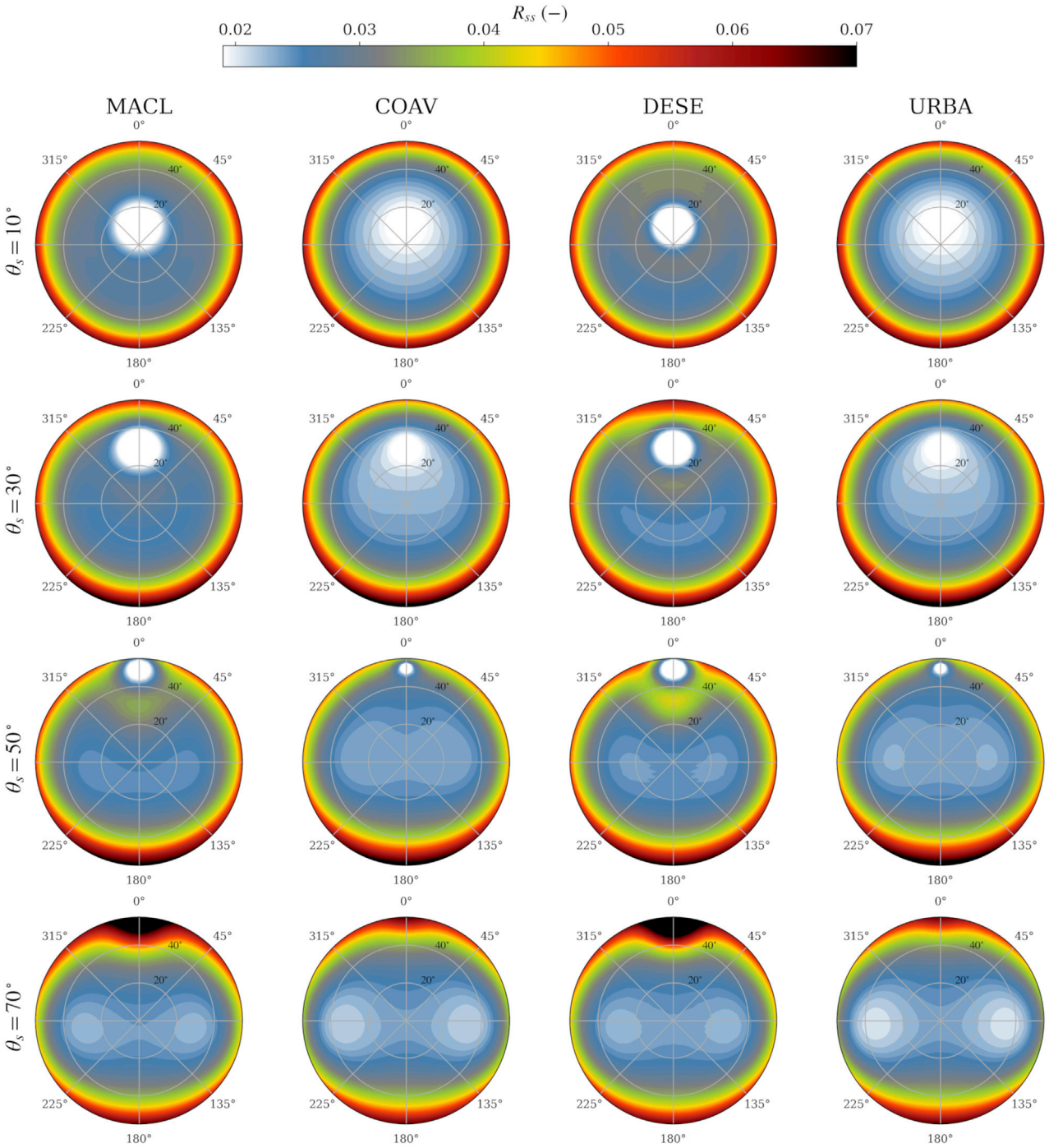


FIGURE 8
Polar diagrams of R_{ss} calculated at 600 nm for several solar zenith angles (rows) and four aerosol models: maritime clean (MACL), continental average (COAV), desert dust (DESE) and polluted urban (URBA). Values are given for an aerosol optical thickness of 0.35 and equivalent Cox-Munk wind speed of 4 m s^{-1} (i.e., σ^2 = 0.0235).

Sun or just left immobile making the relative azimuth change over the course of a day (Harmel et al., 2011). In order to examine the impacts of varying solar and azimuth angles, it is practical to replot the polar diagrams for all the solar zenith angles by fixing the viewing angle. Figure 9 shows this kind of polar diagram for the MACL conditions and several water surface states. Similar figures are provided in the Supplementary Material for the other aerosol models. From this figure, it can be noted that the lowest R_{ss}, i.e., minimizing the sky reflection effect, occur for relative azimuths centered around 90°. In comparison, R_{ss} exhibits higher values along relative azimuth 135°, that is to say the impact of skylight reflection is more pronounced for this viewing geometry. On the other hand, it should be noted that values for

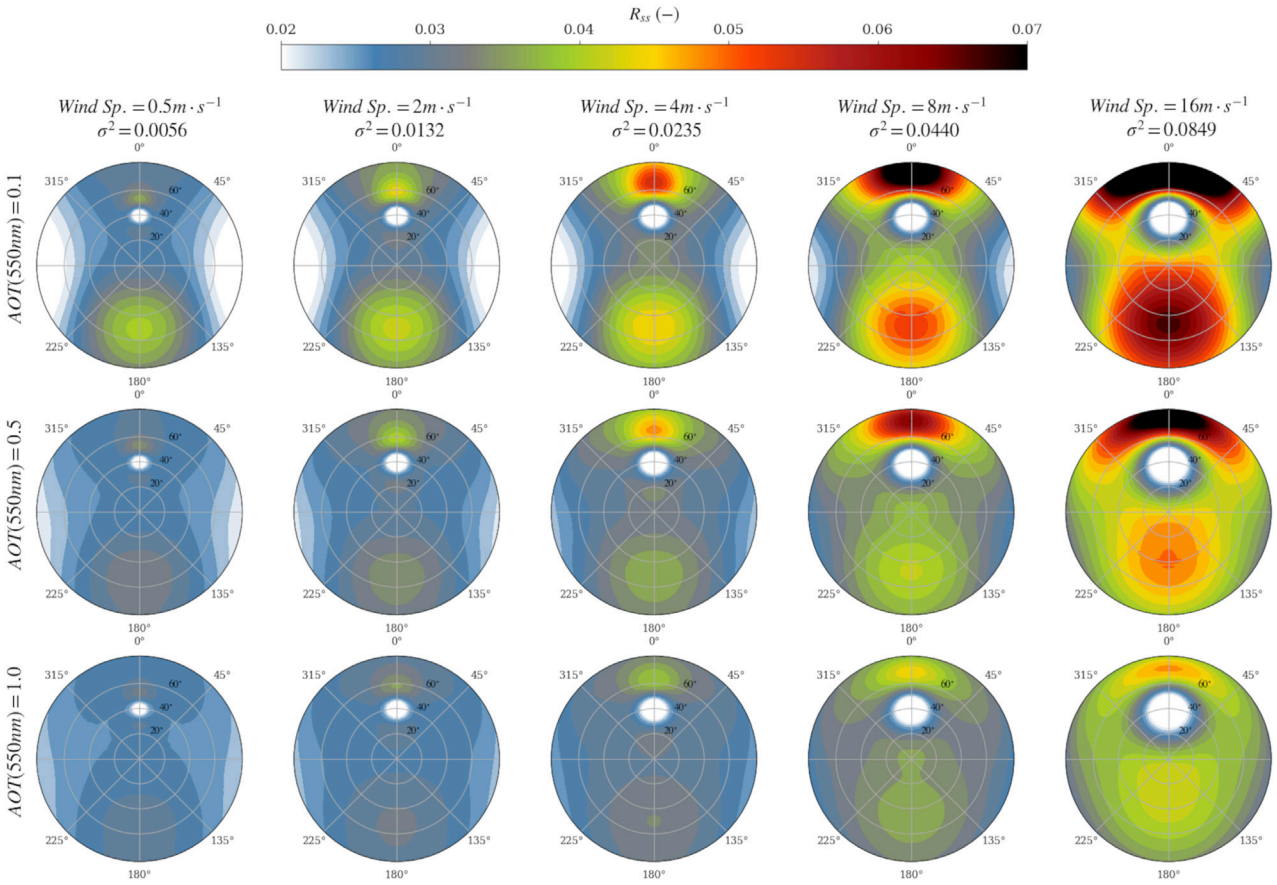


FIGURE 9
(*polar diagram: contour circles indicate solar zenith angles*) Directional values of R_{ss} at 600 nm for a fixed viewing zenith angle of 40° and various loads in *maritime clean* (MACL) aerosols (rows) and water surface states (columns).

relative azimuths between roughly 120° and 250° are significantly increased in high wind speed conditions. In any case, the exact viewing configuration should be accurately known to obtain the corresponding surface-to-sky radiance ratio for practical correction within the AWR processing scheme.

3.3 Uncertainties

3.3.1 Aerosol models

As shown in the previous figures, the aerosol optical thickness and the aerosol model produce significant modifications of the skylight reflected by the air-water interface toward the AWR sensor. In practice, it is far from being obvious to exactly know the exact optical properties of the aerosol load in presence. The directional variability of R_{ss} was shown in Figure 9 for a given aerosol model mimicking typical salt aerosols retrieved in the maritime environment. It is of interest to quantify the variation of this term due to unknown aerosol models. For this purpose, the coefficient of variation (CV) due to unknown aerosol models was computed over the four aerosol models based on Eq. 20. The resulting CV are shown in Figure 10 for several atmosphere turbidites and water surface states. The variations are obviously minimal for low aerosol optical thickness but can reach a few percent for high solar zenith angle, in particular at the relative azimuth of 90°. In comparison, CV is smaller when using a relative azimuth of 135° for measurements with values below 2%. On the contrary, CV values significantly increase for relative azimuths of 180° or smaller than 90°. Choosing an appropriate relative azimuth for a given solar zenith angle might help minimize uncertainty in the surface radiance correction even if the aerosol type is unknown.

3.3.2 Propagation of errors from aerosol optical thickness and wind speed

The uncertainties of the surface-to-sky radiance ratio were computed based on Eqs 21 and 22 to account for the propagation of the errors attached to the input parameters. The two numerical parameters τ_a and ws were taken into account enabling proper analytical derivation in the calculation. The absolute uncertainty was then divided by corresponding R_{ss} to obtain the relative uncertainty as shown in Figure 11 for wavelength 600 nm. Similar figures for wavelengths 350 and 1,000 nm are provided in the Supplementary Material. From those figures, it is clearly seen that the uncertainty is very variable from one given observing geometry to another with values starting from tens of percent up to over 15%. Interestingly, the uncertainties decrease with the atmosphere turbidity set through the aerosol optical thickness, τ_a. This can

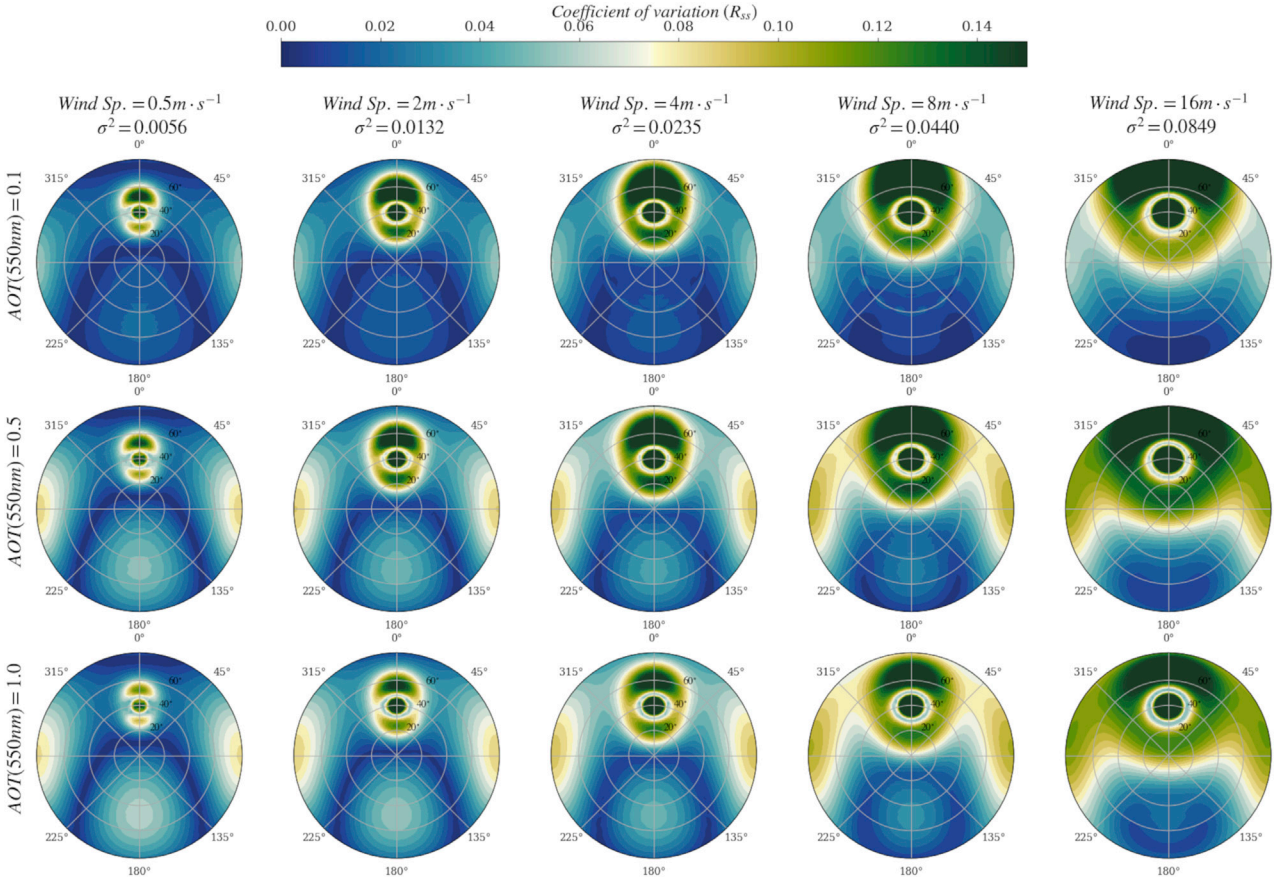


FIGURE 10
(*polar diagram: contour circles indicate solar zenith angles*) Coefficient of variation due to unknown aerosol model computed from the following OPAC models: Maritime clean, Continental average, Desert dust, Urban for a relative humidity of 70%. Values computed at 600 nm for a viewing angle of 40° for diverse (columns) wind speeds (or wave slope variances, σ^2) and (rows) aerosol optical thicknesses.

be explained by two different effects: (i) the relative error in τ_a decreases with increasing aerosol load, (ii) the skylight distribution gets more isotropic under turbid atmosphere conditions. The first effect comes from the error model used for τ_a in which it is assumed that the relative error diminishes with increasing τ_a; this assumption is due to the fact that actual measurements of the optical thickness are more precise for greater values of τ_a (Knobelspiesse et al., 2004). For instance, based on Eq. 22, relative error is 0.7 for τ_a = 0.1 and 0.25 for τ_a = 1.0. The second effect is more physical. When the aerosol optical thickness increases, more multiple scattering occurs in the atmosphere inducing a more isotropic distribution of the sky radiance. As a result, the skylight reflection on the waves at the water surface is less sensitive to the orientation of their facets. Therefore, errors in the wave slope distribution produce a lesser impact on R_{ss} computed for such conditions.

Another interesting aspect is the angular distribution of the uncertainty. Finding the viewing geometry to minimize the uncertainty might help improve the performances of the overall AWR process. For clear atmosphere conditions (i.e., τ_a = 0.1) and low wind speed, it can be seen in Figure 11 that the uncertainty strongly increase with solar zenith angle for relative azimuth 90°, with values exceeding 10% for θ_s >50°. On the contrary, the uncertainty values remain under 2% for the same conditions when taking a relative azimuth of 135°. A specific angular zone between scattering angle 120° and 140° was noticed to provide lesser uncertainty, this zone is delimited by the two black lines in Figure 11, similar patterns are also observed in the absolute uncertainty values. It is worth noting that this geometrical zone provides the lowest uncertainty values whatever the parameters τ_a and *ws* considered. This provides a way to minimize AWR uncertainty by adapting the relative azimuth for each specific Sun elevation.

4 Discussion

4.1 Diffuse and direct light

In this study, it has been proposed to separate the contribution of the diffuse skylight from the direct component of the sunglint radiance to correct AWR measurements for surface reflection. This is the main difference with previously proposed values of the sky to surface radiance conversion factor provided by Mobley (1999) assuming unpolarized light and Mobley (2015) which account for polarization where the

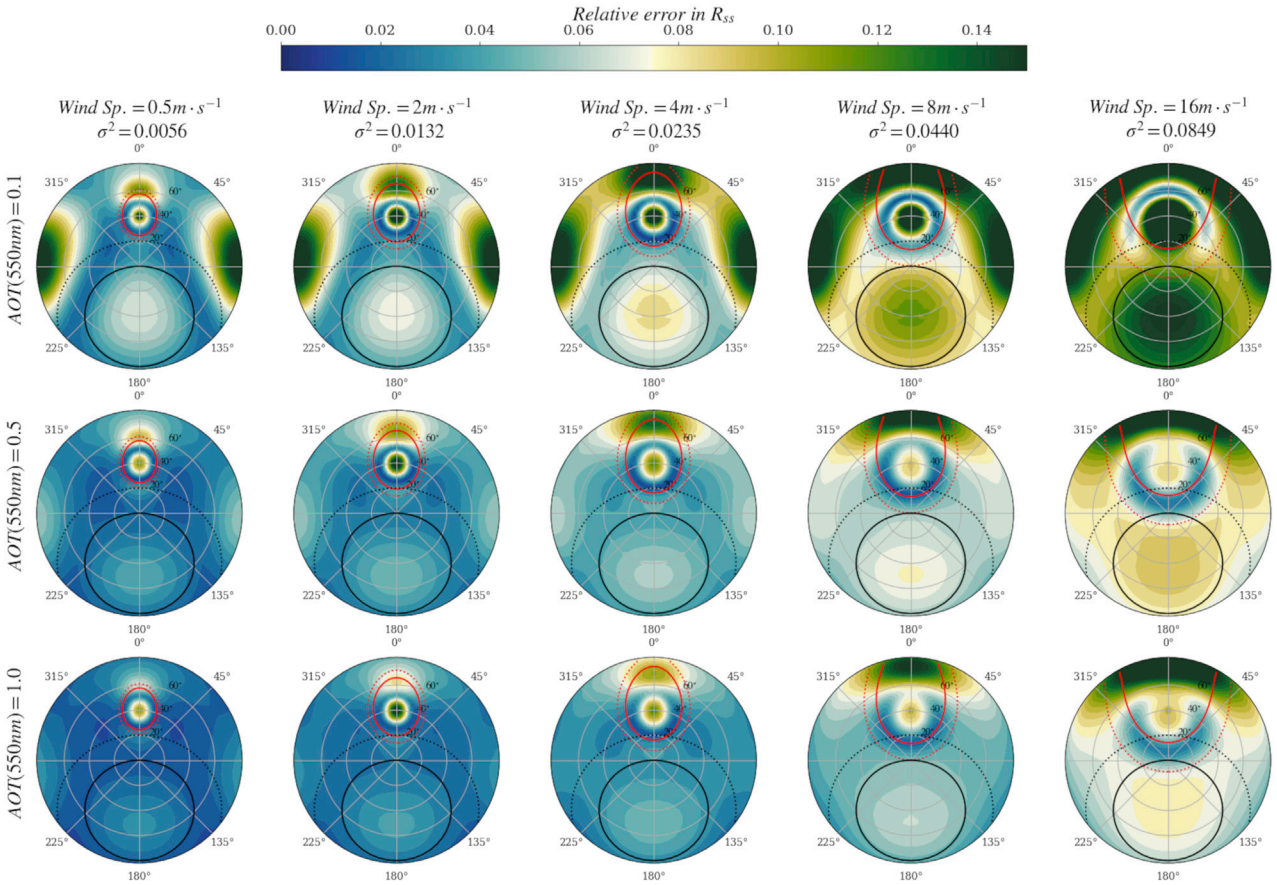


FIGURE 11
(*polar diagram: contour circles indicate solar zenith angles*) Relative uncertainty in R_{ss} at 600 nm and θ_v = 40° due to propagation of errors attached to input aerosol optical thickness and equivalent Cox-Munk wind speed. For information, contour lines for sunglint reflectance of 1% (dotted red line) and 5% (continuous red line) are superimposed based on the Cox-Munk isotropic model. Contour lines of scattering angle 120° (dotted black line) and 140° (continuous black line) are also indicated.

sunglint is embedded. Those values were computed for a fixed wavelength (e.g., 550 nm) assuming the factor is spectrally neutral (Mobley, 2015). It has been shown that the inclusion of the sunglint should also take into account the spectral variation of the direct atmospheric transmittance through the dependency of the total optical thickness including the aerosol effect on it. Other studies provided spectral values of this factor from unpolarized (Lin et al., 2023) or full vector (Gilerson et al., 2018) radiative transfer computations. But, both studies included the sunglint contribution to the final computation. Note that another study explicitly separated the diffuse and direct contributions recommending a two-step procedure for respective corrections of sky and sun lights (Zhang et al., 2017). It has been shown in Figure 4 that inclusion of sunglint induces significant discrepancies especially for low solar zenith angle (i.e., Sun close to zenith). On the other hand, it was already noted that the application of standard procedure that takes the quantile 20% of the measured L_t (Hooker et al., 2002) with factor including the sunglint contribution generally leads to overcorrecting the water signal in the current AERONET-OC processing with increased uncertainty for high Sun elevation (Harmel et al., 2011; Harmel et al., 2012). Moreover, the usual wave statistics fail to reproduce the sunglint signal based on surface wind speed measurements over short time scale and/or small spatial extent (Kay et al., 2009). This study provides spectral values for diffuse light correction for a comprehensive set of environmental conditions that can help to further constrain the dedicated sunglint correction step as recently proposed (Goyens and Ruddick, 2023). It can also be foreseen that preliminary diffuse light correction could help to extract the sunglint signal from spectral measurement where the water-leaving radiance is negligible (e.g., shortwave-infrared) as done for atmospheric correction of optical satellite (Harmel et al., 2018).

4.2 Surface roughness

The presented results are based on the isotropic Cox-Munk wave slopes statistics (Cox and Munk, 1954). This model was used due to its simplicity to be included in radiative transfer calculation. The surface-to-sky radiance ratio has been tabulated using the equivalent Cox-Munk wind speed but also with the variance of the wave slope distribution. This enables the use of the appropriate value based on water surface state information instead of wind speed that may be uncorrelated to actual surface roughness as already mentioned (Kay et al., 2009). Nevertheless, perspectives of this work should include

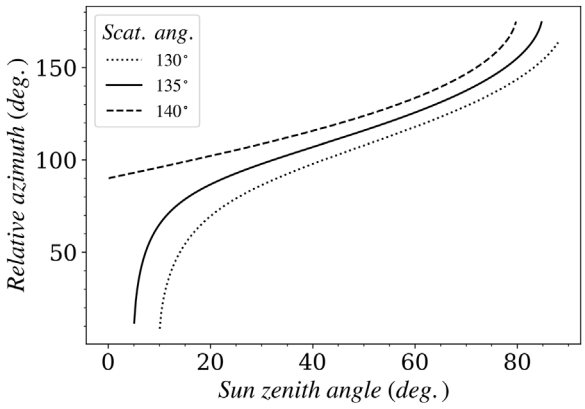


FIGURE 12
Optimal viewing geometry of above-water radiometer for a viewing zenith angle of 40° according to lowest uncertainty attached to the R_{ss} factor which is centered on scattering angle 135°, see Figure 11.

advanced numerical simulations of the wave spectra (from gravities to capillaries) and their slope distributions provided by several theoretical studies based on the Monte-Carlo approach (Mobley, 2015; D'Alimonte and Kajiyama, 2016; Foster and Gilerson, 2016; Hieronymi, 2016). Another approach could be based on direct measurements of the wave distribution from polarimetric measurements (Zappa et al., 2008)) or from multi-angular upwelling radiance measurements as recently suggested (Goyens and Ruddick, 2023).

4.3 Aerosol approach

As it has been shown, the presence of aerosols significantly modifies the surface-to-sky radiance ratio through their optical thickness but also the inherent optical properties defining the aerosol model to be used. These modifications arise even for low values of the aerosol optical thickness. Even if the viewing geometry can be adapted to minimize uncertainty due to partially known aerosol properties, as shown in Figures 10, 11, it is necessary to document the presence of aerosol load during data acquisitions. This can easily be done from the measurements provided by the AERONET-OC network (Zibordi et al., 2009) for which measurements are routinely operated to provide spectral aerosol optical thickness (Zibordi et al., 2021) or further optical properties (Dubovik et al., 2000; O'Neill et al., 2003). For another important network called HYPERNETS, the installed system, the *HYperspectral Pointable System for Terrestrial and Aquatic Radiometry* (HYPSTAR), could also be used to concurrently monitor the aerosol optical properties but it is not currently the case for routine operation (Goyens et al., 2022). A recent study showed the benefits of incorporating a pyranometer in the AWR system enabling distinctive measurements of the direct and diffuse part of the downwelling irradiance (Jordan et al., 2022). For this kind of system, the pyranometer measurements could also be used to retrieve the aerosol parameters (Alexandrov et al., 2002).

Above-water radiometry methods are also deployed on small to big ships including research vessels (Ondrusek et al., 2022), ferries (Nasiha et al., 2022) or even dugout canoes (Marinho et al., 2021). In such conditions, the aerosol properties are not always acquired concurrently. A first approach could be to use the aerosol data provided by the operational reanalysis models such as Copernicus' CAMS or NASA's MERRA which provide aerosol optical properties worldwide with acceptable uncertainties (Gueymard and Yang, 2020). Another practical approach would be to systematically perform aerosol data acquisition within AWR protocols. For this purpose, hand-held sun photometers could be advantageously exploited to provide spectral aerosol optical thickness (Porter et al., 2001; Knobelspiesse et al., 2004).

4.4 Impacts of geometrical configuration

The above-water radiometry procedure is based on a well-calibrated radiometer positioned in predetermined viewing configuration by setting both the viewing zenith angle and the relative azimuth. Even if the choice of viewing geometries for real-world installation may suffer limitations due to the constraints imposed by the vessel/platform superstructure or associated shadowing, it is worth documenting the most optimal geometries that help minimize uncertainties. This study showed that the absolute value of surface-to-sky radiance ratio is very variable with these two parameters but also the uncertainty attached to R_{ss}. This uncertainty originates from errors made in the input parameters to the presented model, i.e., aerosol optical thickness and type as well as the surface roughness parameter. It has been demonstrated that the uncertainty can be minimized by changing the relative azimuth with respect to the Sun elevation to perform the AWR acquisition in a geometry following a constant scattering angle value centered on approximately 135° irrespective of the wavelength. Therefore, it is recommended to adapt the viewing geometry over the course of a day. To do so, the couple $(\theta_s, \Delta\phi)$ needs to be adapted to get a constant value of the scattering angle for a fixed viewing zenith angle, θ_v. The Figure 12 shows this relationship between θ_s and $\Delta\phi$ for $\theta_v = 40°$ for three values of the scattering angles where the uncertainties are minimal. From this figure, it is recommended to perform the acquisition at $\Delta\phi = 90°$ when the Sun is at $\theta_s = 20°$ and at $\Delta\phi = 150°$ when the Sun is at $\theta_s = 80°$, for instance. For robotic setups, the viewing configuration could be automatically adapted from the exact Sun location following this scheme.

5 Conclusion

The impact of aerosols, polarization and water surface roughness on above-water radiometry (AWR) measurements was analyzed based on full vector radiative transfer computations. Based on theoretical and practical considerations, the parameter to convert the downward sky radiance measurements into the surface-reflected radiance was renamed *surface-to-sky radiance ratio*, R_{ss}, in order to avoid misuse of the term *reflectance* as often encountered in the literature. Angular values of R_{ss} were computed for a large set of input parameters with surface roughness both expressed in wave slope variances (0.0056–0.0849) or equivalent Cox-Munk wind speeds

(0.5–16 m s^{-1}), aerosol optical thicknesses (0–1.5 at 550 nm), aerosol types covering maritime, continental, desert and polluted conditions, and for wavelengths ranging from 350 to 1,000 nm. Here, the use of the slope variances is due to the fact that statistics between roughness and wind speed might not hold for time and space scales encountered in AWR measurements. Following previous studies, diffuse (skylight) and direct (sunglint) light component have been separated to provide R_{ss} values for diffuse light only. Comparison with former tabulated values including sunglint might explain the overestimation of the surface radiance when the Sun is high on the horizon.

It has been shown that knowledge on aerosol load and type is critical to correct for reflected skylight even for very low amounts in the atmosphere. Uncertainties attached to R_{ss} were computed based on the two input parameters slope variance (wind speed) and aerosol optical thickness. The uncertainty is very sensitive to the viewing direction and Sun elevation exhibiting lower values for geometries defined by a scattering angle between 120° and 140°. This enabled defining the most appropriate couple of viewing and azimuth angles to reduce uncertainty for a given Sun angle. For instance, it has been recommended to perform acquisition for viewing zenith angle 40° and relative azimuth 90° when the Sun zenith angle is 20° and relative azimuth 150° when the Sun zenith angle is 80°. Such adaptable geometries could be implemented in robotic AWR systems to reduce uncertainty budget. Even if the uncertainty due to unknown aerosol optical properties can be minimized, it is advocated to accompany AWR acquisitions with concurrent aerosol measurements to further constrain the surface-reflected light correction.

The computations presented in this study still need to be further applied on actual *in situ* data sets. To this end, tabulated values are provided as a multidimensional data set based on the network Common Data Form (netCDF file). It is worth highlighting that the tabulated values must be used under clear sky conditions only since heterogeneous atmospheres with clouds or fully overcast conditions were not considered. Nevertheless, those values could be used to develop optimal methods to proceed with non-ideal conditions as in (Groetsch et al., 2017; Pitarch et al., 2020; Borges et al., 2022). The correction of the sunglint component is not taken into account in the tabulated values but methods based on separation of diffuse and direct light developed for atmospheric correction could be further investigated (Harmel et al., 2018). Even if the results have been discussed for monodirectional radiometer, the tabulated values are also suitable for correction of AWR multi-view radiometric camera if the viewing geometry of each pixel is known (Carrizo et al., 2019; Gilerson et al., 2020). Finally, the theoretical scheme presented here could be easily adapted to provide spectral values to correct polarimetric measurements of the water system.

Data availability statement

The original contributions presented in the study are included in the article/supplementary material, further inquiries can be directed to the corresponding author.

Author contributions

TH: Conceptualization, Data curation, Funding acquisition, Investigation, Methodology, Software, Visualization, Writing–original draft.

Funding

The author(s) declare financial support was received for the research, authorship, and/or publication of this article. French National Program for Remote Sensing (PNTS-2019-13).

Acknowledgments

The author is thankful to Alexandre Castagna and the *GEO AquaWatch* Nomenclature Group for insightful discussions. The editor and the two reviewers are also gratefully acknowledged for their subtle and enriching comments.

Conflict of interest

TH was employed by Magellium Artal Group.

Publisher's note

All claims expressed in this article are solely those of the authors and do not necessarily represent those of their affiliated organizations, or those of the publisher, the editors and the reviewers. Any product that may be evaluated in this article, or claim that may be made by its manufacturer, is not guaranteed or endorsed by the publisher.

Supplementary material

The Supplementary Material for this article can be found online at: https://www.frontiersin.org/articles/10.3389/frsen.2023.1307976/full#supplementary-material

References

Adams, J. T., and Kattawar, G. W. (1997). Neutral points in an atmosphere-ocean system. 1: upwelling light field', *Applied Optics. Opt. Soc. Am.* 36 (9), 1976–1986. doi:10.1364/ao.36.001976

Alexandrov, M. D., Lacis, A. A., Carlson, B. E., and Cairns, B. (2002). Remote sensing of atmospheric aerosols and trace gases by means of multifilter rotating shadowband radiometer. Part II: climatological applications. *J. Atmos. Sci.* 59 (3), 544–566. doi:10.1175/1520-0469(2002)059<0544:rsoaaa>2.0.co;2

Antoine, D., d'Ortenzio, F., Hooker, S. B., Bécu, G., Gentili, B., Tailliez, D., et al. (2008). Assessment of uncertainty in the ocean reflectance determined by three satellite ocean color sensors (MERIS, SeaWiFS and MODIS-A) at an offshore site in the Mediterranean Sea (BOUSSOLE project). J. Geophys. Res. *Am. Geophys. Union* 113 (C7), C07013. doi:10.1029/2007JC004472

Bodhaine, B. A., Wood, B. N., Dutton, G., and Slusser, R. J. (1999). On Rayleigh optical depth calculations. *J. Atmos. Ocean. Technol.* 16 (11), 1854–1861. doi:10.1175/1520-0426(1999)016<1854:ORODC>2.0.CO;2

Borges, H. D., Martinez, J. M., Harmel, T., Cicerelli, R. E., Olivetti, D., and Roig, H. L. (2022). Continuous monitoring of suspended particulate matter in tropical inland waters by high-frequency, above-water radiometry. *Sensors* 22 (22), 8731. doi:10.3390/S22228731

Carrizo, C., Gilerson, A., Foster, R., Golovin, A., and El-Habashi, A. (2019). Characterization of radiance from the ocean surface by hyperspectral imaging', *Optics Express. Opt. Publ. Group* 27 (2), 1750. doi:10.1364/oe.27.001750

Chami, M., Lafrance, B., Fougnie, B., Chowdhary, J., Harmel, T., and Waquet, F. (2015). OSOAA: a vector radiative transfer model of coupled atmosphere-ocean system for a rough sea surface application to the estimates of the directional variations of the water leaving reflectance to better process multi-angular satellite data over the ocean', *Optics Express. OSA* 23 (21), 27829–27852. doi:10.1364/OE.23.027829

Chami, M., Santer, R., and Dilligeard, E. (2001). Radiative transfer model for the computation of radiance and polarization in an ocean-atmosphere system: polarization properties of suspended matter for remote sensing. *Appl. Opt.* 40 (15), 2398–2416. doi:10.1364/ao.40.002398

Chandrasekhar, S. (1947). The transfer of radiation in stellar atmospheres. *Bull. Amer. Math. Soc.* 53, 641–711. doi:10.1090/s0002-9904-1947-08825-x

Chandrasekhar, S. (1960). *Radiative transfer*. New York: Dover.

Cox, C., and Munk, W. (1956). in *Slopes of the sea surface deduced from photographs of sun glitter, Scripps Institution of Oceanography*. Editors C. Cox and W. Munk La Jolla, CA, United States: (Scripps Institution of Oceanography).

Cox, C., and Munk, W. H. (1954). Statistics of the sea surface derived from sun glitter. *J. Mar. Res.* 13 (2), 198–227.

D'Alimonte, D., and Kajiyama, T. (2016). Effects of light polarization and waves slope statistics on the reflectance factor of the sea surface', *Optics Express. Opt. Soc. Am.* 24 (8), 7922. doi:10.1364/OE.24.007922

Deuze, J. L., Herman, M., and Santer, R. (1989). Fourier-series expansion of the transfer equation in the atmosphere ocean system. *J. of Quantitative Spectrosc. Radiat. Transf.* 41 (6), 483–494. doi:10.1016/0022-4073(89)90118-0

Dubovik, O., Smirnov, A., Holben, B. N., King, M. D., Kaufman, Y. J., Eck, T. F., et al. (2000). Accuracy assessments of aerosol optical properties retrieved from Aerosol Robotic Network (AERONET) Sun and sky radiance measurements. *J. Geophys. Res.* 105 (D8), 9791–9806. doi:10.1029/2000jd900040

Foster, R., and Gilerson, A. (2016). Polarized transfer functions of the ocean surface for above-surface determination of the vector submarine light field. *Appl. Opt.* 55 (33), 9476–9494. doi:10.1364/AO.55.009476

Franz, B. A., Bailey, S. W., Werdell, P. J., and McClain, C. R. (2007). Sensor-independent approach to the vicarious calibration of satellite ocean color radiometry. *Appl. Opt.* 46 (22), 5068–5082. doi:10.1364/ao.46.005068

Fraser, R. S. (1968). Atmospheric neutral points over water. *JOSA* 58 (8), 1029–1031. doi:10.1364/JOSA.58.001029

Gasteiger, J., and Wiegner, M. (2018). MOPSMAP v1.0: a versatile tool for the modeling of aerosol optical properties. *Copernic. GmbH* 11 (7), 2739–2762. Geoscientific Model Development. doi:10.5194/GMD-11-2739-2018

Giardino, C., Brando, V. E., Gege, P., Pinnel, N., Hochberg, E., Knaeps, E., et al. (2019). Imaging spectrometry of inland and coastal waters: state of the art, achievements and perspectives. *Surv. Geophys.* 40 (3), 401–429. doi:10.1007/s10712-018-9476-0

Gilerson, A., Carrizo, C., Foster, R., and Harmel, T. (2018). Variability of the reflectance coefficient of skylight from the ocean surface and its implications to ocean color. *Opt. Express* 26 (8), 9615–9633. doi:10.1364/OE.26.009615

Gilerson, A., Carrizo, C., Ibrahim, A., Foster, R., Harmel, T., El-Habashi, A., et al. (2020). Hyperspectral polarimetric imaging of the water surface and retrieval of water optical parameters from multi-angular polarimetric data. Appl. Opt. *Opt. Soc.* 59 (10), C8. doi:10.1364/ao.59.0000c8

Gilerson, A., Herrera-Estrella, E., Agagliate, J., Foster, R., Gossn, J. I., Dessailly, D., et al. (2023). Determining the primary sources of uncertainty in the retrieval of marine remote sensing reflectance from satellite ocean color sensors II. Sentinel 3 OLCI sensors. Front. Remote Sens. *Front.* 4, 1146110. doi:10.3389/FRSEN.2023.1146110

Goyens, C., Beyer, J. E., Xiao, X., and Hambright, K. D. (2022). Using hyperspectral remote sensing to monitor water quality in drinking water reservoirs. *Remote Sens.* 14 (21), 5607. doi:10.3390/RS14215607

Goyens, C., and Ruddick, K. (2023). Improving the standard protocol for above-water reflectance measurements: 1. Estimating effective wind speed from angular variation of sunglint. *Appl. Opt.* 62 (10), 2442. doi:10.1364/ao.481787

Groetsch, P. M. M., Gege, P., Simis, S. G. H., Eleveld, M. A., and Peters, S. W. M. (2017). Validation of a spectral correction procedure for sun and sky reflections in above-water reflectance measurements', *Optics Express. Opt. Soc. Am.* 25 (16), A742. doi:10.1364/OE.25.00A742

Gueymard, C. A., and Yang, D. (2020). Worldwide validation of CAMS and MERRA-2 reanalysis aerosol optical depth products using 15 years of AERONET observations, *Atmospheric Environment* 117216. doi:10.1016/j.atmosenv.2019.117216

Harmel, T., and Chami, M. (2012). Determination of sea surface wind speed using the polarimetric and multidirectional properties of satellite measurements in visible bands', *Geophysical Research Letters. AGU* 39 (19), L19611. doi:10.1029/2012GL053508

Harmel, T., Chami, M., Tormos, T., Reynaud, N., and Danis, P.-A. (2018). Sunglint correction of the Multi-Spectral Instrument (MSI)-SENTINEL-2 imagery over inland and sea waters from SWIR bands. *Remote Sens. Environ.* 204, 308–321. doi:10.1016/j.rse.2017.10.022

Harmel, T., Gilerson, A., Hlaing, S., Tonizzo, A., Legbandt, T., Weidemann, A., et al. (2011). Long island sound coastal observatory: assessment of above-water radiometric measurement uncertainties using collocated multi and hyperspectral systems. *Appl. Opt.* 50 (30), 5842–5860. doi:10.1364/AO.50.005842

Harmel, T., Gilerson, A., Hlaing, S., Weidemann, A., Arnone, R., and Ahmed, S. (2012). Long Island Sound Coastal Observatory: assessment of above-water radiometric measurement uncertainties using collocated multi and hyper-spectral systems: reply to comment. Appl. Opt. *OSA* 51 (17), 3893–3899. doi:10.1364/AO.51.003893

Harmel, T., Gilerson, A., Tonizzo, A., Chowdhary, J., Weidemann, A., Arnone, R., et al. (2012). Polarization impacts on the water-leaving radiance retrieval from above-water radiometric measurements. *Appl. Opt.* 51 (35), 8324–8340. doi:10.1364/AO.51.008324

Hess, M., Koepke, P., and Schult, I. (1998). Optical properties of aerosols and clouds: the software package OPAC. *Bull. Am. Meteorological Soc.* 79 (5), 831–844. doi:10.1175/1520-0477(1998)079<0831:OPOAAC>2.0.CO;2

Hieronymi, M. (2016). Polarized reflectance and transmittance distribution functions of the ocean surface', *Optics Express. Opt. Soc. Am.* 24 (14), A1045–A1068. doi:10.1364/OE.24.0A1045

Hooker, S. B., Lazin, G., Zibordi, G., and McLean, S. (2002). An evaluation of above- and in-water methods for determining water-leaving radiances. *J. Atmos. Ocean. Technol.* 19 (4), 486–515. doi:10.1175/1520-0426(2002)019<0486:aeoaai>2.0.co;2

Hooker, S. B., Morrow, J. H., and Matsuoka, A. (2013). Apparent optical properties of the Canadian Beaufort Sea - Part 2: the 1% and 1 cm perspective in deriving and validating AOP data products. *Biogeosciences* 10 (7), 4511–4527. doi:10.5194/BG-10-4511-2013

Hu, C., Carder, K. L., and Muller-Karger, F. E. (2001). How precise are SeaWiFS ocean color estimates? Implications of digitization-noise errors. *Remote Sens. Environ.* 76 (2), 239–249. doi:10.1016/s0034-4257(00)00206-6

Hulburt, E. O. (1934). The polarization of light at sea. *J. of Opt. Soc. of Am.* 24 (2), 35–42. doi:10.1364/josa.24.000035

Jordan, T. M., Simis, S. G. H., Grötsch, P. M. M., and Wood, J. (2022). Incorporating a hyperspectral direct-diffuse pyranometer in an above-water reflectance algorithm. *Remote Sens.* 14 (10), 2491. doi:10.3390/RS14102491

Kay, S., Hedley, J. D., and Lavender, S. (2009). Sun glint correction of high and low spatial resolution images of aquatic scenes: a review of methods for visible and near-infrared wavelengths', *Remote Sensing. Mol. Divers. Preserv. Int.* 1 (4), 697–730. doi:10.3390/rs1040697

Kedenburg, S., Vieweg, M., Gissibl, T., and Giessen, H. (2012). Linear refractive index and absorption measurements of nonlinear optical liquids in the visible and near-infrared spectral region', *Optical Materials Express. Opt. Soc. Am.* 2 (11), 1588–1611. doi:10.1364/OME.2.001588

Knobelspiesse, K. D., Pietras, C., Fargion, G. S., Wang, M., Frouin, R., Miller, M. A., et al. (2004). Maritime aerosol optical thickness measured by handheld sun photometers. *Remote Sens. Environ.* 93 (1–2), 87–106. doi:10.1016/j.rse.2004.06.018

Lee, Z. P., Ahn, Y. H., Mobley, C., and Arnone, R. (2010). Removal of surface-reflected light for the measurement of remote-sensing reflectance from an above-surface platform', *Optics Express. Opt. Soc. Am.* 18 (25), 26313–26324. doi:10.1364/oe.18.026313

Lenoble, J., Herman, M., Deuzé, J., Lafrance, B., Santer, R., and Tanré, D. (2007). A successive order of scattering code for solving the vector equation of transfer in the earth's atmosphere with aerosols. *J. Quantitative Spectrosc. Radiat. Transf.* 107 (3), 479–507. doi:10.1016/j.jqsrt.2007.03.010

Levy, R. C., Mattoo, S., Munchak, L. A., Remer, L. A., Sayer, A. M., Patadia, F., et al. (2013). The Collection 6 MODIS aerosol products over land and ocean. *Atmos. Meas. Tech.* 6 (11), 2989–3034. doi:10.5194/amt-6-2989-2013

Lin, J., Lee, Z., Tilstone, G. H., Liu, X., Wei, J., Ondrusek, M., et al. (2023). Revised spectral optimization approach to remove surface-reflected radiance for the estimation of remote-sensing reflectance from the above-water method. *Opt. Express* 31 (14), 22964–22981. doi:10.1364/OE.486981

Marinho, R. R., Harmel, T., Martinez, J. M., and Filizola Junior, N. P. (2021). Spatiotemporal dynamics of suspended sediments in the negro river, amazon basin, from *in situ* and sentinel-2 remote sensing data. *ISPRS Int. J. Geo-Information* 10 (2), 86. doi:10.3390/ijgi10020086

Max, J.-J. J., and Chapados, C. (2009). Isotope effects in liquid water by infrared spectroscopy. III. H2O and D2O spectra from 6000 to 0 cm(-1). *J. Chem. Phys.* 131 (18), 184505. doi:10.1063/1.3258646

McClain, E. P., and Strong, A. E. (1969). On anomalous dark patches in satellite-viewed sunglint areas. *Mon. Weather Rev.* 97 (12), 875–884. doi:10.1175/1520-0493(1969)097<0875:OADPIS>2.3.CO;2

Mishchenko, M. I., Videen, G., Babenko, V. A., Khlebtsov, N. G., Wriedt, T., et al. (2004). T-matrix theory of electromagnetic scattering by particles and its applications: a comprehensive reference database. *J. Quant. Spectrosc. Radiat. Transf.* 88, 357–406. doi:10.1016/j.jqsrt.2004.05.002

Mishchenko, M. I., Hovenier, J. W., and Travis, L. D. (2000). in *Light scattering by nonspherical particles: theory, measurements, and applications*. Editors M. I. Mishchenko, J. W. Hovenier, and L. D. Travis (San Diego: Academic Press).

Mobley, C. D. (1999). Estimation of the remote-sensing reflectance from above-surface measurements. *Appl. Opt.* 38 (36), 7442–7455. doi:10.1364/AO.38.007442

Mobley, C. D. (2015). Polarized reflectance and transmittance properties of windblown sea surfaces', *Applied Optics. Opt. Soc. Am.* 54 (15), 4828. doi:10.1364/AO.54.004828

Mobley, C. D., Chai, F., Xiu, P., and Sundman, L. K. (2015). Impact of improved light calculations on predicted phytoplankton growth and heating in an idealized upwelling-downwelling channel geometry. *J. Geophys. Res. Oceans* 120 (2), 875–892. doi:10.1002/2014JC010588

Mueller, J. L., and Austin, R. W. (1995). in Ocean Optics Protocols for SeaWiFS validation, revision 1, SeaWiFS technical report series. *Greenbelt, Maryland: NASA technical memorandum 104566*. Editors S. B. Hooker, E. R. Firestone, and J. G. Acker

Munk, W. (2009). An inconvenient sea truth: spread, steepness, and skewness of surface slopes', *annual Review of marine science. Annu. Rev.* 1 (1), 377–415. doi:10.1146/annurev.marine.010908.163940

Nasiha, H. J., Wang, Z., Giannini, F., and Costa, M. (2022). Spatial variability of *in situ* above-water reflectance in coastal dynamic waters: implications for satellite match-up analysis', *Frontiers in remote sensing. Frontiers* 3, 876748. doi:10.3389/FRSEN.2022.876748

Ondrusek, M., Wei, J., Menghua, W., Eric, S., Charles, K., Alex, G., et al. (2022) Report for dedicated JPSS VIIRS ocean color calibration/validation cruise: gulf of Mexico in april 2021. doi:10.25923/X2Q6-9418

O'Neill, N. T., Eck, T. F., Smirnov, A., Holben, B. N., and Thulasiraman, S. (2003). Spectral discrimination of coarse and fine mode optical depth. J. Geophys. Res. *Am. Geophys. Union* 108 (D17), 4559. doi:10.1029/2002JD002975

Pahlevan, N., Mangin, A., Balasubramanian, S. V., Smith, B., Alikas, K., Arai, K., et al. (2021). ACIX-Aqua: a global assessment of atmospheric correction methods for Landsat-8 and Sentinel-2 over lakes, rivers, and coastal waters. *Remote Sens. Environ.* 258, 112366. doi:10.1016/j.rse.2021.112366

Perrin, F. (1942). Polarization of light scattered by isotropic opalescent media. *J. Chem. Phys.* 10, 415–427. doi:10.1063/1.1723743

Pitarch, J., Talone, M., Zibordi, G., and Groetsch, P. (2020). Determination of the remote-sensing reflectance from above-water measurements with the "3C model": a further assessment', *Optics Express. Opt. Soc.* 28 (11), 15885. doi:10.1364/oe.388683

Porter, J. N., Miller, M., Pietras, C., and Motell, C. (2001). Ship-based sun photometer measurements using microtops sun photometers. *J. Atmos. Ocean. Technol.* 18 (5), 765–774. doi:10.1175/1520-0426(2001)018<0765:SBSPMU>2.0.CO;2

Preisendorfer, R. W., and Mobley, C. D. (1986). Albedos and glitter patterns of a wind-roughened sea surface. *J. Phys. Oceanogr.* 16, 1293–1316. doi:10.1175/1520-0485(1986)016<1293:AAGPOA>2.0.CO;2

Quan, X., and Fry, E. S. (1995). Empirical equation for the index of refraction of seawater.', *Applied optics. Opt. Soc. Am.* 34 (18), 3477–3480. doi:10.1364/AO.34.003477

Ruddick, K. G., Voss, K., Boss, E., Castagna, A., Frouin, R., Gilerson, A., et al. (2019). A review of protocols for fiducial reference measurements of water-leaving radiance for validation of satellite remote-sensing data over water. *Remote Sens.* 11 (19), 2198. doi:10.3390/RS11192198

Segelstein, D. J. (1981). *The complex refractive index of water*. Kansas City, USA: University of Missouri–Kansas City.

Spooner, J. (1822). Sur la lumière des ondes de la mer. *Corresp. Astro. Baron Zach.* 6, 331–338.

Stokes, G. G. (1852). On the composition and resolution of streams of polarized light from different sources. *Trans. Camb. Philos. Soc.* 3 (9), 233–259.

Werdell, P. J., McKinna, L. I., Boss, E., Ackleson, S. G., Craig, S. E., Gregg, W. W., et al. (2018). An overview of approaches and challenges for retrieving marine inherent optical properties from ocean color remote sensing. *Prog. Oceanogr.* 160, 186–212. doi:10.1016/j.pocean.2018.01.001

Yang, P., Feng, Q., Hong, G., Kattawar, G. W., Wiscombe, W. J., Mishchenko, M. I., et al. (2007). Modeling of the scattering and radiative properties of nonspherical dust-like aerosols. *J. Aerosol Sci.* 38 (10), 995–1014. doi:10.1016/J.JAEROSCI.2007.07.001

Zappa, C. J., Banner, M. L., Schultz, H., Corrada-Emmanuel, A., Wolff, L. B., and Yalcin, J. (2008). Retrieval of short ocean wave slope using polarimetric imaging', *Measurement Science and Technology. IOP Publ.* 19 (5), 055503. doi:10.1088/0957-0233/19/5/055503

Zhai, P. W., Hu, Y., Chowdhary, J., Trepte, C. R., Lucker, P. L., and Josset, D. B. (2010). A vector radiative transfer model for coupled atmosphere and ocean systems with a rough interface. *J. Quantitative Spectrosc. Radiat. Transf.* 111 (7–8), 1025–1040. doi:10.1016/j.jqsrt.2009.12.005

Zhang, X., He, S., Shabani, A., Zhai, P. W., and Du, K. (2017). Spectral sea surface reflectance of skylight. *Opt. Express* 25 (4), A1–A13. doi:10.1364/OE.25.0000A1

Zibordi, G. (2016). Experimental evaluation of theoretical sea surface reflectance factors relevant to above-water radiometry', *Optics Express. OSA* 24 (6), A446. doi:10.1364/oe.24.00a446

Zibordi, G., et al. (2019). "Protocols for satellite ocean colour data validation," *in Situ optical radiometry*. Editors K. J. Voss, B. C. Johnson, and J. L. Mueller (Dartmouth, NS, Canada: IOCCG Protocol Series IOCCG Ocea). IOCCG 3. doi:10.25607/OBP-691

Zibordi, G., Holben, B. N., Talone, M., D'Alimonte, D., Slutsker, I., Giles, D. M., et al. (2021). Advances in the ocean color component of the aerosol robotic network (AERONET-OC)', *Journal of Atmospheric and oceanic Technology. Am. Meteorological Soc.* 38 (4), 725–746. doi:10.1175/JTECH-D-20-0085.1

Zibordi, G., Hooker, S. B., Berthon, J. F., and D'Alimonte, D. (2002). Autonomous above-water radiance measurements from an offshore platform: a field assessment experiment. *J. Atmos. Ocean. Technol.* 19 (5), 808–819. doi:10.1175/1520-0426(2002)019<0808:aawrmf>2.0.co;2

Zibordi, G., Mélin, F., Berthon, J. F., Holben, B., Slutsker, I., Giles, D., et al. (2009). AERONET-OC: a network for the validation of ocean color primary products. *J. Atmos. Ocean. Technol.* 26, 1634–1651. doi:10.1175/2009jtecho654.1

Zieger, P., Fierz-Schmidhauser, R., Weingartner, E., and Baltensperger, U. (2013). Effects of relative humidity on aerosol light scattering: results from different European sites. *Atmos. Chem. Phys.* 13 (21), 10609–10631. doi:10.5194/ACP-13-10609-2013

frontiers | Frontiers in Remote Sensing

TYPE Erratum
PUBLISHED 27 February 2024
DOI 10.3389/frsen.2024.1379573

Check for updates

OPEN ACCESS

APPROVED BY
Frontiers Editorial Office,
Frontiers Media SA, Switzerland

*CORRESPONDENCE
Frontiers Production Office,
production.office@frontiersin.org

RECEIVED 31 January 2024
ACCEPTED 31 January 2024
PUBLISHED 27 February 2024

CITATION
Frontiers Production Office (2024), Erratum: Apparent surface-to-sky radiance ratio of natural waters including polarization and aerosol effects: implications for above-water radiometry.
Front. Remote Sens. 5:1379573.
doi: 10.3389/frsen.2024.1379573

COPYRIGHT
© 2024 Frontiers Production Office. This is an open-access article distributed under the terms of the Creative Commons Attribution License (CC BY). The use, distribution or reproduction in other forums is permitted, provided the original author(s) and the copyright owner(s) are credited and that the original publication in this journal is cited, in accordance with accepted academic practice. No use, distribution or reproduction is permitted which does not comply with these terms.

Erratum: Apparent surface-to-sky radiance ratio of natural waters including polarization and aerosol effects: implications for above-water radiometry

Frontiers Production Office*

Frontiers Media SA, Lausanne, Switzerland

KEYWORDS

above-water radiometry, aerosol, water-leaving radiance, polarization, cal/val activities

An Erratum on
Apparent surface-to-sky radiance ratio of natural waters including polarization and aerosol effects: implications for above-water radiometry

by Harmel T (2023). Front. Remote Sens. 4:1307976. doi: 10.3389/frsen.2023.1307976

Due to a production error, the supplementary file called Supplementary Data Sheet 1 was not published. This document provides complementary figures to the main manuscript.

The publisher apologizes for this mistake. The original version of this article has been updated.

frontiers | Frontiers in Remote Sensing

TYPE Original Research
PUBLISHED 08 January 2024
DOI 10.3389/frsen.2023.1295855

Check for updates

OPEN ACCESS

EDITED BY
Kevin Ruddick,
Royal Belgian Institute of Natural Sciences, Belgium

REVIEWED BY
Peng-Wang Zhai,
University of Maryland, Baltimore County, United States
Martin Hieronymi,
Helmholtz-Zentrum Hereon, Germany
Agnieszka Bialek,
National Physical Laboratory, United Kingdom

*CORRESPONDENCE
Frédéric Mélin,
frederic.melin@ec.europa.eu

RECEIVED 17 September 2023
ACCEPTED 11 December 2023
PUBLISHED 08 January 2024

CITATION
Mélin F, Cazzaniga I and Sciuto P (2024), Verification of uncertainty estimates of autonomous field measurements of marine reflectance using simultaneous observations. *Front. Remote Sens.* 4:1295855. doi: 10.3389/frsen.2023.1295855

COPYRIGHT
© 2024 Mélin, Cazzaniga and Sciuto. This is an open-access article distributed under the terms of the Creative Commons Attribution License (CC BY). The use, distribution or reproduction in other forums is permitted, provided the original author(s) and the copyright owner(s) are credited and that the original publication in this journal is cited, in accordance with accepted academic practice. No use, distribution or reproduction is permitted which does not comply with these terms.

Verification of uncertainty estimates of autonomous field measurements of marine reflectance using simultaneous observations

Frédéric Mélin*, Ilaria Cazzaniga and Pietro Sciuto

European Commission, Joint Research Centre (JRC), Ispra, Italy

The primary ocean color product is the spectrum of remote sensing reflectance R_{RS} that allows the quantification of in-water optically significant constituents and all ocean color applications. The determination of its uncertainties is thus key to the creation of comprehensive uncertainty budgets for all derived ocean color products. The assessment of satellite R_{RS} uncertainties has largely relied on corresponding field measurements but this process is solid only if these field measurements are in turn fully characterized. Uncertainty budgets have therefore been defined and reported for the radiometric measurements collected in the framework of the Ocean Color component of the Aerosol Robotic Network (AERONET-OC). The contemporaneous deployment of two autonomous systems for 5.5 years on the Acqua Alta Oceanographic Tower (AAOT) located in the northern Adriatic Sea led to the collection of 4,449 pairs of coincident observations (collected with a time difference lower than 10 min) distributed over 659 days of data acquisitions that can be used to verify reported uncertainty values. The comparison of matched pairs showed a good agreement for R_{RS} (with differences of typically 2%–3% between 412 and 560 nm), as well as for the aerosol optical thickness τ_a (3%–6%). Differences between data from the two systems appear generally consistent with their stated uncertainties, indicating that they are metrologically compatible and that uncertainties reported for AERONET-OC data are usually trustworthy (with possible exceptions depending on the level of error correlation between measurements from the two systems). Using uncertainty cone diagrams, this result holds across the range of uncertainty values with few exceptions. Independent uncertainty estimates associated with non-systematic error contributions were obtained using a collocation framework allowing for error correlation between measurements from the two systems. The resulting uncertainties appeared comparable with the reported values for τ_a and R_{RS}. The related mathematical development also showed that the centered root-mean-square difference between data collected by two systems is a conservative estimate of the uncertainty associated with these data (excluding systematic contributions) if these data show a good agreement (expressed by a slope of method II regression close to 1) and if their uncertainties can be assumed similar with errors moderately correlated (typically lower than 0.5).

KEYWORDS

ocean color, optical radiometry, uncertainty, metrology, AERONET-OC

1 Introduction

Ocean color products derived from data of water-leaving radiance L_W or remote sensing reflectance R_{RS} offer an extensive array of applications (IOCCG, 2008), including environmental monitoring or climate science, in the context of which L_W is listed as an Essential Climate Variable (ECV) (GCOS, 2011). But the use of ocean color remote sensing is only trustworthy if these products are accompanied by uncertainty estimates (IOCCG, 2019), a requirement increasingly recognized in explicit terms in related projects (Donlon et al., 2012; Hollmann et al., 2013; Ahmad et al., 2019). Much of what is known about uncertainties of ocean color data relies on comparison with field measurements, a process termed validation. In the context of climate studies, validation activities are actually required by the Global Climate Observing System (GCOS) for the generation of ECV products (GCOS, 2010). Among the field data used for validation activities, Fiducial Reference Measurements (FRM) have a central role to play as data of particularly high quality; they must fulfill some criteria on measurement and quality control protocols, uncertainty characterization, and traceability to standards (Ruddick et al., 2019; Donlon et al., 2014; Fahy et al., 2022). However, the validity of uncertainty estimates associated with FRMs should also be verified, a process that can rely on inter-comparison exercises (Donlon et al., 2014). Even though such exercises have proved useful for an improved characterization of radiometric measurements and associated uncertainties (e.g., Hooker and Maritorena, 2000; Hooker et al., 2002; Zibordi et al., 2004; Vabson et al., 2019; Alikas et al., 2020; Tilstone et al., 2020), they have often been limited to short periods of time.

Since 2002, the Ocean Color (OC) component of the Aerosol Robotic Network (Holben et al., 1998), AERONET-OC (Zibordi et al., 2021), has provided standardized radiometric measurements collected by autonomous Sun photometers operating from offshore structures in coastal regions or lakes. AERONET-OC radiometric measurements have been extensively used for the validation of satellite radiometric products (normalized water leaving radiance L_{WN} or R_{RS}) from a variety of satellite missions (e.g., Zibordi et al., 2009a; Zibordi et al., 2022b; Mélin et al., 2011; Mélin et al., 2012; Pahlevan et al., 2021; McCarthy et al., 2023) as well as for other applications such as the assessment of detection methods for specific types of phytoplankton (Cazzaniga et al., 2021; Cazzaniga et al., 2023), the testing of multi-mission merging techniques (Mélin and Zibordi, 2007; Mélin et al., 2009) or system vicarious calibration (Mélin and Zibordi, 2010). They benefit from a calibration traceable to standards (Johnson et al., 2021) and a comprehensive set of quality control procedures (Zibordi et al., 2022a; D'Alimonte and Zibordi, 2006; Giles et al., 2019). Studies by Gergely and Zibordi (2014) and Cazzaniga and Zibordi (2023) also described an approach to compute uncertainty estimates for each AERONET-OC L_{WN} record.

In October 2017, the AERONET-OC system operating on the Acqua Alta Oceanographic Tower (AAOT), located in the northern Adriatic Sea (45.314°N, 12.508°E), was updated with the installation of a CE-318T Sun photometer with enhanced capabilities but the previous CE-318 instrument was kept in operation till March 2023, which has provided 5.5 years of simultaneous measurements from similar instruments. This dual configuration and the resulting large body of data offer a unique opportunity to assess the AERONET-OC observations and their uncertainty budget by analysing if the differences observed between measurements of two instruments are compatible with their associated uncertainties. The first objective of this study is thus to verify the uncertainty estimates reported for the AAOT AERONET-OC data as well as to validate the approach devised to compile these uncertainties. The second objective is more methodological, i.e., to present a metrologically sound approach for such an assessment that could be applied to other cases of simultaneous observations.

2 Materials and methods

The Acqua Alta Oceanographic Tower (AAOT) in the northern Adriatic Sea has been hosting a SeaWiFS[1] Photometer Revision for Incident Surface Measurements (SeaPRISM or simply PRS hereafter) CE-318 system since 2002 and is the precursor site for AERONET-OC. This site is characterized by a large variability in bio-optical quantities since located in a transition region between open sea and coastal waters affected by the input from several rivers (Zibordi et al., 2009a). The aerosol type is mostly continental, occasionally maritime (Mélin and Zibordi, 2005; Mélin et al., 2006).

In October 2017, a more recent SeaPRISM system (CE-318T, Zibordi et al., 2021) was additionally deployed on AAOT. The two instruments were located a short distance apart (~65 cm) and observed the same portion of the sea (see Zibordi et al., 2021, for a view of the setting). The two systems (hereafter called PRS_0 and PRS_1 for CE-318T and CE-318, respectively) operated simultaneously from October 2017 to March 2023. CE-318 and CE-318T differ mainly in the number of measurement sequences performed and the number of the center-wavelengths at which measurements are acquired, which are both higher for PRS_0 (CE-318T). Every hour, whereas CE-318 instruments perform two sequences of measurements, CE-318T instruments perform two triplets of measurement sequences. Each triplet is composed of three complete measurement sequences typically completed within 10 min.

CE-318 acquires measurements at eight bands with nominal center-wavelengths at 412.5, 442.5, 490.0, 532.0, 551.0, 667.0, 870.0 and 1,020.0 nm, while CE-318T acquires measurements at 11 bands with nominal center-wavelengths matching those of the Ocean and Land Colour Imager (OLCI, Donlon et al., 2012), at 400.0, 412.5, 442.5, 490.0, 510.0, 560.0, 620.0, 665.0, 779.0, 865.0, and 1,020.0 nm. Exact center-wavelengths actually vary with each deployment, with a maximum deviation of 4.4 nm for CE-318 (maximum in the range 551–555 nm) and 0.3 nm for CE-318T. In the considered observation period (Oct. 2017-March 2023), 2 and 5 instruments were alternatively deployed for PRS_0 and PRS_1, respectively. These instruments were regularly substituted for maintenance and re-calibration: the considered period was associated with seven deployments for PRS_0 and 8 deployments for PRS_1, so that the pair of instruments in operation varied at irregular intervals. Even though comparison statistics may

1 standing for Sea-viewing Wide Field-of-view Sensor

somewhat vary from one pair of instruments to another (Zibordi et al., 2021), the observations collected by successive deployments of CE-318T and CE-318 were considered as a single time-series covering the whole period for PRS_0 and PRS_1, respectively, which is consistent with the way the respective data sets are distributed through the AERONET-OC portal[2] for the "AAOT" and "Venice" sites.

2.1 PRS measurements

The water-leaving radiance L_W at wavelength λ is quantified by PRS measurements in the following way (Zibordi et al., 2021, and references therein):

$$L_W(\lambda,\theta,\theta_0,\phi) = L_T(\lambda,\theta,\theta_0,\phi) - \rho(\theta,\theta_0,\phi,w)L_i(\lambda,\theta',\theta_0,\phi) \quad (1)$$

where L_T is the total radiance measured by the instrument pointed at the sea surface with the geometry defined by the zenith viewing angle θ (fixed at 40°) and relative azimuth with respect to the solar plane ϕ (fixed at 90°) with a solar zenith angle θ_0, and L_i is the sky radiance collected with a viewing angle $\theta' = 180° - \theta$. The sea-surface reflectance factor ρ is computed as a function of geometry and sea state represented by wind speed w (Mobley, 1999; Mobley, 2015). For each measurement sequence, 11 measurements of L_T and 3 measurements of L_i are performed. Selected values of L_T and L_i are then obtained by averaging all L_i measurements and the lowest 2 out of 11 measurements of L_T, aiming at minimizing the impact of wave perturbations, as described in Zibordi et al. (2021) and in D'Alimonte et al. (2021).

The conversion from L_W to the normalized water-leaving radiance L_{WN} is performed through:

$$L_{WN}(\lambda) = \frac{L_W(\lambda,\theta,\theta_0,\phi)}{d^2\cos\theta_0 t_d(\lambda,\theta_0)} C_Q(\lambda,\theta,\theta_0,\phi,OP,w) \quad (2)$$

where d is the inverse normalized Earth-Sun distance, and t_d is the diffuse atmospheric transmittance (Deschamps et al., 1983). The remote sensing reflectance R_{RS} is simply defined as L_{WN}/E_0, where E_0 is the mean extra-terrestrial solar irradiance (Thuillier et al., 2003). In effect, the product $d^2\cos\theta_0 E_0 t_d$ normalizes L_W by the incident downward irradiance. C_Q is a factor correcting for bidirectional effects associated for non-nadir illumination and observation conditions. It is here modeled as a function of geometry, wind speed and the optical properties of the water (labeled *OP*), represented either by chlorophyll-a concentration (*Chl*) according to Morel et al. (2002) or by Inherent Optical Properties (IOP) according to Lee et al. (2011). Both correction methods are provided for AERONET-OC data and corresponding R_{RS} values are hereafter referred to as R_{RS}^{Chl} and R_{RS}^{IOP}, respectively.

As indicated above, wavelengths associated with any two systems differ slightly. This could be corrected with a band-shift correction such as that described in Zibordi et al. (2009a) and applied to L_{WN}. This shift includes a correction for E_0 (which is here embedded in the conversion to R_{RS}) and a component modeling spectral changes in IOPs of the water, themselves computed with L_{WN} with a regional algorithm. This part of the correction may be associated with significant uncertainties (Mélin and Sclep, 2015; Salem et al., 2023) that are not easily quantified for all records. Thus, considering that differences in wavelengths are relatively small and that comparison statistics actually do not improve when applying the correction, it is not applied here.

For completeness, it is recalled that AERONET-OC sites also function as generic AERONET sites for the determination of the aerosol optical thickness τ_a using direct solar irradiance measurements (Holben et al., 1998; Smirnov et al., 2000). Reported uncertainties for τ_a measurements are typically decreasing with wavelength from the blue to the near-infrared (NIR) in the interval 0.010–0.015 (Eck et al., 1999; Schmid et al., 1999). In the comparison between τ_a collected by instruments at different wavelengths, a band-shifting procedure is applied by modeling the spectrum of τ_a as a second-order polynomial (in log-space) (O'Neill et al., 2001; Mélin et al., 2007; Mélin et al., 2013).

2.2 Uncertainties associated with PRS ocean color measurements

In this work, only Level 2.0 AERONET-OC data, i.e., measurements that passed the highest level of quality control (QC), were used. A first automated QC process, fully described in Zibordi et al. (2022a), discarded measurements potentially affected by clouds, high aerosol load, high variability in both illumination and water surface conditions. Additionally, until March 2023, data were qualified as Level 2.0 after an expert-based quality control procedure. For more recent data, an automated comprehensive QC procedure was instead applied, which included former automated checks and mimicked the expert analysis during the final QC of AERONET-OC data.

The measurement function associated with the AERONET-OC systems and its related error sources is displayed in an uncertainty analysis diagram (also called uncertainty tree) following Mittaz et al. (2019) (Figure 1). In the works by Gergely and Zibordi (2014) and Cazzaniga and Zibordi (2023), the combined standard uncertainty (with a coverage factor $k = 1$) associated with AERONET-OC L_W data, $u(L_{W,j})$ for record j, was expressed by the law of uncertainty propagation applying a first-order Taylor series development to Eq. 1 (Ku, 1966; GUM, 2008) leading to (omitting the spectral dependence for simplicity):

$$u^2(L_{W,j}) = \left(L_{T,j}u_{\%}(L_T)\right)^2 + \left(L_{i,j}u_{\%}(L_i)\rho_j\right)^2 + \left(L_{i,j}u_{\%,j}(\rho)\rho_j\right)^2 \quad (3)$$

where $u_{\%}(L_T)$ and $u_{\%}(L_i)$ are L_T and L_i relative uncertainty values, respectively, which include the uncertainty affecting instrument calibration, the decay of instrument sensitivity during a deployment and the short-term environmental perturbations $u_{env}(L_T)$ and $u_{env}(L_i)$ (Figure 1) (the notation $u_{\%}$ will indicate relative uncertainties in % throughout the manuscript). Since only PRS_0 systems provide triplets of measurements, used to estimate $u_{env}(L_T)$ and $u_{env}(L_i)$, $u_{\%}(L_i)$ and $u_{\%}(L_T)$ were calculated as in Cazzaniga and Zibordi (2023) only for PRS_0 time series, and their average values were applied too when calculating PRS_1 uncertainties. For those PRS_1 center-wavelengths which were not available from PRS_0, these average values were interpolated

2 https://aeronet.gsfc.nasa.gov/new_web/ocean_color.html

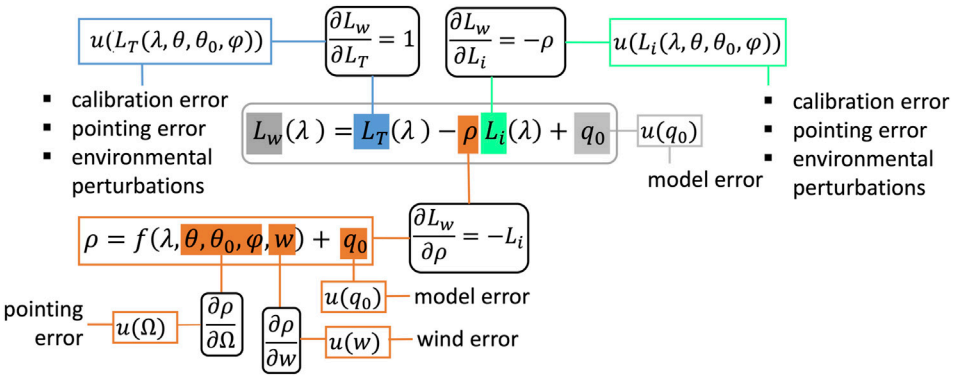


FIGURE 1
Uncertainty tree diagram for the AERONET-OC L_W measurement function (associated with Eq. 3). The measurement function is in the grey rectangle, expressing the measurand as a function of its influence quantities (or input quantities). For each input, the associated error sources are traced with various colors to their contributing factors. Rounded black rectangles indicate the sensitivity factors (expressed as partial derivatives), i.e., the extent to which an error in an input impacts the measurand. For all equations in the diagram, q_0 is a generic notation indicating a possible model error. Ω is a short notation for the geometry of observation and illumination.

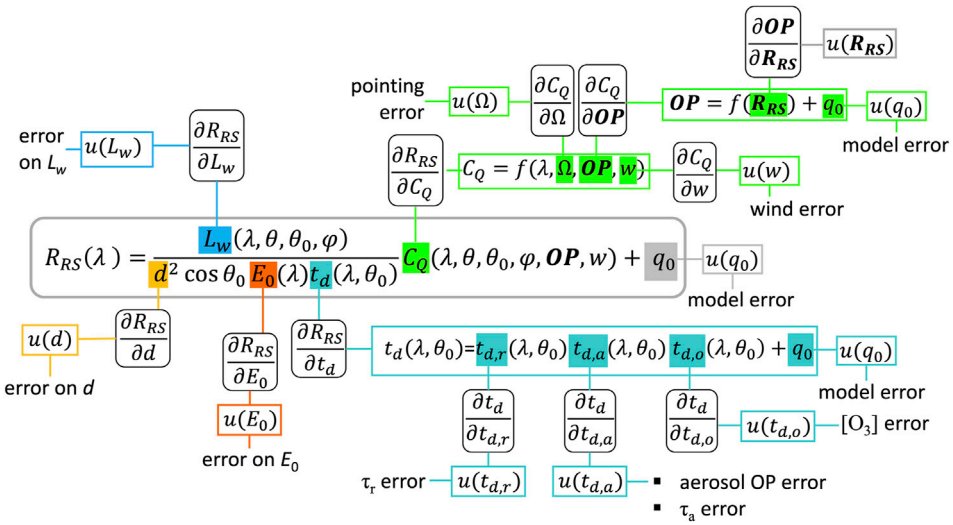


FIGURE 2
Uncertainty tree diagram for the conversion from L_W to R_{RS} (associated with Eq. 4). Its construction is similar to Figure 1. Bold notations indicate a spectrum of values for R_{RS} or for optical properties *OP*. $t_{d,r}$, $t_{d,a}$, and $t_{d,o}$ are transmittance associated with air molecules (Rayleigh), aerosol and ozone. τ_r is the Rayleigh optical thickness (dependent on tabulated values at the standard atmospheric pressure and the actual atmospheric pressure).

spectrally. Finally, $u_{\%,j}(\rho)$, relative uncertainty for ρ, was calculated for each $L_{W,j}$ value as in Cazzaniga and Zibordi (2023). It is acknowledged that Eq. 3 does not include error correlation terms that are deemed insufficiently characterized.

The conversion from L_W to the normalized water-leaving radiance L_{WN} or, equivalently, to the remote sensing reflectance R_{RS} (L_{WN} and R_{RS} merely differ by the factor E_0, Eq. 2) is illustrated by the uncertainty tree diagram of Figure 2. For each record j, the combined standard uncertainty for L_{WN}, $u(L_{WN,j})$, was calculated from $u(L_{W,j})$ and the law of uncertainty propagation applied to Eq. 2, according to (also ignoring correlated terms):

$$u^2\left(L_{WN,j}\right)=\left(C_{Q,j}C_{A,j}u\left(L_{W,j}\right)\right)^2+\left(L_{W,j}u_{\%}\left(C_{Q,j}\right)C_{Q,j}C_{A,j}\right)^2+\left(L_{W,j}u_{\%}\left(C_{A,j}\right)C_{A,j}C_{Q,j}\right)^2 \quad (4)$$

where $C_{A,j}=d_j^2\cos\theta_{0,j}t_{d,j}$, and its relative uncertainty $u_{\%}(C_A)$ is assumed constant for all center-wavelengths and equal to 1.5% (Zibordi et al., 2009b). This estimate encompasses several sources of error such as those due to aerosol, ozone and Rayleigh optical thickness and related optical properties (Figure 2). The relative uncertainty associated with C_Q (term correcting for bidirectional effects), $u_{\%}(C_{Q,j})$, is calculated for each record j as in Cazzaniga and Zibordi (2023), differently

when considering *Chl*-based or IOP-based bidirectional correction functions. Uncertainty values associated with R_{RS} were eventually obtained from $u(L_{WN})$ by dividing by E_0 considered as well known [in reality, this step could introduce an additional, spectrally-varying, uncertainty contribution of the order of 1%, Figure 2, Thuillier et al. (1998)]. Finally, uncertainty estimates shown in this work could slightly vary from those reported in Cazzaniga and Zibordi (2023) due to an updated AERONET-OC time-series which includes more recent data.

2.3 Statistics of comparison

For each day of operation of PRS_0 and for each measurement, the data collected by PRS_1 were searched for the record with the closest time of acquisition, and the pair of coincident measurements was selected for comparison if the time difference was smaller than Δt. From the data set of N pairs of matched data $(x_{0,i})_{i=1,N}$ and $(x_{1,i})_{i=1,N}$ associated with PRS_0 and PRS_1, respectively, statistics of comparison were computed (Mélin and Franz, 2014; IOCCG, 2019), such as:

$$\Delta = \sqrt{\frac{1}{N}\sum_{i=1}^{N}\left(x_{1,i} - x_{0,i}\right)^2} \tag{5}$$

$$\delta = \frac{1}{N}\sum_{i=1}^{N}\left(x_{1,i} - x_{0,i}\right) = \overline{x_1} - \overline{x_0} \tag{6}$$

$$\Delta_c = \sqrt{\frac{1}{N}\sum_{i=1}^{N}\left(x_{1,i} - x_{0,i} + \overline{x_0} - \overline{x_1}\right)^2} = \sqrt{\Delta^2 - \delta^2} \tag{7}$$

where the overbar indicates an average value. Δ, the root-mean-square (RMS) difference between x_0 and x_1 (Eq. 5), can be expressed as the sum (in quadratic form) of the average difference (also called bias), δ, and the centered RMS difference Δ_c.

Acknowledging that there was no reason to consider one measurement better than the other, relative differences were quantified using their unbiased (or symmetric) form, i.e., taking the average of x_0 and x_1 as a reference (at the denominator) (e.g., Hooker and Morel, 2003; Mélin and Franz, 2014).

$$|\psi_u|_m = \text{median}\left(\frac{2|x_{1,i} - x_{0,i}|}{x_{0,i} + x_{1,i}}\right)_{i=1,N} \tag{8}$$

$$\psi_{u,m} = \text{median}\left(\frac{2\left(x_{1,i} - x_{0,i}\right)}{x_{0,i} + x_{1,i}}\right)_{i=1,N} \tag{9}$$

The "median" operator was adopted to reduce the possible impact of outliers; $|\psi_u|_m$ is the median unbiased absolute relative difference (here "absolute" refers to the use of the modulus operator $|\ |$, Eq. 8) and $\psi_{u,m}$ is the median unbiased relative difference (Eq. 9).

The Pearson correlation coefficient r between coincident PRS_0 and PRS_1 measurements (R_{RS} or τ_a) was also computed.

2.4 Error model for collocation statistics

Going beyond simple comparison statistics, collocation analysis underpinned by an error model can provide more elaborate statistics characterizing uncertainties (Stoffelen, 1998; Toohey and Strong, 2007). Here the following error model was adopted for the records $(x_{0,i})_{i=1,N}$ and $(x_{1,i})_{i=1,N}$ associated with PRS_0 and PRS_1, respectively:

$$x_{0,i} = t_i + \epsilon_{0,i} \tag{10}$$

$$x_{1,i} = \alpha + \beta t_i + \epsilon_{1,i} \tag{11}$$

where t is a reference value and the ϵ's are zero-mean random error terms. The term t that serves as a link between x_0 and x_1 can be related to the true value and is not impacted by non-systematic effects that are captured by ϵ. Additive and multiplicative biases, α and β, respectively, further relate x_0 and x_1. Besides systematic effects, uncertainties of x_0 and x_1 could be characterized by the standard deviation of the associated $(\epsilon_i)_{i=1,N}$, σ_ϵ.

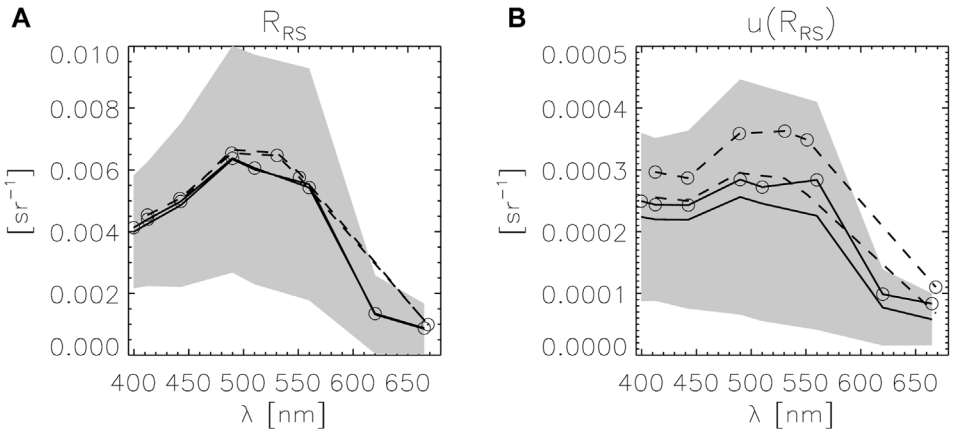


FIGURE 3
Overall average statistics: **(A)** Spectrum of median R_{RS} for PRS_0 (line) and PRS_1 (dashed line), for R_{RS}^{Chl} (line and circle) and for R_{RS}^{IOP} (simple line), the grey envelope representing ± the standard deviation of $R_{RS,0}^{IOP}$; **(B)** Median uncertainty u (R_{RS}) for PRS_0 (line) and PRS_1 (dashed line), for $u(R_{RS}^{Chl})$ (line and circle) and for $u(R_{RS}^{IOP})$ (simple line), the grey envelope representing ± the standard deviation of $u(R_{RS,0}^{IOP})$.

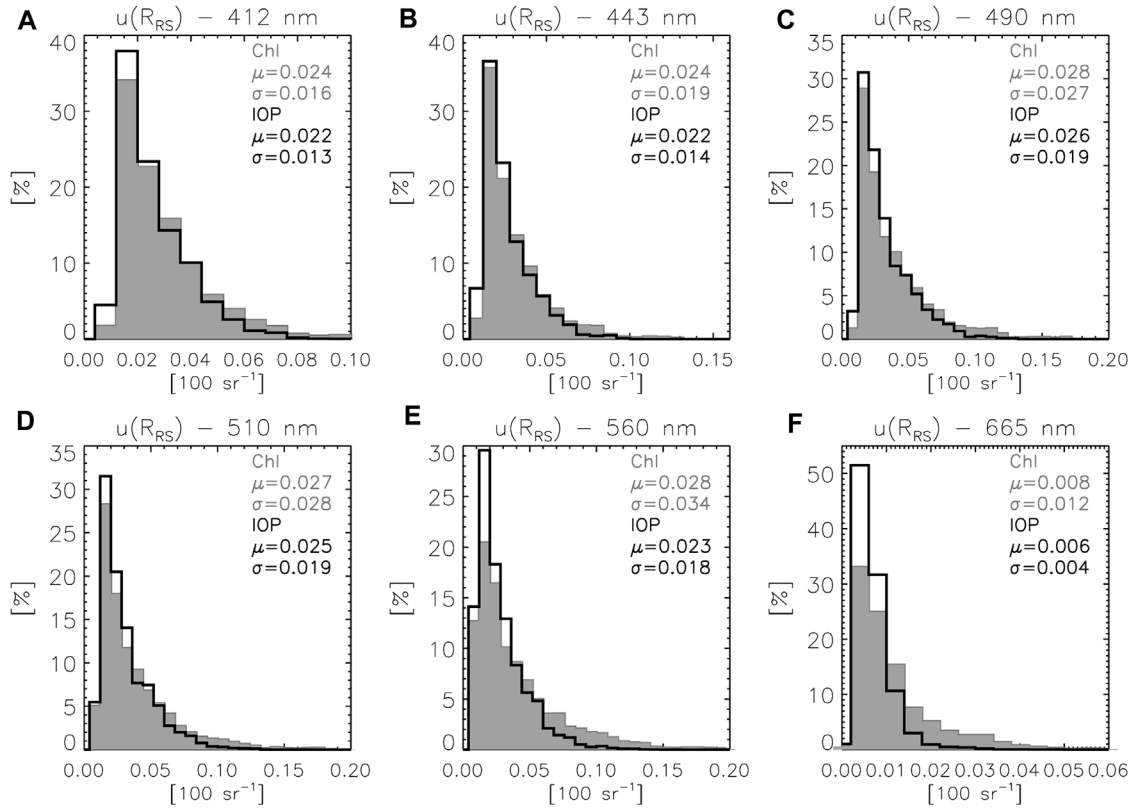


FIGURE 4
Normalized distribution functions of the uncertainties $u(R_{RS})$ for PRS_0 at **(A)** 412 nm, **(B)** 443 nm, **(C)** 490 nm, **(D)** 510 nm, **(E)** 560 nm and **(F)** 665 nm. Grey histogram and statistics are associated with $u(R_{RS}^{Chl})$, while black line and statistics are associated with $u(R_{RS}^{IOP})$. μ and σ give median and standard deviation, respectively.

This framework was adopted to investigate uncertainties of satellite values (Mélin, 2010; Mélin et al., 2016; Mélin, 2021; Mélin, 2022) with the assumption that the ϵ terms were uncorrelated with t and with each other. Considering that the simultaneous determination of R_{RS} by the 2 PRS systems share some elements (Figures 1, 2), this assumption is not warranted here and the framework was extended to the case where ϵ_0 and ϵ_1 are correlated with a coefficient r_ϵ. Writing the variance and covariance terms associated with x_0 and x_1 in that case leads to:

$$\sigma_0^2 = \sigma_t^2 + \sigma_{\epsilon 0}^2 \tag{12}$$

$$\sigma_{01} = \beta\sigma_t^2 + r_\epsilon\sigma_{\epsilon 0}\sigma_{\epsilon 1} \tag{13}$$

$$\sigma_1^2 = \beta^2\sigma_t^2 + \sigma_{\epsilon 1}^2 \tag{14}$$

where σ_0 and σ_1 are the standard deviation of x_0 and x_1, respectively, and $\sigma_{\epsilon 0}$ and $\sigma_{\epsilon 1}$ the standard deviation of ϵ_0 and ϵ_1, respectively.

This system can be rewritten by removing σ_t from Eqs 12, 14 using Eq. 13:

$$\sigma_0^2 = \frac{\sigma_{01} - r_\epsilon\sigma_{\epsilon 0}\sigma_{\epsilon 1}}{\beta} + \sigma_{\epsilon 0}^2 \tag{15}$$

$$\sigma_1^2 = \beta(\sigma_{01} - r_\epsilon\sigma_{\epsilon 0}\sigma_{\epsilon 1}) + \sigma_{\epsilon 1}^2 \tag{16}$$

This system with two equations and four unknowns can be solved if the ratio $\sigma_{\epsilon 1}/\sigma_{\epsilon 0}$, noted η, and r_ϵ are known. This leads to a second-order polynomial with the solution:

$$\beta = \frac{\sigma_1^2 - \eta^2\sigma_0^2 + \sqrt{(\sigma_1^2 - \eta^2\sigma_0^2)^2 + 4(\sigma_{01} - r_\epsilon\eta\sigma_0^2)(\eta^2\sigma_{01} - r_\epsilon\eta\sigma_1^2)}}{2(\sigma_{01} - r_\epsilon\eta\sigma_0^2)} \tag{17}$$

The case $r_\epsilon = 0$ reduces β to the slope of the model II regression, and to the slope of a simple major-axis regression if additionally $\eta = 1$ (Legendre and Legendre, 1998).

The value of β finally leads to $\sigma_{\epsilon 0}$ and $\sigma_{\epsilon 1}$ that are considered as the uncertainties associated with x_0 and x_1 (excluding systematic effects).

$$\sigma_{\epsilon 0}^2 = \frac{\beta\sigma_0^2 - \sigma_{01}}{\beta - r_\epsilon\eta} \tag{18}$$

$$\sigma_{\epsilon 1}^2 = \frac{\sigma_1^2 - \beta\sigma_{01}}{1 - \beta r_\epsilon/\eta} \tag{19}$$

3 Results

3.1 General statistics on data and uncertainties

During the common period of operations (~5.5 years), PRS_0 produced Level 2.0 data over 1,112 days totaling 14,700 records,

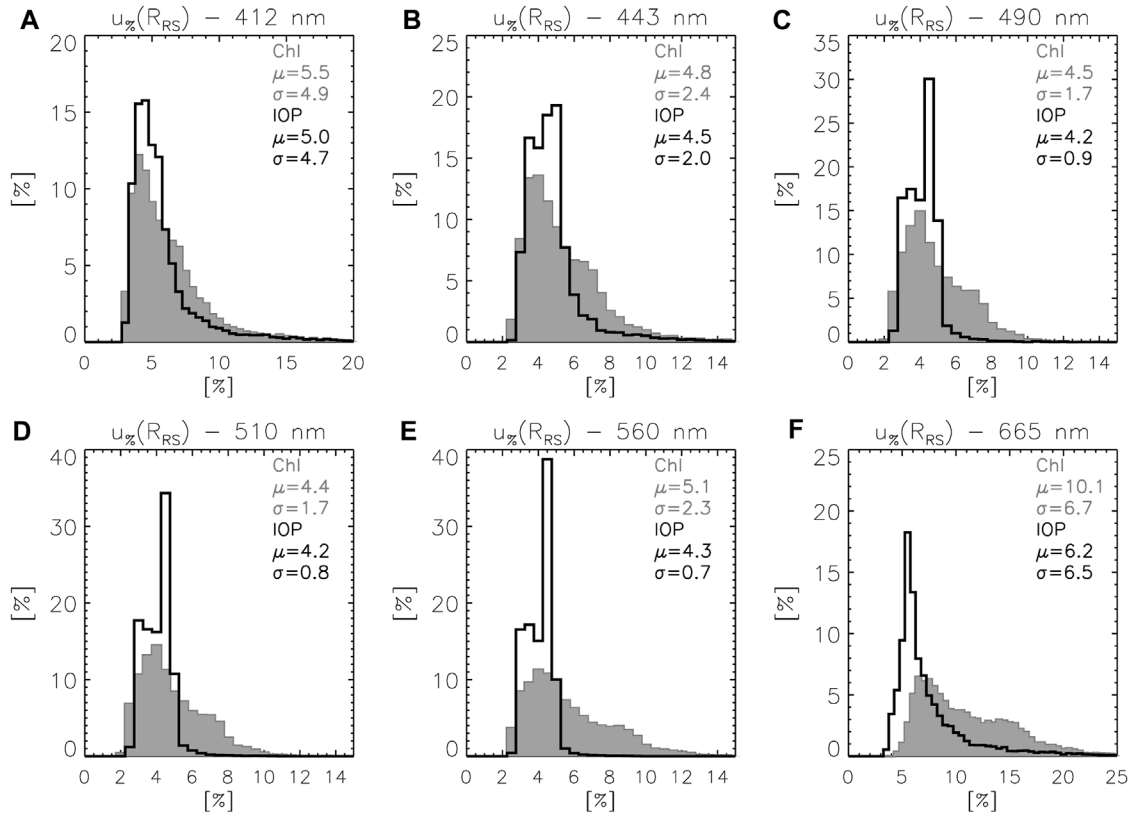


FIGURE 5
Normalized distribution functions of the relative uncertainties $u_{\%}(R_{RS})$ for PRS_0 at **(A)** 412 nm, **(B)** 443 nm, **(C)** 490 nm, **(D)** 510 nm, **(E)** 560 nm and **(F)** 665 nm. Grey histogram and statistics are associated with $u_{\%}(R_{RS}^{Chl})$, while black line and statistics are associated with $u_{\%}(R_{RS}^{IOP})$. μ and σ give median and standard deviation, respectively.

while data were collected by PRS_1 in 811 days (3,059 records). The difference in the number of acquisitions is mostly explained by the higher frequency of observation granted by the CE-318T system (PRS_0).

Figure 3 shows the median values for R_{RS} and associated median uncertainty $u(R_{RS})$ for both terms R_{RS}^{Chl} and R_{RS}^{IOP}. R_{RS} values are typical of the AAOT site, representative of coastal waters with moderately turbid conditions and a peak at 490–530 nm (or secondarily at 555–560 nm) (e.g., Zibordi et al., 2021). The median spectra R_{RS} display a remarkable agreement, both between methods (R_{RS}^{Chl} and R_{RS}^{IOP}) and between systems (PRS_0 and PRS_1), in the latter case when wavelengths are coincident. The spectra $u(R_{RS})$ have a broadly similar shape, with the highest values in the interval 490–560 nm, with lower values in the blue and much lower values in the red. The median spectra $u(R_{RS})$ for PRS_1 usually appear higher than for PRS_0, which is due mostly to the different amounts of data (these differences largely disappear when considering common records, see below).

The overall median aerosol optical thickness τ_a decreases from 0.167 (standard deviation, s.d., 0.133) at 412 nm to 0.054 (s.d. 0.051) at 865 nm for PRS_0, and from 0.166 (s.d. 0.143) at 412 nm to 0.055 (s.d. 0.056) at 869 nm for PRS_1. The median Ångström exponent [computed with a log-transformed linear regression for bands between 412 and 869 nm, Ångström, (1964)] is equal to 1.55 (s.d. 0.30) and 1.52 (s.d. 0.31) for PRS_0 and PRS_1, respectively. These values are also typical for the site and representative of the continental aerosols encountered in the region (Mélin and Zibordi, 2005; Mélin et al., 2006; Clerici and Mélin, 2008).

Focusing on the uncertainties of R_{RS} (calculated assuming uncorrelated inputs, see Section 2.2), Figure 4 shows the distribution functions of $u(R_{RS}^{Chl})$ and $u(R_{RS}^{IOP})$ for PRS_0, (results for PRS_1 are similar with slightly higher values). Results are consistent with those given by Cazzaniga and Zibordi (2023), with median $u(R_{RS}^{Chl})$ and $u(R_{RS}^{IOP})$ in the interval 2.2–2.8 10^{-4} sr^{-1} for wavelengths below 665 nm for PRS_0 (2.5–3.6 10^{-4} sr^{-1} for PRS_1). For PRS_0, median values at 665 nm are 0.83 10^{-4} sr^{-1} for $u(R_{RS}^{Chl})$ and 0.58 10^{-4} sr^{-1} for $u(R_{RS}^{IOP})$ (1.1 and 0.68 10^{-4} sr^{-1} for PRS_1 at 667 nm). The distributions for $u(R_{RS}^{Chl})$ and $u(R_{RS}^{IOP})$ are fairly similar, with the former showing a longer tail of high values. In that respect, the corresponding distributions for the relative uncertainties (Figure 5) show more pronounced differences, with $u_{\%}(R_{RS}^{Chl})$ extending towards larger values. Considering both PRS_0 and PRS_1, the median $u_{\%}(R_{RS}^{IOP})$ is in the interval 4.2%–5.4% for wavelengths below 665 nm, and increases to ~6.2% at 665–667 nm; the median $u_{\%}(R_{RS}^{Chl})$ is slightly higher, in the interval 4.4%–6.4% for wavelengths below 665 nm, and 10.1%–12.1% at 665–667 nm.

3.2 Comparison of τ_a and R_{RS} data

Selecting a maximum time difference Δt of 10 min, 659 days have at least one pair of matching observations, amounting to a total

TABLE 1 Comparison statistics for τ_a with determination coefficient r^2, RMS difference Δ, median unbiased absolute relative difference $|\psi_u|_m$ and median unbiased relative difference $\psi_{u,m}$. Positive values indicate that τ_a from PRS_1 is higher than from PRS_0.

Wavelength λ [nm]	412	443	490	560	665	865
r^2	0.994	0.994	0.989	0.990	0.987	0.977
Δ	0.0103	0.0094	0.0112	0.0095	0.0079	0.0075
$\|\psi_u\|_m$ [%]	3.1	2.6	3.7	5.1	4.5	6.5
$\psi_{u,m}$ [%]	−1.4	−1.1	−0.9	−3.1	−1.3	−2.0

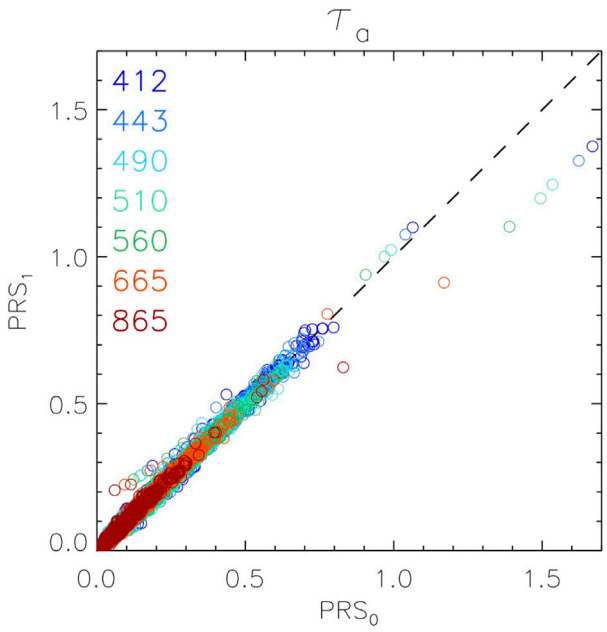


FIGURE 6
Scatter plot of τ_a between PRS_0 and PRS_1 for the indicated wavelengths. Statistics of comparison are given in Table 1.

of 4,449 pairs. This short time difference is associated with similar conditions of illumination, with a mean absolute difference of 0.49° for the solar zenith angle and 1.9° for the solar azimuth angle. In this matching exercise, several members of each PRS_0 triplet (up to 3) can be associated with the same PRS_1 record. Enforcing the occurrence of the PRS_1 data in one matching pair only would reduce the number of matching pairs by half: it would exclude some members of the associated PRS_0 triplet and ultimately a considerable number of valid observations in an arbitrary way. The option adopted here is to consider all PRS_0 data as valid independent observations to be compared to PRS_1 observations. Importantly, besides a lower number of match-ups, results are not affected by this choice.

The comparison between τ_a from PRS_0 and PRS_1 shows a remarkable agreement with a determination coefficient r^2 decreasing from 0.994 at 412 nm to 0.977 at 865 nm, maximum RMS differences Δ of ~0.01 in the spectral range 412–560 nm, and median unbiased absolute relative differences $|\psi_u|_m$ lower than 5% (6.5% at 865 nm) (see Table 1 and Figure 6). There are very few outliers that might be associated with cases of rapid changes in the atmosphere. For instance on 25 February 2020 (the case associated with the highest τ_a in Figure 6), PRS_0 detected three values of τ_a (412) in a hour, 1.26, 1.25 and 1.67, while PRS_1 recorded only one value (1.38) 6 min before the third PRS_0 record.

The R_{RS} data from the two systems also agree very well with very few outliers (Figure 7) in agreement with preliminary results found in Zibordi et al. (2021). This is true for both R_{RS}^{Chl} and R_{RS}^{IOP}, with Δ of the order of 3 10^{-4} sr^{-1} (except ~1.66 10^{-4} sr^{-1} at 665 nm), $|\psi_u|_m$ of 2%–3% (except 5.8% at 665 nm), median unbiased relative differences $\psi_{u,m}$ around or below 1% (except 2.5% at 665 nm) and r^2 in the range 0.967–0.994 (Table 2).

3.3 Uncertainty estimates *versus* comparison statistics

Considering the similar conditions of observations associated with the matched data and the common method to derive uncertainty estimates, $u(R_{RS})$ from PRS_0 and PRS_1 are expected to be close, which is indeed verified by Figure 8. For both $u(R_{RS}^{Chl})$ and $u(R_{RS}^{IOP})$, r^2 between the two distributions is ~0.98. For $u(R_{RS}^{Chl})$, Δ is ~0.2 10^{-4} sr^{-1}, except at 560 nm where it is 0.6 10^{-4} sr^{-1}. In the case of the green band, there are more outliers and an overestimate of the uncertainty from PRS_0 with respect to $u(R_{RS}^{Chl})$ from PRS_1. This can not be easily explained by differences in center wavelengths, as R_{RS} would tend to decrease (and likely its related uncertainty) from 551–555 nm (typical of PRS_1) to 560 nm (associated with PRS_0). Except few outliers, the agreement is slightly better for $u(R_{RS}^{IOP})$ (Figure 8B) with Δ in the interval 0.15–0.25 10^{-4} sr^{-1} between 412 and 560 nm (and 0.08 10^{-4} sr^{-1} at 665 nm); in agreement with Figure 4, there are also less $u(R_{RS}^{IOP})$ values in the upper range (and none above 1.4 10^{-3} sr^{-1}).

The uncertainty estimates should now be related to the differences between coincident records of R_{RS} from PRS_0 and PRS_1 documented in the previous Section 3.2. The uncertainty associated with the difference $R_{RS,1} - R_{RS,0}$ can be expressed with (Mélin, 2021):

$$u^2(R_{RS,1} - R_{RS,0}) = u^2(R_{RS,0}) + u^2(R_{RS,1}) - 2r(e(R_{RS,0}), e(R_{RS,1}))u(R_{RS,0})u(R_{RS,1}) \quad (20)$$

where $r(e(R_{RS,0}), e(R_{RS,0}))$ is the correlation between the errors associated with $R_{RS,0}$ and $R_{RS,1}$. If this correlation is null in Eq. 20, the uncertainty associated with the difference is the sum of the uncertainties (in quadratic form) [e.g., Immler et al. (2010)]. The following inequality may then be introduced (Kacker et al., 2010; Mélin, 2021):

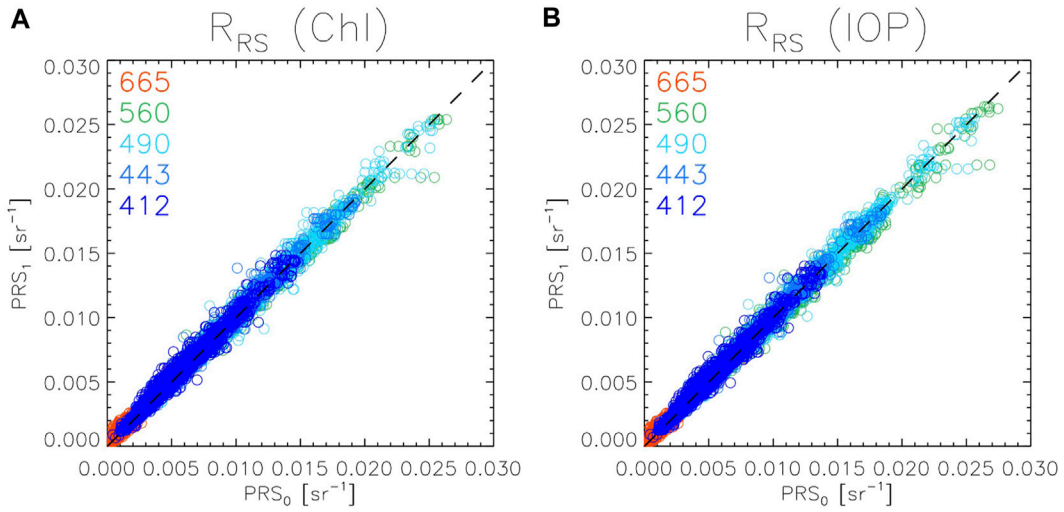


FIGURE 7
Scatter plots comparing **(A)** R_{RS}^{Chl} and **(B)** R_{RS}^{IOP} from PRS_0 and PRS_1 for the indicated wavelengths. Statistics of comparison are given in Table 2.

TABLE 2 Comparison statistics for R_{RS}^{Chl} (upper part) and R_{RS}^{IOP} (lower part) with determination coefficient r^2, RMS difference Δ, median unbiased absolute relative difference $|\psi_u|_m$ and median unbiased relative difference $\psi_{u,m}$. Positive values indicate that R_{RS} from PRS_1 is higher than from PRS_0.

Wavelength λ [nm]	412	443	490	560	665
r^2	0.982	0.991	0.993	0.994	0.967
Δ [10^{-4} sr^{-1}]	3.24	2.90	3.33	3.01	1.66
$\|\psi_u\|_m$ [%]	3.2	2.4	2.0	2.6	5.8
$\psi_{u,m}$ [%]	+1.2	+0.5	+0.3	+0.6	+2.6
r^2	0.981	0.991	0.994	0.992	0.969
Δ [10^{-4} sr^{-1}]	3.01	2.69	2.99	3.64	1.62
$\|\psi_u\|_m$ [%]	3.2	2.3	1.8	3.0	5.8
$\psi_{u,m}$ [%]	+1.2	+0.5	+0.3	+0.5	+2.5

$$|R_{RS,1} - R_{RS,0}| < k\sqrt{u^2(R_{RS,0}) + u^2(R_{RS,1}) - 2r(e(R_{RS,0}), e(R_{RS,1}))u(R_{RS,0})u(R_{RS,1})} \quad (21)$$

where k is the so-called coverage factor. With a normal hypothesis, this inequality would be true in 68% of cases with a coverage factor $k = 1$. Strictly speaking, this reasoning is valid for a hypothetical situation where multiple measurements are repeated in identical conditions; it was here extended to the current match-up data set where R_{RS} (and their uncertainties) are associated with varying conditions experienced during years of operations. No estimate is readily available to quantify the term associated with error correlation (see further on for discussion on this issue) and four cases were considered (with the correlation coefficient assumed constant across the data set): no correlation, low correlation (0.2), moderate correlation (0.5) and high correlation (0.7). The percentage κ of records where Eq. 21 is true appears much higher than 68% for R_{RS}^{Chl} (Table 3); only in the worst case scenario ($r = 0.7$) does κ become slightly lower than 68% at 412 and 665 nm. For R_{RS}^{IOP} between 412 and 490 nm, κ is only slightly lower than for R_{RS}^{Chl} (and mostly well above 68% except at 412 nm for $r = 0.7$) but is noticeably lower at 560 and 665 nm, and lower than 68% for an error correlation above 0.5. Average differences between PRS_0 and PRS_1 are similar for R_{RS}^{Chl} and R_{RS}^{IOP} (actually higher in the latter case at 560 nm, Table 2), while uncertainty estimates tend to be lower for R_{RS}^{IOP} than for R_{RS}^{Chl} (Figures 4, 5), which explains why Eq. 21 is less often verified for R_{RS}^{IOP}, and ultimately the degraded results obtained for κ associated with R_{RS}^{IOP}.

The previous analysis was conducted with statistics compiled over the whole data set; taking advantage of the amount of data available, it can be completed by a more detailed analysis along the range of uncertainties. The set of uncertainties $u(R_{RS})$ was split into 20 bins of equal sample size for which the average value was computed. Then, the centered RMS difference Δ_c (Eq. 7) and average difference δ (Eq. 6) between R_{RS} from PRS_0 and PRS_1 were computed using the records associated with each bin.

Results for R_{RS}^{Chl} and R_{RS}^{IOP} are shown for representative wavelengths in the uncertainty "cone diagrams" of Figures 9, 10, respectively. For each bin, the vertical bar represents $\pm\Delta_c$ (that is the standard deviation of $R_{RS,1} - R_{RS,0}$) while the circle shows δ (the dotted lines being the ±1:1 lines). This type of graphs is more readily used to verify uncertainty estimates when a data set y (typically satellite retrievals) is compared with reference data x (typically field data) (e.g., Ghent et al., 2019). If the error associated with x is negligible, Δ_c is the standard deviation of the errors associated with y and the extremities of the vertical bars should follow the dotted lines (with the assumption that the errors of x and y are not correlated). The dotted uncertainty lines are not extended to 0: in the case of a comparison with reference data, the cone is extended on the lower range by horizontal lines that represent the uncertainty associated with these reference data, considered as the minimum possible value (in the current case the uncertainty lines are only displayed for the available range). Vertical bars exceeding the conic envelope of the dotted lines would indicate that the uncertainty values are

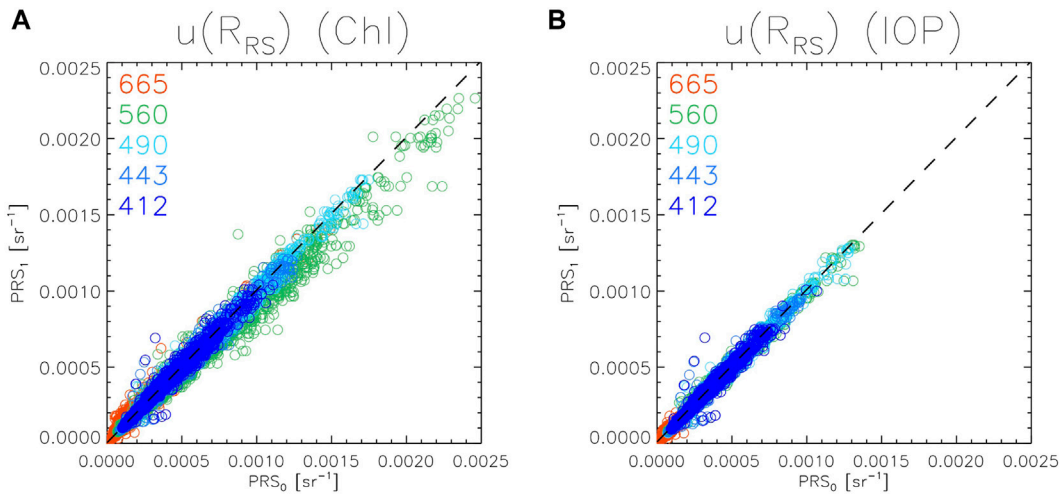


FIGURE 8
Scatter plots comparing **(A)** $u(R_{RS}^{Chl})$ and **(B)** $u(R_{RS}^{IOP})$ from PRS_0 and PRS_1 for the indicated wavelengths.

TABLE 3 Fractions κ (given in %) of records where Eq. 21 is verified for R_{RS}^{Chl} (upper part) and R_{RS}^{IOP} (lower part) and for the four cases of error correlation.

Wavelength λ [nm]	412	443	490	560	665
$r = 0$	89	92	94	93	81
$r = 0.2$	85	89	92	90	78
$r = 0.5$	78	82	86	83	70
$r = 0.7$	67	73	77	73	63
$r = 0$	87	90	93	81	67
$r = 0.2$	83	87	91	76	63
$r = 0.5$	74	80	85	65	55
$r = 0.7$	63	70	75	53	46

underestimated (i.e., that the actual uncertainties would be higher), while vertical bars well contained within the dotted envelope would suggest the opposite. In the current study, neither PRS_0 nor PRS_1 can be taken as a reference value, which means that the comparison between estimated uncertainties and Δ_c remains imperfect. It can just be noted that if the true value of R_{RS} happened to be always in the interval $[R_{RS,0}; R_{RS,1}]$, then Δ_c would be larger than the uncertainty.

At almost all wavelengths and across the range of reported uncertainties, the average differences δ between $R_{RS,0}$ and $R_{RS,1}$ is well below the uncertainty (circles in the dotted cone in Figures 9, 10), the exception being the case of R_{RS}^{IOP} at 665 nm where δ is close to $u(R_{RS}^{IOP})$ (Figure 10C). For R_{RS}^{Chl} between 412 and 560 nm, the extremities of the vertical bars $\pm\Delta_c$ tend to follow the uncertainty estimates (the dotted lines) in the low range of values; in the higher range of uncertainty values, $\pm\Delta_c$ remains further away from the conic envelop (for instance, at 560 nm Δ_c tends to remain stable above uncertainties of 3 10^{-4} sr^{-1}, Figure 9B), suggesting that uncertainty values could actually be too high. The same behavior is seen at 665 nm but the extremities of $\pm\Delta_c$ follow the uncertainty estimates for almost the entire uncertainty range (Figure 9C). For R_{RS}^{IOP} (Figure 10), the extremities of $\pm\Delta_c$ closely follow the cone lines (or are included within the cone) across the range of reported uncertainties from 412 to 560 nm, while at 665 nm, they exceed the uncertainty estimates, suggesting that reported uncertainties may be too low. This is of course coherent with the relatively low values obtained for κ in that case (Table 3). Again, the interpretation that can be given about the positions of the vertical bars $\pm\Delta_c$ within (or beyond) the uncertainty cone implicitly assumes that the error correlation between the PRS_0 and PRS_1 records is negligible. If this is not the case, conclusions drawn from the cone diagrams are too favorable to an extent dependent on the error correlation (Section 3.6). The cone diagram analysis is still valuable as complementary to the analysis conducted with all data (Table 3) as it looks at the behavior of statistics across the range of uncertainties.

3.4 Uncertainty estimates *versus* collocation statistics for τ_a

The collocation approach was first applied to the aerosol optical thickness data τ_a. Considering the agreement of the τ_a data from PRS_0 and PRS_1 (Figure 6), the choice of $\eta = 1$ (ratio of the σ_ϵ's) appears justified. A value for the error correlation is also required and four cases are again considered with r_ϵ equal to 0, 0.2, 0.5 and 0.7. For the case of $r_\epsilon = 0$, the value of β varies between 0.996 and 1.011 (at 865 nm) (Table 4), values that are barely affected by the choice of r_ϵ. σ_ϵ tends to decrease with wavelength, e.g., from 0.0072 at 412 nm to 0.0053 at 865 nm for $r_\epsilon = 0$. Contrary to β, σ_ϵ increases with r_ϵ (following Eqs. 18, 19), from 0.0072 for $r_\epsilon = 0$ to 0.0131 for $r_\epsilon = 0.7$ at 412 nm, or from 0.0053 to 0.0096 at 865 nm. These results are mostly lower than reported uncertainties (Eck et al., 1999; Schmid et al., 1999) of 0.01–0.015 (in the interval 412–865 nm, decreasing with wavelength) but are very close in the case of $r_\epsilon = 0.7$. Similar

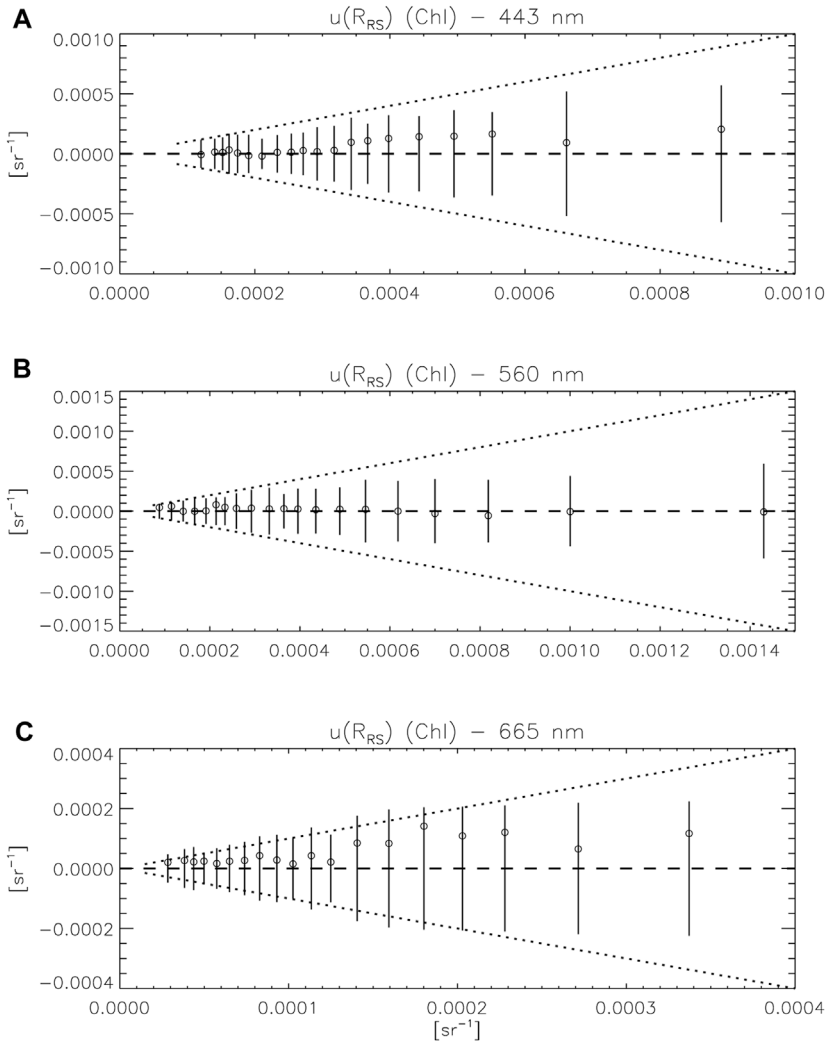


FIGURE 9
Comparison between uncertainty estimates $u(R_{RS}^{Chl})$ and comparison statistics through an uncertainty cone diagram at **(A)** 443 nm, **(B)** 560 and **(C)** 665 nm. The vertical bars represented $\pm\Delta_c$ computed between $R_{RS,0}^{Chl}$ and $R_{RS,1}^{Chl}$ for each bin of increasing uncertainty $u(R_{RS}^{Chl})$. Circles are the associated average difference between $R_{RS,0}^{Chl}$ and $R_{RS,1}^{Chl}$. Dotted lines are $\pm$1:1 lines.

inputs in environmental variables used in τ_a retrieval, such as atmospheric pressure for the determination of the Rayleigh optical depth or ozone concentration and properties, would result in an error correlation for two instruments functioning simultaneously, whereas effects such as instrument noise would not. While determining the relative weights of correlated and uncorrelated effects in τ_a retrievals is out of the scope of this work, it can be said that, unless the contribution to the uncertainty budget from environmental variables is dominant, leading to the upper value of the error correlation, σ_ϵ is found somewhat lower than reported uncertainty values; but it is also stressed that σ_ϵ does not contain contributions from systematic effects (these would be captured by α and β in Eqs. 10, 11), which can be significant (Giles et al., 2019). For completeness, it is noted that the median difference between τ_a from PRS_0 and PRS_1 varies (in modulus) between 0.0010 and 0.0033. Overall, collocation statistics appear consistent with reported uncertainty values for τ_a.

3.5 Uncertainty estimates *versus* collocation statistics for R_{RS}

A similar analysis was conducted with R_{RS} with results reported in Table 5 for the same four cases of error correlation r_ϵ (this time relative to R_{RS}), again under the assumption of $\eta = 1$ considering the agreement in R_{RS} illustrated in Figures 7, 8. The value of β is only given for $r_\epsilon = 0$ since it hardly varies with r_ϵ (with values very close to 1). As for τ_a and according to Eqs 18, 19, σ_ϵ increases with r_ϵ for both R_{RS}^{Chl} and R_{RS}^{IOP}, typically from ~2 to ~3 10^{-4} sr^{-1} (for wavelengths between 412 and 560 nm) when r_ϵ increases from 0 to 0.5. σ_ϵ increases again significantly if r_ϵ is increased from 0.5 to 0.7 (reaching ~4 10^{-4} sr^{-1}).

Values of σ_ϵ can eventually be compared with other statistics presented in the previous sections, the median uncertainty estimate $u(R_{RS})$ (for both PRS_0 and PRS_1, computed with the common records of the match-up data set) and the RMS difference between R_{RS} from PRS_0 and PRS_1 in its centered form Δ_c since σ_ϵ does not include systematic

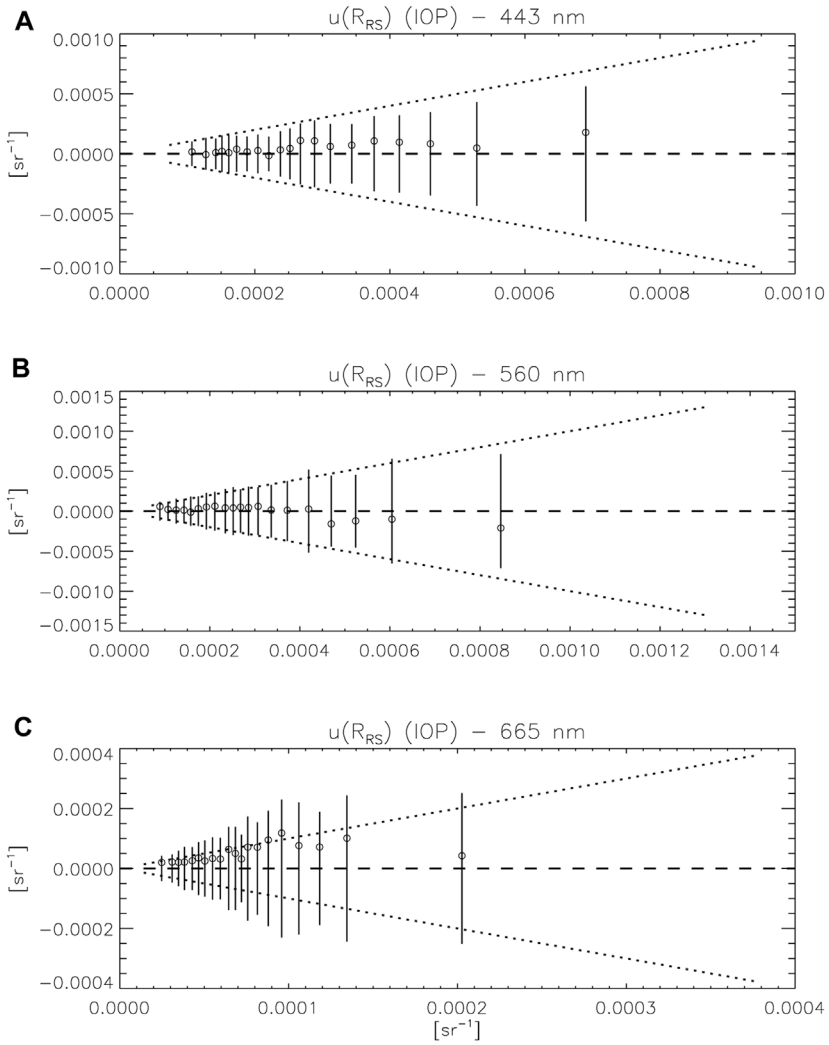


FIGURE 10
Comparison between uncertainty estimates $u(R_{RS}^{IOP})$ and comparison statistics through an uncertainty cone diagram at **(A)** 443 nm, **(B)** 560 and **(C)** 665 nm. The vertical bars represented $\pm\Delta_c$ computed between $R_{RS,0}^{IOP}$ and $R_{RS,1}^{IOP}$ for each bin of increasing uncertainty $u(R_{RS}^{IOP})$. Circles are the associated average difference between $R_{RS,0}^{IOP}$ and $R_{RS,1}^{IOP}$. Dotted lines are $\pm$1:1 lines.

TABLE 4 Collocations statistics: regression slope β for $r_\epsilon = 0$, and σ_ϵ for τ_a for four cases of error correlation r_ϵ.

Wavelength λ [nm]	412	443	490	560	665	865
β; $r_\epsilon = 0$	1.007	0.996	0.998	1.00	1.04	1.011
σ_ϵ; $r_\epsilon = 0$	0.0072	0.0065	0.0079	0.0064	0.0056	0.0053
σ_ϵ; $r_\epsilon = 0.2$	0.0080	0.0073	0.0089	0.0071	0.0062	0.0059
σ_ϵ; $r_\epsilon = 0.5$	0.010	0.0092	0.0112	0.0090	0.0079	0.0075
σ_ϵ; $r_\epsilon = 0.7$	0.0131	0.0119	0.0145	0.0117	0.0102	0.0096

contributions (the average difference δ is also illustrated for completeness and comparison with non-systematic terms). In agreement with Section 2.1 and Figure 4, the median $u(R_{RS}^{IOP})$ is lower than $u(R_{RS}^{Chl})$ (compare Figures 11A, B), while the related Δ_c are comparable, except at 560 nm, where values are higher for R_{RS}^{IOP}. As a result, for R_{RS}^{Chl}, $u(R_{RS})$ is similar or higher than Δ_c except at 665 nm where $u(R_{RS})$ becomes lower (Figure 11A), while for R_{RS}^{IOP}, $u(R_{RS})$ is clearly lower than Δ_c at 560 and 665 nm (Figure 11B). For low values of r_ϵ (0 and 0.2), σ_ϵ associated with R_{RS}^{Chl} is lower than $u(R_{RS})$ except at 665 nm, while for R_{RS}^{IOP}, σ_ϵ is lower than $u(R_{RS})$ for 412–490 nm, similar

TABLE 5 Collocations statistics β for $r_\epsilon = 0$, and σ_ϵ (in 10^{-4} sr^{-1}) for R_{RS}^{Chl} (upper part) and R_{RS}^{IOP} (lower part) and for four cases of error correlation r_ϵ.

Wavelength λ [nm]	412	443	490	560	665
β; $r_\epsilon = 0$	1.013	1.012	1.008	0.984	0.996
σ_ϵ; $r_\epsilon = 0$	2.2	2.0	2.3	2.1	1.1
σ_ϵ; $r_\epsilon = 0.2$	2.5	2.2	2.6	2.3	1.2
σ_ϵ; $r_\epsilon = 0.5$	3.1	2.8	3.3	2.9	1.6
σ_ϵ; $r_\epsilon = 0.7$	4.0	3.6	4.2	3.7	2.0
β; $r_\epsilon = 0$	1.007	1.007	1.003	0.976	0.992
σ_ϵ; $r_\epsilon = 0$	2.0	1.9	2.1	2.5	1.1
σ_ϵ; $r_\epsilon = 0.2$	2.3	2.1	2.3	2.8	1.2
σ_ϵ; $r_\epsilon = 0.5$	2.9	2.6	3.0	3.5	1.5
σ_ϵ; $r_\epsilon = 0.7$	3.7	3.4	3.8	4.5	2.0

for 560 nm and higher for 665 nm. Interestingly, σ_ϵ is very close to Δ_c if $r_\epsilon = 0.5$. For the case of highest correlation (0.7), σ_ϵ is to a varying extent higher than both Δ_c and $u(R_{RS})$.

The relation between Δ_c and σ_ϵ can be further discussed by relating Δ_c with terms of variance and covariance of $(x_{0,i})_{i=1,N}$ and $(x_{1,i})_{i=1,N}$ in Eqs 12–14, starting from:

$$\Delta_c^2 = \sigma_0^2 + \sigma_1^2 - 2\sigma_{01} \tag{22}$$

Eq. 22 then leads to:

$$\Delta_c^2 = (\beta - 1)^2\sigma_0^2 + (\beta(2 - \beta) + \eta^2 - 2r_\epsilon\eta)\sigma_{\epsilon 0}^2 \tag{23}$$

In the case where $\eta \sim 1$, if $\beta \to 1$, then $\Delta_c^2 \to 2(1 - r_\epsilon)\sigma_\epsilon^2$, that is equal to σ_ϵ^2 if $r_\epsilon = 0.5$ (if η is different from 1, the same phenomenon happens at a different value of r_ϵ), a behavior noted in Figure 11. This is actually an important result, predicting that the centered RMS difference between data collected by two systems is a conservative estimate of the uncertainty associated with these data (excluding systematic contributions) if these uncertainties can be assumed similar (η around 1) with errors moderately correlated (typically lower than 0.5) and if the slope of the major-axis regression between the two data sets is close to 1. If the errors can be assumed uncorrelated, then Δ_c is actually twice the uncertainty σ_ϵ. Values of η different from 1 would just vary the relative values of Δ_c and σ_ϵ, while a departure of β from 1 would make these results more dependent on the considered data set (through the first right-hand side term in Eq. 23 proportional to σ_0).

3.6 Error correlation associated with matched R_{RS} observations

The issue of the correlation of the errors associated with the matched R_{RS} data from PRS_0 and PRS_1 has appeared in the previous analyses, when comparing reported uncertainty estimates and comparison statistics (Section 3.3; Eq. 21) and when computing collocation statistics (Section 3.5). Admittedly, additional analyses would be required to quantify the level of correlation between errors affecting simultaneous measurements of R_{RS}. It could change with observation conditions and would certainly vary with wavelength as the weights of different contributing factors in the uncertainty budget varies spectrally (Cazzaniga and Zibordi, 2023). The following discussion attempts to provide an approximate range of values for the error correlation between L_{WN} (or R_{RS}) data from PRS_0 and PRS_1 by defining informed guesses on the error correlation associated with these contributing factors. Cazzaniga and Zibordi (2023) detail five major contributions to the overall uncertainty budget for L_{WN}, the uncertainties due to: i) the calibration of the sensor, u_{cal}, ii) the sea surface reflectance factor ρ, u_ρ, iii) the normalization term for downwelling irradiance $C_A = 1/(d^2\mu_0 t_d)$

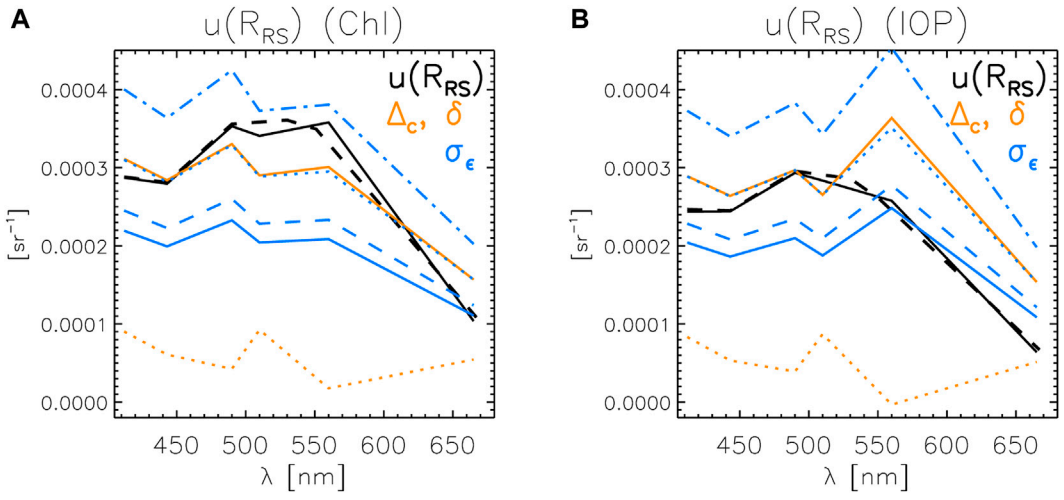


FIGURE 11
Spectra of the median reported uncertainty u (R_{RS}) (black line for PRS_0 and black dashed line for PRS_1) computed for coincident measurements, spectra of centered RMS differences Δ_c (orange line) and average differences δ (orange dotted line), and spectra of σ_ϵ for $r_\epsilon = 0$ (blue line), 0.2 (blue dashed line), 0.5 (blue dotted line) and 0.7 (blue dashed-dotted line). Results are given for **(A)** R_{RS}^{Chl} and **(B)** R_{RS}^{IOP}.

(Eq. 2), u_{C_A}, iv) the correction for bi-directional effects C_Q (Eq. 2), u_{C_Q}, and v) the environmental variability, u_{env} (note that these terms represent uncertainty contributions to the overall uncertainty and not uncertainties of the single quantities; e.g., u_ρ is not the uncertainty $u(\rho)$ associated with ρ but the part of the total uncertainty on R_{RS} that ultimately depends on ρ). For each contribution, a triplet of correlation values will be proposed [low, medium, high].

Starting with the measurement function of L_W (Figure 1), evaluating the correlation of errors due to the calibration of the instruments would require assumptions on the behavior of specific calibration lamps or plaques and on the aging of the sensors, while instrument noise that could additionally affect L_T and L_i would not introduce correlated errors. As a guess for the associated error correlation r_{cal}, the triplet [0, 0.1, 0.3] is proposed. Environmental perturbations may affect the terms of the measurement function L_T, L_i and ρ in a similar way for the two systems but quantifying this relationship is not straightforward and only an arbitrary choice for the associated error correlation r_{env} is selected here, [0, 0.1, 0.3]. The case of ρ can be further discussed, particularly with respect to wind (input to the expression of ρ, Figure 1). In the processing of AERONET-OC data, wind speed is provided by re-analysis products of coarse temporal and spatial resolutions and would have virtually the same value for two measurements collected at short time intervals. If the local wind can be assumed constant for the matched measurements (i.e., in a time interval shorter than 10 min), then the error associated with the use of the re-analysis product will be identical for the two measurements, suggesting a high error correlation affecting ρ for PRS_0 and PRS_1. However, parameterizing the state of the air-sea interface at a precise moment as a function of wind speed is a simplification (represented by the term of model error q_0 in Figure 1). The two instruments are looking at virtually the same small spot on the sea surface (with a full-angle field of view of ~ 1.2°, Holben et al., 1998, the footprint is similar to the distance between the instruments on the supporting platform), but their acquisitions can be minutes apart with variations in surface orientation impacting the actual ρ value (D'Alimonte et al., 2021) in an uncorrelated way. Ultimately, progress on that issue could be achieved by a realistic description of the sea surface at an appropriate time frequency coupled with radiative transfer modelling. Considering these elements, for the purpose of that discussion, a moderately high level of correlation r_ρ can be selected for the errors associated with ρ, [0.1, 0.3, 0.5].

Error correlations may be more easily identified in relation to the conversion from L_W to L_{WN} (or R_{RS}) (Figure 2), introduced by quantities depending on common environmental variables such as the transmittance t_d or C_Q (as well as by E_0). The modeling of the term C_Q contributes significantly to the overall uncertainty budget to an extent that varies with wavelength and water type (Talone et al., 2018; Cazzaniga and Zibordi, 2023). Considering that R_{RS} provided by the two systems are very close (Figure 7), the derived IOPs and *Chl* used to calculate C_Q will also be very similar with correlated errors with respect to the actual IOPs and *Chl* (errors that would depend on the bio-optical model and on R_{RS}). In addition, C_Q models representing the correction for bidirectional effects as a function of IOPs or *Chl* are imperfect [e.g., Gleason et al. (2012); Talone et al. (2018)], which is again represented by the term q_0 associated with C_Q in Figure 2; considering that the same C_Q model was adopted when comparing data from PRS_0 and PRS_1, error correlations r_{C_Q} associated with C_Q can be assumed fairly high, [0.5, 0.7, 0.9]. A similar discussion could be undertaken with t_d that depends on atmospheric variables (e.g., τ_a, ozone, surface pressure) that are very close for matched R_{RS} observations, while the model for computing t_d is identical for both systems. Thus, the triplet of r_{C_A} values associated with C_A is also taken as [0.5, 0.7, 0.9].

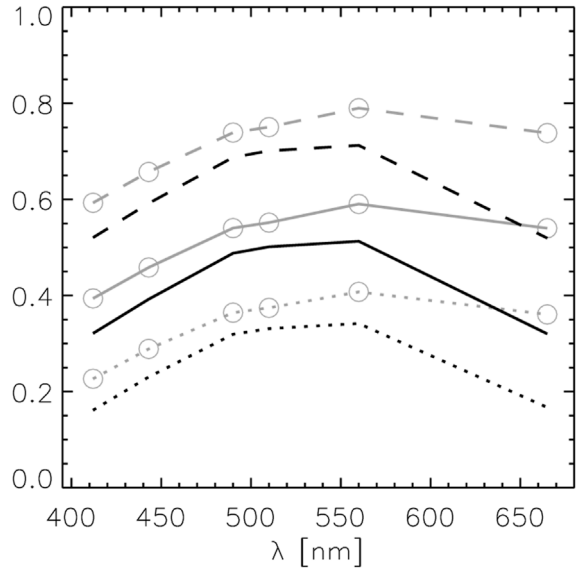


FIGURE 12
Spectra of the error correlation coefficient obtained with Eq. 26 associated with R_{RS}^{Chl} (grey line and circles) and R_{RS}^{IOP} (black lines) from PRS_0 and PRS_1 for the cases of low (dotted lines), medium and high (dashed lines) correlations. For the low case, [r_{cal}, r_ρ, r_{C_Q}, r_{C_A}, r_{env}], is equal to [0, 0.1, 0.5, 0.5, 0], for the medium case [0.1, 0.3, 0.7, 0.7, 0.1] and for the high case [0.3, 0.5, 0.9, 0.9, 0.3].

For each system PRS_j (j = 0 or 1), the error ϵ_j of a given measurement can be written as the sum of errors associated with the contributions discussed above:

$$\epsilon_j = \epsilon_{cal,j} + \epsilon_{\rho,j} + \epsilon_{C_Q,j} + \epsilon_{C_A,j} + \epsilon_{env,j} \quad (24)$$

As said for the uncertainty contributions, it is stressed that the terms of Eq. 24 are representing error contributions to the final value of R_{RS} errors and not errors of the single quantities (e.g., ϵ_ρ is not the error on ρ but the error on R_{RS} that ultimately depends on an error on ρ). Assuming that the errors from different contributions are uncorrelated between PRS_0 and PRS_1 (e.g., that the errors due to environmental variability for PRS_0 are uncorrelated with errors due to C_Q for PRS_1), a calculation of the covariance $\sigma_{\epsilon_0\epsilon_1}$ between ϵ_0 and ϵ_1 gives:

$$\sigma^2_{\epsilon_0\epsilon_1} = \sigma^2_{\epsilon_0\epsilon_1,cal} + \sigma^2_{\epsilon_0\epsilon_1,\rho} + \sigma^2_{\epsilon_0\epsilon_1,C_Q} + \sigma^2_{\epsilon_0\epsilon_1,C_A} + \sigma^2_{\epsilon_0\epsilon_1,env} \quad (25)$$

where, e.g., $\sigma_{\epsilon_0\epsilon_1,cal}$ is the covariance of $\epsilon_{cal,j}$ and $\epsilon_{cal,j}$. Considering that a covariance between two terms is the product of their variance and their correlation, Eq. 25 can be rewritten as:

$$r = \frac{1}{u_0 u_1}\left[r_{cal}u_{0,cal}u_{1,cal} + r_{\rho}u_{0,\rho}u_{1,\rho} + r_{C_Q}u_{0,C_Q}u_{1,C_Q} + r_{C_A}u_{0,C_A}u_{1,C_A} + r_{env}u_{0,env}u_{1,env}\right] \quad (26)$$

where u_0 and u_1 are the combined standard uncertainties for PRS_0 and PRS_1 data while the u_0 and u_1 terms on the right-hand side are associated with the contributions indicated in subscript (Cazzaniga and Zibordi, 2023).

Eq. 26 is applied for the three scenarios (low, medium and high values of the triplets) to calculate an informed guess of the error correlation associated with R_{RS} from PRS_0 and PRS_1 (Figure 12). With the various cases considered, the resulting error correlation could take values in the broad interval 0.2–0.8 with the medium case in the interval of approximately 0.4–0.6. By assuming error correlation coefficients spectrally constant for each type of contribution, the overall correlation is seen to increase from the blue to 560 nm, which can be related to the larger weight of u_{C_Q} in the uncertainty budget at that wavelength (Cazzaniga and Zibordi, 2023); it then decreases in the red, where environmental variability and ρ have a larger relative contribution with respect to the other bands. It is stressed that this spectral shape would be affected if the error correlation associated with specific contributions had a spectral dependence.

Looking back at Figure 11A, $u(R_{RS}^{Chl})$ and σ_ϵ (obtained from collocation statistics) agree well for a correlation coefficient r_ϵ of 0.5 at 412 and 443 nm, ~0.6 at 490–560 nm, and 0–0.2 at 665 nm. In the case of R_{RS}^{IOP} (Figure 11B), $u(R_{RS}^{IOP})$ and σ_ϵ agree for r_ϵ between 0.2 and 0.5 at 412–443 nm, 0.5 at 490–510 nm, and 0–0.2 at 560 nm. At 665 nm, the fact that $u(R_{RS}^{IOP})$ is lower than σ_ϵ obtained with r_ϵ = 0 would again suggest that it might be too low. The correlation analysis performed in this section (Figure 12) aimed at giving some sensitivity on the level of error correlation that could characterize the two systems PRS_0 and PRS_1, and the collocation statistics allowed some degree of cross-checking; this being said, a more detailed investigation would be required for more definite conclusions on this issue.

4 Conclusion

This study has taken advantage of a large body of radiometric data collected simultaneously by two instruments to assess uncertainty estimates reported for R_{RS} (and secondarily τ_a). The first objective was to verify these uncertainty estimates for the specific case of the AERONET-OC data collected at AAOT. τ_a and R_{RS} collected by the two systems appear very close (Figures 6, 7; Tables 1 and 2) and measurements generally agree within their stated uncertainties (Section 3.3), i.e., they are metrologically compatible (Kacker et al., 2010). Actually the analysis comparing uncertainty estimates $u(R_{RS})$ with comparison statistics suggested that $u(R_{RS})$ could be slightly too high in some cases (but too low for $u(R_{RS}^{IOP})$ at 665 nm and even at 560 nm if the error correlation between measurements of the two systems exceeds 0.5, see Table 3). However in the absence of solid estimates of error correlations linking the two systems, no definite conclusions can be stated in that respect. Uncertainty estimates also appeared compatible with uncertainty values σ_ϵ obtained using a collocation approach (again making space for undefined error correlations). Based on these considerations, even though the R_{RS} uncertainty budget could be further refined, the uncertainty values reported for AAOT by Cazzaniga and Zibordi (2023) generally appear trustworthy (with some exceptions where they could be too low, and for error correlation coefficients deemed realistic, i.e., not exceeding 0.7, see Section 3.6). This lends confidence to the general approach developed to calculate the AERONET-OC uncertainties, and indirectly to the resulting uncertainties associated with other sites (Cazzaniga and Zibordi, 2023, propose uncertainty estimates that are site-specific). This warrants the status of these data as reference measurements and fully supports their use for the validation of satellite data (e.g., Zibordi et al., 2022b; Mélin, 2022) and the determination of their uncertainties (Mélin, 2021).

The second objective was more methodological, aiming at applying a metrology-sound protocol to verify uncertainty estimates using simultaneous measurements, while identifying related challenges and limitations. The construction of uncertainty tree diagrams (Mittaz et al., 2019) appears very valuable for a comprehensive view of all error sources affecting a measurement system. Strictly speaking, the measuring system under study here is one quantifying the difference between R_{RS} observed by two instruments (i.e., $R_{RS,1} - R_{RS,0}$) but for ease of illustration, uncertainty tree diagrams were given for an individual PRS system (Figures 1, 2). Uncertainty cone diagrams (Figures 9, 10) provided a mean to compare uncertainty estimates $u(R_{RS})$ with comparison statistics across their range of values. Collocation statistics also proved valuable by providing an independent method of verification. These methods could be applied to other cases where a sufficient number of coincident measurements from different systems are available, starting with the AAOT site that is regularly hosting other instruments (Vansteenwegen et al., 2019; Tilstone et al., 2020; Brando and Vilas, 2023).

The collocation framework used in previous comparison analyses (e.g., Mélin, 2021; Mélin, 2022) was here extended to cases allowing correlation between errors associated with non-systematic effects (leading to a revised expression for the slope of the model II regression, Eq. 17). This approach is powerful to verify uncertainty estimates but has also limitations. To be solved, the system of Eqs 15, 16 requires assumptions on the ratio η of uncertainties σ_ϵ and the error correlation r_ϵ. The first assumption (on the value of η) is not a major limitation as long as the σ_ϵ can be assumed comparable since the results are not strongly dependent on η (for instance η = 1.21 would multiply $\sigma_{\epsilon,1}$ by 1.1 and $\sigma_{\epsilon,0}$ by 0.91). As shown by Figure 11, the choice of r_ϵ has a stronger impact on σ_ϵ, and its actual value should be better characterized as acknowledged in Section 3.6. Another limitation of the collocation approach is that it provides only one general value for the whole data set (even though the current data set is actually large enough to permit computing collocation statistics on subsets of increasing R_{RS}) and therefore allows only the verification of average statistics of the reported uncertainties $u(R_{RS})$.

The collocation analysis has also led to a practical result, i.e., that the centered root-mean-square difference Δ_c between data collected by two systems can directly serve to quantify the uncertainty associated with these data (excluding systematic contributions); this is valid if these data show a good agreement (expressed by a slope of method II regression close to 1) and if their uncertainties are comparable (η not largely different from 1) with moderate error correlation. If the error correlation is negligible, Δ_c is actually twice

the uncertainty, while it happens to be a good estimate of the uncertainty for an error correlation of 0.5. For highly correlated errors, Δ_c would be an underestimate of the uncertainty.

As more data sets come with documented uncertainties, and new observing networks emerge (e.g., for field radiometric measurements, Brown et al., 2007; Białek et al., 2020; Goyens et al., 2021; Lin et al., 2022; Cazzaniga and Zibordi, 2023), appropriate metrologically-based methods will be required to verify uncertainty estimates and ensure that they are trustworthy for validation activities. This work illustrates how the simultaneous operation of multiple systems can help in that regard, but also that a comprehensive understanding of the contributing factors to the uncertainty budget is required for a solid interpretation of differences between matching observations.

Data availability statement

Publicly available datasets were analyzed in this study. This data can be found here: https://aeronet.gsfc.nasa.gov/new_web/ocean_color.html.

Author contributions

FM: Conceptualization, Formal Analysis, Investigation, Methodology, Writing–original draft, Writing–review and editing. IC: Data curation, Formal Analysis, Investigation, Methodology, Writing–original draft, Writing–review and editing. PS: Data curation, Writing–review and editing.

Funding

The author(s) declare financial support was received for the research, authorship, and/or publication of this article. Partial funding was given by the EMPIR grant 19ENV07 associated with the MetEOC-4 project under the EMPIR programme. Additional funding was provided by DG DEFIS, i.e., the European Commission Directorate-General for Defence Industry and Space, and by DG JRC (Joint Research Centre).

Acknowledgments

This work was supported by the MetEOC-4 project through the EURAMET European Metrology Programme for Innovation and Research (EMPIR) under Grant 19ENV07. The EMPIR programme is co-financed by the Participating States and from the European Union's Horizon 2020 research and innovation programme. The support provided by DG DEFIS, i.e., the European Commission Directorate-General for Defence Industry and Space, and the Copernicus Programme is also gratefully acknowledged. G. Zibordi and B. Bulgarelli are thanked for their contribution to the operation of the AAOT AERONET-OC site.

Conflict of interest

The authors declare that the research was conducted in the absence of any commercial or financial relationships that could be construed as a potential conflict of interest.

Publisher's note

All claims expressed in this article are solely those of the authors and do not necessarily represent those of their affiliated organizations, or those of the publisher, the editors and the reviewers. Any product that may be evaluated in this article, or claim that may be made by its manufacturer, is not guaranteed or endorsed by the publisher.

References

Ahmad, Z., Cetinić, I., Franz, B., Karaköylü, E., McKinna, L., Patt, F., et al. (2019). "Data product requirements and error budgets consensus document," in *NASA technical memorandum 2018-219027. NASA goddard space flight center*. Editors I. Cetinić, C. McClain, and P. Werdell (Greenbelt, Maryland), 6. of *PACE Technical Report Series*. 55pp.

Alikas, K., Vabson, V., Ansko, I., Tilstone, G., Dall'Olmo, G., Nencioli, F., et al. (2020). Comparison of above-water Seabird and TriOS radiometers along an atlantic meridional transect. *Remote Sens.* 12, 1669. doi:10.3390/rs12101669

Ångström, A. (1964). The parameters of atmospheric turbidity. *Tellus* 26, 64–75. doi:10.1111/j.2153-3490.1964.tb00144.x

Białek, A., Vellucci, V., Gentili, B., Antoine, D., Gorroño, J., Fox, N., et al. (2020). Monte Carlo-based quantification of uncertainties in determining ocean remote sensing reflectance from underwater fixed-depth radiometry measurements. *J. Atmos. Ocean. Tech.* 37, 177–196. doi:10.1175/JTECH–D–19–0049.1

Brando, V., and Vilas, L. G. (2023). Initial sample of HYPERNETS hyperspectral water reflectance measurements for satellite validation from the VEIT site (Italy). *Zenodo*. doi:10.5281/zenodo.8057531

Brown, S., Flora, S., Feinholz, M., Yarbrough, M., Houlihan, T., Peters, D., et al. (2007). "The Marine Optical BuoY (MOBY) radiometric calibration and uncertainty budget for ocean color satellite vicarious calibration," in Proc. SPIE 6744, Sensors, Systems, and Next-Generation Satellites XI (Florence, Italy: SPIE Remote Sensing 2007), 67441M.

Cazzaniga, I., and Zibordi, G. (2023). AERONET-OC L_{WN} uncertainties: revisited. *J. Atmos. Ocean. Tech.* 40, 411–425. doi:10.1175/jtech-d-22-0061.1

Cazzaniga, I., Zibordi, G., and Mélin, F. (2021). Spectral variations of the remote sensing reflectance during coccolithophore blooms in the western Black Sea. *Remote Sens. Environ.* 264, 112607. doi:10.1016/j.rse.2021.112607

Cazzaniga, I., Zibordi, G., and Mélin, F. (2023). Spectral features of ocean colour radiometric products in the presence of cyanobacteria blooms in the Baltic Sea. *Remote Sens. Environ.* 287, 113464. doi:10.1016/j.rse.2023.113464

Clerici, M., and Mélin, F. (2008). Aerosol direct radiative effect in the Po Valley region derived from AERONET measurements. *Atmos. Chem. Phys.* 8, 4925–4946. doi:10.5194/acp-8-4925-2008

D'Alimonte, D., Kajiyama, T., Zibordi, G., and Bulgarelli, B. (2021). Sea-surface reflectance factor: replicability of computed values. *Opt. Exp.* 29, 25217–25241. doi:10.1364/oe.424768

D'Alimonte, D., and Zibordi, G. (2006). Statistical assessment of radiometric measurements from autonomous systems. *IEEE Trans. Geosci. Remote Sens.* 44, 719–728. doi:10.1109/tgrs.2005.862505

Deschamps, P.-Y., Herman, M., and Tanré, D. (1983). Modeling of the atmospheric effects and its application to the remote sensing of ocean color. *Appl. Opt.* 22, 3751–3758. doi:10.1364/ao.22.003751

Donlon, C., Berruti, B., Buongiorno, A., Ferreira, M.-H., Féménias, P., Frerick, J., et al. (2012). The global monitoring for environment and security (GMES) Sentinel-3 mission. *Remote Sens. Environ.* 120, 37–57. doi:10.1016/j.rse.2011.07.024

Donlon, C., Wimmer, W., Robinson, I., Fisher, G., Ferlet, M., Nightingale, T., et al. (2014). A second-generation blackbody system for the calibration and verification of

seagoing infrared radiometers. *J. Atmos. Oceano. Tech.* 31, 1104–1127. doi:10.1175/jtech-d-13-00151.1

Eck, T., Holben, B., Reid, J., Dubovik, O., Smirnov, A., O'Neill, N., et al. (1999). The wavelength dependence of the optical depth of biomass burning, urban and desert dust aerosols. *J. Geophys. Res.* 104, 31333–31350. doi:10.1029/1999JD900923

Fahy, J., Fox, N., Gardiner, T., Green, P., Hunt, S., Mittaz, J., et al. (2022). *General guidance on a metrological approach to fundamental data records (FDR), thematic data products (TDPS) and fiducial reference measurements (FRMs) - Metrology theoretical basis.* (QA4EO).

GCOS (2010). Guideline for the geenration of datasets and products meeting GCOS requirements. GCOS-143).

GCOS (2011). *Systematic observation requirements for satellite-based products for climate.* (GCOS-154, Supplemental details to the satellite-based component of the "Implementation plan for the Global Observing System for Climate in Support of the UNFCC").

Gergely, M., and Zibordi, G. (2014). Assessment of AERONET-OC L_{WN} uncertainties. *Metrologia* 51, 40–47. doi:10.1088/0026-1394/51/1/40

Ghent, D., Veal, K., Trent, T., Dodd, E., Sembhi, H., and Remedios, J. (2019). A new approach to defining uncertainties for MODIS land surface temperature. *Remote Sens.* 11, 1021. doi:10.3390/rs11091021

Giles, D., Sinyuk, A., Sorokin, M., Schafer, J., Smirnov, A., Slutsker, I., et al. (2019). Advancements in the Aerosol Robotic Network (AERONET) Version 3 database - automated near-real-time quality control algorithm with improved cloud screening for Sun photometer aerosol optical depth (AOD) measurements. *Atmos. Meas. Tech.* 12, 169–209. doi:10.5194/amt-12-169-2019

Gleason, A., Voss, K., Gordon, H., Twardowski, M., Sullivan, J., Trees, C., et al. (2012). Detailed validation of the bidirectional effect in various Case I and Case II waters. *Opt. Exp.* 20, 7630–7645. doi:10.1364/oe.20.007630

Goyens, C., Vis, P. D., and Hunt, S. (2021). "Automated generation of hyperspectral fiducial reference measurements of water and land surface reflectance for the HYPERNETS networks," in Proceedings of the IEEE International Geoscience and Remote Sensing Symposium, July 11-16, 2021 (Brussels, Belgium: IGARSS). 4pp. doi:10.1109/IGARSS47720.2021.9553738

GUM (2008). Evaluation of measurement data – guide to the expression of uncertainty in measurements, JCGM 100 (Joint Committee for Guides in Metrology, Bureau International des Poids et Mesures).

Holben, B., Eck, T., Slutsker, I., Tanré, D., Buis, J., Setzer, A., et al. (1998). AERONET - a federated instrument network and data archive for aerosol characterization. *Remote Sens. Environ.* 66, 1–16. doi:10.1016/s0034-4257(98)00031-5

Hollmann, R., Merchant, C., Saunders, R., Downy, C., Buchwitz, M., Cazenave, A., et al. (2013). The ESA climate change initiative: satellite data records for essential climate variables. *Bull. Am. Meteorol. Soc.* 94, 1541–1552. doi:10.1175/bams-d-11-00254.1

Hooker, S., Lazin, G., Zibordi, G., and McLean, S. (2002). An evaluation of above- and in-water methods for determining water-leaving radiances. *J. Atmos. Ocean. Tech.* 19, 486–515. doi:10.1175/1520-0426(2002)019<0486:aeoaai>2.0.co;2

Hooker, S., and Maritorena, S. (2000). An evaluation of oceanographic radiometers and deployment methodologies. *J. Atmos. Ocean. Tech.* 17, 811–830. doi:10.1175/1520-0426(2000)017<0811:aeoora>2.0.co;2

Hooker, S., and Morel, A. (2003). Platform and environmental effects on above-water determinations of water-leaving radiances. *J. Atmos. Ocean. Tech.* 20, 187–205. doi:10.1175/1520-0426(2003)020<0187:paeeoa>2.0.co;2

Immler, F., Dykema, J., Gardiner, T., Whiteman, D., Thorne, P., and Vömel, H. (2010). Reference quality upper-air measurements: guidance for developing GRUAN data products. *Atmos. Meas. Tech.* 3, 1217–1231. doi:10.5194/amt-3-1217-2010

IOCCG (2008)., No. 7. Dartmouth, Canada: IOCCG. of Reports of the International Ocean Colour Coordinating Group.Why Ocean colour? The societal benefits of ocean-colour technology

IOCCG (2019). *Uncertainties in ocean Colour remote sensing*, No. 18. Dartmouth, Canada: IOCCG. of Reports of the International Ocean Colour Coordinating Group.

Johnson, B., Zibordi, G., Brown, S., Feinholz, M., Sorokin, M., Slutsker, I., et al. (2021). Characterization and absolute calibration of an AERONET-OC radiometer. *Appl. Opt.* 60, 3380–3392. doi:10.1364/ao.419766

Kacker, R., Kessel, R., and Sommer, K.-D. (2010). Assessing differences between results determined according to the guide to the expression of uncertainty in measurement. *J. Res. Natl. Inst. Stand. Technol.* 115, 453–459. doi:10.6028/jres.115.031

Ku, H. (1966). Notes on the use of propagation of error formulas. *J. Res. Natl. Bureau Stand.* 70C, 263–273. doi:10.6028/jres.070c.025

Lee, Z.-P., Du, K., Voss, K., Zibordi, G., Lubac, B., Arnone, R., et al. (2011). An inherent-optical-property-centered approach to correct the angular effects in water-leaving radiance. *Appl. Opt.* 50, 3155–3167. doi:10.1364/AO.50.003155

Legendre, P., and Legendre, L. (1998). *Numerical ecology*. 2nd edition. Amsterdam: Elsevier, 853pp.

Lin, J., Dall'Olmo, G., Tilstone, G., Brewin, R., Vabson, V., Ansko, I., et al. (2022). Derivation of uncertainty budgets for continuous above-water radiometric measurements along an Atlantic Meridional Transect. *Opt. Exp.* 30, 45648–45675. doi:10.1364/oe.470994

McCarthy, S., Crawford, S., Wood, C., Lewis, M., Jolliff, J., Martinolich, P., et al. (2023). Automated atmospheric correction of nanosatellites using coincident ocean color radiometer data. *J. Mar. Sci. Eng.* 11, 660. doi:10.3390/jmse11030660

Mélin, F. (2010). Global distribution of the random uncertainty associated with satellite derived Chla. *IEEE Geosci. Remote Sens. Lett.* 7, 220–224. doi:10.1109/lgrs.2009.2031825

Mélin, F. (2021). From validation statistics to uncertainty estimates: application to VIIRS ocean color radiometric products at European coastal locations. *Front. Mar. Sci.* 8, 1790948. doi:10.3389/fmars.2021.790948

Mélin, F. (2022). Validation of ocean color remote sensing reflectance data: analysis of results at European coastal sites. *Remote Sens. Environ.* 280, 113153. doi:10.1016/j.rse.2022.113153

Mélin, F., Clerici, M., Zibordi, G., and Bulgarelli, B. (2006). Aerosol variability in the Adriatic Sea from automated optical field measurements and sea-viewing Wide field-of-view sensor (SeaWiFS). *J. Geophys. Res.* 111, D22201. 2006JD007226. doi:10.1029/2006jd007226

Mélin, F., and Franz, B. (2014). "Assessment of satellite ocean colour radiometry and derived geophysical products," in *Optical radiometry for oceans climate measurements. Experimental methods in the physical sciences*. Editors G. Zibordi, C. Donlon, and A. Parr (San Diego: Academic Press), 47, 609–638.

Mélin, F., and Sclep, G. (2015). Band-shifting for ocean color multi-spectral reflectance data. *Opt. Exp.* 23, 2262–2279. doi:10.1364/oe.23.002262

Mélin, F., Sclep, G., Jackson, T., and Sathyendranath, S. (2016). Uncertainty estimates of remote sensing reflectance derived from comparison of ocean color satellite data sets. *Remote Sens. Environ.* 177, 107–124. doi:10.1016/j.rse.2016.02.014

Mélin, F., and Zibordi, G. (2005). Aerosol variability in the Po Valley analyzed from automated optical measurements. *Geophys. Res. Lett.* 32, L03810. doi:10.1029/2004gl021787

Mélin, F., and Zibordi, G. (2007). Optically based technique for producing merged spectra of water-leaving radiances from ocean color remote sensing. *Appl. Opt.* 46, 3856–3869. doi:10.1364/ao.46.003856

Mélin, F., and Zibordi, G. (2010). Vicarious calibration of satellite ocean color sensors at two coastal sites. *Appl. Opt.* 49, 798–810. doi:10.1364/ao.49.000798

Mélin, F., Zibordi, G., and Berthon, J.-F. (2012). Uncertainties in remote sensing reflectance from MODIS-Terra. *IEEE Geosci. Remote Sens. Lett.* 9, 432–436. doi:10.1109/lgrs.2011.2170659

Mélin, F., Zibordi, G., Berthon, J.-F., Bailey, S., Franz, B., Voss, K., et al. (2011). Assessment of MERIS reflectance data as processed with SeaDAS over the European seas. *Opt. Exp.* 19, 25657–25671. doi:10.1364/oe.19.025657

Mélin, F., Zibordi, G., and Djavidnia, D. (2009). Merged series of normalized water leaving radiances obtained from multiple satellite missions for the Mediterranean Sea. *Adv. Space Res.* 43, 423–437. doi:10.1016/j.asr.2008.04.004

Mélin, F., Zibordi, G., and Djavidnia, S. (2007). Development and validation of a technique for merging satellite derived aerosol optical depth from SeaWiFS and MODIS. *Remote Sens. Env.* 108, 436–450. doi:10.1016/j.rse.2006.11.026

Mélin, F., Zibordi, G., and Holben, B. (2013). Assessment of the aerosol products from the SeaWiFS and MODIS ocean color missions. *IEEE Geosci. Remote Sens. Lett.* 10, 1185–1189. doi:10.1109/lgrs.2012.2235408

Mittaz, J., Merchant, C., and Woolliams, E. (2019). Applying principles of metrology to historical Earth observations from satellites. *Metrologia* 56, 032002. doi:10.1088/1681–7575/ab1705

Mobley, C. (1999). Estimation of the remote-sensing reflectance from above-surface measurements. *Appl. Opt.* 38, 7442–7455. doi:10.1364/ao.38.007442

Mobley, C. (2015). Polarized reflectance and transmittance properties of windblown sea surfaces. *Appl. Opt.* 54, 4828–4849. doi:10.1364/ao.54.004828

Morel, A., Antoine, D., and Gentili, B. (2002). Bidirectional reflectance of oceanic waters: accounting for Raman emission and varying particle scattering phase function. *Appl. Opt.* 41, 6289–6306. doi:10.1364/ao.41.006289

O'Neill, N., Eck, T., Holben, B., Smirnov, A., Dubovik, O., and Royer, A. (2001). Bimodal size distribution influences on the variation of Ångström derivatives in spectral and optical depth space. *J. Geophys. Res.* 106, 9787–9806. doi:10.1029/2000jd900245

Pahlevan, N., Mangin, A., Balasubramanian, S., Smith, B., Alikas, K., Arai, K., et al. (2021). ACIX-Aqua: a global assessment of atmospheric correction methods for Landsat-8 and Sentinel-2 over lakes, rivers and coastal waters. *Remote Sens. Environ.* 258, 112366. doi:10.1016/j.rse.2021.112366

Ruddick, K., Voss, K., Boss, E., Castagna, A., Frouin, R., Gilerson, A., et al. (2019). A review of protocols for fiducial reference measurements of water-leaving radiance for validation of satellite remote-sensing data over water. *Remote Sen.* 11, 2190. doi:10.3390/rs11192198

Salem, S., Higa, H., Ishizaka, J., Pahlevan, N., and Oki, K. (2023). Spectral band-shifting of multispectral remote-sensing reflectance products: insights for amtchup and

cross-mission consistency assessments. *Remote Sens. Environ.* 299, 113486. doi:10.1016/j.rse.2023.113846

Schmid, B., Michalsky, J., Halthore, R., Beauharnois, M., Harrison, L., Livingston, J., et al. (1999). Comparison of aerosol optical depth from four solar radiometers during the Fall 1997 ARM intensive observation period. *Geophys. Res. Lett.* 26, 2725–2728. doi:10.1029/1999gl900513

Smirnov, A., Holben, B., Eck, T., Dubovik, O., and Slutsker, I. (2000). Cloud screening and quality control algorithms for the AERONET database. *Remote Sens. Environ.* 73, 337–349. doi:10.1016/s0034-4257(00)00109-7

Stoffelen, A. (1998). Toward the true near-surface wind speed: error modeling and calibration using triple collocation. *J. Geophys. Res.* 103, 7755–7766. doi:10.1029/97jc03180

Talone, M., Zibordi, G., and Lee, Z.-P. (2018). Correction for the non-nadir viewing geometry of AERONET-OC above water radiometry data: an estimate of uncertainties. *Opt. Exp.* 26, A541–A561. doi:10.1364/oe.26.00a541

Thuillier, G., Hersé, M., Labs, D., Foujols, T., Peetermans, W., Gillotay, D., et al. (2003). The solar spectral irradiance from 200 to 2400 nm as measured by the SOLSPEC spectrometer from the ATLAS and EURECA missions. *Sol. Phys.* 214, 1–22. doi:10.1023/A:1024048429145

Thuillier, G., Hersé, M., Simon, P., Labs, D., Mandel, H., Gillotay, D., et al. (1998). The visible solar spectral irradiance from 350 to 850 nm as measured by the SOLSPEC spectrometer during the ATLAS I mission. *Sol. Phys.* 177, 41–61. doi:10.1023/a:1004953215589

Tilstone, G., Dall'Olmo, G., Hieronymi, M., Ruddick, K., Beck, M., Ligi, M., et al. (2020). Field intercomparison of radiometer measurements for ocean colour validation. *Remote Sens.* 12, 1587. doi:10.3390/rs12101587

Toohey, M., and Strong, K. (2007). Estimating biases and error variances through the comparison of coincident satellite measurements. *J. Geophys. Res.* 112, D13306. doi:10.1029/2006JD008192

Vabson, V., Kuusk, J., Ansko, I., Vendt, R., Alikas, K., Ruddick, K., et al. (2019). Field intercomparison of radiometers used for satellite validation in the 400-900 nm range. *Remote Sens.* 11, 1129. doi:10.3390/rs11091129

Vansteenwegen, D., Ruddick, K., Cattrijsse, A., Vanhellemont, Q., and Beck, M. (2019). The pan-and-tilt hyperspectral radiometer system (PANTHYR) for autonomous satellite validation measurements—prototype design and testing. *Remote Sens.* 11, 1360. doi:10.3390/rs11111360

Zibordi, G., Berthon, J.-F., Mélin, F., D'Alimonte, D., and Kaitala, S. (2009a). Validation of satellite ocean color primary products at optically complex coastal sites: northern Adriatic Sea, Northern Baltic Proper and Gulf of Finland. *Remote Sens. Environ.* 113, 2574–2591. doi:10.1016/j.rse.2009.07.013

Zibordi, G., D'Alimonte, D., and Kajiyama, T. (2022a). Automated quality control of AERONET-OC L_{WN} data. *J. Atmos. Ocean. Technol.* 39, 1961–1972. doi:10.1175/jtech–d–22–0029.1

Zibordi, G., Holben, B., Slutsker, I., Giles, D., D'Alimonte, D., Mélin, F., et al. (2009b). AERONET-OC: a network for the validation of ocean color primary products. *J. Atmos. Ocean. Tech.* 26, 1634–1651. doi:10.1175/2009JTECHO654.1

Zibordi, G., Holben, B., Talone, M., D'Alimonte, D., Slutsker, I., Giles, D., et al. (2021). Advances in the Ocean Color component of the Aerosol Robotic Network (AERONET-OC). *J. Atmos. Ocean. Technol.* 38, 725–746. doi:10.1175/jtech–d–20–0085.1

Zibordi, G., Kwiatkowska, E., Mélin, F., Talone, M., Cazzaniga, I., Dessailly, D., et al. (2022b). Assessment of OLCI-A and OLCI-B radiometric data products across European seas. *Remote Sens. Environ.* 272, 112911. doi:10.1016/j.rse.2022.112911

Zibordi, G., Mélin, F., Hooker, S., D'Alimonte, D., and Holben, B. (2004). An autonomous above-water system for the validation of ocean color radiance data. *IEEE Geosci. Remote Sens.* 42, 401–415. doi:10.1109/tgrs.2003.821064

frontiers | Frontiers in Remote Sensing

TYPE Perspective
PUBLISHED 24 January 2024
DOI 10.3389/frsen.2024.1336494

Check for updates

OPEN ACCESS

EDITED BY
Vittorio Ernesto Brando,
National Research Council (CNR), Italy

REVIEWED BY
Tristan Harmel,
Magellium, France

*CORRESPONDENCE
Robert J. W. Brewin,
r.brewin@exeter.ac.uk

RECEIVED 10 November 2023
ACCEPTED 08 January 2024
PUBLISHED 24 January 2024

CITATION
Brewin RJW, Sun X, Aurin DA, Viljoen JJ, Walsh C and Sathyendranath S (2024), Superyachts could support satellite ocean colour validation.
Front. Remote Sens. 5:1336494.
doi: 10.3389/frsen.2024.1336494

COPYRIGHT
© 2024 Brewin, Sun, Aurin, Viljoen, Walsh and Sathyendranath. This is an open-access article distributed under the terms of the Creative Commons Attribution License (CC BY). The use, distribution or reproduction in other forums is permitted, provided the original author(s) and the copyright owner(s) are credited and that the original publication in this journal is cited, in accordance with accepted academic practice. No use, distribution or reproduction is permitted which does not comply with these terms.

Superyachts could support satellite ocean colour validation

Robert J. W. Brewin[1]*, Xuerong Sun[1], Dirk A. Aurin[2], Johannes J. Viljoen[1], Christopher Walsh[3] and Shubha Sathyendranath[4]

[1]Centre for Geography and Environmental Science, University of Exeter, Penryn, United Kingdom, [2]NASA Goddard Space Flight Center (USRA), Greenbelt, MD, United States, [3]Seafari Marine Services, Stony Brook, NY, United States, [4]Plymouth Marine Laboratory, Plymouth, United Kingdom

Visible spectral radiometry of seawater, often referred to as ocean colour, from space, provides a synoptic view of surface phytoplankton, and other optically-active constituents, at high temporal resolution, that is unsurpassed by any other technology. Yet, *in-situ* observations of ocean colour are critical to the success of the satellite, tracking the calibration of the radiometers and validating atmospheric correction algorithms. Owing to the high cost of commercial field radiometers, as well as the high costs associated with ocean-based field work, ocean colour scientists are plagued by a sparsity of high quality *in-situ* radiometric observations, particularly in remote regions. In this perspective article, we highlight potential to increase the number of *in-situ* observations of ocean colour by harnessing superyachts. Using openly-available data processing software, we show that automated ocean colour data collected using a superyacht can be used for the validation of an ocean colour satellite, with comparable results to traditional validation studies. Reaching out to wealthy citizen scientists may help fill gaps in our ability to monitor the colour of the ocean.

KEYWORDS

satellite, validation, ocean colour, superyacht, remote sensing

1 Introduction

Ocean colour is defined as spectral variations in water leaving radiance, or reflectance, in visible bands of the electromagnetic spectrum. A primary application of ocean-colour data is to observe the dynamics of phytoplankton in the ocean. The optical signal is processed to retrieve information on the major phytoplankton pigment, chlorophyll-a. Methods are also available to infer phytoplankton community structure from ocean-colour data, by exploiting spectral differences in the optical signatures of different types of phytoplankton, as well as other important optically-active constituents, such as the types of coloured dissolved organic matter (CDOM) in the water and non-algal particles. Recognised as an Essential Climate Variable, ocean-colour data helps to address many important issues, such as changing ocean biogeochemical cycles, collapsing fisheries, climate change, and shifts in waterborne diseases (Sathyendranath et al., 2023).

Ocean-colour sensors mounted on satellites, such as NASA's Moderate Resolution Imaging Spectroradiometer (MODIS) sensors, provide ocean-colour data on a daily basis (clouds permitting) at global scale, with a resolution of a few kilometres. Continual satellite observations since the late 1980's mean that these products provide an excellent platform for monitoring and interpreting regional, seasonal and interannual variations in marine plankton populations and their activity, over multiple decades (Sathyendranath et al., 2019).

Ocean-colour data can be formally combined with numerical models of ocean circulation and ecosystems to provide state estimates of the system (i.e., using the models as an interpolation tool) and these data can be used to constrain parameters of the models which can then be used in prognostic mode (IOCCG, 2020).

A critical component of successful satellite ocean colour remote sensing, is the validation and calibration of the satellite data using *in-situ* measurements, collected at the ocean surface (Mélin, 2022). Despite large efforts by the scientific community to collect and archive *in-situ* measurements of ocean colour (Valente et al., 2022), a paucity of *in-situ* data limits our capability to validate and calibrate satellite ocean-colour data, meaning the satellite data cannot be harnessed to their full extent. This is driven by the high cost of commercial *in-situ* radiometers, as well as the costs associated with ocean-based field work, particularly in remote regions (Lauro et al., 2014). Solutions to this issue include harnessing optical sensors mounted on autonomous platforms (Demeaux and Boss, 2022), mounting sensors on ships-of-opportunity (Simis and Olsson, 2013; Raitsos et al., 2014; Brando et al., 2016; Wang and Costa, 2022) and using citizen science (Lauro et al., 2014; Vanhellemont et al., 2022). Citizen science (or participatory science), requires allocating a task, usually conducted by professionals, to a network of voluntary citizens. If successfully administered, it can improve public understanding of science by disseminating knowledge through different social classes, and tackle expensive, demanding and intractable scientific data collection (Bresnahan et al., 2022). Typically, use of citizen science for evaluating ocean colour data has focused on low cost options, tapping into mobile phones, either for logging data using low cost tools (Novoa et al., 2014; Busch et al., 2016; Brewin et al., 2019; George et al., 2021), or harnessing mobile phone camera sensors (Leeuw and Boss, 2018; Burggraaff et al., 2022). Although these low cost options have proven remarkably robust (e.g., see Brewin et al., 2023), they can lack the quality required for accurate validation and calibration (Lin et al., 2022).

In this perspective article, we discuss opportunities to expand *in-situ* measurements of ocean colour by engaging wealthier citizen scientists who own superyachts, who can afford to purchase commercial *in-situ* radiometers, who have an active interest in environmental monitoring, and who often sail to remote areas that are not routinely covered by research vessels or ships-of-opportunity. We begin by demonstrating results from a pilot study, where automated ocean colour data were collected on a superyacht and used for the validation of an ocean colour satellite, and finish by discussing challenges that need to be addressed for this strategy to be successful.

2 Pilot study on the Archimedes yacht

2.1 Archimedes yacht setup and data collection

A Surface Acquisition System (SAS) Solar Tracker Aiming unit was acquired from Sea-Bird Scientific (https://www.seabird.com/), equipped with two HyperOCR radiance sensors (with a field of view of 11.5° in air), measuring hyperspectral total water radiance (L_t) and sky radiance (L_i) at an angle of 40° from nadir and zenith respectively, a HyperOCR irradiance sensor, measuring downwelling irradiance (E_s), and a infrared radiation pyrometer, for measuring sea surface temperature (SST, not used in this study). The system is designed to maintain the correct pointing angle with respect to the Sun, permitting autonomous operation (Figure 1A). The SAS Solar Tracker Aiming unit was mounted to the bow of the Archimedes Yacht (Figure 1B), following Sea-Bird Scientific (2017) assembly instructions, and aligned to point forward, offering the best placement for viewing total water radiance (L_t) at angles relative to the yacht's center line. The placement of the SAS Solar Tracker Aiming unit at the bow minimised errors from shading and reflection due to the yacht, and ensures that the water sampled is undisturbed by the yacht's wake. This placement also considered the position of the E_s sensor, being far from the yacht's bridge and cabins, minimising shading and reflection effects, with the exception of a thin telescopic removable mast which was occasionally erected near the bow of the yacht (see Figure 1B for image when erected) and may have impacted E_s data collected (see discussion of this aspect in Section 3). The system was deployed on Archimedes Yacht in calm seas at various periods over 3 years (2018–2020), when stationary and moving, and sampled a wide range of geographical locations and optical water types, including: the east coast of the United States, the Caribbean, the northern and equatorial Atlantic, coastal regions of the United Kingdom and Ireland, the Mediterranean Sea, the South Pacific, and the Antarctic Peninsular. By the end of 2020, the system had begun to degrade following extensive environmental exposure and required repair (see Figure 1D).

2.2 *In-situ* data processing

Data were collected using SatView software, Sea-Bird Scientific/Satlantic's real time data logging and display software for Microsoft Windows, with ".raw" files logged on an hourly interval. Data were processed using NASA's open source HyperInSPACE software (https://github.com/nasa/HyperCP). Originally developed to provide hyperspectral *in-situ* support for NASA's Plankton, Aerosol, Cloud, ocean Ecosystem (PACE) mission, HyperInSPACE is specifically designed to process automated, above-water, hyperspectral ocean color radiometry data, and supports data collected using the Sea-Bird Scientific SAS Tracker Aiming unit. HyperInSPACE offers the user a range of processing options, among which include various quality assurance methods and protocols, uncertainty estimation, sky and sunglint correction, and convolution of data to satellite wavebands. The software also outputs files formatted to text files for submission to NASA's SeaBASS database.

For this pilot study, the Archimedes data were processed as follows: 1) SatView Level 0 ".raw" files were periodically transferred from the yacht via File Transfer Protocol (FTP) and processed to Level 1A (Hierarchical Data Format 5 ".hdf") using a solar zenith angle filter that discarded data greater than 60° (Brewin et al., 2016); 2) Level 1A files were processed to Level 1AQC by removing data with absolute rotator angles greater than 40° and less than −40°, removing data with azimuth angles less than 90° and greater than 135° (Mobley, 1999; Zhang et al., 2017), and deglitching the data using default HyperInSPACE settings; 3) Level 1AQC files were processed to Level 1B, correcting for dark counts, applying instrument calibration files, and interpolating to common set of timestamps and a common set of wavebands (at 3.3 nm resolution); 4) Level 1B files were processed to Level 1BQC, using the Zhang et al. (2017) glint correction, which required downloading GMAO MERRA2 ancillary data (see https://oceancolor.gsfc.nasa.gov/

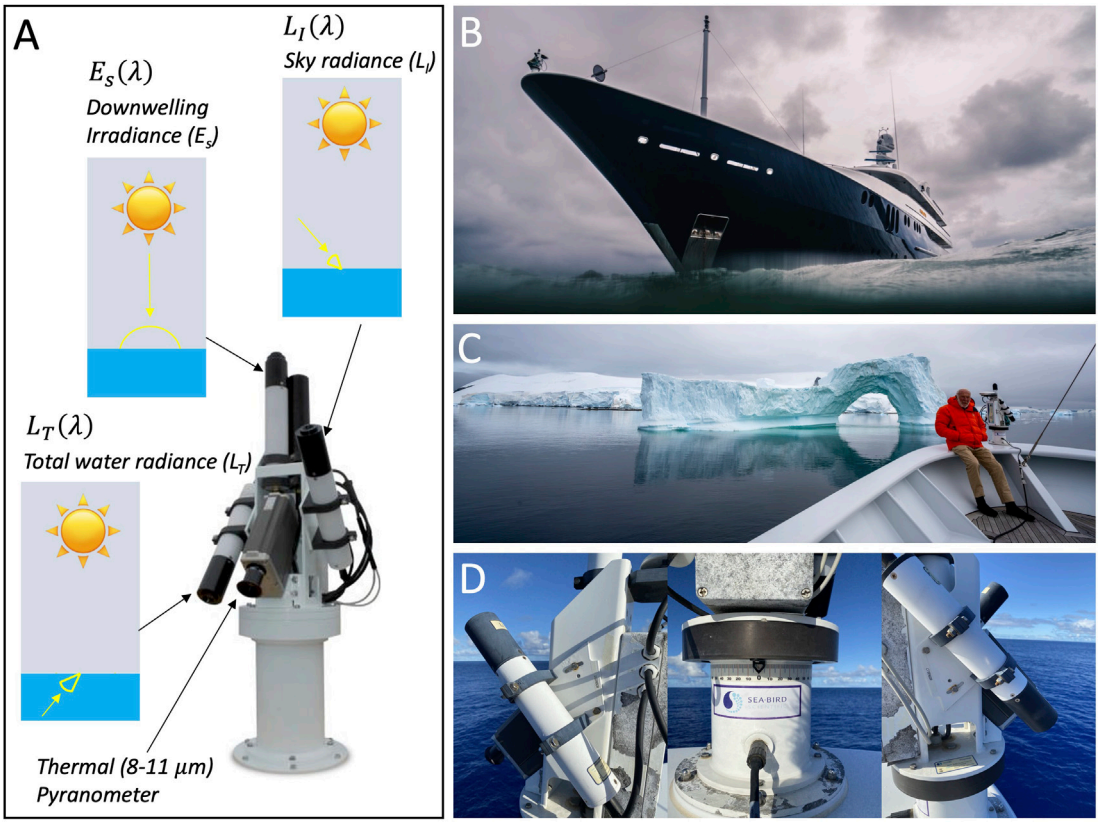


FIGURE 1
(A) Sea-Bird Scientific Solar Tracker Aiming System measuring total water radiance and sky radiance at a solid angle, and downwelling irradiance, which are used to compute remote sensing reflectance. Reproduced with permission from Sea-Bird Scientific (2017). **(B)** Position of the Sea-Bird Scientific Solar Tracker on the bow of the Archimedes Yacht. **(C)** Jim Simons, owner of the Archimedes Yacht alongside the Sea-Bird Scientific Solar Tracker in Antarctica, a remote region where few satellite validation studies have been performed. **(D)** Images showing degradation of the Sea-Bird Scientific Solar Tracker after 3 years of operation (note the corrosion of the instrumentation on the base and junction box of the Solar Tracker).

resources/docs/ancillary/) through HyperInSPACE, removing data with wind speed $>10\,ms^{-1}$ (Mueller et al., 2003), removing data with solar zenith angles outside the window of 20°–60° (Brewin et al., 2016; Zhang et al., 2017), filtering data for spectral outliers using default HyperInSPACE settings (see https://github.com/nasa/HyperCP for details), and using a set of meteorological flags filtering for clouds by removing data where $L_i(750)/E_s(750 > 1.0$ and $E_s(470)/E_s(680) < 1.0$, removing unusually low downwelling irradiance at 480 nm ($< 2.0\ \mu W\,cm^{-2}\,nm^{-1}$), and removing data likely impacted by high relative humidity or rain ($E_s(720)/E_s(370) < 1.095$) (Mobley, 1999; Wernand et al., 2002; Ruddick et al., 2006; Garaba et al., 2012; Simis and Olsson, 2013); 5) Level 1BQC files were processed to Level 2, this required processing data within an optional time interval (we selected the default of 5 min), selecting only the darkest 10% of $L_t(780)$ data to minimise sun glint, then computing the average spectra for E_s, L_i, and L_t and their variability (standard deviations), computing the skyglint/sunglint correction factor (ρ) following Zhang et al. (2017), computing remote sensing reflectance ($R_{rs} = [L_t - \rho L_i]/E_s$), performing an near infrared residual correction following Ruddick et al. (2006), and removing any negative spectra. Uncertainties in R_{rs} were estimated for each ensemble using sum of squares propagation of the standard deviations in L_i, L_t, E_s, and ρ from each ensemble. The data were also convolved to the spectral bands of MODIS-Aqua, using the spectral response functions of the satellite.

In total, 2,402 hyperspectral R_{rs} spectra made it through the processing chain, 314 collected in 2018, 1,605 in 2019, and 483 in 2020 (Figures 2A–D). Data were outputted as NASA SeaBASS formatted text files and are openly available through the Simons Collaborative Marine Atlas Project (https://simonscmap.com) and NASA SeaBASS website (https://seabass.gsfc.nasa.gov/experiment/SUPERYACHT_SCIENCE). This perspective article is focused on demonstrating the potential of augmenting superyachts with automated ocean colour radiometers, rather than testing all the potential combinations of settings in HyperInSPACE, and hence we have used a standard set of settings we think sensible for this dataset. However, all the Level 0 ".raw" data and instrument calibration files are openly available in the NASA SeaBASS archive, for future work testing and comparing different settings, or for reprocessing as and when new updates to HyperInSPACE are introduced.

2.3 Satellite MODIS-Aqua match-ups

In-situ R_{rs} spectra at six wavebands (412, 443, 488, 531, 555, 667 nm, convolved to the spectral bands of MODIS-Aqua), and their

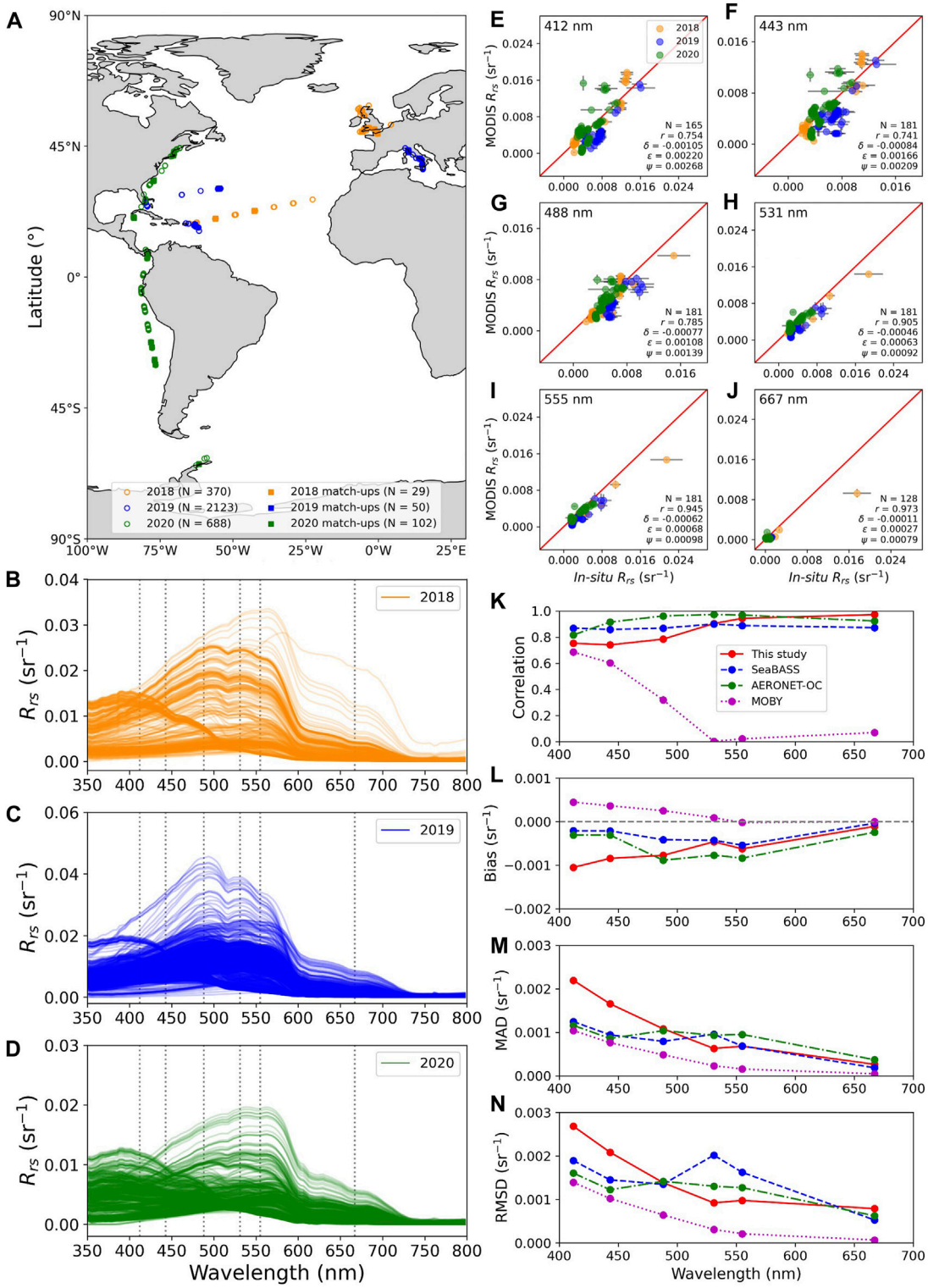


FIGURE 2
(A) Map showing locations of Archimedes remote-sensing reflectance data (R_{rs}) at 443 nm, processed using HyperInSPACE and the locations of MODIS-Aqua match-ups (N refers to the number of spectra). **(B–D)** R_{rs} as a function of wavelength, for Archimedes data collected in 2018, 2019 and 2020, respectively. The dotted lines represent the six wavelengths (412, 443, 488, 531, 555, 667 nm) of MODIS-Aqua satellite data used in the satellite validation. **(E–J)** Comparison of *in-situ* (after BRDF correction) and MODIS-Aqua-derived R_{rs} at six wavelengths (412, 443, 488, 531, 555, 667 nm respectively). The error bar on the x-axis direction is the uncertainty in the *in-situ* measurements, the error bar on the y-axis direction is the standard deviation of MODIS-Aqua-derived data. The statistical tests include correlation (r), bias (δ), mean absolute difference (MAD, denoted ϵ), and root mean squared difference (RMSD, denoted Ψ). **(K–N)** MODIS-Aqua validation statistics (correlation, bias, MAD, and RMSD, respectively) from this study as a function of wavelength compared with validation results obtained from NASA SeaBASS, including SeaBASS, AERONET-OC, and MOBY.

corresponding uncertainties, were used for comparison with Level 2 (L2) MODIS-Aqua data. To compare the *in-situ* R_{rs} data more directly with MODIS-Aqua R_{rs}, we performed a bidirectional reflectance distribution function (BRDF) correction following the method of Lee et al. (2011), inputting information on sun and viewing angles, and environmental conditions. *In-situ* data were matched with MODIS-Aqua L2 data through a python tool available through NASA SeaBASS (fd_matchup.py, https://seabass.gsfc.nasa.gov/wiki/validation_matchup_tools#Satellite%20Match-Up%20Extractor). Each *in-situ* sample was matched in time (within the ±4 h window) and space (closest latitude and longitude) with a MODIS-Aqua L2 image. From 3,181 *in-situ* data, 2,402 had matching MODIS-Aqua L2 images (R2022 reprocessing), resulting in a total of 228 images, which were downloaded automatically from NASA's ocean colour website (https://oceandata.sci.gsfc.nasa.gov/directdataaccess/) on 2 October 2023.

Each *in-situ* sample was paired with its corresponding MODIS-Aqua L2 image in space by extracting a 3 × 3 pixel window centred on the location of the *in-situ* sample. The mean and standard deviation of satellite-derived R_{rs} was calculated from nine pixels, and was retained if the following conditions were met: 1) at least five valid pixels were available from the nine, and 2) the closest satellite pixel contained a valid value. In total, 181 samples fulfilled these criteria, with 29, 50, and 102 samples in 2018, 2019 and 2020 respectively (Figure 2A). To compare the Archimedes *in-situ* data with MODIS-Aqua, we computed four statistical metrics, commonly used in validation exercises (e.g., Brewin et al., 2015), including the correlation coefficient (r), mean difference (bias, denoted δ), mean absolute difference (MAD, denoted ϵ), and root mean squared difference (RMSD, denoted Ψ), all computed in linear space.

To compare the validation results from Archimedes with those from more traditional validation studies conducted by ocean colour scientists, we computed the same statistical metrics, for MODIS-Aqua derived R_{rs} (R2022 processing), using *in-situ* R_{rs} match-ups available in the NASA SeaBASS website (https://seabass.gsfc.nasa.gov/search#val, accessed on 3 October 2023, using standard settings in the tool). These included results from SeaBASS, AERONET-OC, and MOBY. The SeaBASS, AERONET-OC, and MOBY datasets contain a maximum (wavelength-depended) of 730, 6663, and 776 samples, respectively.

3 Augmenting superyachts with ocean colour radiometers

Archimedes *in-situ* R_{rs} data compare well with MODIS-Aqua R_{rs} at the six wavelengths studied (Figures 2E–J). Statistical metrics obtained in the validation exercise using Archimedes are in good agreement with those using other data collected by scientists (Figures 2K, L). Overall, Archimedes R_{rs} biases, MAD and RMSD are slightly higher for blue wavelengths (412 and 443 nm), but lower than, or comparable to, other validation studies, between 488 and 665 nm (Figures 2L–N). Considering MODIS-Aqua blue bands are sensitive to temporal degradation (Lee et al., 2019), poorer statistics in blue wavelengths for Archimedes likely reflects that this validation was conducted in more recent years (2018–2020), in comparison with the other validation studies that include data from an earlier time period (see also recent study by Pardo et al., 2023). These result demonstrate that automated R_{rs} data collection on superyachts can provide very useful data for the validation of satellite ocean colour measurements. When considering superyachts visit remote regions (e.g., in the case of Archimedes, the Antarctic peninsular, see Figure 1C), this may help provide quality *in-situ* radiometric observations in regions rarely sampled. Furthermore, with increasing numbers of ocean-colour satellites being launched, long-term investments in sustaining the time-series of ocean colour data (e.g., through the ESA's Sentinel 3 program), and new exciting hyperspectral ocean-colour satellites being developed (e.g., NASA's PACE mission), it is critical that the international community continues investing in the collection of R_{rs} *in-situ* data and explore new ways to expand the temporal and spatial coverage of these datasets. Augmenting superyachts with ocean colour radiometers could be one opportunity to do this. Nonetheless, for this strategy to be successful, certain challenges need to be considered:

- The scientific community needs to find ways to engage with superyacht communities, to highlight the value and benefits of collecting *in-situ* data. We may be better positioned to do this if we team up with other marine scientists, who are developing automated tools for collecting other useful oceanography data (e.g., microplastsics, see Setälä et al., 2022), possible bringing these instruments together into a simple data collection package that would benefit a broader range of marine scientists. Scientists should consider ways in which they could motivate superyacht owners to collect *in situ* data, building on citizen-science based principles (Garcia-Soto et al., 2021) and existing initiatives (e.g., https://yachtsforscience.com), promoting financial investment that adds to existing funding for validation. Satellite validation work could also extend beyond ocean colour data, for example, collecting SST data for validation of satellite thermal radiometers, by utilising state-of-the-art *in-situ* methods (e.g., Donlon et al., 2014). Ocean colour scientists may also benefit from integration of radiometric systems with other automated systems for monitoring the inherent optical properties of the water (e.g., Slade et al., 2010).
- Availability of automotive radiometric systems is a potential issue for ocean colour validation on superyachts. Unfortunately, a few years after the Sea-Bird Scientific SAS Solar Tracker Aiming unit was purchased for Archimedes, the manufacturer decommissioned the system. However, similar systems are now being developed. For example, the EU Monocle project saw the development of a Solar-tracking Radiometry platform (So-Rad) system (see https://www.monocle-h2020.eu/Sensors_and_platforms/Solar_tracking_radiometry_platform_en) designed to be operated with commercial radiometers (TriOS RAMSEs), with a high degree of automation and low-power consumption. The So-Rad designs are open-source and the system can be installed on non-stationary platforms like superyachts.
- It is essential there is a close dialog between the crew of the superyacht and scientists, so as to ensure these systems are set-up appropriately and for support during operation. This was key to the success of the pilot study on the Archimedes yacht. Sea-Bird Scientific SAS Solar Tracker Aiming unit was placed right at the bow of Archimedes, and carefully set-up by the vessels caption and crew, and removed and replaced during periods of rough and calm weather. In hindsight, it would have been useful to

document when the telescopic mast was erected (see Figure 1B) so as to quantity any effect it may have had on the E_s data. Future efforts may benefit from placing the E_s elsewhere on the vessel (e.g., at top of the telescopic mast). Such a dialog requires a good relationship between scientists and crew.

- For the pilot study on the Archimedes yacht, data were periodically transferred via FTP. This worked well, but meant data were not processed in near real time. Adopting a near real time data transfer/upload system could be useful for operational applications and identifying any issues with the data that could be resolved quickly (both *in situ* and satellite).
- The pilot study on the Archimedes yacht benefited from the development of HyperInSPACE software, allowing for the rapid processing of radiometric data, with full traceability, building on community developed and supported protocols (IOCCG, 2019). The software is also designed to ingest new developments in radiometric data processing, as and when they appear. Increasing efforts are being placed on quantifying uncertainties with full SI traceability (Ruddick et al., 2019; Banks et al., 2020; Tilstone et al., 2020; Lin et al., 2022; Pardo et al., 2023), that should be incorporated in these software in the future, bringing further rigor to the quality of the measurements.
- It is essential that appropriate data archiving systems are maintained and available to support initiatives like this. These need to be open source, to maximise data usage, and must be designed to cater for the raw radiometric measurements, the processed data, with full traceability between the two, so users can reprocess the data if needed, using different settings, or future reprocessing can be made, should new knowledge come to light. The NASA SeaBASS archive is ideally suited for this. Additionally, these data should also be ingested into other archives or data complications, to broaden the user community and allow for integration with other data streams. For the pilot study on the Archimedes yacht, we also submitted the dataset to the Collaborative Marine Atlas Project (CMAP), an open-source data portal designed for retrieving, visualizing, and analysing diverse ocean datasets (see https://simonscmap.com). It strives to enable scientists and the public to dive into the vast ocean datasets without going through the time-consuming process of finding and harmonizing data from different sources (Ashkezari et al., 2021). Such an atlas maybe useful for the development of future ocean colour algorithms and for widening the use of radiometric datasets.

4 Summary and outlook

Due to the high cost of ocean-based field work and commercial field radiometers, there is a paucity of high quality *in-situ* radiometric observations required for satellite validation of ocean colour data. In this perspective article, we have highlighted potential to increase *in-situ* data collection by harnessing superyachts. Utilising openly-available data processing and archiving software, we demonstrate that automated ocean colour data collected from a superyacht can be used for the validation of an ocean colour satellite, with comparable results to more traditional validation studies. We discuss challenges and future work needed for this strategy to be successful.

Data availability statement

The datasets presented in this study can be found in online repositories. The names of the repository/repositories and accession number(s) can be found below: https://seabass.gsfc.nasa.gov/experiment/SUPERYACHT_SCIENCE; and https://oceandata.sci.gsfc.nasa.gov/directdataaccess/.

Ethics statement

Written informed consent was obtained from the individual(s) for the publication of any potentially identifiable images or data included in this article.

Author contributions

RB: Conceptualization, Formal Analysis, Funding acquisition, Investigation, Methodology, Project administration, Resources, Software, Validation, Visualization, Writing–original draft, Writing–review and editing. XS: Formal Analysis, Investigation, Methodology, Writing–review and editing. DA: Formal Analysis, Methodology, Resources, Software, Writing–review and editing. JV: Writing–review and editing. CW: Data curation, Resources, Writing–review and editing. SS: Conceptualization, Resources, Writing–review and editing.

Funding

The author(s) declare financial support was received for the research, authorship, and/or publication of this article. RB is funded by a UKRI Future Leader Fellowship (MR/V022792/1) and by the Simons Foundation Project "Processing and distribution of hyperspectral radiometer data from ships of opportunity for monitoring phytoplankton in the ocean" (654879). SS is supported by the Simons Foundation Project Collaboration on Computational Biogeochemical Modeling of Marine Ecosystems (CBIOMES; 549947, SS).

Acknowledgments

The authors would like to thank all the crew of the Archimedes yacht who assisted in the collection of *in-situ* data. We thank Jim Simons, his family, Marian Carlson and the Simons Foundation, for supporting this work. We thank all those who have supported the development of the HyperInSPACE software and NASA for providing MODIS-Aqua data used in the work.

Conflict of interest

Author CW was employed by Seafari Marine Services.

The remaining authors declare that the research was conducted in the absence of any commercial or financial relationships that could be construed as a potential conflict of interest.

Publisher's note

All claims expressed in this article are solely those of the authors and do not necessarily represent those of their affiliated organizations, or those of the publisher, the editors and the reviewers. Any product that may be evaluated in this article, or claim that may be made by its manufacturer, is not guaranteed or endorsed by the publisher.

References

Ashkezari, M. D., Hagen, N. R., Denholtz, M., Neang, A., Burns, T. C., Morales, R. L., et al. (2021). Simons Collaborative Marine Atlas Project (Simons CMAP): an open-source portal to share, visualize, and analyze ocean data. *Limnol. Oceanogr. Methods* 19, 488–496. doi:10.1002/lom3.10439

Banks, A. C., Vendt, R., Alikas, K., Bialek, A., Kuusk, J., Lerebourg, C., et al. (2020). Fiducial reference measurements for satellite ocean colour (FRM4SOC). *Remote Sens.* 12, 1322. doi:10.3390/rs12081322

Brando, V. E., Lovell, J. L., King, E. A., Boadle, D., Scott, R., and Schroeder, T. (2016). The potential of autonomous ship-borne hyperspectral radiometers for the validation of ocean color radiometry data. *Remote Sens.* 8, 150. doi:10.3390/rs8020150

Bresnahan, P., Cyronak, T., Brewin, R. J. W., Andersson, A., Wirth, T., Martz, T., et al. (2022). A high-tech, low-cost, internet of things surfboard fin for coastal citizen science, outreach, and education. *Cont. Shelf Res.* 242, 104748. doi:10.1016/j.csr.2022.104748

Brewin, R. J. W., Brewin, T. G., Phillips, J., Rose, S., Abdulaziz, A., Wimmer, W., et al. (2019). A printable device for measuring clarity and colour in lake and nearshore waters. *Sensors* 9, 936–1026. doi:10.3390/s19040936

Brewin, R. J. W., Dall'Olmo, G., Pardo, S., van Dongen-Vogel, V., and Boss, E. S. (2016). Underway spectrophotometry along the Atlantic Meridional Transect reveals high performance in satellite chlorophyll retrievals. *Remote Sens. Environ.* 183, 82–97. doi:10.1016/j.rse.2016.05.005

Brewin, R. J. W., Pitarch, J., Dall'Olmo, G., van der Woerd, H. J., Lin, J., Sun, X., et al. (2023). Evaluating historic and modern optical techniques for monitoring phytoplankton biomass in the Atlantic Ocean. *Front. Mar. Sci.* 10. doi:10.3389/fmars.2023.1111416

Brewin, R. J. W., Sathyendranath, S., Müller, D., Brockmann, C., Deschamps, P.-Y., Devred, E., et al. (2015). The Ocean colour climate change initiative: III. A round-robin comparison on in-water bio-optical algorithms. *Remote Sens. Environ.* 162, 271–294. doi:10.1016/j.rse.2013.09.016

Burggraaff, O., Werther, M., Boss, E. S., Simis, S. G. H., and Snik, F. (2022). Accuracy and reproducibility of above-water radiometry with calibrated smartphone cameras using RAW data. *Front. Remote Sens.* 3. doi:10.3389/frsen.2022.940096

Busch, J. A., Bardaji, R., Ceccaroni, L., Friedrichs, A., Piera, J., Simon, C., et al. (2016). Citizen bio-optical observations from coast-and ocean and their compatibility with ocean colour satellite measurements. *Remote Sens.* 8, 879–919. doi:10.3390/rs8110879

Demeaux, C. B., and Boss, E. (2022). Validation of remote-sensing algorithms for diffuse attenuation of downward irradiance using BGC-Argo floats. *Remotre Sens.* 14, 4500. doi:10.3390/rs14184500

Donlon, C. J., Wimmer, W., Robinson, I., Fisher, G., Ferlet, M., Nightingale, T., et al. (2014). A second-generation blackbody system for the calibration and verification of seagoing infrared radiometers. *J. Atmos. Ocean. Technol.* 31, 1104–1127. doi:10.1175/JTECH-D-13-00151.1

Garaba, S. P., Schulz, J., Wernand, M. R., and Zielinski, O. (2012). Sunglint detection for unmanned and automated platforms. *Sensors* 12, 12545–12561. doi:10.3390/s120912545

Garcia-Soto, C., Seys, J. J. C., Zielinski, O., Busch, J. A., Luna, S. I., Baez, J. C., et al. (2021). Marine citizen science: current state in Europe and new technological developments. *Front. Mar. Sci.* 8. doi:10.3389/fmars.2021.621472

George, G., Menon, N. N., Abdulaziz, A., Brewin, R. J. W., Pranav, P., Gopalakrishnan, A., et al. (2021). Citizen scientists contribute to real-time monitoring of lake water quality using 3D printed mini Secchi disks. *Front. Water* 3. doi:10.3389/frwa.2021.662142

IOCCG (2019). Ocean optics and biogeochemistry protocols for satellite Ocean colour sensor validation, volume 3.0: protocols for satellite Ocean colour data validation: *In Situ optical radiometry. Tech. Rep dartmouth, NS, Canada, International Ocean-Colour Coordinating Group (IOCCG), 67pp. (IOCCG protocol series)*, China, IEEE, G. Zibordi, K. J. Voss, B. C. Johnson, and J. L. Mueller

IOCCG (2020). "Synergy between ocean colour and biogeochemical/ecosystem models," in *IOCCG report series, No. 19*. Editors T. rep. and S. Dutkiewicz (Dartmouth, Canada: International Ocean Colour Coordinating Group).

Lauro, F. M., Senstius, S. J., Cullen, J., Neches, R., Jensen, R. M., Brown, M. V., et al. (2014). The common oceanographer: crowdsourcing the collection of oceanographic data. *PLoS Biol.* 12, e1001947. doi:10.1371/journal.pbio.1001947

Lee, S., Meister, G., and Franz, B. (2019). MODIS Aqua reflective solar band calibration for NASA's r2018 ocean color products. *Remote Sens.* 11, 2187. doi:10.3390/rs11192187

Lee, Z. P., Du, K., Voss, K. J., Zibordi, G., Lubac, B., Arnone, R., et al. (2011). An inherent-optical-property-centered approach to correct the angular effects in water-leaving radiance. *Appl. Opt.* 50, 3155–3167. doi:10.1364/AO.50.003155

Leeuw, T., and Boss, E. (2018). The HydroColor App: above water measurements of remote sensing reflectance and turbidity using a smartphone camera. *Sensors* 18, 256. doi:10.3390/s18010256

Lin, J., Dall'Olmo, G., Tilstone, G. H., Brewin, R. J. W., Vabson, V., Ansko, I., et al. (2022). Derivation of uncertainty budgets for continuous above-water radiometric measurements along an Atlantic Meridional Transect. *Opt. Express* 30, 45648–45675. doi:10.1364/OE.470994

Mélin, F. (2022). Validation of ocean color remote sensing reflectance data: analysis of results at European coastal sites. *Remote Sens. Environ.* 280, 113153. doi:10.1016/j.rse.2022.113153

Mobley, C. D. (1999). Estimation of the remote-sensing reflectance from above-surface measurements. *Appl. Opt.* 38, 7442–7455. doi:10.1364/ao.38.007442

Mueller, J. L., Morel, A., Frouin, R., Davis, C. O., Arnone, R., Carder, K. L., et al. (2003). *Ocean optics protocols for satellite Ocean color sensor validation, revision 4*, Vol. III. Greenbelt, MD: NASA Goddard Space Flight Center.

Novoa, S., Wernand, M. R., and van der Woerd, H. J. (2014). The modern Forel-Ule scale: a 'do-it-yourself' colour comparator for water monitoring. *J. Eur. Opt. Soc. - Rapid Publ.* 9, 1–10. doi:10.2971/jeos.2014.14025

Pardo, S., Tilstone, G. T., Brewin, R. J. W., Dall'Olmo, G., Lin, J., Nencioli, F., et al. (2023). Radiometric assessment of OLCI, VIIRS, and MODIS using fiducial reference measurements along the atlantic meridional transect. *Remote Sens. Environ.* 299, 113844. doi:10.1016/j.rse.2023.113844

Raitsos, D. E., Pradhan, Y., Lavender, S. J., Hoteit, I., McQuatters-Gollop, A., Reid, P. C., et al. (2014). From silk to satellite: half a century of ocean colour anomalies in the Northeast Atlantic. *Glob. Change Biol. Press* 20, 2117–2123. doi:10.1111/gcb.12457

Ruddick, K. G., De Cauwer, V., Park, Y.-J., and Moore, G. (2006). Seaborne measurements of near infrared water-leaving reflectance: the similarity spectrum for turbid waters. *Limnol. Oceanogr.* 51, 1167–1179. doi:10.4319/lo.2006.51.2.1167

Ruddick, K. G., Voss, K., Boss, E., Castagna, A., Frouin, R., Gilerson, A., et al. (2019). A review of protocols for Fiducial Reference Measurements of water-leaving radiance for validation of satellite remote-sensing data over water. *Remote Sens.* 11, 2198. doi:10.3390/rs11192198

Sathyendranath, S., Brewin, R. J. W., Brockmann, C., Brotas, V., Calton, B., Chuprin, A., et al. (2019). An ocean-colour time series for use in climate studies: the experience of the Ocean-Colour Climate Change Initiative (OC-CCI). *Sensors* 19, 4285. doi:10.3390/s19194285

Sathyendranath, S., Brewin, R. J. W., Ciavatta, S., Jackson, T., Kulk, G., Jönsson, B., et al. (2023). Ocean biology studied from space. *Surv. Geophys.* 44, 1287–1308. doi:10.1007/s10712-023-09805-9

Sea-Bird Scientific (2017). Product manual SAS solar tracker (document: SAT-DN-635). *Tech. Rep. Sea-Bird Scientific*.

Setälä, O., Tirroniemi, J., and Lehtiniemi, M. (2022). Testing citizen science as a tool for monitoring surface water microplastics. *Environ. Monit. Assess.* 194, 851. doi:10.1007/s10661-022-10487-w

Simis, S. G., and Olsson, J. (2013). Unattended processing of shipborne hyperspectral reflectance measurements. *Remote Sens. Environ.* 135, 202–212. doi:10.1016/j.rse.2013.04.001

Slade, W. H., Boss, E., Dall'Olmo, G., Langner, M. R., Loftin, J., Behrenfeld, M. J., et al. (2010). Underway and moored methods for improving accuracy in measurement of spectral particulate absorption and attenuation. *J. Atmos. Ocean. Technol.* 27, 1733–1746. doi:10.1175/2010JTECHO755.1

Tilstone, G., Dall'Olmo, G., Hieronymi, M., Ruddick, K., Beck, M., Ligi, M., et al. (2020). Field intercomparison of radiometer measurements for ocean colour validation. *Remote Sens.* 12, 1587. doi:10.3390/rs12101587

Valente, A., Sathyendranath, S., Brotas, V., Groom, S., Grant, M., Jackson, T., et al. (2022). A compilation of global bio-optical *in situ* data for ocean colour satellite applications – version three. *Earth Syst. Sci. Data* 14, 5737–5770. doi:10.5194/essd-14-5737-2022

Vanhellemont, Q., Brewin, R. J. W., Bresnahan, P. J., and Cyronak, T. (2022). Validation of Landsat 8 high resolution sea surface temperature using surfers. *Estuar. Coast. Shelf Sci.* 265, 107650. doi:10.1016/j.ecss.2021.107650

Wang, Z., and Costa, M. (2022). Autonomous shipborne *in situ* reflectance data in optically complex coastal waters: a case study of the Salish sea, Canada. *Front. Remote Sens.* 3. doi:10.3389/frsen.2022.867570

Wernand, M. R. (2002). "Guidelines for (ship bourne) auto-monitoring of coastal and ocean color," in *Ocean optics XVI*. Editors S. Ackleson and C. Trees (Santa Fe, NM, USA: Ocean).

Zhang, X., He, S., Shabani, A., Zhai, P.-W., and Du, K. (2017). Spectral sea surface reflectance of skylight. *Opt. Express* 25, A1–A13. doi:10.1364/OE.25.0000A1

frontiers | Frontiers in Remote Sensing

TYPE Original Research
PUBLISHED 08 February 2024
DOI 10.3389/frsen.2023.1290110

Check for updates

OPEN ACCESS

EDITED BY
Nima Pahlevan,
Science Systems and Applications, Inc., United States

REVIEWED BY
Zhigang Cao,
Chinese Academy of Sciences (CAS), China
Lin Qi,
University of South Florida, United States

*CORRESPONDENCE
David Doxaran,
david.doxaran@imev-mer.fr

RECEIVED 07 September 2023
ACCEPTED 11 December 2023
PUBLISHED 08 February 2024

CITATION
Doxaran D, ElKilani B, Corizzi A and Goyens C (2024), Validation of satellite-derived water-leaving reflectance in contrasted French coastal waters based on HYPERNETS field measurements. *Front. Remote Sens.* 4:1290110. doi: 10.3389/frsen.2023.1290110

COPYRIGHT
© 2024 Doxaran, ElKilani, Corizzi and Goyens. This is an open-access article distributed under the terms of the Creative Commons Attribution License (CC BY). The use, distribution or reproduction in other forums is permitted, provided the original author(s) and the copyright owner(s) are credited and that the original publication in this journal is cited, in accordance with accepted academic practice. No use, distribution or reproduction is permitted which does not comply with these terms.

Validation of satellite-derived water-leaving reflectance in contrasted French coastal waters based on HYPERNETS field measurements

David Doxaran[1]*, Boubaker ElKilani[1], Alexandre Corizzi[1] and Clémence Goyens[2]

[1]Laboratoire d'Océanographie de Villefranche, UMR7093 CNRS, Sorbonne Université, Villefranche-sur-Mer, France, [2]Operational Directorate Natural Environment, Royal Belgian Institute of Natural Sciences (RBINS), Brussels, Belgium

Since 2021, two autonomous HYPERNETS (A new hyperspectral radiometer integrated in automated networks of water and land bidirectional reflectance measurements for satellite validation) stations are operated in contrasted French coastal waters: one in the center of an optically complex coastal lagoon and one at the mouth of a highly turbid estuary. These stations perform predefined sequences of above-water hyperspectral radiometric measurements following a strict viewing geometry. The data recorded by the ®HYPSTAR radiometer is automatically transmitted to servers for quality-controls then computation of the water-leaving reflectance signal. Numerous matchups were identified with high (Sentinel2-MSI and Landsat8/9-OLI) and medium (Sentinel3-OLCI and Aqua-MODIS) spatial resolution satellite data and are analyzed to assess the performance of different atmospheric correction algorithms (Sen2Cor, ACOLITE, POLYMER, iCOR, C2RCC, GRS, BPAC, NIR-SWIR). Considering the specifications of each site (i.e., spatial and temporal variations of water optical properties), optimized matchup protocols are first established to guaranty high quality comparisons between satellite products and field measurements. The matchup results highlight the failure and limits of several atmospheric correction algorithms in complex/turbid coastal waters. The importance of accurate sun glint corrections in low to moderately-turbid waters (with the good performances of POLYMER, C2RCC and GRS processors, e.g., errors (MAPE) lower than 25% in the green spectral region) is also shown while the use of dark targets and spectral fitting to estimate the aerosol contributions is proved to be the most accurate method in the case of turbid waters (with Sen2Cor and ACOLITE errors (MAPE) lower than 20% in the visible and near-infrared spectral regions).

KEYWORDS

ocean color, atmospheric corrections, validation, autonomous system, coastal waters

1 Introduction

In coastal, nearshore and inland waters, many new applications have been developed using high quality medium to high spatial resolution satellite data notably provided by the Sentinel3 (S3) Ocean and Land Colour Instrument (OLCI), Sentinel2 (S2) MultiSpectral Instrument (MSI), and Landsat8&9 (L8&9) Operational Land Imager (OLI) sensors. These applications include the monitoring of water quality, sediment transport and dredging activities, aquaculture, detection of (harmful) algal blooms and pollutants from anthropogenic activities (e.g., Doxaran et al., 2009; Gernez et al., 2014; 2017; 2023; Vanhellemont and Ruddick, 2018; Katlane et al., 2020). This statement has been even reinforced with the distribution of hyperspectral (e.g., PRISMA, EnMap) and meter-scale spatial resolution (e.g., Pléiades, PlanetScope) satellite data (Vanhellemont and Ruddick, 2019; 2023; Luo et al., 2020; Pellegrino et al., 2023). Such satellite data is potentially very useful to complement field observations, as long as measurements carried out at the top of the atmosphere can be accurately corrected for complex atmospheric, adjacency and sun glint effects to retrieve the water-leaving reflectance signal (Rhow in the present study, equivalent to ρ_w, dimensionless, used in other studies (e.g., Goyens et al., 2022)). This multiple-correction step is crucial before deriving from Rhow other water optical and biogeochemical properties used for scientific and/or operational monitoring purposes.

Several recent studies assessed the performance of existing atmospheric correction processors used to retrieve Rhow from S2-MSI, L8-OLI and S3-OLCI satellite data in coastal and inland waters (e.g., Pahlevan et al., 2017a; 2017b; 2021; De Keukelaere et al., 2018; Ilori et al., 2019; Pereira-Sandoval et al., 2019; Warren et al., 2019; Soomets et al., 2020; Vanhellemont and Ruddick, 2021). These studies, based on matchups between satellite data and field radiometric measurements provided by the AERONET-OC network (Zibordi et al., 2009; 2020) or dedicated campaigns, revealed significant to high errors associated to satellite-derived Rhow values. These errors are usually around 30% in green and red spectral bands but increase (60% and over) towards short (blue) and near-infrared (NIR) wavebands due to, respectively, higher atmospheric contribution and low water-leaving signal (De Keukelaere et al., 2018; Ilori et al., 2019; Vanhellemont and Ruddick, 2021). Moreover, these studies did not identify any specific AC processor outperforming the others over the wide range of optically complex waters encountered in coastal and inland environments and most recommend a classification of optical water types before selecting the most appropriate atmospheric correction processor (Pereira-Sandoval et al., 2019; Soomets et al., 2020; Pahlevan et al., 2021).

The validation of Rhow values derived from satellite data therefore requires high-quality field radiometric measurements in various coastal, nearshore and inland water environments, at high temporal and radiometric resolutions, to multiply matchups with all satellite data covering all seasonal conditions. Only autonomous systems can satisfy such requirements. The AERONET-OC network is certainly the network of reference around the world; however, it only provides multi-spectral radiometric measurements at a minimum distance from the coast, which is quite limited in terms of current satellite wavebands and excludes nearshore and most inland waters. A new autonomous network has been recently designed to complement radiometric measurements provided by AERONET-OC stations: HYPERNETS[1]. As described by Goyens et al. (2022), the HYPERNETS system includes a new radiometer, the HYperspectral Pointable System for Terrestrial and Aquatic Radiometry (HYPSTAR)[2] mounted on a pointable device. In several fixed locations around the world, this system already executes predefined sequences of above-water radiometric measurements during satellite overpasses. It allows multiplying matchups with satellite data to assess the performance of processing algorithms used to derive the water-leaving reflectance signal from top-of-atmosphere (TOA) measurements. Since 2021, two HYPERNETS stations are operated in France in contrasted nearshore waters: one at the center of an optically complex and dynamic Mediterranean coastal lagoon (Berre), and a second at the mouth of a highly turbid macrotidal estuary (the Gironde, Bay of Biscay).

The present study describes the radiometric measurements carried out aboard these two stations, the quality-control of the data so as the adaptation of existing matchup protocols in the case of dynamic nearshore waters. The resulting matchups are detailed and analyzed to document the respective performance of various atmospheric/glint/adjacency correction algorithms applied to medium (OLCI) and high (MSI, OLI) spatial resolution satellite data. Conclusions and perspectives are finally presented for a future autonomous validation network and improvements of satellite data processing algorithms.

2 Materials and methods

The section first presents the HYPERNETS system and its implementation in the first two French sites. It then describes the considered satellite data and tested processing algorithms used to correct for atmospheric, glint and adjacency effects in order to retrieve the water-leaving reflectance signal. It finally explains how site-specific matchup protocols are established to compare satellite products and field radiometric measurements.

2.1 The HYPERNETS system, data and processing

The HYPSTAR sensor has been developed in the frame of the H2020 HYPERNETS project and is part of the HYPERNETS network (Goyens et al., 2022). The model designed for water applications is the HYPSTAR-SR radiometer which takes radiance (field of view (FOV) = 2°) and irradiance (FOV = 180°) measurements from 380 to 1020 nm with a spectral sampling of 0.5 nm (i.e., Full Width Half Maximum is 3 nm).

As part of the HYPERNETS project, a system has also been developed to operate the HYPSTAR in autonomous mode and outdoor conditions. This system is mainly composed of a pan-tilt unit, to accurately point the radiometer towards specific directions, and a water-proof main box. This box contains an electronic card to

1 https://www.hypernets.eu/from_cms/summary

2 https://hypstar.eu

switch ON/OFF the system, a rugged PC, a GPS antenna and a 3G card for data transmission. Ancillary sensors are used to measure humidity, temperature and pressure inside the main box. Deported sensors are used to detect rainfall and measure ambient light conditions. Two webcams, one pointing towards the system, the other towards the target/surrounding waters, are used for remote control and detection of potential presence of floating debris, animals or boats which could contaminate the radiometric measurements, respectively. The whole system is powered by a 12V battery connected to a solar panel for long-term autonomous operation. The hypernets_tools software[3] is installed on the rugged PC to execute predefined measurement sequences when environmental conditions (e.g., enough light and no rain) are favorable and store recorded data. After the execution of each measurement sequence, the recorded data is also automatically transferred (3G) to a remote server for quality-controls and further processing (i.e., computation of the water-leaving reflectance signal) (see Goyens et al. (2022) for details). The 3G communication also allows to modify remotely the data acquisition procedure. At night the system is OFF to minimize power consumption with the HYPSTAR pointing to nadir. The system wakes up every morning to execute measurement sequences at predefined times, typically every 15 or 30 min.

When executing a "water standard" measurement sequence, the system first detects the Sun position to adopt a +/- 90° or +/- 135° azimuth angle. The sensor is then successively pointed towards the zenith to measure the downwelling irradiance, (Ed), then at zenith angles of 140° and 40° to measure respectively the sky (Ls) and upwelling (Lu) radiances. These viewing angles are the ones recommended by Mobley (1999) based on computations and by Ruddick et al. (2006) based on field measurements. The duration of this sequence varies from 2 to 3 min, depending on light conditions and contains 6 measurements of each parameter recorded in this order: 3 Ed, 3 Ls, 6 Lu, 3 Ls and 3 Ed spectra.

The data transferred to servers are processed using the HYPERNETS Processor[4]. The data quality controls and computation of the remote sensing reflectance signal (Rrs in sr^{-1}) which is multiplied by π sr to obtain the water-leaving reflectance (Rhow, dimensionless) spectra are detailed in Goyens et al. (2022). Spectra are distributed to users as Rhow and Rhow_nosc values, i.e., with or without applying the NIR similarity correction (Ruddick et al., 2005), which was proved to be no longer valid in highly turbid waters (Doron et al., 2011). However, note that the quality checks are slightly different from one HYPERNETS site to another (and in some conditions from one application to another). Here, we have used quality checks that do not rely on the NIR similarity correction.

2.1.1 First French station: Berre coastal lagoon

The first HYPERNETS station operated in France was implemented in February 2021 in the central part of the Berre lagoon (Figure 1). This coastal lagoon, located North-West of Marseille and connected to the Mediterranean Sea, is the second largest in Europe. With a mean depth of 6 m, it is highly influenced by the freshwater discharge of three small rivers and by the massive discharge of turbid freshwater from a power plant (Électricité de France). These natural and human-controlled river inputs regularly provide high loads of nutrients which enhance the primary production with regular intensive phytoplankton blooms at the end of the summer period. They also induce a strong density stratification of water masses which may generate anoxic crises when wind conditions do not guaranty an efficient mixing of the water column for long periods. The lagoon is also surrounded by many industrial zones which have contributed in the past to several pollution events with significant impacts on water quality affecting the pelagic and benthic ecosystems. In the central part of the Berre lagoon, concentrations of suspended particulate matter (SPM) and chlorophyll-a (Chla) typically vary from 0.1 to 10 g m^{-3} and from 0.1 to 5 mg m^{-3}, within surface waters, with peaks of concentrations up to 100 g m^{-3} and 30 mg m^{-3}, respectively, during exceptional phytoplankton bloom events (Elkilani 2020).

To prevent such events, the GIPREB company was created in2000[5] notably to monitor the water quality in different parts of the Berre lagoon, based on monthly field measurements and laboratory analyses of key parameters. The implementation of the HYPERNETS station in collaboration with GIPREB in this sensitive area was done with the objective to locally calibrate and validate ocean color satellite products (e.g., optical and biogeochemical parameters) for the monitoring of water quality in the lagoon. The HYPERNETS station was implemented on a fixed platform in the center of the lagoon to guaranty optically-deep waters (9 m depth) and minimize adjacency effects on satellite data (Figure 1). Since its implementation in February 2021, standard water sequence measurements have been executed every 30 min during day time. Note that several minor technical problems occurred with this version 1 of the HYPERNETS system; these issues were rapidly fixed to provide the acquisition of good quality measurements more than 90% of the operation phase.

On a cloud-free day in Berre (e.g., in July 2021, see Figure 2), illumination conditions are very stable so that the 6 Ed spectra recorded during a water standard measurement sequence are almost superimposed. The measured Ls (6 spectra) also show almost negligible variations. During calm wind conditions, the Lu is also expected to be quite stable as the water surface is plane and the water mass is usually homogeneous in the central part of the lagoon. In such conditions, the spectra easily pass the following quality controls, i.e., temporal variability in Ed, Ls and Lu is low with differences between consecutive scans at 550 nm not exceeding 25%, and the resulting Rhow spectra can be computed (Figure 1). Note than applying the near-infrared similarity correction is useful to minimize imperfect correction of skylight reflection effects on Lu. The resulting Rhow spectra are typical of moderately turbid waters, with also a significant decrease around 675 nm indicating the presence of phytoplankton pigments (Gernez et al., 2017; 2023).

The Figure 2 (bottom plots) summarizes the resulting water reflectance spectra measured at the BEFR station in March, August and November 2021.

3 https://github.com/HYPERNETS/hypernets_tools

4 https://github.com/HYPERNETS/hypernets_processor

5 https://etangdeberre.org



FIGURE 1
Locations of the two autonomous HYPERNETS stations operated in France since 2021: (i) at the mouth of the Gironde Estuary (South-West of France, Atlantic coast) (top left) and (ii) in the central part of the Berre coastal lagoon (South-East of France, Mediterranean Sea) (bottom right). Pictures of the HYPERNETS stations in the Gironde (turbid brown waters) and Berre lagoon (blue optically dynamic waters) (bottom left).

2.1.2 Second French station: Gironde Estuary

A second French site was implemented in November 2021 with the version 2 of the HYPERNETS system, i.e., a more robust and technically improved system. The location of this station is at the mouth of the macro-tidal Gironde Estuary, South-West of France, connected to the Atlantic Ocean (Figure 1). This estuary is characterized by well-developed maximum turbidity zones, with high concentrations of suspended sediments which strongly vary according to daily to fortnightly tidal cycles (e.g., Doxaran et al., 2009). The mouth of the Gironde Estuary actually represents a limit between sediment-rich turbid waters (inside the estuary) and phytoplankton-rich productive waters (in the adjacent coastal zone). The limits between predominantly brown and green waters have been often observed using satellite data in this transition zone, where the mixing of water masses depends on the river discharge and tidal currents (e.g., Novoa et al., 2017; Luo et al., 2020; Renosh et al., 2020). At the mouth of the Gironde Estuary, SPM and Chla concentrations typically vary from 10 to 600 g m^{-3} and from 0.1 to 5 mg m^{-3}, within surface waters (Doxaran et al., 2009; Jalón-Rojas et al., 2021).

From November 2021 to September 2022, the HYPERNETS station was operated on the West shore of the estuary, on a fixed platform located at the beginning of a pontoon (50 m from the shore, station MAFR1 in Figure 1) where is located the MAGEST-Verdon autonomous station which provides continuous measurements of water turbidity, salinity and temperature (Jalón-Rojas et al., 2021). In September 2022, in order to improve the quality of comparisons between satellite and field data, the HYPERNETS station was moved 400 m away from the shore to face estuarine waters and minimize potential land contamination on satellite data (station MAFR2 in Figure 1). Taking into account the strong variations of water turbidity with tidal currents, water standard measurement sequences were recorded every 15 min in this location, during day time.

Selecting a cloud-free day over the Gironde Estuary (e.g., end of September 2022, see Figure 2), quite stable illumination conditions logically result in 6 almost superimposed Ed spectra measured over a full sequence. The same is observed for the 6 Ls spectra, while a low but significant variability is observed amongst the 6 Lu spectra. These variations can result from fast variations of water turbidity in the estuary, but also heterogeneous waters with mixed suspended sediment and phytoplankton particles. In such conditions, the data quality controls (see Section 2.1.1) are successfully passed and the

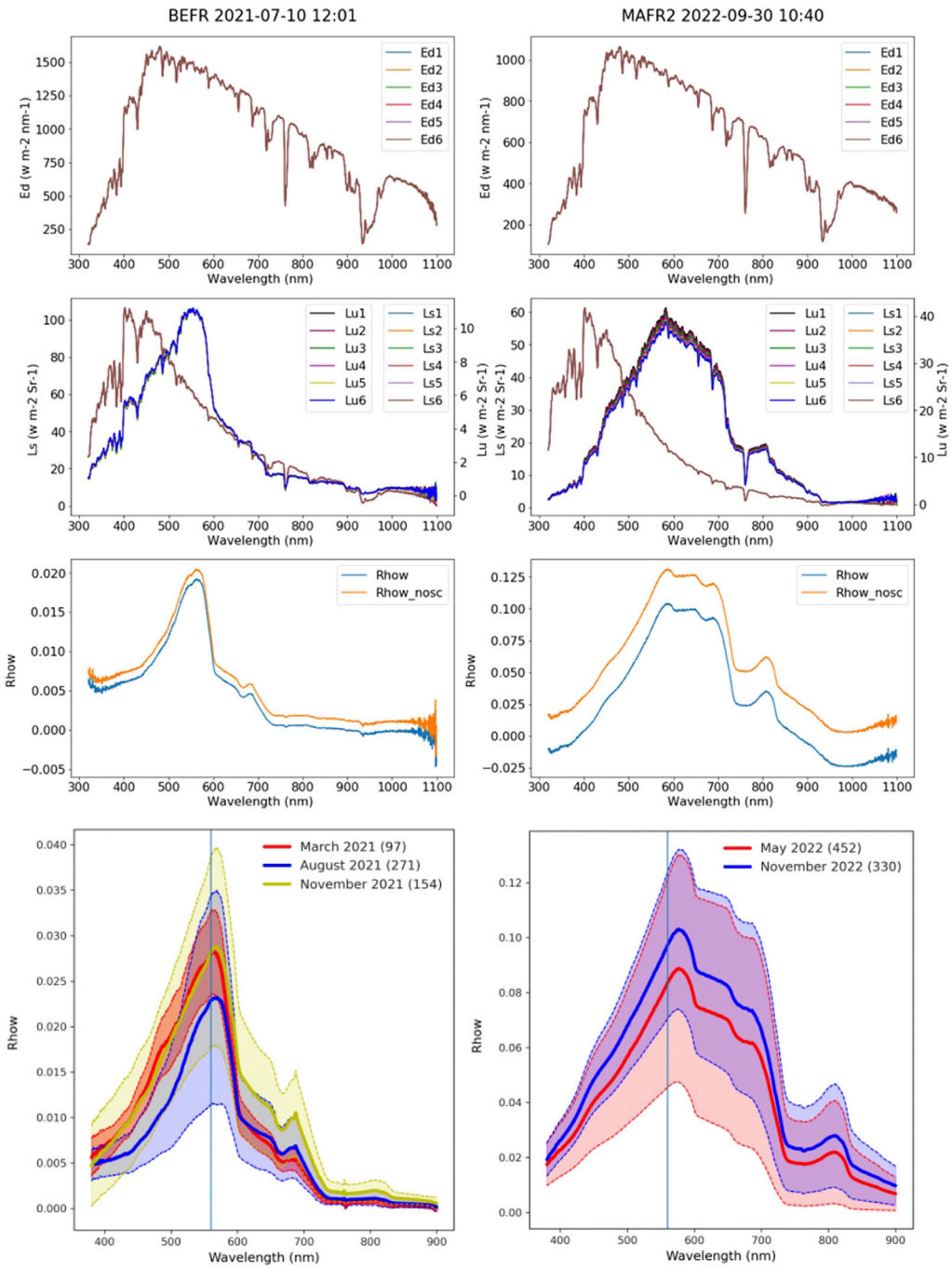


FIGURE 2
Processing and quality controls applied to above-water HYPERNETS radiometric measurements (downwelling irradiance (Ed), upwelling (Lu) and sky (Ls) radiances) used to compute the water-leaving reflectance after applying or not the NIR similarity correction (Rhow and Rhow_nosc, respectively, see the text for details). Typical measurement sequences recorded at the Berre [BEFR, **(A)**] and Gironde [MAFR2, **(B)**] stations. Bottom left: plain lines are the averaged reflectance spectra measured during March (97 spectra), August (271 spectra) and November (154 spectra) 2021 at the BEFR station with the shaded area delimited by dashed lines being +/- standard deviation around the average. Bottom right: plain lines are the resulting averaged reflectance spectra during May (452 spectra) and November (330) 2022 at the MAFR station with the shaded area being the +/- standard deviation around the average.

water reflectance signal can be computed. Dealing with quite turbid waters, the obtained Rhow values are about ten times higher than in the Berre coastal lagoon, with a very strong signal in the red and NIR parts of the spectrum. However, the presence of phytoplankton cells can be detected with a significant decrease of Rhow around 675 nm, the second absorption peak of chlorophyll-a. Finally note that applying the NIR similarity correction in such turbid waters generates negative values at the two extremities of the spectrum (<400 nm and >850 nm), i.e., the Rhow_nosc values must be considered in such waters.

TABLE 1 List of satellite sensors and atmospheric correction algorithms tested.

Satellite sensor	Atmospheric correction	Version
S2-MSI	C2RCC	1.1
	GRS	1.5
	Polymer	4.13
	iCOR	3
	ACOLITE	20221025
	ACOLITE-GLINT	20221025
	Sen2Cor	2.11
L8/9-OLI	C2RCC	1.1
	C2X	1.1
	iCOR	3
	ACOLITE	20221025
	ACOLITE-GLINT	20221025
S3-OLCI	C2RCC	2.1
	BAC	1.5
	Polymer	4.13
	iCOR	3
	ACOLITE	20221025
	ACOLITE-GLINT	20221025
AQUA-MODIS	NIR-SWIR	2007

The Figure 2 (bottom plots) summarizes the resulting water reflectance spectra measured at the MAFR station in May and November 2022.

2.2 Satellite data and products

Satellite data considered in the present study were selected based on their specifications in terms of spatial, temporal and spectral resolutions which should be adapted to monitor water quality parameters in estuaries and coastal lagoons. As already highlighted (Doxaran et al., 2009; Ody et al., 2016; 2022; Novoa et al., 2017; Renosh et al., 2020), the combined S2A&B-MSI and S3A&B-OLCI satellite sensors from the European Space Agency (ESA) have great capabilities in this scope. S2-MSI has 12 wavebands from the visible to the shortwave-infrared (SWIR) with different spatial resolutions ranging from 10 to 60 m. The S2A&B-MSI sensors in activity since 2015 and 2017, respectively, provide a revisit time period of about 4 days at mid-latitudes. Comparatively, the S3A&B-OLCI sensors in activity since 2016 and 2018, respectively, provide daily observations at 300 m spatial resolution with 21 wavebands in the visible and NIR spectral regions. Level-1 data and Level-2 products were downloaded from CREODIAS[6].

The L8 and L9-OLI sensors provide since 2013 and 2021, respectively, observations at high spatial resolution (30 m), with 9 wavebands from the visible to the SWIR and a revisit time period of about 9 days at mid-latitudes. These sensors are operated by NASA, the National Aeronautics and Space Administration. Data and products were downloaded from USGS[7].

Finally, the Aqua-MODIS (Moderate-resolution Imaging Spectroradiometer) sensor (NASA) was also considered as it provides daily observations since 2002 at spatial resolutions of 250, 500 and 1000 m (19 wavebands from the visible to the SWIR). Level-1 data were downloaded from the NASA ocean color data portal[8] to generate level-2 products at 250 m spatial resolution using the SeaWiFS Data Analysis System (SeaDAS) l2gen function. This processing, however, is known to be limited in confined areas such as estuaries, bays and lagoons as only two wavebands are available at 250 m and since the wavebands at 1000 m spatial resolution are used to apply atmospheric corrections (i.e., water pixels partly on land will be masked).

2.2.1 Atmospheric correction algorithms

For each satellite sensor, atmospheric correction algorithms specifically developed for coastal turbid and dynamic waters were considered (Novoa et al., 2017; Warren et al., 2019; Renosh et al., 2020; Pahlevan et al., 2021). Note that some of these algorithms also integrate a correction for sun glint effects and/or also explicitly or implicitly a correction (which can be activated or not) for adjacency effects. Table 1 summarizes, the atmospheric correction algorithms tested for each sensor (and the corresponding versions).

C2RCC–The C2RCC processor has been developed for different satellite sensors (Brockmann et al., 2016). It is an advanced neural network (NN) algorithm trained for several water types including highly backscattering waters (rivers, estuaries and lakes). In this study, C2RCC processors available in SNAP 9.0 were used to process S2-MSI, S3-OLCI and L8&9-OLI satellite data. Here the default values were used for the water salinity (35 PSU) and temperature (15°C), as field data were not always available to document these parameters.

GRS–The Glint Removal for Sentinel2 (GRS) processor was initially develop to correct S2-MSI satellite data for sun glint effect. It now also incorporates a Rayleigh correction and applies a spectral fitting approach to estimate aerosol radiances (Harmel et al., 2018). Selected S2-MSI images were processed on demand by T. Harmel for the purpose of this study.

Polymer–The Polynomial Spectral Matching based algorithm applied to MERIS (Polymer) is an algorithm specially designed for waters with and without glint contamination (Steinmetz et al., 2011). Polymer works on the principle of the spectral matching method. This method depends upon a polynomial function to model the spectral reflectance of the atmosphere and sun glint with the help of a water reflectance model covering the visible and NIR (700–900 nm) spectral regions using the similarity spectrum for turbid waters (Ruddick et al., 2006). It was used to process S2-MSI and S3-OLCI satellite data. Note that the processing of L8&9-OLI

6 https://browser.creodias.eu/

7 https://earthexplorer.usgs.gov

8 https://oceancolor.gsfc.nasa.gov

10.3389/frsen.2023.1290110

TABLE 2 List of satellite images considered for matchups with field data on the two study sites: the Berre coastal lagoon (BEFR on the left) and Gironde Estuary on the right (MAFR1 up to June 2022 and MAFR2 since September 2022).

BEFR			MAFR		
Satellite sensor	Date (dd/mm/yyyy)	Time (UT)	Satellite sensor	Date (dd/mm/yyyy)	Time (UT)
S2A-MSI	18/11/2021	10:48	S2A-MSI	03/05/2022	11:08
S2A-MSI	15/12/2021	10:38	S2A-MSI	13/05/2022	11:08
S2A-MSI	18/12/2021	10:48	S2A-MSI	02/06/2022	11:08
S2B-MSI	04/04/2021	10:38	S2B-MSI	28/05/2022	11:08
S2B-MSI	03/06/2021	10:38	S2B-MSI	03/01/2023	11:03
S2B-MSI	13/06/2021	10:38	S2A-MSI	29/11/2022	11:04
S2B-MSI	01/09/2021	10:38	S2A-MSI	19/11/2022	11:03
S2B-MSI	11/10/2021	10:38	L8-OLI	30/04/2022	10:47
S2B-MSI	30/11/2021	10:38	L8-OLI	16/05/2022	10:47
S2A-MSI	28/02/2021	10:38	L9-OLI	03/01/2023	10:48
S2A-MSI	28/07/2021	10:38	L9-OLI	07/11/2022	10:54
S2A-MSI	09/10/2021	10:48	L8-OLI	07/10/2022	10:48
S2A-MSI	26/10/2021	10:38	S3A-OLCI	09/05/2022	10:39
S2A-MSI	07/01/2022	10:48	S3A-OLCI	29/05/2022	10:20
S2A-MSI	14/01/2022	10:38	S3B-OLCI	05/05/2022	10:03
S2A-MSI	17/01/2022	10:48	S3B-OLCI	07/05/2022	10:52
S2B-MSI	12/01/2022	10:48	S3B-OLCI	08/05/2022	10:26
L8-OLI	14/03/2021	10:23	S3B-OLCI	13/05/2022	09:56
L8-OLI	20/07/2021	10:23	S3B-OLCI	28/05/2022	10:07
L8-OLI	05/08/2021	10:23	S3B-OLCI	01/06/2022	10:03
L8-OLI	08/10/2021	10:24	S3B-OLCI	13/11/2022	10:27
S3A-OLCI	25/06/2021	09:43	S3B-OLCI	12/11/2022	10:53
S3A-OLCI	10/07/2021	09:54	S3A-OLCI	05/12/2022	09:56
S3A-OLCI	03/08/2021	09:32	S3A-OLCI	19/11/2022	10:11
S3A-OLCI	10/08/2021	09:50	S3A-OLCI	08/10/2022	09:59
S3A-OLCI	30/08/2021	09:32	S3B-OLCI	26/10/2022	10:33
S3A-OLCI	14/10/2021	10:05	S3B-OLCI	09/10/2022	10:35
S3A-OLCI	06/11/2021	10:09	AQUA- MODIS	04/05/2022	13:07
S3A-OLCI	14/11/2021	10:01	AQUA- MODIS	07/05/2022	13:37
S3A-OLCI	18/11/2021	09:58	AQUA- MODIS	09/05/2022	13:25
S3A-OLCI	16/12/2021	09:32	AQUA- MODIS	10/05/2022	12:30
S3A-OLCI	18/12/2021	10:20	AQUA- MODIS	11/05/2022	13:12
S3A-OLCI	20/12/2021	09:28	AQUA- MODIS	16/05/2022	13:30
S3B-OLCI	14/03/2021	10:14	AQUA- MODIS	18/05/2022	13:17
S3B-OLCI	12/05/2021	09:44	AQUA- MODIS	25/05/2022	13:22
S3B-OLCI	01/07/2021	09:48	AQUA- MODIS	30/05/2022	13:40
S3B-OLCI	20/07/2021	09:56			

(Continued on following page)

TABLE 2 (*Continued*) List of satellite images considered for matchups with field data on the two study sites: the Berre coastal lagoon (BEFR on the left) and Gironde Estuary on the right (MAFR1 up to June 2022 and MAFR2 since September 2022).

BEFR			MAFR		
Satellite sensor	Date (dd/mm/yyyy)	Time (UT)	Satellite sensor	Date (dd/mm/yyyy)	Time (UT)
S3B-OLCI	15/08/2021	10:22			
S3B-OLCI	20/08/2021	09:52			

data has been recently implemented in Polymer (v4.14) (e.g., see Kabir et al., 2023).

iCOR–Image correction for atmospheric effects (iCOR) is an image-based atmospheric correction tool which first identifies land and water pixels based on a band threshold then uses land pixels to estimate the aerosol optical thickness (AOT) (De Keukelaere et al., 2018). Multiple steps allow retrieving AOT values over land which are extrapolated over water. An adjacency correction can be applied using the SIMilarity Environmental Correction (SIMEC) approach (Sterckx et al., 2015). For consistency with the other processing algorithms, SIMEC was not applied in the present study. Finally, look-up-tables (LUT) are used to solve the radiative transfer equation and an additional correction for Fresnel reflectance is applied over water pixels. iCOR can be implemented into the SNAP software and was used here to process S2-MSI, S3-OLCI and L8&9-OLI satellite data.

ACOLITE–This generic processor was developed for atmospheric correction of multi-sensor satellite data (incl. L8&9-OLI, S2-MSI, S3-OLCI) for coastal and inland water applications. The default correction uses the dark spectrum fitting (DSF) approach (Vanhellemont and Ruddick, 2018; 2021; Vanhellemont and Ruddick, 2019; 2019; 2020). It is exclusively image-based, hence does not need external inputs such as measured AOT values, and assumes that the atmospheric path reflectance can be predicted from multiple dark targets in the scene (or sub-scene). The GRS correction for glint effects (Harmel et al., 2018) can be activated in ACOLITE (method called here ACOLITE-GLINT).

Sen2Cor–Sen2Cor is the processor supported by ESA to generate standard S2-MSI level-2 products distributed by Copernicus. It performs the atmospheric-, terrain- and cirrus correction of TOA data. Sen2Cor creates Bottom-Of-Atmosphere and cirrus corrected reflectance images, and additionally, AOT (Main-Knorn et al., 2017) using look-up-tables generated with the LIBRADTRAN radiative transfer model (Mayer and Killing, 2005). While Sen2Cor was designed for land processing with no water application, it was tested here as this standard level-2 product may perform well in highly turbid estuarine waters.

BAC–The Baseline Atmospheric Correction algorithm (BAC) is a combination of NIR-based black pixel assumption accommodated with the multiple scattering of air molecules and aerosols together with the bright pixel atmospheric correction approach (Moore et al., 2017). Initially developed for MERIS it was updated using OLCI wavebands. The BPAC corrects for the contribution of sediments on Rhow before estimating the atmospheric contribution in the NIR bands and applying the standard atmospheric correction scheme. It is the standard level-2 OLCI product distributed by Copernicus.

NIR-SWIR–This method of ocean color data processing combines the use of NIR and SWIR wavebands for the atmospheric correction of Aqua-MODIS satellite data (Wang and Shi, 2007). A turbid water index is used to discriminate clear and turbid waters. The standard (open ocean) atmospheric correction algorithm is applied in the first case, whereas for identified turbid waters MODIS SWIR bands are used to estimate the aerosol contribution on Rayleigh-corrected satellite data.

2.2.2 Matchup protocols

For validating satellite-derived products using *in situ* data in coastal and inland waters, Concha et al. (2017) raised the need to adapt matchup protocols to each site, depending on spatiotemporal collocation criteria. This approach was cautiously applied here taking into account the temporal variations of field measurements nearshore in the macro-tidal Gironde Estuary and in the center of the dynamic Berre coastal lagoon, and considering the high and medium spatial resolutions of satellite observations.

2.3 Statistical analyses

The list of high-quality matchups, identified in 2021 and 2022 between satellite data and HYPERNETS measurements, is presented in Table 2, for each satellite sensor and HYPERNETS station. These quality matchups were identified based on the availability of HYPERNETS field data and cloud-free satellite data.

Before comparing satellite-derived and field-measured Rhow values, the HYPERNETS Rhow spectra were convolved with the relative spectral responses of each satellite sensor to obtain band-equivalent Rhow values (e.g., see section 2.3.1 in Renosh et al. (2020) for details). The quantitative comparisons were then based on five different statistical indicators: the slope, intercept and determination coefficient (R^2) of the best-fitted linear regression, the root mean square error (RMSE) (Eq. 1) and mean absolute percentage error (MAPE) (Eq. 2):

$$RMSE = \sqrt{\frac{\sum_{i=1}^{n} (Rhow_sat(\lambda) - Rhow_HYP(\lambda))^2}{n}} \quad (1)$$

$$MAPE(\%) = \frac{1}{n}\left[\sum_{i=1}^{n} \frac{|(Rhow_sat(\lambda) - Rhow_HYP(\lambda))|}{Rhow_HYP(\lambda)}\right] \times 100 \quad (2)$$

10.3389/frsen.2023.1290110

TABLE 3 S2-MSI matchup results (statistics for Berre lagoon).

Panel A C2RCC							GRS					
W (nm)	N	slope	Intercept	R^2	MAPE (%)	RMSE	N	slope	Intercept	R^2	MAPE (%)	RMSE
443	17	0.43	0.002	0.32	38	0.005	17	0.69	−0.000	0.56	50	0.005
492	17	0.46	0.003	0.46	33	0.008	17	0.81	0.000	0.91	25	0.044
560	17	0.73	−0.000	0.86	28	0.008	17	0.77	0.000	0.97	22	0.006
665	17	0.69	0.001	0.89	22	0.002	17	0.75	0.000	0.75	31	0.002
704	17	0.67	0.001	0.84	26	0.001	17	0.68	0.001	0.62	37	0.002
740	17	0.68	0.000	0.80	28	0.001	17	0.35	0.002	0.03	>100	0.002
783	17	0.74	0.000	0.80	26	0.001	17	0.10	0.003	0.00	>100	0.002
833	17	0.34	0.000	0.83	51	0.001	17	0.41	0.002	0.05	>100	0.001
Sen2Cor							iCOR					
W (nm)	N	slope	Intercept	R^2	MAPE (%)	RMSE	N	slope	Intercept	R^2	MAPE (%)	RMSE
443	17	0.87	0.014	0.25	>100	0.001	17	1.19	0.007	0.70	98	0.001
492	17	0.82	0.015	0.52	99	0.009	17	1.17	0.004	0.84	44	0.008
560	17	0.86	0.011	0.76	37	0.009	17	0.93	0.004	0.90	16	0.004
665	17	0.49	0.011	0.11	>100	0.009	17	0.95	0.004	0.69	60	0.004
704	17	−0.10	0.012	0.00	>100	0.009	17	1.04	0.004	0.59	>100	0.005
740	17	−3.00	0.013	0.17	>100	0.009	17	1.51	0.004	0.18	>100	0.005
783	17	−3.45	0.013	0.17	>100	0.009	17	0.93	0.006	0.07	>100	0.006
833	17	−2.96	0.011	0.13	>100	0.009	17	1.06	0.005	0.07	>100	0.005
Panel B ACOLITE							ACOLITE_glint					
W (nm)	N	slope	Intercept	R^2	MAPE (%)	RMSE	N	slope	Intercept	R^2	MAPE (%)	RMSE
443	17	1.35	0.009	0.73	>100	0.01	17	1.35	0.008	0.69	>100	0.001
492	17	1.14	0.007	0.87	67	0.009	17	0.86	0.008	0.74	50	0.001
560	17	0.94	0.005	0.94	17	0.004	17	0.94	0.003	0.93	14	0.001
665	17	0.95	0.004	0.67	56	0.004	17	1.06	0.002	0.82	34	0.003
704	17	0.84	0.005	0.41	99	0.005	17	1.05	0.002	0.66	57	0.003
740	17	0.43	0.005	0.01	>100	0.005	17	1.39	0.003	0.24	>100	0.003
783	17	0.31	0.005	0.01	>100	0.005	17	1.32	0.003	0.25	>100	0.003
833	17	0.45	0.004	0.01	>100	0.005	17	1.79	0.001	0.40	>100	0.002

Polymer						
W (nm)	N	slope	intercept	R^2	MAPE (%)	RMSE
443	15	0.71	0.003	0.74	28	0.002
492	15	0.78	0.003	0.93	14	0.001
560	15	0.68	0.002	0.89	21	0.005
665	15	0.79	−0.001	0.47	36	0.002
704	15	0.64	−0.001	0.37	59	0.002
740	15	−0.22	0.001	0.04	70	0.001
783	15	−1.66	0.003	0.42	62	0.001

10.3389/frsen.2023.1290110

TABLE 4 S2-MSI matchup results (statistics for Gironde Estuary).

Panel A C2RCC							GRS					
W (nm)	N	slope	Intercept	R^2	MAPE (%)	RMSE	N	slope	Intercept	R^2	MAPE (%)	RMSE
443	7	−0.24	0.022	0.04	79	0.040	7	−0.78	0.074	0.25	26	0.015
492	7	−0.05	0.023	0.00	72	0.052	7	−0.50	0.089	0.15	25	0.020
560	7	−0.17	0.068	0.01	55	0.065	7	0.19	0.066	0.07	20	0.025
665	7	−0.20	0.054	0.21	57	0.067	7	0.69	0.010	0.73	23	0.023
704	7	−0.14	0.046	0.13	45	0.056	7	0.68	0.007	0.80	26	0.023
740	7	0.04	0.011	0.16	47	0.029	7	0.59	0.001	0.82	43	0.017
783	7	0.06	0.011	0.37	47	0.029	7	0.55	0.003	0.87	34	0.016
833	7	0.16	0.002	0.98	66	0.029	7	0.51	0.004	0.91	31	0.016
Polymer							iCOR					
W (nm)	N	slope	Intercept	R^2	MAPE (%)	RMSE	N	slope	Intercept	R^2	MAPE (%)	RMSE
443	7	1.10	−0.027	0.20	45	0.023	7	2.50	0.052	0.02	>100	0.131
492	7	1.96	−0.095	0.21	36	0.031	7	2.04	0.042	0.06	>100	0.124
560	7	1.13	−0.045	0.34	27	0.034	7	0.77	0.150	0.13	>100	0.130
665	7	0.34	0.021	0.38	39	0.045	7	0.98	0.120	0.80	>100	0.132
704	7	0.26	0.019	0.44	44	0.045	7	0.94	0.135	0.87	>100	0.149
740	7	0.08	0.011	0.14	47	0.028	7	1.16	0.127	0.90	>100	0.162
783	7	−0.07	0.017	0.04	68	0.031	7	1.17	0.124	0.90	>100	0.162
833	7	0.00	0.003	0.00	76	0.035	7	1.07	0.130	0.86	>100	0.218
Panel B ACOLITE							ACOLITE_GLINT					
W (nm)	N	slope	Intercept	R^2	MAPE (%)	RMSE	N	slope	Intercept	R^2	MAPE (%)	RMSE
443	7	−0.19	0.062	0.05	8	0.006	7	−0.84	0.089	0.27	11	0.007
492	7	0.32	0.047	0.04	9	0.007	7	−0.68	0.112	0.30	13	0.011
560	7	0.15	0.084	0.05	10	0.013	7	0.06	0.092	0.01	12	0.015
665	7	0.87	0.012	0.86	9	0.010	7	0.81	0.009	0.82	14	0.014
704	7	0.84	0.012	0.86	11	0.011	7	0.81	0.009	0.86	14	0.013
740	7	0.75	0.005	0.89	21	0.009	7	0.82	0.004	0.95	18	0.007
783	7	0.74	0.008	0.93	23	0.008	7	0.82	0.004	0.96	16	0.006
833	7	0.82	0.009	0.96	41	0.007	7	0.80	0.003	0.98	12	0.006

Sen2Cor						
W (nm)	N	slope	Intercept	R^2	MAPE (%)	RMSE
443	7	1.05	0.009	0.08	24	0.015
492	7	1.04	0.007	0.14	17	0.016
560	7	1.01	0.005	0.34	11	0.014
665	7	1.09	−0.003	0.87	12	0.012
704	7	1.09	0.001	0.90	16	0.013
740	7	0.92	0.008	0.74	38	0.013
783	7	0.84	0.012	0.70	45	0.015
833	7	0.85	0.013	0.64	54	0.016

10.3389/frsen.2023.1290110

TABLE 5 L8/9-OLI matchup results (statistics for Berre lagoon).

C2RCC							C2X				
W (nm)	N	slope	intercept	R^2	MAPE (%)	RMSE	slope	intercept	R^2	MAPE (%)	RMSE
443	5	0.42	0.003	0.45	88	0.002	0.50	0.003	0.49	81	0.0024
483	5	0.45	0.005	0.48	99	0.003	0.51	0.005	0.45	>100	0.0037
561	5	0.43	0.008	0.80	96	0.004	0.44	0.009	0.61	>100	0.0051
665	5	0.23	0.003	0.37	86	0.001	0.12	0.004	0.17	93	0.0019
865	5	0.31	0.000	0.40	42	0	0.09	0.000	0.06	50	0.0001
ACOLITE							ACOLITE_glint				
W (nm)	N	slope	intercept	R^2	MAPE (%)	RMSE	slope	intercept	R^2	MAPE (%)	RMSE
443	5	1.81	0.001	0.83	>100	0.006	0.53	0.011	0.04	>100	0.01
483	5	1.41	0.003	0.97	>100	0.006	0.52	0.012	0.14	>100	0.01
561	5	0.84	0.008	0.91	>100	0.006	0.49	0.013	0.37	>100	0.01
665	5	1.15	0.003	0.49	>100	0.004	0.49	0.005	0.09	>100	0
865	5	−0.36	0.004	0,2	>100	0.005	3.91	0.001	0.20	>100	0

iCOR						
W (nm)	N	slope	intercept	R^2	MAPE (%)	RMSE
443	5	1.35	0.012	0.65	>100	0.014
483	5	1.14	0.012	0.90	>100	0.012
561	5	0.77	0.014	0.85	>100	0.011
665	5	1.20	0.009	0.51	>100	0.009
865	5	4.01	0.009	0.01	>100	0.010

Where $Rhow_sat(\lambda)$ is the water-leaving reflectance derived from the satellite at the waveband λ, and $Rhow_HYP(\lambda)$ is the water-leaving reflectance derived from the HYPERNETS field measurements within the same waveband λ.

3 Results

Matchup results are presented separately for each satellite sensor in different sections and for each HYPERNETS site as scatterplots, indicating the overall statistics (combining all wavebands) and comparing the different atmospheric correction methods tested. Detailed statistical results are also presented separately for each waveband in Tables 2–12. The results obtained are assumed to be representative of the uncertainties associated to satellite-derived water reflectance values.

3.1 Site-specific matchup protocols

Around the HYPERNETS station operated in Berre, the spatial dynamics of the water reflectance was characterized using 20 S2-MSI and 20 S3-OLCI images here corrected for atmospheric effects using ACOLITE-GLINT (Figure 3). Independently of the spatial resolution (20 m S2-MSI, and, 300 m S3 OLCI, respectively), mean values of Rhow (555) in the 3 × 3 and 5 × 5 pixels boxes, respectively, show a very good agreement with the Rhow (555) values of the central pixel (where is located the station). This homogeneity is even confirmed when mapping the variations (in %) of Rhow (555) compared to the Rhow (555) value in the central pixel over a larger area (Figure 3). These variations are typically lower than 15% on S2-MSI images (despite some apparent residual glint effects) and lower than 7% on S3-OLCI images (Figure 3). Now looking at the temporal variations of field-measured Rhow (555) values (HYPERNETS data), between 10 h and 14 h (local time) over a 10 months period, these variations within +/-30 and +/-60 min time windows do not usually exceed 6%. Rare maximum variations of 10% are also detected. This could be explained by the presence of algal blooms causing higher diurnal variability in the optical properties of the water (i.e., August). This period of time also corresponds to higher variability in the HYPERNETS *in-situ* reflectance spectra (see Figure 2). Therefore, as a local adaptation of matchup protocols, extracting the mean satellite-derived value over the 3 × 3 pixels box and field measurements

10.3389/frsen.2023.1290110

TABLE 6 L8/9-OLI matchup results (statistics for Gironde Estuary).

C2RCC							C2X				
W (nm)	N	slope	intercept	R^2	MAPE (%)	RMSE	slope	intercept	R^2	MAPE (%)	RMSE
443	5	−0.72	0.044	0.13	83	0.044	−0.13	0.020	0.01	73	0.038
483	5	−0.90	0.074	0.21	81	0.058	−0.28	0.042	0.05	64	0.046
561	5	−1.14	0.169	0.23	66	0.084	−0.05	0.065	0.00	48	0.059
655	5	−0.07	0.062	0.00	52	0.064	1.12	−0.029	0.16	26	0.034
865	5	−0.05	0.008	0.05	63	0.019	−0.15	0.051	0.00	>100	0.036
ACOLITE							ACOLITE_glint				
W (nm)	N	slope	intercept	R^2	MAPE (%)	RMSE	slope	intercept	R^2	MAPE (%)	RMSE
443	5	0.45	0.035	0.03	20	0.015	0.87	0.011	0.08	22	0.014
483	5	0.14	0.064	0.01	16	0.014	0.57	0.032	0.07	18	0.014
561	5	0.04	0.106	0.00	12	0.017	0.34	0.068	0.06	13	0.018
655	5	0.63	0.038	0.17	13	0.018	0.45	0.054	0.10	14	0.020
865	5	1.66	0.015	0.47	>100	0.035	−0.12	0.041	0.01	100	0.024

iCOR						
W (nm)	N	slope	intercept	R^2	MAPE (%)	RMSE
443	5	−2.07	0.178	0.26	51	0.032
483	5	−1.19	0.168	0.17	30	0.029
561	5	−0.20	0.144	0.01	16	0.025
655	5	0.51	0.065	0.07	12	0.024
865	5	−1.09	0.133	0.14	>100	0.092

averaged within a +/-30 min time windows around the satellite data acquisition time seems appropriate in the central part of the Berre lagoon.

The spatiotemporal dynamics of the water reflectance at the mouth of the Gironde Estuary significantly differ from that observed in Berre (Figure 4). Around the HYPERNETS station located at the extremity of the pontoon (left shore), the high spatial resolution of S2-MSI pixels (7 images) show limited variations of the water reflectance signal (Rhow (665) within boxes of 1–5 × 5 pixels boxes (once the pontoon is accurately masked). This is no longer the case on S3-OLCI pixels which coarser spatial resolution results in a more significant scatter, as Rhow (665) values within boxes of 3 × 3 to 5 × 5 pixels are partly contaminated by the shore and the pontoon itself (Figure 4). As for the temporal variations of the water reflectance measured in the field, time windows of maximum +/-30 min must be considered to avoid variations larger than 20% (as the turbidity of the water, and consequently the water reflectance, strongly varies with tidal currents [e.g., Doxaran et al. (2009)]. This is also confirmed by Figure 2 with the very high variability in water reflectance expected at the Gironde especially in May and, slightly less, in November. Therefore, at the mouth of the Gironde Estuary, the site-specific matchup protocol consists in extracting the satellite-derived value of the closest pixel to the HYPERNETS station and average the field measurements within a +/-15 min time window.

3.2 S2-MSI matchup results

3.2.1 Berre coastal lagoon

Based on 17 quality matchups identified in the Berre lagoon, the C2RCC, GRS and Polymer processors provide results highly correlated with field measurements (R^2 > 0,90), but all tend to underestimate (by about 25%) high Rhow values (Figure 5). C2RCC and Polymer provide accurate retrievals of low reflectance values (negligible intercepts) while GRS results are significantly noisier. Results obtained with iCOR, ACOLITE (with or without glint correction) are overall satisfactory (slope close to 1), but associated to more scatter especially for low Rhow values. The difference between satellite-derived and field-measured values is significantly lower when applying a glint correction, which was expected as S2-MSI data over the lagoon are often affected by sun glint (sensor pointing close to nadir). Sen2Cor results clearly overestimate field measurements (significant intercept) and are associated to a high scatter, as this processor is not designed to perform well in clear to moderately turbid waters and does not correct for glint effects.

TABLE 7 S3-OLCI matchup results (statistics for Berre lagoon) (part ½).

		BAC					C2RCC				
W (nm)	N	slope	intercept	R^2	MAPE (%)	RMSE	slope	intercept	R^2	MAPE (%)	RMSE
400	20	−1.12	0.018	0.25	>100	0.01	0.64	0.004	0.55	40	0.002
412	20	−0.91	0.016	0.18	>100	0.01	0.72	0.004	0.63	40	0.002
442	20	−0.21	0.009	0.02	86	0.01	0.83	0.004	0.74	37	0.003
490	20	0.28	0.005	0.17	46	0.01	0.82	0.005	0.80	26	0.003
510	20	0.41	0.005	0.43	35	0.01	0.85	0.004	0.84	19	0.003
560	20	0.56	0.005	0.86	23	0.01	0.81	0.002	0.83	15	0.004
620	20	0.50	0.001	0.69	36	0.005	0.94	0.001	0.92	11	0.001
665	20	0.39	0.001	0.48	47	0.004	1.00	0	0.93	9	0.001
673	20	0.36	0.001	0.42	48	0.004	0.97	−0.001	0.92	14	0.001
681	20	0.41	0.001	0.58	46	0.004	0.85	0	0.88	20	0.001
708	20	0.38	0.000	0.47	50	0.003	0.82	0	0.89	12	0.001
753	20	0.06	0.001	0.00	62	0.001	0.81	0	0.88	14	0
778	20	0.17	0	0.16	80	0.001	0.96	0	0.88	19	0
865	20	0.18	0	0.27	80	0	0.58	0	0.89	23	0
885	20	0.14	0	0.38	80	0	0.52	0	0.86	36	0
1020	20	−0.29	0.002	0.01	>100	0.001	0	0	0.20	>100	0

TABLE 8 S3-OLCI matchup results (statistics for Berre lagoon) (part 2/2).

		ACOLITE_glint					Polymer				
W (nm)	N	slope	intercept	R^2	MAPE (%)	RMSE	slope	intercept	R^2	MAPE (%)	RMSE
400	20	0.0	0.03	0.0	>100	0.03	0.82	0	0.59	35	0.002
412	20	−0.1	0.03	0.0	>100	0.02	0.77	0.002	0.67	18	0.002
443	20	0.2	0.03	0.0	>100	0.02	0.62	0.004	0.73	19	0.002
490	20	0.7	0.02	0.4	>100	0.02	0.60	0.004	0.79	16	0.004
510	20	0.8	0.02	0.5	>100	0.02	0.63	0.004	0.86	16	0.004
560	20	0.9	0.02	0.6	93	0.02	0.64	0.005	0.92	16	0.005
620	20	0.8	0.02	0.6	>100	0.01	0.61	0.002	0.95	16	0.002
665	20	0.7	0.01	0.4	>100	0.01	0.62	0.001	0.91	21	0.002
674	20	0.7	0.01	0.3	>100	0.01					
682	20	0.5	0.01	0.3	>100	0.01	0.63	0.001	0.90	18	0.002
709	20	0.7	0.01	0.2	>100	0.01	0.67	0	0.85	37	0.002
754	20	−0.0	0.01	0.0	>100	0.01	0.40	0.001	0.41	90	0.002
768	20	0.6	0.01	0.0	>100	0.01	0.50	0.001	0.72	40	0.0
865	20	−0.1	0.01	0.0	>100	0.01					
1020	20	−0.2	0.01	0.0	>100	0.01	−1.50	0.002	0.04	>100	0.002

TABLE 9 S3-OLCI matchup results (statistics for Gironde Estuary) (part 1/3).

		BAC					C2RCC				
W (nm)	N	slope	intercept	R^2	MAPE (%)	RMSE	slope	intercept	R^2	MAPE (%)	RMSE
400	15	0.83	−0.013	0.63	67	0.018	−0.49	0.033	0.01	64	0.024
412	15	0.47	−0.003	0.07	63	0.024	−0.19	0.028	0.00	58	0.025
443	15	0.80	−0.012	0.22	45	0.024	0.23	0.020	0.01	47	0.028
490	15	0.79	−0.006	0.45	29	0.021	0.50	0.016	0.08	30	0.027
510	15	0.72	0.004	0.51	22	0.020	0.51	0.022	0.14	25	0.025
560	15	0.67	0.020	0.63	14	0.019	0.62	0.022	0.36	21	0.028
620	15	0.85	0.001	0.83	18	0.021	0.73	0.009	0.72	21	0.028
665	15	0.86	0.000	0.83	20	0.020	0.62	0.009	0.73	29	0.035
673	15	0.85	0.000	0.83	21	0.020	0.58	0.009	0.72	32	0.038
681	15	0.85	0.001	0.83	21	0.020	0.59	0.009	0.73	31	0.037
708	15	0.84	0.002	0.84	23	0.019	0.69	0.008	0.80	22	0.026
753	15	0.66	0.006	0.77	17	0.015	0.57	0.006	0.76	25	0.018
778	15	0.70	0.003	0.73	18	0.010	0.62	0.007	0.76	22	0.017
865	15	0.72	0.002	0.75	16	0.008	0.51	0.002	0.72	35	0.014
885	15	0.51	0.005	0.34	>100	0.004	0.53	0.002	0.72	34	0.011
1020	15	0.53	0.004	0.16	>100	0.004	0.21	0.004	0.00	>100	0.008

TABLE 10 S3-OLCI matchup results (statistics for Gironde Estuary) (part 2/3).

		ACOLITE					ACOLITE_glint				
W (nm)	N	slope	intercept	R^2	MAPE (%)	RMSE	slope	intercept	R^2	MAPE (%)	RMSE
400	15	1.33	−0.008	0.77	24	0.010	1.41	−0.010	0.85	23	0.010
412	15	1.10	−0.003	0.74	18	0.009	1.17	−0.005	0.82	17	0.008
443	15	1.02	−0.001	0.80	11	0.008	1.09	−0.004	0.87	10	0.007
490	15	0.85	0.007	0.79	8	0.009	0.91	0.004	0.88	7	0.008
510	15	0.75	0.015	0.74	10	0.012	0.82	0.010	0.84	8	0.010
560	15	0.68	0.032	0.61	12	0.018	0.74	0.024	0.75	10	0.014
620	15	0.84	0.009	0.74	16	0.021	0.94	−0.001	0.83	14	0.017
665	15	0.86	0.004	0.79	16	0.020	0.98	−0.005	0.87	15	0.016
673	15	0.85	0.004	0.79	16	0.020	0.97	−0.005	0.87	15	0.016
681	15	0.86	0.004	0.79	17	0.020	0.98	−0.006	0.87	16	0.016
708	15	0.84	0.003	0.80	22	0.020	0.99	−0.007	0.91	21	0.014
753	15	0.74	0.007	0.75	41	0.014	0.95	0.002	0.90	43	0.008
778	15	0.73	0.006	0.75	37	0.014	0.94	0.001	0.90	38	0.008
865	15	0.76	0.003	0.66	32	0.012	0.88	0.002	0.83	31	0.006
885	15	0.83	0.001	0.68	41	0.011	0.87	0.001	0.81	40	0.006
1020	9	0.53	0.004	0.16	>100	0.004	0.31	0.004	0.05	95	0.004

10.3389/frsen.2023.1290110

TABLE 11 S3-OLCI matchup results (statistics for Gironde Estuary) (part 3/3).

		iCOR					Polymer				
W (nm)	N	slope	intercept	R^2	MAPE (%)	RMSE	slope	intercept	R^2	MAPE (%)	RMSE
400	15	0.89	0.019	0.03	68	0.027	−0.04	0.013	0.04	57	0.028
412	15	1.18	0.009	0.07	54	0.025	−0.04	0.016	0.10	55	0.030
443	15	1.04	0.007	0.11	34	0.023	−0.01	0.025	0.00	51	0.039
490	15	0.64	0.031	0.07	22	0.022	0.01	0.038	0.00	46	0.048
510	15	0.55	0.040	0.07	20	0.022	0.02	0.045	0.01	42	0.052
560	15	0.53	0.054	0.13	16	0.024	0.09	0.064	0.20	50	0.057
620	15	0.86	0.012	0.49	19	0.027	0.31	0.033	0.50	29	0.060
665	15	0.86	0.009	0.53	22	0.028	0.36	0.023	0.56	38	0.059
673	15	0.86	0.009	0.53	22	0.028					
681	15	0.86	0.009	0.53	23	0.028	0.38	0.022	0.58	37	0.057
708	15	0.83	0.008	0.56	27	0.028	0.38	0.013	0.62	45	0.058
753	15	0.66	0.013	0.32	56	0.025	0.25	0.009	0.54	42	0.040
778	15	0.68	0.013	0.34	54	0.025	0.26	0.009	0.54	41	0.040
865	15	0.62	0.012	0.17	98	0.023	0.17	0.006	0.42	44	0.032
885	15	0.59	0.014	0.13	>100	0.024					
1020	15	0.84	0.015	0.02	>100	0.024	−0.07	0.006	0.14	>100	0.014

TABLE 12 Aqua-MODIS matchup results (statistics for Gironde Estuary).

	NIR-SWIR					
W (nm)	N	slope	intercept	R^2	MAPE (%)	RMSE
412	11	−0.24	0	0.01	>100	0.03
443	11	−1.03	0.05	0.20	67	0.03
469	11	−0.80	0.06	0.16	54	0.03
488	11	−0.53	0.06	0.07	43	0.03
531	11	0.76	0	0.10	26	0.02
555	11	1.28	−0.05	0.44	32	0.03
645	11	1.22	−0.04	0.92	47	0.03
667	11	0.44	0	0.70	60	0.02
678	11	0.43	0	0.47	58	0.02
748	11	1.50	−0.01	0.51	>100	0.01
859	11	2.24	−0.01	0.41	>100	0.01

Distinguishing S2-MSI wavebands (Table 3), the performance of C2RCC is overall satisfactory and stable, except at short visible wavebands (<500 nm). The inverse is observed for GRS and Polymer with good performances for visible wavebands and worst results in the NIR spectral region. Rather surprisingly, Sen2Cor performance is higher at short visible wavebands (<600 nm), but systematically with a high overestimation. The performance of iCOR is spectrally-stable except for the specific 740 nm waveband. The best ACOLITE results are obtained at wavebands when field Rhow values are maximum (500–700 nm),

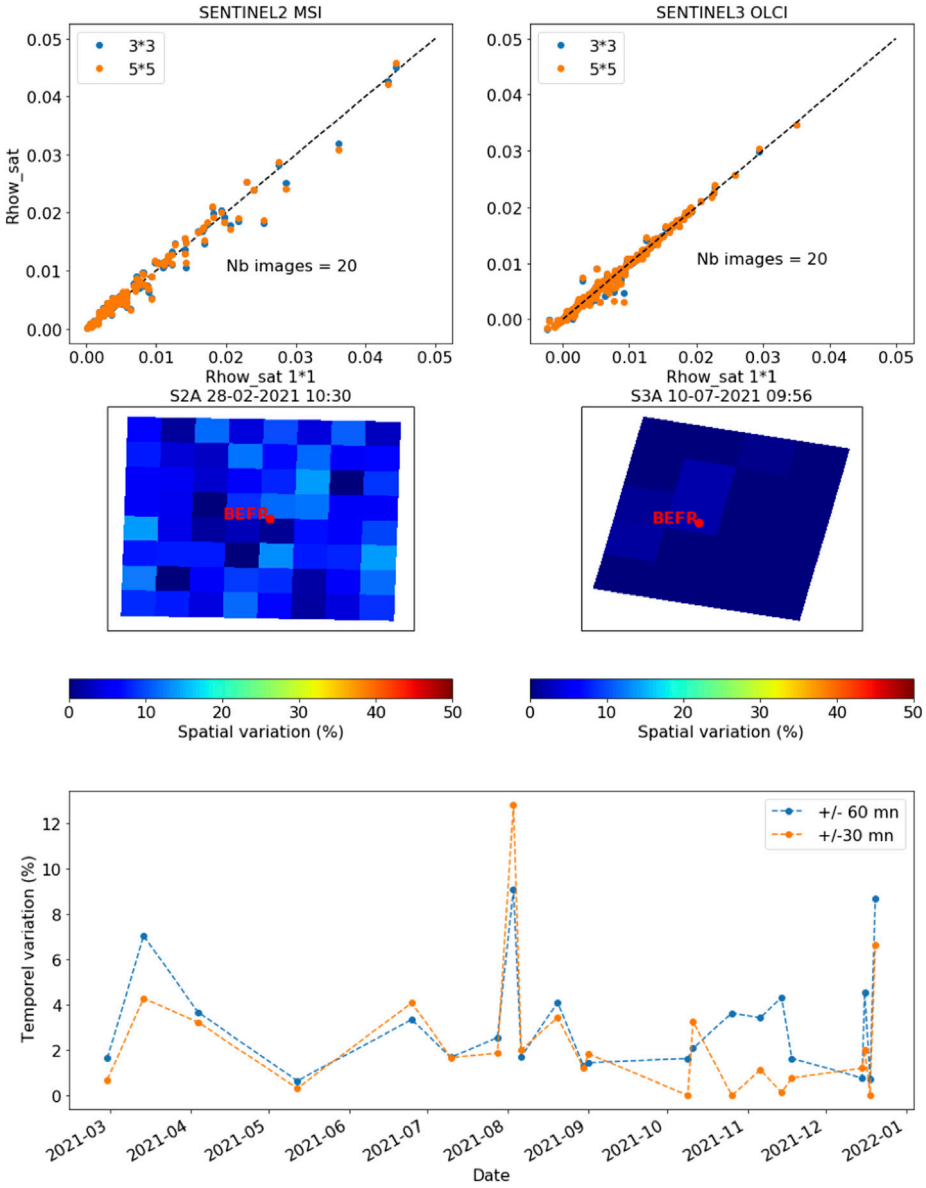


FIGURE 3
Observed spatial and temporal variations of the water-leaving reflectance (Rhow at 560 nm) at and around the Berre HYPERNETS station. Spatial variations are derived from S2-MSI (top left) and S3-OLCI (top right) satellite products respectively generated using the ACOLITE and BAC algorithms (20 images; the number of points correspond to the number of images multiplied by the number of each sensor spectral bands). Scatterplots of mean reflectance values within the 3 × 3 and 5 × 5 pixels centered on the HYPERNETS station *versus* the reflectance value of the single pixel containing the HYPERNETS station (top). Spatial variation of Rhow (560) in % around the station (center). Temporal variations (in %) observed on HYPERNETS -derived Rhow (560) (mean values within +/- 30 and 60 min) on selected dates from March 2021 to January 2022.

while activating the glint correction tends to provide slightly underestimated Rhow values.

Overall, all the tested processing algorithms (except Sen2Cor) provide rather satisfactory results in such complex waters (low water-leaving signal, glint and potentially adjacency effects). Their results are actually complementary with best performances obtained either at short visible, visible or NIR wavebands. A glint correction module on top of atmospheric corrections appears to be crucial when selecting a specific processor. The C2RCC algorithm provides the minimum differences with field-measured values.

3.2.2 Mouth of the Gironde Estuary

Based on 7 quality matchups with S2-MSI satellite data, one of the first striking result is the failure of the C2RCC and Polymer processors which both strongly underestimate Rhow values measured in the field (Figure 6). These two processing algorithms require to be trained using datasets representative of such waters (e.g., Knaeps et al., 2018). GRS performs significantly better but also provides underestimated reflectance values. The overall performances of ACOLITE (with or without glint correction) but also Sen2Cor is impressive; these two algorithms are simply well designed for highly turbid waters.

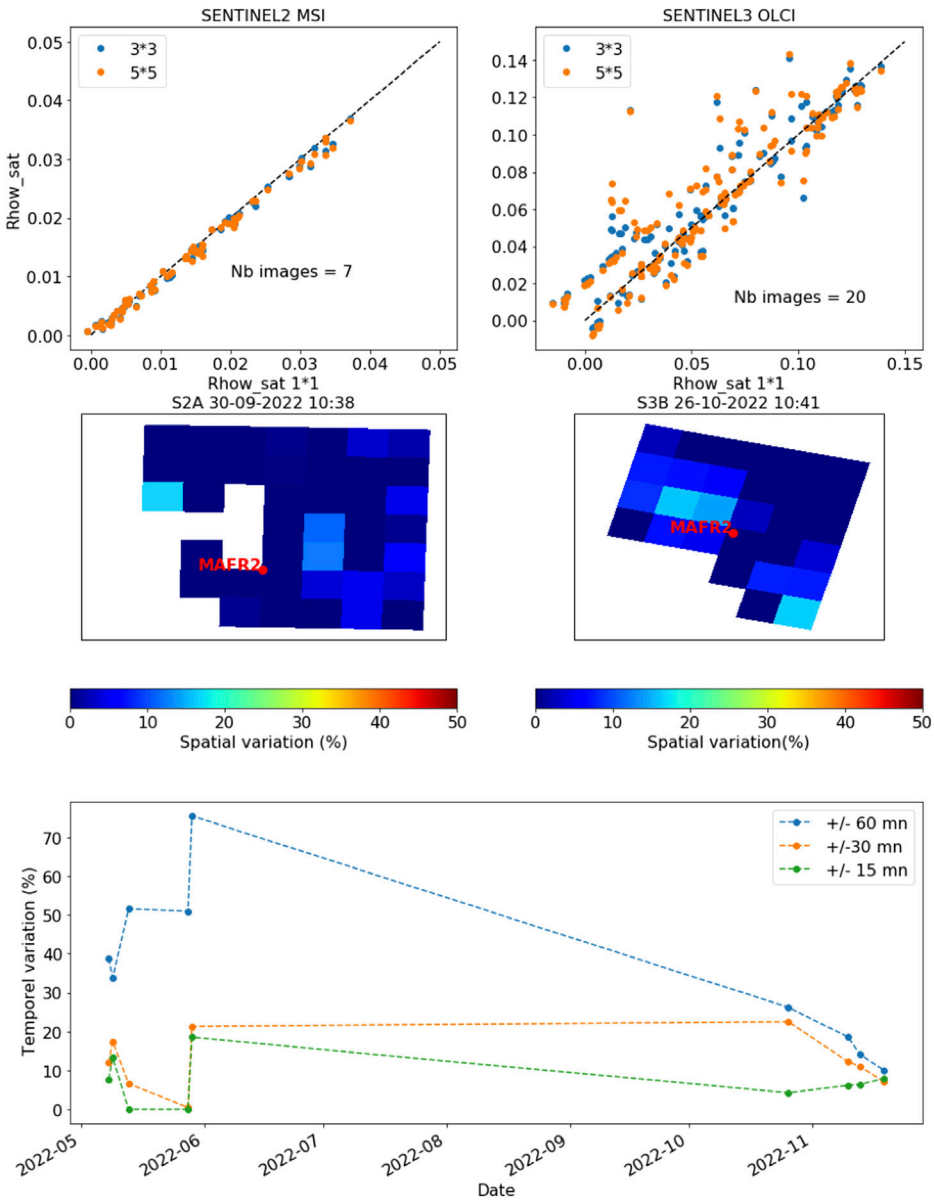


FIGURE 4
Observed spatial and temporal variations of the water-leaving reflectance (Rhow at 665 nm) at and around the Gironde HYPERNETS station. Spatial variations are derived from S2-MSI (top left) and S3-OLCI (top right) satellite products generated using the ACOLITE algorithm (7 and 20 images, respectively; the number of points correspond to the number of images multiplied by the number of each sensor spectral bands). Scatterplots of mean reflectance values within the 3 × 3 and 5 × 5 pixels centered on the HYPERNETS station *versus* the value right at the HYPERNETS station (top). Spatial variation of Rhow (560) in % around the station (center). Temporal variations (in %) observed on HYPERNETS -derived Rhow (665) (mean values within +/- 15, 30 and 60 min) on selected dates from May to November 2022.

When looking at wavebands separately, the C2RCC processor is clearly not adapted to highly turbid waters (Table 4), while the worst performance of GRS this time is observed at short visible wavelengths (<500 nm). It is also at these shortest wavebands that iCOR clearly fails and overestimates Rhow by a factor 2, while much better results are obtained at longer wavebands. This is actually the inverse for Polymer which provides better results in this specific spectral region. ACOLITE (especially with the glint correction activated) definitely generates the minimum differences between satellite and field Rhow values (<18%); the results obtained with Sen2Cor are not as good but still quite satisfactory.

Overall, the best results are obtained with processing algorithms which do not make assumptions on the water reflectance but rather rely on dark (land) targets to estimate the aerosol contribution on recorded satellite data.

3.3 L8&9-OLI matchup results

Only few (5) quality matchups between L8&9-OLI satellite products and HYPERNETS field data are available in both the Berre lagoon and Gironde Estuary to assess the performance of

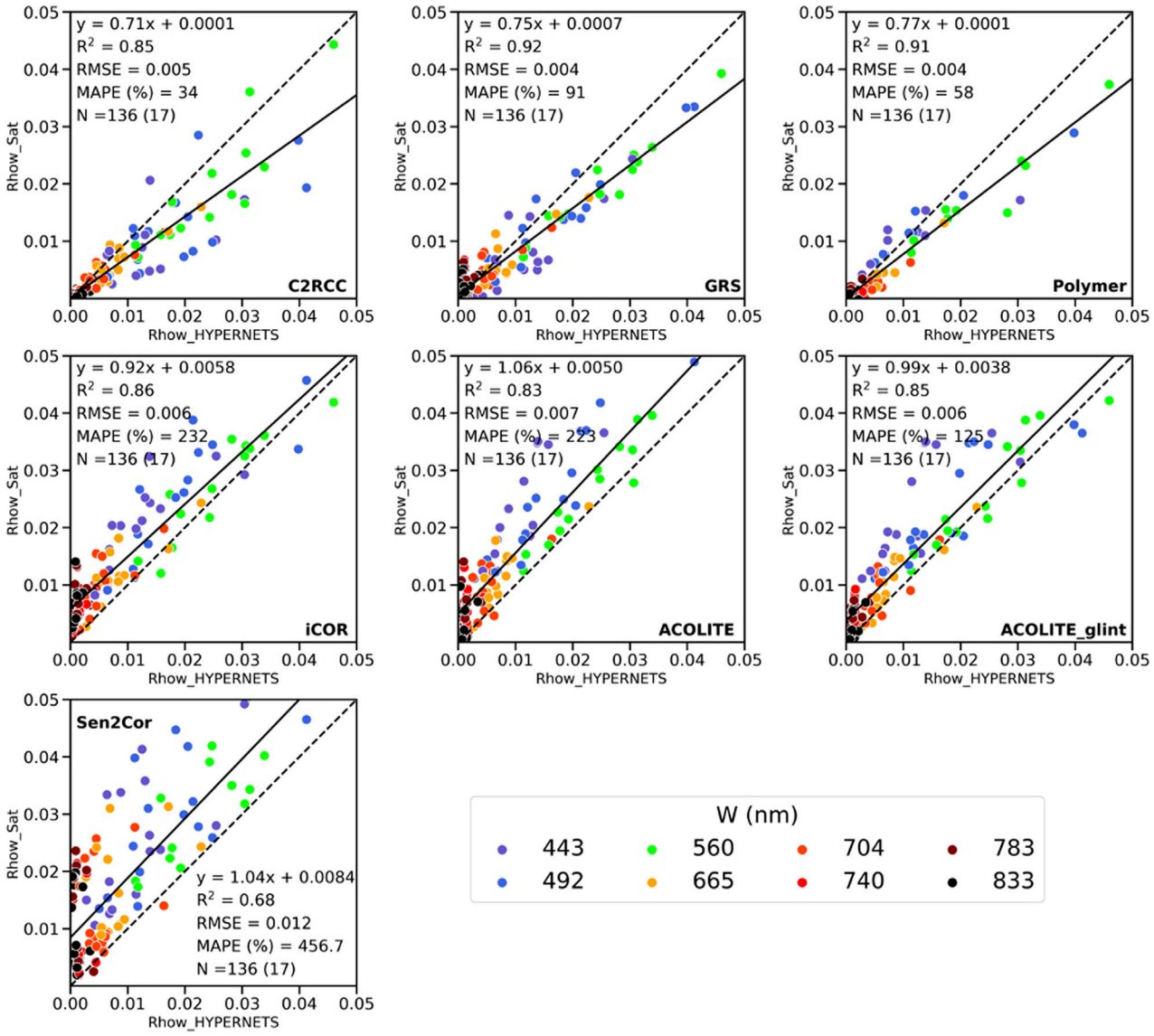


FIGURE 5
Matchup results (Berre coastal lagoon) obtained between Rhow derived from HYPERNETS field measurements (x-axis) and S2-MSI satellite-derived Rhow product (y-axis) when applying the different atmospheric correction algorithms tested in this study. Colors represent the satellite wavebands. For each scatterplot, statistics are presented as the best-fitted linear regression and associated determination coefficient, the RMSE and MAPE, the number of points (N) and processed satellite images (in brackets).

existing processing algorithms and estimate the uncertainties associated to the water reflectance products. These results, however, tend to confirm those obtained with S2-MSI, with quite satisfactory results obtained with C2RCC in Berre (Figure 7; Table 5) and with ACOLITE-GLINT in the Gironde (Figure 8; Figure 5B).

3.4 S3-OLCI matchup results

Comparatively to S2-MSI and L8&9-OLI, numerous matchups were available (20 and 15, respectively, in the Berre lagoon and Gironde Estuary) to assess the validity of S3-OLCI satellite products generated using different processing algorithms.

3.4.1 Berre coastal lagoon

In the Berre lagoon, the poor performance of the standard (BAC) processor is clearly highlighted as the results obtained are quite scattered and satellite-derived Rhow values underestimated by up to 39% (Figure 9; Tables 7–11). Poor results are also obtained with ACOLITE, even when activating the glint correction, with a very significant scatter and a strong overestimation of field-measured Rhow values. The two best performers for S3-OLCI data are clearly C2RCC and Polymer, in this order, with a slope of 1 and differences of 20% on average for C2RCC, while Polymer results show a higher determination factor (0.95) but a significant underestimation of high Rhow values. Clearly the best results are obtained with C2RCC while the Polymer processing should be improved for turbid waters.

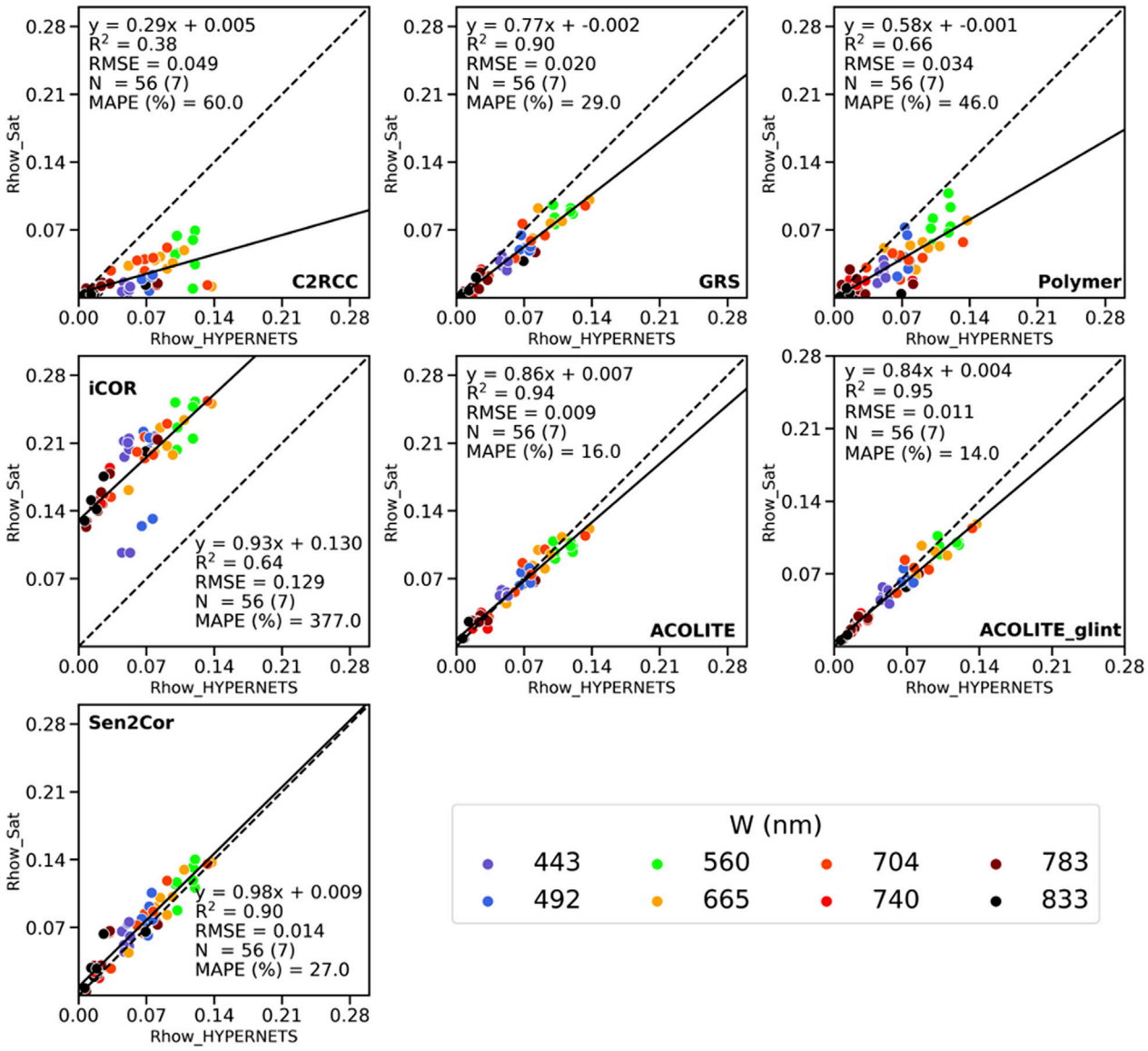


FIGURE 6
Matchup results (Gironde Estuary) obtained between Rhow derived from HYPERNETS field measurements (x-axis) and S2-MSI satellite-derived Rhow product (y-axis) when applying the different atmospheric correction algorithms tested in this study. Colors represent the satellite wavebands. For each scatterplot, statistics are presented as the best-fitted linear regression and associated determination coefficient, the RMSE and MAPE, the number of points (N) and processed satellite images (in brackets).

3.4.2 Mouth of the Gironde Estuary

Several processing algorithms provide satisfactory results in the moderately to highly turbid waters encountered at the mouth of the Gironde Estuary (Figure 10). First the standard (BAC) product is highly correlated to field measurements (R^2 = 0.89), but tends to underestimate field-measured Rhow values with overall differences of 35%. Results obtained with C2RCC are still reasonable but correspond to significantly underestimated (by 29%) satellite-derived Rhow values, especially in presence of highly turbid waters, and slightly higher differences (42%) overall. This is no longer the case when considering satellite-derived Rhow values generated using Polymer, with a significant underestimation of field values. This processor clearly reaches its limits for Rhow values higher than 0.02. Satisfactory results are obtained using iCOR over the whole range of Rhow values measured in the field, but with a significant scatter (R^2 = 0.65) and differences higher than 70%. Once again in the case of turbid waters, the best results are obtained using the ACOLITE processor, especially when activating the glint correction [slope close to 1, negligible intercept and high correlation (R^2 = 0.92)], with mean differences lower than 30% between satellite-derived and field measured Rhow values (Figure 10; Tables 7–11).

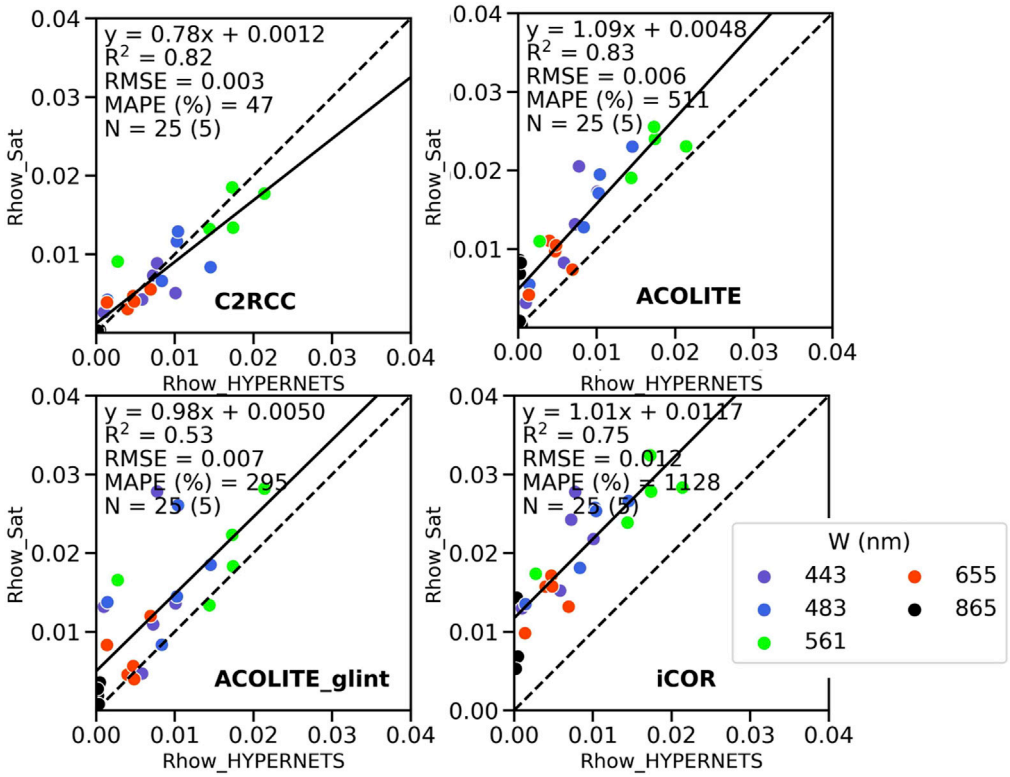


FIGURE 7
Matchup results (Berre coastal lagoon) obtained between Rhow derived from HYPERNETS field measurements (x-axis) and L8&9-OLI satellite-derived Rhow product (y-axis) when applying the different atmospheric correction algorithms tested in this study. Colors represent the satellite wavebands. For each scatterplot, statistics are presented as the best-fitted linear regression and associated determination coefficient, the RMSE and MAPE, the number of points (N) and processed satellite images (in brackets).

3.5 Aqua-MODIS matchup results

Doxaran et al. (2009) used the "surface reflectance" MODIS land product at full spatial resolution (250 m) to retrieve and map concentrations of suspended particulate matter (SPM) in the whole Gironde Estuary. Here, the more conventional NIR-SWIR atmospheric correction method was applied to estimate water reflectance values at the mouth of the estuary characterized by moderately to highly turbid waters. The SeaDAS l2gen function allowed retrieving Rhow values at 250 m spatial resolution at all MODIS visible to NIR wavebands, by interpolation, for comparisons with HYPERNETS Rhow field measurements.

Unfortunately, the use of the l2gen function is problematic in inland and nearshore turbid waters such as estuaries and bays as atmospheric corrections and application of land, cloud and other masks rely on wavebands at 1000 m resolution. Therefore, as expected, few MODIS products satisfy matchup criteria and only 11 images provide matchups with MAFR HYPERNETS data. Including all MODIS wavebands, the matchup results show a significant but not satisfactory linear correlation (R^2 = 0.62) between satellite-derived and field-measured Rhow values (Figure 11). The NIR-SWIR processing clearly tends to underestimate actual Rhow values, by about 30%. Results are inverse and satisfactory (slope of 1.2, negligible intercept and R^2 = 0.92) only at 645 nm, a band with a native spatial resolution of 250 nm and wavelengths sensitive to moderately to highly turbid waters (Table 12). Therefore, despite the potential of specific MODIS wavebands, accurately retrieving Rhow values in confined and turbid estuarine waters remains challenging using the ocean color l2gen function.

4 Discussion

4.1 The HYPERNETS system for nearshore waters

As part of the HYPERNETS project, a new network of autonomous field optical stations has been developed and is already in operation around the world for the validation of multi-sensor satellite products. It notably includes coastal and inland water sites such as estuaries, lagoons and reservoirs, i.e., optically complex water bodies where only few measurements are available in this scope (e.g., Pahlevan et al., 2021). These stations provide daily hyperspectral above-water radiance and irradiance measurements, recorded with a precise

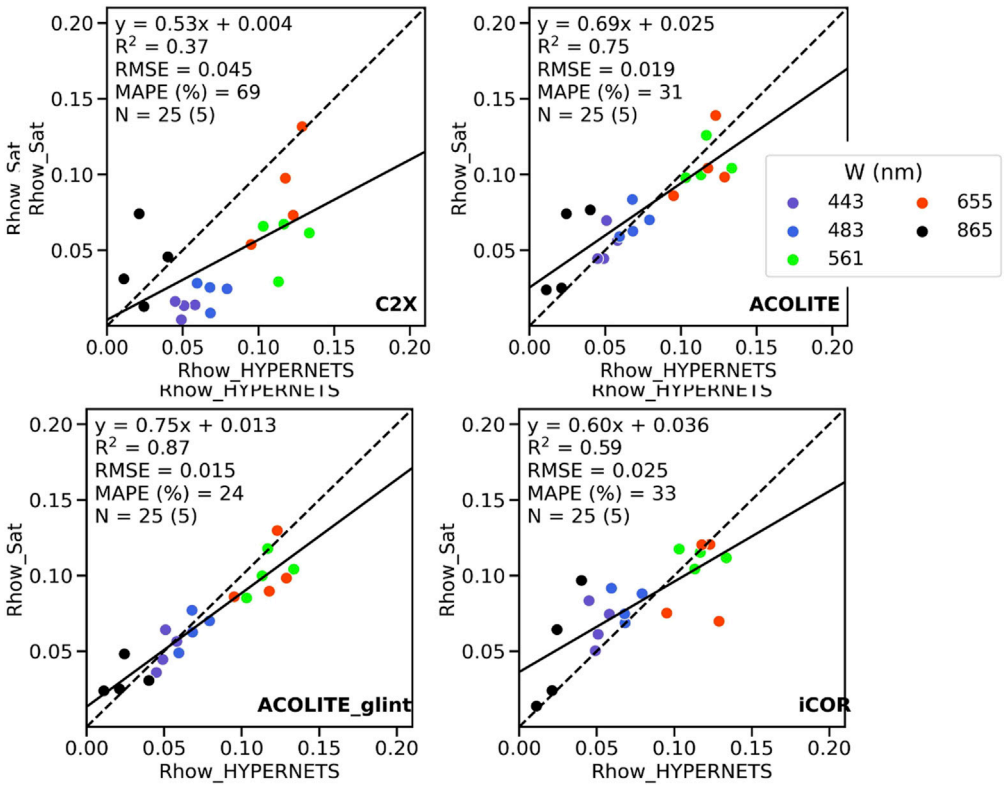


FIGURE 8
Matchup results (Gironde Estuary) obtained between Rhow derived from HYPERNETS field measurements (x-axis) and L8&9-OLI satellite-derived Rhow product (y-axis) when applying the different atmospheric correction algorithms tested in this study. Colors represent the satellite wavebands. For each scatterplot, statistics are presented as the best-fitted linear regression and associated determination coefficient, the RMSE and MAPE, the number of points (N) and processed satellite images (in brackets).

viewing geometry and used to accurately compute the water-leaving reflectance signal (Goyens et al., 2022). The autonomous system operating the HYPSTAR radiometer was already proved to be robust as successfully operated in wet and windy environments for more than 2 years over a wide range of air temperatures. This system guaranties accurate pointing geometries and provides useful information on environmental conditions (e.g., illumination, rainfall, humidity, air pressure, floating debris) to help operators optimizing their sampling strategy and anticipate technical problems.

The HYPERNETS network will certainly help characterizing the complex optical properties of nearshore coastal waters and confined inland waters (coastal lagoon, estuaries, rivers). These new field datasets will be of great benefit to complement existing ones such as AERONET-OC datasets (Zibordi et al., 2018; 2020), the SeaWiFS Bio-optical Archive and Storage System (SeaBASS), GLORIA (a globally representative hyperspectral *in situ* dataset for optical sensing of water quality) (Lehmann et al., 2023) or Lake Bio-optical Measurements and Matchup Data for Remote Sensing data (LIMNADES) (Pahlevan et al., 2021). The field datasets in generation will certainly enlarge our knowledge in terms of optical (and biogeochemical) properties of natural waters, extending the ranges of water dynamics and turbidity currently covered for the training of reflectance models used to develop inversion algorithms.

4.2 Performances and failures of atmospheric correction algorithms

The first aim of HYPERNETS stations operated in water sites is to validate atmospheric, sun glint and adjacency corrections applied to multi-sensor high and medium spatial resolution satellite data. Matchups between field and satellite data in dynamic and often turbid nearshore waters is challenging and matchup protocols previously defined for open ocean then coastal waters must be revised (Concha et al., 2021). In the present study, the analysis of field radiometric measurements and ocean color satellite data has highlighted the need to adapt to each site matchup protocols in contrasted environments such as estuaries and coastal lagoons. Strict quality controls are also required and applied to field radiometric measurements to remove any suspicious or contaminated data (Goyens et al., 2022).

Operating two HYPERNETS stations in France for less than 2 years has already provided numerous matchups with high (L8&9-OLI, S2-MSI) and medium (S3-OLCI, Aqua-MODIS) spatial resolution satellite data. These new matchup datasets will grow and rapidly complement recent attempts to validate the processing of radiometric satellite data in coastal and inland waters and assess the uncertainties associated to satellite-derived optical and biogeochemical properties (e.g., Novoa et al., 2017; Warren et al., 2019; Renosh et al., 2020; Pahlevan et al., 2021).

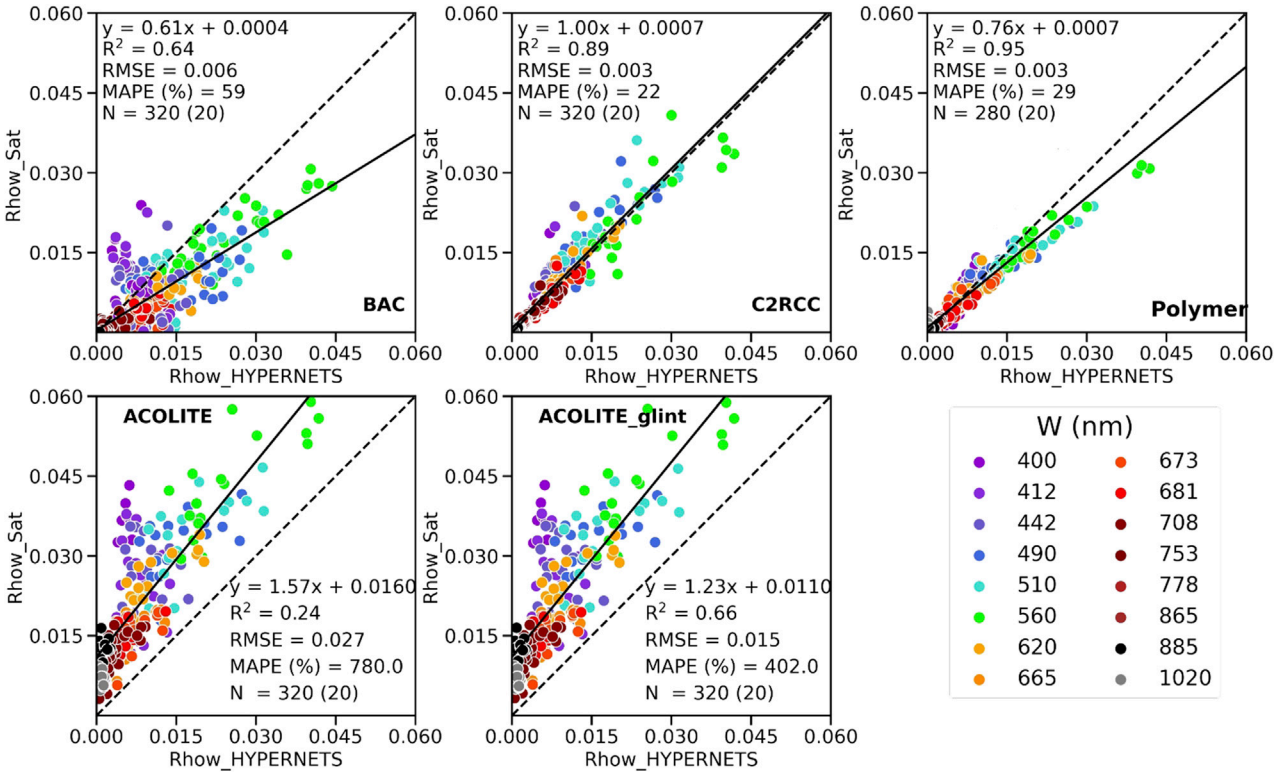


FIGURE 9
Matchup results (Berre coastal lagoon) obtained between Rhow derived from HYPERNETS field measurements (x-axis) and S3-OLCI satellite-derived Rhow product (y-axis) when applying the different atmospheric correction algorithms tested in this study. Colors represent the satellite wavebands. For each scatterplot, statistics are presented as the best-fitted linear regression and associated determination coefficient, the RMSE and MAPE, the number of points (N) and processed satellite images (in brackets).

The first results obtained using the two HYPERNETS stations operated in contrasted French coastal waters confirm that the water-leaving reflectance retrieved using most atmospheric correction processors is associated to significant (>20%) to critical (>60%) errors in nearshore waters (here a coastal lagoon and the mouth of an estuary), as already pointed out by previous studies (e.g., De Keukelaere et al., 2018; Ilori et al., 2019; Warren et al., 2019). These errors typically increase from green and/or red wavebands where the Rhow signal is usually maximum towards the blue and NIR spectral regions; several atmospheric correction algorithms, in their current version, simply generate unreliable results (Warren et al., 2019). There is no processor outperforming others, i.e., providing satisfactory results over the wide diversity of coastal and nearshore waters (Pereira-Sandoval et al., 2019), so that a prior optical water type classification is recommended for selecting the most appropriate atmospheric correction processor (e.g., Soomets et al., 2020; Pahlevan et al., 2021). In moderately turbid coastal lagoon waters, our results show that C2RCC and Polymer provide satisfactory results (errors respectively lower than 30% in visible wavebands and lower than 40% from 443 to 800 nm), as already reported by Pereira-Sandoval et al. (2019) for inland waters where glint and adjacency corrections of satellite data may be as important as atmospheric corrections. Now our study actually shows that the current versions of these two processors reach their limits in turbid to highly turbid waters (with errors higher than 40% at all wavebands). The failure most probably comes from the water reflectance models used in these processors, i.e., models which do not yet account for the large variations of Rhow in the NIR part of the spectrum (Knaeps et al., 2018). The HYPERNETS network will provide new validation datasets to complement the lack of matchups between field and satellite data in highly turbid waters (Knaeps et al., 21018; Goyens et al., 2022), but also contribute to tune then adopt adapted water reflectance models (e.g., Lee et al., 2016; Luo et al., 2018) in atmospheric correction processors. In such waters, our results clearly highlight the very satisfactory performances of ACOLITE (with errors lower than 20% over the visible to NIR parts of the spectrum, when the glint correction is applied) but also Sen2Cor (errors lower than 30% in visible wavebands), i.e., processors which do not make (potentially erroneous) assumptions on the water-leaving reflectance signal to be retrieved from the signal recorded at the top of the atmosphere. Similar results were obtained by Vanhellemont and Ruddick (2021) in moderately turbid coastal waters.

Our results therefore complement previous studies quantifying atmospheric correction errors and understanding the implication on downstream data, such as the concentrations of algal and non-algal particles, water turbidity (and transparency) and light absorption by colored dissolved organic matter (CDOM) (e.g., Ansper and Alikas, 2019; Pahlevan et al., 2021). In turbid estuarine waters, several processors certainly provide satisfactory results in order to accurately estimate the water turbidity and SPM concentration, but also Chla concentrations using a NIR to red edge algorithm (Gernez et al., 2017). In moderately turbid lagoon waters, a

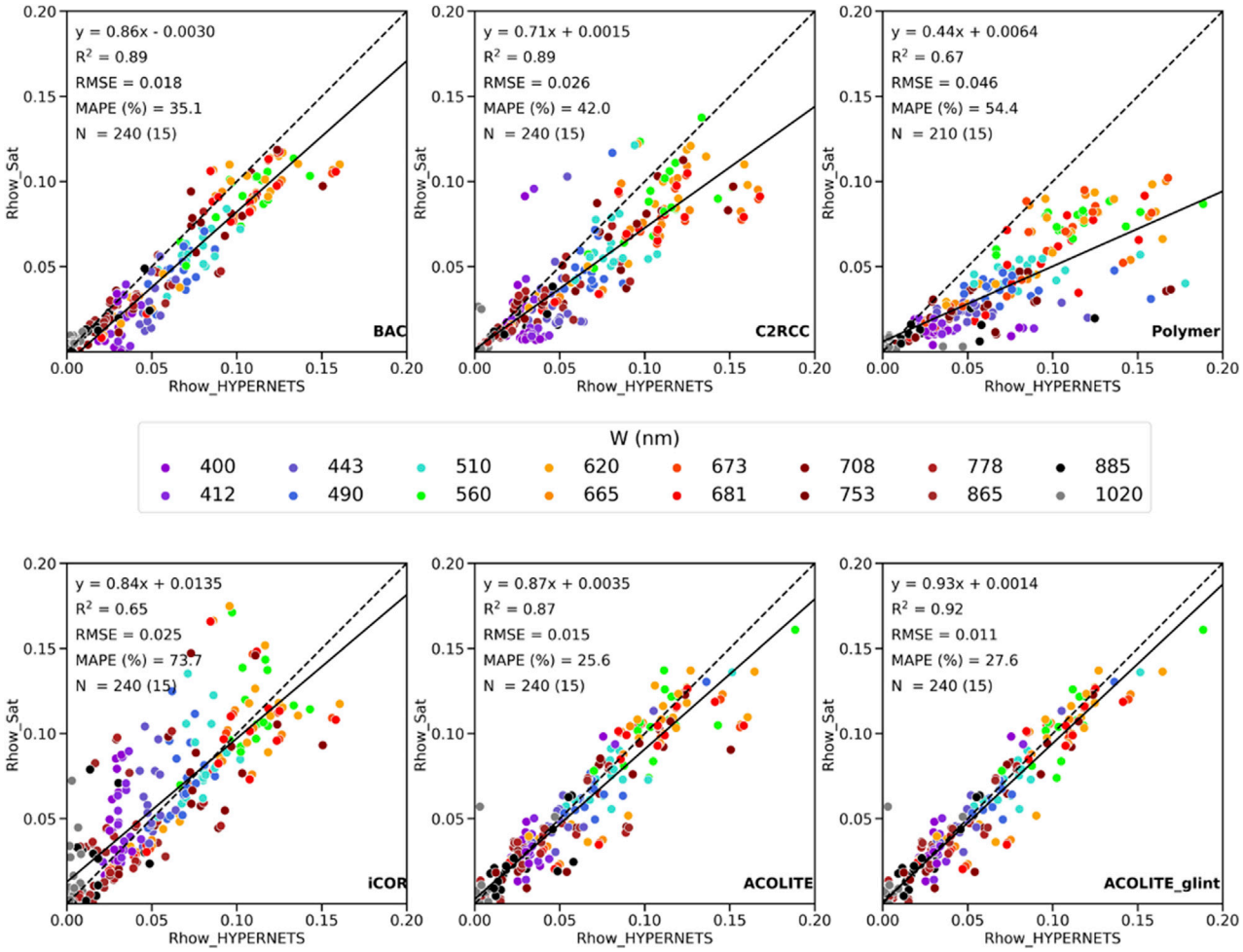


FIGURE 10
Matchup results (Gironde Estuary) obtained between Rhow derived from HYPERNETS field measurements (x-axis) and S3-OLCI satellite-derived Rhow product (y-axis) when applying the different atmospheric correction algorithms tested in this study. Colors represent the satellite wavebands. For each scatterplot, statistics are presented as the best-fitted linear regression and associated determination coefficient, the RMSE and MAPE, the number of points (N) and processed satellite images (in brackets).

processor such as C2RCC (neural networks) is expected to provide satisfactory results to estimate SPM concentrations (using Rhow in the green or red waveband) but also Chla concentrations using a blue-to-green ratio (Erena et al., 2019; Jiménez-Quiroz et al., 2021) or preferably using a NIR-red ratio algorithm where waters are more turbid and/or more productive (Tavares et al., 2021; Zhan et al., 2022). The retrieval of CDOM optical properties is certainly more challenging, as all atmospheric correction processors are associated to significant errors at short visible wavelengths (<450 nm).

5 Conclusion

This study shows the great potential of hyperspectral radiometric measurements recorded on nearshore water sites when operated by autonomous pointing and recording systems. While the new HYPSTAR sensor allows a fine characterization of the spectral signatures in the visible and NIR, the accuracy of the pointing system guaranties the quality of the radiometric measurements for the computation of the water-leaving reflectance signal (after applying several steps of strict quality controls on recorded data). The system specifically designed as part of the HYPERNETS project also provides to users a high flexibility in order to adapt the sampling strategy to changing environmental conditions. HYPERNETS stations are already operated as part of an international network that will generate optical datasets needed to extend existing ocean color algorithms to nearshore and inland waters (e.g., estuaries, rivers, coastal lagoons, lakes).

Based on data recorded by two stations operated over the last 2 years in contrasted French waters, concluding results were already obtained concerning the first objective of HYPERNETS field measurements: the validation of atmospheric corrections applied to satellite data. These stations provide numerous quality matchups with data recorded aboard any satellite or airborne platform that will help better understanding atmospheric but also sun glint and adjacency effects on remote sensing data. In turbid estuarine waters, our results

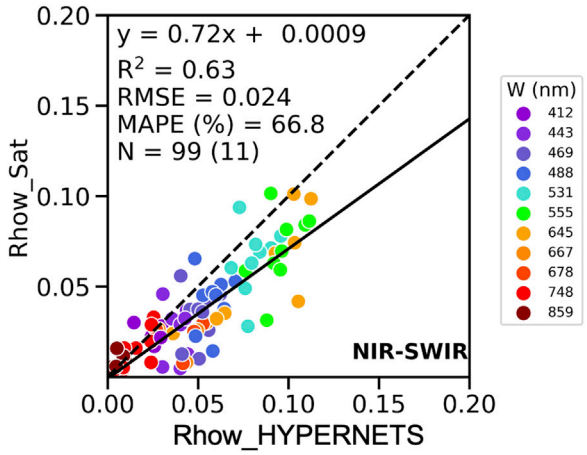


FIGURE 11
Matchup results (Gironde Estuary) obtained between Rhow derived from HYPERNETS field measurements (x-axis) and AQUA-MODIS satellite-derived Rhow product (y-axis) when applying the NIR-SWIR atmospheric correction algorithm. Colors represent the satellite wavebands. Statistics are presented as the best-fitted linear regression and associated determination coefficient, the RMSE and MAPE, the number of points (N) and processed satellite images (in brackets).

showed that the use of dark targets on each satellite image processed to estimate the aerosol contribution provides an accurate retrieval of the water-leaving reflectance signal (errors lower than 30% from short visible to NIR wavelengths). Other atmospheric processors (e.g., NN) still require improvements in such highly scattering waters by updating the reflectance model used, i.e., the assumptions made on the water-leaving reflectance signal. In less turbid coastal lagoon waters, by opposition, corrections of sun glint effects can be as important as atmospheric corrections. In all cases, adjacency effects are certainly significant, highly wavelength-dependent and should not be ignored. Our first and future results obtained using HYPERNETS field measurements are expected to be useful in order to improve existing processing algorithms, then validate satellite products to be used for the operational monitoring of coastal, nearshore and inland waters.

Data availability statement

Parts of the HYPERNETS data from the Berre (BEFR site) and Gironde (MAFR site) stations are available and can be accessed here: https://zenodo.org/records/8057777 (BEFR), https://zenodo.org/records/8057789 (MAFR).

Author contributions

DD: Methodology, Supervision, Writing–original draft. BE: Data curation, Investigation, Validation, Writing–review and editing. AC: Conceptualization, Software, Visualization, Writing–review and editing. CG: Data curation, Investigation, Software, Validation, Writing–review and editing.

Funding

The author(s) declare financial support was received for the research, authorship, and/or publication of this article. HYPSTAR deployments and maintenance, data processing and analysis were funded by the H2020 Project HYPERNETS (grant number: 775983). Field campaigns and data processing were co-funded by CNES through the TOSCA program (HYPERVAL project).

Acknowledgments

The authors address special thanks to local collaborators in the Berre lagoon (GIPREB) and Gironde Estuary (Port de Bordeaux) who allowed the deployment and maintenance of the HYPERNETS stations.

Conflict of interest

The authors declare that the research was conducted in the absence of any commercial or financial relationships that could be construed as a potential conflict of interest.

Publisher's note

All claims expressed in this article are solely those of the authors and do not necessarily represent those of their affiliated organizations, or those of the publisher, the editors and the reviewers. Any product that may be evaluated in this article, or claim that may be made by its manufacturer, is not guaranteed or endorsed by the publisher.

References

Concha, J., Bracaglia, M., and Brando, V. (2021). Assessing the influence of different validation protocols on Ocean Colour match-up analyses. *Remote Sens. Environ.* 259, 112415. doi:10.1016/j.rse.2021.112415

De Keukelaere, L., Sterckx, S., Adriaensen, S., Knaeps, E., Reusen, I., Giardino, C., et al. (2018). Atmospheric correction of Landsat-8/OLI and Sentinel-2/MSI data using iCOR algorithm: validation for coastal and inland waters. *Eur. J. Remote Sens.* 51, 525–542. doi:10.1080/22797254.2018.1457937

Doron, M., Bélanger, S., Doxaran, D., and Babin, B. (2011). Spectral variations in the near-infrared ocean reflectance. *Remote Sens. Environ.* 115, 1617–1631. doi:10.1016/j.rse.2011.01.015

Doxaran, D., Froidefond, J. M., Castaing, P., and Babin, M. (2009). Dynamics of the turbidity maximum zone in a macrotidal estuary (the Gironde, France): observations from field and MODIS satellite data. *Estuar. Coast. Shelf Sci.* 81, 321–332. doi:10.1016/j.ecss.2008.11.013

Erena, M., Domínguez, J. A., Aguado-giménez, F., Soria, J., and García-Galiano, S. (2019). Monitoring coastal lagoon water quality through remote sensing: the mar menor as a case study. *Water* 11 (7), 1468. doi:10.3390/w11071468

Gernez, P., Barillé, L., Lerouxel, A., Mazeran, C., Lucas, A., and Doxaran, D. (2014). Remote sensing of suspended particulate matter in turbid oyster-farming ecosystems. *J. Geophys. Res. - Oceans* 119, 7277–7294. doi:10.1002/2014JC010055

Gernez, P., Doxaran, D., and Barillé, L. (2017). Shellfish aquaculture from Space: potential of Sentinel2 to monitor tide-driven changes in turbidity, chlorophyll concentration and oyster physiological response at the scale of an oyster farm. *Front. Mar. Sci.* 4. doi:10.3389/fmars.2017.00137

Gernez, P., Zoffoli, M. L., Lacour, T., Hernandez Farinas, T., Navarro, G., Caballero, I., et al. (2023). The many shades of red tides: sentinel-2 optical types of highly-concentrated harmful algal blooms. *Remote Sens. Environ.* 287, 113486. doi:10.1016/j.rse.2023.113486

Goyens, C., Lavigne, H., Dille, A., and Vervaeren, H. (2022). Using hyperspectral remote sensing to monitor water quality in drinking water reservoirs. *Remote Sens.* 14, 5607. doi:10.3390/rs14215607

Harmel, T., Chami, M., Tormos, T., Reynaud, N., and Danis, P.-A. (2018). Sunglint correction of the multi-spectral instrument (MSI)-SENTINEL-2 imagery over inland and sea waters from SWIR bands. *Remote Sens. Environ.* 204, 308–321. doi:10.1016/j.rse.2017.10.022

Ilori, C. O., Pahlevan, N., and Knudby, A. (2019). Analyzing performances of different atmospheric correction techniques for Landsat 8: application for coastal remote sensing. *Remote Sens.* 11, 469. doi:10.3390/rs11040469

Jalón-Rojas, I., Dijkstra, Y. M., Schuttelaars, H. M., Brouwer, R. L., Schmidt, S., and Sottolichio, A. (2021). Multidecadal evolution of the turbidity maximum zone in a macrotidal river under climate and anthropogenic pressures. *J. Geophys. Res. Oceans* 126, e2020JC016273. doi:10.1029/2020JC016273

Jiménez-Quiroz, M. C., Martell-Dubois, R., Cervantes-Duarte, R., and Cerdeira-Estrada, S. (2021). Seasonal pattern of the chlorophyll-a in a coastal lagoon from the southern Baja California (Mexico), described with *in situ* observations and MODIS-Aqua imagery. *Oceanologia* 63, 329–342. doi:10.1016/j.oceano.2021.03.003

Kabir, S., Pahlevan, N., O'Shea, R. E., and Barnes, B. B. (2023). Leveraging Landsat-8/-9 underfly observations to evaluate consistency in reflectance products over aquatic environments. *Remote Sens. Environ.*, 296. doi:10.1016/j.rse.2023.113755

Katlane, R., Dupouy, C., El Kilani, B., and Berges, J.-C. (2020). Estimation of chlorophyll and turbidity using sentinel 2A and EO1 data in Kneiss Archipelago Gulf of Gabes, Tunisia. *Int. J. Geosciences* 11, 708–728. doi:10.4236/ijg.2020.1110035

Knaeps, E., Doxaran, D., Dogliotti, A. I., Nechad, B., Ruddick, K. G., Raymaekers, D., et al. (2018). The SeaSWIR dataset. *Earth Syst. Sci. Data* 10, 1439–1449. doi:10.5194/essd-10-1439-2018

Lee, Z., Shang, S., Lin, G., Chen, J., and Doxaran, D. (2016). On the modeling of hyperspectral remote-sensing reflectance of high-sediment-load waters in the visible to shortwave-infrared domain. *Appl. Opt.* 55, 1738–1750. doi:10.1364/ao.55.001738

Lehmann, M. K., Gurlin, D., Pahlevan, N., Alikas, K., Conroy, T., Anstee, J., et al. (2023). GLORIA - a globally representative hyperspectral *in situ* dataset for optical sensing of water quality. *Sci. Data* 10, 100. doi:10.1038/s41597-023-01973-y

Luo, L., Doxaran, D., and Vanhellemont, Q. (2020). Retrieval and validation of water turbidity at metre-scale using Pléiades satellite data: a case study in the Gironde estuary. *Remote Sens.* 12, 946. doi:10.3390/rs12060946

Luo, Y., Doxaran, D., Ruddick, K. G., Shen, F., Gentili, B., Yan, L., et al. (2018). Saturation of water reflectance in extremely turbid media based on field measurements, satellite data and bio-optical modelling. *Opt. Express* 26 (8), 10435. doi:10.1364/OE.26.010435

Main-Knorn, M., Pflug, B., Louis, J., Debaecker, V., Müller-Wilm, U., and Gascon, F. (2017). "Sen2Cor for sentinel-2," in *SPIE remote sensing* (Bellingham, WA, USA: SPIE), 12.

Mayer, B., and Kylling, A. (2005). Technical note: the libRadtran software package for radiative transfer calculations - description and examples of use. *Atmos. Chem. Phys.* 5, 1855–1877. doi:10.5194/acp-5-1855-2005

Mobley, C. D. (1999). Estimation of the remote-sensing reflectance from above-surface measurements. *Appl. Opt.* 38, 7442. doi:10.1364/ao.38.007442

Moore, G., Mazeran, C., and Huot, J. P. (2017). MERIS ATBD 2.6 case II bright pixel atmospheric correction (BPAC). *Eur. Space Agency* 5, 3.

Novoa, S., Doxaran, D., Ody, A., Vanhellemont, Q., Lafon, V., Lubac, B., et al. (2017). Atmospheric corrections and multi-conditional algorithm for multi-sensor remote sensing of suspended particulate matter in low-to-high turbidity levels coastal waters. *Remote Sens.* 9, 61. doi:10.3390/rs9010061

Ody, A., Doxaran, D., Vanhellemont, Q., Nehad, B., Novoa, S., Many, G., et al. (2016). Potential of high spatial and temporal ocean color satellite data to study the dynamics of suspended particles in a micro-tidal river plume. *Remote Sens.* 8 (3), 245. doi:10.3390/rs8030245

Ody, A., Doxaran, D., Verney, R., Bourrin, F., Morin, G. P., Pairaud, I., et al. (2022). Ocean color remote sensing of suspended sediments along a continuum from rivers to river plumes: concentration, transport, fluxes and dynamics. *Remote Sens.* 14, 2026. doi:10.3390/rs14092026

Pahlevan, N., Mangin, A., Balasubramanian, S. V., Smith, B., Alikas, K., Arai, K., et al. (2021). ACIX-Aqua: a global assessment of atmospheric correction methods for Landsat-8 and Sentinel-2 over lakes, rivers, and coastal waters. *Remote Sens. Environ.* 258, 112366. doi:10.1016/j.rse.2021.112366

Pahlevan, N., Sarkar, S., Franz, B. A., Balasubramanian, S. V., and He, J. (2017a). Sentinel-2 MultiSpectral instrument (MSI) data processing for aquatic science applications: demonstrations and validations. *Remote Sens. Environ.* 201, 47–56. doi:10.1016/j.rse.2017.08.033

Pahlevan, N., Schott, J. R., Franz, B. A., Zibordi, G., Markham, B., Bailey, S., et al. (2017b). Landsat 8 remote sensing reflectance (R rs) products: evaluations, intercomparisons, and enhancements. *Remote Sens. Environ.* 190, 289–301. doi:10.1016/j.rse.2016.12.030

Pellegrino, A., Fabbretto, A., Bresciani, M., Lima, T., Braga, F., Pahlevan, N., et al. (2023). Assessing the accuracy of PRISMA standard reflectance products in globally distributed aquatic sites. *Remote Sens.* 15, 2163. doi:10.3390/rs15082163

Pereira-Sandoval, M., Ruescas, A., Urrego, P., Ruiz-Verdú, A., Delegido, J., Tenjo, C., et al. (2019). Evaluation of atmospheric correction algorithms over Spanish inland waters for sentinel-2 multi spectral imagery data. *Remote Sens.* 11, 1469. doi:10.3390/rs11121469

Renosh, P. R., Doxaran, D., De Keukelaere, L. 2, and Gossn, J. I. (2020). Evaluation of atmospheric correction algorithms for sentinel-2-MSI and sentinel-3-OLCI in highly turbid estuarine waters. *Remote Sens.* 12, 1285. doi:10.3390/rs12081285

Ruddick, K., De Cauwer, V., and Van Mol, B. (2005). "Use of the near infrared similarity reflectance spectrum for the quality control of remote sensing data," in *Remote sensing of the coastal oceanic environment*. Editors R. J. Frouin, M. Babin, and S. Sathyendranath (Bellingham, WA, USA: SPIE).588501

Ruddick, K. G., De Cauwer, V., Park, Y. J., and Moore, G. (2006). Seaborne measurements of near infrared water-leaving reflectance: the similarity spectrum for turbid waters. *Limnol. Oceanogr.* 51, 1167–1179. doi:10.4319/lo.2006.51.2.1167

Soomets, T., Uudeberg, K., Jakovels, D., Brauns, A., Zagars, M., and Kutser, T. (2020). Validation and comparison of water quality products in Baltic Lakes using Sentinel-2 MSI and Sentinel-3 OLCI data. *Sensors* 20, 742. doi:10.3390/s20030742

Sterckx, S., Knaeps, S., Kratzer, S., and Ruddick, K. (2015). SIMilarity Environment Correction (SIMEC) applied to MERIS data over inland and coastal waters. *Remote Sens. Environ.* 157, 96–110. doi:10.1016/j.rse.2014.06.017

Tavares, M. H., Lins, R. C., Harmel, T., Fragoso, C. R., Jr., Martínez, J. M., and Motta-Marques, (2021). Atmospheric and sunglint correction for retrieving chlorophyll-a in a productive tropical estuarine-lagoon system using Sentinel-2 MSI imagery. *ISPRS J. Photogrammetry Remote Sens.* 174, 215–236. doi:10.1016/j.isprsjprs.2021.01.021

Vanhellemont, Q., and Ruddick, K. (2018). Atmospheric correction of metre-scale optical satellite data for inland and coastal water applications. *Remote Sens. Environ.* 216, 586–597. doi:10.1016/j.rse.2018.07.015

Vanhellemont, Q., and Ruddick, K. (2021). Atmospheric correction of Sentinel-3/OLCI data for mapping of suspended particulate matter and chlorophyll-a concentration in Belgian turbid coastal waters. *Remote Sens. Environ.* 256, 112284. doi:10.1016/j.rse.2021.112284

Wang, M., and Shi, W. (2007). The NIR-SWIR combined atmospheric correction approach for MODIS ocean color data processing. *Opt. Express* 15, 15722–15733. doi:10.1364/oe.15.015722

Warren, M., Simis, S., Martinez-Vicente, V., Poser, K., Bresciani, M., Alikas, K., et al. (2019). Assessment of atmospheric correction algorithms for the Sentinel-2A MultiSpectral Imager over coastal and inland waters. *Remote Sens. Environ.* 225, 267–289. doi:10.1016/j.rse.2019.03.018

Zhan, Y., Delegido, J., Erena, M., Soria, J., Ruiz-Verdu, A., Urrego, P., et al. (2022)). Menor lagoon (SE Spain) chlorophyll-a and turbidity estimation with Sentinel-2. *Limnetica* 41, 253. doi:10.23818/limn.41.18

Zibordi, G., Holben, B. N., Talone, M., D'Alimonte, D., Slutsker, I., Giles, D. M., et al. (2020). Advances in the ocean color component of the aerosol robotic network (AERONET-OC). *J. Atmos. Ocean. Technol.* 38, 725–746. doi:10.1175/JTECH-D-20-0085.1

Zibordi, G., Mélin, F., Berthon, J. F., Holben, B., Slutsker, I., Giles, D., et al. (2009). AERONET-OC: a network for the validation of ocean color primary products. *J. Atmos. Ocean. Technol.* 26, 1634–1651. doi:10.1175/2009jtecho654.1

frontiers | Frontiers in Remote Sensing

TYPE Original Research
PUBLISHED 12 February 2024
DOI 10.3389/frsen.2024.1305787

Check for updates

OPEN ACCESS

EDITED BY
Vittorio Ernesto Brando,
National Research Council (CNR), Italy

REVIEWED BY
Tristan Harmel,
Earth Observation Unit, France
Anna Windle,
Goddard Space Flight Center, United States

*CORRESPONDENCE
Maximiliano Arena,
marena@iado-conicet.gob.ar

RECEIVED 02 October 2023
ACCEPTED 30 January 2024
PUBLISHED 12 February 2024

CITATION
Arena M, Pratolongo P, Loisel H, Tran MD, Jorge DSF and Delgado AL (2024), Optical water characterization and atmospheric correction assessment of estuarine and coastal waters around the AERONET-OC Bahia Blanca. *Front. Remote Sens.* 5:1305787. doi: 10.3389/frsen.2024.1305787

COPYRIGHT
© 2024 Arena, Pratolongo, Loisel, Tran, Jorge and Delgado. This is an open-access article distributed under the terms of the Creative Commons Attribution License (CC BY). The use, distribution or reproduction in other forums is permitted, provided the original author(s) and the copyright owner(s) are credited and that the original publication in this journal is cited, in accordance with accepted academic practice. No use, distribution or reproduction is permitted which does not comply with these terms.

Optical water characterization and atmospheric correction assessment of estuarine and coastal waters around the AERONET-OC Bahia Blanca

Maximiliano Arena[1,2]*, Paula Pratolongo[3,2], Hubert Loisel[4], Manh Duy Tran[4], Daniel Schaffer Ferreira Jorge[4] and Ana Laura Delgado[1,5]

[1]Instituto Argentino de Oceanografía (IADO-CONICET-UNS), Bahía Blanca, Argentina, [2]Departamento de Biología Bioquímica y Farmacia, Universidad Nacional del Sur (UNS), Bahía Blanca, Argentina, [3]Centro de Recursos Renovables de la Zona Semiárida (CERZOS-CONICET-UNS), Bahía Blanca, Argentina, [4]Laboratoire d'Océanologie et de Géosciences, Université du Littoral-Côte-d'Opale, Université Lille, CNRS, IRD, UMR, LOG, Wimereux, France, [5]Institut Mediterrani d'Estudis Avançats (IMEDEA-CSIC-UIB), Esporles, Spain

The site AERONET-OC Bahía Blanca (BB-AERONET-OC) is located at the mouth of the Bahía Blanca Estuary, Argentina (Southwestern Atlantic Ocean), a coastal system defined by its high suspended loads and relatively low colored dissolved organic matter. The typically high turbidity of these waters makes the BB-AERONET-OC distinctive within the AERONET-OC network stations, providing exceptional opportunities not only for the validation of atmospheric correction algorithms but also for the development of regional algorithms for coastal complex waters. A SeaWiFS Photometer Revision for Incident Surface Measurements (SeaPRISM) instrument was deployed in January 2020 in the upper rail of a Mareograph Tower, a 15 m tall structure, located 10 miles away from the coast in optically deep waters. In this work we used the remote sensing reflectance (R_{rs}) derived from the BB-AERONET-OC measurements along with *in situ* hyperspectral radiometric data to classify optical water types (OWTs). We assigned each $R_{rs}(\lambda)$ spectra to one of the five OWTs defined by Tran et al., and OWTs were further characterized with the concentrations of optically significant components (chlorophyll-a and suspended particulate matter) and inherent optical properties (absorptions of phytoplankton, non-algal particles, and dissolved organic matter), retrieved from water samples obtained simultaneously with radiometric spectra. Based on a match-up exercise with *in situ* data, different schemes of atmospheric correction methods were applied to Sentinel-3 Ocean and Land Colour Instrument (OLCI) images. The operational product OLCI Level 2 European Space Agency (ESA) standard (hereafter referred to as "Standard Neural Network (NN)") proves to be the most suitable atmospheric correction algorithm, which was then used to describe spatial patterns and temporal variability of the different OWTs in the region. The BB-AERONET-OC site is located in a sharp transition between estuarine and coastal waters that present contrasting optical conditions: OWT 4 dominates over time (73.72% of the observations), followed by OWT 3 (24.74%) and OWT 5 (1.53%). OWTs 4 and 5 are associated with turbid waters of the Bahía Blanca Estuary, especially OWT 5, which typifies the very turbid waters from the inner estuary, with the particulate

load dominated by mineral sediments and detritus. OWT 3, in turn, depicts the eutrophic coastal waters of the inner shelf. The variability of OWTs and the relative contribution of organic and inorganic compounds to the suspended material would be mostly related with the prevalence of northwest winds in the area, which would drive the export of estuarine sediments to the shelf.

KEYWORDS

AERONET-OC, optical water types, atmospheric correction, Sentinel-3 OLCI, coastal waters

1 Introduction

The Aerosol Robotic Network (AERONET) is a global network of ground-based Sun and sky radiometers and data archive managed by the National Aeronautics and Space Administration (NASA) Goddard Space Flight Center (GSFC) in partnership with the Laboratoire d'Optique Atmosphérique (LOA) of the University of Lille (France) (Holben et al., 1998). The instruments collect high-quality data on aerosol optical thickness, size distribution, and other atmospheric properties. The AERONET Ocean Color Project (AERONET-OC) is an extension of AERONET's capabilities to support ocean color research, providing information to calibrate and validate ocean color measurements taken from space-borne instruments. The network is composed of radiometers deployed at coastal sites and marine environments to gather accurate ground-based measurements, which are then used to validate the satellite-derived ocean color data. Thus, AERONET-OC plays a crucial role in improving the accuracy and reliability of satellite-derived ocean color products (Zibordi and Talone, 2020), allowing a more comprehensive understanding of the oceans and their essential functions, and leading to better-informed decisions and policies related to environmental conservation and management.

AERONET-OC sites collect radiometric measurements of the spectral normalized water-leaving radiance, L_{wn} (λ; mW cm^{-2} sr^{-1} μm^{-1}) (λ represents wavelength of visible light expressed in units of nm). The spectral remote-sensing reflectance, R_{rs}(λ), can be converted from L_{wn}(λ) and is the fundamental parameter from which bio-optical properties and the concentrations of optically significant substances in water are retrieved. Global Climate Observing System (GCOS, 2011) defines a target accuracy requirement for the water-leaving radiance of 5% specifically for the blue and green wavelengths. This accuracy is achievable in the so-called Case-1 waters (typically oceanic environments), whose inherent optical properties (IOPs) primarily depend on phytoplankton and associated dissolved and particulate matters (Morel and Prieur, 1977). In optically complex waters of estuarine, coastal, and inland environments, IOPs are significantly influenced by other particulate and dissolved constituents mainly from terrestrial origin whose concentrations do not covary with the phytoplankton concentration. In these waters, commonly referred to as Case-2 (Morel and Prieur, 1977), the optical budget depends on the relative contribution of these substances, significantly increasing the uncertainties of R_{rs} (λ) retrievals and derived ocean color products (Bi et al., 2023).

A methodological approach to solve the problem of estimating the concentration of relevant optically significant substances in complex waters, includes a classification of R_{rs} (λ) spectra into optical water types (OWTs) (*e.g* Lubac and Loisel, 2007; Vantrepotte et al., 2012; Hieronymi et al., 2017; Wei et al., 2022; Hieronymi et al., 2023). R_{rs}(λ) spectra vary in different shapes and magnitudes, in response to the absorption and backscattering of optically significant substances suspended and dissolved in water (Kirk, 2011). Thus, the classification in OWTs provides information about the optically significant components in each class and allows analyzing the variability and trends of the biogeochemical and biological variables they are proxy of (Botha et al., 2020). Statistical methods for clustering, such as k-means, hierarchical clustering and fuzzy clustering are widely used based on the spectral shape or spectral magnitude of R_{rs}(λ) spectra. For instance, Vantrepotte et al. (2012) identified different OWTs for contrasted turbid coastal areas of the eastern English Channel, southern North Sea and French Guiana using a clustering approach performed on the spectrally normalized reflectance spectra. More recently, Tran et al. (2023) used this same approach as a classification of R_{rs}(λ) spectra into five different OWTs as a preliminary step to obtain optimized Chl-a retrievals.

In January 2020 the site AERONET-OC Bahía Blanca (BB-AERONET-OC) was established at the mouth of Canal Principal, the main navigation channel of the Bahía Blanca Estuary. This is a complex coastal system characterized by large temporal and spatial variations in turbidity. Previous work by Arena et al. (2022), based on a time series of Landsat 8 - Operational Land Imager (L8-OLI) showed that larger turbidity values consistently characterized the middle section of Canal Principal, and turbidity progressively decreased through the mouth of Canal Principal. Around the location of the site BB-AERONET-OC, a synoptic overview of the average turbidity over the entire time series showed a sharp transition from the turbid waters characterizing Canal Principal, to the clearer water conditions typical of the coastal zone out of the estuary. In turn, the temporal analysis revealed large changes in turbidity in response to meteorological forcings, demonstrating a variety of water types at this site location.

The objective of the present study is to characterize the optical variability around the BB-AERONET-OC site whose R_{rs}(λ) measurements can also be used to assess the accuracy of atmospheric correction algorithms (Zibordi and Talone, 2020). In this work we used the R_{rs}(λ) from the BB-AERONET-OC and spectral radiometric measurements obtained from field campaigns, along Canal Principal, to describe the optical variability of waters around the site. We assigned each normalized R_{rs}(λ) spectra to one of the five OWT's proposed by Tran et al. (2023) and the different OWTs found in the area were then characterized using the concentrations of optically significant components namely the chlorophyll-*a*, Chl-*a*, (in mg.m^{-3}) and

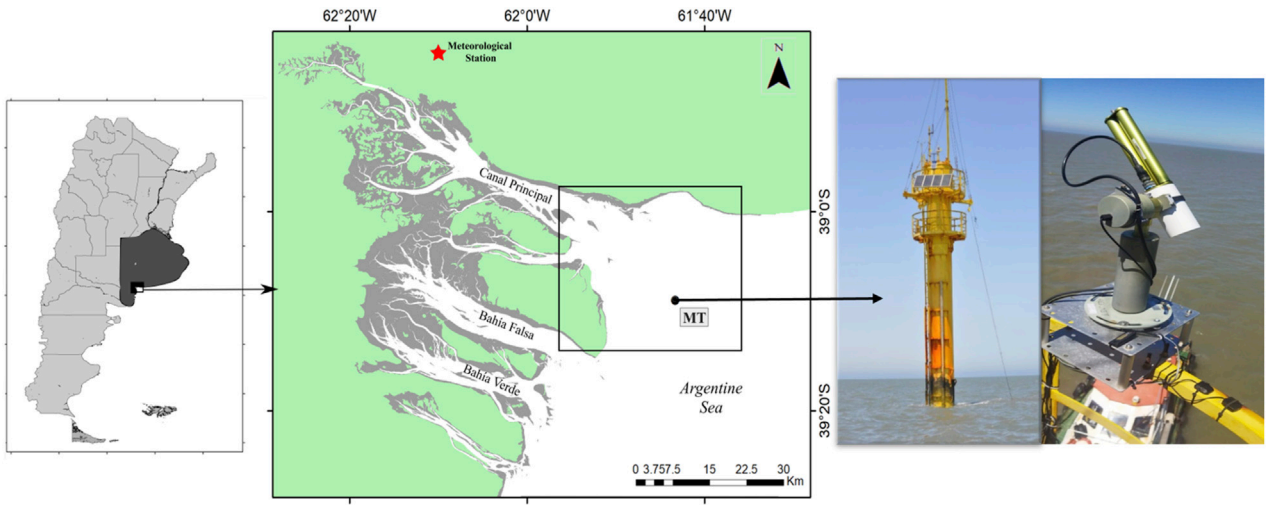


FIGURE 1
Geographical location of AERONET Bahía Blanca site, Argentina. Red star indicates the location of the meteorological station and the black dot represents the position of the Mareographic Tower (MT).

suspended particulate matter, SPM, (in g.m^{-3}) concentrations, absorption coefficients by phytoplankton, a_{ph} (443, in m^{-1}), non-algal particulate matter, a_{nap} (443, in m^{-1}) and colored dissolved organic matter, a_{cdom} (443, in m^{-1}), retrieved from *in situ* water samples collected along with the radiometric measurements. Afterwards, five freely available atmospheric correction algorithms were tested on Ocean and Land Colour Instrument (OLCI) images through a match up exercise using data from the site BB-AERONET-OC. The best performing atmospheric correction algorithm was then applied to all the OLCI images available since 2020 and used to describe spatial patterns and temporal variability of the different OWTs in the study area. Our results emphasize the optical complexity of the waters located around the BB-AERONET-OC and can be used to inform future development of inverse algorithms to accurately retrieve bio-optical parameters in extremely dynamic coastal environments.

2 Materials and methods

2.1 Study area

The Bahía Blanca Estuary (38° 45′S; 62° 22′W) is a mesotidal system, located in a temperate region of the Argentine Sea. The estuary is composed of a series of major tidal channels, oriented NW to SE, separated from each other by extensive intertidal flats, salt marshes, and islands (Pratolongo et al., 2017). The northern portion of the estuarine area is dominated by Canal Principal (Figure 1), the main navigation channel, that extends over more than 60 km and varies in width from about 3 to 4 km at the mouth (22 m depth) to 200 m at the head (3 m depth) (Piccolo and Perillo, 1990; Perillo et al., 2004). This is a complex coastal system characterized by a widespread erosion in mudflats and saltmarshes of the inner section, and strong tidal currents are responsible for the typically high suspended loads in the channel. Off the estuarine influence, a wide inner shelf extends to the 40 m isobath. In this shallow region, called El Rincón, mixing due to wind and tides produces a vertically homogeneous water column throughout the year (Martos and Piccolo, 1988).

Previous work, based on *in situ* observations in the inner section of Canal Principal (Arena et al., 2019), showed that the absorption budget (at 443 nm) of turbid waters close to the head of the estuary were dominated by a_{nap} (70%) followed by a_{ph} (20%), while a_{cdom} presented the lowest contribution (10%). In the coastal waters of the inner shelf, where the phytoplankton community is mainly dominated by diatoms, a_{ph} (443) varied from 0.02 to 0.13 m^{-1} with a mean value of 0.052 m^{-1}, (Delgado et al., 2019). The hydrographic evidence presented by Delgado et al. (2017), coupled with the prevalence of phytoplankton groups well-adapted to turbulent and turbid conditions, such as diatoms which are the most abundant phytoplankton group over coccolithophores, nano-flagellates, and dinoflagellates, suggest that the coastal zone off the mouth of Canal Principal is influenced by relatively turbid water (ranging between 50–100 FNU) outflowing the Bahía Blanca Estuary.

2.2 *In situ* measurements

2.2.1 Radiometric measurements from the AERONET station

Since January 2020 the site BB-AERONET-OC has been operational at the mouth of Canal Principal, the main navigation channel of the Bahía Blanca Estuary. AERONET-OC collects data from worldwide distributed autonomous above-water CIMEL CE-318 (Cimel Electronique, France) sun-photometers adapted to perform marine radiometric measurements for determining the $L_{wn}(\lambda)$, in addition to measurements for retrieving aerosol optical properties. This CIMEL-based system, called SeaWiFS Photometer Revision for Incident Surface Measurements (SeaPRISM), performs

multiple sky- and sea-radiance measurements at programmable viewing and azimuth angles at eight center-wavelengths (nominal bands: 412, 443, 488, 531, 551, 667, 870, and 1020 nm) (Zibordi et al., 2009). At the BB-AERONET-OC site, a SeaPRISM instrument was deployed in the upper rail of the Mareographic Tower, a 15 m tall structure, located 10 miles away from the coast (15 m depth). Data provided by NASA (https://aeronet.gsfc.nasa.gov/) include L_{wn} values determined from measurements screened and processed according to Zibordi et al. (2009).

Level 1.5 data cloud-screened and quality-controlled data collected by the SeaPRISM instrument from January 2020 to May 2023 were downloaded from https://aeronet.gsfc.nasa.gov/. In addition to the AERONET-OC LWN_f/Q data corrected for bidirectional effects (Morel et al., 2002), the alternative LWN_IOP products (Lee et al., 2011) are available. While LWN_f/Q data are generally recommended for applications related to Chla-dominated waters, the alternative products LWN_IOP appear more suitable for optically complex waters (Zibordi et al., 2022; Cazzaniga and Zibordi, 2023). These authors warned that the correction based on Morel et al. (2002; i.e., f/Q) is likely to be affected by large uncertainties. An experimental study focused on the comparison of f/Q- and IOP-based methods (Talone et al., 2018), indicates relative spectrally and water dependent uncertainties varying between 20% and 60% for the f/Q-based approach, with the highest values affecting the blue and red regions. Conversely, the IOP-based approach shows relative uncertainties within 20%–35% and lower dependence on wavelength and water type. These results have motivated the implementation of the IOP-based correction approach in the AERONET-OC processing in addition to the f/Q (Zibordi et al., 2022). The L_{wn} measured at the site BB-AERONET-OC, corrected using the IOP-based scheme (L_{wn}-IOP; Lee et al., 2011). was transformed into $R_{rs}(\lambda)$ using Eq. 1 and the solar irradiance spectrum, (F_0, mW cm^2 μm^{-1}) from Thuillier et al. (2003).

$$Rrs(\lambda) = \frac{L_{wn}(\lambda)}{F_0(\lambda)} \quad (1)$$

2.2.2 Field measurements

In situ measurements of hyperspectral $R_{rs}(\lambda)$ were obtained from above-water spectral measurements of water leaving radiance, downwelling radiance reflected from a Spectralon plaque, and sky radiance. Measurements were performed using an Ocean Optics Spectroradiometer HR4000CG (200–1100 nm), (Ocean Optics, Inc.; United States of America), following the NASA-Ocean Optics Protocols for satellite ocean color sensor validation (Mueller et al., 2003). Sampling was always performed under clear sky conditions and low wind speed (<30 km h^{-1}), within 2 h around noon and adopting a viewing angle θ of 40° and a relative azimuth φ of 90°. $R_{rs}(\lambda)$ was estimated as follows:

$$Rrs(\lambda) = \frac{L_u(\lambda) - L_{sky}(\lambda)^{*}\rho}{\pi \frac{1}{0.99} L_d(\lambda)} \quad (2)$$

where L_u is the upward radiance from the water surface, L_{sky} is the downward sky radiance, L_d is the radiance measured off a horizontally positioned standard Spectralon plaque, ρ is the effective sea-surface reflectance (with an approximate value of 0.028, Mobley (1999)) and 0.99 is the reflectance of the plaque provided by the manufacturer.

Radiometric measurements were taken during September 2017—July 2023 aboard sailboats or small artisanal fishing boats at different sampling points along Canal Principal, from the inner section to the mouth of Canal Principal (38.79°S; 62.27°W) and the coastal zone out of the estuary (39°S–62.5°W; 41.5°S–60°W). To further characterize the optical properties of waters in the Patagonian Shelf, out of the estuarine area and the coastal zone under study (mid shelf and shelf-break), optical and biochemical measurements were collected during a dedicated oceanographic cruise onboard the R/V Dr. Bernardo Houssay (25–28th of March, 2019). A total of 135 surface water samples were taken simultaneously with $R_{rs}(\lambda)$ measurements, and analyzed to obtain turbidity (T, FNU), chlorophyll a concentration (Chl-*a*, μg L^{-1}), concentration of suspended particulate matter (SPM, g m^{-3}), a_{ph} (443), a_{nap} (443) and a_{cdom} (443).

Turbidity was measured using a Hach 2100Q IS portable turbidimeter (FNU). Estimates were obtained by triplicate, after seawatersamples were mixed by gently tumbling the closed 5 L container around several times before subsampling. Turbidity values were then used to set the filtration volume for SPM estimation and to detect problems with sample mixing during subsampling. The dry weight concentration of SPM (mg m^{-3}) was determined by gravimetry, following the protocol proposed by Neukermans et al. (2012). Briefly, a known volume of seawater was passed through a pre-treated and pre-weighed 47 mm Whatman GFF glass fiber filter, with a nominal pore size of 0.7 μm. Filters were pre-treated by ashing at 450°C for 1 h, gently washing in 0.5 L of distilled water to remove loose fractions, drying at 65°C for 1 h, and pre-weighing to the nearest 0.1 mg. Seawater samples were filtered by triplicate on pre-treated filters with an applied vacuum of 300–400 mmHg. Filtration volume was set after Neukermans et al. (2012), considering the previously measured turbidity; for the present study, optimal filtration volumes ranged 0.5–2 L. After filtration, filters were washed with 250 mL of distilled water to remove salts, dried for 48 h at 65°C and re-weighed on the same weighing scale.

Chl-*a* was estimated by filtering 50 mL of seawater through a Whatman GF/F filter (nominal pore size 0.7 μm) at low vacuum pressure (<5 PSI). Immediately after filtration, all filters were packed individually in aluminum foil and stored in an ultrafreezer at −80°C until analysis. Pigments were extracted in methanol 100% (8 mL), during 12 h at −20°C, in dark, and Chl-*a* concentration was estimated using the selective fluorometric technique proposed by Welschmeyer (1994). Extract fluorescence was measured with a spectrofluorometer Shimadzu RF 5301 PC (Ex/Em wavelengths: 436/680 nm). To derive the absorption spectra of suspended particulate matter, water samples were filtered and stored using the same procedure described for Chl-a. Total particulate absorption spectra ($a(\lambda)$, m^{-1}) were estimated through the quantitative filter technique using the quadratic equation of Mitchell (1990). The spectral absorption of each sample was measured using a double beam spectrophotometer Shimadzu UV2450 with integrating sphere, in the 300–800 nm spectral range. After total particulate absorption spectra were measured, the filters were treated with

methanol (15 mL; 1 h), and measurements repeated to obtain a_{nap} (443). a_{ph} (443) was finally estimated by subtracting a_{nap} (443) from $a(\lambda)$. Finally, a_{cdom} was estimated from filtered seawater (pre-combusted filters Whatman GF/F, nominal pore size 0.7 µm) using glassware pre-washed according to Mitchell and stramska (2002) from the NASA-Ocean Optics Protocols For Satellite Ocean Color Sensor Validation (HCl 10%; 12 h). Absorption spectra in the 250–750 nm spectral range were measured with a spectrophotometer UV–VIS (Agilent Cary 60), using a 0.1 m pathlength quartz cell.

2.3 Optical water types (OWTs)

Hyperspectral $R_{rs}(\lambda)$ data obtained with the hand-held spectroradiometer were resampled to multispectral data using the spectral response functions of the 6 visible OLCI bands (412, 443, 490, 510, 560, and 665 nm) (https://sentinels.copernicus.eu/web/sentinel/technical-guides/sentinel-3-olci/olci-instrument/spectral-characterisation-data). The obtained curves, along with data from the site BB-AERONET-OC, were normalized by considering the ratio between the original $R_{rs}(\lambda)$ values and the area below the curve in order to perform the classification introduced by Tran et al. (2023). Regarding BB-AERONET-OC spectra, which are provided in nominal bands, it is worth noting that only six specific wavelengths matching to OLCI bands were considered as inputs for the classification.

In the work by Tran et al. (2023), an unsupervised classification was applied to the normalized spectra derived from worldwide distributed field campaigns along contrasted coastal areas. This unsupervised classification was performed using the Ward's clustering method. It is a variance analysis used to quantify the distance between different clusters, minimizing the sum of squares of any pair of clusters defined at each step of the procedure. This classification led to the definition of 5 optical water types with distinct R_{rs} spectral shapes. Those OWTs were then used for labeling inputs of R_{rs} spectra (e.g., hyperspectral data resampled to multispectral format, multispectral AERONET-OC data, or satellite R_{rs}) to each of those OWTs defined from their *in situ* dataset, which are characterized by specific mean and covariance matrices.

For OWT membership computation, we used in this work the normalized R_{rs} spectra (derived from both Hyperspectral, resampled to OLCI bands, and multispectral AERONET-OC data) as an inputs to assign them into each of the pre-defined OWTs. This was done by using the Mahalanobis distance (Δ^2_{ic}) applied to the log-transformed normalized R_{rs} spectra to estimate the distance between our input spectra (x) and a given OWT (ic), computed as:

$$\Delta^2_{ic} = (x - \mu_{ic})^T \sum_{ic}^{-1} (x - \mu_{ic}) \quad (3)$$

where T indicates the matrix transpose, according to the characteristic covariance ($\sum$) and mean (μ) matrices of each OWT provided by the author. This Mahalanobis distance was used to compute the probability of a given spectra to belong to the spectra of the 5 OWTs predefined in Tran et al. (2023). Finally, the label assigned to the input spectra is determined by the highest probability of belonging to a given OWT.

2.4 Satellite data and evaluation of atmospheric correction (AC) algorithms

OLCI is a multispectral radiometer currently operational on-board Sentinel-3A (launched in 2016) and B (launched in 2018) observing the Earth at 21 spectral bands from 400 to 1020 nm, with a full spatial resolution at approximately 300 m. We downloaded daily S3/OLCI images Level 1 (full resolution) from the Copernicus Online Data Access (CODA) hosted at EUMETSAT (coda.eumetsat.int). Top-of-atmosphere Level 1 products were processed considering the following atmospheric correction (AC) schemes:

1- "POLYMER" (POLYnomial-based algorithm applied to MERis; v. 4.13) based on an iterative coupled ocean-atmosphere and polynomial spectral matching technique (Steinmetz et al., 2011).
2- "SeaDAS"/l2gen (SeaWiFS Data Analysis System; v8.1, OBPG) algorithm from NASA's SeaDAS with default settings for OLCI using the 2 bands 779 nm and 865 nm multi-scattering algorithm with Relative Humidity based model selection and iterative NIR correction (Ahmad et al., 2010; Bailey et al., 2010).
3- "SeaDAS-ALT", an alternative processing for SeaDAS/l2gen using the 2 bands 865/1020 nm multi-scattering algorithm (aerosol mode option = − 2: Multi-scattering with 2-band, RH-based model selection and iterative NIR correction, and Bidirectional reflectance correction = 7; Morel f/Q + Fresnel solar + Fresnel sensor).
4- "ACOLITE/DSF" (Atmospheric correction for OLI 'lite'/Dark Spectrum Fitting), an imaged-base adapted method for OLCI imagery implemented in ACOLITE using an assumed homogeneous atmosphere over a scene (Vanhellemont and Ruddick, 2021). The atmospheric path reflectance is predicted from multiple dark targets, which are selected accordingly to the lowest observed top of atmosphere reflectance values in all the bands.
5- "Standard NN", the operational product OLCI L2 ESA standard approach in which atmospheric parameters and water-leaving reflectances are inverted through dedicated neural networks. (EUMETSAT, 2019).

To test the performance of the different AC schemes, we considered $L_{wn}(\lambda)$ data measured at the site BB-AERONET-OC at the following wavelengths: 412, 443, 490, 510, 560, 665. The match-up exercise was based on the protocol developed in Bailey and Werdell, (2006). The selection criteria included a time window of ±3 h between the satellite overpass and the *in situ* measurement, and the $L_{wn}(\lambda)$ extraction was performed considering a pixel box of 3-by-3 pixels centered at the location of the BB-AERONET-OC site. A match-up was accepted if at least 6 of 9 pixels of the box were valid (Bailey and Werdell, 2006; Jamet el al., 2011). Afterwards, a spatial uniformity criterion was applied for bands between 412 and 665 nm, based on the coefficient of variation (cv = standard deviation/mean*100). If the cv was higher than 15% the match-up was discarded. A set of quality flags, integrated into the output of each processor, served to determine the validity of individual pixels. Pixels deemed invalid were masked based on criteria such

as invalidity, land, cloud, suspicion, high sun-glint, whitecaps, high zenith angle, saturation, and AC failure (Bailey and Wedell, 2006). Additional flags varied depending on the atmospheric correction (AC) method employed. For the "Standard NN," flags included the adjacency effect and Lwn negative value between 412 and 665 nm, as well as flags indicating being out of range for atmospheric correction neural nets. POLYMER employed flags for negative back-scattering coefficient, out of bounds, exception, thick aerosol, high air mass, and inconsistency. NASA, on the other hand, utilized stray light, very low 560-nm water-leaving radiance Lw (560 nm), and navigation fail flags.

Regarding the data derived from the site BB-AERONET-OC, as mentioned above the L_{wn}-IOP (Lee et al., 2011) approach was considered to correct for the anisotropy of the water-leaving radiance (Zibordi et al., 2022; Cazzaniga and Zibordi, 2023). In contrast, AC algorithms currently consider different approaches for bidirectional effects. The OLCI "Standard NN" product is a directional water-leaving reflectance not corrected for bidirectional effects (EUMETSAT, 2021), as well as "ACOLITE/DSF". Meanwhile, POLYMER and SeaDAS l2gen products are already corrected for bidirectional effects as described in Steinmetz et al. (2011) and Bailey et al. (2010).

The assessment of each AC algorithm was performed through linear regression analyses between *in situ* measurements and satellite $L_{wn}(\lambda)$ estimates, and their goodness-of-fit was evaluated through the root mean-square error (RMSE, Eq. (3)), the normalized mean absolute error (NMAE, Eq. (4)), and the Bias (Eq. (5)).

$$RMSE = \sqrt{\frac{1}{n}\sum [y - x]^2} \tag{3a}$$

$$NMAE = \sum \frac{|y - x|/x}{n} \tag{4}$$

$$bias = \frac{1}{n}\sum y - x \tag{5}$$

where x is $L_{wn}(\lambda)$ measured *in situ*, y the satellite estimated and n the number of match-ups.

2.5 Spatial and temporal variability of OWTs membership

A continuous monitoring of a significant storm event in the estuary was possible in March 2022, since OLCI captured scenes of pre- and post-storm conditions. A cyclone with tropical characteristics influenced the central region of Argentina and particularly the southwest part of Buenos Aires province during March 24–26th, 2022. The Bahía Blanca area was particularly affected by heavy rains within a cumulative rainfall of 120 mm in 48 h, and powerful hurricane-force winds blowing from the southwest sector during the storm passage. Daily atmospherically corrected OLCI data, were used to monitor the impact of wind and storm events on OWT variability. Due to the heavy cloud coverage during the storm event, only four clear-sky images were available to compare spatial-temporal variations of computed OWTs maps before the event (March 22–23th) to those after (March 27–28th) the storm.

Wind speeds and directions, coincident with the BB-AEROENT-OC sampling period were recorder at the meteorological station Comandante Espora, Bahía Blanca (−38.733 S; −62.167 W, https://www.meteobahia.com.ar/index.php?estacion=Bahia%20Blanca%20(Espora)). The station is equipped with a wind sensor positioned 10 m above the surface, recording wind intensity (m s^{-1}) and direction at a 2-minute frequency. To characterize wind speeds, we considered the arithmetic mode 24 h before the AERONET-OC acquisition date and time.

On the other hand, to analyze the long-term statistical distribution of each OWT, all available daily OLCI Lwn data collected between 2016 and 2023 were associated with the five optical OWTs. Subsequently, the most frequent OWTs observed for each pixel over the OLCI time period were mapped.

3 Results

3.1 *In situ* R_{rs} spectra of contrasting waters from estuarine, coastal and mid-outer shelf environments

All $R_{rs}(\lambda)$ spectra collected *in situ* between 2017 and 2023 with a hand-held spectroradiometer, were grouped and their mean ± standard deviation values were plotted (Figure 2) according to the location of sample collection: estuarine, coastal, and mid-outer shelf environments (maps in Figure 2A). These spectra show a wide range of signal amplitudes and shapes across the region mirroring the large variability in types and concentration of optically significant compounds present in these waters.

The $R_{rs}(\lambda)$ spectra obtained in the estuarine environment (Figure 2B) correspond to a shallow and turbulent water column, with the highest turbidity values and variations of the study area. These $R_{rs}(\lambda)$ spectra vary over a wide range of magnitudes and spectral shapes, but a common pattern is that values sharply increase over the blue and green regions of the spectrum, with a strong reflectance peak around 570 nm, and then a moderate decrease in magnitude over the red domain. The R_{rs} depression around 670 nm may be caused by the maximum absorption of Chl-a, while the small R_{rs} peaks around 680 nm can be attributed to the Chl-*a* fluorescence peak. A clear R_{rs} maximum appears at 800 nm, that is characteristic of highly turbid waters with high SPM concentrations (Doxaran et al., 2002).

In contrast, $R_{rs}(\lambda)$ data from clear waters of the mid-outer shelf (Figure 2D) present the lowest $R_{rs}(\lambda)$ values and relatively flat spectra, in accordance with the low concentration of optically significant components, a typical attribute of blue waters. These curves exhibit maximum reflectance values in the blue part of the visible spectrum and the lowest in the red, but R_{rs} values are comparatively lower than those observed in coastal and estuarine waters. These spectral curves show a wide plateau between 500 and 570 nm, and do not show any absorption valley or fluorescence peak around 670–680 nm. R_{rs} values are negligible for longer wavelengths.

In an intermediate position, spectral curves obtained in the coastal region out of the estuary (Figure 2C) have a typical reflectance peak at 570 nm, the depression around 670 nm, and a fluorescence peak around 680 nm can be also observed, but all these features appear to be diminished when compared with estuarine

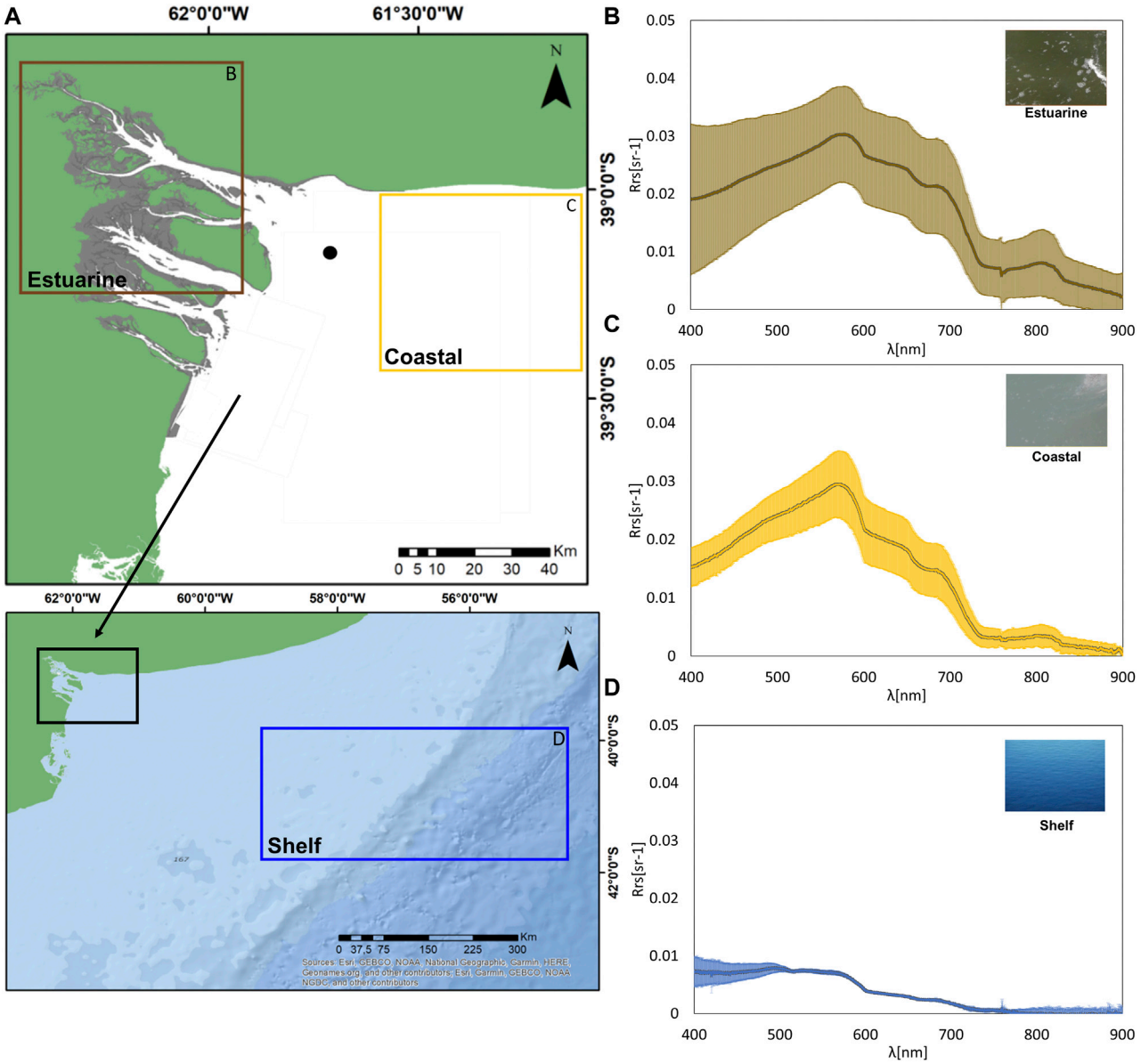


FIGURE 2
Radiometric remote sensing reflectance (R_{rs} (λ)) spectra obtained in cruise campaigns (2017–2023) from **(A)** Estuarine (<10 m depth (z), brown square), **(B)** Coastal (10 m < z < 50 m, yellow square) and **(C)** Shelf waters (z > 50 m, blue square). Note that **(B–D)** figures are not in the same scale. The black dot represents the position of the BB-AERONET-OC site. The solid line stands for the mean values and the colored area for the standard deviation of the R_{rs} (λ).

waters. The reflectance peak at 800 nm and R_{rs} values at longer wavelengths at not negligible, but their magnitudes are much lower than those in estuarine waters, suggesting a minor contribution of SPM to the signal.

3.2 Optical water type classification

Five different OWTs were depicted across the wide range of oceanographic conditions in the area, including R_{rs} spectra obtained in the mid-outer shelf. Figure 3A displays the averaged normalized R_{rs} spectra, resampled to OLCI bands, obtained for each OWT, based on the field measurements previously considered in Section 3.1. Figure 3B–F present a synoptic overview of optically active constituents (concentrations of Chl-*a* and SPM) and inherent optical properties (a_{ph} (443), a_{nap} (443) and a_{cdom} (443)) estimated from water samples corresponding to each class.

Waters belonging to OWTs 1 and 2 present the typical spectral shapes of oligotrophic and mesotrophic shelf waters with minimum turbidity values (SPM concentrations from 8.60E-04 to 1.57E-03 g m^{-3}). All samples in these classes were collected in the mid-shelf and shelf break, out of the coastal zone and the estuarine

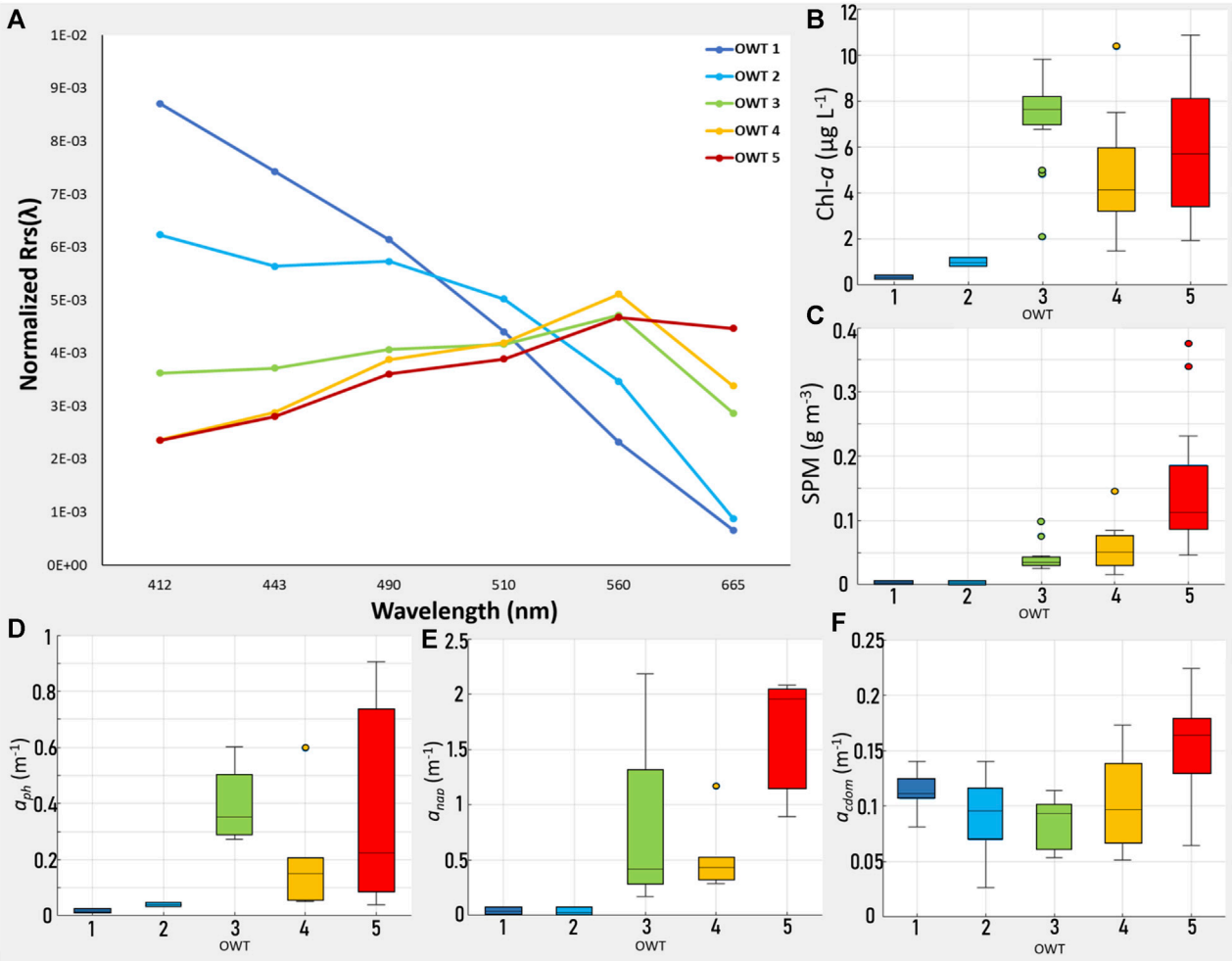


FIGURE 3
(A) Averaged normalized (R_{rs} (λ)) spectra corresponding to the OWTs; box plots illustrating the distribution of Chl-*a* (µg L^{-1}, **(B)**, SPM (g m^{-3}, **(C)**, a_{ph} (443, m^{-1}; **(D)**, a_{nap} (443, m^{-1}; **(E)**, a_{cdom} (443, m^{-1}; **(F)**.

influence. Both OWTs present higher values in the blue portion of the spectrum and it is in agreement with the low Chl-*a* concentrations (both classes ranging from 0.36 to 1.19 µg L^{-1}), small values of a_{ph} (443) (0.009–0.03 m^{-1}) as well as a_{nap} (443) (0.007–0.01 m^{-1}).

The averaged normalized spectrum for OWT 3 has lower reflectance values in the blue, with a plateau between 490–510 nm, and a relatively small peak around 560 nm. Most samples that belong to this class were collected in the coastal zone, out of the estuarine area, but there are also 16 samples collected in the middle section of Canal Principal. OWT 3 characterizes mesotrophic waters with and intermediate turbidity, with Chl-*a* concentrations ranging 2.10–9.82 µg L^{-1} and higher absorption of phytoplankton and NAP (a_{ph} (443) 0.27–0.6 m^{-1}; a_{nap} (443) 0.17–2.18 m^{-1}), compared to OWTs 1 and 2.

OWTs 4 and 5 corresponded to turbid and highly turbid waters, and all samples in these types were collected within the Bahía Blanca Estuary. Both classes present a reflectance peak at 560 nm and similar Chl-*a* concentrations, ranging from 2.85 to 10.36 µg L^{-1}. A major difference is that OWT 5 presents a higher reflectance at 665 nm, related with more turbid conditions and a higher concentration of suspended materials that enhance particulate backscattering. Waters belonging to the OWT 4 have SPM concentrations and a_{nap} ranging from 0.016 to 0.145 g m^{-3} and 0.28 to 1.16 m^{-1}, respectively, while in waters in OWT 5 SPM and a_{nap} varied from 0.046 to 0.375 g m^{-3} and 0.9 to 2.07 m^{-1}, respectively. The absorption of CDOM presented low and similar values through the five classes depicted.

Restricting the analysis to samples collected within estuarine and coastal waters, in a radius of 100 km around the BB-AERONET-OC (n = 129), we explored the association of the available biochemical and bio-optical parameters to better characterize the OWT that may be found at the site. On average, the highest Chl-*a* concentrations along with lowest concentrations of SPM characterized the OWT 3. At the opposite end, OWT 5 has the highest SPM concentrations, but a large variability in Chl-*a* is observed. Considering the Chl-*a*/SPM ratio (Figure 4A), the largest values corresponded to OWT 3 (2.06×10^{-1}), while OWT 5 presented the lowest ratio (4.96×10^{-2}), suggesting that phytoplankton (pigmented particles) would not have a significant contribution to the SPM in OWT 5. Considering the

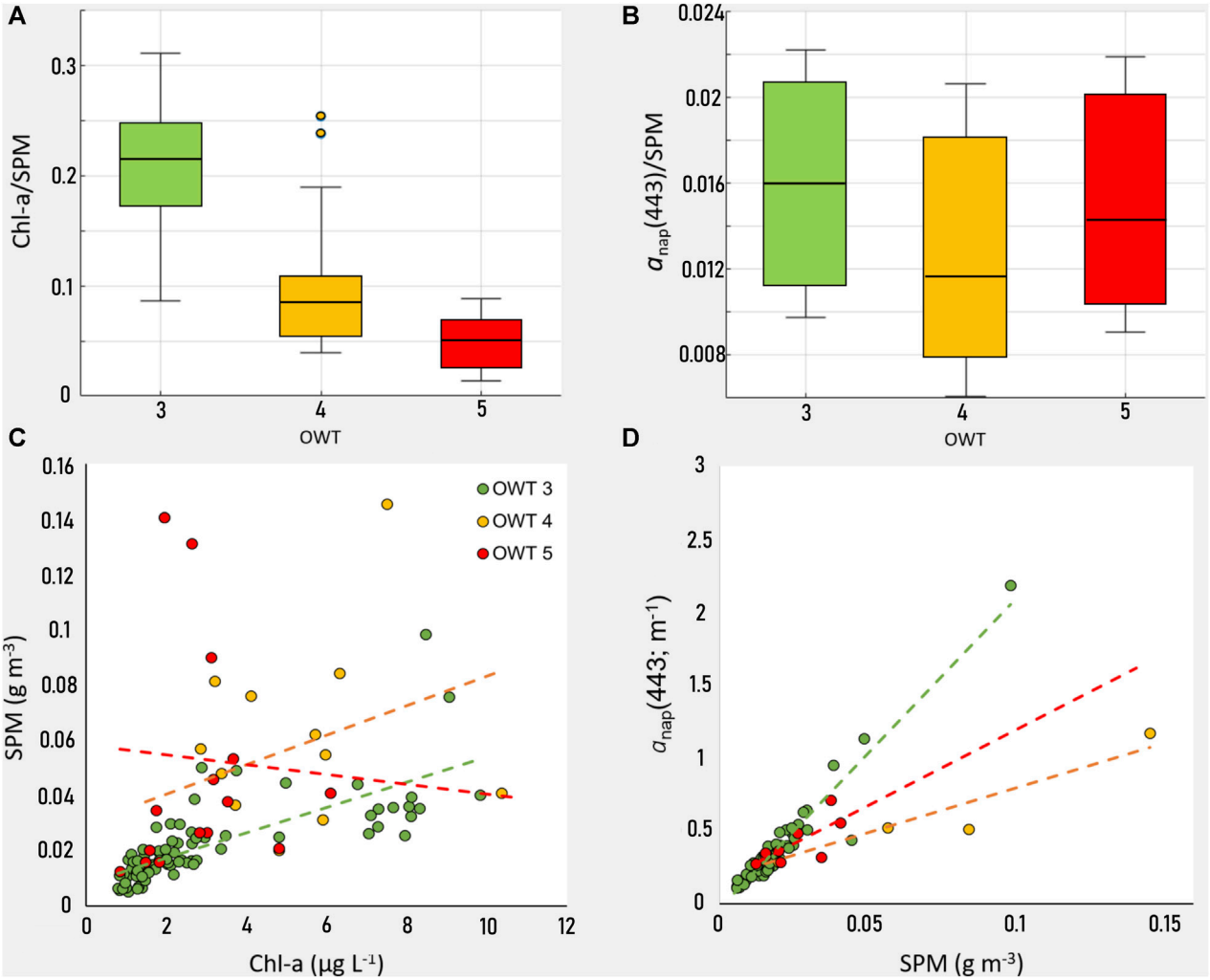


FIGURE 4
Boxplot distribution of coastal OWTs regarding their Chl-a/SPM ratio **(A)** and anap (443)/SPM ratio **(B)** Scatter plots of Chl-a vs. SPM **(C)** and SPM vs. a_{nap} (443) **(D)**. The colors indicate the OWT: OWT 3, in green, OWT 4, in yellow, and OWT 5 in red.

covariation between Chl-*a* and SPM concentrations (Figure 4C), the strongest correlation was observed in OWT 3 ($R^2 = 0.56$) compared to OWT 4 and 5 ($R^2 = 0.14$ and 0.027, respectively), emphasizing the idea of a strong contribution of phytoplankton to the particulate material in OWT 3. On the opposite, the complete lack of a positive correlation between Chl-*a* and SPM concentrations in OWT 5 are indicative of an allochthonous origin for the particulate material, either mineral sediments or detrital matter derived from sources other than phytoplankton. Also, a strong positive linear correlation was obtained between a_{nap} and SPM (Figures 4B, D) in OWT 3 ($R^2 = 0.91$), suggesting that detrital material, possibly derived from phytoplankton, may also have a significant contribution to the SPM.

3.3 Validation of OLCI (Sentinel 3A-B) $L_{wn}(\lambda)$

Scatterplots comparing *in situ* $L_{wn}(\lambda)$ measurement derived from the BB-AERONET-OC site and OLCI (Sentinel 3A-B) $L_{wn}(\lambda)$ is presented in Figure 5. For all the AC schemes considered, the number of match-ups generated was 34, with the exception of the 'SeaDAS' algorithm, that only generated 30 match-ups. Overall, the "Standard NN" presented the most accurate results, with the highest coefficients of determination (R^2) at 443 (0.32), 490 (0.5), 510 (0.55), and 560 (0.52) nm. It also presented the lowest bias at every band, with estimated $L_{wn}(\lambda)$ values closer to the 1:1 line. For all AC schemes, large uncertainties were observed in the blue bands (412 and 443 nm), with RSME >0.29 mW cm^{-2} sr^{-1} µm^{-1}, but better precisions were attained at longer wavelengths.

At 412 nm, the "Standard NN" presented the lowest RSME (0.29 mW cm^2 sr µm)$^{-1}$ and NMAE (12%) (Supplementary Figure S2, Supplementary Material). Similar results were obtained with the l2gen processor whose performance was relatively intermediate (RSME: 0.51 and 0.73, and NMDE: 24 and 38 at 412 nm for "SeaDAS" and "SeaDAS-ALT", respectively). Results from "SeaDAS", "SeaDAS-ALT" and "ACOLITE-DSF" were similar, with a slight tendency to overestimation in all cases. In the case of blue-green bands, overestimation resulted in large biases, NMDEs and offsets (Figure 5). POLYMER consistently underestimated

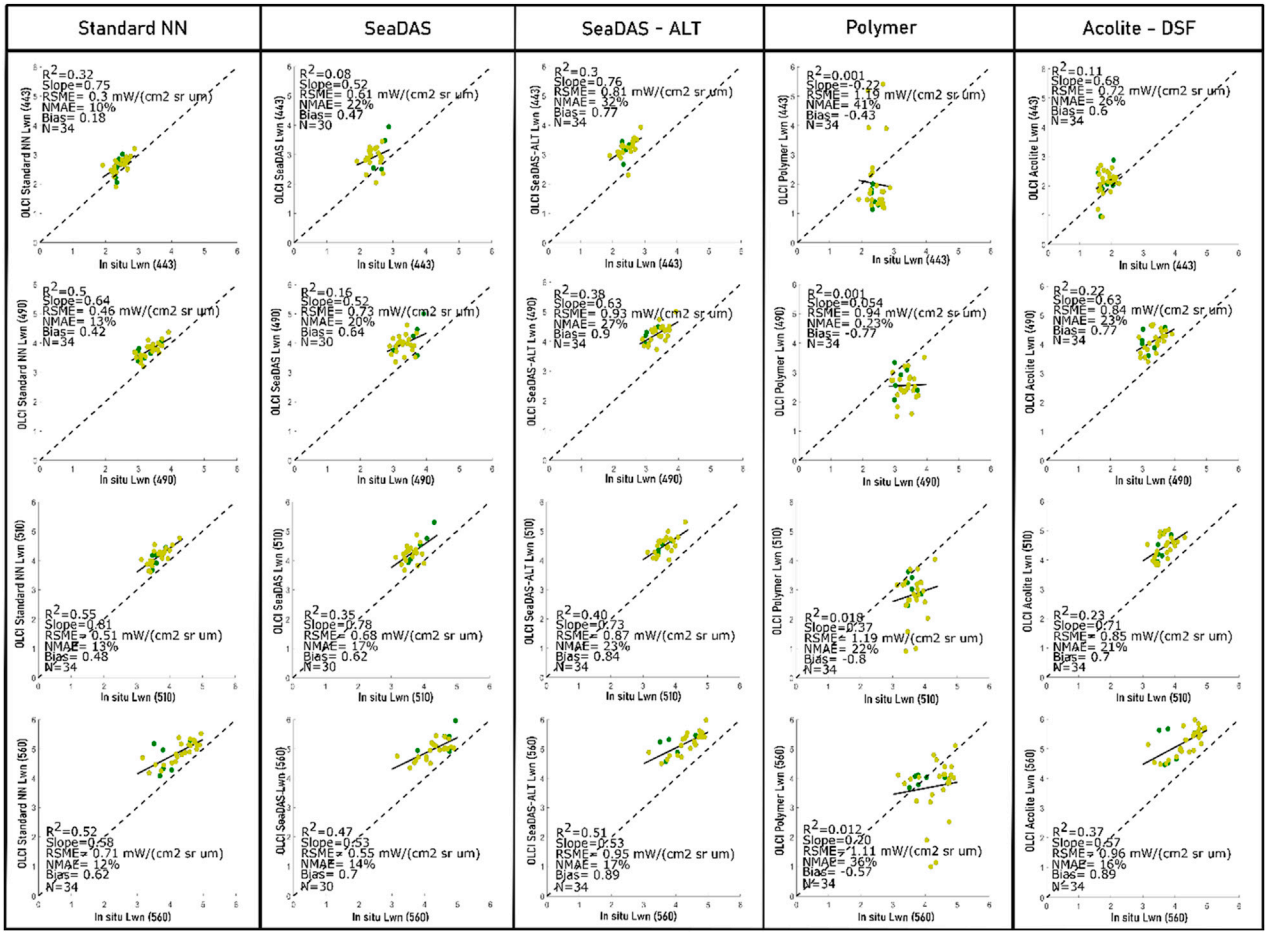


FIGURE 5
Scatterplots of the match-up exercise of the atmospheric correction algorithm (AC) retrieval and the in situ L_{wn} (443, 490, 510, 560 nm). Colors indicate the OWT: OWT 3 in green, OWT 4 in yellow.

Lwn (λ) with negative biases and lower coefficients of determination. It has to be noted that POLYMER performance improved at 510, 560, and 665 nm, but large RSMEs and NMAEs, as well as larger dispersion were observed when compared to the operational algorithm (Figure 5).

3.4 Spatial and temporal variability of R_{rs}(λ) and OWTs in the study area

R_{rs}(λ) values derived from all the L_{wn}(λ) measured at the site BB-AERONET-OC, from January 2020 to May 2023 are displayed in Figure 6A. The spectra exhibit typical features of coastal turbid waters, with a peak at 560 nm indicating the minimum absorption of Chl-*a* and dispersion by inorganic particles and non-algal particulate matter. R_{rs} (560) derived from L_{wn}(λ) varied from 0.0153 to 0.0292 sr^{-1} with an average value of 0.0232 ± 0.0020 sr^{-1} (Figure 6A). There was a good agreement in shape and magnitude between the spectral curves obtained with the hand-held spectroradiometer in the area around the Mareograph Tower and values measured at the site BB-AERONET-OC.

According to the classification of all spectra collected at the site, OWT 4 was the most frequent OWT (73.72% of the observations), followed by OWT 3 (24.74%) and OWT 5 was the less frequent (1.53%, Figure 6B). It was also noted that in 7 out of the 392 valid spectra analyzed, a secondary peak appeared at 667 nm that typifies the OWT 5 (Figure 6A, red spectral lines). The common feature for these samples was a prevalence of northwest winds in the area (Figure 6D).

Remote sensing applications provide an effective approach to monitor water quality conditions over large coastal systems to support the tracking of sediment re-suspension and transport along transitional zones. The significant storm event registered in the estuary had a short duration but strong wind speeds (>60 km h^{-1}; Figure 7A).

Figure 7 presents the distribution of each OWT before (B-C) and after (D-E) the storm passage in the study area. Under regular wind conditions before the storm OWT 3 and 4 dominated the mouth of Canal Principal and the coastal zone next to the estuary. In these conditions, OWT 5 only appeared in the inner zone of Canal Principal and the major channels to the south. The lack of data in the image corresponding to March 23th might respond to the cloud coverage at the beginning of the storm. Also, the prevalent

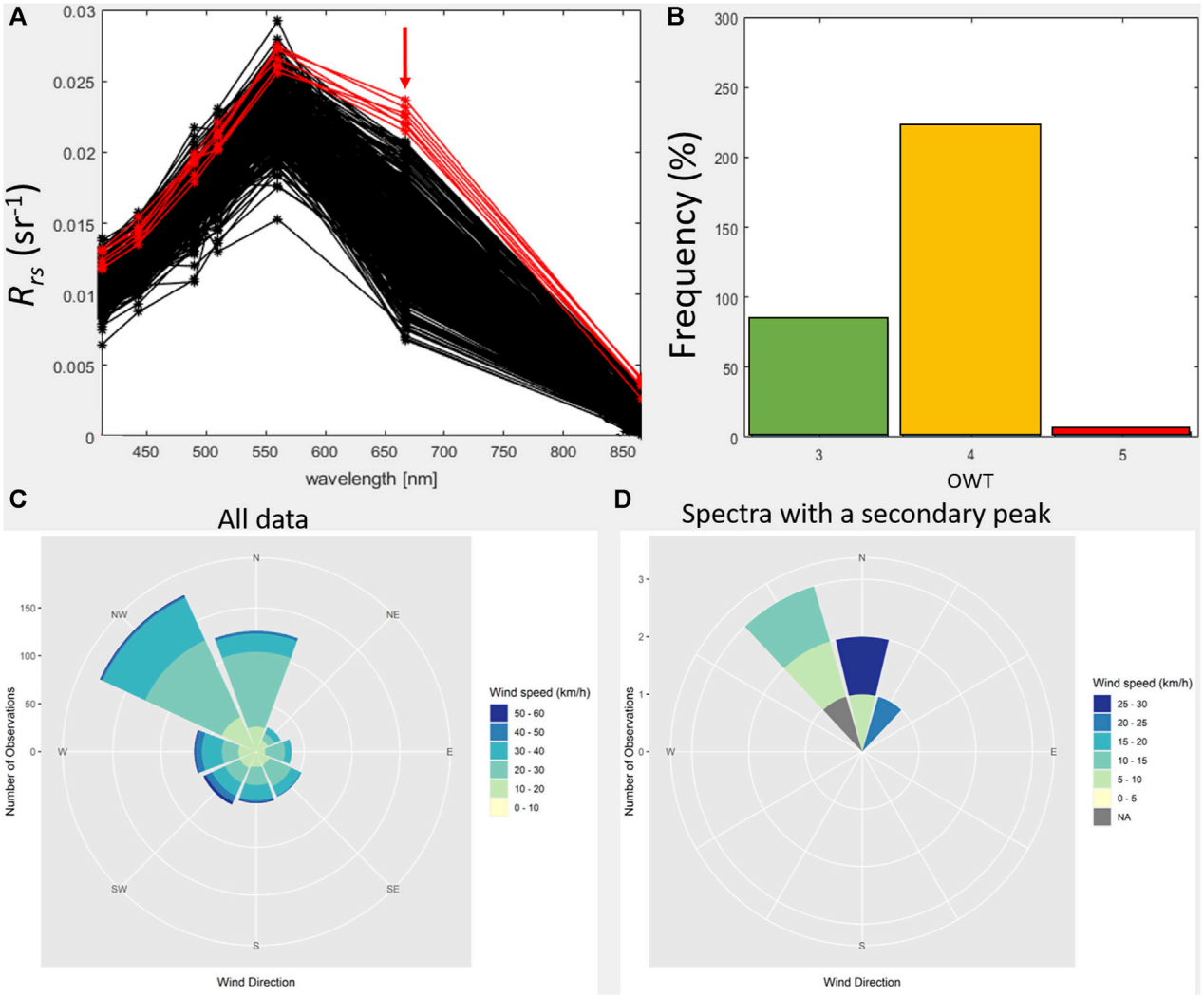


FIGURE 6
SeaPRISM-measured remote sensing reflectance (R_{rs}) spectra in AERONET-BB site **(A)** and frequency distribution of the depicted OWTs **(B)**. **(C)** Climatological wind conditions (2003–2023) and **(D)** 24 h s wind conditions for the R_{rs} spectra in red.

wind direction suddenly changed to the south, what may have caused the observed difference in the extension of OWT 4 between March 22 and 23th. During the storm, wind speeds significantly augmented, causing resuspension in the shallower inner section of major channels, causing a large increase in the suspended load. Run-off during the storm may have also contributed sediments from terrestrial sources to the estuary. After the storm, sustained northwest winds aided to the outflow of these suspended materials and their export off the estuarine area. The remote sensing mapping post-storm revealed that the region was under extremely turbid conditions as it is shown by the wide distribution of the OWT 5 along the whole estuarine system and their extension towards the open coast.

To provide a synthetic overview of the regional long-term pattern of OWTs distribution in the coastal zone, Figure 8 illustrates the most frequently observed OWT for each OLCI pixel over the period 2016–2023. A general transitional gradient is evident from the estuary to the adjacent coastal shelf, with OWT 5 dominating estuarine waters, while OWT 3 characterizes the coastal region out of the estuarine influence. The transitional region among those OWTs, which includes the location of the BB-AERONET-OC, can be described by the OWT 4.

4 Discussion

Coastal waters share common features and represent the interface between terrestrial environments and open oceans (Spyrakos et al., 2018; Botha et al., 2020). The $R_{rs}(\lambda)$ curves presented here showed typical spectral of complex waters, with intermediate to high levels of turbidity, and where the spectral characteristics are dominated by optically significant constituents other than phytoplankton. The backscattering of suspended particles tend to produce a flat spectrum increasing water reflectance from the blue wavelengths through the NIR region, but the distinct absorption of the different components produces

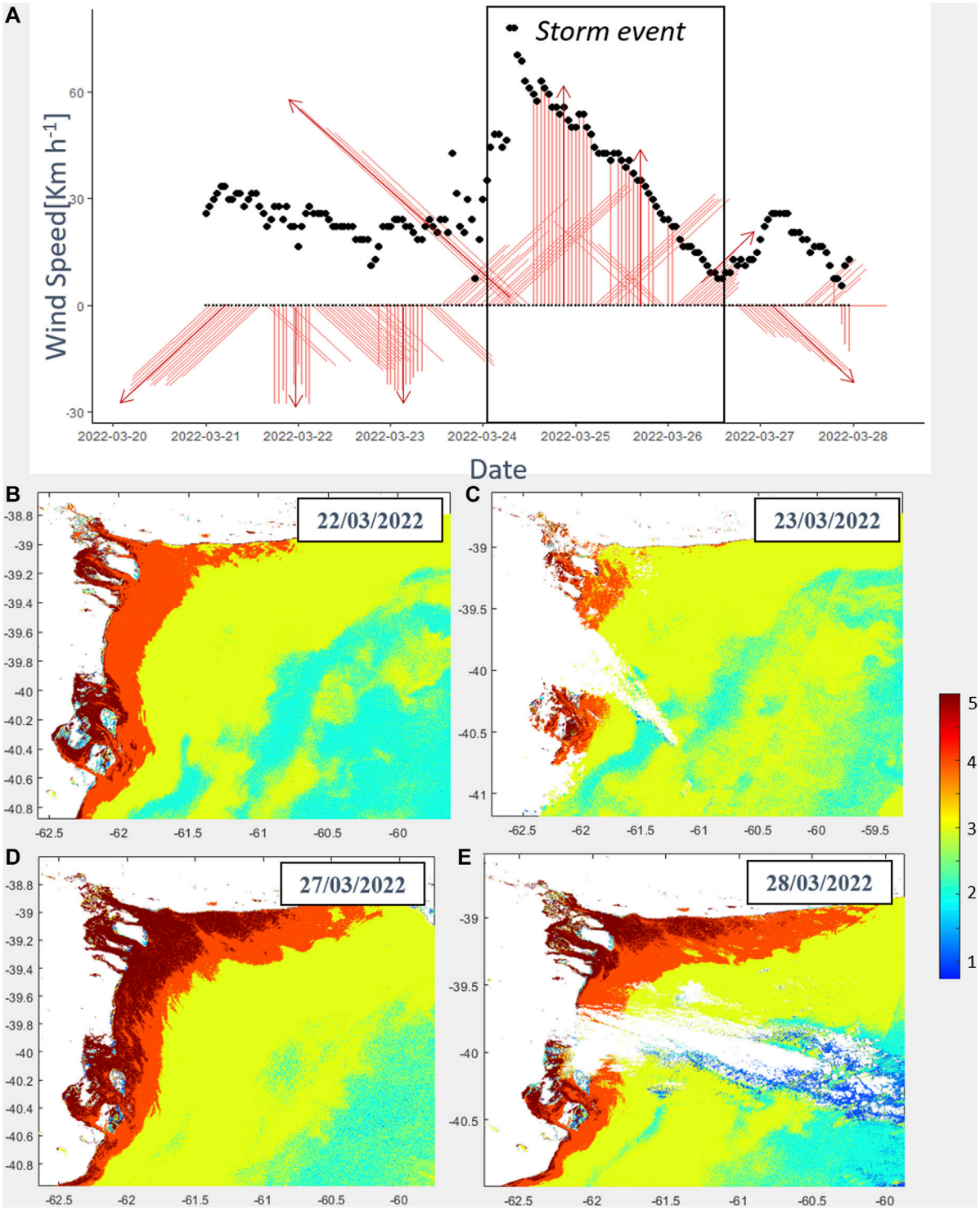


FIGURE 7
Hourly variation of wind speed (black dots) and direction (red arrows) in response to a storm that occurred in March 2022 **(A)**. Spatial distribution of each OWTs during pre-storm (March 22nd and 23th, 2022) **(B, C)** and post-storm (March 27th and 28th, 2022) **(D, E)** conditions in the study area.

the large variety of spectral curves presented here. In this context, OWTs represent snapshots of the continuum of these optical conditions (Moore et al., 2014). We identified water types adopting the same methodological approach presented in Tran et al. (2023), which was developed based on a globally distributed database of $R_{rs}(\lambda)$ of contrasting waters of coastal areas. In the present work, we used our site-specific radiometric data and the associated optical properties and biochemical determinations obtained from water samples in coastal and transitional areas surrounding the BB-AERONET-OC site to explore their OWT

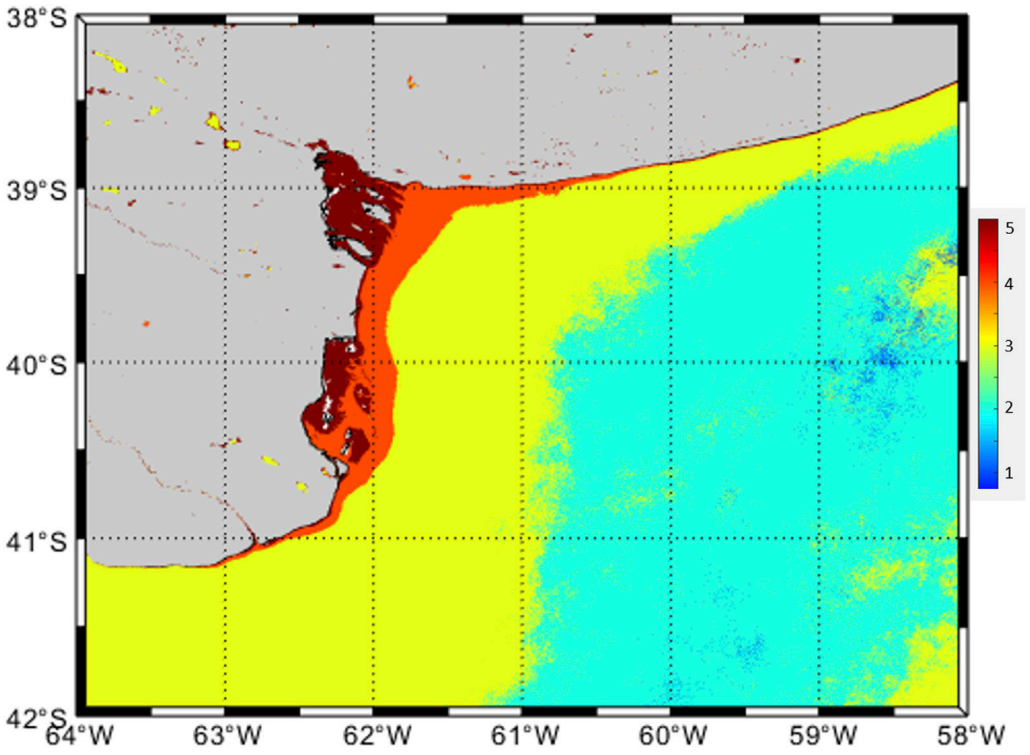


FIGURE 8
Distribution of the most frequent OWTs considering daily OLCI data between 2016 and 2023.

membership. Thus, they represent locally more refined indicators of water quality.

4.1 The optical water types and $R_{rs}(\lambda)$ of the BB-AERONET-OC site

In our study area, there was a large bio-optical and biogeochemical variability among regions, as a function of the a_{nap}, SPM, and Chl-*a* concentrations derived from field samples. On average, in the inner portion of the estuary, SPM concentration was approximately 50 times higher, and Chl-a was 1.2 times higher, compared to samples obtained in the inner shelf. Our results are in line with those reported in the North Sea, where there were two orders of magnitude of variation in SPM and Chl-*a* concentrations when the coastal zone was compared with the open marine environment (Babin et al., 2003; Astoreca et al., 2012). According to the supervised classification applied to our regional hyperspectral dataset of normalized $R_{rs}(\lambda)$ spectra, water types present a full range of variations from estuarine and coastal waters to open waters in the mid shelf and shelf break. OWTs 3 to 5 characterize waters within the Bahía Blanca Estuary and the coastal area under its influence, while OWTs 1 and 2 define waters from the mid-shelf and the shelf-break, where IOPs primarily depend on the phytoplankton contributions and those optically significant constituents covarying with Chl-a concentrations.

Regarding the area around the BB-AERONET-OC, across the transition between the estuary to the coastal zone, large differences in $R_{rs}(\lambda)$ magnitude, especially in the blue and red domains reflect differences in the concentrations of SPM that characterize different sections of the system, from the extremely turbid and eutrophic conditions of the inner estuary, where waters classify OWT 4 and 5, through more diluted waters near the mouth of Canal Principal, at the site itself, where OWT 4 is the dominant type, but OWT 3 is also present almost 25% of the time. In the coastal zone out of the estuarine influence, waters classified as OWT 3. $R_{rs}(\lambda)$ spectra have a generally lower magnitude, still mirroring the presence of significant loads of suspended materials, but diminished in magnitude, and a less pronounced fluorescence peak. This agrees with less turbid and mesotrophic conditions of the inner-shelf (Delgado et al., 2019). Within the estuary, the resuspension and transport of suspended loads through Canal Principal is largely induced by winds (Arena et al., 2022) suggesting their large influence in determining the temporal variations of optical properties at the site BB-AERONET-OC. Comparing our results with different AERONET-OC sites (from 2020 to the present), OWT 4 was not observed or less frequent in other regions. For instance, at the LISCO site (Long Island Sound Coastal Observatory, NY, United States of America) the dominant type was OWT 3 (95.83%), while OWT 4 had a low frequency (4.16%). Similarly, the AERONET-OC site, in a platform off the coast of Venice (Italy) presented a dominance of OWT 3 (80% of the observations), followed by OWT 2 (19.57%) and the OWT 1 was the less frequent (0.34%). Finally, the AERONET-OC site located in Lucinda Bay (northeast Australia) was also dominated by OWT 3 (95.34% of the observations) followed by OWT 2 (4.64%).

The SPM contains all organic and mineral material above 0.5–0.7 μm, which can be present as particulate organic carbon

(POC), including autotrophic and heterotrophic organisms, and detritus (organic particles), or as inorganic carbon (PIC) which comes mainly from carbonates (Loisel et al., 2009). Around the site, many differences in the spectral shape of $R_{rs}(\lambda)$ may derive from the relative contribution of phytoplankton to the SPM budget, as shown by the Chl-a/SPM ratio. This was also observed in other coastal environments where different classification approaches were considered for determining OWTs (*e.g* Lubac and Loisel, 2007; Vantrepotte et al., 2012; Hieronymi et al., 2017; Wei et al., 2022; Hieronymi et al., 2023). For instance, Lubac and Loisel (2007) explored the mechanisms of variation on $R_{rs}(\lambda)$ spectra along the eastern English Channel and southern North Sea, covering a wide range of in-water bio-optical properties. They conclude that POC/SPM ratio progressively increase from class 1 (where POC is dominated by phytoplankton) to class 5 (dominated by mineral particles). For instance, OWT 5, that dominates in the inner estuary, has the lowest Chl-*a*/SPM ratio, and the lowest correlation between a_{nap} and SPM, suggesting a dominance in the contribution of inorganic sediments (Babin et al., 2003).

The opposite situation was observed in the OWT 3, the only water type presents out of the estuarine influence, where phytoplankton seems to be dominant in the SPM composition, and their degradation products may contribute to a large a_{nap} - SPM correlation. Although data on POC and PIC concentrations are missing in our analysis, previous work (Arena et al., 2019) suggest that within the inner section of Canal Principal (dominated by OWT 5), turbidity is mainly promoted by fine silts and clays, from resuspension processes and transport over the intertidal and subtidal flats. According to the results presented here, the source of turbidity would progressively change to phytoplankton biomass and their degradation products to the coastal region out of the estuary (OWT 3), as suggested by the highest Chl-*a*/SPM ratio and strongest correlation between a_{nap} and SPM.

4.2 Validation of AC algorithms

Highly dynamic environments, such as the Bahía Blanca Estuary and the shallow coastal waters of our study area, become a challenge for AC purposes due to the presence of contrasted water masses, ranging from clear to very turbid environments, in response to rapid changes linked to several geomorphological, oceanographic and meteorological settings (Miller et al., 2011). In addition, narrow and restricted water bodies, different radiometric signals tend to overlap on the same subset, printing sharp transitional areas among OWTs and their effects cannot be treated separately. Overall, for the water and atmospheric conditions observed at the site BB-AERONET-OC, the operational product ("Standard NN") showed good agreement with the *in situ* measurements. We tested different AC approaches where in general, the accuracy of L_{wn} retrievals had an increasing performance towards longer wavelengths (560–865 nm), with large uncertainties over blue bands likely affected by the presence of atmospheric absorbing aerosols that algorithms could accurately differentiate (Wei et al., 2018). Overestimations of L_{wn} at blue bands correlated with underestimations of the aerosol optical depth at 865 nm (Zibordi et al., 2018). According to the distribution of Ångström Exponent observed in our study area, we found a predominance of small size aerosol particles (Supplementary Figure S1, Supplementary Material). Specifically, algorithms based on the usage of two-band iterative approaches, as the case of "SEADAS" and "SEADAS-ALT", might be affected by the presences of fine mode aerosols greatly impact the signal in the blue and become transparent with increasing wavelength, i.e., optical thickness rapidly decreases with wavelength making this AC methods more error-prone in the blue bands due to the insufficient extrapolation of the aerosol contribution from NIR bands to the visible (Frouin et al., 2019; IOCCG, 2020).

In the study area, POLYMER showed a poor performance in retrieving $L_{wn}(\lambda)$. This algorithm relies on a spectral optimization approach and uses the whole spectral range to decouple the atmospheric and surface components based on bio-optical models that might be unable to represent higher reflectance in highly turbid waters (Mogran et al., 2019; Vanhellemont and Ruddick, 2021) resulting in an underestimation of $L_{wn}(\lambda)$. In addition to this, Lain et al. (2014) addresses that the assumptions made in the in-water model used in POLYMER may not be suitable for eutrophic waters, where different IOP models produce contrasting outputs with varying phytoplankton concentrations. Similarly, POLYMER tended to underestimate the Rrs of turbid inland and coastal waters (see Liu et al., 2021 and references therein). The underestimations are partially caused by the bio-optical model in POLYMER that seems not suitable for optically complex waters, in which particulate and CDOM absorptions do not covary with chlorophyll concentration. The lower performance might also be caused by complex aerosols (Liu et al., 2021). The Ångström coefficient of aerosol in POLYMER is assumed to be 1, whereas the coefficient can vary in our study area between 0–1.8 with a median of 0.76 indicating that small size aerosol particles are present.

Nevertheless, validations performed in medium-turbid environments, reported better estimations for this algorithm than in the present work (*e.g.* Alikas et al., 2020; Li et al., 2022). Our results agree with those found by Vanhellemont and Ruddick (2021), who presented a poor performance of POLYMER in Belgian coastal waters, meanwhile the "Standard NN" OLCI product performed relatively well.

The significant underestimations of $L_{wn}(\lambda)$ resulted from "ACOLITE-DSF" in the study area, might be attributed to the fact that this algorithm does not perform a pixel-by-pixel AC. Instead, a homogeneous atmosphere is assumed over the entire sub-scenes, and its relatively poor performance could be due to variations of the aerosol type across the estuary and the lack of "dark pixels" in the area (Supplementary Figure S1, Supplementary Material). This algorithm has been previously tested in L8-OLI scenes of the Bahía Blanca Estuary using BB-AERONET-OC measurements of $L_{wn}(\lambda)$ and it was concluded that the use of a spatially invariant aerosols defined for the whole scene would not be appropriate for this study area (Arena et al., 2021; 2022).

In line with our results, previous works reported a good performance of the operational AC OLCI product ("Standard NN") for most part of the spectrum in case-2 waters (Tilstone et al., 2021; Vanhellemont and Ruddick, 2021; Windle et al., 2022). One of the reasons could be that the improvements made in reprocessed OLCI Collection 3, including updates to system vicarious calibration gains, bright pixel correction, cloud masking, flags and whitecap correction (Frouin et al., 1996;

Stramska and petelski, 2003; Wang and Shi, 2006), resulted in retrievals more suitable for coastal areas (Zibordi et al., 2022). Finally, we consider our dataset representative enough to conclude that the operational product of OLCI can be applied without major disturbances and avoiding negative retrievals along the transitional waters (OWT 3 and 4) of the BB-AERONET-OC site.

4.3 Variability of OWT and $R_{rs}(\lambda)$ in the BB-AERONET-OC site related to hydrometeorological conditions

Coastal regions are highly susceptible to optically complex waters conditions as consequence of their proximity to the land and adjacent highly urbanized areas (*e.g.* runoff of sediments, nutrients and organic matter) and also are under the influence of wind-induced flow patterns causing re-suspension of shallow bottom sediments. The use of optical classification schemes in coastal environments are a powerful tool for the pre-processing of $R_{rs}(\lambda)$ spectra as a previous step to obtain optimized bio-optical algorithms (Lubac and Loisel, 2007; Le et al., 2011; Vantrepotte et al., 2012; Tran et al., 2023). Monitoring the variability of OWTs can also help to differentiate the environment and choose the most suitable algorithm for the given environmental conditions (Moore et al., 2014). In this work, we were able to describe the spatial distribution and variability for each OWT detected in the study area with validated OLCI $L_{wn}(\lambda)$ images.

During the analyzed storm event, wind speeds significantly increased, with prevalent wind directions from the south producing resuspension in the shallower inner sections of major channels in the Bahía Blanca Estuary, increasing the suspended load over those areas. Before the storm the $R_{rs}(\lambda)$ spectra derived from the BB site in the red and NIR part of spectrum presented values of 7.28 $10^{-3} \pm 1.20\ 10^{-3}$ sr^{-1} and 3.44 $10^{-4} \pm 2.38\ 10^{-4}$ at 667 and 865 nm respectively). After the storm, sustained northwest winds aided to the export of suspended sediments through the mouth of these major channels, including Canal Principal, where the BB-AERONET-OC site is located. During this period the $R_{rs}(\lambda)$ maximum values in the red and NIR part of the spectrum peak around 2.11 $10^{-2} \pm 1.61\ 10^{-3}$ sr^{-1} at 667 and 3.81 $10^{-3} \pm 9.42\ 10^{-4}$ sr^{-1} at 865. The post-storm OWTs map revealed that the region was under extremely turbid conditions as it is shown by the wide distribution of the OWT 5, covering the entire estuarine system and the adjacent coastal area. The large differences observed before and after the storm reveal the strong variability in the temporal distribution of the OWTs and their association with re-suspended solids induced by hydro meteorological forcing, as well as sediment inputs via run-off.

5 Conclusion

The relevance of turbid waters outflowing the Bahía Blanca Estuary has been previously suggested by several authors as a major influence over the adjacent inner-shelf. This finding was supported by hydrographic and biological evidence (Delgado et al., 2015; Delgado et al., 2017). Arena et al. (2022) also concluded that turbidity, at the mouth of Canal Principal, mainly responds to winds that control sediment resuspension and export. Thus, winds would be critical for the sedimentary budget of the estuary and could explain the high turbidity values observed in the adjacent region. This study represents the first one describing the OWT variability around the AERONET-OC site, allowing for better characterization of the bio-optical environment of this site, which is useful by itself but also for further applications of OWT based bio-optical algorithms. According to the classification of all spectra collected at the BB-AERONET-OC site, OWT 4 was the most frequent water type (73.72% of the observations), followed by OWT 3 (24.74%) and OWT 5 was the less frequent (1.53%). In the present study, the "Standard NN" product of OLCI performed well across coastal transitional waters (OWT 3 and 4) of the BB-AERONET-OC site. The classification applied to OLCI scenes over the AERONET-BB site showed an alternance of multiple water types at the AERONET-BB site and a large spatial variability as result of hydrometeorological variations, emphasizing the optical complexity of the site. The typically turbidity of these waters and large variability makes the BB site distinctive among the different AERONET-OC stations, providing exceptional opportunities for the validation of atmospheric correction algorithms.

Data availability statement

The original contributions presented in the study are included in the article/Supplementary Material, further inquiries can be directed to the corresponding author.

Author contributions

MA: Data curation, Formal Analysis, Investigation, Methodology, Writing–original draft, Writing–review and editing. PP: Funding acquisition, Supervision, Writing–review and editing, Conceptualization. HL: Funding acquisition, Project administration, Resources, Supervision, Writing–review and editing, Conceptualization, Methodology. MT: Data curation, Investigation, Methodology, Writing–review and editing. DJ: Data curation, Methodology, Writing–review and editing. AD: Funding acquisition, Project administration, Supervision, Validation, Writing–review and editing, Conceptualization.

Funding

The author(s) declare financial support was received for the research, authorship, and/or publication of this article. The authors would like to thank the Consejo Nacional de Investigaciones Científicas y Técnicas (CONICET) for their financial support. This research was done in the frame of CO2BAHIA project founded by the ECOS2020 initiative (Programa de Cooperación Científico-Tecnológica entre el Ministerio de Ciencia, Tecnología e Innovación de la República Argentina, MNCyT, y ECOS-Sud de Francia), of ANR CO2COAST project (Grant Nos. ANR-20-CE01-0021), of

PICT2020-Serie A-02309 founded by the Agencia Nacional de Promoción de la Investigación, el Desarrollo Tecnológico y la Innovación and of "B8" Pampa Azul (MNCyT). The present research was carried out within the framework of the activities of the Spanish Government through the "María de Maeztu Centre of Excellence" accreditation to IMEDEA(CSIC-UIB) (CEX 2021-001198-M). A.L. Delgado acknowledges funding by an individual postdoctoral fellowship "Vicenç Mut" (PD/002/2022) from Govern de les Illes Balears and Fondo Social Europeo.

Acknowledgments

We specially thank the Cámara de Pescadores Artesanales de Monte Hermoso y Pehuén Co (Eduardo Flores and Juancito) and the Consorcio del Puerto de Bahía Blanca for their valuable help, since the collection of in situ samples would not have been possible without their continual contribution. Finally, the authors would like to thank EUMETSAT for the freely distribution of OLCI-A and OLCI-B data, and the AERONET Team for processing and distributing the AERONET-OC data.

Conflict of interest

The authors declare that the research was conducted in the absence of any commercial or financial relationships that could be construed as a potential conflict of interest.

Publisher's note

All claims expressed in this article are solely those of the authors and do not necessarily represent those of their affiliated organizations, or those of the publisher, the editors and the reviewers. Any product that may be evaluated in this article, or claim that may be made by its manufacturer, is not guaranteed or endorsed by the publisher.

Supplementary material

The Supplementary Material for this article can be found online at: https://www.frontiersin.org/articles/10.3389/frsen.2024.1305787/full#supplementary-material

References

Ahmad, Z., Franz, B. A., McClain, C. R., Kwiatkowska, E. J., Werdell, J., Shettle, E. P., et al. (2010). New aerosol models for the retrieval of aerosol optical thickness and normalized water-leaving radiances from the SeaWiFS and MODIS sensors over coastal regions and Open Oceans. *Appl. Opt.* 49 (29), 5545. doi:10.1364/ao.49.005545

Alikas, K., Ansko, I., Vabson, V., Ansper, A., Kangro, K., Uudeberg, K., et al. (2020). Consistency of radiometric satellite data over lakes and coastal waters with local field measurements. *Remote Sens.* 12 (4), 616. doi:10.3390/rs12040616

Arena, M., Delgado, A. L., Celleri, C., and Pratolongo, P. D. (2019). Preliminary assessment of spatial and short-term variability of bio-optical properties in a tidal dominated estuary (Bahía Blanca, Argentina). *Regional Stud. Mar. Sci.* 29, 100639. doi:10.1016/j.rsma.2019.100639

Arena, M., Delgado, A. L., Pratolongo, P., Celleri, C., and Vitale, A. (2021). "Validation of the atmospheric correction of Landsat OLI imagery and turbidity retrievals using AERONET-OC data from the Bahía Blanca site," in 2021 XIX Workshop on Information Processing and Control (RPIC) (IEEE), 1–6.

Arena, M., Pratolongo, P., Delgado, A. L., Celleri, C., and Vitale, A. (2022). Spatial and temporal distribution of satellite turbidity in response to different environmental variables in the Bahía Blanca Estuary, South-Western Atlantic. *Int. J. Remote Sens.* 43 (10), 3714–3743. doi:10.1080/01431161.2022.2105175

Astoreca, R., Doxaran, D. A. V. I. D., Ruddick, K., Rousseau, V., and Lancelot, C. H. R. I. S. T. I. A. N. E. (2012). Influence of suspended particle concentration, composition and size on the variability of inherent optical properties of the Southern North Sea. *Cont. Shelf Res.* 35, 117–128. doi:10.1016/j.csr.2012.01.007

Babin, M., Stramski, D., Ferrari, G. M., Claustre, H., Bricaud, A., Obolensky, G., et al. (2003). Variations in the light absorption coefficients of phytoplankton, nonalgal particles, and dissolved organic matter in coastal waters around Europe. *J. Geophys. Res. Oceans* 108 (C7). doi:10.1029/2001jc000882

Bailey, S. W., Franz, B. A., and Werdell, P. J. (2010). Estimation of near-infrared water-leaving reflectance for satellite ocean color data processing. *Opt. express* 18 (7), 7521–7527. doi:10.1364/oe.18.007521

Bailey, S. W., and Werdell, P. J. (2006). A multi-sensor approach for the on-orbit validation of ocean color satellite data products. *Remote Sens. Environ.* 102 (1-2), 12–23. doi:10.1016/j.rse.2006.01.015

Bi, S., Hieronymi, M., and Röttgers, R. (2023). Bio-geo-optical modelling of natural waters. *Front. Mar. Sci.* 10, 1196352. doi:10.3389/fmars.2023.1196352

Botha, E. J., Anstee, J. M., Sagar, S., Lehmann, E., and Medeiros, T. A. (2020). Classification of Australian waterbodies across a wide range of optical water types. *Remote Sens.* 12 (18), 3018. doi:10.3390/rs12183018

Cazzaniga, I., and Zibordi, G. (2023). AERONET-OC L WN uncertainties: revisited. *J. Atmos. Ocean. Technol.* 40 (4), 411–425. doi:10.1175/jtech-d-22-0061.1

Delgado, A. L., Guinder, V. A., Dogliotti, A. I., Zapperi, G., and Pratolongo, P. D. (2019). Validation of MODIS-Aqua bio-optical algorithms for phytoplankton absorption coefficient measurement in optically complex waters of El Rincón (Argentina). *Cont. Shelf Res.* 173, 73–86. doi:10.1016/j.csr.2018.12.012

Delgado, A. L., Loisel, H., Jamet, C., Vantrepotte, V., Perillo, G. M., and Piccolo, M. C. (2015). Seasonal and inter-annual analysis of chlorophyll-a and inherent optical properties from satellite observations in the inner and mid-shelves of the south of Buenos Aires Province (Argentina). *Remote Sens.* 7 (9), 11821–11847. doi:10.3390/rs70911821

Delgado, A. L., Menéndez, M. C., Piccolo, M. C., and Perillo, G. M. E. (2017). Hydrography of the inner continental shelf along the southwest Buenos Aires Province, Argentina: influence of an estuarine plume on coastal waters. *J. Coast. Res.* 33 (4), 907–916. doi:10.2112/jcoastres-d-16-00064.1

Doxaran, D., Froidefond, J. M., Lavender, S., and Castaing, P. (2002). Spectral signature of highly turbid waters: application with SPOT data to quantify suspended particulate matter concentrations. *Remote Sens. Environ.* 81 (1), 149–161. doi:10.1016/s0034-4257(01)00341-8

EUMETSAT (2019). *Sentinel-3 product notice – OLCI level-2 ocean Colour*. EUM/OPSSEN3/TEN/19/1068317.

EUMETSAT (2021). *Sentinel-3 OLCI L2 report for baseline collection OL_L2M_003*. https://www.eumetsat.int/media/47794.

Frouin, R., Schwindling, M., and Deschamps, P. Y. (1996). Spectral reflectance of sea foam in the visible and near-infrared: *in situ* measurements and remote sensing implications. *J. Geophys. Res. Oceans* 101 (C6), 14361–14371. doi:10.1029/96jc00629

Frouin, R. J., Franz, B. A., Ibrahim, A., Knobelspiesse, K., Ahmad, Z., Cairns, B., et al. (2019). Atmospheric correction of satellite ocean-color imagery during the PACE era. *Front. Earth Sci.* 7, 145. doi:10.3389/feart.2019.00145

GCOS (2011). *Systematic observation requirements for satellite-based products for climate*, 154. . Geneva: WMO GCOS Rep., 127. 2011 update.

Hieronymi, M., Bi, S., Müller, D., Schütt, E. M., Behr, D., Brockmann, C., et al. (2023). Ocean color atmospheric correction methods in view of usability for different optical water types. *Front. Mar. Sci.* 10, 1129876. doi:10.3389/fmars.2023.1129876

Hieronymi, M., Müller, D., and Doerffer, R. (2017). The OLCI neural network swarm (ONNS): a bio-geo-optical algorithm for open ocean and coastal waters. *Front. Mar. Sci.* 4, 140. doi:10.3389/fmars.2017.00140

Holben, B. N., Eck, T. F., Slutsker, I. A., Tanré, D., Buis, J. P., Setzer, A., et al. (1998). AERONET—a federated instrument network and data archive for aerosol characterization. *Remote Sens. Environ.* 66 (1), 1–16. doi:10.1016/s0034-4257(98)00031-5

Kirk, J. (2011). *Light and photosynthesis in aquatic ecosystems*. 3rd ed. Cambridge, UK: Cambridge University Press.

Lain, L. R., Bernard, S., and Evers-King, H. (2014). Biophysical modelling of phytoplankton communities from first principles using two-layered spheres: equivalent Algal Populations (EAP) model. *Opt. express* 22 (14), 16745–16758. doi:10.1364/oe.22.016745

Le, C., Li, Y., Zha, Y., Sun, D., Huang, C., and Zhang, H. (2011). Remote estimation of chlorophyll a in optically complex waters based on optical classification. *Remote Sens. Environ.* 115 (2), 725–737. doi:10.1016/j.rse.2010.10.014

Lee, Z. P., Du, K., Voss, K. J., Zibordi, G., Lubac, B., Arnone, R., et al. (2011). An inherent-optical-property-centered approach to correct the angular effects in water-leaving radiance. *Appl. Opt.* 50 (19), 3155–3167. doi:10.1364/ao.50.003155

Li, Q., Jiang, L., Chen, Y., Wang, L., and Wang, L. (2022). Evaluation of seven atmospheric correction algorithms for OLCI images over the coastal waters of Qinhuangdao in Bohai Sea. *Regional Stud. Mar. Sci.* 56, 102711. doi:10.1016/j.rsma.2022.102711

Liu, H., He, X., Li, Q., Hu, X., Ishizaka, J., Kratzer, S., et al. (2021). Evaluation of ocean color atmospheric correction methods for Sentinel-3 OLCI using global automatic *in situ* observations. *IEEE Trans. Geoscience Remote Sens.* 60, 1–19. doi:10.1109/tgrs.2021.3136243

Loisel, H., Mériaux, X., Poteau, A., Artigas, L. F., Lubac, B., Gardel, A., et al. (2009). Analyze of the inherent optical properties of French Guiana coastal waters for remote sensing applications. *J. Coast. Res.*, 1532–1536.

Lubac, B., and Loisel, H. (2007). Variability and classification of remote sensing reflectance spectra in the eastern English Channel and southern North Sea. *Remote Sens. Environ.* 110 (1), 45–58. doi:10.1016/j.rse.2007.02.012

Martos, P., and Piccolo, M. C. (1988). Hydrography of the Argentine continental shelf between 38° and 42°S. *Cont. Shelf Res.* 8 (9), 1043–1056. doi:10.1016/0278-4343(88)90038-6

Miller, R. L., Liu, C. C., Buonassissi, C. J., and Wu, A. M. (2011). A multi-sensor approach to examining the distribution of total suspended matter (TSM) in the Albemarle-Pamlico estuarine system, NC, USA. *Remote Sens.* 3 (5), 962–974. doi:10.3390/rs3050962

Mitchell, B. G. (1990). *Algorithms for determining the absorption coefficient for aquatic particulates using the quantitative filter technique*, 1302. . Orlando, FL: SPIE, 137–148. Ocean optics X.

Mitchell, B. G., and Stramska, M. (2002). Determination of spectral absorption coefficients of particles, dissolved material and phytoplankton for. *Ocean Opt. Protoc. Satell. ocean color Sens. validation Revis.* 3, 231, 210004.

Mobley, C. D. (1999). Estimation of the remote-sensing reflectance from above-surface measurements. *Appl. Opt.* 38 (36), 7442–7455. doi:10.1364/ao.38.007442

Moore, T. S., Dowell, M. D., Bradt, S., and Verdu, A. R. (2014). An optical water type framework for selecting and blending retrievals from bio-optical algorithms in lakes and coastal waters. *Remote Sens. Environ.* 143, 97–111. doi:10.1016/j.rse.2013.11.021

Morel, A., and Prieur, L. (1977). Analysis of variations in ocean color 1. *Limnol. Oceanogr.* 22 (4), 709–722. doi:10.4319/lo.1977.22.4.0709

Mueller, J. L., Davis, C. O., Arnone, R. A., Frouin, R., Carder, K. L., Lee, Z. P., et al. (2003). Above-water radiance and remote sensing measurement and analysis protocols. Ocean Optics protocols for Satellite Ocean-color sensor validation, revision 4, vol. III: radiometric measurements and data analysis protocols. NASA Tech. Memo, 21162.

Neukermans, G., Ruddick, K., Loisel, H., and Roose, P. (2012). Optimization and quality control of suspended particulate matter concentration measurement using turbidity measurements. *Limnol. Oceanogr. Methods* 10 (12), 1011–1023. doi:10.4319/lom.2012.10.1011

Perillo, G. M. E., Piccolo, M. C., Palma, E. D., Pérez, D. E., and Pierini, J. O. (2004). *Oceanografía física: ecosistema del estuario de Bahía Blanca*, 61–67.

Piccolo, M. C., and Perillo, G. M. (1990). Physical characteristics of the Bahía Blanca estuary (Argentina). *Estuar. Coast. Shelf Sci.* 31 (3), 303–317. doi:10.1016/0272-7714(90)90106-2

Pratolongo, P., Piovan, M. J., Cuadrado, D. G., and Gómez, E. A. (2017). Coastal landscape evolution on the western margin of the Bahía Blanca Estuary (Argentina) mirrors a non-uniform sea-level fall after the mid-Holocene highstand. *Geo-Marine Lett.* 37 (4), 373–384. doi:10.1007/s00367-016-0480-4

Spyrakos, E., O'Donnell, R., Hunter, P. D., Miller, C., Scott, M., Simis, S. G., et al. (2018). Optical types of inland and coastal waters. *Limnol. Oceanogr.* 63 (2), 846–870. doi:10.1002/lno.10674

Steinmetz, F., Deschamps, P. Y., and Ramon, D. (2011). Atmospheric correction in presence of sun glint: application to MERIS. *Opt. express* 19 (10), 9783–9800. doi:10.1364/oe.19.009783

Stramska, M., and Petelski, T. (2003). Observations of oceanic whitecaps in the north polar waters of the Atlantic. *J. Geophys. Res. Oceans* 108 (C3). doi:10.1029/2002jc001321

Talone, M., Zibordi, G., and Lee, Z. (2018). Correction for the non-nadir viewing geometry of AERONET-OC above water radiometry data: an assessment of uncertainties. *Opt. Express* 26, A541–A561. doi:10.1364/OE.26.00A541

Thuillier, G., Hersé, M., Labs, D., Foujols, T., Peetermans, W., Gillotay, D., et al. (2003). The solar spectral irradiance from 200 to 2400 nm as measured by the SOLSPEC spectrometer from the ATLAS and EURECA missions. *Sol. Phys.* 214, 1–22.

Tilstone, G. H., Pardo, S., Simis, S. G., Qin, P., Selmes, N., Dessailly, D., et al. (2021). Consistency between satellite ocean colour products under high coloured dissolved organic matter absorption in the Baltic Sea. *Remote Sens.* 14 (1), 89. doi:10.3390/rs14010089

Tran, M. D., Vantrepotte, V., Loisel, H., Oliveira, E. N., Tran, K. T., Jorge, D., et al. (2023). Band ratios combination for estimating chlorophyll-a from sentinel-2 and sentinel-3 in coastal waters. *Remote Sens.* 15 (6), 1653. doi:10.3390/rs15061653

Vanhellemont, Q., and Ruddick, K. (2021). Atmospheric correction of Sentinel-3/OLCI data for mapping of suspended particulate matter and chlorophyll-a concentration in Belgian turbid coastal waters. *Remote Sens. Environ.* 256, 112284. doi:10.1016/j.rse.2021.112284

Vantrepotte, V., Loisel, H., Dessailly, D., and Mériaux, X. (2012). Optical classification of contrasted coastal waters. *Remote Sens. Environ.* 123, 306–323. doi:10.1016/j.rse.2012.03.004

Wang, M., and Shi, W. (2006). Cloud masking for ocean color data processing in the coastal regions. *IEEE Trans. Geoscience Remote Sens.* 44 (11), 3196–3105. doi:10.1109/tgrs.2006.876293

Wei, J., Lee, Z., Garcia, R., Zoffoli, L., Armstrong, R. A., Shang, Z., et al. (2018). An assessment of Landsat-8 atmospheric correction schemes and remote sensing reflectance products in coral reefs and coastal turbid waters. *Remote Sens. Environ.* 215, 18–32. doi:10.1016/j.rse.2018.05.033

Wei, J., Wang, M., Mikelsons, K., Jiang, L., Kratzer, S., Lee, Z., et al. (2022). Global satellite water classification data products over oceanic, coastal, and inland waters. *Remote Sens. Environ.* 282, 113233. doi:10.1016/j.rse.2022.113233

Welschmeyer, N. A. (1994). Fluorometric analysis of chlorophyll a in the presence of chlorophyll b and pheopigments. *Limnol. Oceanogr.* 39 (8), 1985–1992. doi:10.4319/lo.1994.39.8.1985

Windle, A. E., Evers-King, H., Loveday, B. R., Ondrusek, M., and Silsbe, G. M. (2022). Evaluating atmospheric correction algorithms applied to olci sentinel-3 data of Chesapeake Bay Waters. *Remote Sens.* 14 (8), 1881. doi:10.3390/rs14081881

Zibordi, G., D'Alimonte, D., and Kajiyama, T. (2022). Automated quality control of AERONET-OC L WN data. *J. Atmos. Ocean. Technol.* 39 (12), 1961–1972. doi:10.1175/jtech-d-22-0029.1

Zibordi, G., Mélin, F., and Berthon, J. F. (2018). A regional assessment of OLCI data products. *IEEE Geoscience Remote Sens. Lett.* 15 (10), 1490–1494. doi:10.1109/lgrs.2018.2849329

Zibordi, G., Mélin, F., Berthon, J. F., Holben, B., Slutsker, I., Giles, D., et al. (2009). AERONET-OC: a network for the validation of ocean color primary products. *J. Atmos. Ocean. Technol.* 26 (8), 1634–1651. doi:10.1175/2009jtecho654.1

Zibordi, G., and Talone, M. (2020). On the equivalence of near-surface methods to determine the water-leaving radiance. *Opt. Express* 28 (3), 3200–3214. doi:10.1364/oe.28.003200

frontiers | Frontiers in Remote Sensing

TYPE Original Research
PUBLISHED 14 March 2024
DOI 10.3389/frsen.2024.1335627

Check for updates

OPEN ACCESS

EDITED BY
Kevin Ruddick,
Royal Belgian Institute of Natural Sciences, Belgium

REVIEWED BY
Pieter De Vis,
National Physical Laboratory, United Kingdom
Astrid Bracher,
Alfred Wegener Institute Helmholtz Centre for Polar and Marine Research (AWI), Germany
B. Carol Johnson,
National Institute of Standards and Technology (NIST), United States

*CORRESPONDENCE
Jing Tan,
jit079@ucsd.edu

RECEIVED 09 November 2023
ACCEPTED 14 February 2024
PUBLISHED 14 March 2024

CITATION
Tan J, Frouin R, Häentjens N, Barnard A, Boss E, Chamberlain P, Mazloff M and Orrico C (2024), Reconstructing hyper-spectral downwelling irradiance from multi-spectral measurements. *Front. Remote Sens.* 5:1335627. doi: 10.3389/frsen.2024.1335627

COPYRIGHT
© 2024 Tan, Frouin, Häentjens, Barnard, Boss, Chamberlain, Mazloff and Orrico. This is an open-access article distributed under the terms of the Creative Commons Attribution License (CC BY). The use, distribution or reproduction in other forums is permitted, provided the original author(s) and the copyright owner(s) are credited and that the original publication in this journal is cited, in accordance with accepted academic practice. No use, distribution or reproduction is permitted which does not comply with these terms.

Reconstructing hyper-spectral downwelling irradiance from multi-spectral measurements

Jing Tan[1]*, Robert Frouin[1], Nils Häentjens[2], Andrew Barnard[3], Emmanuel Boss[2], Paul Chamberlain[1], Matt Mazloff[1] and Cristina Orrico[4]

[1]Scripps Institution of Oceanography, University of California, San Diego, La Jolla, CA, United States, [2]School of Marine Sciences, University of Maine, Orono, ME, United States, [3]College of Earth, Ocean, and Atmospheric Sciences, Oregon State University, Corvallis, OR, United States, [4]Sea-Bird Scientific, Philomath, OR, United States

Checking the radiometric calibration of satellite hyper-spectral sensors such as the PACE Ocean Color Instrument (OCI) while they operate in orbit and evaluating remote sensing reflectance, the basic variable from which a variety of optical and biogeochemical ocean properties can be derived, requires measuring upwelling radiance just above the surface (L_w) and downwelling planar irradiance reaching the surface (E_s). For this, the current HyperNav systems measure L_w at about 2 nm spectral resolution in the ultraviolet to near infrared, but E_s in only four 10 nm wide spectral bands centered on 412, 489, 555, and 705 nm. In this study, the E_s data acquired in these spectral bands in clear sky conditions are used to reconstruct via a multi-linear regression model the hyper-spectral E_s signal at 0.5 nm resolution from 315 to 900 nm, the OCI spectral range, allowing an estimate of E_s at the HyperNav, OCI, and other sensors' resolutions. After correction of gaseous absorption and normalization by the top-of-atmosphere incident solar flux, the atmospheric diffuse transmittance is expressed as a linear combination of E_s measured in those 4 spectral bands. Based on simulations for Sun zenith angles from 0 to 75° and a wide range of (i.e., expected) atmospheric, surface, and water conditions, the E_s spectrum is reconstructed with a bias of less than 0.4% in magnitude and an RMS error (RMSE) ranging from 0% to 2.5%, depending on wavelength. The largest errors occur in spectral regions with strong gaseous absorption. In the presence of typical noise on E_s measurements and uncertainties on the ancillary variables, the bias and RMSE become −2.5% and 7.0%, respectively. Using a General Additive Model with coefficients depending on Sun zenith angle and aerosol optical thickness at 550 nm improves statistical performance in the absence of noise, especially in the ultraviolet, but provides similar performance on noisy data, indicating more sensitivity to noise. Adding spectral bands in the ultraviolet, e.g., centered on 325, 340, and 380 nm, yields marginally more accurate results in the ultraviolet, due to uncertainties in the gaseous transmittance. Comparisons between the measured and reconstructed E_s spectra acquired by the MOBY spectroradiometer show agreement within predicted uncertainties, i.e., biases less than 2% in magnitude and RMS differences less than 5%. Reconstruction can also be achieved accurately with other sets of spectral bands and extended to cloudy conditions since cloud optical properties, like aerosol properties, tend to vary regularly with wavelength. These results indicate that it is sufficient, for many

scientific applications involving hyper-spectral E_s, to measure E_s in a few coarse spectral bands in the ultraviolet to near infrared and reconstruct the hyperspectral signal using the proposed multivariate linear modeling.

KEYWORDS

HyperNav, downwelling planar irradiance, multivariate regression, generalized additive model, ocean Color, MOBY, PACE

1 Introduction

Water-leaving radiance (L_w) and remote sensing reflectance (R_{rs}, or the ratio of L_w and downwelling planar irradiance reaching the air-water interface E_s), $R_{rs} = L_w/E_s$, are basic aquatic optical variables from which properties of the water body can be retrieved for a variety of scientific and societal applications (e.g., IOCCG, 2008; Frouin et al., 2019). System Vicarious Calibration (SVC), an important procedure to ensure that satellite L_w estimates meet requirements for biogeochemistry (Evans and Gordon, 1994; Gordon, 1997; IOCCG, 2013), necessitates measuring L_w accurately at the time of satellite overpass (Franz et al., 2007; Zibordi et al., 2015). Inversion schemes to retrieve inherent optical properties (IOPs) and biogeochemical characteristics of the water body require R_{rs} (or similar normalized L_w variables) as input (e.g., Werdell et al. (2018)). Measurements of R_{rs} are therefore essential to develop algorithms for inferring those properties/characteristics, and to evaluate their retrieval. Diverse instrumentation, installed on fixed platforms or deployed from ships, has been used to measure L_w and E_s (therefore R_{rs}) spectrally, and deployment/measurement protocols defined to provide best data quality with associated uncertainties (e.g., Mueller et al. (2003); Ruddick et al. (2019a) for L_w; Ruddick et al. (2019b) for E_s).

For the upcoming PACE mission, which will carry into polar orbit the Ocean Color Instrument (OCI), the HyperNav spectroradiometer/float system (Barnard et al., 2024, this issue) was designed to measure L_w at about 2 nm resolution (full width at half maximum) from 250 to 900 nm. The system is also equipped with a commercial (SeaBird, Inc.) cosine sensor that measures E_s in 4 spectral bands about 10 nm wide centered on 412, 489, 555, and 705 nm. The E_s measurements do not allow direct normalization of L_w into R_{rs} over the entire spectral range and at the spectral resolution of the L_w measurements, but this is highly desirable for evaluating the PACE OCI hyper-spectral R_{rs} retrievals at 5 nm resolution. Accurate reconstruction of the E_s spectrum from measurements in a few coarse spectral bands is possible, however, because the solar irradiance reaching the surface is strongly correlated spectrally, even though gaseous absorption only modulates specific regions of the solar spectrum, which requires proper treatment.

In the following, a methodology is presented and evaluated to reconstruct E_s at 0.5 nm resolution from 315 to 900 nm (the OCI spectral range) in clear sky conditions from E_s measurements in 10 nm bands centered on 412, 489, 555, and 705 nm. The methodology is based on multi-linear regression and includes uncertainty estimation via Monte Carlo propagation (Section 2). Simulations for expected (realistic) atmospheric, surface, and aquatic conditions and Sun zenith angles are described in Section 3. Performance is evaluated theoretically in the absence and presence of noise in Section 4, as well as the merits of an additive varying coefficient model with aerosol optical thickness and Sun zenith angle as auxiliary variables. The methodology is checked experimentally on E_s spectral measurements collected at and near the MOBY site in Section 5. The applicability to other sets of spectral bands, and the advantage and drawback of including additional bands in the ultraviolet, is discussed in Section 6, as well as the ability to reproduce accurately E_s at the HyperNav and OCI spectral resolutions. The study is summarized in Section 7, with conclusions on the accuracy of the reconstruction and the possible extension to cloudy conditions since cloud properties, like aerosol properties, tend to vary smoothly with wavelength, and recommendations, in view of the applications, on the need for hyper-spectral E_s sensors instead of multi-band sensors.

2 Methodology

In clear atmosphere, the downwelling planar solar irradiance reaching ocean surface, E_s, can be modeled accurately as in Eq. 1 (e.g., Tanré et al., 1979):

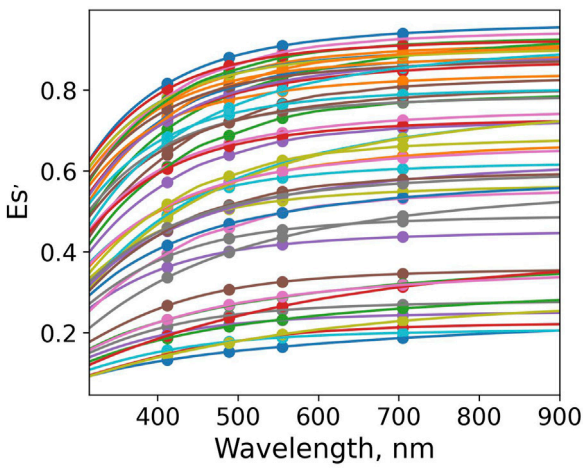


FIGURE 1
Es'of the 50 cases simulated using ARTDECO with parameters randomly selected, i.e., different aerosol models (maritime clean, continental, urban, desert), aerosol optical thickness at 550 nm from 0 to 0.8, aerosol scale height from 0.5 to 5 km, relative humidity from 60% to 90%, ozone amount from 250 to 450 Dobson, water vapor from 0.1 to 7 g cm^{-2}, surface pressure from 1,000 to 1,025 mb, solar zenith angle from 0° to 75°, wind speed from 5 to 15 m s^{-1}, and chlorophyll concentration from 0.3 to 30 mg m^{-3}. Dots represent the Es' values at 412, 489, 555, and 705 nm.

$$E_s = E_0 \cos(\theta_s) T_g T_a / (1 - S_a A) \quad (1)$$

where E_0 is the extraterrestrial (top-of-atmosphere, TOA) solar irradiance corrected for Earth Sun distance, θ_s is the solar zenith angle, T_g and T_a denote the downward gaseous transmittance and total (direct plus diffuse) atmospheric transmittance, respectively, S_a is the spherical albedo of the atmosphere, and A is the surface albedo.

The hypothesis that it is feasible to reconstruct E_s at hyperspectral resolution using measurements at only a few bands is based on the fact that E_s after the correction of gaseous absorption and normalization using the extraterrestrial solar irradiance, i.e., $E_s' = E_s/(E_0 T_g)$, essentially becomes $T_a \cos(\theta_s)/(1 - S_a A)$, which varies smoothly with wavelength (Figure 1). However, even though E_s' does not exhibit an irregular spectral dependence, its reconstruction via interpolation/extrapolation of measurements in a few bands may not be sufficiently accurate (see Section 4). Therefore, we tested two different models:

1. Multivariate linear model with constant coefficients (Eq. 2).

$$E_s'(\lambda) = a_0 + \sum_i a_i E_s'(\lambda_i) \quad (2)$$

where a_0 is a constant, λ represents wavelength, $E_s'(\lambda_i)$ and a_i are the E_s' and the corresponding linear coefficients at λ_i, the center wavelengths i of the 412, 489, 555, and 705 nm bands.

2. Generalized additive model (GAM; Hastie and Tibshirani, 1993) with coefficients as functions of geometric and/or geophysical parameters (Eq. 3).

$$E_s'(\lambda) = f_0(p_1, p_2, \ldots, p_n) + \sum_i f_i(p_1, p_2, \ldots, p_n) E_s'(\lambda_i) \quad (3)$$

where $p_1, p_2, \ldots, p_n$ represent the various geometric and/or geophysical parameters to be used, and f are functions of these variables. The parameters p are selected based on analysis of the data. The f functions constitute the free parameters of the model and will be estimated from the data. The shapes of f are largely unspecified in the fitting procedure, while the resulting number of degrees of freedom are controlled to avoid overfitting. This is achieved via penalized smoothing splines.

Once E_s' is retrieved, E_s can be derived from E_s' since E_0 is known and T_g can be accurately estimated (see Section 4). Uncertainties of the two methods are quantified by introducing noise to the input E_s at the four wavelengths, together with assigning noise to T_g, which will then be propagated to estimate the uncertainties in reconstructed E_s using the Monte-Carlo method (e.g., JCGM, 2008; Bialek et al., 2020. This requires the probability distribution functions for the input components in the model equation (content of gaseous absorbers in the multilinear model with constant coefficients and, additionally, the auxiliary variables in the additive varying coefficient model), from which many random realizations are selected in the calculation of the output, providing the uncertainty of the output value.

The reconstruction of E_s described above is accomplished with respect to the extraterrestrial solar spectrum E_0 used in the radiative transfer (RT) model. One has to be aware of this in calibration/validation activities and make sure that the same E_0 is used. Using a different E_0, however, does not require re-determining the coefficients of the E_s' model (Eq. 2).

3 Simulations

Radiative transfer simulations were performed from 315 to 900 nm at 0.5 nm resolution with the Atmospheric Radiative Transfer Database for Earth Climate Observation (ARTDECO) code (Dubuisson et al., 2016) for a variety of geometric and geophysical conditions. The ARTDECO radiative transfer model accounts for scattering and absorption by air molecules, aerosols, and cloud droplets, and interactions between scattering and absorption. The radiative transfer equation is solved using the discrete ordinate method. The atmosphere is assumed plane-parallel and positioned above a wavy air-sea interface. In the code, the high-resolution extraterrestrial solar spectrum is from Chance and Kurucz (2010), mean Earth-Sun distance is used, and gaseous absorption is accounted for by applying the correlated-k technique (Lacis and Oinas, 1991) with appropriate k-distribution coefficients. The optical properties of aerosols and clouds are selected from the Optical Properties of Aerosols and Clouds (OPAC) database (Hess et al., 1998). The vertical distribution of the scatterers and absorbers can be specified. The bidirectional reflectance of the wavy interface is modeled based on Fresnel equations and the Cox-Munk wind-dependent wave slope probability density distribution. The diffuse water reflectance (Case 1 waters only) is assumed Lambertian and modeled as a function of chlorophyll concentration according to Morel and Maritorena (2001). This model, limited to the visible, was extended to 300 nm using Hydrolight (Hedley and Mobley, 2019) inherent optical properties. The water body is considered black at wavelengths longer than 700 nm. This treatment is sufficient because the impact of photons leaving the water that are backscattered by the atmosphere to the surface is relatively small.

The total downwelling solar irradiance arriving at the ocean surface E_s was simulated from 315 to 900 nm with a 0.5 nm resolution for a clear atmosphere (i.e., no clouds). The corresponding extraterrestrial solar irradiance E_0 was also output in the simulations. In the code, the AFGL US standard atmosphere profile (Anderson et al., 1986) was used and adapted to the input concentrations of gases, i.e., ozone, water vapor, and oxygen. Note that by explicitly varying the oxygen amount the absorption from other gases including CH_4, CO_2, and N_2O was considered since the molar fraction of these gases are fixed with respect to oxygen in the ARTDECO code. Since absorption from NO_2 was not modeled in ARTDECO, transmittance of NO_2 was estimated based on Schneider et al. (1987) and applied to the simulated E_s. In this study, the following three different datasets were generated.

1. Dataset for calibrating the models for E_s reconstruction, referred as the calibration dataset.

In this dataset, four different aerosol models from the OPAC database were considered, i.e., maritime clean, continental clean, urban, and desert, including both absorbing and non-absorbing aerosols. The computations were conducted for total aerosol optical thickness values (AOT550) ranging from 0 to 0.8 at 550 nm. The

aerosol concentration was set to decrease with altitude according to an exponential law with a typical scale height (SH) from 0.5 to 5 km. The relative humidity (RH) in the atmosphere was set to randomly vary from 60% to 90%. The amount of ozone (U_o3) and water vapor (U_h2o) were from 250 to 450 Dobson and from 0.1 to 7 g cm^{-2}, respectively. The oxygen amount is defined using surface pressure (PS), which was varied from 1,000 to 1,025 mb. Simulations were carried out for Sun zenith angles (SZAs) ranging from 0° to 75° (view zenith and relative azimuth were fixed as 0° and 90°, since they do not affect $\boldsymbol{E_s}$). The wind speed (U) was set to vary from 5 to 15 m s^{-1}. The optical properties of the diffuse boundary marine reflectance were specified for chlorophyll concentration (Chl) varying from 0.03 to 30 mg m^{-3}. A total of 10,000 simulations were performed, with aerosol types, aerosol optical thickness, scale height, humidity, ozone, surface pressure, water vapor, Sun zenith angle, wind speed, chlorophyll concentration randomly varied in the ranges described above. For each simulation with gaseous absorption, the case of no gaseous absorption was also generated to obtain $\boldsymbol{E_{s0}}$, i.e., $\boldsymbol{E_s}$ after correction of gaseous absorption ($\boldsymbol{E_s} = \boldsymbol{E_{s0}}\boldsymbol{T_g}$).

2. Dataset for developing the Look-Up Table (LUT) of $\boldsymbol{T_g}$, referred as the LUT dataset.

In this dataset, the ranges of different geometric and geophysical parameters are the same as those in the calibration dataset. What is different is that the input amount of ozone, water vapor and oxygen as well as Sun zenith angles were set to be discrete values as below.

- SZA (degree): 0, 10, 20, 30, 40, 50, 60, 65, 70, and 75
- U_o3 (Dobson): 250, 300, 350, 400, 450
- U_h2o (g cm^{-2}): 0.1, 0.2, 0.3, 0.4, 0.5, 0.6, 0.7, 0.8, 0.9, 1, 2, 3, 4, 5, 6, 7
- PS (mb): 1,000, 1,005, 1,010, 1,015, 1,020, 1,025

Both simulations with and without gaseous absorption were made. The aerosol properties and surface conditions have a small impact on $\boldsymbol{T_g}$, except in strong water vapor absorption bands, where the coupling between aerosol scattering and water vapor absorption becomes effective, but such bands occur above 900 nm. Therefore these parameters were fixed for each simulation, i.e., AOT550 = 0.1, RH = 90%, SH = 2 km, maritime aerosol, U = 5 m/s, and Ch1 = 0.1 mg/m^3. The LUT has four axes, i.e., Sun zenith angle, ozone and water vapor amounts, and pressure.

3. Dataset for validating the models for $\boldsymbol{E_s}$ reconstruction, referred as the validation dataset.

Instead of using the four different OPAC aerosols, this dataset uses mixed aerosols, i.e., all aerosol species were mixed up for each simulation. The aerosol species include black carbon (OPAC urban), dust (OPAC Desert), organic carbon (OPAC continental), and sea salt (OPAC maritime). Global hourly MERRA-2 reanalysis data (Gelaro et al., 2017) for the entire year 2006 were acquired to extract the optical thickness corresponding to each aerosol species, which were then randomly selected (covering global ocean) and input to ARTDECO. Other parameters were set in the same predefined ranges as in the calibration dataset but with totally different values. There are 10,000 simulations with gaseous absorption and another 10,000 without gaseous absorption. Noise was also added to this dataset to evaluate the sensitivity of the models to noise, of which the details are described in Section 4.

For the calibration and validation datasets, the $\boldsymbol{E_s}$ and $\boldsymbol{E_{s0}}$ simulations at 0.5 nm resolution were further processed into the values in the 412, 488, 555, and 705 nm bands by using the average within ±5 nm of the center wavelengths (the exact spectral response of the bands was unknown).

4 Theoretical results

The LUT developed in Section 3 was used to estimate $\boldsymbol{T_g}$ for the 10,000 cases in the calibration dataset and another 10,000 cases in the validation dataset using the prescribed solar zenith angle, ozone, amount, surface pressure, and water vapor amount as input and linearly interpolating within the LUT. Figure 2 shows that the LUT method produces accurate estimation of $\boldsymbol{T_g}$, with the bias ranging from −0.6% to 0.3% and from −2.5% to 0.4% and RMS error (RMSE) within 2.5% and within 3%, for the calibration and validation dataset, respectively. The bias and RMSE for the calibration and validation dataset are different because the input parameters to the LUT are not exactly the same. Remember that −2.5% bias is equivalent a bias of −0.004, which is very small. As expected, degradation of accuracy is found at the wavelengths with gaseous absorption, for example, the ultra-violet (UV) and 500–700 nm with ozone absorption, ~688 nm and ~760 nm with strong oxygen absorption, and near-infrared with water vapor absorption, while at the wavelengths almost without gaseous absorption the bias and RMS error are close to 0. This is with the assumption that the amount of ozone, surface pressure, and water vapor are perfectly known. In practice, noise in these quantities will introduce uncertainties in the estimated $\boldsymbol{T_g}$ and the impact on the $\boldsymbol{E_s}$ reconstruction is investigated, as described in the text below.

$\boldsymbol{E_s'}$ at 0.5 nm resolution from 315 nm to 900 nm can be accurately reconstructed using the values at 412, 489, 555, and 705 nm using multivariate linear regression (Figure 3). The $\boldsymbol{a_0}$ and $\boldsymbol{a_i}$ coefficients in Eq. 2, are irregular spectrally (Figure 4), an indication that simple interpolation/extrapolation would not capture spectral $\boldsymbol{E_s'}$ variability as well as the multilinear model. Bias is 0 for all the wavelengths, which is not surprising because the model is supposed to be unbiased. The RMSE is less than 0.1% starting from 400 nm and increases to 0.6% in the UV wavelengths. The relatively high error in the UV is probably due to the fact that the input four wavelengths are from 400 to 700 nm, which may fail to properly capture some of the spectral characteristics at the UV. The $\boldsymbol{E_s}$ spectra were computed using $\boldsymbol{E_0}$ and the estimated $\boldsymbol{T_g}$. The bias, ranging from −0.2% to 0.4%, and RMSE, from 0% to 2.5%, are basically the total of $\boldsymbol{T_g}$ and $\boldsymbol{E_s'}$ errors, although some compensation occurs so that the values are slightly lower.

The prescribed $\boldsymbol{E_s'}$ was further modeled as a function of all other variables, including the estimated $\boldsymbol{E_s'}$ ($\boldsymbol{E_{s,est}'}$), SZA, AOT550, SH, aerosol model (A), Chl, U, RH, and PS, following the procedure of Bisson et al. (2021) using a Bayesian approach to multivariate

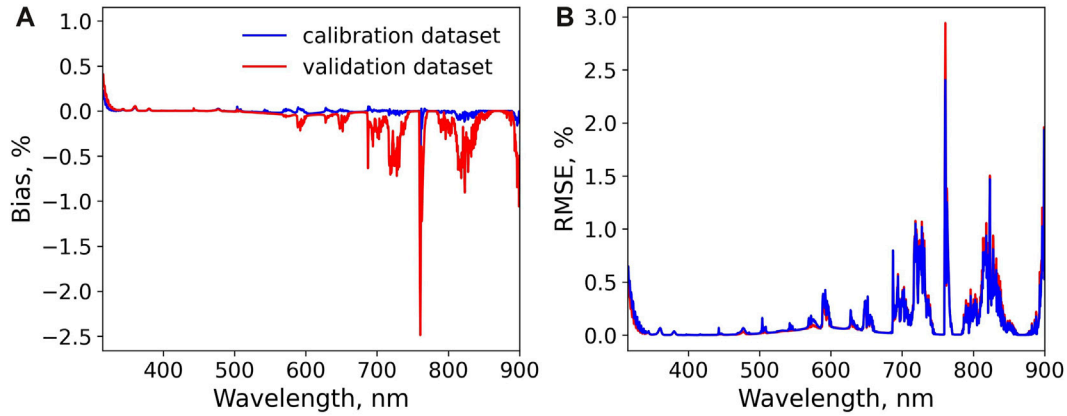


FIGURE 2
Percent bias **(A)** and RMSE **(B)** of T_g estimation using the calibration (blue) and validation (red) dataset.

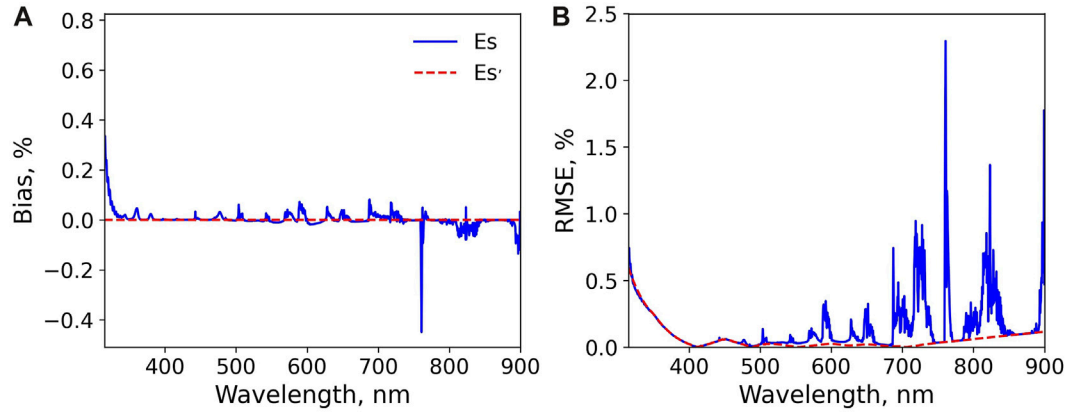


FIGURE 3
Percent bias **(A)** and RMSE **(B)** of $E_s^{'}$ (red dashed) and E_s (blue solid) estimation using the calibration dataset and multivariate linear regression.

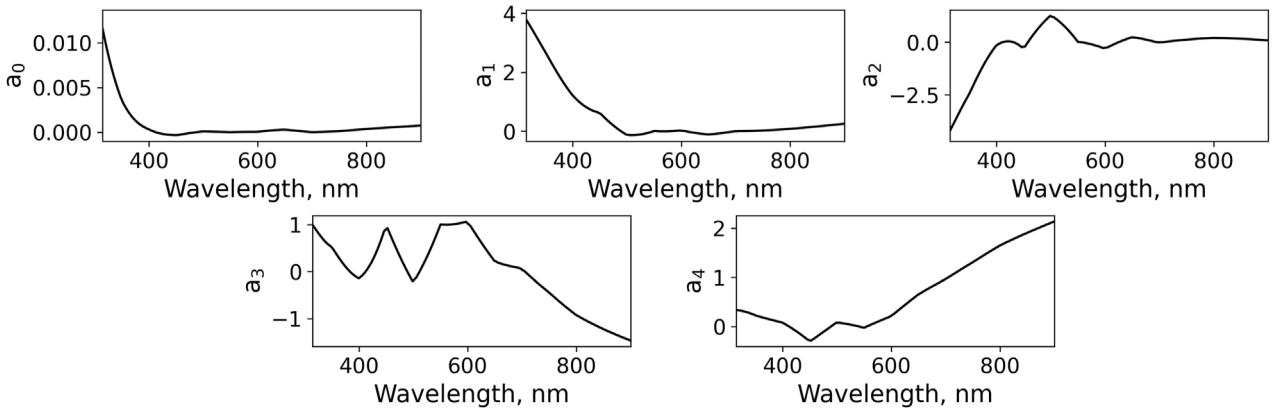


FIGURE 4
Coefficients of the multilinear model (see Eq. 2).

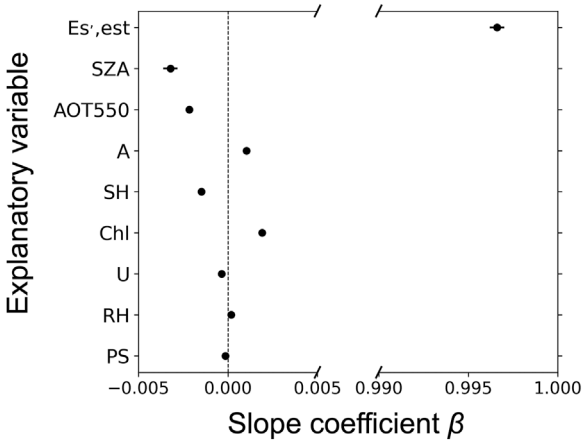


FIGURE 5
Forest plot of the slope coefficients for wavelength 320.25 nm. The y axis shows the coefficients β for each explanatory variable, i.e., estimated E_s' ($E_{s,est}'$), solar zenith angle (SZA), aerosol optical thickness (AOT550), aerosol model (A), scale height (SH), chlorophyll concentration (Chl), wind speed (U), relative humidity (RH), and surface pressure (PS), and the x axis shows the scale of the coefficients. The circle presents the mean of the posterior and the error bar represents the standard deviation of the distribution.

regression analysis. U_o3 and U_h2o were not included because E_s' is the quantity after gaseous absorption. The regression model is assumed to follow a normal distribution with the mean μ modeled as in Eq. 4

$$\mu = \beta_0 E_{s,est}' + \beta_1 SZA + \beta_2 AOT550 + \beta_3 SH + \beta_4 A + \beta_5 Chl + \beta_6 U + \beta_7 RH + \beta_8 PS + \alpha \quad (4)$$

Each variable was standardized by subtracting the mean and dividing by the standard deviation to shift the distribution to have a mean of zero and a standard deviation of one. By doing so, the intercept bias α essentially becomes zero and the slope coefficients β_i illustrate a one-to-one correspondence between the dependent and independent variables. In the model, the prior distribution of β_i is assumed weakly informative, with mean of zero and a standard deviation of 100. For example, at 320.25 nm, the slope coefficient β_0 is very close to 1, i.e., ~0.997 (Figure 5), indicating strong correspondence between E_s' and $E_{s,est}'$. The β for other variables all deviate from 0, although the deviations are small, indicating their contribution to residual errors. Based on the magnitude of the β values, the three variables with the highest absolute values are SZA, AOT550, and Chl. Large percent errors are typically found to be associated with small E_s', which is not easy to model accurately. When SZA is large, it means longer travelling path and more interactions of the light with aerosols and molecules in the atmosphere. The larger AOT550, the more aerosol scattering and absorption, depending on the aerosol types. Both variables lead to small E_s' and may explain their relatively large contributions in the residual errors. The variations in chlorophyll concentration affect the ocean surface albedo. In the UV, when chlorophyll concentration is small, the ocean surface albedo becomes relatively large and the spherical albedo of the atmosphere is increased, hence the surface impact introduced by the term $1/(1 - S_a A)$ may cause perturbations in E_s' and inaccuracy in the modeling.

The variables SZA, AOT550, aerosol type, SH, Chl, U, RH, and PS were then tested in the GAM model. These variables were introduced one by one and only those that brought in significant model improvement were selected, i.e., SZA and AOT550 in this study. The GAM model therefore becomes Eq. 5:

$$E_s'(\lambda) = f_0(SZA, AOT550) + \sum_i f_i(SZA, AOT550) E_s'(\lambda_i) \quad (5)$$

With the coefficients as a function of SZA and AOT550 instead of assumed constant, the accuracy of E_s' reconstruction is improved (Figure 6). The bias is not discussed here because both models are unbiased. The change of percent RMSE with wavelength shows a pattern similar to that obtained using multivariate linear regression, i.e., the closer the wavelength is to one of the input four bands the smaller the RMSE. Overall, the magnitude is lower for GAM as opposed to the linear model, especially in the wavelengths shorter than 400 nm and those longer than 700 nm. For example, the error drops from 0.6% to 0.2% in the UV and from 0.1% to 0.06% at 900 nm. An even stronger decrease of RMSE in the UV and from 850 to 900 nm is observed for the E_s reconstruction when using GAM. The terms of the five components (i.e., the functions f_0,f_1,f_2,

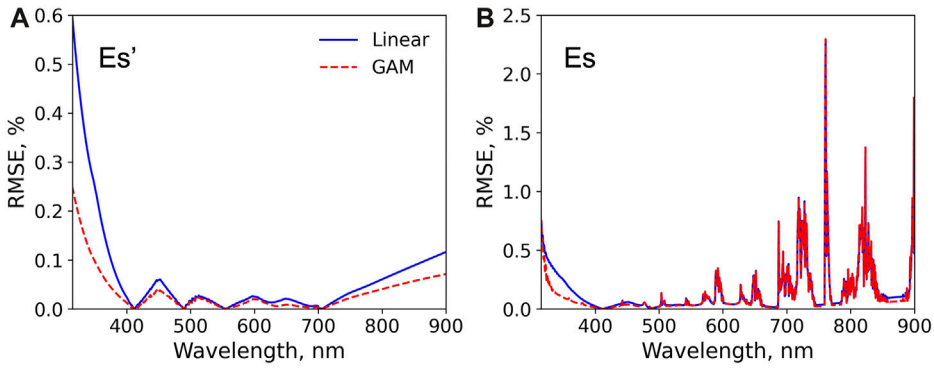


FIGURE 6
Percent RMSE of E_s' **(A)** and E_s **(B)** estimation using the calibration dataset with both models: (blue) multivariate linear regression and (red) GAM. Percent bias is not shown as both models result in almost identical bias for E_s' and E_s.

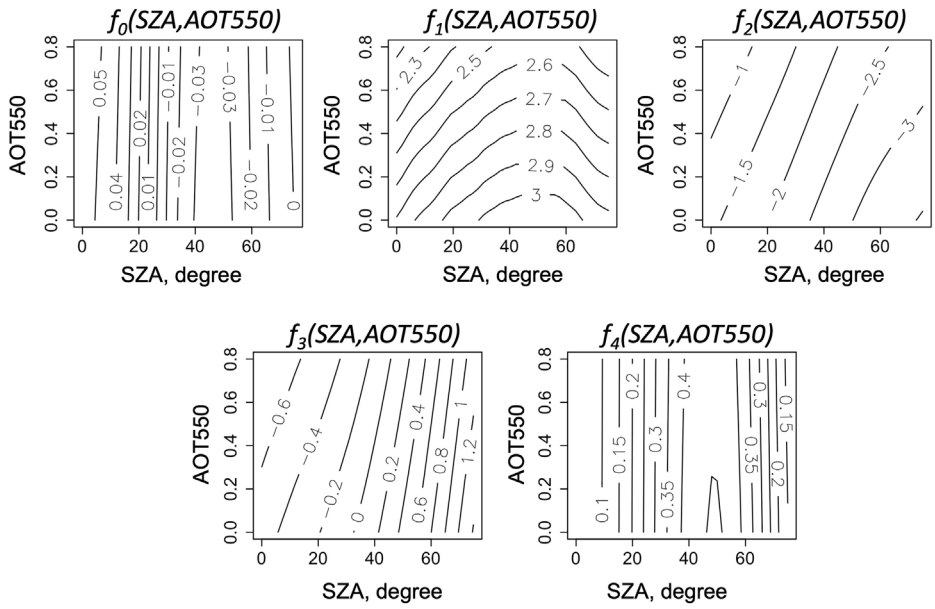


FIGURE 7
The five component smooth functions (f_0, f_1, f_2, f_3, and f_4) of the GAM model fitted on the calibration data at 320.25 nm.

f_3 and f_4) of the GAM model at 320.25 nm and 410.25 nm are displayed in Figures 7, 8, respectively. It is thus clear that the intercept as well as the coefficients for $E_s^{'}$ at the four wavelengths are not constant and the contours show how the values of f_i change with SZA and AOT550. The gradients of the component smooth functions f_i at 410.25 nm are much smaller than those at 310.25 nm, which is expected as the residual errors in $E_s^{'}$ attributed to SZA and AOT550 are more pronounced in the UV. At 320.25 nm the gradient of each f_i changes with SZA, while the impact AOT550 is more obvious on f_1, f_2, and f_3 and becomes less important for f_0 and f_4. This is the same with 410.25 nm, i.e., the changes in f_i with respect to AOT550 decrease with wavelength, probably due to that aerosol scattering is stronger at shorter than longer wavelengths. Although the impact of AOT550 may be small and negligible depending on the smooth functions and the wavelength, AOT550 is kept in the GAM model so that we do not need to optimize the model for each wavelength, which is out of the scope of this study.

Performance of both models in reconstructing $E_s^{'}$ and E_s with the validation dataset are very similar to those with the calibration dataset (Figure 9). For $E_s^{'}$ reconstruction, the percent bias is from −0.15% to 0.03% for the multivariate linear model and from −0.01% to 0.02% for the GAM model, and the precent RMSE from 0% to 0.55% and from 0% to 0.15%, respectively. The bias and RMSE of E_s are higher than those with the calibration dataset (Figure 2), from −2.5% to −0.5% and from 0% to 3%, respectively, mainly attributed to the errors in T_g estimation (Figure 2). Figure 10 shows that simply using interpolation/extrapolation to reconstruct the hyperspectral $E_s^{'}$ from only four values typically yield much larger errors when compared to the multivariate linear model and GAM, especially in the ultraviolet wavelengths and at high Sun zenith angles.

In practice the *in-situ* measurements may be biased due to instrument calibration uncertainty and other uncertainties, (e.g., data processing). It is important to check the *in-situ* dataset against radiative transfer calculations before performing the spectral reconstruction, which can be accomplished by comparing measurements and modeled values in ideal conditions, i.e., very clear atmosphere with low aerosol content. Assuming such check has been performed and environmental uncertainty is negligible, the remaining noise, i.e., which defines the E_s calibration uncertainty, is about ±1%, according to Bialek et al. (2020) for an ideal case with no bias.

This noise was added to E_s in the validation dataset based on Eq.6 displayed below,

$$E_{s,noisy} = E_s(1 + e) \tag{6}$$

where e is a gaussian distributed variable with standard deviation of 0.01. Note that there are other sources of uncertainty in the E_s, such as that caused by converting the 0.5 nm simulated E_s to multispectral values, but here only the calibration error e is considered. In addition, noise was added to U_o3, U_h2o, and PS, i.e., ±10 Dobson, ±20%, and ±5 mb, respectively, to account for the uncertainty in the MERRA-2 data. No uncertainty in E_o and in the radiative transfer modeling was considered. The Monte Carlo approach described in JCGM (2008) was used to quantify the final uncertainties in the reconstructed E_s. A total of 100 hyperspectral E_s were reconstructed with random realizations of noise specified above and the bias and RMSE were calculated against the prescribed values.

When using the multivariate linear model on the noisy data, the percent bias and RMSE in $E_s^{'}$ could reach 0.3% and about 2.0%, respectively (Figure 11), which generally increase in the UV and near infrared and decrease (i.e., less than 0.1% and 0.5%, respectively) in the visible. The errors in E_s are larger, with the largest bias and RMSE being −2.5% and 7.0% respectively. Relatively large errors are typically found in the spectral region of the gaseous absorption bands and at UV wavelengths. The GAM model produces very similar level of

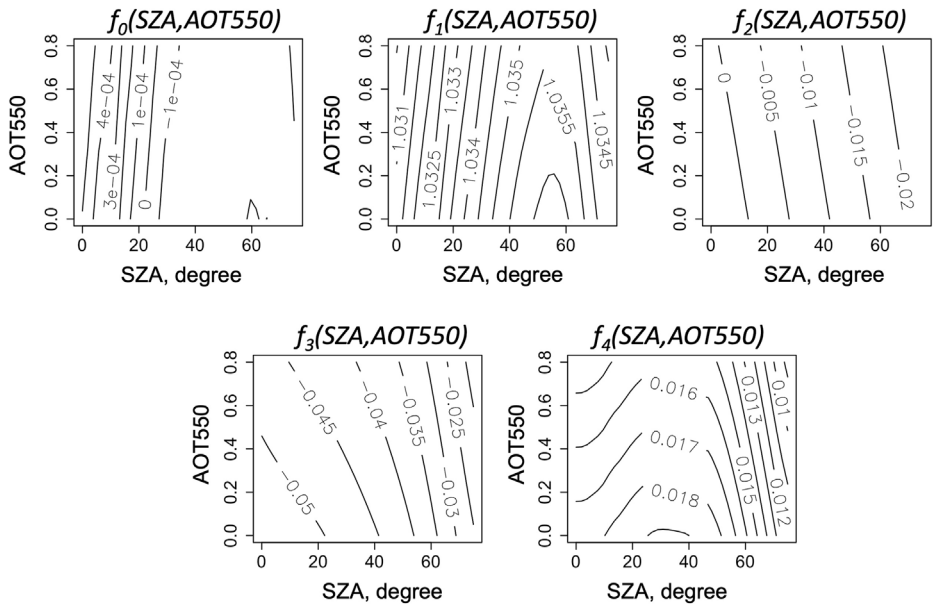


FIGURE 8
Same as Figure 7, but for 410.25 nm.

bias and RMSE in the $E_s^{'}$ estimation. Considering that the GAM model is more accurate than the multivariate linear model, especially in the UV, as well as that the uncertainty of GAM estimated $E_s^{'}$ was calculated assuming AOT550 is perfectly known, the results suggest that the GAM model is slightly more sensitive to noise, as the bias and RMSE between the two models become closer after introducing noise. In fact, the bias and RMSE for E_s are very similar for both models and much larger than those for $E_s^{'}$, indicating the large impact from the noise in T_g.

5 Evaluation against *in situ* measurements

The performance of E_s reconstruction when applied to *in-situ* measurements was evaluated. Only the multivariate linear model was used since it is sufficiently accurate and slightly less sensitive to noise. In this study, two different *in-situ* datasets were used. The first one is the MOBY dataset, which has been collected off Lanai, Hawaii since 1997 (Clark et al., 1997; Clark et al., 2002) and used for vicarious calibration of many NASA, NOAA, and international satellite programs. MOBY is a spar buoy tethered to a slack-line moored buoy and has 3 underwater arms fixed at approximately 1, 5, and 9 m to take measurements of upwelling radiance and downwelling irradiance. Above-water downwelling irradiance is also measured using the E_s sensor mounted on top of the buoy, which is about 2.5 m above the surface float. For more details see Clark et al., 1997; Clark et al., 2002. The MOBY E_s data is hyperspectral and sampled every 0.8 nm from 344 nm to 750 nm, with the spectral resolution of approximately 0.9 nm for the blue (<620 nm) and 1.2 nm for the red (>620 nm). The data is publicly available at https://www.star.nesdis.noaa.gov/socd/moby/filtered_spec/. October 2016 reprocessing was applied. Note that the E_s data below 380 nm is affected by stray light in the spectrometer (Feinholz et al., 2009). Only the data flagged as good were used in this study and there are a total of 7,036 data files available. In each data file, three columns of E_s are provided, to match the measurements taken at the three underwater arms. The three E_s values are very similar since they were taken in a short time period and only E_s corresponding to the times of measurements by the middle arm were used. These MOBY data were checked against ARTDECO simulations made using MERRA-2 data corresponding to the MOBY observation time and a minor wavelength shift, i.e., 0.3 nm toward short wavelengths, was noticed. Since the MOBY data are very close to the ARTDECO simulations (i.e., within uncertainties in the modeling), no bias adjustment was made, but the wavelength shift was corrected for each measurement.

Figure 12 displays one example of the reconstructed MOBY E_s on 27 May 2017. The measured and reconstructed E_s are in very good agreement with the relative percent difference mostly within 10% over the entire wavelength range and less than 5% above 450 nm. The reconstruction at the UV wavelengths is noisier, attributed to the model noise and the stray light issue of the MOBY E_s sensor. The relative error is also higher in the gaseous absorption bands. Uncertainties of the reconstructed E_s were calculated by introducing the typical uncertainties in MOBY E_s, i.e., approximately ±1.5% for the laboratory and ±3.0% for the field (Voss et al., 2015), ±10 Dobson for U_o3, ±20% for U_h2o, ±5 mb for PS, as well as the model noise shown in Figure 3 (blue line, right panel). After that, 100 random realizations were generated, and the final uncertainty, i.e., the

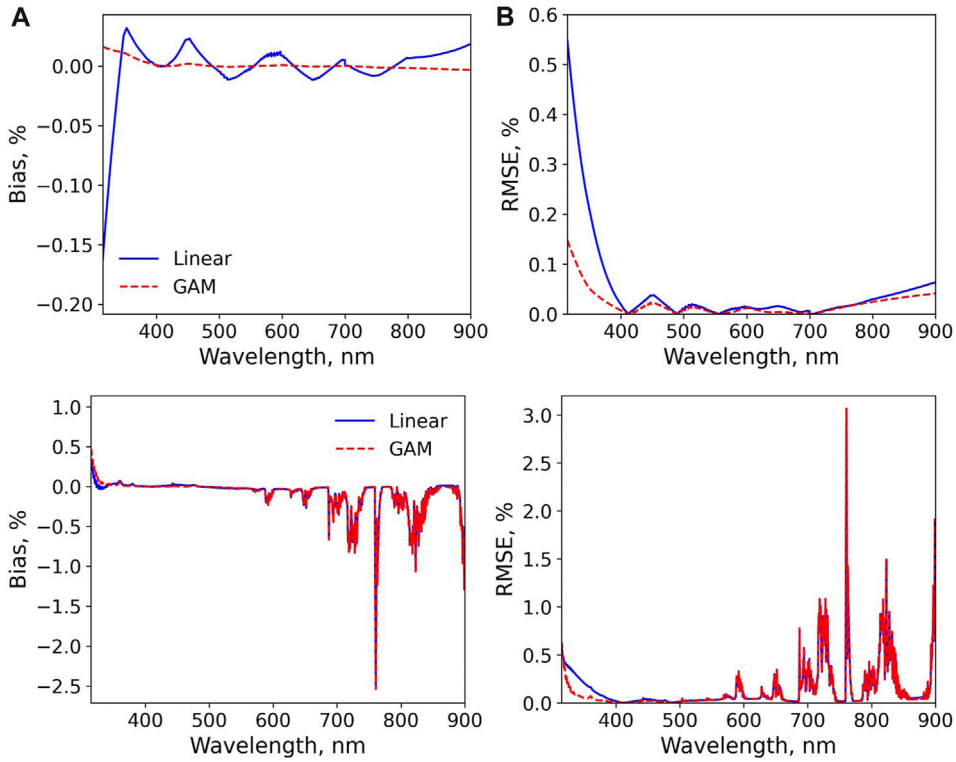


FIGURE 9
Percent bias and RMSE in the reconstructed of $E_s^{'}$ **(A)** and E_s **(B)** using the multivariate linear model (blue) and GAM (red) with the validation data set.

standard deviation of E_s with noise, was calculated using all realizations. The measured values are generally within the uncertainties of the reconstructed E_s (Figure 13). For all the 7,036 cases, the reconstructed E_s are in very good agreement with the measured values, with the bias less than 2% and RMSE less than 5% (Figure 14). The bias and RMSE at wavelengths affected by gaseous absorption are larger. For example, at 688 nm and 720 nm, corresponding to oxygen and water vapor absorption, the corresponding bias and RMSE are 2.2% and 3.6%, and −4.2% and 6.3%, respectively. Such uncertainties are higher than those obtained using the theoretical data (Figure 11, bottom panel), which may be due to noise that are not accounted for when evaluating the model performance using the theoretical data.

The second E_s dataset used for evaluation was acquired with a Sea-Bird Scientific HyperOCR radiometer from June 10 to 16 June 2021 within sight of the MOBY buoy in Hawaii (20° 49′ 54.582″ N, 157° 11′ 19.062″ W). The measurements were made from the top of a 30 feet fishing vessel with an unobstructed view of the sky between 10:00 and 14:00 local time. The HyperOCR radiometer was calibrated by Sea-Bird Scientific with an FEL lamp pre and post deployment. The HyperOCR E_s ranges from 349 to 801 nm and is sampled every 3 nm, with a spectral resolution of 10 nm. Only the data collected during clear sky conditions were used, which resulted in only one measurement on 16 June 2021. A check with ARTDECO code corresponding to the field observation time and conditions (obtained from MERRA-2 data) suggested that the HyperOCR E_s values are biased, with the difference up to about 20 μW/cm^2/nm (Figure 15). After adjusting the E_s at the four wavelengths to the simulated values, the reconstruction was performed, with the uncertainties quantified in the same way as for the MOBY data. The measured values are mostly outside the uncertainty of the reconstructed E_s, confirming the possible bias existing in the measurements. The relative errors between the reconstructed and simulated E_s using the 4 spectral bands are within 5% from 380 to 800 nm and go up to ~9% at 350 nm. It is within expectation that the relative differences between the reconstructed and measured 10-nm resolved HyperOCR E_s are lower than those with MOBY data, which has approximately 1 nm resolution.

6 Discussion

As demonstrated in the previous sections, both the multivariate linear and GAM models are capable of accurately reconstructing E_s at 0.5 nm from four 10 nm wide spectral bands centered on 412, 489, 555, and 705 nm. The multivariate linear model is straightforward, easy to interpret, and well suited for the problem in this study, i.e., E_s, after normalization of the incoming TOA solar irradiance and correction of gaseous absorption, exhibits a smooth wavelength-dependent behavior. Conversely, the GAM model is more sophisticated and has advantages in complex nonlinear relationships. By varying the coefficients as

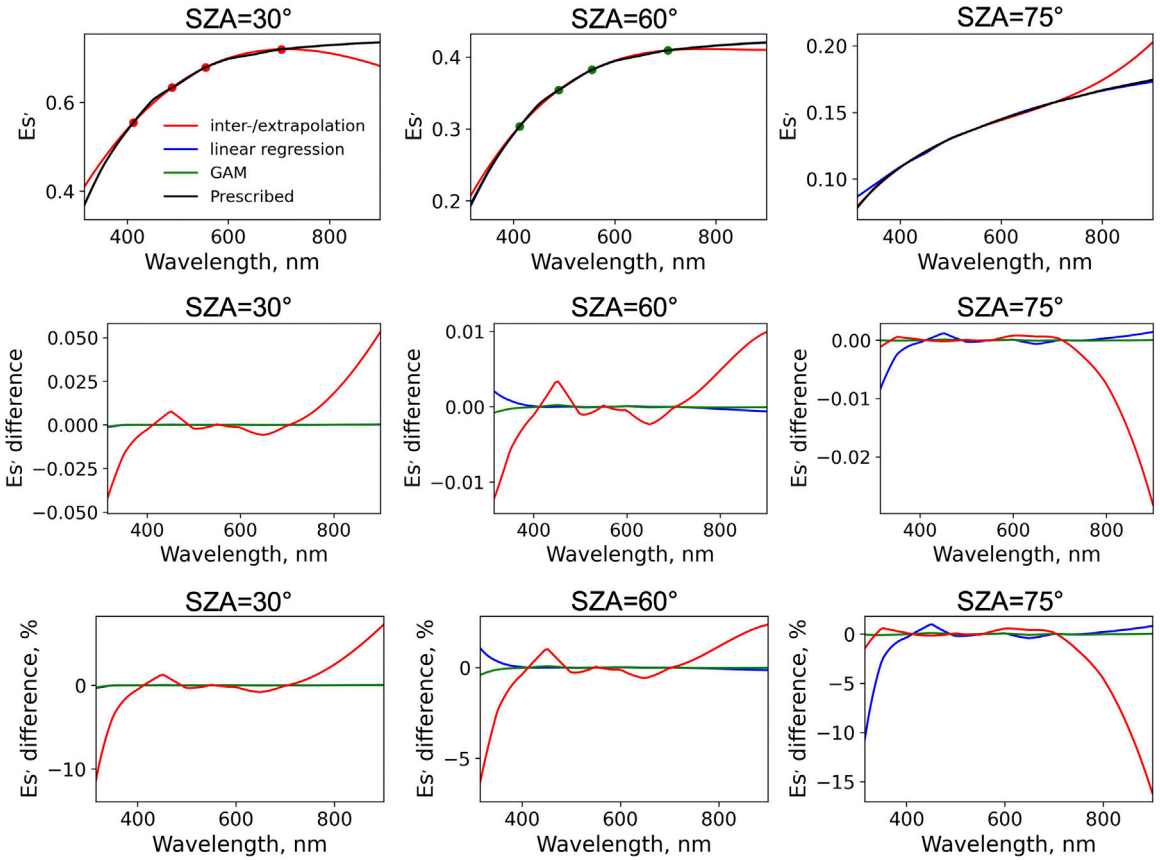


FIGURE 10
Comparison of the reconstructed $E_s^{'}$ using interpolation/extrapolation, multivariate linear model, and GAM for three cases in the calibration dataset with solar zenith angle (SZA) of 30°, 60°, and 75°. $E_s^{'}$ difference is defined as the prescribed minus the reconstructed value.

functions of SZA and AOT550 in the GAM, the accuracy in reconstructing E_s is slightly improved. This is consistent with the analysis of the correspondence between $E_s^{'}$ and different variables (Figure 5). This analysis suggests that only small residual errors exist between the $E_s^{'}$ and $E_{s,est}^{'}$, which indicates that the relation between the $E_s^{'}$ to be reconstructed and the $E_s^{'}$ at the four 10-nm bands is almost linear, and such residual errors can be explained by parameters including SZA and AOT550, the two parameters with the highest β compared to other geophysical parameters. Moreover, it is worth noting that the GAM model is more sensitive to noise. As a result, it is concluded that multivariate linear model is a more suitable choice in this study in terms of model accuracy and sensitivity.

Instead of just utilizing the four multi-spectral bands at 412, 489, 555, and 705 nm, it is also possible to use other sets of wavelengths. For example, if we incorporate three additional wavelengths at UV, i.e., 325, 340, and 380 nm, the optional wavelengths that can be customized to the commercial Sea-Bird, Inc. OCR multi-spectral (7-band) radiometer, the RMSE of $E_s^{'}$ at UV exhibits significant reduction, with the maximum dropped from 0.6% to 0.02% and mostly remaining below 0.01% (Figure 16). The errors at other wavelengths also decrease to a certain extent, but not as much as in the UV. One may also be tempted to add more bands in the near infrared so that the RMSE can be further reduced in this range. However, one needs to have in mind that the major uncertainty comes from the estimation of T_g.

In the evaluation of the model sensitivity to noise, it is found that the instrument calibration noise is the major contributor to the uncertainties in $E_s^{'}$. For example, at 320.25 nm, with no noise the percent bias and RMSE in $E_s^{'}$ are −0.01% and 0.50%, respectively; the percent RMSE increases to 1.82% if added noise and the percent bias remains the same. The noise in the input PS, U_o3, and U_h2o affect the estimation of T_g, and this is another important source of uncertainties in the final restitution of E_s, especially at wavelengths affected by gaseous absorption. When T_g noise is included, the percent RMS of E_s increases from 1.86% to 1.94% at 320.25 nm, but changes from 2.78% to 3.60% in the oxygen band near 760 nm. To ensure accurate E_s reconstruction, it should be verified that the input multispectral E_s is not biased, for example by checking against radiative transfer simulations during very clear sky conditions (i.e., with small aerosol content), as indicated in Section 2. If the input E_s is biased, one may expect that the reconstructed E_s will be biased and the uncertainties could be large.

Since the presented method is capable of accurately reconstructing E_s at 0.5 nm resolution, it can be easily adapted to different sensors with varying spectral characteristics. One

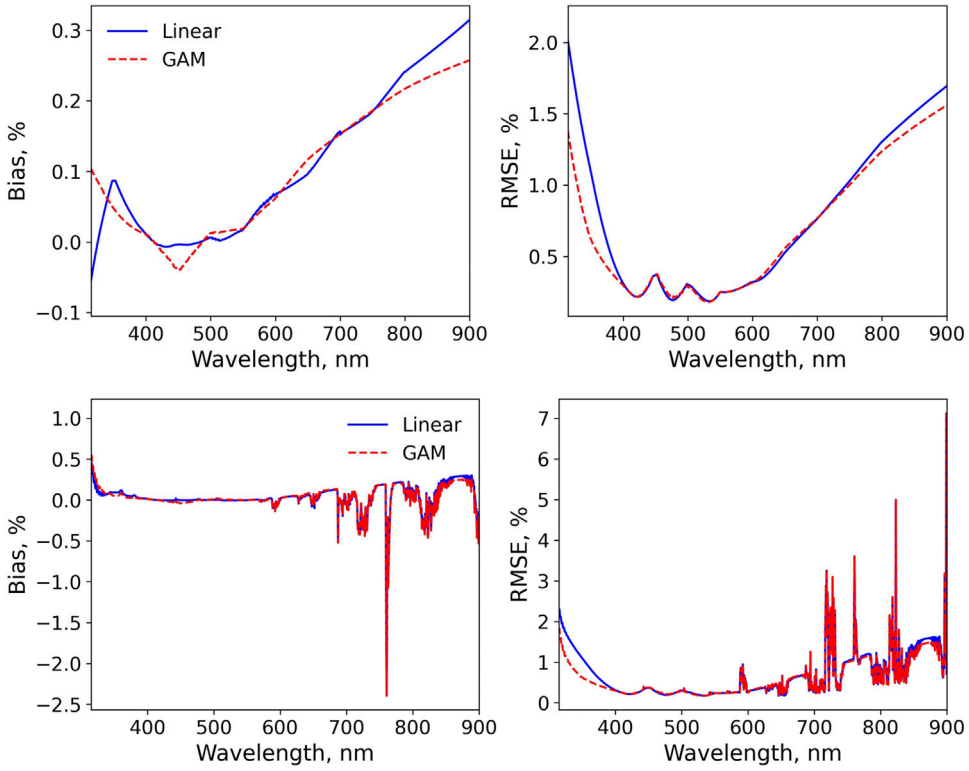


FIGURE 11
Same as Figure 9, but with noise added to E_s in the validation dataset and typical noise added to U_h2o, U_o3, and PS in T_g estimation. See text for more details.

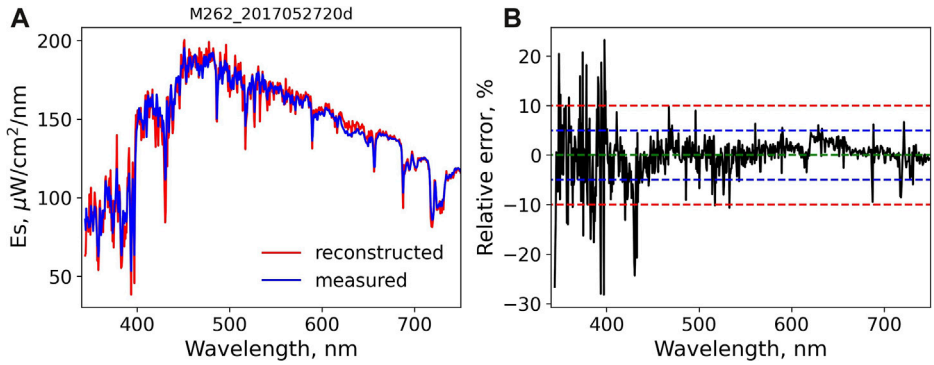


FIGURE 12
(A) Measured and reconstructed MOBY E_s on 27 May 2017, and **(B)** percent relative error between the measured and reconstructed E_s. Green, blue, and red dashed lines correspond to 0, 5, and 10% errors, respectively.

potential and important use in the context of the upcoming PACE mission (scheduled to launched in February 2024) is reconstructing the OCI hyper-spectral E_s signal using measurements in the four multi-spectral measurements of the current HyperNav system. Figure 17 illustrates an example of reconstructed E_s at OCI wavelengths using simulated HyperNav E_s measurements for a clear day. Results show that the OCI E_s can be reconstructed accurately, with the relative differences within 1% from 360 nm to 900 nm. In the UV, the errors increase with wavelength, with the highest values of ~4% and ~7%, depending on the Sun zenith angle (high Sun zenith angle means low E_s and relatively large uncertainties). With such reconstructed E_s data, the HyperNav system is able to provide hyper-spectral R_{rs} by normalizing the measured hyper-spectral L_w against E_s, which has great significance for the calibration and validation of the PACE mission.

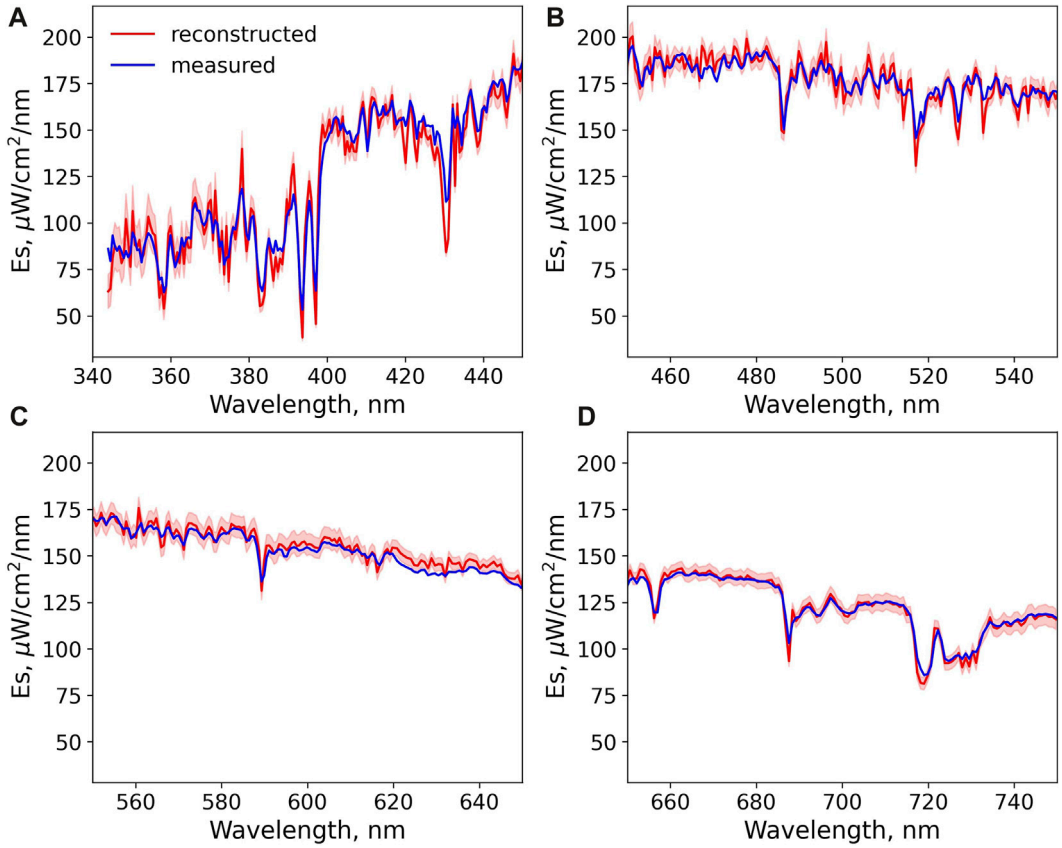


FIGURE 13
Comparisons between measured and reconstructed MOBY E_s on 27 May 2017 at **(A)** 340–450 nm, **(B)** 450–550 nm, **(C)** 550–650 nm, and **(D)** 650–750 nm. Shaded areas indicate the uncertainties of the reconstructed E_s.

7 Summary and conclusion

Spectral E_s at 0.5 nm resolution can be reconstructed accurately from E_s measurements in 4 spectral bands 10 nm-wide centered on 412, 489, 555, and 705 nm, such as those by an OCR SeaBird, Inc. planar irradiance sensor mounted on the HyperNav spectroradiometer/float system, using a multivariate linear model with constant coefficients or a GAM with coefficients dependent on SZA and AOT550. The models require as input, in addition to the 4 E_s measurements, the content of gaseous absorbers (vertically integrated content for ozone and water vapor and surface pressure for oxygen and other gases). In the absence of noise, both models yield biases less than 0.4% in magnitude and RMSEs less than 2.5%. The largest errors are obtained in regions of strong absorption bands. Errors are smaller in the UV with the GAM model, i.e., 0.2% instead of 0.6%. In the presence of typical noise on the input variables, biases and RMSEs are generally less than 1.5% in magnitude and 3.5%, respectively, except in the center of the oxygen A-band (−2.7% and 5.3%). The GAM model is more sensitive to noise, i.e., the gain in accuracy in the UV in the absence of noise is practically lost in the presence of noise. The complexity of the GAM model, therefore, may not be justified, unless the typical noise in the input variables can be reduced. Using additional bands in the UV, i.e., at 325, 340, and 380 improves theoretical performance in the UV without noise, but marginally in practice because the E_s error is dominated by T_g uncertainties.

Evaluation of the multivariate linear model with constant coefficients against *in-situ* hyper-spectral E_s measurements at the MOBY site revealed E_s spectra reconstructed with biases less than 2% in magnitude and RMSE ranging from 1% to 2% in the visible to 5% in the UV, in agreement with theoretical uncertainties estimated using the Monte Carlo method. It is important, however, before doing any reconstruction, to check whether the multi-band E_s measurements are not biased (e.g., due to exposure, calibration, or processing errors), which can be accomplished by comparing the measurements to accurate radiative transfer calculations under favorable conditions. This revealed a significant bias in the HyperOCR E_s data acquired near the MOBY site.

The methodology, by providing a way to accurately reconstruct E_s at 0.5 nm resolution from E_s measurements at a few 10 nm-wide spectral bands, as demonstrated theoretically and experimentally, allows normalization of hyper-spectral L_w data acquired by HyperNav systems for validation activities of the PACE mission. The modeling does not replace hyper-spectral E_s measurements, such as those made by the MOBY system, but is adequate in many

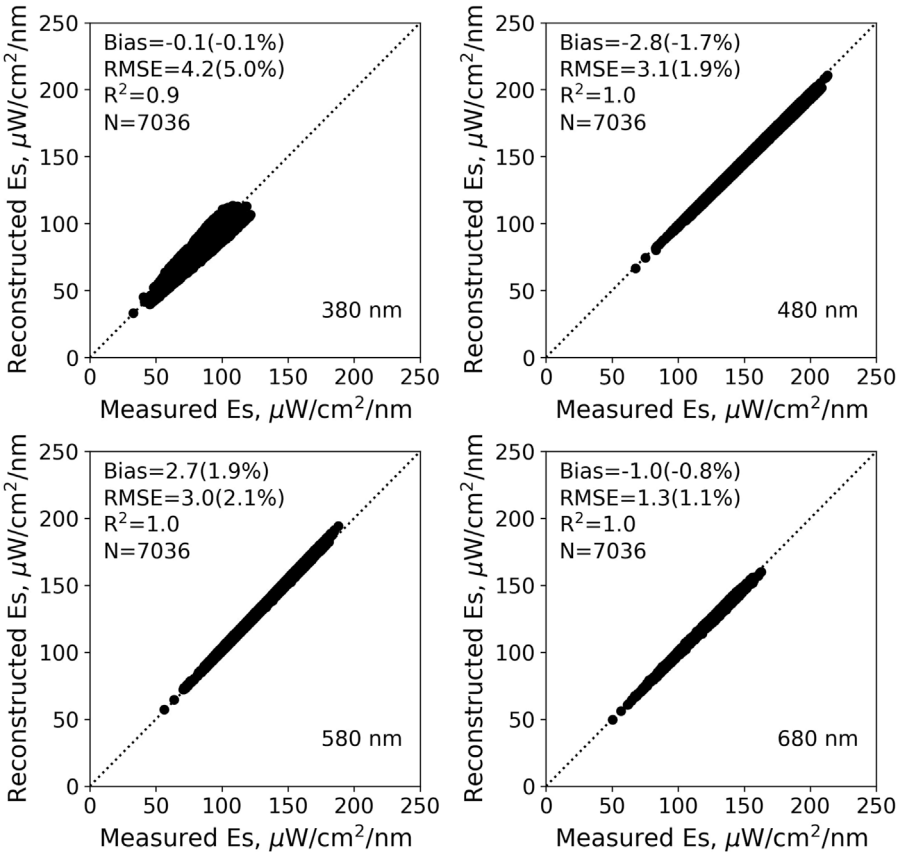


FIGURE 14
Comparisons between measured and reconstructed MOBY E_s at 380, 480, 580, and 680 nm.

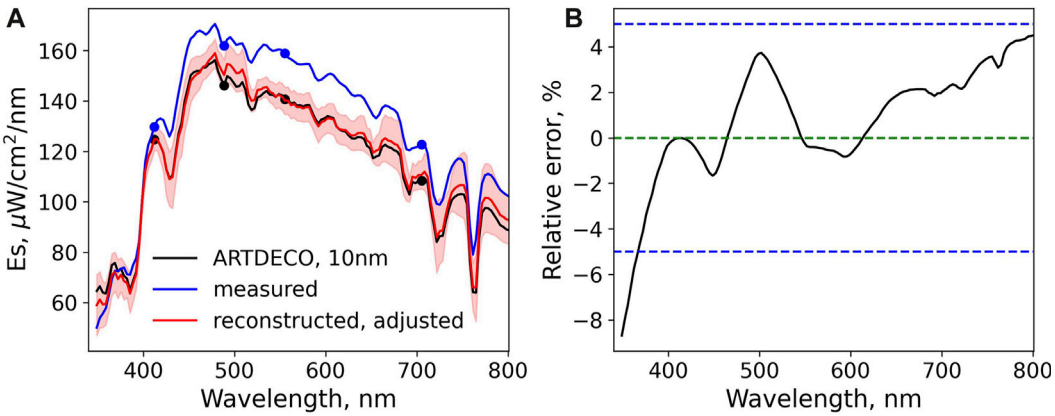


FIGURE 15
(A) Measured (blue solid) HyperOCR E_s on 16 June 2021. ATDECO simulations (black solid) show that the HyperOCR E_s is off and needs to be adjusted. The reconstructed E_s after adjustment (red solid) shows good agreement with the ARTDECO simulated values. Shaded areas indicate the uncertainties of the reconstructed E_s. **(B)** Percent relative error between the ARTDECO simulated and the reconstructed E_s after adjustment. Green and blue dashed lines correspond to 0% and 5% errors, respectively. Blue and black dots represent the E_s measured before and after adjustment.

aquatic optics applications, for which the acquisition of a relatively expensive hyper-spectral E_s sensor, costly to maintain and calibrate, may therefore not be necessary. The methodology is applicable to other sets of spectral bands, i.e., those of other multi-band radiometers than the Seabird Inc. OCR used here, but accuracy of the reconstruction will depend on the bands position in the solar spectral range. Now, because the optical properties of clouds, like those of aerosols, and their effects on E_s vary

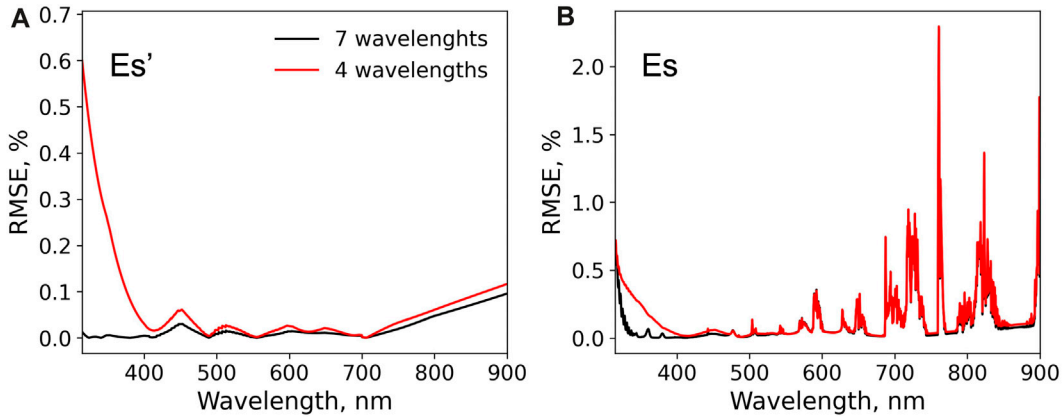


FIGURE 16
Percent RMSE of E_s' **(A)** and E_s **(B)** estimation using multivariate linear regression with three extra wavelengths in the UV, i.e., 325, 340, and 380 nm (black), in comparison to original four input wavelengths (red) as shown in Figure 6. The regression was performed using the calibration dataset without noise.

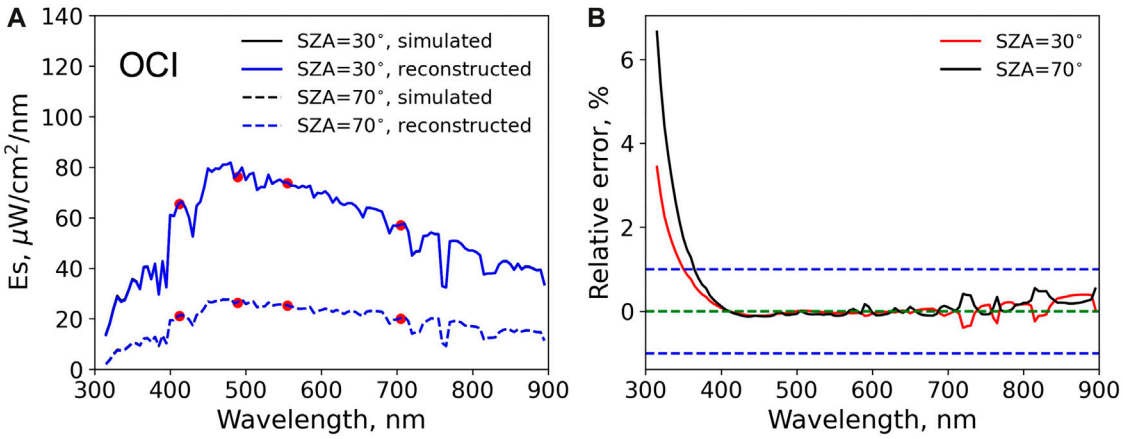


FIGURE 17
(A) The simulated (black) and reconstructed (blue) E_s at PACE OCI wavelengths. The simulations are for a clear day with U_o3 = 300 Dobson, U_h2o = 2 g/cm^2, PS = 1,015 mb, Chl = 0.1 mg m^{-3}, AOT550 = 0.1, maritime aerosol, relative humidity of 70%, SH = 2 km, and wind speed of 5 m s^{-1}. Two different SZA were used, i.e., 30° and 70°. The reconstruction was done using the simulated HyperNav values at the four wavelengths (red dots), i.e., 412, 489, 555, and 705 nm. **(B)** Percent relative error between the simulated and the reconstructed E_s. Green and blue dashed lines correspond to 0% and 1% errors, respectively. No noise has been added to the model input parameters.

relatively smoothly with wavelength in the UV to near infrared, the modeling can be extended to estimating spectral E_s in all sky conditions, although the coupling between absorption by gases and scattering by cloud droplets may complicate the treatment of T_g in some spectral regions. Such extension is envisioned in future work.

Data availability statement

The original contributions presented in the study are included in the article, further inquiries can be directed to the corresponding author. The code for reconstructing from E_s measurements at 412, 489, 555, and 705 nm is publicly available at https://github.com/jit079/Es_reconstruction.

Author contributions

JT: Conceptualization, Investigation, Methodology, Writing–original draft, Writing–review and editing. RF: Conceptualization, Investigation, Methodology, Supervision, Writing–review and editing. NH: Writing–review and editing. AB: Writing–review and editing. EB: Writing–review and editing. PC: Writing–review and editing. MM: Writing–review and editing. CO: Writing–review and editing.

Funding

The author(s) declare that financial support was received for the research, authorship, and/or publication of this article. This work

was supported by the National Aeronautics and Space Administration NASA under Grant 80GFC22CA050.

Acknowledgments

The authors gratefully acknowledge the MOBY team for generating, maintaining, and distributing the MOBY data used in this study, and the HyperNav engineers and technicians at SeaBird, Inc. for their help with HyperNav operations.

Conflict of interest

Author CO was employed by Sea-Bird Scientific.

The remaining authors declare that the research was conducted in the absence of any commercial or financial relationships that could be construed as a potential conflict of interest.

The author(s) declared that they were an editorial board member of Frontiers, at the time of submission. This had no impact on the peer review process and the final decision.

Publisher's note

All claims expressed in this article are solely those of the authors and do not necessarily represent those of their affiliated organizations, or those of the publisher, the editors and the reviewers. Any product that may be evaluated in this article, or claim that may be made by its manufacturer, is not guaranteed or endorsed by the publisher.

References

Anderson, G. P., Clough, S. A., Kneizys, F. X., Chetwynd, J. H., and Shettle, E. P. (1986). AFGL atmospheric constituent profiles (0-120 km). *Environ. Res. Pap.*, 954.

Barnard, A., Boss, E., Haëntjens, N., Orrico, C., Frouin, R., Klumpp, J., et al. (2024). Design, characterization, and verification of a highly accurate *in situ* hyperspectral radiometric measurement system (HyperNAV). Submitted to *Frontiers in Remote Sensing*.

Białek, A., Douglas, S., Kuusk, J., Ansko, I., Vabson, V., Vendt, R., et al. (2020). Example of Monte Carlo method uncertainty evaluation for above-water ocean colour radiometry. *Remote Sens.* 12, 780. doi:10.3390/rs12050780

Bisson, K. M., Boss, E., Werdell, P. J., Ibrahim, A., Frouin, R., and Behrenfeld, M. J. (2021). Seasonal bias in global ocean color observations. *Appl. Opt. AO* 60, 6978–6988. doi:10.1364/AO.426137

Chance, K., and Kurucz, R. L. (2010). An improved high-resolution solar reference spectrum for earth's atmosphere measurements in the ultraviolet, visible, and near infrared. *J. Quantitative Spectrosc. Radiatve Transf.* 111, 1289–1295. doi:10.1016/j.jqsrt.2010.01.036

Clark, D. K., Gordon, H. R., Voss, K. J., Ge, Y., Broenkow, W., and Trees, C. (1997). Validation of atmospheric correction over the oceans. *J. Geophys. Res. Atmos.* 102, 17209–17217. doi:10.1029/96JD03345

Clark, D. K., Yarbrough, M. A., Feinholz, M. E., Flora, S., Broenkow, W., Johnson, B. C., et al. (2002). "MOBY, a radiometric buoy for performance monitoring and vicarious calibration of satellite ocean color sensors: measurement and data analysis protocols," in *Ocean optics protocols for satellite Ocean color sensor validation, revision 3. Greenbelt, MD, NASA goddard Space flight center*. Editors J. L. Mueller, and G. S. Fargion, 2. NASA/TM–2002-21004:138-170.

Dubuisson, P., Labonnote, L. C., Riedi, J., Compiegne, M., and Winiarek, V. (2016). "ARTDECO: atmospheric radiative transfer database for earth and climate observation," in International Radiation Symposium 2016, Auckland, New Zealand, April 2016, 17–22.

Evans, R. H., and Gordon, H. R. (1994). Coastal zone color scanner "system calibration": a retrospective examination. *J. Geophys. Res. Oceans* 99, 7293–7307. doi:10.1029/93JC02151

Feinholz, M. E., Flora, S. J., Yarbrough, M. A., Lykke, K. R., Brown, S. W., Johnson, B. C., et al. (2009). Stray light correction of the marine optical system. *J. Atmos. Ocean. Technol.* 26, 57–73. doi:10.1175/2008JTECHO597.1

Franz, B. A., Bailey, S. W., Werdell, P. J., and McClain, C. R. (2007). Sensor-independent approach to the vicarious calibration of satellite ocean color radiometry. *Appl. Opt. AO* 46, 5068–5082. doi:10.1364/AO.46.005068

Frouin, R. J., Franz, B. A., Ibrahim, A., Knobelspiesse, K., Ahmad, Z., Cairns, B., et al. (2019). Atmospheric correction of satellite ocean-color imagery during the PACE era. *Front. Earth Sci.* 7, 00145. doi:10.3389/feart.2019.00145

Gelaro, R., McCarty, W., Suárez, M. J., Todling, R., Molod, A., Takacs, L., et al. (2017). The modern-era retrospective analysis for research and applications, version 2 (MERRA-2). *J. Clim.* 30, 5419–5454. doi:10.1175/JCLI-D-16-0758.1

Gordon, H. R. (1997). Atmospheric correction of ocean color imagery in the Earth Observing System era. *J. Geophys. Res. Atmos.* 102, 17081–17106. doi:10.1029/96JD02443

Hastie, T., and Tibshirani, R. (1993). Varying-coefficient models. *J. R. Stat. Soc. Ser. B Methodol.* 55, 757–779. doi:10.1111/j.2517-6161.1993.tb01939.x

Hedley, J. D., and Mobley, C. (2019). *HydroLight 6.0 - EcoLight 6*. 0 Users' Guide Numerical Optics Ltd.

Hess, M., Koepke, P., and Schult, I. (1998). Optical properties of aerosols and clouds: the software package OPAC. *Bull. Am. Meteorological Soc.* 79, 831–844. doi:10.1175/1520-0477(1998)079<0831:OPOAAC>2.0.CO;2

IOCCG (2008). "Why ocean colour? The scocietal benefits of ocean-colour technology," in *Report No. 7 of the international ocean-colour coordinating group*. Editors T. Platt, N. Hoepffner, V. Stuart, and C. Brown, Dartmouth, Canada: (Dartmouth: NS: IOCCG), 141.

IOCCG (2013). "In-flight calibration of satellite ocean-colour sensors," in *Report No. 14 of the international ocean-colour coordinating group*. Editor R. Frouin, Dartmouth, Canada: (Dartmouth, NS: IOCCG), 106.

JCGM (2008). Evaluation of measurement data – supplement 1 to the "Guide to the expression of uncertainty in measurement" – propagation of distributions using a Monte Carlo method. Guidance Document. Avaialable at: https://www.bipm.org/documents/20126/2071204/JCGM_101_2008_E.pdf/325dcaad-c15a-407c-1105-8b7f322d651c.

Lacis, A. A., and Oinas, V. (1991). A description of the correlated k distribution method for modeling nongray gaseous absorption, thermal emission, and multiple scattering in vertically inhomogeneous atmospheres. *J. Geophys. Res. Atmos.* 96, 9027–9063. doi:10.1029/90JD01945

Morel, A., and Maritorena, S. (2001). Bio-optical properties of oceanic waters: a reappraisal. *J. Geophys. Res. Oceans* 106, 7163–7180. doi:10.1029/2000JC000319

Mueller, J. L., Davis, C., Arnone, R., Frouin, R., Carder, K., Lee, Z. P., et al. (2003). "Above-water radiance and remote sensing reflectance measurements and analysis protocols," in *Ocean optics protocols for satellite Ocean color sensor validation revision 4; national aeronautical and Space administration* (MD, USA: Greenbelt), III, 21–31. Chapter 3.

Ruddick, K. G., Voss, K., Banks, A. C., Boss, E., Castagna, A., Frouin, R., et al. (2019a). A review of protocols for fiducial reference measurements of downwelling irradiance for the validation of satellite remote sensing data over water. *Remote Sens.* 11, 1742. doi:10.3390/rs11151742

Ruddick, K. G., Voss, K., Boss, E., Castagna, A., Frouin, R., Gilerson, A., et al. (2019b). A review of protocols for fiducial reference measurements of water-leaving radiance for validation of satellite remote-sensing data over water. *Remote Sens.* 11, 2198. doi:10.3390/rs11192198

Schneider, W., Moortgat, G. K., Tyndall, G. S., and Burrows, J. P. (1987). Absorption cross-sections of NO2 in the UV and visible region (200 – 700 nm) at 298 K. *J. Photochem. Photobiol. A Chem.* 40, 195–217. doi:10.1016/1010-6030(87)85001-3

Tanré, D., Herman, M., Deschamps, P. Y., and Leffe, A. de (1979). Atmospheric modeling for space measurements of ground reflectances, including bidirectional properties. *Appl. Opt. AO* 18, 3587–3594. doi:10.1364/AO.18.003587

Voss, K., Johnson, B. C., and Yarbrough, M. A. (2015). MOBY past, current, and future. Available at https://mlml.sjsu.edu/moby/wp-content/uploads/sites/20/2017/05/TH-14-15-Keynote7-Voss-InSitu.ppt.

Werdell, P. J., McKinna, L. I. W., Boss, E., Ackleson, S. G., Craig, S. E., Gregg, W. W., et al. (2018). An overview of approaches and challenges for retrieving marine inherent optical properties from ocean color remote sensing. *Prog. Oceanogr.* 160, 186–212. doi:10.1016/j.pocean.2018.01.001

Zibordi, G., Mélin, F., Voss, K. J., Johnson, B. C., Franz, B. A., Kwiatkowska, E., et al. (2015). System vicarious calibration for ocean color climate change applications: requirements for *in situ* data. *Remote Sens. Environ.* 159, 361–369. doi:10.1016/j.rse.2014.12.015

frontiers | Frontiers in Remote Sensing

TYPE Original Research
PUBLISHED 18 March 2024
DOI 10.3389/frsen.2024.1330317

Check for updates

OPEN ACCESS

EDITED BY
Enner Alcântara,
São Paulo State University, Brazil

REVIEWED BY
Yulong Guo,
Henan Agricultural University, China
Shun Bi,
Helmholtz Association of German Research Centres (HZ), Germany

*CORRESPONDENCE
Luis González Vilas,
luis.gonzalezvilas@artov.ismar.cnr.it

RECEIVED 30 October 2023
ACCEPTED 15 February 2024
PUBLISHED 18 March 2024

CITATION
González Vilas L, Brando VE, Concha JA, Goyens C, Dogliotti AI, Doxaran D, Dille A and Van der Zande D (2024), Validation of satellite water products based on HYPERNETS *in situ* data using a Match-up Database (MDB) file structure.
Front. Remote Sens. 5:1330317.
doi: 10.3389/frsen.2024.1330317

COPYRIGHT
© 2024 González Vilas, Brando, Concha, Goyens, Dogliotti, Doxaran, Dille and Van der Zande. This is an open-access article distributed under the terms of the Creative Commons Attribution License (CC BY). The use, distribution or reproduction in other forums is permitted, provided the original author(s) and the copyright owner(s) are credited and that the original publication in this journal is cited, in accordance with accepted academic practice. No use, distribution or reproduction is permitted which does not comply with these terms.

Validation of satellite water products based on HYPERNETS *in situ* data using a Match-up Database (MDB) file structure

Luis González Vilas[1]*, Vittorio E. Brando[1], Javier A. Concha[1,2], Clèmence Goyens[3], Ana I. Dogliotti[4,5], David Doxaran[6], Antoine Dille[3] and Dimitry Van der Zande[3]

[1]CNR-ISMAR, Istituto di Scienze Marine, Consiglio Nazionale delle Ricerche, Rome, Italy, [2]Serco S.p.A. c/o ESA-ESRIN, Rome, Italy, [3]RBINS, Royal Belgian Institute of Natural Sciences (RBINS), Operational Directorate Natural Environment, Brussels, Belgium, [4]Instituto de Astronomía y Física del Espacio, Consejo Nacional de Investigaciones Científicas y Técnicas (IAFE, CONICET/UBA), Buenos Aires, Argentina, [5]Instituto Franco-Argentino para el Estudio del Clima y sus Impactos (UMI-IFAECI, CNRS CONICET-UBA), Buenos Aires, Argentina, [6]Laboratoire d'Océanographie de Villefranche UMR7093—CNRS/SU, Villefranche-sur-Mer, France

A Match-up Database (MDB) file structure and tools were developed to ease the validation analysis of satellite water products and to improve the exchange and processing of match-up data from different sites, missions and atmospheric correction processors. *In situ* remote sensing reflectance (*Rrs*) measurements were available from the HYPSTAR® (HYperspectral Pointable System for Terrestrial and Aquatic Radiometry), a new automated hyperspectral radiometer. An MDB file is a NetCDF file containing all the potential match-ups between satellite and *in situ* data on a specific site and within a given time window. These files are generated and manipulated with three modules developed in Python to implement the validation protocols: extract satellite data, associate each extract with co-located *in situ* radiometry data, and then perform the validation analysis. This work provides details on the implementation of the open-source MDB file structure and tools. The approach is demonstrated by a multi-site matchup comparison based on satellite data from the Sentinel-2 MSI and Sentinel-3 OLCI sensors, and HYPSTAR® data acquired over six water sites with diverse optical regimes from February 2021 to March 2023.The analysis of Sentinel-3 OLCI matchups across the six sites shows consistency with previous comparisons based on AERONET-OC data over extended reflectance range. We evaluated Sentinel-2 MSI reflectance data corrected with two atmospheric correction processors (ACOLITE and C2RCC) over four sites with clear to highly turbid waters. Results showed that the performance of the processors depends on the optical regime of the sites. Overall, we proved the suitability of the open-source MDB-based approach to implement validation protocols and generate automated matchup analyses for different missions, processors and sites.

KEYWORDS

ocean color, satellite validation, hyperspectral reflectance, Sentinel-3 OLCI, Sentinel-2 MSI, Match-up Database (MDB)

1 Introduction

In remote sensing, validation aims at evaluating quantitatively if satellite data meet the mission requirements and are suitable for the intended applications (IOCCG, 2012). Justice et al. (2000) defined validation as "the process of evaluating by independent means the accuracy of satellite-derived [land or water] products and quantifying their uncertainties by analytical comparison with reference data. According to Bailey and Werdell (2006), "validation is the process of determining the spatial and temporal error fields of a given biological or geophysical data product." In practice, quality of satellite-derived products over time and space is often assessed by the direct comparison with (quasi-)coincident *in situ* measurements, defining a match-up as a pair of satellite and *in situ* measurements (Clark et al., 1997; Zibordi et al., 2009a; Zibordi et al., 2018). Hence, *in situ* measurements are assumed to be representative of the truth, at least within their own reported uncertainties that need to be determined for each site (Loew et al., 2017).

In ocean colour remote sensing, water reflectance, usually expressed as remote-sensing reflectance (*Rrs*) or normalized water-leaving radiance (L_{WN}), is the standard input for retrieving bio-geophysical parameters (e.g., chlorophyll-a, total suspended matter, chromophoric organic dissolved organic matter) from most of the optical models (Concha et al., 2021 and references therein). Validation of *Rrs* is hence essential to assess the atmospheric correction processors converting the satellite top-of-atmosphere signal into *Rrs* data and ensure the quality of ocean colour data for water quality monitoring (Clark et al., 1997; Gordon, 2021; Pahlevan et al., 2021).

Reference data for radiometric validation are typically based on under- or above-water radiometry data from ships or fixed platforms, with both multispectral and hyperspectral resolution (Concha et al., 2021 and references therein).

A new automated hyperspectral radiometer, i.e., the HYPSTAR® (HYperspectral Pointable System for Terrestrial and Aquatic Radiometry), has been developed within the European Union's HORIZON 2020 project HYPERNETS. This radiometer provides high-quality above-water hyperspectral radiometry data in the visible to near infrared (VNIR) from 380 to 1,020 nm with a spectral resolution of 5 nm (or better), and in the short-wavelength infrared (SWIR) from 1,000 to 1700 nm with a spectral resolution of 10 nm (Goyens et al., 2022; De Vis et al., 2024). During the project, HYPSTAR® radiometers were deployed using fixed platforms at 7 water sites and 7 land sites in order to provide measurements at high spectral and temporal resolutions and for the multi-mission validation of satellite products. After the project, and at the time of writing this manuscript, the network of water sites (WATERHYPERNET) includes six operative sites and is expected to continue to deliver data in future (Ruddick et al., 2024, submitted in the current special issue).

Efforts have been made by the ocean colour (OC) community to establish the protocols to obtain Fiducial Reference Measurements (FRM) from *in situ* radiometry data (see review in Ruddick et al., 2019) or to perform validation exercises based on match-ups of satellite and reference data (Bailey and Werdell, 2006; Zibordi et al., 2009b; Concha et al., 2021). However, there is a lack of a standard data formats or database structures to facilitate the sharing of match-up data and validation results. To this aim, the Match-up Database (MDB) concept was first introduced by EUMETSAT (EUMETSAT, 2019). MDB files are designed to include all the potential match-ups between satellite and reference (*in situ*) Rrs data and to be used as input for the implementation of validation analysis.

Moreover, several satellite validation tools are available within the OC community. EUMETSAT has developed ThoMaS (https://gitlab.eumetsat.int/eumetlab/oceans/ocean-science-studies/ThoMaS, accessed on 18 January 2024), a toolkit to create matchups of bio-geophysical *in situ* data (in SeaBASS/OCDB-like format) with satellite OC products from Sentinel-3 OLCI. ThoMaS is also an open-source MDB-based approach developed in Python sharing many features with the approach presented in this work, such as user-defined validation protocols and metrics and plots production. The SeaWiFS Bio-optical Archive and Storage System (SeaBASS) maintained by the NASA Ocean Biology Processing Group (OBPG) has also developed a set of Satellite Validation Match-Up Tools (https://seabass.gsfc.nasa.gov/wiki/validation_matchup_tools, accessed on 18 January 2024) as part of its software package. Its approach includes the satellite data finder and the match-up extractor, both designed to work only with NASA's Ocean Biology Distributed Active Archive Center (OB.DAAC) Level-2 products. The satellite validation navy tool (SAVANT) was developed by the Naval Research Laboratory (Lawson et al., 2021). SAVANT implements validation analysis in three steps: ingestion of satellite and *in situ* data into a database in addition to a set of metadata; match-up filtering according to the quality control criteria defined by the user; and production of validation graphs and statistical information. Unfortunately, at the time of writing this manuscript, SAVANT was temporally unavailable for the OC community (personal communication, Lawson et al., 2021).

In this work, and in the framework of HYPERNETS project, we developed an open-source MDB file structure and a set of Python tools to implement validation analysis of satellite water products using hyperspectral data as reference.

The rest of this document is organized as follows. First, we describe the MDB structure and validation tools. Then, as an example of the MDB-based approach, we present the results of a multi-site validation exercise using match-ups of satellite data from Sentinel-3 OLCI and Sentinel-2 MSI sensors with HYPSTAR® data from six water sites between January 2021 to March 2023. And we finalize with a brief discussion and conclusions.

2 Methods

Several satellite validation tools are available within the OC community. In this study, we built on the MDB concept that was first introduced by EUMETSAT (EUMETSAT, 2019). MDB files were designed to include all the potential match-ups between satellite and reference (*in situ*) *Rrs* data and to be used as input for the implementation of validation analysis.

EUMETSAT has developed ThoMaS (https://gitlab.eumetsat.int/eumetlab/oceans/ocean-science-studies/ThoMaS, accessed on 18 January 2024), a toolkit to create match-ups of bio-geophysical *in situ* data (in SeaBASS/OCDB-like format) with satellite OC products from Sentinel-3 OLCI. ThoMaS is also an open-source MDB-based approach developed in Python sharing many features with the approach presented in this work, such as

user-defined validation protocols and metrics and plots production. Moreover, it provides some interesting options, as direct access to the EUMETSAT Sentinel-3 products from the EUMETSAT data store to generate the extracts or the optional application of the bi-directional reflectance correction (BRDF) to the *in situ Rrs* data.

The SeaWiFS Bio-optical Archive and Storage System (SeaBASS) maintained by the NASA Ocean Biology Processing Group (OBPG) has also developed a set of Satellite Validation Match-Up Tools (https://seabass.gsfc.nasa.gov/wiki/validation_matchup_tools, accessed on 18 January 2024) as part of its software package. Its approach includes two steps: the satellite data finder, aimed at locating satellite granules given an *in situ* point in space and time; and the match-up extractor, which creates the satellite extracts and obtain the match-ups values by applying the default validation protocols proposed by Bailey and Werdell (2006), although the user can define some options as the size extract, the minimum percent of valid pixels or the maximum time difference between the satellite and *in situ* observations. The main limitations are that these tools are designed to work only with NASA's Ocean Biology Distributed Active Archive Center (OB.DAAC) Level-2 products, and production of metrics and plots is not implemented in the software.

The satellite validation navy tool (SAVANT) was developed by the Naval Research Laboratory (Lawson et al., 2021). SAVANT implements validation analysis in three steps: ingestion of satellite and *in situ* data into a database in addition to a set of metadata; match-up filtering according to the quality control criteria defined by the user; and production of validation graphs and statistical information. The system was tested using *in situ* data from the Marine Optical Buoy (MOBY) and the Aerosol Robotic Network—Ocean Color (AERONET-OC) network and support satellite data from different sources, including Suomi National Polar-orbiting Partnership (SNPP) Visible Infrared Imaging Radiometer Suite (VIIRS), NOOA-20 VIIRS or Sentinel-3 OLCI, but the back-end database was designed to be flexible and open-ended. Unfortunately, at the time of writing this manuscript, SAVANT was temporally unavailable for the OC community (personal communication, Lawson et al., 2021).

2.1 MDB file structure

In this study, MDB files include all the potential match-ups between satellite and reference (*in situ*) *Rrs* data, and are then used for validation analysis. MDB files use the open-source NetCDF-4 (Network Common Data Form) file format (https://www.unidata.ucar.edu/software/netcdf), which is built on top of the Hierarchical Data Format version 5 (HDF5) (https://hdfgroup.github.io/hdf5). HDF5 supports large, complex and heterogenous data by using a directory-like structure to organize the data within the file.

Data in MDB files are stored in variables, i.e., multi-dimensional arrays of values of the same type. The shape of the arrays is defined using the following dimensions:

- *satellite_id*: satellite measurements (i.e., satellite *Rrs* extracts). It is defined as unlimited to enable appending more data. Its actual length is the number of satellite measurements included in the file.
- *insitu_id*: *in situ* measurements (i.e., *in situ Rrs* spectra). Its length indicates the maximum number of *in situ* measurements that could be associated with a specific satellite measurement.
- *row* and *columns*: spatial coordinates of the satellite extracts, which are defined as squared boxes of *n* rows by *n* columns centered on the *in situ* site location being *n* an uneven number of pixels.
- *satellite_bands*: satellite spectral bands. Its length depends on the number of bands of the sensor and/or the AC processor.
- *insitu_original_bands*: *in situ* spectral bands. Its length depends on the instrument (e.g., HYPSTAR® include 1,600 bands).
- *mu_id*: match-up of a satellite and an *in situ* measurement at a specific wavelength. It is also defined as unlimited. Its actual length is the number of satellite measurements by the number of satellite bands included in the validation analysis.

The list of variables with their corresponding dimensions is summarized in Table 1. All the variables (except for *time_difference*) could be grouped in the following groups: satellite variables (*satellite* prefix); *in situ* variables (*insitu* prefix); match-ups variables (*mu* prefix); and flag variables (*flag* prefix).

The MDB file also contains metadata (global attributes) to fully characterize and identify the file, including satellite and *in situ* sensor, name, latitude and longitude of the site, creation date, etc., (Supplementary Material MDB file structure, Section 2; Table 3).

2.2 MDB tools

We developed a set of Python tools to work with MDB files (Supplementary Material MDB User Manual). Tools are organized in three modules: SAT_EXTRACT, MDB_builder and MDB_reader, which are included in the *hypernets_val* repository available from the HYPERNETS project GitHub (https://github.com/HYPERNETS/hypernets_val). Figure 1 summarizes the workflow for the implementation of validation analysis based on the MDB-approach.

2.2.1 Extraction module (SAT_EXTRACT)

This module aims at extracting data from a specific satellite product for a box centered on the specified site location. The extract size can be defined by the user depending on the satellite resolution and/or site characteristics. By default, it is set to 25 × 25 pixels, which is enough for applying all the validation protocols proposed in literature for both medium- and high-resolution satellites (see review in Concha et al., 2021).

Different Python extracts tools were developed for working with specific satellite sensors and/or AC processors. For the multi-site validation exercise presented in this article, we used the tools for Sentinel-3 WFR, Sentinel-2 C2RCC and Sentinel-2 ACOLITE.

The output of the extract tools is a single NetCDF extract file for each satellite product and site, including a set of variables named

TABLE 1 List of variables included in the MDB file. Unix time is the number of seconds since 1 January 1970 00:00:00 UTC.

Variable	Description (units)	Dimensions
satellite_bands	Band wavelengths (nm)	*satellite_bands*
satellite_time	Overpass time (Unix time)	*satellite_id*
satellite_Rrs	Satellite-derived *Rrs* (sr^{-1})	*satellite_id, satellite_bands, rows, columns*
satellite_latitude	Latitude (degrees North)	*satellite_id, rows, columns*
satellite_longitude	Longitude (degrees East)	
satellite_AOT_0865p50	Aerosol Optical Thickness (unitless)	
satellite_WQSF	Flags Data Set (Sentinel-3 WFR) (unitless)	
satellite_OAA	Observation Azimuth Angle (°)	
satellite_OZA	Observation Zenith Angle (°)	
satellite_SAA	Sun Azimuth Angle (°)	
satellite_SZA	Sun Zenith Angle (°)	
insitu_original_bands	Instrument wavelengths (nm)	*insitu_original_bands*
insitu_time	Measurement time	*satellite_id, insitu_id*
insitu_Rrs	*In situ Rrs* (sr^{-1})	*satellite_id, insitu_original_bands, insitu_id*
insitu_Rrs_nosc	*In situ Rrs* without correction for the NIR similarity spectrum (sr^{-1})	
insitu_quality_flag	Quality Flag Dataset (unitless)	*satellite_id, insitu_id*
insitu_site_flag	Site Flag Dataset (unitless)	
insitu_OAA	Observation Azimuth Angle (°)	
insitu_OZA	Observation Zenith Angle (°)	
insitu_SAA	Sun Azimuth Angle (°)	
insitu_SZA	Sun Zenith Angle (°)	
mu_ins_rrs	Match-up *in situ Rrs* (sr^{-1})	*mu_id*
mu_sat_rrs	Match-up satellite *Rrs* (sr^{-1})	
mu_wavelength	Match-up wavelength (nm)	
mu_satellite_id	Match-up *satellite_id* (unitless)	
mu_valid	Match-up validity (unitless)	*satellite_id*
mu_insitu_id	Match-up *insitu_id* (unitless)	
mu_ins_time	Match-up *in situ* time (Unix time)	
mu_sat_time	Match-up satellite time (Unix time)	
mu_time_diff	Match-up time difference (seconds)	
flag_ac	Atmospheric correction (unitless)	*satellite_id*
flag_site	Site (unitless)	
flag_satellite	Satellite mission (unitless)	
flag_sensor	Satellite sensor (unitless)	
time_difference	Time difference (seconds)	*satellite_id*

with the prefix *satellite* (see Table 1). The variable used in the validation is *satellite_Rrs*, containing extracts of *Rrs* values for each satellite band. Other variables store the overpass time, the band wavelengths, the geographic coordinates (*satellite_latitude* and *satellite_longitude*) and data useful for the quality control, as sun and observation angles (e.g., *satellite_OZA*), aerosol optical thickness (*satellite_AOT_0865p50*) or *flag* bands for masking (e.g., *satellite_WQSF*).

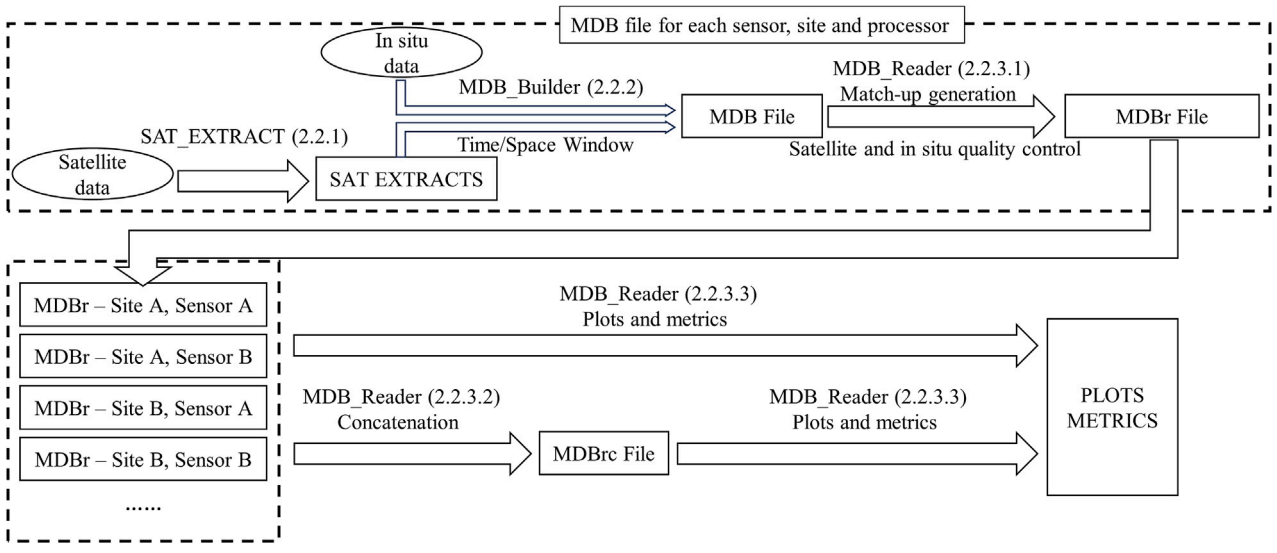


FIGURE 1
Workflow for the implementation of validation analysis using the MDB-based approach.

2.2.2 Building module (MDB_builder)

The MDB_builder module aims at generating MDB files containing all the potential match-ups between satellite and *in situ* data. A single MDB file is produced for each satellite sensor, atmospheric correction processor and site.

The output MDB file includes: 1) the extracts of satellite data generated in the previous step, which are stored in the variables with the *satellite* prefix; and 2) the corresponding *in situ* data () available for the specific site within a time window from the satellite overpass time, which are stored in the variables identified with the *insitu* prefix (Table 1). *insitu_Rrs* contain the quality-assured Level-2 *Rrs in situ* spectra associated with each satellite extract. In this work for the HYPSTAR® spectra, *Rrs* with (*insitu_Rrs*) and without (*insitu_Rrs_nosc*) applying the correction for the NIR similarity spectrum were stored. Other variables include measurement time (*insitu_time*), band wavelengths (*insitu_original_bands*), geometry information (e.g., *insitu_SZA*) or *flags* datasets for masking (*insitu_quality_flags* or *insitu_site_flags*).

The time window, i.e., the maximum time difference between the *in situ* and satellite measurements, is defined by the user. Hence, the maximum number of *in situ* observations associated with a specific satellite extract (length of dimension *insitu_id*) depends on this time window and the *in situ* measurement frequency. This value is automatically determined from data or set by the user.

In this work, defaults are set to a time window of 3 h and a maximum of 40 *in situ Rrs* spectra. Depending on the site, HYPSTAR® collects automatically data with a time interval between 10 and 30 min, although the number of available spectra is not always the same one as some measurements are not processed to quality-assured level-2 *Rrs* spectra. Overall, the default (3 h) time window enable to collect enough data for maximizing the number of valid match-ups for all the sites.

2.2.3 Reader module (MDB_reader)

The MDB_reader module includes a set of tools for performing the validation analysis starting from the MDB files produced in the previous step. The approach consists of three steps: 1) Match-up generation; 2) Optional concatenation for multi-mission, multi-site and multi-processor analysis; 3) Plot production and metric computation.

2.2.3.1 Match-up generation

The match-up generation tool aims at producing match-ups, i.e., pairs of satellite and *in situ Rrs* at a given wavelength for the later plot production and metric computation. It uses as input a specific MDB file (The required quality control options for the satellite and *in situ* data and the spatiotemporal colocation protocols are defined by the user (Concha et al., 2021).

The process is divided into four steps:

1) Quality checking of satellite data: Satellite measurements are evaluated and identified as valid or invalid according to the criteria defined by the user, such as the size of the satellite extract and minimum number of valid pixels, masks based on flag lists or band (*Rrs* or geometry) thresholds, or spatial homogeneity tests based on the coefficient of variation or other extract statistics.
2) Quality checking of *in situ* data: *In situ* spectra are also defined as valid or invalid according to the criteria defined by the user, such as flag datasets or *Rrs* thresholds for specific spectral ranges.
3) Match-up preparation: Match-ups, i.e., pairs of satellite and *in situ Rrs* values, are obtained for all the available satellite bands or for a band list defined by the user. Satellite *Rrs* are derived from the satellite extract according to the user options, including the reported quantity (mean or median) and the possibility of applying outliers based on the standard deviation

or the interquartile range. *In situ Rrs* are derived from the closest valid spectra to the satellite acquisition time. The user can decide if the *Rrs* value for each wavelength is retrieved as the value at the nearest wavelength to the satellite band or applying the spectral response function of the satellite sensor.

4) Match-up validity: A match-up is defined as valid if both the satellite and *in situ* measurements are valid (steps 1 and 2) and if the time difference between both acquisitions is lower than a threshold defined by the user.

Output data are stored in a set of new variables identified with the *mu* prefix (Table 1) and saved in an extended copy of the MDB file (MDBr). Data available for each match-up include *Rrs* (*mu_sat_rrs* and *mu_ins_rrs*), identifiers (*mu_satellite_id* and *mu_insitu_id*) and acquisition times (*mu_sat_time* and *mu_ins_time*) for both satellite and *in situ* measurements, as well as wavelength (*mu_wavelength*), validity (*mu_valid*) and time difference (*mu_time_diff*).

2.2.3.2 MDB concatenation

The concatenation tool creates a new MDB file (MDBrc) by assembling the match-ups from single MDB files with match-up values generated in the previous step. Therefore, results from different satellite/sensor, processed with different AC algorithms and/or based on *in situ* data from different sites are combined in a single file to obtain multi-mission, multi-processor and/or multi-site validation results.

The match-ups are correctly identified in the extended MDBrc file using new variables identified with the *flag* prefix (Table 1), as *flag_ac* (for the AC processor), *flag_satellite*, *flag_sensor* or *flag_site*.

2.2.3.3 Plots and metrics

The plot tool aims as obtaining different types of plot (e.g., scatter plots, average spectra) and metrics based on the recommendations in literature (Concha et al., 2021). It uses extended MDB files with match-ups (MDBr or MDBrc) as input. Options and parameters are defined by the user. Examples of plots are shown in the results for Sentinel-3 and Sentinel-2 in Section 3.1; Section 3.2, respectively.

Metrics used in this work are the determination coefficient (R^2), Root Mean Square Deviation (RMSD); Absolute Percent Difference (APD), Relative Percent Difference (RPD) and bias, which are computed by the following equations (Eqs 1–5) using the *in situ* (x) and satellite (y) *Rrs* values:

$$R^2 = \frac{\sum_{i=1}^{N}(x_i-\bar{x})(y_i-\bar{y})}{\sqrt{\sum_{i=1}^{N}(x_i-\bar{x})^2}\sqrt{\sum_{i=1}^{N}(y_i-\bar{y})^2}} \quad (1)$$

$$RMSD = \sqrt{\frac{\sum_{i=1}^{N}(y_i-x_i)^2}{N}} \quad (2)$$

$$APD = \frac{1}{N}\sum_{i=1}^{N}\frac{|y_i-x_i|}{x_i}\times 100\% \quad (3)$$

$$RPD = \frac{1}{N}\sum_{i=1}^{N}\frac{y_i-x_i}{x_i}\times 100\% \quad (4)$$

$$bias = \frac{1}{N}\sum_{i=1}^{N} y_i - x_i \quad (5)$$

R^2 (unitless) assesses the agreement between the satellite and *in situ Rrs* ranging from 0 (no agreement) to 1 (perfect agreement). RMSD and APD quantify the differences between the satellite and *in situ* measurements in *Rrs* units (sr^{-1}) and in percentage, respectively. RPD measures the relative error in percentage, whereas the bias (in *Rrs* units: sr^{-1}) is useful for checking if there is overestimation (positive values) or underestimation (negative values). Some metrics are displayed in the scatter plot of *Rrs* match-ups in addition to the identity line ($y = x$) and the linear regression line based on the least square method (Figures 5, 10, 11).

2.3 Validation of Sentinel-3 OLCI level 2 WFR

We applied the MDB-based approach for a multi-site validation of Sentinel-3 OLCI Level 2 Water Full Resolution (WFR) product using HYPSTAR® data from six sites of the WATERHYPERNET network. Data were collected during the HYPERNETS deployment phase between January 2021 and March 2023.

2.3.1 Satellite and *in situ* data

The OLCI WFR product is operationally processed by EUMETSAT for both Sentinel-3A (from April 2016 to present) and 3B (from May 2018 to present) missions using the OLCI L2 processor IPF-OL-2 version 07 (EUMETSAT, 2021; Zibordi et al., 2022). OLCI WFR provides *Rrs* for 16 bands (all the OLCI bands except those dedicated to atmospheric measurements) between 400 nm and 1,020 nn at 300 m resolution, and with a revisit time of 1 day combining both missions. It also includes a pixel classification band, i.e., Water Quality and Science Flags (WQSF), which is imported into the MDB file (*satellite_ WQSF*, see Table 1). Data were available from the EUMETSAT Ocean Colour baseline collection OL_L2M.003.

In this study, HYPSTAR® publicly available datasets acquired at six water sites were included in the validation analysis (Table 2): Acqua Alta Oceanographic Tower in Venice (AAOT), Italy (VEIT) (Brando et al., 2023a); Garda Lake, Italy (GAIT) (Brando et al., 2023b); Berre, France (BEFR) (Doxaran and Corizzi, 2023a); Magest station—GIRonde estuary (MAGIR), France (MAFR) (Doxaran and Corizzi, 2023b); Rio de la Plata (RdP-EsNM), Argentina (LPAR) (Dogliotti et al., 2023); and Zeebrugge, Belgium (M1BE) (Goyens and Gammaru, 2023). The optical water types at the six sites range from clear to highly turbid waters (Table 2).

The reference data from HYPSTAR® are processed with the "hypernets processor" (https://github.com/HYPERNETS/hypernets_processor) and assumed to be quality-assured Level 2 *Rrs* data (with site specific quality checks, see Tables 3, 4, but without extrapolation of the viewing and illumination geometry).

Rrs data are calculated according to Eq. 6, i.e., the measured above water upwelling radiance, L_u *(θ, Δφ, θs, λ) is* corrected for the reflectance at the air-water interface and is normalized by the downwelling irradiance, E_d *(θs, λ)*. The symbols θ, $\Delta\varphi$, θs, and λ stand for the viewing zenith angle, the relative azimuth angle between sun and sensor, the solar zenith angle and wavelength, respectively. The reflectance at the air-water interface is the product of the air-water interface reflectance factor, ρF *(θ, Δφ, θs, ws)*, taken from Mobley (1999) and with *ws* being the wind speed, and, the downwelling radiance, L_d, measured at a an angle reciprocal to the measurement of L_u, i.e., θ-140°. More details on the HYPSTAR® data

TABLE 2 WATERHYPERNET sites included in the Sentinel-3 validation analysis.

Site	Site code	Country	Water type	Location	Installation date
Berre	BEFR	France	Inland—productive and turbid	43°28′09″ N 5°05′03″ E	2021-02-24
AAOT	VEIT	Italy	Moderately to turbid coastal waters	45°18′51.29″ N 12°30′29.70″ E	2021-04-16
MAGIR	MAFR	France	Estuarine turbid to highly turbid	45°32′43.69″ N 1°02′24.62″ W	2021-11-08
RdP-EsNM	LPAR	Argentina	Estuarine highly turbid	34°49′4.76″ S 57°53′45.28″ W	2021-12-14
Lake Garda	GAIT	Italy	Inland—clear waters (macrophytes)	45°34′35.93″ N 10°34′47.80″ E	2022-06-08
Zeebrugge	M1BE	Belgium	Marine—very turbid	51°21′43.2″ N 3°07′12″ E	2022-11-22

processing are available in Goyens et al., 2021, Goyens et al., 2022 and De Vis et al. 2024.

$$Rrs(\theta,\Delta\varphi,\theta s,\lambda) = [L_u(\theta,\Delta\varphi,\theta s,\lambda) - \rho F(\theta,\Delta\varphi,\theta s,ws).L_d(\theta,\Delta\varphi,\theta s,\lambda)] / Ed(\theta s,\lambda) \quad (6)$$

For most sites the NIR similarity correction (Ruddick et al., 2024) has been applied to correct the spectra for remaining glint. However, for some sites the theory of the NIR Similarity correction is not valid, in particular in very turbid waters, explaining why the *Rrs* data without the NIR similarity spectrum correction is used. Both *Rrs* variables (*insitu_Rrs* and *insitu_Rrs_nosc*) are delivered by the "hypernets processor" and are available in the MDB files (see Table 1). It is at the discretion of the end-user to select the appropriate final product. The HYPSTAR® Level-2 files also provide flags (imported into the MDB file as *insitu_quality_flag*) that are useful for checking the validity of the *Rrs* spectra.

2.3.2 MDB-based approach and validation protocols

As explained in Section 2.2, the MDB-based approach consists of three steps:

a) Satellite extract: Production of satellite extracts from OLCI WFR images for all the sites and dates with available *in situ* data (Section 2.2.1).
b) MDB building: Preparation of 12 MDB files including satellite and *in situ* data for each platform (Sentinel-3A and 3B) and site (2 platforms x 6 sites) (Section 2.2.2).
c) MDB reader: Match-ups generation for each single MDB implementing the corresponding validation protocols; concatenation to produce a single MDB file; and production of plots and statistics (Section 2.2.3)

Validation protocols are summarized in Table 3. Default options are based on the recommendations available in literature for Sentinel-3 OLCI (Concha et al., 2021; EUMETSAT, 2022). Protocols were adapted for some sites with specific characteristics.

All the available bands were included in the analysis except for 1,020 nm, since the combination of a greater variability of the HYPSTAR® spectra in the near infrared and the low signal (except for LPAR and MAFR) leads to unreliable results.

Regarding the satellite quality control, the same flag list based on the WQSF flag band was implemented for all the sites. With respect to the default parameters, the main difference is the application of only one valid pixel in the measurement window for GAIT and MAFR (instead of the strict criterium of 9 valid pixels) because of the proximity of the coastline. Moreover, considering that WQSF RNEG flags allow for low negative values up to a defined threshold, we masked negative pixels at some stations in the blue spectral range in order to reduce noise (Table 3).

In situ Rrs data were extracted as the HYPSTAR® L2 values at the nearest wavelength to the corresponding satellite band. Data without the NIR similarity spectrum correction were used for the validation of the sites with high turbid waters (i.e., MAFR, LPAR, and M1BE, Table 2).

2.4 Validation of Sentinel-2 MSI processed using ACOLITE and C2RCC

We used the MDB-based approach for a multi-site and multi-processor validation exercise of Sentinel-2 MSI based on HYPSTAR® data from four WATERHYPERNET sites acquired between January 2021 and March 2023.

2.4.1 Satellite and *in situ* data

Sentinel-2A and 2B Level 1B images available from ESA (revisit time varies between 3 and 5 days combining both missions) were processed to produce Level-2 *Rrs* products at 20 m resolution using two AC processors: the Case 2 Regional Coast Colour, C2RCC (Doerffer and Schiler, 2007; Brockmann et al., 2016) and ACOLITE/DSF (Vanhellemont, 2019a). ACOLITE provides remote sensing reflectance data for 11 bands between 442 nm and 2,200 nm at 20 m spatial resolution. The Version 2 of C2RCC (https://c2rcc.org/

TABLE 3 Default and site-specific protocols implemented in the OLCI WFR validation analysis. Superscripts in the flag list indicate the flags used in the flag groups shown in Figure 3 (1: S3_CLOUD; 2: S3_RWNEG; 3: S3_INVALID; 4: HIGHGLINT; 5: HISOLZEN).

Default	
Wavelength (in nm): 400, 412.5, 442.5, 490, 510, 560, 620, 665, 673.75, 681.25, 708.75, 753.75, 778.75,865, 885	
Measurement window size: 3 × 3 pixels	
Minimum number of valid pixels: 9	
Flag List (WQSF): LAND, COASTLINE, CLOUD[1], CLOUD_AMBIGUOUS[1], CLOUD_MARGIN[1], RWNEG_O2[2], RWNEG_O3[2], RWNEG_O4[2], RWNEG_O5[2], RWNEG_O6[2], RWNEG_O7[2], RWNEG_O8[2], INVALID[3], AC_FAIL[3], SUSPECT[3], HIGHGLINT[4], HISOLZEN[5], COSMETIC, SATURATED, SNOW_ICE, WHITECAPS	
Reported quantity: Average after excluding outliers	
Geometry thresholds	
Solar Zenith Angle (SZA) > 70°	
Viewing Zenith Angle (OZA) > 70°	
Spatial Homogeneity Test: CV > 20% at 560 nm	
Time window: 2 h	
Site-specific protocols	
BEFR	Default
	Masked pixels with negative Rrs at 400 nm, 412.5 nm or 442.5 nm
VEIT	Default
MAFR	Default
	Minimum number of valid pixels: 1
	Masked pixels with negative Rrs at 442.5 nm
	NIR similarity spectrum correction is not applied for in situ data
LPAR	Default
	Masked pixels with negative Rrs at 442.5 nm
	NIR similarity spectrum correction is not applied for in situ data
GAIT	Default
	Minimum number of valid pixels: 1
M1BE	Default
	NIR similarity spectrum correction is not applied for in situ data

neural-nets/) provides *Rrs* data for 8 MSI bands between 442 nm and 865 nm at 20 m spatial resolution. In addition to the atmospheric correction, the pixels are also classified to flag non-water and/or cloud contaminated pixels. Therefore, the IdePix software (v2.2.10, algorithm update 8.0.3), available as a SNAP processor, is used. How the data has been processed is detailed in Van der Zande et al. (2022). This document also provides a description of both AC algorithms, and their respective assumptions. Note, however, that the complementary quality tests coming from the AC algorithms suggested by the authors have not been applied here. The IdePix classes used for flagging are given in Table 4.

Four sites were included in the analysis (Table 2): Acqua Alta Oceanographic Tower (VEIT), Berre (BEFR), MAGIR (MAFR), and Rio de la Plata (LPAR). As compared to Sentinel-3 (see Section 2.3.1), Lake Garda (GAIT) and Zeebrugge (M1BE) were excluded because only a small number of match-ups was available since most of the images were affected by sun glint (GAIT) or the deployment period was too short (M1BE).

2.4.2 MDB-based approach and validation protocols

The MDB-based approach (see Section 2.2) was based on three steps:

a) Satellite extract (Section 2.2.1): Production of satellite extracts from ACOLITE and C2RCC images for all the sites and dates with available *in situ* data.
b) MDB building (Section 2.2.2): Generation of 16 MDB files including satellite and *in situ* data for each platform (Sentinel-2A and 2B), AC processor (ACOLITE and C2RCC) and site (2 platforms x 2 AC processors x 4 sites).

TABLE 4 Default and site-specific protocols implemented in the MSI validation analysis. Superscripts in the flag list indicate the flags used in the flag groups shown in Figure 8 (1: S2_CLOUD; 2: S2_SHADOW; 3: S2_WHITE/BRIGHT). Note that the same flagging based on IdePix software was applied to both C2RCC and ACOLITE processors.

Default	
Wavelengths (in nm): 442.7, 492.4, 559.8, 664.6, 704.1, 740.5, 782.8, 864.7	
Measurement window size: 17 × 17 pixels	
Inner masked window size: 3 × 3 pixels	
Minimum number of valid pixels: 140	
Flag List: INVALID, CLOUD[1], CLOUD_AMBIGUOUS[1], CLOUD_SURE[1], CLOUD_BUFFER[1], CIRRUS_SURE[1], CIRRUS_AMBIGUOUS[1], COASTLINE, LAND, CLEAR_LAND, VEG_RISK, CLOUD_SHADOW[2], MOUNTAIN_SHADOW[2], POTENTIAL_SHADOW[2], CLUSTERED_CLOUD_SHADOW[2], SNOW_ICE, WHITE[3], BRIGHTWHITE[3]	
Reported quantity: Average after excluding outliers	
Geometry thresholds	
Solar Zenith Angle (SZA) > 70°	
Viewing Zenith Angle (OZA) > 70°	
Spatial Homogeneity Test: CV > 20% at 559.8 nm	
Time window: 2 h	
Site-specific protocols	
VEIT	Default
BEFR	Default
MAFR	Default
	Minimum number of valid pixels: 62
	NIR similarity spectrum correction is not applied for *in situ* data
LPAR	Default
	NIR similarity spectrum correction is not applied for *in situ* data

c) MDB reader (Section 2.2.3): Match-ups generation for each single MDB implementing the corresponding validation protocols; concatenation to produce a single MDB file; and production of plots and statistics.

Table 4 summarizes the validation protocols. Default options follow the recommendations available in the literature for high-resolution sensors (Concha et al., 2021). As with Sentinel-3, some variations were implemented to adapt the protocols to the site-specific characteristics.

We included in the validation analysis the eight bands available for both AC processors, using the same flag list based on IdePix (Table 4). Due to the broad band width in Sentinel-2, we implemented Spectral Response Functions (SRF) specific for each Sentinel-2 mission in order to extract the *in situ Rrs* values matching to each satellite band (https://sentinels.copernicus.eu/web/sentinel/user-guides/sentinel-2-msi/document-library/-/asset_publisher/Wk0TKajiISaR/content/sentinel-2a-spectral-responses, accessed on 19 January 2024) Moreover, the NIR similarity spectrum correction was not applied to the HYPSTAR® L2 spectra for the sites with high turbid waters (i.e., MAFR and LPAR) consistently with the Sentinel-3 analysis.

3 Results

3.1 Sentinel-3 OLCI WFR

3.1.1 Coverage

We obtained 1955 match-ups combining data from both Sentinel-3A and 3B missions at the six sites. 595 of these match-ups (around 30%) were classified as valid after applying the quality control (see Section 2.3).

Figure 2 summarizes the temporal distribution showing the total and valid number of match-ups by month and site. The highest number of match-ups are from VEIT and BEFR, as HYPSTAR® radiometers at these sites were working for a longer period with some interruptions since the first half of 2021 until February 2023. Data from GAIT and MAFR were available with some interruptions since beginning 2022, LPAR was working during two short periods (December 2021-February 2022 and May 2022-September 2022) and data from M1BE were not available until February 2023. Note that up to 40 potential match-ups could be obtained for a specific site and month because two match-ups (one per mission) are available for some days.

The temporal distribution of valid match-ups is a result of the percentage of valid match-ups with respect to the total number of

10.3389/frsen.2024.1330317

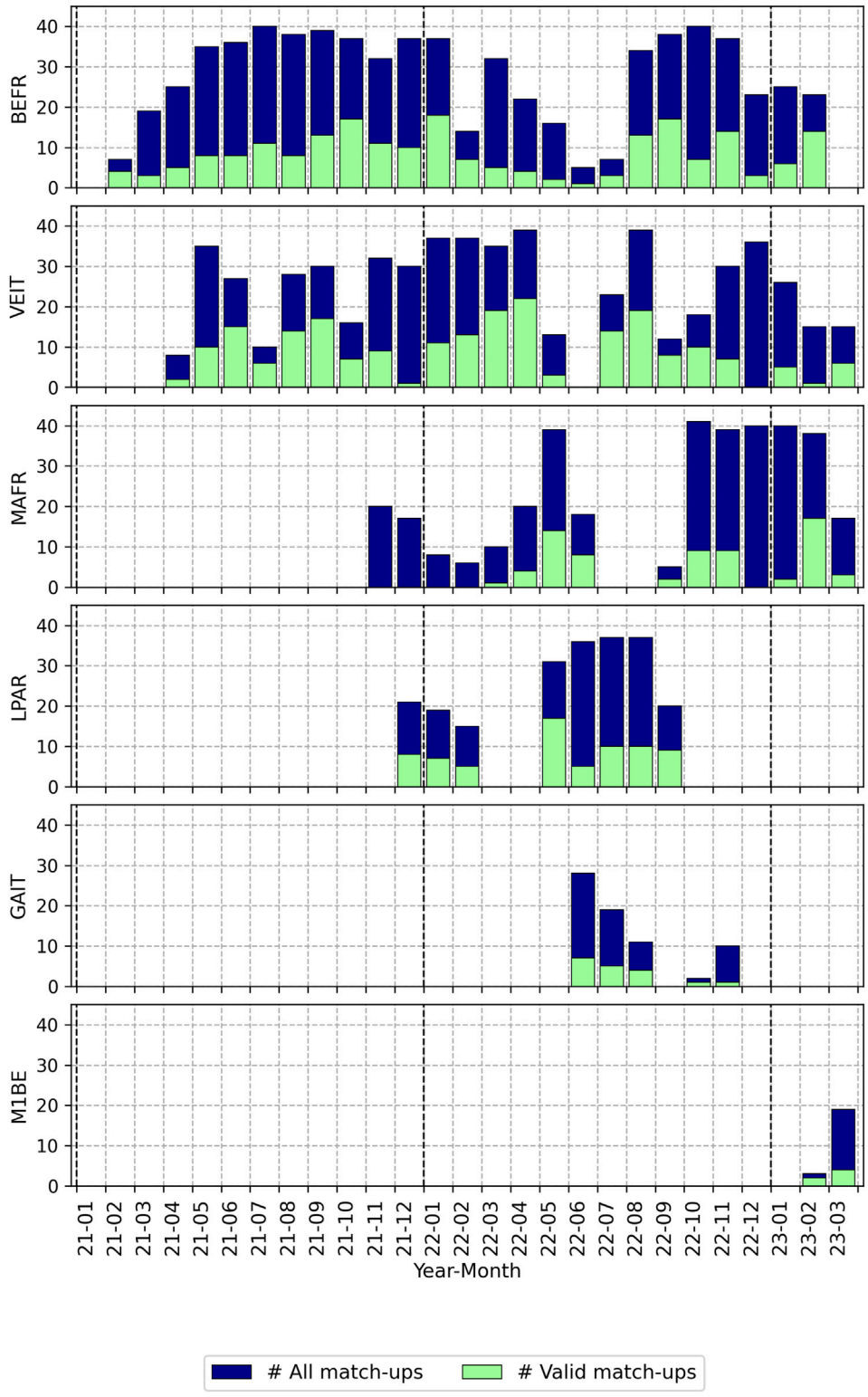


FIGURE 2
Number of total and valid Sentinel-3 WFR match-ups per month and site.

match-ups per site (Figure 3A) and the satellite flags affecting each site (Figure 3B). For instance, VEIT shows the highest validity rates (37.06%), with more than 15 valid match-ups in some months (Figure 2). On the other hand, the lowest percentage is found in MAFR (19.27%), which is explained by the higher impact of the cloud coverage (almost 80%, see Figure 3B). Coverage results from

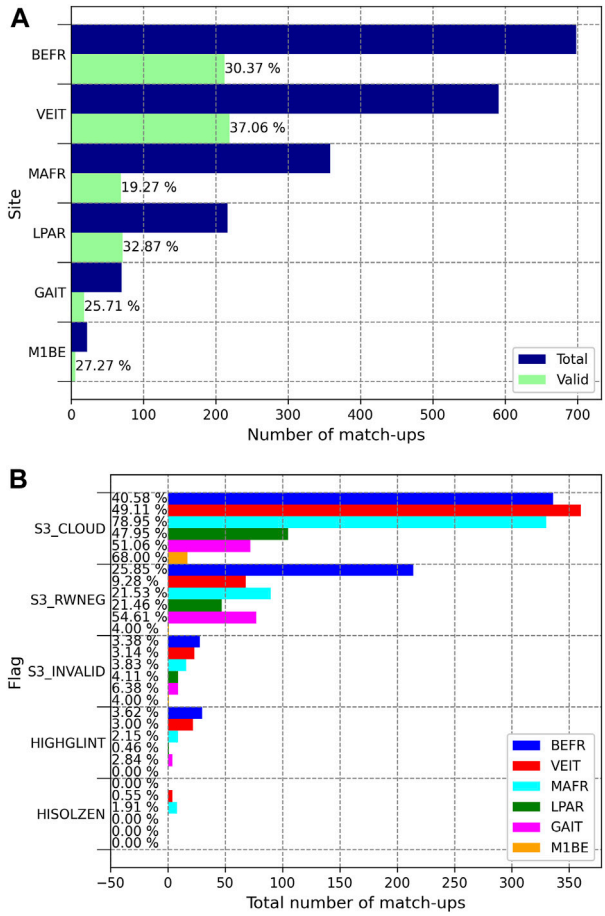


FIGURE 3
(A) Number of total and valid match-ups for each site. Validity rate is also shown. **(B)** Number of match-ups with at least one pixel affected by a specific flag within the measurement window, and percentage with respect to the total number of potential match-ups. Flags included in each flag group are shown in Table 1.

M1BE or GAIT, with values around 25%, are less significant as coming from a shorter deployment period.

Most of invalid match-ups are caused by the cloud coverage (Figure 3B), with percentages varying between 40% and 80%. Moreover, negative reflectance values (S3_RWNEG) also have an important impact, especially at sites characterized by low signals in the blue part of the spectrum as BEFR. In fact, VEIT shows a better global coverage than BEFR despite of its higher cloud coverage (49.11% versus 40.58%) because of the lower impact of S3_RWNEG (9.28% versus 49.11%). Other flags have a less significant effect as they only affect a limited number of match-ups (always lower than 7%).

3.1.2 Comparison of *in situ* and satellite spectra

Figure 4 shows the comparison between satellite and *in situ* spectra for each site. Overall, at all the sites the *in situ* and satellite radiometry show similar spectral shape but WFR tends to underestimate the *in situ Rrs* values. Overall, there is a greater variability in the blue part of the spectrum and a higher overlap towards the red and NIR spectral range, with exception of GAIT.

VEIT is characterized by optically complex waters. oligotrophic to mesotrophic waters in function of the phytoplankton seasonal dynamics, some moderately turbid waters occur due to wind and wave driven re-suspension or coastal currents. The *Rrs* spectra are thus characterized by a high variability in the blue and green spectral range (400-560 nm) and low *Rrs* values between 665 nm and 708.75 nm.

BEFR is characterized by moderately turbid waters with rather stable concentrations of CDOM and non-algal particles along the year, and strong seasonal dynamics of phytoplankton with peaks of chl-a concentrations occurring at the end of the summer period. BEFR shows a higher CDOM absorption and lower *Rrs* values than VEIT in the blue part of the spectrum.

As compared to VEIT or BEFR, LPAR, and MAFR sites are characterized by highly turbid sediment-dominated waters with higher *Rrs* ranges. Strong tidal currents and river discharges strongly influence the dynamics of suspended sediment concentrations and therefore the water optical properties. Both sites show also similar spectral shapes except for the 560 nm–708.75 nm spectral range: LPAR shows lower *Rrs* values at 560 nm and higher *Rrs* values between 665 nm and 708.75 nm, specially at 708.75 nm. Compared to LPAR, MAFR shows higher but less variable *Rrs* values in lower wavelengths (400–510 nm) and lower but more variable *Rrs* in the NIR (753.75–885 nm).

GAIT is characterized by clear oligo/meso-trophic lake waters with *Rrs* spectra with a peak centred in the 442.5–510 nm spectral range. As the radiometer is installed in a steep transitional zone, due to varying lake water levels it can measure some shallow waters that may not be captured by the satellite footprint: *Rrs* values between 665 nm and 708.75 nm were consistently higher for the *in situ* spectra than Sentinel-3 WFR. Furthermore a 753.75 nm peak in satellite data not observed in the *in situ* spectra may be due to adjacency effects or the lake elevation not addressed adequately by the atmospheric correction.

Results from M1BE are not significant as they come from only 11 valid match-ups. However, the *Rrs* range, similar to those from LPAR and MAFR, indicates that the site is mainly characterized by turbid waters. This is also in agreement with the literature showing turbid coastal waters around this station (e.g., Vanhellement and Ruddick, 2021 and references therein).

3.1.3 Validation results

Figure 5 shows the scatter plots between satellite and *in situ Rrs* for each wavelength and grouped by site. A high data dispersion and poor correlation (R^2 < 0.35) are observed at 400 nm and 442.5 nm. Better correlations are attained with increasing wavelengths, mainly between 510 nm and 865 nm (R^2 > 0.90), whereas a relative worse fitting is obtained at 442.5 nm or 885 nm. As also observed in Figure 4, a negative bias was found across the whole spectral range. Regression lines also show negative deviations with respect to the identity line ($y = x$). These negative deviations increase with *Rrs* and are mainly linked with match-ups from turbid sites (MAFR, LPAR or M1BE) with *Rrs* values higher that 0.010 sr^{-1}.

Spectral variation of some metrics for each site is shown in Figure 6 (except for M1BE as only 11 match-ups were available). Overall, RMSD values are lower in the 708.75–865 nm spectral range and higher in the blue part of the spectrum. The determination coefficients (R^2) are always higher between 490 nm and 708.75 nm, with a peak at 560 nm and lower values in the blue and towards the

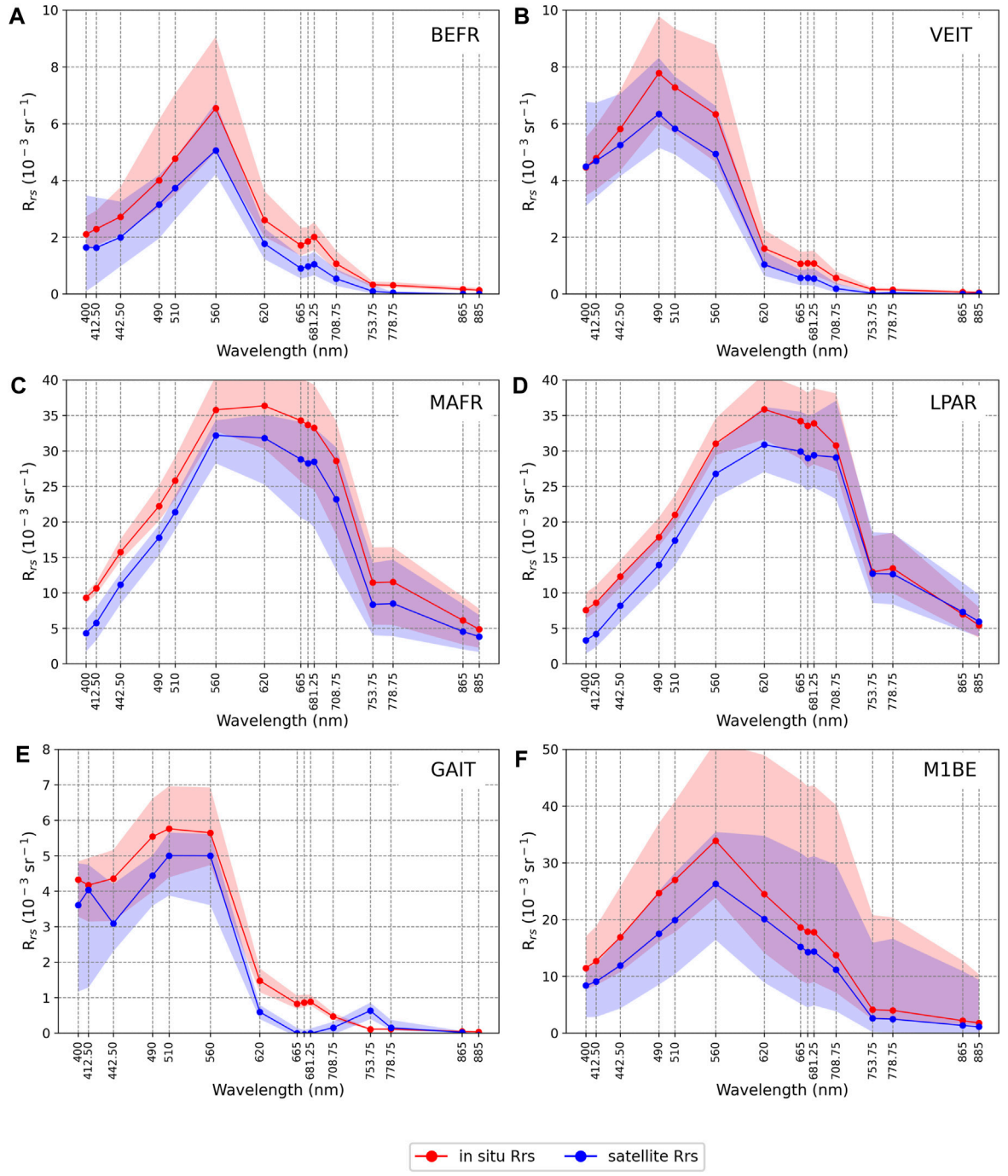


FIGURE 4
Comparison between satellite (Sentinel-3 WFR) and *in situ* (HYPSTAR® L2) spectra for each site: **(A)** BEFR; **(B)** VEIT; **(C)** MAFR; **(D)** LPAR; **(E)** GAIT; **(F)** M1BE. Lines show the average spectra and shadow areas indicate the interquartile range. Note that spectral shapes and Rrs ranges reveal, to some extent, the specific optical characteristics of each site.

red parts of the spectrum. The bias values are always negative, expect for some values near zero (see also Figure 4). Lower bias values are observed in the 708.75–855 nm spectral range.

Analysing the validation metrics by site, VEIT and BEFR show similar global results (including all the bands) in terms of determination coefficient (VEIT: 0.83; BEFR: 0.85), bias (VEIT: −5.9 10^{-4} sr^{-1}: BEFR: −5.8 10^{-4} sr^{-1}) or RMSD (VEIT: 1.6 10^{-3} sr^{-1}; BEFR: 1.1 10^{-3} sr^{-1}). Moreover, bias follows a similar spectral pattern for both sites (Figure 6) despite of the different spectral shape (Figure 4), with negative values between 442.5 nm and 708.75 nm and near zero in the remaining bands (Figures 4, 6). There are also some differences, as BRFR results are better in the 490–560 nm spectral range with higher correlation coefficients and lower bias and RMSD values.

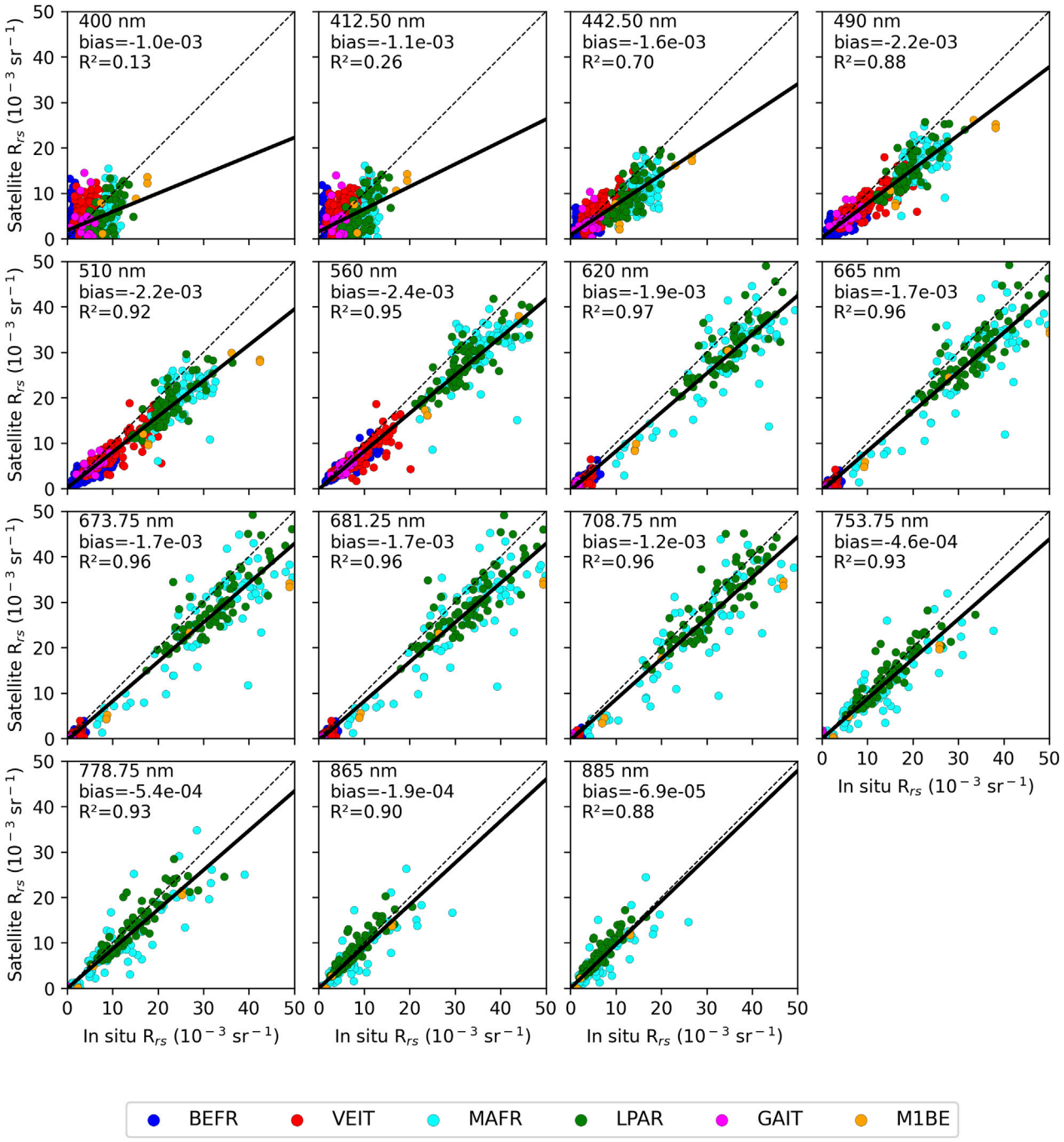


FIGURE 5
Scatter plot of *Rrs* match-ups between satellite (Sentinel-3 WFR) and *in situ* (L2 HYPSTAR®) measurements for each OLCI band. Data points are coloured by site. Statistics are computed including the six sites.

As compared to VEIT/BEFR, sites characterized by highly turbid waters (i.e., MAFR and LPAR) show remarkably higher RMSD and bias values across the whole spectrum, but mainly in the 400–681.25 spectral range, and a better fitting (higher R^2 values) between 665 nm and 885 nm. These differences are mainly explained because *Rrs* data from MAFR/LPAR present a higher range (with values up to 0.060 sr^{-1}) causing a higher bias and RMSD, but also better results in terms of correlation. Comparing both turbid sites, results from LPAR are better than those from MAFR in terms of correlation, bias and RMSD for almost all the spectral bands.

Results from GAIT are affected by higher uncertainties in the *Rrs* data because of the low water level in the Lake Garda due to a prolongated drought, which could cause shallow waters and bottom effects. In fact, results from this site are worse in terms of correlation, with only a determination coefficient higher than 0.6 at 560 nm, and bias, with a positive value at 753.75 (Figures 4, 6). Regarding RMSD,

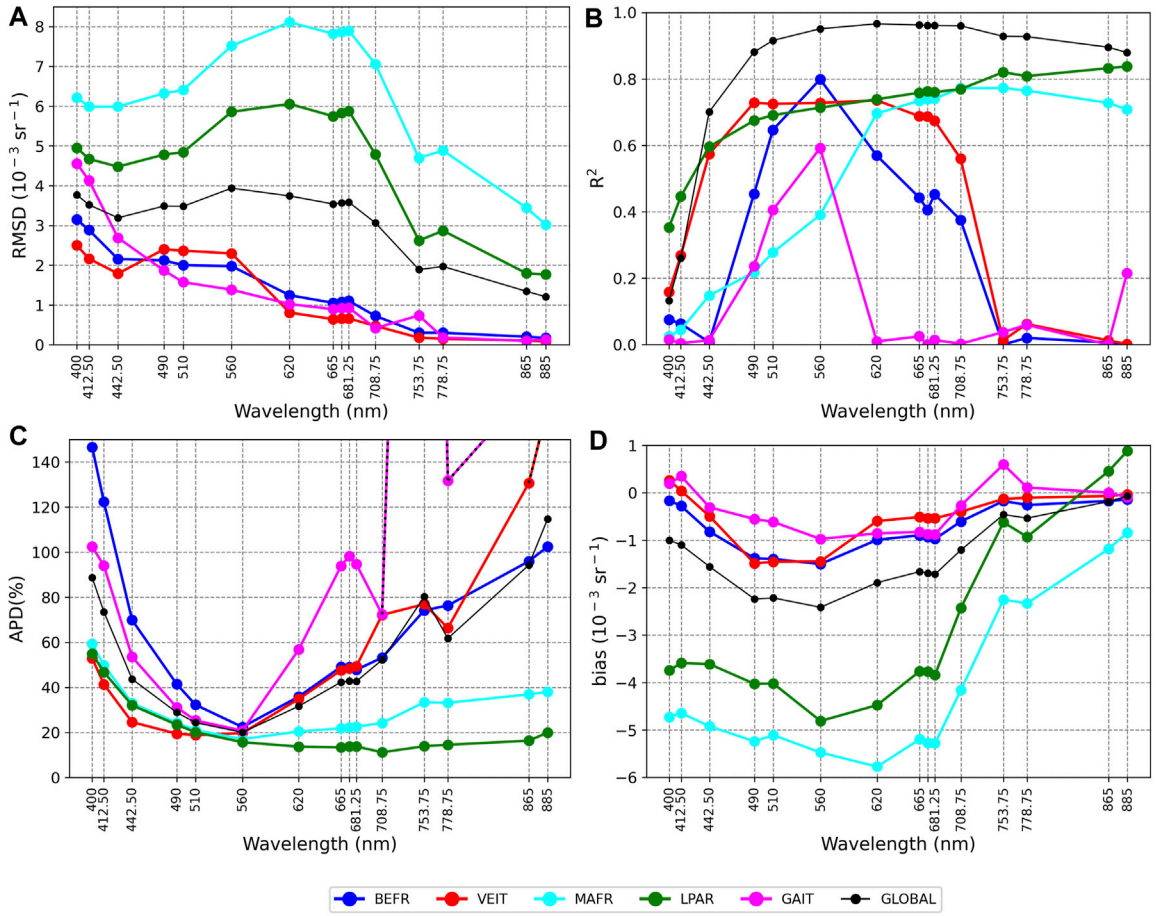


FIGURE 6
Spectral variation of the validation metrics computed for each site from the Sentinel-3 WFR match-ups with HYPSTAR® L2 *in situ* data. **(A)** RMSD (in *Rrs* units: sr^{-1}). **(B)** Determination coefficient (R^2). **(C)** Absolute percentage difference (in percentage). **(D)** Bias (in *Rrs* units: sr^{-1}).

values are similar to those from BEFR except for the blue region (400 nm–442.5 nm).

3.2 Sentinel-2 MSI (ACOLITE and C2RCC)

3.2.1 Coverage

We obtained 508 potential match-ups combining Sentinel-2A and 2B missions and the four WATERHYPERNET sites (BEFR, VEIT, LPAR and MAFR). Since we used a common flagging framework, we obtained almost the same number of valid match-ups for both processors: 226 for ACOLITE and 229 for C2RCC. Validation analysis was only based on common valid match-ups resulting in 221 valid match-ups (~44%), distributed as follows: 99 from BEFR, 77 from VEIT, 32 from LPAR and 11 from MAFR (see also Table 3). As compared to Sentinel-3, GAIT and M1BE were discarded from further analysis because of the small number of valid match-ups.

Figure 7 shows the temporal distribution of the potential and valid match-ups grouped by site. As compared to Sentinel-3, the temporal distribution patterns of potential match-ups are quite similar as a result of the same availability of HYPSTAR® data (Figures 2, 7). However, the total number of match-ups is more limited because of the longer revisit time (3-5 days vs. 1 day) with only 12 potential match-ups as maximum for each single month and site. Regarding the number of valid match-ups, we obtained on average 4 match-ups by site and month, with a peak of 10 valid match-ups available in August 2022 for VEIT (Figure 7).

The rates of valid match-ups with respect to the total number of match-ups (Figure 8A) were similar at BEFR, VEIT and LPAR, with values around 45%. In these three sites, validity rates were higher than those attained using Sentinel-3 OLCI WFR (Figure 3A). This difference is more remarkable at BEFR (48.56% with MSI versus 30.37% with OLCI WFR) because of the impact of negative reflectance values (flag RWNEG, Figure 3B) on WFR match-ups. Finally, MAFR shows a lower validity rate (22%) as a consequence of the cloudiness impact (72.73%), with similar percentages to those obtained with OLCI WFR (Figure 3).

Figure 8B shows the impact of some satellite flags on the match-ups for each site. As with Sentinel-3 WFR, cloud coverage was the most common flag leading to invalid match-ups for all the sites, affecting more than 70% of match-ups at MAFR and around 50% at the other sites. Moreover, bright or white pixels and shadow also had a significant impact.

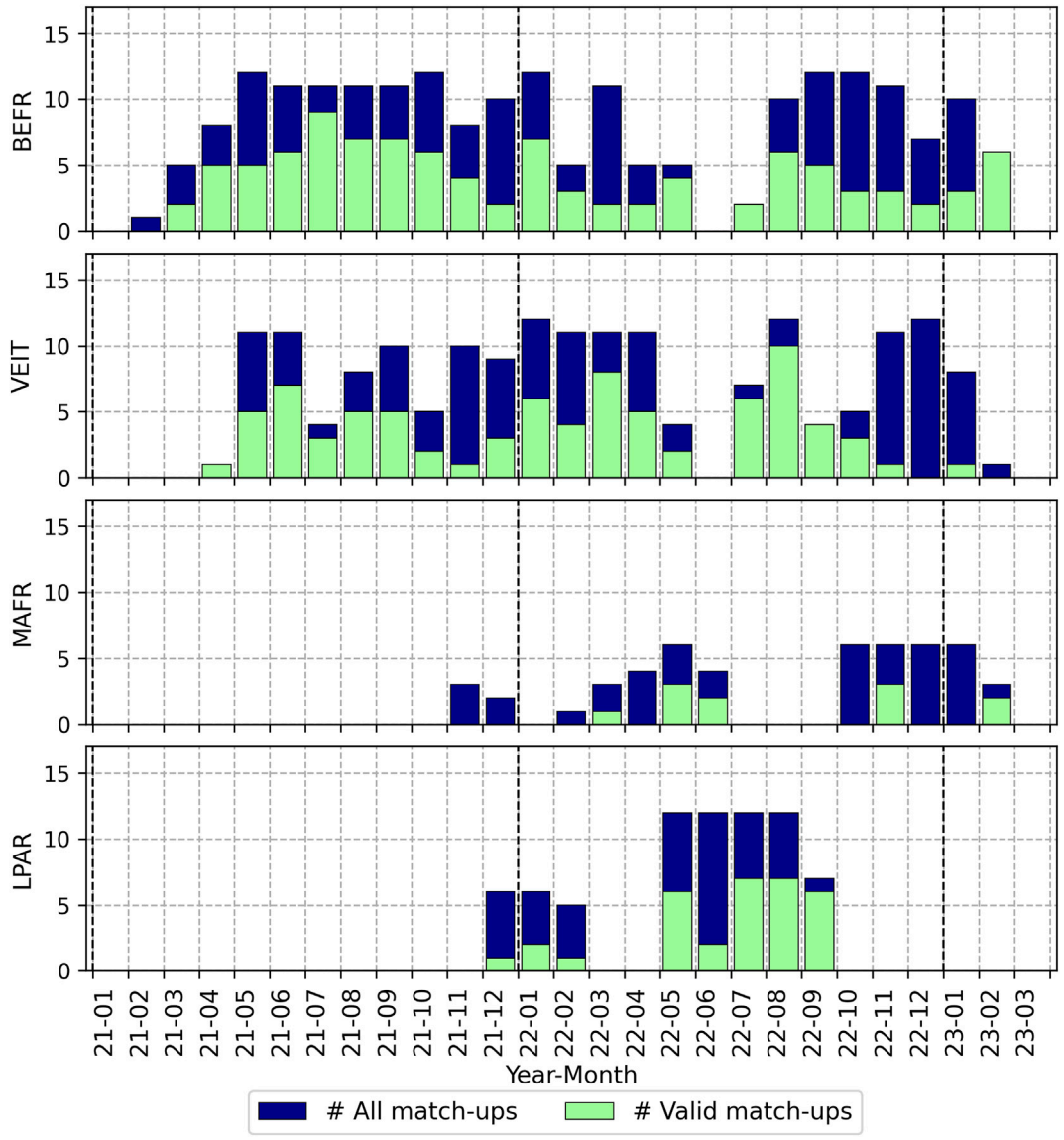


FIGURE 7
Number of total and valid Sentinel-2 match-ups per month and site. The valid number of match-ups include only common match-ups for ACOLITE and C2RCC.

3.2.2 Comparison of *in situ* and satellite spectra

Figure 9 shows the comparison between satellite and *in situ* spectra using both C2RCC and ACOLITE, highlighting the differences between both processors.

At VEIT and BEFR, ACOLITE follows correctly the spectral shape except for the increasing *Rrs* between 442.7 nm and 492.4 nm at VEIT. However, it tends to overestimate keeping a positive bias across the whole spectral range, with values around 1 10^{-3} sr^{-1} (Figures 9A, B).

C2RCC also keeps better the spectral shape at these two sites but with a opposite behaviour as compared to ACOLITE: it tends to underestimate showing non-uniform negative bias, with higher deviations between 442.7 nm and 559.8 nm and lower bias values lower (<0.2 10^{-3} sr^{-1}) with wavelengths greater than 704.1 nm (Figures 9A, B).

At the sites characterized by highly turbid waters, i.e., LPAR and MAFR, C2RCC is able to follow the spectral shape but with a high negative bias across the whole spectra. At LPAR, ACOLITE shows a similar pattern but with lower negative deviations, whereas at MAFR it shows a greater overlap with wavelengths lower than 704.1 nm and overestimation towards the near infrared part of the spectrum (Figures 9B, C).

3.2.3 Validation results

Figure 10 compares the validation results of both AC processors with the metrics computed for each wavelength and site.

In case of VEIT and BEFR, C2RCC outperforms ACOLITE considering almost all the metrics and wavelengths (Figure 10), although ACOLITE shows higher R^2 values in the 442.7–559.8 spectral range (Figure 10B). As also observed in Figure 9, there is a difference in the bias sign: ACOLITE tends to overestimate the *in situ Rrs* (positive bias) whereas C2RCC shows a negative bias nearer zero (Figure 10D). C2RCC follows a similar

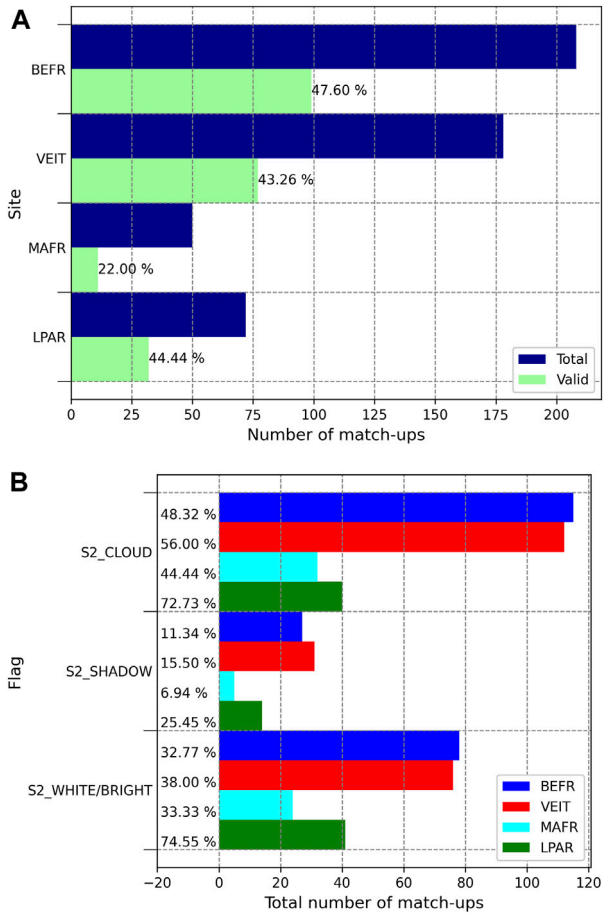


FIGURE 8
(A) Number of total and valid match-ups (based on common match-ups for ACOLITE and C2RCC) for each site. Validity rate is also shown. **(B)** Number of match-ups with at least one pixel affected by a specific flag within the measurement window, and percentage with respect to the total number of potential match-ups. Flags included in each flag group are shown in Table 3.

pattern in both sites with comparable values in terms of RMSD, bias and APD (except for the highest APD at 864.7 nm at VEIT, Figure 10), although the R^2 values are higher at VEIT for all the wavelengths (Figure 10B). The main limit of ACOLITE performance at these two sites is the *Rrs* retrieval in the red and infrared spectral range (wavelengths >664.6 nm), leading to extreme APD values (up to 2000%, Figure 10C).

On the contrary, ACOLITE shows better results than C2RCC at LPAR and MAFR considering almost all the metrics and wavelengths (Figure 10). The main issue of C2RCC at these sites is the high negative bias (Figures 9C, D) despite of the relatively good correlation results observed specially at MAFR (Figure 10B). Regarding ACOLITE, it shows comparable results in terms of error (RMSD and APD, Figures 10A, C) at both sites and higher R^2 values at LPAR (Figure 10B). The ACOLITE bias values are negative at LPAR for all the wavelengths (Figures 9D, 10D), whereas the bias goes from negative to positive values with increasingly wavelengths at MAFR (Figures 9C, 10D).

As with Sentinel-3 OLCI WFR, the higher RMSD magnitudes at LPAR and MAFR are caused by the higher *Rrs* range (Figure 10A) while the APD values for C2RCC were comparable to VEIT and BEFR as this metric isn't sensitive to the signal intensity.

Figure 11 shows the scatter plots of *Rrs* match-ups between ACOLITE and *in situ Rrs* for each wavelength grouped by site. The best results were achieved in the central bands between 559.8 nm and 704.1 nm, with R^2 values around 0.95 and bias lower than 1.0 10^{-3} sr^{-1}. On the contrary, higher dispersion and worse results were attained at 442.7 and 864.7 nm, whereas the remaining bands were found in between with correlation coefficients around 0.78. The scatter plots confirm the overall good results at LPAR and MAFR, with most of the data points around the identity line, whereas bad results are observed at VEIT and BEFR with wavelengths greater than 740.5 nm.

Figure 12 presents the scatter plots of match-ups between C2RCC and *in situ Rrs*. The best results in terms of correlation were achieved with wavelengths between 559.8 nm and 704.1 nm ($R^2 > 0.95$). However, increase negative deviations of the regression line with respect to the identity line were observed with increasing wavelengths, which are mainly caused by the bad results (with a clear underestimation) at LPAR and MAFR.

4 Discussion

The MDB-based approach presented in this work has proven to be a useful tool for the implementation of satellite validation analysis based on *in situ* reference data. The main strong points are: 1) it is an open-source approach open to the community; 2) it provides a common format facilitating the sharing of match-up data and validation results; 3) it allows users to adapt different validation protocols; and 4) it is suitable to perform automated analysis and compare results from different missions, atmospheric correction processors and/or sites. This approach requires both satellite and *in situ* reference data as input.

Regarding satellite data, they should be provided as single NetCDF extract files for each site, satellite sensor and AC processor. Different tools have already been implemented for the generation of these extract files. For instance, the methodology was adapted for a round-robin comparison of four AC algorithms for Sentinel-3 in the Baltic Sea (González Vilas et al., 2024), and for the validation exercises required for the implementation of new level-3 CMEMS datasets. In case of satellite products without a specific extract tool available in the code, users could also provide their own extract files, which should follow the format requirements (see Section 2.2.1).

Regarding the *in situ* reference data, the MDB-based approach was first implemented in the framework of HYPERNETS project to work with HYPSTAR® data. Moreover, it has already been adapted to use *Rrs* data from multispectral instruments collected at fixed platforms, such as AERONET-OC/SeaPRISM, and from shipborne hyperspectral radiometers (González Vilas et al., 2024). In addition to radiometric data, the approach has also been implemented for the validation of chlorophyll-a concentration (González Vilas et al., 2024). Users could also provide their own *in situ* data (radiometry or bio-geochemical parameters) by using the csv format.

The MDB-based approach mainly aimed at the systematic collection of match-up data to evaluate the quality of satellite products. In this work, examples of multi-site comparison were

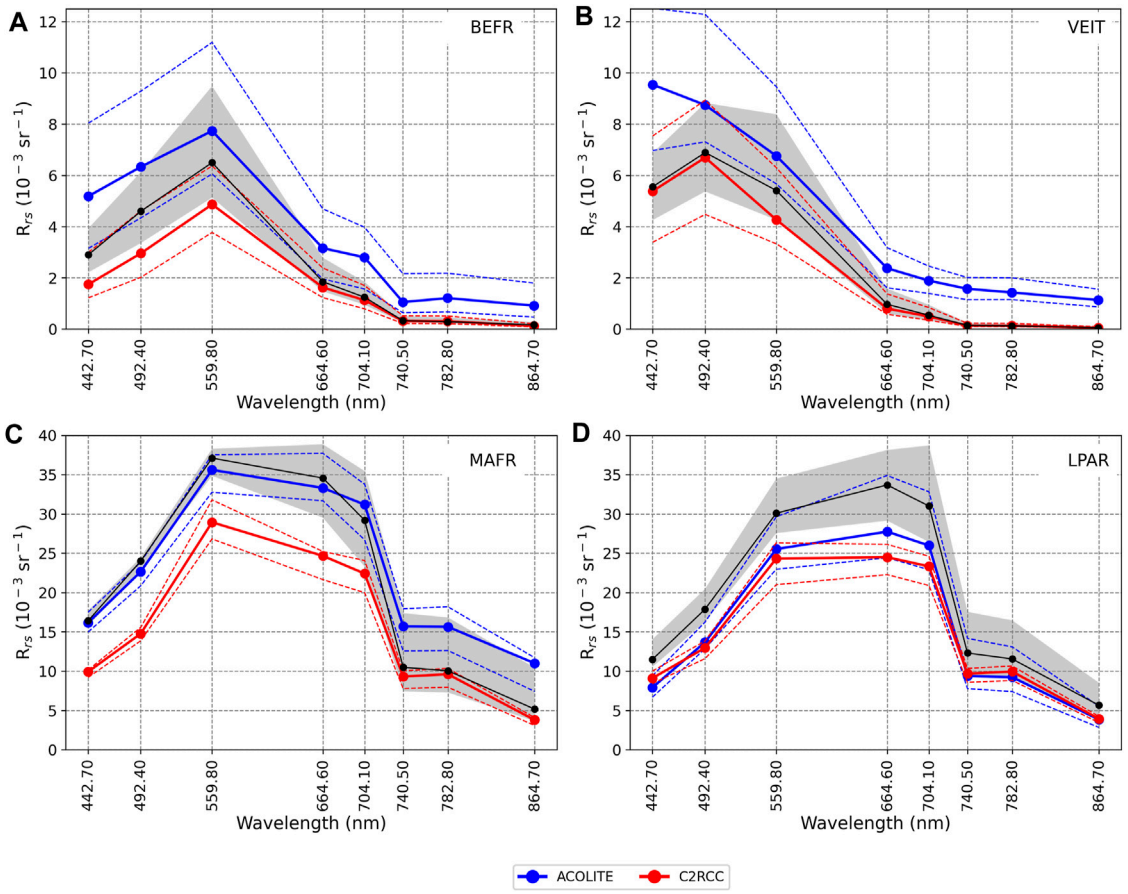


FIGURE 9
Comparison between satellite (Sentinel-2 ACOLITE and C2RCC) and *in situ* (HYPSTAR® L2) spectra for each site: **(A)** VEIT; **(B)** BEFR; **(C)** LPAR; **(D)** MAFR. Solid lines show the average spectra, whereas the grey shadow area and the dashed lines limit the interquartile range for *in situ* and satellite data, respectively.

performed for Sentinel-3 OLCI and Sentinel-2 MSI as these sensors are representative of different spatial, spectral and temporal resolutions, although the methodology could be adapted to other sensors and/or processors.

In case of Sentinel-3 OLCI WFR product, the average percentage of valid match-ups reached 30% with more than 15 match-ups obtained in some months and sites. The comparison across sites with different optical properties enabled an evaluation of the sensor performance over a rather extended reflectance range with values greater than 0.0001 10^{-3} sr^{-1} and up to 50 10^{-3} sr^{-1}. The satellite and *in situ* spectra showed similar spectral shapes at all the sites (except for GAIT), but the satellite product tends to underestimate the *in situ Rrs* with a negative deviation across the spectra and a higher overlap towards the red. The comparison between Sentinel-3A and Sentinel-3B (results not shown in this work, see Ruddick et al., 2024) yielded a similar number of match-ups for both platforms and showed that values of the uncertainty metrics were practically identical.

Moreover, Sentinel-3 OLCI WFR validation results at VEIT were consistent with the comparison based on AERONET-OC/SeaPRISM multispectral data for optically complex waters performed by Zibordi et al., 2022. They limit their analysis to the 400–665 nm spectral range and used data from four sites, including Acqua Alta Oceanographic Tower (AAOT), which is located in the same platform as the HYPSTAR® instrument at VEIT. Their metrics follow a similar spectral pattern as observed in Figure 6. For instance, the correlation coefficient (R^2) shows lower values in the 400–442.5 nm spectral range and higher values between 490 nm and 665 nm, whereas the APD follows a U-shape pattern with higher values between 400 nm and 442.5 nm and between 620 nm and 665 nm but lower values in the 490–560 nm spectral range. In absolute terms, their metrics are better but results are not directly comparable as they include four sites. A more detailed comparison between both instruments (HYPTAR® and SeaPRISM) located at the same platform is expected to be performed in future to verify the consistency of the measurements, similarly to the comparison between two SeaPRISM systems by Mélin et al., 2024.

Regarding Sentinel-2 MSI, we evaluated two atmospheric correction processors, i.e., ACOLITE and C2RCC, using data from four sites. Coverage was lower than using Sentinel-3 due to the difference in the revisit time (3–5 days against 1 day), although we were able to obtain up to 10 valid math-up in a single month (i.e., MAFR). Results evidence that the selection of the optimal processor depends on the optical regime of the sites, i.e., ACOLITE performed better in very turbid waters (LPAR, MAFR) while better

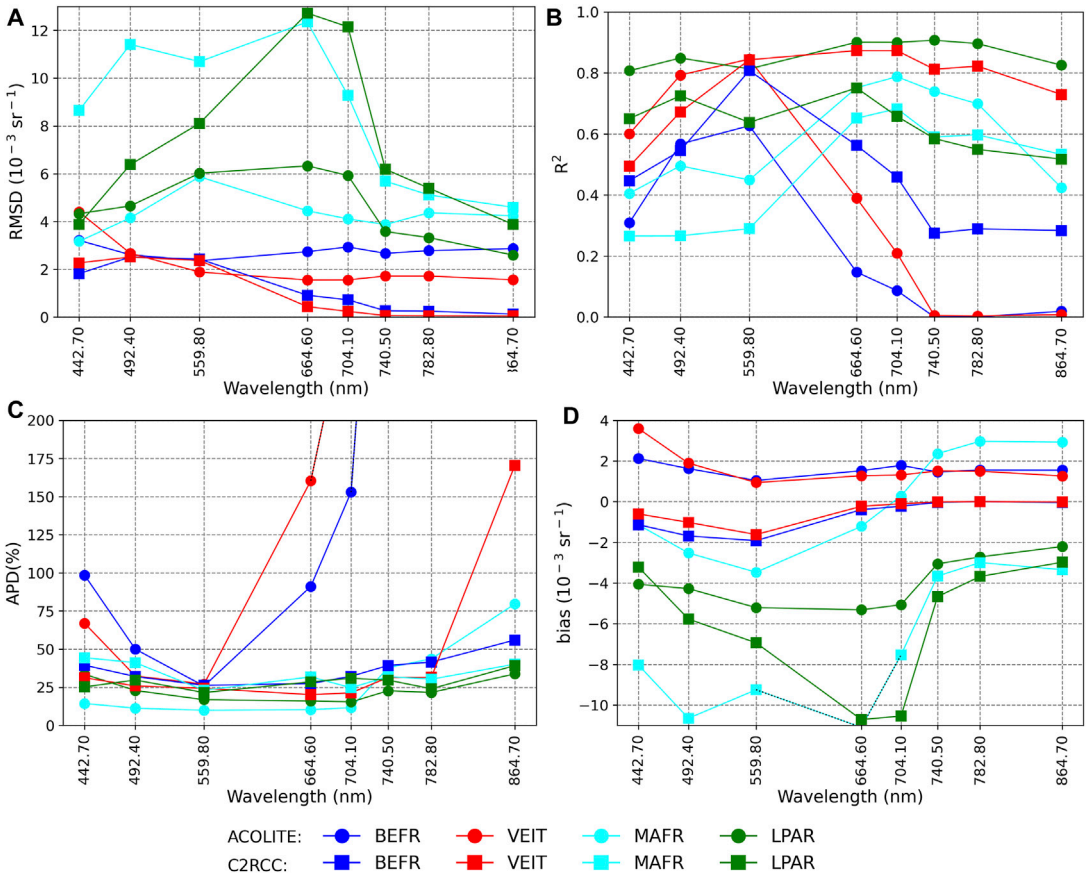


FIGURE 10
Spectral variation of the validation metrics computed for each site from the Sentinel-2 ACOLITE and C2RCC match-ups with HYPSTAR® L2 *in situ* data. **(A)** RMSD (in *Rrs* units: sr^{-1}). **(B)** Determination coefficient (R^2). **(C)** Absolute percentage difference (in percentage). **(D)** Bias (in *Rrs* units: sr^{-1}).

results were attained using C2RCC at the other two sites (BEFR, VEIT). This is in agreement with findings in literature, while C2RCC is designed to handle optically complex waters (Brockman et al., 2016; Warren et al., 2019; Soriano-González et al., 2022), its effectiveness in highly turbid conditions might be limited (Katlane et al., 2023). At the opposite, ACOLITE is known to perform well in moderately and highly turbid waters (Maciel and Pedocchi, 2022; Renosh et al., 2020; Vanhellemont and Ruddick, 2016). Note that both processors were run using default parameters and results could hence be improved by applying specific options depending on the particular site characteristics (e.g., using the glint correction from the ACOLITE processor; Katlane et al., 2023; Tavares et al., 2021).

The application of hyperspectral instruments as HYPSTAR® for validation analysis provide some advantages as compared to multispectral data. Firstly, it enables to obtain results for bands that could be missing in case of multispectral instruments (e.g., 709 nm, 754 nm, and 885 nm in case of AERONET-OC). Secondly, it does not require the use of the band shifting procedure for estimating the *in situ Rrs* at a specific satellite wavelength, which could introduce some uncertainty (Mélin and Sclep, 2015). And finally, it enables the application of spectral response functions, which is especially useful in case of satellite sensors with a large band width as Sentinel-2 MSI. Note also that some WATERHYPERNET sites are located in very turbid waters (LPAR, MAFR, M1BE, see Table 1), showing a higher signal in the NIR bands (between 709 and 885 nm) facilitating the validation analysis in this spectral range.

Overall, as compared to other validation software available for OC validation, our approach is more generic and flexible and enable users to work with different satellite sensors and AC processors, as well as *in situ* sources. For instance, ThoMaS and SeaBASS are designed to use EUMETSAT Sentinel-3 OLCI and OB.DAAC Level-2 products as input, respectively. Hence, they could not be used for the multi-processor validation exercises as the one presented in this work for Sentinel-2 or the one for the Sentinel-3 OLCI in the Baltic Sea (González Vilas et al., 2024). Moreover, our tools also support validation from shipborne *in situ* measurements (González Vilas et al., 2024).

The main limitation of the proposed approach is that the download of the satellite sources and AC processing are not integrated in the software package, so that these tasks must be performed using external tools. Moreover, some features are not still incorporated, as BRDF correction or validation based on reference pixels to avoid perturbations at sub-pixel level and/or within the validation window (e.g., Vanhellemont, 2019b).

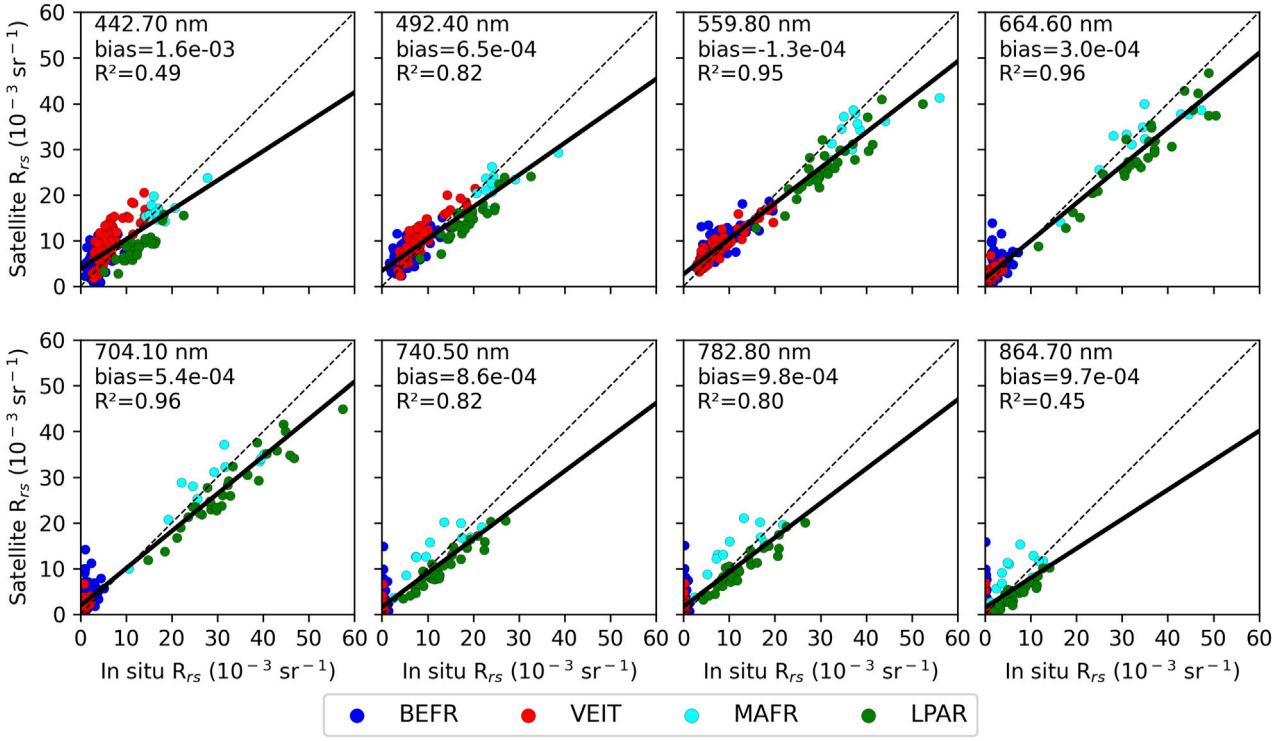


FIGURE 11
Scatter plot of *Rrs* match-ups between satellite (Sentinel-2 ACOLITE) and *in situ* (HYPSTAR® L2) measurements for each MSI band. Data points are coloured by site. Statistics are computed including the four sites.

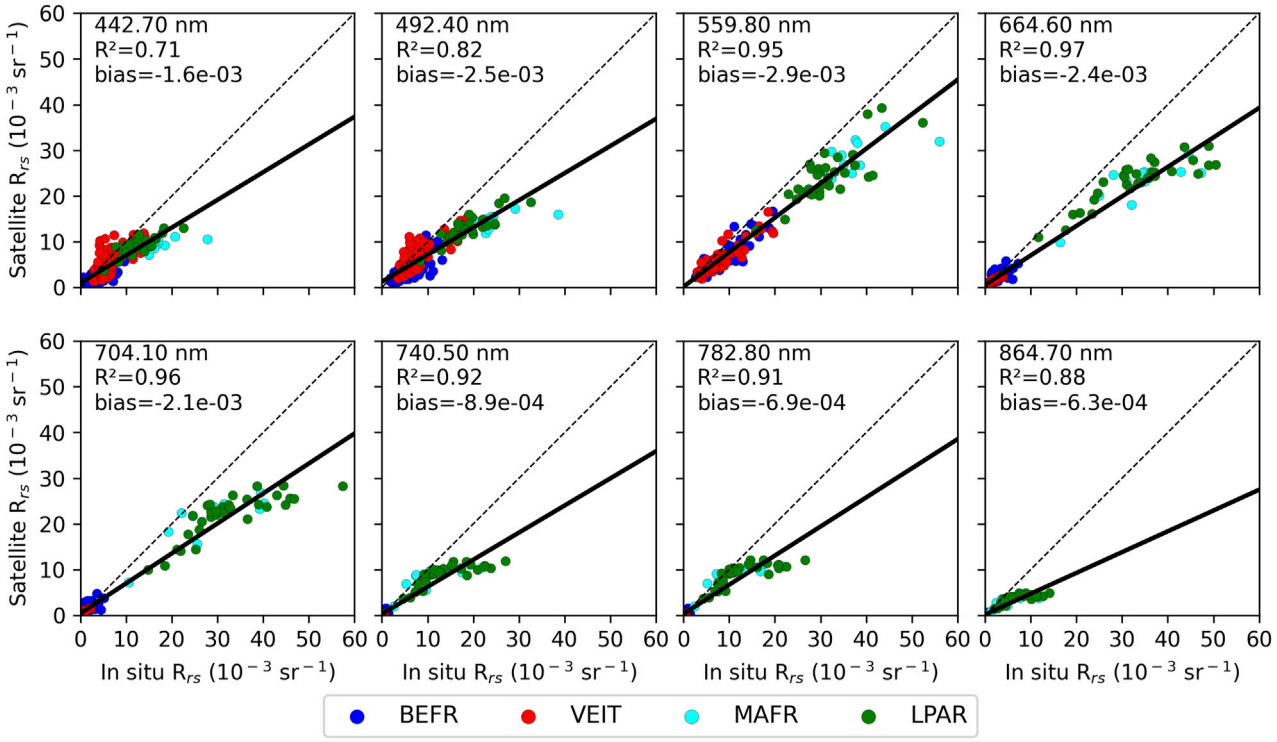


FIGURE 12
Scatter plot of *Rrs* match-ups between satellite (Sentinel-2 C2RCC) and *in situ* (HYPSTAR® L2) measurements for each wavelength. Data points are coloured by site. Statistics are computed including the four sites.

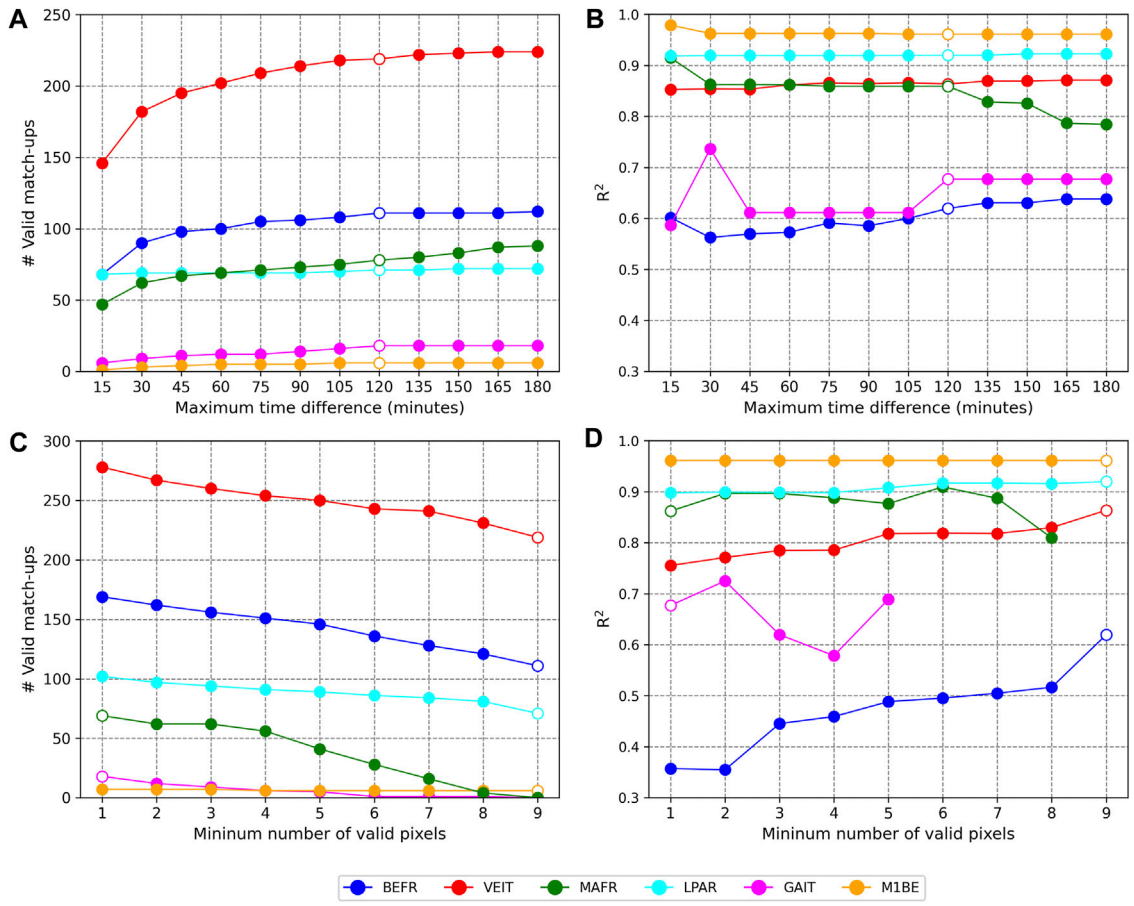


FIGURE 13
(A,B) Variation of the number of valid match-ups **(A)** and the correlation coefficient R^2 **(B)** with the maximum time difference between the satellite and *in situ* acquisitions. **(C,D)** Variation of the number of valid match-ups **(C)** and the correlation coefficient R^2 **(D)** with the minimum number of valid pixels in the extraction window. All the plots are based on the Sentinel-3 OLCI WFR validation protocols shown in Table 3, varying only the indicated parameter (maximum time difference or minimum number of valid pixels). The empty dots indicated the selected options for each site in the validation results presented in this work.

The set of tools presented in this work could also be useful for assessing the influence of different validation protocols on the results, as Concha et al. (2021) show that the number of the valid match-ups and metrics differ between methods. The most evident possibility is repeating the full analysis using different quality control options to compare the results. Moreover, two useful alternatives have also been implemented: one is the flag analysis (see Figures 3B, 8B) and the other one is the evaluation of the results by applying different values of a specific quality control parameter (Figure 13).

As an example, Figure 13 shows the variation of the number of valid match-ups and R^2 using the Sentinel-3 OLCI WFR match-ups with: 1) the maximum time difference between the satellite and *in situ* measurements (Figures 13A, B), and 2) the minimum number of valid pixels in the satellite extract (Figures 13C, D). For each case, the remaining quality control options (Table 3) are kept fixed. Note also that R^2 is reported for the match-ups for all the OLCI bands, although the analysis could also be implemented for other metrics or specific bands.

The valid match-ups are always based on the valid *in situ* measurement closest in time to the satellite overpass. HYPSTAR® measures each 10 min (MAFR), 15 min (VEIT), 20 min (LPAR and GAIT) or 30 min (BEFR or M1BE), and hence most of valid match-ups are expected to show a time difference between both acquisitions lower than 30 min. However, as valid spectra are not always available within this interval, the number of valid match-ups usually increases with the maximum time difference (Figure 13A). Validation metrics (as R^2) also vary with the number of match-ups included in the analysis (Figure 13B).

The use of match-ups with a higher time difference is expected to introduce uncertainties in dynamic environments (Bailey and Werdell, 2006; Concha et al., 2021). In this work, a maximum time difference of two hours was selected to try to balance the number of valid match-ups and the quality of the validation results (Figures 13A, B). At LPAR, more than 95% of match-ups show a time difference lower than 15 min and R^2 keeps almost constant. At BEFR, VEIT, and MAFR, around 80% of the valid match-ups were obtained with time differences lower than 30 min with an abrupt change between 15 and 30 min followed by a slower growth. At these sites, the global correlation keeps constant (or with a slight increase) after 30 min, with a decrease after the 120 min threshold only at

MAFR. GAIT and M1BE show a lower number of valid match-ups as compared to the other sites because of the shorter deployment time, so that the time difference threshold enables to maximize the number of valid match-ups.

As the minimum number of valid pixels in the extraction window increases, the number of valid match-ups decreases but validation metrics are expected to improve, since higher uncertainties in the satellite measurement are expected when invalid (masked) pixels are present within the extraction window (Zibordi et al., 2009b; Concha et al., 2021). In this study, we selected the strict criterium of 9 valid pixels (i.e., not allowing invalid pixels in the 3 × 3 extraction window) at BEFR, VEIT, LPAR, and M1BE with the aim of obtaining the best possible validation results at the cost of a lower number of match-ups (Figures 13C, D). In terms of global correlation, the improvement is more evident at VEIT and mainly at BEFR (Figure 13D). On the contrary, we relaxed the criterium at MAFR and GAIT because these two sites are nearer to the coastline so that land masked pixels are always present in the extraction window. In fact, we opted for maximizing the number of valid match-ups requiring only one valid pixel (Figure 13C).

5 Conclusion

This work demonstrated the satellite validation analysis based on the MDB approach using the HYPSTAR® demonstration datasets acquired at six water sites collected during the deployment phase of the HYPERNETS project (February 2021–March 2023). The results of the matchup analyses were consistent with recent findings based on other *in situ* radiometric data proving that the data collected by the network of automated *in situ* measurements of hyperspectral water reflectance (WATERHYPERNET) are suitable to communicate conclusions about the quality of the satellite data streams to the corresponding agencies (e.g., ESA/EUMETSAT/Copernicus) and satisfying the multi-mission radiometric validation needs. At the time of writing, the WATERHYPERNET network includes six sites and is expected to continue to deliver publicly available data in the future (Ruddick et al., 2024, submitted in the current special issue).

The MDB-based approach for satellite validation analysis enables open science and repeatability as the generated NetCDF files containing the potential match-ups between satellite and *in situ* data can be shared with collaborators and manipulated consistently with the open-source Python modules to implement the validation protocols.

Furthermore, the open-source MDB-based approach is already being implemented as a standard for the validation of Copernicus Ocean Colour Thematic Assembly Centre (OCTAC) products using *in situ* reference data from different sources, including radiometric networks as WATERHYPERNET or AERONET-OC as well as ship-based measurements and it was adapted to also assess merged multi-sensor satellite data time series.

Data availability statement

The six HYPSTAR® demonstration datasets used in this study are publicly available on Zenodo: Brando et al. (2023a), Brando et al. (2023b), Dogliotti et al. (2023b), Doxaran and Corizzi (2023a), Doxaran and Corizzi (2023b), Goyens and Gammaru (2023). The 28 MDB files generated and analysed in this work are publicly available on Zenodo: González Vilas et al. (2024).

Author contributions

LG: Conceptualization, Data curation, Formal Analysis, Methodology, Software, Validation, Visualization, Writing–original draft. VB: Conceptualization, Data curation, Formal Analysis, Funding acquisition, Methodology, Validation, Writing–original draft. JC: Conceptualization, Methodology, Software, Writing–review and editing. CG: Data curation, Software, Writing–review and editing. AID: Funding acquisition, Writing–review and editing. DD: Funding acquisition, Writing–review and editing. AD: Data curation, Software, Writing–review and editing. DV: Data curation, Software, Writing–review and editing.

Funding

The author(s) declare financial support was received for the research, authorship, and/or publication of this article. This work has been performed in the context of the HYPERNETS project funded by the European Union's Horizon 2020 research and innovation programme (Grant agreement no 775983), the HYPERNETS-POP project funded by the European Space Agency (contract no 4000139081/22/I-EF), the ArcticFlux TOSCA research project funded by the French Spatial Agency CNES and the ANPCyT PICT-2020/2636 project.

Acknowledgments

The MDB-based approach for satellite validation analysis presented in this work builds on open source codes developed by Ilaria Cazzaniga while she was working at EUMETSAT. The whole HYPERNETS Team is acknowledged for the development of the HYPSTAR® radiometer and its data processing, as well as for the installation and maintenance of the water sites. In particular, the installation and maintenance of the six sites was supported by: Alexander Corrizzi and local collaborators at GIPREB (BEFR); Mauro Bastianini, the skipper and crew of the AAOT and R/V Litus (VEIT); Estefania Piegari, Lucas Rubinstein, Pablo Perna, Escuela Naval Militar (LPAR); Alexander Corrizzi and local collaborators at Port de Bordeaux (MAFR), Claudia Giardino, Mariano Bresciani, Salvatore Mangano (GAIT); Anabel Gammaru, Benoot Broes from the Flemish Government, department Maritieme Dienstverlening en Kust for providing access and technical support to the platform (M1BE). EUMETSAT and ESA are acknowledged for the provision of the Copernicus Sentinel-3 Full Resolution and the Copernicus Sentinel-2 MSI data. The ESA Sentinel Application Platform and Sentinel tool-box development teams is thanked for making the SNAP software freely available. We are grateful to Vega Forneris and Flavio

Lapadula for maintaining the satellite data processing and the satellite data archive at CNR-ISMAR. The authors would like to thank Adam Lawson for his information about SAVANT.

Conflict of interest

Author JC was employed by Serco S.p.A. c/o ESA-ESRIN.

All authors are likely to receive future research funding for WATERHYPERNET data acquisition and/or exploitation.

The authors declare that these interests do not affect the statements and findings of this paper, which has been written according to the normal scientific ethics and values of the academic community.

Publisher's note

All claims expressed in this article are solely those of the authors and do not necessarily represent those of their affiliated organizations, or those of the publisher, the editors and the reviewers. Any product that may be evaluated in this article, or claim that may be made by its manufacturer, is not guaranteed or endorsed by the publisher.

Supplementary material

The Supplementary Material for this article can be found online at: https://www.frontiersin.org/articles/10.3389/frsen.2024.1330317/full#supplementary-material

References

Bailey, S. W., and Werdell, P. J. (2006). A multi-sensor approach for the on-orbit validation of ocean color satellite data products. *Remote Sens. Environ.* 102 (1-2), 12–23. doi:10.1016/j.rse.2006.01.015

Brando, V., González Vilas, L., Bresciani, M., Mangano, S., Concha, J. A., and Goyens, C. (2023b). Initial Sample of HYPERNETS hyperspectral water reflectance measurements for satellite validation at Lake Garda, GAIT site (Italy) (v1.2). *Zenodo*. doi:10.5281/zenodo.8057823

Brando, V. E., González Vilas, L., Concha, J. A., and Goyens, C. (2023a). Initial Sample of HYPERNETS hyperspectral water reflectance measurements for satellite validation from the VEIT site (Italy). *Zenodo*. doi:10.5281/zenodo.8057531

Brockmann, C., Doerffer, R., Peters, M., Stelzer, K., Embacher, S., and Ruescas, A. (2016). *Evolution of the C2RCC neural network for Sentinel 2 and 3 for the retrieval of Ocean Colour products in normal and extreme optically complex waters" in proceedings of living planet symposium*. Prague, Czech Republic: ESA-SP, 740.

Clark, D. K., Gordon, H. R., Voss, K. J., Ge, Y., Broenkow, W., and Trees, C. (1997). Validation of atmospheric correction over the oceans. *J. Geophys. Res.-Atmos.* 102, 17209–17217. doi:10.1029/96jd03345

Concha, J. A., Bracaglia, M., and Brando, V. E. (2021). Assessing the influence of different validation protocols on Ocean Colour match-up analyses. *Remote Sens. Environ.* 259, 112415. doi:10.1016/j.rse.2021.112415

De Vis, P., Goyens, C., Hunt, S., Vanhellemont, Q., Ruddick, K., and Bialek, A. (2024) Generating hyperspectral reference measurements for surface reflectance from the LANDHYPERNET and WATERHYPERNET networks. *Front. Remote Sens.* 5, 1347230. doi:10.3389/frsen.2024.1347230

Doerffer, R., and Schiller, H. (2007). The MERIS Case 2 water algorithm. *Int. J. Remote Sens.* 28, 517–535. doi:10.1080/01431160600821127

Dogliotti, A. I., Piegari, E., Rubinstein, L., and Perna, P. (2023). Initial Sample of HYPERNETS hyperspectral water reflectance measurements for satellite validation from the LPAR site (Argentina). *Zenodo Dataset*. doi:10.5281/zenodo.8057728

Doxaran, D., and Corizzi, A. (2023a). Initial Sample of HYPERNETS hyperspectral water reflectance measurements for satellite validation at Berre coastal lagoon, BEFR site (France). *Zenodo Dataset*. doi:10.5281/zenodo.8057777

Doxaran, D., and Corizzi, A. (2023b). Initial Sample of HYPERNETS hyperspectral water reflectance measurements for satellite validation at the mouth of the Gironde estuary, MAFR site (France). *Zenodo Dataset*. doi:10.5281/zenodo.8057789

EUMETSAT (2019). EUMETSAT OCDB user manual. Copyright 2019, Copernicus revision 763d8907. Available at: https://ocdb.readthedocs.io/en/latest/ocdb-MDB-user-manual.html (Accessed October 17, 2023).

EUMETSAT (2021). Sentinel-3 OLCI L2 report for baseline collection OL_L2M_003 - EUM/RSP/REP/21/1211386. Available at: https://www.eumetsat.int/media/47794 (Accessed October 17, 2023).

EUMETSAT (2022). Recommendations for sentinel-3 OLCI Ocean Colour product validations in comparison with *in situ* measurements – matchup protocols. Available at: https://www.eumetsat.int/media/44087 (Accessed October 17, 2023).

González Vilas, L., Brando, V. E., Di Cicco, A., Colella, S., D'Alimonte, D., Kajiyama, T., et al. (2024). Assessment of ocean color atmospheric correction methods and development of a regional ocean color operational dataset for the Baltic Sea based on Sentinel-3 OLCI. *Front. Mar. Sci.* 10, 1256990. doi:10.3389/fmars.2023.1256990

González Vilas, L., Brando, V., Concha, J. A., Goyens, C., Dogliotti, A. I., Doxaran, D., et al. (2024). Match-up Database (MDB) files for the validation of satellite water products from Sentinel-3 OLCI and Sentinel-2 MSI using the initial samples of HYPERNETS *in situ* data. *Zenodo*. doi:10.5281/zenodo.10721333

Gordon, H. R. (2021). Evolution of Ocean Color atmospheric correction: 1970–2005. *Remote Sens.* 13, 5051. doi:10.3390/rs13245051

Goyens, C., De Vis, P., and Hunt, S. E. (2021). Automated generation of hyperspectral fiducial reference measurements of water and land surface reflectance for the hypernets networks. *Bruss. Belg.*, 7920–7923. doi:10.1109/IGARSS47720.2021.9553738

Goyens, C., and Gammaru, A. (2023). *Initial Sample of HYPERNETS hyperspectral water reflectance measurements for satellite validation at the measurement tower MOW1*. Zenodo, M1BE site. (Belgium) (v1.2) [Data set]. doi:10.5281/zenodo.8059881

Goyens, C., Lavigne, H., Dille, A., and Vervaeren, H. (2022). Using hyperspectral remote sensing to monitor water quality in drinking water reservoirs. *Remote Sens.* 14 (21), 5607. doi:10.3390/rs14215607

IOCCG (2012). "Mission requirements for future ocean-colour sensors," in *Reports of the international Ocean Colour coordinating group (IOCCG), No. 13*. Editors C. R. McClain and G. Meister (Canada: IOCCG).

Justice, C., Belward, A., Morisette, J., Lewis, P., Privette, J., and Baret, F. (2000). Developments in the 'validation' of satellite sensor products for the study of the land surface. *Int. J. Remote Sens.* 21 (17), 3383–3390. doi:10.1080/014311600750020000

Katlane, R., Doxaran, D., ElKilani, B., and Trabelsi, C. (2023). Remote sensing of turbidity in optically shallow waters using sentinel-2 MSI and PRISMA satellite data. *PFG - J. Photogramm. Remote Sens. Geoinf.* doi:10.1007/s41064-023-00257-9

Lawson, A., Bowers, J., Ladner, S., Crout, R., Wood, C., Arnone, R., et al. (2021). Analyzing satellite Ocean Color match-up protocols using the satellite validation navy tool (SAVANT) at MOBY and two AERONET-OC sites. *Remote Sens.* 14, 2673. doi:10.3390/rs13142673

Loew, A., Bell, W., Brocca, L., Bulgin, C. E., Burdanowitz, J., Calbetet, X., et al. (2017). Validation practices for satellite-based Earth observation data across communities. *Rev. Geophys.* 55, 779–817. doi:10.1002/2017RG000562

Maciel, F. P., and Pedocchi, F. (2022). Evaluation of ACOLITE atmospheric correction methods for Landsat-8 and Sentinel-2 in the Río de la Plata turbid coastal waters. *Int. J. Remote Sens.* 43 (1), 215–240. doi:10.1080/01431161.2021.2009149

Mélin, F., Cazzaniga, I., and Sciuto, P. (2024). Verification of uncertainty estimates of autonomous field measurements of marine reflectance using simultaneous observations. *Front. Remote Sens.* 4, 1295855. doi:10.3389/frsen.2023.1295855

Mélin, F., and Sclep, G. (2015). Band shifting for ocean color multi-spectral reflectance data. *Opt. Express* 23, 2262. doi:10.1364/OE.23.002262

Pahlevan, N., Mangin, A., Balasubramanian, S. V., Smith, B., Alikas, K., Arai, K., et al. (2021). ACIX-Aqua: a global assessment of atmospheric correction methods for Landsat-8 and Sentinel-2 over lakes, rivers, and coastal waters. *Remote Sens. Environ.* 258, 112366. doi:10.1016/j.rse.2021.112366

Renosh, P. R., Doxaran, D., Keukelaere, L. D., and Gossn, J. I. (2020). Evaluation of atmospheric correction algorithms for sentinel-2-MSI and sentinel-3-OLCI in highly turbid estuarine waters. *Remote Sens.* 12, 1285. doi:10.3390/rs12081285

Ruddick, K., Brando, V. E., Corizzi, A., Dogliotti, A., Doxaran, D., Goyens, C., et al. (2024). WATERHYPERNET: a prototype network of automated *in situ* measurements of hyperspectral water reflectance for satellite validation and water quality monitoring. *Submitt. Front. Remote Sens.*

Ruddick, K., De Cauwer, V., Park, Y., and Moore, G. (2024). Seaborne measurements of near infrared water-leaving reflectance: the similarity spectrum for turbid waters. *Limnol. Oceanogr.* 51 (2), 1167–1179. doi:10.4319/lo.2006.51.2.1167

Ruddick, K. G., Voss, K., Boss, E., Castagna, A., Frouin, R., Gilerson, A., et al. (2019). A review of protocols for fiducial reference measurements of water-leaving radiance for validation of satellite remote-sensing data over water. *Remote Sens.* 11, 2198. doi:10.3390/rs11192198

Soriano-González, J., Urrego, E. P., Sòria-Perpinyà, X., Angelats, E., Alcaraz, C., Delegido, J., et al. (2022). Towards the combination of C2RCC processors for improving water quality retrieval in Inland and Coastal Areas. *Remote Sens.* 14, 1124. doi:10.3390/rs14051124

Tavares, M. H., Lins, R. C., Harmel, T., Fragoso, C. R., Martínez, J. M., and Motta-Marques, D. (2021). Atmospheric and sunglint correction for retrieving chlorophyll-a in a productive tropical estuarine-lagoon system using Sentinel-2 MSI imagery. *ISPRS J. Photogramm. Remote Sens.* 174, 215–236. doi:10.1016/j.isprsjprs.2021.01.021

Van der Zande, D., Stelzer, K., Lebreton, C., Dille, A., Shevchuk, R., Santos, J., et al. (2022). Copernicus marine service, quality information document, ref: CMEMS-HR-OC-QUID-009-201to212. Available at: https://catalogue.marine.copernicus.eu/documents/QUID/CMEMS-HR-OC-QUID-009-201to212.pdf (Accessed October 26, 2023).

Vanhellemont, Q. (2019a). Adaptation of the dark spectrum fitting atmospheric correction for aquatic applications of the Landsat and Sentinel-2 archives. *Remote Sens. Environ.* 225, 175–192. doi:10.1016/j.rse.2019.03.010

Vanhellemont, Q. (2019b). Adaptation of the dark spectrum fitting atmospheric correction for aquatic applications of the Landsat and Sentinel-2 archives. *Remote Sens. Environ.* 225, 175–192. doi:10.1016/j.rse.2019.03.010

Vanhellemont, Q., and Ruddick, K. (2016). "*ACOLITE for sentinel-2: aquatic applications of MSI imagery" in proceedings of the 2016 ESA living planet symposium*, Prague. ESA Special Publication.

Vanhellemont, Q., and Ruddick, K. (2021). Atmospheric correction of Sentinel-3/OLCI data for mapping of suspended particulate matter and chlorophyll-a concentration in Belgian turbid coastal waters. *Remote Sens. Environ.* 256, 112284. doi:10.1016/j.rse.2021.112284

Warren, M. A., Simis, S. G., Martinez-Vicente, V., Poser, K., Bresciani, M., Alikas, K., et al. (2019). Assessment of atmospheric correction algorithms for the sentinel-2a multispectral imager over Coastal and Inland Waters. *Remote Sens. Environ.* 225, 267–289. doi:10.1016/j.rse.2019.03.018

Zibordi, G., Berthon, J.-F., Mélin, F., D'Alimonte, D., and Kaitala, S. (2009a). Validation of satellite ocean color primary products at optically complex coastal sites: northern Adriatic Sea, Northern Baltic Proper and Gulf of Finland. *Remote Sens. Environ.* 113 (12), 2574–2591. doi:10.1016/j.rse.2009.07.013

Zibordi, G., Holben, B., Slutsker, I., Giles, D., Dalimonte, D., Melin, F., et al. (2009b). AERONET-OC: a network for the validation of Ocean Color primary products. *J. Atmos. Ocean. Technol.* 26, 1634–1651. doi:10.1175/2009JTECHO654.1

Zibordi, G., Kwiatkowska, E., Mélin, F., Talone, M., Cazzaniga, I., Dessailly, D., et al. (2022). Assessment of OLCI-A and OLCI-B radiometric data products across European seas. *Remote Sens. Environ.* 272, 112911. doi:10.1016/j.rse.2022.112911

Zibordi, G., Mélin, F., and Berthon, J.-F. (2018). A regional assessment of OLCI data products. *IEEE Geosci. Remote Sens. Lett.* 15, 1490–1494. doi:10.1109/LGRS.2018.2849329

frontiers | Frontiers in Remote Sensing

TYPE Original Research
PUBLISHED 22 March 2024
DOI 10.3389/frsen.2024.1354662

Check for updates

OPEN ACCESS

EDITED BY
Wenhan Qin,
Science Systems and Applications, Inc.,
United States

REVIEWED BY
Peter Gege,
German Aerospace Center (DLR), Germany
Samantha Jane Lavender,
Pixalytics Ltd, United Kingdom

*CORRESPONDENCE
Ana I. Dogliotti,
adogliotti@conicet.gov.ar

RECEIVED 12 December 2023
ACCEPTED 12 March 2024
PUBLISHED 22 March 2024

CITATION
Dogliotti AI, Piegari E, Rubinstein L, Perna P and Ruddick KG (2024), Using the automated HYPERNETS hyperspectral system for multi-mission satellite ocean colour validation in the Río de la Plata, accounting for different spatial resolutions.
Front. Remote Sens. 5:1354662.
doi: 10.3389/frsen.2024.1354662

COPYRIGHT
© 2024 Dogliotti, Piegari, Rubinstein, Perna and Ruddick. This is an open-access article distributed under the terms of the Creative Commons Attribution License (CC BY). The use, distribution or reproduction in other forums is permitted, provided the original author(s) and the copyright owner(s) are credited and that the original publication in this journal is cited, in accordance with accepted academic practice. No use, distribution or reproduction is permitted which does not comply with these terms.

Using the automated HYPERNETS hyperspectral system for multi-mission satellite ocean colour validation in the Río de la Plata, accounting for different spatial resolutions

Ana I. Dogliotti[1,2]*, Estefanía Piegari[1,3], Lucas Rubinstein[1,4], Pablo Perna[1] and Kevin G. Ruddick[5]

[1]Instituto de Astronomía y Física del Espacio, Consejo Nacional de Investigaciones Científicas y Técnicas (IAFE, CONICET/UBA), Buenos Aires, Argentina, [2]Instituto Franco-Argentino para el estudio del Clima y sus impactos (UMI-IFAECI, CNRS CONICET-UBA), Buenos Aires, Argentina, [3]Instituto de Investigación e Ingeniería Ambiental (IIIA, CONICET/UNSAM), Buenos Aires, Argentina, [4]Laboratorio de Acústica y Electroacústica (LACEAC), FIUBA, Buenos Aires, Argentina, [5]Royal Belgian Institute of Natural Sciences (RBINS), Brussels, Belgium

Validation of water reflectance using *in situ* data is essential to ensure the quality of ocean colour satellite-derived products useful for water quality monitoring, like turbidity and chlorophyll-a concentration. Since December 2021, the HYPERNETS automated hyperspectral system has been collecting data in the optically complex and highly turbid waters of the Río de la Plata, an ideal scenario for testing atmospheric correction algorithms' performance. The site, located 60 km south of Buenos Aires (Argentina), is described in relation to the water reflectance spectral features and variability using high spatial resolution imagery and a methodology is proposed to objectively select a sensor-specific location of a reference pixel for satellite validation. Six months of data is used to evaluate surface water reflectance operational products from multi-spectral systems like Landsat 8&9/OLI (L89/OLI), Sentinel-2/MSI (S2/MSI) & Sentinel-3/OLCI (S3/OLCI), and PlanetScope SuperDoves (PS/SD), and also non standard products for Aqua/MODIS (Aqua/MODIS) and SNPP&JPSS1/VIIRS (SJ/VIIRS) missions. Moreover, the standard surface water reflectance product from the hyperspectral PRISMA mission could also be evaluated. The matchups show general good results when *in situ* measurements are compared to L2 standard products of high spatial resolution sensors that use land-based atmospheric correction approach, if sun glint contamination is avoided. Low mean relative percentage difference was found for S2/MSI (2.45%) and L89/OLI (–3.52%), but higher for PS/SD (30.7%). In turn, S3/OLCI medium resolution also showed low mean relative differences (2.31%), while SJ/VIIRS and Aqua/MODIS showed larger and negative differences (–16.35 for SJ/VIIRS and –35.6% for Aqua/MODIS) which showed a clear increase towards the shortest blue bands. The results show the

great potential of the HYPERNETS automated system to provide high quality and quantity of data for validation of satellite data at all visible and near infrared (VNIR, 400–900 nm) wavelengths in a multi-mission perspective.

KEYWORDS

ocean colour, satellite validation, hyperspectral reflectance, autonomous system, Río de la Plata, turbid waters, LPAR

1 Introduction

Declining water quality of coastal and estuarine waters has become a global issue of concern affecting human health, ecosystems and the economic environment (IOCCG, 2018). Given the increasing anthropogenic activities and water pollution issues in populated coastal areas, there is a strong need to perform integrated and regular water monitoring to improve the present strategies concerning water treatment and management, as well as governance. While traditional *in situ* water sampling and measurements are expensive, both in cost and time, satellite remote sensing technology has shown to be a cost-effective tool for proving synoptic data for monitoring large scale and long-term water quality (Mumby et al., 1999). Therefore, it is essential to validate satellite-derived products, in particular water reflectance (ρ_w), using *in situ* data to ensure the quality of derived parameters useful for water quality monitoring, like turbidity and chlorophyll-*a* concentration.

The Río de la Plata (RdP) estuary, located in the Southwestern South Atlantic (~35°S), is the natural boundary limit between Argentina and Uruguay where the respective capital cities of Buenos Aires and Montevideo are located. The estuary and its area of influence is of great social, economical and ecological importance being the source of drinking water for millions of people, a region for tourism, transportation, and fishing activities, and the location of big harbours and industrial centers. It is a highly active and human impacted area that receives the discharge of domestic and industrial effluents as well as agro-chemicals that drain from large areas of intensive agricultural production, leading to an important increase in nutrient loading, showing symptoms of eutrophication (Nagy et al., 2002; García-Alonso et al., 2019). Moreover, cyanobacterial blooms have become a recurrent phenomenon in the estuary, especially in the last 2 decades along the northern Uruguayan coast (De León and Yunes, 2001; Aubriot et al., 2020; Kruk et al., 2021), and also on the Argentine coast (Sathicq et al., 2014; Dogliotti et al., 2021), although less frequent and intense.

Therefore, water quality control and regular monitoring of the trophic status of this estuarine system are very important for which remote sensing is a powerful tool. However, due to the optical complexity of RdP waters, *i.e.*, high inorganic suspended matter, they represent a challenging scenario for both atmospheric correction and bio-optical algorithm development.

The use of autonomous systems, like AERONET-OC, has shown to be effective for increasing the number of validation match-ups (Zibordi et al., 2009; Zibordi et al., 2020). However, the multispectral nature of the instrument used in the AERONET-OC network, prevents its use to validate hyperspectral missions and missions with different spectral band configurations. Within the H2020/HYPERNETS project, a new hyperspectral radiometer with a pointing system and auxiliary sensors has been developed to provide fine spectral resolution radiometric data in the visible and near infrared (VNIR) region with high quality measurements at lower cost. One of these autonomous hyperspectral systems has been deployed for the first time in the turbid waters of Río de la Plata estuary, close to the city of Buenos Aires, gathering high quality radiometric information since December 2021. At the moment of writing other five HYPERNETS systems have been deployed in a wide variety of water types, *i.e.*, in coastal waters with moderately (Aqua Alta Oceanographic Tower in Italy) to more turbid (Zeebrugge in Belgium) waters, in inland water bodies with clear (Garda Lake in Italy) and turbid and productive (Etang de Berre in France) waters, and in estuaries with turbid to highly turbid waters like the Gironde estuary, in France, with similar optical characteristics to the highly turbid waters in the Río de la Plata estuary (LPAR site).

The objectives of the present paper are to introduce the hyperspectral automated fixed station deployed in the turbid waters of the Río de la Plata estuary in support for long-term multi-mission satellite ocean colour validation, evaluate the spatial variability of water reflectance around the site in order to select the location of reference pixel to be used for satellite validation, and to show its potential to provide high quality and quantity of data by evaluating surface water reflectance operational products from existing satellite missions operating in the visible and near infrared (VNIR, 400–900 nm) spectral bands that are used for aquatic applications.

2 Data and methods

2.1 HYPERNETS system and HYPSTAR® *in situ* reflectance data

The HYPERNETS System, deployed at the LPAR site, is comprised of an advanced hyperspectral VNIR spectrometer with an embedded RGB imaging camera, a relative calibration LED source, a pan-tilt mechanism that allows positioning and pointing the radiometer in different directions, and auxiliary sensors (pressure, humidity, temperature, rain, light, and two external cameras). A detailed description of the system and sensor can be found in Kuusk et al. (submitted to this same Frontiers Research Topic). All the controlling, positioning, and data transmitting parts of the system are located in a water-proof main box and the whole system is powered by a 12 V battery that is connected to a solar panel and charge controler.

The HYPSTAR® (HYperspectral Pointable System for Terrestrial and Aquatic Radiometry) Standard Range (HYPSTAR®-SR), developed within the European Union's H2020 HYPERNETS project, is a hyperspectral radiometer system with radiance (Field Of View, FOV 2°) and irradiance (FOV 180°) optical entrances that are optically multiplexed to one VNIR spectrometer module that collects data between 380 and 1,020 nm with a FWHM of 3 nm (https://hypstar.eu/). Since the same spectrometer is used for both radiance and irradiance measurements, the three measurements needed to derive water reflectance (ρ_w), *i.e.*, the downwelling sky radiance (L_d), upwelling radiance from the water (L_u) and downwelling irradiance (E_d), are measured sequentially. The system is programmed to collect data every 20 min between 09:00 to 17:00 local time, and data is saved in a local device and automatically transferred (3G) to a remote server where it is processed and quality controlled using the HYPERNETS processor (https://github.com/HYPERNETS/hypernets_processor, see Goyens et al., 2022 for details).

The standard water measurement sequence consists of sequential measurements of E_d (three replicates), L_d (three replicates), L_u (six replicates), and three more replicates of L_d and E_d after the L_u measurements. The zenith angles of the sea- and sky-viewing radiance sensors are 40° and the relative azimuth angle with respect to the sun is ±90° as in Zibordi et al. (2009). This geometry is kept constant throughout the day thanks to the automated pan/tilt mechanism that rotates the radiometer. Data from a sequence that pass quality control are mean averaged, and if sufficient replicates are available, *i.e.*, at least 3 replicates of each parameter, the water-leaving radiance reflectance (ρ_w) is computed by:

$$\rho_w(\lambda) = \pi \frac{L_u(\lambda) - \rho_F L_d(\lambda)}{E_d(\lambda)}$$

Where ρ_F is the air-water interface reflectance factor that is approximated as a function of the sun and viewing geometry and wind speed (Mobley, 1999). Wind speed is derived from NCEP/GDAS (National Centers for Environmental Prediction, National Weather Service, NOAA, U.S. Department of Commerce, 2015) when available or fixed to 2 m/s otherwise. As part of the WATERHYPERNET network, an international prototype network of sites running automated systems of pointable hyperspectral radiometers with common data acquisition and processing, a common quality control of the data is performed (Goyens et al., 2022; De Vis et al.; Ruddick et al. *submitted this same Frontiers Research Topic*) and further LPAR site-specific quality control is applied in order to reduce perturbations from the structure, *e.g.*, avoiding certain viewing and illuminating geometry, and removing variable ρ_w, *i.e.*, with a coefficient of variation (standard deviation to mean ratio) CV<10% in the VIS 400–900 nm. Further details the HYPSTAR® data processing are available in Goyens et al. (2022), and De Vis et al., *submitted this same Frontiers Research Topic*). The quality-controlled hyperspectral water reflectance spectra have been convoluted to the spectral response of the different multi-spectral sensors analyzed in this study (Supplementary Figures S1, S2) and smoothed using a moving average filter (15 window size) for comparison with PRISMA data.

2.2 LPAR fixed station

The La Plata Argentine site (LPAR) is located 60 km south of the city of Buenos Aires (Argentina) in the coastal waters of the highly turbid of Río de la Plata middle estuary (Figure 1). The fixed structure, that belongs to the "Escuela Naval Militar" (Naval Academy), is located at the end of the 1.1 km long and 50 cm wide jetty (34°49′04.8″ S, 57°53′45.3″ W), with a size of 5 × 5 m and a height of ~8.5 m above water surface. Water flows freely under the jetty, thus minimising impact of the jetty on the hydrodynamics and ambient water colour. The HYPSTAR® is located in the northwestern corner in the first level of this platform. The LPAR site is located between a regional water intake that distributes drinking water to 2.5 million people in the Buenos Aires province and the active commercial harbour of La Plata city, an area where intense phytoplankton blooms (including toxic Cyanobacteria) have been recorded frequently since 2020 (Dogliotti et al., 2021) presenting human health risks and causing occasional problems for the water intake site.

The Río de la Plata (RdP) is a large and shallow funnel shaped estuary with high values of suspended particulate matter, ranging from 100 to 300 g m^{-3} (Framiñan et la. 2006) and reaching 940 g m^{-3} in the maximum turbidity zone. The region is therefore an ideal site to test atmospheric correction algorithm performance (Shi and Wang et al., 2009; Gossn et al., 2019; Maciel et al., 2022). The LPAR site is located in the southern limit of the middle estuary and the average water depth is ~4 m.

In situ HYPSTAR® data at LPAR have been automatically collected from 2021-12-16 until 2022-09-19, with some downtime periods, and operating from 09:00 to 17:00 local time every 20 min. Spectra collected during this period were quite fluctuating depending on the month of the year, but spectral shapes and magnitude are consistent with measured spectra collected in this part of the estuary during previous campaigns (Gossn et al., 2019; Dogliotti et al., 2021). Examples of monthly mean spectra +/- 1 standard deviation collected in February and July 2022 are shown in Figure 2. Data collected in July show typical turbid waters water spectra features, *i.e.*, highest ρ_w values in the 550–700 nm part of the spectra (0.10–0.14), a peak around 810 nm, due to a local minimum of the water pure absorption, and relatively high ρ_w values in the NIR (0.025–0.075). In turn, spectra collected in February showed features more related to moderately productive waters with indications of cyanobacteria presence, *i.e.*, a clear strong decrease in ρ_w around 675 nm (second peak of chlorophyll-*a* absorption) and slight decrease in ρ_w around 620 nm (characteristic absorption peak of Phycocyanin, a typical pigment found in cyanobacteria). Moreover, samples collected during a field campaign on 2022-02-16 confirmed the presence of high amount of phytoplankton cells, high chlorophyll-*a* concentration (25 mg/m^3) and the presence of cyanobacteria cells (Dogliotti et al., 2023).

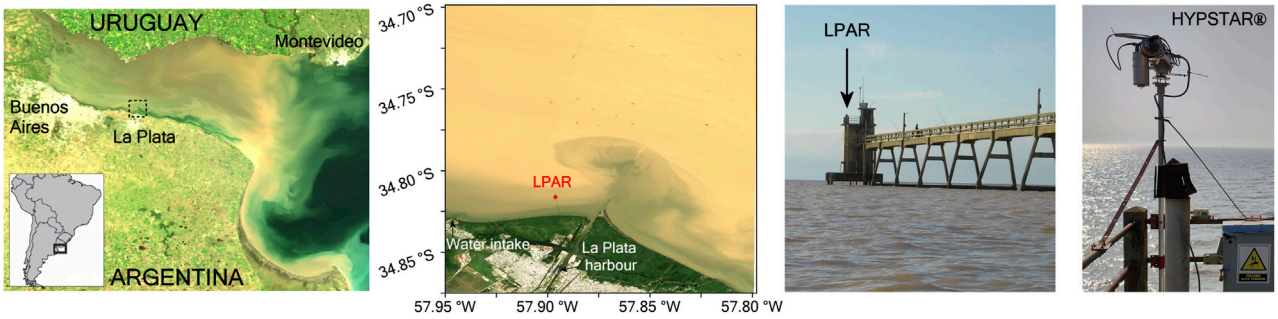


FIGURE 1
Location of the LPAR site next to La Plata harbor on the Sentinel-3A/OLCI (left) and Sentinel-2A/MSI images taken 2022-09-05 and photos of the platform and HYPSTAR® sensor (right).

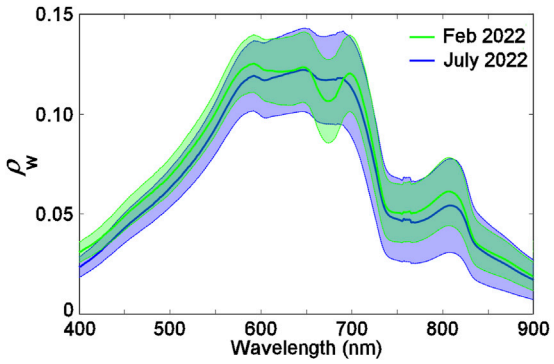


FIGURE 2
In situ HYPSTAR® L2 average spectra (bold lines) collected at LPAR on February (green) and July (blue) 2022. The shadowed areas delimit the +/-1 standard deviation respect to the average of all available spectra for each month.

2.3 Satellite data

With the aim of demonstrating the capability of HYPERNETS system, different available optical VSWIR satellite missions, with varying band sets and widths and spatial and temporal resolutions, have been chosen. Satellite data acquired from 2021-12-16 to 2022-09-19 covering the LPAR site were downloaded and compared to HYPSTAR® L2 data. Given that the OBPG Level 2 standard products fails in the turbid waters of RdP and pixels are generally masked (Dogliotti et al., 2011), Level 1A MODIS and VIIRS data have been downloaded and processed using alternative atmospheric correction, *i.e.*, the black pixel approach using the SWIR bands (more details below). For the other sensors, operational standard Level 2 images have been downloaded. All the evaluated systems are summarized in Table 1 and described below.

SuperDove (SD) satellites, third generation of PlanetScope Earth-imaging constellation, are currently in orbit and produce imagery with 8 spectral bands in the VNIR region at a ground sampling distance at nadir of 3–6 m (Planet, 2022). Six of the SD bands match and have similar relative spectral responses (RSRs) to S2/MSI bands (Supplementary Figure S1). The absolute calibration is performed using near-simultaneous SuperDove and S2/MSI observations and validated with RadCalNet data (Collison et al., 2022). Level-2 surface reflectance (ρ_s) orthorectified GeoTIFF files with 3 m pixel size have been downloaded from the Planet Explorer website (https://www.planet.com/explorer). Cloud free images (CMO processor v4.1.4) over the LPAR site have been selected during the deployment period.

Landsat 8 and 9 satellites, on orbit since 2013 and 2021 respectively, carry the Operational Land Imager (OLI) that provides data at 9 spectral bands, eight of which at 30 m spatial resolution and one panchromatic band at 15 m. Considering both satellites together, the revisit time for data collection is every 8 days. Level 2 Collection 2 images over the LPAR site (path row 225/084)

TABLE 1 Characteristics of the systems evaluated in the present study.

Platform/sensor	Pixel Size (m)	Spectral bands (400–1,000 nm)	Revisit frequency (at equator)	Launch
PlanetScope/SuperDove	3–6	8	Daily	2021onward
Landsat 8-9/OLI	30	5	8 days (2 sats)	2013/2021
Sentinel-2 A-B/MSI	10/20/60	9 (4/6/3)	5 days (2 sats)	2015/2017
Sentinel-3 A-B/OLCI	300	21	Daily (2 sats)	2016/2018
Aqua/MODIS	250/500/1,000	2/2/9	Daily	2000
SNPP-JPPS/VIIRS	750	7	Daily	2011/2017
PRISMA	30	66	On demand	2019

have been downloaded from USGS EarthExplorer (http://earthexplorer.usgs.gov/). Landsat 8/9 Level 2 science surface reflectance (ρ_s) products are generated using the Land Surface Reflectance Code (LaSRC) algorithm (Version 1.5.0).

Sentinel-2 A and B satellites, launched in 2015 and 2017 respectively, carry the MultiSpectral Imager (MSI) with 13 bands in the Visible to ShortWave InfraRed (VSWIR) part of the spectrum with 4 bands at 10 m, 6 bands at 20 m and 3 bands at 60 m spatial resolution. The revisit frequency of each single S2 satellite is 10 days and the combined constellation revisit is 5 days. Level 1C images over the LPAR site (tile 21HVA) have been downloaded from the Sentinel Scientific Data Hub (https://scihub.copernicus.eu/) and processed using Sen2Cor v2.11 atmospheric correction (Louis et al., 2016) algorithm. The default configuration was used giving the same as for the L2A "Core" Products processing in Sentinel-2 Ground Segment with L2A processing baseline 04.00. Surface reflectance (ρ_s) at all bands were resampled to 10 m resolution using Sentinel Applications Platform (SNAP v9.0.0).

Sentinel-3 A and B satellites, launched in 2016 and 2018 respectively, carry the Ocean and Land Colour Instrument (OLCI) with 21 bands in the VSWIR at 300 m spatial resolution. Being an instrument designed for water applications, OLCI have more and narrower bands (Supplementary Figures S1, S2) with higher signal-to-noise ratio compared to land sensors. The two in-orbit S3 satellites enable a short revisit time of less than 2 days for OLCI at the equator. S3/OLCI Level 2-Water Full Resolution (L2-WFR) images, processed by EUMETSAT with the Instrument Processing Facility (IPF) IPF-OL-1-EO version 7.00 (EUMETSAT, 2021; Zibordi et al., 2022), were downloaded from the Copernicus Online Data Access hosted by EUMETSAT (coda.eumetsat.int). Data were available from the EUMETSAT Ocean Colour baseline collection OL_L2M.003.

The Moderate Resolution Imaging Spectroradiometer (MODIS), onboard of Terra and Aqua platforms launched in 1999 and 2002, has 36 spectral bands, with 19 bands in the VSWIR range at 250 m (2 bands), 500 m (5 bands) and 1,000 m (9 bands) spatial resolution. Only MODIS-Aqua imagery is here evaluated given the difficulties in characterizing the MODIS instrument on board of Terra satellite and its calibration history (Franz et al., 2008). Level-1A images covering LPAR site in cloud-free days were acquired from NASA ocean color website (https://oceancolor.gsfc.nasa.gov) and processed to Level 2 at 1,000 m resolution using SeaWiFS Data Analysis System (SeaDAS) ocssw/l2gen processor version 8.1. The output product, the remote sensing reflectance (R_{rs} in sr^{-1}), is multiplied by π sr to obtain the water reflectance (ρ_w). A two-band multiple scattering extrapolative approach, similar to Gordon and Wang (1994), was used but using two SWIR bands (Shi and Wang, 2009), *i.e.*, the aerosol signal was computed accounting for multiple scattering effects and assuming black water in two specified bands in the SWIR (GW94-SWIR). Given that four out of ten detectors for the Aqua/MODIS SWIR2 band (1,640 nm) are inoperable and cannot be used, the SWIR1 (1,240 nm) and SWIR3 (2,130 nm) bands are used (SWIR13). Given the high reflectance of Río de la Plata waters, the following l2gen configuration parameters have been modified compared to the default processing. The bidirectional reflectance distribution function correction (BDRF), based on the blue-to-green ratio chlorophyll estimation, was disabled (brdf_opt = 0) given that it generally degrades performance in turbid waters (Li et al., 2019). The gaseous absorption correction was set to account for ozone, carbon dioxide, nitrogen dioxide, and water vapor (gas_opt = 15). Clouds were masked using the SWIR3 band using a threshold 0.018 and pixels with high sun zenith angle ($\theta_s > 60^\circ$) and view zenith angle ($\theta_v > 70^\circ$) were also masked. The high radiance (maskhilt = 0) and straylight (maskstlight = 0) standard masks were switched off since they usually erroneously mask turbid water pixels.

The Suomi National Polar-orbiting Partnership (Suomi-NPP) and two Joint Polar Satellite System satellites (JPSS-1 and JPSS-2 or NOAA-20 and NOAA-21), launched in 2011, 2017 and 2022, carry the Visible Infrared Imaging Radiometer Suite (VIIRS) with 22 spectral bands that ranges from the blue (410 nm) to the long wave infrared (12.5 μm). Five imaging (I) bands, covering the red, near-, shortwave-, medium-, and long wave infrared, have a spatial resolution of 375 m while the 16 moderate (M) resolution bands and the day/night panchromatic band have 750 m spatial resolution. VIIRS-JPPS/SNPP Level-1A cloud-free images covering LPAR site were downloaded from NASA ocean color website (https://oceancolor.gsfc.nasa.gov) and processed to Level 2 using SeaDAS v8.1. The output product, the remote sensing reflectance (R_{rs} in sr^{-1}), is multiplied by π sr to obtain the water reflectance (ρ_w). The same atmospheric correction approach (WG94-SWIR) and l2gen configuration parameters were applied, but given that VIIRS has the three operating SWIR bands compared to MA, VIIRS data was processed using three sets of SWIR band combinations, *i.e.*, SWIR12, SWIR13, and SWIR23.

The hyperspectral PRISMA (PRecursore IperSpettrale della Missione Applicativa) mission was launched by the Italian Space Agency (ASI) in 2019. The hyperspectral camera takes images in a continuum of spectral bands with 66 bands in the VNIR range (400–1,010 nm) and 173 bands in the SWIR range (920–2,500 nm) at 30 m spatial resolution. As acquisitions are taken by request, only four cloud-free PRISMA images have been acquired during the LPAR deployment period here analyzed. Level 2C images from the PRISMA archive were downloaded from the ASI portal (https://prisma.asi.it/). PRISMA Level 2 surface reflectance (ρ_s) product is generated based on MODTRAN v6.0 and using a multi-dimensional LUT approach. The processing uses a land-based atmospheric correction where retrieval of aerosol optical thickness is based on the Dense Dark Vegetation algorithm approach. A full description of the algorithms is available in the PRISMA Algorithm Theoretical Basis Document (ASI, 2021).

2.4 Match-up analysis

The comparison between *in situ* and satellite data (match-up) has been performed by extracting a 3 × 3 pixel window centered at the reference location for the LPAR site depending on the spatial resolution of the system being evaluated. The location of the reference pixel, as described later in Section 3.1, was selected by evaluating the natural spatial variability of the water reflectance around the platform using S2/MSI 2016-2022 time series at 10 m spatial resolution imagery. If less than 50% of the pixels in the 3 × 3 window were valid, *i.e.*, less than 5 pixels out of 9, the matchup was discarded, otherwise the mean and standard deviation were calculated. Invalid pixels were determined by applying mission-

TABLE 2 List of satellite/sensors, level-2 processor, and flags used for quality control of satellite data.

Satellite/Sensor	Processor	Flags
PS/SD	CMO processor	-
S2/MSI	Sen2Cor	Saturated_defective; dark_feature_shadow; cloud_shadow; unclassified; cloud_Midium/high_proba; thin_cirrus; snow_ice, ρ_s(~1,600)>0.05
L89/OLI	LaSRC	ρ_s(~1,600)>0.05
S3/OLCI	IPF-OL-2	INVALID, LAND, CLOUD and CLOUD_AMBIGUOUS
JS/VIIRS	l2gen	ATMFAIL, HIGHGLINT,NAVFAIL, LAND,HISATZEN, CLDICE,HISOLZEN
Aqua/MODIS	l2gen	ATMFAIL, HIGHGLINT,NAVFAIL, LAND,HISATZEN, CLDICE,HISOLZEN
PRISMA	L2C v2.05	-

specific recommended flags which varied with the sensor/processor analyzed. Flags considered for each system are listed in Table 2. For the L2 standard land products, which do not correct for sun glint but have SWIR bands, pixels were masked if ρ_s(~1,600)>0.05. In order to minimize the effect of outliers on the calculated mean value, pixels beyond median ±1.5* standard deviation were excluded as in Bailley and Werdell (2006). Finally, in order to evaluate spatial homogeneity, the mean value of the valid pixels was used if the median of the CV of ρ_w between 412 and 560 nm was less than 0.15 (Bailey and Werdell, 2006). The closest HYPSTAR® observation in time with the satellite overpass, within 30 min, was selected and, if bounding observations within a window of maximum 40 min were available, observations were linearly interpolated to the satellite overpass time and convolved to the relative spectral responses (RSR) of the different sensors analyzed (Supplementary Figures S1, S2). Vertical bars in the scatter plots corresponds to the standard deviation of the 3 × 3 window, for satellite data, and the horizontal bars, half the absolute difference between the bounding observations for HYPSTAR® data. The time difference between *in situ* and satellite overpass was always within 10 min.

2.5 Statistics

To describe the difference between satellite and *in situ* data, regression analysis and a set of statistics were calculated. Linear regressions between predicted (satellite) and observed (*in situ*) water reflectance were performed using a reduced major axis (RMA) type II regression analysis given that both satellite and *in situ* measurements are subject to errors. Typical linear regression statistics were obtained, *i.e.*, slope, intercept, and coefficient of determination R^2. Considering N match-ups, the differences between *in situ* (x) and satellite (y) data are quantified by the mean relative percentage difference (RPD) or bias, and the absolute percentage difference (APD), both in percent

$$APD = \frac{1}{N}\sum_{i=1}^{N}\frac{|y_i - x_i|}{x_i} \times 100$$

$$RPD = \frac{1}{N}\sum_{i=1}^{N}\frac{y_i - x_i}{x_i} \times 100$$

The root mean square difference (RMSD) is also computed, which gives the uncertainty in the same units as the evaluated variable.

$$RMSD = \sqrt{\frac{1}{N}\sum_{i=1}^{N}(y_i - x_i)^2}$$

3 Results

3.1 Selection of reference pixel location

The radiometer is located at the end of a slender (50 cm) 1.1 km long jetty. Given its relative closeness to land, it is important to understand the natural horizontal variability of the water reflectance around the deployment site in order to evaluate its suitability to validate sensors with different spatial resolutions. Therefore, an analysis is performed here considering different satellite spatial resolutions in order to decide whether the site exact location or a reference pixel is preferred and if the latter, select the optimal location. To evaluate the spatial homogeneity of the area, a 6 years time-series of Sentinel-2 (A & B) images resampled to 10, 300, 700 and 1,000 m resolutions was used. For each image, the reflectance value from the 10 m resolution imaged at all bands have been extracted at the exact location of the measurement site and used to calculate the relative percentage difference between this value and each pixel of the same image (Figure 3).

Similar daily maps have been calculated for the whole time series comparing the original value at the site at 10 m resolution to the pixels of the resampled images at the other spatial resolutions for the same date (Figure 4).

It can be observed that lower relative differences are found for shorter (*e.g.*, 492 nm) compared to longer wavelengths (*e.g.*, 865 nm). To determine the region with lower spatial variability, the frequency of pixels with APD lower than 15% per band was calculated. Given that the NIR band showed the highest variability, this band was used to define the reference pixel (with its corresponding 3 × 3 window) to use for typical spatial resolutions sensors. For the medium and lower resolutions, *i.e.* 300, 700 and 1,000 m, the reference pixel was

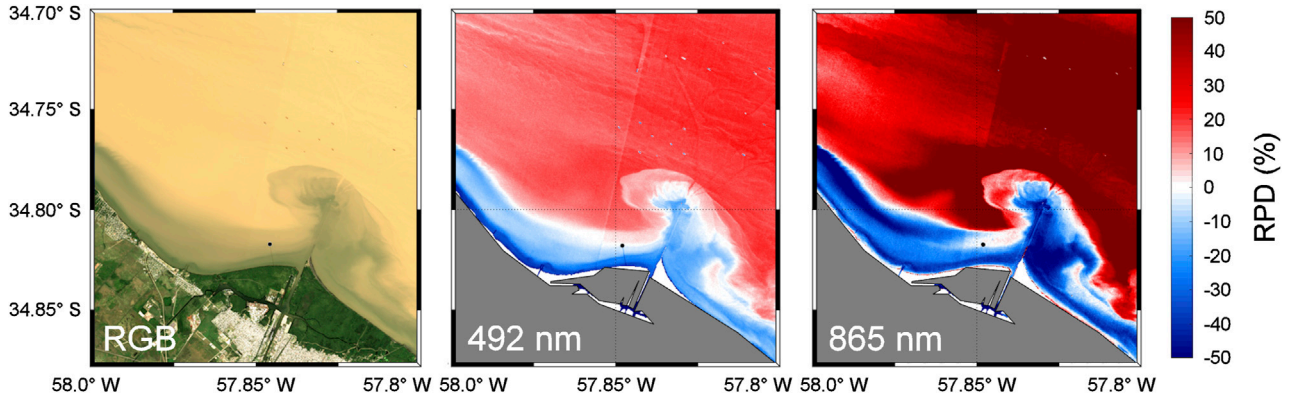


FIGURE 3
Sentinel-2A/MSI RGB composite of ρ_w for LPAR site taken on 2020-02-28 (left) and relative percentage difference calculated at each pixel respect to the value at LPAR site location for 492 nm (centre) and 865 nm (right) bands.

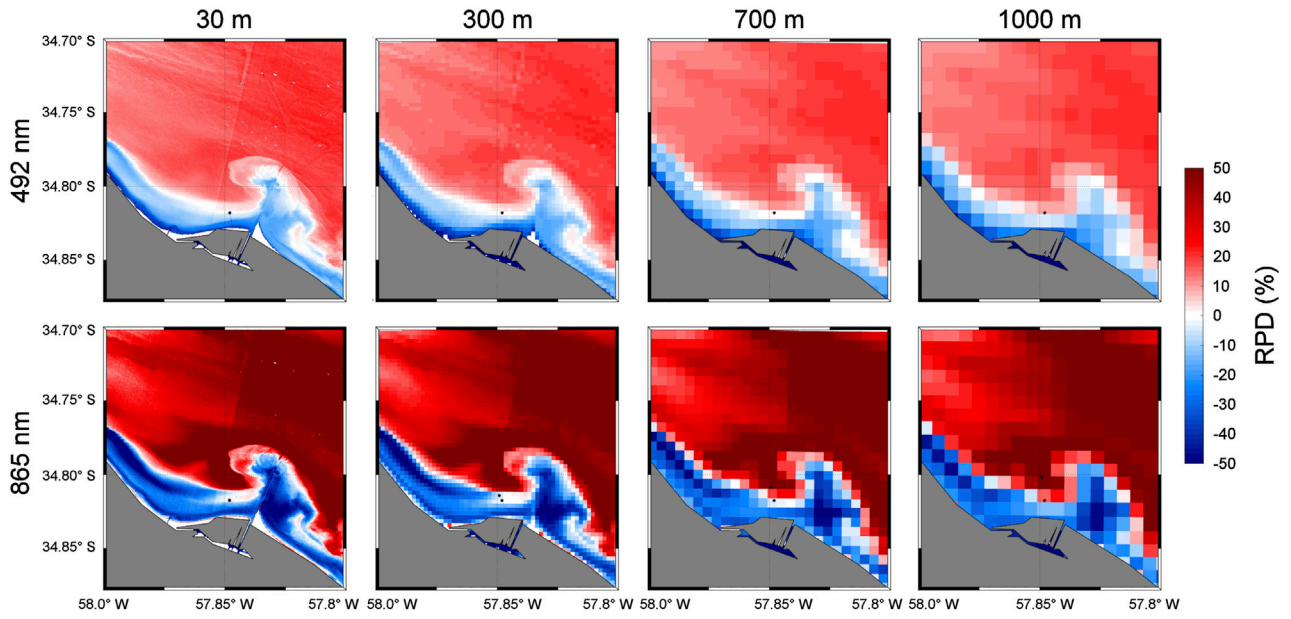


FIGURE 4
Sentinel-2A/MSI relative percentage difference maps taken on 2020-02-28 calculated at each pixel respect to the value at LPAR site location for 492 nm (top row) and 865 nm (bottom row) bands for resampled images at different spatial resolutions (columns).

selected within the region of lower variability (high frequency of APD< 15%) and at a certain distance to the coast, considering the satellite pixel size, in order to avoid contamination (Figure 5).

In turn, for the higher spatial resolution sensors, *i.e.* 3 (PS), 10 (MSI) and 30 (OLI) m, the closest pixel to the platform to the Northwest, considering also the 3 × 3 pixel window, is selected in order to avoid contamination from the platform structure (Figure 6). In this way the location of the reference pixel to be used, depending on the resolution of the sensor to evaluate, are shown in Figure 6 and listed in Table 3. Statistics for the 492 nm and 865 nm bands are also presented in Table 3.

3.2 Spectral consistency

Comparison of satellite and *in situ* ρ_w spectra for all the sensors analyzed in this study are shown in Figure 7. In general, the average spectral shape of all sensors were consistent with the *in situ* data, however clear differences are obvious and varied for each sensor. The average spectra of PS/SD tended to overestimate *in situ* data, especially in the blue (400–500 nm) and NIR (800–900 nm) parts of the spectra. In turn, L89/OLI and S2/MSI tended to overestimate *in situ* data between 500 and 700 nm, while similar values (average) and variability (standard deviation) were found in the blue and NIR part of the spectra. The average ρ_w spectra of S3/OLCI was slightly lower (higher) at wavelengths shorter (longer) than 600 nm. Both

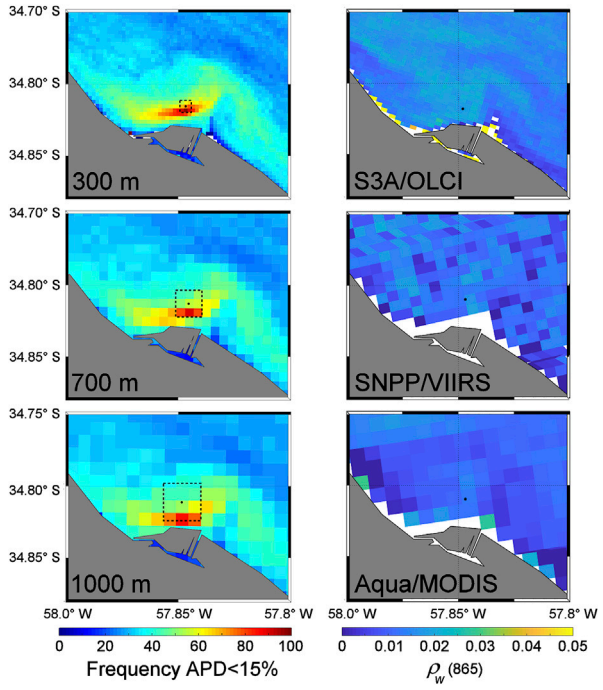


FIGURE 5
Frequency of APD values lower than 15% calculated using the whole S2/MSI time series (left) and ρ_w at 865 nm for S3A/OLCI (300 m), SNPP/VIIRS (750 m), and Aqua/MODIS (1,000 m) images taken on 2022-09-05 (right). Location of the reference pixel (black round symbol) and the corresponding 3 × 3 pixel window (dashed black square) are indicated.

Aqua/MODIS and SJ/VIIRS sensors, processed using OCSSW/l2gen and SWIR bands, systematically underestimated *in situ* ρ_w data. For SJ/VIIRS, increased overestimation can be observed when SWIR12 and SWIR13 bands are used compared to SWIR23. In general, differences increased towards the shorter wavelengths, retrieving negative ρ_w values in the blue bands, especially for Aqua/MODIS. Finally, PRISMA also showed a systematic underestimation of the *in situ* ρ_w throughout the spectra.

3.3 Matchups analysis

Comparisons between satellite-derived and HYPSTAR® *in situ* water reflectance data for the six multispectral sensors (PS/SD, L89/OLI, S2/MSI, S3/OLCI, JS/VIIRS, and Aqua/MODIS) considering all bands together, are shown in Figure 8. A first evaluation of JS/VIIRS atmospheric correction results comparing the three SWIR bands combination showed that, even though a general underestimation at all bands is evident for all configurations, differences between satellite and *in situ* data were lower when the SWIR23 bands were used (Figure 8 and Supplementary Figures S3, S4). Therefore the analysis of JS/VIIRS matchups using only the SWIR23 band combination are presented in the following results. Given that comparisons with *in situ* measurements (plots and statistics) for the same instrument on board of different satellites are comparable, all data from each sensor regardless of the satellite were analyzed and plotted together, *i.e.*, OLI from Landsat-8/9, MSI from S2A/B, and VIIRS from JPPS/SNPP. A breakdown per satellite sensor statistics and scatterplots can be found in Supplementary Figures S5–S12.

A high correlation for all bands together was found for all sensors ($R^2 > 0.8$), being higher ($R^2 > 0.9$) for L89/OLI and S2/MSI (Figure 8). The latter also showed the lowest average RPD (−3.52 and 2.45), APD (14.67 and 12.20) and RMSD (0.0124 and 0.0091) for L89/OLI and S2/MSI respectively. In both cases, higher underestimation is found at higher water reflectance values (slope <1).

It is interesting to note that if images contaminated with sun glint are not removed (using the ρ_s(~1,600)>0.05 criterion) and are thus included in the analysis (grey symbols in Figures 8, 9 for S2/MSI and L89/OLI), correlations decrease (R^2 = 0.65 and 0.81) and all statistics increase (Table 4). Moreover, higher overestimation (RPD = 29.74% and 7.4%) and scatter (APD = 37.14% and

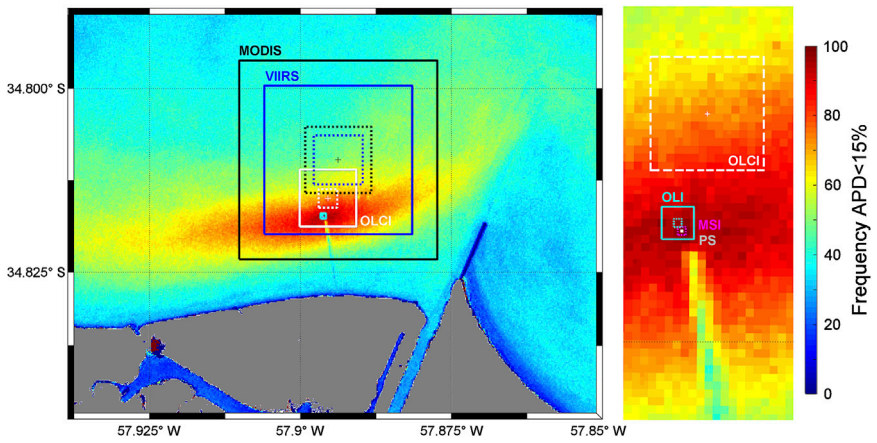


FIGURE 6
Frequency map of APD values lower than 15% where the location of the reference pixel and corresponding 3 × 3 pixel window are indicated for different sensors: PS (grey), MSI (magenta), OLI (cyan), OLCI (white), VIIRS (blue), and MODIS (black). Detailed view of the LPAR site (right).

TABLE 3 Reference pixel location depending on the spatial resolution of the systems and statistics for 492 and 865 nm bands. medAPD: median absolute percentage difference (%), medRPD: median relative percentage difference (%).

Resolution [m]	Sensor	Latitude [°]	Longitude [°]	Statistics	492 nm	865 nm
3	SD	−34.817570	−57.896118			
10/20	MSI	−34.817493	−57.896960	medAPD	1.44	1.58
				medRPD	0.05	0.12
				RMSD	0.0014	0.0009
30	OLI/PRISMA	−34.817356	−57.896229	medAPD	1.17	2.67
				medRPD	0.51	0.60
				RMSD	0.0018	0.0033
300	OLCI	−34.814934	−57.895401	medAPD	2.85	7.14
				medRPD	1.72	2.48
				RMSD	0.0040	0.0058
700	VIIRS	−34.809700	−57.893700	medAPD	4.75	12.47
				medRPD	3.43	7.56
				RMSD	0.0057	0.0087
1,000	MODIS	−34.809700	−57.893700	medAPD	4.63	11.18
				medRPD	2.80	6.14
				RMSD	0.0051	0.0077

24.11%) of the data is found for both S2/MSI and L89/OLI, respectively when sun glinted images are not removed (Table 4). The RMSD not only decrease for both sensors at all bands, but its spectral shape changes from almost spectrally flat (when sun glinted images are included) to a shape that resembles water reflectance when contaminated images are excluded (Figure 9).

Results for PS/SD indicate lower correlation ($R^2 = 0.88$) and on average higher scatter (APD = 33.63%, RMSD = 0.0165) and positive bias (RPD = 30.75%) tending in general to overestimate *in situ* data especially at low reflectance values. For mid- and low-spatial resolution sensors, *i.e.*, S3/OLCI, JS/VIIRS, and Aqua/MODIS, higher APD (20%–30%) and RMSD (0.014–0.025) were found, with Aqua/MODIS showing higher scatter (APD = 36.30% and RMSD = 0.0259). Both JS/VIIRS and Aqua/MODIS clearly tend to underestimate *in situ* values at all bands, even retrieving negative values in the shorter bands. While S3/OLCI showed better results, it also retrieved some negative values in the blue, demonstrating clear problems of the atmospheric correction in these turbid waters. PS/SD standard ρ_s products tend to over(under) estimate *in situ* values at low(high) water reflectance values (Supplementary Table S1). Given that only a few PRISMA images were available for the period analyzed, only the four match-ups spectra are shown in Figure 10. In general water reflectances were underestimated over the whole spectra, except for the image on 2022-08-25 which showed good correspondence in the region between 550 and 710 nm and overestimation below and above those wavelengths. In general, the PRISMA spectra shape resembles that of the HYPSTAR measurements, although some strange features can be observed, *i.e.*, there is an increase in water reflectance in the 400–420 nm part of the spectra and there is a spike at ~760 nm that could be an artifact due to the proximity to the region of atmospheric oxygen absorption (Ruddick et al., 2023).

The spectral variation of the statistics is shown in Figure 11. In general, for all multi-spectral sensors here analyzed, higher scatter (APD = 20–90%) and worse fits ($R^2 < 0.5$, Supplementary Table S1) are found at the shorter bands (<550 nm), but while the average relative difference is positive for S2 (RPD = 2–6%), and PS/SD (RPD = 3–54%), it is negative for L89/OLI (RPD = −3/-10%), S3/OLCI (RPD = −40/-10%), JS/VIIRS (−50/-10%), and Aqua/MODIS (−25/-90%). The absolute relative differences also increases towards the NIR (>700 nm), varying from 10% to 140%, with a general overestimation of the *in situ* values for all sensors except for VIIRS and MODIS which show a clear underestimation. Furthermore, JS/VIIRS and Aqua/MODIS show a negative bias across the whole spectrum, indicating a general overestimation of the atmospheric path reflectance that increases from the near infrared to the shortest blue bands with RPD, varying from −2.5% to −50% for JS/VIIRS and from −18% to −90% for Aqua/MODIS (Figure 12). S2/MSI and L89/OLI spectral RMSD resemble the shape of water reflectance spectra, with higher values between 500 and 700 nm (0.014–0.017) and lower in the shorter and longer wavelength (~0.007). A similar shape can also be observed for S3/OLCI, but with higher RMSD at all bands, and for JS/VIIRS but with higher RMSD at shorter wavelengths (~0.015), while a general increase of RMSD with decreasing wavelength is observed for Aqua/MODIS, evidencing an imperfect correction of the atmospheric path reflectance. In turn, PS/SD shows high RMSD towards both the shorter and longer wavelengths reaching maxima of 0.022 and 0.025, respectively. Results for PS/SD indicate on average low differences with

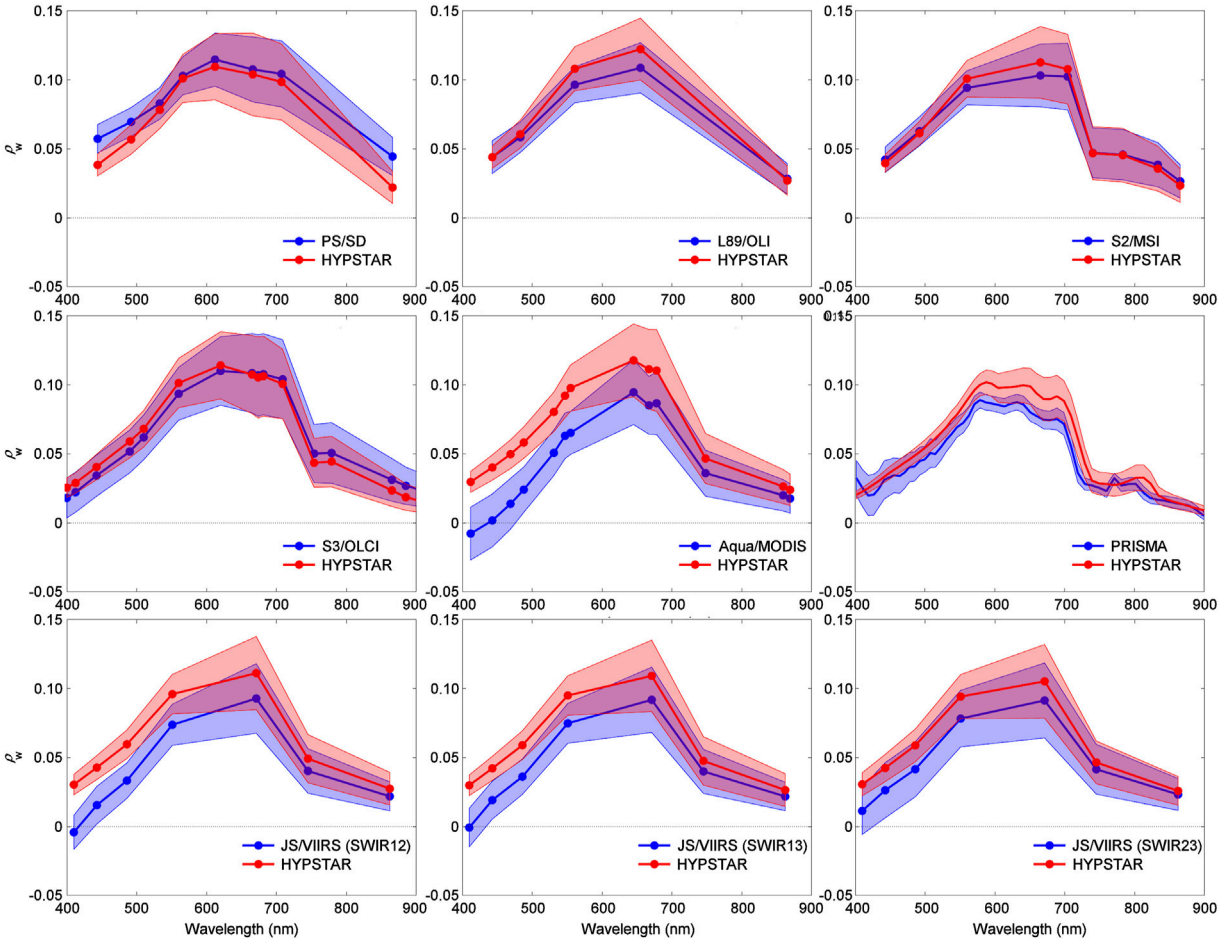


FIGURE 7
Comparison of ρ_w spectra of satellite-derived (blue) and *in situ* HYPSTAR® data (red). Bold lines are the mean and the thin lines are the +/-1 standard deviation respect to the average of all available spectra: PS/SD, L89/OLI, S2/MSI, S3/OLCI, Aqua/MODIS, PRISMA, and JS/VIIRS using SWIR12, SWIR13, and SWIR23 configurations.

HYPSTAR® observations for the five bands between 553 and 707 nm, with mean absolute relative differences (APD) 8.4%–12%, while differences increases for the shorter bands 442–490 nm (APD = 25.7 and 54.2%) and the longest NIR band (APD = 135.0%), showing in all cases a positive bias. Root mean square differences are also lower for bands between 492 and 707 nm (RMSD = 0.011–0.016) and higher scatter is found for the first (444 nm) and the last (866 nm) bands (RMSD = 0.022 and 0.025).

4 Discussion

4.1 Spatial homogeneity

The quality of the match-ups at a test site will depend on how representative is the point radiometric measurement at the site compared to the satellite pixel of a given size. This will depend the spatial homogeneity of the water and also on the proximity of the site to land (possible mixed pixels or spatial straylight). Different strategies/solutions to address this problem have been proposed, like manually shifting the extraction window to avoid the influence of the structure (Vanhellemont, 2019) or to extract a large pixel window and discard the central pixels to minimize platform contamination (Ilori et al., 2019). For more examples see Table 3 in Concha et al. (2021). In the present study a different and more objective strategy is proposed. High spatial resolution imagery was used to evaluate the spatial variability (homogeneity) and the closeness to land at different length scales in order to select the location of a reference pixel as a function of sensor spatial resolution. Matchup statistics improved when extracting satellite information using the reference pixel location compared to the exact location of the radiometer (Supplementary Figure S13)

4.2 Water reflectance standard product performance

For the eight band SuperDoves satellites, 54 matchups from 44 unique satellites have been obtained showing high consistency for all 44 different satellites. Match-up results obtained in this study

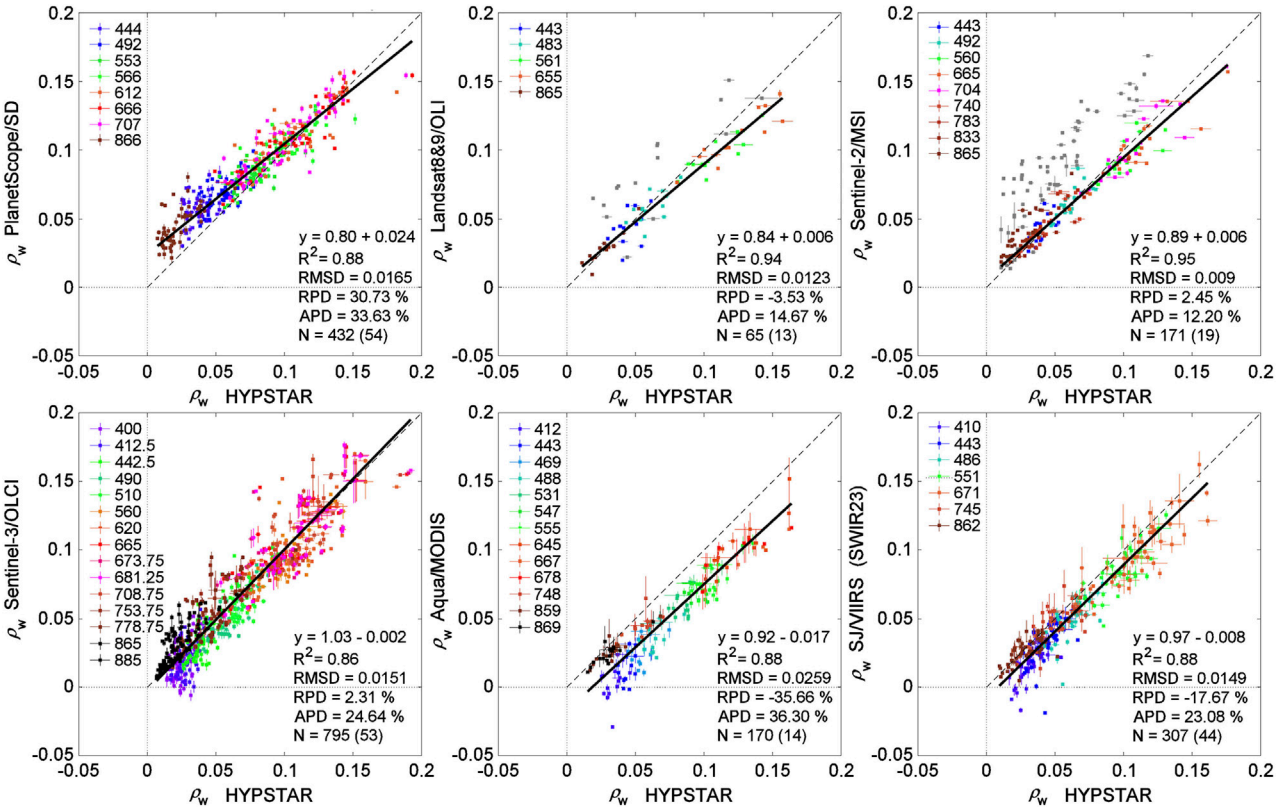


FIGURE 8
Scatter plots of *in situ* HYPSTAR *versus* satellite-derived water reflectance (ρ_w) for PS/SD, L89/OLI, S2/MSI, S3/OLCI, Aqua/MODIS, SJ/VIIRS. Statistics are presented as the best-fitted SMA linear regression and associated determination coefficient, the RMSD, RPD, APD and the number of data (N) and processed images (in brackets). For L89/OLI and S2/MSI, grey symbols correspond to discarded match-ups due to sun glinted images.

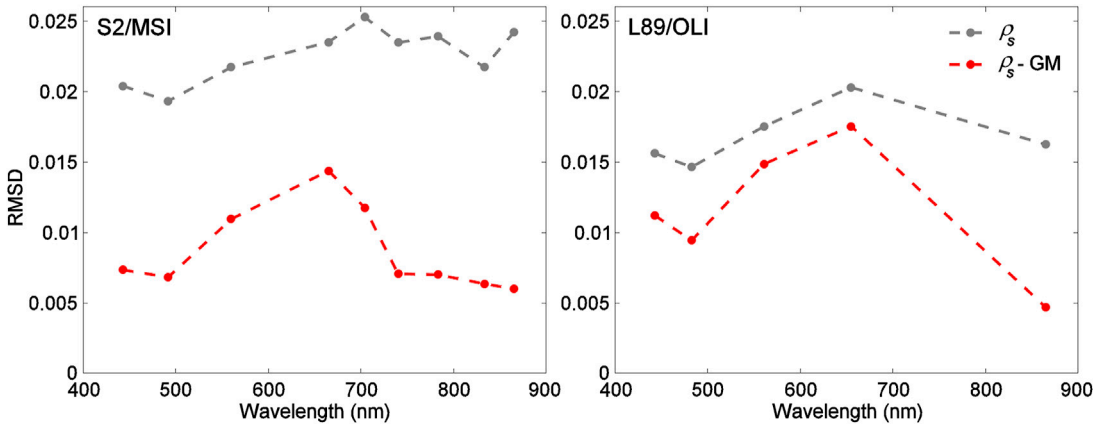


FIGURE 9
RMSD spectra for S2/MSI (left) and L89/OLI (right) for ρ_s matchups using all coincident images (grey) and masking sun glinted images (GM) (red).

were similar to the ones obtained for the turbid waters of the Belgian Coastal Zone (Vanhellemont, 2023), *i.e.*, low relative errors between 566 and 707 nm (APD = 8.4–12%) and larger relative differences (APD = 25–134%) in the blue (444 nm) and NIR (866 nm) bands, but reaching lower and higher values than in the BCZ, with APD = 15–20% and APD = 30–99.4%, respectively. The general overestimation found in this study could be related, as suggested in Vanhellemont (2023), to the use of ancillary (not from image) aerosol optical thickness that could be biased low, especially for the blue band, and due to not corrected sun glint.

TABLE 4 Validation statistics for OLI and MSI matchups considering all possible matchups and only non-glinted images (GM: Glint Masked).

Statistics	L89	L89-GM	S2	S2-GM
R^2	0.81	0.94	0.65	0.95
APD	24.11	14.67	37.14	12.20
RPD	7.40	−3.52	29.74	2.45
RMSD	0.0170	0.0124	0.0227	0.0091
N	80	65	225	171

Even though L89/OLI and S2/MSI standard L2 products use land remote sensing algorithms for the atmospheric correction, they showed better results compared to the other systems and considering all bands together (Figure 9). Similar results have been found in other turbid waters. Kuhn et al. (2019) found that L8 standard land surface reflectance product had the best performance in the highly scattering (turbid) waters of the Lower Amazon river, with median APD of 4%–17% and RMSD 0.003–0.0157 across the spectrum and varying on the tidal condition (high or low water) of the river. Li et al. (2023) also showed good results for S2 images over turbid waters using Sen2Cor. For turbid waters, aerosol reflectance contributes relatively less to the top of atmosphere signal. A crude aerosol correction can therefore be sufficient and is more robust than typical extrapolative algorithms for aerosol correction.

It is common that nadir-viewing sensors, like L89/OLI, S2/MSI and PS/SD, are frequently affected by sun glint on the air water

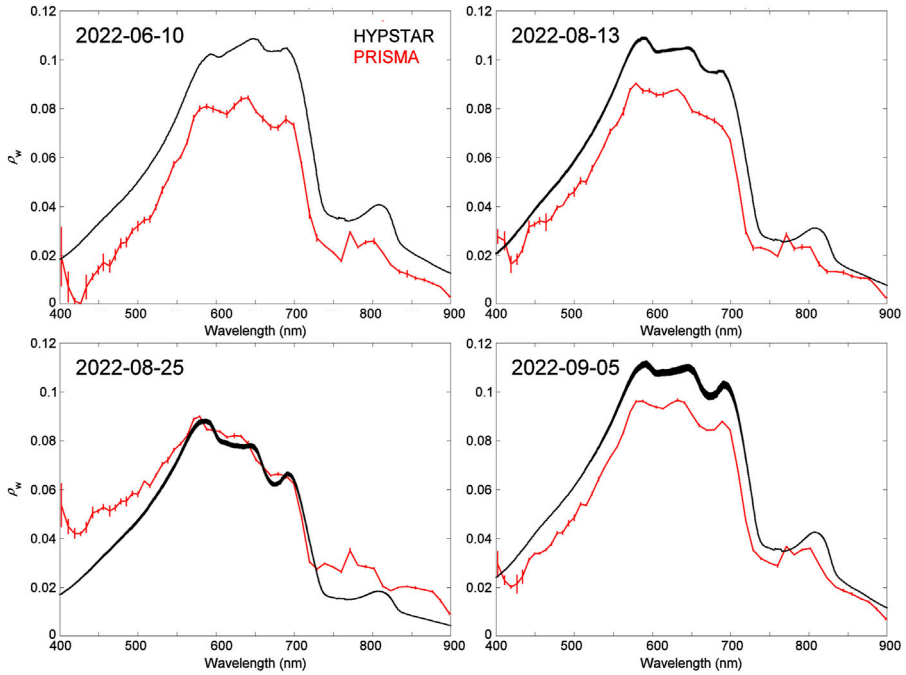


FIGURE 10
In situ HYPSTAR ρ_w (black) and PRISMA standard Level-2 ρ_s (red) spectra.

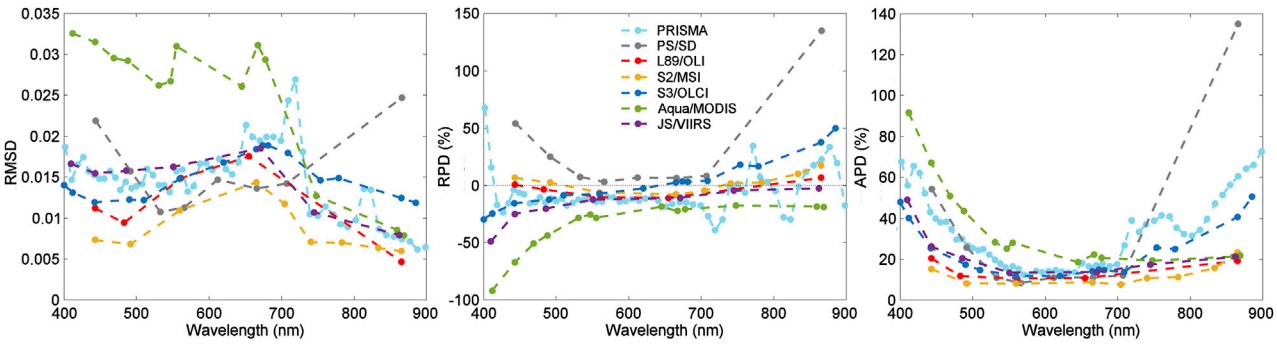


FIGURE 11
Spectra of RMSD (left), RPD (centre) and APD (right) for the different satellite-sensors evaluated: PS/SD (grey), L89/OLI (red), S2/MSI (orange), S3/OLCI (blue), Aqua/MODIS (green), JS/VIIRS (violet), and PRISMA (light blue).

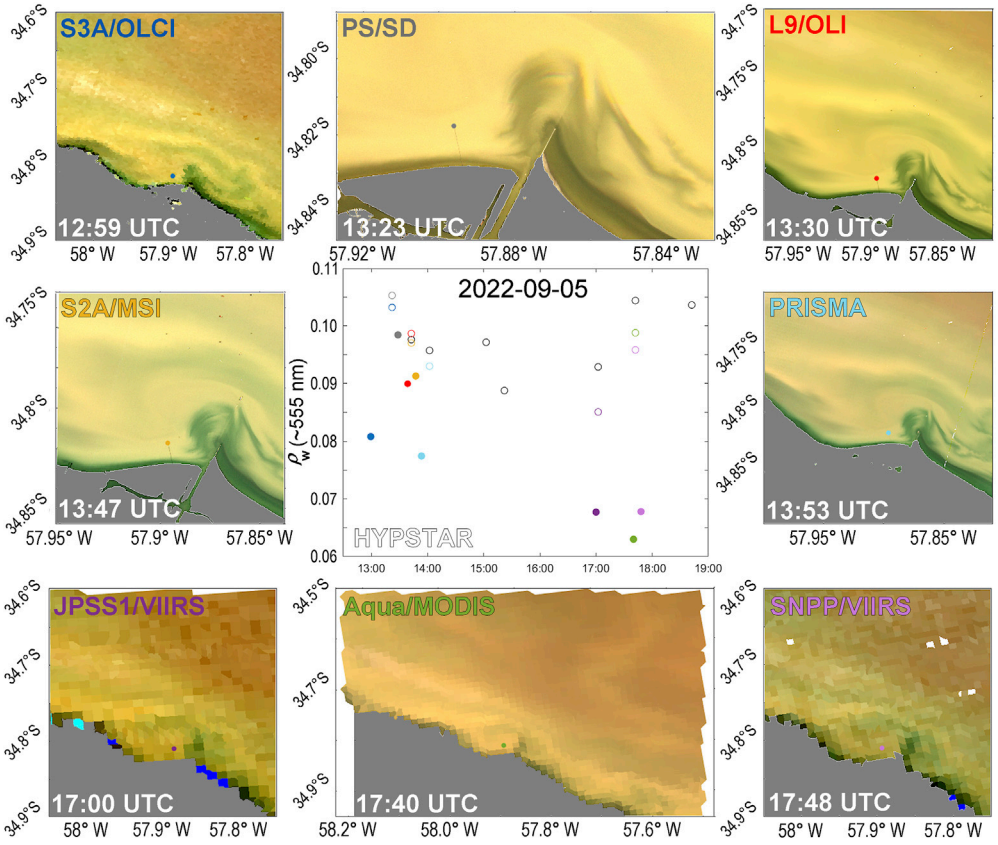


FIGURE 12
Example of matchups between eight sensors (circles) and HYPSTAR *in situ* (open circles) reflectance data at ~555 nm on 2022-09-05 (centre). RGB images from: S3A/OLCI at 12:59 UTC, PS/SD at 13:23UTC, L9/OLI 13:30 UTC, S2A/MSI 13:47 UTC, PRISMA 13:53 UTC, JPSS1/VIIRS 17:00 UTC, Aqua/MODIS 17:40 UTC, SNPP/VIIRS 17:48 UTC. The coloured coded circles on the RGB composites show the reference location use for the matchup.

interface (Vanhellemont, 2019; Lavigne et al., 2023). Given that standard land approaches do not correct for this additional contribution of scattered light to the satellite observed signal, in this study a simple mask using a threshold on water reflectance in the SWIR was applied for L89/OLI and S2/MSI imagery. Even if it is not a correction, a simple masking greatly improved the statistics, evidencing the importance of either correcting or avoiding sun glint contaminated images. The same masking could not be performed to PS/SD imagery because they lack SWIR bands. Glint removal methods have been developed in alternative aquatic atmospheric correction approaches (Harmel et al., 2018; Vanhellemont, 2019) showing improved S2 and L8 retrievals (Vanhellemont, 2020; Maciel et al., 2022), but solutions for sun glint correction of sensors without SWIR bands are still needed (Lavigne et al., 2023).

Matchup results obtained here for MODIS and VIIRS sensors are in agreement with previous comparisons made in the turbid waters of Río de la Plata for both MODIS and VIIRS instruments using the WG94-SWIR atmospheric correction (Dogliotti et al., 2014; Gossn et al., 2021). Namely, retrievals tend to underestimate water reflectance at all wavelengths with increasing differences and scatter from the near infrared to the shortest blue bands, frequently retrieving negative water reflectance, evidencing an overcorrection of the reflectance in visible bands probably due to overestimation of the aerosol component.

The spectral shape of PRISMA water reflectance resembled that of the HYPSTAR® *in situ* measurements, but a general underestimation was found for the whole spectra except at one date. It has already been found that the PRISMA L2 standard product has better performance in more turbid and productive waters (like the Trasimeno Lake) compared to more clear waters and slightly influenced by suspended particles, like the Venice lagoon at Aqua Alta Oceanographic Tower (Braga et al., 2022). Even though Trasimeno Lake and Río de la Plata have different optical characteristics, similar statistics have been found considering all bands together with high correlation (R^2 = 0.82) and scatter (APD~32%).

The current protocol used to process HYPSTAR data is based on the standard protocol generally used to process above-water measurements, *i.e.*, it uses measurements of the upwelling radiance from the water (L_u) and downwelling sky radiance (L_{sky}) and an external source for wind speed data to estimate the estimate the air-water interface reflectance factor using Cox–Munk wave-slope statistics (Mobley, 1999). In the case of HYPERNETS, wind is obtained either from NCEP/GDAS or fixed to 2 m/s, if the former is not available (De Vis et al. *submitted this same Frontiers Research Topic*). Even if a fixed wind speed might be more appropriate to use at LPAR because waves will be fetch-limited, using either modelled or fixed wind speed can lead to errors if they

defer from the actual wind speed at the moment of the measurement. In a recent revision of the AERONET-OC L_w uncertainties, Cazzaniga and Zibordi (2023) found that the largest contribution to uncertainties was the sea surface reflectance factor ρ_F which was mainly explained by the uncertainties in wind speed estimation. Analyzing data from six AERONET-OC sites they found median relative uncertainties ranging from 3.2% to 4.3%. In turn, using HYPSTAR data from Blankaart reservoir, Goyens and Ruddick (2023) calculated that errors on ρ_w in the blue and NIR can reach up to 75% and 50%, respectively, when wind speed is overestimated by 2 m/s in clear waters, but reaching lowers errors in more turbid waters (up to 25%). This is because the error on water reflectance due to errors in wind speed is an absolute error, *i.e.*, independent of water reflectance, and thus the percentage error is inversely proportional to water reflectance. This is encouraging considering that sediment-rich turbid waters are usually found at LPAR site. However, further analysis on the error introduced by using a fixed or modelled wind speed value is needed and will be assessed when *in situ* wind speed will be available, a meteorological station is planned to be deployed at LPAR site this year.

5 Conclusion

In this study, the first fixed automated hyperspectral system deployed in South America is described and the natural spatial variability of water reflectance around the site is characterized using high spatial resolution imagery. A methodology is proposed to objectively select a sensor-specific location of a reference pixel for satellite validation.

The water reflectance data collected during the first six operating months after deployment are used to evaluate the performance of operational level-2 products of many optical VSWIR satellite missions with different band sets and widths, from the multispectral metre scale 8-band SuperDoves, the medium S3/OLCI and low spatial resolution VIIRS and MODIS sensors, to the hyperspectral PRISMA sensor. It is shown that in these highly turbid waters, standard level-2 that uses land-based atmospheric correction approaches work reasonable well provided that sun glint contamination is avoided. The S2/MSI and L89/OLI high spatial resolution sensors showed the best results with low absolute percentage difference (APD~10%) and slight understimation in the bands with the highest water reflectance, *i.e.*, bands between 490 and 704 nm. PS/SD also showed low errors in this spectral region (RPD <10%), but increased overestimation and absolute relative difference in the shorter (blue) and longer (NIR) bands (APD>100%). In general performance decreased for the shorter wavebands for all systems, evidencing the need to improve the atmospheric correction in these challenging turbid waters for these approaches that relay on the extrapolation of the atmospheric path reflectance from the longer to the shorter bands. Finally, the mid-to low-spatial resolution VIIRS and MODIS imagery using the assumption of black pixel in the SWIR, showed the worst performance with a general underestimation of the reflectance across the whole spectra, increasing the difference from the longer (RPD ~ −20%) to the shorter wavelengths (RPD ~ −100%).

This work shows the power and the great potential of the HYPERNETS hyperspectral automated system to provide, on a routine basis, high quality and quantity of data for validation of satellite data at all wavelengths in a multi-mission perspective, fundamental in a context of massive and constantly growing Earth observing missions. As an example, in just 1 day level-2 products from eight missions could be evaluated at the LPAR site (Figure 12). These range from the typical "ocean colour" missions, like Aqua/MODIS and S3/OLCI, to "land" missions, like S2/MSI and L89/OLI that are used for coastal and inland waters applications, to the existing and planned hyperspectral missions, like PRISMA, ENMAP and future PACE, as well as geostationary GOCI and future GLIMR missions that provide information at high temporal resolution. Moreover, LPAR as well as other HYPERNETS sites are part the WATERHYPERNET international network (Ruddick et al., 2022; 2024 *submitted this same Frontiers Research Topic*), which are currently collecting data in very different optical water types in different regions of the world thus generating invaluable standardized radiometric data for satellite validation.

Data availability statement

The datasets presented in this study can be found in online repositories. The names of the repository/repositories and accession number(s) can be found below: https://doi.org/10.5281/zenodo.8048425.

Author contributions

AD: Conceptualization, Data curation, Formal Analysis, Funding acquisition, Investigation, Methodology, Project administration, Validation, Visualization, Writing–original draft, Writing–review and editing. EP: Investigation, Methodology, Resources, Writing–review and editing. LR: Investigation, Methodology, Resources, Software, Writing–review and editing. PP: Investigation, Methodology, Resources, Software, Writing–review and editing. KR: Funding acquisition, Investigation, Project administration, Resources, Supervision, Writing–review and editing.

Funding

The author(s) declare financial support was received for the research, authorship, and/or publication of this article. This study has been carried out in the context of HYPERNETS project funded by the European Union's Horizon 2020 research and innovation programme (Grant agreement n° 775983). Field campaigns and data processing were co-funded by the ANPCyT (PICT-2020/2636) and PIDT-PA-2020/B8 Pampa Azul (MiNCyT) projects.

Acknowledgments

Planet is thanked for research access to SuperDove data. NASA/USGS and ESA/EUMETSAT Copernicus are thanked for the acquisition and free distribution of Landsat and Sentinel-2 and Sentinel-3 images. NASA and NOAA are thanked for the acquisition and free distribution of MODIS and VIIRS imagery. The Italian Space Agency is thanked for the acquisition and distribution of

PRISMA data. The Escuela Naval Militar (EsNM) and Servicio de Hidrografia Naval (SHN) are thanked for permission and access to the LPAR platform and installation support. Fabricio Idoeta, Javier Pardiñas, and Ubaldo Hereñú are thanked for the logistics and technical support. HYPERNETS colleagues: Joel Kuusk, Alexander Corizi, Clémence Goyens, and Pieter de Vis are gratefully thanked for developing the radiometer, system, processor, and general support.

Conflict of interest

The authors declare that the research was conducted in the absence of any commercial or financial relationships that could be construed as a potential conflict of interest.

Publisher's note

All claims expressed in this article are solely those of the authors and do not necessarily represent those of their affiliated organizations, or those of the publisher, the editors and the reviewers. Any product that may be evaluated in this article, or claim that may be made by its manufacturer, is not guaranteed or endorsed by the publisher.

Supplementary material

The Supplementary Material for this article can be found online at: https://www.frontiersin.org/articles/10.3389/frsen.2024.1354662/full#supplementary-material

References

ASI – Italian Space Agency, (2021). PRISMA algorithm theoretical basis document (ATBD), issue 1. http://prisma.asi.it/missionselect/docs.php (Accessed March 3, 2023). Date 14/12/2021.

Aubriot, L., Zabaleta, B., Bordet, F., Sienra, D., Risso, J., Achkar, M., et al. (2020). Assessing the origin of a massive cyanobacterial bloom in the Río de la Plata (2019): towards an early warning system. *Water Res.* 181, 115944. doi:10.1016/j.watres.2020.115944

Bailey, S. W., and Werdell, P. J. (2006). A multi-sensor approach for the on-orbit validation of ocean color satellite data products. *Remote Sens. Environ.* 102, 12–23. doi:10.1016/j.rse.2006.01.015

Braga, F., Fabbretto, A., Vanhellemont, Q., Bresciani, M., Giardino, C., Scarpa, G. M., et al. (2022). Assessment of PRISMA water reflectance using autonomous hyperspectral radiometry. *ISPRS J. Photogramm. Remote Sens.* 192, 99–114. doi:10.1016/j.isprsjprs.2022.08.009

Cazzaniga, I., and Zibordi, G. (2023). AERONET-OC LWN uncertainties: revisited. *J. Atmos. Ocean. Tech.* 40, 411–425. doi:10.1175/jtech-d-22-0061.1

Collison, A., Jumpasut, A., and Bourne, H. (2022). On-orbit radiometric calibration of the Planet satellite fleet. *Planet Labs PBC.* https://assets.planet.com/docs/radiometric_calibration_white_paper.pdf (Accessed November 14, 2023).

Concha, J., Bracaglia, M., and Brando, V. (2021). Assessing the influence of different validation protocols on Ocean Colour match-up analyses. *Remote Sens. Environ.* 259, 112415. doi:10.1016/j.rse.2021.112415

De León, L., and Yunes, J. (2001). First report of a microcystin-containing bloom of the cyanobacterium Microcystis aeruginosa in the La Plata River, South America. *Environ. Toxicol. Water Qual.* 16, 110–112. doi:10.1002/1522-7278(2001)16:1<110::aid-tox1012>3.3.co;2-q

De Vis, P., Goyens, C., Hunt, S., Quinten Vanhellemont, Q., Ruddick, K., and Bialek, A., Generating hyperspectral reference measurements for surface reflectance from the LANDHYPERNET and WATERHYPERNET networks. *Submitt. this Special Issue Front. Remote Sens.*

Dogliotti, A. I., Ruddick, K., Nechad, B., and Lasta, C. (2011). "Improving water reflectance retrieval from MODIS imagery in the highly turbid waters of La Plata River," in Proceedings of VI International Conference "Current problems in optics of natural waters" (ONW'2011), Saint-Petersburg, Russia (Publishing House "Nauka" of RAS), 152.6-10 September, 2011

Dogliotti, A. I., O'Farrel, I., Yema, L., and Merlo, R. (2023). Validation of Sentinel-2/MSI water reflectance and water quality products in the turbid waters of Río de la Plata estuary using fixed automated hyperspectral *in situ* observations. *Proceedings of SPIE, the International Society for Optical Engineering*, 12728-1.

Dogliotti, A. I., Camiolo, M., Simionato, C., Jaureguizar, A., Guerrero, R., and Lasta, C. (2014). "First optical observations in the turbidity maximum zone in the Río de la Plata estuary: A challenge for atmospheric correction algorithms," in. *Proceeding of Ocean Optics XXII Conference*. Portland: United States of America.

Dogliotti, A. I., Gossn, J. I., Gonzalez, C., Yema, L., Sanchez, L., and O'Farrell, L. (2021). "Evaluation of multi- and hyper-spectral Chl-a algorithms in the Río de la Plata turbid waters during a cyanobacteria bloom," in 2021 IEEE International Geoscience and Remote Sensing Symposium IGARSS, 7442–7445. doi:10.1109/IGARSS47720.2021

Eumetsat, (2021). Sentinel-3 OLCI L2 report for baseline collection OL_L2M_003-EUM/RSP/REP/21/1211386. Available at: https://www.eumetsat.int/media/47794 (Accessed October 20, 2023).

Eumetsat, (2022). Recommendations for sentinel-3 OLCI Ocean Colour product validations in comparison with *in situ* measurements – matchup protocols. Available at: https://www.eumetsat.int/media/44087 (Accessed October 20, 2023).

Franz, B. A., Kwiatkowska, E. J., Meister, G., and McClain, C. R. (2008). Moderate resolution imaging spectroradiometer on Terra: limitations for ocean color applications. *J. Appl. Remote Sens.* 2, 023525. doi:10.1117/1.2957964

García-Alonso, J., Lercari, D., and Defeo, O. (2019). "R_ıo de la Plata: a neotropical Estuarine system," in *Coasts and estuaries*. Editors E. Wolanski, J. W. Day, M. Elliott, and R. Ramachandran (Amsterdam: Elsevier), 45–56.Chap. 3

Gordon, H. R., and Wang, M. (1994). Retrieval ofWater-leaving radiance and aerosol optical thickness over the oceans with SeaWIFS: a preliminary algorithm. *Appl. Opt.* 33, 443–452. doi:10.1364/ao.33.000443

Gossn, J. I., Frouin, R., and Dogliotti, A. I. (2021). Atmospheric correction of satellite optical imagery over the Río de la Plata highly turbid waters using a SWIR-based principal component decomposition technique. *Remote Sens.* 13 (6), 1050. doi:10.3390/rs13061050

Gossn, J. I., Ruddick, K. G., and Dogliotti, A. I. (2019). Atmospheric correction of OLCI imagery over extremely turbid waters based on red, NIR and 1016nm bands and a new baseline residual technique. *Remote Sens.* 11 (220), 1–24. doi:10.3390/rs11030220

Goyens, C., Lavigne, H., Dille, A., and Vervaeren, H. (2022). Using hyperspectral remote sensing to monitor water quality in drinking water reservoirs. *Remote Sens.* 14 (21), 5607. doi:10.3390/rs14215607

Goyens, C., and Ruddick, K. (2023). Improving the standard protocol for above-water reflectance measurements: 1. Estimating effective wind speed from angular variation of sunglint. *Appl. Opt.* 62 (February), 2442. doi:10.1364/AO.481787

Harmel, T., Chami, M., Tormos, T., Reynaud, N., and Danis, P.-A. (2018). Sunglint correction of the Multi-Spectral Instrument (MSI)-SENTINEL-2 imagery over inland and sea waters from SWIR bands. *Remote. Sens. Environ.* 204, 308–321. doi:10.1016/j.rse.2017.10.022

Ilori, O. C., Pahlevan, N., and Knudby, A. (2019). Analyzing performances of different atmospheric correction techniques for Landsat 8: application for coastal remote sensing. *Remote Sens.* 11, 469. doi:10.3390/rs11040469

IOCCG, (2018). "Earth observations in support of global water quality monitoring," in *IOCCG Report Series, No. 17*. Editors S. Greb, A. Dekker, and C. Binding (Dartmouth, Canada: International Ocean Colour Coordinating Group), 17, 125.

Kruk, C., Martíınez, A., Martíınez de la Escalera, G., Trinchin, R., Manta, G., Segura, A. M., et al. (2021). Rapid freshwater discharge on the coastal ocean as a mean of long distance spreading of an unprecedented toxic cyanobacteria bloom. *Sci. Total Environ.* 754, 142362. doi:10.1016/j.scitotenv.2020.142362

Kuhn, C., de Matos Valerio, A., Ward, N., Loken, L., Oliveira Sawakuchi, H., Kampel, M., et al. (2019). Performance of landsat-8 and sentinel-2 surface reflectance products for river remote sensing retrievals of chlorophyll-a and turbidity. *Remote Sens. Environ.* 224, 104–118. doi:10.1016/j.rse.2019.01.023

Kuusk, J., Corizzi, A., Doxaran, D., Duong, K., Flight, K., Kivastik, J., et al. HYPSTAR: a hyperspectral pointable system for terrestrial and aquatic radiometry. *Front. remote sens.*

Lavigne, H., Vanhellemont, Q., Ruddick, K., and Vansteenwegen, D. (2023). Turbid water sun glint removal for high resolution sensors without SWIR. *Proc. SPIE 12728, Remote Sens. Ocean, Sea Ice, Coast. Waters, Large Water Regions* 2023, 1272804. doi:10.1117/12.268391217 October

Li, J., Yin, Z., Lu, Z., Ye, Y., Zhang, F., Shen, Q., et al. (2019). Regional vicarious calibration of the SWIR-based atmospheric correction approach for MODIS-aqua measurements of highly turbid inland water. *Remote Sens.* 11, 1670. doi:10.3390/rs11141670

Li, W., Huang, Y., Shen, Q., Yao, Y., Xu, W., Shi, J., et al. (2023). Assessment of seven atmospheric correction processors for the sentinel-2 multi-spectral imager over lakes in qinghai province. *Remote Sens.* 2023 (15), 5370. doi:10.3390/rs15225370

Maciel, F. P., and Pedocchi, F. (2022). Evaluation of ACOLITE atmospheric correction methods for Landsat-8 and Sentinel-2 in the Rıo de la Plata turbid coastal waters. *Inter J. Remote Sens.* 43 (1), 215–240. doi:10.1080/01431161.2021.2009149

Mobley, C. D. (1999). Estimation of the remote-sensing reflectance from above-surface measurements. *Appl. Opt.* 38, 7442–7455. doi:10.1364/ao.38.007442

Mumby, P. J., Green, E. P., Edwards, A. J., and Clark, C. D. (1999). The cost-effectiveness of remote sensing for tropical coastal resources assessment and management. *J. Environ. Manag.* 55 (3), 157–166. doi:10.1006/jema.1998.0255

Nagy, G. J., Gomez-Erache, M., L_opez, C. H., and Perdomo, A. C. (2002). "Distribution patterns of nutrients and symptoms of eutrophication in the Rio de la Plata River Estuary system," in *Nutrients and eutrophication in estuaries and coastal waters. Developments in hydrobiology*. Editors E. Orive, M. Elliott, and V. N. de Jonge (Dordrecht, Netherlands: Springer), 164, 125–139.

National Centers for Environmental Prediction, National Weather Service, Noaa, U.S. Department of Commerce, (2015). *Ncep gdas/fnl 0.25 degree global tropospheric analyses and forecast grids*. National Centers for Environmental Prediction, National Weather Service, Noaa, U.S. Department of Commerce. Maryland, MD, USA.

Planet, (2022). Planet: Planet imagery product specifications. https://assets.planet.com/docs/Planet_Combined_Imagery_Product_Specs_letter_screen.pdf.

Prisma, (2020). PRISMA products specification. Available online: http://prisma.asi.it/missionselect/docs/PRISMA%20Product%20Specifications_Is2_3.pdf (Accessed on November 20, 2023).

Ruddick, K., Brando, V. E., Corizzi, A., Dogliotti, A. I., Doxaran, D., and Goyens, C., WATERHYPERNET: a prototype network of automated *in situ* measurements of hyperspectral water reflectance for satellite validation and water quality monitoring. *Front. Remote Sens.*

Ruddick, K. G., De Vis, P., Goyens, C., Kuusk, J., Lavigne, H., and Vanhellemont, Q. (2023). Second derivative water reflectance spectra for phytoplankton species detection: origin, impact, and removal of spectral wiggles. *Proc. SPIE 12728, Remote Sens. Ocean, Sea Ice, Coast. Waters, Large Water Regions* 2023, 127280A. doi:10.1117/12.268433617 October

Sathicq, M., Gómez, N., Andrinolo, D., Sedán, D., and Donadelli, J. (2014). Temporal distribution of cyanobacteria in the coast of a shallow temperate estuary (Río de la Plata): some implications for its monitoring. *Environ. Monit. Assess.* 186 (11), 7115–7125.

Shi, W., and Wang, M. (2009). An assessment of the black ocean pixel assumption for MODIS SWIR bands. *Remote Sens. Environ.* 113 (2009), 1587–1597. doi:10.1016/j.rse.2009.03.011

Vanhellemont, Q. (2019). Adaptation of the dark spectrum fitting atmospheric correction for aquatic applications of the Landsat and sentinel-2 archives. *Remote Sens. Environ.* 1197 (225), 175–192. doi:10.1016/j.rse.2019.03.010

Vanhellemont, Q. (2020). Sensitivity analysis of the dark spectrum fitting atmospheric correction for metre-and decametrescale satellite imagery using autonomous hyperspectral radiometry. *Opt. Express* 28 (20), 29948–29965. doi:10.1364/oe.3974562020

Vanhellemont, Q. (2023). Evaluation of eight band SuperDove imagery for aquatic applications. *Opt. Express* 31 (9), 13851. doi:10.1364/oe.48341824 Apr 2023

Zibordi, G., Holben, B. N., Talone, M., D'Alimonte, D., Slutsker, I., Giles, D. M., et al. (2020). Advances in the Ocean color component of the aerosol robotic network (AERONET-OC). *J. Atmos. Ocean. Technol.* 38, 725–746. doi:10.1175/jtech-d-20-0085.1

Zibordi, G., Kwiatkowska, E., Mélin, F., Talone, M., Cazzaniga, I., Dessailly, D., et al. (2022). Assessment of OLCI-A and OLCI-B radiometric data products across European seas. *Remote Sens. Environ.* 272, 112911. doi:10.1016/j.rse.2022.112911

Zibordi, G., Melin, F., Berthon, J. F., Holben, B., Slutsker, I., Giles, D., et al. (2009). AERONET-OC: a network for the validation of ocean color primary products. *J. Atmos. Ocean. Technol.* 26, 1634–1651. doi:10.1175/2009jtecho654.12009

frontiers | Frontiers in Remote Sensing

TYPE Perspective
PUBLISHED 10 April 2024
DOI 10.3389/frsen.2024.1372085

Check for updates

OPEN ACCESS

EDITED BY
Zhigang Cao,
Chinese Academy of Sciences (CAS), China

REVIEWED BY
Joseph L. Garrett,
NTNU, Norway
Shun Bi,
Helmholtz Association of German Research Centres (HZ), Germany

*CORRESPONDENCE
Kevin G. Ruddick,
kruddick@naturalsciences.be

RECEIVED 17 January 2024
ACCEPTED 14 March 2024
PUBLISHED 10 April 2024

CITATION
Ruddick KG, Bialek A, Brando VE, De Vis P, Dogliotti AI, Doxaran D, Goryl P, Goyens C, Kuusk J, Spengler D, Turpie KR and Vanhellemont Q (2024), HYPERNETS: a network of automated hyperspectral radiometers to validate water and land surface reflectance (380–1680 nm) from all satellite missions.
Front. Remote Sens. 5:1372085.
doi: 10.3389/frsen.2024.1372085

COPYRIGHT
© 2024 Ruddick, Bialek, Brando, De Vis, Dogliotti, Doxaran, Goryl, Goyens, Kuusk, Spengler, Turpie and Vanhellemont. This is an open-access article distributed under the terms of the Creative Commons Attribution License (CC BY). The use, distribution or reproduction in other forums is permitted, provided the original author(s) and the copyright owner(s) are credited and that the original publication in this journal is cited, in accordance with accepted academic practice. No use, distribution or reproduction is permitted which does not comply with these terms.

HYPERNETS: a network of automated hyperspectral radiometers to validate water and land surface reflectance (380–1680 nm) from all satellite missions

Kevin G. Ruddick[1]*, Agnieszka Bialek[2], Vittorio E. Brando[3], Pieter De Vis[2], Ana I. Dogliotti[4], David Doxaran[5], Philippe Goryl[6], Clémence Goyens[1], Joel Kuusk[7], Daniel Spengler[8], Kevin R. Turpie[9] and Quinten Vanhellemont[1]

[1]Royal Belgian Institute of Natural Sciences (RBINS), Brussels, Belgium, [2]National Physical Laboratory (NPL), Teddington, United Kingdom, [3]CNR-ISMAR, Istituto di Scienze Marine, Consiglio Nazionale delle Ricerche, Rome, Italy, [4]Instituto de Astronomía y Física del Espacio, Consejo Nacional de Investigaciones Científicas y Técnicas (IAFE, CONICET/UBA, University of Buenos Aires), Buenos Aires, Argentina, [5]Laboratoire d'Océanographie de Villefranche (LOV), Sorbonne Université/CNRS, Villefranche-sur-Mer, France, [6]European Space Agency (ESA), Frascati, Italy, [7]Tartu Observatory, University of Tartu (UT), Tartu, Estonia, [8]Deutsches GeoForschungsZentrum (GFZ), Potsdam, Germany, [9]University of Maryland Baltimore County (UMBC), Baltimore, MD, United States

Satellites are now routinely used for measuring water and land surface reflectance and hence environmentally relevant parameters such as aquatic chlorophyll *a* concentration and terrestrial vegetation indices. For each satellite mission, radiometric validation is needed at bottom of atmosphere for all spectral bands and covering all typical conditions where the satellite data will be used. Existing networks such as AERONET-OC for water and RadCalNet for land provide vital information for validation, but (AERONET-OC) do not cover all spectral bands or (RadCalNet) do not cover all surface types and viewing angles. In this Perspective Article we discuss recent advances in instrumentation, measurement methods and uncertainty estimation in the field of optical radiometry and put forward the viewpoint that a new network of automated hyperspectral radiometers is needed for multi-mission radiometric validation of water and land surface reflectance. The HYPERNETS federated network concept is described, providing a context for research papers on specific aspects of the network. This network is unique in its common approach to both land and water surfaces. The common aspects and the differences between land and water measurements are explained. Based on early enthusiasm for HYPERNETS data from validation-oriented workshops, it is our viewpoint that this new network of automated hyperspectral radiometers will be useful for multi-mission radiometric validation of water and multi-angle land surface reflectance. The HYPERNETS network has strong synergy with other measurement networks (AERONET,

AERONET-OC, RadCalNet, FLUXNET, ICOS, skycam, etc.) and with optional supplementary measurements, e.g., water turbidity and fluorescence, land surface temperature and soil moisture, etc.

KEYWORDS

satellite validation, hyperspectral reflectance, *in situ* measurements, automated network, radiometry

1 Introduction

1.1 Motivation

Satellites are now routinely used for measuring water and land surface reflectance and hence parameters such as aquatic chlorophyll *a* concentration and terrestrial vegetation indices. Since these remotely sensed parameters may be significantly affected by errors in top of atmosphere calibration and atmospheric correction, radiometric validation at the bottom of atmosphere is needed for quality control, ensuring that data reaching end-users are of known quality and that quality issues are reported to satellite data providers for improvement.

For each satellite mission, radiometric validation is needed for all spectral bands and covering all typical conditions where the satellite data will be used, including various water/land types, sun angles, atmospheric conditions (aerosols, absorbing gases, scattered and semi-transparent clouds), surface altitudes, spatial heterogeneity, etc.

1.2 User needs

The users of *in situ* measurements of water and land surface reflectance are identified as:

- Satellite operators, including international and national space agencies and "Newspace" commercial data providers—see Supplementary Material S1 for a list of target missions.
- Developers of atmospheric correction algorithms and software.
- Environmental agencies and scientists using *in situ* measurements to monitor water or land surface properties.

The user requirements for *in situ* measurements of water and land surface reflectance are identified as (Goyens et al., 2018):

- Hyperspectral coverage 380–1020 nm for water and minimally 380–1700 nm but preferably 380–2500 nm for land.
- Spectral resolution of 5 nm Full Width at Half Maximum (FWHM) for 380–1020 nm and 10 nm FWHM for 1020–1700 nm.
- Measurements every 30 min during daylight.
- Data provided publicly in Near Real Time (e.g., <1 day) by web service.
- Fiducial Reference Measurement (FRM) quality, including full estimate of uncertainty.
- Full nadir/azimuth coverage up to 60° nadir for land surface reflectance.

In addition to the reflectance measurements, users request pictures from cameras and information on aerosols and direct/diffuse irradiance ratio.

Atmospheric applications are specifically excluded here because aerosol parameters are already well-measured by AERONET (Holben et al., 1998) and because measurement of absorbing atmospheric gases (Verhoelst et al., 2021) generally requires much finer spectral resolution, e.g., sub-nanometre.

1.3 Precursor networks

The user needs of Section 1.2 are partially met by the existing networks, AERONET-OC for water and RadCalNet for land.

The AERONET-OC 12 band instrument (Zibordi et al., 2021) matches well the spectral bands of "ocean colour" sensors, but less well the wide bands of "land" sensors such as Sentinel-2/MSI, Landsat-8/9, Planet Superdoves, etc.—see Figure 1. Validation of the new generation of hyperspectral sensors by multispectral ground measurements is also insufficient (Giardino et al., 2020; Braga et al., 2022). While aerosol correction can be assessed by a limited set of multispectral bands, the new potential of hyperspectral satellite data, e.g., spectral curvature/derivative algorithms (Dierssen et al., 2020; Lavigne et al., 2022), will require hyperspectral *in situ* data.

RadCalNet (Bouvet et al., 2019) is designed to provide hyperspectral radiance at top of atmosphere for the purpose of satellite vicarious (in-flight) calibration. RadCalNet sites are located in optimal locations with horizontal homogeneity of the surface and clear, stable atmosphere and do not cover the more difficult surfaces required for a complete sensor validation plan. Some sites do not use hyperspectral instruments. RadCalNet provides only nadir-viewing data.

While both AERONET-OC and RadCalNet must continue to provide vital data for calibration and validation of satellite missions, **it is our viewpoint that a new *in situ* measurement network is needed to fully satisfy the user requirements for multi-mission water and land surface reflectance validation**. This was the motivation for setting up HYPERNETS, a federated network of sites running autonomous hyperspectral radiometer systems to provide validation data at all spectral bands in the range 380–1700 nm for all satellite missions with a surface reflectance product.

1.4 The difference between land and water

The land and water optical remote sensing communities have traditionally operated very separately with different data processing chains, atmospheric correction algorithms, etc. This separation is driven by the different user groups and data products, and by different physical processes, particularly those relevant for atmospheric correction.

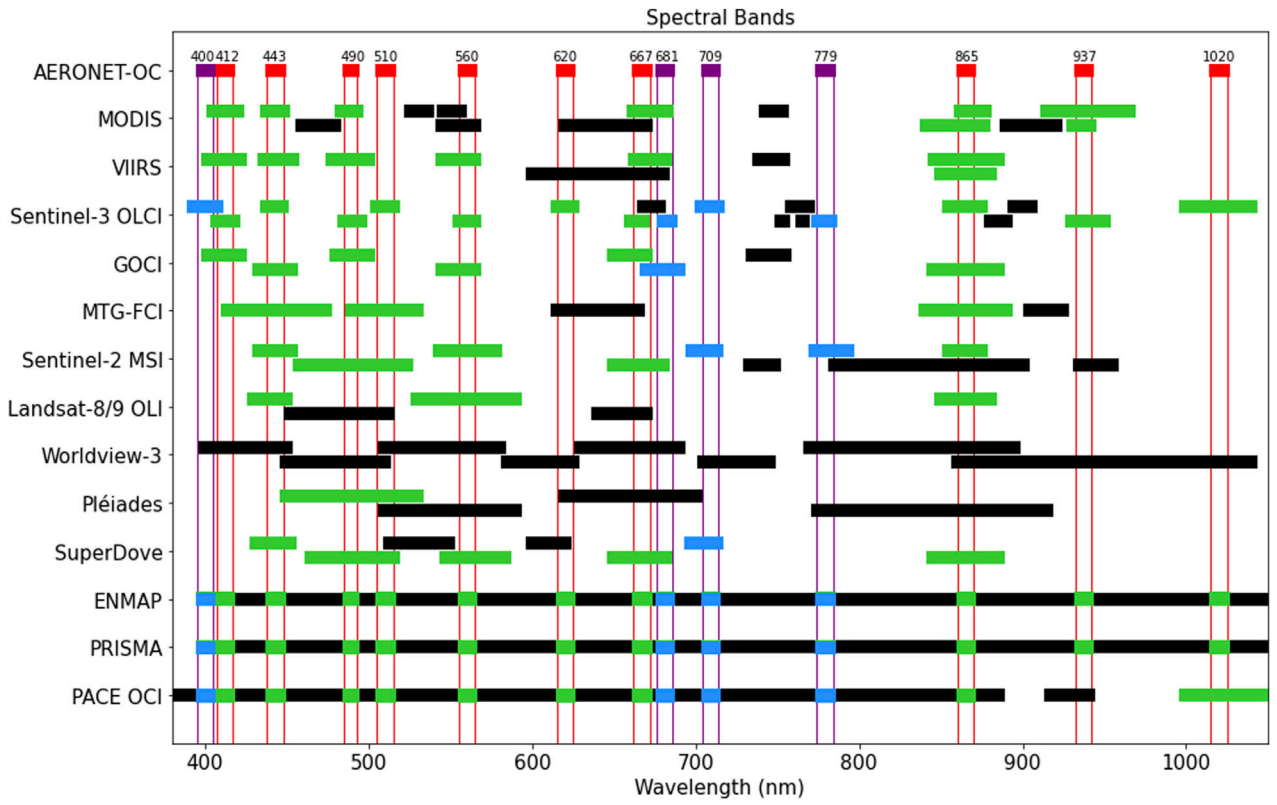


FIGURE 1
Spectral bands of typical satellite missions to be validated compared with (top row) the CIMEL CE318TV-12 used in AERONET-OC. The two versions of the CE318TV-12 instrument are displayed with common bands in red and optional bands in violet. The variant CE318TV-12-LC ("lake colour") has bands 681 nm and 709 nm, while the CE318TV-12-OC ("ocean colour") variant CE318TV-12-OC has bands 400 nm and 779 nm. The CE318-TU12 instrument used for multispectral land surface reflectance measurements (Meygret et al., 2011) has a different set of 9 or 12 spectral bands.[1] Satellite bands with central wavelength falling inside a CE318TV-12 common/optional band are shown in green/blue respectively and those falling outside such bands are shown in black.

Water is generally much darker than land, exacerbating challenges for aerosol correction, adjacency effect correction, vicarious calibration, absorbing aerosol detection/correction, etc. Removal of air-water interface reflection is an additional challenge, particularly as regards sunglint removal for near nadir-viewing sensors. However, there are algorithms that can apply over both water and land surfaces, e.g., iCOR (Keukelaere et al., 2018) and ACOLITE/DSF (Vanhellemont, 2019).

Land surfaces may have higher spatial heterogeneity at short length scales (<30 m) and high angular but low temporal variability of upwelling radiance.

Despite these differences, the HYPERNETS consortium decided to develop instrumentation and processing for both water and land surfaces, benefitting from the economy of scale for radiometer, host system and processor development and offering a larger customer base for the new radiometer. The commonality in data processing and distribution for the land and water network will also facilitate validation of land and water surface reflectance simultaneously and open up new opportunities to study complex interactions between water and land environments.

1.5 Scope and overview of this Perspective Article

In this Perspective Article we discuss recent advances in optical radiometry and describe the HYPERNETS federated network concept (Figure 2). HYPERNETS integrates two branches for the different surface types: WATERHYPERNET (Ruddick et al., 2024) and LANDHYPERNET (De Vis et al., 2024a). Both branches use the newly developed HYPSTAR® radiometer system, which is the main focus of this article. The PANTHYR/TriOS radiometer system (Vansteenwegen et al., 2019) is also included in WATERHYPERNET and in the summary of results of Section 3.

2 Optical radiometry state of the art and HYPERNETS network design

2.1 Measurement method

For water reflectance measurements, automated above water radiometry (Zibordi et al., 2009) has proven to be cost-effective. HYPERNETS adopts the same approach as AERONET-OC for measurement of water-leaving radiance, L_w, but makes direct measurement of downwelling irradiance, E_d, using a flat diffuse

1 https://www.cimel.fr/solutions/ce318-t/#specifications

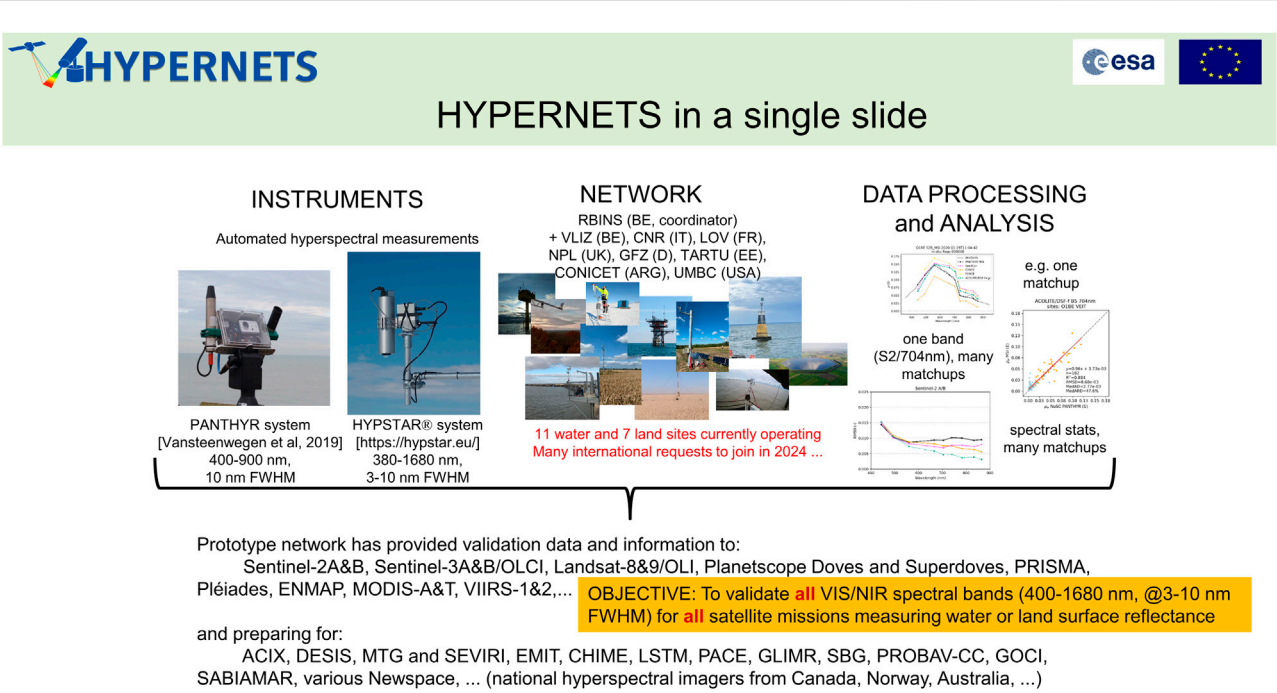


FIGURE 2
Overall concept of the HYPERNETS network.

collector with approximately cosine angular response instead of sun photometry—see Ruddick et al. (2024).

For land surface reflectance measurements, protocols for automated radiometry are less mature. Most measurements are supervised and use a reflectance based method with a reflectance standard as a reference (Slater et al., 1987). An autonomous multiangle surface reflectance protocol was developed by Meygret et al. (2011) for measurement of Hemispherical Conical Reflectance Factor (HCRF) with a multispectral instrument. This protocol could not be implemented by HYPERNETS due to the hyperspectral measurement time, power and data transfer requirements. HYPERNETS developed a sequential acquisition protocol (De Vis et al., 2024b), measuring E_d before and after a series of upwelling radiance, L_u, measurements at nadir and azimuth angles corresponding to typical viewing geometries of polar-orbiting satellites—see Supplementary Material S3.

While the basic water and land reflectance measurement scenarios are sufficient, complementary measurements can be added, e.g., sunglint pointing for estimation of wave slope statistics (Goyens and Ruddick, 2023); direct sun radiance measurement, potentially supplemented with various sky radiance measurements, for comparison with the direct E_d measurement; a more complete measurement of land surface HCRF, etc.

2.2 Hyperspectral radiometers

The user requirements of Section 1.2, particularly the spectral requirements and the need for a pointable radiometer could not be met by any Commercial Off The Shelf (COTS) radiometer—see Kuusk et al. (2024). The HYPERNETS consortium therefore designed a new hyperspectral radiometer, the HYPSTAR®. This innovative design (Kuusk et al., 2024) is based on spectrometers covering 380–1020 nm at 3 nm FWHM with 0.5 nm sampling interval and (land units only) 1020–1680 nm at 10 nm FWHM and 3 nm sampling interval. The spectrometers are multiplexed between alternative optical paths, one for radiance and one for irradiance, reducing cost and minimising impact of thermal sensitivity and some absolute calibration uncertainties on reflectance products. One innovative feature of the HYPSTAR® radiometer design is the integration of an external LED source, which can be used at night for monitoring the long term stability of radiometric calibration. Another useful feature, first suggested in the OSPREY design (Hooker et al., 2012), is an embedded RGB camera. This camera has proven extremely useful for troubleshooting equipment failures and strange radiometric data—at some sites it is not unusual to see a bird sitting on the radiometer, partially obscuring the field of view!

2.3 Autonomous system

The HYPSTAR® system integrates the radiometer with a pointing system, a PC, a power source and data transmission hardware and associated software/firmware (Doxaran et al., 2024; Kuusk et al., 2024).

For autonomous systems deployed with minimal maintenance requirements, and in potentially hostile environments (hot, cold, wet, salty), remote connection capabilities should be ensured and all components must be selected for reliability. HYPSTAR® has only two moving parts, the radiometer multiplexer and the pointing system.

Over the last decade, technological improvements and mass COTS production have been significant for: pointing systems (now ubiquitous for security cameras), data transmission (4G), photovoltaic power and solid state drives.

The HYPSTAR® system (Kuusk et al., 2024), integrates a Will-Burt Bowler RX pointing system with a Cincoze rugged PC and a custom-made board integrating relays for efficient power management. Components were selected for an operating temperature range of −25°C to +45°C and housings are rated with Ingress Protection IP66, IP67 or IP68.

Power supply is site-specific, preferably grid power, but otherwise photovoltaic or wind power with associated battery and controller. Data transmission is generally by cellular or cabled internet, but may be manual for some locations, e.g., Gobabeb and Antarctica.

System components are attached to mounting structures, which vary from large platforms to standalone masts. The choice of platform and mounting location is important for data quality and should be made to limit optical perturbations of the radiometric targets by the structure and maximise acceptable viewing angles—see Section 3.3 of Ruddick et al. (2024).

2.4 Validation sites

A validation network should include sites covering a wide range of surface types and atmospheric conditions, in particular including the "difficult cases" where atmospheric correction may fail or produce poor results.

Water sites should cover a range of turbidity, phytoplankton biomass and species, Coloured Dissolved Organic Matter absorption, sun zenith angle, clouds, aerosols, etc. Sites at high altitude and with strong adjacency effects are also needed.

Land sites should cover a range of substrates and vegetation including non-vegetated, snow/ice, grassland, agricultural with various crops and practices, forest with various species, age and canopy cover, etc.

When comparing satellite and matchup *in situ* measurements it is necessary to consider additional uncertainties associated with the different wavelength, space, time and angular coordinates.

A key question for each validation site is the spatial heterogeneity. Each validation site should be characterised in terms of spatial variability to give the additional uncertainty involved in a matchup comparison as function of length scale, e.g., Dogliotti et al. (2015), Dogliotti et al. (2024), Doxaran et al. (2024) for water and Morris et al. (2024) for land.

Temporal variability at a validation site, also of importance in satellite/*in situ* matchups, can be characterised from time series of the *in situ* radiometer measurements (Doxaran et al., 2024).

For land sites, the angular variability of upwelling radiance is very high for many surface types, particularly for vegetated surfaces and shadowing surfaces. The BRDF needs to be modelled for each site (Schunke et al., 2023), using measurements at multiple sun and viewing zenith and azimuth angles. The separation of spatial and angular variability may be complex, but should be feasible if data are collected over sufficient time and for multiple sun and viewing angles.

The list of currently operated HYPERNETS validation sites is provided in Supplementary Material S2.

2.5 Data processing and quality control

Network data processing and quality control (De Vis et al., 2024a) must be centralised and automated to ensure efficient operations and reliability of data provided to users. Measurements are acquired at the validation sites every 15–30 min during daylight. Raw data and metadata are transmitted to computer servers, one for water and one for land processing.

Identical processing is applied for water and land sites up to the level of calibrated radiances and irradiances with associated uncertainties. The derivation of water and land surface reflectance then uses different measurement functions, but within a common software framework. This integration of land and water processing facilitates joint use of quality control tests, e.g., comparison of E_d with a clear sky model to check for clouds and obstructions (including birds).

2.6 Uncertainty estimation

An important feature of the HYPERNETS processor, of relevance to Fiducial Reference Measurements (Donlon and Zibordi, 2014; Goryl et al., 2023), is the propagation of measurement uncertainties from their sources to the final reflectance data using a Monte Carlo approach (International Standards Organisation ISO, 2008). The implementation, using the open source CoMet toolkit,[2] preserves temporal and spectral uncertainty covariance. The covariance information (De Vis et al., 2024b) provided with the output reflectance ensures that the uncertainty of downstream products, such as Normalised Difference Vegetation Index (NDVI) or aquatic chlorophyll *a* concentration, can be correctly evaluated.

2.7 Data distribution and network user support

For optimal user uptake, data from the network will be publicly distributed through an interactive user interface, and an Application Programming Interface (API). Data are provided in NetCDF format with relevant metadata, following the INSPIRE directive, and are covered by a CC-BY-ND open data licence.

HYPERNETS provides support for both site operators and data users. Site operators receive installation and troubleshooting advice, share experiences on site operations and data exploitation in scientific discussions and receive radiometer calibration and characterisation services.

A common request from space agencies is for a list of validation site coordinates to be used in prioritising acquisitions, e.g., during a

2 https://www.comet-toolkit.org/

commissioning phase. The coordinates of HYPERNETS sites are provided in Supplementary Material S2.

3 Summary of demonstration results

In Supplementary Material S4, findings from exploitation of early prototype HYPERNETS data can be found. This includes both the new HYPSTAR® system and the PANTHYR system (Vansteenwegen et al., 2019), which is based on the mature COTS TriOS/RAMSES radiometer.

So far, PANTHYR (Vanhellemont, 2020; Vanhellemont and Ruddick, 2021; Braga et al., 2022; Vanhellemont, 2023; Ruddick et al., 2024) and HYPSTAR® (Dogliotti et al., 2024; Doxaran et al., 2024; Gonzalez Vilas et al., 2024; Ruddick et al., 2024) data have been used for validation of water reflectance from Landsat-8&9/OLI, Sentinel-2/MSI, Sentinel-3/OLCI, PRISMA, Aqua/MODIS, SNPP&JPSS1/VIIRS, and the constellation of PlanetScope Dove and Superdove satellite data, generally comparing different atmospheric correction algorithms.

HYPSTAR® data have been used for validation of land surface reflectance from Sentinel-2/MSI and Landsat-8&9/OLI for a deciduous forest site (Morris et al., 2024).

HYPERNETS data have also been used for monitoring of water quality and phytoplankton species (Goyens et al., 2022; Ruddick et al., 2024).

Finally, the HYPERNETS instrument system and data processing is also relevant for vicarious calibration of satellites at top of atmosphere if the deployment site is sufficiently spatially homogeneous and well-characterised. E.g., De Vis et al. (2024a) demonstrates use of the HYPSTAR® at Gobabeb (Namibia) and the Princess Elisabeth Antarctica base for vicarious calibration of Sentinel-2, Landsat-9 and PRISMA. The HYPSTAR®/Gobabeb site (Sinclair et al., 2023) has been submitted to the official application process to become a RadCalNet site.

4 Discussion

We suggest that a new network of automated hyperspectral radiometers is needed for multi-mission radiometric validation of water and land surface reflectance. The corresponding HYPERNETS federated network, now at the stage of demonstrated prototype, has been described.

A new hyperspectral radiometer has been designed, manufactured and tested. This radiometer provides high quality data according to user needs and will be commercialised by the new company RSware OÜ (https://hypstar.eu).

A host system, built from both COTS and customised components has been assembled and tested with improvements in reliability (uptime) over the successive prototype versions.

The new hyperspectral radiometer and associated host system have been deployed at 22 sites, of which 10 water and 8 land sites are expected to continue in 2024. The network is expected to expand slowly in 2024–26 by addition of new international partners.

Data are transmitted from validation sites to central servers, and are processed daily using automated routines. Data distribution will be public from web data portals. Pending completion of these data portals, prototype "beta-release" datasets have been publicly distributed via www.zenodo.org—see Supplementary Material S5.

Measurement uncertainties are propagated in data processing using Monte Carlo modelling. The current status includes uncertainties from replicate noise and radiometric calibration. Measurement uncertainties from the following processes are in preparation for future implementation: a) radiometer thermal sensitivity, straylight and angular response, b) mounting platform optical perturbations (shading/reflection) and, for water, c) air-water interface reflected light. Additional uncertainties relating to space and time differences when using HYPERNETS data for satellite validation are also being addressed (Dogliotti et al., 2024; Doxaran et al., 2024; Morris et al., 2024).

While HYPERNETS is designed as a standalone single measurand network there is a strong interest in collaboration with other networks. Some HYPERNETS sites are already co-located with sites from the AERONET, AERONET-OC, RadCalNet, FLUXNET, IR-ILICO, ICOS, ROMA[3] and skycam networks, and co-location of one or more sites with the PANDONIA[4] network is foreseen. The synergy between co-located networks provides both economic and scientific benefits: site infrastructure and maintenance visits can be combined for multiple instruments providing an economy of scale; data from HYPERNETS can be intercompared directly with similar measurands using different methods/instruments from other networks, e.g., surface reflectance from AERONET-OC and RadCalNet; HYPERNETS could benefit from information on aerosol properties from AERONET and atmospheric absorbing gases from PANDONIA[4]. HYPERNETS sites can be supplemented by other measurements, e.g., water turbidity and fluorescence, land surface temperature and soil moisture, etc.

Based on early enthusiasm from data users, HYPERNETS seems useful for radiometric validation of water and multi-angle land surface reflectance. The cost effectiveness of the approach is clearly demonstrated, e.g., validation of Landsat-8&9/OLI, Sentinel-2/MSI, Sentinel-3/OLCI, the PlanetScope/SuperDoves constellation, SNPP&JPSS1/VIIRS, AQUA/MODIS and PRISMA satellite data at the La Plata Estuary site (Dogliotti et al., 2024). Exploitation of HYPERNETS data for other applications, e.g., satellite vicarious calibration (De Vis et al., 2024b) and water quality monitoring (Goyens et al., 2022), is also promising.

Data availability statement

The original contributions presented in the study are included in the article/Supplementary Material, further inquiries can be directed to the corresponding author.

3 https://aeronet.gsfc.nasa.gov/; https://aeronet.gsfc.nasa.gov/new_web/ocean_color.html; https://ceos.org/home-2/wgcv-radcalnet/; https://fluxnet.org/; https://www.ir-ilico.fr/; https://www.icos-cp.eu/; https://roma.conicet.gov.ar/

4 https://www.pandonia-global-network.org/

Author contributions

KR: Conceptualization, Funding acquisition, Methodology, Project administration, Writing–original draft, Writing–review and editing. AB: Conceptualization, Funding acquisition, Methodology, Project administration, Writing–review and editing. VB: Conceptualization, Funding acquisition, Methodology, Project administration, Writing–review and editing. PD: Conceptualization, Methodology, Writing–review and editing. AD: Conceptualization, Funding acquisition, Methodology, Project administration, Writing–review and editing. DD: Conceptualization, Funding acquisition, Methodology, Project administration, Writing–review and editing. PG: Conceptualization, Funding acquisition, Methodology, Project administration, Writing–review and editing. CG: Conceptualization, Funding acquisition, Methodology, Project administration, Writing–review and editing. JK: Conceptualization, Funding acquisition, Methodology, Project administration, Writing–review and editing. DS: Funding acquisition, Methodology, Project administration, Writing–review and editing. KT: Funding acquisition, Methodology, Project administration, Writing–review and editing. QV: Conceptualization, Methodology, Writing–review and editing.

Funding

The authors declare that financial support was received for the research, authorship, and/or publication of this article. This work was carried out in the context of: the H2020/HYPERNETS project funded by the European Union's Horizon 2020 research and innovation programme (Grant agreement n° 775983), the HYPERNET-POP project funded by the European Space Agency (contract n° 4000139081/22/I-EF), by the PICT-2020/2636 project funded by the ANPCyT, and by NASA grant 80NSSC24K0479 in support of the Surface Biology and Geology mission development and a NASA grant in support of Plankton, Aerosol, Cloud, ocean Ecosystem (PACE) Mission Validation.

Acknowledgments

Over the last 6 years we have benefited from input, discussions and support from many colleagues. We thank all colleagues from the H2020/HYPERNETS and FRM4SOC projects as well as external experts and project advisers including particularly: Giuseppe Zibordi, Nigel Fox, Craig Donlon, Tania Casal, Erwin Goor, Miroslaw Darecki, Ewa Kwiatkowska, Juan Gossn, Kevin Alonso Gonzalez, Fabrizio Niro and Dimitry Van der Zande. Acknowledgement of these individuals does not constitute endorsement of or responsibility for the content of this work but is merely an expression of thanks for their suggestions and support. The Escuela Naval Militar (EsNM) and Servicio de Hidrografia Naval (SHN) are thanked for permission and access to the LPAR platform and installation support.

Conflict of interest

Co-authors from University of Tartu and Sorbonne University may benefit from future commercialisation of the HYPSTAR® radiometer and system. One author (PG) represents a funding agency. All other authors are likely to receive future research funding for HYPERNETS-related data acquisition and/or exploitation. The authors declare that these interests do not affect the statements and findings of this paper, which has been written according to the normal scientific ethics and values of the academic community.

The remaining authors declare that the research was conducted in the absence of any commercial or financial relationships that could be construed as a potential conflict of interest.

The authors declared that they were an editorial board member of Frontiers, at the time of submission. This had no impact on the peer review process and the final decision.

Publisher's note

All claims expressed in this article are solely those of the authors and do not necessarily represent those of their affiliated organizations, or those of the publisher, the editors and the reviewers. Any product that may be evaluated in this article, or claim that may be made by its manufacturer, is not guaranteed or endorsed by the publisher.

Supplementary material

The Supplementary Material for this article can be found online at: https://www.frontiersin.org/articles/10.3389/frsen.2024.1372085/full#supplementary-material

References

Bouvet, M., Thome, K., Berthelot, B., Bialek, A., Czapla-Myers, J., Fox, N. P., et al. (2019). RadCalNet: a radiometric calibration network for earth observing imagers operating in the visible to shortwave infrared spectral range. *Remote Sens.* 11 (20), 2401. doi:10.3390/rs11202401

Braga, F., Fabbretto, A., Vanhellemont, Q., Bresciani, M., Giardino, C., Scarpa, G. M., et al. (2022). Assessment of PRISMA water reflectance using autonomous hyperspectral radiometry. *ISPRS J. Photogrammetry Remote Sens.* 192, 99–114. doi:10.1016/j.isprsjprs.2022.08.009

De Vis, P., Goyens, C., Hunt, S., Vanhellemont, Q., Ruddick, K. G., and Bialek, A. (2024a). Generating hyperspectral reference measurements for surface reflectance from the LANDHYPERNET and WATERHYPERNET networks. *Front. Remote Sens.* doi:10.3389/frsen.2024.1347230

De Vis, P., Howes, A., Vanhellemont, Q., Bialek, A., Morris, H., Sinclair, M., et al. (2024b). Feasibility of satellite vicarious calibration using HYPERNETS surface reflectances from Gobabeb and princess Elisabeth Antarctica sites. *Front. Remote Sens.* (submitted).

Dierssen, H., Bracher, A., Brando, V., Loisel, H., and Ruddick, K. (2020). Data needs for hyperspectral detection of algal diversity across the globe. *Oceanography* 33 (1), 74–79. doi:10.5670/oceanog.2020.111

Dogliotti, A. I., Gossn, J., Vanhellemont, Q., and Ruddick, K. G. (2015). *Evaluation of two sites for ocean color validation in the Turbid waters of the rio de La Plata (Argentina) (2015) Proceedings of the Sentinel-3 for Science Workshop held in Venice-Lido, Italy, 2-5 June 2015, ESA Special Publication SP-734, Paris, France.*

Dogliotti, A. I., Piegari, E., Rubinstein, L., Perna, P., and Ruddick, K. G. (2024). Using the automated HYPERNETS hyperspectral system for multimission Satellite Ocean Colour validation in the Río de La Plata, accounting for different spatial resolutions. *Front. Remote Sens.* doi:10.3389/frsen.2024.1354662

Donlon, C. J., and Zibordi, G. (2014). "*In situ* optical radiometry," in *Optical radiometry for ocean climate measurements* (Amsterdam, Netherlands: Elsevier), 245–246.

Doxaran, D., Elkilani, B., Corizzi, A., and Goyens, C. (2024). Validation of satellite-derived water-leaving reflectance in contrasted French coastal waters based on HYPERNETS field measurements. *Front. Remote Sens.* 4, 1290110. doi:10.3389/frsen.2023.1290110

Giardino, C., Bresciani, M., Braga, F., Fabbretto, A., Ghirardi, N., Pepe, M., et al. (2020). First evaluation of PRISMA level 1 data for water applications. *Sensors* 20, 4553. doi:10.3390/s20164553

Gonzalez Vilas, L., Brando, V. E., Concha, J. A., Goyens, C., Dogliotti, A. I., Doxaran, D., et al. (2024). Validation of satellite water products based on HYPERNETS *in situ* data using a match-up Database file (MDB) structure. *Front. Remote Sens.* 5, 1330317. doi:10.3389/frsen.2024.1330317

Goryl, P., Fox, N., Donlon, C., and Castracane, P. (2023). Fiducial reference measurements (FRMs): what are they? *Remote Sens.* 15 (20), 5017. doi:10.3390/rs15205017

Goyens, C., Lavigne, H., Dille, A., and Vervaeren, H. (2022). Using hyperspectral remote sensing to monitor water quality in drinking water reservoirs. *Remote Sens.* 14 (21), 5607. doi:10.3390/rs14215607

Goyens, C., and Ruddick, K. (2023). Improving the standard protocol for above-water reflectance measurements: 1. Estimating effective wind speed from angular variation of sunglint. *Appl. Opt.* 62, 2442. doi:10.1364/AO.481787

Goyens, C., Ruddick, K., and Kuusk, J. (2018). "Spectral requirements for the development of a new hyperspectral radiometer integrated in automated networks - the HYPERNETS sensor," in 2018 9th Workshop on Hyperspectral Image and Signal Processing: Evolution in Remote Sensing (WHISPERS), Amsterdam, Netherlands, September, 2018, 1–5. doi:10.1109/WHISPERS.2018.8747259

Holben, B. N., Eck, T. F., Slutsker, I., Tanré, D., Buis, J. P., Setzer, A., et al. (1998). AERONET—a federated instrument network and data archive for aerosol characterization. *Remote Sens. Environ.* 66 (1), 1–16. doi:10.1016/S0034-4257(98)00031-5

Hooker, S. B., Bernhard, G., Morrow, J. H., Booth, C. R., Comer, T., Lind, R. N., et al. (2012). "Optical sensors for planetary radiant energy (OSPREY): calibration and validation of current and next-generation NASA missions," in *NASA technical memorandum 2012–215872* (Greenbelt, MD, USA: NASA).

International Standards Organisation (ISO) (2008). *Evaluation of measurement data - guide to the expression of uncertainty in measurement*. JCGM 100:2008. Geneva, Switzerland: International Standards Organisation ISO.

Keukelaere, L. D., Sterckx, S., Adriaensen, S., Knaeps, E., Reusen, I., Giardino, C., et al. (2018). Atmospheric correction of Landsat-8/OLI and Sentinel-2/MSI data using iCOR algorithm: validation for coastal and inland waters. *Eur. J. Remote Sens.* 51 (1), 525–542. doi:10.1080/22797254.2018.1457937

Kuusk, J., Corizzi, A., Doxaran, D., Duong, K., Flight, K., Kivastik, J., et al. (2024). HYPSTAR: a hyperspectral pointable system for terrestrial and aquatic radiometry. *Front. Remote Sens.* (submitted).

Lavigne, H., Ruddick, K., and Vanhellemont, Q. (2022). Monitoring of high biomass *Phaeocystis globosa* blooms in the Southern North Sea by *in situ* and future spaceborne hyperspectral radiometry. *Remote Sens. Environ.* 282, 113270. doi:10.1016/j.rse.2022.113270

Meygret, A. R., Santer, P., and Berthelot, B. (2011). ROSAS: a robotic station for atmosphere and surface characterization dedicated to on-orbit calibration. in *Proceedings of SPIE - the international society for optical engineering* (San Diego, California, USA: SPIE). doi:10.1117/12.892759

Morris, H., Sinclair, M., De Vis, P., and Białek, A. (2024). Utilising LANDHYPERNETS data products over a deciduous broadleaf forest to validate Sentinel-2 and Landsat surface reflectance products. *Front. Remote Sens.*, doi:10.3389/frsen.2024.1322760

Ruddick, K. G., Brando, V. E., Corizzi, A., Dogliotti, A. I., Doxaran, D., Goyens, C., et al. (2024). WATERHYPERNET: a prototype network of automated *in situ* measurements of hyperspectral water reflectance for satellite validation and water quality monitoring. *Front. Remote Sens.* (submitted).

Schunke, S., Leroy, V., and Govaerts, Y. (2023). Retrieving BRDFs from UAV-based radiometers for fiducial reference measurements: caveats and recommendations. *Front. Remote Sens.* 4. doi:10.3389/frsen.2023.1285800

Sinclair, M., Bialek, A., Vis, P. D., and Bouvet, M. (2023). "HYPERNETS land network: HYPSTAR®-XR deployment and validation in Namibia, Africa," in IGARSS 2023 - 2023 IEEE International Geoscience and Remote Sensing Symposium, Pasadena, CA, USA, July, 2023, 4625–4627. doi:10.1109/IGARSS52108.2023.10282079

Slater, P. N., Biggar, S. F., Holm, R. G., Jackson, R. D., Mao, Y., Moran, M. S., et al. (1987). Reflectance- and radiance-based methods for the in-flight absolute calibration of multispectral sensors. *Remote Sens. Environ.* 22 (1), 11–37. doi:10.1016/0034-4257(87)90026-5

Vanhellemont, Q. (2019). Adaptation of the Dark Spectrum fitting atmospheric correction for aquatic applications of the Landsat and sentinel-2 archives. *Remote Sens. Environ.* 225, 175–192. doi:10.1016/j.rse.2019.03.010

Vanhellemont, Q. (2020). Sensitivity Analysis of the Dark Spectrum fitting atmospheric correction for metre- and decametre-scale satellite imagery using autonomous hyperspectral radiometry. *Opt. Express* 28 (20), 29948–29965. doi:10.1364/OE.397456

Vanhellemont, Q. (2023). Evaluation of eight band SuperDove imagery for aquatic applications. *Opt. Express* 31 (9), 13851–13874. doi:10.1364/OE.483418

Vanhellemont, Q., and Ruddick, K. (2021). Atmospheric correction of Sentinel-3/OLCI data for mapping of suspended particulate matter and chlorophyll-a concentration in Belgian turbid coastal waters. *Remote Sens. Environ.* 256, 112284. doi:10.1016/j.rse.2021.112284

Vansteenwegen, D., Ruddick, K., Cattrijsse, A., Vanhellemont, Q., and Beck, M. (2019). The pan-and-tilt hyperspectral radiometer system (PANTHYR) for autonomous satellite validation measurements – prototype design and testing. *Remote Sens.* 11 (11), 1360. doi:10.3390/rs11111360

Verhoelst, T., Compernolle, S., Pinardi, G., Lambert, J.-C., Eskes, H. J., Eichmann, K.-U., et al. (2021). Ground-based validation of the Copernicus Sentinel-5P TROPOMI NO_2 measurements with the NDACC ZSL-DOAS, MAX-DOAS and pandonia global networks. *Atmos. Meas. Tech.* 14 (1), 481–510. doi:10.5194/amt-14-481-2021

Zibordi, G., Holben, B., Slutsker, I., Giles, D., D'Alimonte, D., Mélin, F., et al. (2009). AERONET-OC: a network for the validation of ocean color primary products. *J. Atmos. Ocean. Technol.* 26, 1634–1651. doi:10.1175/2009jtecho654.1

Zibordi, G., Holben, B. N., Talone, M., D'Alimonte, D., Slutsker, I., Giles, D. M., et al. (2021). Advances in the ocean color component of the aerosol robotic network (AERONET-OC). *J. Atmos. Ocean. Technol.* 38 (4), 725–746. doi:10.1175/JTECH-D-20-0085.1

frontiers | Frontiers in Remote Sensing

TYPE Original Research
PUBLISHED 10 April 2024
DOI 10.3389/frsen.2024.1320454

Check for updates

OPEN ACCESS

EDITED BY
Sawaid Abbas,
University of the Punjab, Pakistan

REVIEWED BY
Dingtian Yang,
Chinese Academy of Sciences (CAS), China
B. Carol Johnson,
National Institute of Standards and Technology (NIST), United States

*CORRESPONDENCE
Viktor Vabson,
viktor.vabson@ut.ee

RECEIVED 12 October 2023
ACCEPTED 21 March 2024
PUBLISHED 10 April 2024

CITATION
Vabson V, Ansko I, Duong K, Vendt R, Kuusk J, Ruddick K, Bialek A, Tilstone GH, Gossn JI and Kwiatkowska E (2024), Complete characterization of ocean color radiometers. *Front. Remote Sens.* 5:1320454. doi: 10.3389/frsen.2024.1320454

COPYRIGHT
© 2024 Vabson, Ansko, Duong, Vendt, Kuusk, Ruddick, Bialek, Tilstone, Gossn and Kwiatkowska. This is an open-access article distributed under the terms of the Creative Commons Attribution License (CC BY). The use, distribution or reproduction in other forums is permitted, provided the original author(s) and the copyright owner(s) are credited and that the original publication in this journal is cited, in accordance with accepted academic practice. No use, distribution or reproduction is permitted which does not comply with these terms.

Complete characterization of ocean color radiometers

Viktor Vabson[1]*, Ilmar Ansko[1], Kim Duong[1], Riho Vendt[1], Joel Kuusk[1], Kevin Ruddick[2], Agnieszka Bialek[3], Gavin H. Tilstone[4], Juan Ignacio Gossn[5] and Ewa Kwiatkowska[5]

[1]Tartu Observatory, University of Tartu, Tartu, Estonia, [2]Royal Belgian Institute of Natural Sciences, Brussels, Belgium, [3]National Physical Laboratory, Climate and Earth Observation Group, Teddington, United Kingdom, [4]PML—Plymouth Marine Laboratory, Plymouth, United Kingdom, [5]European Organisation for the Exploitation of Meteorological Satellites (EUMETSAT), Darmstadt, Germany

Verifying and validating waterleaving radiance measurements from space for an accurate derivation of Ocean/Water Colour biogeophysical products is based on concurrent high-quality fiducial reference measurements (FRM) carried out on the ground or water body. The FRM principles established by the Committee on Earth Observation Satellites (CEOS) recommend that *in situ* Ocean Colour radiometers (OCR) have a documented history of SI traceable calibrations including uncertainty budgets. Furthermore, there can be significant differences between calibration and use of the instruments in the field due to differences in operating temperature, angular variation of the light field (especially for irradiance sensors), the intensity of the measured radiation, and spectral variation of the target, among others. Each of these factors may interact with individual properties of the instrument when deployed in the field, and estimation of such uncertainties requires instrument characterization in addition to the absolute radiometric calibration if expanded uncertainties within $\pm$10% (k = 2) are the aim. The FRM4SOC Phase 2 project - funded by the European Commission in the frame of the Copernicus Programme and implemented by EUMETSAT - contributes to these efforts, aiming at developing an operational and sustained network of radiometric measurements of FRM quality. Within FRM4SOC-2, scientists from the Tartu Observatory (TO) of the University of Tartu performed an unprecedented batch of calibrations and characterizations on a set of 37 hyperspectral field radiometers representative of the most used OCR classes within the OC community. The calibrations and characterizations performed include the determination of radiometric responsivity, long-term stability, the accuracy of the spectral scale, non-linearity and accuracy of integration times, spectral stray light, angular response of irradiance sensors in air, dark signal, thermal sensitivity, polarization sensitivity, and signal-to-noise ratio of individual OCRs. Consistent correction of biases and extended uncertainty analysis procedures of *in situ* data obtained from different instruments and measurement models need to be clearly defined, which is the objective of this paper.

KEYWORDS

fiducial reference measurements, SI-traceability, measurement uncertainty, radiometric calibration, characterization, hyperspectral radiometers

1 Introduction

Fiducial reference measurements (FRM) provide independent ground measurement results with uncertainty estimates suitable for validation of the satellite remote sensing data products (Vendt et al., 2021). Scientists from the Tartu Observatory (TO) of the University of Tartu have lead the FRM4SOC (Fiducial Reference Measurements for Satellite Ocean Colour) project funded by the European Commision's Copernicus Programme, initially (2016–2019) launched by the European Space Agency (ESA) (Banks et al., 2020) and followed-up in a second phase (FRM4SOC-2) (2021–2023) by the European Organization for the Exploitation of Meteorological Satellites EUMETSAT ("EUMETSAT | FRM4SOC Phase-2," 2023). The necessary conditions for water remote sensing (Vendt et al., 2021) are traceability of measurements to the International System of Units (SI) (Białek et al., 2020b; BIPM, 2019) and evaluation of uncertainty of each measurement result (Białek et al., 2020a; JCGM 100:2008," 2008).

Any field radiometer used for the validation of satellite ocean color radiometry data must have a documented history of SI traceable calibrations including uncertainty statements (Mueller et al., 2003; Zibordi et al., 2019; Vabson et al., 2022). For this, regular calibration and complete characterization of OCRs is required due to non-negligible drifts observed in the responsivity of sensors, frequently observed biases of single instruments from the ideal realization of specification values, and to account for environmental factors that may affect the results. Moreover, there can be significant differences between calibration and later field use regarding operating temperature, angular variation of the light field (especially for irradiance sensors), the intensity of the measured radiation, spectral variation of the target, etc. Each of these factors may interact with individual properties of the instrument when used in the field, and estimation of uncertainties therefore requires instrument characterization in addition to the absolute radiometric calibration (Vabson et al., 2019a; Vabson et al., 2019b; Zibordi et al., 2019; Vabson et al., 2022). Characterization results describe the properties of individual radiometers. A system of two or three radiometers however, is often used for the determination of remote-sensing reflectance and/or fully normalized water-leaving radiance [see, e.g. Zibordi et al., 2019; Ruddick et al., 2019a; Ruddick et al., 2019b]. Data handling of a three-radiometer system, including uncertainty contributions, is substantially more complicated compared to that for a single radiometer. For a single radiometer, some parameters that make a significant contribution to the uncertainty budget may have almost no effect on a three-radiometer system. For evaluating specific uncertainty contributions to the total uncertainty of final measurands, a particular measurement model and a full set of relevant input quantities must be known. Besides calibration/characterization (cal/char) results, the input quantities of the measurement model include additional information, that must be acquired during field measurements.

Characterising the spectral radiation measurands associated with the OC remote sensing products (irradiance, radiance, remote-sensing reflectance, etc.) for the above-described effects allows assessing:

- steady drift and random variations of the radiometric responsivity,
- individual differences of radiometers,
- environmental conditions influencing the data.

This study focuses on the two most common OCR instrument models used for Fiducial Reference Measurements:

- TriOS RAMSES,
- Sea-Bird Scientific HyperOCR.

The selection of radiometers reflects the typical choice of instruments used for *in situ* validation of satellite-derived water reflectance ("ocean color validation"), by the marine ocean optics community. According to the above-water field measurement protocols (Mobley, 1999; Mueller et al., 2003; Ruddick et al., 2019a; Zibordi et al., 2019; Ruddick et al., 2019b) usually a system with three radiometers denoted by the combination "(2L, 1E)" is used: two radiance sensors, for upwelling (water) and downwelling (sky) radiances, respectively, and an irradiance sensor, measuring downwelling irradiance. For the RAMSES and HyperOCR this is generally achieved by three separate radiometers (Hooker and Lazin, 2000; Ruddick et al., 2006), although the measurement can also be achieved with two radiometers, one irradiance and one radiance, if the latter is mounted on a pointing system for both water- and sky-viewing (Vansteenwegen et al., 2019).

In total, 37 OCRs were calibrated and characterized in TO in the frame of FRM4SOC phase-2. In Section 2, the description of the calibrated and characterized instruments, and a short review about the measurement of parameters needed for correction of biases and for the full description of uncertainty contributions is given. Calibration and characterization results are presented in Section 3. The majority of OCRs involved in FRM4SOC-2 project were subject to a full list of characterizations as presented in (Zibordi et al., 2019). In this paper, besides the calibration results, the outcomes of only a few characterizations (angular response of irradiance sensors in air, non-linearity of radiometric response, steady-state and dynamic thermal sensitivity) are described. In Section 4, some specific problems related with correcting *in situ* results are considered. Specifically, the size of corrections may depend on measurement configuration and will be substantially different when evaluating measurements done with a single OCR compared to those done with three-radiometer systems. Discussion about the calibration and characterisation results and conclusions are presented in Section 5. Throughout the article, *above water* measurements are discussed. The calibration and characterization procedures of OCRs used at the optical laboratory of TO are the same for in air and in water instruments, except for the immersion factors which are additionally needed for the in water measurements. The terminology and nomenclature (L_u, L_d, E_d) used for the above water measurements is based on (Ruddick et al., 2019a; 2019b; Goyens and Ruddick, 2023).

2 Materials and methods

2.1 Description of radiometers subject to calibration and characterization

A list of key parameters of TriOS RAMSES and Sea-Bird Scientific HyperOCR radiometers for both irradiance E and radiance L sensors

TABLE 1 Key parameters of the radiometers.

Parameter	Unit	RAMSES		HyperOCR	
		Irradiance	Radiance	Irradiance	Radiance
Mass	kg	0.9		1.1	0.95
Length	mm	295	330	395	355
Diameter	mm	48		60(70)	60
Supply voltage	V	6. . .11		9. . .18	
Average power consumption	W	0.85		4	
Temperature range	°C	+2. . .+40		−10. . .+50	
Temperature control		without temperature stabilisation			
Field of view (full angle at half maximum in air)	°	180, hemispherical	7	180, hemispherical	6
Input aperture diameter	mm	7	15	21	20
Si photodiode array	-	CMOS logic compatible			
Active area	-	pixel pitch: 25 µm; height: 2.5 mm			
Wavelength range	nm	350. . .1000		305. . .900	
Wavelength step	nm	3.3			
Spectral bandwidth (FWHM)	nm	9.5			
Pixel count	-	256, with 16 dark covered		256	
Integration time	ms	4. . .8192			
Minimum sampling interval	s	1		0.25	
Bits per sample	-	16			
Responsivity @ 500 nm and 1 ms	$\mu W^{-1}m^2nm$	0.6	N/A	0.7	N/A
Responsivity @ 500 nm and 1 ms	$\mu W^{-1}m^2nmsr$	N/A	0.1	N/A	0.02
Internal shutter	-	NO, dark CCD pixels used		yes	
Internal temperature sensor	-	no		yes	

are given in Table 1. The information are based on documents supplied by the manufacturers of OCRs and components/modules, and on the results of on-site testing of instruments. At first, OCRs were radiometrically calibrated, then characterized according to parameters listed in Table 2, and then recalibrated. These radiometers measure radiation from the atmosphere or water in the spectral range from 350 to 900 or 1000 nm with a resolution of 10 nm. The radiometers contain a spectrometer module (Zeiss MMS-1), proprietary front-end electronics and optical input elements in a watertight housing. The housing is cylindrically symmetrical, with the optical input and electrical connector in the opposite ends of the cylinder. The housing is fabricated from stainless steel (RAMSES) or Acetron (HyperOCR). The optical axis is expected to coincide with the center of the cylinder. The wavelength scale and some other parameters are defined in the calibration files provided by the manufacturer.

2.2 Radiometric characterization

The complete calibration and characterization scheme for the OCRs was designed by following the guidelines of the IOCCG protocols (Zibordi et al., 2019) and the measurements performed in FRM4SOC Phase-1 (Vabson et al., 2019b; 2019a). Characterization procedures of OCRs used at the optical lab of TO are largely based on former studies and publications carried out for similar radiometers. A full list of characterized parameters, which can affect field measurements and are needed for correction of biases and evaluation of uncertainties is given in Table 2.

Limitations in the design and construction of OCRs inhibit significantly the characterization and the use of characterization results for correcting *in situ* data. Changes in the radiometric response due to the self-heating in stable laboratory conditions can distort the calibration and characterization results. For example, small deviations in spectra due to sensitivity to the polarization state and/or angular effects can be of the same magnitude as the thermal responsivity change of the radiometer. The radiometer's response will drift with the varying internal temperature, which in turn depends on the data acquisition process/rate. Due to internal self-heating, achieving good reproducibility of the calibration and characterization results may be difficult.

TABLE 2 List of characterized OCR properties and references where the characterization procedures are described.

Parameter	References
Absolute calibration for radiometric responsivity	Hooker et al. (2002), Mueller et al. (2003), Ylianttila et al. (2005), Seckmeyer (2010), Johnson et al. (2014), Salim et al. (2014)
Long term stability	Vabson et al. (2019a)
Spectral stray light and out of band response	Slaper et al. (1995), Kostkowski (1997), Zong et al., (2007), Zong et al., (2006), Feinholz et al. (2009), Nevas et al. (2012), Talone et al. (2016), Schinke et al. (2019)
Immersion factor (radiance, irradiance)	Zibordi et al. (2004), Zibordi (2006)
Angular response of irradiance sensors in air	Zibordi and Bulgarelli, (2007); Pulli et al. (2017)
Field of view of radiance sensors in air	Not addressed in this paper
Non-linearity	Pacheco-Labrador et al. (2014); Pulli et al. (2017); Talone and Zibordi, (2018); Talone et al. (2020)
Accuracy of integration times	Not addressed in this paper
Dark signal	Kuusk, (2011); Xing and Lagunas-Morales, (2018)
Thermal sensitivity	Baczynska et al. (2011); Salim et al. (2011); Price et al. (2014); Li et al. (2017); Li et al. (2018); Zibordi et al. (2017)
Polarization sensitivity	Talone and Zibordi, (2016); Voss and Costa, (2016)
Wavelength scale	Not addressed in this paper
Signal-to-noise ratio	Not addressed in this paper

2.2.1 Absolute calibration for radiometric responsivity

Absolute radiometric calibration of OCRs is needed to derive values of measured quantities accompanied by the specific SI unit and an estimate of measurement uncertainty from field results obtained in arbitrary units. This approach makes results obtained by using different sensors at different times comparable. The spectral responsivity of a radiometer is usually calibrated by measuring a known radiation source aligned at a specified distance. Procedures for this are well established and validated (Hooker et al., 2002; Mueller et al., 2003; Ylianttila et al., 2005; Seckmeyer, 2010; Johnson et al., 2014; Salim et al., 2014). Radiometric calibration of the irradiance and radiance sensors and their uncertainty budgets for the optics laboratory at TO are described in (Vabson et al., 2019a) and in more detail in (Vabson et al., 2022). The uncertainty of radiometric calibration described in (Vabson et al., 2019a) has been validated by an international comparison between four participants (TO, National Physical Laboratory, Joint Research Centre, and TriOS) in 2016, and, since 2018, is accredited by the Estonian Accreditation Centre (EAK).

2.2.2 Angular response of irradiance sensors in air

For determination of the angular response, a pseudo-collimated light beam is needed. Such a beam could be formed by using a point source with collimating optics using lenses, spherical or parabolic mirrors or the bare point source far enough away from the radiometer's input diffuser. The latter is impractical due to too low irradiance levels for most of the OC radiometers. The collimated beam defines the optical axis of the setup. The radiometer should be rotated in the plane coplanar to the optical axis so that the crossing of the optical and rotation axes stays in the center of the diffuser's surface. For an ideal diffuser, the radiometer's output signal should follow the cosine law with respect to the rotation angle θ over all wavelengths of the radiometer. To guarantee reproducibility of characterization results, for angular measurements of irradiance sensors the sensor's azimuth angle shall be clearly defined and recorded in the characterization report.

2.2.3 Non-linearity of radiometric response

For determination of the radiometric non-linearity, a stable light source (e.g., the calibration source) was measured by using at least two different integration times. Following (Vabson et al., 2019a; Lin et al., 2022), the absolute non-linearity error $\Delta DN(\lambda)$ was determined, from which, using Eq. (1), the relative non-linearity error $\delta x(\lambda)$ and non-linearity coefficient $\alpha(\lambda)$ were calculated:

$$\alpha(\lambda) = \frac{\delta x(\lambda)}{DN(\lambda)} = \frac{\Delta DN(\lambda)}{[DN(\lambda)]^2}, \quad (1)$$

where $DN(\lambda)$ is the dark and linearity corrected spectrum in digital numbers derived from laboratory measurements. The non-linearity coefficient $\alpha(\lambda)$ is an inherent property of a particular radiometer, and, in contrast to the relative non-linearity error $\delta x(\lambda)$, does not depend on the shape of the measured spectra. Thus, coefficient $\alpha(\lambda)$ can be used for correcting raw spectra of any shape limited only by the uncertainty. The non-linearity determination method described by the Eq. (1) can be modified by using a stable, adjustable monochromatic source set to the central wavelength of a certain (measured) pixel of the radiometer. Re-adjusting at each measured wavelength the radiation intensity and the integration time of the radiometer, a more effective selection of signal level and, as a result, better signal-to-noise ratio in ultraviolet (UV) and near infrared (NIR) parts of the spectrum can be achieved.

2.2.4 Dark signal

Radiometers usually have a non-null output called dark signal without any input flux at the entrance optics (Zibordi et al., 2019). Dark signal is caused by the photodetector dark current and

additional contributions such as the electronic offset and varies largely with temperature and integration time. Due to varying conditions, frequent measurements of the dark signal are essential. The optimal way during both the characterization and the field measurements is to measure the dark signal and the illuminated signal with equal integration times and as close in time as possible to minimize internal temperature drifts between these measurements.

2.2.5 Thermal sensitivity

Temperature is among the most significant environmental factors impacting OCR response (Zibordi et al., 2017; Vabson et al., 2022). Both the radiometric responsivity and the dark signal of a sensor are temperature sensitive. For determination of the thermal coefficients, the radiometer was immersed in a cylindrical thermally controlled water tank, equipped with an optical grade fused silica window. Although any climate chamber with an optical window might be suitable, submersion of the OCRs in a liquid tank is preferable for frequent repetition since this provides much better thermal contact with the environment and faster thermal adaptation, compared to in air adaptation times which can exceed hours. The characterization setup with a lamp (in the case of irradiance sensor) or a lamp-plaque or lamp-sphere (in the case of radiance sensors) is similar to the corresponding radiometric calibration setups. The crucial parameter of the light source is temporal stability, while the absolute irradiance/radiance output is not that important.

For determination of the thermal coefficients, temperature setpoints were selected as +5 °C, +10 °C, +20 °C, +30 °C, +35 °C and +40 °C to cover the temperature range expected during field use. The temperature was maintained at each selected setpoint for about an hour for reaching thermal equilibrium. Three integration times of the radiometer were used at each temperature setpoint to account for the non-linearity effect. At least two scans were performed for each radiometer, with temperature ramping up and down, respectively.

Accounting for thermal effects with varying temperature is complicated, but in field conditions, the temperature is usually varying. Therefore, dynamic tests have been performed in a thermostat to evaluate the possible effects from changing temperature on the radiometer measurement signal by sweeping the temperature from 5°C up to 40°C and back down to 5°C. Temperature sweeping rate was 0.5°C/min with a full test length of 4 h.

2.2.6 Polarization sensitivity

For the characterization of the polarization sensitivity of a radiance sensor, a linearly polarized source is required (Talone and Zibordi, 2016). The source can be created by using an unpolarized radiance source (an integrating sphere or lamp-plaque setup) and a linear polarizer with known properties. The sensor's azimuth angle is defined and recorded in the same way as for angular measurements.

2.2.7 Wavelength scale

For calibration of the wavelength scale, fixed narrow-band sources with known wavelength reference values such as lasers, gas discharge lamps, certified sharp absorption line filters or tuned narrow-band sources such as monochromators and tunable lasers can be used. According to the specifications of the manufacturers (TriOS, 2019; Sea-Bird Scientific, 2024), the wavelength accuracy of TriOS RAMSES and Seabird HyperOCR radiometers is within ±0.3 nm. Therefore, the characterization setup has to provide reference values with smaller or at least with the same uncertainty.

2.2.8 Signal-to-noise ratio

The signal-to-noise ratio (SNR) is determined as the ratio of an averaged signal with subtracted dark to the standard deviation of a single measurement accounting for the variance of both light and dark signal.

3 Calibration and characterization results

3.1 Radiometric responsivity

In the context of the FRM4SOC projects, all radiometers involved in inter-comparison exercises must be uniformly calibrated immediately before comparison. The calibration state of sensors before calibration at the optical lab of TO and after calibration is shown in Figure 1A (Vabson et al., 2019a) and in Figure 1B. Agreement of measurement results for irradiance (E) and radiance (L) sensors were evaluated as a standard deviation calculated from the individual comparison spectra normalized by the consensus value (e.g., mean or median). The relative standard deviation of individual differences of the radiometers estimated with the previous calibration coefficients was found to be within 5%–10% if the same stable radiation source was measured in controlled laboratory conditions (using an integrating sphere for the radiance, and a Quartz Tungsten Halogen (QTH) lamp on the optical axis for the irradiance sensors). Just after calibration, calculating the same results with the fresh determined calibration coefficients the relative standard deviation was within ±1%. Agreement between OCRs before FRM4SOC phase 2 is shown in Figure 1B where for RAMSES and HyperOCR sensors the relative standard deviation of individual differences was within 2% and 10%, respectively. These results highlight the crucial role of reliable SI-traceable radiometric calibrations in improving agreement between the OCRs used by participants in all comparison exercises performed in the frame of the FRM4SOC projects (Vabson et al., 2019b; 2019a; Alikas et al., 2020; Tilstone et al., 2020).

Variation of the radiometric responsivity over many years for selected instruments is shown in Figure 1C. Responsivity drift is monitored in the spectral range from 400 nm to 800 nm. Average drift is close to −1% per year (shown with broad blue line). Occasionally however, a responsivity jump of several percent may happen. Due to drift of the OCRs, recalibration is advisable before and after each deployment. Yearly re-calibration is recommended as a minimum requirement to achieve FRM standards. More frequent checking of responsivity is also recommended, e.g., using field portable light sources or natural light sources, especially for long-term unsupervised systems where fore-optics contamination may occur.

Variation of the radiometric responsivity as a function of the measurement conditions for freshly calibrated radiometers is

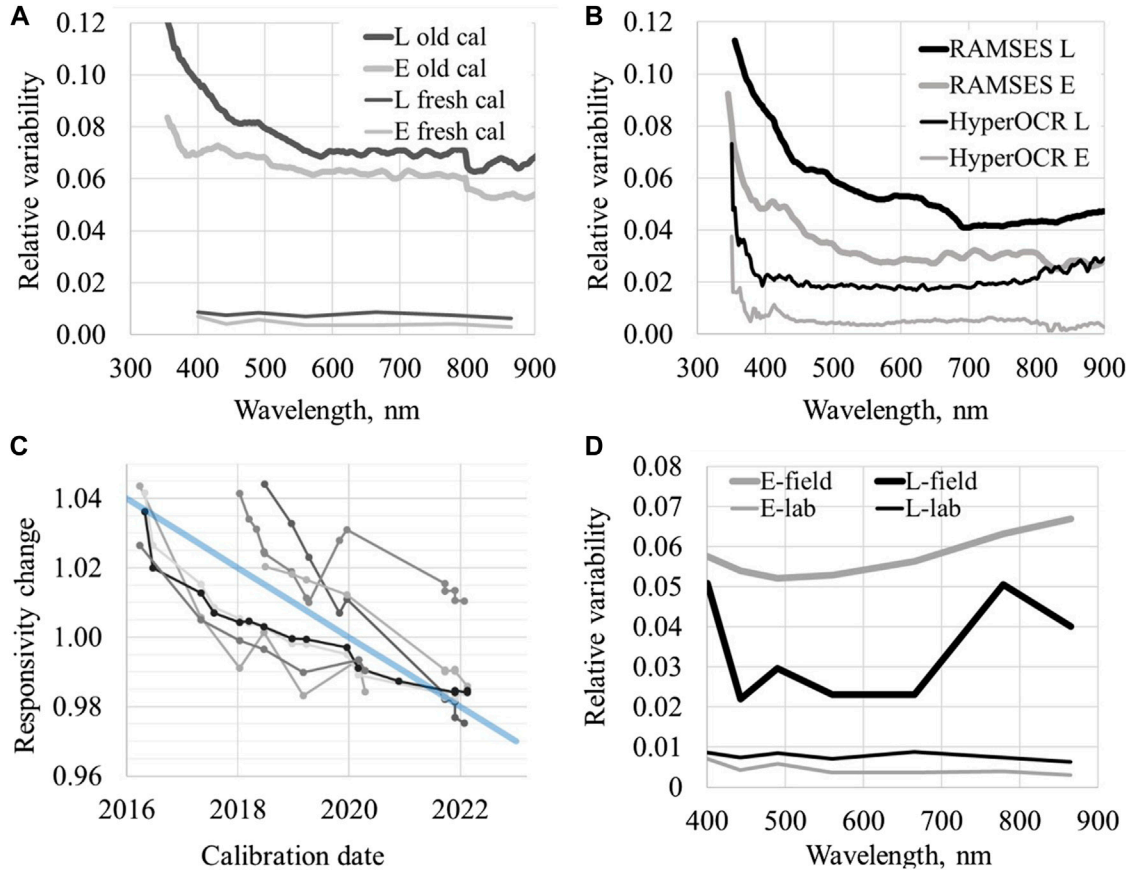


FIGURE 1
Agreement of measurement results for irradiance (E) and radiance (L) sensors as a function of calibration state and environmental conditions. **(A)** Agreement between OCRs before FRM4SOC-1 (thick lines), after calibration during FRM4SOC-1 (thin lines). **(B)** Agreement between OCRs before FRM4SOC-2; RAMSES sensors (thick lines), and HyperOCR sensors (thin lines). **(C)** Responsivity drift at 550 nm of selected OCRs with the thick blue line representing a 1% annual responsivity drop (linear fit). **(D)** Agreement between OCRs with fresh calibration during the field comparison (thick lines), and during the laboratory comparison (thin lines) without any characterisation corrections applied.

shown in Figure 1D. The relative standard deviation of individual differences during the field intercomparison of radiometers was around 5% (thick lines), and during the laboratory intercomparison below 1% (thin lines) (Vabson et al., 2019b; 2019a). Any corrections that rely on characterization of radiometers during these exercises were not applied. Spread of the laboratory intercomparison results was small as the measurement conditions were close to the calibration conditions. Due to significant difference in conditions of the field deployments, instrument characterisation in addition to the absolute radiometric calibration and respective corrections are needed if expanded uncertainties below ±10% (k = 2) are to be achieved.

3.2 Angular response of irradiance sensors in air

The cosine response in air of a HyperOCR irradiance sensor is shown in Figure 2A. The cosine response error for HyperOCR sensors is usually within ±2% in the range of incident angles from −60° to +60°. The cosine response in air for a RAMSES irradiance sensor is shown in Figure 2B. The cosine response error for RAMSES sensors is often significantly larger than the cosine response error of HyperOCR sensors, with greater variability between individual sensors. Measurements at TO have shown that RAMSES sensors may have large cosine errors that are around ±10% (Vabson et al., 2019b). In addition, angular response of RAMSES irradiance sensors is often markedly more asymmetrical than for HyperOCR.

The determination of cosine response of irradiance sensors depends strongly on the radiation source used and the measurement geometry. Therefore, careful choice of the source, proper baffling of the measurement beam and evaluation of the beam's spatial uniformity are required. As the results are extremely sensitive to small misalignments, repeating the full alignment and validating it against the opposite azimuth is advisable by rotating the radiometer around its axis by 180°. Azimuth planes differing in 180° should coincide, but with opposite sign of the incident angle. Accounting for temporal and thermal drifts is also necessary. Due to asymmetry of the cosine response, the azimuth angle of the OCR should be specified during characterization and during field deployments (and an azimuthal reference must therefore be marked on the OCR).

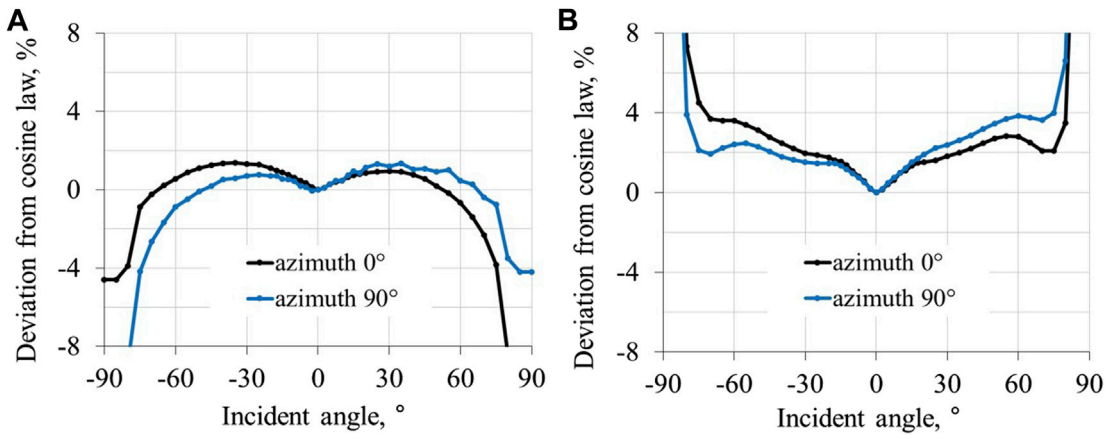


FIGURE 2
Angular response of irradiance sensor as a function of OCR's azimuth plane. **(A)** Deviation from cosine law of one HyperOCR sensor. **(B)** Deviation from cosine law of one RAMSES sensor.

3.3 Non-linearity of radiometric response

Figure 3A shows the difference between non-linearity coefficients α(λ) determined using two methods. During radiometric calibration, the full-spectrum α(λ) was determined in 2018 and twice in 2022. Determination with an adjustable monochromatic source was made in 2022. In the central spectral part, the agreement between the results is satisfactory. Determination by using the adjustable monochromatic source is clearly preferable due to a better signal to noise ratio in the UV and NIR parts of the spectrum. This method is therefore considered as validation/reference for the full-spectrum results.

The range of non-linearity coefficients for 16 RAMSES sensors is shown in Figure 3B and for 9 HyperOCR sensors in Figure 3C. The range of variation in $\alpha(\lambda)$ for the RAMSES sensors is larger than the HyperOCR sensors, and significantly larger than the uncertainty of an individual non-linearity coefficient. The difference between mean $\alpha(\lambda)$ values of RAMSES and HyperOCR sensors is clearly seen in Figure 3D, while the difference between irradiance and radiance sensors in Figures 3B, C is insignificant.

The influence of integration times on the accuracy of the non-linearity coefficient is shown in Figure 3E. The integration time initially set to 64 ms was changed by ±0.1%. This small deviation from the correct set value 64 ms will cause changes in α which are comparable with the measured spread of non-linearity coefficients shown for the RAMSES sensors in Figure 3B. Thus, non-linearity determination based on two different integration times will give reliable results only when the relative uncertainty of setting integration times is better than 0.03%.

3.4 Thermal sensitivity

In Figure 4A the thermal coefficients for the radiance sensors after correction for non-linearity for RAMSES (black) and for HyperOCR (gray) are given together with expanded uncertainty (k = 2) of the temperature coefficients.

Class-specific temperature coefficients at equilibrium conditions for 17 individual characteristics of RAMSES sensors (9L and 8E) is given in Figure 4B and for 8 HyperOCR sensors (4L and 4E) is given in Figure 4C. Additionally, the results of the Joint Research Centre (JRC) (Zibordi et al., 2017) based on data of four RAMSES sensors are shown in Figure 4B. There is no significant difference between TO and JRC. The spread of JRC results is smaller than the spread of TO data given that it contains much larger group of individual characteristics. Distributions of the RAMSES sensors partly cover each other, but the spread of the irradiance sensors is about twice the spread of the radiance sensors. Distributions of the HyperOCR radiance and irradiance sensors are clearly separated (Figure 4B), but the spread of both radiance and irradiance sensors is much smaller than the typical range for the RAMSES sensors. Larger difference between the HyperOCR radiance and irradiance sensors is likely to be caused by the high thermal sensitivity of the material, polytetrafluoroethylene (PTFE), used for the construction of the cosine collector. The phase transition of PFTE at 19°C can cause relative change of the optical transmittance around 3% (Ylianttila and Schreder, 2005). The manufacturer does not provide details of the diffuser material for the HyperOCR irradiance sensors, however, the discontinuity in the thermal dependence of these radiometers around 19 °C ambient temperature resembles the properties of PTFE. Responsivity-temperature plots for HyperOCR radiance sensor are shown in Figure 4D and for irradiance sensor in Figure 4E. Responsivity-temperature relationship of the radiance sensor is well-suited for applying a linear model to estimate the temperature coefficient, but for the irradiance sensor due to a stepwise change in the signal at 19°C the linear model is much less convenient. The uncertainty of the HyperOCR irradiance sensors increases, especially if measurements are performed within a temperature range that contains this point (Figure 4E).

3.5 Dynamic thermal sensitivity

A rather large difference between external and internal temperature of an OCR will be seen if a radiometer is equipped

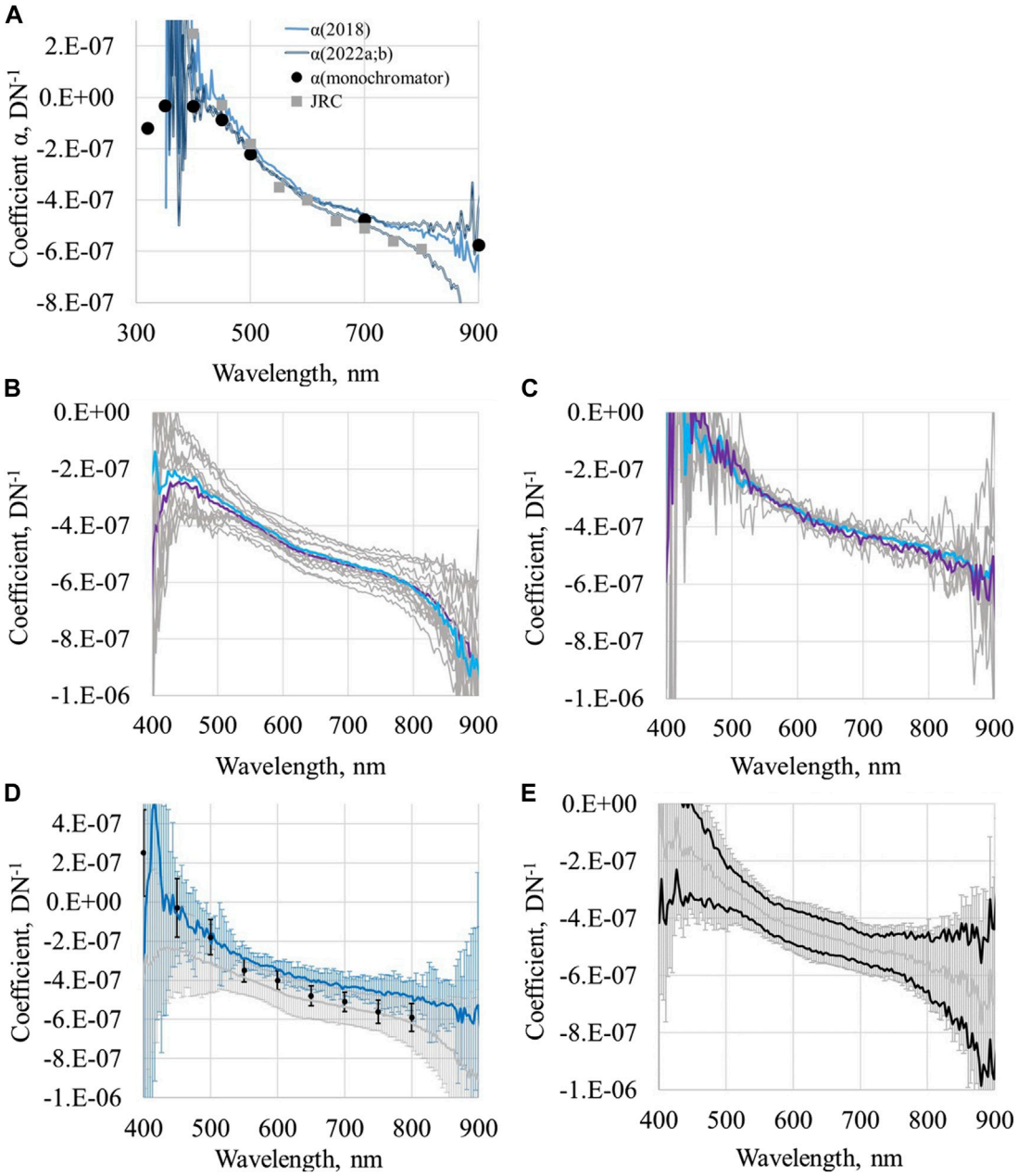


FIGURE 3
Non-linearity of radiometric response of OCRs. **(A)** Non-linearity coefficient $\alpha(\lambda)$ of a RAMSES radiance sensor (SAM_821E) determined during calibration with a FEL lamp (in 2018 blue line, in 2022 gray lines), using an adjustable monochromatic source (dots), and results from JRC (squares) (Talone and Zibordi, 2018; Talone et al., 2020). **(B)** Spread of non-linearity coefficients determined during FRM4SOC-2 for RAMSES. Mean of E sensors (violet line), and L sensors (blue line). **(C)** Spread of non-linearity coefficients determined during FRM4SOC-2 for HyperOCR. **(D)** Class-specific presentation of non-linearity coefficients with expanded uncertainty for RAMSES (gray) and HyperOCR (blue), including results from JRC (Talone and Zibordi, 2018; Talone et al., 2020) shown as dots. **(E)** Sensitivity of non-linearity coefficient to small changes in integration time. Class-specific distribution: gray showing expanded uncertainty; non-linearity coefficients for integration time changed by ±0.1%: black.

with an internal temperature sensor. For the HyperOCR sensor immersed into a water thermal bath, the difference between internal and external temperatures is about (2...3) ˚C (Figure 5A), depending how data are acquired, and on the ambient fluid. The temperature difference of the same sensor used in air can be much larger, even reaching 5 ˚C.

Strong hysteresis of the optical signal of the radiometers is evident if the signal is presented as a function of the ambient temperature (see Figures 5B, D). As well as the responsivity change at 400 nm and 700 nm, the radiometer's dark signal is shown. Hysteresis of the optical signal contributes significantly to the measurement uncertainty. The situation is similar to field measurements, where the temperature is obtained with an external temperature sensor. In this case, uncertainty due to hysteresis can be similar or even larger than the change in thermal responsivity. Hysteresis becomes significantly smaller if

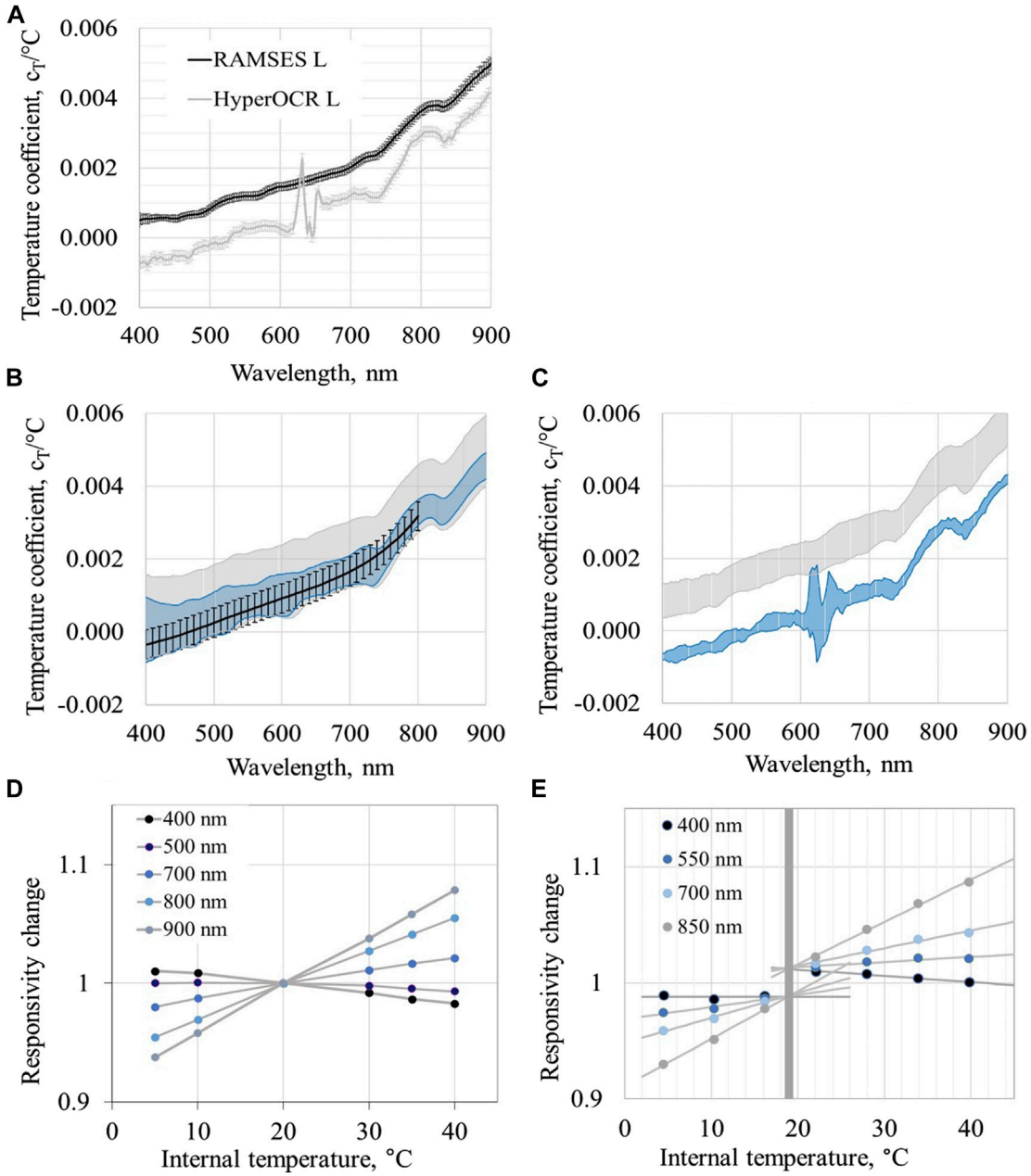


FIGURE 4
Steady-state thermal properties of the OCRs. **(A)** Individual temperature coefficient of one RAMSES (black) and one HyperOCR (gray) radiance sensor with expanded uncertainties. **(B)** Class-specific temperature coefficients for RAMSES radiance (blue region) and irradiance (gray region). Data from JRC (Zibordi et al., 2017) are indicated by a black line. **(C)** Same as B but for HyperOCR. **(D)** Responsivity-temperature plots for HyperOCR radiance sensor and **(E)** for HyperOCR irradiance sensor.

the same data are presented as a function of temperature measured with the internal temperature sensor of the radiometer (Figure 5C). In this case, the contribution from the temperature correction will dominate. This clearly shows the importance of an internal temperature sensor of a radiometer used under variable environmental conditions. In addition, correcting for temperature effects is inefficient without an internal temperature sensor due to the large uncertainty of the determined temperature difference under calibration and found in the field.

Hysteresis of the optical signal of the HyperOCR irradiance sensor is shown in Figures 5D, E. As seen in Figures 5B–E, and the variations in the dark signal of both radiance and irradiance sensors are very similar, implying that thermal effects on both optical sensors are comparable. The behavior of the optical and dark signal of the radiance sensor (Figures 5B, C) is also similar indicating a common source of hysteresis. For irradiance sensors, the cosine collector, which is known to have an abrupt change of transmittance at around 19°C, is located on the external surface, causing additional hysteresis compared to

10.3389/frsen.2024.1320454

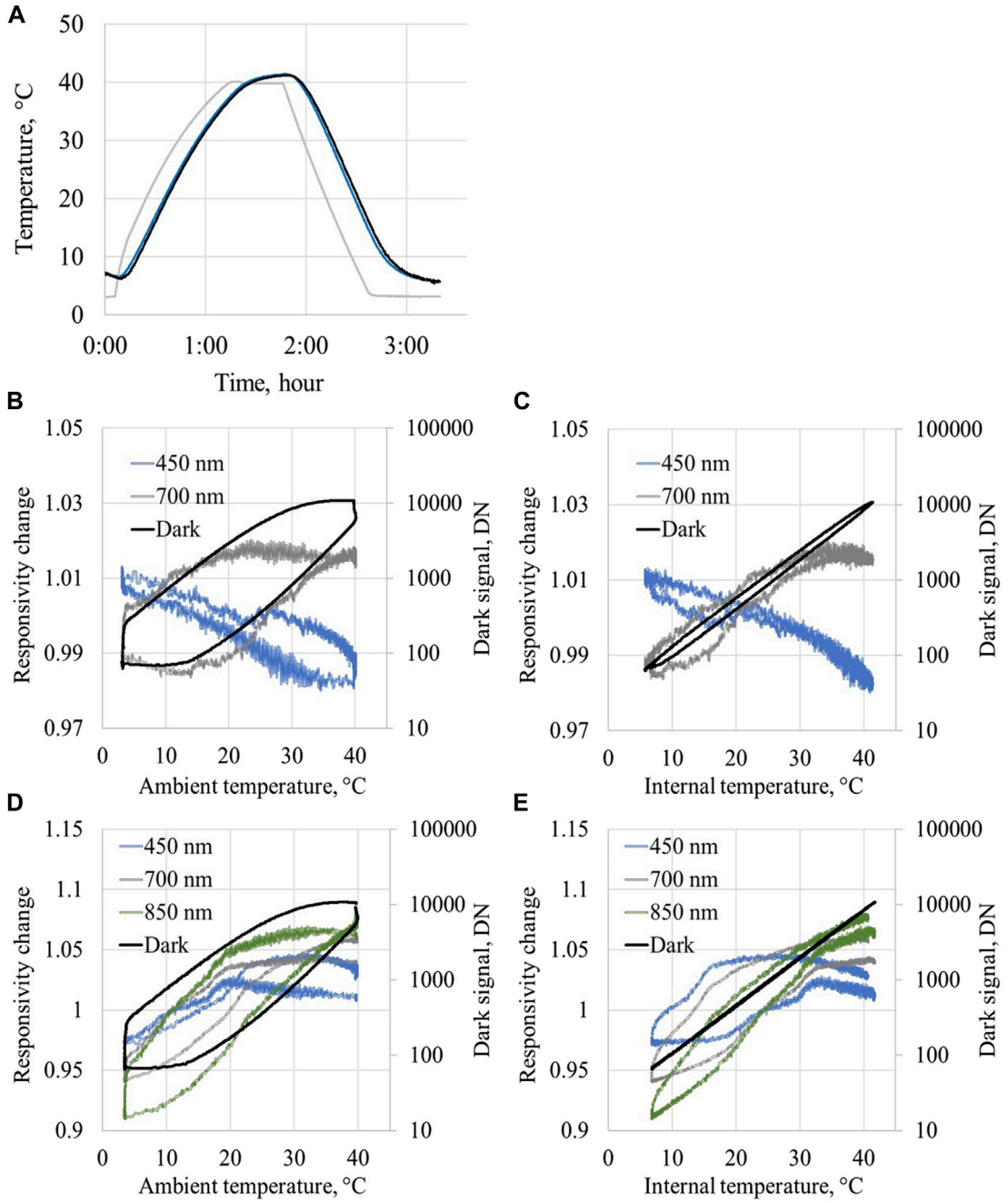


FIGURE 5
Dynamic thermal properties of the radiance and irradiance OCRs. **(A)** Time lags and differences between different temperature sensors (gray: ambient temperature sensor, blue: internal temperature sensor (added *ad hoc* in the case of TriOS): black: temperature calculated from the dark signal) at varying temperatures measured for a radiometer immersed in water. **(B)** Relative variations of optical signal of HyperOCR radiance sensor as a function of ambient temperature (blue: 400 nm, gray: 700 nm). Variation of the dark signal (black) is shown using logarithmic scale. **(C)** Optical and dark signal of HyperOCR radiance sensor as a function of internal temperature. **(D)** Optical and dark signal of HyperOCR irradiance sensor as a function of ambient temperature. **(E)** Optical and dark signal of HyperOCR irradiance sensor as a function of internal temperature.

the radiance sensors. Consequently, hysteresis of the optical signal did not decrease substantially when presented as a function of the internal temperature sensor (Figure 5E), although the dark signal hysteresis is removed, as expected. Thus, for HyperOCR irradiance sensors, using internal temperature will not avoid an increase in uncertainty due to hysteresis.

4 Correcting *in situ* data

The measurement data may lead to different measurement results and uncertainties depending on how the measurement process is modeled. This is dependent on which statistical assumptions are used, which approximations are applied, and which environmental factors are taken into account. For

radiometric *in situ* measurements, at least three levels of measurement outputs should be distinguished:

- instrument indications or readings—raw data level;
- measurement results of a single radiometer—values attributed to the measured target (e.g., water, sky, upper hemisphere), accompanied by a measurement unit and an uncertainty estimate;
- measurement results of a multi-radiometer system–calculated from two or more radiometers.

If a three radiometer system is used, accounting for the correlations between input quantities is crucial. Strong correlations are likely to occur if the same calibration standards have been used for calibration of different radiometers within a short time period from calibration, if the characteristics of the radiometers, and measurement environmental conditions are similar. Small differences in internal heating of the synchronously working individual radiometers and/or slightly deviating measurement conditions of the three-radiometer system used in the field however, may significantly change the correlations between the data of the radiometers.

A comprehensive characterization of the radiometers and the implementation of correction schemes enables a reduction in the uncertainties of field data. If only a single radiometer is used, the application of cal/char data is quite straightforward, and cal/char uncertainties contribute entirely to the overall uncertainty budget of the measurement data. For example, relative temperature correction for six individual radiometers as a function of difference from the calibration temperature is shown in Figure 6A. During field use, possible thermal full scale effect for these radiometers will remain within ±10%. In Figure 6B, thermal effects of the three-radiometer system with large discrepancy between individual thermal coefficients of radiance and irradiance sensors are presented for maximum bias from the calibration temperature of ±20°C. The effect is proportional to both (i) the deviation of the in-field temperature from the calibration temperature, and (ii) to the difference between the thermal coefficients of the radiance and irradiance sensors.

For a two-radiometer scheme, cal/char contributions to the uncertainty can be rather similar to the single radiometer case. For example, with two radiance sensors, which can be used for determination of the water leaving radiance L_w. If for the determination of remote-sensing reflectance the system of three radiometers is used however, then data handling, including uncertainty contributions, can be far more complex. For above-water measurements, often three different radiometers are concurrently used, one measuring the upwelling radiance from the water, $L_u(\lambda)$, the second measuring the downwelling radiance from the sky, $L_d(\lambda)$, and third, the downwelling irradiance, $E_d(\lambda)$.

The water-leaving reflectance spectra can be calculated from the synchronized time series measured with the three-radiometer system. Calculations include the following steps:

- all measured radiance and irradiance spectra are corrected for the spectral stray light, non-linearity, thermal effects, etc.;
- spectral response functions of a satellite sensor are used to convolute L_u, L_d and E_d spectra into the satellite spectral bands (Burggraaff, 2020);
- the remote sensing reflectance $R_{rs}(\lambda)$ is calculated as

$$R_{rs}(\lambda) = \frac{L_u(\lambda) - \rho_F L_d(\lambda)}{E_d(\lambda)}, \quad (2)$$

where $L_u(\lambda)$ is the upwelling water radiance, $L_d(\lambda)$ is the downwelling sky radiance, $E_d(\lambda)$ is the downwelling irradiance and ρ_F is the "effective Fresnel reflectance coefficient" for a roughened water surface (Goyens and Ruddick, 2023), obtained as a function of the wind speed, Sun zenith angle, and relative azimuth angle from the Look Up Table 1 of (Mobley, 1999), provided online[1]. The spectra of E_d, L_u and L_d are presented in Figure 6C as an example of the simultaneous use of three radiometers. In Figure 6D, remote sensing reflectance is calculated from these spectra; at first, the spectra are convoluted to OLCI bands to compensate for differences in wavelength scales of the OCRs, and then Eq. 2 is used with the obtained band values. Some environmental conditions affecting radiometers are similar or almost the same (ambient temperature) for all sensors. Some are very different, such as the intensity of radiation, and spatial or spectral distribution (Figure 6C). As the angular response of irradiance sensor is specific to only one sensor in the three-radiometer system, its contribution cannot be reduced or compensated for by the similar behavior of other radiometers.

If the same standard lamp has been used for radiometric calibration of all the sensors of a three-radiometer system measuring, E_d, L_u and L_d, then due to correlation of calibration coefficients (Johnson et al., 2014) uncertainty in remote sensing reflectance is notably reduced (Figure 6D), and the relative expanded uncertainty of the system due to calibration of radiometers is about 2% which was typical for the FRM4SOC projects. Only contributions from the mechanical alignment of the lamp, plaque and sensors, inadequate baffling, short-time instability of the irradiance standard, and uncertainty of the plaque reflectance are significant. This is valid only if the same standard lamp has been used for all the sensors in a short space of time. If the same three radiometers are calibrated at three independent laboratoriess equipped with the same high-level calibration standards, expanded uncertainty of the three-radiometer system due to calibration of radiometers will be about 5%. If the calibration state of radiometers used in a three-radiometer system is such as described in Figure 1A, the expanded uncertainty of the remote sensing reflectance can be more than 40% due to inconsistent calibration of the radiometers (Figure 6D). Therefore, careful and regular radiometric calibration of OCR is extremely important for SI-traceability of the OCRs and this is a major factor in obtaining satisfactory agreement in the measurement results.

Similarly, if we assume an identical behavior for thermal sensitivity of all three sensors the temperature correction will cancel out. Thus, for the three-radiometer system (with all radiometers belonging to the same class) class-based temperature corrections would have no significant effect on the results. This does not imply that in the case of a three-radiometer system, the temperature corrections are always insignificant. If real individual

1 https://www.oceanopticsbook.info/packages/iws_l2h/conversion/files/rhoTable_AO1999.txt

10.3389/frsen.2024.1320454

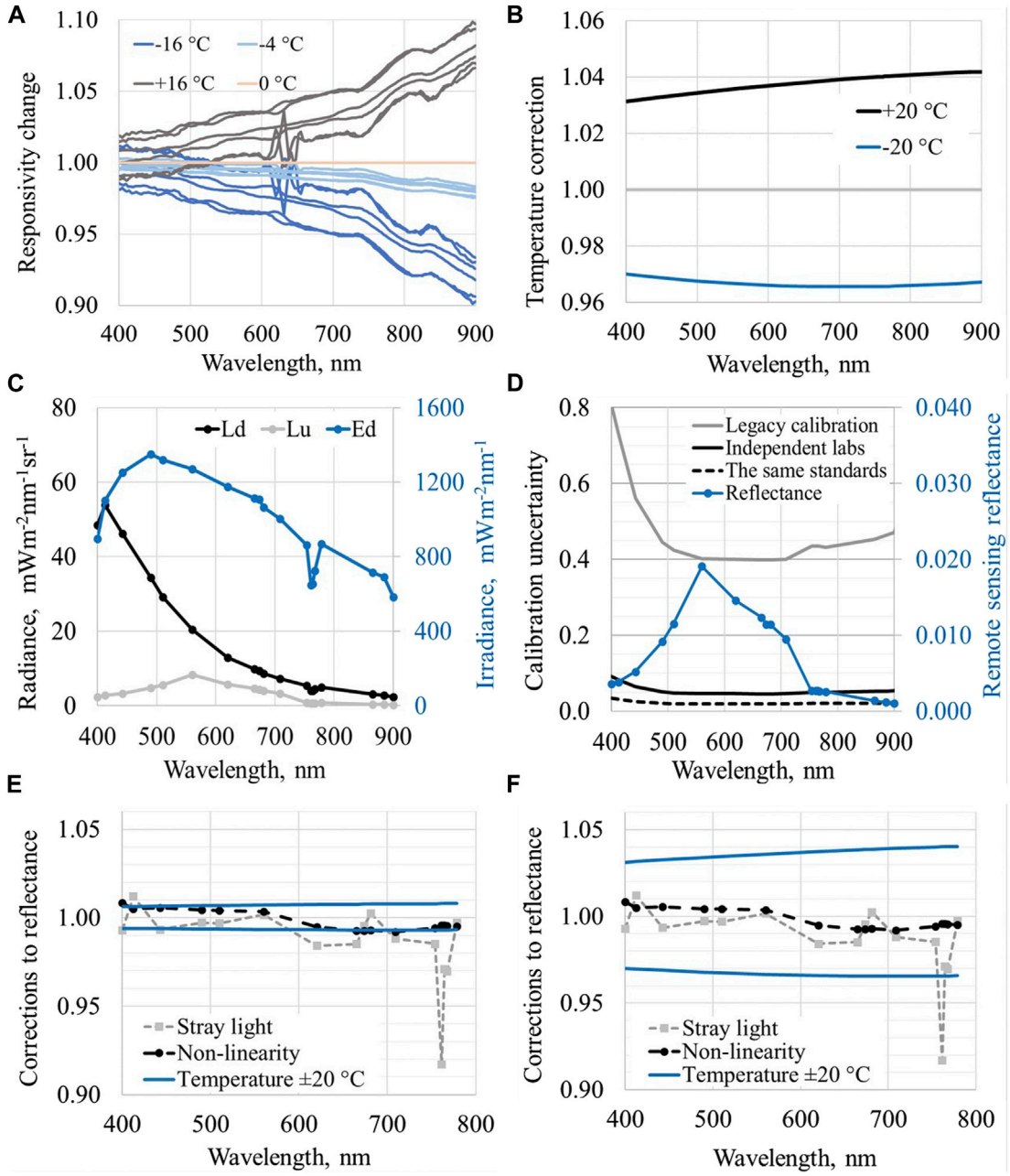


FIGURE 6
Size of corrections for a single OCR and for a three-radiometer system. **(A)** Temperature corrections as a function of the difference from the calibration temperature for six OCRs. **(B)** Bias of the three-radiometer HyperOCR system at ±20 °C from the calibration temperature. **(C)** Spectra measured with three radiometers for determination of the remote sensing reflectance. **(D)** Relative expanded uncertainty of the three-radiometer system due to contributions from the individual calibration uncertainties of the applied radiometers is shown with solid lines. Remote sensing reflectance convoluted to OLCI bands is given with a blue line. **(E)** Simulation of the joint relative effects with three RAMSES sensors due to spectral stray light, non-linearity, and temperature difference during calibration and later use. **(F)** The joint relative effects for similar system with three HyperOCR sensors.

temperature characteristics are used, the thermal correction for a deviation of about 10°C from the temperature during calibration may be several percent (Figure 6B). Here, the differences between the thermal coefficients of different sensors are critical, and due to different thermal loads of the radiometers, temperature differences from calibration points may be different.

For the three-radiometer system, the correction coefficients for non-linearity and spectral stray light, even based on the same (class-specific) characteristics will lead to different corrections for individual radiometers due to significant spectral differences of the target signals. Individual characteristics of radiometers are certainly preferable. For uncertainty contributions of the three-radiometer system, instead of individual characterization parameters, the differences between the radiometers will be more relevant.

An example showing the combined contributions of different uncertainty sources for a three-radiometer system of RAMSES and

HyperOCR radiometers is presented in Figures 6E, F. Here, the relative contribution due to spectral stray light is shown with gray dotted lines, due to non-linearity with black dotted lines and the limits of relative biases due to temperature differences during calibration and later use are given as with blue lines. Large variation in the thermal effect (Figure 6F) is due to difference in thermal coefficients of the HyperOCR radiance and irradiance sensors (Figure 4C). Here, possible differences among internal temperatures of the three radiometers during the field deployment are not accounted for.

5 Conclusion

During the FRM4SOC Phase 2 project 37 hyperspectral field radiometers, including both irradiance and radiance sensors for TriOS RAMSES and Sea-Bird Scientific HyperOCR systems, were calibrated and characterized. There was good agreement between the characterizations made in this study and results from previous studies (Zibordi et al., 2017; Talone and Zibordi, 2018; Talone et al., 2020). The spread of individual results of many parameters has been expanded compared with previous studies however, and as a consequence, class specific characterization of these parameters may no longer be suitable. To provide individual characterizations of a large number of radiometers, several highly specialized calibration/ chararcterization laboratories are needed. Using characterization results to correct field data is also time consuming and complex, as additional measurement information (e.g., OCR's internal temperature) is needed in the measurement equation of remote sensing reflectance and whilst in-field measurement protocols need to be strictly followed (Ruddick et al., 2019a; Zibordi et al., 2019; Ruddick et al., 2019b; Ruddick, 2023).

For some properties of radiometers, dynamic tests are essential. The anomalous thermal dependence of the HyperOCR irradiance sensors was revealed only during the continuous change in temperature as opposed to thermal equilibrium. Another important feature detected during dynamic tests is the hysteresis of optical response and its dependence on a particular sensor used for temperature determination. Such an effect may significantly contribute to the uncertainty of the field results. In order to account for dynamic effects during field measurements, the best solution would be to have two temperature sensors installed in each radiometer: one sensor close to the location of the optical sensor and the other would be located on the surface of the radiometer. Differences between sensors will show the speed of temperature variation and give input for dynamic influences.

Although in comparison with RAMSES the cosine error and asymmetry of HyperOCR irradiance sensors is often smaller, the diffuser material used in HyperOCR irradiance sensors can cause significant errors, evident as strong hysteresis patterns in the responsivity as a function of ambient temperature (Figure 5), which cannot be compensated due to unknown temperature of the diffuser in variable environmental conditions. HyperOCR instruments have an internal temperature logger, whereas RAMSES do not, so recording internal temperature in RAMSES sensors in the varying field conditions is almost impossible.

Most of the OCR parameters that produce the greatest bias also contribute significantly to the combined uncertainty for individual radiometers, but using the three-radiometer system this effect is far less. The size of individual specific thermal effects over the range from 400 nm to 800 nm is up to ±10% if the bias from the calibration temperature is ±20°C. Relative joint thermal correction for the three-radiometer system is within ±4% if the discrepancies between the temperature coefficients of radiance and irradiance sensors is large, and almost zero if the thermal characteristics are similar. Joint non-linearity and spectral stray light corrections are also usually smaller than individual corrections and are within a few percent. Contrary to this, the angular response of the irradiance sensors cannot be reduced as it does not cancel out and therefore contributes to the uncertainty budget of a three-radiometer system (up to ±10%).

Characterization of radiometers is important if *in situ* OC expanded uncertainties below 10% level are aimed at. However, without very careful regular radiometric calibration of OCRs the advantages of the characterization cannot be achieved (Figure 6D) as the differences due to unsatisfactory calibration state can be much larger than possible biases, which is revealed in the characterization. Some parameters that contribute significantly to measurements with a single radiometer may be negligible in a two- or three-radiometer system. Consistent correction of biases and extended uncertainty analysis of *in situ data* obtained by different measurement models and instrument configurations need further attention.

Data availability statement

Publicly available datasets were analyzed in this study. This data can be found here: The cal/char data presented in this study can be found in online repositories Fiducial Radiometer Database (FidRadDB) and Ocean Colour *In-Situ* Database (OCDB) at https://ocdb.eumetsat.int.

Author contributions

VV: Conceptualization, Data curation, Methodology, Visualization, Writing–original draft, Writing–review and editing, Formal Analysis. IA: Conceptualization, Formal Analysis, Investigation, Methodology, Software, Visualization, Writing–review and editing. KD: Data curation, Formal Analysis, Methodology, Visualization, Writing–review and editing. RV: Conceptualization, Formal Analysis, Methodology, Project administration, Writing–review and editing. JK: Formal Analysis, Methodology, Writing–review and editing. KR: Formal Analysis, Methodology, Writing–review and editing. AB: Formal Analysis, Methodology, Writing–review and editing. GT: Formal Analysis, Methodology, Writing–review and editing. JG: Formal Analysis, Methodology, Writing–review and editing. EK: Formal Analysis, Methodology, Project administration, Writing–review and editing.

Funding

The author(s) declare financial support was received for the research, authorship, and/or publication of this article. The work presented in this article was performed in the framework of the project Fiducial Reference Measurements for Satellite Ocean Color

(FRM4SOC) Phase-2 (EUMETSAT contract no. EUM/CO/21/460002539/JIG) funded by European Commission (Copernicus Programme) and implemented by EUMETSAT. The work has also made use of the laboratory facilities of Tartu Observatory, University of Tartu, supported by the Estonian Research Council project TT8 (grant number TT8) and the Estonian State Shared Service Center project KosEST [grant number SLTTO20562T (2014-2020.4.01.20-0284)].

Acknowledgments

The authors would like to thank Giuseppe Zibordi, Carol Johnson and Julian Gröbner for valuable comments during FRM4SOC Phase 2 project.

Conflict of interest

The authors declare that the research was conducted in the absence of any commercial or financial relationships that could be construed as a potential conflict of interest.

Publisher's note

All claims expressed in this article are solely those of the authors and do not necessarily represent those of their affiliated organizations, or those of the publisher, the editors and the reviewers. Any product that may be evaluated in this article, or claim that may be made by its manufacturer, is not guaranteed or endorsed by the publisher.

References

Alikas, K., Ansko, I., Vabson, V., Ansper, A., Kangro, K., Uudeberg, K., et al. (2020). Consistency of radiometric satellite data over lakes and coastal waters with local field measurements. *Remote Sens.* 12, 616. doi:10.3390/rs12040616

Baczynska, K., O'Hagan, J. B., Pearson, A. J., and Eriksen, P. (2011). Temperature correction of UV spectral solar measurements for ICEPURE project. *Photochem. Photobiol.* 87, 1464–1467. doi:10.1111/j.1751-1097.2011.00981.x

Banks, A. C., Vendt, R., Alikas, K., Bialek, A., Kuusk, J., Lerebourg, C., et al. (2020). Fiducial reference measurements for Satellite Ocean Colour (FRM4SOC). *Remote Sens.* 12, 1322. doi:10.3390/rs12081322

Białek, A., Douglas, S., Kuusk, J., Ansko, I., Vabson, V., Vendt, R., et al. (2020a). Example of Monte Carlo method uncertainty evaluation for above-water Ocean Colour radiometry. *Remote Sens.* 12, 780. doi:10.3390/rs12050780

Białek, A., Goodman, T., Woolliams, E., Brachmann, J., Schwarzmaier, T., Kuusk, J., et al. (2020b). Results from verification of reference irradiance and radiance sources laboratory calibration experiment campaign. *Remote Sens.* 12, 2220. doi:10.3390/rs12142220

BIPM, (2019). *The international system of units (SI)*, 9th ed. Sèvres: BIPM.

Burggraaff, O. (2020). Biases from incorrect reflectance convolution. *Opt. Express* 28, 13801–13816. doi:10.1364/OE.391470

EUMETSAT | FRM4SOC Phase-2 (2023). EUMETSAT | FRM4SOC phase-2 [WWW document]. Available at: https://frm4soc2.eumetsat.int/ (Accessed February 17, 2023).

Feinholz, M. E., Flora, S. J., Yarbrough, M. A., Lykke, K. R., Brown, S. W., Johnson, B. C., et al. (2009). Stray light correction of the marine optical system. *J. Atmos. Ocean. Technol.* 26, 57–73. doi:10.1175/2008JTECHO597.1

Goyens, C., and Ruddick, K. (2023). Improving the standard protocol for above-water reflectance measurements: 1. Estimating effective wind speed from angular variation of sunglint. *Appl. Opt.* 62, 2442–2455. doi:10.1364/AO.481787

Hooker, S. B., Firestone, E. R., McLean, S., Sherman, J., Small, M., Lazin, G., et al. (2002). *The seventh SeaWiFS intercalibration round-robin experiment (SIRREX-7), TM-2003- 206892*, 17. Greenbelt: NASA Goddard Space Flight Center.

Hooker, S. B., and Lazin, G. (2000). *SeaWiFS postlaunch technical report series volume 8, the SeaBOARR-99 field campaign*.

JCGM 100 (2008). *Evaluation of measurement data — guide to the expression of uncertainty in measurement (GUM)*. First Edition. Available online: https://www.bipm.org/en/committees/jc/jcgm/publications.

Johnson, C., Yoon, H., Rice, J. P., and Parr, A. C. (2014). "Chapter 1.2 - principles of optical radiometry and measurement uncertainty," in *Experimental methods in the physical Sciences, optical radiometry for ocean climate measurements*. Editors G. Zibordi, C. J. Donlon, and A. C. Parr (Academic Press), 13–67. doi:10.1016/B978-0-12-417011-7.00003-9

Kostkowski, H. (1997). *Reliable spectroradiometry. Spectroradiometry consulting.*

Kuusk, J. (2011). Dark signal temperature dependence correction method for miniature spectrometer modules. *J. Sens.* 608157, 1–9. doi:10.1155/2011/608157

Li, L., Dai, C., Wu, Z., and Wang, Y. (2017). Temperature and nonlinearity correction methods for commercial CCD array spectrometers used in field (Proc. SPIE 10463, AOPC 2017: Space Optics and Earth Imaging and Space Navigation), 104631K. doi:10.1117/12.2285634

Li, L., Dai, C., Wu, Z., and Wang, Y. (2018). Temperature correction method for commercial CCD array spectrometers used in spectral radiometry measurement. *J. Phys. Conf. Ser.* 972, 012020. doi:10.1088/1742-6596/972/1/012020

Lin, J., Dall'Olmo, G., Tilstone, G. H., Brewin, R. J. W., Vabson, V., Ansko, I., et al. (2022). Derivation of uncertainty budgets for continuous above-water radiometric measurements along an Atlantic Meridional Transect. *Opt. Express* 30, 45648–45675. doi:10.1364/OE.470994

Mobley, C. D. (1999). Estimation of the remote-sensing reflectance from above-surface measurements. *Appl. Opt.* 38, 7442–7455. doi:10.1364/AO.38.007442

Mueller, J. L., Morel, A., Frouin, R., Davis, C., Arnone, R., Carder, K., et al. (2003). Ocean optics protocols for satellite Ocean color sensor validation, Revision 4. Volume III: Radiometric Measurements and Data Analysis Protocols. doi:10.25607/OBP-62

Nevas, S., Wübbeler, G., Sperling, A., Elster, C., and Teuber, A. (2012). Simultaneous correction of bandpass and stray-light effects in array spectroradiometer data. *Metrologia* 49, S43–S47. doi:10.1088/0026-1394/49/2/S43

Pacheco-Labrador, J., Ferrero, A., and Martín, M. P. (2014). Characterizing integration time and gray-level-related nonlinearities in a NMOS sensor. *Appl. Opt.* 53, 7778–7786. doi:10.1364/AO.53.007778

Price, L. L. A., Hooke, R. J., and Khazova, M. (2014). Effects of ambient temperature on the performance of CCD array spectroradiometers and practical implications for field measurements. *J. Radiol. Prot.* 34, 655–673. doi:10.1088/0952-4746/34/3/655

Pulli, T., Nevas, S., Gawhary, O. E., Berg, S. van den, Askola, J., Kärhä, P., et al. (2017). Nonlinearity characterization of array spectroradiometers for the solar UV measurements. *Appl. Opt.* 56, 3077–3086. doi:10.1364/AO.56.003077

Ruddick, K. (2023). *D-6 measurement procedure document (MPROCD).*

Ruddick, K. G., De Cauwer, V., Park, Y.-J., and Moore, G. (2006). Seaborne measurements of near infrared water-leaving reflectance: the similarity spectrum for turbid waters. *Limnol. Oceanogr.* 51, 1167–1179. doi:10.4319/lo.2006.51.2.1167

Ruddick, K. G., Voss, K., Banks, A. C., Boss, E., Castagna, A., Frouin, R., et al. (2019a). A review of protocols for fiducial reference measurements of downwelling irradiance for the validation of satellite remote sensing data over water. *Remote Sens.* 11, 1742. doi:10.3390/rs11151742

Ruddick, K. G., Voss, K., Boss, E., Castagna, A., Frouin, R., Gilerson, A., et al. (2019b). A review of protocols for fiducial reference measurements of water-leaving radiance for validation of satellite remote-sensing data over water. *Remote Sens.* 11, 2198. doi:10.3390/rs11192198

Salim, S. G. R., Fox, N. P., Theocharous, E., Sun, T., and Grattan, K. T. V. (2011). Temperature and nonlinearity corrections for a photodiode array spectrometer used in the field. *Appl. Opt.* 50, 866–875. doi:10.1364/AO.50.000866

Salim, S. G. R., Woolliams, E. R., and Fox, N. P. (2014). Calibration of a photodiode array spectrometer against the copper point. *Int. J. Thermophys.* 35, 504–515. doi:10.1007/s10765-014-1609-1

Schinke, C., Franke, M., Bothe, K., and Nevas, S. (2019). Implementation and uncertainty evaluation of spectral stray light correction by Zong's method. *Appl. Opt.* 58, 9998–10009. doi:10.1364/AO.58.009998

Sea-Bird Scientific, (2024). Specifications for HyperOCR radiometer [WWW Document]. Available at: https://www.seabird.com/hyperspectral-radiometers/

hyperocr-radiometer/family?productCategoryId=54627869935 (accessed (accessed January.31.2019).

Seckmeyer, G., Bais, A., Bernhard, G., Blumthaler, M., Drüke, S., Kiedron, P., et al. (2010). *Instruments to measure solar ultraviolet radiation Part 4: array spectroradiometers*. Geneva, Switzerland: WMO/TD No. 1538, 39pp.

Slaper, H., Reinen, H. a. J. M., Blumthaler, M., Huber, M., and Kuik, F. (1995). Comparing ground-level spectrally resolved solar UV measurements using various instruments: a technique resolving effects of wavelength shift and slit width. *Geophys. Res. Lett.* 22, 2721–2724. doi:10.1029/95GL02824

Talone, M., and Zibordi, G. (2016). Polarimetric characteristics of a class of hyperspectral radiometers. *Appl. Opt.* 55, 10092–10104. doi:10.1364/AO.55.010092

Talone, M., and Zibordi, G. (2018). Non-linear response of a class of hyper-spectral radiometers. *Metrologia* 55, 747–758. doi:10.1088/1681-7575/aadd7f

Talone, M., Zibordi, G., Ansko, I., Banks, A. C., and Kuusk, J. (2016). Stray light effects in above-water remote-sensing reflectance from hyperspectral radiometers. *Appl. Opt.* 55, 3966–3977. doi:10.1364/AO.55.003966

Talone, M., Zibordi, G., and Bialek, A. (2020). Reduction of non-linearity effects for a class of hyper-spectral radiometers. *Metrologia* 57, 025008. doi:10.1088/1681-7575/ab6277

Tilstone, G., Dall'Olmo, G., Hieronymi, M., Ruddick, K., Beck, M., Ligi, M., et al. (2020). Field intercomparison of radiometer measurements for Ocean Colour validation. *Remote Sens.* 12, 1587. doi:10.3390/rs12101587

TriOS (2019). RAMSES technische spezifikationen [WWW document]. TriOS Mess-Datentech. Available at: https://www.trios.de/ramses.html (Accessed January 31, 2019).

Vabson, V., Ansko, I., Vendt, R., and Kuusk, J. (2022). *Technical Report D12: harmonised cal/char lab guidelines, including lab protocols for FRMOCnet OCR models*.

Vabson, V., Kuusk, J., Ansko, I., Vendt, R., Alikas, K., Ruddick, K., et al. (2019a). Laboratory intercomparison of radiometers used for satellite validation in the 400–900 nm range. *Remote Sens.* 11, 1101. doi:10.3390/rs11091101

Vabson, V., Kuusk, J., Ansko, I., Vendt, R., Alikas, K., Ruddick, K., et al. (2019b). Field intercomparison of radiometers used for satellite validation in the 400–900 nm range. *Remote Sens.* 11, 1129. doi:10.3390/rs11091129

Vansteenwegen, D., Ruddick, K., Cattrijsse, A., Vanhellemont, Q., and Beck, M. (2019). The pan-and-tilt hyperspectral radiometer system (PANTHYR) for autonomous satellite validation measurements—prototype design and testing. *Remote Sens.* 11, 1360. doi:10.3390/rs11111360

Vendt, R., Vabson, V., Ansko, I., and Kuusk, J. (2021). Maapealse tugiväärtuse mõõtmine satelliitkaugseire andmete valideerimiseks. *Kaugseire Eest. 2021. Artik. Tõravere Tartu. Obs. 2021*, 10–20. lk.

Voss, K. J., and Costa, L.B. da (2016). Polarization properties of FEL lamps as applied to radiometric calibration. *Appl. Opt.* 55, 8829–8832. doi:10.1364/AO.55.008829

Xing, X., and Lagunas-Morales, J. (2018). "Laboratory results on the dependence of dark current upon environmental temperature variability for Satlantic's OCR504 radiometers," in *Optical precision manufacturing, testing, and applications. Presented at the optical precision manufacturing, testing, and applications, SPIE*. Editors J. McBride, J. Tan, S. Han, and X. Zhang (Beijing, China), 11. doi:10.1117/12.2504241

Ylianttila, L., and Schreder, J. (2005). Temperature effects of PTFE diffusers. *Opt. Mater.* 27, 1811–1814. doi:10.1016/j.optmat.2004.11.008

Ylianttila, L., Visuri, R., Huurto, L., and Jokela, K. (2005). Evaluation of a single-monochromator diode array spectroradiometer for sunbed UV-radiation measurements¶. *Photochem. Photobiol.* 81, 333–341. doi:10.1111/j.1751-1097.2005.tb00192.x

Zibordi, G. (2006). Immersion factor of in-water radiance sensors: assessment for a class of radiometers. *J. Atmos. Ocean. Technol.* 23, 302–313. doi:10.1175/JTECH1847.1

Zibordi, G., and Bulgarelli, B. (2007). Effects of cosine error in irradiance measurements from field ocean color radiometers. *Appl. Opt.* 46, 5529–5538. doi:10.1364/AO.46.005529

Zibordi, G., Hooker, S. B., Mueller, J., and Lazin, G. (2004). Characterization of the immersion factor for a series of in-water optical radiometers. *J. Atmos. Ocean. Technol.* 21, 501–514. doi:10.1175/1520-0426(2004)021<0501:COTIFF>2.0.CO;2

Zibordi, G., Talone, M., and Jankowski, L. (2017). Response to temperature of a class of *in situ* hyperspectral radiometers. *J. Atmos. Ocean. Technol.* 34, 1795–1805. doi:10.1175/JTECH-D-17-0048.1

Zibordi, G., Voss, K. J., Johnson, B. C., and Mueller, J. L. (2019). *IOCCG ocean optics and biogeochemistry protocols for Satellite Ocean Colour sensor validation*, 3.0. Dartmouth, NS, Canada: IOCCG. doi:10.25607/OBP-691

Zong, Y., Brown, S. W., Johnson, B. C., Lykke, K. R., and Ohno, Y. (2006). Simple spectral stray light correction method for array spectroradiometers. *Appl. Opt.* 45, 1111–1119. doi:10.1364/ao.45.001111

Zong, Y., Brown, S. W., Meister, G., Barnes, R. A., and Lykke, K. R. (2007). Characterization and correction of stray light in optical instruments, 67441L–67511L. doi:10.1117/12.737315

frontiers | Frontiers in Remote Sensing

TYPE Original Research
PUBLISHED 29 April 2024
DOI 10.3389/frsen.2024.1322760

Check for updates

OPEN ACCESS

EDITED BY
Quan Wang,
Shizuoka University, Japan

REVIEWED BY
Andreas Hueni,
University of Zurich, Switzerland
Xingwen Lin,
Zhejiang Normal University, China

*CORRESPONDENCE
Harry Morris,
harry.morris@npl.co.uk

RECEIVED 16 October 2023
ACCEPTED 06 February 2024
PUBLISHED 29 April 2024

CITATION
Morris H, Sinclair M, De Vis P and Bialek A (2024), Utilising LANDHYPERNET data products over a deciduous broadleaf forest to validate Sentinel-2 and Landsat surface reflectance products. *Front. Remote Sens.* 5:1322760. doi: 10.3389/frsen.2024.1322760

COPYRIGHT
© 2024 Morris, Sinclair, De Vis and Bialek. This is an open-access article distributed under the terms of the Creative Commons Attribution License (CC BY). The use, distribution or reproduction in other forums is permitted, provided the original author(s) and the copyright owner(s) are credited and that the original publication in this journal is cited, in accordance with accepted academic practice. No use, distribution or reproduction is permitted which does not comply with these terms.

Utilising LANDHYPERNET data products over a deciduous broadleaf forest to validate Sentinel-2 and Landsat surface reflectance products

Harry Morris*, Morven Sinclair, Pieter De Vis and Agnieszka Bialek

Climate and Earth Observation, National Physical Laboratory, Teddington, United Kingdom

This paper demonstrates the use of a novel, autonomous hyperspectral surface reflectance data collected at Wytham Woods, United Kingdom (WWUK) as part of the LANDHYPERNET network for the validation of multispectral data from Sentinel-2, Landsat 8 and Landsat 9. The deployment of the HYPSTAR instrument at the site and the corresponding quality control of the data products is described. In addition, a methodology based upon metrological principles is outlined showing the propagation of uncertainties from the LANDHYPERNET and satellite data products to enable conformity testing of the satellite products using the satellite mission requirements. A total of 9 matchups are found for satellite validation at the site, where there is a cloud-free satellite scene and a corresponding LANDHYPERNET sequence, which has passed all quality checks, within two hours of the overpass. An analysis of the impact of the spatial variability of the site is presented and can account for up to 40% of the uncertainty associated with the *in-situ* surface reflectance data. There is no systematic bias in the Bottom-Of-Atmosphere reflectance data obtained from the LANDHYPERNET data in comparison to the satellite data. In the best case, differences of less than 2% are found for certain spectral bands. However, in the worst cases, relatively large differences are found which exceed 100%, this is affected by the relatively low reflectance values found in the visible bands. These differences could be caused by the spatial and temporal mismatch between the *in-situ* and satellite measurement, or due to shadowing caused by the flux tower. Further data quality control and assurance is needed to best choose data sets suitable for satellite validation. Incorporating a Bidirectional Reflectance Distribution Function model into the processing chain for the forest canopy is recommended. Overall, although there are areas to further characterise, the site provides a useful benchmark for which to develop techniques for validation of satellite surface reflectance products over a challenging environment.

KEYWORDS

LANDHYPERNET, HYPERNETS, hyperspectral, validation, surface reflectance, uncertainty, fiducial reference measurement, earth observation

1 Introduction

Data from Earth Observation (EO) satellites are increasingly being used for commercial and scientific purposes. Long-term time series of this data are being utilised to develop records of environmental change (Fensholt et al., 2009; Yang et al., 2013). Users are combining data sets from multiple satellites to either increase the data coverage or extend the time series beyond the operational range of a single satellite (Li and Roy, 2017; Claverie et al., 2018). Although pre-launch calibration of the instruments is performed for many satellite missions, ongoing validation on their products performance is needed against independent sources to provide users with the confidence in the quality of the data products to ensure performance and remove satellite degradation effects, which change characteristics after launch and are not captured by the pre-flight calibration efforts (Justice et al., 2000). The main satellite-derived products which are used as inputs for terrestrial monitoring are the Bottom-Of-Atmosphere (BOA) products, also referred to as Surface Reflectance (SR) products. BOA products are generated by applying Atmospheric Correction (AC) algorithms from the Top-Of-Atmosphere (TOA) products, removing the influence of the atmosphere to the TOA signal (Liang et al., 2012). AC algorithms introduce more uncertainties into the SR products, which in the visible and near infra-red (VNIR) and short wave infra-red (SWIR) can be mainly attributed to the uncertainties associated with the aerosol and water vapour optical properties (Li et al., 2018). Currently European Space Agency (ESA) SR products do not have per-pixel uncertainty estimates, which can be considered a key limitation in subsequently derived bio-geophysical retrieval algorithms (Niro et al., 2021). Presently, there are no global networks systematically collecting ground-data for the validation of surface reflectance products over land.

There is a long history of using *ad hoc* campaigns, ground and airborne measurements for the validation of EO products (Badawi et al., 2019). However, there are limitations to *ad hoc* campaign validation approaches including inclement weather conditions, time and cost constraints and personal availability which minimises the number of validation matchups. Moreover, attempts to validate multiple sensors with different overpass times and dates can be difficult to achieve using campaign validation models (Malthus et al., 2019). Recent advances in automated techniques have been developed to overcome some of these challenges, whilst maintaining similar results to those obtained from traditional validation campaigns. One such system which has been extensively used for the vicarious calibration to TOA products is the Radiometric Calibration Network (RadCalNet) (Banks et al., 2017; Bouvet et al., 2019; Jing et al., 2019), which was developed by the RadCalNet working group under the Committee on Earth Observation Satellites (CEOS) Working Group on Calibration and Validation (WGCV) and the Infrared Visible Optical Sensors (IVOS). However, there are still significant challenges and gaps which affect our ability to assess the radiometric quality of BOA products such as the limited geographical coverage of existing validation datasets and temporal and spatial mismatches between the reference datasets and the satellite data products (Niro et al., 2021).

Alternatively, indirect validation of SR products can be performed, such as the joint ESA-NASA Atmospheric Correction Inter-Comparison Exercise (ACIX) (Doxani et al., 2018) utilising the AERONET stations (Holben et al., 1998), to obtain a globally representative set of surface and climatological conditions.

The Horizon 2020 LANDHYPERNET project aimed to fill the gap in the validation of SR products by developing a network of land and water sites with automated, hyperspectral platforms which can make continuous measurements over a variety of surface types (Goyens et al., 2021). As part of this project, 9 test sites were deployed and formed a LANDHYPERNET network. The sites are: DEMMIN, Germany (DEGE), Wytham Woods, United Kingdom (WWUK), Princess Elisabeth, Antarctica (PEAN), ATB, Germany (ATGE), Gobabeb, Namibia (GHNA), IFEVA, Argentina (IFAR), Järvselja, Estonia (JAES), Tõrravere, Estonia (TOES) and Barrax, Spain (BASP). They include various land cover types such as deciduous broadleaf forest, cropland, bare soil, snow and ice, desert, grassland and needleleaf forest. All sites are equipped with the Hyperspectral Pointable System for Terrestrial and Aquatic Radiometry, (HYPSTAR®) instrument deployed as part of the LANDHYPERNET project. This paper describes the deployment of the HYPSTAR® instrument at the Wytham Woods, United Kingdom site. An overview of the LANDHYPERNET and satellite-derived SR products are presented. Then, the spatial variability of the site and validation results for two different high-resolution satellite missions: Sentinel-2 (S2), Landsat-8 and Landsat-9 (Landsat) are presented. Finally, the suitability of the site for use as a calibration and validation site for surface reflectance products and future steps are discussed.

2 Materials and methods

2.1 WWUK

The Wytham Woods United Kingdom (WWUK) site is a site of special scientific interest (SSSI) and has a long history of scientific research, including for the validation of satellite products (Brown et al., 2021), understanding the dynamics of canopy bio-physical properties (Brown et al., 2020) and carbon sequestration (Calders et al., 2022). Being a SSSI, it is a protected area in the United Kingdom and is representative of its natural fauna and flora. The site is managed by the University of Oxford and the area surrounding the flux tower is primarily ancient seminatural woodlands with the main species being ash (*Fraxinus excelsior*), beech (*Fagus sylvatica*), hazel (*Corylus avellana*), oak (*Quercus robur*) and sycamore (*Acer pseudoplatanus*) (Figure 1 left). The HYPSTAR® extended range (-XR)[1] instrument was deployed at the top of a flux tower (N 51.77503°, W1.33906°) in November 2021, at a height of 28 m above the ground, on an extended 6 m horizontal boom to minimise the impact of the tower on the field of view (Figure 1 right). Data is collected every 30 min between 9 a.m. and 6 p.m. local time (UTC+0 in winter months and UTC+1 in British Summer Time) between viewing zenith angles of 0–30° and viewing azimuth angles of 83, 98, 113, 263, 278 and 293° corresponding to the typical viewing geometry of satellites on sun-synchronous orbits.

1 https://hypstar.eu/

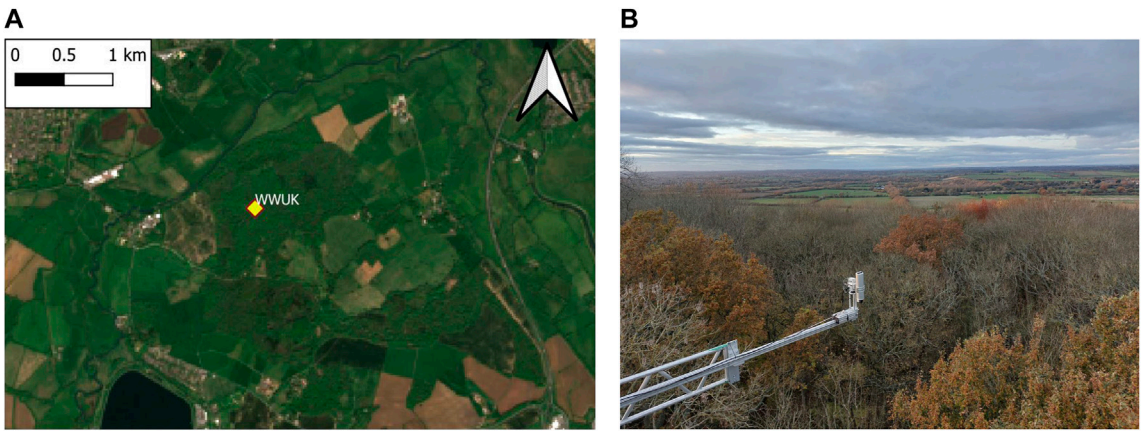


FIGURE 1
Wytham Woods United Kingdom (WWUK) site location **(A)** and mast **(B)**. Contains modified Copernicus Sentinel data (2022) obtained from Copernicus Data Space Ecosystem.

The deployment of the instrument was not optimal, being on the North facing side of the flux tower due to local topography and the presence of other instruments on the flux tower.

The site is highly variable due to the annual phenological cycle of the vegetation changing the surface reflectance values and the structure of the canopy over the growing season. Moreover, diurnal variability in the surface reflectance is caused by variable shadowing affecting the site in different illumination conditions. Shadowing, caused by both the flux tower and the trunks of the tree, particularly impacted the sequences obtained in leaf-off conditions between mid-October and mid-April.

2.2 LANDHYPERNET data

The HYPSTAR® XR instrument has been deployed as part of the LANDHYPERNET network. The instrument contains two modules; the first collecting visible and near-infrared spectra (VNIR, 380–1,000 nm) and the second collecting shortwave-infrared spectra (SWIR) up to 1700 nm with a 5° FOV for radiance measurements and 180° for irradiance measurements. The spectral sampling is 0.5 nm in the VNIR and 3 nm in the SWIR, with a spectral resolution of 3 nm and 10 nm respectively. All sequences have been processed using the HYPERNET_PROCESSOR (Goyens et al., 2021) (De Vis et al., in prep) which automatically generates data products at different levels from raw counts (L0), up to surface reflectance (L2A) values for each angle by combining the radiance and irradiance measurements from each sequence. The surface reflectance product is defined as the Hemispherical-directional Reflectance Factor (HDRF) (Schaepman-Strub et al., 2006), which can be used as a proxy to measured Hemispherical-conical Reflectance Factor (HCRF), under the assumption that the relatively small instrument FOV (5°) and the small physical size of the fore optic allows us to make this approximation. Each data product comes with random and systematic uncertainties propagated using the CoMet toolkit (www.comet-toolkit.org) which applies a rigorous metrological approach (GUM, 2008).

A detailed description of the processing steps and the uncertainty propagation performed in the HYPERNET_PROCESSOR can be found in De Vis et al. (in prep) or in the HYPERNET_PROCESSOR documentation[2]. In total 5,572 sequences have been collected since the instrument has been deployed up to the 31 August 2023, of which 4,254 sequences have been processed to surface reflectance products (L2A) without any issues.

In addition to the standard checks in the HYPERNET_PROCESSOR two additional screening procedures are developed to remove outliers and only supply the best quality data suitable for satellite validation. These two additional checks are firstly that the spectrum matches a typical vegetation spectrum and the sigma-clipping approach, both are described in detail below. Only data between April and October, corresponding to the leaf on period, are considered to be checked against a nominal vegetation spectrum. Spectra need to pass three tests: that there is a peak in the green portion of the visible wavebands (560 nm), that a red edge is detected and that their Normalized Difference Vegetation Index (NDVI) exceeds 0.42. The threshold of NDVI >0.42 was selected as it allowed for consistency between spectrum from the HYPSTAR instrument corresponding to vegetation and pixels classified as vegetation in the scene classification layer of S2 SR products (Main-Knorn et al., 2017).

After the vegetation quality flags are applied and spectra that failed any of the three tests have been removed, a sigma-clipping method is used to remove remaining outliers. First reflectances are extracted in separate 2 hour windows throughout the day (to account for BRDF differences due to different solar position) for 4 different wavelengths (500, 900, 1,100 and 1,600 nm). Outliers in these reflectances are then identified by iteratively calculating the mean reflectance trend with time (by binning the data per maximum 30 data points), calculating the standard deviation from this trend, and masking any data that is more than 3 standard deviations away from the trend. This process is repeated on the unmasked data until

2 https://LANDHYPERNET-processor.readthedocs.io/en/latest/

the standard deviation does not vary by more than 5% between two iterations. The masks for the 4 different wavelengths are then combined (keeping only measurements for which none of the 4 wavelengths is an outlier). The reflectances and associated uncertainties for any masked series (i.e., a geometry that is masked either by the sigma-clipping procedure or from the masks of the HYPERNETS_processor) are replaced by NaNs. Any sequence that has more than half of its series masked is removed entirely. After this second screening procedure is applied 396 sequences remain. This data is open access and the first version available (Morris et al., 2023)[3] which contains data from April 2022–April 2023. Additional data files from May–August 2023 have been used in this study which are not currently included in the zenodo dataset but will be included in the next release.

2.3 Satellite data

2.3.1 Sentinel-2

The Sentinel-2 (S2) Copernicus mission is a high spatial resolution (10 m–60 m), multi-spectral optical imaging mission. Two sun-synchronous satellites, S2A and S2B, launched in June 2015 and March 2017 respectively, are phased at 180° to each other, providing a revisit time of 5 days (Drusch et al., 2012). Onboard these satellites is a multispectral instrument (MSI), which has 13 spectral bands covering the visible, infrared and short wave infrared. Surface reflectance data, which corresponds to the directional hemispherical reflectance at a surface (Schaepman-Strub et al., 2006), is provided to users in the Level-2A products which have been generated using the atmospheric correction processor Sen2Cor (Main-Knorn et al., 2017).

There have been a limited number of studies which have attempted to evaluate the performance of S2 Level-2A products (Origo et al., 2020; Pancorbo et al., 2021). Systematic evaluation of the performance of S2 SR products is conducted by the S2 Mission Performance Cluster (S2MPC) (S2MPC, 2023). Total uncertainty of SR retrieval with Sen2Cor was estimated as 7% (k = 1) over bright RadCalNet sites and 17% over bare soil and meadow sites in Germany (Pflug et al., 2022). Utilising the data collected by Pflug et al., the S2MPC found that 79% of retrieved SR values are within the mission uncertainty requirement goals of S2, (0.05 * reflectance value +0.005). The conventional S2 Level-2A product does not come with any associated uncertainty values. However, a recently released tool, the S2L2 Radiometric Uncertainty Tool (RUT) which utilises a multivariate MonteCarlo Model (MCM) to derive uncertainty and spectral correlation information for a S2 region of interest, has been used in this study to obtain uncertainties, using the standard parameters provided (Gorroño et al., 2023).

All available S2 L2A surface reflectance products and their corresponding top of atmosphere L1C products, from April 2022 to August 2023, which have been processed using Sen2cor version 4.0.0 (Main-Knorn et al., 2017), were downloaded from the Copernicus Open Access Hub (https://scihub.copernicus.eu/).

3 https://doi.org/10.5281/zenodo.7962557

2.3.2 Landsat 8/9

Landsat 8 (L8) and Landsat 9 (L9) are the most recently launched missions (February 2013 and September 2021 respectively) of the NASA/USGS Landsat program, which has been operational since the 1970s (Wulder et al., 2019). Both satellites have two instruments onboard: the Operational Land Imager (OLI) and the Thermal Infrared Sensor (TIRS). OLI provides 15–30 m imagery in 9 multispectral bands covering the visible, near infrared and shortwave infrared. TIRS measures land surface temperature in two infrared bands. Both satellites orbit in a sun-synchronous, near-polar orbit (98.2° inclination) with a 16-day repeat cycle (Markham et al., 2015; Masek et al., 2020). Validation of L8 and L9 L2 products has found differences of 3.3%–10% in comparison to *in-situ* datasets over a number of land cover types (Wulder et al., 2019; Teixeira Pinto et al., 2020; Eon et al., 2023). The current radiometric calibration accuracy and stability mission requirement targets are within 5% (k = 1) absolute spectral radiance; within 3% top-of-atmosphere reflectance and within 2% thermal infrared spectral radiance.

The Landsat 8/9 data was extracted using the cloud based platform of Google Earth Engine (Gorelick et al., 2017). For both satellites the corresponding Collection 2 Level-2 Tier 1 surface reflectance products were used (L8[4], L9[5]). The surface reflectance products are generated using the Land Surface Reflectance Code (LaSRC), version 1.5.0 (Vermote et al., 2016).

2.3.3 Understanding the spatial heterogeneity of the site

One of the areas of interest in this study has been to assess the representativeness of the region of interest (ROI) measured by the HYPSTAR®XR instrument in comparison to the pixel extraction from the satellite. As previously mentioned, variability in the forest canopy can be caused by a variety of factors including different tree species, an undulating surface at the top of canopy, hot spots and shadowing.

The uncertainty associated with the spatial variability of the site at the HYPSTAR ROI scale was quantified using hyperspectral airborne data captured over the site on the 17 July 2021. This data was captured by the University of Zurich (UZH) Airborne Research Facility for Earth System (ARES) using the Airborne Visible/Infrared Imaging Spectrometer Next-Generation (AVIRIS-NG) instrument developed by the National Aeronautics and Space Administration (NASA) Jet Propulsion Laboratory (JPL). The data covered the spectral range of 380–2,510 nm with a 5 nm full width half maximum per band and a spatial resolution of 3 m. This data was radiometrically, atmospherically and geometrically corrected in house by JPL (Thompson et al., 2018; Chapman et al., 2019).

For each of the corresponding extracted ROIs from the satellite data the uncertainty associated with the spatial variability of the site at the HYPSTAR measurement size is determined from the standard

4 https://developers.google.com/earth-engine/datasets/catalog/LANDSAT_LC08_C02_T1_L2

5 https://developers.google.com/earth-engine/datasets/catalog/LANDSAT_LC09_C02_T1_L2

deviation in the spread of the reflectance values per band. The spatial uncertainty is first interpolated to 1 nm bands then band integrated using the spectral response function of the HYPSTAR bands, before being propagated into the final uncertainty budget for the HYPSTAR measurements.

2.3.4 Identifying matchups between WWUK LANDHYPERNETS and satellite data

Once the satellite data has been downloaded, a python script identifies matchups to the nearest LANDHYPERNET sequence. A match-up is only considered, if there is a corresponding sequence within 2 hours of a cloud-free satellite overpass. In the case of multiple sequences, the sequences with the smallest difference in time is selected. As each sequence contains multiple reflectance scans taken at different viewing geometries, a matching procedure was used based upon the VAA of the satellite matchup and using the maximum VZA (30°), to maximise the top of canopy area sampled by the HYPSTAR instrument.

The hyperspectral data from the HYPSTAR instrument was integrated into the multispectral bands of each satellite using the specific relative spectral response (RSR) function of the sensor. This was obtained for both S2A and S2B[6] as well as for OLI L8 (Barsi et al., 2014) and OLI L9 (Barsi et al., 2019).

Frtom each S2 scene, a 5 × 5 pixel extraction centered on the flux tower was acquired, corresponding to a 100 m × 100 m ROI. For Landsat scenes, a 3 × 3 pixel extraction was acquired corresponding to a 90 m × 90 m ROI. Pixels were flagged in each product using the corresponding quality flags provided with the products to remove pixels affected by cloud, cirrus cloud, no-data, saturated, degraded or otherwise contaminated pixels. For Landsat matchups, the mean and the standard deviation of all valid pixels per band was taken as the mean and spatial uncertainty associated with the extraction. For Sentinel-2 matchups, the average value was calculated as the mean of all valid pixels, whereas the uncertainty was calculated using the S2L2 RUT using its default parameters and running for 250 iterations of the MonteCarlo Model.

There were 32 S2 scenes available over the site during this study. Of these, 13 were affected by cloud cover and an additional 15 had no corresponding sequence that had passed all quality checks. There are 4 good quality S2 matchups found for the site over the two growing seasons. For Landsat 8 and 9 there are 62 potential matchups for this study. 45 of these are removed due to cloud cover and an additional 13 have no corresponding sequence. This leaves 5 good quality Landsat matchups for the site. Therefore in total there are 9 matchups between LANDHYPERNET and satellites used in this study. Matchups from the summer of 2022 were affected by periods of downtime, as the instrument is a prototype and needed maintenance, additionally, the summer of 2023 has been unseasonably cloudy affecting the majority of the matchups. Although, the current number of matchups is lower than expected for the site, in the future we hope to be able to provide greater statistics from this site. Details of all of the matchups can be found in Table 1, including time of observations, viewing and solar geometries. Plots for every matchup are given in the Supplementary Appendix S1.

$$bias = \frac{\rho_{\text{sat}}}{\rho_{\text{band,LANDHYPERNET}}} - 1 \quad (1)$$

For each match-up the reflectances from the LANDHYPERNET sequence can be compared directly to the satellite observations. The bias is calculated using Eq. 1 as the uncertainties are represented as relative in this study. Where $\rho_{\text{band,LANDHYPERNET}}$ are the relevant satellites band-integrated BOA reflectances and ρ_{sat} are the observed BOA satellite reflectances. In the visible parts of the spectrum, reflectance values are very low over the dark vegetated site and therefore representing bias as a ratio leads to a lack of precision. Therefore, for these bands the results are compared in absolute reflectances in addition to relative signals. Each bias measurement comes with an associated uncertainty calculated using Eq. 2

$$u_{\text{total}} = \sqrt{u_{sat}^2 + u_{LANDHYPERNET}^2 + u_{comp}^2} \quad (2)$$

where u_{sat} is the uncertainty associated with the satellite observation, $u_{LANDHYPERNET}$ is the measurement uncertainty associated with the LANDHYPERNETS data and u_{comp} is the comparison uncertainty accounting for differences in the measurements between the satellite and the HYPSTAR. The spatial variability of the site derived from the airborne data is used as the lower limit estimator of u_{comp} in this study. This is likely to be an underestimation of u_{comp} as it does not take into account other factors such as the BRDF of the canopy, shadowing and a mixture of the above and below canopy reflectance, pointing errors in the HYPSTAR and changes in both the viewing and solar geometries within the match-up window (Widlowski et al., 2015; Nevalainen et al., 2017). As the data from the LANDHYPERNET instrument and the satellite data has an associated uncertainty, conformity testing of the satellite SR products is performed using the mission requirements to define the upper and lower limits of the tolerance intervals. For each matchup the absolute difference between the WWUK data and the satellite data is used for evaluation. This difference also has an associated uncertainty derived using Eq. 2, accounting for the uncertainty associated with the satellite and LANDHYPERNET data and the comparison uncertainty. A measurement is conforming if the difference combined with the total uncertainty (u_{total}), is within the mission requirements. Shown in Eq. 3 for Sentinel-2 at $k = 1$. A measurement can also be inconclusive or nonconforming if one or both of the requirements are not met (ISO, 2003).

$$\left|\rho_{sat} - \rho_{band,LANDHYPERNETS}\right| + u_{total} \leq 0.05\,\rho_{band,LANDHYPERNETS} + 0.05$$

and

$$\left|\rho_{sat} - \rho_{band,LANDHYPERNETS}\right| - u_{total} \geq -0.05\,\rho_{band,LANDHYPERNETS} - 0.05 \quad (3)$$

3 Results

3.1 Spatial variability

The heterogeneity of the site within a satellite ROI extraction can be seen in Figure 2, which shows the average airborne reflectance spectra (red data series) and the variability of the spectra within a

6 https://sentinels.copernicus.eu/web/sentinel/user-guides/sentinel-2-msi/document-library/-/asset_publisher/Wk0TKajiISaR/content/sentinel-2a-spectral-responses

TABLE 1 Details of the matchups between the observations for WWUK with Landsat and Sentinel satellites. The viewing and solar zenith and azimuth angles are measured clockwise from North.

Satellite	Date	Satellite observation (UTC)	WWUK observation (UTC)	VZA satellite, HYP* (°)	VAA satellite, HYP* (°)	SZA satellite, HYP* (°)	SAA satellite, HYP* (°)
L8	14/05/2022	10:58:29	11:00:37	1.9, *30.0	131.6, *113.0	35.4, *35.0	153.5, *155.8
L8	12/08/2023	11:04:37	11:00:42	7.3, *30.0	280.6, *278.0	41.4, *39.2	155.9, *153.7
L9	22/05/2022	10:58:05	11:00:38	1.7, *30.0	133.5, *113.0	33.7, *33.3	152.3, *154.9
L9	26/08/2022	10:58:48	11:40:38	1.9, *30.0	129.8, *113.0	43.7, *44.7	155.3, *150.5
L9	20/08/2023	11:04:33	11:00:38	7.3, *30.0	280.6, *278.0	41.4, *41.5	155.9, *155.3
S2A	26/04/2022	11:06:31	11:32:43	3.6, *30.0	126.6, *113.0	39.3, *38.5	162.1, *169.8
S2A	16/10/2022	11:21:21	09:40:42	10.1, *30.0	295.3, *293.0	61.0, *66.57	173.2, *145.4
S2A	22/08/2023	11:21:21	11:00:37	10.1, *30.0	295.2, *293.0	41.0, *35.0	164.4, *156.8
S2B	14/05/2022	11:21:09	11:00:37	10.1, *30.0	294.6, *293.0	33.8, *34.9	165.0, *156.4

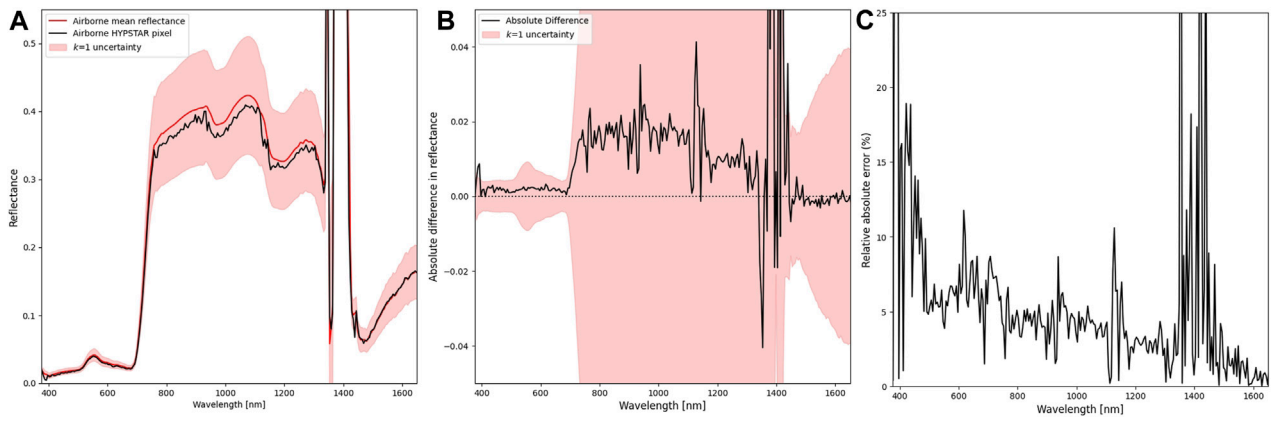


FIGURE 2
(A) Reflectance profiles for the central pixel and the ROI average with the standard deviation (k = 1) of the ROI plotted. **(B)** The absolute difference per wavelength between the ROI average and the central pixel, with the standard deviation (k = 1) of the ROI plotted. **(C)** The spectral relative absolute error (RAE) between the central and ROI spectra.

100 m × 100 m area around the flux tower (red shaded area) and the reflectance spectra from the exact pixel of the deployment of the HYPSTAR instrument from the airborne data (black data series). The spatial variability is expressed as k = 1 uncertainty and derived as the standard deviation of all pixels in ROI of airborne data. There is a slight underestimation in the HYPSTAR pixel in the NIR and SWIR bands in comparison to the average for the ROI. For all bands, this difference is less than the variability of the spectra within the ROI. The absolute difference between the two spectra in the visible range is less than 0.01, increasing to between 0.01 and 0.04 in 800–1,400 nm (Figure 2).

The Spectral Relative Absolute Error (RAE) was used to evaluate the representativeness of the airborne spectral reflectance profile of the pixel where the HYPSTAR instrument is deployed in comparison to the ROI average spectral reflectance profile (Xu et al., 2016). A smaller RAE value means the location of the HYPSTAR instrument is representative of the ROI at the spatial scale of the airborne data (Hakuba et al., 2013). In Figure 2 it can be seen that the location of the HYPSTAR instrument is representative of the overall 100 m × 100 m ROI. In the visible and NIR bands a near perfect relationship is seen with an RAE less than 20% at 400 nm and decreasing to less than 10% from 500 nm onwards. There are a few increases in the RAE values corresponding to bands affected by aerosols and water vapour bands in the atmosphere which would affect the airborne data.

The relative uncertainty associated with the airborne spectra at different spatial resolutions was calculated as the standard deviation of the airborne spectra divided by the mean airborne spectra for the ROI size. The relative variability was highest in the blue bands reaching 40% variability and averaging 20% variability for all wavelengths between 500–1,300 nm at k = 1 coverage factor (Figure 3). With an increase within the red-edge portion of tree species present at the site. The relative uncertainty increased as the size of the region of interest increased up to the decametric scale of the satellite data as shown in Figure 3. At any scale greater than this the uncertainties stabilised as the variability between the tree species

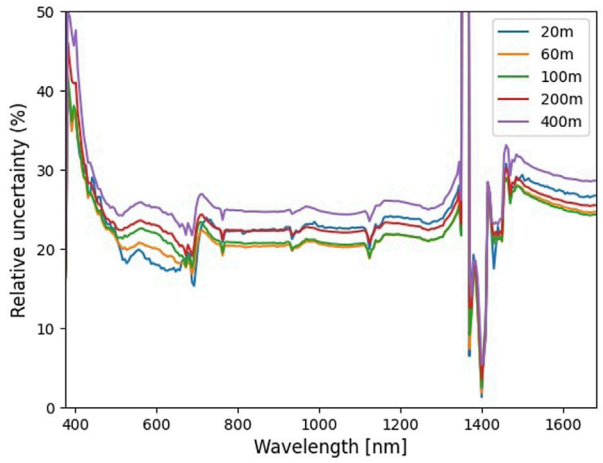


FIGURE 3
The relative spatial variability in the airborne data with k = 1 uncertainty for different spatial scales around the flux tower.

and gaps in the canopy become less predominant. This pattern was found for all wavelengths across the visible, NIR and SWIR bands.

3.2 S2 comparison

Observations of the BOA reflectance from S2 and from the corresponding LANDHYPERNET sequences show a similar spatial pattern for all of the matchups, whereby the WWUK data has a similar spectral profile to the S2 files, falling within the LANDHYPERNET uncertainties. In the visible wavelengths, both SR products have very low reflectances varying between 0.02–0.1. In the NIR and SWIR range, both products increase to the region of 0.35–0.5 (Figure 4).

For the WWUK data products, two uncertainties are included accounting for the measurement uncertainty and also the spatial representativeness uncertainty, corresponding to the grey and orange shaded areas respectively. For each of the S2 bands the bias between the band-integrated WWUK data and the S2 bands has been calculated and plotted in the figures as a percentage. In the matchup from the 26 April 2022 shown in Figure 4, B01 has the greatest relative bias, at 27%. In absolute terms, this difference is 0.0071 which slightly exceeds the mission requirements of 0.0066 for the low reflectance. For the bands in the visible region, the relative bias ranges between −17.6% and 27.2%. The best agreement is found in bands B06, B07, B08 and B8A, with differences of less than 2% relative bias between the two datasets. Overall, these bands have the lowest relative biases across all of the S2 matchups. For all of the matchups the absolute biases between the LANDHYPERNETS data and the S2 extractions are less than the total combined uncertainty.

Additionally, an assessment into the temporal variability of the matchups between S2 and WWUK are presented. The percentage difference (bias) for all matchups are shown in Table 2, for all bands, there is a marked increase in the bias between the WWUK and S2 products from 2022 to 2023. This increasing bias between the two data sets could be caused by a number of factors such as a change in the vegetation conditions or degradation of the HYPSTAR via a build up of dust or dirt on the fore optics. However, to truly characterise this phenomenon, more matchups with satellite SR products over the next growing season are needed.

The uncertainties in the S2 BOA reflectance products derived from the S2L2RUT tool are presented in Table 3. The tool gives the uncertainties at coverage k = 1. The lowest relative uncertainty (in the range of 3%–5%) occurs in the bands in the NIR and SWIR. The visible bands have higher uncertainties, ranging from 25% to 60%, for all S2 scenes. This is due to the relatively low reflectance values in these bands. These are represented in Figure 4 as error bars on the S2 values.

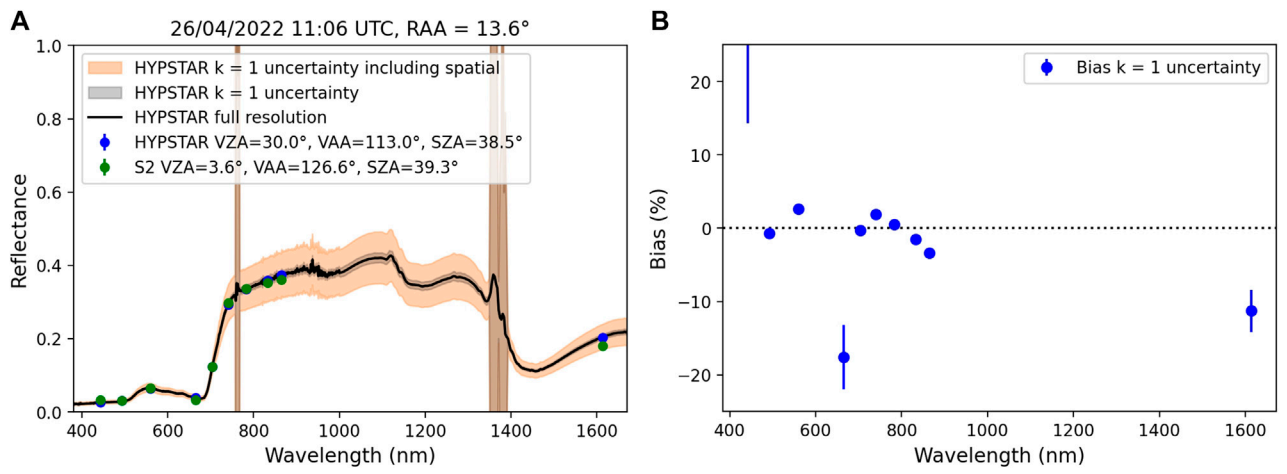


FIGURE 4
(A) The full resolution and band-integrated LANDHYPERNET data compare to Sentinel-2 data for the WWUK matchup on 26 April 2022. The two shaded areas represent the uncertainty (k = 1) of the LANDHYPERNET data only considering the instrument uncertainty (grey) or the instrument and the spatial representativeness uncertainty of the measurement (orange). The uncertainty bars on the S2 data are derived using the S2L2RUT tool. **(B)** The percentage difference (bias) between the band-integrated LANDHYPERNET data and the S2 data. A few points are off the graph due to the absolute values in reflectance being very small.

TABLE 2 The relative bias (%) per S2 band for all matchups used in this study.

Date	B01 (%)	B02 (%)	B03 (%)	B04 (%)	B05 (%)	B06 (%)	B07 (%)	B08 (%)	B8A (%)	B11 (%)
26/04/2022	27.2	−0.7	2.7	−17.6	−0.3	1.9	0.5	−1.5	−11.3	−3.4
14/05/2022	93.5	114.0	47.6	87.0	49.8	17.5	12.1	10.8	20.8	8.7
16/10/2022	−32.5	12.3	60.0	70.2	84.8	0.3	−9.0	−8.6	6.0	−8.5
22/08/2023	93.2	92.1	44.9	39.5	24.6	1.4	−1.7	15.9	−18.2	−7.4

TABLE 3 The uncertainty (k = 1) (%) associated per band for the S2 data derived from the S2L2RUT tool.

Date	B01 (%)	B02 (%)	B03 (%)	B04 (%)	B05 (%)	B06 (%)	B07 (%)	B08 (%)	B8A (%)	B11 (%)
26/04/2022	39.1	27.5	11.8	16	4.7	3.6	3.4	3.2	3.7	3.5
14/05/2022	54.8	29.2	10.7	18.9	4.8	3.5	3.3	3.3	3.8	3.4
16/10/2022	163.3	69.5	31.3	36.5	10.2	4.2	3.7	3.3	4.1	3.9
22/08/2023	44.8	26.55	16.7	19.6	8.1	3.8	3.75	3.7	3.9	3.9

The performance of the matchups against the mission requirements for S2 are shown in Figure 6 left. Overall, there is good agreement with the mission requirements for all bands, with an overall bias of - 0.01 in the S2 data. However, for all bands except Band 5 (704.1 nm), which has two non-conforming measurements, all measurements are inconclusive when assessing their conformity in comparison to the S2 mission requirements. As the absolute difference falls within the mission requirements and agrees within the combined uncertainties, there is no evidence that the S2 mission requirements are not being met. However, further work on reducing the comparison contributions towards the combined uncertainty would improve the conformity results from the analysis.

Overall, the results are similar to other validation results which found an absolute bias of 0.005 ± 0.02 for validation sites over much brighter and homogeneous surfaces (Pflug et al., 2022).

3.3 Landsat comparison

A comparison of Landsat SR and the corresponding LANDHYPERNET sequence from the 20 August 2023 is shown in Figure 5. In this example, there is relatively good agreement between the BOA reflectance from the two products with an underestimation (where Landsat reflectance is less than the LANDHYPERNETS) of less than 10% for B03 and B04. For all Landsat matchups there was an overestimation in B01 and B02, however these are reasonably small in absolute terms. Moreover, the agreement between the LANDHYPERNET data and Landsat was consistently worse than for S2, with significant differences in the NIR bands. This may suggest that the matchup approach adopted in this study, selecting the corresponding scan from a VZA of 30°, may need a BRDF correction implemented to minimise the different in VZA between the two datasets.

Finally, the overall performance of the matchups against the mission requirements are presented in Figure 6 right. For all of the bands, none of the measurements from the matchups are conforming to the mission requirements. However, this is partially due to the dominance of the comparison uncertainties in the total uncertainty budget. Overall, the performance is worse for Landsat than S2 with a higher bias of 0.04 from the HYPERNETS data in comparison to the Landsat data. In addition, there is a larger spread in the results, which can be seen in Band 5 (865.0 nm), with matchups both over and underestimating the reflectance in comparison to the satellite data. These results are similar, to those of Eon et al. (2023) which found a difference of 2% in the VNIR and 5%–8% in the SWIR region between UAV and Landsat SR products when performing SR validation over desert sites.

4 Discussions

The results presented in the previous section indicate that in its current set up, the WWUK site is suitable for use as a validation site for surface reflectance. However, as the site is operational for longer it will develop the understanding of the spatial variability at the site. There is no systematic bias between the WWUK data and the satellite data. As discussed in Section 2.1 the instrument deployment was compromised due to the presence of other instruments at the ideal location upon the flux tower. Additionally, as the instrument is deployed facing North, it is quite likely that the shadow from the structure of the flux tower is influencing the upwelling radiance measurements taken from the measurement area of the instrument, an example of which can be seen in Figure 7 as the shadow moves across the measurement area across the day. There is a large variability in the surface reflectance measurements obtained by the instrument for a particular VAA depending on the VZA as demonstrated in Figure 8. As the VZA increases the area of the top of canopy being measured will increase, with a lower gap fraction obtained at higher VZA, minimising the area of the understory being measured.

As shown in Figure 8 measurements at 30° VZA do have the highest reflectance values. However, for measurements approaching

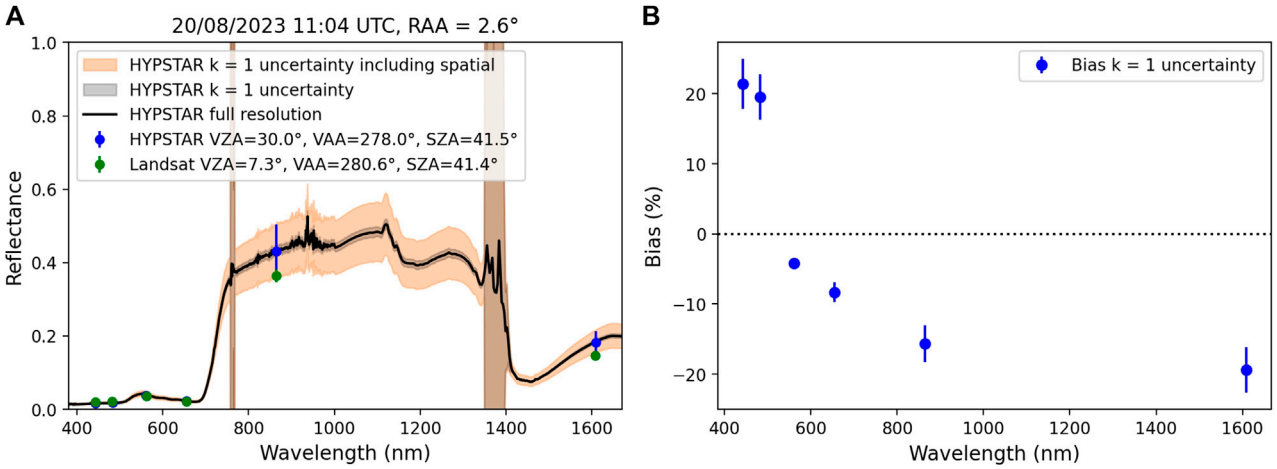


FIGURE 5
(A) The full resolution and band-integrated LANDHYPERNET data compare to Landsat data for the WWUK matchup on 20 August 2023. The two shaded areas represent the uncertainty (k = 1) of the LANDHYPERNET data only considering the instrument uncertainty (grey) or the instrument and the spatial representativeness uncertainty of the measurement (orange). The uncertainty bars on the Landsat data correspond to the standard deviation of the reflectances within the ROI. **(B)** The percentage difference (bias) between the band-integrated LANDHYPERNET data and the Landsat data. The error bars on the differences are derived using Eq. 2.

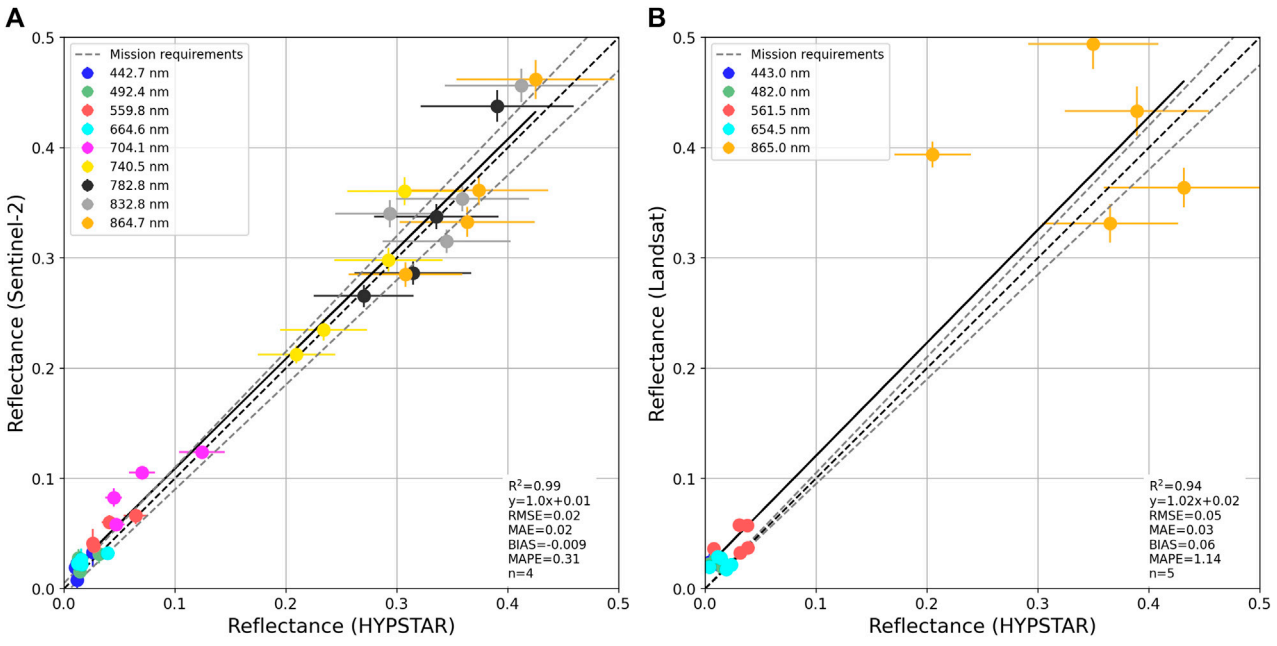


FIGURE 6
Evaluation of **(A)** S2 and **(B)** Landsat SR products against LANDHYPERNET products. The black dashed line represents a 1:1 relationship, the grey dashed lines represent the corresponding satellite mission requirements and the black solid line is the line of best fit between the WWUK data and the satellite matchups. The error bars on the plots correspond to the (k = 1) uncertainty associated with the LANDHYPERNET and satellite data.

nadir, there is no consistent pattern between the days, suggesting individual measurements could be affected by shadowing. To fully understand this further, additional measurements taken at more VZA and VAA angles would give us a better understanding of the variability in the reflectance due to the structure of the canopy. Therefore, in this study, the maximum VZA was used for comparisons. The uncertainty of using a different VZA in comparison to the satellite data was assessed through simulations based upon MODIS BRDF albedo products (MCD43A1) (Strahler et al., 1999) by generating reflectance for the same VZA measured by HYPSTAR (0°, 5°, 10°, 20°, 30°). Overall, a maximum difference in reflectance values of 25% in wavelengths 841 nm–876 nm was found comparing VZA of 0° and 30° within the solar principle plane, suggesting that a full BRDF model for the forest canopy would help



FIGURE 7
Webcam images of the HYPSTAR instrument from the 26th of August 2022. **(A)** image from 11:41, **(B)** image from 12:21 and **(C)** image from 13:01.

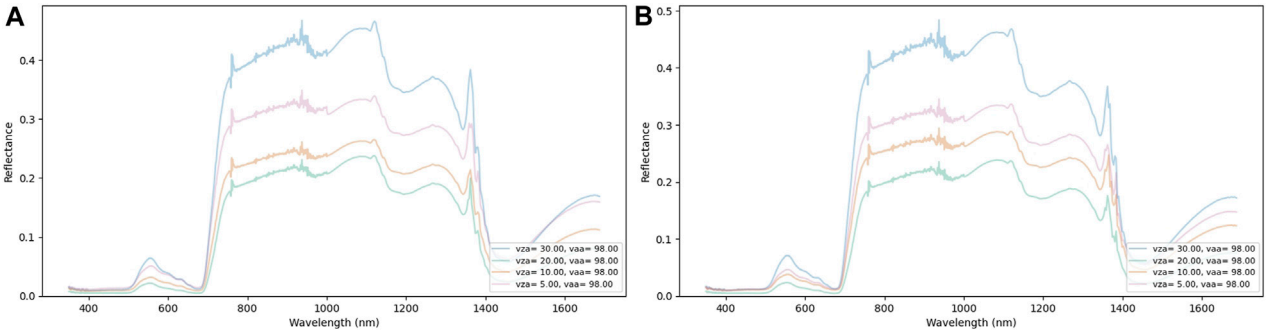


FIGURE 8
Examples of the different surface reflectances from the 98° VAA for some of the WWUK sequences. **(A)** 11:32 26 April 2022. **(B)** 11:40 30 April 2022.

to correct for this variability. However, due to the overpass time of the satellite observations used in this study, measurements are taken with a relative azimuth angle of 5°–15°which would reduce the BRDF effect.

To minimise the impact of changes in local environmental and illumination conditions the closest, valid, HYPSTAR sequence within a 2 hour window was selected for the comparison. For the majority of the comparisons a matchup was available within 30 min, leading to a change in SZA of <1°(viewing geometries for matchups are presented in Table 1). However, for the match up on the 16 October 2022, the closest available sequence was at 09:40 from the HYPSTAR instrument in comparison to an S2 overpass of 11:21. As such there was a change in the SZA from 66.57° to 61° between the matchups. The change in SZA for this matchup, may have been a significant factor in the differences for the disagreement between the SR as we are not yet able to correct for the forest BRDF effect.

Another issue which could be affecting the measurements is the height above the canopy that the HYPSTAR instrument is deployed at and the corresponding small FOV of the *in-situ* measurements. For nadir measurements the maximum canopy footprint of the HYPSTAR instrument is 4.69 m^2 assuming the instrument is pointing at a gap in the canopy and measuring the ground surface. However, it is likely to be a lot smaller than this due to the height of the surrounding trees, which average 24 m in the surrounding area (Calders et al., 2022). Therefore the measurements from different viewing angles and different days are susceptible to a number of unknown assumptions such as the BRDF of the foliage elements, the BRDF of the background, the spatial variability of the background BRDF and the temporal dynamics of these characteristics. These assumptions were identified in the RAMI-IV exercise as all having an influence on the retrieved reflectance (Widlowski et al., 2015). Additionally, the illumination conditions of the understory and overstory vegetation could be different, both of which could be measured within the FOV of a HYPERNETS scan whereas in summer, when the canopy is at maximum coverage, the satellite signal is dominated by the overstory vegetation (Nevalainen et al., 2017). For future studies, this could be estimated at the site by measuring the distance to the canopy and the understory at various viewing angles from the location of the sensor by using a laser range finding instrument. This information could then be utilised in a 3D-model of the site to be incorporated for satellite matchups at different viewing geometries.

Ideally to assess the accuracy of the surface reflectance obtained by the HYPSTAR instrument and fully validate its measurements uncertainty estimates a comparison against an independent instrument would be performed at the site (Kuester et al., 2001). A comparison of the HYPSTAR against a RadCalNet instrument has been performed at the Gobabeb site for BOA data from both instruments. Comparisons over a six-month period displays initial difference to within 5% in the visible and near infrared (VNIR), as well as 1%–2.5% agreement in the short-wave infrared (SWIR) (Sinclair et al., 2023). However, there are currently no independent, point, multiangular hyperspectral

measurements taken at WWUK over where the instrument is positioned. Future work involving UAV mounted sensors could provide an independent method for assessing the accuracy of the HYPSTAR system.

Additionally, further work is needed to expand the uncertainties associated with the HYPSTAR measurements. In the current version of the data used in this paper, uncertainties associated with the stray light correction and the spectral positioning of the LANDHYPERNET bands are not included in the full uncertainty budget.

Accounting for the spatial heterogeneity of the site was one of the key considerations applied in the validation methodology in this study. The spatial variability of the site at the satellite was included as the comparison uncertainty (u_{comp}) in the overall uncertainty calculation to account for this variability. However, the spatial uncertainty becomes the dominant component in the combined uncertainty over a heterogeneous target. The issue of spatial mismatch between *in-situ* and satellite SR is frequently discussed in the literature (Gamon et al., 2006; Hill et al., 2006; Román et al., 2009; Song et al., 2019). Consequently, validation of SR products tends to be conducted over homogeneous targets (Wulder et al., 2019; Origo et al., 2020; Teixeira Pinto et al., 2020; Pflug et al., 2022; Eon et al., 2023). Nevertheless, it is important to assess the performance of these products over multiple landcover types, especially forests, which biophysical products such as leaf area index are derived from satellite SR products. Additionally, as far as we are aware this is the first validation of high spatial resolution satellite data using a multi-angular hyperspectral imaging system and therefore the results presented here give us a baseline for expected performance, which will be improved as the understanding of spatial variability increases.

Finally, although the use of the airborne data helped to quantify the spatial variability of the site at the satellite scale, there are improvements that could be made in this analysis. The collection of hyperspectral data over the site using sensors mounted on Unmanned Aerial Vehicles would address two limitations of the current technique. Firstly, the spatial resolution of such data is on the order of tens of time smaller than that of the currently used airborne data, allowing more precise information about the spatial representativeness for different viewing angles to be understood (Fawcett et al., 2020). Secondly, in comparison to airborne campaigns, UAV campaigns are relatively low cost to perform which could allow for a more frequent sampling interval across the growing season to see how the spatial variability varies across the year which would improve the uncertainty assessment associated with the spatial variability (Arroyo-Mora et al., 2019).

5 Conclusions

This paper demonstrates the use of a novel, autonomous hyperspectral surface reflectance data collected at Wytham Woods, United Kingdom (WWUK) as part of the LANDHYPERNET network for the validation of multispectral data from Sentinel-2 and Landsat 8 and Landsat 9. The deployment of the HYPSTAR instrument at the site, the corresponding quality control of the data products is described. In this paper the first satellite validation activity of Sentinel-2 and Landsat 8 and 9 has been performed using the BOA products produced by the HYPERNET_PROCESSOR at the WWUK site. This is the first study using autonomous, hyperspectral *in-situ* measurements for the validation of surface reflectance land products over forests using a point measurement and therefore provides an understanding of the minimum performance expected using such a system. In addition, a methodology based upon metrological principles has been outlined showing the propagation of uncertainties from the LANDHYPERNET and satellite data products to enable conformity testing of the satellite products using the satellite mission requirements. Overall for the WWUK site, the initial findings from this comparison indicate good agreeement between the reflectance products produced by the HYPSTAR instrument and the satellite product. The strongest agreement is with bands in the red and NIR. Additionally, in absolute terms, the differences in the visible bands are within the mission requirements for Sentinel-2 but are inconclusive due to the large uncertainties associated with the in-situ data.

These differences could be reduced by mounting the HYPSTAR instrument on a higher tower above the surrounding forest canopy, increasing the FOV of the instrument and minimising the impact of local shadowing on the instrument. A longer time series from the site will improve the analysis by leading to more satellite matchups, additionally incorporating a BRDF model of the local vegetation could improve the matchups between the *in-situ* and satellite products. Furthermore, expanding the analysis to include leaf-off conditions will allow for a more comprehensive understanding of the temporal dynamics of the satellite products. Finally, this analysis focused on multispectral satellite products, further analysis could be conducted on hyperspectral missions such as CHIME, ENMAP, PRISMA and GLIMR further exploiting the relatively fine spectral resolution of the LANDHYPERNET data products.

Data availability statement

The raw data supporting the conclusion of this article will be made available by the authors, without undue reservation.

Author contributions

HM: Writing–original draft, Writing–review and editing, Conceptualization, Data curation, Formal Analysis, Investigation, Methodology, Project administration, Resources, Software, Supervision, Validation, Visualization. MS: Conceptualization, Data curation, Methodology, Validation, Visualization, Writing–review and editing. PD: Conceptualization, Data curation, Methodology, Software, Validation, Visualization, Writing–review and editing. AB: Conceptualization, Data curation, Funding acquisition, Methodology, Project administration, Resources, Supervision, Validation, Visualization, Writing–review and editing.

Funding

The author(s) declare financial support was received for the research, authorship, and/or publication of this article. The HYPERNETS project is funded by the European Union's Horizon

2020 research and innovation program under grant agreement No. 775983 and by the HYPERNET-POP project funded by the European Space Agency (contract no. 4000139081/22/I-EF). The CoMet toolkit was developed using funding from the ESA-funded Instrument Data quality Evaluation and Assessment Service—Quality Assurance for Earth Observation (IDEAS-QA4EO) contract funded by ESA-ESRIN (no. 4000128960/19/I-NS) and the United Kingdom's Department for Business, Energy and Industrial Strategy's (BEIS) National Measurement System (NMS) programme.

Acknowledgments

We thank the Copernicus program, the U.S. Geological Survey for the use of their data. The authors extend their gratitude to Nigel Fisher and the University of Oxford for facilitating access to Wytham Woods, in addition to Curt Lambert for his technical support in the establishment and maintenance of the Wytham Woods site. We thank Andreas Hueni and his team from the University of Zürich for the collection of the AVIRIS-NG airborne data over Wytham Woods used in this study.

Conflict of interest

The authors declare that the research was conducted in the absence of any commercial or financial relationships that could be construed as a potential conflict of interest.

Publisher's note

All claims expressed in this article are solely those of the authors and do not necessarily represent those of their affiliated organizations, or those of the publisher, the editors and the reviewers. Any product that may be evaluated in this article, or claim that may be made by its manufacturer, is not guaranteed or endorsed by the publisher.

References

Arroyo-Mora, J. P., Kalacska, M., Inamdar, D., Soffer, R., Lucanus, O., Gorman, J., et al. (2019). Implementation of a uav–hyperspectral pushbroom imager for ecological monitoring. *Drones* 3, 12. doi:10.3390/drones3010012

Badawi, M., Helder, D., Leigh, L., and Jing, X. (2019). Methods for earth-observing satellite surface reflectance validation. *Remote Sens.* 11, 1543. doi:10.3390/rs11131543

Banks, A. C., Hunt, S. E., Gorroño, J., Scanlon, T., Woolliams, E. R., and Fox, N. P. (2017). A comparison of validation and vicarious calibration of high and medium resolution satellite-borne sensors using radcalnet. *Sensors, Syst. Next-Generation Satell. XXI* 10423, 246–254. doi:10.1117/12.2278528

Barsi, J. A., Lee, K., Kvaran, G., Markham, B. L., and Pedelty, J. A. (2014). The spectral response of the landsat-8 operational land imager. *Remote Sens.* 6, 10232–10251. doi:10.3390/rs61010232

Barsi, J. A., Markham, B. L., McCorkel, J., McAndrew, B., Donley, E., Morland, E., et al. (2019). The operational land imager-2: prelaunch spectral characterization. *Earth Obs. Syst. XXIV* 11127, 35–45. doi:10.1117/12.2529776

Bouvet, M., Thome, K., Berthelot, B., Bialek, A., Czapla-Myers, J., Fox, N. P., et al. (2019). Radcalnet: a radiometric calibration network for earth observing imagers operating in the visible to shortwave infrared spectral range. *Remote Sens.* 11, 2401. doi:10.3390/rs11202401

Brown, L. A., Camacho, F., García-Santos, V., Origo, N., Fuster, B., Morris, H., et al. (2021). Fiducial reference measurements for vegetation bio-geophysical variables: an end-to-end uncertainty evaluation framework. *Remote Sens.* 13, 3194. doi:10.3390/rs13163194

Brown, L. A., Ogutu, B. O., and Dash, J. (2020). Tracking forest biophysical properties with automated digital repeat photography: a fisheye perspective using digital hemispherical photography from below the canopy. *Agric. For. Meteorology* 287, 107944. doi:10.1016/j.agrformet.2020.107944

Calders, K., Verbeeck, H., Burt, A., Origo, N., Nightingale, J., Malhi, Y., et al. (2022). Laser scanning reveals potential underestimation of biomass carbon in temperate forest. *Ecol. Solutions Evid.* 3, e12197. doi:10.1002/2688-8319.12197

Chapman, J. W., Thompson, D. R., Helmlinger, M. C., Bue, B. D., Green, R. O., Eastwood, M. L., et al. (2019). Spectral and radiometric calibration of the next generation airborne visible infrared spectrometer (aviris-ng). *Remote Sens.* 11, 2129. doi:10.3390/rs11182129

Claverie, M., Ju, J., Masek, J. G., Dungan, J. L., Vermote, E. F., Roger, J.-C., et al. (2018). The harmonized landsat and sentinel-2 surface reflectance data set. *Remote Sens. Environ.* 219, 145–161. doi:10.1016/j.rse.2018.09.002

Doxani, G., Vermote, E., Roger, J.-C., Gascon, F., Adriaensen, S., Frantz, D., et al. (2018). Atmospheric correction inter-comparison exercise. *Remote Sens.* 10, 352. doi:10.3390/rs10020352

Drusch, M., Del Bello, U., Carlier, S., Colin, O., Fernandez, V., Gascon, F., et al. (2012). Sentinel-2: esa's optical high-resolution mission for gmes operational services. *Remote Sens. Environ.* 120, 25–36. doi:10.1016/j.rse.2011.11.026

Eon, R., Gerace, A., Falcon, L., Poole, E., Kleynhans, T., Raqueño, N., et al. (2023). Validation of landsat-9 and landsat-8 surface temperature and reflectance during the underfly event. *Remote Sens.* 15, 3370. doi:10.3390/rs15133370

Fawcett, D., Panigada, C., Tagliabue, G., Boschetti, M., Celesti, M., Evdokimov, A., et al. (2020). Multi-scale evaluation of drone-based multispectral surface reflectance and vegetation indices in operational conditions. *Remote Sens.* 12, 514. doi:10.3390/rs12030514

Fensholt, R., Rasmussen, K., Nielsen, T. T., and Mbow, C. (2009). Evaluation of earth observation based long term vegetation trends—intercomparing ndvi time series trend analysis consistency of sahel from avhrr gimms, terra modis and spot vgt data. *Remote Sens. Environ.* 113, 1886–1898. doi:10.1016/j.rse.2009.04.004

Gamon, J. A., Rahman, A., Dungan, J., Schildhauer, M., and Huemmrich, K. (2006). Spectral network (specnet)—what is it and why do we need it? *Remote Sens. Environ.* 103, 227–235. doi:10.1016/j.rse.2006.04.003

Gorelick, N., Hancher, M., Dixon, M., Ilyushchenko, S., Thau, D., and Moore, R. (2017). Google earth engine: planetary-scale geospatial analysis for everyone. *Remote Sens. Environ.* 202, 18–27. doi:10.1016/j.rse.2017.06.031

Gorroño, J., Guanter, L., Graf, L. V., and Gascon, F. (2023). A software tool for the estimation of uncertainties and spectral error correlation in sentinel-2 level-2a data products. *EarthArXiv*. doi:10.31223/X5GM33

Goyens, C., De Vis, P., and Hunt, S. E. (2021). Automated generation of hyperspectral fiducial reference measurements of water and land surface reflectance for the hypernets networks. *IEEE Int. Geoscience Remote Sens. Symposium IGARSS*, 7920. doi:10.1109/IGARSS47720.2021.9553738

GUM (2008). Evaluation of measurement data—guide to the expression of uncertainty in measurement. *Int. Organ. Stand. Geneva* 50, 134. doi:10.59161/JCGM100-2008E

Hakuba, M. Z., Folini, D., Sanchez-Lorenzo, A., and Wild, M. (2013). Spatial representativeness of ground-based solar radiation measurements. *J. Geophys. Res. Atmos.* 118, 8585–8597. doi:10.1002/jgrd.50673

Hill, M., Held, A., Leuning, R., Coops, N., Hughes, D., and Cleugh, H. (2006). Modis spectral signals at a flux tower site: relationships with high-resolution data, and co2 flux and light use efficiency measurements. *Remote Sens. Environ.* 103, 351–368. doi:10.1016/j.rse.2005.06.015

Holben, B. N., Eck, T. F., Slutsker, I. a., Tanré, D., Buis, J., Setzer, A., et al. (1998). Aeronet—a federated instrument network and data archive for aerosol characterization. *Remote Sens. Environ.* 66, 1–16. doi:10.1016/s0034-4257(98)00031-5

ISO (2003). Statistical methods: guidelines for the evaluation of conformity with specified requirements: Part 1: general principles. *Int. Organ. Stand*. doi:10.3403/30398733u

Jing, X., Leigh, L., Teixeira Pinto, C., and Helder, D. (2019). Evaluation of radcalnet output data using landsat 7, landsat 8, sentinel 2a, and sentinel 2b sensors. *Remote Sens.* 11, 541. doi:10.3390/rs11050541

Justice, C., Belward, A., Morisette, J., Lewis, P., Privette, J., and Baret, F. (2000). Developments in the'validation'of satellite sensor products for the study of the land surface. *Int. J. Remote Sens.* 21, 3383–3390. doi:10.1080/014311600750020000

Kuester, M., Thome, K., Krause, K., Canham, K., and Whittington, E. (2001). "Comparison of surface reflectance measurements from three asd fieldspec fr

spectroradiometers and one asd fieldspec vnir spectroradiometer," in IGARSS 2001. Scanning the Present and Resolving the Future. Proceedings. IEEE 2001 International Geoscience and Remote Sensing Symposium, China, 09-13 July 2001 (IEEE), 72–74.1

Li, J., and Roy, D. P. (2017). A global analysis of sentinel-2a, sentinel-2b and landsat-8 data revisit intervals and implications for terrestrial monitoring. *Remote Sens.* 9, 902. doi:10.3390/rs9090902

Li, Y., Chen, J., Ma, Q., Zhang, H. K., and Liu, J. (2018). Evaluation of sentinel-2a surface reflectance derived using sen2cor in north America. *IEEE J. Sel. Top. Appl. Earth Observations Remote Sens.* 11, 1997–2021. doi:10.1109/jstars.2018.2835823

Liang, S., Li, X., and Wang, J. (2012). Atmospheric correction of optical imagery. *Adv. Remote Sens.* 117. doi:10.1016/B978-0-12-385954-9.00005-8

Main-Knorn, M., Pflug, B., Louis, J., Debaecker, V., Müller-Wilm, U., and Gascon, F. (2017).Sen2cor for sentinel-2, *Image Signal Process. Remote Sens. XXIII*, 10427, 37–48. doi:10.1117/12.2278218

Malthus, T., Ong, C., Lau, I., Fearns, P., Byrne, G., Thankappan, M., et al. (2019). *A community approach to the standardised validation of surface reflectance data. A technical handbook to support the collection of field reflectance data*.

Markham, B., Storey, J., and Morfitt, R. (2015). Landsat-8 sensor characterization and calibration. *Remote Sens.* 7, 2279–2282. doi:10.3390/rs70302279

Masek, J. G., Wulder, M. A., Markham, B., McCorkel, J., Crawford, C. J., Storey, J., et al. (2020). Landsat 9: empowering open science and applications through continuity. *Remote Sens. Environ.* 248, 111968. doi:10.1016/j.rse.2020.111968

Morris, H., Bialek, A., Sinclair, M., and De Vis, P. (2023). *Initial Sample of HYPERNETS hyperspectral surface reflectance measurements for satellite validation from the Wytham Woods site in the United Kingdom*.

Nevalainen, O., Honkavaara, E., Tuominen, S., Viljanen, N., Hakala, T., Yu, X., et al. (2017). Individual tree detection and classification with uav-based photogrammetric point clouds and hyperspectral imaging. *Remote Sens.* 9, 185. doi:10.3390/rs9030185

Niro, F., Goryl, P., Dransfeld, S., Boccia, V., Gascon, F., Adams, J., et al. (2021). European space agency (esa) calibration/validation strategy for optical land-imaging satellites and pathway towards interoperability. *Remote Sens.* 13, 3003. doi:10.3390/rs13153003

Origo, N., Gorroño, J., Ryder, J., Nightingale, J., and Bialek, A. (2020). Fiducial reference measurements for validation of sentinel-2 and proba-v surface reflectance products. *Remote Sens. Environ.* 241, 111690. doi:10.1016/j.rse.2020.111690

Pancorbo, J., Lamb, B. T., Quemada, M., Hively, W. D., Gonzalez-Fernandez, I., and Molina, I. (2021). Sentinel-2 and worldview-3 atmospheric correction and signal normalization based on ground-truth spectroradiometric measurements. *ISPRS J. Photogrammetry Remote Sens.* 173, 166–180. doi:10.1016/j.isprsjprs.2021.01.009

Pflug, B., Louis, J., de los Reyes, R., Pflug, K., Mueller-Wilm, U., Quang, C., et al. (2022). "Evaluation of sen2cor surface reflectance products over land surface with reference measurements on ground," in *IGARSS 2022-2022 IEEE international geoscience and Remote sensing symposium* (China: IEEE), 4308–4311.

Román, M. O., Schaaf, C. B., Woodcock, C. E., Strahler, A. H., Yang, X., Braswell, R. H., et al. (2009). The modis (collection v005) brdf/albedo product: assessment of spatial representativeness over forested landscapes. *Remote Sens. Environ.* 113, 2476–2498. doi:10.1016/j.rse.2009.07.009

S2MPC (2023). Data quality report - MSI L2A (June 2023) *(Copernicus Sentinel optical mission performance cluster)*.

Schaepman-Strub, G., Schaepman, M. E., Painter, T. H., Dangel, S., and Martonchik, J. V. (2006). Reflectance quantities in optical remote sensing—definitions and case studies. *Remote Sens. Environ.* 103, 27–42. doi:10.1016/j.rse.2006.03.002

Sinclair, M., Bialek, A., De Vis, P., and Bouvet, M. (2023). "Hypernets land network: hypstar®-xr deployment and validation in Namibia, africa," in *IGARSS 2023-2023 IEEE international geoscience and Remote sensing symposium* (China: IEEE), 4625. –4627.

Song, R., Muller, J.-P., Kharbouche, S., and Woodgate, W. (2019). Intercomparison of surface albedo retrievals from misr, modis, cgls using tower and upscaled tower measurements. *Remote Sens.* 11, 644. doi:10.3390/rs11060644

Strahler, A. H., Muller, J., Lucht, W., Schaaf, C., Tsang, T., Gao, F., et al. (1999). Modis brdf/albedo product: algorithm theoretical basis document version 5.0. *MODIS Doc.* 23, 42–47.

Teixeira Pinto, C., Jing, X., and Leigh, L. (2020). Evaluation analysis of landsat level-1 and level-2 data products using *in situ* measurements. *Remote Sens.* 12, 2597. doi:10.3390/rs12162597

Thompson, D. R., Natraj, V., Green, R. O., Helmlinger, M. C., Gao, B.-C., and Eastwood, M. L. (2018). Optimal estimation for imaging spectrometer atmospheric correction. *Remote Sens. Environ.* 216, 355–373. doi:10.1016/j.rse.2018.07.003

Vermote, E., Justice, C., Claverie, M., and Franch, B. (2016). Preliminary analysis of the performance of the landsat 8/oli land surface reflectance product. *Remote Sens. Environ.* 185, 46–56. doi:10.1016/j.rse.2016.04.008

Widlowski, J.-L., Mio, C., Disney, M., Adams, J., Andredakis, I., Atzberger, C., et al. (2015). The fourth phase of the radiative transfer model intercomparison (rami) exercise: actual canopy scenarios and conformity testing. *Remote Sens. Environ.* 169, 418–437. doi:10.1016/j.rse.2015.08.016

Wulder, M. A., Loveland, T. R., Roy, D. P., Crawford, C. J., Masek, J. G., Woodcock, C. E., et al. (2019). Current status of landsat program, science, and applications. *Remote Sens. Environ.* 225, 127–147. doi:10.1016/j.rse.2019.02.015

Xu, B., Li, J., Liu, Q., Huete, A. R., Yu, Q., Zeng, Y., et al. (2016). Evaluating spatial representativeness of station observations for remotely sensed leaf area index products. *IEEE J. Sel. Top. Appl. Earth Observations Remote Sens.* 9, 3267–3282. doi:10.1109/jstars.2016.2560878

Yang, J., Gong, P., Fu, R., Zhang, M., Chen, J., Liang, S., et al. (2013). The role of satellite remote sensing in climate change studies. *Nat. Clim. change* 3, 875–883. doi:10.1038/nclimate1908

frontiers | Frontiers in Remote Sensing

TYPE Original Research
PUBLISHED 13 May 2024
DOI 10.3389/frsen.2024.1347230

Check for updates

OPEN ACCESS

EDITED BY
Sawaid Abbas,
University of the Punjab, Pakistan

REVIEWED BY
Syed Muhammad Irteza,
Urban Unit, Pakistan
Yu Fenghua,
Shenyang Agricultural University, China

*CORRESPONDENCE
Pieter De Vis,
pieter.de.vis@npl.co.uk

†These authors have contributed equally to this work and share first authorship

RECEIVED 30 November 2023
ACCEPTED 08 March 2024
PUBLISHED 13 May 2024

CITATION
De Vis P, Goyens C, Hunt S, Vanhellemont Q, Ruddick K and Bialek A (2024), Generating hyperspectral reference measurements for surface reflectance from the LANDHYPERNET and WATERHYPERNET networks.
Front. Remote Sens. 5:1347230.
doi: 10.3389/frsen.2024.1347230

COPYRIGHT
© 2024 De Vis, Goyens, Hunt, Vanhellemont, Ruddick and Bialek. This is an open-access article distributed under the terms of the Creative Commons Attribution License (CC BY). The use, distribution or reproduction in other forums is permitted, provided the original author(s) and the copyright owner(s) are credited and that the original publication in this journal is cited, in accordance with accepted academic practice. No use, distribution or reproduction is permitted which does not comply with these terms.

Generating hyperspectral reference measurements for surface reflectance from the LANDHYPERNET and WATERHYPERNET networks

Pieter De Vis[1*†], Clemence Goyens[2†], Samuel Hunt[1], Quinten Vanhellemont[2], Kevin Ruddick[2] and Agnieszka Bialek[1]

[1]National Physical Laboratory, Teddington, United Kingdom, [2]Royal Belgian Institute of Natural Sciences (RBINS), Operational Directorate Natural Environment, Brussels, Belgium

The LANDHYPERNET and WATERHYPERNET networks (which together make up the HYPERNETS network) consist of a set of autonomous hyperspectral spectroradiometers (HYPSTAR®) acquiring fiducial reference measurements of surface reflectance at various sites covering a wide range of surface types (both land and water) for use in satellite Earth observation validation and remote sensing applications. This paper describes the processing algorithm for the HYPSTAR® data products. The HYPERNETS_PROCESSOR is a Python software package to process the LANDHYPERNET and WATERHYPERNET *in-situ* hyperspectral raw data, collected from the measurement network under the standard measurement protocols, to the designated products, through data transmission and conversion, application of calibration, evaluation of reflectance and other variables, and, archiving for distribution to users. In order to achieve fiducial reference measurement quality, uncertainties are propagated through each step of the processing chain, taking into account temporal and spectral error-covariance. Such detailed uncertainty information is unique for any satellite validation network. We also describe the HYPSTAR® products acquired until 2023–04–31, consisting of 12,190 LANDHYPERNET sequences and 55,514 WATERHYPERNET sequences (of which respectively 11,802 and 44,412 were successfully processed to surface reflectance).

KEYWORDS

HYPERNETS, LANDHYPERNET, WATERHYPERNET, hyperspectral, validation, reflectance, uncertainty, fiducial reference measurements

1 Introduction

In recent years, there has been a growing fleet of high-quality optical Earth observation satellite sensors with various spectral bands and/or resolutions. As a result, there is a growing need for high-quality hyperspectral *in-situ* optical reflectance validation observations, for both land and water. Particularly, the European Space Agency (ESA) has highlighted the need for a network for validating surface reflectance in their Calibration/Validation strategy for optical land-imaging satellites (Niro et al., 2021). There is also an increasing focus on data quality, with the objective to make traceable and uncertainty-

quantified measurements, referred to as Fiducial Reference Measurements (FRMs; Goryl et al., 2023).

By moving from mobile measurement setups to the use of autonomous platforms over a variety of surface types, there are many more matchups available for a given satellite. When this is combined with taking hyperspectral measurements and integrating over the satellite spectral response function, the data from a single site can be used to reconstruct the signal for many optical missions (S2, S3, PROBA-V, MODIS, VIIRS, L8, Pléiades, ENMAP, PRISMA, SABIAMAR, PACE, *etc.*). The existing AERONET-OC (Zibordi et al., 2009; Zibordi et al., 2021) and RadCalNet (Bouvet et al., 2019) networks provide reference *in situ* measurements, and have been shown to be suitable for performing validation of satellite products (e.g., Alonso et al., 2019; Ishizaka et al., 2022; Zibordi et al., 2022). However both these networks are based on multispectral instruments (with the exception of the Chinese RadCalNet sites), which require spectral interpolation and modelling associated uncertainties to cover all spectral bands of all sensors.

The Horizon 2020 HYPERNETS project set out to meet these needs by developing a network of autonomous field sites for the measurement of high-quality, hyperspectral surface reflectance. To achieve this, a new hyperspectral radiometer, HYPSTAR® (Hyperspectral Pointable System for Terrestrial and Aquatic Radiometry; Kuusk et al., in this issue), with instrument pointing capabilities has been developed and is currently operational at several land (LANDHYPERNET; Bialek et al., in this issue) and water (WATERHYPERNET; Ruddick et al., in this issue) sites. The data from these new instruments are centrally processed, with consistent processing for water and land reflectances, by the HYPERNETS_PROCESSOR to radiance, irradiance and reflectance products with associated uncertainties. The HYPERNETS satellite validation network is expected to become the main source of surface reflectance validation data for all spectral bands of VNIR-SWIR optical missions with detailed uncertainty estimates and including error-correlation information. It is the first network with such a detailed metrological approach in terms of uncertainty analysis.

The HYPERNETS_PROCESSOR is the network processor to handle both water and land data from HYPSTAR® acquisitions through transmission, conversion, application of calibration, interpolation, evaluation of reflectance and other products and archiving for web distribution. Quality control is performed at different stages throughout the processing. The data are managed in line with the Findable, Accessible, Interoperable and Re-useable (FAIR) principles of data management (Wilkinson et al., 2016). Measurement and calibration uncertainty is propagated through the full processing chain, including treatment of temporal and wavelength error-covariance following a metrological approach as defined in the Guide to the Expression of Uncertainty in Measurement (JCGM 100:2008, 2008). These data are now publicly available as part of the WATERHYPERNET and LANDHYPERNET network respectively.

This paper presents the reference description of the v2.0 of the HYPERNETS_PROCESSOR and its products. Previously, a summarised description of a beta version of the HYPERNETS_PROCESSOR was presented in Goyens et al. (2021). In Section 2, some information on the HYPERNETS project and HYPSTAR® instrument are summarised. Section 3 details the processing algorithms used, including the different steps used as well as the different quality checks and the uncertainty propagation. In Section 4, the different data products produced by the HYPERNETS_PROCESSOR and their distribution are described. In Section 5, some examples and processing statistics are provided. Section 6 lists some of the improvements that are foreseen in the near future. Finally, Section 7 provides the conclusions.

2 HYPERNETS

2.1 HYPSTAR® instrument

HYPSTAR® (Hyperspectral Pointable System for Terrestrial and Aquatic Radiometry; www.hypstar.eu) is an autonomous hyperspectral radiometer system dedicated to surface reflectance validation of all optical Copernicus satellite data products. For a complete description of the HYPSTAR® system, we refer to Kuusk et al. (in this issue). HYPSTAR® takes radiance and irradiance measurements using the same spectrometer (though with different optical paths for radiance and irradiance). Two slightly different instruments are used for water and land: (1) The Standard Range (SR) model provides visible and near-infrared (VNIR, 380–1,020 nm) data and is used on water sites, (2) the eXtended Range (XR) models have an additional shortwave-infrared (SWIR) spectrometer module which extends the spectral range up to 1680 nm. The XR models are meant to be used on the land sites. Pictures of the SR and XR models of the HYPSTAR® are shown in Figure 1, together with some example field sites. The instrument characteristics are summarised in Table 1.

The spectral sampling of the HYPSTAR® is 0.5 nm in the VNIR and 3 nm in the SWIR, and the spectral resolution full-width half-maximum (FWHM) is 3 nm in the VNIR and 10 nm in the SWIR. The SWIR sensor is actively cooled (typically to 0 °C, but this can be configured) to ensure the stability of the measurements. The field of view of the radiance measurements is ~ 2° for the SR model and ~ 5° for the XR model. The irradiance measurements observe the full hemisphere, i.e. 180°. The HYPSTAR® system is mounted on a low-cost pointing system which allows the acquisition of autonomous, multi-angular measurements. A GPS, light and rain sensors as well as cameras to image the target and the sensor heads are also included. Data acquired by the HYPSTAR® is saved in separate binary '.spe' files for each viewing geometry. These acquisitions are sent to the central server for processing, together with some 'rgb' images taken by the camera within the system, a file with meteorological information (i.e., relative humidity, temperature and pressure measured within the system and illuminance measured by an external light sensor), log files made during the acquisition and data transfer, and a metadata file.

The HYPSTAR instruments are calibrated by Tartu University[1] (See Kuusk et al. in this issue). Currently this includes radiometric calibration (gains) and non-linearity calibration (non-linearity coefficients). Measurements of the temperature responsivity and stray light are also planned/in progress, but these characterisations are not yet used in the processing of the data in the current processor version. The lab calibration also includes a wavelength calibration.

1 https://kosmos.ut.ee/en/laboratory



FIGURE 1
Picture of the Standard Range (SR) HYPSTAR® system (including validation module) used for the WATERHYPERNET network (top left) and the eXtended Range (XR) HYPSTAR® system (including validation module) used for the LANDHYPERNET network (top right). A picture of one of the water sites (Aqua Alta, bottom left) and one of the land sites (Gobabeb, bottom right) is also shown.

TABLE 1 Instrument characteristics for the water HYPSTAR® (SR model) and land HYPSTAR® (XR model, consisting of VNIR and SWIR module) sensors. All values in the table are approximate values. Precise values might be slightly different and vary from instrument to instrument.

Parameter	VNIR water	VNIR land	SWIR land
spectral resolution FWHM	3 nm	3 nm	10 nm
spectral sampling interval	0.5 nm	0.5 nm	3 nm
L2B wavelength range	380–1,020 nm	380–1,000 nm	1,000–1,680 nm
number of L2B channels	1,300	1,260	220
field of view radiance sensor	2°	5°	5°
field of view irradiance sensor	180°	180°	180°

The wavelengths for each instrument will thus be slightly different, and the radiance and irradiance measurements can also have slightly different wavelengths for each spectral pixel (see Section 3.2.4.1). The wavelength calibration assigns a wavelength to each spectral pixel in the raw data, but not all the raw data pixels will be used in the final product. This is either because these wavelengths (e.g., in the UV) cannot be calibrated due to the spectral limits of the radiometric calibration references used, or because these wavelengths are simply too noisy to be used. In the final publicly distributed data (L2B products) the wavelength range is limited to the ranges specified in Table 1 in order to only supply the user with the best quality data.

2.2 HYPERNETS measurement protocol and terminology

Radiometer measurements are taken in a defined set of geometries called a sequence. For the WATERHYPERNET network, the output of a single sequence is the resulting water-leaving reflectance (possibly measured at different relative azimuth angles between Sun and sensor) and associated uncertainty and quality flags. For the LANDHYPERNET network, it is a set of surface reflectance measurements for different viewing geometries with associated uncertainties and quality flags. The set of acquisitions at each viewing geometry in a sequence is called a series, and it is composed of a set of

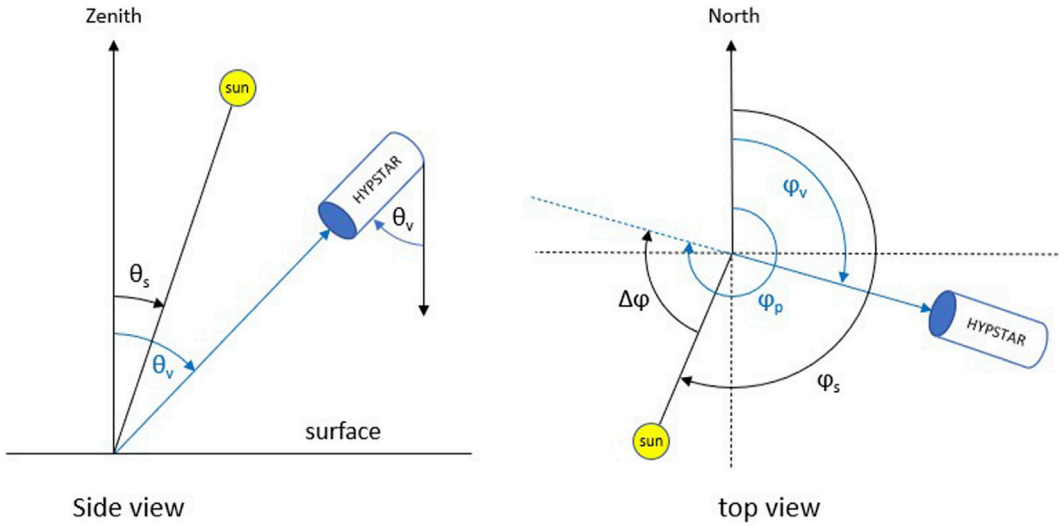


FIGURE 2
Left: Side-view diagram defining viewing zenith angles θ_v and solar zenith angles θ_s. Right: Top-view diagram defining the viewing azimuth angles φ_v, 'pointing-to' azimuth angle φ_p and solar azimuth angles φ_s, measured clockwise from North. The relative azimuth angle $\Delta\varphi$ is defined as the difference between φ_p and φ_s. All angles are defined in the reference frame centred on the measurement location on the surface.

repeat measurements called scans (which will be averaged). Hence, one scan results in a single unique spectrum with a specific integration time. The number of repeat scans in a single series depends on the desired parameter and its natural variability, potentially constrained by the total duration and power consumption. For the land XR instruments, the SWIR sensors typically have larger integration times than the VNIR sensors (in order to optimally use the dynamic range of the sensor). Typically, a fixed number (the default is 10) of SWIR scans will be set, and the VNIR sensor will keep taking scans until the SWIR sensor has completed its scans (leading to a larger number of scans for VNIR than for SWIR).

The geometries for the HYPERNETS network are defined in Figure 2. Each of the angles are defined in the reference frame centred on the measurement location on the surface. The viewing angles are thus defined as the sensor 'viewing from' a particular direction. In the side view, the viewing zenith angles are computed from Nadir to Zenith, i.e., a viewing zenith angle, θ_v, of 180° is looking upward (e.g., for downwelling irradiance measurements). The solar zenith angle is measured from Zenith. In the top view, the viewing azimuth angle, φ_v, is the angle measured clockwise from the absolute North to the direction of the sensor (i.e., the line from the target to the sensor). This definition of the viewing azimuth angle matches that of most optical satellite geometries (such as those of Sentinel-2, Sentinel-3, Landsat 8). Two additional azimuth angles are defined, i.e., the 'pointing-to' azimuth angle, φ_p, measured clockwise from the absolute North to the pointing direction (i.e., the line from the sensor to the target, or, φ_v+180°), and, the relative azimuth angle, $\Delta\varphi$, measured clockwise from the Sun to the pointing direction (i.e., φ_p-φ_s). In this definition, $\Delta\varphi = 0$ means the instrument is looking towards the Sun, and $\Delta\varphi = 180$ means the instrument is looking away from the Sun. Our definitions of φ_p and $\Delta\varphi$ match the definitions in Ruddick et al. (2019) for their viewing azimuth and $\Delta\varphi$, respectively (see their Figure 1).

Figure 3 illustrates the measurement protocol for a WATERHYPERNET sequence. The current standard water protocol follows commonly used measurement protocols (Ruddick et al., 2019, and references therein). Upwelling above-water radiance, L_u, series are taken at $\theta_v = 40°$ and sun-sensor relative azimuths, $\Delta\varphi$, at ± 90° and/or ± 135° (to avoid Sun glint and high skylight reflectance within the sensor field of view). Each series of L_u is preceded and followed by a series of above-water downwelling (sky) radiance, L_d, in the specular reflection direction for the correction of the reflected skylight (i.e., θ_v for $L_u = 180° - \theta_v$ for L_d). Downwelling irradiance, E_d, series are taken at the beginning and the end of each sequence. A standard water sequence (including only one single azimuth angle) lasts approximately 5 min and is executed every 15–30 min during daylight.

The LANDHYPERNET sequences also start and end with downwelling irradiance series, but have multiple upwelling radiance series covering a range of different viewing geometries (including a minimum of five view zenith and six view azimuth angles). The design of the land measurement protocol aims to optimise the viewing geometry during satellite's overpass times and by its repeats through the day to obtain information about Bidirectional Reflectance Distribution Function (BRDF) properties of the site. A plot illustrating the different viewing geometries for a land sequence is illustrated in Figure 4. Land sequences do not measure the downwelling (sky) radiance. A standard land sequence typically lasts approximately 15 min (depending on illumination) and is executed every 30 min during daylight.

WATERHYPERNET and LANDHYPERNET sequences following the above protocols are called 'standard' sequences.

2.3 HYPERNETS_PROCESSOR design

The HYPERNETS_PROCESSOR module is an open source Python package, with the code actively developed on GitHub[2]. It has a modular design that enables simple development. The various processing steps (described in the next section) have been

2 https://github.com/HYPERNETS/hypernets_processor

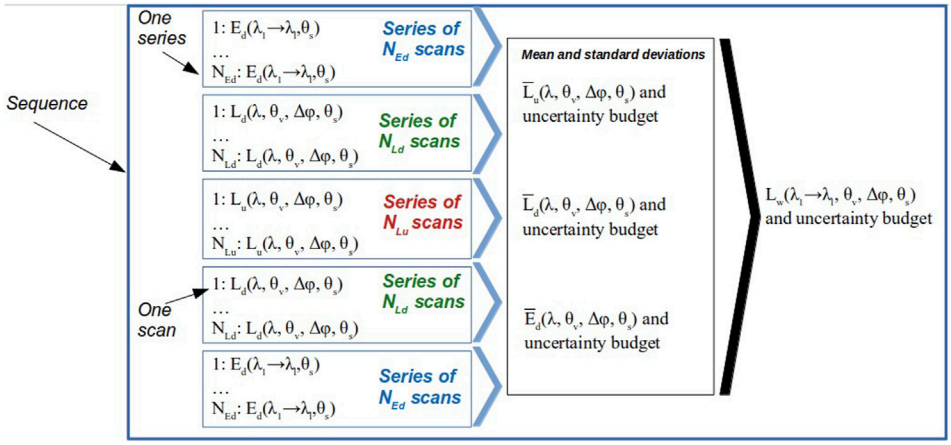


FIGURE 3
Diagram illustrating the measurement protocol for the WATERHYPERNET network with a sequence being a series of scans of upwelling radiance L_u preceded and followed by a series of scans of downwelling irradiance, E_d, and a series of scans of downwelling radiance L_d. In the figure N_x, λ, θ_v, θ_s, and, $\Delta\phi$ stand for number of scans, wavelength, viewing zenith angle, solar zenith angle and relative azimuth angle, respectively.

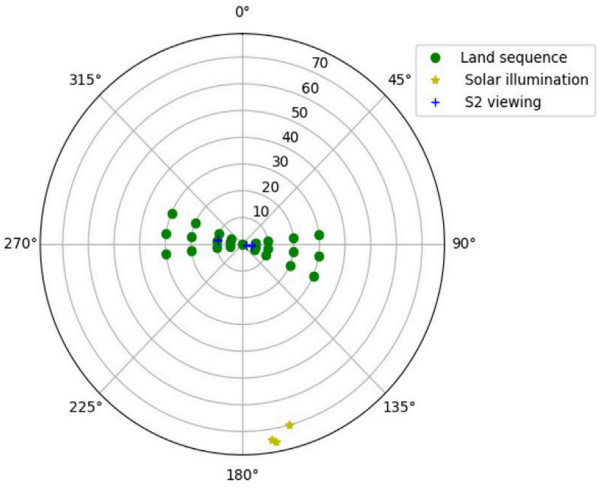


FIGURE 4
Polar plot showing the typical land protocol viewing geometries for the LANDHYPERNET network. As an example, the Sentinel-2 viewing geometries and solar geometries (during Sentinel-2 overpass) for the NPL Wytham Woods site in January 2022 are shown for comparison.

implemented within a flexible framework, so that rapid advances in instrumentation and systems can be easily accommodated. The software is run through a command-line interface (CLI) and ingests data and processes with 24/7/365 operation including automated monitoring of diagnostics both for the network operator and for the site operators. Installation instructions are available in the HYPERNETS_PROCESSOR documentation[3].

The HYPERNETS_PROCESSOR has a number of different categories of usage or modes of operation, to provide context to the rest of the design, they are initially described here. The first distinction is between the LANDHYPERNET processor and the WATERHYPERNET processor.

- LANDHYPERNET processor - processing for data taken by the LANDHYPERNET Network.
- WATERHYPERNET processor - processing for data taken by the WATERHYPERNET Network.

Where possible, the processing of the LANDHYPERNET and WATERHYPERNET is done as consistently as possible, with deviations between them only in the L1C and L2A processing (Figure 5). Also, there is a distinction between whether the measured data are from a standard measurement sequence or custom measurement sequence.

- Standard Sequence - dataset containing the standard set of measurements defined by the LANDHYPERNET or WATERHYPERNET network (as described in Section 2.2).
- Custom Sequence - dataset containing any other set of measurements.

Standard sequences are automatically processed to L2A, whereas custom sequences are only processed to L1B (flags and anomalies will be raised, triggering an anomaly that will stop the processing, see Section 3.3). Finally, there is the distinction between the two potential use cases, network processing or field use.

- Network Processing - automated processing to prepare standard sequences retrieved from network sites for distribution to users.
- Field Use - *ad hoc* processing of particular field acquisitions, for example, for testing instrument operation in the field.

3 https://hypernets-processor.readthedocs.io/en/latest/content/developers/getting_started.html

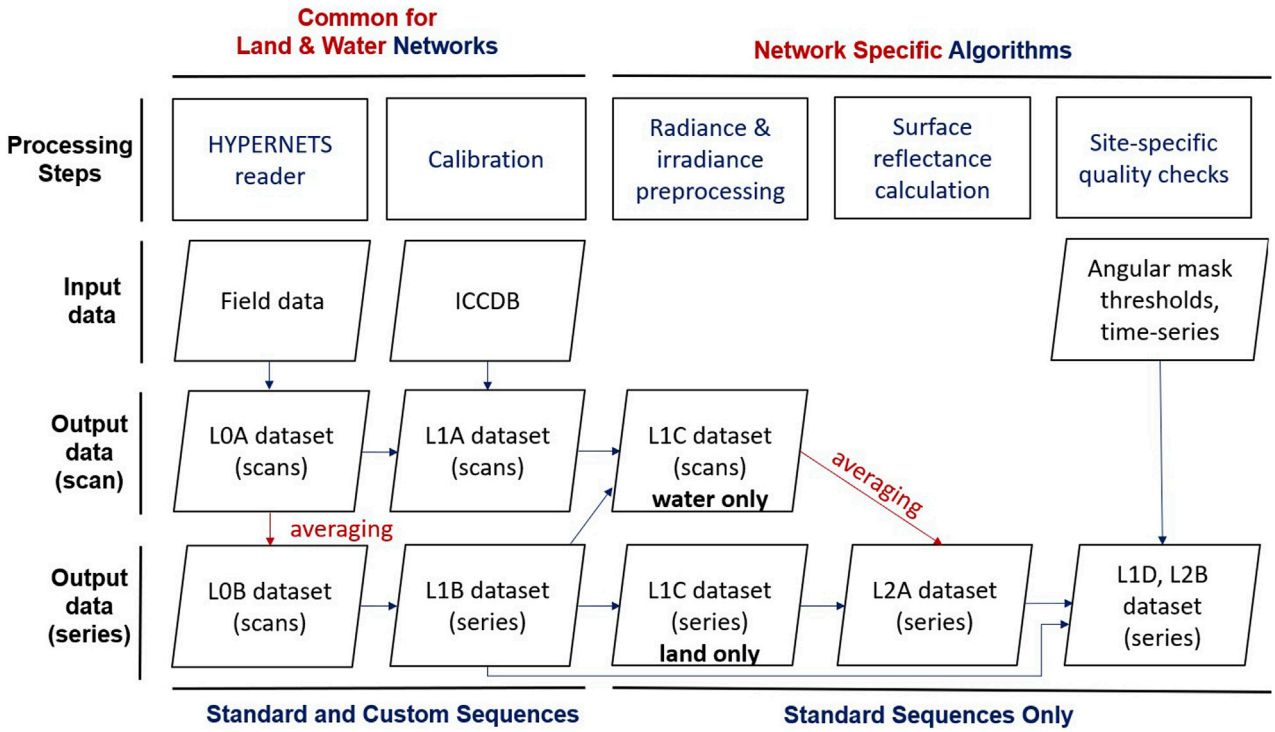


FIGURE 5
Design diagram for the HYPERNETS_PROCESSOR. Inputs from raw field acquisitions and the instrument characterisation and calibration database (ICCDB) are processed in various steps to the L0A-L2B HYPERNETS products. The processing steps row indicates what step of the processor has been used to create the output files in that column. The averaging processing step is applied at different stages throughout the processing, as indicated with the red arrows.

In the remainder of this paper, we will mainly focus on the network processing of standard sequences. For further information on the use case of field use, we refer the reader to the corresponding page in the HYPERNETS_PROCESSOR documentation[4].

2.4 HYPERNETS_PROCESSOR options

There are many options that can be fine-tuned in the running of the HYPERNETS_PROCESSOR, from controlling which measurement functions are used, where to store the output data and what plots and output files are produced, to details like number of Monte Carlo iterations used in the uncertainty propagation, thresholds of the quality checks or what ancillary data to use in the calculation of the air-water interface reflection factor (referred to as 'rhof_option'). These options can be controlled through three config files. The *processor.config* file contains all the options that are in common between all sites (different *processor.config* files are used for the WATERHYPERNET and LANDHYPERNET network, though with most values in common). The *job.config* file controls all site-specific options. Finally, there is also a *scheduler.config* file which controls how often the HYPERNETS_PROCESSOR checks for new data and how many sequences can be processed in parallel.

Set up routines are available to set up the processor (and the processor.config file using default values), to set up a new job (i.e., the processing of a new site, including what directory to check for new data) and to start the scheduler. The HYPERNETS_PROCESSOR documentation provides more information on how to set up and run the automated processing[5].

2.5 HYPERNETS_PROCESSOR versions

The version of the HYPERNETS_PROCESSOR described in this paper is v2.0. This is the first version that is intended for operational use. Previous versions include a beta version (as described in Goyens et al., 2021), and a v1.0 which was used to produce the first public dataset on Zenodo (see Section 4.4). A new version of the dataset on Zenodo will be released upon publication of this paper, using the v2.0 of the HYPERNETS_PROCESSOR.

The version number is made up of two numbers. The first indicates the major version number. Changes to this number indicate significant changes and improvements to the code, and

4 https://hypernets-processor.readthedocs.io/en/latest/content/users/adhoc.html

5 https://hypernets-processor.readthedocs.io/en/latest/content/users/automated.html

major changes to the datafiles. The second number, called the minor version, is incremented when there are minor feature changes or notable fixes which do not significantly change how the data products should be used.

Compared to the v1.0, there are a few changes in the v2.0 HYPERNETS_PROCESSOR worth noting, so that any HYPERNETS results using the v1.0 data products can be understood.

- The first important difference is in the definition of the viewing azimuth angles, which have changed by 180° in order to be consistent with satellite viewing azimuth angles in v2.0 (see Section 2.2). The pointing azimuth angles in v2.0 are equal to the viewing azimuth angles in v1.0. Pointing azimuth angles are mainly of interest for the WATERHYPERNET network as it is commonly used (Ruddick et al., 2019, and references therein) to compute the relative azimuth angles.
- Uncertainty propagation is now consistently applied to all WATERHYPERNET products, in the same way as for the LANDHYPERNET network.
- Output files and their names have slightly changed, e.g., there are now L0A and L0B files as opposed to only L0 files, and, the relative azimuth angle, used for the approximation of the air-water interface reflection factor within the WATERHYPERNET network, is also added to the L1C and L2A product names.
- Reflectance files with site specific quality checks applied are called L2B files in v2.0 (see Section 3.3.7), as opposed to L2A files in v1.0. These are the main files to be distributed.
- There were many minor changes (e.g., to the metadata and the quality checks) that are not worth noting individually but do make a difference to the produced HYPERNETS products.

3 Processing algorithm

3.1 Processing overview

The network processing is done centrally on the LANDHYPERNET and WATERHYPERNET servers, through a command line interface, which continuously checks for new data, and processes it as soon as it comes in. The HYPERNETS_PROCESSOR takes the data from acquisition (raw data) to application of calibration and quality controls, computation of correction factors (e.g., air-water interface reflectance correction for water processing), temporal interpolation to coincident timestamps, processing to surface reflectance and averaging per series. A diagram showing the design for the network processing is provided in Figure 5.

The inputs are the raw field acquisitions and the instrument characterisation and calibration database (ICCDB). The main outputs are the various L0A-L2B NetCDF datasets listed in Table 2. The HYPERNETS_PROCESSOR also produces various plots and SQL databases of successfully processed products and anomalies (Section 4.3). The different processing steps and the plots produced are described in the next section. As part of the processing, quality checks are performed which either add quality flags to the produced data processing, or in some cases raise anomalies and halt the processing. These quality checks are described in Section 3.3. Uncertainties are also propagated through each of the processing steps, as described in Section 3.4. Details on the produced products are provided in Section 4.

3.2 Processing steps

3.2.1 HYPERNETS reader

The hypernets_reader module processes the raw dataset (in spe-binary file format) to the L0A data product (readable NetCDF file). It reads the metadata file of the sequence (ASCII file), as well as the spe-binary data file for each series (the different scans are concatenated per series). According to the metadata file and the filename of the spe-binary file, the processing reorders the scans to L0A radiance, irradiance and darks and outputs for each of those a NetCDF with the different scans. The module also copies and renames the RGB images taken from the target and/or the sky during the sequence with the time of acquisition, the series number and the viewing and (relative) azimuth angle.

3.2.2 Calibration

After the raw L0A data has been read in, it needs to be quality checked and calibrated in order to get the radiance and irradiance L1A data products. The first step consists of assigning wavelengths to each of the spectral pixels based on laboratory characterisation measurements (and omitting pixels outside the calibration range). Next, the L0A dark scans are combined with the L0A (ir)radiance files, assigning each dark to the right (ir)radiance series. Next, the quality checks described in Section 3.3.2 are applied. In order to get calibrated (ir)radiances, the calibration coefficients and non-linearity coefficients (as determined by the calibration laboratory at Tartu University[6]) are then applied to the raw data. Figure 6 shows the raw L0A data and the calibrated L1A data for an land sequence example.

When multiple calibration files are available (i.e., at different calibration dates) the one nearest to the acquisition time is used, though only looking backward. When reprocessing data, calibration dates after the acquisition date are thus ignored. Interpolation between pre-deployment and post-deployment calibrations will be explored in the future (see Section 6).

The exact measurement function to be used can be specified manually by providing the measurement function as a standalone Python script. If no custom measurement function is provided, a default measurement function is used. This measurement function is defined by:

```
def meas_function(digital_number,gains,dark_signal,non_linear,
                  int_time):
    DN = digital_number-dark_signal
    non_lin_func = np.poly1d(np.flip(non_linear))
    corrected_DN = DN / non_lin_func(DN)

    return gains*corrected_DN/(int_time/1000)
```

where each of the arguments is a NUMPY array, digital_number gives the measured signal (in digital numbers), dark_signal gives the dark signal in digital numbers, gains gives the calibration coefficients,

6 https://kosmos.ut.ee/en/laboratory

TABLE 2 HYPERNETS_PROCESSOR processing levels.

Network	Level_Type	Description	Dimensions
Both	Ancillary	Generic term covering non-measurement data used in processing chain	-
Both	Spe files	Raw binary files (.spe format)	wavelength, scan
Both	jpg files	RGB images taken by the HYPSTAR®	image
Both	L0A_RAD	Raw data for radiance scans, stored in NetCDF files	wavelength, scan
Both	L0A_IRR	Raw data for irradiance scans, stored in NetCDF files	wavelength, scan
Both	L0A_BLA	Raw data for dark scans, stored in NetCDF files	wavelength, scan
Both	L0B_RAD	Raw data for radiance, averaged per series and corresponding dark scans, averaged per series	wavelength, series
Both	L0B_IRR	Raw data for irradiance, averaged per series and corresponding dark scans, averaged per series	wavelength, series
Both	L1A_RAD	Calibrated data for radiance scans, corrected for dark samples and any other instrument corrections (e.g., non-linearity)	wavelength, scan
Both	L1A_IRR	Calibrated data for irradiance scans, corrected for dark samples and any other instrument corrections (e.g., non-linearity)	wavelength, scan
Both	L1B_RAD	Calibrated data for radiance averaged over scans within one series, stored in NetCDF files	wavelength, series
Both	L1B_IRR	Calibrated data for irradiance averaged over scans within one series, stored in NetCDF files	wavelength, series
Land	L1C_ALL	LANDHYPERNET network file with (upwelling) radiance and irradiance which has been temporally and spectrally interpolated to match the radiance series	wavelength, series
Water	L1C_ALL	WATERHYPERNET network file with downwelling radiance and irradiance which has been temporally and spectrally interpolated to match the upwelling radiance scans and wavelength, upwelling radiance scans, and, estimated water-leaving radiance and reflectance with and without the NIR similarity correction (see below Section 3.2.4.2)	wavelength, upwelling radiance scan
Land	L2A_REF	LANDHYPERNET network file with surface reflectances per series	wavelength, series
Water	L2A_REF	WATERHYPERNET network file with water-leaving radiance, and, surface reflectance with and without the NIR similarity correction Ruddick et al. (2005)	wavelength, series
Both	L2B_REF	Only includes L2A_REF measurements which have passed site specific quality checks	wavelength, series
Both	L1D_RAD	Only includes L1B_RAD measurements which have passed site specific quality checks	wavelength, series
Both	L1D_IRR	Only includes L1B_IRR measurements which have passed site specific quality checks	wavelength, series

non_linear has the polynomial non-linearity coefficients, and int_time is the integration time of the measurement (in ms). An update to this default measurement function is foreseen in a future release, which will include temperature and spectral straylight corrections. The gains and non-linearity coefficients are taken from the most recent calibration data for the given instrument.

The same measurement function is applied for radiance and irradiance measurements, but the gains (as well as the measurements themselves) will be different. Note that the non-linearity coefficients are the same for both radiance and irradiance head (assuming that the non-linearity results from the sensor and internal electronics). For the LANDHYPERNET network, the VNIR and SWIR sensors also both use the same measurement function, and each have their own set of calibration and non-linearity coefficients.

Uncertainties on each of the input quantities (i.e., digital_number, gains, dark_signal, non_linear and int_time) can optionally be propagated to the L1A products using PUNPY uncertainty propagation package. More details are provided in Section 3.4.

3.2.3 Averaging

In order to get the best averaged results and associated uncertainties per series, the most robust approach is to first average the L0A data (i.e., radiance, irradiance and dark scans in digital numbers). Only the scans that passed the L1A quality checks (see Section 3.3.2) are used in the mean. The averaged raw data make up the L0B datasets. Next, the averaged results in the L0B datasets are calibrated using the same approach as in the previous section.

For the WATERHYPERNET network these calibrated results are directly saved as the L1B datasets, which are an important output of the HYPERNETS_PROCESSOR as these are made publicly available. for the LANDHYPERNET network, after applying the calibration, the VNIR and SWIR data are combined (for the WATERHYPERNET network no SWIR data are acquired, and this step is skipped). This is done by simply appending all VNIR measurements with wavelengths smaller than 1,000 nm with all SWIR measurements with wavelengths larger than 1,000 nm. The VNIR-SWIR combined, averaged data are then saved as the L1B datasets. An example L1A plot for irradiance is shown in the right panel of Figure 6.

3.2.4 Radiance and irradiance preprocessing

3.2.4.1 LANDHYPERNET network interpolation

The L1C processing for the LANDHYPERNET network consists of two interpolation steps that are applied to the irradiance

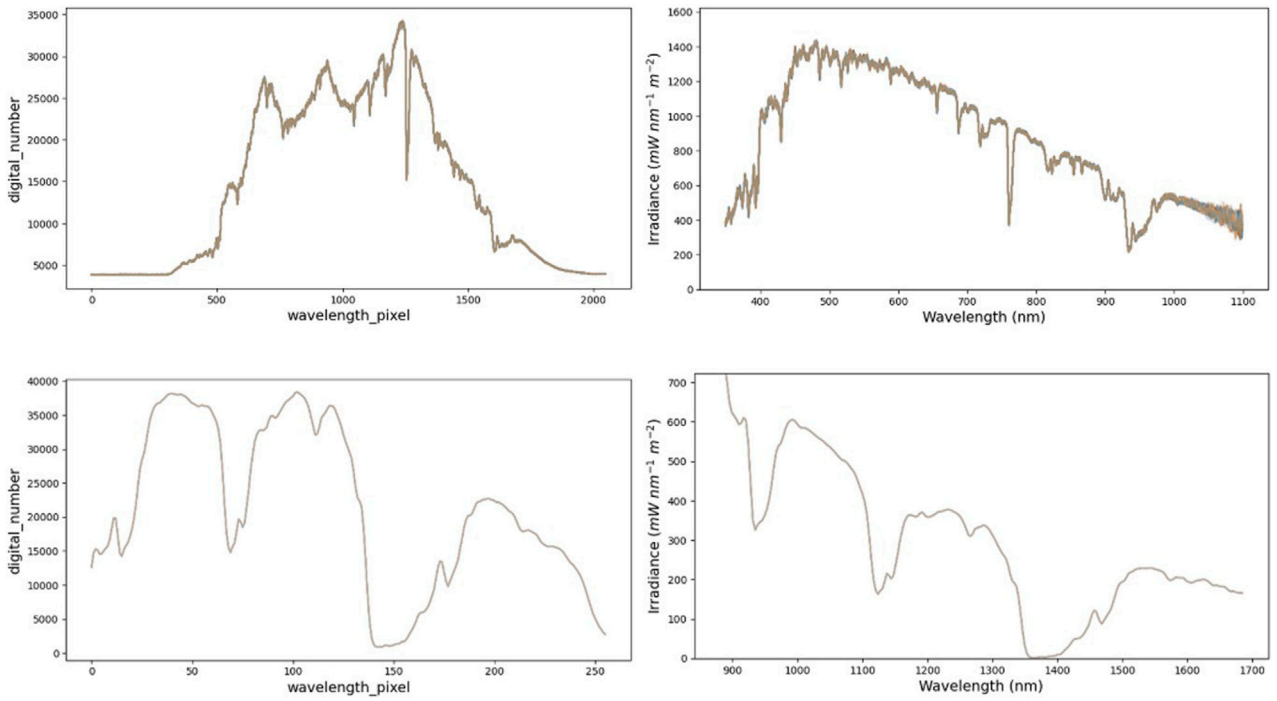


FIGURE 6
Example of the calibration process for the Gobabeb hyperspectral Namibia site (GHNA) sequence on 2022–10–06 at 9 a.m. UTC. The left panels show the digital numbers (L0A) for the irradiance series at the start of the sequence (all scans plotted) of the VNIR (top) and SWIR (bottom) sensors. The right panels show the calibrated irradiance scans (L1A) of the VNIR (top) and SWIR (bottom) sensors.

measurements in order to bring them to the same wavelength scale and timestamps as the radiance measurements.

- Spectral interpolation: The irradiances are spectrally interpolated to the wavelengths of the radiance measurements (which are not identical to the irradiance measurements). Currently, we use a simple linear interpolation.
- Temporal interpolation: Next, we use a similar method to perform a temporal interpolation. In this case, we interpolate the irradiance measurements at the start and end of the sequence, to each of the timestamps of the radiance measurements. A correction is applied to take into account the change in solar zenith angle during the sequence.

The output of the L1C processing is a product with irradiances that now have the same wavelengths and timestamps as the radiance measurements. The radiances in the L1C dataset are unchanged from the L1B dataset. An example of the L1C interpolated irradiances is shown in Figure 7.

There are multiple options available for the interpolation. For the temporal interpolation, the default option includes a correction for the change in solar zenith angle throughout the sequence. Prior to the interpolation, the irradiances are divided by the cosine of the solar zenith angle at the time of the irradiance acquisition. After the interpolation, the irradiances are multiplied by the cosine of the solar zenith angle at the timestamps of the radiances. Alternatively, there is also an option to not apply the solar zenith angle correction (i.e., only linear interpolation).

By default, the linear interpolation method is used for both the spectral and temporal interpolations. However, optionally, the HYPERNETS_PROCESSOR can also be set up to do interpolation following a model. This is done using the interpolation tool within the NPL CoMet toolkit to interpolate between the irradiance wavelengths using a high-resolution reference[7]. The high resolution reference for the spectral irradiance interpolation comes from a clear-sky model, which gives a good first-order approximation of the short scale variability. This model is then scaled to go through the measured irradiance data, while taking into account the spectral response function of the different HYPSTAR® measurements.

The interpolation option using a high resolution model has been implemented, but is not currently operationally used. Further investigations are required to assess whether these alternative interpolation methods lead to sufficient improvement in the performance to justify their significantly slower runtime.

3.2.4.2 WATERHYPERNET network

The L1C processing for the WATERHYPERNET network consists of multiple steps including (1) water-specific quality

7 https://comet-maths.readthedocs.io/en/latest/content/interpolation_atbd.html

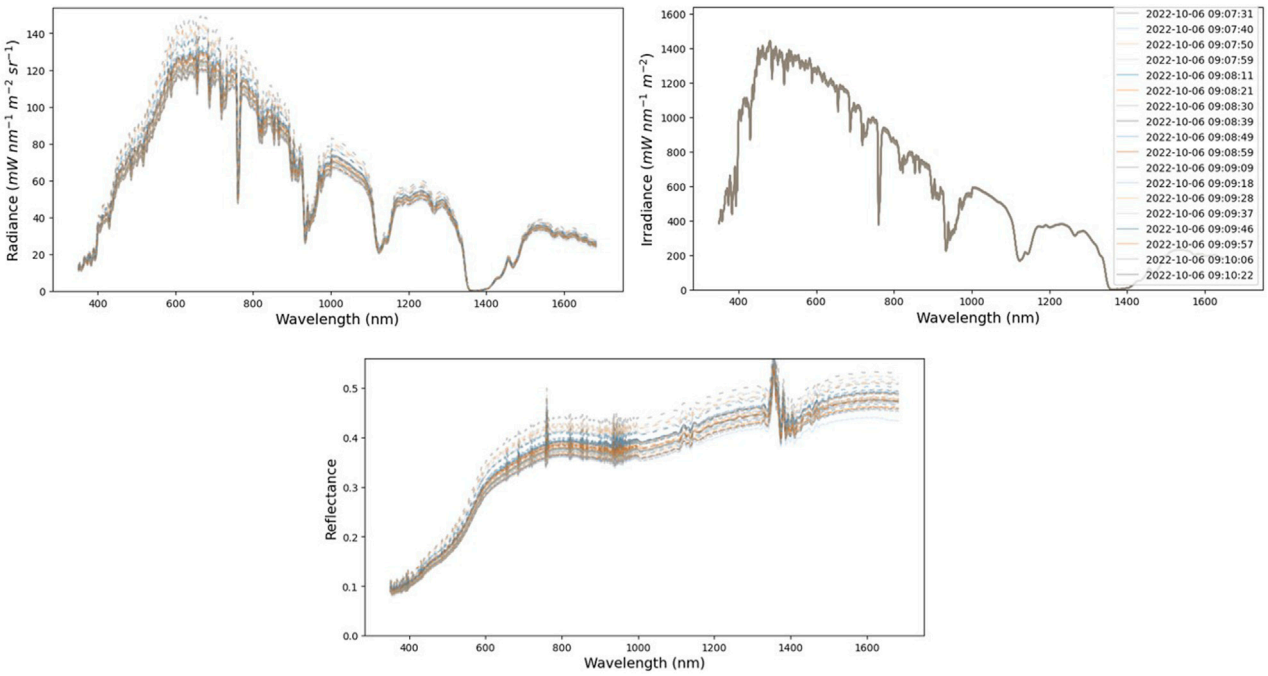


FIGURE 7
Example of the interpolation and surface reflectance calculation for the GHNA sequence on 2022–10–06 at 9 a.m. UTC. The top left panel shows 45 radiance series (L1B/L1C), which each have a different geometry, and which were acquired one after another. The top right panel shows the irradiance series (L1C), spectrally and temporally interpolated to match the radiance series. The various interpolated lines are very close to each-other. The bottom panel shows the surface reflectances (L2A) calculated using the radiances and irradiances in the L1C dataset.

checks, (2) temporal and spectral interpolation steps mirroring the land processing, and, (3) computation of the water-leaving radiance and reflectance for each upwelling radiance scan. For the latter, the HYPERNETS_PROCESSOR uses a water specific processing component, referred to as RHYMER (Reliable processing of HYperspectral MEasurement of Radiance, version on 2020–10–16, written by Quinten Vanhellemont and adapted for the water HYPERNETS_PROCESSOR by Clémence Goyens).

In its current version, RHYMER provides all the required functions to process above water measurements to water-leaving radiance and water-leaving reflectance (referred hereafter as water reflectance), including the estimation of the air-water interface reflection coefficient using Mobley (1999), Mobley (2015). RHYMER is written such that it can easily be adapted to use alternative look-up-tables, processing functions and/or quality flags. Note that the L1C processing takes as input the L1A files (i.e., not the L1B files as done for the LANDHYPERNET network processing) as it checks for water specific quality flags per upwelling radiance scan. In addition, if the processor encounters measurements made at different relative azimuth angles (and provided that the standard measurement protocol is followed), the processor will estimate the reflectance at each relative azimuth angle $\Delta\varphi$. Therefore, the final dimensions of the L1C data level are wavelength and the number of quality-checked scans of the upwelling radiance measurements. A separate L1C data file is created for each relative azimuth angle.

The L1C radiance and irradiance processing steps are the following.

- Cycle parse: The processor parses through the sequence and verifies, for a single azimuth angle and after applying the required quality checks (see Section 3.3), if the sequence has the required number of downward irradiance ($\theta_v = 180^\circ$) and radiance ($\theta_v = 140^\circ$) scans and corresponding upward radiance scans ($\theta_v = 40^\circ$). If these requirements are not met, the sequence is not further processed and an anomaly is raised (see Section 3.3).
- Spectral interpolation: Likewise for the LANDHYPERNET network processing, the irradiance measurements are spectrally interpolated in order to bring them to the same wavelength scale as the radiance measurements.
- Temporal interpolation: Next, the downwelling radiance and irradiance measurements are averaged per series and each series is temporally interpolated to the same timestamps as the upwelling radiance measurements (including a correction to account for viewing zenith angle, likewise the temporal interpolation of the land processing mentioned above).
- Auxiliary data retrieval: All the required parameters for the computation of the water-leaving radiance and reflectance, i.e., wind speed, *ws*, and the air-water interface reflection factor, ρ_f (θ_v, θ_s, $\Delta\varphi$, *ws*), are retrieved. The default wind speed is taken from NCEP/GDAS (National Centers for Environmental Prediction, National Weather Service, NOAA, U.S. Department of Commerce, 2015) and is spatially and temporally interpolated according to the site location and the measurement date and time. Other data sources or a constant value for wind speed can also be used. Based on the retrieved wind speed, ρ_f (θ_v, θ_s, $\Delta\varphi$, *ws*)

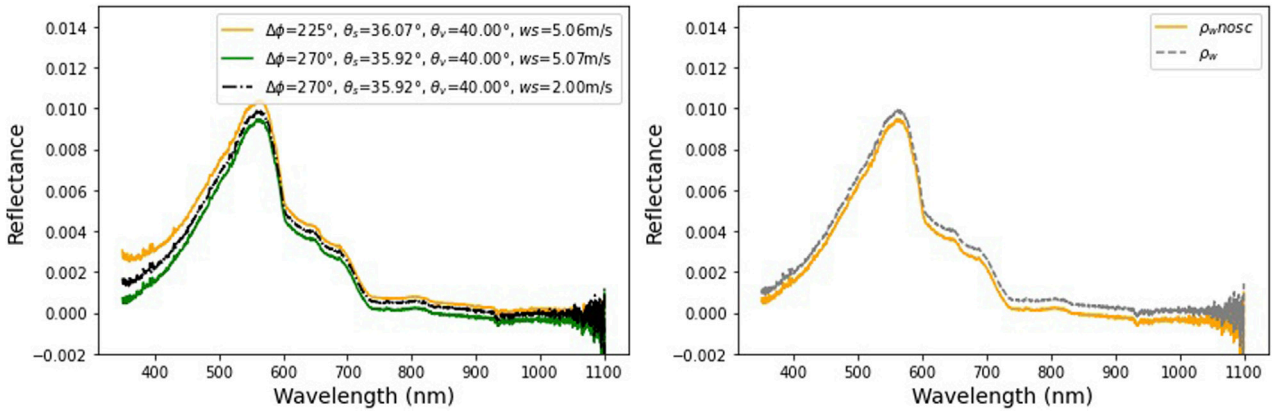


FIGURE 8
Example of the water-leaving reflectances for the Wraysbury Reservoir, UK site (WRUK) sequence on 2023–07–07 at 1:45 p.m. UTC. The left panel shows reflectance without NIR similarity correction ($\rho_{w,nosc}$) for different relative azimuth angles ($\Delta\varphi$ equals 225° and 270°, respectively) and wind sources (i.e., retrieved from NCEP/GDAS and default 2 m^{-1}). The right panel shows the reflectance with (ρ_w) and without the NIR similarity correction ($\rho_{w,nosc}$).

can be extracted from different look-up tables, e.g., Mobley (1999) or Mobley (2015). Figure 8 (left panel) shows an example of the estimated reflectance for a single sequence, but for different $\Delta\varphi$ (i.e., 225° and 270°) and wind speeds (retrieved from NCEP/GDAS (default) and using a constant value of 2 m^{-1}). The options used for the retrieval of the wind speed and the air water interface reflectance factor can be set in the configuration file (e.g., *rhof_option*: Mobley1999 and *wind_ancillary*: GDAS) and are recorded in the metadata of each processed datafile for traceability.

- Retrieval of water-leaving radiance and reflectance: For each L_u scan and from the averaged and temporally interpolated L_d, the water-leaving radiance, L_w, is computed as in Eq. 1 below.

$$L_w(\theta_v, \Delta\varphi, \lambda, \theta_s) = L_u(\theta_v, \Delta\varphi, \lambda, \theta_s) - \left[\rho_f(\theta_v, \Delta\varphi, \lambda, \theta_s, ws) L_d(180 - \theta_v, \Delta\varphi, \lambda, \theta_s)\right] \quad (1)$$

The water-leaving radiance is then converted into water reflectance (omitting illumination and viewing dimensions for brevity) in Eq. 2 below using the downwelling (hemispherical) irradiance E_d:

$$\rho_{w,nosc}(\lambda) = \pi \frac{L_w(\lambda)}{E_d(\lambda)} \quad (2)$$

with *nosc* referring to *non similarity corrected* reflectance. Indeed, although most acquisition protocols attempt to avoid Sun glint, over wind roughened surfaces the target radiance may still contain some Sun glint. Therefore, a spectrally flat correction, ϵ, based on the "near infrared (NIR) similarity spectrum" correction from Ruddick et al. (2006), is applied. The constant ϵ is estimated in Eq. 3 using two wavelengths in the NIR (default for λ_1 and λ_2 are 780 and 870 nm, respectively).

$$\epsilon(\lambda_1, \lambda_2) = \frac{\alpha \rho_{w,nosc}(\lambda_2) - \rho_{w,nosc}(\lambda_1)}{\alpha - 1} \quad (3)$$

α is the similarity spectrum ratio for the bands used (the default is, α(780,870) = 1.912). The water reflectance ρ_w is given in Eq. 4 below.

$$\rho_w(\lambda) = \rho_{w,nosc}(\lambda) - \epsilon(\lambda_1, \lambda_2) \quad (4)$$

Figure 8 (right panel) shows an example of the estimated reflectance for a single sequence with and without the NIR similarity correction. The data shown in this figure are for the WRUK site, an inland water basin with relatively clear waters. Hence, the NIR similarity correction can be applied (in contrast to turbid water sites such as MAFR or M1BE, see Table 5).

3.2.5 Surface reflectance calculation

3.2.5.1 LANDHYPERNET network

For the LANDHYPERNET network, the surface reflectances can now be calculated from the L1C radiances, L_u, and irradiances, E_d in Eq. 5 below.

$$\rho = \pi \frac{L_u}{E_d} \quad (5)$$

We note that this surface reflectance is technically the hemispherical-conical reflectance factor and not the bidirectional reflectance factor, as the contribution from sky reflectance is included in the measurements and the field-of-view of the LANDHYPERNET is 5°.

An example with all the different series is shown in the right panel of Figure 7. In addition, Figure 9 shows additional useful plots produced by the HYPERNETS_PROCESSOR. This includes plots showing the reflectance variation for a fixed value of viewing azimuth angle (98°) and viewing zenith angle (30°), as well as a polar plot showing the reflectances at 900 nm for each of the included geometries. This shows the smooth variation of the surface reflectance with different angles. In the future, we will investigate whether BRDF models can be fitted to these data (Section 6). These data might in the future be provided as a L2C or L2D dataset.

3.2.5.2 WATERHYPERNET network

For each L1C data file (one per relative azimuth angle), the surface reflectances and water radiances (computed at each L_u timestamp) are averaged. This results in L2A files containing one spectrum for each variable (i.e., water-leaving radiance, and, water

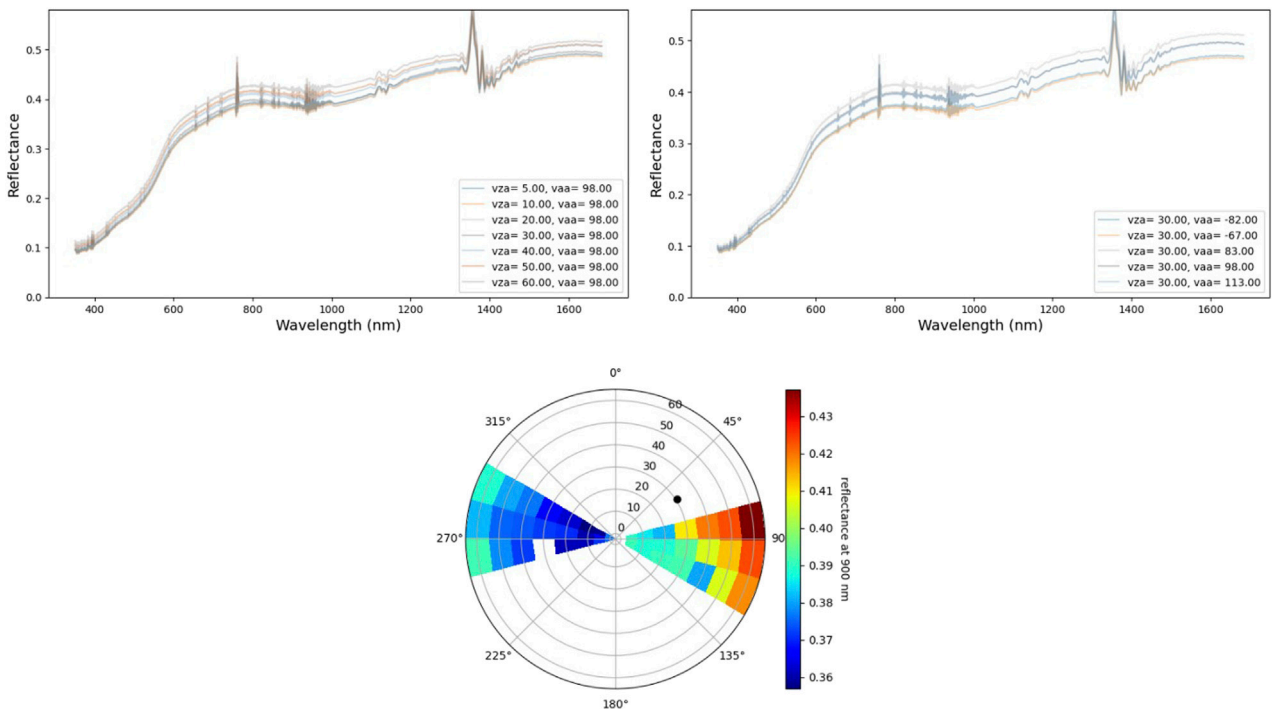


FIGURE 9
Example of the surface reflectances for the GHNA sequence on 2022–10–06 at 9 a.m. UTC. The top left panel shows the variation with viewing zenith angle for the scans with a viewing azimuth angle of 98°. The top right panel shows the variation with viewing azimuth angle for the scans with a viewing zenith angle of 30°. The bottom panel shows a polar plot with the 900 nm reflectances for each of the different included viewing geometries (zenith angle for radial axis, azimuth angle for angular axis). The solar geometry is shown by the black dot.

reflectance with and without the NIR similarity correction) and the associated uncertainties. Figure 10 shows an example of the reflectance spectra measured at the WRUK site on 2023–07–07 from the L1C processing level and the averaged L2A reflectance spectrum. Measurements were made at two different relative azimuth angles, i.e., 225° (or −135°) and 270° (or −90°). Hence, as shown in Figure 10, more variability in the L1C reflectance spectra results in higher uncertainties for the L2A reflectance spectrum (see Section 3.4 for more details about uncertainties).

3.2.6 Site-specific quality checks

Once the L2A datasets have been produced, a final set of site-specific quality checks and masks are applied. The site-specific quality checks and masks are determined after inspection of the first months of data in consultation of the site owners - see Section 3.3.7. The resulting masks are applied to the L2A dataset and stored as L2B. The same masks are also applied to the L1B datasets and stored as L1D. Only the L1D and L2B data will be distributed to satellite validation users.

3.3 Quality checks, quality flags and anomalies

Throughout the different processing steps described in the previous section, a number of quality checks are applied. These quality checks are described below. When a given quality check fails, there are two possible outcomes.

- When the quality check is critical for having useful data, failure of the quality check results in halting of the processing, and an anomaly is raised and stored in the anomaly database (see Section 4.3). In Tables 3, 4, it is indicated which quality checks halt the processing and what anomaly is raised.
- On the other hand, there are some quality check where failure does not necessarily mean the entire sequence cannot be used. In some cases only part of the data might be affected (e.g., a single series in the sequence), or in other cases the quality check is only a warning the data should be used with caution. In each of these cases, a quality flag is added to the data, and the processing is continued. In some cases, it is still useful to also raise an anomaly and store it in the anomaly database for future reference. The different quality checks, the triggered flags and raised anomalies are listed in Tables 3, 4.

3.3.1 L0A: Read raw data

While reading in the data, there are quality checks that verify whether the metadata.txt file is appropriate and all required raw data files exist. If these checks fail, an anomaly is raised (see Section 4.3) and the processing halts. There is also a quality check which checks whether the file with meteorological information exists. If it does not, an anomaly is added to the SQL database, but the processing is continued. In addition, for traceability, if the latitude and/or longitude are unknown (i.e., not included in the metadata.txt file), latitude and longitude are taken from the processor

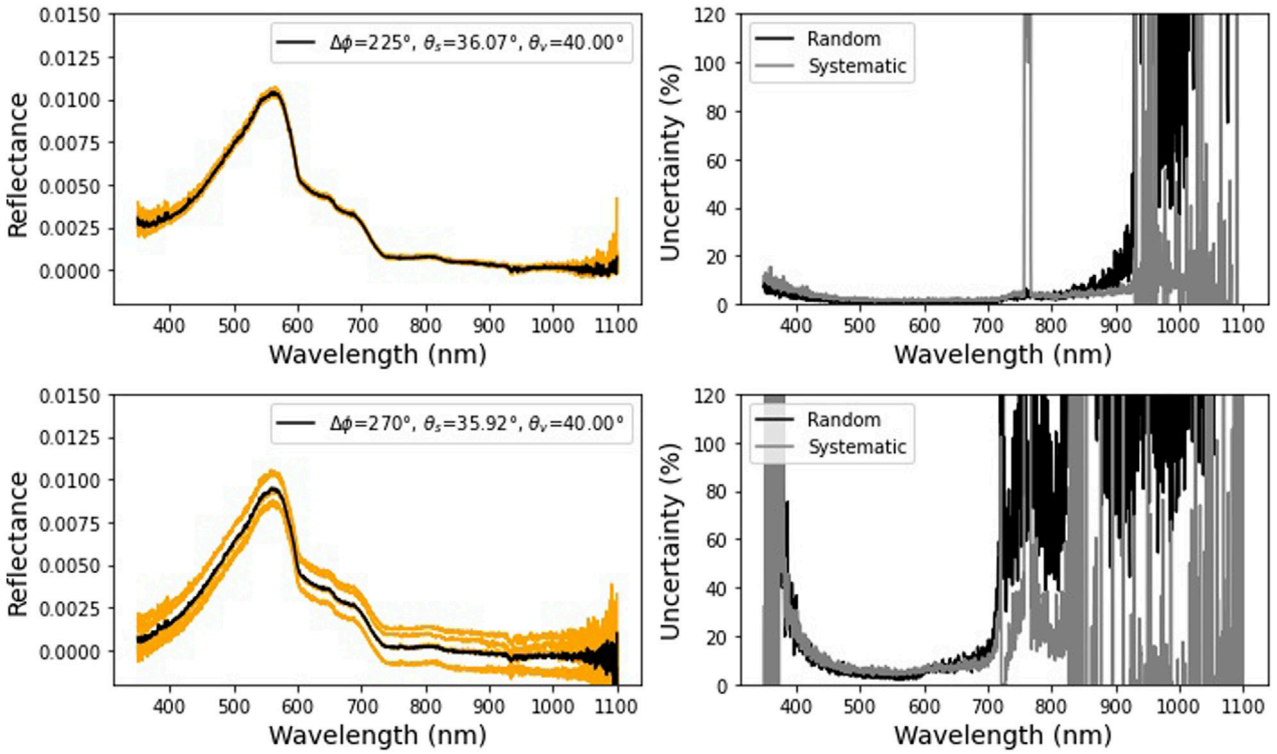


FIGURE 10
Example of the water-leaving reflectances (without NIR similarity correction ($\rho_{w,nosc}$)) for the WRUK sequence on 2023–07–07 at 1:45 p.m. UTC. The left panel shows reflectance of the L1C processing level (orange) together with the averaged L2A spectrum (black) for the two different relative azimuth angles ($\Delta\varphi$) equal 225° and 270° (top and bottom, respectively). The right panel shows the relative random and systematic uncertainties for each averaged L2A spectrum for the relative azimuth angles ($\Delta\varphi$) equal 225° and 270° (top and bottom, respectively).

configuration file and the 'lon_default' and/or 'lat_default' flags are triggered. Next, the pointing accuracy of the pan/tilt is also verified. If the requested pan or tilt angle differs by more than 3° with the effective pan or tilt angle, the 'bad_pointing' flag is raised for the given scan.

3.3.2 L1A: Check raw data prior to calibrating

Before calibrating each of the individual scans in the L0 data, a number of quality checks is applied. If the spectrally integrated signal of a scan is more than 3 times the standard deviation, or more than 25% (whichever is largest) removed from the mean, it is masked and will not be used when averaging the series. This process is repeated until convergence and applied to the measured (ir)radiances and to the darks. The L0 data are also checked for saturation (digital number $DN \geq 64{,}000$) and for discontinuities (missing values or $\Delta DN > 10^4$). A flag is also added to the L1 data if any of the dark scans have been masked by the above processes. Scans not satisfying the quality checks are flagged, but no data are removed at this stage.

3.3.3 L0B: Average valid scans

When averaging, only scans that passed the L1A quality checks are used. There are a few quality checks that check the number of scans being averaged is sufficient. By default, the threshold number of scans is three. If there are fewer than three scans for one of the dark, radiance or irradiance series, no reliable uncertainty can be calculated, and the series is flagged. If less than half of the radiance or irradiance scans of a series pass the L1A checks, the series is flagged, as this likely indicates something has gone wrong.

3.3.4 L1B: Check calibrated data are fit for purpose

After calibrating the L0B file, we check all the required measurements to form a standard sequence are included and have not been flagged by the previous 'not_enough_dark_scans', 'not_enough_rad_scans' or 'not_enough_irr_scans' flags. If any series are missing or flagged, the 'series_missing' is added to all the series in the sequence. If there are no valid radiance or irradiance measurements, the processing is halted.

Next, quality checks on the irradiance measurements are applied. First, their viewing angles are checked (which must be 180°, with a tolerance of 2°, as irradiance measurements have to be pointing up). Next, the irradiance is compared to a simulated clear-sky model. This clear sky model is made using the libRadtran radiative transfer software package (Emde et al., 2016), assuming its mid-latitude summer standard atmosphere and its standard desert surface (for land sites) and its standard ocean surface (for water sites). Note that the surface does not make a big difference as it is only second-order effects that affect the downwelling irradiance

10.3389/frsen.2024.1347230

TABLE 3 HYPERNETS_PROCESSOR flags applied up to L1B.

Name	Network	Level	Description	Flag triggered	Anomaly raised	Processing halted
metadata_miss	L, W	L0A	metadata file is missing, or one of the raw files listed in the Metadata file is missing		'm'	✓
meteo_miss	L, W	L0A	File with meteorological information is missing		's'	
lon_default	L, W	L0A	Default longitude as given in the configuration file is used (missing Lon in metadata)	✓		
lat_default	L, W	L0A	same as 'lon_default' but for latitude	✓		
pt_ref_invalid	L, W	L0A	No effective pan/tilt is returned and the requested pan/tilt was used instead	✓		
bad_pointing	L, W	L0A	Difference between requested and effective pan/tilt angle is > = 3°	✓	'a'	
outliers	L, W	L1A	Scans that are outliers are flagged and will not be included when averaging scans	✓		
L0_threshold	L, W	L1A	Check if any of the spectral pixels are saturated, i.e., digital number $DN \geq 64{,}000$	✓		
L0_discontinuity	L, W	L1A	Check if there are missing values in the spectrum, or significant discontinuities ($\Delta DN > 10^4$)	✓		
dark_masked	L, W	L1A	If any of the darks have been masked by 'outliers', 'L0_thresholds', and/or, 'L0_discontinuity'	✓		
half_of_scans_masked	L, W	L0B	Less than half of the scans for a series passed quality checks 'bad_pointing', 'outliers', 'L0_thresholds', and, 'L0_discontinuity'	✓		
not_enough_dark_scans	L, W	L0B	Not enough valid dark scans for this series (# valid dark scans < n_valid_dark from the config file)	✓	'nld'	
not_enough_rad_scans	L, W	L0B	Not enough valid radiance scans for this series (# valid radiance scans < n_valid_rad from the config file)	✓	'nlu'	
not_enough_irr_scans	L, W	L0B	Not enough valid irradiance scans for this series (# valid irradiance scans < n_valid_irr from the config file)	✓	'ned'	
series_missing	L, W	L1B	Check if there are any missing series (either not present or flagged by 'not_enough_dark_scans', 'not_enough_irr_scans', 'not_enough_rad_scans' or 'vza_irradiance')	✓	'ms'	
vza_irradiance	L, W	L1B	One of the irradiance measurements did not have θ_v = 180° (within 2° tolerance), so has been masked	✓		
no_clear_sky_irradiance	L, W	L1B	More than 10% of the wavelength bands have a difference of more than 50% with the clear sky model	✓		
variable_irradiance	L, W	L1B	More than 10% difference between start and end E_d at 550 nm	✓		
negative_unc	L, W	L1B	There are negative uncertainties		'u'	✓
half_of_unc_too_big	L, W	L1B	More than 50% of data has random error above 100% (likely corrupted or dark data)	✓	'o'	
discontinuity_VNIR_SWIR	L	L1B	Checks if the VNIR and SWIR are different by more than 25%	✓	'd'	

used in the clear sky model. The surface is assumed to be at sea-level and the TSIS solar irradiance model is used (Coddington et al., 2021). Given the downwelling irradiance measures the full hemisphere, the only relevant angle is the solar zenith angle. A clear sky model is calculated using solar zenith angles of 0°, 10°, 20°, 40°, 60°, 70° and 80°. These irradiance data are provided at 0.1 nm resolution to the HYPERNETS_PROCESSOR.

When performing the clear sky quality check, the irradiance data are band integrated to the HYPSTAR® bands (which vary slightly from instrument to instrument), as defined by the

TABLE 4 HYPERNETS_PROCESSOR flags applied during L1C processing.

Name	Network	Level (C)	Description	Flag triggered	Anomaly raised	Processing halted
check_valid_irradiance	L, W	L1	Halt processing if 'variable_irradiance' flag was triggered at previous level		'nu'	✓
check_valid_sequence	L, W	L1	Halt processing if there are no valid series (flagged by 'not_enough_dark_scans', 'not_enough_irr_scans', 'not_enough_rad_scans' or 'vza_irradiance')		'in'	✓
single_irradiance_used	L, W	L1	If only one series of irradiance is used for the computation of the reflectance	✓		
no_clear_sky_sequence	L, W	L1	If all irradiance series are flagged with the 'no_clear_sky_irradiance' flag	✓	'cl'	
variable_radiance	W	L1	More than 10% difference between start and end L_d at 550 nm		'nd'	✓
single_skyradiance_used	W	L1	If only one series of downwelling radiance is used for the computation of the reflectance	✓		
lu_eq_missing	W	L1	If there is no upwelling and downwelling radiance pair with similar pointing azimuth angles (within 1° tolerance)	✓	'l'	✓
rhof_angle_missing	W	L1	If there are no downwelling radiance scans at the appropriate viewing zenith angle (i.e., 180°-θ_v) (within 1° tolerance)	✓	'l'	✓
rhof_default	W	L1	If the viewing geometry of the upwelling and downwelling radiance measurements are outside the viewing geometry range of the selected LUT for the 'rhof_option' (e.g., $\Delta\phi > 180°$ when using the LUT from Mobley (1999)), a default ρ_F is used for the air-water interface correction factor (default: $\rho_F = 0.0256$)	✓		
temp_variability_irr	W	L1	If the difference in $E_d(\lambda)$ scans exceeds a given threshold between two neighbouring scans (default: threshold = 25% and $\lambda = 550$, see also Ruddick et al. (2006))	✓		
temp_variability_rad	W	L1	If the difference in $L_d(\lambda)$ or $L_u(\lambda)$ scans exceeds a given threshold between two neighbouring scans (default: threshold = 25% and $\lambda = 550$, see also Ruddick et al. (2006))	✓		
min_nbred/lu/lsky	W	L1	If the total number of scans not flagged by either 'L0_threshold', 'bad_pointing' or 'outliers', is less than a given threshold (default: 3)	✓	'ned' 'nlu' 'nld'	✓
def_wind_flag	W	L1	If a default wind speed is used (by default: wind speed = 2 m^{-1})	✓		
simil_fail	W	L1	If the quality check applied on the NIR similarity spectrum is not verified as suggested by Ruddick et al. (2005) (see Section 3.2 and Figure 4 in Ruddick et al. (2005)) with default values for the computation of the NIR Similarity being 780 and 870 nm, the reference wavelength 670 nm and the threshold 5%	✓		

calibration data, using the MATHEO[8] tool. The measured HYPERNETS irradiances are then scaled (assuming cosine response) to match the nearest solar zenith angle among the provided clear sky models. In Figure 11, we show an example of the clear sky checks applied to the irradiance. We note that the clear sky models are not always very close, as a mid-latitude summer atmosphere at sea-level was used as opposed to a more realistic site-specific model. Therefore this quality check only fails if there are significant differences of more than 50% with the clear sky model (for more than 10% of the wavelength bands). Overcast conditions consistently trigger this quality flag.

Then, there is a quality check verifying that the irradiance has not changed more than 10% (after correcting for differences in solar zenith angle) between the measurements at the start and end of the sequence. At this stage the resulting irradiance series are flagged and the L1B file is produced. However if this 'variable_

8 https://matheo.readthedocs.io/en/latest/

TABLE 5 Examples of site name conventions for water and land sites.

Site ID	Site Name
BSBE	Blankaart South, Belgium
TBBE	Thornton-C, Belgium
M1BE	Zeebrugge MOW-1, Belgium
MAFR	MAGEST station, Gironde estuary, France
LPAR	LA PLATA, La Plata River, Argentina
BEFR	Etang de BERRE, France
VEIT	Aqua Alta Oceanographic Tower, Venice, Italy
WRUK	Wraysbury Reservoir, UK
ATGE	ATB, Germany
BASP	Barrax SRIX4VEG site, Spain
DEGE	Demmin, Germany
GHNA	Gobabeb HYPERNETS, Namibia
IFAR	IFEVA, Argentina
JAES	Jarvselja, Estonia
PEAN	Princess Elisabeth Research Station, Antarctica
WWUK	Wytham Woods, UK

irradiance' check is triggered the processing will be halted at the L1C stage.

There are also some quality checks on the uncertainties. These check that there are no negative uncertainties and that less than 50% of the random uncertainties (i.e., less than half of the spectral channels) on radiance and irradiance have values below 100% (this indicates corrupted or dark data, e.g., measurements at night fail this check).

For the LANDHYPERNET network, there is an additional check that there is no strong discontinuity (larger than 25%) between the VNIR and SWIR parts of the spectrum for both radiances and irradiances.

3.3.5 L1C: Check if all required data for L1C processing is valid

Before interpolating the irradiances, there are a number of checks verifying the data are valid. If the 'variable_irradiance' flag was raised in previous levels, we cannot perform reliable interpolation and the processing is halted. Next, the processing is halted if there are no valid series for either radiance or irradiance (checking 'not_enough_dark_scans', 'not_enough_irr_scans', 'not_enough_rad_scans' or 'vza_irradiance' flags). When all irradiance series have the 'no_clear_sky_irradiance' flag, the processing is continued, as overcast products might still be useful to some users (available by request). A flag is added to all series to indicate this is a sequence without clear sky irradiance. No L1D/L2B data will be produced (and thus this data will not be provided publicly). When only one irradiance series is available (due to 'vza_irradiance' or missing measurements), the processing is continued, and the same irradiance is used for every radiance series (instead of temporally interpolating), with a correction for the changing solar zenith angle throughout the sequence. A flag is added to the entire sequence to indicate only one irradiance has been used.

For the WATERHYPERNET network, there are a number of additional quality checks. First, similarly to the 'variable_irradiance' flag, it checks if the downwelling sky radiance, L_d, at 550 nm remains constant over the entire sequence (i.e., coefficient of variation for L_d (550) < 10%). Indeed, if L_d varies significantly between the start and the end of the sequence, the downwelling sky radiance can not be temporally interpolated to the timestamps of the L_u scans and the processing is therefore halted. Note however that the threshold of 10% difference may be subject to further research in order to select the best threshold. Next, an anomaly (i.e., 'l') is raised and the processor is halted if the upwelling and downwelling radiance pair does not have a similar pointing azimuth angle (within 1° accuracy), or, if the viewing geometry does not satisfy θ_v for L_d equals 180-θ_v for L_u (within 1° accuracy).

The processor also checks for the temporal variability within each series. Scans for E_d, L_u and L_d at 550 nm, should not vary by more than a certain threshold with their neighbouring scans (default threshold is 25%). Note, those flags are not expected to be raised as scans with high temporal variability should have been removed by previous flags, i.e., 'outliers' or 'L0_discontinuty' flags. However, these flags are kept to ensure consistency with other common water network processing (Ruddick et al., 2006; Vansteenwegen et al., 2019).

The number of scans per series is important to assess the uncertainties. Hence, if the number of scans, not flagged by 'bad pointing', 'outliers', 'L0_thresholds', or 'L0_discontinuity', for E_d, L_u and L_d is below a given threshold, an anomaly is raised, and the processing is halted. The current default value is three which is a compromise between sequence duration and measurement replicates.

If the viewing geometry of the upwelling and downwelling radiance measurements are outside the viewing geometry range of the selected LUT for the 'rhof_option', the flag 'rhof_default' is raised. Similarly, a 'def_wind_flag' is used to trace spectra processed with a default wind speed value.

Finally, the flag 'simil_fail' is raised if the quality check applied on the NIR similarity spectrum is not verified as suggested by Ruddick et al. (2005). Note, this flag should only be considered for water types satisfying the NIR Similarity spectrum theory (i.e., clear to moderately turbid waters).

3.3.6 L2A: Calculate reflectance

Currently, no further quality checks are applied. For the WATERHYPERNET network, water radiance and reflectance are averaged only for the L_u scans which are not flagged for temporal variability, i.e., 'temp_variability_irr' and 'temp_variability_rad', or 'rhof_default'.

3.3.7 Site-specific quality checks

The site-specific quality checks range from angular masks, i.e., viewing geometries that are expected to be affected by shadows or part of the installation (such as a mast) in the field-of-view, to quality checks that are very specific to the surface for a given site (e.g., ensuring vegetation is measured for the Wytham Woods UK (WWUK) site, or checking abnormal high reflectance values over clear or low turbid waters). Such site-specific checks often use thresholds (determined from analysis of the first months/year of data) checking the reflectance (or ratios

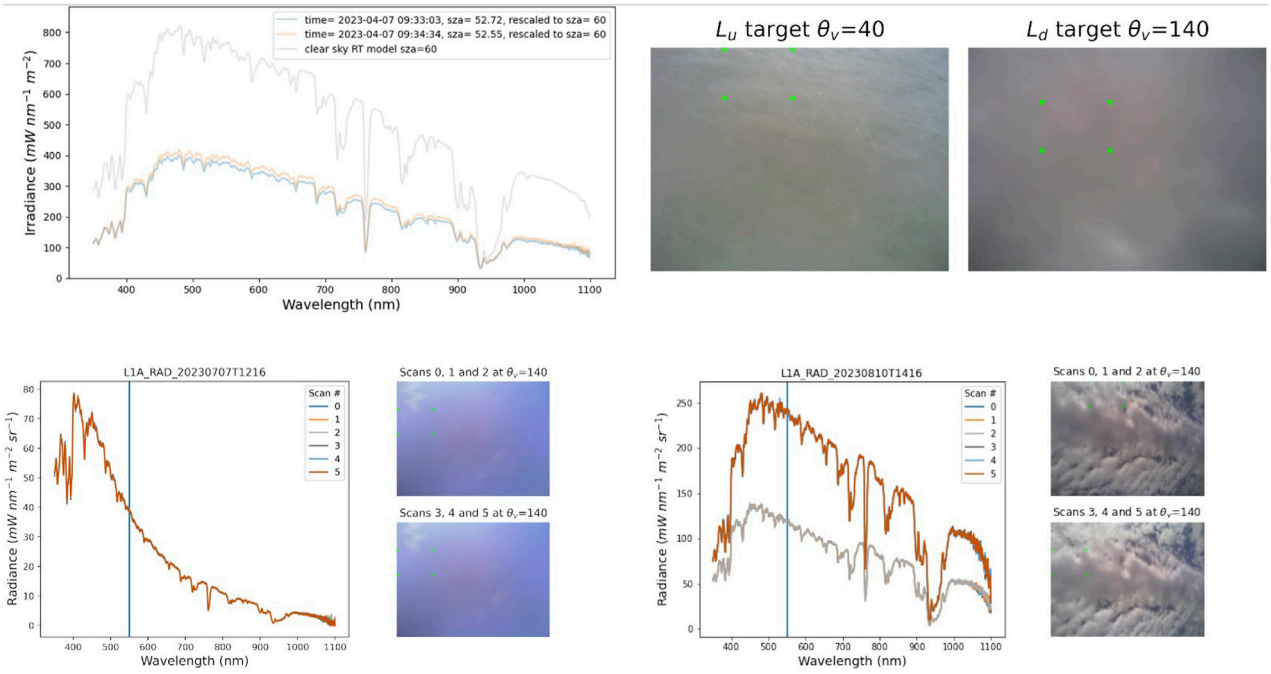


FIGURE 11
Example of the quality checks on the illumination applied in the L1B and L1C data processing for the downwelling irradiance and radiance, respectively. The top row shows the irradiance measurements not passing the 'no_clear_sky_irradiance' check taken at Zeebrugge MOW-1 Belgium (M1BE) site on the 2023–04–07 at 09:32 together with the simulated clear sky (for the same illumination geometries). Images of the sky (θ_v = 140°) and the water (θ_v = 40°) for this sequence are also shown. Bottom row shows (1) an example of downwelling radiance scans passing the quality criteria for constant downwelling radiance taken at WRUK on 2023–07–07 and the images taken with the camera during the measurements (bottom left panels), and, (2) an example of downwelling radiance scans not passing this quality check (variable_radiance flag is raised), and, the images taken with the camera during the measurements taken on 2023–08–10 at WRUK (bottom right panels).

of reflectances, e.g., epsilon for water sites, or NDVI for vegetated sites) at specific wavelengths. Additionally, the site owners can provide specific date-time ranges to mask, e.g., because something went slightly wrong during the deployment of the instrument (e.g., alignment).

Another important quality check is that the surface reflectances are compared to a time-series of similar measurements (matching viewing geometry and time of day) at the same site, to identify outliers so that they can be investigated. If these outliers are found to come from invalid data, further quality checks can be added to remove such cases.

The resulting site-specific masks are applied on a sequence-by-sequence basis to both L2A data (resulting in L2B dataset) and to the L1B dataset (resulting in L1D dataset). The same mask is applied to both L2A and L1B so that they remain consistent with each-other.

3.4 Uncertainties

3.4.1 Uncertainty propagation

The HYPERNETS_PROCESSOR uses a Monte Carlo (MC) approach (see Supplement one to the "Guide to the expression of uncertainty in measurement" (JCGM 101:2008, 2008), to propagate uncertainties and error-correlations between product levels. This MC approach is implemented using the PUNPY module from the open-source CoMet toolkit. PUNPY is a Python software package to propagate random, structured and systematic uncertainties through a given measurement function. For further info on PUNPY, we refer to De Vis & Hunt (in this issue), the CoMet website[9] and the PUNPY documentation[10].

In short, we first implement each of the processing steps as a numerical measurement function (e.g., measurement function in Section 3.2.2), i.e., a Python function which takes the input quantities (for which we are propagating the uncertainties) as arguments and returns the measurand (for which we are calculating the uncertainties as output). PUNPY then generates MC samples of the input quantities (taking into account the error correlation) proportional to the joint Probability Distribution Function (PDF) of the provided input quantities. Each of these samples is then run through the numerical measurement function to produce a sample of measurands. Finally, these output samples are analysed to obtain the uncertainties and error-correlation in the measurand. The uncertainties are propagated in this way through the measurement functions of each processing step discussed in Section 3.2.

9 www.comet-toolkit.org

10 https://punpy.readthedocs.io/en/latest/

3.4.2 Storing uncertainty information as digital effects tables

As previously mentioned, detailed error-correlation information is calculated as part of the uncertainty propagation. Storing this information in a space-efficient way is not trivial. To do this we use the OBSARRAY module[11] of the CoMet toolkit. OBSARRAY uses a concept called 'digital effects tables' to store the error-correlation information. This concept takes the parameterised error-correlation forms defined in the Quality Assurance Framework for Earth Observation (QA4EO) project[12] and stores them in a standardised metadata format. By using these parameterised error-correlation forms, it is not necessary to explicitely store the error-correlation along all dimensions. Instead only the error-correlation with wavelength is explicitly stored, and error-correlation with scans/series is captured as the 'random' or 'systematic' error-correlation forms.

Another benefit to using OBSARRAY, is that it allows for straightforward encoding of the uncertainty and error-correlation variables. The error-correlation (with respect to wavelength) does not need to be known at a very high precision. It can be saved as an 8-bit integer (leading to about a 0.01 precision in the error-correlation coefficient). Similarly, the uncertainties can be encoded using a 16-bit integer to a precision of 0.01%. Together, these encodings significantly reduce the amount of space required to store the uncertainty information.

Finally, having the HYPERNETS products saved as 'digital effects tables' means they can easily be used in further uncertainty propagation where all the error-correlation information is automatically taken into account. See De Vis & Hunt (in this issue) and the CoMet toolkit examples[13] for further information (note there is one example specific to HYPERNETS).

3.4.3 Uncertainty contributions

Three uncertainty contributions are tracked throughout the processing.

- Random uncertainty: Uncertainty component arising from the noise in the measurements, which does not have any error-correlation between different wavelengths or different repeated measurements (scans/series/sequences). The random uncertainties on the L0 data are taken to be the standard deviation between the scans that passed the quality checks. These uncertainties are then propagated all the way up to L2A.
- Systematic independent uncertainty: Uncertainty component combining a range of different uncertainty contributions in the calibration. Only the components for which the errors are not correlated between radiance and irradiance are included. These include contributions from the uncertainties on the distance, alignment, non-linearity, wavelength, lamp (power, alignment, interpolation) and panel (calibration, alignment, interpolation, back reflectance) used during the calibration. Since the same lab calibration is used within the HYPERNETS_PROCESSOR for repeated measurements (scans/series/sequences), the errors in the systematic independent uncertainty are assumed to be fully systematic (error-correlation of one) with respect to different scans/series/sequences. With respect to wavelength, we combine the different error-correlations of the different contributions and calculate a custom error-correlation matrix between the different wavelengths. These uncertainties are included in the L1A-L2A data products.
- Systematic uncertainty correlated between radiance and irradiance: Uncertainty component combining a range of different uncertainty contributions in the calibration. Only the components for which the errors are correlated between radiance and irradiance are included. This error-correlation means this component will become negligible when taking the ratio of radiance and irradiance (i.e., in the L2A reflectance products), which is why we separate it from the systematic independent uncertainty. The systematic uncertainty correlated between radiance and irradiance includes contributions from the uncertainties on the lamp (calibration, age) because the same lamp was used for the radiance and irradiance HYPSTAR calibrations in Tõravere. Since the same lab calibration is used within the HYPERNETS_PROCESSOR for repeated measurements (scans/series/sequences), the errors in the systematic independent uncertainty are assumed to be fully systematic (error-correlation made up of ones) with respect to different scans/series/sequences. With respect to wavelength, we combine the different error-correlations of the different contributions and calculate a custom error-correlation matrix between the different wavelengths. These uncertainties are present in the L1A-L1C products.

The temperature and spectral straylight uncertainties will be improved in future versions (Section 6). Additionally, there is an uncertainty to be added on the HYPSTAR responsivity change since calibration (drift/ageing of spectrometer and optics). More post-deployment calibrations are necessary before we can quantify this contribution. Other uncertainty contributions not yet included in the uncertainty budget will also be considered in the future, such as uncertainties on the sensitivity to polarisation, uncertainties in the cosine response of the irradiance optics, the effects of the platform/mast on the observed upwelling radiances (e.g., Talone and Zibordi, 2018), or on the air-water interface reflectance corrections. Uncertainties on the Spectral Response Functions (SRF) of the radiance and irradiance sensors (particularly the difference between the two is important when calculating reflectance) should also be considered (see also Ruddick et al., 2023). To account for these missing uncertainty contributions, a placeholder uncertainty of 2% is added to the systematic independent uncertainty, assuming systematic spectral correlation. In the strong atmospheric absorption features (i.e., 757.5–767.5 nm and 1,350–1,390 nm), an additional placeholder uncertainty of 50% (assuming random spectral error correlation) is added to account for the difference in SRF becoming dominant. Examples of the different uncertainty contributions are shown in Section 5.3.

11 https://obsarray.readthedocs.io/en/latest/

12 www.QA4EO.org

13 https://www.comet-toolkit.org/examples/

4 HYPERNETS products

4.1 Product format, variables and metadata

The main output files produced by the HYPERNETS_PROCESSOR are in NetCDF CF-convention version 1.8 format. There are also plots, typically produced in png format, and SQL databases (see Section 4.3).

The different NetCDF files contain a range of different variables and metadata. The main measurands, as well as their dimensions for the different levels of data files are described in Table 2. For these measurand variables, there are also uncertainty variables for each of the components described in Section 3.4, as well as error-correlation variables for the systematic uncertainty components.

In addition to these there are coordinate variables, wavelength and series/scans, as well as a number of common variables (i.e., present in each of the data products) that provide additional details about the measurement. Acquisition time, viewing zenith and azimuth angle, solar zenith and azimuth angle are examples of common variables with series or scans as dimension. Bandwidth is also a common variable which has the wavelength dimension. Then there are a few additional variables such as the quality flag variable and variables specifying the number of valid and total VNIR scans and specifying the number of valid and total SWIR scans (for the LANDHYPERNET network).

There are also a number of variables that are only present in some of the data products. For example, there is some additional information in the L0A files, such as integration times, values of the accelerometers, the requested and returned pan/tilt angles. This information is propagated to the L1A and L0B files, but not beyond.

The quality flag field consists of 32 bits. Every bit is related to the absence or presence of a flag as described in Section 3.3. The quality flag value given in each data level is the compound value of the specific bits of each raised flag. The specific flags associated with each bit are given in the quality flag field metadata. Some flags are left as placeholders for future updates. Tables 3, 4 present the flags used in the current version.

The are is also a range of metadata contained within the files. For each variable, there is metadata such as the standard name, long name, units and uncertainty components (where relevant). The uncertainty variables will have additional metadata describing their error correlation (see Section 3.4). Finally, there is also a range of global metadata, describing information about how, and when the data was processed, what data files it used, information about the site (e.g., latitude and longitude) *etc.*

4.2 File naming

The naming convention is intended to allow the unique identification of all product files and to summarise the contents. It is composed of a defined sequence of data fields, separated by an underscore. For the HYPERNETS measurement data, the file name is composed as follows:

SYSTEM NETWORK SITEID LEVEL TYPE ACQUISITIONDATETIME PROCESSINGDATETIME_version.nc.

where.

- System: "HYPERNETS"
- Network: Name of product network, i.e., W and L for WATERHYPERNET and LANDHYPERNET network, respectively.
- Siteid: Abbreviated site names defined in Table 5.
- Level: Data processing Level as defined in Table 2. For the RGB images the level is "IMG".
- Type: Name of product type. Values may be abbreviated product type names defined in Table 2.
- Acquisitiondatetime: Denotes the acquisition datetime (start of sequence) as UTC, formatted as "YYYYMMDDTHHMM".
- Processingdatetime: Denotes the processing datetime as UTC, formatted as "YYYYMMDDTHHMM".
- Zenith: For the RGB images only–viewing nadir angle ranging from 0° (looking down) to 180° (looking up).
- Azimuth: For the RGB images only and the L1C and L2A/B WATERHYPERNET network files–relative azimuth angle between Sun and sensor ranging from 0° to 360°.
- Version: Denotes data version number, formatted as "vX.X" as described in Section 2.5.

For instance, for a L1B product processed by the HYPERNETS_PROCESSOR version two of WATERHYPERNET network acquired at Blankaart South at 11:30 UTC on 2023–10–04 and processed at 11:30 UTC on 2023–10–05, the filename should be:

HYPERNETS_W_BSBE_L1B_RAD_20231004T1130_20231005T1130_v2.0.nc,

and the related L2A files for standard measurement protocols taken at 90° and 135° $\Delta\phi$ should be:

HYPERNETS_W_BSBE_L1B_RAD_20231004T1130_20231005T1130_v2.0.nc, and,

HYPERNETS_W_BSBE_L2A_REF_20231004T1130_20231005T1130_135_v2.0.nc.

Table 5 defines the abbreviated name convention applicable to the individual HYPERNETS sites. Site name convention is a 4 letter abbreviation [LLCC] with LL standing for the location and CC for the country.

4.3 SQL databases

The HYPERNETS_PROCESSOR produces SQL Database entries to keep track of successfully processed sequences and anomalies in the processing. These entries are combined into the following three databases, each stored in the SQLite format:[14]

- Archive Database: SQLite database listing all successfully processed data products, together with auxiliary information to enable queries (e.g., product_name, datetime, sequence_name, site_id, latitude, longitude, solar and viewing angles, etc.).
- Anomaly Database: There are a number of anomalies to track where there are issues in the processing of the data (e.g., incomplete sequence data, instrument failure etc.). The different anomalies are defined above in Tables 3, 4 as well

14 https://hypernets-processor.readthedocs.io/en/latest/content/atbd/products/anomalies.html

as in the HYPERNETS_PROCESSOR documentation. Each of the anomalies is identified with a letter and every occurrence is stored in the Anomaly SQLite database, together with auxiliary information to enable queries (e.g., sequence_name, site_id, datetime, viewing and solar angles, etc.). Some of these anomalies will raise an error (e.g., metadata file missing), and cause the processing of the data to be stopped. Other anomalies (e.g., clear sky check failed) indicate an issue, but do not halt the processing of the data (e.g., measurements with overcast conditions might still be useful to some users). In such cases, a quality flag is always added to the data so that users can easily identify the affected sequences without having to look in the anomaly database (see Section 3.3).

- Metadata Database: SQLite database of all network metadata, e.g., site info, instrument info *etc.* Contains all the metadata that is also present in the product files (stored in database to enable querying this information).

These databases can be used to produce processing statistics, or to find a set of sequences/anomalies that matched a certain set of criteria using SQL queries.

4.4 Data management and distribution

To follow the Findable-Accessible-Interoperable and Reusable principles (FAIR), particular attention is given to the data format and metadata, and, data accessibility. Files are in the NetCDF CF-convention version 1.8 format. Common metadata (e.g., metadata section added with each data product) follow the INSPIRE directives[15] in accordance with the EN ISO 19115 for the metadata elements and the Dublin Core Metadata Initiative[16]. Instrument, component and system metadata are bound by a unique metadata key (i.e., system_id) allowing to trace the history of the system (e.g., replacement, maintenance, system updates or instrument setup improvements).

The distribution of Near Real-Time (NRT, 24 h between data acquisition and data availability) LANDHYPERNET and WATERHYPERNET data will happen through the data portals for the LANDHYPERNET (www.landhypernet.org.uk) and WATERHYPERNET (www.waterhypernet.org). However, during the current prototype phase, where improvement of the quality checks is still ongoing, and further site-specific quality checks are still being added by the site-owners, these data portals are restricted to consortium members. In addition, for the WATERHYPERNET network the distribution may be delayed to ensure that the NCEP/GDAS forecast data for wind speed are made available for the latest sequence (should be less than 24 h). Data transfer from the system to the server may also delay the NRT processing (e.g., due to poor 4G connections on the field). In the near future, these data portals will be opened to the public and will become the reference source of data for HYPERNETS.

In the meantime, a subset of the HYPERNETS data until 2023–04–31 is publicly available and can be found on Zenodo (Brando et al., 2023; Brando and Vilas, 2023; De Vis et al., 2023; Dogliotti et al., 2023; Doxaran and Corizzi, 2023a; Doxaran and Corizzi, 2023b; Piegari et al., 2023; Goyens and Gammaru, 2023; Morris et al., 2023; Saberioon et al., 2023a; Saberioon et al., 2023b; Sinclair et al., 2023). The initial datasets provided here in June 2023 were produced using the v1.0 of the HYPERNETS_PROCESSOR (see Section 2.5). A new version of the datasets on Zenodo will be released upon publication of this paper, using the v2.0 of the HYPERNETS_PROCESSOR.

5 Results

5.1 LANDHYPERNET network example

In this section, we discuss the results of the processing of a few example land sequences. Two examples are included, one for the WWUK site on 2022–06–26 at 11:40 UTC and one for the GHNA site on 2022–08–04 at 10:00 UTC. Figure 12 shows a few of the plots created by the HYPERNETS_PROCESSOR for these two sequences.

The radiance plots show a lot more variability between different viewing zenith angles for the WWUK site than for the GHNA site, which is to be expected as GHNA is expected to be especially homogeneous and near-Lambertian, whereas the WWUK is a vegetated site, which has spatial heterogeneity and significant bidirectional reflectance distribution function (BRDF) effects. When the irradiances are inspected and compared to the clear sky models, we see that for each of these cases, the clear-sky model matches the observed radiances quite well. We note that this will not always be the case, as the clear sky model does not take into account the different surface reflectance, pressure or aerosol properties for each site.

The bottom two rows of Figure 12 show how the surface reflectances vary with viewing zenith and azimuth angles. Typical reflectances for vegetation (WWUK) and deserts (GHNA) are found. Again, much more variation is seen between the reflectances for the different geometries for WWUK than for GHNA, as expected. There are some blips in the reflectance around the absorption features (e.g., around 760 nm and 1,370 nm), which are likely caused by differences in the SRF of the radiance and irradiance sensors (See also Ruddick et al., 2023). Uncertainties have been increased to account for these SRF differences (see Sections 3.4; 5.3).

5.2 WATERHYPERNET network example

The last column in Figure 12 shows the plots provided by the WATERHYPERNET processor for a sequence at M1BE on 2022–06–19 at 08:02 UTC. Measurements were made at a relative azimuth angle, $\Delta\phi$, of 90° and the wind speed retrieved from NCEP/GDAS was around 6.2 m^{-1}. Top plot shows the averaged radiance scans for two series of L_d (two times three scans) and one series of L_u (six scans). It was a clear blue sky at M1BE on that day, and illumination during the sequence seemed to be constant. This is confirmed by the downwelling radiance (top right panel) and irradiance (second row right panel) series that are similar at the start and the end of the sequence. The bottom right panel show the final averaged reflectance product, i.e., the L2A reflectance. This figure shows that the water at M1BE was green and turbid on that day with a reflectance peak around 550 nm and relatively high red-NIR values.

15 http://inspire.ec.europa.eu/glossary/Metadata

16 https://www.dublincore.org/specifications/dublin-core/dcmi-terms/

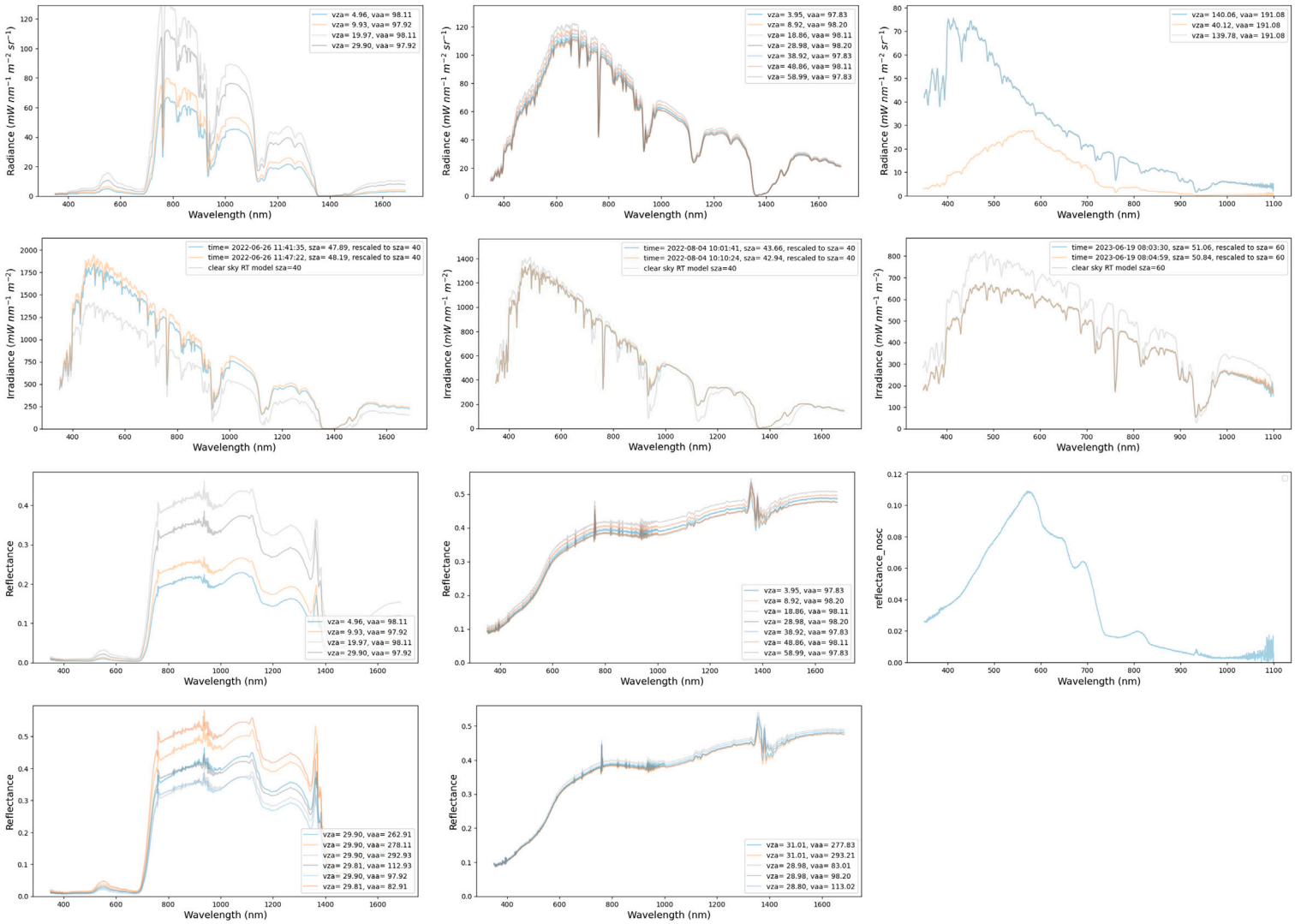


FIGURE 12
HYPERNETS_PROCESSOR plots for the WWUK site on the 2022–06–26 at 11:40 (left column), GHNA site on the 2022–08–04 at 10:00 (centre column) and the water site M1BE on 2022–06–19 at 08:02 (right column). The top row shows the L1B radiances at different viewing zenith angles, second row L1B irradiances together with clear sky model used in quality check. The third row shows the L2A reflectances at different viewing zenith angles for land and the non similarity corrected reflectance for water. The bottom row shows the L2A reflectances at different azimuth angles for land. Note the different wavelength range along the *x*-axis for the land (WWUK and GHNA) and water (M1BE) sites.

10.3389/frsen.2024.1347230

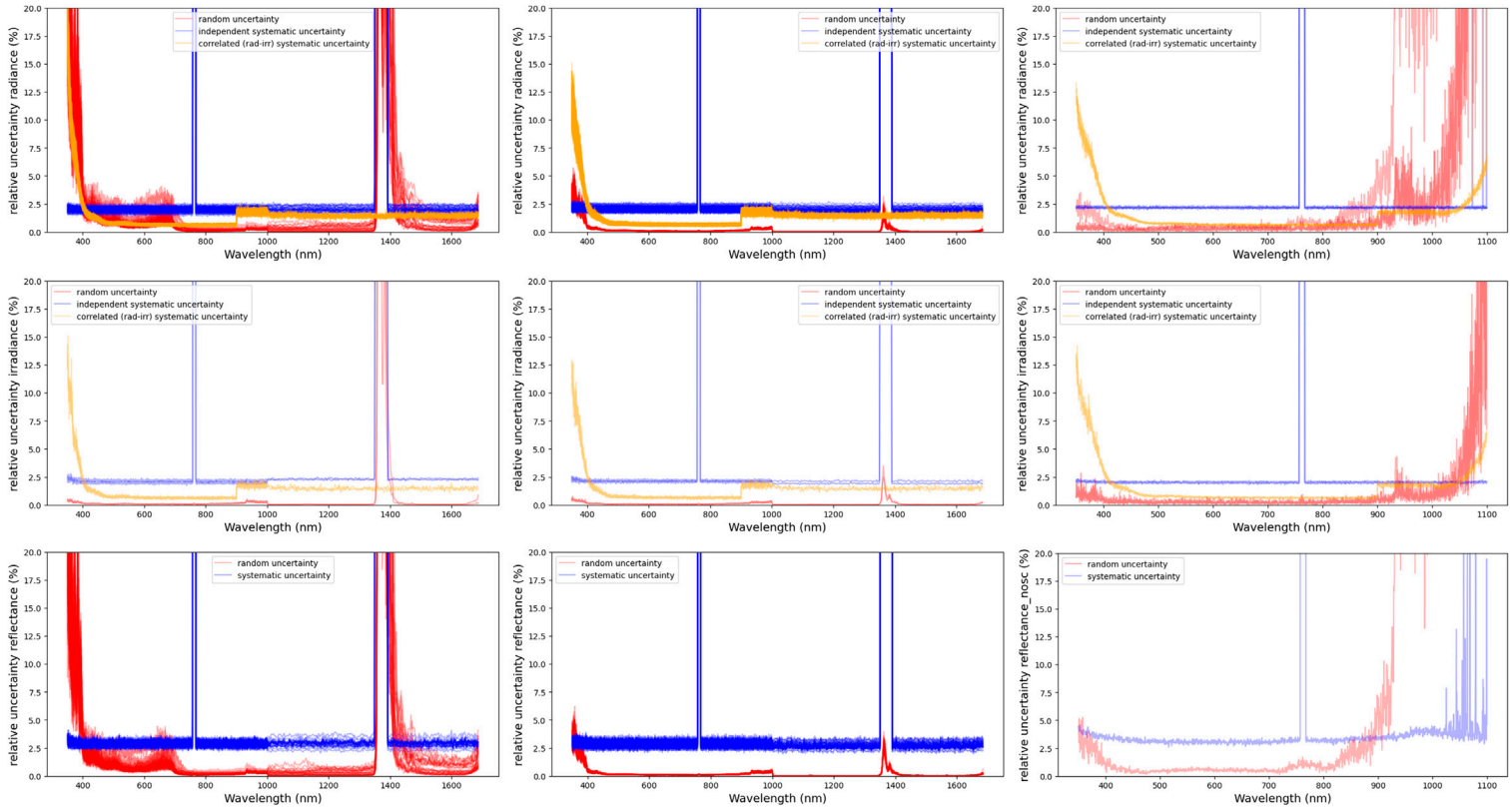


FIGURE 13
Example HYPERNETS_PROCESSOR plots illustrating the uncertainties (in percent) on L1B radiances (top row), L1B irradiances (second row) and L2A reflectances (third row) for the WWUK site on 2022–06–26 at 11:40 (left column), GHNA site on 2022–08–04 at 10:00 (centre column) and the water site M1BE on 2022–06–19 at 08:02 (right column). Note the different wavelength range along the *x*-axis for the land (WWUK and GHNA) and water (M1BE) sites.

10.3389/frsen.2024.1347230

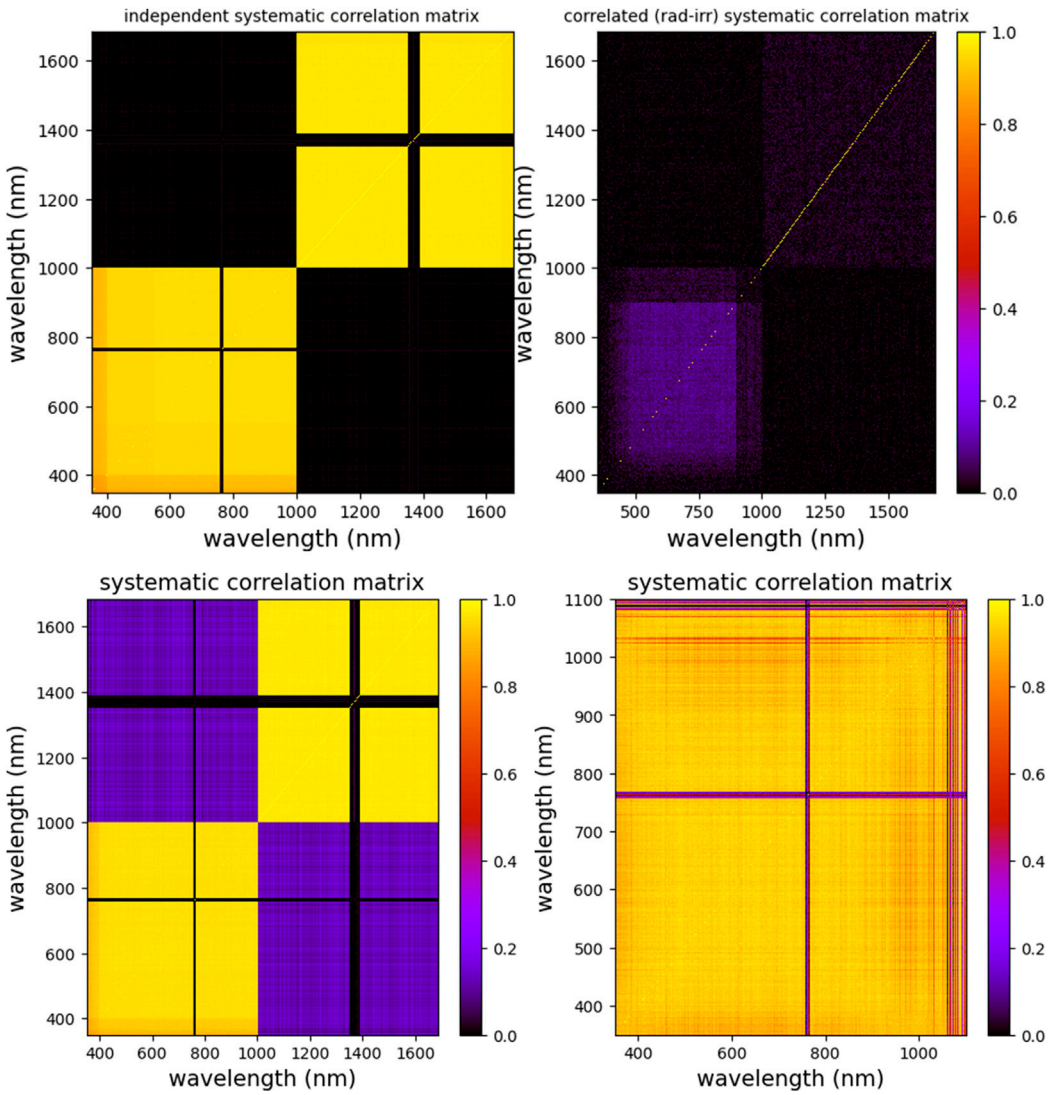


FIGURE 14
Example of the error-correlation matrices for the systematic independent uncertainty on GHNA L1B radiance (top left), the systematic uncertainty on GHNA L1B radiance correlated between radiance and irradiance (top right), the systematic uncertainty on GHNA L2A reflectance (bottom left) and systematic uncertainty on M1BE L2A reflectance (bottom right). Note that the M1BE error-correlation matrices have a reduced wavelength range.

5.3 Uncertainty example

We have illustrated the typical relative uncertainties of the LANDHYPERNET and WATERHYPERNET products in Figure 13, using the same three examples (GHNA, WWUK & M1BE) as discussed in the previous sections. For radiance (top row), the three uncertainty components are shown (one line for each series) for the three sites. The two systematic components are very similar between each of the sites, though for the water example (M1BE), the wavelength range is different compared to the land sites. This similar shape of the systematic uncertainties is expected as the instruments deployed at three sites are calibrated in the same way and thus have similar calibration uncertainties. These systematic components are also the same for each sequence for these sites, as the same calibration is applied for every sequence. The random uncertainty on the radiance is more variable, as it is dependent on illumination conditions, the nature of the target, and the stability of the instrument. Smaller relative uncertainties are found for brighter surfaces. Note the difference in wavelength range between the land and water sites with, subsequently, higher uncertainties in the blue and NIR spectral for the water site as it corresponds to the extremes of the wavelength range. The uncertainty plots for irradiance in Figure 13 are very similar than for radiance. The main difference, in particular for the land sites, is that there are fewer series (only two), and the relative random uncertainties are a bit smaller (due to higher signal in irradiance).

For reflectance, there are only two uncertainty components as the systematic component for which the errors in radiance and irradiance are correlated become negligible. For most wavelengths, the (independent) systematic component dominates over the random uncertainties. The random uncertainties will become even smaller when averaging measurements or integrating over the SRF of a satellite sensor (e.g., De Vis et al., in this issue), as opposed to the systematic uncertainties which will remain constant. For the water site, the random uncertainty is higher compared to the

systematic uncertainty in the NIR spectral range. This is due to the usually very low water signal in this spectral range.

Finally, Figure 14 top row shows the error-correlation between the different wavelength channels of the systematic component(s) for the L1B radiances of the GHNA example, i.e., the error-correlation matrix for the independent systematic uncertainty (left) and the correlated (between radiance and irradiance) systematic uncertainty (right). The bottom plots show the error-correlation for the L2A (independent) systematic uncertainties on reflectance for the land (left) and water (right) examples (GHNA and M1BE, respectively). For the independent systematic error correlations for land, there is a strong correlation between the wavelengths within the VNIR and SWIR sensors, but not between VNIR and SWIR. The strong wavelength correlation comes from various components, with a strong contribution from the placeholder uncertainty. As this placeholder is replaced by more realistic contributions, this error-correlation structure might become more complex. For the water example, correlations remain high at all wavelengths between the blue and red wavelengths.

5.4 Processing statistics of H2020 HYPERNETS data

In this section we briefly provide some of the processing statistics for both the LANDHYPERNET and WATERHYPERNET networks until the end of April 2023. for the LANDHYPERNET, there were a total of 12,190 sequences acquired. 11,802 of these (97%) were successfully processed to L2A. The remainder had an anomaly which halted the processing (Section 3.3). Stringent site specific quality checks were applied to the L2A data, and a total of 4,256 sequences were provided on the Zenodo database.

For the WATERHYPERNET, there were 55,514 sequences acquired. 44,412 of these (80%) were succesfully processed to L2A. Stringent site specific quality checks were applied to the L2A data, and a total of 4,931 sequences were provided on the Zenodo database. Note that the data provided on Zenodo are still a subset of the entire dataset and that the number of processed and quality checked sequences is expected to increase since the first version of the processor has been considerably improved (e.g., additional and more appropriate flagging, processing issues and bugs have been solved, accounting for different relative azimuth angles, retrieving wind speed from a different data source, i.e., NCEP/GDAS) to the current v2.0 of the HYPERNETS_PROCESSOR.[17]

6 Future work

There are a number of improvements that are foreseen in the near future.

- There are a number of improvements that will be made to the calibration measurement function, such as the inclusion of a temperature and spectral straylight correction. As soon as lab-based characterisation of these effects is concluded, appropriate corrections will be implemented and added to the calibration measurement function (see Section 3.3.2).
- Post-deployment calibration will be implemented in the future. This means it would be possible to do a reprocessing of the data between the calibration dates and interpolate the calibration data between the pre-deployment data and post-deployment data. Post-deployment data should be gathered prior to any cleaning being done to the instrument. Further investigations will be performed to compare results from interpolating calibrations, to calibrations done using the previous available date. This will also include assessments of the uncertainty on the calibration due to drift/ageing of the sensor and optics.
- There are still missing uncertainty contributions that currently are just provided as a combined placeholder uncertainty (see Section 3.4). These include uncertainties related to the temperature and spectral straylight corrections, as well as uncertainties due to the angular accuracy, polarisation, the effects of the platform/mast on the observed upwelling radiances (e.g., Talone and Zibordi, 2018) and the uncertainty in the retrieval of the air-water interface correction methodology. Uncertainties on the SRF will also be more precisely included. All these uncertainties need dedicated studies in order to be quantified, and will be added to the HYPERNETS_PROCESSOR as soon as they have been quantified. The placeholder uncertainty will be adjusted when new uncertainty components are added, with the aim of eventually not needing any placeholder uncertainty any more.
- The current angular tolerance on the viewing zenith angle for the irradiance measurements is set to 2°. This leads to acceptable irradiances, but improvements can still be made by correcting the irradiance measurements for any deviation from *vza* = 180, taking into account the solar azimuth angles, and relative azimuth angles.
- Further investigations will be performed of the potential improvements of using high resolution models in the spectral and temporal interpolation of the irradiances (See Section 3.2.4.1).
- In future versions of the processor we will further investigate whether using a sliding average would be useful where, for the overlapping wavelengths, a weighted (by inverse of uncertainties) mean is taken between VNIR and SWIR so that there is a smooth transition. The overlapping wavelength range spans from about 880–1,100 nm, with worse performance towards the ends of the wavelength range of each detector.
- Work is ongoing to continuously improve the common quality checks being applied as part of the automated processing, as well as the site-specific quality checks. These improvements will include improved checks such as angular masks for shadowing effects by the mast/platform, non-linearity checks and more robust comparisons with expected reflectance.
- BRDF modelling will be investigated for a number of LANDHYPERNET sites. This would allow for better outlier detection compared to the BRDF model, as well as allow interpolation over missing geometries.
- The current standard protocol for measurement of water reflectance uses external sources for the retrieval of the wind speed and approximates the air–water interface reflectance factor following Mobley (1999). However, it is known that these methods present some limitations (see Goyens and Ruddick

17 https://landhypernet.org.uk/

(2023) and references therein). In the future, new methods and models may be explored and integrated into the processor.
- The LANDHYPERNET and WATERHYPERNET data portals (see also Section 4.4) will be fully opened to the public.
- A web interface allowing to visualise the latest incoming data, the archived data, and the anomalies and flags of the processed data, may also be build to help debugging and tracing issues in the sensor deployments and the processing.
- An API will be developed to access and download the L1D and L2B HYPERNETS data through a Python tool which will also include command-line functionality. This API will use credentials for the LANDHYPERNET and WATERHYPERNET data portals.
- Future version of the processor might make additional data products available to the public, such as irradiance and surface reflectance measurements during fully overcast conditions (which are not useful for satellite validation but might be of interest to other user communities), and products including additional water (e.g., turbidity) and atmospheric (e.g., aerosol optical depth) products. Any of these additional products would require significant validation before they could be made public so are not expected in the near future.

Some of these improvements will be present in the next major version (v3.0) of the HYPERNETS_PROCESSOR.[18] The documentation[19] will also be kept up to date with any modifications made to the HYPERNETS_PROCESSOR.

7 Conclusion

The HYPERNETS_PROCESSOR is a software package for ground processing of the hyperspectral HYPSTAR® data from the autonomous field sites of the LANDHYPERNET and WATERHYPERNET networks. it continuously processes new acquisitions taken by the HYPSTAR® instrument, through various processing levels, to the surface reflectance products required for validation of satellite measurements. Uniquely for this type of processing, multiple different types of uncertainty (including error-correlations) are propagated through each of the processing levels. The processor is now operationally running for a series of networked validation sites, revealing plausible results and a well constrained uncertainty budget.

Data availability statement

The datasets generated for this study (Brando et al., 2023; Brando and Vilas, 2023; De Vis et al., 2023; Dogliotti et al., 2023; Doxaran and Corizzi, 2023a; Doxaran and Corizzi, 2023b; Piegari et al., 2023; Goyens and Gammaru, 2023; Morris et al., 2023; Saberioon et al., 2023a; Saberioon et al., 2023b; Sinclair et al., 2023) can be found on Zenodo (https://zenodo.org/).

18 https://waterhypernet.org/

19 https://hypernets-processor.readthedocs.io/en/latest/

Author contributions

PD: Conceptualization, Data curation, Investigation, Methodology, Software, Validation, Visualization, Writing–original draft. CG: Conceptualization, Data curation, Investigation, Methodology, Software, Validation, Visualization, Writing–original draft. SH: Conceptualization, Methodology, Software, Writing–review and editing. QV: Methodology, Writing–review and editing. KR: Funding acquisition, Project administration, Writing–review and editing. AB: Funding acquisition, Project administration, Writing–review and editing.

Funding

The author(s) declare that financial support was received for the research, authorship, and/or publication of this article. The HYPERNETS project is funded by the European Union's Horizon 2020 research and innovation program under grant agreement No. 775983 and by the HYPERNET-POP project funded by the European Space Agency (contract No. 4000139081/22/I-EF). This work (and the CoMet toolkit used within) has also received funding from the ESA-funded Instrument Data quality Evaluation and Assessment Service-Quality Assurance for Earth Observation (IDEAS-QA4EO) contract funded by ESA-ESRIN (No. 4000128960/19/I-NS) and the UK's Department for Science, Innovation and Technology (DSIT) National Measurement System (NMS) programme.

Acknowledgments

The HYPERNETS partners, especially Tartu University and Sorbonne University are thanked for technical support and development of the HYPSTAR® instrument and system. The HYPERNETS PI (Kevin Ruddick), co-PIs (Agnieszka Bialek, Vittorio Brando, Ana Dogliotti, David Doxaran, Joel Kuusk, Mohammadmehdi Saberioon) as well as all other contributors are gratefully acknowledged for their useful inputs, discussion and comments. Paul Green and Joel Kuusk are thanked for useful comments.

Conflict of interest

The authors declare that the research was conducted in the absence of any commercial or financial relationships that could be construed as a potential conflict of interest.

Publisher's note

All claims expressed in this article are solely those of the authors and do not necessarily represent those of their affiliated organizations, or those of the publisher, the editors and the reviewers. Any product that may be evaluated in this article, or claim that may be made by its manufacturer, is not guaranteed or endorsed by the publisher.

References

Alonso, K., Bachmann, M., Burch, K., Carmona, E., Cerra, D., de los Reyes, R., et al. (2019). Data products, quality and validation of the dlr earth sensing imaging spectrometer (desis). *Sensors* 19, 4471. doi:10.3390/s19204471

Bouvet, M., Thome, K., Berthelot, B., Bialek, A., Czapla-Myers, J., Fox, N. P., et al. (2019). Radcalnet: a radiometric calibration network for earth observing imagers operating in the visible to shortwave infrared spectral range. *Remote Sens.* 11, 2401. doi:10.3390/rs11202401

Brando, V., Gonzalez Vilas, L., Bresciani, M., Mangano, S., Concha, J. A., and Goyens, C. (2023). Initial sample of HYPERNETS hyperspectral water reflectance measurements for satellite validation at lake garda, GAIT site (Italy). Zendo. doi:10.5281/zenodo.8057823

Brando, V., and Vilas, L. G. (2023). Initial sample of HYPERNETS hyperspectral water reflectance measurements for satellite validation from the VEIT site (Italy). Zendo. doi:10.5281/zenodo.8057531

Coddington, O. M., Richard, E. C., Harber, D., Pilewskie, P., Woods, T. N., Chance, K., et al. (2021). The tsis-1 hybrid solar reference spectrum. *Geophys. Res. Lett.* 48, e2020GL091709. doi:10.1029/2020GL091709

De Vis, P., Bialek, A., and Sinclair, M. (2023). Initial sample of HYPERNETS hyperspectral surface reflectance measurements for satellite validation from the Gobabeb site in Namibia. Zendo. doi:10.5281/zenodo.8039303

Dogliotti, A. I., Piegari, E., Rubinstein, L., and Perna, P. (2023). Initial sample of HYPERNETS hyperspectral water reflectance measurements for satellite validation from the LPAR site (Argentina). Zendo. doi:10.5281/zenodo.8057728

Doxaran, D., and Corizzi, A. (2023a). Initial sample of HYPERNETS hyperspectral water reflectance measurements for satellite validation at berre coastal lagoon, BEFR site (France). Zendo. doi:10.5281/zenodo.8057777

Doxaran, D., and Corizzi, A. (2023b). Initial sample of HCYPERNETS hyperspectral water reflectance measurements for satellite validation at the mouth of the gironde estuary, MAFR site (France). Zendo. doi:10.5281/zenodo.8057789

Emde, C., Buras-Schnell, R., Kylling, A., Mayer, B., Gasteiger, J., Hamann, U., et al. (2016). The libradtran software package for radiative transfer calculations (version 2.0.1). *Geosci. Model Dev.* 9, 1647–1672. doi:10.5194/gmd-9-1647-2016

Goryl, P., Fox, N., Donlon, C., and Castracane, P. (2023). Fiducial reference measurements (frms): what are they? *Remote Sens.* 15, 5017. doi:10.3390/rs15205017

Goyens, C., De Vis, P., and Hunt, S. E. (2021). "Automated generation of hyperspectral fiducial reference measurements of water and land surface reflectance for the hypernets networks," in 2021 IEEE International Geoscience and Remote Sensing Symposium IGARSS, Brussels, Belgium, 11-16 July 2021 (IEEE), 7920–7923. doi:10.1109/IGARSS47720.2021.9553738

Goyens, C., and Gammaru, A. (2023). Initial sample of HYPERNETS hyperspectral water reflectance measurements for satellite validation at the measurement tower MOW1, M1BE site (Belgium). Zendo. doi:10.5281/zenodo.8059881

Goyens, C., and Ruddick, K. (2023). Improving the standard protocol for above-water reflectance measurements: 1. estimating effective wind speed from angular variation of sunglint. *Appl. Opt.* 62, 2442–2455. doi:10.1364/AO.481787

Ishizaka, J., Yang, M., Fujii, N., Katano, T., Hori, M., Mine, T., et al. (2022). Use of aeronet-oc for validation of sgli/gcom-c products in ariake sea, Japan. *J. Oceanogr.* 78, 291–309. doi:10.1007/s10872-022-00642-9

JCGM 100:2008 (2008). Evaluation of measurement data — Guide to the expression of uncertainty in measurement. Joint Committee for Guides in Metrology. JCGM 100: 2008.

JCGM 101:2008 (2008). Evaluation of measurement data — Supplement 1 to the "Guide to the expression of uncertainty in measurement" — propagation of distributions using a Monte Carlo method. Joint Committee for Guides in Metrology. JCGM 101:2008.

Mobley, C. D. (1999). Estimation of the remote-sensing reflectance from above-surface measurements. *Appl. Opt.* 38, 7442–7455. doi:10.1364/AO.38.007442

Mobley, C. D. (2015). Polarized reflectance and transmittance properties of windblown sea surfaces. *Appl. Opt.* 54, 4828–4849. doi:10.1364/AO.54.004828

Morris, H., Bialek, A., Sinclair, M., and De Vis, P. (2023). Initial sample of HYPERNETS hyperspectral surface reflectance measurements for satellite validation from the Wytham Woods site in the United Kingdom. Zendo. doi:10.5281/zenodo.7962557

National Centers for Environmental Prediction, National Weather Service, NOAA, U.S. Department of Commerce (2015). *Ncep gdas/fnl 0.25 degree global tropospheric analyses and forecast grids*. NOAA.

Niro, F., Goryl, P., Dransfeld, S., Boccia, V., Gascon, F., Adams, J., et al. (2021). European space agency (esa) calibration/validation strategy for optical land-imaging satellites and pathway towards interoperability. *Remote Sens.* 13, 3003. doi:10.3390/rs13153003

Piegari, E., Dogliotti, A., Grings, F., Perna, P., Rubinstein, L., and Cordon, G. (2023). Initial sample of HYPERNETS hyperspectral surface reflectance measurements for satellite validation from the IFEVA site in Argentina. Zendo. doi:10.5281/zenodo.8048425

Ruddick, K., De, V., Ab, C., and Mol, B. (2005). Use of the near infrared similarity reflectance spectrum for the quality control of remote sensing data. *Proc. SPIE - Int. Soc. Opt. Eng.* 5885, 615152. doi:10.1117/12.615152

Ruddick, K. G., De Cauwer, V., Park, Y.-J., and Moore, G. (2006). Seaborne measurements of near infrared water-leaving reflectance: the similarity spectrum for turbid waters. *Limnol. Oceanogr.* 51, 1167–1179. doi:10.4319/lo.2006.51.2.1167

Ruddick, K. G., De Vis, P., Goyens, C., Kuusk, J., Lavigne, H., and Vanhellemont, Q. (2023). "Second derivative water reflectance spectra for phytoplankton species detection: origin, impact, and removal of spectral wiggles," in *Remote sensing of the ocean, sea ice, coastal waters, and large water regions 2023*. Editors C. R. B. Jr. and X. Neyt (International Society for Optics and Photonics SPIE). doi:10.1117/12.2684336

Ruddick, K. G., Voss, K., Boss, E., Castagna, A., Frouin, R., Gilerson, A., et al. (2019). A review of protocols for fiducial reference measurements of water-leaving radiance for validation of satellite remote-sensing data over water. *Remote Sens.* 11, 2198. doi:10.3390/rs11192198

Saberioon, M., Spengler, D., Hohmann, C., and Itzerott, S. (2023a). Initial sample of HYPERNETS hyperspectral surface reflectance measurements for satellite validation from the agricultural land at demmin, Germany. Zendo. doi:10.5281/zenodo.8048348

Saberioon, M., Spengler, D., Hohmann, C., Wille, C., and Itzerott, S. (2023b). Initial sample of HYPERNETS hyperspectral surface reflectance measurements for satellite validation from the bare soil at marquardt, Germany. Zendo. doi:10.5281/zenodo.8044522

Sinclair, M., Morris, H., Bialek, A., De Vis, P., Gammaru, A., and Goyens, C. (2023). Initial sample of HYPERNETS hyperspectral surface reflectance measurements for satellite validation from the barrax site in Spain. Zendo. doi:10.5281/zenodo.8060798

Talone, M., and Zibordi, G. (2018). Non-linear response of a class of hyper-spectral radiometers. *Metrologia* 55, 747–758. doi:10.1088/1681-7575/aadd7f

Vansteenwegen, D., Ruddick, K., Cattrijsse, A., Vanhellemont, Q., and Beck, M. (2019). The pan-and-tilt hyperspectral radiometer system (PANTHYR) for autonomous satellite validation measurements—prototype design and testing. *Remote Sens.* 11, 1360. doi:10.3390/rs11111360

Wilkinson, M. D., Dumontier, M., Aalbersberg, I. J., Appleton, G., Axton, M., Baak, A., et al. (2016). The fair guiding principles for scientific data management and stewardship. Zendo. doi:10.1038/sdata.2016.18

Zibordi, G., Holben, B. N., Talone, M., D'Alimonte, D., Slutsker, I., Giles, D. M., et al. (2021). Advances in the ocean color component of the aerosol robotic network (aeronet-oc). *J. Atmos. Ocean. Technol.* 38, 725–746. doi:10.1175/JTECH-D-20-0085.1

Zibordi, G., Kwiatkowska, E., Mélin, F., Talone, M., Cazzaniga, I., Dessailly, D., et al. (2022). Assessment of olci-a and olci-b radiometric data products across european seas. *Remote Sens. Environ.* 272, 112911. doi:10.1016/j.rse.2022.112911

Zibordi, G., Mélin, F., Berthon, J.-F., Holben, B., Slutsker, I., Giles, D., et al. (2009). AERONET-OC: a network for the validation of ocean color primary products. *J. Atmos. Ocean. Technol.* 26, 1634–1651. doi:10.1175/2009JTECHO654.1

frontiers | Frontiers in Remote Sensing

TYPE Original Research
PUBLISHED 28 June 2024
DOI 10.3389/frsen.2024.1369769

Check for updates

OPEN ACCESS

EDITED BY
Agnieszka Bialek,
National Physical Laboratory, United Kingdom

REVIEWED BY
Giuseppe Zibordi,
National Aeronautics and Space Administration (NASA), United States
B. Carol Johnson,
National Institute of Standards and Technology (NIST), United States

*CORRESPONDENCE
Andrew Barnard,
barnaran@oregonstate.edu

RECEIVED 12 January 2024
ACCEPTED 07 June 2024
PUBLISHED 28 June 2024

CITATION
Barnard A, Boss E, Haëntjens N, Orrico C, Frouin R, Tan J, Klumpp J, Dewey M, Walter D, Mazloff M and Chamberlain P (2024), Design and verification of a highly accurate *in-situ* hyperspectral radiometric measurement system (HyperNav).
Front. Remote Sens. 5:1369769.
doi: 10.3389/frsen.2024.1369769

COPYRIGHT
© 2024 Barnard, Boss, Haëntjens, Orrico, Frouin, Tan, Klumpp, Dewey, Walter, Mazloff and Chamberlain. This is an open-access article distributed under the terms of the Creative Commons Attribution License (CC BY). The use, distribution or reproduction in other forums is permitted, provided the original author(s) and the copyright owner(s) are credited and that the original publication in this journal is cited, in accordance with accepted academic practice. No use, distribution or reproduction is permitted which does not comply with these terms.

Design and verification of a highly accurate *in-situ* hyperspectral radiometric measurement system (HyperNav)

Andrew Barnard[1]*, Emmanuel Boss[2], Nils Haëntjens[2], Cristina Orrico[3], Robert Frouin[4], Jing Tan[4], Justin Klumpp[5], Michael Dewey[5], David Walter[3], Matthew Mazloff[4] and Paul Chamberlain[4]

[1]College of Earth, Ocean and Atmospheric Sciences, Oregon State University, Corvallis, OR, United States, [2]School of Marine Sciences, University of Maine, Orono, ME, United States, [3]Formerly at Sea-Bird Scientific LTD, Bellevue, WA, United States, [4]Scripps Institute of Oceanography, University of California San Diego, San Diego, CA, United States, [5]Sea-Bird Scientific LTD, Bellevue, WA, United States

Hyperspectral optical observations of the Earth's surface oceans from space offer a means to improve our understanding of ocean biology and biogeochemistry. NASA's Plankton, Aerosol, Cloud, ocean Ecosystem (PACE) satellite mission, which includes a hyperspectral ocean color instrument (OCI), will provide radiometric observations of surface ocean with near continuous spectral resolution across the near UV to NIR range. Maintaining sufficient accuracy over the lifetime of satellite ocean color missions requires a robust program for system vicarious calibration (SVC) and product validation. The system vicarious calibration process combines satellite sensor data with *in-situ* radiometric/optical measurements to remove potential biases due to the combined errors from both satellite radiometric sensor calibration and atmospheric correction. As such, high accuracy, high-spectral resolution *in-situ* radiometric measurements are required to provide a principal source of truth for the satellite-derived products. To meet the requirements, a novel *in-situ* radiometric system, called HyperNav, has been developed, rigorously characterized and field tested. Key attributes of HyperNav are dual upwelling radiance heads coupled to individual spectrometers, spectral resolution of ~2.2 nm (full width, half-maximum) across 320–900 nm, integrated shutter systems for dark measurements, and integrated tilt and pressure sensors. The HyperNav operational modes include traditional profiling and surface modes, as well as integration with an autonomous profiling float for unattended deployment, offering a new capability for a network of autonomous platforms to support the long-term needs for hyperspectral ocean color remote sensing observations. This paper describes the HyperNav design, *in-situ* operational modes, and field verification results.

KEYWORDS

ocean color remote sensing, system vicarious calibration, radiometry, hyperspectral, ocean optics, instrumentation

1 Introduction

The NASA Plankton, Aerosol, Clouds and ocean Ecosystem (PACE) mission builds on past ocean color remote sensing efforts to provide a global observational basis for understanding the living ocean and for improving skill in forecasts and projections of Earth System variability over a wide range of time and space scales (Werdell et al., 2019). The primary instrument of the PACE satellite, the Ocean Color Instrument (OCI), includes significant advances in ocean color remote sensing, namely, a wider spectral range extending into the UV and near-infrared with bandwidth of 5.0 nm spectral resolution (2.5 nm spectral steps). These advancements drive new requirements for *in-situ* radiometric measurement capabilities to ensure the ocean color satellite is accurately ground-truthed through a process known as system vicarious calibration, SVC (Gordon, 1998; Franz et al., 2007; Frouin, 2013). Relative to existing *in-situ* ocean radiometer technology, advancements are needed with regard to the extended spectral range into the UV and the increased spectral resolution. For the latter, a desire to create aggregate spectral bands of 5–10 nm imposes a need to sample the ocean remote sensing reflectance spectra at approximately one-half of the spectral resolution of the satellite instrument, and in the case of *in-situ* upwelling radiance, may require sub-nanometer resolution in the blue spectral region (Zibordi et al., 2017).

Concurrent with the enhanced capabilities of OCI has been a need to evolve ocean color *in-situ* SVC approaches. Historically, *in-situ* SVC measurements have been collected from mooring-based radiometric systems such as the Marine Optical BuoY (MOBY) located off Lana'i, Hawaii (Brown et al., 2007) and the Boussole mooring located in the Ligurian Sea (Antoine et al., 2008). While such mooring-based approaches have been successful in providing *in-situ* SVC data, it is advantageous to collect *in-situ* SVC observations using a variety of measurement techniques across multiple SVC sites to reduce the time needed to achieve vicarious calibration post-launch (Voss et al., 2010) and to assure accuracy in the SVC coefficients. However, all *in-situ* SVC systems must meet stringent instrument performance and uncertainty requirements to ensure equivalency in the quality of the radiometric data (Zibordi et al., 2015). Specifically for the NASA PACE mission SVC program, these requirements include a radiometric spectral range spanning 350–890 nm, spectral resolution < 3 nm (ideally 1 nm), with spectral radiometric uncertainty ($< 4\%$ over blue-green spectral region, ~5% in the red), and radiometric stability (~1% per deployment). Uncertainties presented throughout this paper are at $k = 1$ confidence level (i.e. 68% of the measurements fall within the specified uncertainty relative to the 'true' values). Additional capability requirements include autonomous field operation, full laboratory and field characterizations, and full autonomous delivery of data in near real time.

A new hyperspectral radiometric sensor, HyperNav, has been developed to finely and accurately resolve the upwelling radiance spectrum to meet the *in-situ* SVC requirements of the PACE mission OCI. The design of HyperNav focused on providing the most accurate and lowest uncertainty spectral upwelling radiance measurements with emphasis on achieving these measurements as close to the sea surface as possible to meet the needs of *in-situ* SVC data production. Additionally, design criteria for the radiometric measurement system included a capability to be integrated with an autonomous profiling float. As such, mechanical, electrical and data interfaces were developed to enable onboard data collection and sampling, as well as data transmission to shore when integrated with an autonomous profiling float. As part of HyperNav design criteria, optimal mission operation modalities (frequency of profile trade-off against mission duration, vertical resolution, surface observations for extended periods, etc.; see Claustre (2011)) were considered to ensure cost-effective operations of deployments of the system. In this paper, we describe the HyperNav radiometric system, the modes of operation, the integration of the system with an autonomous float, and the methods and field results used to evaluate the system performance against the stated *in-situ* SVC requirements.

Our effort resulted in the creation of new radiometers able to collect accurate and precise radiometric measurements of upwelling radiance in the ocean environment at high spectral resolution, 2.2 nm full width at half maximum (FWHM) over the 320–800 nm spectral region. While Zibordi et al. (2015) and Zibordi et al. (2017) recommended a finer spectral resolution requirement, the radiometric spectral resolution of our system does meet the NASA PACE mission SVC stated requirement of < 3 nm. The integration of two such radiometers onboard autonomous profiling floats creates a new system that can be deployed at many location adding a spatially extensive component to existing fixed-location sites, such as MOBY, for vicarious calibration of ocean color satellites. The addition of a fleet float-based HyperNav systems to the suite of *in-situ* SVC platforms will permit significant reduction in the uncertainty of the onboard calibration and will significantly increase the number of radiometric observations available for vicarious calibration efforts post-launch. Such data can be used to examine potential effects such as out-of-band response, changes in the adopted representation of the ocean Bidirectional Reflectance Distribution Function (BRDF), and atmospheric corrections of the satellite ocean color sensor data.

2 HyperNav system Description

The design objectives for HyperNav focused primarily on providing the most accurate and lowest uncertainty spectral upwelling radiance measurements with emphasis on achieving these measurements as close to the sea surface as possible to reduce the uncertainty in extrapolating upwelled radiance measurements from depth to the air-sea interface. HyperNav includes two independent upwelling radiance sensors, oriented 180° apart from the main body (Figure 1). The purpose of including dual upwelling radiance sensors on the HyperNav system was three-fold: 1) to provide redundancy in the key upwelled radiance measurements in case of failure of one radiance system, 2) to characterize uncertainties in measurements over time by comparing the measurements from the different radiometers, and 3) to reduce the effects of shading by the float and arms on the radiance measurements. With respect to item 1, the design of the HyperNav system includes separate and independent optical paths and spectrometers for each of the upwelled radiance measurement sensors. The only shared elements of the two radiance measurement sensors are the command and control electronic

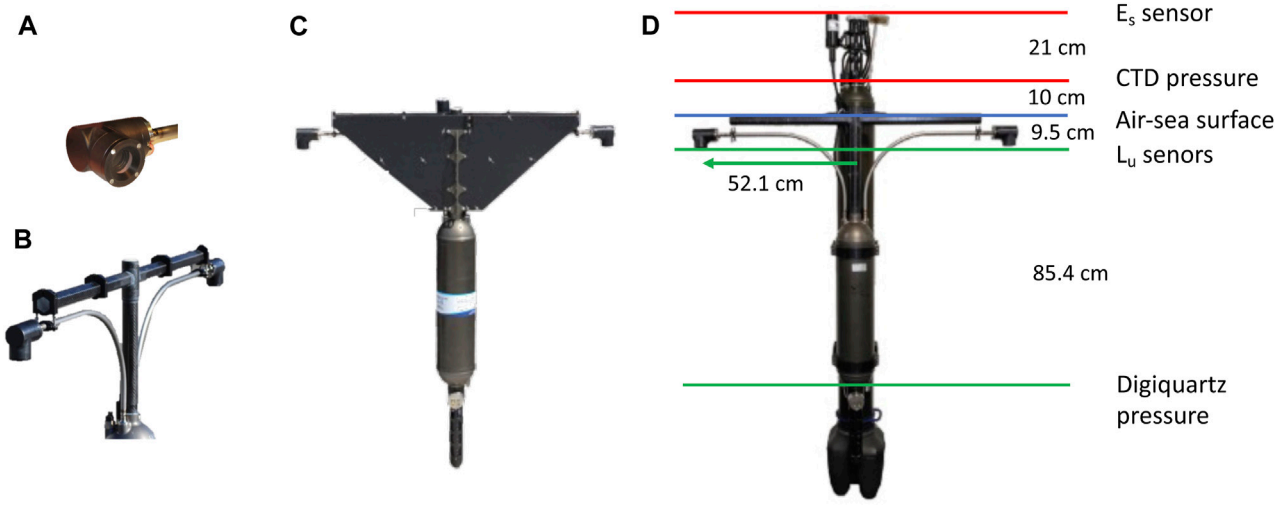


FIGURE 1
Photos of the HyperNav system. **(A)** Upwelling radiance sensor fore-optics head, **(B)** Upper section of the HyperNav radiance system with fiber optic conduits and support structure, **(C)** HyperNav configured for real-time profiling, and **(D)** a HyperNav system attached to a Navis float with locations and distances for each sensor system.

boards and the HyperNav physical body. Thus, the two measurements are independent and provide, by the difference between them and its change over time, a validation of the measurements within their uncertainties. Details of the HyperNav system design, functionality, and characterization methods are provided in the following sections.

2.1 HyperNav Opto-mechanical design

Meeting the spectral range and resolution requirements for PACE necessitated the design of new radiometers, as no commercial option for in water upelling radiometers with appropriate specifications was available. In the early stages of our development project a search for commercially available spectrometers was undertaken and three potential spectrometers were selected for further laboratory evaluation. Evaluation was based on radiometer requirements detailed in Mueller (2003). Tests included determining sensitivity, saturation, digital resolution, polarization sensitivity, absolute wavelength accuracy, wavelength resolution, linearity, thermal sensitivity, and stray light rejection.

After extensive laboratory characterization, the Zeiss CGS CCD UV-NIR spectrometer was selected based on the required performance criteria. The Zeiss spectrometer has a stated 190–1,015 nm spectral range, with a spectral resolution (FWHM) of 2.2 nm and 2.5 nm in the UV-VIS and NIR region respectively, high dynamic range obtained from a 16 bit ADC digitization and multiple integration times, with high sensitivity, low stray light perturbations, and low temperature drift. The CCD detector uses 2048 pixels to sample the spectral range, providing ~0.41 nm sampling interval. Additionally, the compact size, SMA (SubMiniature A connector) optical interface, low stray light characteristics, and a wide range of integration times provided significant advantages in the design of the HyperNav.

The HyperNav design choice was to position the fore-optics of the radiance radiometers at the end of arms extended horizontally outward from the body of the HyperNav using pressured sealed titanium conduits (Figure 1) for strength, weight, and corrosion considerations. The impact of the arm extension and the fore-optics from the main housing with respect to the effects of self shading on the radiance measurements was determined using a Monte Carlo self shading models (SimulO software[1], Leymarie et al. (2010)) and was taken into account in the float design. The fore-optics, contained within in a small sealed pressure housing, are located 52 cm from the center-line of the main HyperNav pressure housing (Figure 1). Armored, solarization-resistant (to mitigate the effects of UV degradation), 600 μm core optical fibers are used to couple the light between each spectrometer (located in the main underwater housing) and the fore-optics. A low power bi-stable shutter is integrated into the radiance fore-optics heads (in front of the fore-optics fiber) to enable collection of dark measurements near the time when light data is taken. The use of the fiber optic coupler (via the titanium conduit) necessitated a plane mirror oriented at 45° to make a 90° angle in the direction of the light propagation in the fore optics. This, combined with the optical elements in the HyperNav radiance sensor, presented a potential issue of increased polarization sensitivity. To reduce the polarization sensitivity of the optical train, a liquid crystal polymer depolarizing filter with anti-reflection coating was integrated between the mirror and the pressure window. Inclusion of the depolarizing filter significantly reduced the polarization sensitivity of the optical train over the 350–700 nm range to less than 1%, and increases to 2% from 700 to 800 nm.

1 http://omtab.obs-vlfr.fr/SimulO

The in-water field of view (FOV) of the HyperNav radiance sensor was designed to be 4.5° (half-angle, half-max) in water. To verify, the FOV was measured in a seawater tank, with the radiance head rotated in a beam of collimated light from a FEL lamp into the tank with the face of the radiance head oriented perpendicular to the incident beam. To minimize scattering, the water was filtered and allowed time to settle for bubbles to escape. The field-of-view was determined to be 4.5° (half-angle, half-max) for all wavelengths, with the response dropping to 0.35% of maximum at 10° (half-angle) with no secondary reflections observed.

The main pressure housing of the HyperNav system contains the dual spectrometers, electronic boards, external cable connectors, as well as a pitch and roll sensor and a pressure sensor. Simulations were conducted to ensure that the HyperNav system maintained low tilt due to the drag of the HyperNav system. Drag simulation models predicted a pitching moment of only 0.002 J/rad parallel to the arms. Because the ocean upwelling radiance decreases exponentially with depth their position in the vertical is needed in high accuracy. Thus, the sensors were placed as close to the surface as possible (but below the surface to avoid reflections from air-water interface), and a Paroscientific Digiquartz® pressure sensor was integrated to provide accurate and high-resolution measurements of depth.

The inclusion of the titanium conduits (fore-optics to the main HyperNav body) necessitated a support structure to ensure stability of the fore optics in rough ocean surface conditions. The support structure used is fabricated from carbon fiber tubing filled with castable syntactic foam. Test results showed the design was able to support approximately 200 J/rad of torque while retaining its original shape.

To obtain a pressure rating for the HyperNav system, testing of the main pressure housing and the fore-optics head housing were conducted down to ~1,200 dbar without failure occurring. Pressure testing of the full HyperNav system was conducted to 825 dbar without failures occurring. Based on these results, we estimated the pressure rating as 1,200 dbar. To date, no destructive pressure testing of the full system has been completed. However, during a recent field deployment of the HyperNav system integrated with an autonomous profiling float, the system was mistakenly commanded to go down to 1700 m but survived and continued to work properly without any effects on the system. Thus we expect the system to be able to reach depths of 1,500 m without failures occurring.

The HyperNav system also supports integration of an external four-channel downwelling irradiance sensor (a Sea-Bird Scientific OCR-504). The OCR-504 is enabled by using an underwater cable connected to an electrical connector on the top of the HyperNav system's pressure housing. The OCR-504 is mounted to a support structure located at the highest point on the platform to avoid reflections and shadowing effects on the measurement. The purpose of including the OCR-504 sensor on the HyperNav system was to capture potential varying sky conditions during the surface upwelling radiance measurement acquisitions. Recent work by Tan et al. (2024) has shown potential that the full hyperspectral above surface downwelling irradiance can be reconstructed accurately using *in-situ* irradiance measurements from 4 select spectral bands. Finally, the HyperNav system also includes a combined chlorophyll fluorescence, colored dissolved organic matter fluorescence, and backscattering sensor (Sea-Bird Scientific MCOMS). However, data acquisition integration for this sensor within the HyperNav system is not completed as of yet, but will be pursued in the future. The purpose of including this sensor is to provide an independent method of assessing the water column properties to meet the SVC criteria of spatial/vertical homogeneity.

2.2 Electronics and firmware functionality

Due to the number of sensors integrated into the HyperNav system, the large volume of data from the spectrometers, and the real-time requirements, the electronics design required implementation of two microprocessors as well as analog to digital interface electronics to the spectrometers to provide more flexibility and capabilities in optimizing the radiometric signals and control. In the free-fall system (i.e., real time acquisition mode, see HyperNav operation modes section below), this significantly limits the frame rate (one sample every ~ 3 seconds). In the float implementation, frames are collected and stored locally on the spectrometer interface board (one sample every ~1.15 s). In the float implementation, typical float ascent rates are between 0.05 m s^{-1} (in the upper 10 m of the water column) and 0.08 m s^{-1} (below 10 m), providing radiance measurements every 0.06 m–0.09 m. When the float is at the surface, and after data collection is complete, the frames are transferred to the controller board for permanent storage and transmission via Iridium to the Router-Based Unrestricted Digital Internetworking Connectivity Solutions (RUDICS) server.

The HyperNav system's firmware has an on-board automatic integration time adjustment feature, where the integration time of each spectrometer is controlled based on the nearest neighbor sampled light (unshuttered) and dark (shuttered) measurements. This control algorithm functions as follows: a light measurement is taken, and the maximum count (i.e., highest value as a function of wavelength) value is determined and compared to a user configurable saturation count value. If the maximum light count value exceeds the saturation count level, the firmware automatically switches the integration time of the spectrometer to the next shortest integration time. Conversely, the mean of the spectral dark (with the shutter closed) counts is computed and compared with the most recent light sample. If the light measurement is near the dark count average, the firmware automatically changes the integration time to the next longest integration time. The available spectrometer integration times are 11, 20, 40, 80, 160, 320, 640, 1,280, and 1920 ms, which enable over 7 orders of magnitude of range in radiance.

Ancillary sensors on board the HyperNav sensor, pitch and roll and pressure sensors, are sampled continuously during operation. At the time of a radiance measurement acquisition, the nearest pitch/roll and pressure measurements are collected and integrated into the radiance data output frame, along with the date/time of measurement. Additionally, all measured data are recorded to internal memory, which has a capacity of 4GB, (roughly 1,000 HyperNav profiles) on the HyperNav system which can be downloaded post-deployment.

2.3 HyperNav operational modes

Each HyperNav system can be configured to operate in one of two modes: 1) a real-time (RT) mode, also known as "freefall", where a cable is used to connect the HyperNav to an external power source and for data/command transmissions, and, 2) a fully autonomous profiling (AP) mode, where the HyperNav system is coupled to an autonomous profiling float to move the system through the water column, supply power to the HyperNav system and enable remote telemetry of HyperNav data to shore using the Iridium modem of the float. Switching between the two modes requires installation of separate firmware on the HyperNav controller board which can be accomplished using a direct cabled connection to HyperNav prior to deployment by the user. Both modes support the on-board automatic integration time adjustment feature.

2.3.1 HyperNav real-time (RT) mode of operation

The simplest method of operating a HyperNav system is via a short cable to connect an external 12 V DC power supply and a serial (RS-232) interface to the power/communications port of HyperNav. A terminal program, such as Tera Term, can be used to send various commands to the HyperNav, for example, to start/stop sampling, change and store configuration settings, manually change integration times, change the interval of light and dark sampling, and to offload collected data from the internal memory of HyperNav. This is the typical method used for laboratory testing and for calibration of the radiance sensors. HyperNav command, configuration, and data capture and visualization can also be accomplished using the open source software Inlinino[2] (Haëntjens and Boss, 2020) which has been updated to include many of the features listed above.

The RT mode of operation also enables using the HyperNav for conducting shallow (< 150 m) ocean vertical profiles and for data collection at the near surface when deployed from small boats (similar to the capabilities of legacy Sea-Bird Scientific HyperPro II systems in profiling and buoy modes of operation). In this case, a set of fins fitted with syntactic foam are mounted to the HyperNav radiometric system to aid in maintaining attitude and orientation of the system as it profiles through the water column (Figure 1C). The rate of descent can be adjusted by changing buoyancy through addition/removal of weights to the HyperNav nosecone. Likewise, to collect a time series of data from just below the surface ocean only, weights are removed from the HyperNav such that it is positively buoyant at the surface (the buoyant wing structure near the top increases the righting moment when tilted by waves). A 12 V DC (nominal) power supply is connected to a Satlantic/Sea-Bird Scientific Micro-Deck Unit (MDU) located on the deck of the boat, connected to an external power supply, and to a serial (RS-232) interface of a computer. The MDU serves two purposes, first to convert input voltage from the 12 V DC to 48 V DC and second to convert between RS-232 telemetry and RS-422 levels. Both are needed to reduce power and data transmission line loss when using long cables. A sea-cable is used to connect the MDU to a Micro-Water Unit (MWU) that is externally mounted on the HyperNav. The MWU converts the 48 V DC power from the sea-cable to 12 V DC and converts the RS-232 telemetry coming from the HyperNav to RS-422 levels so that it can be sent through the sea-cable to the MDU. A short underwater cable is used to connect the MWU to the power/communications connector on the HyperNav system.

In RT mode, samples are acquired continuously from each radiance sensor as well as from the integrated pressure and pitch/roll sensors. The measurements are used to build a data frame for each radiance sensor, which includes the serial number of the radiance head, date and time of the radiance measurement, pressure, pitch and roll, and the 2048 spectral count values from the radiance sensor. This data frame creation is performed in real-time and is transmitted through the HyperNav power/communications port. The rate of sampling varies, as the integration time of the spectrometer at the time of measurement depends on the *in-situ* light level, and as well as the processing time needed to create data frames for both radiance sensors in real-time. Typical sampling rates in RT mode vary from 0.25 Hz to 0.5 Hz. Additionally, a hyperspectral surface downwelling irradiance sensor (e.g., a HyperOCR irradiance sensor) can be mounted on a ship/platform near the HyperNav deployment location, to evaluate temporal changes in the downwelling surface irradiance during the period of the HyperNav radiance profiling.

2.3.2 HyperNav autonomous profiling float (AP) mode of operation

The AP mode, where the HyperNav system is integrated with a buoyancy-driven autonomous profiling float (a Sea-Bird Scientific Navis float), enables fully autonomous operational capabilities for collection of quality radiometric data. The Navis float firmware was modified to enable power, sampling, and data transmission for the HyperNav system during deployments. Two sets of black plastic (Delrin) brackets are used to mount the HyperNav system firmly to the Navis body such that the radiance sensor faces of HyperNav are ~10 cm below the water when the float is at the surface. A set of small brackets is used to mount the downwelling irradiance sensor (OCR-504) to the CTD guard such that the sensing face is at the highest point of the float. Currently, the downwelling surface irradiance data (i.e., the OCR-504) from the system are used primarily for QA/QC purposes to evaluate the incident light field variability with respect to the observations of near surface upwelling radiance from HyperNav (i.e., the presence/variation of clouds). The integrated HyperNav float system is ballasted at the Sea-Bird Scientific facility before deployment to achieve a nominal ascent rate of 0.08 m s^{-1} over the profiling range (i.e., park depth to the surface). The system typically performs one profile per day, surfacing ±20 min of the user programmed mission surfacing time, which can be changed through a new mission upload to the Navis system through the Iridium modem.

The HyperNav firmware for AP mode includes user configurable settings that define the radiance sampling interval as a function of depth for three depth ranges. A typical radiance sampling profile is shown in Figure 2. HyperNav uses the integrated pressure sensor to decide when to collect data based on the pre-assigned sampling configuration settings. A maximum of 300 data frames (150 per radiance sensor) of radiance data is collected per vertical profile. When the Navis float reaches the

2 https://github.com/OceanOptics/Inlinino

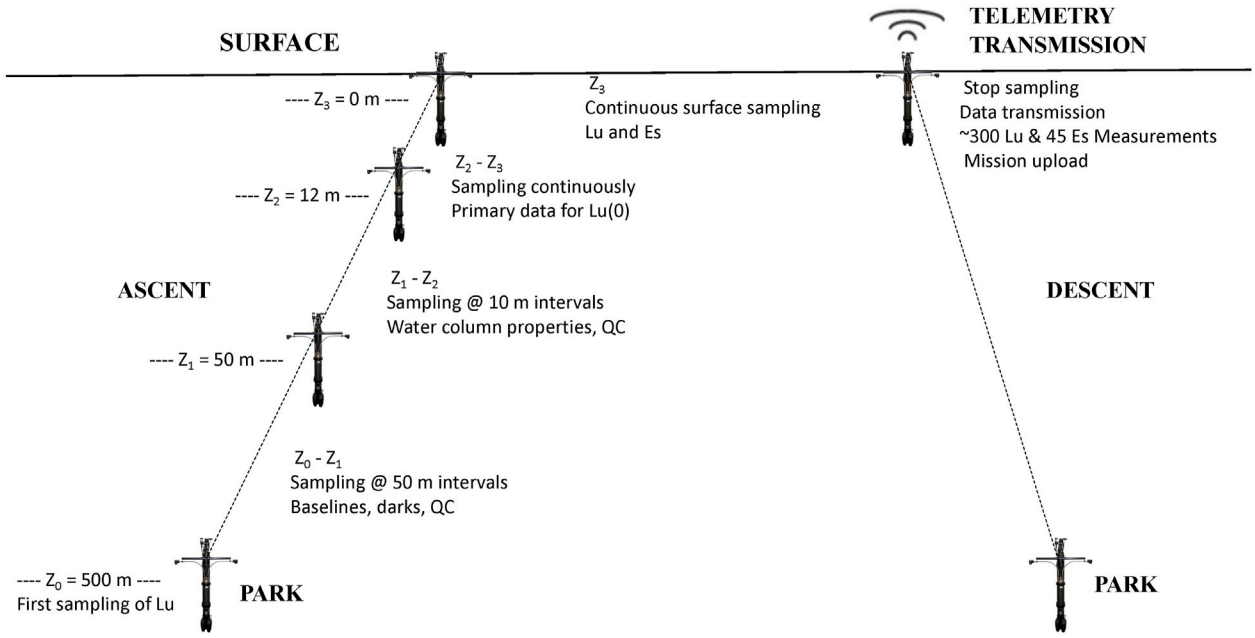


FIGURE 2
Typical HyperNav float profile mission sequence: Each radiance sensor obtains 8 measurements between 500 and 50 (50 m intervals), 4 measurements between 50 and 12 m (10 m intervals), and 138 measurements between 12 m to the surface including the continuous surface hold sampling.

surface, it transmits a message to the HyperNav to complete its sample collection. The Navis controller then establishes an Iridium connection and transmits standard Navis data and control through the Iridium link. Upon completion of this transmission of Navis data, the Navis system transfers modem control to HyperNav, which then initiates transfer of the HyperNav data through the Iridium link. When HyperNav indicates it has completed its transmission, or when a timeout is reached, Navis powers down HyperNav and the system descends to its programmed park depth.

2.4 Radiometric characterizations and uncertainties summary

An expansive series of radiometric characterizations have been conducted on the HyperNav radiance sensors. The results of these characterizations were used to produce a total uncertainty budget for HyperNav radiance measurements. Potential sources of uncertainty included: Calibration, Instrument, and Field uncertainties as described in Zibordi et al. (2015). While the results of these characterization studies and the associated uncertainties are the subject of a companion paper to follow, for convenience, we include Table 1, which summarizes the combined uncertainty (k = 1) estimates for 6 wavelengths of the HyperNav radiance sensors.

Pre- and post-deployment calibrations are performed on each of the radiance sensors to track potential drift or offsets over the deployment duration. Note that while the spectrometers used in the HyperNav radiance sensor have a broad spectral range (i.e 190-1015 nm), the current calibration process extends a smaller spectral range (320–800 nm) primarily due to the light source (i.e., FEL lamp) used in calibration. All calibrations are logged and tracked as a function of date to evaluate and identify long-term changes for each radiance sensor. Additionally, a pre- and post-deployment wavelength registration characterization process is performed to track any changes over the deployment period.

3 Field results of radiometric measurements

A field campaign was conducted over 3 weeks in June 2021 near the Hawaiian Islands. Deployments included a) a HyperNav radiometric sensor (in RT mode) at the Mauna Loa Observatory, HI (MLO), b) a HyperNav radiometric system (in RT mode) deployed near the MOBY site, off Lanai, HI, and c) two HyperNav float systems (in AP mode) deployed west of Kona, HI (Figure 3). The purpose of the campaign was to evaluate HyperNav system performance, radiometric quality, and to validate estimates of measurement uncertainty. In this section we present results from a subset of the data collections at MLO and from the HyperNav float deployments west of Kona, HI. The results from the HyperNav deployment near MOBY and further details and results of the deployment at MLO will be presented in forthcoming papers.

3.1 HyperNav radiometric comparison against the solar spectral irradiance

A HyperNav system operating in RT mode was deployed on an observing platform at the Mauna Loa Observatory, Hawaii on 20 June 2021. The primary objective was to evaluate the accuracy

TABLE 1 HyperNav radiance sensor percent uncertainty at several wavelengths (nm) computed at a k = 1 confidence level. Note that for each source of uncertainty, Type A (i.e., based on statistical analyses of data collected), Type B (i.e., estimated from published literature results), or a combination of both were used to derive the uncertainty values (indicated superscript).

Source of uncertainty	380	412	443	490	510	550	665
Calibration sources of uncertainty							
Irradiance standard[B]	0.55	0.51	0.48	0.44	0.42	0.4	0.34
Reflectance target[B]	1.1	1.1	1	0.9	0.8	0.8	0.9
Geometric effects[B]	1.4	1.4	1.4	1.4	1.4	1.4	1.4
Reproducability[A]	0.23	0.23	0.23	0.23	0.23	0.23	0.23
Instrumental sources of uncertainty							
Polarization[A]	0.9	0.5	0.4	0.1	0.06	0.07	0.5
Thermal[A]	0.08	0.08	0.08	0.08	0.08	0.08	0.08
Immersion[A,B]	0.43	0.45	0.45	0.36	0.4	0.39	0.3
Integration Time Linearity[A]	0.05	0.05	0.05	0.05	0.05	0.05	0.05
Counts Linearity[A, NIST]	0	0	0	0	0.01	0.03	1
Stray Light[A, NIST]	0.12	0.1	0.09	0.08	0.05	0.04	0.09
Wavelength uncertainty (In calibration)[A]	0.19	0.15	0.13	0.09	0.08	0.06	0.03
Wavelength uncertainty (in field)[A]	1	0.1	0.1	0.2	0.5	0.2	0.1
Field sources of uncertainty							
Self-shading effects[A]	0.3	0.26	0.22	0.24	0.32	0.56	2.7
Tilt effects[A,B]	2.2	2.2	2.2	2.2	2.2	2.2	2.2
Biofouling[B]	1	1	1	1	1	1	1
Wave focusing effects[B]	0.5	0.5	0.5	0.5	0.5	0.5	0.5
Depth measurement[A,B]	0.7	0.56	0.54	0.54	0.82	1.14	4
Surface transmittance[B]	0.1	0.1	0.1	0.1	0.1	0.1	0.1
Combine Total Uncertainty (k = 1)	3.5	3.2	3.2	3.1	3.2	3.3	5.8

and uncertainty of the laboratory determined spectral wavelength registrations of the HyperNav radiance sensors using the Sun as the light source. A second objective was to develop and test methods for calibrating the HyperNav radiance sensors pre- and post-deployment that can be accomplished in the field. The MLO site offered significant advantages to test this method due to its high altitude, low aerosol content, and low variability in atmospheric properties. Importantly, it also provided a wealth of data on the atmospheric conditions (i.e., irradiance, aerosol concentration and type, relative humidity) to validate the approach. The approach used was based on the solar reflectance calibration technique described in Cattrall et al. (2002) adapted for estimating HyperNav spectral registrations. Briefly, a calibrated reflectance plaque was positioned below a HyperNav radiance sensor normal to the Hypernav radiance and measurements were made to collect the total (i.e., direct plus diffuse) spectral incident radiance. A fixture mounted to the HyperNav radiance face was used to reduce the in-air FOV to ensure the FOV was centered within the reflectance plaque and were constrained within the dimensions of the plaque. This was accomplished by using a lower reflectance material placed on the plague and changing its location until a reduction in the observed radiance was found. While the exact FOV of the sensor in this setup was not determined, every effort was made to ensure the radiance sensor was in the center of the plaque with at least 25% away from the plaque edges. The spectral sampling (~0.41 nm and spectral resolution ~2.2 nm) of the HyperNav radiance sensors offer the potential to resolve fine-scale spectral absorption lines (e.g., Fraunhofer lines) in the incident radiance associated with chemical elements in the solarsphere and the Earth's atmosphere, and thus the spectral accuracy of the HyperNav radiometric sensors.

A series of radiance measurements were collected from 8: 45 HST to 10:45 HST, with each set of measurements lasting ~60 s in duration. Sky conditions on 20 June 2021 clear, with few cirrus clouds near the horizon. The mean total radiance spectrum at 10:16 HST is shown in Figure 4. This data was used to evaluate the spectral wavelength accuracy of the HyperNav radiance sensor by comparing the center wavelengths of eleven Fraunhofer lines (Figure 4) with the center wavelength of HyperNav that had the lowest radiance value near each Fraunhofer line. The mean wavelength difference was 0.23 nm with a standard deviation and standard error of 0.73 nm and 0.07 nm respectively. Considering that the spectral sampling of the HyperNav radiance (~0.41 nm) is larger than the mean difference derived using the above method, we conclude that uncertainty in

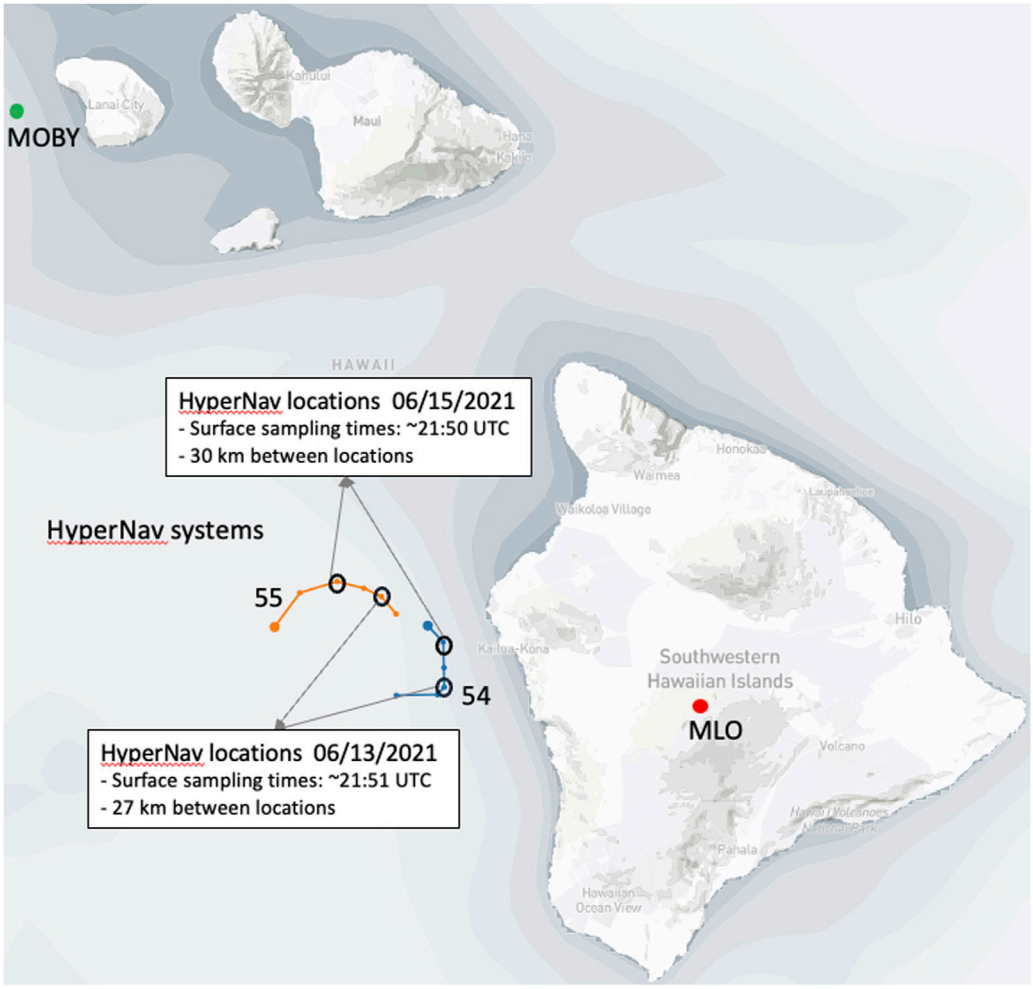


FIGURE 3
Map of deployment locations during the June 2021 HyperNav field campaign; site of the Marine Optical BuoY, MOBY, (green circle), Mauna Loa Observatory, MLO, (red circle), HyperNav float positions (orange circles/line for HyperNav 55, blue circles/line HyperNav 54). Locations of the HyperNav float systems on 16 June 2021 are also shown.

HyperNav spectral registration is low and meets the requirements for *in-situ* SVC measurements.

3.2 Comparisons between HyperNav systems

Two HyperNav float systems (54 and 55) were deployed west of the Island of Hawaii from 9 June 2021 to 20 June 2021. On 17 June 2021, both systems were recovered and were subsequently redeployed on 18 June 2021. The purpose of these deployments was to evaluate the accuracy of the radiance measurements of each system and between systems. Data collected on June 13 and 15, 2021 from the two HyperNav float systems were used to examine the surface upwelling radiance measurements. Recall that each HyperNav system has two independent upwelling radiance sensors, which allows for intra-comparisons of measurements, and as two HyperNav systems, inter-comparisons of HyperNav systems deployed in the same region. Below we present results of the surface upwelling radiance observations from HyperNav float systems 54 and 55 acquired on June 13 and 15, 2021 (Figure 3). Surface radiance measurements from the two floats systems on 13 June 2021 were collected at 21:50 UTC and 21:51 UTC for systems 54 and 55 respectively, with a 27 km distance between the two HyperNav systems sampling locations. Surface radiance measurements from the two floats systems on 15 June 2021 were collected at 21:53 UTC and 21:46 UTC for systems 54 and 55 respectively, with a 30 km distance between the two HyperNav systems sampling locations.

Pre-deployment calibrations for each of the individual radiance sensors (4 radiance sensors, two sensors per HyperNav system) were applied to the raw field data collected. As shown in Figure 2, the HyperNav float based system profiling sequence includes a near surface data acquisition sequence, typically collecting ~1–2 min of radiance measurements while the system is at the surface. The surface data collected on June 13 and 15, 2021 off Kona, HI (Figure 3) from both HyperNav systems (~50 samples, 1.5 min) were used to derive the mean upwelling radiance spectrum for each radiance head based on the following criteria: 1) include only Lu observations collected from depths shallower than 0.2 m depth, and 2) include observations

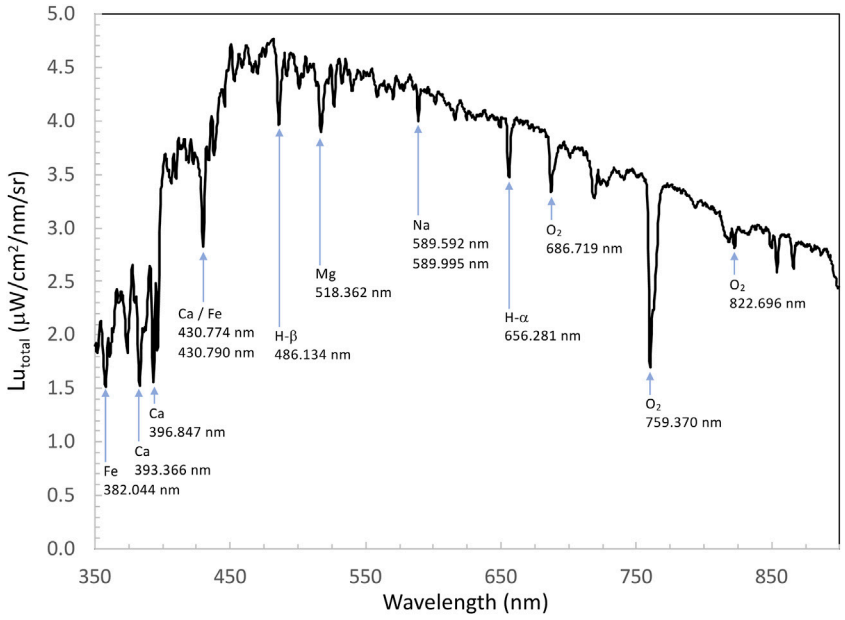


FIGURE 4
Mean total upwelled radiance spectrum obtained from a HyperNav radiance sensor at Mauna Loa Observatory on 20 June 2021 at 10:16 HST using the method described in section 3.1. Various Fraunhofer lines are also shown.

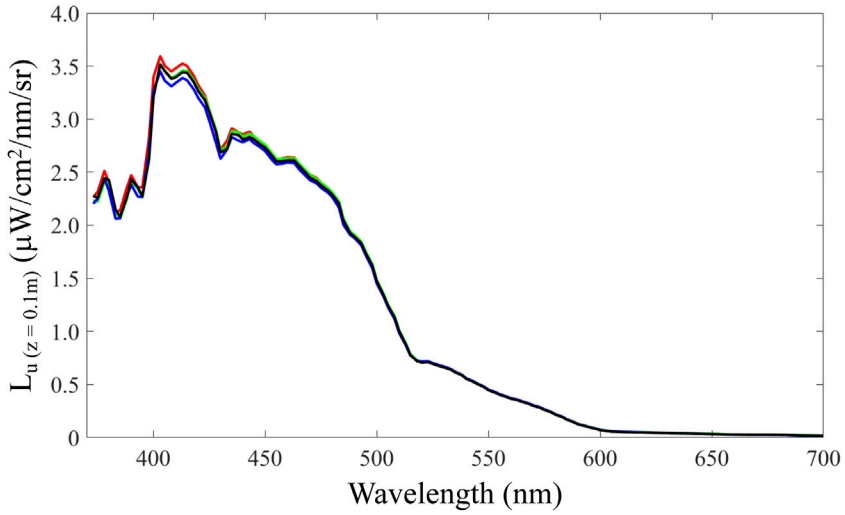


FIGURE 5
Mean near surface (z = ~0.1 m) upwelling radiance spectrum obtained on June 13 and 15, 2021 from HyperNav systems 54 and 55 off Kona, HI. Spectral plots are for 13 June 2021 from HyperNav system 54 (red line) and 55 (green line), and 15 June 2021 from HyperNav system 54 (blue line) and 55 (black line) respectively. Data were binned to the NASA PACE OCI wavelengths in this figure.

with a measured platform tilt angle of $< 5^{\circ}$. Limiting the upwelling radiance observations to depths < 0.2 m and the tilt to $< 5^{\circ}$ reduces the potential errors in extrapolation of radiance to the surface and the potential effects of off-nadir biases due to platform tilt. The mean depth during the surface observations was 0.09 m and 0.10 m for systems 54 and 55 respectively.

To accommodate spectral comparisons between two radiance sensors, the mean surface spectrum for each of the 4 radiance sensors was binned by wavelength to match the PACE OCI remote sensing reflectance center wavelengths using the OCI spectral weighting functions[3]. The mean surface upwelling radiance spectra were derived for each radiance sensor on each for the 2 days during the deployments off Kona, HI. We selected the radiance sensor with the highest mean spectra from each of the two

3 https://oceancolor.gsfc.nasa.gov/data/pace/characterization/

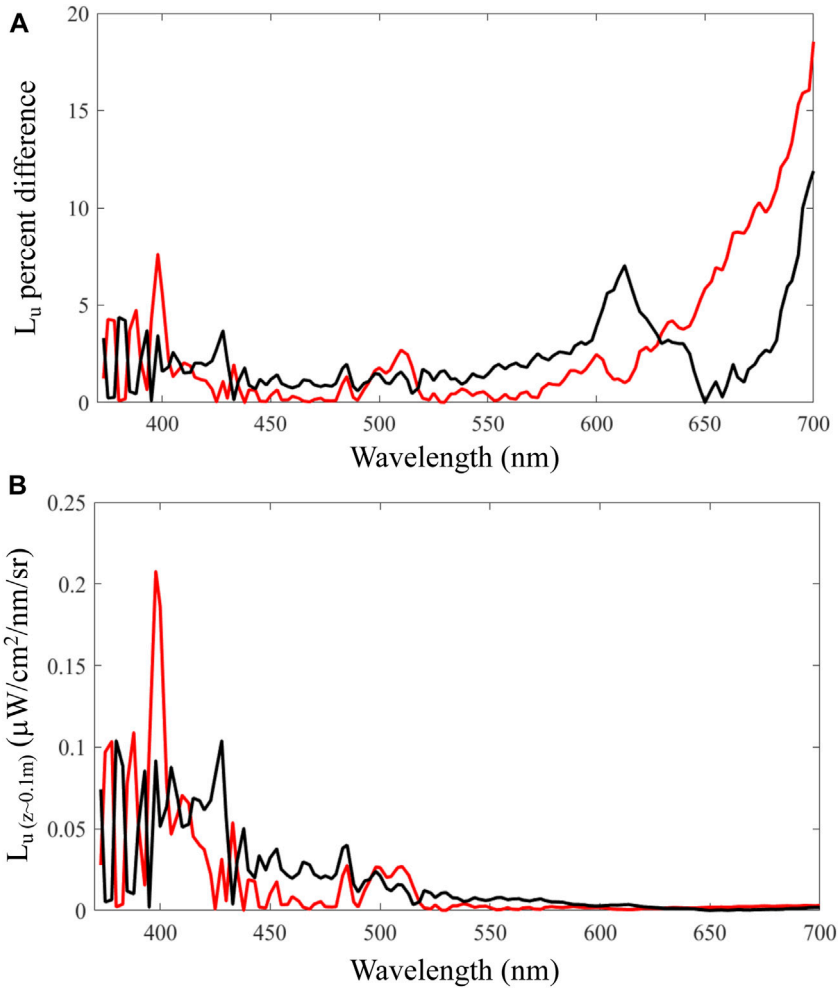


FIGURE 6
Comparison of the mean near surface (z ~ 0.1 m) upwelling radiance spectrum obtained on June 13 (red line) and 15 (black line), 2021 from HyperNav systems 54 and 55 off of Kona, HI. **(A)** Absolute (unsigned) relative difference. **(B)** Absolute (unsigned) difference.

HyperNav systems to use in the below comparisons (Figure 5) assuming that the lower values were due to partial shading of the other radiometer. We examined the relative and absolute differences of the mean upwelling radiance spectrum measured from each HyperNav system on each of the 2 days selected is presented in Figure 6. The mean spectral (373–700 nm) absolute relative difference is 2.02% and 0.1%) for June 13 and 15, 2021 respectively. The mean spectral (373–700 nm) absolute difference is 0.0085 μW cm^{-2} nm^{-1} sr^{-1} and 0.0124 μW cm^{-2} nm^{-1} sr^{-1} for June 13 and 15, 2021 respectively.

While the spectral relative and absolute differences shown in Figure 6 are very low, the largest differences are observed in two spectral regions, 370–400 nm and 600–700 nm. In the 370–400 nm region, note that several Fraunhofer absorption lines are very narrow and tightly spaced (see Figure 4), which contributes to the high spectral variability in the upwelling radiance in this region. Note that even with the 0.41 nm channel spacing of the HyperNav, slight errors (< 0.4 nm) in the center wavelength registrations can contribute to larger relative difference errors between two sensors across these distinct Fraunhofer absorption lines, even after applying the band weighting response functions of OCI and binning to 3 nm. Also note that the source light used for the HyperNav radiance sensor (i.e., a FEL 1000 W tungsten-halogen lamp) is very weak in the 305–400 nm range. At the standard integration time (40 msec) used during calibration, the typical light output from the source lamp is only 1%–2% above the signal-to-noise level (e.g., 60 counts above the 6,000 counts dark signal). Additionally, the depolarizer filter used in the radiance sensor reduces the light transmission in the 350–400 nm region (approx. 80% as compared to 95% in the 500–700 nm region). As such we expect higher uncertainty in both the percent and absolute difference between radiance sensors in this spectral region. A future area of investigation is to utilize a stable light source for the UV region, or to calibrate the radiance sensors at longer integration times and stitch the calibrations across the UV and Blue-NIR spectrum. At wavelengths greater than 600 nm, large absolute percent differences (> ± 5%) are observed, however, the absolute differences are small. This is a region where the absorption by water increases rapidly and is temperature and salinity dependent. In clear waters such as those experienced on the 2 days in June 2021 off Kona, HI, the primary absorbing

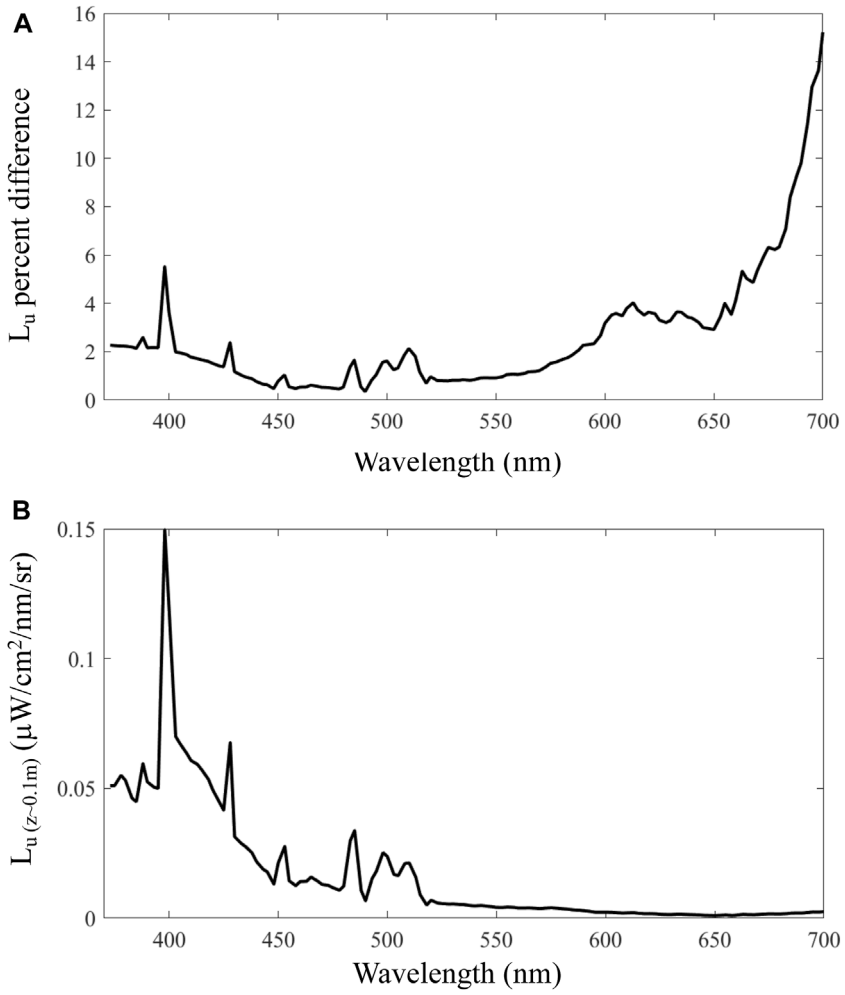


FIGURE 7
Comparison of the mean near surface (z ~ 0.1 m) upwelling radiance spectrum between June 13 and 15, 2021 from HyperNav systems 54 and 55 off of Kona, HI. **(A)** Mean absolute relative difference. **(B)** Mean absolute difference.

substance *in-situ* is water, which may account for lowest upwelled radiances in this wavelength region.

As shown in Figure 5, the upwelling radiance spectra from each of the radiance sensors on each of the 2 days were very similar across both HyperNav systems, and thus, merited a comparison between the 2 days of observations. When comparing the mean spectral upwelling radiances across the 2 days (Figure 7), we find the derived relative and absolute spectral differences (unsigned) are 1.7% and 0.025 μW cm^{-2} nm^{-1} sr^{-1} respectively. We find these results to be highly encouraging in meeting the SVC *in-situ* criteria given that this comparison includes measurements from four independent upwelling sensors that two HyperNav systems collected on two separate days.

4 Summary and future directions

We have accomplished the selection of components, build, and testing of a new hyperspectral field radiometer. The initial results show that HyperNav radiance radiometer has high spectral resolution, is portable, stable, with high accuracy. Field testing results suggest it is ready to be used for *in-situ* SVC for the PACE OCI sensor. Future work includes improvement to firmware to increase sampling frequency, improved integration with ancillary sensors, and accelerated telemetry.

Operating and maintaining a fleet of HyperNav systems will provide means to vicariously calibrate space-based sensors faster than previously possible by obtaining sufficient match-ups earlier. In conjunction with moored SVC facilities they could reduce the time needed to estimate the Ocean Color sensor gain from 2 years with matchups from a single site Franz et al. (2007) to a few months. While the focus of this paper has been to describe a new radiometric technology for obtaining high spectral resolution and accuracy upwelling radiance measurements for *in-situ* SVC, we envision these measurements will be useful for various studies that utilize ocean color hyperpectral imagery. Such applications include validation of SVC gain values over the OCI mission, atmospheric correction verification/improvement studies, as well as PACE satellite data product algorithm development and validation that utilize hyperspectral data.

Data availability statement

The datasets presented in this study can be found in online repositories. The names of the repository/repositories and accession number(s) can be found below: Data from field deployments of the HyperNav float based system are available at https://misclab.umeoce.maine.edu/HyperNAV/.

Author contributions

AB: Conceptualization, Funding acquisition, Investigation, Methodology, Project administration, Writing–original draft, Writing–review and editing. EB: Conceptualization, Data curation, Investigation, Validation, Writing–review and editing. NH: Data curation, Formal Analysis, Investigation, Methodology, Validation, Writing–review and editing. CO: Conceptualization, Project administration, Writing–original draft. RF: Conceptualization, Investigation, Methodology, Validation, Writing–review and editing. JT: Formal Analysis, Investigation, Validation, Writing–review and editing. JK: Methodology, Software, Writing–original draft. MD: Formal Analysis, Investigation, Methodology, Writing–review and editing. DW: Conceptualization, Methodology, Writing–original draft. MM: Formal Analysis, Investigation, Methodology, Writing–review and editing. PC: Conceptualization, Methodology, Writing–review and editing.

Funding

The author(s) declare financial support was received for the research, authorship, and/or publication of this article. Funding for the HyperNav system has been provided by NASA's Ocean Biology and Biogeochemistry program, from contract numbers 80GSFC20C0101 and 180GSFC22CA050.

Acknowledgments

The authors gratefully recognize and thank Ronnie Van Dommelen, Keith Brown, Burkhard Plache, Scott Feener, and Marlon Lewis, formerly of Satlantic LP for their many innovative contributions to the project which included the initial design, characterization and field testing of the HyperNav. Their contributions were seminal to successful development of the HyperNav system. We thank the staff of the Mauna Loa Observatory for providing logistic support, access to the site, and technical and scientific support. We thank Eric Rehm, Sea-Bird Scientific for useful comments in preparation and review of this manuscript.

Conflict of interest

Authors CO and DW were formerly employed by Sea-Bird Scientific.

Authors JK and MD are employed by Sea-Bird Scientific.

The remaining authors declare that the research was conducted in the absence of any commercial or financial relationships that could be construed as a potential conflict of interest.

The author(s) declared that they were an editorial board member of Frontiers, at the time of submission. This had no impact on the peer review process and the final decision.

Publisher's note

All claims expressed in this article are solely those of the authors and do not necessarily represent those of their affiliated organizations, or those of the publisher, the editors and the reviewers. Any product that may be evaluated in this article, or claim that may be made by its manufacturer, is not guaranteed or endorsed by the publisher.

References

Antoine, D., Guevel, P., Desté, J.-F., Bécu, G., Louis, F., Scott, A. J., et al. (2008). The "boussole" buoy—a new transparent-to-swell taut mooring dedicated to marine optics: design, tests, and performance at sea. *J. Atmos. Ocean. Technol.* 25, 968–989. doi:10.1175/2007JTECHO563.1

Brown, S. W., Flora, S. J., Feinholz, M. E., Yarbrough, M. A., Houlihan, T., Peters, D., et al. (2007). "The marine optical buoy (MOBY) radiometric calibration and uncertainty budget for ocean color satellite sensor vicarious calibration," in *Sensors, systems, and next-generation satellites XI*. Editors S. Habib, R. Meynart, S. P. Neeck, and H. Shimoda (SPIE: International Society for Optics and Photonics), 6744. doi:10.1117/12.737400

Cattrall, C., Carder, K. L., Thome, K. J., and Gordon, H. R. (2002). Solar-reflectance-based calibration of spectral radiometers. *Geophys. Res. Lett.* 29, 1–4. doi:10.1029/2002GL015130

Claustre, H. (2011). Bio-optical sensors on argo floats. *Tech. Rep.*

Franz, B. A., Bailey, S. W., Werdell, P. J., and McClain, C. R. (2007). Sensor-independent approach to the vicarious calibration of satellite ocean color radiometry. *Appl. Opt.* 46, 5068–5082. doi:10.1364/ao.46.005068

Frouin, R. (2013). In-flight calibration of satellite ocean-colour sensors. *Tech. Rep.*

Gordon, H. R. (1998). In-orbit calibration strategy for ocean color sensors. *Remote Sens. Environ.* 63, 265–278. doi:10.1016/S0034-4257(97)00163-6

Haëntjens, N., and Boss, E. (2020). Inlinino: a modular software data logger for oceanography. *Oceanography* 33, 80–84. doi:10.5670/oceanog.2020.112

Leymarie, E., Doxaran, D., and Babin, M. (2010). Uncertainties associated to measurements of inherent optical properties in natural waters. *Appl. Opt.* 49, 5415–5436. doi:10.1364/AO.49.005415

Mueller, J. L. (2003). Ocean optics protocols for satellite ocean color sensor validation, revision 4: instrument specifications, characterization, and calibration. *Tech. Rep.*

Tan, J., Frouin, R., Häentjens, N., Barnard, A., Boss, E., Chamberlain, P., et al. (2024). Reconstructing hyper-spectral downwelling irradiance from multi-spectral measurements. *Front. Remote Sens.* 5. doi:10.3389/frsen.2024.1335627

Voss, K. J., McLean, S., Lewis, M., Johnson, C., Flora, S., Feinholz, M., et al. (2010). An example crossover experiment for testing new vicarious calibration techniques for satellite ocean color radiometry. *J. Atmos. Ocean. Technol.* 27, 1747–1759. doi:10.1175/2010JTECHO737.1

Werdell, P. J., Behrenfeld, M. J., Bontempi, P. S., Boss, E., Cairns, B., Davis, G. T., et al. (2019). The plankton, aerosol, cloud, ocean ecosystem mission: status, science, advances. *Bull. Am. Meteorological Soc.* 100, 1775–1794. doi:10.1175/BAMS-D-18-0056.1

Zibordi, G., Mélin, F., Voss, K. J., Johnson, B. C., Franz, B. A., Kwiatkowska, E., et al. (2015). System vicarious calibration for ocean color climate change applications: requirements for *in situ* data. *Remote Sens. Environ.* 159, 361–369. doi:10.1016/j.rse.2014.12.015

Zibordi, G., Talone, M., Voss, K. J., and Johnson, B. C. (2017). Impact of spectral resolution of *in situ* ocean color radiometric data in satellite matchups analyses. *Opt. Express* 25, A798–A812. doi:10.1364/OE.25.00A798

frontiers | Frontiers in Remote Sensing

TYPE Original Research
PUBLISHED 04 July 2024
DOI 10.3389/frsen.2024.1359709

Check for updates

OPEN ACCESS

EDITED BY
Kevin Ruddick,
Royal Belgian Institute of Natural Sciences, Belgium

REVIEWED BY
Maycira Costa,
University of Victoria, Canada
Ilaria Cazzaniga,
Joint Research Centre, Italy

*CORRESPONDENCE
Victor Martinez-Vicente,
vmv@pml.ac.uk
Gaia Gleratti,
gaia.gleratti@gmail.com

RECEIVED 21 December 2023
ACCEPTED 10 June 2024
PUBLISHED 04 July 2024

CITATION
Gleratti G, Martinez-Vicente V, Atwood EC, Simis SGH and Jackson T (2024), Validation of full resolution remote sensing reflectance from Sentinel-3 OLCI across optical gradients in moderately turbid transitional waters. *Front. Remote Sens.* 5:1359709. doi: 10.3389/frsen.2024.1359709

COPYRIGHT
© 2024 Gleratti, Martinez-Vicente, Atwood, Simis and Jackson. This is an open-access article distributed under the terms of the Creative Commons Attribution License (CC BY). The use, distribution or reproduction in other forums is permitted, provided the original author(s) and the copyright owner(s) are credited and that the original publication in this journal is cited, in accordance with accepted academic practice. No use, distribution or reproduction is permitted which does not comply with these terms.

Validation of full resolution remote sensing reflectance from Sentinel-3 OLCI across optical gradients in moderately turbid transitional waters

Gaia Gleratti[1,2]*, Victor Martinez-Vicente[3]*, Elizabeth C. Atwood[3], Stefan G. H. Simis[3] and Thomas Jackson[4]

[1]School of Marine Science and Engineering, University of Plymouth, Plymouth, United Kingdom, [2]Now at A-2-Sea Solutions Ltd., Romsey, United Kingdom, [3]Plymouth Marine Laboratory, Plymouth, United Kingdom, [4]European Organisation for the Exploitation of Meteorological Satellites (EUMETSAT), Darmstadt, Germany

Estuarine and coastal transitional waters present a challenge for the interpretation of radiometric remote sensing. Neighbouring water masses have strongly contrasting optical properties at small spatial scales. Adjacency of land adds optical contaminations (adjacency effect) and further complicates satellite use in near-shore waters. In these areas, the lack of *in situ* observations has been the bottleneck for the characterisation of the uncertainty of satellite products. Radiometric underway measurements (e.g., ferries, ships of opportunity, autonomous vehicles) produce large volumes of *in situ* observations that can be used for radiometric validation. In this study, we evaluate the performance of the POLYMER atmospheric correction algorithm for the Ocean and Land Colour Instrument (OLCI) onboard Sentinel-3 (S3) for the retrieval of remote sensing reflectance $R_{rs}(\lambda)$ in the transitional waters of Plymouth, United Kingdom using hyperspectral radiometric underway measurements. We explored the effect of the selection of time window, averaged areas around the *in situ* measurement and quality control flags into the matchup procedure. We selected matchups only within 1 pixel and $\pm$30 min of the satellite overpass. Accuracy (RMSD) decreased spectrally from blue to red wavelengths (from 0.0015 to 0.00025 sr^{-1}) and bias (Median Percentage Difference) was mostly positive (up to more than 100%) in relation to *in situ* observations. We segregated the dataset with respect to optical water types and distance to shore. Although no statistically significant difference was observed among those factors on the measures of performance for the reflectance retrieval, RMSD was the most sensitive metric. Our study highlights the potential to use OLCI full resolution imagery in nearshore areas and the need for more *in situ* data to be collected in the more turbid waters.

KEYWORDS

reflectance, matchup, validation, Sentinel-3 OLCI, atmospheric correction, coastal waters

1 Introduction

Spaceborne data collection offers a cost-effective solution to global scale monitoring to complement *in situ* efforts. Ocean colour remote sensing using coarse and medium resolution optical sensors is especially relevant for monitoring water quality. Water quality indicators (i.e., chlorophyll-a, suspended particulate matter, coloured dissolved organic matter) derived from satellite remote sensing reflectance (R_{rs}) are used to monitor changes in the coastal zone. Some of these indicators are used for enabling the monitoring of compliance with international agreements (e.g., OSPAR) and would benefit from the daily revisit times of imaging spectrometers such as OLCI on Sentinel-3.

Despite improvements in the spectral, temporal, and spatial resolutions of optical sensors over time, environmental variability poses challenges in the interpretation of the remote sensing signal when studying the aquatic environment, particularly close to the shore (Hieronymi et al., 2017). Accurate atmospheric correction remains an essential component towards reliable remote sensing of ocean colour since 80%–90% of the measured signal comes from the atmosphere, primarily caused by molecular and aerosol scattering (IOCCG, 2010). Other factors such as Sun glint and whitecaps pose further challenge to remote sensing of ocean colour, and in coastal waters, the adjacency of land also needs to be considered (Bulgarelli and Zibordi, 2018; Warren et al., 2019; Vanhellemont and Ruddick, 2021). These effects represent the bulk of estimated ocean colour product uncertainty, while optical complexity of the water column is non-negligible (Mélin and Vantrepotte, 2015; Spyrakos et al., 2018). Optically active constituents such as phytoplankton, phytodetritus, colour dissolved organic matter (CDOM) and suspended sediments contribute to the bulk optical properties. Optical water types, each one representing the different contributions of the optically active constituents (Moore et al., 2001; Jackson et al., 2017; Spyrakos et al., 2018), may provide an avenue to disentangle the effects of in-water optical complexity from the artefacts produced by contamination outside the water (i.e., adjacency of land, complex changes in aerosols) in satellite ocean colour products near the coasts (Pahlevan et al., 2021).

To assess the reliability of remotely sensed products over gradients of optical diversity, validation of the atmospherically corrected signal with concurrent field measurements is usually done. Although a great effort has been put into estimating uncertainty of ocean colour products, validation is still limited by the scarcity of validation data. Consequently, taking advantage of automated platforms will help to increase the amount of field observations (Zibordi et al., 2006; Simis and Olsson, 2013; Vansteenwegen et al., 2019; Goyens et al., 2022).

Past research has successfully exploited the Aerosol Robotic Network-Ocean Colour (AERONET-OC) dataset to validate ocean colour products in offshore waters (Zibordi et al., 2006; Mélin et al., 2016). From a combination of automatic and cruise measurements, the uncertainty in R_{rs} mainly in the open ocean has been estimated per optical water type (Moore et al., 2015). More work is required in specific areas, particularly optically complex coastal waters, where uncertainties in blue and red bands are still in the order of 10%–20% (Moore et al., 2015). Over lakes, rivers, and coastal waters, a similar exercise has been conducted to assess atmospheric correction methods for Landsat-8, MODIS-Aqua, VIIRS, Sentinel-2 and Sentinel-3 using AERONET-OC data (Liu et al., 2021; Pahlevan et al., 2021; Tilstone et al., 2022; Arena et al., 2024). Several recent studies have concentrated efforts on the Sentinel-3 OLCI in a range of optically complex water bodies through ground station and shipborne data, including turbid waters such as the Eastern English Channel (Mograne et al., 2019; Vanhellemont and Ruddick, 2021) and British Columbia (Giannini et al., 2021), or CDOM-dominated waters like the Baltic Sea (Alikas et al., 2020). Compared to phytoplankton-dominated waters where atmospheric correction uncertainties are highest in the blue-green bands, documented uncertainty from remote sensing reflectance (R_{rs}) measurements in optically complex waters is particularly high in the red and near-infrared (NIR; Morel and Prieur, 1977).

High uncertainty in the red and near-infrared documented in optically complex waters can be explained by the adjacent land as it is the spectral region where the contrast between land and water is the highest, with water efficiently absorbing light whilst land is highly reflective (Bulgarelli and Zibordi, 2018). The adjacency effect has been shown to be a significant issue at distances of up to 25 km for SeaWiFS and 30 km for MODIS observations in the Northern Adriatic Sea. When considering mid-latitude coastal regions, it is expected to be more pronounced in summer months, for off-nadir views, for observations from over the land and for a lower aerosol optical thickness (Bulgarelli et al., 2014). Whilst the effect is strong in the NIR (865 nm) due to significant differences between the respective reflectance of the terrestrial and the marine environments, additional uncertainty in the blue-green region (412–510 nm) originates from a difference in the angular distribution of the water-leaving radiance (Bulgarelli and Zibordi, 2018). High dependence on the reflectance of the neighbouring land has been demonstrated, further affecting its sensitivity to the viewing geometry and the optical water type. Whilst it tends to be a serious concern for inland water bodies, it also poses a significant challenge to nearshore coastal environments (Warren et al., 2019). In addition, unlike clear oceanic waters, no assumption can be made about total absorbance of seawater in the NIR in these waters (Ruddick et al., 2000; Goyens et al., 2013). In order to reduce these uncertainties in near coastal waters, *in situ* observations automated systems from vessels have been recently deployed (Martinez-Vicente et al., 2013; Giannini et al., 2021; Wang and Costa, 2022).

Despite all these difficulties, it is important to persevere on efforts to quantify uncertainty in R_{rs} in coastal waters on medium resolution satellite radiometers as their daily revisit times allow for monitoring of coastal processes in SPM flows that could be linked to novel pollutants (Sullivan et al., 2023), as well as to extend the climate quality datasets to coastal waters such as the Ocean Colour Climate Change initiative (Sathyendranath et al., 2019) and develop further products to support biodiversity monitoring.

The present study aims to quantify the uncertainty in R_{rs} satellite data in the optically complex waters surrounding the Tamar Estuary, Plymouth (Western English Channel) and identify its potential sources in the context of optimising ocean colour products in optically complex waters. The focus is on the role of optical water types and distance from land on the discrepancies between

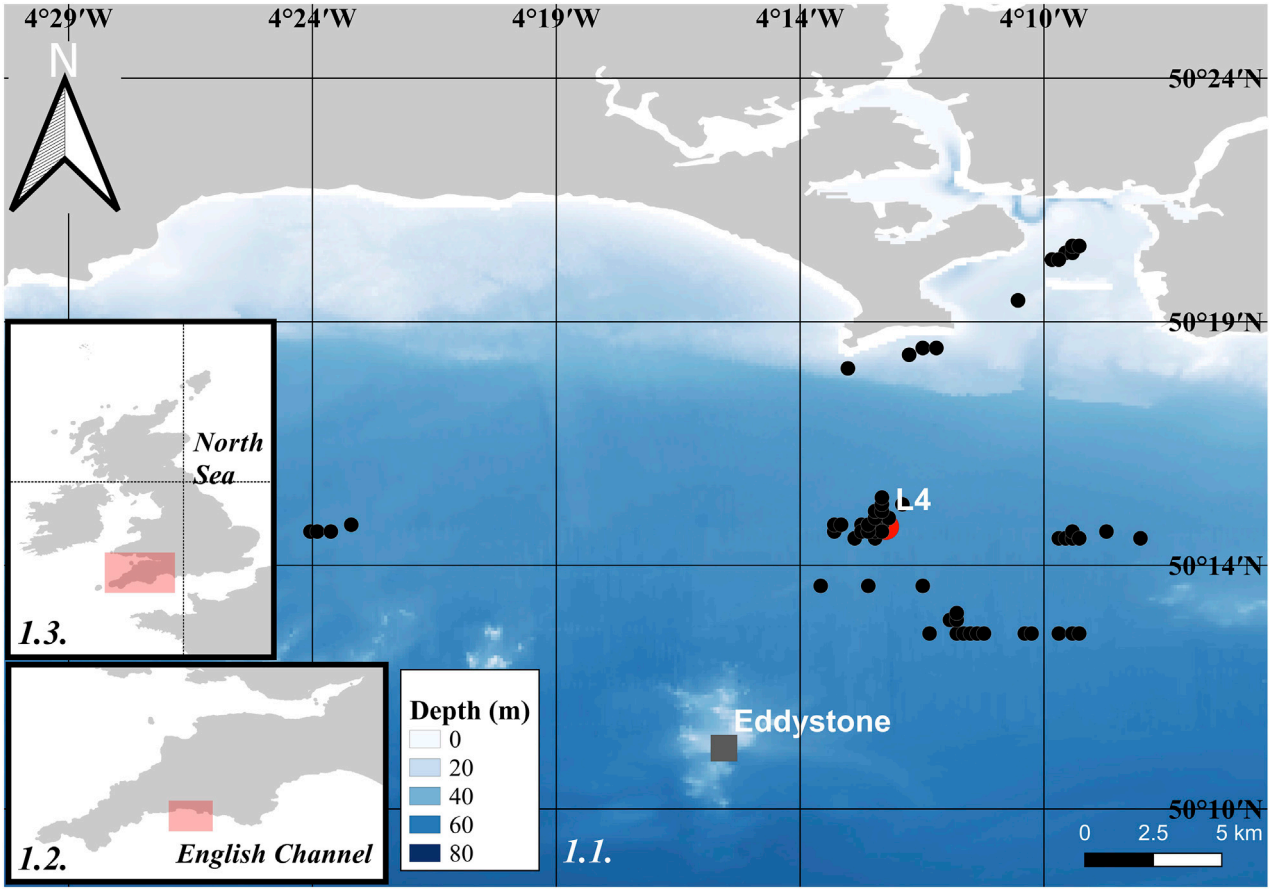


FIGURE 1
Location of the matchup data points from the coastal waters surrounding Plymouth (1.1.), in the Western English Channel (1.2.) in the South West of the United Kingdom (1.3.). The colour scheme represents the local bathymetry.

satellite and *in situ* R_{rs}. This is achieved by comparing shipborne and remotely sensed reflectance from Sentinel-3 OLCI at full resolution (300 m).

2 Materials and methods

2.1 Study area

The coastal waters surrounding Plymouth (United Kingdom) are located on the North Western European Continental Shelf, a dynamic environment heavily influenced by freshwater, tidal and marine currents (Figure 1). The tidal cycle of the estuary governs hydrodynamic processes in the area (Siddorn et al., 2007). In combination with biological seasonality, these influence the dynamics of the optically active constituents (total suspended matter concentration, TSM; coloured dissolved organic matter, CDOM and phytoplankton chlorophyll concentration, Chla; Doxaran et al., 2006). Offshore, in coastal waters around station L4 (water column depth 55 m, Figure 1), optically active constituents are mostly influenced by biological seasonality and river outflows. Phytoplankton dominates during spring/summer bloom events and TSM (mainly made of inorganic particles) and/or CDOM in winter (Groom et al., 2009; Martinez-Vicente et al., 2010). Low concentrations of optically active constituents are present in the area, with concentrations of chlorophyll-a around 1.5 mg m^{-3}, reaching 4 mg m^{-3} during spring bloom at L4 station and TSM concentrations generally around 1 g m^{-3}, reaching 9.94 g m^{-3} in winter months (Martinez-Vicente et al., 2010).

2.2 Earth observation data

Ocean and Land Colour Instrument (OLCI) data were acquired for the period between December 2016 and March 2021. The data evaluated in this study are the fully normalised water-leaving reflectance (ρ_w) full resolution (300 m × 300 m) for 15 selected bands: 400, 412, 443, 490, 510, 560, 620, 665, 674, 681, 709, 754, 779, 865 and 885 nm. For comparison to field measurements, these were then transformed to remote sensing reflectance (R_{rs}) by dividing by π.

The processing stages included atmospheric correction using the POLYMER v4.15 algorithm and the IDEPIX mask generation. The POLYMER atmospheric correction algorithm was originally developed for MERIS open water products to remove Sun glint (Steinmetz et al., 2011), using a BRDF correction from Park and Ruddick (2005) and selected because of its high performance for Sentinel product (Mograne et al., 2019; Giannini et al., 2021).

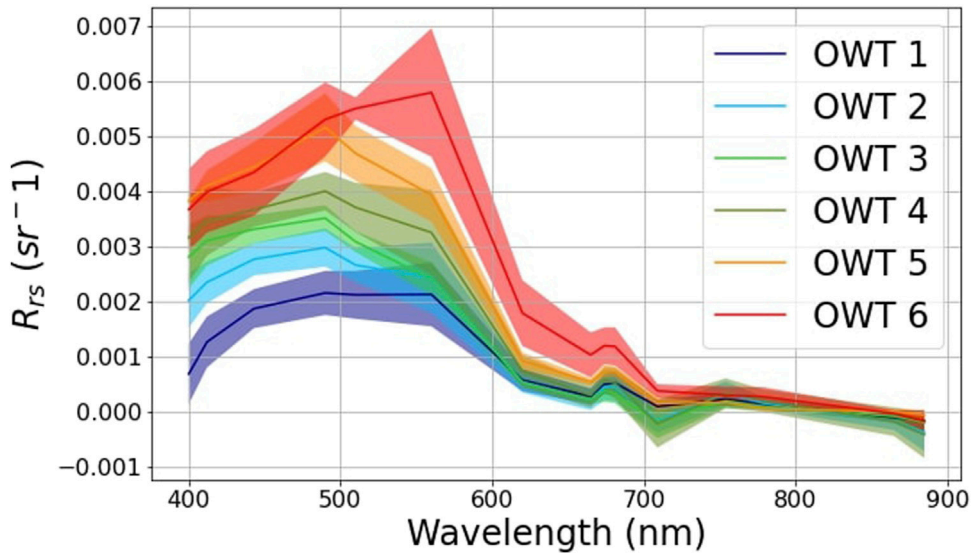


FIGURE 2
The reflectance (Rrs) means and standard deviation of the six optical water types represented in the selected transitional waters of Plymouth, Southwest, United Kingdom. The means were calculated from the training dataset spanning 2016 to 2021.

IDEPIX (Identification of Pixel properties, in SNAP 8) masking is used to remove land, cloud and spurious data points with high uncertainty. The processing chain follows that developed in Warren et al., 2019.

For the creation of a set of optical water types (OWTs), a spatial/temporal subset of the processed satellite data acted as a training dataset to represent the observed variability in the reflectance spectra in the region of interest (Jackson et al., 2017). The optical water type classification first involved the standardisation of the output products by subtracting the mean and dividing by the standard deviation for each band. Principal component analysis was then performed on the standardised data whereby the resulting principal components were used in the cluster analysis to classify the coastal waters into OWTs. The cluster analysis consisted of a fuzzy c-means clustering procedure using a cluster validity function to generate clusters (Xie and Beni, 1991; Moore et al., 2001). The clustering approach resulted in 6 OWTs in the study area (Figure 2). Memberships to all OWT classes were calculated for every satellite data matchup and assigned a dominant OWT class based on highest membership value. The *in situ* spectra associated with that satellite matchup pixel were assigned the same OWT class.

2.3 *In situ* observation data: collection, processing and quality control

During field campaigns in 2017, 2018 and 2020, above-water radiometric measurements were collected with the unsupervised Hyperspectral Sur-face Acquisition System (HSAS, SeaBird Inc.). The sky and water leaving radiance measurements were acquired from the bow of R/V Plymouth Quest at about 5 m above the water surface, whilst out at sea. R/V Plymouth Quest is a 21.5 m length scientific vessel that has been used in previous works (Martinez-Vicente et al., 2013; Jordan et al., 2023). The downward looking radiometer has a field of view of 6°, which corresponds to about 0.6 m at the sea surface. The downwelling irradiance sensor was located at the top of the wheelhouse, on the extreme side of the top of a T shaped mast, away from any superstructure. The sensors and the setup provide accuracy similar to other sensors and approaches (Tilstone et al., 2020). The system continuously recorded downwelling irradiance (E_d), sky radiance (L_s) and water leaving radiance (L_t) at 169 wavelengths with 3.3 nm spectral resolution between 340.0 and 897.7 nm. The scanning frequency was between 4 and 0.5 Hz, depending on the sensor optics. The optical data were converted to physical units and processed to Level3a using the manufacturer's software (Prosoft v7.7.16) which merged the data to 1 Hz. R_{rs} was inferred following: $R_{rs}(\lambda) = L_{w+(}\lambda)/E_d(\lambda)$ where $L_{w+(}\lambda) = L_t(\lambda) - \rho_s L_s(\lambda)$ with L_{w+} the water leaving radiance above the surface and ρ_s the surface reflectance factor (Martinez-Vicente et al., 2013). At the normal speed of R/V Plymouth Quest, the average number of R_{rs} spectra data per OLCI FR pixel (300 m) is 150. The spatial structure of reflectance dataset collected underway from R/V Plymouth Quest is discussed in detail in Jordan et al. (2023). Sensors were factory calibrated every year.

The data were then processed following the fingerprint approach (Simis and Olsson, 2013; QC0 in Table 1) to resolve ρ_s for each observation. Following the procedure, data flagged as valid were retained and filtered according to published recommendations. Quality control was done using characteristics of the spectral shape (Simis and Olsson, 2013; Qin et al., 2017; IOCCG, 2019; Warren et al., 2019). Quality control consisted of removing spectra affected by significantly negative values (QC1 in Table 1; Qin et al., 2017), removing spectra affected by Sun glint and whitecaps (QC2 and QC3 in Table 1; Qin et al., 2017; IOCCG, 2019), removing the effect of the oxygen absorption feature from the instrument calibration (QC4 in Table 1; Qin et al., 2017). It also consisted of accurately selecting spectra representative of the study area

TABLE 1 Summary of *in situ* data filtering criteria with the number (N) of retained spectra per year. φ_s is the viewing azimuth angle relative to the Sun.

	Criteria	2017	2018	2020	Total
QC0	Minimisation of atmospheric absorption features	76,873	46,269	51,254	174,396
QC1	$\sum_{\lambda=340}^{400} \frac{R_{rs}(\lambda)}{(400-340)} \geq -0.0005\, sr^{-1}$ and $\sum_{\lambda=800}^{900} \frac{R_{rs}(\lambda)}{(900-800)} \geq -0.0005\, sr^{-1}$	23,719	12,811	22,327	58,857
QC2	$90° \leq \varphi_s \leq 136°$	3,814	4,241	5,630	13,685
QC3	$R_{rs}(400 - 885) < 0.015\, sr^{-1}$	3,639	3,156	5,627	12,422
QC4	$Max\, R_{rs}(760 - 770) < 0.1 \times Min\, R_{rs}(560 - 600)$	3,072	2,692	4,497	10,261
QC5	$Max\, R_{rs}(\lambda)\, at\, \lambda < 600\, nm$	3,072	2,262	3,731	9,065

TABLE 2 Number of *in situ* spectra retained after distinct matchup selection criteria, with different spatial and temporal windows considered. Bold writing shows the number of in situ spectra used in the main analysis and discussion of this study.

Temporal window	3 h		30 min	
Spatial window	1 × 1 pixel	3 × 3 pixel	1 × 1 pixel	3 × 3 pixel
Matchup Selection	2,817	2,772	432	427
Filtering	2,732	2,215	430	170
Median	583	409	**71**	49

where dominance of mineral particles compared to coloured dissolved organic matter can be found (QC5 in Table 1; Qin et al., 2017; Warren et al., 2019). By applying those successive gating criteria, the number of observations was reduced from 174,396 to 9,065 (Table 1).

In situ spectra that passed the filtering criteria were convolved to the spectral response functions of the OLCI, instrument on Sentinel-3A.

The distance to land (including smaller features such as islands and breakwaters) for each *in situ* measurement was computed using the great-circle distance (Distance to Nearest Hub tool in QGIS). All data points were within 15 km of land. These were grouped into three categories (namely, 0–5 km, 5–10 km, and 10–15 km), and used to investigate the effect of land adjacency on the satellite data quality as described in Section 2.5.

2.4 Extraction and matchup routine

The selection of spatial and temporal windows has been documented to potentially affect validation performance statistics (Concha et al., 2021). Therefore, different matchup selection routines were explored in this study. Two temporal windows (±30 min and ±3 h) and two spatial windows (1 pixel and 3 × 3 pixels) were considered (Table 2). In the case of the 3 × 3 pixel area, only matchups yielding a minimum of six pixels and a coefficient of variation <0.15 were retained (Brewin et al., 2016; Bailey and Werdell, 2006). The mean *in situ* spectra were then used to reduce the satellite data to unique validation points for comparison purposes. A detailed study on the variability within different spatial windows is not the subject of this paper and has been explored elsewhere (Nasiha et al., 2022; Jordan et al., 2023).

The satellite matchup data points were filtered (as shown in 'Filtering' step in Table 2) for significantly negative values ($<-0.0005\, sr^{-1}$) to allow for consistency with the *in situ* dataset (QC1 in Table 1; Qin et al., 2017). In the case that multiple field measurements were present in the same pixel, the median value was taken ('Median' step in Table 2).

For very dynamic waters or stations close to the coast, EUMETSAT (2021) states that reduction of the matchup time window to 1 hour and the spatial window to 1 pixel is acceptable. Thus, given the spatiotemporal variability in the study area, the ±30 min and 1 × 1 pixel matchup selection routine was selected. The resulting matchup *in situ* spectra span across 19 sampling dates, covering a transect of approximately 12 km (Respective *in situ* spectra retained: 0–5 km: N = 11, 5–10 km: N = 38, 10–15 km, N = 22) and spanning six optical water types. The environmental conditions for those sampling dates were clear to slightly overcast skies for all days other than 14th July 2020 showing hazy skies. Most matchups occurred in OWTs 1 and 3 with N = 23 and N = 18, respectively.

From the initial 174,396 reflectance spectra collected, 430 were preserved, and converted to 71 median spectra that were then used for the statistical matchup, coming from a temporal window of 30 min and a spatial window of 1 × 1 pixel.

2.5 Matchup metrics

A set of performance metrics was then calculated to describe the difference between the OLCI and *in situ* data. Root Mean Square Difference (RMSD), Median Absolute Percentage Difference (MdAPD) and Median Percentage Difference (MdPD) were computed to quantify the accuracy, dispersion and bias of the data, respectively, with x the *in situ* data, y the satellite data and N the number of matchups 1–3:

$$RMSD = \sqrt{\frac{1}{N} * \sum_{i=1}^{N} (y_i - x_i)^2} \quad (1)$$

$$MdAPD = Median \left| \frac{y_i - x_i}{x_i} \right| * 100 \quad (2)$$

$$MdPD = Median \frac{y_i - x_i}{x_i} * 100 \quad (3)$$

These metrics were chosen since they are most common in validation exercises within the Ocean Colour Radiometry

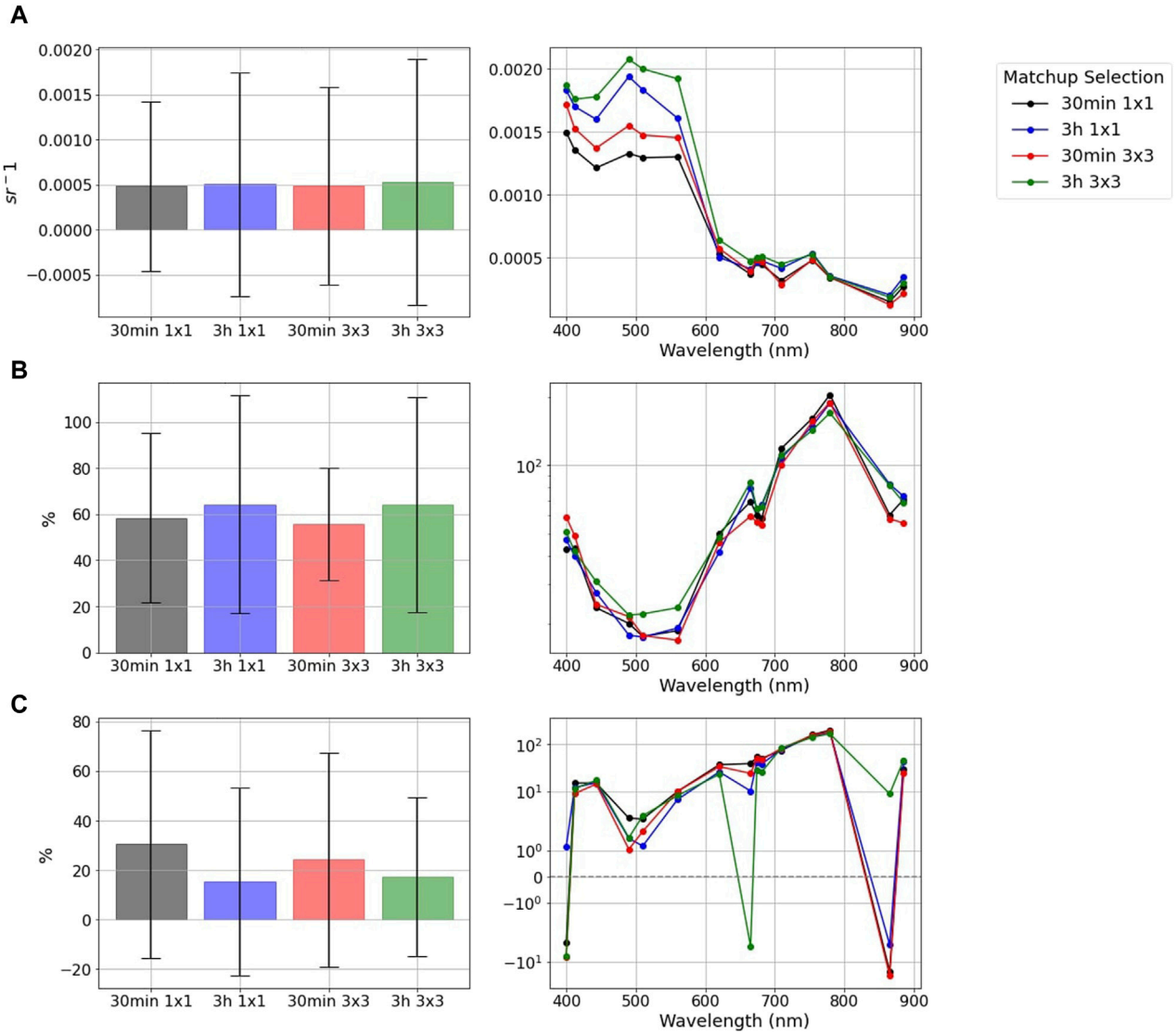


FIGURE 3
Performance metrics for the respective matchup selection routines averaged over the electromagnetic spectrum and represented spectrally for the selected wavelengths. **(A)** Root Mean Square Difference (RMSD), **(B)** Median Absolute Percentage Difference (MdAPD), **(C)** Median Percentage Difference (MdPD). The plots of MdAPD and MdPD are shown on a log scale due to the large variation between wavelengths.

community (Concha et al., 2021). In addition, the distribution of the datasets was investigated.

Data were then segregated by distance to land and by optical water types. Performance metrics were then calculated for subsets depending on the OWT and distance from land. Following a Levene's test for heterogeneity of variance and Shapiro-Wilk test for normality of distribution, non-parametric tests were used. Mann-Whitney tests were carried out to test for statistically significant differences. A permutational analysis of variance (PERMANOVA) with 1,000 permutations based on Euclidian distances was conducted to test for differences in the performance metrics between the distinct OWTs and distance from land.

A comparison of performance metrics between the various matchup selection routines can be found in Section 3.1. Results and discussion are, however, mainly focused on the matchups with a temporal window of 30 min and a spatial window of 1 × 1 pixel, on all data and on data segregated by OWT dominance and distances to the shore. Scatterplots, histograms and descriptive statistics for the other spatial and temporal match up windows explored (as described in Section 2.4) are provided in Supplementary Materials S2–S4.

3 Results

3.1 Discrepancies between satellite and *in situ* data across various matchup selection routines

First, satellite and *in situ* data were compared using various matchup selection criteria using distinct temporal and spatial

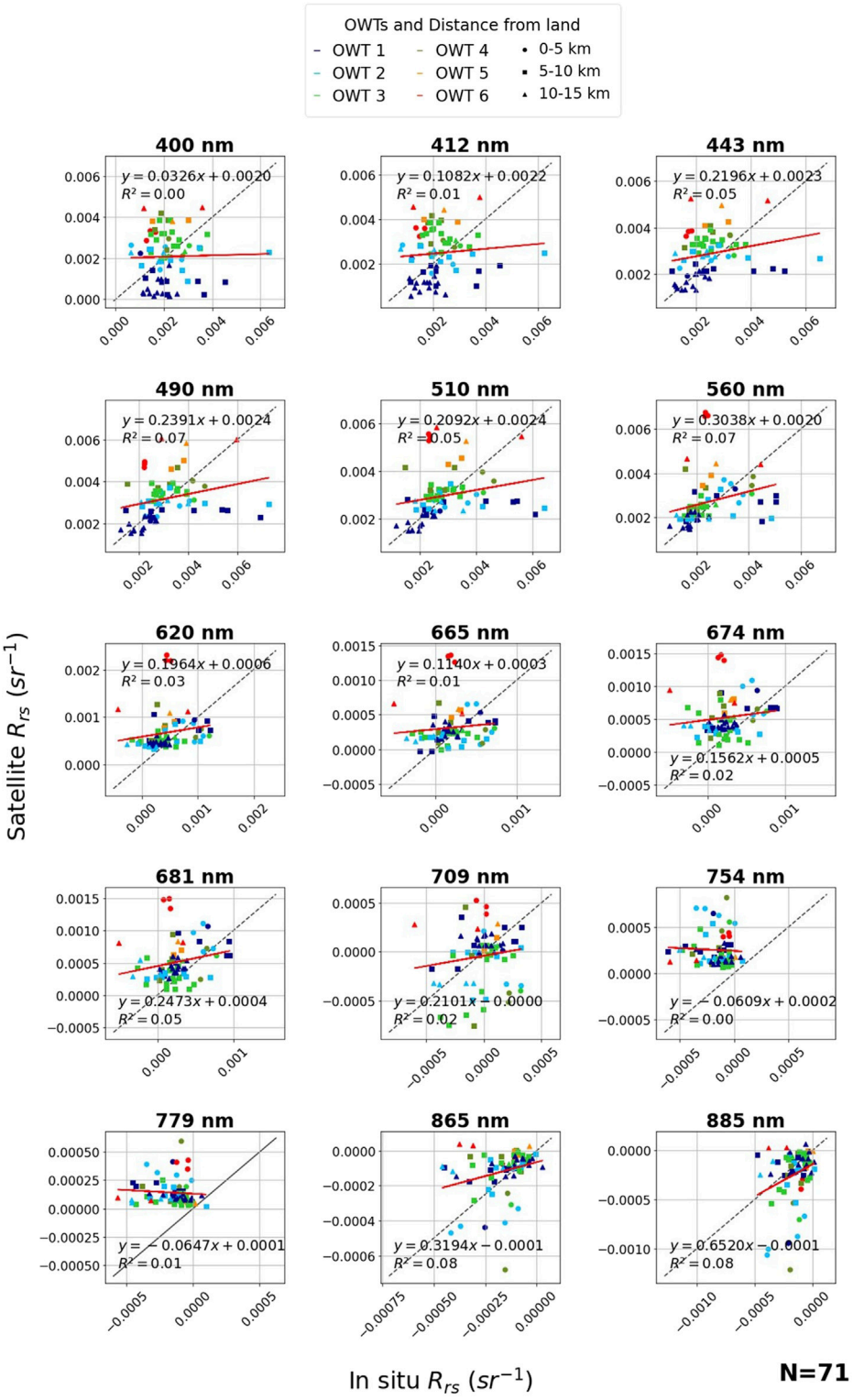


FIGURE 4
Per-band scatter plots. The dotted line represents the 1:1 ratio line. The red line represents the line of best fit between the satellite and *in situ* Rrs, with the regression equation and coefficient of determination (R^2) noted in the plot. Details of the respective optical water types (OWTs) and distance to land have been included. Temporal window of 30 min and spatial window of 1 × 1 pixel (300 × 300 m).

windows. The respective performance metrics were calculated across the spectrum and for each spectral band, and further displayed in Figure 3.

The spectral distribution in the RMSD was similar across data from all matchup selection routines with a peak at 490 nm with an overall decrease with a smaller temporal and spatial window, going

10.3389/frsen.2024.1359709

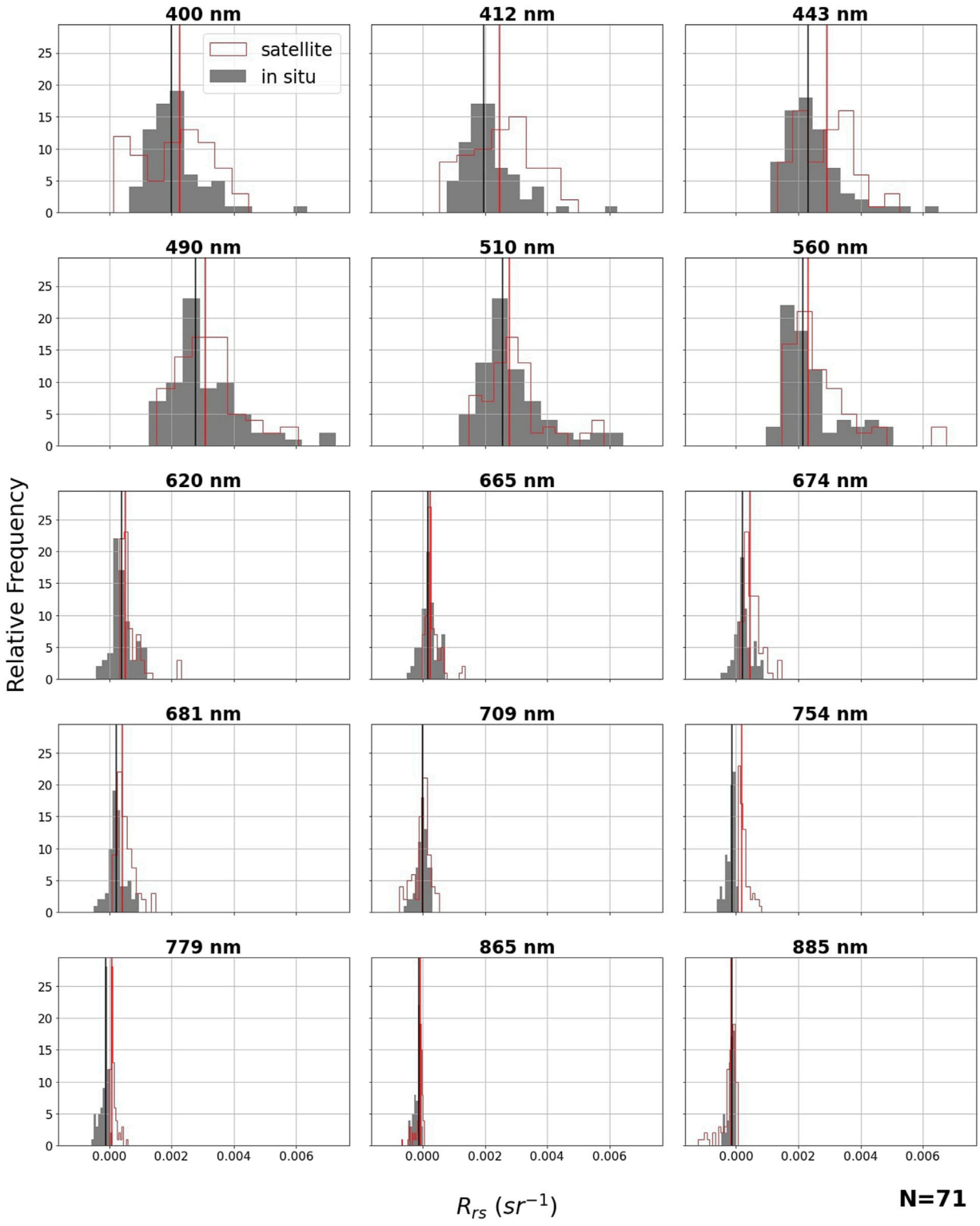


FIGURE 5
Relative frequency distribution of Rrs of the *in situ* data (grey bars) compared with Sentinel-3 OLCI data (red outline bars). Asterisks refer to statistically significant differences between the datasets (Mann-Whitney test, N = 71, $p < 0.01$). Median for each distribution is indicated by the solid line, grey for the *in situ* dataset, red for the satellite dataset. Temporal window of 30 min and spatial window of 1 × 1 pixel (300 × 300 m).

from 0.0021 sr^{-1} with a ±3 h and 3 × 3 pixel window to 0.0013 sr^{-1} with a ±30 min and 1 × 1 pixel window (Figure 3A). Similarly, the spectral distribution of the MdAPD was consistent across all data with a higher median value of 64% for the matchup data selected within a 3-h window (Figure 3B). On the other hand, the highest median MdPD value could be observed for the most stringent

TABLE 3 Performance metrics over the electromagnetic spectrum: Root Mean Square Difference (RMSD), Median Absolute Percentage Difference (MdAPD), Median Percentage Difference (MdPD).

(nm)	RMSD (sr^{-1})	MdAPD (%)	MdPD (%)
400	1.50×10^{-3}	42.72	−3.87
412	1.36×10^{-3}	43.05	15.15
443	1.22×10^{-3}	23.58	15.09
490	1.33×10^{-3}	20.12	2.72
510	1.30×10^{-3}	17.62	2.59
560	1.30×10^{-3}	18.68	10.03
620	5.36×10^{-4}	50.17	37.08
665	3.70×10^{-4}	69.16	39.28
674	4.63×10^{-4}	60.26	53.99
681	4.47×10^{-4}	58.4	20.91
709	3.22×10^{-4}	118.3	73.76
754	4.83×10^{-4}	161.1	161.1
779	3.44×10^{-4}	204.3	200.9
865	1.51×10^{-4}	60.48	−16.04
885	2.74×10^{-4}	70.72	30.43

dataset (±30 min 1 × 1 pixel selection window) with a peak of 200% depicted at 779 nm (Figure 3C).

3.2 Discrepancies between satellite and *in situ* data for the dataset as a whole

Next, the most stringent matchup selection criteria (±30 min and 1 pixel) were delved into further. Overall, when comparing the satellite reflectance estimates with *in situ* measurements, small differences were observed, yet a positive bias could be seen over most of the spectral range. To illustrate any discrepancies between satellite and *in situ* R_{rs} for the whole matchup dataset (N = 71), scatter plots and histograms for each of the S3-OLCI bands are shown in Figures 4, 5. The distribution of the data can further be observed in relation to optical water types and distance to land as depicted in Figure 4. Performance metrics were then calculated for each spectral band (Table 3; Figure 6).

In general, there was a large scatter across the wavelengths, but a positive slope of the regression between satellite and *in situ* R_{rs} can be seen for all wavelengths but 754 nm and 779 nm (Figure 4). A positive bias of the satellite estimates can be observed in relation to *in situ* measurements for most wavelengths, except in the range from 490 to 560 nm, Figure 4. It is, however, essential to notice that the R^2 values depicted are very small (≤0.08, Figure 4). It is also worth noticing, that when looking at the distribution of the data points in relation to optical water types, measurements in waters dominated by OWT 6 were particularly out of range (Figure 4).

As the range of observations is limited, another way to visualise the data is by means of histograms. The histograms show a maximum range of 0.007 sr^{-1} at 490 nm (Figure 5). Figure 5 shows the non-normal distribution of R_{rs} at most wavebands (Shapiro-Wilk normality test, $p < 0.05$, N = 71) except 412 nm (W = 0.98, $p = 0.25$) and 443 nm (W = 0.97, $p = 0.11$) in the satellite dataset and 665 nm (W = 0.98, $p = 0.21$) and 674 nm (W = 0.97, $p = 0.08$) in the *in situ* dataset. The data also showed overall positive skewness, particularly for the satellite dataset where outliers were present in three of the bands, namely, 560, 620 and 665 nm.

Testing for the differences between performance metrics, statistically, we found that significant differences between the median R_{rs} were shown for some of the bands (Mann-Whitney test, $p < 0.05$, N = 71) where there was a general shift towards higher reflectance values in the satellite dataset as suggested by the bias metric (Figure 6). This was clear at 674 nm, 681 nm, 754 nm and 779 nm where the median satellite reflectance values were at least double the *in situ* measurements (e.g., Median $R_{rs_\ satellite}$ (674) = 4.57×10^{-4} sr^{-1} vs. Median $R_{rs_\ in\ situ}$ (674) = 2.10×10^{-4} sr^{-1}).

When comparing the satellite with the *in situ* measured reflectance, we used a set of metrics commonly used in the field. RMSD (a measure of accuracy) increased from 0.0001 to 0.001 sr^{-1} from the red to the blue parts of the spectrum (Figure 6A), which is small compared to the range in R_{rs} in the blue (i.e. 0.001 sr^{-1} at 490 nm; Table 3). Conversely, the MdAPD (a measure of dispersion), was lower in the green (~30%) than in the red bands (MdAPD(779) = 204%; Table 3). This was similar to strongly negative bias at 400 nm (MdPD (400) = −4%) and 865 nm (MdPD(865) = −16%; Table 3). The rest of the wavelengths exhibited a positive bias ranging between 2.59% and 201% (Table 3). A gradual increase was observed between 510 nm and 779 nm, both in the dispersion and the bias metrics (Figures 6B, C).

Overall, this validation exercise at relatively low reflectance values in coastal waters depicted that full resolution OLCI R_{rs} using POLYMER produced lower accuracy and higher dispersion at shorter wavelengths than at higher wavelengths compared to underway above water R_{rs}. To try to disentangle the causes affecting this performance, the matchup datasets were then separated in terms of optical water types and distance to the coast.

3.3 Discrepancies between satellite and *in situ* data for the dataset segregated by optical water types

3.3.1 Spatial distribution of optical water types

Membership values to the optical water type clusters for the matchup R_{rs} spectra were calculated and spectra grouped by dominant optical water type are shown in Figure 7. All OWTs in the study area depict a peak in reflectance between 490 nm and 560 nm (Figure 7). Both OWT 1 and OWT two show a peak in R_{rs} at 490 nm (R_{rs} (490) = 0.007 sr^{-1}; Figure 7). A seemingly good accordance between the *in situ* and satellite datasets can be seen for OWT 2, whilst a more defined peak can be seen in the *in situ* dataset for OWT 1. A peak in R_{rs} between 490 nm and 560 nm can be seen, once again, for OWTs 3 and 4 with, however, a smaller range of reflectances with a maximum value of 0.004–0.005 sr^{-1} at 490 nm (Figure 7). Despite the lack of matchup data for OWT 5, a clear peak can be observed at 490 nm whilst a defined peak at 560 nm is present for OWT 6 (Figure 7).

From the matchup dataset, the dominant OWTs found in each zone of the study area were the following: OWT 2 in 0–5 km, OWT 3 in 5–10 km and OWT 1 in 10–15 km, representing 36%, 42% and

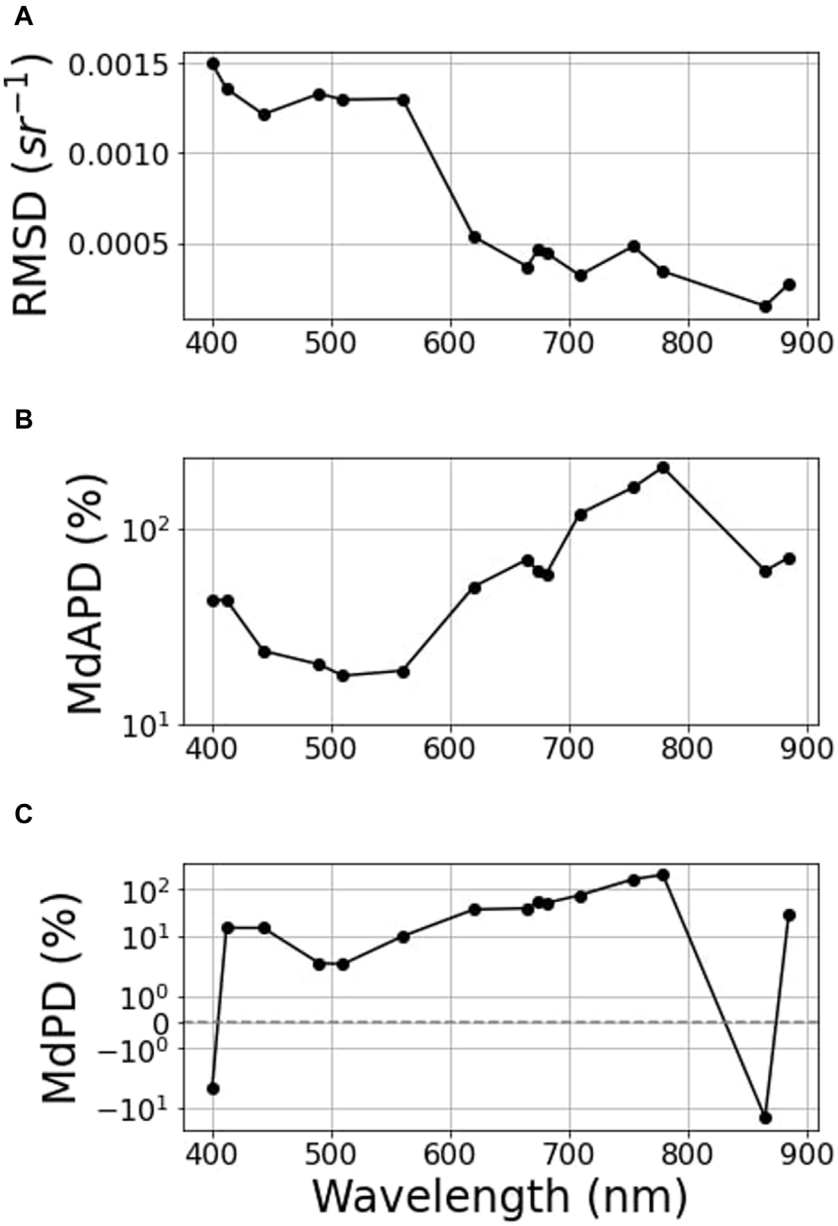


FIGURE 6
Performance metrics for different wavelengths: **(A)** Root Mean Square Difference (RMSD), **(B)** Median Absolute Percentage Difference (MdAPD), **(C)** Median Percentage Difference (MdPD). The plots of MdAPD and MdPD are shown on a log scale. Number of matchups (N) N = 71.

64% of the data, respectively (Figure 8). It is also worth noticing the presence of OWTs 1 and 2 in nearshore waters (0–5 km) corresponding to two distinct days: 6th July 2017 and 26th June 2018, respectively. OWTs 5 and 6, on the other hand, were found in more offshore waters (10–15 km) corresponding to data collected on 5th April 2017 (Figure 8).

3.3.2 Performance metrics: dataset segregated by optical water types

The discrepancy metrics between satellite and field measurements of R_{rs} were investigated separating the matchups by optical water types (OWT). Although no statistically significant difference was found among the groups (PERMANOVA, F5 = 0.845, $R^2 = 0.063$, $p = 0.388$), separation by the distinct OWTs was observed. Performance metrics were calculated for subsets of the matchup dataset averaged across all wavelengths (Figure 9) and on a per-wavelength basis (Figure 10). Concerning the satellite vs. *in situ* matchup metrics grouped by optical water types, the RMSD metric indicated higher uncertainty in the OWT 6 subset with a mean value of 0.0014 sr^{-1}, double the RMSD for the rest of the OWTs found in the study area (Figure 9A). Spectrally, RMSD peaked at 560 nm with a value of 0.004 sr^{-1} (Figure 10A). The measure of dispersion per optical water type, the median MdAPD metric, was high, ranging between 60% and 91% (for OWTs 3 and 4, respectively; Figure 9B). Spectrally, peaks were present for

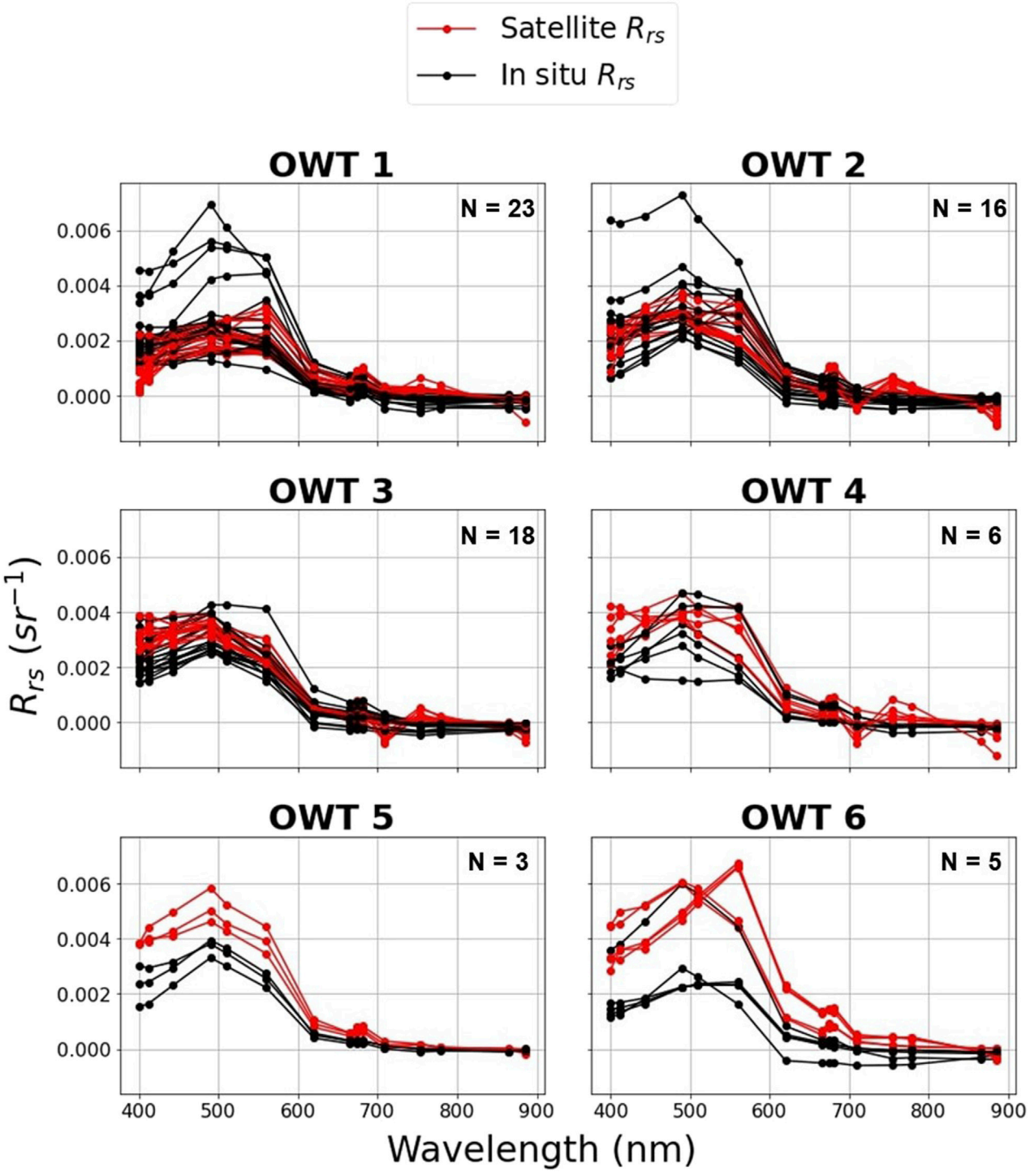


FIGURE 7
The reflectance (Rrs) spectra of the six optical water types represented in the selected transitional waters of Plymouth, Southwest, United Kingdom. Both satellite (red) and *in situ* spectra are displayed.

OWTs 1-3 with a main peak at 400 nm (MdAPD = 289%) for OWT 1 followed by a second peak at 779 nm (MdAPD = 186–241%) for OWTs 1–3 (Figure 10B). OWTs 4-6 depicted a generally higher MdAPD at longer wavelengths (665–885 nm) with a peak at 865 nm (Figure 10B). Concerning the measure of bias, the MdPD metric was on average positive, ranging between 11 and 74 with a general increase from OWTs 1 towards 6 (Figure 9C). Yet, the comparison of the satellite reflectance estimates with *in situ* measurements revealed negative bias (negative MdPD) between 400 and 560 nm for OWT 1, only at 400 nm for OWT 2, and at 865 nm for OWTs 1, three and 6 (Figure 10C).

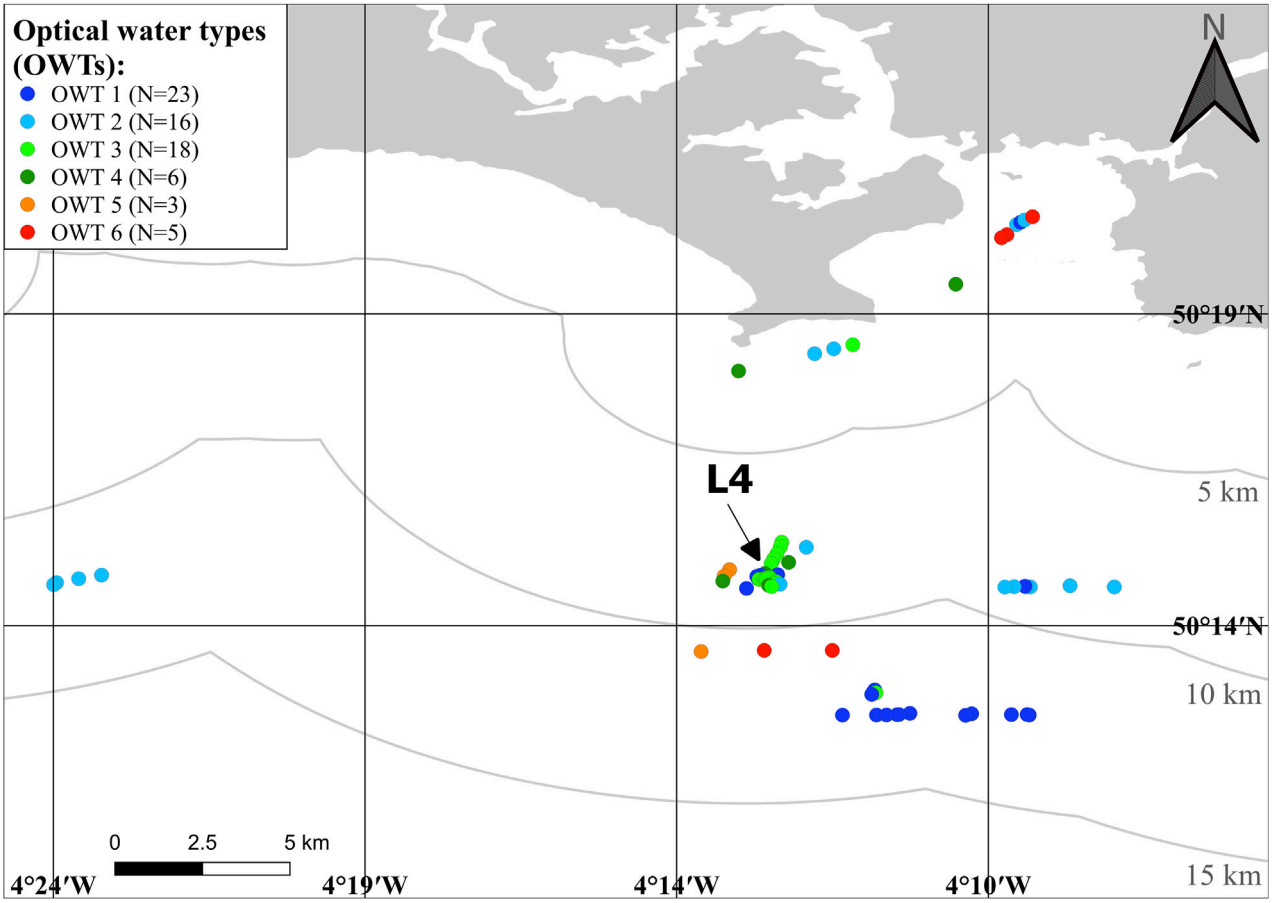


FIGURE 8
Location of the matchup data points from the study area with the colour scheme representing the respective optical water types (OWTs). Contour lines represent successive distance from shore (5 km, 10 km and 15 km). Location of the Western Channel Observatory station L4 is among the dots and marked with an arrow for clarity.

Overall, the dispersion measures were similar across the optical water types in this study, with the two extremes (clearest waters from OWT 1 and more turbid waters of OWT 6) being well defined spectrally. Negative bias appeared at the shorter parts of the spectrum in OWT 1, while lower accuracy (higher RMSD) was more evident in middle parts of the spectrum. On the other hand, OWTs two to 4 seemed to have similar performance statistics.

3.4 Discrepancies between satellite and *in situ* data for the dataset segregated by distance to land

The discrepancy metrics between satellite and field measurements of R_{rs} were investigated separating the matchups by their distance to land. Despite no statistically significant relationship (PERMANOVA, F2 = −0.049, R^2 = −0.001, p = 0.969), the influence of varying distance from land on discrepancies was observed and summarised through performance metrics (Figure 11).

The RMSD metric had a higher mean value for measurements in the nearshore waters (RMSD = 0.001 sr^{-1} for 0–5 km to land) compared to more offshore waters (RMSD = 0.0006 sr^{-1} for 10–15 km to land; Figure 11A). A clear peak was associated with the 560 nm for the 0–5 km to land group (RMSD (560) = 0.002 sr^{-1}; Figure 11D) coinciding with the peak observed in OWT 6 (Figure 10A). From the location of the matchups (Figure 8), OWT 6 appeared both within the <5 km to land and 10–15 km to land regions. The averaged MdAPD (dispersion) was similar for the three groups, and varied between 64% and 72% across all wavelengths (Figure 11B), with a peak at the 709 nm for waters <5 km to land (MdAPD(709) = 142%) and at 779 nm for the two groups further offshore (MdAPD(779) = 210–221%; Figure 11E). Spectrally, the minimum for this metric was found at 443 nm for 0–5 km (MdAPD(443) = 15%), at 510 nm for 5–10 km (MdAPD(510) = 18%) and at 560 nm for 10–15 km (MdAPD(560) = 12%; Figure 11E). The MdPD metric (Bias) was overall positive (MdPD = 35–46%). This indicates a positive bias of satellite estimates in relation to in situ observations across all distance partitions considered (Figure 11C). When looking at the spectral variation of this metric, however, matchups at 5–10 km from the shore were the only ones revealing a positive bias of the satellite derived reflectance (Figure 11F). At other distances (0–5 km and 10–15 km), bias was variable and sometimes negative.

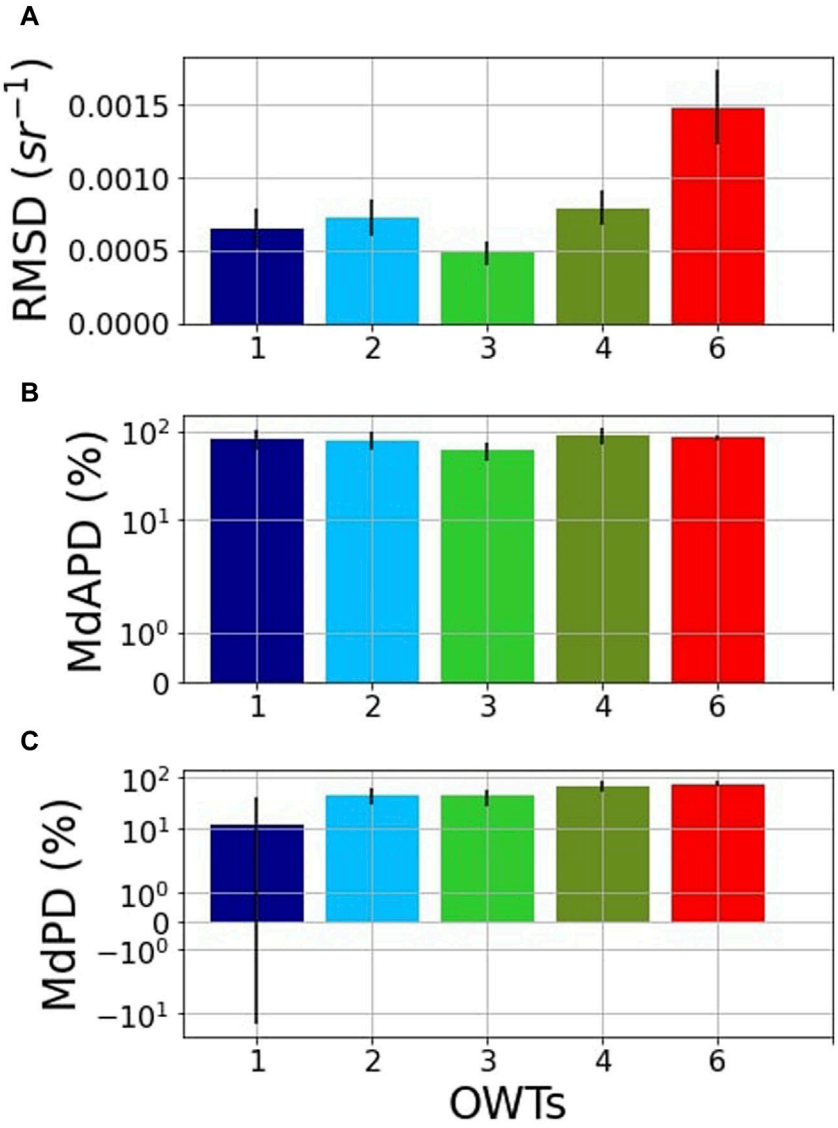


FIGURE 9
Spectrally averaged performance metrics per optical water types (OWTs). **(A)** Root Mean Square Difference (RMSD), **(B)** Median Absolute Percentage Difference (MdAPD), **(C)** Median Percentage Difference (MdPD). The plots of MdAPD and MdPD are shown on a log scale. OWT 1 N = 23, OWT 2 N = 16, OWT 3 N = 18, OWT 4 N = 6, OWT 6 N = 5. Error bars are the standard deviation.

4 Discussion

4.1 Performance compared to other studies for OLCI full resolution in coastal waters

Previous studies assessing the performance of atmospheric correction processors have highlighted that disparities in results between study areas arise from differences in reflectance ranges, in part due to varying degrees of turbidity (Vanhellemont and Ruddick, 2021).

The coastal areas assessed in the present study can be classed as moderately turbid, with total suspended matter concentrations between 1 and 10 g/m^3 (Martinez-Vicente et al., 2010). These turbidity conditions differ substantially from those of recent studies (Mograne et al., 2019; Alikas et al., 2020; Giannini et al., 2021), which included moderately turbid to very turbid water bodies with reflectance values 10 times greater in magnitude (0.02–0.05 sr^{-1}) than the values observed in the present study (0.003 sr^{-1}, Figure 4). The study area, characterised by a narrow range of relatively low reflectances (Figure 4), revealed a positive bias of satellite estimates in relation to *in situ* observations. Although the present observations are low in magnitude, they are in line with previous measurements in the area (Martinez-Vicente et al., 2013; Jordan et al., 2023). They align with the lower end of values recorded in coastal waters by Giannini et al. (2021) (at 443 nm they report *in situ* R_{rs} less than 0.005 sr^{-1}). They are also similar to more offshore waters in the Canadian coast (Vishnu and Costa, 2023).

When comparing the performance metrics for the whole dataset of this study to other studies, similarities arise with regards to the wavelength dependency. The dispersion and bias metrics indicated higher dispersion and bias at the edges of the spectral band range (<490 nm and >674 nm) with a peak in the red region (Figure 6C).

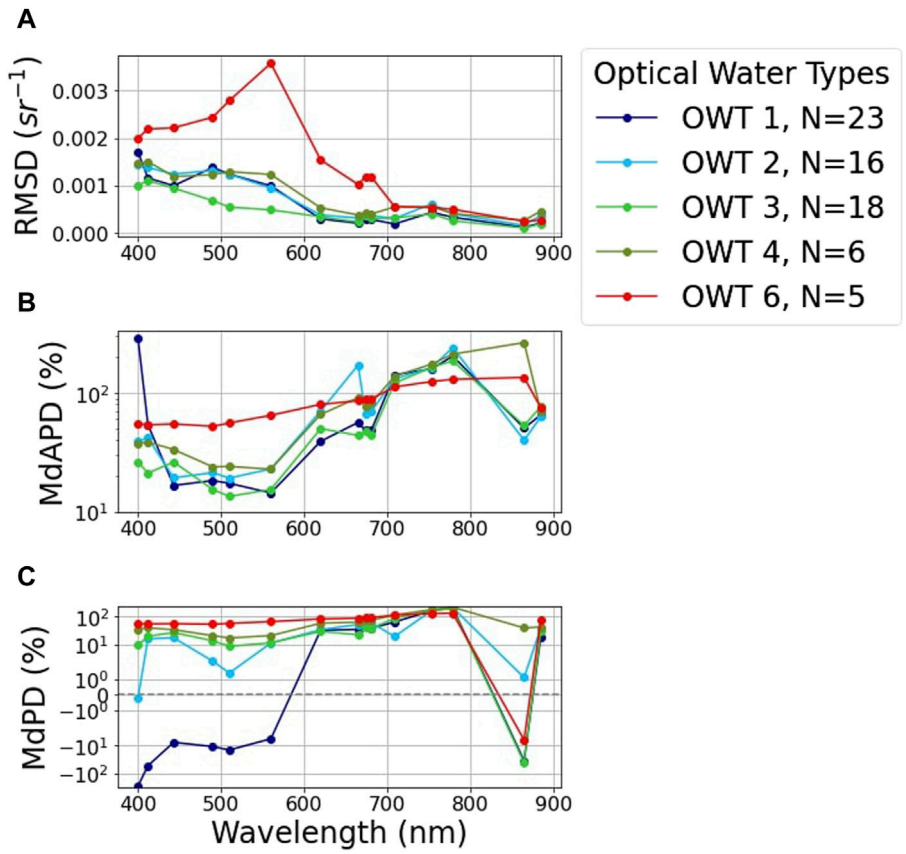


FIGURE 10
Spectrally resolved performance metrics for optical water types (OWTs). **(A)** Root Mean Square Difference (RMSD), **(B)** Median Absolute Percentage Difference (MdAPD), **(C)** Median Percentage Difference (MdPD). The plots of MdAPD and MdPD are shown on a log scale.

The spectral differences in the dispersion and bias metrics are consistent with the metrics obtained by selecting different spatial or temporal windows explored in this study (Figures 3B, C). Lower performance at 400 nm and 865 nm may result from the low R_{rs} signal, given that there is a relationship between the dispersion metric and the intensity of the signal (Vanhellemont and Ruddick, 2021), and less likely to come from high absorption and backscattering by optically active constituents (Mograne et al., 2019). Larger uncertainties at shorter wavelengths could also be attributed to difficulties with aerosol correction (Soppa et al., 2021). Larger uncertainties at longer wavelengths, however, may instead be attributed to the small R_{rs} signal from increasing water absorption (Soppa et al., 2021). The positive bias of the satellite derived R_{rs} at 865 nm in relation to the *in situ* observations (Figure 6C) was also indicated by the MPD (Mean Percentage Difference) metric in Alikas et al. (2020) despite larger bias being observed ($MdPD_{present}$ = −16%, MPD_{Alikas} = −50%).

Conversely, the RMSD metric suggested lower accuracy at shorter wavelengths than other studies (Figure 6A; Mograne et al., 2019; Vanhellemont and Ruddick, 2021). Also, the RMSD depicted strong differences with changes in the spatial and temporal matchup windows (Figure 3). An increase in RMSD (decrease in accuracy) was observed, mainly, at shorter wavelengths (<600 nm) between the strictest matchup selection routine (30 min and 1 × 1 pixel) and the most relaxed one (3 h and 3 × 3 pixels). Different causes have been proposed in the literature. Giannini et al. (2021) raise the fact that POLYMER does not consider the CDOM contribution to the optical signal adequately, leading to uncertainties in shorter wavelengths. This is particularly important in regions where the optical signal is significantly affected by CDOM absorption, e.g., British Columbia a_{CDOM} (440) 0.23–4.91 m^{-1} (Giannini et al., 2021). The more offshore part of our study area is not affected by high CDOM, with a_{CDOM}(440) 0.05–0.20 m^{-1} levels around L4 station (10–15 km from shore, Groom et al., 2009). Higher concentrations of CDOM are, however, expected in nearshore waters that could result in error in the shorter wavelengths. Warren et al. (2019) point out that the curve follows the wavelength dependency of the aerosol optical thickness with particular difficulty in removing aerosol contributions in shorter wavelengths, specifically at 443 nm (Pahlevan et al., 2021). Vanhellemont and Ruddick (2021) propose the under correction of the increasing atmospheric path reflectance between the NIR and the UV to be a potential cause.

Disparity between the present results and other studies can also be explained by the differences in the matchup selection criteria and in the data processing chain, including atmospheric correction methods and *in situ* data filtering. Not only have previous studies assessed more turbid types of coastal waters, different matchup selection routines and data filtering

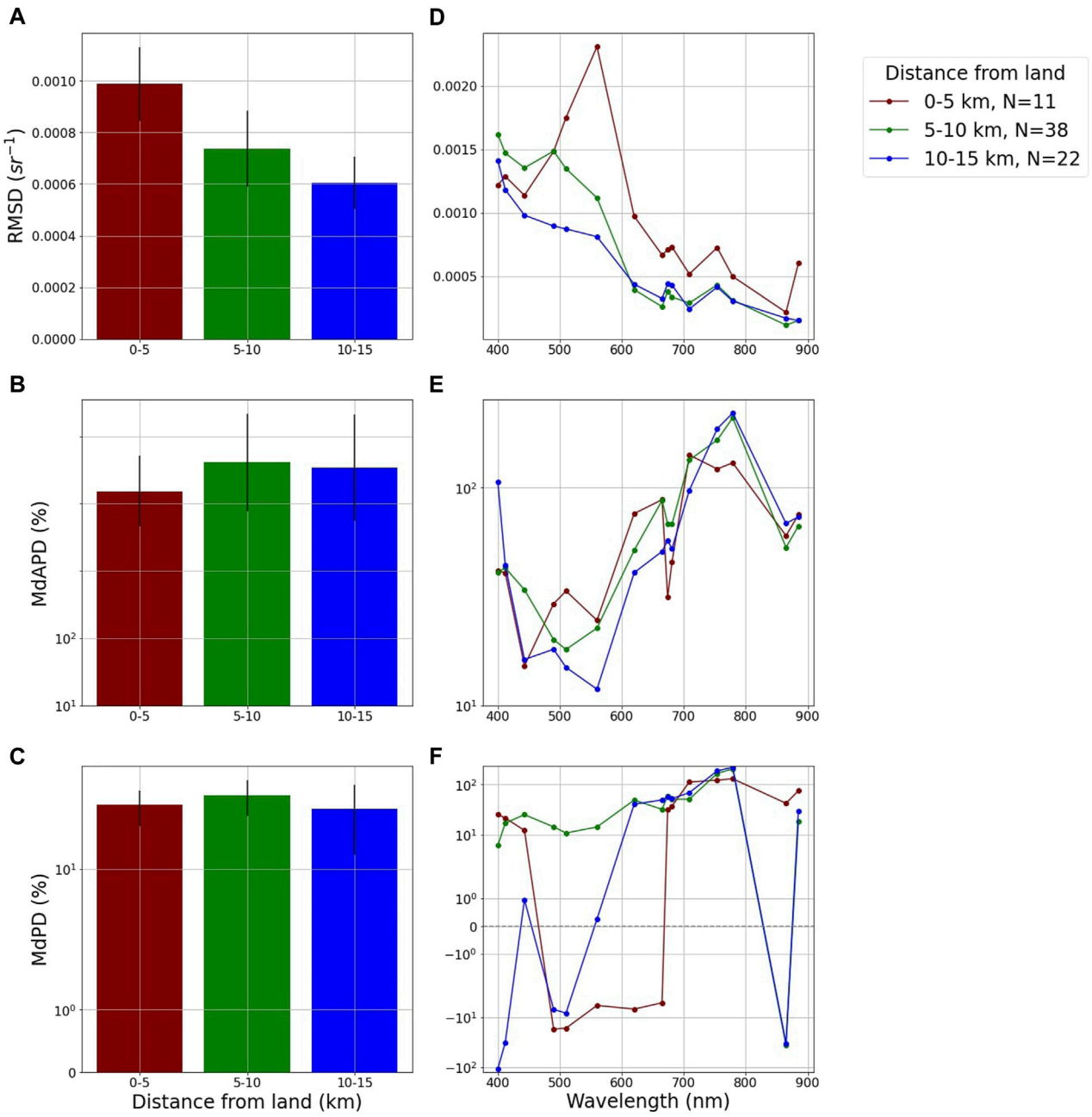


FIGURE 11
Spectrally averaged performance metrics with the distance from land and spectrally resolved. Averaged performance metrics in sub-figures **(A–C)**. Per wavelength performance metrics in sub-figures **(D–F)**. Root Mean Square Difference (RMSD), Median Absolute Percentage Difference (MdAPD), Median Percentage Difference (MdPD).

procedures have been used resulting in possible mismatch between satellite and field measurements. In this study we have selected the matchups very strictly (30 min difference between satellite and *in situ* observations), however for sun-synchronous satellites such as MERIS or Sentinel-3 OLCI, tidal dynamics are a known cause of bias in ocean colour products, for instance TSM concentrations in estuaries (Eleveld et al., 2014). Appropriate matchup selection criteria are therefore critical according to the spatiotemporal variability of the study area (Concha et al., 2021). It is also worth pointing out that the present study and previous studies cited have used different methods of atmospheric correction, with various versions of POLYMER used as well as different flags or correction methods to target bidirectional effects (Table 4).

Whilst both matchup selection and quality control are crucial for high quality data to support satellite ocean colour validation activities (IOCCG, 2019), strict criteria cause a large proportion of the acquired data to be discarded. Particular attention should be given to the sampling strategy and the validation protocol to obtain high quality ground measurements for accurate measures of

TABLE 4 Summary of atmospheric correction steps used in the present study compared to past research. BRDF = Bidirectional Reflectance Distribution Function.

Reference	POLYMER version	Data flags	BRDF correction
This study, 2024	v4.15	IDEPIX masking	Correction using Park and Ruddick (2005)
Alikas et al. (2020)	v4.10	POLYMER internal masking: Bitmask	None
Giannini et al. (2021)	v4.9	POLYMER internal masking	Correction using Park and Ruddick (2005)
Mograne et al. (2019)	v4.10	Negative back-scattering coefficient, out of bounds, exception, thick aerosol, high air mass, and inconsistency flags	None
Vanhellemont and Ruddick (2021)	v4.13	POLYMER internal masking: Bitmask, Case 2 waters flags, Inconsistency flags	None

performance. Users should follow accepted protocols (IOCCG, 2019; EUMETSAT, 2021).

4.2 Effects of optical water types and land adjacency on the results

Few sources in the literature describe the performance of atmospheric correction models while considering optical water types or distance from land (as proxy for adjacency effects) as potential contamination factors (Pereira-Sandoval et al., 2019; Warren et al., 2019; Pahlevan et al., 2021; Hieronymi et al., 2023).

When considering nearshore waters (0–5 km from land), the large RMSD values were present at the 560 nm band and could be a result of either nearshore enhanced TSM scattering (OWT 6) and/or adjacency from neighbouring land (Groom et al., 2009). The latter was suggested by Warren et al. (2019) when assessing the performance of atmospheric correction models for the Sentinel-2 MSI data. In their study, the RMSD at 560 nm increased by 25%–55% between the coastal and inland matchup datasets. With distance from land ranging between 0.2 and 1.2 km, this was associated with the contribution of land adjacency to the atmospheric path reflectance. The under correction of the land adjacency effect could explain the positive bias of the satellite derived reflectance in such waters. This is supported by the decreasing tendency observed in RMSD with increasing distance to land. When considering the RMSD metric, the results of the current study therefore point to the adjacency effect from neighbouring land as being a potential issue for Sentinel-3 OLCI data up to approximately 5 km from land. The dispersion (MdAPD) and bias (MdPD) metrics do, however, not show similar tendencies. This could be the result of other factors such as environmental conditions at the time of sampling such as aerosol optical depth, Sun and observation geometry. Increased efforts in the *in situ* R_{rs} sampling collocated with aerosol optical properties measurements within that distance to the shoreline would help to reduce uncertainties and improve confidence on Sentinel-3 OLCI to increase its use in water quality monitoring applications. Concerning the relationship between OWT and performance statistics, the accuracy (RMSD) and the dispersion (MdPD) measures provide the worse results, pointing to worse R_{rs} retrievals in more optically complex waters. This points to an application of OWT to flag coastal areas where satellite retrievals should be used with caution.

Finally, several limitations could be attributed to this analysis, in particular related to *in situ* data collection and analysis of radiometric data from unsupervised equipment. Non-ship superstructure, uncertainties associated with instruments and possible environmental conditions affect all measurements collected in this manner and have been discussed in specifically designed intercomparisons (e.g., Tilstone et al., 2020). In addition, some variations could come from the processing approach, which has been discussed extensively elsewhere (Groetsch et al., 2017). Ideally, optical instruments should be collected in tandem to provide closure, however, this is not always possible in the context of satellite validation from opportunistic, unsupervised platforms, which, in contrast, provide large amounts of data with the possibility to filter them. Progress could be made in the direction of improving the automatic orientation of the platform. In this way, data would be collected in the best conditions.

5 Conclusion

The present study assessed the performance of the POLYMER atmospheric correction processor for data from the Ocean and Land Colour Instrument (OLCI) onboard Sentinel-3. The focus was on the coastal regions of Plymouth Sound and the Western English Channel, dynamic ecosystems characterised by a complex geomorphology and influenced by tides. The validation activity carried out used high spatial resolution hyperspectral R_{rs} *in situ* data allowing convolution over the spectral response function of OLCI to emulate satellite data. These *in situ* data were strictly filtered and matched very closely to satellite data (to within 30 min and 300 m). The performance of POLYMER was evaluated by grouping matchup datasets according to optical water types and varying distance offshore.

The study demonstrated positive bias of the satellite R_{rs} estimates in relation to the *in situ* measurements collated in these relatively clear coastal waters, especially pronounced in nearshore more turbid regions. Considering that the *in situ* data can also have large uncertainties, and for the Near-Infrared (NIR) bands often have negative reflectance, we cannot state that this bias corresponds

purely to an error in the satellite measurement. Issues related to aerosol correction by POLYMER have, however, been proposed as well as potential errors related to the adjacency of land and the low level of signal coming out of the water in nearshore regions.

Differences in the performance of POLYMER were observed across optical water types. Notably, poorer performance was observed in waters classified as OWT 6. Future sampling efforts in field campaigns should target optically active constituents to better characterise water types, specifically for OWT 6 and within 5 km of the shoreline to improve characterisation of uncertainties in those areas and improvement of products usability. These should be organised as close as possible to the satellite overpass to increase the size of the matchup dataset whilst considering the regional variability (tides, river flushing times, *etc.*) to limit spatial and temporal mismatch.

Data availability statement

The datasets presented in this study can be found in online repositories available at: https://github.com/ggleratti/datasets_insitu_S3_validation.git.

Author contributions

GG: Conceptualization, Formal Analysis, Investigation, Software, Visualization, Writing–original draft, Writing–review and editing. VM-V: Conceptualization, Formal Analysis, Investigation, Methodology, Project administration, Resources, Supervision, Validation, Writing–review and editing. EA: Methodology, Resources, Investigation, Writing–review and editing. SS: Data curation, Methodology, Resources, Writing–review and editing. TJ: Methodology, Resources, Writing–review and editing, Data curation.

Funding

The author(s) declare that financial support was received for the research, authorship, and/or publication of this article. This work has been supported by the CERTO project (Copernicus Evolution–Research for harmonised and Transitional water Observation) that has received funding from the European Union's Horizon 2020 research and innovation programme under grant agreement No. 870349 and by the European Space Agency (ESA) FutureEO-1 Biodiversity + precursors Bicome project: Biodiversity of the coastal ocean: Monitoring with Earth Observation, grant number 4000135756/21/I-EF. EA was partially funded by NERC through its Earth Observation Data Acquisition and Analysis Service (NEODAAS). The publication of this research was funded by the United Kingdom Natural Environment Research Council (NERC) through its National Capability Long-term Single Centre Science Programme, Climate Linked Atlantic Sector Science, grant number NE/R015953/1, contributing to 4—Fixed Point Observations (Western Channel Observatory).

Acknowledgments

We thank the staff at the Plymouth Marine Laboratory who participated in the *in situ* data sampling.

Conflict of interest

Author GG is now employed at A-2-Sea Solutions Ltd.

The remaining authors declare that the research was conducted in the absence of any commercial or financial relationships that could be construed as a potential conflict of interest.

Publisher's note

All claims expressed in this article are solely those of the authors and do not necessarily represent those of their affiliated organizations, or those of the publisher, the editors and the reviewers. Any product that may be evaluated in this article, or claim that may be made by its manufacturer, is not guaranteed or endorsed by the publisher.

Supplementary material

The Supplementary Material for this article can be found online at: https://www.frontiersin.org/articles/10.3389/frsen.2024.1359709/full#supplementary-material

References

Alikas, K., Ansko, I., Vabson, V., Ansper, A., Kangro, K., Uudeberg, K., et al. (2020). Consistency of radiometric satellite data over lakes and coastal waters with local field measurements. *Remote Sens.* 12, 616. doi:10.3390/rs12040616

Arena, M., Pratolongo, P., Loisel, H., Tran, M. D., Jorge, D. S. F., and Delgado, A. L. (2024). Optical water characterization and atmospheric correction assessment of estuarine and coastal waters around the AERONET-OC Bahia Blanca. *Front. Remote Sens.* 5, 1305787. doi:10.3389/frsen.2024.1305787

Bailey, S. W., and Werdell, P. J. (2006). A multi-sensor approach for the on-orbit validation of ocean color satellite data products. *Remote Sens. Environment* 102 (1-2), 12–23. doi:10.1016/j.rse.2006.01.015

Brewin, R. J. W., Dall'Olmo, G., Pardo, S., van Dongen-Vogels, V., and Boss, E. S. (2016). Underway spectrophotometry along the Atlantic Meridional Transect reveals high performance in satellite chlorophyll retrievals. *Remote Sens. Environ.* 183, 82–97. doi:10.1016/j.rse.2016.05.005

Bulgarelli, B., Kiselev, V., and Zibordi, G. (2014). Simulation and analysis of adjacency effects in coastal waters: a case study. *Appl. Opt.* 53, 1523–1545. doi:10.1364/AO.53.001523

Bulgarelli, B., and Zibordi, G. (2018). On the detectability of adjacency effects in ocean color remote sensing of mid-latitude coastal environments by SeaWiFS, MODIS-A, MERIS, OLCI, OLI and MSI. *Remote Sens. Environ.* 209, 423–438. doi:10.1016/j.rse.2017.12.021

Concha, J. A., Bracaglia, M., and Brando, V. E. (2021). Assessing the influence of different validation protocols on Ocean Colour match-up analyses. *Remote Sens. Environ.* 259, 112415. doi:10.1016/j.rse.2021.112415

Doxaran, D., Cherukuru, N., and Lavender, S. J. (2006). Apparent and inherent optical properties of turbid estuarine waters: measurements, empirical quantification relationships, and modeling. *Appl. Opt.* 45, 15. doi:10.1364/AO.45.002310

Eleveld, M. A., van der Wal, D., and van Kessel, T. (2014). Estuarine suspended particulate matter concentrations from sun-synchronous satellite remote sensing: tidal and meteorological effects and biases. *Remote Sens. Environ.* 143, 204–215. doi:10.1016/j.rse.2013.12.019

EUMETSAT (2021). *Recommendations for Sentinel-3 OLCI Ocean Colour product validations in comparison with* in situ *measurements*.

Giannini, F., Hunt, B. P. V., Jacoby, D., and Costa, M. (2021). Performance of OLCI sentinel-3A satellite in the northeast pacific coastal waters. *Remote Sens. Environ.* 256, 112317. doi:10.1016/j.rse.2021.112317

Goyens, C., Jamet, C., and Schroeder, T. (2013). Evaluation of four atmospheric correction algorithms for MODIS-Aqua images over contrasted coastal waters. *Remote Sens. Environ.* 131, 63–75. doi:10.1016/j.rse.2012.12.006

Goyens, C., Lavigne, H., Dille, A., and Vervaeren, H. (2022). Using hyperspectral remote sensing to monitor water quality in drinking water reservoirs. *Remote Sens.* 14, 5607. doi:10.3390/rs14215607

Groetsch, P. M. M., Gege, P., Simis, S. G. H., Eleveld, M. A., and Peters, S. W. M. (2017). Validation of a spectral correction procedure for sun and sky reflections in above-water reflectance measurements. *Opt. Express. OE* 25, A742–A761. doi:10.1364/OE.25.00A742

Groom, S., Martinez-Vicente, V., Fishwick, J., Tilstone, G., Moore, G., Smyth, T., et al. (2009). The western English Channel observatory: optical characteristics of station L4. *J. Mar. Syst.* 77, 278–295. doi:10.1016/j.jmarsys.2007.12.015

Hieronymi, M., Bi, S., Müller, D., Schütt, E. M., Behr, D., Brockmann, C., et al. (2023). Ocean color atmospheric correction methods in view of usability for different optical water types. *Front. Mar. Sci.* 10. doi:10.3389/fmars.2023.1129876

Hieronymi, M., Müller, D., and Doerffer, R. (2017). The OLCI neural network swarm (ONNS): a bio-geo-optical algorithm for open ocean and coastal waters. *Front. Mar. Sci.* 4. doi:10.3389/fmars.2017.00140

IOCCG (2010). *Atmospheric correction for remotely-sensed ocean-colour products*. Dartmouth, Canada: IOCCG. Available at: https://www.ioccg.org/reports/report10.pdf (Accessed October 6, 2023).

IOCCG (2019). *Ocean optics and biogeochemistry protocols for satellite Ocean colour sensor validation, volume 3.0: protocols for satellite Ocean colour data validation:* in situ *optical Radiometry*. Dartmouth, Canada: IOCCG. doi:10.25607/OBP-691

Jackson, T., Sathyendranath, S., and Mélin, F. (2017). An improved optical classification scheme for the Ocean Colour Essential Climate Variable and its applications. *Remote Sens. Environ.* 203, 152–161. doi:10.1016/j.rse.2017.03.036

Jordan, T. M., Simis, S. G., Selmes, N., Sent, G., Ienna, F., and Martinez-Vicente, V. (2023). Spatial structure of *in situ* reflectance in coastal and inland waters: implications for satellite validation. *Front. Remote Sens.* 4. doi:10.3389/frsen.2023.1249521

Liu, H., He, X., Li, Q., Hu, X., Ishizaka, J., Kratzer, S., et al. (2021). Evaluation of ocean color atmospheric correction methods for Sentinel-3 OLCI using global automatic *in situ* observations. *IEEE Trans. Geoscience Remote Sens.* 60, 1–19. doi:10.1109/TGRS.2021.3136243

Martinez-Vicente, V., Land, P. E., Tilstone, G. H., Widdicombe, C., and Fishwick, J. R. (2010). Particulate scattering and backscattering related to water constituents and seasonal changes in the Western English Channel. *J. Plankton Res.* 32, 603–619. doi:10.1093/plankt/fbq013

Martinez-Vicente, V., Simis, S. G. H., Alegre, R., Land, P. E., and Groom, S. B. (2013). Above-water reflectance for the evaluation of adjacency effects in Earth observation data: initial results and methods comparison for near-coastal waters in the Western Channel, UK. *J. Eur. Opt. Soc. - Rapid Publ.* 8, 13060. doi:10.2971/jeos.2013.13060

Mélin, F., Sclep, G., Jackson, T., and Sathyendranath, S. (2016). Uncertainty estimates of remote sensing reflectance derived from comparison of ocean color satellite data sets. *Remote Sens. Environ.* 177, 107–124. doi:10.1016/j.rse.2016.02.014

Mélin, F., and Vantrepotte, V. (2015). How optically diverse is the coastal ocean? *Remote Sens. Environ.* 160, 235–251. doi:10.1016/j.rse.2015.01.023

Mograne, M. A., Jamet, C., Loisel, H., Vantrepotte, V., Mériaux, X., and Cauvin, A. (2019). Evaluation of five atmospheric correction algorithms over French optically-complex waters for the sentinel-3A OLCI ocean color sensor. *Remote Sens.* 11, 668. doi:10.3390/rs11060668

Moore, T. S., Campbell, J. W., and Feng, H. (2001). A fuzzy logic classification scheme for selecting and blending satellite ocean color algorithms. *IEEE Trans. Geosci. Remote Sens.* 39, 1764–1776. doi:10.1109/36.942555

Moore, T. S., Campbell, J. W., and Feng, H. (2015). Characterizing the uncertainties in spectral remote sensing reflectance for SeaWiFS and MODIS-Aqua based on global *in situ* matchup data sets. *Remote Sens. Environ.* 159, 14–27. doi:10.1016/j.rse.2014.11.025

Morel, A., and Prieur, L. (1977). Analysis of variations in ocean color 1. *Limnol. Oceanogr.* 22 (4), 709–722. doi:10.4319/lo.1977.22.4.0709

Nasiha, H. J., Wang, Z., Giannini, F., and Costa, M. (2022). Spatial variability of *in situ* above-water reflectance in coastal dynamic waters: implications for satellite match-up analysis. *Front. Remote Sens.* 3, 876748. doi:10.3389/frsen.2022.876748

Pahlevan, N., Mangin, A., Balasubramanian, S. V., Smith, B., Alikas, K., Arai, K., et al. (2021). ACIX-Aqua: a global assessment of atmospheric correction methods for Landsat-8 and Sentinel-2 over lakes, rivers, and coastal waters. *Remote Sens. Environ.* 258, 112366. doi:10.1016/j.rse.2021.112366

Park, Y. J., and Ruddick, K. (2005). Model of remote-sensing reflectance including bidirectional effects for case 1 and case 2 waters. *Appl. Opt.* 44 (7), 1236–1249. doi:10.1364/AO.44.001236

Pereira-Sandoval, M., Ruescas, A., Urrego, P., Ruiz-Verdú, A., Delegido, J., Tenjo, C., et al. (2019). Evaluation of atmospheric correction algorithms over Spanish inland waters for sentinel-2 multi spectral imagery data. *Remote Sens.* 11, 1469. doi:10.3390/rs11121469

Qin, P., Simis, S. G. H., and Tilstone, G. H. (2017). Radiometric validation of atmospheric correction for MERIS in the Baltic Sea based on continuous observations from ships and AERONET-OC. *Remote Sens. Environ.* 200, 263–280. doi:10.1016/j.rse.2017.08.024

Ruddick, K. G., Ovidio, F., and Rijkeboer, M. (2000). Atmospheric correction of SeaWiFS imagery for turbid coastal and inland waters. *Appl. Opt.* 39, 897–912. doi:10.1364/AO.39.000897

Sathyendranath, S., Brewin, R., Brockmann, C., Brotas, V., Calton, B., Chuprin, A., et al. (2019). An Ocean-colour time series for use in climate studies: the experience of the Ocean-colour climate change initiative (OC-CCI). *Sensors* 19, 4285. doi:10.3390/s19194285

Siddorn, J. R., Allen, J. I., Blackford, J. C., Gilbert, F. J., Holt, J. T., Holt, M. W., et al. (2007). Modelling the hydrodynamics and ecosystem of the North-West European continental shelf for operational oceanography. *J. Mar. Syst.* 65, 417–429. doi:10.1016/j.jmarsys.2006.01.018

Simis, S. G. H., and Olsson, J. (2013). Unattended processing of shipborne hyperspectral reflectance measurements. *Remote Sens. Environ.* 135, 202–212. doi:10.1016/j.rse.2013.04.001

Soppa, M. A., Silva, B., Steinmetz, F., Keith, D., Scheffler, D., Bohn, N., et al. (2021). Assessment of polymer atmospheric correction algorithm for hyperspectral remote sensing imagery over coastal waters. *Sensors* 21, 4125. doi:10.3390/s21124125

Spyrakos, E., O'Donnell, R., Hunter, P. D., Miller, C., Scott, M., Simis, S. G., et al. (2018). Optical types of inland and coastal waters. *Limnol. Oceanogr.* 63, 846–870. doi:10.1002/lno.10674

Steinmetz, F., Deschamps, P.-Y., and Ramon, D. (2011). Atmospheric correction in presence of sun glint: application to MERIS. *Opt. Express* 19, 9783–9800. doi:10.1364/OE.19.009783

Sullivan, E., Cole, M., Atwood, E. C., Lindeque, P. K., Chin, P. T., and Martinez-Vicente, V. (2023). *In situ* correlation between microplastic and suspended particulate matter concentrations in river-estuary systems support proxies for satellite-derived estimates of microplastic flux. *Mar. Pollut. Bull.* 196, 115529. doi:10.1016/j.marpolbul.2023.115529

Tilstone, G., Dall'Olmo, G., Hieronymi, M., Ruddick, K., Beck, M., Ligi, M., et al. (2020). Field intercomparison of radiometer measurements for ocean colour validation. *Remote Sens.* 12 (10), 1587. doi:10.3390/rs12101587

Tilstone, G. H., Pardo, S., Simis, S. G., Qin, P., Selmes, N., Dessailly, D., et al. (2022). Consistency between satellite ocean colour products under high coloured dissolved organic matter absorption in the Baltic Sea. *Remote Sens.* 14 (1), 89. doi:10.3390/rs14010089

Vanhellemont, Q., and Ruddick, K. (2021). Atmospheric correction of Sentinel-3/OLCI data for mapping of suspended particulate matter and chlorophyll-a concentration in Belgian turbid coastal waters. *Remote Sens. Environ.* 256, 112284. doi:10.1016/j.rse.2021.112284

Vansteenwegen, D., Ruddick, K., Cattrijsse, A., Vanhellemont, Q., and Beck, M. (2019). The pan-and-tilt hyperspectral radiometer system (PANTHYR) for autonomous satellite validation measurements—prototype design and testing. *Remote Sens.* 11, 1360. doi:10.3390/rs11111360

Vishnu, P. S., and Costa, M. (2023). Evaluating the performance of Sentinel-3A OLCI products in the subarctic northeast Pacific. *Remote Sens.* 15 (13), 3244. doi:10.3390/rs15133244

Wang, Z., and Costa, M. (2022). Autonomous shipborne *in situ* reflectance data in optically complex coastal waters: a case study of the salish sea, Canada. *Front. Remote Sens.* 3, 867570. doi:10.3389/frsen.2022.867570

Warren, M. A., Simis, S. G. H., Martinez-Vicente, V., Poser, K., Bresciani, M., Alikas, K., et al. (2019). Assessment of atmospheric correction algorithms for the Sentinel-2A MultiSpectral Imager over coastal and inland waters. *Remote Sens. Environ.* 225, 267–289. doi:10.1016/j.rse.2019.03.018

Xie, X. L., and Beni, G. (1991). A validity measure for fuzzy clustering. *IEEE Trans. Pattern Anal. Mach. Intell.* 13, 841–847. doi:10.1109/34.85677

Zibordi, G., Holben, B., Hooker, S. B., Mélin, F., Berthon, J.-F., Slutsker, I., et al. (2006). A network for standardized ocean color validation measurements. *Eos Trans. Am. Geophys. Union* 87, 293–297. doi:10.1029/2006EO300001

frontiers | Frontiers in Remote Sensing

TYPE Technology and Code
PUBLISHED 16 July 2024
DOI 10.3389/frsen.2024.1347507

Check for updates

OPEN ACCESS

EDITED BY
Enner Alcântara,
São Paulo State University, Brazil

REVIEWED BY
Matteo Ottaviani,
National Aeronautics and Space Administration (NASA), United States
Mhd. Suhyb Salama,
University of Twente, Netherlands

*CORRESPONDENCE
Joel Kuusk,
joel.kuusk@ut.ee

RECEIVED 30 November 2023
ACCEPTED 12 June 2024
PUBLISHED 16 July 2024

CITATION
Kuusk J, Corizzi A, Doxaran D, Duong K, Flight K, Kivastik J, Laizans K, Leymarie E, Muru S, Penkerc'h C and Ruddick K (2024), HYPSTAR: a hyperspectral pointable system for terrestrial and aquatic radiometry.
Front. Remote Sens. 5:1347507.
doi: 10.3389/frsen.2024.1347507

COPYRIGHT
© 2024 Kuusk, Corizzi, Doxaran, Duong, Flight, Kivastik, Laizans, Leymarie, Muru, Penkerc'h and Ruddick. This is an open-access article distributed under the terms of the Creative Commons Attribution License (CC BY). The use, distribution or reproduction in other forums is permitted, provided the original author(s) and the copyright owner(s) are credited and that the original publication in this journal is cited, in accordance with accepted academic practice. No use, distribution or reproduction is permitted which does not comply with these terms.

HYPSTAR: a hyperspectral pointable system for terrestrial and aquatic radiometry

Joel Kuusk[1]*, Alexandre Corizzi[2], David Doxaran[2], Kim Duong[1], Kenneth Flight[1], Joosep Kivastik[1], Kaspars Laizans[1], Edouard Leymarie[2], Silvar Muru[1], Christophe Penkerc'h[2] and Kevin Ruddick[3]

[1]Tartu Observatory, University of Tartu, Tõravere, Estonia, [2]Laboratoire d'Océanographie de Villefranche, UMR7093 CNRS, Sorbonne Université, Villefranche-sur-Mer, France, [3]Royal Belgian Institute of Natural Sciences, Brussels, Belgium

Optical Earth observation satellites provide vast amounts of data on a daily basis. The top-of-atmosphere radiance measured by these satellites is usually converted to bottom-of-atmosphere radiance or reflectance which is then used for deriving numerous higher level products used for monitoring environmental conditions, climate change, stock of natural resources, etc. The increase of available remote sensing data impacts decision-making on both regional and global scales, and demands appropriate quality control and validation procedures. A HYperspectral Pointable System for Terrestrial and Aquatic Radiometry (HYPSTAR®) has been designed to provide automated, *in-situ* multiangular reflectance measurements of land and water targets. HYPSTAR-SR covers 380–1020 nm spectral range at 3 nm spectral resolution and is used at water sites. For land sites the HYPSTAR-XR variant is used with the spectral range extended to 1680 nm at 10 nm spectral resolution. The spectroradiometer has multiplexed radiance and irradiance entrances, an internal mechanical shutter, and an integrated imaging camera for capturing snapshots of the targets. The spectroradiometer is mounted on a two-axis pointing system with 360° range of free movement in both axes. The system also incorporates a stable light emitting diode as a light source, used for monitoring the stability of the radiometric calibration during the long-term unattended field deployment. Autonomous operation is managed by a host system which handles data acquisition, storage, and transmission to a central WATERHYPERNET or LANDHYPERNET server according to a pre-programmed schedule. The system is remotely accessible over the internet for configuration changes and software updates. The HYPSTAR systems have been deployed at 10 water and 11 land sites for different periods ranging from a few days to a few years. The data are automatically processed at the central servers by the HYPERNETS processor and the derived radiance, irradiance, and reflectance products with associated measurement uncertainties are distributed at the WATERHYPERNET and LANDHYPERNET data portals.

KEYWORDS

satellite validation, hyperspectral surface reflectance, automated field spectroradiometry system, WATERHYPERNET, LANDHYPERNET, HYPSTAR

1 Introduction

Data from multispectral spaceborne optical imaging satellites, such as Sentinel-2/MSI, Sentinel-3/OLCI, Landsat-(8/9)/OLI, and Suomi NPP/VIIRS, are used operationally for environmental applications on land and water. Data from a new generation of hyperspectral satellite missions, including PRISMA (Cogliati et al., 2021), ENMAP (Storch et al., 2023), EMIT (Green et al., 2023), and PACE (Gorman et al., 2019) are gaining traction. Commercial "NewSpace" operators are also providing optical imaging data, typically from smaller nanosatellite platforms without on-board calibration devices. The top-of-atmosphere data from all these missions must be calibrated and atmospherically corrected to provide the water and land surface reflectance products from which the higher level end-user products, e.g., chlorophyll *a* concentration in water and fraction of absorbed photosynthetically active radiation (FAPAR), are derived. The quality and usability of the derived products depends on the quality of the reflectance measurements. Imperfect atmospheric correction often leads to contamination of data reaching end-users making the need for radiometric validation at bottom of atmosphere crucial.

For water reflectance, the AERONET-OC network (Zibordi et al., 2009), based on the multispectral Cimel SeaPRISM radiometer, met this need for ocean colour sensors with narrow bands, but did not cover well the spectral bands required for validation of neither the upcoming hyperspectral sensors, nor the wide and non-square bands of the "land-dedicated" missions such as Sentinel-2/MSI and Landsat-8/OLI. For land surface reflectance, very little data were available outside of the RadCalNet network (Bouvet et al., 2019) of sites optimised for vicarious calibration. It was therefore decided in 2017 to develop the HYPERNETS network of validation sites with automated measurement of water and land surface reflectance, based on a new hyperspectral radiometer and commercial off-the-shelf (COTS) pointing system (Ruddick et al., 2024a).

While some hyperspectral radiometers, such as the TriOS/RAMSES, DALEC (Slivkoff, 2014), Sea-Bird/HyperSAS (Carswell et al., 2017) and Biospherical/OSPREy (Hooker et al., 2012) based on the Zeiss MMS 1 spectrometer, do provide hyperspectral coverage and have been integrated into automated measurement systems, they have only 10 nm full width at half maximum (FWHM) spectral resolution which is not high enough for validation of PACE/OCI that has 5 nm spectral resolution (Gorman et al., 2019). The RoX system (Cesana et al., 2021) and WISPstation (Peters et al., 2018) do provide higher spectral resolutions (1.5 nm and 4.6 nm FWHM, respectively).

The design spectral requirements for the new hyperspectral radiometer are summarised in Goyens et al. (2018) as:

- coverage of the spectral range 380–1020 nm for water applications with typically 5 nm FWHM, or preferably 1 nm FWHM resolution;
- coverage of at least 1000–1700 nm or preferably 1000–2500 nm for land applications with typically 5–10 nm FWHM.

Additionally it was necessary to:

- integrate the radiometer with a COTS pointing system with both pan and tilt capabilities, and suitable controller, power supply, and data transmission;
- achieve a complete automated measurement system suitable for reliable long-term deployments in hostile environments (from polar to desert regions and remotes seas);
- consider the requirements of the IOCCG protocols (Zibordi et al., 2019) as far as possible regarding radiometer specification, calibration, and characterisation.

The tilt capability, not included in some precursor water reflectance systems such as DALEC, HyperSAS, RoX, and WISPstation, is considered important to protect the fore-optics when not measuring and is essential for land reflectance measurements where a range of nadir- and azimuth-viewing geometries are required.

The HYperspectral Pointable System for Terrestrial and Aquatic Radiometry (HYPSTAR®) described in the current paper is intended to be a standalone low-maintenance automated data source for the WATERHYPERNET (Ruddick et al., 2024b) and LANDHYPERNET (De Vis et al., 2024b) networks that provide end-users with processed and calibrated water and land reflectance data and associated measurement uncertainties (De Vis et al., 2024b) akin to the existing AERONET-OC and RadCalNet concepts. Following the recommendations of the FRM4SOC project (Banks et al., 2020), the properties of the HYPSTAR spectroradiometers were thoroughly studied in the laboratory and the results are presented in Section 3. Only a brief description and average values are given for each parameter to illustrate the typical performance of the HYPSTAR spectroradiometers. Detailed analysis would warrant an individual research article for each subsection.

The HYPSTAR systems have been deployed at 10 water and 11 land sites. Some of these were only brief campaigns or technology testing experiments while others have been capturing the *in-situ* satellite validation data for months or even years (Dogliotti et al., 2024; Doxaran et al., 2024; Morris et al., 2024). The deployments have been made at a wide range of environments from Antarctica to the Gobabeb desert and the North Sea (De Vis et al., 2024a; González Vilas et al., 2024). The infrastructure available at the test sites has varied from grid power and Ethernet to solar power and sneakernet. The data are transmitted to and automatically processed at the central WATERHYPERNET and LANDHYPERNET servers by the HYPERNETS processor to radiance, irradiance, and reflectance products with associated measurement uncertainties (De Vis et al., 2024b).

2 System description

The interconnection among the different components of HYPSTAR system in a typical configuration is shown in Figure 1:

- *Measurement unit* is the hyperspectral radiometer used for radiance and irradiance measurements and target image acquisition;

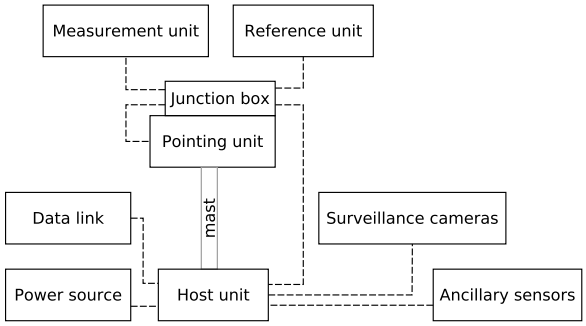


FIGURE 1
Block diagram of a HYPSTAR system.

- *Reference unit* is a stabilised light emitting diode (LED) light source for *in-situ* monitoring the long-term stability of the entire optical path of the spectroradiometer, including the optical windows subject to fouling;
- *Pointing unit* is an electrical pan-tilt pointing system (PT) which is mounted directly on a site-specific mast and provides full-sphere rotational coverage of the spectroradiometer;
- *Junction box* is a passive connection box intended for splitting up connections from single cable coming from the controller into localised connections on top of the mast for the reference LED, spectroradiometer, and PT;
- *Host unit* is the system controller that handles scheduling and all the communications with subsystems as well as with external sources. The heart of the host unit is an industrial grade personal computer (PC) with Linux-based operating system which executes scheduling and acquisition software for control and data acquisition. The host unit also contains a custom-made real time clock (RTC) based control mechanism that supports scheduled power control of the system. This allows a mode of deep sleep to conserve energy between captures. The whole unit is housed in a weatherproof wall-mountable box with sealed external ports for power input and connections to other subsystems;
- *Ancillary sensors* comprise a rain sensor and a broadband photodiode. The rain sensor is used to save energy by preventing sequences during rain. The photodiode is intended for monitoring the stability of the downwelling irradiance during the hyperspectral radiance measurements;
- *Power source* is a site-specific source of 12 V direct current (DC) power bus. This can be a solar panel array or wind turbine with battery backup or a generic AC/DC converter capable of supplying at least 4 A of sustained current;
- *Data link* is a site-specific internet connection for uploading the data to the network server and accessing the system remotely for troubleshooting, configuration changes, and software updates;
- *Surveillance cameras* are optional components of the system that can be used for diagnostics and monitoring for external influences, such as equipment damage, vandalism, etc.

The technical specifications of the HYPSTAR systems are listed in Table 1.

2.1 Spectroradiometer

The *measurement unit* in Figure 1 is the hyperspectral radiometer that performs acquisition of radiance and irradiance spectra and target imagery. Two different versions of the radiometer have been developed for various applications:

- HYPSTAR-SR (Standard Range) has a single 2048 pixel Si detector array for visible and near-infrared (VNIR) spectral range and is mainly intended for above-water measurements;
- HYPSTAR-XR (eXtended Range) has an additional thermally stabilised 256 pixel InGaAs array for extending the spectral range into short-wavelength infrared (SWIR) which is useful for measuring land (surface) targets.

In small scale engineering and manufacturing a main cost driver is non-recurring engineering costs, i.e., person-hours used for development and testing. One way of working around this issue is creating systems consisting of generic modules that can be reused for multiple systems. This approach was used in designing the HYPSTAR instruments. The main difference between the SR and XR radiometers is the support for extended spectral range via the inclusion of an additional spectrometer module. Most of the system components (host and pointing systems, internal electronics and optical paths, firmware and supporting software) have been designed to be as modular and interchangeable as possible. Based on this, most of the following text will be about the SR system, but is also applicable to the XR, except where explicitly mentioned.

2.1.1 Optical path

The optical path is based around the idea of multiplexing radiance and irradiance optical entrances into a single spectrometer module, or a set of modules in the case of the XR variant. The benefits compared to parallel acquisition using duplicated signal chains are:

- reduced laboratory characterisation effort;
- correlations between radiance and irradiance measurement reduce the uncertainties (e.g., from laboratory calibration, spectrometer responsivity drift and/or thermal sensitivity) of the calculated reflectance;
- the multiplexer acts as a shutter, providing dark signal when neither entrance is selected;
- reduced cost, size, mass, and power consumption.

The price to pay for the aforementioned benefits is that simultaneous acquisition of radiance and irradiance measurements is not possible. This is not a major issue for satellite validation application, since automated operation enables the collection of large amounts of data. The best data for validating optical satellites are collected in stable atmospheric and illumination conditions when downwelling irradiance changes slowly and in a predictable manner. Another downside of the multiplexed design is the reduced optical throughput due to the losses in the extended optical path.

The Ibsen FREEDOM UV-NIR FSA-101 spectrometer module with the 2048-pixel Hamamatsu S11639-01 CMOS detector array is used for both SR and XR units. The VNIR module has 3 nm FWHM

TABLE 1 Technical specifications of the HYPSTAR.

Model	HYPSTAR-SR	HYPSTAR-XR
Weight of top-of-the-mast assembly	6.3 kg	7.8 kg
Power supply (entire system)	12 VDC, 40 W	12 VDC, 50 W
Operating temperature	−25°C to 45°C	
Storage temperature	−35°C to 70°C	
Spectroradiometer		
Measured quantity	radiance and irradiance (multiplexed)	
Field of view	2° (radiance), 180° (irradiance)	5° (radiance), 180° (irradiance)
Detector array	2048 px Si	2048 px Si, 256 px InGaAs
Spectral range	380–1020 nm	380–1680 nm
Spectral sampling interval	0.5 nm	0.5 nm (VNIR), 3 nm (SWIR)
Spectral resolution	3 nm	3 nm (VNIR), 10 nm (SWIR)
ADC resolution	16 bit	
Integration time	1–65000 ms, independent for VNIR and SWIR	
Shutter	internal	
Target camera	5 MP, RGB, 57° vertical and 44° horizontal FOV	
Communication interface	RS-485, half duplex, 115.2–8000 kbit s^{-1}	
Housing material	anodised marine grade aluminium	
Environmental protection	IP 67	
Dimensions (DxL)	ϕ 110 mm × 267 mm	ϕ 110 mm × 434 mm
Weight	1.5 kg	3 kg
Power supply	8–30 VDC, 6 W	8–30 VDC, 25 W
Reference unit		
Light source	ϕ 42 mm diffuse, white LED spectrum	
Communication interface	RS-485, half duplex, 115.2 kbit s^{-1}	
Housing material	anodised marine grade aluminium	
Environmental protection	IP 67	
Dimensions (DxL)	ϕ 110 mm × 108 mm	
Weight	0.8 kg	
Power supply	8–30 VDC, 10 W	
Pointing unit		
Communication interface	RS-485, half duplex, 2.4 kbit s^{-1}, PELCO D protocol	
Range	360° pan and tilt	
Speed	24° s^{-1} pan, 6° s^{-1} tilt	
Repeatability	< 1°	
Backlash	< 0.15°	
Housing material	painted die cast aluminium	
Environmental protection	IP 68	
Weight	1.9 kg	

(Continued on following page)

TABLE 1 (*Continued*) Technical specifications of the HYPSTAR.

Model	HYPSTAR-SR	HYPSTAR-XR
Host unit		
Operating system	Linux	
Communication interface	Ethernet, WiFi, mobile	
Data storage	64 GB solid state drive	
Enclosure material	polycarbonate	
Environmental protection	IP 66	
Dimensions (HxWxD)	500 mm × 400 mm × 210 mm	
Weight	10 kg + cables 4 kg	

spectral resolution. The spectral sampling interval is 0.5 nm at 800 nm and decreases slightly at longer and shorter wavelengths, reaching 0.46 nm in ultraviolet (UV). Considering the number of pixels and the sampling interval, the spectral range of the VNIR spectrometer module is 165–1145 nm, however, the responsivity is highest around 750 nm and decreases towards longer and shorter wavelengths. In addition, the bottom-of-atmosphere solar irradiance drops rapidly in UV. Thus, the signal-to-noise ratio (SNR) drops at both ends of the spectral range and the nominal VNIR spectral range reported in Table 1 is limited to 380–1020 nm although the signal from all the 2048 sensor pixels are stored.

The XR units are also equipped with the Ibsen Rock NIR RSM-420 spectrometer module having a 256-pixel Hamamatsu G9203-256SA thermoelectrically stabilised InGaAs detector array for covering the SWIR spectral range up to 1680 nm. The spectral resolution in the SWIR is 10 nm, sampling interval varies from 3.6 nm in near-infrared (NIR) to 2.6 nm in SWIR. Integration time can be adjusted in the range of 1–65000 ms for both spectrometer modules separately. Since the Ibsen Rock NIR RSM-420 does not include an order sorting filter, an external filter is used for blocking the VNIR radiation that would cause higher order diffraction pattern on the SWIR detector array. The stabilisation temperature of the SWIR detector array is user configurable. In most cases a 0 °C setpoint is used except for extremely hot locations where ambient temperature exceeding 40°C can be expected (e.g., Gobabeb, Namibia, where the SWIR detector is stabilised to 10°C).

The radiance and irradiance entrances are both connected to the input multiplexer (MUX in Figure 2) using multimode optical fibres. The multiplexer radiance and irradiance channel outputs are simultaneously connected to both VNIR and SWIR spectrometer modules (where the SWIR module is present) using a multi-branch fibre bundle. Single fibres in the bundle are mixed in such a way as to provide both spectrometer modules with signals from both input arms. Since most of the measurements during the sequence are made via the radiance entrance and the targets are often rather dark (e.g., water), 80% of the fibres in the bundle are allocated for the radiance channel to reduce the sequence duration and increase the signal-to-noise ratio of the radiance measurements. The nominal radiance field of view (FOV) is 2° and 5° for the SR and XR unit, respectively. These FOV values were chosen as a compromise between resolving the angular dependence of radiance and averaging over small scale spatial heterogeneities (compared to any satellite pixel). The spatial

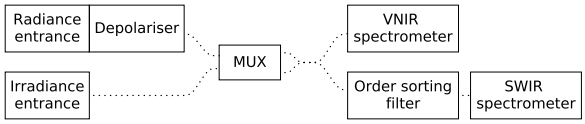


FIGURE 2
Block diagram of the optical path of the HYPSTAR-XR spectroradiometer. The dotted lines represent optical fibres. The HYPSTAR-SR variant does not have the SWIR spectrometer module, the order sorting filter, and the fibre arm entering the filter. MUX is a multiplexer/shutter.

averaging can be improved by increasing the distance from the target, but there are practical limitations on the height of the mast.

The radiance and irradiance optical paths passing through the multiplexer are permanently aligned. The active channel is selected by aligning the aperture of a solid rotating disk with a respective channel while the disk blocks the other channel. When the aperture is not aligned with either of the channels, the disk performs as a shutter. The disk with aperture is the only moving part in the multiplexer assembly which makes the design relatively robust and insensitive to small multiplexer positioning errors. The downside is reduced optical throughput due to illuminating only part of the fibres in the bundle at any given time.

All the windows and lenses in the optical path of the HYPSTAR radiometers are made of borosilicate glass. A fused silica diffuser is used for the cosine collector of the irradiance entrance. Fused silica is preferred due to superior thermal properties to another commonly used diffuser material polytetrafluoroethylene (PTFE) (Ylianttila and Schreder, 2005; Vabson et al., 2024). The depolariser of the radiance entrance is made of quartz. The geometry of the cosine collector was optimised with TracePro opto-mechanical design software and further adjusted according to laboratory characterisation on a goniometer setup to provide the lowest cosine error throughout the entire spectral range.

2.1.2 Target camera

Target monitoring is done using an RGB camera that provides compressed JPEG images with resolutions up to 2,560 px × 1920 px and 68° diagonal FOV featuring automatic exposure control, with a dynamic range large enough to tolerate direct-Sun pointing. The imaging RGB camera coaligned with the radiance and irradiance

optical entrances is a very useful tool for identifying and understanding anomalies in the measured spectra (foreign objects inside the FOV, pointing errors) or for visualising the state and evolution of the target (waves, phenology) during the potentially long periods of unattended measurements. The camera images are captured in portrait orientation.

2.1.3 Mechanics

The mechanical design using anodised marine grade ϕ110 mm aluminium tubing for the body of the spectroradiometer provides sufficient corrosion resistance in harsh marine conditions (salt spray, biofouling, etc.) and is stable for long-term outdoor deployments (solar UV radiation, variable temperature, ice and snow, etc.). O-ring seals are used to cap off both ends to create an IP-67-rated enclosure. One end cap contains the optical entrances, while the other houses the connection port and heat sink for the XR units. The XR variant is longer and heavier compared to the SR units to accommodate the additional SWIR spectrometer module. CA Bayonet connectors designed to VG95234 specifications ensure appropriate environmental protection and robust mating. The use of a ϕ110 mm body also enables creation of *ad-hoc* test stands and jigs from water supply industry standard clamps.

2.1.4 Ancillary sensors

Internal environment monitoring consists of pressure, relative humidity, 3D acceleration and various temperature sensors, as well as voltage and current monitors. Internal pressure and humidity are used in conjunction with internal temperature to gauge the state of sealing. Leakage increases humidity, which in turn could lead to internal fogging of the fore-optics in low temperature regions or damage to the electronics if the leak is significant. Acceleration data can be used for estimating the pointing precision. Each spectrum captured is provided with 3-axial acceleration data together with statistics for the duration of acquisition. A high standard deviation in accelerometer data can be indicative of excessive swaying during windy conditions. Other uses for acceleration data converted into gravity vector are verification of pointing angle and assistance of instrument levelling during initial setup in poor visibility. It is also useful in challenging conditions, such as the typical setup for land measurements where the system is mounted at the end of a cantilever, to enable nadir reflectance measurements. Internal power bus voltage and current monitoring provides information for troubleshooting purposes. Various internal temperature sensors (on both photodetector arrays, SWIR module body and heat sink, internal ambient) assist with evaluation of the system state and correction for the thermal dependence of the radiometric measurements.

2.1.5 Communication interface

The communications scheme employing the industrial TIA-485 standard (also known as RS-485) and half-duplex physical layer enables system evaluation by using any generic TIA-485 transceiver and a PC. The default baud rate of 115200 with 8N1 frames is supported by most generic devices. The same interface is often used to control various PT units available on the market albeit at lower baud rates. The lack of high baud rate support on PT units means that multi drop communications among the host, pointing, and measurement units are not used. To increase throughput, binary data encoding as well as data rates up to 8 Mbit s^{-1} can be used (in transceivers that support it). All datasets have cyclic redundancy check (CRC) checksums and are split into packets of up to 1 KiB that each have their own checksum. Communications are handled by an open source Linux driver[1] that exposes C/C++ and Python 3 application programming interfaces for integration into custom software. This driver handles all the setting-up, acquisition and data downloads as well as managing any communication issues with minimal user intervention. The end user application developer does not have to worry about specific differences between instrument models or versions, since all the data packets and structures are unified.

2.1.6 Power supply

The power supply circuitry within the spectroradiometer generates all the internal power rails necessary for operation from the provided power input of 8–30 V. Support for off-grid 24 V supply rail during active charging at 27–29 V is present, but currently not used due to constraints from the other parts of the system. Automotive load dump and battery-reverse protection to ISO 16750–2 levels implemented in the design of the power supply protect the most valuable parts of the spectroradiometer.

2.1.7 Firmware

The firmware of the spectroradiometer is remotely upgradeable. This allows not only for bugfixes, but also implementation of some site-specific user requests. As an example, typically automatic integration time adjustments are started from some low-mid range value. For low brightness targets the optimisation algorithm has to extend the integration time for each measurement which increases total sequence time. Per user request, inverted logic was implemented, where the integration time of the previous measurement was used as a starting point, thus reducing the total duration of each sequence.

Graceful degradation is the ability of a system to retain partial functionality even when a portion of the overall system has been rendered inoperative. Damage of non-essential parts (environmental sensors, RGB camera) is reported by the instrument, all the while allowing to perform the other tasks.

2.2 Reference LED

One of the main requirements for the HYPSTAR is low maintenance need during field operations. Performing high quality optical measurements is a difficult task even in laboratory, let alone in field conditions. In order to automatically assess the responsivity of the instrument on regular basis, a stable LED-based reference light source is added to the system. The LED source is not used for absolute radiometric calibration of the

1 https://github.com/HYPERNETS/libhypstar, accessed on 15 November 2023.

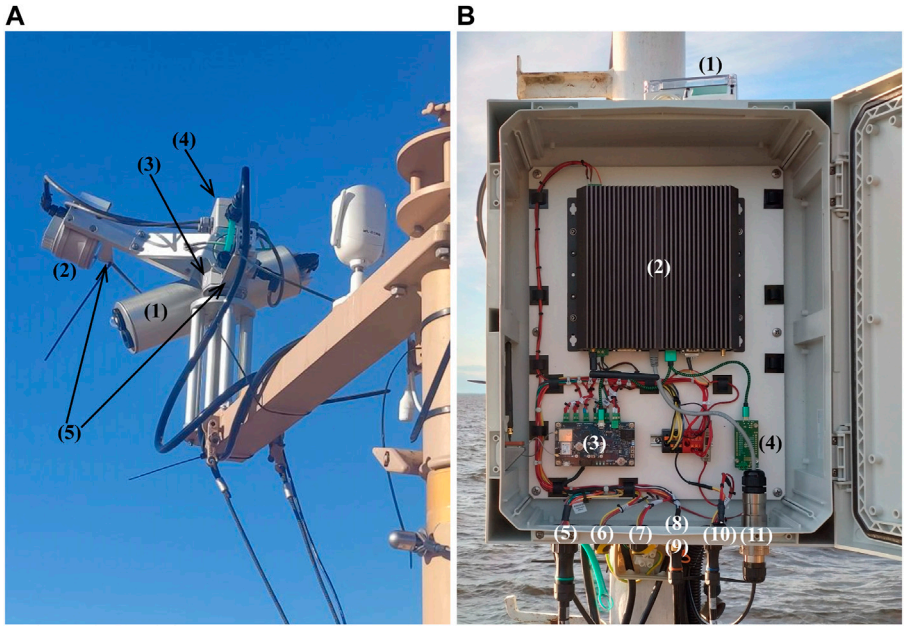


FIGURE 3
(A) Top-of-the-mast assembly of the HYPSTAR-XR system deployed in Gobabeb, Namibia–spectroradiometer (1), reference LED (2), pointing system (3), junction box (4), and cable supports (5). The vertical axis of the pointing system (3) is fixed to the mast and the entire assembly above (and including) the lower cable support (5) moves when panning. **(B)** HYPSTAR host unit with the enclosure door open–monitor photodiode and rain sensor (1), PC (2), Yocto-Pictor (3), high speed RS-485 transceiver for the spectroradiometer communications (4), cable to junction box (5), surveillance camera power connectors (6) and (7) (unused in this image), cable to monitor photodiode and rain sensor (8), connector for external GNSS/WiFi/mobile antenna (9) (unused in this image), system power supply input (10), and Ethernet connection (11).

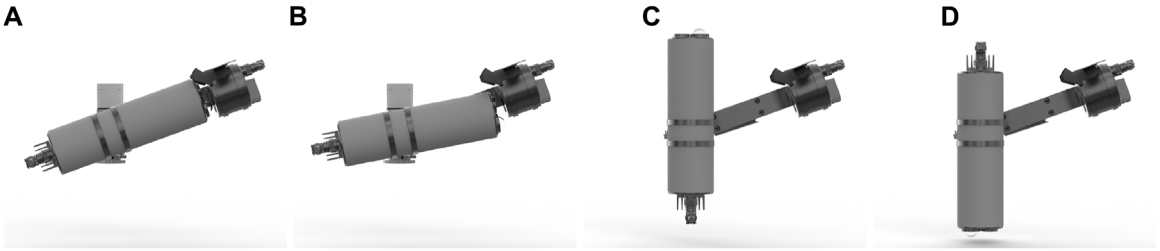


FIGURE 4
Different tilt positions of the radiometer: measurement of the reference LED using irradiance **(A)** and radiance **(B)** entrance; measurement of downwelling irradiance **(C)**; measurement of nadir radiance and parking **(D)**.

instrument but should enable identification of variation of responsivity during a long deployment from processes such as spectrometer ageing or fore-optics contamination. It is considered an unknown but stable source and repeated measurement of that source in identical measurement conditions should give identical results. Detected variations in the measured brightness are used to inform on potential instrument servicing.

LEDs have high radiant efficacy which is relevant for off-grid systems and their vibration and shock tolerance is also much higher than that of any incandescent light source. LEDs exhibit temperature dependence for both emission wavelength and intensity (Eugène and Deswert, 2009; Cengiz et al., 2022), but this can be mitigated with thermal monitoring and stabilisation.

The radiometer is pointed towards the reference LED by tilt axis movement of the PT (see Figures 3, 4). The pointing accuracy is determined by the repeatability and backlash of the pointing system. A quite large ϕ42 mm diffuse source is used as a reference, in order to limit the sensitivity to pointing accuracy. A borosilicate glass window protects the fused silica diffuser of the reference LED from the elements.

A broadband white LED with emissions in the range of 400–800 nm is used for the VNIR range. Due to rather high losses in the optical paths (the source diffuser coupled with the radiometer diffuser in the case of irradiance measurement) a high-power source is required. Excess heat from the power LED is transported to the external aluminium casing which houses a heat sink. The LED temperature is monitored via an adjacent sensor on the circuit board. When the temperature reaches the setpoint the reference unit reports back to the spectroradiometer that the reference measurement can be performed. The setpoint is

determined automatically based on the ambient temperature and the user configurable LED current and is typically 30°C or 40°C for mid-latitude summer.

2.3 Pointing unit and instrument mounting

An active pointing system is required due to the single body design and the taking of both irradiance and radiance measurements at various angles. For estimating remote-sensing reflectance of water using above-water instruments (Mobley, 1999; Ruddick et al., 2019), the measurements have to be made in three directions: downwelling irradiance (zenith), sky radiance (tilted upwards), and water radiance (tilted downwards). In addition, the optimal azimuth of sky and water measurements is at a fixed relative angle to the Sun. A PT allows following the diurnal movement of the Sun and switching between positive and negative relative azimuth as necessary to avoid pointing at the superstructure or its shadow. Zenith pointing capability can also be used for more advanced water measurement protocols (Goyens and Ruddick, 2023). The directional effects of surface reflectance for land targets (Kuusk et al., 2014; Gatebe and King, 2016) can be captured with an active pointing system, thus, matching the view geometry of different satellite sensors.

The HYPSTAR system incorporates the Will-Burt Bowler RX dual axis side-mount PT, with 360° range in both axes providing fully spherical coverage. This PT requires 12 V DC power supply and provides rotation speeds of $24^{\circ}s^{-1}$ and $6^{\circ}s^{-1}$ for pan and tilt, respectively, with better than 1° precision.

The top-of-the-mast assembly of a HYPSTAR-XR system deployed in Gobabeb, Namibia, is shown in Figure 3A. The PT serves as an interface between the superstructure and the measurement and reference units, which are mounted on the pointing unit using custom design mounting brackets and a junction box to reduce the number of cables necessary to connect the whole setup to the host unit. Splitting a single cable above the rotation point reduces the load on the PT as well as the possibility of damaging the cabling due to repeated rubbing action while rotating. The mounting brackets incorporate cable supports that elevate cabling to prevent entangling, rubbing, and relieve bending stresses on the electrical connectors.

The reference unit is fixed to the body of the PT and pans together with the radiometer, which ensures that no measurement direction is blocked by the reference unit, but requires over 180° tilt range of the pointing unit. The reference LED is located slightly higher than the tilt axis so that the source window is inclined downward, which provides some protection against fouling (see Figure 4). At the same time the body of the reference unit remains entirely below the cosine collector of the spectroradiometer during the downwelling irradiance measurements. Rainwater and bird droppings are diverted from draining down the source window of the reference LED by a 3D-printed shroud.

The PT is mounted on the mast with a flange fixed to the end of the pan axis, and a slip-ring fastened with three stainless steel bolts. When the bolts are slightly loosened, the flange still supports the assembly while allowing it to be pointed to the desired position. Since the pan axis is locked to the mast, any pan movement rotates the body of the PT (and everything attached to it) instead.

The reference unit and the spectroradiometer are aligned in the mounting brackets with the help of a 3D-printed alignment tool which allows for aligning laterally, vertically, and rotationally. It also doubles as a physical support during transportation of the top-of-the-mast assembly.

2.4 Host unit

HYPSTAR setups require a control system that deals with scheduling, power and communications management as well as data offloading to network. The host unit is built around the industrial-grade PC Cincoze DE-1000 running a Linux operating system. Either Debian Stable or Manjaro has been used for the prototype systems deployed so far.

As shown in Figure 3B, an IP-66-rated box houses the PC and:

- an RTC that keeps track of the time and power-up schedule;
- six power management relays that are used for turning the other subsystems on and off;
- a global navigation satellite system (GNSS) receiver for location data and time synchronisation;
- a high speed RS-485 transceiver used for communicating with the spectroradiometer;
- intra-system communications ports that are used to connect other external parts of the system: the pointing, measurement, and reference units at the top of the mast, the rain/light sensors, external web cameras, Ethernet port, external WiFi or mobile antenna, and power input.

The RTC, relays, and GNSS are integrated into a bespoke Yocto-Pictor device manufactured by Yoctopuce (Geneva, Switzerland). The six relays provide power to the PC, PT, spectroradiometer and reference LED, heated rain sensor, and independently up to two surveillance cameras. The PC relay is controlled by the RTC; the switching of all other relays is managed by the PC software.

Power management is performed by a dedicated RTC which controls the power relays in a timed fashion. Typically, the measurement sequences are performed at certain time slots (usually every 15–30 min) during daytime, when light conditions are sufficient for obtaining meaningful data. The whole system, with exception of the low-power RTC, shuts down between sequences. The RTC contains also a programmable watchdog timer that powers off all the subsystems if the measurement sequence has not been finished and the system gracefully shut down. The watchdog prevents the system from draining the batteries of off-grid setups or just hanging indefinitely in the case of a software bug.

At the start of a sequence, the RTC powers up the PC which starts execution of open source scheduler software[2] written in Python 3. This software first checks the rain sensor to verify that external weather conditions are suitable for performing the measurements. If rain is detected, the PT is requested to point the spectroradiometer towards nadir (in case it was not already

2 https://github.com/HYPERNETS/hypernets_tools, accessed on 15 November 2023.

parked for some reason, e.g., hard power-off by the watchdog timer at the end of the previous sequence) to protect the entrance optics from contamination and the system is shut down until the next programmed timeslot.

If no rain is detected, a series of basic checks is performed as the units are sequentially powered up. The user-defined sequence containing PT movements, spectroradiometric measurements, and RGB camera captures, is then executed. The broadband photodiode (ROHM Semiconductor BH1751FVI photometric light sensor) signal is recorded at 1 Hz rate during the sequence for monitoring the stability of the downwelling irradiance. Once all the measurements have taken place the system is shut down. For power and time saving reasons the data are uploaded to the network as a background process during the next measurement sequence. Local copies of the data are preserved until they are manually deleted by the operator.

Two 12 V independent power sockets are available to power up the optional surveillance cameras (in our case, commercial-grade ABUS TVIP6256x-series cameras). The data link to the cameras depends on the site infrastructure and can be either wired or wireless. Wireless connection directly to the PC is possible if the PC is configured as a WiFi access point. The cameras can be scheduled to record a snapshot during each measurement sequence.

A GNSS receiver is used as a backup time synchronisation device in case network time is not available. Since these systems are intended for fixed-site installation, the correct time and location data are only used to calculate the Sun angle.

Various external communications and power supply possibilities are available. For sites with grid power an AC/DC converter and, where available, fixed Ethernet connection might provide the best results. For remote and off-shore installations a battery-backed solar panel system is preferred, with WiFi or mobile connection for data transmission.

Each of the host units establishes a reverse-SSH connection to either the WATERHYPERNET or LANDHYPERNET data server for remote access during measurement time. This can be used to connect to the host unit remotely even in environments with dynamic IP address assignment (such as mobile networks). Once connection is established, subsequent scheduled power-down can be prevented allowing time necessary for performing remote maintenance or updates.

The system is designed for automated operation and is not meant to be used as a general purpose radiometer. Hence, the rather minimalistic graphical user interface is provided only to perform basic functional tests on the subsystems.

2.5 Power and data budgets and standard measurement sequences

The power and data budgets of the HYPSTAR setup depend on various parameters and are not very deterministic. The main drivers are the scheduling and sequence configurations which determine how often the system is powered up and which data are acquired. For example, the integration time of the spectroradiometer depends on the downwelling irradiance and target radiance. The power consumption of the SWIR detector thermal stabilisation is driven by the difference between the setpoint and the ambient temperatures. The JPEG compression ratio of the camera images depends on the image content.

The approximate power consumptions of the main system components during operation are:

- host system (PC, Yocto-Pictor, stationary PT): 14 W;
- HYPSTAR-SR spectroradiometer: 4 W;
- HYPSTAR-XR spectroradiometer, SWIR temperature stabilised to 0°C at 20°C ambient: 8 W;
- PT movement: 2 W;
- reference LED at 1 A: 5 W;
- ABUS surveillance camera: 1.5 W.

It should be noted, however, that the instantaneous peak consumptions at the moment of switching on the loads and charging the internal capacitors of the subsystem power supplies or during PT acceleration and deceleration can be substantially higher. If the system is powered from an AC/DC converter, it must have good load regulation capability for handling the load transients, otherwise the voltage may sag temporarily to a level that causes the HYPSTAR system to reboot.

A standard measurement sequence of the HYPSTAR-SR systems integrated into the WATERHYPERNET network contains the following:

- 3 × downwelling irradiance + 3 × dark + picture;
- 3 × sky radiance + 3 × dark + picture;
- 6 × water radiance + 3 × dark + picture;
- 3 × sky radiance + 3 × dark + picture;
- 3 × downwelling irradiance + 3 × dark + picture;
- picture of the Sun (for checking the pointing accuracy);
- park to nadir.

The water sequence is usually executed every 15–30 min for 8–12 h centred around the local noon and takes typically 4–7 min. The daily data budget is usually 25–50 MB for the spectra and target images, and 3–8 MB for the snapshots of the surveillance cameras. Typical daily power consumption is 30–60 W h d^{-1}. More details about the data acquisition protocol and data processing of the WATERHYPERNET systems can be found in (De Vis et al., 2024b; Ruddick et al., 2024b).

The HYPSTAR-XR systems of the LANDHYPERNET measure the multiangular reflectance of the target according to the following standard sequence:

- 10 × downwelling irradiance + 3 × dark + picture;
- (10 × surface radiance + 3 × dark) in 27 directions + nadir picture;
- 10 × downwelling irradiance + 3 × dark + picture;
- park to nadir.

The land sequence takes longer to execute due to the larger number of captured spectra. Typical run time at a vegetated site is 8–12 min. The sequences are executed every 20–30 min. The much larger number of captured spectra compared to the water systems increases the daily data budget to 150–200 MB. Typical daily power consumption is 150–250 W h d^{-1} for the LANDHYPERNET HYPSTAR-XR systems. More details about the

LANDHYPERNET data acquisition protocol are presented in (De Vis et al., 2024b).

3 Calibration and characterisation

The HYPSTAR spectroradiometer prototypes were manufactured in three batches during the H2020/HYPERNETS project. The performance of all the units was thoroughly studied in laboratory and field conditions, and the design refined between batches. The third batch contained nine HYPSTAR-SR and eight HYPSTAR-XR units. The calibration and characterisation results are presented in the following sections as the mean and standard deviation of the parameters of the third batch HYPSTAR instruments.

3.1 Radiometric calibration and noise metrics

The link between the digital number (DN) output of the radiometer and the international system of units (SI) is established by measuring a known source with SI-traceable (ir)radiance. Common setups use the direct illumination of a calibrated quartz-tungsten-halogen (QTH) lamp for the irradiance calibration (Schinke et al., 2020), and a diffusing plaque with calibrated reflectance illuminated by the same (or similar) lamp for the radiance calibration (Białek et al., 2020).

The signal-to-noise ratio (SNR) depends on the measured signal and settings of the measurement device. Many sources of noise can affect photosensors (Konnik and Welsh, 2014). Generally, the overall noise is expressed as the sum of the photon noise, the dark noise, the readout noise, and the digitisation noise (Moses et al., 2012). The photon noise (also known as shot noise or Poisson noise) is related to the quantised nature of light and the random fluctuations in the arrival and detection of the photons (Hasinoff, 2014). The standard deviation of the photon noise increases with the square root of the signal. The dark noise is driven by the shot noise of the thermally generated electrons recorded by the photodetector. Since the dark signal increases with sensor temperature and integration time, so does the dark noise. The readout and digitisation noise are related to reading the signal from the photodetector and analogue-to-digital conversion, respectively, and do not depend on the measured signal.

The highest SNR is achieved when the signal approaches the saturation level at the lowest integration time, thus, minimising the dark noise. This situation is obviously not guaranteed during field measurements as we are limited by the intensity of the natural illumination. The noise level was analysed from the radiometric calibration data which represents more realistic use case in terms of using the dynamic range of the sensor and selecting the integration time.

The radiometric calibration was performed using a 1 kW FEL lamp (and plaque, for radiance) positioned at a distance of 500 mm. The integration time during the radiance (irradiance) calibration was automatically adjusted to 32 ms (512 ms) and 128 ms (2048 ms) for the VNIR and SWIR modules, respectively. The SNR was calculated as in Eq. (1) below:

$$\mathrm{SNR}(\lambda) = \frac{S(\lambda) - D(\lambda)}{\sigma_S(\lambda)}, \tag{1}$$

where $S(\lambda)$ and $D(\lambda)$ are the mean light and dark signal at wavelength λ, respectively, and $\sigma_S(\lambda)$ is the standard deviation of the light signal. The noise equivalent irradiance difference (NEdI) and noise equivalent radiance difference (NEdR) are the (ir)radiance values corresponding to SNR = 1 and were calculated as the (ir)radiance of the calibration standard divided by the SNR.

The noise metrics calculated from the radiometric calibration data are presented in Figure 5. The SNR values correlate with the raw signal level peaking at 300 for the VNIR and at 3000 for the SWIR modules. The lower mean SNR of the HYPSTAR-XR irradiance measurements in Figure 5A is due to the lower raw signal level when measuring the irradiance calibration standard. While the mean peak raw signal value before subtracting the dark was between 47000 DN and 49000 DN for the irradiance calibration of the SR and radiance calibration of both the SR and XR units, the average peak signal of the XR irradiance measurements remained below 41000 DN, but still within the target range of the automatic integration time adjustment.

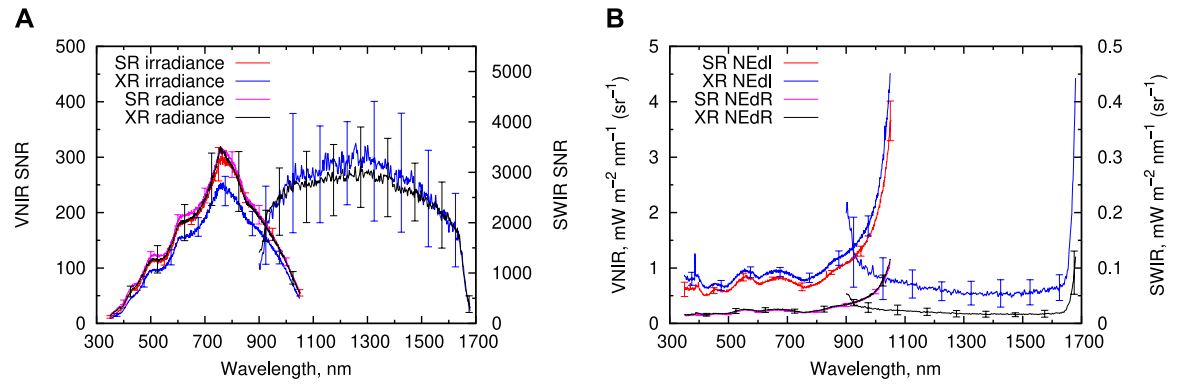


FIGURE 5
Mean **(A)** signal-to-noise ratio (SNR) and **(B)** noise equivalent radiance difference (NEdR) and noise equivalent irradiance difference (NEdI) of the HYPSTAR spectroradiometers during radiometric calibration. The error bars indicate the standard deviation of the results of nine SR and eight XR units.

Finally, we note that for field measurements the SNR can be improved by averaging over replicates.

3.2 Non-linearity

The radiance and irradiance levels measured in the field depend on various parameters (solar zenith angle (SZA), target reflectance, atmospheric composition, wavelength, etc.) and can vary over an order of magnitude. The raw output signal of the spectroradiometer is usually calibrated using single (ir)radiance levels.

The linearity of the VNIR and SWIR spectrometer modules was tested using two different methods: the "flux addition" method (Sanders, 1972), where the integration time was kept constant and the source radiance was changed and the "constant source" method (Pacheco-Labrador et al., 2014) where the source radiance was kept constant and the integration time was changed. The non-linearity factor α for the flux addition method was calculated as:

$$\alpha = \frac{I(A+B)}{I(A)+I(B)} - 1, \tag{2}$$

where $I(A)$ and $I(B)$ are the dark-subtracted signals when the spectrometer is illuminated by flux A and B, respectively, and $I(A+B)$ is the signal when illuminated by both fluxes simultaneously. As suggested by Sanders (1972), the fluxes $I(A)$ and $I(B)$ were adjusted to be roughly equal. If the system is linear, $\alpha = 0$.

The non-linearity factor for the constant source method can be expressed as:

$$\alpha = \frac{I(t)}{n\,I\left(\frac{t}{n}\right)} - 1, \tag{3}$$

where t is the integration time and n is an arbitrary multiplier. The results are directly comparable to the flux addition method if $n = 2$. There was good agreement between the non-linearity factors determined with these two methods for both the VNIR and SWIR modules, the mean absolute difference was 0.002 and 0.001, respectively. Since the constant source method is easier to implement, it was chosen for linearity characterisation of all HYPSTAR spectroradiometers.

The radiance of the source as well as the responsivity of the spectrometer vary with wavelength, resulting in different pixel values in a single spectrum. No wavelength dependence of the non-linearity factor was evident, except for some SWIR modules, and the entire dynamic range of the sensor could be covered with measurements at only a few different integration times. The non-linearity factors obtained using the constant source method did not depend on the source radiance used for the measurements.

The non-linearity factor defined by Eqs 2, 3 describes the non-linearity of the dark-subtracted raw signal in digital counts with respect to the signal that the same instrument would record in the case of half the radiant flux when using the same instrument settings (flux addition method) or in the case of half the integration time when measuring the same radiant flux (constant source method). For instance, $\alpha = -0.04$ at 60000 counts implies that measuring the same source using half the integration time would yield a result of 31250 counts instead of the 30000 counts that a perfectly linear system would measure. At the same time, the non-linearity factor at 30000 counts describes the non-linearity with respect to 15000 counts and so on. No particular number of digital counts can be considered to be the "correct" level.

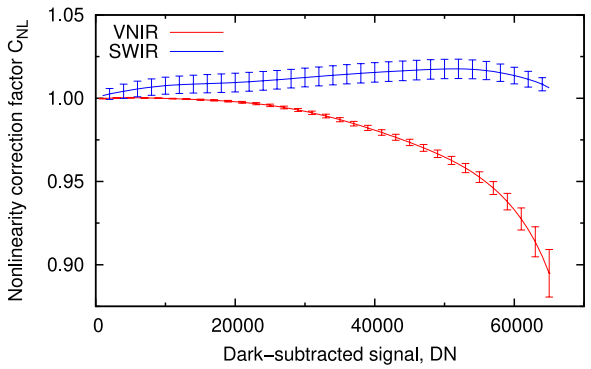


FIGURE 6
Mean non-linearity correction factor C_{NL} for the VNIR and SWIR spectrometer modules of the HYPSTAR spectroradiometers. The error bars indicate the standard deviation of the correction factors of 17 VNIR and eight SWIR modules.

A polynomial function $f(x)$ with zero intercept was fitted to the factor α. The polynomial was sixth-order for the VNIR modules and fourth-to-12th-order for the SWIR modules, depending on the manufacturing quality of each detector. Next, the fitted polynomials were used to calculate the non-linearity correction factors C_{NL} for each possible pixel value x in the range 1–65535 DN as shown in Eq. (4) below. 1 DN was arbitrarily chosen as the "correct" level and the non-linearity factors were iteratively multiplied until 1 DN value was reached:

$$C_{NL}(x) = \prod_{i=0}^{\frac{x}{2^i}<1} f\left(\frac{x}{2^i}\right). \tag{4}$$

For non-linearity correction, the dark-subtracted pixel value x has to be divided by the correction factor $C_{NL}(x)$. The mean $C_{NL}(x)$ is presented in Figure 6.

3.3 Thermal sensitivity

Thermal sensitivity of the spectroradiometer can be a significant source of bias and uncertainty for radiometric measurements, especially in the NIR spectral region for instruments without thermal stabilisation for the silicon photodetectors (Salim et al., 2011; Zibordi et al., 2017; Vabson et al., 2024).

During the characterisation, the instrument was placed inside an environmental chamber. The flux from a stabilised QTH source located outside the chamber was coupled to the radiance or irradiance entrance of the HYPSTAR with an optical fibre. The temperature inside the chamber was ramped from 20°C up to 40°C and maintained for 1 hour, then ramped down to −20°C and maintained for 1 hour and then ramped back up to 20°C. The ramp-up and ramp-down rates were approximately 1°C min^{-1}. During the experiment the lamp signal and the dark signal were alternately recorded. The dark-subtracted lamp signals were

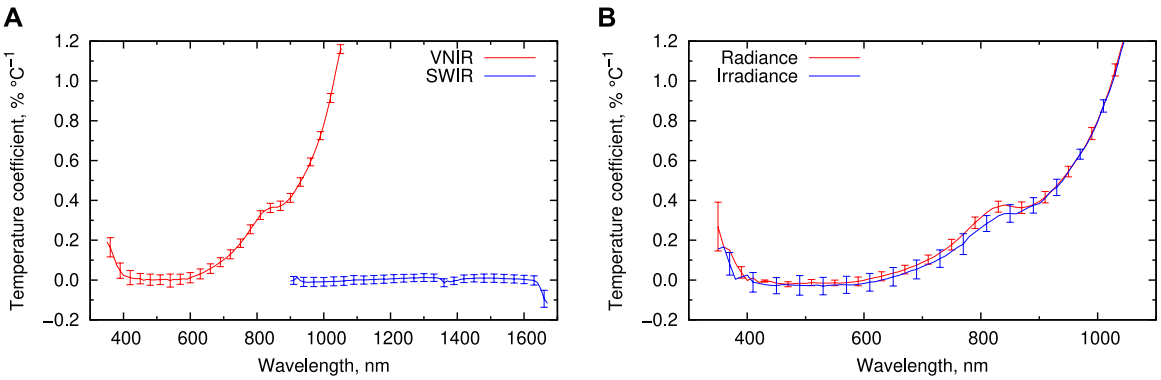


FIGURE 7
(A) Mean temperature coefficient of the VNIR and SWIR spectrometer modules of the HYPSTAR spectroradiometers measured at 30 °C using the irradiance entrance; **(B)** mean temperature coefficient of three VNIR spectrometer modules (of one XR and two SR units) measured with the radiance and irradiance entrances at 30°C. The error bars indicate the standard deviation of the temperature coefficients of 17 VNIR and eight SWIR modules **(A)** and three VNIR modules for both radiance and irradiance measurements **(B)**.

normalised to 30°C and the thermal dependence of responsivity was approximated with a second order polynomial for each spectral band.

Second order fit implies that the thermal coefficients were not constant throughout the characterised temperature range. However, the coefficients of the second degree terms of the fitted polynomials were small and the deviation from linear dependence was not significant. The temperature coefficients characterised at 30°C are presented as a function of wavelength in Figure 7. The thermal dependence was characterised using only the irradiance entrance for most of the units. The characterisation was repeated with radiance entrance for three units and the results obtained with radiance and irradiance entrances agreed within the standard deviations as shown in Figure 7B.

3.4 Angular response

Irradiance entrance optics should collect hemispherical radiation with an angular response that varies as the cosine of the incident angle. Deviations from this ideal behaviour are expressed by the "cosine error" $f_2(\theta,\lambda)$ in Eq. (5) below (Pulli et al., 2013):

$$f_2(\theta,\lambda) = \left[\frac{S(\theta,\lambda)}{\cos(\theta)S(0^\circ,\lambda)} - 1\right] \cdot 100\%, \quad (5)$$

where $S(\theta)$ is the dark-subtracted signal at wavelength λ when the incident angle is θ. The integral cosine error $f_2(\lambda)$ which accounts for the impact of cosine error over the hemisphere is defined as (Pulli et al., 2013):

$$f_2(\lambda) = \int_{0^\circ}^{85^\circ} |f_2(\theta,\lambda)| \sin(2\theta)\, d\theta. \quad (6)$$

Each radiometer was mounted on a computer-controlled rotation stage and illuminated by flux from a 450 W Xenon short arc gas discharge lamp (e.g., Mekaoui and Zibordi (2013) and references therein). The apparent size of the source was 1° which is roughly double the apparent size of the Sun. The integral cosine error defined by Eq. (6) was calculated after averaging the cosine errors $f_2(\theta,\lambda)$ measured at equal negative and positive incidence angles θ. The mean cosine error is shown in Figure 8.

The angular response of the radiance entrance was characterised for only a few HYPSTAR spectroradiometers using a setup similar to cosine response characterisation, but instead of the Xe source a H1 QTH lamp with a very small filament was used. As an example the characterisation result of a single HYPSTAR-SR unit measured in two orthogonal planes is shown in Figure 9. The slight asymmetry, nonuniform response within the FOV, and the FOV somewhat narrower than the nominal value given in Table 1 were characteristic to all the HYPSTAR units for which the radiance angular response was measured.

3.5 Polarisation sensitivity

Light reflected or scattered from some natural targets like sky or water surface can be linearly polarised to some degree (Brewster, 1815; Hansen and Travis, 1974). If polarising targets are observed with a polarisation-sensitive spectroradiometer, the measured signal depends on the alignment of the sensor relative to the target. Such sensitivity increases the measurement uncertainty unless appropriate models are used to exploit the additional information carried by the polarisation signatures.

The polarisation sensitivity of the HYPSTAR spectroradiometers was characterised by measuring the signal of an unpolarised stable source (integrating sphere illuminated by a QTH lamp) through a wire-grid polariser (Thorlabs WP50L-UB with typical extinction ratio over 2500 at 350 nm and increasing with wavelength) at 15° increments of the polariser rotation angle. The polarisation sensitivity, in percent, is defined as in Eq. (7) below (Zibordi et al., 2019):

$$P(\lambda) = 100\% \cdot \frac{DN_M(\lambda) - DN_m(\lambda)}{DN_M(\lambda) + DN_m(\lambda)}, \quad (7)$$

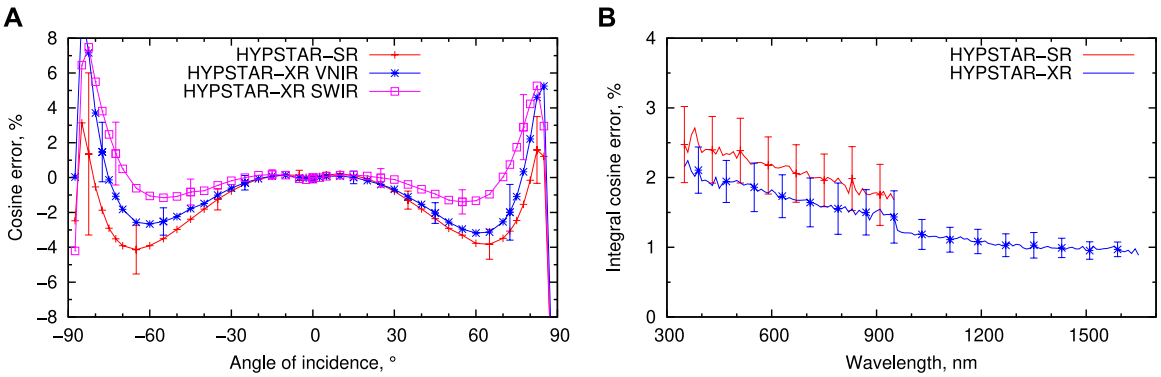


FIGURE 8
(A) Mean cosine error and **(B)** mean integral cosine error of the HYPSTAR spectroradiometers. The error bars indicate the standard deviation of the cosine error of nine SR and eight XR units.

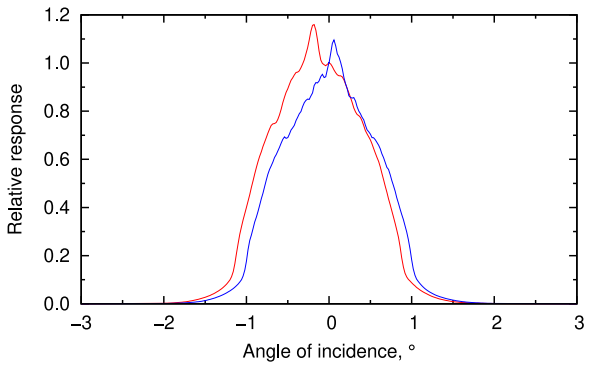


FIGURE 9
Angular response of a single HYPSTAR-SR spectroradiometer measured in two orthogonal planes and normalised to 0° incidence.

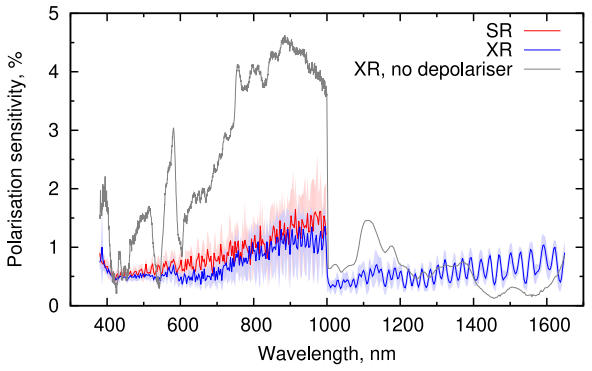


FIGURE 10
Mean sensitivity to linear polarisation. The shaded backgrounds indicate the standard deviation of the results of nine SR and seven XR units.

where $DN_m(\lambda)$ and $DN_M(\lambda)$ are the minimum and maximum values of the dark-subtracted sphere signal while rotating the polariser. The results are presented in Figure 10. The polarisation sensitivity of an early prototype of HYPSTAR-XR which did not have a depolariser in the radiance optical path is also shown for reference. The polarisation sensitivity was strongest in NIR and was reduced significantly by adding the depolariser. However, the depolariser introduced short wavelength spectral oscillations in the polarisation sensitivity similar to the MERIS scrambler described in Caron et al. (2017). For irradiance measurement mode the polarisation sensitivity was negligible due to the depolarising nature of the diffuser.

3.6 Spectral calibration

Spectral emission lines of Xe, HgAr, and Kr Pen-Ray gas discharge lamps were used for spectral calibration. The Pen-Ray lamps were measured with both optical entrances. The lamp was placed as close as possible to the irradiance entrance, without touching the protective glass dome. Behind the lamp was a white sheet of PTFE which covered the entire FOV of the radiance optics, therefore, radiance measurement recorded the lamp flux that was diffusely scattered from the PTFE.

Gaussian functions were fitted to some selected spectral emission lines. A fourth-order polynomial was used to fit the series of Gaussian means. The regression coefficients correspond to the spectral calibration coefficients used to convert pixel index to wavelength.

The different optical paths of the radiance and irradiance measurement inside the HYPSTAR result in different spectral response functions. The mean difference between the radiance and irradiance spectral calibrations is shown in Figure 11.

3.7 Spectral stray light

A fraction of incoming photons of a certain wavelength are scattered inside the spectrometer and incorrectly recorded by pixels corresponding to some other wavelength. The full recorded spectrum corresponding to monochromatic input and normalised to peak value is called a spectral line spread function (LSF) (Zong

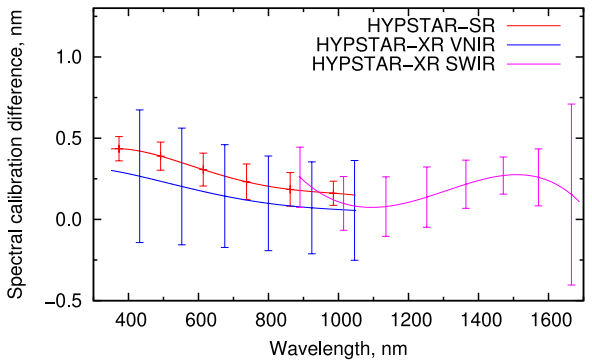


FIGURE 11
Mean difference between the radiance and irradiance spectral calibration. The error bars indicate the standard deviation of the results of nine SR and eight XR units.

et al., 2006). By tuning an adjustable monochromatic source through the entire spectral range of the sensor and recording the LSFs corresponding to each pixel, a spectral stray light matrix (SLM) can be constructed.

The SLM was determined for all the VNIR and SWIR spectrometer modules without the rest of the components (entrance optics, fibres, multiplexer) of the radiance and irradiance optical paths. A double monochromator illuminated by a QTH broadband source was used as the adjustable source of monochromatic excitation and the light was guided into the spectrometer module with a single core multimode fibre. A condenser lens was used to couple the light from the monochromator into the fibre at geometry corresponding to the nominal numerical aperture of the spectrometer module. The measured SLMs of a single VNIR and SWIR module are shown in Figure 12. The visible stray light features were found roughly similar yet with varying intensity in all units.

The spectral stray light characteristics of a spectrometer module depend on illumination geometry (Kuusk et al., 2018). The different optical paths of the radiance and irradiance measurements modes of each HYPSTAR sensor result in different LSFs. Figure 13 shows the radiance and irradiance of a green diode laser measured by a HYPSTAR-SR unit compared to the corresponding LSF of its VNIR spectrometer module (a single column of the SLM shown in Figure 12A). The centre wavelength and width of the main peak is slightly different for all these three measurements. The narrow peak at double the excitation wavelength is the second order diffraction that is largely suppressed (over three orders of magnitude) but not entirely blocked.

The measurement time was 12–15 h and over 2 h for each VNIR and SWIR module, respectively. Characterising the radiance and irradiance modes separately with the optical throughput reduced by the full optical path would extend the characterisation time of a single HYPSTAR to hundred(s) of hours. The experiment time could be reduced by measuring the LSF at selected wavelengths and modelling (Ylianttila et al., 2005; Kreuter and Blumthaler, 2009; Shen et al., 2009) or interpolating (Barlier-Salsi, 2014) the full SLM. This approach would likely give good results for the SWIR module since the SLM does not have fine features and varies smoothly across the spectral range (Figure 12B). However, the SLM of the VNIR module shown in Figure 12A is much more complex and has fine features that can not be easily modelled or interpolated. The most practical characterisation approach likely involves the combination of LSFs measurements for each pixel (or at least every few pixels) at shorter wavelengths and for a more sparse set of pixels in the NIR.

The stray light of the VNIR module significantly increases above 1100 nm, but the effect on field measurements is marginal due to the very low sensitivity of the silicon detector in this spectral region. Likewise, the sensitivity drops in the UV (as well as the natural illumination) and the stray light was not characterised below 300 nm.

The temperature coefficient in the UV increases, as can be seen in Figure 7. Similar results obtained for a spectrometer with a silicon charge-coupled device (CCD) array detector have been explained by the temperature-dependent reflectivity coefficients of the silicon

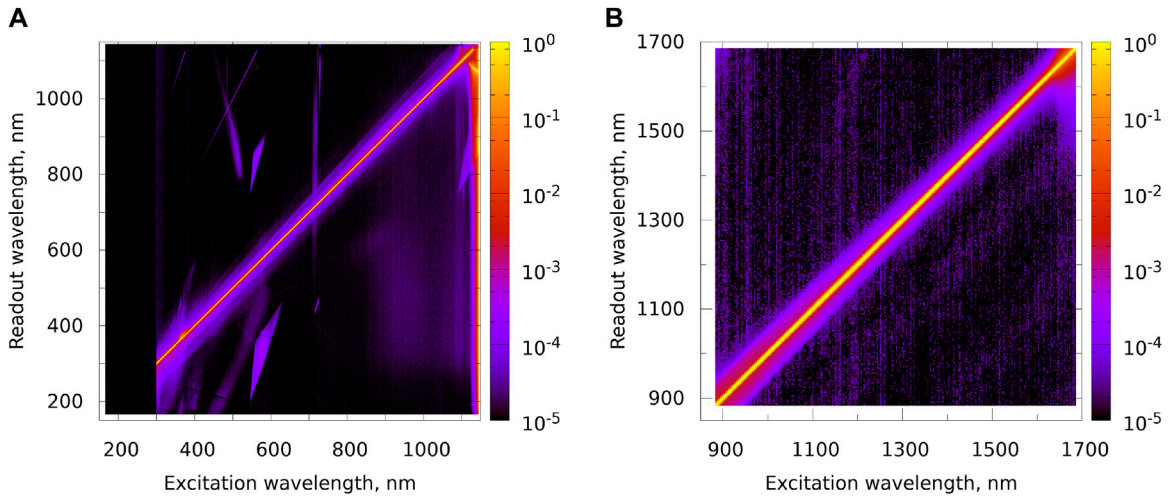


FIGURE 12
Spectral stray light matrices of only a single VNIR **(A)** and SWIR **(B)** spectrometer module measured without the rest of the HYPSTAR optical path.

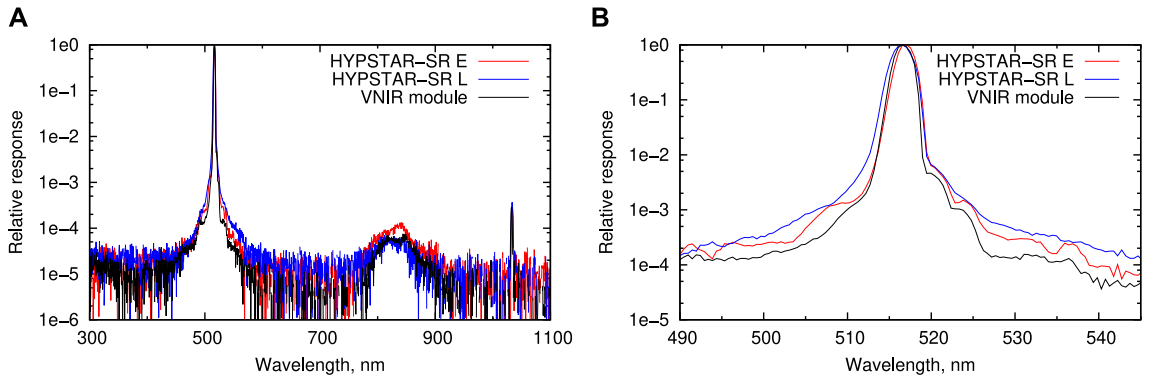


FIGURE 13
(A) The normalised signal of a green diode laser measured with the radiance (L) and irradiance (E) entrance of a HYPSTAR-SR and the line spread function (LSF) of the VNIR spectrometer module measured without the rest of the HYPSTAR optical path and **(B)** zoom in to the main peak at the excitation wavelength.

material (see Nevas et al. (2012) and references therein). However, the dark-subtracted raw signal of the incandescent source used for the characterisation was nearly three orders of magnitude lower at 350 nm compared to the peak signal at 760 nm, which gives reason to believe that the increase of the measured temperature coefficient in the UV includes stray light contributions from the longer wavelengths, for which the temperature dependence of the silicon photodetector is stronger.

4 Reference LED measurements and long-term stability

One of the unique features of the HYPSTAR system is the reference LED for monitoring the stability of the radiometric calibration during long-term unsupervised deployment. It is rather common that the responsivity of radiometers change over time (Vabson et al., 2024). In addition to the inherent sensitivity change (usually decay) of the radiometer there is additional external contribution related to long-term unattended outdoor measurements which is the contamination of the sensor's optics by ambient conditions, including weather and wildlife activity. The responsivity change can be monitored by regularly measuring a stable reference source. The HYPSTAR systems are programmed to measure the reference LED at night to reduce the amount of background illumination affecting this measurement. The generally lower nighttime temperatures (and associated lower temperature variations) have the advantage to limit the thermal noise. Moreover, the nightly measurements do not interfere with the daily surface reflectance measurement sequences.

The reference LED measurements are illustrated by the time series of two HYPSTAR deployments. Three measurement sequences of LED and dark acquisitions were scheduled for each night at 1 hour intervals around the local midnight. Initially, due to the limitations of the host unit software, the sequence contained only a single light measurement with the irradiance entrance followed by ten dark acquisitions. After the host system software update in the middle of July 2023 the sequence was changed to ten LED measurements followed by ten dark measurements with both entrances. The optical entrances were individually aligned with the reference LED by tilt axis movement of the PT before the measurement. Some of the scheduled acquisitions were not successful mainly for three reasons: 1) failure to reach the LED temperature setpoint within 2 min; 2) rain detected and sequence aborted or skipped; 3) system downtime either due to the site activities (dredging works at the HYPSTAR-SR location) or software errors (both sites were used for beta-testing the host system software developments which on few occasions required a site visit to fix).

The HYPSTAR-SR system was deployed on 27 April 2023 in the Võrtsjärv Limnological Station (Nõges et al., 2001) on the shore of Lake Võrtsjärv in central Estonia. The reference LED measurements were started on 8 May and 14 July for irradiance and radiance, respectively. The LED acquisition time series is displayed in Figure 14A as percent difference from the mean of the entire time series. Each data point was calculated as the mean light signal minus the mean dark signal and averaged over all the VNIR detector pixels without applying any calibration or corrections to the raw data. The decrease of variability of the irradiance data in the middle of July is caused by better averaging after the light measurement count was increased. Both radiance and irradiance signals decreased at about −0.5 % months^{-1} until in the middle of September there was a sudden decrease of the measured LED signal, especially for the radiance measurements. The radiometer and LED optics were cleaned on 21 September and the measured LED signals returned to the original levels. Before cleaning there were some light spider webs covering the radiance and irradiance entrances, the window of the reference LED looked visually clean.

The HYPSTAR-XR system was deployed on 30 March 2023 in a rural area in South-Eastern Estonia at the Järvselja Experimental Forestry Centre. It is mounted above a mixed forest on top of a 30 m scaffolding mast which is part of the SMEAR-Estonia research station infrastructure (Noe et al., 2015). The irradiance (radiance) reference LED measurements started on 25 May (19 July), and the corresponding time series are shown in Figure 14B. The sensor optics were cleaned on 19 September from spider webs, whitish deposit (possibly dust or pollen) and a brown spot of unknown origin. As for the HYPSTAR-SR, the cleaning procedure restored the LED signals to the initial levels.

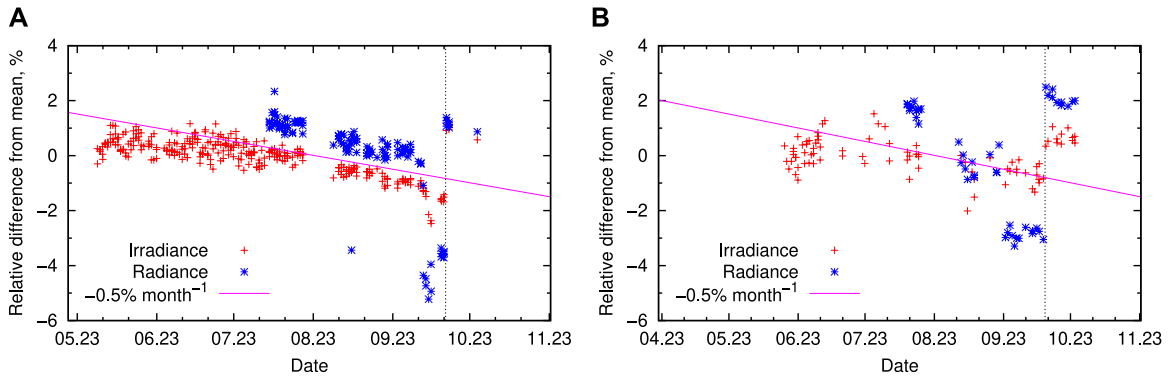


FIGURE 14
Time series of the reference LED signal as percent difference from the mean for HYPSTAR-SR **(A)** and HYPSTAR-XR **(B)**. The horizontal axis starts at the time of field deployment, the vertical dotted lines indicate cleaning of the optical windows of the radiometer and the reference LED. −0.5 % months^{-1} rate is shown for reference.

The reference LED measurement time series presented in Figure 14 indicate that the main contribution of the long-term responsivity change of these two HYPSTAR deployments is caused by the contamination of the entrance optics. If the radiance and irradiance measurement time series have different trends, it is quite likely that the contamination is on the radiometer entrance optics. However, if the trends are similar like for the HYPSTAR-SR in July-August (Figure 14A) it is not possible to determine if the contamination affects the radiometer entrance optics or the LED window. Nevertheless, the reference LED measurements are helpful for detecting major contamination events like the spider webs that appeared in September on both sites.

Most of the HYPSTAR radiometers of the third manufacturing batch have been calibrated only once and there is no calibration history that could be used for evaluation of the long-term stability. Only the two HYPSTARs that were deployed at the Estonian sites have post-deployment calibration available from May 2024. The radiometers were calibrated before and after cleaning the entrance optics to evaluate also the impact of contamination. The mean change of radiometric responsivity of the HYPSTAR-SR (HYPSTAR-XR VNIR; SWIR) compared to the pre-deployment calibration made in January 2023 was −1.5% (0.2%; −0.4%) for radiance and 0.6% (0.4%; 0.4%) for irradiance. The mean impact of fore-optics contamination was −0.8% (−0.8%; −0.4%) for radiance and −2.2% (−1.4%; −0.7%) for irradiance. The change of responsivity over 16 months remained within the calibration uncertainty for both of these HYPSTAR radiometers.

5 Future improvements

The HYPERNETS network is expected to expand slowly in coming years which requires production of new HYPSTAR systems (Ruddick et al., 2024a). There are a number of design refinements that are planned to be implemented:

- During the prototyping and testing phase it was necessary to have easy access to system components inside the enclosure of the host unit. As can be seen in Figure 3B there is a lot of free space inside the host unit and the layout of the components can be optimised which allows using smaller and lighter enclosure.
- Currently the two surveillance cameras are powered by 12 V from the host system and use either wired or wireless data link depending on the site infrastructure. Adding a power over Ethernet (PoE) switch to the host unit and replacing the cameras with PoE-capable ones allows unifying the system topology by using a single cable for both power and data.
- The cables interconnecting the subsystems have plastic IP-68-rated Samtec AccliMate series bayonet connectors. The alignment keys of these circular connectors are rather small and the plastic shell not rigid enough to prevent mismating by 90° or 180° if the contact pin arrangement allows it (e.g., the four-pin input power connector) and slightly more force is applied. The connectors will be replaced by more robust ones that can not be easily mated in wrong orientation.
- It has been observed that LEDs tend to exhibit instability in light output for a period of time right after manufacturing. Example graphs by Liu et al. (2012) show that for the first couple of hundred of hours the luminous efficiency is unstable, but at some point it reaches a plateau before starting to gradually degrade. The LEDs used in the HYPSTAR reference units produced during the H2020/HYPERNETS project were not aged before deployment in the field. Pre-ageing of the LEDs is planned as a future improvement for the next HYPSTAR reference units.
- After powering on with constant current, the LEDs exhibit a short-term optical output power change related to resistance change due to internal heating until thermal equilibrium is reached. During this heating period a drop in diode forward voltage V_f, typically in the −1.5 mV K^{-1} to −2.5 mV K^{-1} range, is observed (Eugène and Deswert, 2009). Since power is a function of both current and voltage, the radiated output power drops along with V_f if the current is held constant. The reference units manufactured so far use only passive temperature monitoring. A setpoint temperature above ambient is chosen and when the LED temperature reaches the setpoint the radiometer is signalled to start the

measurement. The reference unit design can be improved by adding an active thermal control for temperature stabilisation.

- The reference units presently feature a white LED which does not emit in the SWIR. Adding SWIR diode(s) would be desirable for monitoring the calibration stability of the HYPSTAR-XR units. While high-power, VNIR broadband LEDs are readily available thanks to phosphor conversion and common lighting technologies, the broadband SWIR emitters available on the market have a significantly lower power output. Narrowband diodes can alternatively be used, especially because it is not essential to monitor all wavelengths to characterise the calibration stability.
- Characterising the spectral stray light only for the spectrometer module without the entrance optics, fibres, and multiplexer does not adequately represent the spectral stray light of neither radiance nor irradiance measurement. The spectral stray light measurement has to characterise the entire optical path.
- Only radiometric and spectral calibration coefficients and non-linearity correction factors are currently used in the hypernets-processor (De Vis et al., 2024b). The rest of the characterisations described in Section 3 need further work, especially in terms of uncertainty evaluation for being mature enough to be incorporated in the data processing pipeline.

6 Conclusion

A new hyperspectral radiometer system HYPSTAR is described, which enables fully automated field measurements of the multiangular reflectance of land and water targets. The hyperspectral design is suitable to the validation of remote sensing satellite observations from any sensor of choice. The multiangular capability is especially useful for validating the land data with *in-situ* acquisitions captured at (or near) the satellite view geometry.

The HYPSTAR spectroradiometers are available in two configurations. The HYPSTAR-SR variant covers the VNIR spectral range at 3 nm FWHM resolution and is deployed at water sites. The HYPSTAR-XR units, which are used at the land sites, extend the spectral range to 1680 nm with a 10 nm spectral resolution in the SWIR domain. All HYPSTAR radiometers have both radiance and irradiance optical entrances, multiplexed into a single spectrometer module for the SR units and into a set of modules for the XR units. The multiplexer acts as a mechanical shutter when neither of the entrance is selected. This design reduces 1) laboratory characterisation efforts; 2) uncertainties due to correlations between radiance and irradiance measurements; and 3) cost, mass, size, and power consumption. The tradeoffs are reduced optical throughput and the impossibility of making concurrent radiance and irradiance measurements. The spectroradiometers also include a 5 MP RGB camera coaligned with the radiance and irradiance entrances for capturing diagnostic snapshots of the targets.

The spectroradiometer is mounted on a two-axis PT unit that provides full rotational freedom, including towards the LED source used to monitor the stability of the radiometric calibration. The system is controlled by a host unit that takes care of the scheduling and data acquisition, storage, and transfer to the central WATERHYPERNET or LANDHYPERNET server.

The performance of the HYPSTAR spectroradiometers was studied in the laboratory. The characterised parameters include radiometric responsivity, SNR, non-linearity, thermal sensitivity, angular response, polarisation sensitivity, spectral calibration, and spectral stray light. The average and standard deviation of the characteristics of nine SR and eight XR units are presented. Not enough calibration history has been accumulated for evaluating the long-term stability of the HYPSTAR radiometers. The pre- and post-deployment radiometric responsivities agreed within calibration uncertainty after 1 year deployment in the field for one SR and one XR unit.

The reference LED measurements are demonstrated for a HYPSTAR-SR deployment at an inland water site and a HYPSTAR-XR setup in a hemiboreal mixed forest for 4–5 months in the summer and autumn. Decay of the radiometric responsivity was evident for both setups, as well as recovery to the initial level after cleaning the fore-optics.

Data availability statement

The raw data supporting the conclusions of this article will be made available by the authors, without undue reservation.

Author contributions

JK: Conceptualization, Data curation, Formal Analysis, Funding acquisition, Investigation, Methodology, Project administration, Resources, Software, Supervision, Visualization, Writing–original draft, Writing–review and editing, Validation. AC: Investigation, Methodology, Resources, Software, Writing–review and editing. DD: Conceptualization, Funding acquisition, Methodology, Project administration, Supervision, Validation, Writing–review and editing. KD: Investigation, Resources, Visualization, Writing–review and editing. KF: Investigation, Resources, Software, Writing–review and editing. JKi: Methodology, Resources, Writing–review and editing. KL: Data curation, Formal Analysis, Investigation, Methodology, Resources, Software, Visualization, Writing–original draft, Writing–review and editing. EL: Conceptualization, Methodology, Resources, Writing–review and editing. SM: Methodology, Resources, Writing–review and editing. CP: Conceptualization, Methodology, Resources, Software, Writing–review and editing. KR: Conceptualization, Funding acquisition, Methodology, Project administration, Supervision, Validation, Writing–original draft, Writing–review and editing.

Funding

The author(s) declare that financial support was received for the research, authorship, and/or publication of this article. This study was conducted by the HYPERNETS project funded by the European Union's Horizon 2020 research and innovation

programme (grant agreement 775983), by the HYPERNET-POP project funded by the European Space Agency (contract 4000139081/22/I-EF), and using the facilities funded by the Estonian Research Council grant TT8 and the Estonian State Shared Service Centre project KosEST (grant number 2014-2020.4.01.20-0284).

Acknowledgments

The authors would like to thank the partners of the HYPERNETS project for setting up and operating the HYPSTAR systems at several field sites and providing useful feedback for improving the design. The Estonian University of Life Sciences is acknowledged for operating the SMEAR-Estonia and Võrtsjärv Limnological Station infrastructure and hosting the HYPSTAR-XR and HYPSTAR-SR systems. We would like to express our deepest gratitude to the two reviewers whose insightful comments and constructive feedback greatly contributed to the improvement of this manuscript.

Conflict of interest

The intellectual property rights of the HYPSTAR design and know-how belong to University of Tartu and Sorbonne University. The HYPSTAR® trademark is registered by University of Tartu.

JK is the owner and chief executive officer of the private limited company RSware OÜ (Estonia) which is preparing the commercialisation of the HYPSTAR spectroradiometer systems.

The remaining authors declare that the research was conducted in the absence of any commercial or financial relationships that could be construed as a potential conflict of interest.

Publisher's note

All claims expressed in this article are solely those of the authors and do not necessarily represent those of their affiliated organizations, or those of the publisher, the editors and the reviewers. Any product that may be evaluated in this article, or claim that may be made by its manufacturer, is not guaranteed or endorsed by the publisher.

References

Banks, A. C., Vendt, R., Alikas, K., Bialek, A., Kuusk, J., Lerebourg, C., et al. (2020). Fiducial reference measurements for satellite ocean colour (FRM4SOC). *Remote Sens.* 12, 1322. doi:10.3390/rs12081322

Barlier-Salsi, A. (2014). Stray light correction on array spectroradiometers for optical radiation risk assessment in the workplace. *J. Radiol. Prot.* 34, 915–930. doi:10.1088/0952-4746/34/4/915

Białek, A., Goodman, T., Woolliams, E., Brachmann, J. F. S., Schwarzmaier, T., Kuusk, J., et al. (2020). Results from verification of reference irradiance and radiance sources laboratory calibration experiment campaign. *Remote Sens.* 12, 2220. doi:10.3390/rs12142220

Bouvet, M., Thome, K., Berthelot, B., Bialek, A., Czapla-Myers, J., Fox, N. P., et al. (2019). RadCalNet: a radiometric calibration network for earth observing imagers operating in the visible to shortwave infrared spectral range. *Remote Sens.* 11, 2401. doi:10.3390/rs11202401

Brewster, D. (1815). On the laws which regulate the polarisation of light by reflexion from transparent bodies. By David Brewster, LL. D. F. R. S. Edin. and F. S. A. Edin. In a letter addressed to Right Hon. Sir Joseph Banks, Bart. K. B. P. R. S. *Philos. Trans. R. Soc. Lond* 105, 125–159. doi:10.1098/rstl.1815.0010

Caron, J., Bézy, J.-L., Courrèges-Lacoste, G. B., Sierk, B., Meynart, R., Richert, M., et al. (2017). "Polarization scramblers in earth observing spectrometers: lessons learned from Sentinel-4 and 5 phases A/B1," in *International conference on space optics — ICSO 2012*. Editors B. Cugny, E. Armandillo, and N. Karafolas (Bellingham, WA, United States: SPIE). doi:10.1117/12.2309044

Carswell, T., Costa, M., Young, E., Komick, N., Gower, J., and Sweeting, R. (2017). Evaluation of MODIS-Aqua atmospheric correction and chlorophyll products of western North American coastal waters based on 13 years of data. *Remote Sens.* 9, 1063. doi:10.3390/rs9101063

Cengiz, C., Azarifar, M., and Arik, M. (2022). A critical review on the junction temperature measurement of light emitting diodes. *Micromachines* 13, 1615. doi:10.3390/mi13101615

Cesana, I., Bresciani, M., Cogliati, S., Giardino, C., Gupana, R., Manca, D., et al. (2021). Preliminary investigation on phytoplankton dynamics and primary production models in an oligotrophic lake from remote sensing measurements. *Sensors* 21, 5072. doi:10.3390/s21155072

Cogliati, S., Sarti, F., Chiarantini, L., Cosi, M., Lorusso, R., Lopinto, E., et al. (2021). The PRISMA imaging spectroscopy mission: overview and first performance analysis. *Remote Sens. Environ.* 262, 112499. doi:10.1016/j.rse.2021.112499

De Vis, P., Howes, A., Vanhellemont, Q., Bialek, A., Morris, H., Sinclair, M., et al. (2024a). Feasibility of satellite vicarious calibration using HYPERNETS surface reflectances from Gobabeb and Princess Elisabeth Antarctica sites. *Front. Remote Sens.* 5. doi:10.3389/frsen.2024.1323998

De Vis, P., Hunt, S., Vanhellemont, Q., Ruddick, K. G., and Bialek, A. (2024b). Generating hyperspectral reference measurements for surface reflectance from the LANDHYPERNET and WATERHYPERNET networks. *Front. Remote Sens.* 5. doi:10.3389/frsen.2024.1347230

Dogliotti, A. I., Piegari, E., Rubinstein, L., Perna, P., and Ruddick, K. G. (2024). Using the automated HYPERNETS hyperspectral system for multi-mission satellite ocean colour validation in the Río de la Plata, accounting for different spatial resolutions. *Front. Remote Sens.* 5. doi:10.3389/frsen.2024.1354662

Doxaran, D., ElKilani, B., Corizzi, A., and Goyens, C. (2024). Validation of satellite-derived water-leaving reflectance in contrasted French coastal waters based on HYPERNETS field measurements. *Front. Remote Sens.* 4. doi:10.3389/frsen.2023.1290110

Eugène, C., and Deswert, J.-M. (2009). "Photoelectric characterization of electroluminescent photodiodes," in *LEDs for lighting applications*. Editor P. Mottier (John Wiley and Sons, Ltd.), 165–196. doi:10.1002/9780470612019.ch6

Gatebe, C. K., and King, M. D. (2016). Airborne spectral BRDF of various surface types (ocean, vegetation, snow, desert, wetlands, cloud decks, smoke layers) for remote sensing applications. *Remote Sens. Environ.* 179, 131–148. doi:10.1016/j.rse.2016.03.029

González Vilas, L., Brando, V. E., Concha, J. A., Goyens, C., Dogliotti, A. I., Doxaran, D., et al. (2024). Validation of satellite water products based on HYPERNETS *in situ* data using a match-up database (MDB) file structure. *Front. Remote Sens.* 5. doi:10.3389/frsen.2024.1330317

Gorman, E. T., Kubalak, D. A., Patel, D., Dress, A., Mott, D. B., Meister, G., et al. (2019). "The NASA plankton, aerosol, cloud, ocean ecosystem (PACE) mission: an emerging era of global, hyperspectral earth system remote sensing," in *Sensors, systems, and next-generation satellites XXIII*. Editors S. P. Neeck, P. Martimort, and T. Kimura (Bellingham, WA, United States: International Society for Optics and Photonics SPIE). doi:10.1117/12.2537146

Goyens, C., and Ruddick, K. (2023). Improving the standard protocol for above-water reflectance measurements: 1. estimating effective wind speed from angular variation of sunglint. *Appl. Opt.* 62, 2442–2455. doi:10.1364/AO.481787

Goyens, C., Ruddick, K., and Kuusk, J. (2018). "Spectral requirements for the development of a new hyperspectral radiometer integrated in automated networks - the Hypernets sensor," in 2018 9th Workshop on Hyperspectral Image and Signal Processing: Evolution in Remote Sensing (WHISPERS), Amsterdam, Netherlands, 23-26 September 2018, 1–5. doi:10.1109/WHISPERS.2018.8747259

Green, R. O., Mahowald, N., Thompson, D. R., Ung, C., Brodrick, P., Pollock, R., et al. (2023). "Performance and early results from the earth surface mineral dust source investigation (EMIT) imaging spectroscopy mission," in 2023 IEEE Aerospace Conference, Big Sky, MT, USA, 04-11 March 2023, 1–10. doi:10.1109/AERO55745.2023.10115851

Hansen, J. E., and Travis, L. D. (1974). Light scattering in planetary atmospheres. *Space Sci. Rev.* 16, 527–610. doi:10.1007/BF00168069

Hasinoff, S. W. (2014). "Photon, Poisson noise," in *Computer vision: a reference guide*. Editor K. Ikeuchi (Boston, MA: Springer US), 608–610. doi:10.1007/978-0-387-31439-6_482

Hooker, S. B., Bernhard, G., Morrow, J. H., Booth, C. R., Comer, T., Lind, R. N., et al. (2012). *Optical sensors for planetary radiant energy (OSPREy): calibration and*

validation of current and next-generation NASA missions. Tech. rep. Greenbelt, MD, USA: NASA.

Konnik, M., and Welsh, J. (2014). *High-level numerical simulations of noise in CCD and CMOS photosensors: review and tutorial*. ArXiv. doi:10.48550/arXiv.1412.4031

Kreuter, A., and Blumthaler, M. (2009). Stray light correction for solar measurements using array spectrometers. *Rev. Sci. Instrum.* 80, 096108. doi:10.1063/1.3233897

Kuusk, A., Kuusk, J., and Lang, M. (2014). Measured spectral bidirectional reflection properties of three mature hemiboreal forests. *Agric. For. Meteorol.* 185, 14–19. doi:10.1016/j.agrformet.2013.10.011

Kuusk, J., Ansko, I., Bialek, A., Vendt, R., and Fox, N. (2018). Implication of illumination beam geometry on stray light and bandpass characteristics of diode array spectrometer. *IEEE J. Sel. Top. Appl. Earth Obs. Remote Sens.* 11, 2925–2932. doi:10.1109/JSTARS.2018.2841772

Liu, L., Ling, M., Yang, J., Xiong, W., Jia, W., and Wang, G. (2012). Efficiency degradation behaviors of current/thermal co-stressed GaN-based blue light emitting diodes with vertical-structure. *J. Appl. Phys.* 111. doi:10.1063/1.4712030

Mekaoui, S., and Zibordi, G. (2013). Cosine error for a class of hyperspectral irradiance sensors. *Metrologia* 50, 187–199. doi:10.1088/0026-1394/50/3/187

Mobley, C. D. (1999). Estimation of the remote-sensing reflectance from above-surface measurements. *Appl. Opt.* 38, 7442–7455. doi:10.1364/AO.38.007442

Morris, H., Sinclair, M., De Vis, P., and Bialek, A. (2024). Utilising LANDHYPERNET data products over a deciduous broadleaf forest to validate Sentinel-2 and Landsat surface reflectance products. *Front. Remote Sens.* 5. doi:10.3389/frsen.2024.1322760

Moses, W. J., Bowles, J. H., Lucke, R. L., and Corson, M. R. (2012). Impact of signal-to-noise ratio in a hyperspectral sensor on the accuracy of biophysical parameter estimation in case II waters. *Opt. Express* 20, 4309–4330. doi:10.1364/OE.20.004309

Nevas, S., Teuber, A., Sperling, A., and Lindemann, M. (2012). Stability of array spectroradiometers and their suitability for absolute calibrations. *Metrologia* 49, S48–S52. doi:10.1088/0026-1394/49/2/S48

Noe, S. M., Niinemets, Ü., Krasnova, A., Krasnov, D., Motallebi, A., Kängsepp, V., et al. (2015). SMEAR Estonia: perspectives of a large-scale forest ecosystem–atmosphere research infrastructure. *For. stud.* 63, 56–84. doi:10.1515/fsmu-2015-0009

Nõges, P., Kangur, A., Järvalt, A., and Nõges, T. (2001). History of hydrological and biological investigations of lake Võrtsjärv. *Proc. Est. Acad. Sci. Biol. Ecol.* 50, 180–193. doi:10.3176/biol.ecol.2001.3.04

Pacheco-Labrador, J., Ferrero, A., and Martín, M. P. (2014). Characterizing integration time and gray-level-related nonlinearities in a NMOS sensor. *Appl. Opt.* 53, 7778–7786. doi:10.1364/AO.53.007778

Peters, S., Laanen, M., Groetsch, P., Ghezehegn, S., Poser, K., Hommersom, A., et al. (2018). "WISPstation: a new autonomous above water radiometer system," in *Proceedings of the ocean optics XXIV conference* (Croatia: Dubrovnik), 7–12. doi:10.5281/zenodo.2533079

Pulli, T., Kärhä, P., and Ikonen, E. (2013). A method for optimizing the cosine response of solar UV diffusers. *J. Geophys. Res. Atmos.* 118, 7897–7904. doi:10.1002/jgrd.50642

Ruddick, K. G., Bialek, A., Brando, V. E., De Vis, P., Dogliotti, A. I., Doxaran, D., et al. (2024a). HYPERNETS: a network of automated hyperspectral radiometers to validate water and land surface reflectance (380–1680 nm) from all satellite missions. *Front. Remote Sens.* 5. doi:10.3389/frsen.2024.1372085

Ruddick, K. G., Brando, V. E., Corizzi, A., Dogliotti, A. I., Doxaran, D., Goyens, C., et al. (2024b). WATERHYPERNET: a prototype network of automated *in situ* measurements of hyperspectral water reflectance for satellite validation and water quality monitoring. *Front. Remote Sens*. doi:10.3389/frsen.2024.1347520

Ruddick, K. G., Voss, K., Boss, E., Castagna, A., Frouin, R., Gilerson, A., et al. (2019). A review of protocols for fiducial reference measurements of water-leaving radiance for validation of satellite remote-sensing data over water. *Remote Sens.* 11, 2198. doi:10.3390/rs11192198

Salim, S. G. R., Fox, N. P., Theocharous, E., Sun, T., and Grattan, K. T. V. (2011). Temperature and nonlinearity corrections for a photodiode array spectrometer used in the field. *Appl. Opt.* 50, 866–875. doi:10.1364/AO.50.000866

Sanders, C. L. (1972). Accurate measurements of and corrections for nonlinearities in radiometers. *J. Res. Natl. Bur. of Stand. A Phys. and Chem.* 76 (5), 437–453. doi:10.6028/jres.076A.039

Schinke, C., Pollex, H., Hinken, D., Wolf, M., Bothe, K., Kröger, I., et al. (2020). Calibrating spectrometers for measurements of the spectral irradiance caused by solar radiation. *Metrologia* 57, 065027. doi:10.1088/1681-7575/abafc5

Shen, H., Pan, J., Feng, H., and Liu, M. (2009). Stray light errors in spectral colour measurement and two rejection methods. *Metrologia* 46, 129–135. doi:10.1088/0026-1394/46/1/017

Slivkoff, M. M. (2014). "*Ocean colour remote sensing of the Great Barrier Reef waters*". Ph.D. thesis (Bentley, Australia: Curtin University).

Storch, T., Honold, H.-P., Chabrillat, S., Habermeyer, M., Tucker, P., Brell, M., et al. (2023). The EnMAP imaging spectroscopy mission towards operations. *Remote Sens. Environ.* 294, 113632. doi:10.1016/j.rse.2023.113632

Vabson, V., Ansko, I., Duong, K., Vendt, R., Kuusk, J., Ruddick, K., et al. (2024). Complete characterization of ocean color radiometers. *Front. Remote Sens.* 5. doi:10.3389/frsen.2024.1320454

Ylianttila, L., and Schreder, J. (2005). Temperature effects of PTFE diffusers. *Opt. Mater.* 27, 1811–1814. doi:10.1016/j.optmat.2004.11.008

Ylianttila, L., Visuri, R., Huurto, L., and Jokela, K. (2005). Evaluation of a single-monochromator diode array spectroradiometer for sunbed UV-radiation measurements. *Photochem. Photobiol.* 81, 333–341. doi:10.1111/j.1751-1097.2005.tb00192.x

Zibordi, G., Mélin, F., Berthon, J.-F., Holben, B., Slutsker, I., Giles, D., et al. (2009). AERONET-OC: a network for the validation of ocean color primary products. *J. Atmos. Ocean. Technol.* 26, 1634–1651. doi:10.1175/2009JTECHO654.1

Zibordi, G., Talone, M., and Jankowski, L. (2017). Response to temperature of a class of *in situ* hyperspectral radiometers. *J. Atmos. Ocean. Technol.* 34, 1795–1805. doi:10.1175/JTECH-D-17-0048.1

Zibordi, G., Voss, K. J., Johnson, B. C., and Mueller, J. (2019). IOCCG ocean optics and biogeochemistry protocols for satellite ocean colour sensor validation. *IOCCG Protoc. Ser.* 3. doi:10.25607/OBP-691

Zong, Y., Brown, S. W., Johnson, B. C., Lykke, K. R., and Ohno, Y. (2006). Simple spectral stray light correction method for array spectroradiometers. *Appl. Opt.* 45, 1111–1119. doi:10.1364/AO.45.001111

frontiers | Frontiers in Remote Sensing

TYPE Original Research
PUBLISHED 17 July 2024
DOI 10.3389/frsen.2024.1333851

Check for updates

OPEN ACCESS

EDITED BY
Agnieszka Bialek,
National Physical Laboratory, United Kingdom

REVIEWED BY
Frederic Melin,
Joint Research Centre, Italy
Davide D'Alimonte,
University of Algarve, Portugal

*CORRESPONDENCE
Paul Chamberlain,
pachamberlain@ucsd.edu

RECEIVED 06 November 2023
ACCEPTED 18 June 2024
PUBLISHED 17 July 2024

CITATION
Chamberlain P, Frouin RJ, Tan J, Mazloff M, Barnard A, Boss E, Haëntjens N and Orrico C (2024), Selecting HyperNav deployment sites for calibrating and validating PACE ocean color observations.
Front. Remote Sens. 5:1333851.
doi: 10.3389/frsen.2024.1333851

COPYRIGHT
© 2024 Chamberlain, Frouin, Tan, Mazloff, Barnard, Boss, Haëntjens and Orrico. This is an open-access article distributed under the terms of the Creative Commons Attribution License (CC BY). The use, distribution or reproduction in other forums is permitted, provided the original author(s) and the copyright owner(s) are credited and that the original publication in this journal is cited, in accordance with accepted academic practice. No use, distribution or reproduction is permitted which does not comply with these terms.

Selecting HyperNav deployment sites for calibrating and validating PACE ocean color observations

Paul Chamberlain[1]*, Robert J. Frouin[1], Jing Tan[1], Matthew Mazloff[1], Andrew Barnard[2], Emmanuel Boss[3], Nils Haëntjens[3] and Cristina Orrico[4]

[1]Scripps Institution of Oceanography, University of California, San Diego, La Jolla, CA, United States, [2]College of Earth, Ocean, and Atmospheric Sciences, Oregon State University, Corvallis, OR, United States, [3]School of Marine Sciences, University of Maine, Orono, ME, United States, [4]Sea-Bird Scientific, Bellevue, WA, United States

A novel ocean profiling float system for calibrating and validating satellite-based ocean color observations has been developed and tested. The float-based radiometric sampling system, herein referred to as HyperNav, is complementary to traditional moored in-situ observing systems and provides additional capability due to the relatively small platform size and high radiometric accuracy that allows for opportunistic deployments at locations during seasons and conditions that are best for ocean color observations. The purpose of this study is to optimize the deployment locations of an array of HyperNav systems to support the Plankton, Aerosol, Cloud, ocean Ecosystem (PACE) mission by performing System Vicarious Calibration (SVC) observations. Specifically, we present the development of logistical and scientific criteria for selecting suitable sites for developing an SVC network of profiling-float-based radiometric systems capable of calibrating and validating ocean color observations. As part of the analyses described in this paper, we have synthetically deployed HyperNav at potential US-based and international sites, including: north of Crete island; south-east of Bermuda island; south of Puerto Rico island; southwest of Port Hueneme, CA; west of Monterey, CA; west of Kona, HI; and south-west of Tahiti island. The synthetic analyses identified Kona, Puerto Rico, Crete, and Tahiti as promising SVC sites. All sites considered are suitable for generating a significant number of validation match-ups. Optimally deploying HyperNav systems at these sites during the PACE post-launch SVC campaign is expected to cost-effectively provide a large number of SVC match-ups to fulfill the PACE calibration requirements.

KEYWORDS

vicarious calibration, ocean color, upper-ocean, sampling, profiling floats

1 Introduction

For over 40 years, observations from ocean color satellites have inferred surface ocean biogeochemistry on an unprecedented spatial and temporal scale. These data have been important in understanding many of the grand challenges of our age, such as marine pollution, the global marine food web, and global carbon cycles (Groom et al., 2019; Brewin et al., 2023). Reflected sunlight entering the satellite's field of view comes mostly from atmospheric sources and only a small fraction is reflected from within the ocean. The subtleties of ocean color interpretation depend on the accuracy of the retrieved ocean color

signals and, therefore, also the accuracy of the atmospheric correction methods used to obtain these data (Gilerson et al., 2022). As such, correction schemes require that Earth-orbiting ocean color satellites be well calibrated, with known and quantified uncertainties, to obtain precise ocean color radiance spectra with a known accuracy. (Franz et al., 2007; McClain and Meister, 2012; Bisson et al., 2021).

Satellites are calibrated through a combination of pre- and post-launch observations using well-characterized optical targets. Post-launch characterizations of satellite-borne measurements are dependent on signal response for known and well-specified (i.e., lowest uncertainty) oceanic signals in a process known as system vicarious calibration (SVC). Vicarious calibration systems are observational platforms dedicated to collecting in-situ observations that can be compared to satellite ocean color data for calibration. The SVC component of satellite calibration is considered critical to reach the high accuracy necessary to make meaningful ocean color observations (Frouin et al., 2013; Johson et al., 2024). Plankton, Aerosol, Cloud, ocean Ecosystem (PACE) satellite, lauchched on February 6, 2024, carries an Ocean Color Instrument (OCI) capable of resolving reflected ocean light at 5 nm resolution spanning from the UV to the visible and into NIR spectrum and promises to transform our understanding and monitoring of phytoplankton communities and ocean biogeochemistry (Frouin et al., 2019; Werdell et al., 2019). Observations on such a fine spectral scale require substantial calibration and validation efforts to be of known uncertainty and, hence, utility.

Historically, in-situ SVC observations have been collected from two specially designed and equipped moorings: the Marine Optical Buoy (MOBY) mooring (Clark et al., 1997) located off the island of Lanai in the Hawaiian island chain, and the now decommissioned Bouée pour l'acquisition de Séries Optiques à Long Terme (BOUSSOLE) mooring (Antoine et al., 2006) located off the coast of Villefranche-sur-Mer in Southern France. The MOBY and BOUSSOLE moorings have successfully recorded over 20 years of SVC quality observations (Valente et al., 2016) and MOBY remains a critical component of any SVC array. Moorings typically record high-frequency observations at one geographical location over a long time series. These data are useful for long-term inter-calibration and resolving complex time-varying signals, but are poorly suited for resolving large spatial variability. Moorings are expensive and could be difficult to maintain: mooring equipment typically requires complicated shipping and logistics to mobilize; moorings typically require large ships to assemble and place; and surface sensors can quickly foul with biological organisms, which require regular cleaning and maintenance. Another potential limitation is that moored sensors typically collect data at fixed depths, whereas optical profiles can resolve stratification details.

The Argo semi-Lagrangian profiling float (Roemmich et al., 2019) is a complementary platform to moorings and ship-based hydrography. Core Argo floats are typically deployed from ships, then drift at 1,000 m and ascend to the surface once every 10 days to broadcast their collected temperature and salinity profiles. Argo floats only have buoyancy control and are advected by ocean currents. Argo floats are relatively low cost and are typically analyzed in concert over a large array to resolve spatial variability. There are now over 3,800 Argo floats deployed in all the world's oceans. The distributed Core Argo array complemented by targeted moorings has improved our understanding of difficult problems such as ocean currents, steric height, and heat content (Miller, 1990; Servain et al., 1998; Wong et al., 2020).

Since its original introduction, the Argo platform has been modified to carry additional sensors. The HyperNav sensor (Barnard et al., 2022) is an Argo float-borne optical sensor specifically designed for satellite SVC operations. HyperNav typically samples once per day (≈ local noon time), has a relatively small form factor, can be shipped via cargo plane, is easily deployed from a small fishing or utility boat, and costs an order of magnitude less than a comparable mooring. A distributed array of HyperNav systems, like Argo, can sample larger spatial variability than moorings alone and may reduce unexplained biases in satellite-based ocean color (Bisson et al., 2021).

Argo floats executing their standard mission can drift substantial distances over their lifetime (Chamberlain et al., 2023). SVC match-up site locations are carefully chosen to maximize the quality of SVC observations. To maximize the utility of radiometer-equipped floats for SVC match-ups and to recover the sensors for post-calibration, floats should remain in the general vicinity of the original deployment location. To accomplish this, we have devised a novel float navigation method that uses predictions of ocean currents to compute future float displacement at different drift depths. An operator can then transmit optimized mission programming to the float that adjusts the float drift depth to achieve some degree of control over position based on the structure of the ocean currents. Identifying these locations can be done using high-resolution computer simulations.

The flexibility of the HyperNav system, as well as the spatial and temporal variability in atmospheric and oceanic optical properties, motivates the construction of a distributed SVC system. SVC criteria are stringent (Zibordi et al., 2015; Zibordi and Mélin, 2017) and dependent on environmental factors, such as wind speed and aerosol optical thickness, which are seasonally variable. Consequently, the optimal distribution and timing of HyperNav deployments are not obvious but have the possibility to substantially improve the effectiveness of the array. In this publication, we attempt to optimize such a distributed system by evaluating the number of SVC and validation match-ups as well as estimating the number of match-ups per dollar spent on operations at different sites. Here SVC match-ups are calculated using two criteria: the published Zibordi and Mélin (2017) criteria, and a new criteria described and justified in this publication. We also compute a simpler, validation-specific, clear sky criteria.

We first detail the SVC match-up and validation match-up requirements in Section 2, then in Section 3, we describe the HyperNav observing system. In Section 4, we describe the criteria for optimization: a high likelihood of SVC quality match-ups, economical and easy logistics for operations, and the ability to effectively navigate the float by using ocean currents. Finally, in Sections 5 and 6 we present and discuss the results of our optimization.

2 System vicarious calibration and validation requirements

System Vicarious Calibration (SVC), originally developed for the Coastal Zone Colour Scanner (CZCS) (Gordon, 1987; Evans and Gordon, 1994), consists of comparing retrievals of water-leaving

radiance to in-situ measurements at the time of satellite overpass and adjusting the calibration coefficients to force agreement between retrieved and measured quantities. This strategy aims at reducing uncertainties of post-launch radiometric calibration techniques, which are not sufficiently accurate for scientific applications, and biases in atmospheric correction. It has been employed operationally for the processing of imagery from major satellite ocean-color missions (Franz et al., 2007; Frouin et al., 2013).

The suitable SVC sites must satisfy specific and rather strict criteria (Gordon, 1998; Fougnie et al., 1999; Frouin et al., 2013; Zibordi et al., 2015; Zibordi and Mélin, 2017). Firstly, the aerosols should be mostly of maritime origin or at most weakly absorbing with optical thickness below 0.1 in the near-infrared (i.e., very clear atmosphere), and the ocean surface free of whitecaps. In such situations, molecular scattering is the dominant process affecting the top-of-atmosphere (TOA) radiance in the ultraviolet and visible, reducing the impact of uncertainties associated with the atmospheric correction scheme. Selecting situations with little-absorbing aerosols is important because the ensemble of aerosol models to choose from in the operational schemes for atmospheric correction (Ahmad et al., 2010) only includes those aerosol types (i.e., single scattering albedo, $\omega_{aer} > 0.95$ at 440 nm). Secondly, the water-leaving radiance should be uniform over several pixels, and the spatial contrast should be minimal over a distance of about 10 km (Santer and Schmechtig, 2000) to minimize adjacency effects. This generally excludes coastal regions, where aerosols are likely to be absorbing and abundant, spatial variability in water-leaving radiance may be large, and the proximity of land exerts a significant influence on the TOA signal. Furthermore, the sites should experience low cloudiness (to maximize the number of high-quality match-ups) and exhibit low bio-optical complexity (e.g., to properly model/correct bidirectional effects in water-leaving radiance). Another desirable quality is high temporal stability in water and atmosphere optical properties (to minimize atmospheric correction uncertainties), especially when the satellite imagery and the in-situ data are not acquired simultaneously. Oligotrophic waters tend to meet these requirements better than productive waters, despite the water signal exerting a greated influence on the measured TOA radiance in the visible and ultraviolet. This advantage is attributed to their enhanced stability, which minimizes the impacts of satellite spatial resolution and time differences in match-ups. Employing several sites in SVC ensures a more comprehensive, robust, and globally applicable calibration process for satellite ocean color sensors, addressing the challenges associated with the inherent variability of marine environments (Bisson et al., 2021).

The MOBY site in the North Pacific (Clark et al., 2003) and the now decommissioned BOUSSOLE site in the Ligurian Sea (Antoine et al., 2008) have the desired SVC attributes (Gordon, 1998; Zibordi et al., 2015). The operational SVC of current satellite ocean-color sensors has been essentially based on water-leaving radiance data acquired at those two sites. Fougnie et al. (2002, 2010), Zibordi and Mélin (2017), and Kwiatkowska et al. (2022) considered other oceanic sites that have potential for SVC. The focus was on analyzing time series of satellite-derived remote-sensing reflectance, R_{rs}, chlorophyll concentration, Chl, diffuse attenuation coefficient at 490 nm, $K_d(490)$, and aerosol optical thickness, τ_{aer}, and Ångström coefficient, α, according to criteria on magnitude, spatial homogeneity, and temporal stability. Suitable regions were identified in various oceans, especially in the north and southeast Pacific Ocean, the Mediterranean Sea, and the eastern Indian Ocean accompanied by the best-recommended period during the year. Zibordi and Mélin (2017) concluded that the MOBY and BOUSSOLE sites are superior for likely high-quality match-ups but suggested that the Eastern Mediterranean Sea near Crete should be considered as a further SVC site. Kwiatkowska et al. (2022) recommended two sites for Copernicus SVC infrastructure located near El Hierro (Canary Islands, Spain) and Crete (Greece). Note that there is currently no consensus in the published literature regarding the specific selection criteria for SVC. For example, Zibordi and Mélin (2017) used α <1, but Kwiatkowska et al. (2022) did not use α restrictions.

Given the above, multi-year L2 satellite imagery of aerosol and surface variables were systematically analyzed in potentially suitable regions to generate a climatology with spatial and temporal variability characteristics. This allowed one to select, using complementary information about trajectory statistics and logistics considerations, the best sites for operational SVC activities using HyperNav systems. The lack of community consensus on SVC match-up criteria and the multitude of potential applications for the HyperNav data motivated the analysis of two different match-up criteria for SVC: first, the previously advanced Zibordi and Mélin (2017) criteria; second, the new criteria advanced herein.

The new criteria are similar yet somewhat different from those of previous analyses: (1) the site should be free of clouds, as well as the $5\,km^2 \times 5\,km^2$ area centered on the target pixel, to minimize adjacency effects (based on Bailey and Werdell, 2006); (2) the site should be in open Case 1 waters Morel and Prieur (1977), to minimize water complexity and land influence: (3) wind speed should be $<8\ ms^{-1}$, to minimize whitecaps; (4) the coefficient of variation of R_{rs} in the blue (e.g., 443 nm); over a $3\,km^2 \times 3\,km^2$ area should be <20%, to reduce the impact of time differences between satellite and in-situ measurements, (5) τ_{aer} should be <0.1 in the near infrared (e.g., 869 nm), to lessen aerosol influence, and (6) ω_{aer} at 550 nm should be >0.95, to remove moderately to strongly absorbing aerosols. Note that a restriction on α ($\alpha < 1$) would not eliminate dust-type aerosols since they may exhibit values much less than unity - Dubovik et al. (2002) demonstrates α values of 0.4. Such aerosols are relatively frequent over the Mediterranean Sea and off the Atlantic coast of Northern Africa (Saharan dust events). Asian dust is also transported to the Hawaiian islands, with strong influxes during spring (Parrington et al., 1983).

In the following analysis, no constraints were placed on the Sun zenith angle and Chl (all investigated sites were in low latitude Case 1 waters). Results on the potential number of match-ups may differ depending on the satellite mission and time of overpass (e.g., cloudiness may vary with the time of day), as reported by Zibordi and Mélin (2017). We only considered MODIS-Aqua in the statistical analysis (1:30 p.m. equatorial crossing, similar to the upcoming PACE). Therefore, the findings may not be readily generalized to other missions but should nonetheless give a good indication of the expected match-ups for planning SVC activities and the expected match-up for validation at those sites.

For validation purposes, the aforementioned SVC restrictions can be relaxed as long as the satellite retrievals exist (i.e., are not masked), which may exclude pixels contaminated by Sun glint and

high aerosol loadings or located too close to land and clouds in other words, pixels for which the atmospheric correction fails (Bailey and Werdell, 2006). To evaluate the suitability of sites for validation (less stringent criteria), we choose only the clear sky condition used for SVC; however, it should be noted that ocean variability may still pose challenges for validation.

3 HyperNav concept

The HyperNav system was designed to address the next-generation of satellite ocean color imagers, including near-continuous hyper-spectral coverage from the near UV to NIR bands, specifically focused on meeting the SVC needs for the PACE mission and the OCI. The HyperNav system includes 2 independent upwelling radiance sensors, each providing 2.2 nm wavelength resolution across the 350 to 900 nm spectral range. The HyperNav system also includes a 4-channel above-water downwelling irradiance sensor. Additional measurements from the HyperNav sensor system include pressure and tilt of the platform. The HyperNav system has two modes of operation: a free-fall sampling mode and an autonomous profiling float integration. For an in-depth description of the HyperNav system, see Barnard et al., 2024a; Barnard et al., 2024b, this volume. This paper focuses on using the HyperNav integrated with an autonomous profiling float equipped with a sensors for temperature, salinity and depth. We briefly describe a typical profiling sequence of the HyperNav system. The profile sequence includes the following phases: descent, park, profile phase, surface hold, and transmission. The descent phase typically occurs after initial deployment or surface transmission. During this phase, an onboard buoyancy engine negatively ballasts the float, and the float sinks to a desired drift depth. The HyperNav system cannot communicate with shoreside researchers once it leaves the surface. The desired drift depth is programmed via transmitted instruction while the float is at the surface. Once the HyperNav system reaches its desired drift depth, the buoyancy engine neutrally ballasts the HyperNav system, and the HyperNav system enters the park phase. In the park phase, the HyperNav float system drifts at depth in low power mode. The ballast system positively ballasts the HyperNav system at a programmed time, and the profile phase starts. During the profile phase, the HyperNav system ascends through the water column while collecting data for surface transmission. A typical mission sequence is to have the float profile once per day, with the HyperNav radiance sensor data collection concentrated in the upper 20 m, including a surface acquisition period. After the profile and surface acquisition is completed, the data is telemetered to shore-side systems using an Iridium satellite connection. Note that the daily data transmission of the HyperNav sensors can take up to 2 h (depending on satellite coverage). The float receives new mission files from shore-side systems, powers down the HyperNav sensor systems, and descends to the set park depth.

4 Selection of HyperNav deployment sites

The primary objective of the HyperNav mission is to generate a substantial volume of high-quality SVC data at minimal cost. Nevertheless, HyperNav systems are also engineered for the validation of satellite-derived water-leaving radiance (or remote sensing reflectance), which necessitates less stringent criteria regarding atmosphere, surface, and water conditions—essentially requiring clear skies over a limited pixel area. Both ocean and atmospheric conditions are dynamic, impacting the feasibility of SVC or validation match-up criteria. However, certain locations during specific seasons are more likely to align with SVC match-up criteria than others (Zibordi and Mélin, 2017). Additionally, the operational costs vary across deployment sites, with factors such as shipping expenses and boat rentals contributing to disparities.

This poses a fundamental optimization question: what is the best spatio-temporal deployment configuration to maximize the number of SVC match-ups and minimize deployment costs? To answer this question, we consider the likelihood of a deployment site meeting the SVC match-up criteria derived from the ocean color record (Section 4.1) in addition to the cost of operations at a site (Section 4.2). Finally, because the floats are not actively propelled laterally, we quantify the navigability of the current structure of each site and, if required, impose additional logistical expenses for small boat operations to reposition a float during a typical deployment of 60 days (Section 4.3).

4.1 Analysis of atmospheric and surface variables

The Zibordi and Mélin (2017) and herein described match-up criteria were calculated from atmospheric and oceanic variables. Ten years of level-1a MODIS-A images (from 1/1/2010 to 12/31/2019) covering the areas of interest were downloaded from the OBPG website (https://oceancolor.gsfc.nasa.gov) and were processed into level-2 data including chlorophyll-a concentration (Chl-a), aerosol optical thickness at 869 nm, and wind speed using l2gen in SeaDAS. Specifically, the wind speed is originally from the National Centers for Environmental Prediction (NCEP) reanalysis dataset with 1° spatial resolution and 6 h temporal resolution. As one of the ancillary data used in l2gen, wind speed is interpolated to MODIS resolution. The level-2 MODIS-A images were first remapped to a 1.1 km equal-area grid and then remapped to a Plate Carrée (equal-angle) grid with 1.1 km resolution at the equator. The remapping algorithm is exactly the one used by NASA OBPG to generate level-3 binned ocean color products (Campbell et al., 1996). Nearest neighbor interpolation was used to fill missing pixels at the edges. Daily single scattering albedo was extracted and computed from the 0.5° × 0.625° MERRA-2 hourly data for the same time period and interpolated to the binned MODIS grid. The clear sky, Zibordi and Mélin (2017), and herein described SVC match-up probabilities were computed for each month from the year 2010–2019. The clear sky probability is defined as the number of days with valid Chl-a values (hence clear days) in an entire 5 km^2 × 5 km^2 window divided by the total number of days in each month. The herein described SVC criteria probability is defined similarly but with more criteria, i.e., clear sky, aerosol optical thickness at 869 nm <0.1, single scattering albedo >0.95, coefficient of variation of R_{rs} <0.2 over a 3 km^2 × 3 km^2 area, and wind speed <8 ms^{-1}.

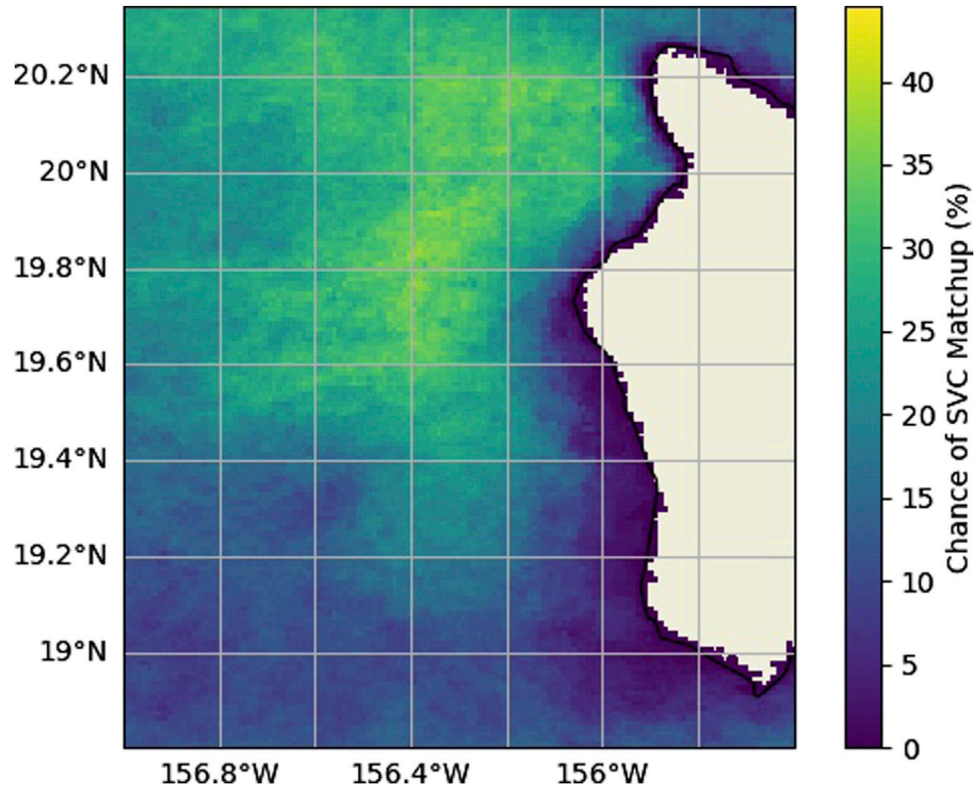


FIGURE 1
Example of conditional SVC match-up probabilities for an August Kona deployment. Colored shading represents the % chance of an SVC match-up. Beige masking represents land.

TABLE 1 Mission deployment and costing information for each deployment site considered. Travel includes round trip transportation and lodging for two people to and from deployment site. Transport includes mobilization logistics for HyperNav system. Boat fee is the daily fee for chartered vessel, fuel, and captain. Modifier is the expected number of boat trips each deployment will require (calculated in Section 4.3.2). Data Transmission includes all iridium satellite transmission fees. Refurbishment includes all replacement batteries and sensor re-calibration. Note that local collaborators in Crete and Puerto Rico eliminate travel costs by generously participating in recovery and deployment operations.

	Deployment site	Travel	Transport	Boat (Modifier)	Data transmission	Refurbishment
Monterey	36.7°N 122.2°W	6,100	4,500	2,500 (X3)	10,893	15,000
Port Hueneme	33.7°N 119.6°W	1,000	960	1800 (X2)	10,893	15,000
Bermuda	32°N 64.5°W	18,600	8,500	2,500 (X3)	10,893	15,000
Kona	19.5°N 156.4°W	10,800	4,900	4,260 (X4)	10,893	15,000
Crete	35.75°N 25°E	0	11,000	5,100 (X2)	10,893	15,000
Puerto Rico	17.8°N 66.7°W	0	8,700	2,600 (X3)	10,893	15,000
Tahiti	17.8°S 149.75°W	13,600	10,600	1,020 (X2)	10,893	15,000

All numbers listed in USD ($) and include university overhead.

match-up probabilities. (Figure 1) illustrates these probabilities for August off Kona, Hawaii, depicting values that reach up to 40% in certain areas.

4.2 Logistics

For the HyperNav project, the assembly and calibration of the HyperNav system are done at Sea-Bird Scientific in Bellevue, WA, and shipping logistics are staged out of Oregon State University in Corvallis, OR. The cost to mobilize logistics around the world is not uniform and needs to be estimated.

Some sites (Crete, Puerto Rico, Port Hueneme) are in close proximity to advanced oceanographic laboratories operated by collaborators willing to perform float deployments, recoveries, and even in-field equipment refreshes. All other sites require more extensive mobilization: first, the HyperNav system has to be shipped from the Pacific Northwest to the site; next, a team of at

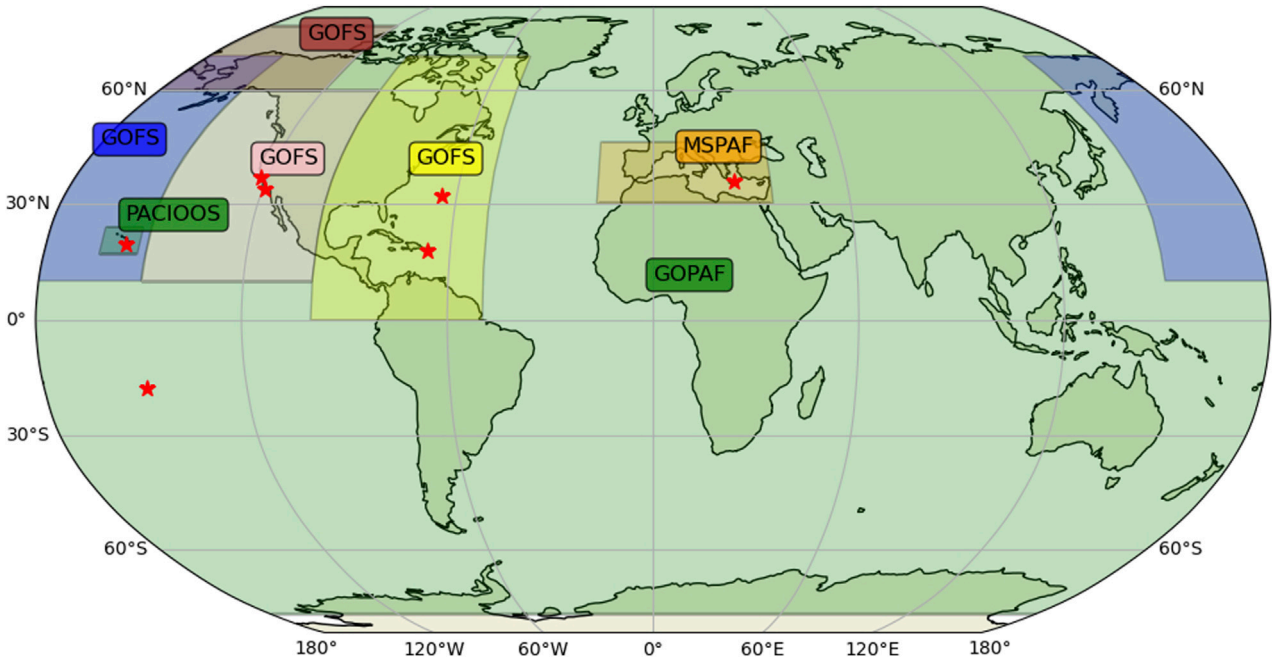


FIGURE 2
Map of regional extent of currently integrated ocean current models. Shaded regions represent coverage area by each model (see Section 4.3.1 for model descriptions). Red stars indicate study regions.

least two people is needed at the site to assemble and test the system, arrange deployment logistics and perform the deployment; after the mission is complete, this process must be done in reverse. The sites considered in this manuscript range in travel distance from a long day's drive to multi-leg international flights across oceans and the differences in logistics costs for float operations between one site and another can be substantial.

To quantify these differences in logistical cost, a simple model was created with information based on previous shipping, daily charter boat rates, and government travel per-diems combined with university overhead (Table 1). We also amortize HyperNav system costs in our deployment cost model. The statistics of HyperNav systems reaching a failure mode after deployments are yet to be determined by our limited number of test deployments; as such, we make the conservative assumption that one float will be lost for every eight deployments (to date one float was lost out of 14 deployments).

4.3 Navigability

The HyperNav system, like all drifting floats, is advected by ocean currents. HyperNav is a variant of the Argo platform, and, without intervention, this advection can cause substantial displacements from the original deployment location over time (Chamberlain et al., 2023). If the HyperNav system leaves the deployment area, it can be problematic for two reasons: first, the deployment sites are chosen for specific atmospheric and ocean optical properties that are conducive for SVC match-up criteria as described in Section 4.1, therefore HyperNav systems that stay in the deployment area are likely to record more SVC match-up observations than those that leave; second, because of the expense of the system and the time of shipping and assembly, the HyperNav project can deploy in more places and collect more data if the floats are recovered after deployment. Float recovery is much easier if the float stays in the deployment area. Also, HyperNav sensors must be post-calibrated to assess uncertainties in the radiometric measurements over the deployment duration. Currently, without post-calibration, the data collected are not considered of sufficient quality for SVC.

The Argo platform is only propelled in the vertical direction and cannot directly relocate itself laterally. Floats can be picked up and repositioned via a small boat, but this can be costly and logistically complicated to do frequently. The strategy for float piloting that we have adopted in this project is directly analogous to that of aeronauts piloting hot air balloons. Substantial vertical changes in current direction and magnitude exist in the ocean. With sufficient prior knowledge of the structure of the currents, the vertical position of a float can be adjusted such that the float moves in the desired direction.

Predictive high-resolution current models (described in Section 4.3.1) have been operationally combined with the open source Probably A Really Computationally Efficient Lagrangian Simulator (PARCELS) (Lange and van Sebille, 2017) software package to replicate the HyperNav system's behavior and predict its displacement in near real-time. PARCELS is designed around a flexible and modular architecture compatible with many ocean circulation models and can simulate particle behaviors. PARCELS solves the equations of particle motions using a fourth-order Runge–Kutta scheme. PARCELS particles are programmed to simulate the HyperNav mission by sinking to a predefined drift depth and waiting there for a predetermined period of time (typically 1–5 days), then ascending through the water column

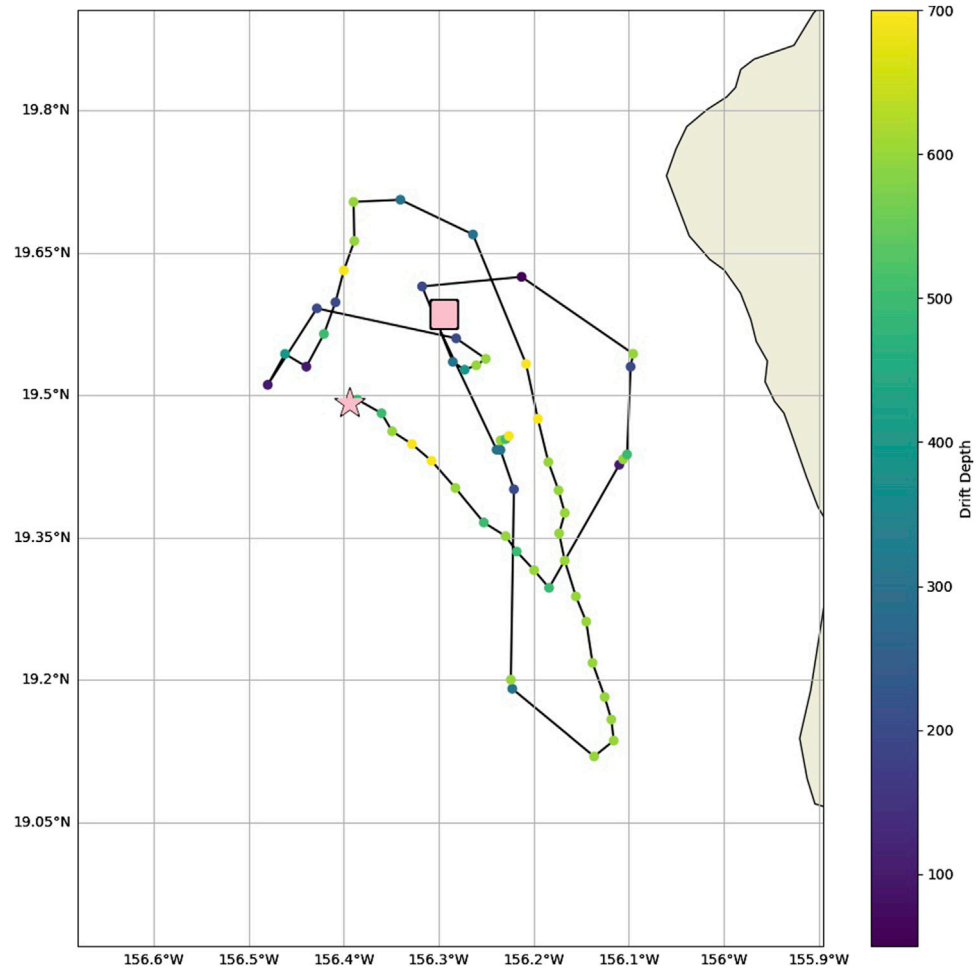


FIGURE 3
Example of Navigability Study for a Kona deployment. Pink star represents deployment location, pink square represents the recovery location, black line represents the HyperNav trajectory, colored dots represent the calculated ideal drift depth, beige shading represents land.

and waiting at the surface for 2 h to simulate data transmission before descending again. Vertical velocities in both ascent and descent are 0.076 ms^{-1}, which is typical of a HyperNav in a fully ballasted or de-ballasted state.

This software has been combined with reanalysis models to gain intuition for the best deployment locations and how a float will behave prior to deployment, as well as predictive current models to dynamically adjust HyperNav drift depths and navigate the system during deployment. The code for our calculations is publicly available (https://github.com/Chamberpain/HyperNav), and details of the predictive skill of this novel system will be described in a future publication. Other computational schemes have predicted Argo trajectories or adapted drift depths to navigate floats (Siiriä et al., 2019; González Santana et al., 2023), but this is the first open-ocean, global adaptive navigation system we are aware of.

4.3.1 Model data

Output from four different models are used to simulate float trajectories. These models were of the highest perceived regional skill for each selected site: 1. Output from the Global Ocean Physics Analysis and Forecast (GOPAF) hosted by Copernicus Marine Service and run on the Nucleous for European Modelling of the Ocean (NEMO) (Escudier et al., 2021) model was used for the Crete island, Tahiti, and Bermuda float trajectory predictions, 2. the Mediterranean Sea Physics Analysis and Forecast (MSPAF) also hosted by Copernicus Marine Service and run on the NEMO model was used for Mediterranean simulations. 3. The Pacific Islands Ocean Observing System (PACIOOS) (Powell, 2018) model output was used for the Kona, HI float trajectory predictions, and 4. The Global Ocean Forecasting System (GOFS) run on the HYbrid Coordinate Ocean Model (HYCOM)(Chassignet et al., 2009; Wallcraft et al., 2009) and the Navy Coupled Ocean Data Assimilation (NCODA) system (Cummings and Smedstad, 2014) was used for all other locations (Figure 2).

The MSPAF is a regional model that covers the Mediterranean Sea. The MSPAF has a horizontal grid spacing of 1/24° and 141 vertical levels (Escudier et al., 2021). MSPAF output has hourly resolution. Relatively high vertical resolution is necessary to capture the complicated vertical dynamics present in the Mediterranean, but are unnecessary for our application and were subsampled to 63 levels.

PACIOOS is a Regional Ocean Modeling System (ROMS) based data assimilating model with approximately 4 km grid spacing.

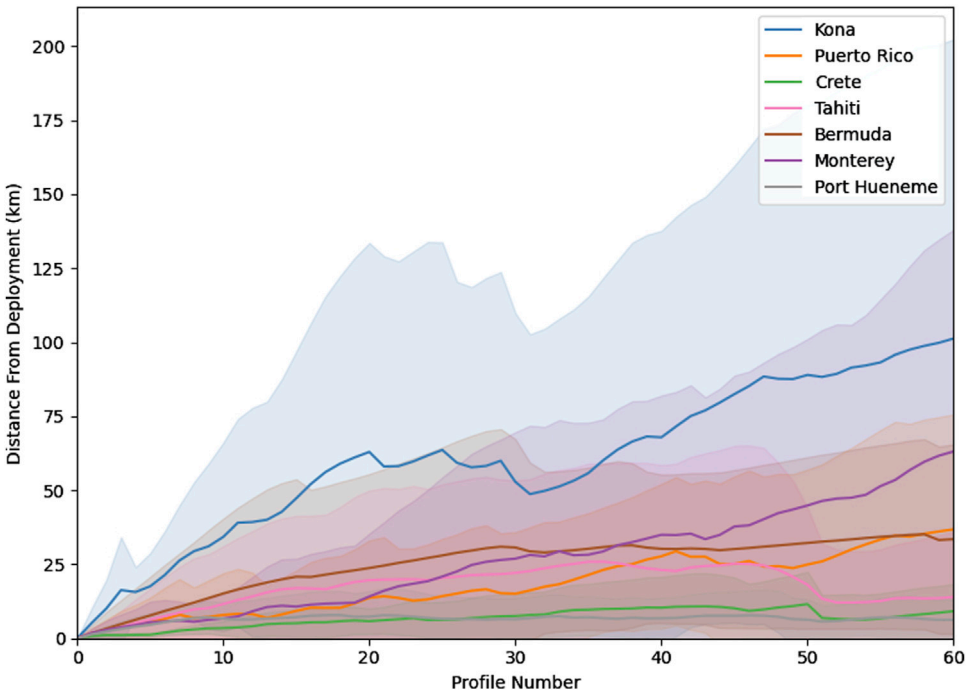


FIGURE 4
Aggregated estimates of site navigability (Section 4.3.2) for 60 profiles at Puerto Rico (orange), Hawaii (blue), Port Hueneme (grey), Monterey (purple), Bermuda (brown), Crete (green), and Tahiti (pink). Solid lines represent the mean estimate of displacement away from the starting point by profile number, shading represents the standard deviation of 20 controlability runs. Smaller distances from the deployment point indicate that the sites have a navigable current structure; larger distances indicate that the site is un-navigable. Sites that exceed a displacement of 20 km are anticipated to need a small boat repostioning as shown in Table 1.

Ocean boundary conditions are provided by HYCOM. 6 days predictions are made using assimilated data from PacIOOS high-frequency radars, Argo floats, autonomous underwater vehicles (AUVs), and satellite-based estimates of sea surface height and sea surface temperature. The subsampled model contains 18 depth levels with 3 h output.

GOFS is a hybrid isopycnal-sigma-pressure assimilating model with global coverage. The HYCOM prediction is generated by the US Naval Oceanographic Office and hosted by the National Oceanographic and Atmospheric Administration's National Centers for Environmental Information. The subsampled model dataset has 30 depth levels, approximately a 1/12° grid cell spacing, and 3 h output.

4.3.2 Navigation test

To quantify the navigability of each site, and ultimately the cost of logistics for repositioning unnavigable floats, we quantified how close we could keep floats to their deployment sites by trying to navigate an ensemble of synthetic floats through hypothetical missions using reanalysis current data from each location. The trajectory prediction computation was described in Section 4.3.

Synthetic floats were initialized at deployment sites selected for a high probability of SVC match-ups as described in Section 4.1. For each profile, future trajectories were calculated for eight drift depths ranging from 50 to 700 m and five drift durations ranging from 1 to 6 days in 1-day increments. The combination of drift depth and drift duration that resulted in the final trajectory location closest to the original deployment location was identified as optimal and the drift depth-duration calculation was repeated for the next profile. Each mission consisted of 60 profiles. Figure 3 shows an example mission off the coast of Kona, HI and illustrates that the optimal drift depth can change many times throughout a deployment. A Monte Carlo simulation conducted these synthetic missions at twenty random deployment times at each deployment site. These trajectory estimates spanned all years and seasons and the results are aggregated (Figure 4).

Unnavigable sites can still have utility for the program if the SVC match-up probability is sufficiently high, but the expense of additional boat time to reposition floats needed to be quantified. Sites where the average float trajectories exceeded a distance of 20 km from the deployment site were deemed to require a small boat repositioning.

Our choice for quantifying site navigability (Figure 4) includes increased logistical expense in locations where we expect to require additional small boat charters to reposition floats that are uncontrollably advected a substantial (greater than 20 km) distance from their deployment site. Based on the rate that distance from the deployment site uncontrollably increased, the sites considered can be grouped into three classifications: sites that are navigable and will not require additional repositioning (Port Hueneme, Crete, Tahiti), sites that are semi-navigable and will likely require one repositioning (Monterey, Bermuda, Puerto Rico), and sites that are unreliably-navigable and will require 2 or more repositionings (Hawaii). The maximum standard deviation of distance from deployment location over the simulations at each site was as much as 84% of the maximum mean distance from

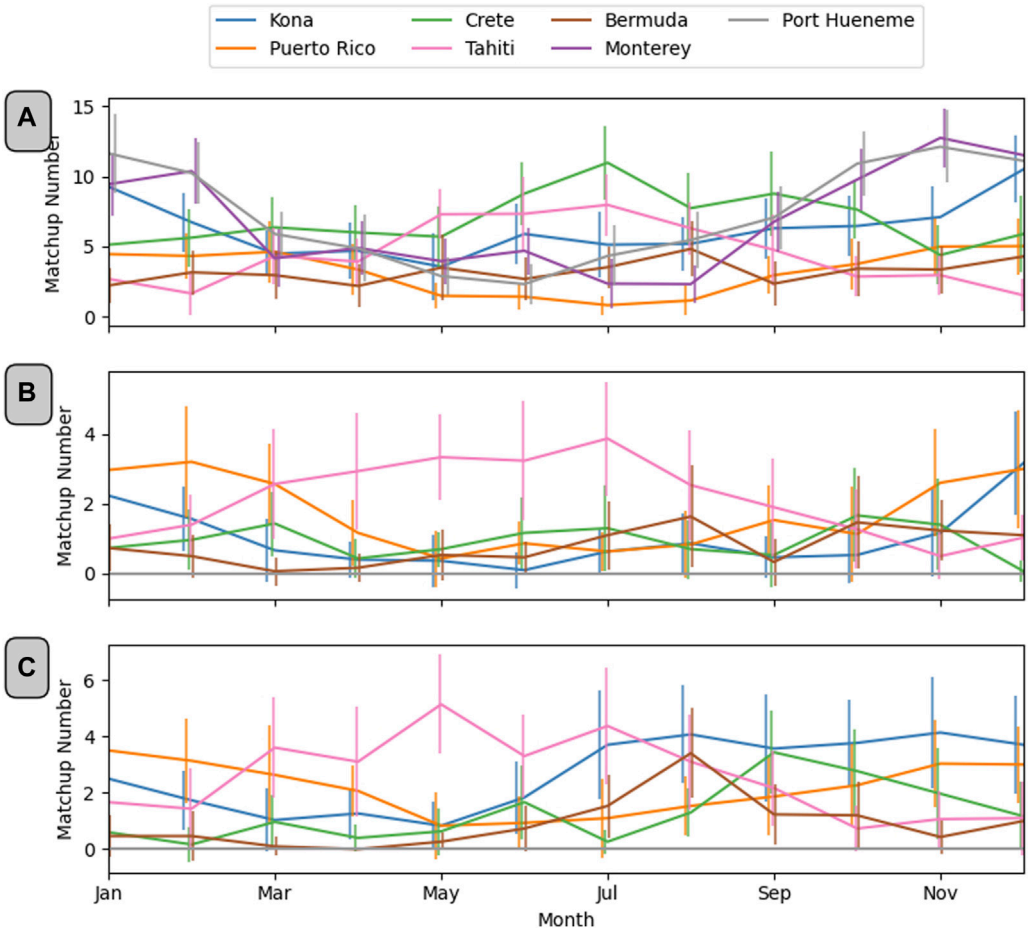


FIGURE 5
Seasonal estimate of number of match-ups recorded by HyperNav system at each site. Colored lines represent estimated seasonal mean (horizontal) and standard deviation (vertical) of match-ups at Port Hueneme (grey), Kona (blue), Crete (green), Tahiti (pink), Puerto Rico (orange), Monterey (purple), and Bermuda (brown) using the clearsky criterion (panel **(A)**), the Zibordi and Mélin (2017) criteria (panel **(B)**), and the criteria described in Section 2 (panel **(C)**).

deployment location, implying large variability among simulations. Of these classifications, we anticipate navigable sites to not need repositioning and only require 2 small boat charters (one for deployment and one for recovery), semi-navigable sites to need 3 small boat charters (one additional charter for repositioning), and unreliably navigable locations to require 4 or more small boat charters for frequent repositionings. These increased expenses are found in the "Boat Modifier" column of Table 1.

5 Prediction of potential match-ups

To estimate the number of seasonal match-ups at each deployment site, we interrogated the SVC probability maps in Section 4.1 at the deployment locations in Section 4.3.2 (Figure 5). The seasonal estimate of the number of match-ups was combined with our estimates for logistical expenses (Section 4.2) informed by the navigability tests (Section 4.3.2) to estimate the seasonally varying cost per SVC match-up at each deployment site. Finally, the cost of each SVC match-up was calculated by dividing the costs (Table 1) associated with each deployment site (Figure 6) by the aggregated mean of likely match-ups at each month.

The stricter SVC match-up criteria of Zibordi and Mélin (2017) and that described in (Section 2) as compared with the clear sky criteria suitable for validation match-ups unsurprisingly resulted in far fewer SVC match-ups, which increased SVC match-up cost by approximately an order of magnitude (Figures 6B, C). Additionally, because of sub-mesoscale coastal processes, Monterey and Port Hueneme have high spatial variability of R_{rs} and were unsuitable for SVC match-ups (Figures 5B, C); however, because of a highly retentive circulation, efficient logistics (low travel and transport costs), and a high likelihood of cloudless days Figure 5A Port Hueneme outperforms other sites half the year (fall and winter) in cost per clear sky match-up. Crete outperforms other sites in clear sky matchups for the other half of the year (spring and summer) (Figure 6A). It should be noted that we have found evidence for strongly recirculating, bathymetry-controlled, retentive eddies at both the Crete and Port Hueneme sites, and these locations should be considered for future observations so long as the clear sky SVC match-up criteria have utility for validating future ocean color products (Figure 4). There exist 2 distinct phases to the

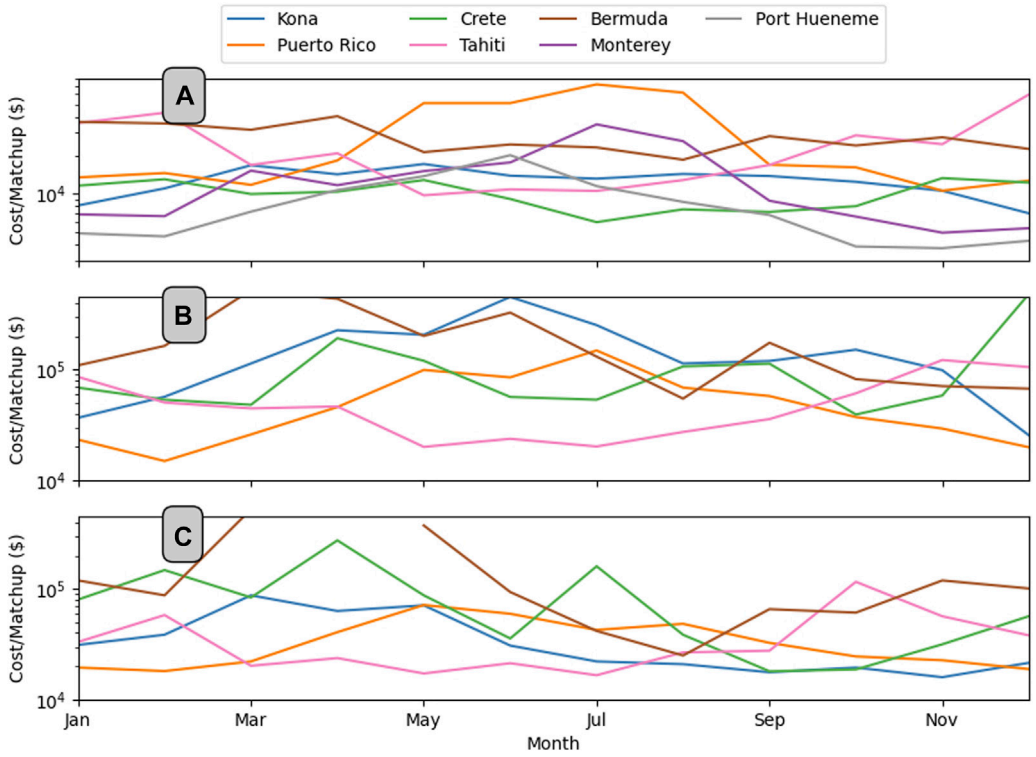


FIGURE 6
Seasonal USD ($) cost per match-up for monthlong deployment at each considered deployment site for **(A)** clear sky criterion described in Section 4.1, **(B)** Zibordi and Mélin (2017) criteria, and **(C)** match-up criteria described in Section 2. Colored lines represent the mean cost of Port Hueneme (grey), Kona (blue), Crete (green), Tahiti (pink), Puerto Rico (orange), Monterey (purple), and Bermuda (brown) deployment sites.

seasonal cycle of clear sky match-up costing: cost of match-ups in North American sites (Monterey, Port Hueneme, Kona, Puerto Rico) all peaking in the summer months and reaching minima in the winter; Tahiti, Bermuda, and Crete had opposite phasing with the price per match-up peaking during the winter months and reaching a minima in the summer. The minimal cost for clear sky match-up of all sites considered were January deployments in Port Hueneme with a cost per match-up of ≈ $4,000; the absolute maxima was June deployments in Puerto Rico with a cost per match-up of ≈ $80,000.

The Zibordi and Mélin (2017) criteria described in Section 2 includes more atmospheric and oceanic processes; therefore, the resulting seasonal distributions are more complex. The seasonal phasing of the Zibordi and Mélin (2017) criteria has similarities with the clear sky criteria in that the cost of match-ups of sites excluding Crete and Bermuda peak follow a predictable hemispheric seasonality. Bermuda and Crete do not exhibit an obvious seasonal signal. The absolute cost minima per match-up is found to be ≈ $15,000–found in February, Puerto Rico deployments and May, Tahiti deployments; The absolute average cost maxima is a March, Bermuda deployment, where the cost per match-up is ≈ $430,000 (Figure 6B).

Finally, the seasonality of the criteria described in Section 4.1 is similar to both the clear sky and Zibordi and Mélin (2017) criteria, except that it is phase shifted earlier in the year, approximately 3 months. The minimal cost per match-up was May deployments in Tahiti of ≈ $14,000. The most expensive was April deployments in Bermuda, where no match-ups were expected (Figure 6C).

6 Discussion

The selection criterion primarily discussed in this publication is cost (Figure 6). The HyperNav program has the additional goals of providing as many SVC match-ups after the PACE launch as possible and providing observations in independent and varying optical regimes. Like many optimizations applied to the real world, simplifying assumptions were made, and our conclusions must be considered in this context. In addition to cost considerations, it is essential to highlight the significance of all considered sites in providing a substantial number of match-ups for validation purposes. For instance, during the winter months, deployments from Port Hueneme in the Southern California Bight could potentially yield over 10 match-ups per month, showcasing diverse environmental conditions for validation. It is noteworthy that deploying at Port Hueneme and Monterey is not suitable for SVC due primarily to ocean variability. However, deploying HyperNav systems at the other sites would benefit both SVC and validation activities. Thus, site selection may consider optimizing both types of activities.

The navigability test, although illuminating, makes fundamental assumptions about the skill of models and the inherent risks of operations. The placement of mesoscale features in many models

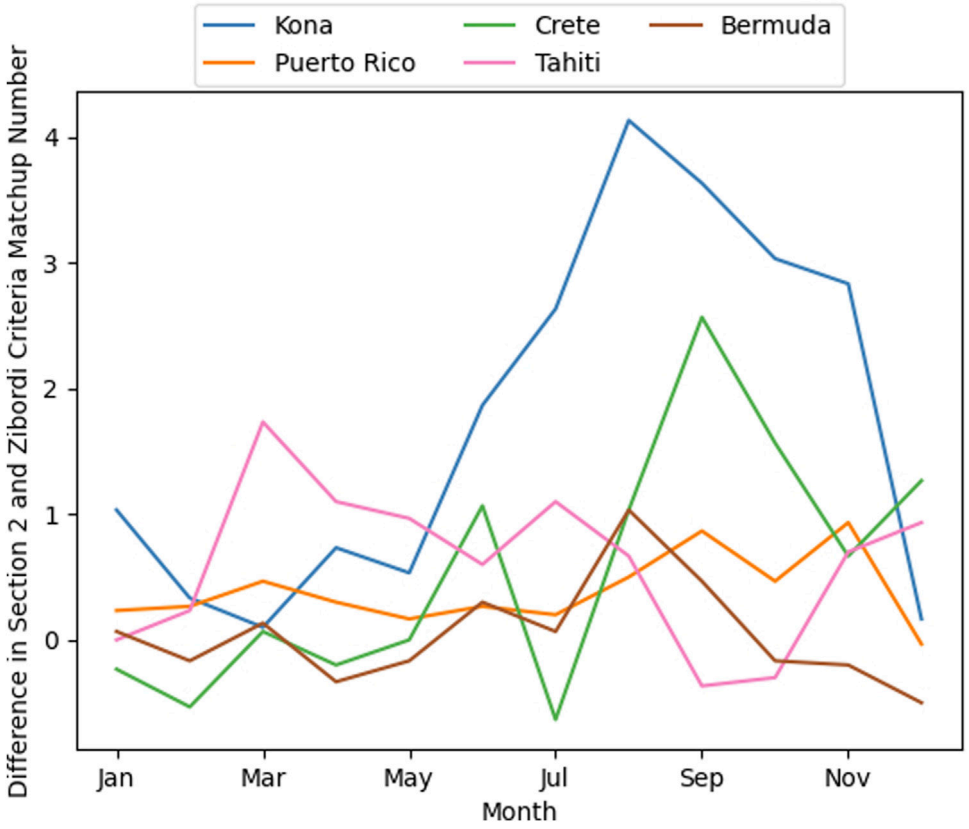


FIGURE 7
Seasonal match-up difference between criteria described in Section 2; Zibordi and Mélin (2017) criteria. Colored lines represent the difference in the estimated seasonal number of match-ups at Kona (blue), Puerto Rico (orange), Tahiti (pink), Crete (green), Bermuda (brown), Monterey (purple), and Port Hueneme (grey). Positive number means that Section 2 criteria allows more match-ups than the Zibordi and Mélin (2017) criteria.

TABLE 2 HyperNav project deployments as of 9 May 2024 with more than 8 quality controlled (QC'd) HyperNav profiles. During initial test deployments, HyperNav system was not turned on or functioning properly for all profiles. Potential match-ups are QC'd HyperNav profiles that satisfy internal system checks and have spectra broadly similar to clear sky models. These data can be accessed from the HyperNav website (https://misclab.umeoce.maine.edu/HyperNAV/).

Deployment ID	Dates	Location	QC'd HyperNav profiles	Potential match-ups
042.D01	2017 November 18–Dec 4	Hawaii	14	14
055.D01	2021 June 9–June 16	Hawaii	8	8
054.D01	2021 June 9–June 16	Hawaii	8	7
053.D04	2022 April 20–May 9	Hawaii	16	16
057.D01	2022 May 24–July 27	Crete	13	11
056.D01	2022 May 24–July 31	Crete	50	45
057.D02	2023 March 25–May 2	Crete	35	32
053.D05	2023 April 10–Jun 4	Port Hueneme	42	38
1,544.D02	2023 November 30–December 10	Port Hueneme	9	9
1,462.D01	2024 February 13–March 30	Puerto Rico	36	24
1,447.D01	2024 February 21–April 10	Crete	40	27
1,311.D02	2024 March 9–March 29	Hawaii	15	10
1,543.D03	2024 April 5–May 7	Puerto Rico	18	12
1,312.D03	2024 April 23–May 8	Hawaii	12	7

(including reanalysis) is commonly wrong. However, we assume the looser condition that the general structure of mesoscale statistics is accurate. The degree to which this condition holds is unclear and is likely regionally specific because the spatial resolutions and model formulations vary by site. Another assumption fundamental to the navigability test is that the predictive models have perfect skill and that while floats are deployed in the field, we can best use ocean circulation predictions. For similar reasons, a given model's predictive skill is unclear and likely regionally specific. Finally, sites where floats are advected uncontrollably away from the deployment location have an inherent and increased risk of becoming lost or damaged. Floats can quickly travel (Figure 4) too far away from local ports to be recovered by small boats and risk never being recovered. Float repositioning also has its own risks. A float drifting at its park depth is far safer than on the rolling deck of a small boat where delicate sensors can be damaged. These risks are not factored into these calculations and should be further studied.

The top three sites considered (Kona, Puerto Rico, and Tahiti) are located within an absolute latitude band of 19.5° to 17.5°. These locations are objectively most suitable for the Zibordi and Mélin criteria and would be the three recommendations if cost optimization were the only criteria considered. However, in the context of a global observing system, restricting the SVC match-up sites to such a limited range of latitudes, during seasons conducive for SVC match-up, may bias the satellite calibration (Bisson et al., 2021). The diversity of observing sites may be an important factor in an unbiased SVC match-up array and is something that the optimization process presented here does not capture. However, the substantial seasonal cycle of SVC match-up cost (Figure 6) highlights the advantage of the flexibility of the HyperNav system. With a small logistical footprint, HyperNav systems can be redeployed globally to anticipate the atmospheric and oceanic conditions that are favorable to SVC match-up and for validation match-up.

Community consensus and guidance do not exist for which SVC match-up criteria should be used for PACE. This is problematic from an operational perspective because, while similarities exist between the Zibordi and Mélin (2017) and Section 2 criteria, there are also substantial differences (Figure 7) and optimizing around unclear SVC match-up criteria could cause sub-optimal deployment choices. These differences are most pronounced for the expected value of fall Crete and summer and fall Kona match-ups. For Crete, this may be due to a reduction of dust storms, which are more common during spring and summer, seasons of increased atmospheric instability over North Africa. For Kona, the Zibordi and Mélin (2017) criteria may eliminate situations of small, non-absorbing aerosols. The Big Island of Hawaii is subjected to volcanic eruptions, generating non-absorbing sulfate aerosols with $\alpha > 1$ that are eliminated by the Zibordi and Mélin (2017) criterion of $\alpha < 1$. Of the sites considered, Section 2 criteria are more permissive, allowing 36 more annual match-ups per year at the sites considered - half of these coming from increased match-ups in Kona.

Despite this lack of consensus, preliminary HyperNav deployments have been initiated for system development and satellite validation purposes, spanning both the pre and post PACE eras. Table 2 presents a subset of the 15 most successful deployments from November 2017 to the present. Data from these ongoing deployments are integrated in near real-time into the NASA PACE SVC effort, highlighting the flexibility and effectiveness of the HyperNav system.

7 Conclusion

A methodology for selecting cost-efficient System Vicarious Calibration (SVC) and validation match-up sites using the HyperNav system has been developed. This versatile methodology is applicable across various locations. Seven specific sites were examined: Puerto Rico, Kona, Port Hueneme, Monterey Bay, Bermuda, Crete, and Tahiti. Evaluation based on three primary criteria, i.e., number of SVC match-ups, logistics, and navigability, revealed substantial differences among the sites and underscored the need for a flexible selection approach. Notably, while Port Hueneme and Monterey did not meet SVC match-up criteria, they emerged as leading sites for validation due to their abundance of clear sky days and diverse environmental conditions. For instance, during the winter months, deployments from Port Hueneme in the Southern California Bight could potentially yield over 10 validation match-ups monthly (Figure 6). Deploying HyperNav systems at the other sites would benefit both SVC and validation activities, highlighting the importance of optimizing both types of activities in site selection processes. The navigability of sites was categorized into three groups: navigable (Crete, Port Hueneme, and Tahiti), semi-navigable (Bermuda, Monterey, and Puerto Rico), and un-navigable (Kona). Semi-navigable or un-navigable sites may require additional small boat charters for float repositioning, and these costs were integrated into the logistics model (Table 1). Based on the evaluation criteria, Kona, Puerto Rico, and Tahiti emerge as promising sites for SVC match-ups.

Data availability statement

The datasets presented in this study can be found in online repositories. The names of the repository/repositories and accession number(s) can be found below: https://github.com/Chamberpain/HyperNav.

Author contributions

PC: Writing–original draft, methodology. RF: Writing–original draft, conceptualization. JT: Writing–original draft, formal analysis. MM: Writing–review and editing. AB: Funding acquisition, Writing–review and editing, EB: Writing–review and editing, methodology, NH: Writing–review and editing, data curation. CO: Writing–review and editing, Project administration.

Funding

The author(s) declare that financial support was received for the research, authorship, and/or publication of

this article. All authors acknowledge support from HyperNav project under NASA awards 80GSFC20C0101 and 180GSFC22CA050.

Acknowledgments

We thank A. Banks and N. Spyridakis of the Helenic Center for Marine Research in Crete for valuable assistance in science, logistics and deployments off Crete. William Hernandez from Environmental Mapping consultants and Fernando Gilbes Santaella and Roy Armstrong from University of Puerto Rico for valuable assistance in science, logistics, and deployments off Puerto Rico. We also thank Neil Davies and the staff of the Gump Station for valuable assistance with deployments off Tahiti. We also thank two reviewers for their helpful comments and suggestions.

Conflict of interest

The authors declare that the research was conducted in the absence of any commercial or financial relationships that could be construed as a potential conflict of interest.

The author(s) declared that they were an editorial board member of Frontiers, at the time of submission. This had no impact on the peer review process and the final decision.

Publisher's note

All claims expressed in this article are solely those of the authors and do not necessarily represent those of their affiliated organizations, or those of the publisher, the editors and the reviewers. Any product that may be evaluated in this article, or claim that may be made by its manufacturer, is not guaranteed or endorsed by the publisher.

References

Ahmad, Z., Franz, B. A., McClain, C. R., Kwiatkowska, E. J., Werdell, J., Shettle, E. P., et al. (2010). New aerosol models for the retrieval of aerosol optical thickness and normalized water-leaving radiances from the seawifs and modis sensors over coastal regions and open oceans. *Appl. Opt.* 49, 5545–5560. doi:10.1364/ao.49.005545

Antoine, D., Chami, M., Claustre, H., d'Ortenzio, F., Morel, A., Bécu, G., et al. (2006). BOUSSOLE: a joint CNRS-INSU, ESA, CNES, and NASA ocean color calibration and validation activity. *Tech. Rep.*

Antoine, D., Guevel, P., Deste, J.-F., Becu, G., Louis, F., Scott, A. J., et al. (2008). The "boussole" buoy—a new transparent-to-swell taut mooring dedicated to marine optics: design, tests, and performance at sea. *J. Atmos. Ocean. Technol.* 25, 968–989. doi:10.1175/2007jtecho563.1

Bailey, S. W., and Werdell, P. J. (2006). A multi-sensor approach for the on-orbit validation of ocean color satellite data products. *Remote Sens. Environ.* 102, 12–23. doi:10.1016/j.rse.2006.01.015

Barnard, A., Van Dommelen, R., Boss, E., Plache, B., Simontov, V., Orrico, C., et al. (2022). A new paradigm for ocean color satellite calibration and validation: accurate measurements of hyperspectral water leaving radiance from autonomous profiling floats (hypernav). *Authorea Prepr.*

Barnard, A., Boss, E., Haëntjens, N., Orrico, C., Frouin, R., Tan, J., et al. (2024a). Design and verification of a highly accurate in-situ hyperspectral radiometric measurement system (HyperNav). *Frontiers in Remote Sensing.* 5, 1369769. doi:10.3389/frsen.2024.1369769

Barnard, A. E., Boss, N., Haëntjens, C., Chamberlain, R., Frouin, M., Tan, J., et al. (2024b). A float-based ocean color vicarious calibration program. *Frontiers in Remote Sensing.*

Brewin, J., Sathyendranath, S., Kulk, G., Rio, M., Concha, J., Bell, T., et al. (2023). Ocean carbon from space: Current status and priorities for the next decade. *Earth-science reviews* 240 (03), 104386. doi:10.1016/j.earscirev.2023.104386

Bisson, K., Boss, E., Werdell, P. J., Ibrahim, A., Frouin, R., and Behrenfeld, M. (2021). Seasonal bias in global ocean color observations. *Appl. Opt.* 60, 6978–6988. doi:10.1364/ao.426137

Campbell, J. W., Blaisdell, J. M., and Darzi, M. (1996). Level-3 sea wifs data products: spatial and temporal binning algorithms. *Oceanogr. Lit. Rev.* 9, 952.

Chamberlain, P., Talley, L. D., Mazloff, M., Van Sebille, E., Gille, S. T., Tucker, T., et al. (2023). Using existing argo trajectories to statistically predict future float positions with a transition matrix. *J. Atmos. Ocean. Technol.* 40, 1083–1103. doi:10.1175/jtech-d-22-0070.1

Chassignet, E. P., Hurlburt, H. E., Metzger, E. J., Smedstad, O. M., Cummings, J. A., Halliwell, G. R., et al. (2009). Us godae: global ocean prediction with the hybrid coordinate ocean model (hycom). *Oceanography* 22, 64–75. doi:10.5670/oceanog.2009.39

Clark, D., Gordon, H., Voss, K., Ge, Y., Broenkow, W., and Trees, C. (1997). Validation of atmospheric correction over the oceans. *J. Geophys. Res. Atmos.* 102, 17209–17217. doi:10.1029/96jd03345

Clark, D. K., Yarbrough, M. A., Feinholz, M., Flora, S., Broenkow, W., Kim, Y. S., et al. (2003). Moby, a radiometric buoy for performance monitoring and vicarious calibration of satellite ocean color sensors: measurement and data analysis protocols. *Ocean Opt. Protoc. Satell. Ocean Color Sens. Validation* 6.

Cummings, J. A., and Smedstad, O. M. (2014). Ocean data impacts in global hycom. *J. Atmos. Ocean. Technol.* 31, 1771–1791. doi:10.1175/jtech-d-14-00011.1

Dubovik, O., Holben, B., Eck, T. F., Smirnov, A., Kaufman, Y. J., King, M. D., et al. (2002). Variability of absorption and optical properties of key aerosol types observed in worldwide locations. *J. Atmos. Sci.* 59, 590–608. doi:10.1175/1520-0469(2002)059<0590:voaaop>2.0.co;2

Escudier, R., Clementi, E., Cipollone, A., Pistoia, J., Drudi, M., Grandi, A., et al. (2021). A high resolution reanalysis for the mediterranean sea. *Front. Earth Sci.* 9, 702285. doi:10.3389/feart.2021.702285

Evans, R. H., and Gordon, H. R. (1994). Coastal zone color scanner "system calibration": a retrospective examination. *J. Geophys. Res. Oceans* 99, 7293–7307. doi:10.1029/93jc02151

Fougnie, B., Deschamps, P.-Y., and Frouin, R. (1999). Vicarious calibration of the polder ocean color spectral bands using *in situ* measurements. *IEEE Trans. geoscience remote Sens.* 37, 1567–1574. doi:10.1109/36.763267

Fougnie, B., Henry, P., Morel, A., Antoine, D., and Montagner, F. (2002). Identification and characterization of stable homogeneous oceanic zones: climatology and impact on in-flight calibration of space sensor over Rayleigh scattering. *Ocean. Opt. XVI*, 18–22. Santa Fe, NM.

Fougnie, B., Llido, J., Gross-Colzy, L., Henry, P., and Blumstein, D. (2010). Climatology of oceanic zones suitable for in-flight calibration of space sensors. *Earth Obs. Syst. XV (SPIE)* 7807, 215–225.

Franz, B. A., Bailey, S. W., Werdell, P. J., and McClain, C. R. (2007). Sensor-independent approach to the vicarious calibration of satellite ocean color radiometry. *Appl. Opt.* 46, 5068–5082. doi:10.1364/ao.46.005068

Frouin, R., et al. (2013). *In-flight calibration of satellite ocean-colour sensors*. Canada: International Ocean-Colour Coordinating Group.

Frouin, R. J., Franz, B. A., Ibrahim, A., Knobelspiesse, K., Ahmad, Z., Cairns, B., et al. (2019). Atmospheric correction of satellite ocean-color imagery during the pace era. *Front. Earth Sci.* 7, 145. doi:10.3389/feart.2019.00145

Gilerson, A., Herrera-Estrella, E., Foster, R., Agagliate, J., Hu, C., Ibrahim, A., et al. (2022). Determining the primary sources of uncertainty in retrieval of marine remote sensing reflectance from satellite ocean color sensors. *Front. Remote Sens.* 3. doi:10.3389/frsen.2022.857530

González Santana, A., Oosterbaan, M., Clavelle, T., Maze, G., Notarstefano, G., Poffa, N., et al. (2023). "Analysis of the global shipping traffic for the feasibility of a structural recovery program of argo floats," in *XXVIII general assembly of the international union of geodesy and geophysics (IUGG)* (GFZ German Research Centre for Geosciences).

Gordon, H. R. (1987). Calibration requirements and methodology for remote sensors viewing the ocean in the visible. *Remote Sens. Environ.* 22, 103–126. doi:10.1016/0034-4257(87)90029-0

Gordon, H. R. (1998). In-orbit calibration strategy for ocean color sensors. *Remote Sens. Environ.* 63, 265–278. doi:10.1016/s0034-4257(97)00163-6

Groom, S., Sathyendranath, S., Ban, Y., Bernard, S., Brewin, R., Brotas, V., et al. (2019). Satellite ocean colour: current status and future perspective. *Front. Mar. Sci.* 6, 1–30. doi:10.3389/fmars.2019.00485

Johnson, B., Zibordi, G., Kwiatkowska, E., Voss, K., Melin, F., Antoine, D., et al. (2024). System Vicarious Calibration requirements for satellite ocean colour missions targeting climate and global long-term operational applications. Available at: https://tsapps.nist.gov/publication/get_pdf.cfm?pub_id=957358 (Accessed July 5, 2024).

Kwiatkowska, E., Babu, K. N., Bojkov, B., Dessailly, D., Gilmore, R., Goryl, P., et al. (2022). *Conclusions of the review of candidate locations for copernicus ocean colour system vicarious calibration infrastructure*. Darmstadt, Germany: EUMETSAT.

Lange, M., and van Sebille, E. (2017). Parcels v0. 9: prototyping a Lagrangian ocean analysis framework for the petascale age. *Geosci. Model Dev.* 10, 4175–4186. doi:10.5194/gmd-10-4175-2017

McClain, C. R., Meister, G., et al. (2012). *Mission requirements for future ocean-colour sensors*. Dartmouth, NS, Canada: International Ocean Colour Coordinating Group (IOCCG).

Miller, R. N. (1990). Tropical data assimilation experiments with simulated data: the impact of the tropical ocean and global atmosphere thermal array for the ocean. *J. Geophys. Res. Oceans* 95, 11461–11482. doi:10.1029/jc095ic07p11461

Morel, A., and Prieur, L. (1977). Analysis of variations in ocean color 1. *Limnol. Oceanogr.* 22, 709–722. doi:10.4319/lo.1977.22.4.0709

Parrington, J. R., Zoller, W. H., and Aras, N. K. (1983). Asian dust: seasonal transport to the Hawaiian islands. *Science* 220, 195–197. doi:10.1126/science.220.4593.195

Powell, B. S. (2018). Regional ocean modeling system (roms): main Hawaiian islands: reanalysis. *Pac. Isl. Ocean. Obs. Syst.* 27.

Roemmich, D., Alford, M. H., Claustre, H., Johnson, K., King, B., Moum, J., et al. (2019). On the future of Argo: a global, full-depth, multi-disciplinary array. *Front. Mar. Sci.* 6, 439. doi:10.3389/fmars.2019.00439

Santer, R., and Schmechtig, C. (2000). Adjacency effects on water surfaces: primary scattering approximation and sensitivity study. *Appl. Opt.* 39, 361–375.

Servain, J., Busalacchi, A. J., McPhaden, M. J., Moura, A. D., Reverdin, G., Vianna, M., et al. (1998). A pilot research moored array in the tropical atlantic (pirata). *Bull. Am. Meteorological Soc.* 79, 2019–2031. doi:10.1175/1520-0477(1998)079<2019:aprmai>2.0.co;2

Siiriä, S., Roiha, P., Tuomi, L., Purokoski, T., Haavisto, N., and Alenius, P. (2019). Applying area-locked, shallow water argo floats in baltic sea monitoring. *J. Operational Oceanogr.* 12, 58–72. doi:10.1080/1755876x.2018.1544783

Valente, A., Sathyendranath, S., Brotas, V., Groom, S., Grant, M., Taberner, M., et al. (2016). A compilation of global bio-optical *in situ* data for ocean-colour satellite applications. *Earth Syst. Sci. Data* 8, 235–252. doi:10.5194/essd-8-235-2016

Wallcraft, A., Metzger, E., and Carroll, S. (2009). Software design description for the hybrid coordinate ocean model (hycom) version 2.2. *Nav. Res. Laboratory*, 13–15.

Werdell, P. J., Behrenfeld, M. J., Bontempi, P. S., Boss, E., Cairns, B., Davis, G. T., et al. (2019). The plankton, aerosol, cloud, ocean ecosystem mission: status, science, advances. *Bull. Am. Meteorological Soc.* 100, 1775–1794. doi:10.1175/BAMS-D-18-0056.1

Wong, A. P., Wijffels, S. E., Riser, S. C., Pouliquen, S., Hosoda, S., Roemmich, D., et al. (2020). Argo data 1999–2019: two million temperature-salinity profiles and subsurface velocity observations from a global array of profiling floats. *Front. Mar. Sci.* 7, 700. doi:10.3389/fmars.2020.00700

Zibordi, G., and Mélin, F. (2017). An evaluation of marine regions relevant for ocean color system vicarious calibration. *Remote Sens. Environ.* 190, 122–136. doi:10.1016/j.rse.2016.11.020

Zibordi, G., Mélin, F., Voss, K. J., Johnson, B. C., Franz, B. A., Kwiatkowska, E., et al. (2015). System vicarious calibration for ocean color climate change applications: requirements for *in situ* data. *Remote Sens. Environ.* 159, 361–369. doi:10.1016/j.rse.2014.12.015

frontiers | Frontiers in Remote Sensing

TYPE Perspective
PUBLISHED 05 August 2024
DOI 10.3389/frsen.2024.1373540

Check for updates

OPEN ACCESS

EDITED BY
Kevin Ruddick,
Royal Belgian Institute of Natural Sciences, Belgium

REVIEWED BY
Xiuqing Hu,
China Meteorological Administration, China
Ewa Kwiatkowska,
European Organisation for the Exploitation of Meteorological Satellites, Germany
Violeta Sanjuan Calzado,
National Aeronautics and Space Administration (NASA), United States

*CORRESPONDENCE
Andrew Barnard,
barnaran@oregonstate.edu

RECEIVED 19 January 2024
ACCEPTED 15 July 2024
PUBLISHED 05 August 2024

CITATION
Barnard A, Boss E, Haëntjens N, Orrico C, Chamberlain P, Frouin R, Mazloff M and Tan J (2024), A float-based Ocean color vicarious calibration program.
Front. Remote Sens. 5:1373540.
doi: 10.3389/frsen.2024.1373540

COPYRIGHT
© 2024 Barnard, Boss, Haëntjens, Orrico, Chamberlain, Frouin, Mazloff and Tan. This is an open-access article distributed under the terms of the Creative Commons Attribution License (CC BY). The use, distribution or reproduction in other forums is permitted, provided the original author(s) and the copyright owner(s) are credited and that the original publication in this journal is cited, in accordance with accepted academic practice. No use, distribution or reproduction is permitted which does not comply with these terms.

A float-based Ocean color vicarious calibration program

Andrew Barnard[1]*, Emmanuel Boss[2], Nils Haëntjens[2], Cristina Orrico[3], Paul Chamberlain[4], Robert Frouin[4], Matthew Mazloff[4] and Jing Tan[4]

[1]College of Earth, Ocean and Atmospheric Sciences, Oregon State University, Corvallis, OR, United States, [2]School of Marine Sciences, University of Maine, Orono, ME, United States, [3]Sea-Bird Scientific, Bellevue, WA, United States, [4]Scripps Institution of Oceanography, University of California San Diego, La Jolla, CA, United States

Ocean color satellites require a procedure known as System Vicarious Calibration (SVC) after launch as the pre-launch and on-orbit calibration accuracy is insufficient. The current approach for determination of post-launch SVC uses a single fixed measurement location and may be susceptible to unexpected biases in satellite processing algorithms. Here we describe a novel SVC program which is based on a high resolution and high accuracy radiometric system integrated with an autonomous profiling float (providing a buoyancy engine, physical observations, and communication). This float + radiometer (HyperNav) system can be shipped via air, land, ocean and is deployable from small boats. This SVC program relies on multiple deployment sites with associated facilities to collect a significant amount of SVC quality data in a relatively short time. It has centralized logistics and command-and-control centers ensuring easy access to information regarding the status of each asset and to ensure floats stay within a certain ocean area. The development of the program has been associated with the launch of NASA's PACE satellite and has been executed by academic institutions in collaboration with an industrial partner. Other approaches for a future float-based operational SVC program are discussed.

KEYWORDS

ocean color remote sensing, system vicarious calibration, ocean optics, radiometry, governance

1 Introduction

Ocean color sensors on satellites require a System Vicarious Calibration (SVC) procedure after launch as the pre-launch ground and on-board calibration uncertainties are insufficient to meet ocean color product requirements (Gordon, 1987; IOCCG, 2012). The SVC process has been used post-launch to evaluate and adjust the calibration factor of visible bands of the ocean color satellite sensor. The SVC method utilizes the *in-situ* water leaving radiance measurements propagated to the top of the atmosphere (TOA) using the same atmospheric correction functions as in operational processing, to provide estimated TOA radiance (Franz et al., 2007). The ratio between the estimated and measured TOA radiance is the vicarious gain (if no correction is necessary this value would be 1). Currently, the SVC process relies on obtaining a sufficient number of matchups (i.e., satellite TOA measurements and *in-situ* water leaving radiance measurements) to determine the average value of the calibration gain factors and their uncertainty. This process results in a lookup table of band-specific gains that are applied to post-launch ocean color observations. Thus, inherently, the SVC process relies

on both the quality of *in-situ* water leaving radiance data, as well as the quality of atmospheric correction models used in ocean color processing. Since the launch of NASA's SeaWiFS in 1997, the strategy for SVC of satellite ocean color radiometers has relied primarily on the deployment of an *in-situ* buoy instrumented with precision radiometers near the island of Lana'i in Hawaii (named Marine Optical BuoY, or MOBY). Historically, it has taken approximately 2–3 years following a satellite launch to determine required SVC gains by obtaining sufficient high-quality match-ups at the MOBY site (i.e., high accuracy *in-situ* radiometric measurements in ocean/atmosphere conditions that meet the SVC criteria, Franz et al. (2007)). Forty high-quality match-ups (concurrent satellite observation and in water observations) that meet acceptable atmosphere and ocean conditions were deemed sufficient to obtain sufficiently small uncertainties in the calibration gain factors of visible bands (Franz et al., 2007). This is because the uncertainty of a gain value scales inversely with the square root of the number of independent match-ups. This process is not designed to correct for drift in the sensor over its lifetime for which other procedures, such as lunar calibrations or on-board solar diffusers, are used. Suitable SVC infrastructure must ensure the lowest uncertainties on the measured radiometry that allow meeting the ocean color mission requirements. The coverage of the ocean color spectral domain and a hyperspectral capability must support SVC needs of the applicable missions.

Suitable SVC sites must satisfy specific and rather strict criteria (Gordon, 1987; IOCCG, 2012; Zibordi and Mélin, 2017). Firstly, the aerosols should be mostly of maritime origin (i.e., non-absorbing) with aerosol optical thickness (AOT) below 0.1 in the visible (i.e., very clear atmosphere), and the surface should be free of whitecaps (i.e., local surface wind speeds $< 15\ ms^{-1}$). In such situations, molecular scattering is the dominant process affecting the top-of-atmosphere (TOA) radiance in the visible, reducing the impact of uncertainties associated with the atmospheric correction scheme. Secondly, the water-leaving radiance should be uniform over several pixels viewed by the satellite, and the spatial contrast should be minimal over a distance of about 10–20 km to minimize adjacency effects. This generally excludes coastal regions, where aerosols are likely to be absorbing and abundant, spatial variability in water-leaving radiance may be large, and the proximity of land could exert a significant influence on the top-of-atmosphere (TOA) satellite signal. Furthermore, the sites should experience low cloudiness to maximize the number of *in-situ* SVC-quality measurements over time. The success of SVC requires an ability to accurately remove the contribution of the atmosphere whose signal dominates the TOA measured radiance in order to compare it with that measured at water-level. Thus, a good SVC site needs to have an atmosphere that can be accurately modeled (e.g., known aerosols concentration and composition), have low spatial in-water optical variability, is typically cloud-free with low wind/wave conditions, is located far enough away from land to reduce adjacency effects, in addition to considerations of logistical costs of system operation.

Multiple sites meeting the SVC specifications can be preferable, providing the highest standard and equivalence in radiometric performance IOCCG (2012). Multiple sites may allow to understand and reduce residual uncertainties in atmospheric correction modelling, if any. A possibility of a seasonal bias in the visible band radiometry and particulate backscattering retrievals in the ocean color sensors processed using the same atmospheric correction code was found in comparisons with MOBY, lidar and profiling floats Bisson et al. (2021b,a). Performing SVC measurements at multiple sites across the globe may thus be a prudent approach.

From the above it follows that to improve on the current approach for SVC, future ocean color SVC programs should include: 1) an increase the number of high quality *in-situ* measurements available for SVC after satellite launch, 2) an increase the number of sites for SVC, and 3) such sites should have a high probability for ocean color satellite match-ups (i.e., meet the stringent criteria for SVC purposes). These improvements will reduce the time to derive stable and accurate SVC gain adjustments for a new ocean color satellite, better constrain potential uncertainties in the atmospheric correction, and reduce the time for scientific use of satellite imagery after launch.

The number of current and future satellite ocean color missions has significantly increased in recent years[1], with each of these missions having different visible spectral bands. In particular, various organizations, such as NASA and European Commission Copernicus Programme, are planning new ocean color satellite missions to observe the Earth's oceans at unprecedented spectral resolution with the goal to improve understanding of the surface biology and biogeochemistry (e.g., phytoplankton functional groups; Werdell et al. (2019)). Thus, future generation of hyperspectral ocean color satellite will require a concordant advancement in *in-situ* hyperspectral radiometric measurements for SVC purposes.

In this paper we describe a novel SVC system, HyperNav, that provides a pathway to meet the current and future needs of ocean color satellite sensors. It is based on high-precision high-accuracy hyperspectral upwelling radiance radiometers (two per system) and utilizes an autonomous profiling float which is portable and can be deployed and retrieved by relatively small coastal vessels. The system includes a command and control platform, termed the HyperNav Portal, to aid in navigation of the float to remain in a bounded region near the deployment site, provide time series of *in-situ* high-accuracy radiometric measurements, and provide open access to collected data from deployed HyperNav float systems. Furthermore, the program is scalable, whereby several HyperNav float systems can be deployed to collect measurements at multiple sites simultaneously, thereby increasing the number of high-quality, low-uncertainty *in-situ* SVC-usable observations. Together with *in-situ* mooring-based SVC measurement approaches such as MOBY (Brown et al., 2007), these systems can provide complementary information, support retrieval and uncertainty analysis of SVC gain factors using independent approaches (i.e., different in hardware and location), and rapid delivery of the gains with multiple floats operating at different sites.

1 https://ioccg.org/resources/missions-instruments/current-ocean-colour-sensors/

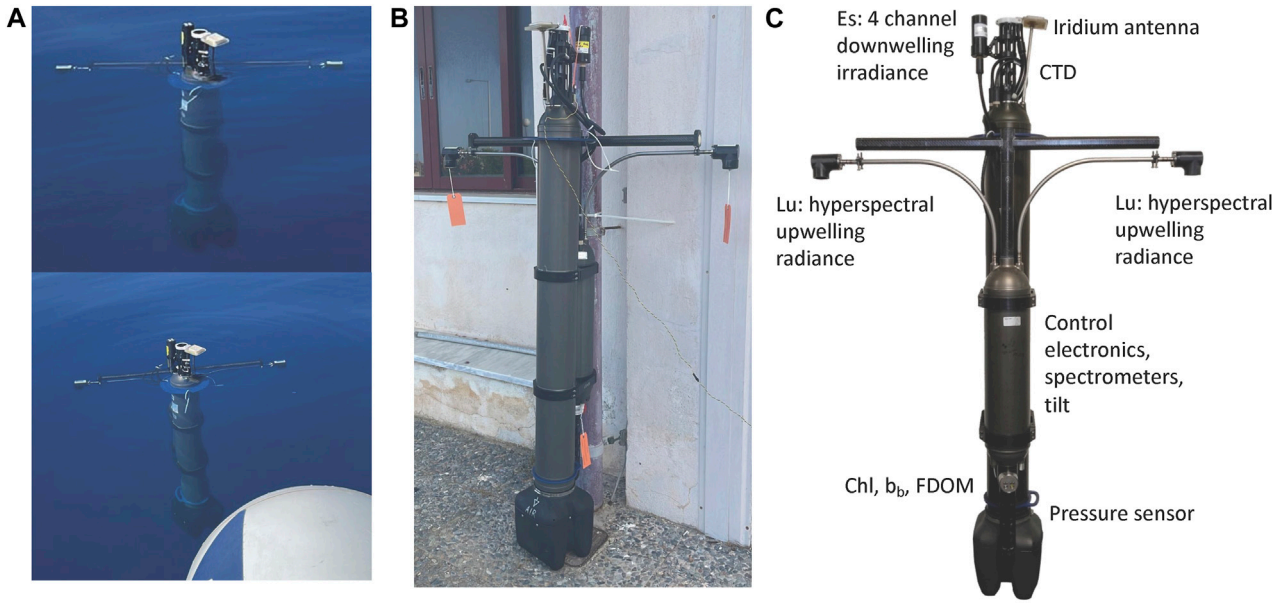


FIGURE 1
The HyperNav float-based system. **(A)** Photos of the system from a test deployment North of Crete. **(B)** Photo of the system taken onshore before deployment during system testing. The Navis float is shown in the forefront. **(C)** Photo of HyperNav showing the locations of the sensors.

2 Components of a float-based SVC system

The idea of using radiometers on profiling floats is not new. In the early 2000s floats equipped with radiometers were used to study the onset of the spring bloom in the sea of Japan (Mitchell, 2003) and have since become an integral part of BGC-Argo (Johnson and Claustre, 2016). The idea of using autonomous profiling floats as a component of an SVC program for *in-situ* radiometric measurements has also been previously explored (Gerbi et al., 2016; Leymarie et al., 2018), including the advantages of putting two upwelling radiometers per float on extended arms (Leymarie et al., 2018) for redundancy and to ensure that there is always a radiometer that is not shaded by the float itself. Redundancy and minimizing shading both contribute to reducing the uncertainty in the *in-situ* radiometric measurements for SVC. Below we expand on the HyperNav end-to-end system that has been designed and tested which we suggest should be part of an ocean color satellite SVC system.

2.1 The float and HyperNav system

The HyperNav float-based profiling system consists of a buoyancy-driven autonomous profiling float with standard Argo sensors (e.g., an Argo-program-like profiling float, Roemmich et al. (2019)) integrated with a high spectral resolution and accuracy radiometric system (HyperNav radiometric sensor, Sea-Bird Scientific (SBS)) equipped with additional sensors to measure pressure and platform orientation and other optical properties. The profiling float we currently use is a SBS Navis float, modified to power the HyperNav system, receive and transmit HyperNav data via Iridium satellite communication to shore, and change mission configurations of the HyperNAV system (Figure 1). The Navis float is equipped with a standard Argo CTD and the Navis firmware has been modified to enable power, sampling, and data transmission for the HyperNav radiometric system.

The integrated HyperNav radiometric system includes dual independent upwelling radiance sensors, integrated pressure and tilt sensor. The sensors, the system, and how they meet the SVC measurment requirements are described in a parallel paper Barnard et al. (2024). The HyperNav sensor system that is integrated with the Navis float includes an SBS OCR-504 four-wavelength downwelling radiometer (providing above water downwelling irradiance) which is mounted to the Navis float CTD stalk. The purpose of the above-water downwelling radiometer is to help ensure conditions for SVC are optimal in terms of atmospheric transmission and account for varying sky conditions during the HyperNav data acquisition period. The HyperNav sensor system also includes integrated pressure and tilt sensors, both of which are used to evaluate the upwelling radiance measurements for SVC observations. The development of the HyperNav sensor system includes a SBS MCOMS triplet sensor (measuring backscattering at 700 nm, chlorophyll and CDOM fluoresence). The purpose of the MCOMS is to provide verification that the upper part of the ocean is not optically stratified, a key requirement of SVC qualified *in-situ* measurements. While MCOMS are included on all HyperNav sensor systems, full data integration and sample sequencing is still under developed, and is intended to be enabled in the near future.

2.2 Float command and control center

As part of the currently funded HyperNav project, an online command and control operations and data delivery site, termed the

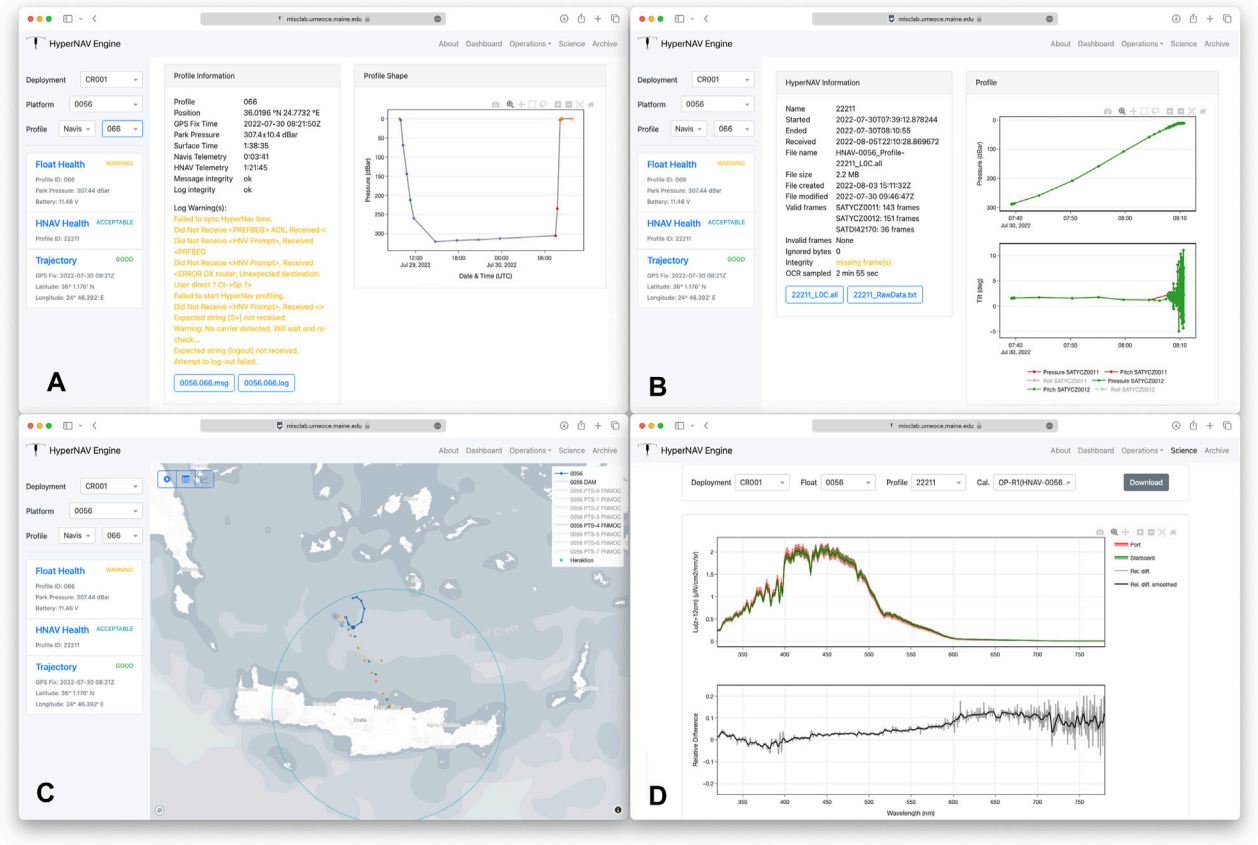


FIGURE 2
Four different screens from the HyperNav Portal site. **(A)** Dive pattern of a given profile. **(B)** HyperNav data acquisition profile. **(C)** Float trajectory for 5 day period North of Crete. **(D)** Water leaving radiance spectra and its uncertainty computed for a given profile. All can be accessed from the HyperNav Portal https://misclab.umeoce.maine.edu/HyperNav/.

HyperNav Portal, was created (http://misclab.umeoce.maine.edu/HyperNav/) where key information is available (Figure 2):

- Displays near-real time float and HyperNav radiometric sensor health status.
- Maps of current and predicted trajectories of HyperNav floats for mission planning.
- Displays radiometric measurements to assess data-quality.
- Links to download near-real time data.
- Links to weather predictions and ocean color satellite overpass dates/times for each site.

Such information is available for current as well historical deployments.

This information allows the operations team to assess the health of each float, the quality of the radiometric data being collected (e.g., to decide whether it needs to be picked up), consult with weather patterns for decision-making of future float surfacing, and consult with circulation models output to navigate and steer the float to remain within the predefined sampling and recovery area. The command and control center also includes hardware such as a Router-Based Unrestricted Digital Internet-working Connectivity Solutions (RUDICS) server, a web server (and backup servers) for two way communication with the float and the on-shore server to enable public distribution/access of the data. All servers are virtual machine hosted in the cloud of the University of Maine and could be transferred to other cloud providers if need be.

2.3 Logistics center

The logistics center of the HyperNav Portal consists of a series of Google worksheets that aggregate all the information regarding the past, present and future status of floats and HyperNav systems and is accessible to all relevant partners. This information is used by the operational team to aid in deployment/recovery and future asset planning. Key attributes includes HyperNav calibration status (e.g., which sensors need to be post-calibrated after a mission), float and HyperNav asset tracking for deployments (i.e., asset availability to support next deployment locations), which is used to plan for future deployments and integration of future builds of float and HyperNav systems (e.g., new systems deliveries and scheduling). The logistics center facilitates coordination with local deployment groups as well as planning and coordination with shipping agents to deliver the systems to the next location in a timely manner.

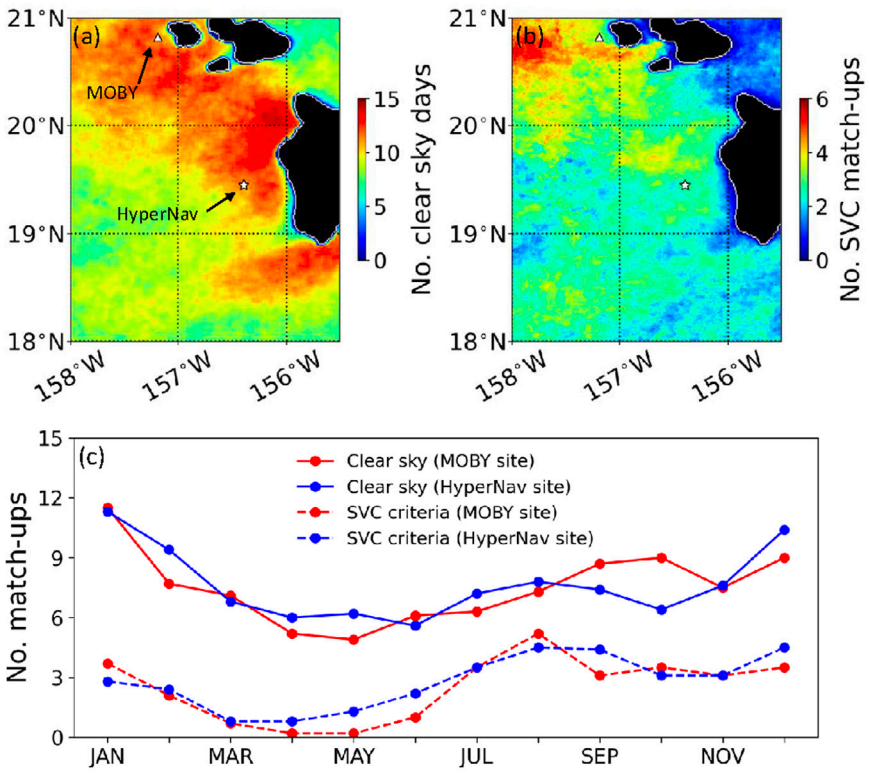


FIGURE 3
(A) Map of the average number of clear sky conditions in January in the seas around Hawaiian islands. White lines delineate the land/water boundaries. **(B)** Same as **(A)** but for the more stringent conditions where the sky is clear, aerosol optical thickness at 869 nm < 0.1, single scattering albedo > 0.95 at 550 nm, coefficient of variation of Rrs at 443 nm < 0.2 over a 3 × 3 km^2 area, and wind speed < 8 m s^{-1}. MODIS-A L2 data at 1.1 km resolution (2010-2019) are used for all variables except single scattering albedo and wind speed, which originate from MERRA-2 and NCEP reanalyses. Clear sky conditions are those where a 5 × 5 km^2 area around each location is free of clouds. **(C)** Monthly time series of potential clear sky and SVC match-ups, solid and dashed lines, respectively, at the selected locations, i.e., MOBY site [20.8°N, 157.2°W] and HyperNav deployment site [19.5°N, 156.4°W], as indicated by a white star in the maps.

2.4 Deployment sites

One key characteristic of the float-based SVC program is its ability to obtain data from multiple sites. Each deployment site is evaluated based on:

- Oceanic and atmospheric suitability to SVC.
- Logistics - cost and ease-of shipping, deployment and servicing of systems at the site.
- Circulation properties likely to allow for the systems to stay within reach (3–4 h of steaming with local vessel) throughout a 60–90 days deployment.

We expand on some of these below and much more in Chamberlain et al. (2024).

We developed partnerships with local scientists and boat operators to facilitate operations in each of the selected regions. All project team members and local personnel are trained in the necessary procedures to assemble a HyperNav system, perform operational system checks before deployment, enable deployment mission configuration, and ensure effective operations at time of deployment and through post deployment. This strategy of utilizing project teams and/or local partners (if available) for deployments, adds flexibility to the HyperNav program to maintain presence in longer-term deployment sites as well as facilitating "seasonal" and sites of opportunity for deployments. In the later case, deployment/logistics actions are performed by a project team that travels to the deployment site for deployment and/or recovery. As part of the deployment planning process, the logistic center includes working with local teams to ensure local knowledge and availability of boat operators in the deployment region that can support deployment/recovery operations on short notice in case a system recovery is needed. Since it will be very useful to have capabilities to replace a float within a system or batteries of a float locally (to avoid shipping the whole float back to the manufacturer), training local personnel in those tasks is performed. Issues of customs are also taken into account in site selection as those add delays as well as costs to the operation.

The selection of deployment sites is based on a comprehensive analysis of various factors to ensure suitability for SVC measurements (e.g., Figure 3). This analysis includes evaluating ocean and atmosphere properties, as discussed in studies by Franz et al. (2007) and Zibordi and Mélin (2017), assessing ocean current fields to guarantee that floats can remain within a predefined region for a 3-month deployment, and considering logistics and associated costs for each site. The process of the HyperNav system site selection, which includes flow analysis, is described in more detail in Chamberlain et al. (2024).

Figure 3 depicts maps illustrating the number of clear sky and SVC days, indicating the potential number of match-ups in January in the Hawaiian region during MODIS-A overpass. The SVC criteria, although similar, differ somewhat from those outlined in previous studies, specifically in their stringency regarding aerosol type and optical thickness thresholds. In particular the influence of absorbing aerosols is minimized. At identified locations such as MOBY and the HyperNav site west of Kona, Hawaii, there are approximately 3 potential SVC match-ups per month from July to January, totaling about 25–30 SVC match-ups annually. In comparison, Franz et al. (2007) obtained roughly 15 SVC match-ups per year at the MOBY site, reflecting the challenges of maintaining continuous measurements throughout the year. Relaxing the SVC criteria would lead to a larger number of potential SVC match-ups, as indicated by the SVC and clear sky curves in Figure 3.

For the PACE mission post-launch support, four sites have been identified for initial operation: West of Kona, Hawaii, United States; North of the island of Crete, Greece; South of Puerto Rico, United States; and South of Moorea, French Polynesia. Over the past 2 years, multiple deployments have been conducted at each location to assess HyperNav performance, evaluate upwelled radiance measurement quality against SVC criteria, and determine the ability of HyperNav float trajectories to remain in the desired location. Additionally, recent deployments off Southern California have contributed to the assessment and refinement of site selection for seasonal and opportunistic future deployments, as well as testing HyperNav system performance with newly delivered systems.

2.5 Data analysis

As data arrives from the *in-situ* HyperNav system to the command and control center via Iridium communication, it is automatically processed in near-real time and subsequently posted to the HyperNav Portal (Haëntjens et al., this issue). This processing includes:

- Application of calibration for conversion to SI units of radiance measurements.
- Computation of the near surface attenuation coefficients based on profile.
- Propagation of upwelled radiance to the surface and through the water-air interface.
- Quality assessment of radiance data (e.g., spike removal).
- Merging of the two upwelled radiance spectra above the surface into a single best estimate with uncertainties.
- Computation of reflectance based on the above upwelled radiance and modelled solar irradiance (Tan et al., 2024).

Following the recovery and post-calibration of the HyperNav is performed, the data is reprocessed, and a delayed-mode data set is generated for the spectrum of upwelled radiance and reflectance. Note that as with ocean color remote sensing, the reflectance computation is based on the measured spectral *in-situ* upwelled radiance and a model-based downwelling irradiance spectrum Tan et al. (2024). In addition, all data and associated metadata (e.g., sensors calibrations) is archived and shared on the HyperNav Portal. Computed products are archived in compliance with the NetCDF Climate and Forecast Metadata Conventions v1.10.

2.6 Liaison to space agency

NASA, the funding agency of HyperNav program, has been interested in both near-real-time and delayed-mode data. A person in the agency and at the SVC program are in regular contact to ensure the SVC system is fit for purpose, and that data flows automatically to the agency as soon as it is available in raw format as well as processed to SI units.

3 Models for operational float-based SVC systems

3.1 Governance structures

The float-based SVC program described here is currently funded as a research and development program. The long-term prospects depend not only on evolving such system to a sustainable operational state, but also on ensuring sustainable funding for such a program in the future. Below we discuss different models that may be chosen for this purpose:

- A private company sells to customer(s) SVC match-ups on a per match-up basis, e.g., based on dollars per match-up in a region of interest. This entity takes care of all the logistics and the command and control parts of the operation itself, or delegates logistics to subcontractor. An example of such data ordered system is that of saildrone.com which collects ocean data in a variety of oceans using drones equipped with a variety of ocean sensors.
- An academic institution or a consortium of academic institutions (as in our current project) maintains and operates the SVC system funded by space agencies interested in the data. Data is available to all in near-real time (to ensure transparency). Local operations may be coordinated with a local marine stations to minimize shipping and travel costs. The MOBY SVC program operates that way with the University of Miami as lead and the Moss Landing Marine Lab as the entity operating the facility.
- An operational group within a space agency is responsible to the SVC operation and data analysis. It has agreements with local entities to take care of the infrastructure but the oversight of data and its analysis is done by the agency. An example is the AERONET-OC consortium and NASA.

Each of these models has advantages and disadvantages. Academic institutions are generally less expensive and nimble (e.g., if there is a need to swap sites) but lack the robustness of services that may be provided via a private company. There may be issues of conflict of interest when a funding agency also operates services, though it is a model that best ensures fitness for purpose.

Whichever governance system is chosen, it is critical to maximize its utility to the oceanographic community, that it

follows the FAIR (findable, accessible, inter-operable, and reusable) data management principles Tanhua et al. (2019); Davidson et al. (2019). In addition, it is expected that data will be made available to users in near-real time for short-term decision making as well as in a delayed mode, following recovery and radiance sensors post-calibration.

3.2 External advisory committee

It is critical that the latest science and technological know-how informs the program operations while providing the funding agency with unbiased information regarding the return on investment. This goal can be achieved by having an external advisory committee which includes outside experts in the subject of ocean optics, radiometry, SVC and metrology, that meets annually to review the program and provide recommendation to the funder as well as the entity responsible for the operation of the SVC program.

4 Summary

In this paper we summarized the features associated with a float-based SVC program building on our experience with the program we have designed and tested to date. More details about the different elements of this program are detailed in accompanying papers Barnard et al. (2024); Chamberlain et al. (2024); Tan et al. (2024). We believe the program to have been very successful and it has been improving continuously. However, such an SVC program is not sustainable in its current form and in order to be operational over ocean color satellite lifetimes, funding agencies interested in its data will need to decide on its future funding and governance structure. We hope this paper has provided sufficient information on the needs, importance, and potential pathways forward to consider for maintaining and sustaining such a critical SVC program in the future.

Data availability statement

The raw data supporting the conclusions of this article will be made available by the authors, without undue reservation.

Author contributions

AB: Conceptualization, Funding acquisition, Investigation, Methodology, Project administration, Supervision, Validation, Writing–original draft, Writing–review and editing. EB: Conceptualization, Investigation, Methodology, Supervision, Validation, Writing–original draft, Writing–review and editing. NH: Formal Analysis, Methodology, Software, Validation, Writing–review and editing. CO: Project administration, Supervision, Writing–review and editing. PC: Conceptualization, Formal Analysis, Methodology, Writing–review and editing. RF: Formal Analysis, Investigation, Methodology, Writing–original draft, Writing–review and editing. MM: Conceptualization, Methodology, Supervision, Writing–review and editing. JT: Formal Analysis, Investigation, Methodology, Writing–review and editing.

Funding

The author(s) declare that financial support was received for the research, authorship, and/or publication of this article. Funding for the HyperNav system has been provided by NASA Goddard Space Flight Center, through the Ocean Biology and Biogeochemistry program, from contract numbers 80GSFC20C0101 and 180GSFC22CA050.

Acknowledgments

We thank Andrew Banks and Nektarios Spiyridakis for extraordinary support for operations in Crete. We thank Eric Rehm for useful comments on an early version of this manuscript.

Conflict of interest

Author CO was employed by company Se-Bird Scientific.

The remaining authors declare that the research was conducted in the absence of any commercial or financial relationships that could be construed as a potential conflict of interest.

Publisher's note

All claims expressed in this article are solely those of the authors and do not necessarily represent those of their affiliated organizations, or those of the publisher, the editors and the reviewers. Any product that may be evaluated in this article, or claim that may be made by its manufacturer, is not guaranteed or endorsed by the publisher.

References

Barnard, A., Boss, E., Häentjens, N., Orrico, C., Frouin, R., Tan, J., et al. (2024). Design and verification of a highly accurate *in-situ* hyperspectral radiometric measurement system (hypernav). *Front. Remote Sens.* 5. doi:10.3389/frsen.2024.1369769

Bisson, K. M., Boss, E., Werdell, P. J., Ibrahim, A., and Behrenfeld, M. J. (2021a). Particulate backscattering in the global ocean: a comparison of independent assessments. *Geophys. Resa Lett.* 48, e2020GL090909. doi:10.1029/2020gl090909

Bisson, K. M., Boss, E., Werdell, P. J., Ibrahim, A., Frouin, R., and Behrenfeld, M. J. (2021b). Seasonal bias in global ocean color observations. *Appl. Opt.* 60, 6978–6988. doi:10.1364/AO.426137

Brown, S. W., Flora, S. J., Feinholz, M. E., Yarbrough, M. A., Houlihan, T., Peters, D., et al. (2007). "The marine optical buoy (MOBY) radiometric calibration and uncertainty budget for ocean color satellite sensor vicarious calibration,". *Sensors, systems, and next-generation satellites XI*. Editors S. Habib, R. Meynart, S. P. Neeck, and H. Shimoda (SPIE: International Society for Optics and Photonics), 6744. doi:10.1117/12.73740067441M

Chamberlain, P., Frouin, R., Tan, J., Mazloff, M., Barnard, A., Boss, E., et al. (2024). Selecting hypernav deployment sites for calibrating and validating pace ocean color observations. *Front. Remote Sens* doi:10.3389/frsen.2024.1333851

Davidson, F., Alvera-Azcárate, A., Barth, A., Brassington, G. B., Chassignet, E. P., Clementi, E., et al. (2019). Synergies in operational oceanography: the intrinsic need for sustained ocean observations. *Front. Mar. Sci.* 6. doi:10.3389/fmars.2019.00450

Franz, B. A., Bailey, S. W., Werdell, P. J., and McClain, C. R. (2007). Sensor-independent approach to the vicarious calibration of satellite ocean color radiometry. *Appl. Opt.* 46, 5068–5082. doi:10.1364/AO.46.005068

Gerbi, G. P., Boss, E., Werdell, P. J., Proctor, C. W., Haëntjens, N., Lewis, M. R., et al. (2016). Validation of ocean color remote sensing reflectance using autonomous floats. *J. Atmos. Ocean. Technol.* 33, 2331–2352. doi:10.1175/JTECH-D-16-0067.1

Gordon, H. R. (1987). Calibration requirements and methodology for remote sensors viewing the ocean in the visible. *Remote Sens. Environ.* 22, 103–126. doi:10.1016/0034-4257(87)90029-0

IOCCG (2012). *Dartmouth*. Canada: IOCCG.

Johnson, K. S., and Claustre, H. (2016). Bringing biogeochemistry into the argo age. *EOS* 97. doi:10.1029/2016EO062427

Leymarie, E., Penkerc'h, C., Vellucci, V., Lerebourg, C., Antoine, D., Boss, E., et al. (2018). Proval: a new autonomous profiling float for high quality radiometric measurements. *Front. Mar. Sci.* 5. doi:10.3389/fmars.2018.00437

Mitchell, B. G. (2003). "Resolving spring bloom dynamics in the sea of Japan," in *ALPS: Autonomous and Lagrangian Platforms and Sensors, Workshop Report*. Editors D. L. Rudnick and M. J. Perry (La Jolla, CA: ALPS), 26 –27.

Roemmich, D., Alford, M. H., Claustre, H., Johnson, K., King, B., Moum, J., et al. (2019). On the future of argo: a global, full-depth, multi-disciplinary array. *Front. Mar. Sci.* 6. doi:10.3389/fmars.2019.00439

Tan, J., Frouin, R., Häentjens, N., Barnard, A., Boss, E., Chamberlain, P., et al. (2024). Reconstructing hyper-spectral downwelling irradiance from multi-spectral measurements. *Front. Remote Sens.* 5. doi:10.3389/frsen.2024.1335627

Tanhua, T., Pouliquen, S., Hausman, J., O'Brien, K., Bricher, P., de Bruin, T., et al. (2019). Ocean fair data services. *Front. Mar. Sci.* 6. doi:10.3389/fmars.2019.00440

Werdell, P. J., Behrenfeld, M. J., Bontempi, P. S., Boss, E., Cairns, B., Davis, G. T., et al. (2019). The plankton, aerosol, cloud, ocean ecosystem mission: status, science, advances. *Bull. Am. Meteorological Soc.* 100, 1775–1794. doi:10.1175/BAMS-D-18-0056.1

Zibordi, G., and Mélin, F. (2017). An evaluation of marine regions relevant for ocean color system vicarious calibration. *Remote Sens. Environ.* 190, 122–136. doi:10.1016/j.rse.2016.11.020

frontiers | Frontiers in Remote Sensing

TYPE Original Research
PUBLISHED 05 August 2024
DOI 10.3389/frsen.2024.1347520

Check for updates

OPEN ACCESS

EDITED BY
Amir Ibrahim,
National Aeronautics and Space Administration, United States

REVIEWED BY
Tristan Harmel,
Earth Observation Unit, Magellium, France
Srinivas Kolluru,
Florida Atlantic University, United States

*CORRESPONDENCE
Kevin G. Ruddick,
kruddick@naturalsciences.be

RECEIVED 30 November 2023
ACCEPTED 10 June 2024
PUBLISHED 05 August 2024

CITATION
Ruddick KG, Brando VE, Corizzi A, Dogliotti AI, Doxaran D, Goyens C, Kuusk J, Vanhellemont Q, Vansteenwegen D, Bialek A, De Vis P, Lavigne H, Beck M, Flight K, Gammaru A, González Vilas L, Laizans K, Ortenzio F, Perna P, Piegari E, Rubinstein L, Sinclair M and Van der Zande D (2024), WATERHYPERNET: a prototype network of automated *in situ* measurements of hyperspectral water reflectance for satellite validation and water quality monitoring. *Front. Remote Sens.* 5:1347520. doi: 10.3389/frsen.2024.1347520

COPYRIGHT
© 2024 Ruddick, Brando, Corizzi, Dogliotti, Doxaran, Goyens, Kuusk, Vanhellemont, Vansteenwegen, Bialek, De Vis, Lavigne, Beck, Flight, Gammaru, González Vilas, Laizans, Ortenzio, Perna, Piegari, Rubinstein, Sinclair and Van der Zande. This is an open-access article distributed under the terms of the Creative Commons Attribution License (CC BY). The use, distribution or reproduction in other forums is permitted, provided the original author(s) and the copyright owner(s) are credited and that the original publication in this journal is cited, in accordance with accepted academic practice. No use, distribution or reproduction is permitted which does not comply with these terms.

WATERHYPERNET: a prototype network of automated *in situ* measurements of hyperspectral water reflectance for satellite validation and water quality monitoring

Kevin G. Ruddick[1]*, Vittorio E. Brando[2], Alexandre Corizzi[3], Ana I. Dogliotti[4], David Doxaran[3], Clémence Goyens[1], Joel Kuusk[5], Quinten Vanhellemont[1], Dieter Vansteenwegen[6], Agnieszka Bialek[7], Pieter De Vis[7], Héloise Lavigne[1], Matthew Beck[1], Kenneth Flight[5], Anabel Gammaru[1], Luis González Vilas[2], Kaspars Laizans[5], Francesca Ortenzio[1], Pablo Perna[4], Estefania Piegari[4], Lucas Rubinstein[4], Morven Sinclair[7] and Dimitry Van der Zande[1]

[1]Royal Belgian Institute of Natural Sciences (RBINS), Brussels, Belgium, [2]Consiglio Nazionale Delle Ricerche (CNR-ISMAR), Rome, Italy, [3]Laboratoire Océanographique de Villefranche (LOV), UMR7093 CNRS, Sorbonne Université (SU), Villefranche-sur-mer, France, [4]Instituto de Astronomía y Física del Espacio, Consejo Nacional de Investigaciones Científicas y Técnicas (IAFE, CONICET/UBA), Buenos Aires, Argentina, [5]Tartu Observatory, University of Tartu (UT), Tartu, Estonia, [6]Flanders Marine Institute (VLIZ), Oostende, Belgium, [7]National Physical Laboratory (NPL), Teddington, United Kingdom

This paper describes a prototype network of automated *in situ* measurements of hyperspectral water reflectance suitable for satellite validation and water quality monitoring. Radiometric validation of satellite-derived water reflectance is essential to ensure that only reliable data, e.g., for estimating water quality parameters such as chlorophyll *a* concentration, reach end-users. Analysis of the differences between satellite and *in situ* water reflectance measurements, particularly unmasked outliers, can provide recommendations on where satellite data processing algorithms need to be improved. In a massively multi-mission context, including Newspace constellations, hyperspectral missions and missions with broad spectral bands not designed for "water colour", the advantage of hyperspectral over multispectral *in situ* measurements is clear. Two hyperspectral measurement systems, PANTHYR (based on the mature TRIOS/RAMSES radiometer) and HYPSTAR® (a newly designed radiometer), have been integrated here in the WATERHYPERNET network with SI-traceable calibration and characterisation. The systems have common data acquisition protocol, data processing and quality control. The choice of validation site and viewing geometry and installation considerations are described in detail. Three demonstration cases are described: 1. PANTHYR data from two sites are used to validate Sentinel-2/MSI (A&B); 2. HYPSTAR® data at six sites are used to validate Sentinel-3/OLCI (A&B); 3. PANTHYR and HYPSTAR® data in Belgian North Sea waters are used to monitor phytoplankton parameters, including *Phaeocystis globosa*, over two 5 month periods. Conclusion are drawn regarding the quality

of Sentinel-2/MSI and Sentinel-3/OLCI data, including indications where improvements could be made. For example, a positive bias (mean difference) is found for ACOLITE_DSF processing of Sentinel-2 in clear waters (Acqua Alta) and clues are provided on how to improve this processing. The utility of these *in situ* measurements, even without accompanying hyperspectral satellite data, is demonstrated for phytoplankton monitoring. The future evolution of the WATERHYPERNET network is outlined, including geographical expansion, improvements to hardware reliability and to the measurement method (including uncertainty estimation) and plans for daily distribution of near real-time data.

KEYWORDS

water colour, satellite validation, hyperspectral reflectance, in situ measurements, phytoplankton

1 Introduction

Spaceborne optical remote sensing from daily 100–1000 m resolution multispectral "water colour" missions such as MODIS (Franz et al., 2005), VIIRS (Wang et al., 2016) and Sentinel-3/OLCI (Garnesson et al., 2019) provides operational data to end-users for applications such as coastal water quality management (eutrophication, sediment transport, etc.). 10–100 m resolution "designed-for-land" missions such as Landsat 8&9 (Pahlevan and Schott, 2013; Vanhellemont and Ruddick, 2014) and Sentinel-2 (Hedley et al., 2018; Vanhellemont, 2019a) have also become popular tools for coastal and inland water monitoring. 1–10 m resolution missions, including large satellites such as the Pléiades series (Vanhellemont and Ruddick, 2018; Luo et al., 2020) and cubesat constellations from Newspace companies such as the PlanetScope Doves (Vanhellemont, 2019b) and SuperDoves (Vanhellemont, 2023), are now emerging, and offer new opportunities for applications inside ports and small lakes, and for monitoring coastal operations (construction, dredging/disposal). This spacescape of low earth orbit missions is supplemented by a new generation of hyperspectral missions, such as DESIS (Alonso et al., 2019), PRISMA (Braga et al., 2022), ENMAP (Kaufmann et al., 2006), EMIT (Thompson et al., 2023) and PACE/OCI (Gorman et al., 2019), which are expected to provide better information on phytoplankton species composition (Dierssen et al., 2020; Lavigne et al., 2022). Finally the multispectral geostationary "water colour" missions, GOCI-1 and GOCI-2 (Ryu et al., 2012), can provide a much higher frequency of data, e.g., for monitoring tidal and diurnal variability, as can the "meteorological" geostationary satellite sensors such as MSG/SEVIRI (Neukermans et al., 2009) and MTG/FCI (Kwiatkowska et al., 2016; Lavigne and Ruddick, 2018) and Himawari-8 (Dorji and Fearns, 2018), albeit with a more challenging signal-to-noise ratio for the latter sensors. A non-exhaustive overview of the present and near-future satellite missions relevant for coastal and inland water quality monitoring can be found in Table 1.

To ensure that the products from all these satellite missions can be trusted by end-users, and particularly to identify any atmospheric correction errors, *in situ* measurements of water reflectance are needed to validate the satellite data products. The multispectral AERONET-OC network (Zibordi et al., 2009; Zibordi et al., 2021) demonstrated clearly that radiometric validation of satellites is most efficiently achieved by a network of automated radiometers with common data acquisition and processing. In fact, the radiometric validation of the operational Sentinel-3/OLCI mission is currently achieved with only AERONET-OC data (EUMETSAT, 2021; Zibordi et al., 2022). Shipborne and buoy data, from SeaBASS (Werdell et al., 2003), CEFAS Smartbuoys (Mills et al., 2003; Neukermans et al., 2012) and the Atlantic Meridional Transect (Tilstone et al., 2021), are used in the validation context only for inherent optical properties and chlorophyll *a* concentration, while the single automated MOBY platform data (Brown et al., 2007) are used for system vicarious calibration. Based on the AERONET-OC success, the prototype WATERHYPERNET network has been set up as an international network of sites running automated systems of pointable hyperspectral radiometers with common data acquisition and processing. WATERHYPERNET provides water reflectance validation data at hyperspectral resolution every cloud-free day for sites with diverse water and atmosphere conditions.

The use of hyperspectral radiometers in this massively multi-mission perspective has a clear advantage (Figure 1) for matching *in situ* data to all satellite data spectral responses (including out-of-band response), and thus avoiding the uncertainties and possible model assumptions associated with band-shifting (Mélin and Sclep, 2015; Pahlevan et al., 2017; Hieronymi, 2019). A disadvantage of the hyperspectral radiometers is the slower integration time, and generally less mature knowledge of instrument characteristics (Vabson et al., 2019; Zibordi et al., 2019).

This paper describes the design of the prototype WATERHYPERNET network, including hardware (radiometer and associated system), software (data acquisition, and data processing and distribution by the HYPSTAR® processor (De Vis et al., 2024)) and current validation sites. Examples are given of exploitation of datasets for satellite validation and water quality monitoring, and future perspectives for a long-term operational network are provided.

To facilitate reading of this paper, a table of acronyms is provided in Supplementary Table S1.

2 The WATERHYPERNET network—overview

2.1 Materials and equipment - hyperspectral radiometer systems

Automated abovewater hyperspectral radiometer systems currently or recently used for measurement of water reflectance

include: 3-sensor TRIOS/RAMSES with fixed azimuth (Arabi et al., 2018); rotating azimuth TRIOS/RAMSES So-Rad (Simis and Olsson, 2013); rotating azimuth DALEC (Slivkoff, 2014; Brando et al., 2016); 3-sensor Seabird/HyperSAS with rotating azimuth (Carswell et al., 2017); the WispStation with six optical paths at two fixed azimuth directions (Peters et al., 2018); and the OSPREY system (Hooker et al., 2012), which includes both zenith and azimuth pointing and both multispectral and hyperspectral detectors. For the WATERHYPERNET a crucial design choice was to use a pan-tilt unit, allowing both azimuth- and zenith-pointing, in contrast to all prior hyperspectral systems except the OSPREY.

WATERHYPERNET currently accepts two abovewater hardware systems: a) the PANTHYR system based on the mature TRIOS/RAMSES radiometer, and b) the HYPSTAR® system based on a newly-designed radiometer.

The PANTHYR (PAN and Tilt HYperspectral Radiometer) system, shown in Figure 2A, is described in detail by (Vansteenwegen et al., 2019), and consists of two TRIOS/RAMSES radiometers (one irradiance, one radiance with 7° Field of View; 400–900 nm at 10 nm Full Width Half Maximum, FWHM) with external camera mounted on a FLIR PTU-D48 E pan-tilt unit controlled by a single-board Beaglebone Black Industrial computer and associated custom-built electronics.

The HYPSTAR® (HYperspectral Pointable System for Terrestrial and Aquatic Radiometry) system, shown in Figure 2B and described in more detail in (Kuusk et al., 2024), consists of a newly-designed hyperspectral radiometer (380–1020 nm at 3 nm FWHM) with integrated radiance and irradiance fore-optics and embedded RGB camera, mounted on a Will-Burt Bowler Rx pan-tilt unit, and controlled by a rugged Cincoze DE-1000 PC. The system has an integrated LED light source for relative calibration monitoring during long deployments–see Figure 2B. This light source is outside the HYPSTAR® system optical path and so monitors not just changes in spectrometer responsivity, but also any contamination of the fore-optics, e.g., from dust or animals (spider webs, bird faeces, etc.).

Both systems include auxiliary sensors for ambient light and rain detection and the HYPSTAR® has an ambient light sensor measuring continuously during radiometry. Power supplies (grid, solar + battery) and data transmission (cabled internet, wifi, 2G/3G/4G) are site dependent.

The systems are programmed to acquire data typically every 20 min during daylight, although site-specific adjustments between 15 and 30 min repeat period and/or limiting to a few hours around local solar noon are possible if justified by scientific needs or power limitations. Both systems follow an abovewater radiometry acquisition protocol based on (Mobley, 1999), termed hereafter M1999. Measurements are acquired at 90° and/or 135° relative azimuth to Sun and potentially both left and right of Sun, when permitted by the local mounting structure and its shadows/reflections. Data are transmitted to land in near real time for automated, centralised processing and quality control. Extension of the processing to generate uncertainty estimates for data value is in progress following the work of the FRM4SOC project (Banks et al., 2020; Ruddick et al., 2019). A data portal is under development to distribute data publicly to users such as satellite mission validation entities and developers of atmospheric correction algorithms. Pending implementation of these developments in an operational processing environment, some prototype datasets have been distributed via ZENODO, and are listed at https://waterhypernet.org/data/.

An important feature of both these systems, also present on the precursor multispectral CIMEL CE318-T-OC (Seaprism) and the hyperspectral OSPREY system but not on other hyperspectral systems, is the use of a pointing system with both pan and tilt possibilities. While many other hyperspectral systems recognise the importance of panning to achieve the desired relative azimuth to Sun, tilting has three important advantages compared to typical fixed zenith/nadir angle systems: 1. Both sky and water radiance measurements can be made with the same radiometer, thus saving on acquisition cost and ensuring identical wavelength scale and radiometer sensitivity and characterisation for both sky and water radiance; 2. When not measuring, the radiometers can be "parked" pointed downwards to reduce fore-optics contamination from atmospheric deposition; 3. It is possible to adopt new pointing scenarios with different zenith/nadir angles from the standard M1999 protocol, e.g., scanning the principal plane into sunglint to better estimate the effective Fresnel reflectance coefficient (Goyens and Ruddick, 2023) or scanning the skydome to check for clouds and/or obstructions or to estimate aerosol properties or Sun/moon pointing for calibration monitoring.

2.2 Validation sites

2.2.1 Choice of validation site

The PANTHYR and HYPSTAR® systems are installed on fixed structures overlooking water enabling a tilt-free, standardised viewing geometry. The network should ideally cover a wide diversity of water, atmosphere and Sun conditions in order to provide validation data everywhere satellite data are used. In contrast to the criteria used for selection of vicarious calibration sites (Zibordi et al., 2015), where optimal water, atmosphere and Sun conditions are preferred, validation data are needed also in the "difficult" or suboptimal conditions including dynamic and patchy waters, waters with bottom reflectance, hazy, variable and partially cloudy atmospheres, very low and very high Sun zenith angles, sites with strong adjacency effects, absorbing aerosols, etc.

Locations close to land are not excluded, since validation data are also needed for the metre-scale satellite missions (Vanhellemont, 2019b) to provide quality control (QC) for their unique applications close to land, e.g., in ports, small lakes and wide rivers, where atmospheric adjacency effects (Reinersman and Carder, 1995; Santer and Schmechtig, 2000), and sensor point spread function effects may be problematic. However, sites close to land will obviously be applicable only to satellite missions with spatial resolution finer than a site-dependent maximum spatial resolution.

Some validation sites in regions of high natural spatial variability are also desirable since users need to understand satellite data quality in such regions, e.g., for dredging/disposal and other sediment transport applications, and for monitoring of patchy phytoplankton distributions. If the natural spatial variability can be characterised, e.g., by analysing satellite data at different spatial resolutions, then appropriate conclusions can be drawn when performing the matchup validation. For example, (Dogliotti et al., 2015) demonstrates for a site close to the front of a coastal current

TABLE 1 Overview of satellite missions used for aquatic applications.

Satellite/Instrument	Agency	Launch date	Spectral coverage
VIIRS	NOAA	Oct 2011	402–2275 nm Multispectral + TIR
Pléiades	CNES/EADS	1A: December 2011 1B: December 2012 Neo3-6: Apr 2021+	450–915 nm Multispectral
Landsat 8/OLI	NASA/USGS	Feb 2013	423–2300 nm Multispectral + TIR
Worldview	DigitalGlobe	WV3: August 2014	400–2365 nm Multispectral
Doves Superdoves Skysats	Planetlabs	2015 + many	430–885 nm Multispectral
Sentinel-2/MSI	ESA (Copernicus)	A: June 2015 B: March 2017 C: 2024? D: ?	442–2202 nm Multispectral
Sentinel-3/OLCI	EUMETSAT/ESA (Copernicus)	A: February 2016 B: Apr 2018 C: 2024? D: ?	400–1020 nm Multispectral
PRISMA	ASI (Italy)	Mar 2019	400–2500 nm Hyperspectral
GOCI-2 (geo)	KIOST	Feb 2020	370–885 nm Multispectral
Landsat 9/OLI	NASA/USGS	Sep 2021	423–2300 nm Multispectral + TIR
ENMAP	DLR (Germany)	Apr 2022	420–2450 nm Hyperspectral
EMIT	NASA	Jul 2022	380–2500 nm Hyperspectral
MTG (geo)	EUMETSAT	I1: December 2022 I2: 2024? I3: 2025? I4: ?	400–2200 nm Multispectral + TIR
PACE	NASA	Feb 2024	Hyperspectral
SABIA-Mar	CONAE	2024?	Multispectral
GLIMR (geo)	NASA	2026?	Hyperspectral
CHIME	ESA	2028?	Hyperspectral
LSTM	ESA (Copernicus)	2028?	Multispectral
SBG	NASA	2028?	Hyperspectral
Newspace	Various	Frequent!	Multispectral+ Hyperspectral
Many others	Various	?	Multispectral+ Hyperspectral

that high spatial resolution sensors will give better agreement than low spatial resolution sensors. If the horizontal patchiness is also variable in time, e.g., because of horizontal advection, then matchup validation results may depend strongly on the time difference between *in situ* and satellite. When performing the matchup analysis it is therefore important to characterise the natural spatial and temporal variability of the water, and estimate the consequent uncertainty relating to the space and time differences between *in situ* and satellite measurements.

While natural space and time variability of the water target is not undesirable, since satellite data need to be validated in all conditions, artificial optical variability of the water target, induced by the measurement platform, is clearly to be avoided/minimised. It is obvious that measurements should not be made where the water-

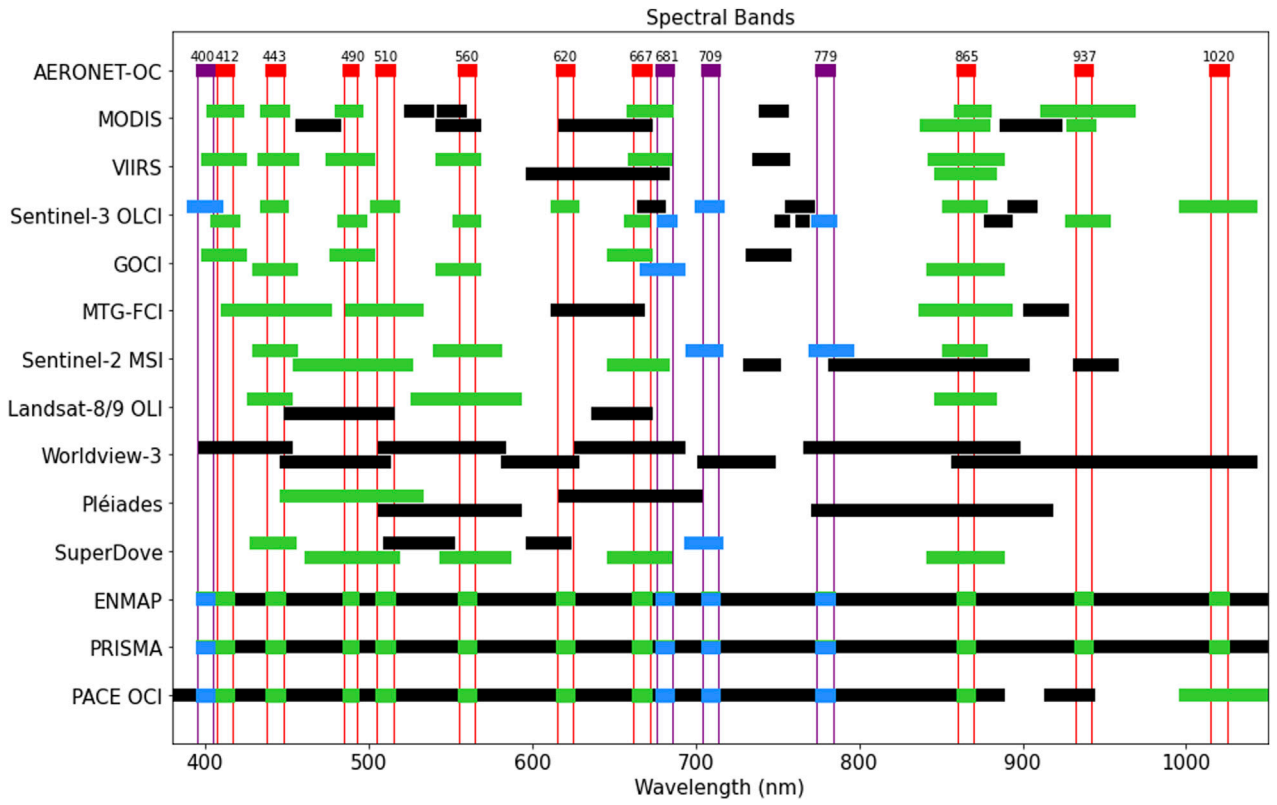


FIGURE 1
Spectral bands of typical satellite missions to be validated compared with (top row) the CIMEL CE318TV-12 (https://www.cimel.fr/solutions/ce318-t/#specifications) used in AERONET-OC. The two versions of the CE318TV-12 instrument are displayed with common bands in red and optional bands in violet. The variant CE318TV-12-LC ("lake colour") has bands 681 nm and 709 nm, while the CE318TV-12-OC ("ocean colour") variant CE318TV-12-OC has bands 400 nm and 779 nm. The CE318-TU12 instrument used for multispectral land surface reflectance measurements (Meygret et al., 2011) has a different set of 9 or 12 spectral bands. Satellite bands with central wavelength falling inside a CE318TV-12 common/optional band are shown in green/blue respectively and those falling outside such bands are shown in black. The latter will be particularly difficult to accurately estimate by band-shifting.

viewing sensor field of view includes either the measurement platform itself or the shadow of the measurement platform (including any underwater shadow). More subtle perturbations of the water target by reflection of Sun and skylight from the measurement platform should also be evaluated within the measurement uncertainty budget (Talone and Zibordi, 2019), and minimised as far as possible. This can be understood intuitively by taking (or imagining taking) a fish-eye photo of the Sun/sky hemisphere at the water surface within the water-viewing sensor field of view. Any portions of such a photo where the sky is replaced by the measurement platform/instrument contribute to artificial contamination of the measurement. This contamination will depend on the solid angle of the artificial structure, the difference in colour compared to the replaced sky, and the zenith angle of the obstruction as seen from the water target.

The measurement platform may also induce local hydrodynamic and hence optical variability, e.g., turbid wakes (Vanhellemont and Ruddick, 2014), and will directly impact the satellite measurement itself, especially at metre and decametre spatial resolutions (Vanhellemont and Ruddick, 2015). These are generally undesirable but unavoidable. There is a clear preference for structures which allow water to freely flow underneath, e.g., offshore platforms or piers/jetties supported by underwater wood/steel beams, or slender structures, e.g., single-legged poles, and a preference to avoid structures which block underwater currents, e.g., concrete walls or wooden breakwaters.

While at the level of network organisation, there is a strategic interest to cover a wide range of water, atmosphere and Sun conditions, in practice the choice of validation sites is mainly opportunistic. Long-term operation of a validation site depends on sustained funding, a supportive platform owner and a very dedicated and motivated scientist acting as Principal Investigator. Over the time scale of a decade, there can be many and diverse disruptive events: funding gaps, platform ownership/policy changes, institutional changes, transfer of staff, priority shifts, interpersonal tensions, damage from natural events (esp storms) or accidents, hardware failures, safety issues, etc. It requires considerable determination to keep things running when difficulties arise.

2.2.2 Viewing geometry and installation considerations

The location of the measurement system on the measurement platform is also important, and should take account of platform shadow and its variation over the day and over the year, as well as any underlying obstructions which may contaminate the field of view and hence restrict useable azimuth angles for the water-viewing measurement. In general location on a corner is therefore preferred. The choice of corner will impact the possible

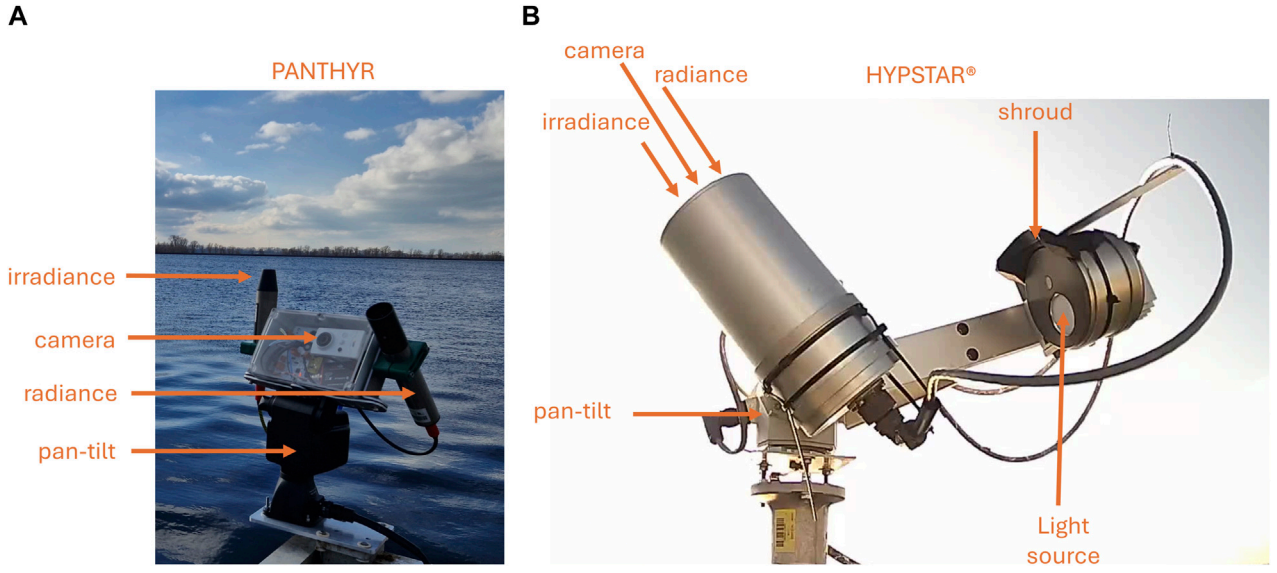


FIGURE 2
(A) PANTHYR radiometer system including separate irradiance sensor, radiance sensor and camera mounted on a pan-tilt unit; **(B)** HYPSTAR® radiometer system with integrated radiance and irradiance sensors, camera and calibration monitoring LED source with plastic shroud. Cable tie spikes are used for bird avoidance.

measurement times (and hence cover satellites with different overpass times). Both the PANTHYR and HYPSTAR® systems have been designed to allow flexible azimuthal pointing, and can be programmed to measure at 90°, 135°, 225° and/or 270° relative (away from) Sun if the angle is optically acceptable (not pointing at platform or platform shadow and pointing sufficiently far away from optical contamination caused by the platform). The M1999 acquisition protocol recommends a relative azimuth to Sun of 135° or 225° in order to minimise sunglint, particularly for moderate/high wave conditions. While such an azimuth is generally appropriate for measurements from the prow of a ship, which can be oriented for the measurement (Ruddick et al., 2006), measurements from the corner of a fixed platform generally have a more limited range of azimuth angles where platform perturbations are minimal. In the AERONET-OC network (Zibordi et al., 2009) the viewing azimuth of 90° or 270° was therefore adopted with a strict QC filtering restricting measurements typically to wind speed not exceeding 5 m/s (Zibordi et al., 2021). The approach in WATERHYPERNET is to define a "keep-out zone" of absolute azimuthal directions where measurements should not be made because data will be contaminated by the platform either directly or indirectly. When the PANTHYR system wakes up to make a measurement, the four potential azimuth angles are checked against the keep-out zone, and acquisitions may be made for all acceptable azimuth angles. In practice generally only one or two of the four potential angles are acceptable. In the case where two azimuth angles are possible there is considerable value in comparing water reflectance between these two angles–clearly these two measurements should agree to within the estimated measurement uncertainty (after viewing angle correction), and if they do not then there is important information on how the measurement should be improved, possibly relating to the viewing angle correction, the skyglint/sunglint correction or optical contaminations from the platform. At the time of writing the keep-out zone is hard-coded per site as an absolute azimuth range, but repeated measurements at different azimuth angles are being analysed to build up a better understanding on a site-by-site basis of data quality as a function of Sun zenith and azimuth angle and viewing azimuth angle relative to Sun.

Both the PANTHYR and HYPSTAR® systems measure downwelling irradiance directly, and hence require an unobstructed Sun/sky hemisphere (as opposed to the CIMEL/SeaPRISM system which estimates downwelling irradiance from a direct Sun measurement, and only requires an unobstructed direct Sun view). This means that the system should therefore ideally be located above all other artificial structures (Mueller et al., 2003). Unfortunately this requirement is almost never possible in practice for offshore structures because of the safety requirements for masts with lights for navigation and for lightning protection rods. The system should therefore be located as high as possible and horizontally distanced from such masts, minimising the impact on the downwelling irradiance measurement. The associated residual uncertainty can be modelled, e.g., (Castagna et al., 2019).

2.2.3 Existing and planned sites

Since the WATERHYPERNET network is at a prototype stage, the location of validation sites may vary considerably in the coming years as funding from the driving projects ceases, and as the network expands with new partners from more diverse funding sources. Despite this long-term (~10 years) and even medium-term (~3 years) uncertainty, the validation managers for many of the missions listed in Table 1 are already looking to WATERHYPERNET as a major source of radiometric validation data, both during the commissioning phases and during routine operations. The existing WATERHYPERNET sites are therefore

TABLE 2 Overview of the first WATERHYPERNET validation sites. Each site has a 4 letter code ("ID").

Location, ID and organisation	System Platform type	Latitude (°)	Longitude (°)	Water type	First measurement passing QC
Acqua Alta (VEIT) CNR	PANTHYR platform	45.31428	12.5083	coastal	2019-09-26
RT1 Oostende (RTBE) VLIZ	PANTHYR monopile	51.24640	2.91933	turbid, coastal	2019-12-23
Etang de Berre (BEFR) LOV	HYPSTAR® monopile	43.44231	5.09718	eutrophic, lake	2021-02-24
Acqua Alta (VEIT) CNR	HYPSTAR® platform	45.31425	12.50825	coastal	2021-04-20
Gironde Estuary (MAFR) LOV	HYPSTAR® quay	45.54389	−1.04195	very turbid	2021-11-10
Rio de la Plata (LPAR) CONICET	HYPSTAR® pier	−34.81799	−57.89591	very turbid, coastal	2021-12-16
Lake Garda (GAIT) CNR	HYPSTAR® rock	45.57694	10.57944	clear/macrophytes, lake	2022-06-09
Zeebrugge (M1BE) RBINS	HYPSTAR® monopile	51.36055	3.11815	very turbid marine	2023-02-26
Thornton Bank (TBBE) RBINS	PANTHYR platform	51.53277	2.95510	coastal	2023-05-11
Wraysbury (WRUK) NPL/RBINS	HYPSTAR® tethered	51.46380	−0.52927	reservoir	2023-07-05

provided in Table 2, and will be updated continuously via the web site www.waterhypernet.org.

The latitude and longitude provided in Table 2 refers to the location of the instrument. When data are used for satellite validation studies it is typical to extract satellite data for a macropixel "doughnut" around the measurement location (Pahlevan et al., 2021) or for a reference pixel horizontally shifted from the measurement platform (Vanhellemont, 2019a). This choice is the responsibility of the validation scientist using WATERHYPERNET data, and will generally be a function of the spatial resolution of the satellite sensor, as well as its viewing geometry and geolocation accuracy (including orthorectification) and site characteristics.

2.3 Demonstration *in situ* datasets

Following the successful AERONET-OC approach, and in the interests of reducing costs and achieving a high degree of standardisation, the WATERHYPERNET data acquisition, transmission, processing and distribution is fully automated in Near Real-Time (NRT, <24 h between data acquisition and data availability), at least for the data using pre-deployment radiometer calibration and default wind speed. Data distribution is foreseen from the www.waterhypernet.org data portal, but, during the current prototype phase, where the automated quality control does not yet meet the desired long-term standard, public release of the NRT data is not yet implemented. Despite this prototype status, while the data currently acquired and processed lack some of the features that will be implemented (full measurement uncertainty estimation, better characterisation of optical perturbations from the platforms, links to spectral convolution and BRDF correction tools), these data are already considered to be very valuable for assessing the quality of satellite data for wavelengths or geographical regions not covered by AERONET-OC.

The WATERHYPERNET v0 data are, for example, probably superior in quality to many shipborne reflectance measurements, because they are less subject to tilt, and certainly provide many more hyperspectral matchups per year than shipborne validation data sources. The WATERHYPERNET data should ideally have arrived at maturity at least 7 years ago, e.g., to support the validation of Sentinel-2 and Landsat 8, and are critically needed now for the validation of hyperspectral missions such as PRISMA, EnMAP, EMIT and PACE. Faced with this dilemma of having v0 prototype data that are considered useful but not of the final quality that is expected for routine operations in 2 years time, the current approach is to publicly release limited datasets via www.zenodo.org with appropriate disclaimers on quality and without the "WATERHYPERNET" branding.

In the present paper examples are given of prototype datasets and their application, for both PANTHYR and HYPSTAR® systems.

3 Methods - WATERHYPERNET

3.1 Data acquisition protocol

For both the PANTHYR and the HYPSTAR® system the data acquisition protocol is based closely on the M1999 measurement

method. For each azimuth angle, $\Delta\phi$, measurements are made of downwelling irradiance, $E_d(\Delta\phi,\lambda)$, upwelling water radiance, $L_u(\Delta\phi,\theta_v,\lambda)$ and downwelling sky radiance, $L_d(\Delta\phi,180°-\theta_v,\lambda)$ for nadir-viewing angle $\theta_v = 40°$ and wavelength λ. The sequence of measurements adopted here is: 3* E_d, 3* L_d, X* L_u, 3* L_d, 3* E_d, where X = 6 for HYPSTAR®, X = 11 for PANTHYR. With the single radiance sensor design concept these measurements cannot be made simultaneously, in contrast to typical shipborne supervised measurements (Ruddick et al., 2006). This non-simultaneous acquisition has the slight disadvantage that measurements will be contaminated if there is significant time variation of illumination conditions, beyond the correctible Sun zenith angle variation, during the full sequence, which lasts typically <2 min for PANTHYR and <7 min for HYPSTAR®. Such contamination occurs primarily if there are scattered clouds near the Sun disk, and can generally be detected when the first and last 3* E_d (and, for HYPSTAR® also first and last 3* L_d) are different by more than a pre-defined threshold and/or when the E_d is much lower than a clear sky model E_d as described in the next two subsections.

During the above-mentioned sequence a simple ambient light sensor measures continuously and can be used for identifying any variation in illumination during the sequential radiometric measurements.

3.2 Data processing and quality control

The primary radiometric measurand produced by WATERHYPERNET is the (directional) water-leaving radiance reflectance as represented by ρ_w hereafter, and defined by:

$$\rho_w(\Delta\phi,\theta_v,\lambda) = \frac{\pi L_w(\Delta\phi,\theta_v,\lambda)}{E_d(\lambda)} \quad (1)$$

where L_w is the water-leaving radiance (with air-water interface reflection removed), and E_d is the planar downwelling irradiance just above the water surface.

L_w is estimated by correction of L_u for light reflected at the air-water interface, assumed to be a multiple of L_d, using the approach of (Mobley, 1999) where the wind-roughened air-water interface is modelled via an "effective Fresnel coefficient", ρ_F:

$$L_w = L_u - \rho_F L_d \quad (2)$$

ρ_F is modelled using the look-up table of (Mobley, 1999) with inputs for the solar zenith angle, viewing zenith angle, relative azimuth angle between Sun and sensor, and the wind speed. See section 4 of (Ruddick et al., 2019) and references therein for a detailed discussion of this approach.

The wind speed is retrieved from the 0.25° gridded, 6-hourly nowcast wind speed provided by the National Centers for Environmental Prediction (NCEP) GDAS (https://rda.ucar.edu/datasets/ds083.3/citation/).

For clear and moderately turbid, but not extremely turbid, water sites, a wavelength-independent "NIR Similarity Spectrum (SimSpec)" correction is applied, following (Ruddick et al., 2005), using the expected constant ρ_w ratio in the NIR (i.e., 780 and 870 nm) to correct for residual Sun glint.

3.2.1 PANTHYR data processing

Measurements are converted from digital counts to (ir)radiance using two laboratory instrument characterisations performed by Tartu Observatory (Estonia) before and after each deployment period. Calibration data for a specific scan are obtained from linear interpolation in time between pre-deployment and post-deployment instrument characterisation. The calibrated scan data are linearly interpolated from the instrument specific wavelengths to a common wavelength grid (355–900 nm, every 2.5 nm). Individual calibrated scans are subjected to quality control as in (Ruddick et al., 2006), i.e., scans differing >25% at 550 nm from their neighbouring scans are rejected. For the E_d measurements, this quality control step takes the change in Sun zenith angle between the measurements into account.

If sufficient calibrated scans are available in the cycle, i.e., ≥5/6 for E_d and L_d and ≥9/11 for L_u, the scans are mean averaged, and the standard deviation is computed. ρ_w is then computed according to (Eqs 1, 2) for mean-averaged L_u, E_d, and L_d, and with ρ_F as described in Section 3.2.

Data are provided both with and without ("nosc" suffix in distributed datasets) the SimSpec correction, since the latter is expected to improve data for clear and moderately turbid waters but is expected to be inappropriate for extremely turbid waters – see (Ruddick et al., 2006; Doron et al., 2011). The SimSpec-corrected data are currently recommended for Acqua Alta (VEIT) and Thornton Bank (TBBE) PANTHYR sites but not Oostende (O1BE).

The ρ_w products are further quality controlled preserving only data fulfilling the following criteria:

1. $L_d(750\,\text{nm})/E_d(750\,\text{nm}) < 0.05$, removing non-clear sky conditions.
2. Variability (coefficient of variation) of $\rho_w(780\,\text{nm})$ <0.1, removing highly variable conditions.
3. $\rho_w(\lambda) \geq 0$ for $350\,\text{nm} \leq \lambda \leq 900\,\text{nm}$, removing spectra with negative reflectance retrievals.
4. $\rho_w(\lambda)$ (840–900 nm) is decreasing with wavelength for $840\,\text{nm} \leq \lambda \leq 900\,\text{nm}$ (Ruddick et al., 2006), removing spectra potentially contaminated by solid objects, either from the platform or floating.
5. Bright water spectra (average VIS ρ_w over 400–700 nm > 0.07 or average NIR ρ_w over 780–950 nm > 0.01) have a local maximum at around 810 nm (805–815 nm) due to the local minimum in pure water absorption, removing potentially contaminated spectra.
6. E_d measurements in the range 860–885 nm are within 20% of the Gregg and Carder (1990) clear sky model with an aerosol optical depth of 0.1 at normal pressure, removing cloudy, shadowed, or very hazy conditions.

An example of PANTHYR spectra for measured L_u, E_d, and L_d and derived L_w and ρ_w are provided in Figure 3.

3.2.2 HYPSTAR® data processing

In the HYPSTAR® data processing, the following steps are performed.

1. The processing scheduler starts processing when a new sequence has been transmitted to the server. It first inspects, and reads the raw spectra and calibration data.

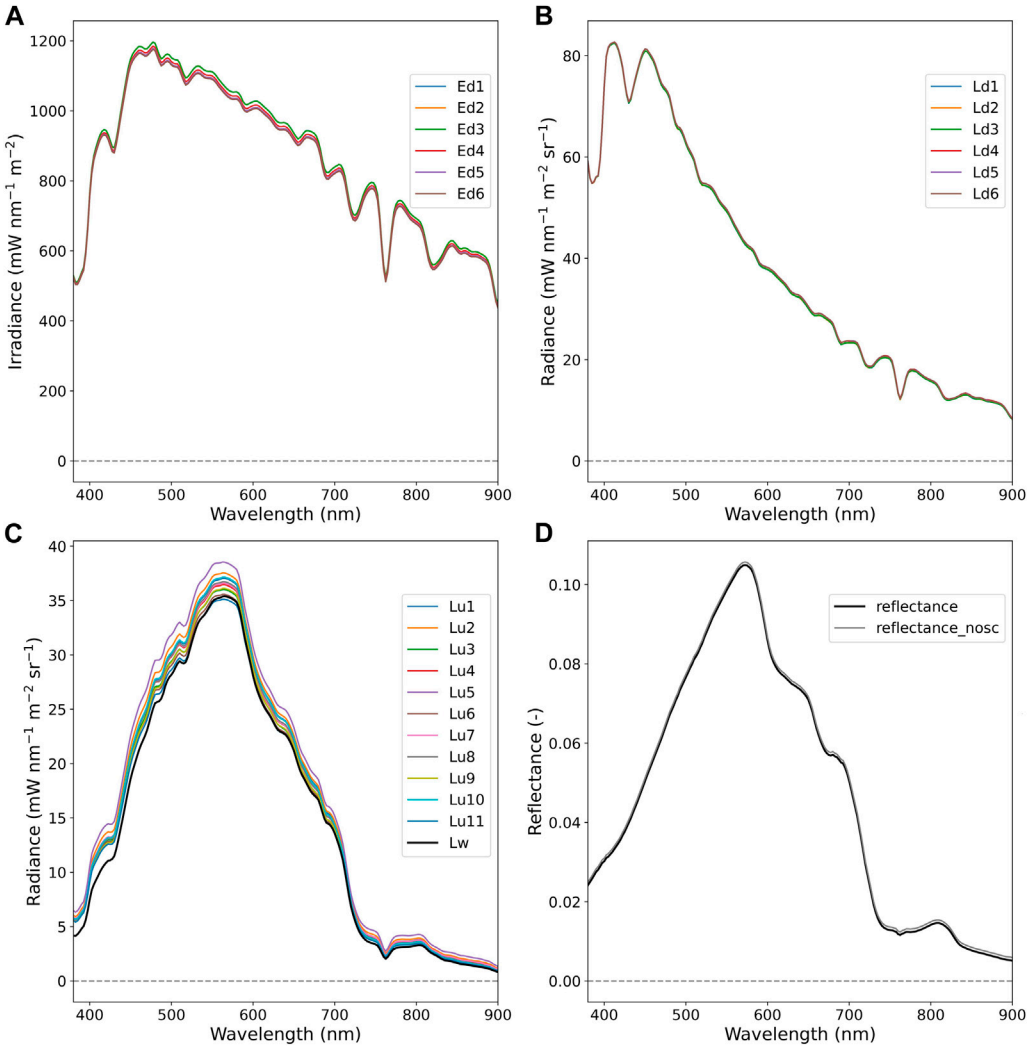


FIGURE 3
Example of processing from PANTHYR data acquired at the Oostende (O1BE) site on 2023-04-29 at 14:40 UTC. **(A)** six scans of downwelling irradiance, E_d. **(B)** six scans of downwelling (sky) radiance, L_d, **(C)** 11 scans of upwelling (water + surface) radiance, L_u, and resulting water-leaving radiance, L_w. **(D)** water-leaving radiance reflectance, ρ_w, with ("reflectance") and without ("reflectance_nosc") Similarity Correction. In this example the six scans of E_d and L_d are almost superimposed.

2. Raw spectra are then corrected for darks before they are calibrated to irradiance and radiance scans using pre-deployment calibration coefficients (post-deployment calibration coefficients are not yet available).
3. Next, since the irradiance and radiance measurements have a slight shift in wavelength, spectral interpolation is performed for the irradiance scans to fit the radiance wavelength scale.
4. L_d and E_d scans are then averaged per series. These series are temporally interpolated to fit the temporal time steps of the L_u scans.
5. ρ_w is then computed for each L_u scan, with the time- and spectrally-coincident L_d and E_d, using (Eqs 1, 2).
6. Finally, the NIR Similarity Spectrum correction is applied, where appropriate, and ρ_w scans are averaged.

The random uncertainties (from the standard deviation between scans) and the systematic uncertainties (from the instrument calibration) are propagated through each of the processing steps listed above using the Monte Carlo method implemented in the CoMet toolkit (www.comet-toolkit.org). Multiple uncertainty components as well as associated error-correlation information are provided in each of the HYPSTAR® products. Although implemented, these uncertainty products are not yet fully tested and will be released in the next version of the processing.

Throughout the abovementioned processing steps, several quality checks are performed to ensure that only high quality data are distributed. These include: 0) Pointing accuracy is checked and measurements with pointing errors >3° are rejected, 1) Raw spectra considered as outliers and/or presenting saturated counts or missing data, are discarded from further processing. Outliers are determined as any spectra for which the spectrally-integrated signal deviates more than three sigma or 25% (whichever is largest) from the mean; 2) After averaging over the scans, the

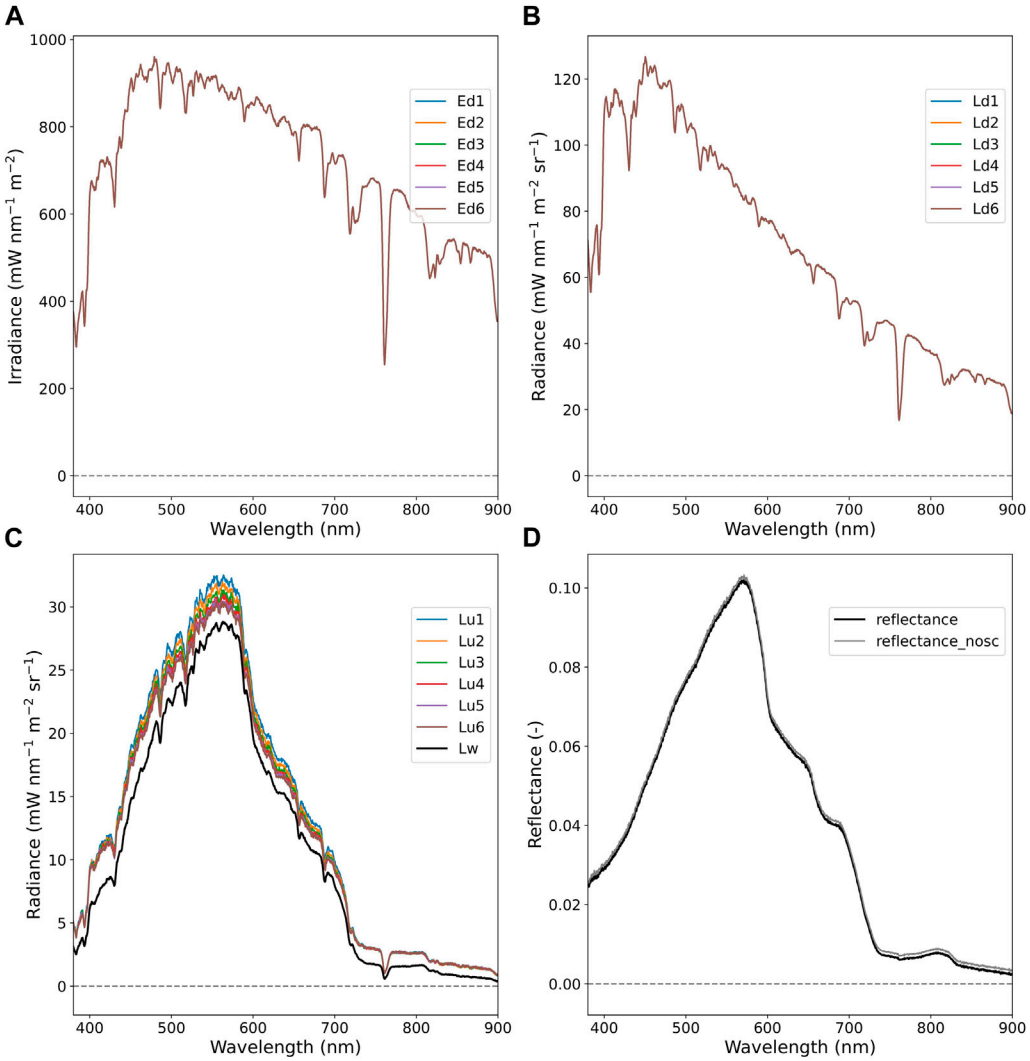


FIGURE 4
Example of processing from HYPSTAR® data acquired at the Zeebrugge (M1BE) site on 2023-04-09 at 13:01 UTC. **(A)** six scans of downwelling irradiance, E_d. **(B)** six scans of downwelling (sky) radiance, L_d, **(C)** six scans of upwelling (water + surface) radiance, L_u, and resulting water-leaving radiance, L_w. **(D)** water-leaving radiance reflectance, ρ_w, with ("reflectance") and without ("reflectance_nosc") Similarity Correction. In this example the six scans of E_d and L_d are superimposed, indicating optimal clear sky conditions, and a difference in scans is visible only for L_u.

E_d series deviating by >50% from a clear sky model or showing high variability over time (>10% deviation with the mean at 550 nm) are discarded from further processing, 3) ρ_w is only computed if there are at least three scans per series for L_u, L_d and E_d, and, 4) final ρ_w spectra are quality checked with site specific requirements. For example, site specific ρ_w thresholds at particular wavelengths or wavelength ranges are used to track suspect spectra (e.g., noisy or non-water spectra), and ρ_w spectra contaminated by nearby structures are also removed using viewing and illumination geometries coinciding with the platform and/or platform shadows.

Full data processing and default quality checks are described in (De Vis et al., 2024). The HYPSTAR® processor is fully accessible via (https://github.com/HYPERNETS/hypernets_processor, accessed on 20 October 2023).

An example of HYPSTAR® spectra for measured L_u, E_d, and L_d and derived L_w and ρ_w are provided in Figure 4.

4 Methods–demonstration cases

Three examples are shown here to demonstrate the usefulness of the WATERHYPERNET data. The corresponding satellite and/or *in situ* data processing is described in the following subsections.

4.1 Sentinel-2 validation–satellite data and matchup procedure

As a follow-up to the study of (Vanhellemont, 2020), Sentinel-2 (A&B) (S2) data are compared to PANTHYR data for the Acqua Alta and Oostende sites.

The S2 satellites have onboard a 13 band MultiSpectral Instrument (MSI) spanning the VSWIR with four bands at 10 m, six bands at 20 m and three bands at 60 m spatial resolution. MSI has

two bands that are not processed to surface reflectance, one at 945 nm for estimation of water vapour, and one at 1.3 μm for the detection of cirrus clouds.

S2 satellite data for both sites were collected as top-of-atmosphere reflectance (ρ_t, "L1C", orthorectified and tiled) and Sen2Cor (Main-Knorn et al., 2017) surface reflectance ("L2SR") for a 3 × 3 km region of interest (ROI), as defined by a bounding box in latitude and longitude, from the Google Earth Engine (GEE) archive (Gorelick et al., 2017) on download dates between 2023-08-10 and 2023-08-13, including acquisitions from 2019-10-01 for Acqua Alta and 2022-02-27 for Oostende and up to 2023-08-11 for both sites. The GEE download uses the latest available processing baseline (from N0208 in late 2019 through N0509 early 2023, see Supplementary Data Sheet S1 for processor versions).

Imagery was processed to water-leaving radiance reflectance (ρ_w) using ACOLITE_DSF using an ACOLITE GitHub clone dated 2023-08-10, with "3bfe8d8" commit (https://github.com/acolite/acolite). Inside the ROI the aerosol optical thickness (AOT) estimation is assumed uniform in this implementation (pixel-by-pixel processing is also possible in ACOLITE but not used here). Output resolution was 10 m, replicating pixels from the 20 and 60 m bands to fill the 10 m grid. S2 imagery was processed using the following two processor options:

1. ACOLITE/DSF with AOT estimated from VNIR bands (no SWIR) (termed "ACOLITE_DSF")
2. ACOLITE/DSF with AOT estimated from VNIR bands (no SWIR) and optional per-pixel SWIR based glint correction (termed "ACOLITE_DSF_GC")

Other processor options (including ancillary datasets for pressure, ozone and water vapour) are used according to the defaults documented in (Vanhellemont, 2020).

Matchups with PANTHYR (using only 225° relative azimuth) were made using a 60 min full width window (i.e., +/-30 min around overpass time), linearly interpolated to the overpass time if possible, i.e., when two bounding measurements are available. PANTHYR data are spectrally convoluted to the Sentinel-2 (A&B) bands in reflectance space with spectral response functions S2-SRF_COPE-GSEG-EOPG-TN-15-0007_3.0 (dated 2018-01).

Satellite data are mean averaged over 11 × 11 10 m pixels centred on a reference location. The reference location used for extraction is located as specified in (Vanhellemont, 2020) for Oostende, i.e., 90 m East of the platform, and for Acqua Alta by (Vanhellemont, 2019a, Supplementary Material S2) avoiding platform and near platform pixels. Quality control was made using a threshold on the 95th percentile (P95) of the 11 × 11 pixel box, rejecting matchups where in this box P95 $\rho_t(1610\,\mathrm{nm}) \geq 0.05$ or $\rho_t(1375\,\mathrm{nm}) \geq 0.005$, respectively filtering non-water and cirrus near the matchup location. The 3 × 3 km subscene data were also used, filtering out subscene P95 $\rho_t(443\,\mathrm{nm}) \geq 0.3$, thus removing scenes with nearby clouds or other very bright objects.

In situ and satellite matchup data are provided in Supplementary Data Sheet S2.

Reduced Major Axis (RMA) regression lines and squared correlation coefficients, R^2 are provided for the comparison between *in situ* and satellite $\rho_w(\lambda)$ measurements, denoted x_i and y_i respectively, where $i = 1 \ldots n$. Error statistics were computed for the Root Mean Squared Difference (RMSD), the Mean Difference (MD), and Mean Absolute Percentage Difference (MAPD) between the *in situ* and satellite measurements as follows:

$$RMSD = \frac{1}{n}\sqrt{\sum_{i=1}^{n}(y_i - x_i)^2} \tag{3}$$

$$MD = \frac{1}{n}\sum_{i=1}^{n}(y_i - x_i) \tag{4}$$

$$MAPD = \frac{100\%}{n}\sum_{i=1}^{n}\frac{|y_i - x_i|}{0.5*(y_i + x_i)} \tag{5}$$

4.2 Sentinel-3/OLCI validation - satellite data

Sentinel-3_OLCI/A&B data between February 2021 and March 2023 were downloaded from the EUMETSAT Data Store as Level 2 Water Full Resolution (WFR) products processed using the OLCI L2 processor IPF-OL-2 version 07 (EUMETSAT, 2021; Zibordi et al., 2022) for the HYPSTAR® deployments at six sites: Acqua Alta Oceanographic Tower (VEIT), Lake Garda (GAIT), Etang de Berre (BEFR), Gironde (MAFR), La Plata (LPAR) and Zeebrugge (M1BE).

An adaptation of the Matchup Data Base (MDB) approach proposed by EUMETSAT (EUMETSAT, 2022) was used to organise the satellite and *in situ* data, and perform the validation analysis (Gonzalez Vilas et al., 2024). Validation protocols were based on the recommendation available in the literature for medium-resolution satellites (Concha et al., 2021), applying the same protocols for all the sites except for the adaptations noted below (1 valid pixel for GAIT and MAFR, negative satellite reflectance masking for BEFR, MAFR and LPAR).

The 15 OLCI bands between 400 and 865 nm are included in the analysis. The 1020 nm band is excluded because the low signal causes unreliable measurements.

Satellite measurements for each band were computed as the average, excluding outliers, for a measurement window of three by three pixels around the site location, using a strict criterium of nine valid pixels for all the sites except for GAIT and MAFR, where only one valid pixel was required because of the proximity of the coastline. Outliers are identified (EUMETSAT, 2022) when the pixel value is lower (or greater) than mean minus (or plus) 1.5 standard deviations, where mean and standard deviation are computed using valid (non-flagged) pixels in the 3 × 3 extraction window. For masking, the default flag list proposed by EUMETSAT (EUMETSAT, 2021) is used and is based on the Water Quality and Science Flags (WQSF) dataset for all the sites. As WQSF RNEG flags allow for low negative values up to a defined threshold, pixels with negative satellite reflectance between 400 nm and 442 nm are also masked for BEFR, MAFR and LPAR.

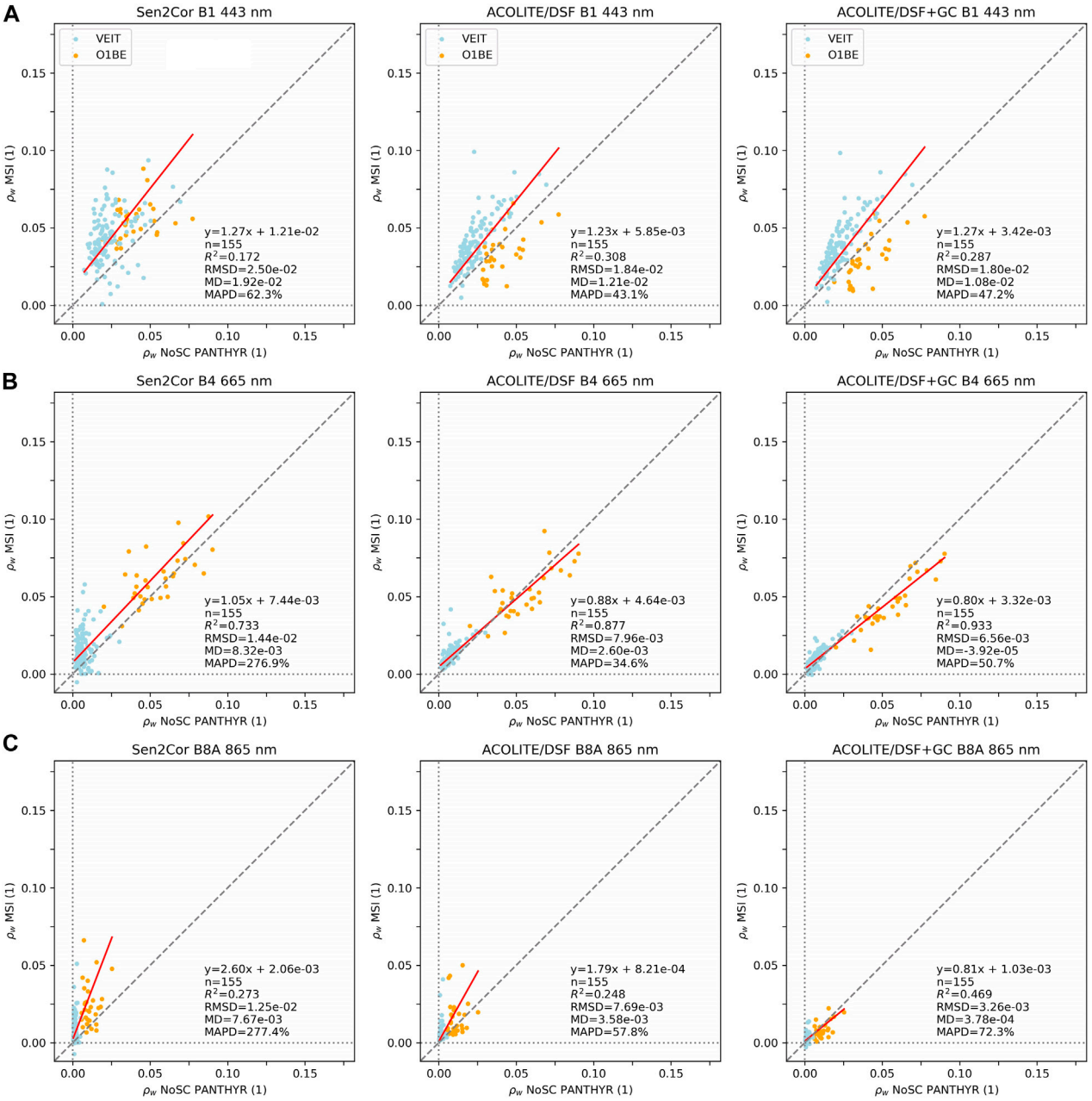


FIGURE 5
Scatterplot of Sentinel-2 (A&B) satellite (*y*-axis) and PANTHYR *in situ* (*x*-axis) water-leaving radiance reflectance measurements for 155 matchups at the Acqua Alta (VEIT: 124 blue points) and Oostende (O1BE: 31 orange points) validation sites for three bands: **(A)** 443 nm, **(B)** 665 nm and **(C)** 865 nm. Satellite data processed by Sen2Cor (left column), ACOLITE_DSF (centre) and ACOLITE_DSF_GC (right column). The linear RMA regression line is shown in red with corresponding statistical metrics in text on each plot. Scatterplots for all other bands are available in Supplementary Data Sheet S3.

In situ measurements for each satellite band were extracted as the HYPSTAR® L2 reflectances convoluted using the mean spectral response function for each Sentinel-3 mission (https://sentinels.copernicus.eu/web/sentinel/technical-guides/sentinel-3-olci/olci-instrument/spectral-characterisation-data, accessed on 8 April 2024) without applying the NIR similarity spectrum correction for the validation of sites with highly turbid waters (i.e., MAFR, LPAR and M1BE).

In situ and satellite matchup data are provided in Supplementary Data Sheet S8.

Reduced Major Axis (RMA) regression lines and squared correlation coefficients, R^2 are provided for the comparison between *in situ* and satellite $\rho_w(\lambda)$ measurements. Error statistics were computed for the Root Mean Squared Difference (RMSD), the Mean Difference (MD), and Mean Absolute Percentage Difference (MAPD) by Eqs 3–5.

4.3 Phytoplankton monitoring time series

Reflectance data from the autonomous systems were used to derive phytoplankton parameters in Belgian North Sea waters over the spring-summer season in 2020 (PANTHYR at Oostende, O1BE, Supplementary Data Sheet S9) and 2023 (HYPSTAR® at Zeebrugge_MOW1, M1BE, Supplementary Data Sheet S10). In this region, *Phaeocystis globosa* is considered as a non-toxic but undesirable phytoplankton species because of the unsightly and sometimes dangerous (Philippart et al., 2020) generation of foam, and because the gelatinous mucus has potential impact on species composition at higher trophic levels (Rousseau et al., 2000).

Chlorophyll *a* concentration (Chl-a hereafter) was calculated using the CRAT method (Ruddick et al., 2001) from reflectance spectra (without SimSpec correction) that have passed quality control. This algorithm, designed for hyperspectral data, is based on the red-NIR reflectance spectrum but contrary to typical semi-analytical red-edge algorithms it avoids calculation of NIR backscattering for moderate-high Chl-a (>13.45 µg/L). This algorithm is less suitable for low Chl-a, but is relevant for the bloom events considered here.

Two indices for *P. globosa* were calculated from reflectance spectra based on existing algorithms which are described in detail in the cited papers, and briefly summarised here.

The Lubac Index (LI), defined in (Lubac et al., 2008), is a binary algorithm (yes/no) indicating if the phytoplankton assemblage is dominated by *P. globosa*, and is based on the shape of the second derivative reflectance spectrum between 420 and 560 nm. The second derivative was calculated following the formulation described by (Lubac et al., 2008; Lavigne et al., 2022) for intervals of 2.5 nm for the PANTHYR data and of 1 nm for the HYPSTAR® data. Before making the second derivative calculation, ρ_w spectra were smoothed to avoid strong outliers in the second derivative. A five-point window (12.5 nm) running average was applied to all PANTHYR spectra, and a nine-point window (8 nm) running average was applied 3 times to all HYPSTAR® data.

The Modified Astoreca Line Height index (MALH), defined in (Lavigne et al., 2022), and based on prior work by (Astoreca et al., 2009) is a line height difference algorithm (Eq. 6) measuring the absorption anomaly at $\lambda_2 = 482.5$ nm with respect to a non-linear baseline between $\lambda_1 = 470$ nm and $\lambda_3 = 490$ nm:

$$MALH = \left\{ \frac{1}{\rho_w(\lambda_2)} - \frac{1}{\rho_w(\lambda_1)^{(1-w)}} \times \frac{1}{\rho_w(\lambda_3)^{w}} \right\} \times a_{w\,NIR} \times \rho_{w\,NIR} \tag{6}$$

where $w = \frac{\lambda_2 - \lambda_1}{\lambda_3 - \lambda_1}$. $a_{w\,NIR}$ and $\rho_{w\,NIR}$ are respectively the pure water absorption and the water-leaving radiance reflectance at a near infrared band, here chosen as $\lambda_{NIR} = 700$ nm, giving $a_{w\,NIR} = 0.57\ m^{-1}$ according to (Kou et al., 1993).

Finally, because MALH depends on the concentration of *P. globosa*, the ratio MALH/Chl-a is calculated as a proxy for the *P. globosa* fractional contribution to phytoplankton absorption. This ratio is calculated from the slope of linear regressions between MALH and Chl-a data available 48 h before and after the measurement date. Hence, a positive value suggests a high fraction of *P. globosa* in the phytoplankton community, and a negative value a low fraction of *P. globosa*. When the regression slope was not significant (p-value ≤5%) results are shown in grey.

5 Results

5.1 Validation of Sentinel-2 (A&B) by PANTHYR deployments at Acqua Alta and Oostende sites

The scatterplots comparing Sentinel-2 (A&B) water-leaving radiance reflectance with matchup PANTHYR *in situ* measurements from the Acqua Alta (VEIT) and Oostende (O1BE) validation sites are shown in Figure 5 for selected spectral bands. Scatterplots for all spectral bands can be found in Supplementary Data Sheet S3. Results for Sentinel-2A and Sentinel-2B were very similar, and are presented together in this scatterplot. The results shown in Figure 5 are quite different for the two validation sites, suggesting different algorithm performance issues for the different turbidity ranges (Acqua Alta moderately turbid, Oostende highly turbid).

For the Sen2Cor processor, the vertical dispersion of points in these scatterplots, and strong positive bias (MD) at all wavelengths with a striking overestimation of ρ_w at 865 nm suggests a general underestimation of aerosol reflectance and/or uncorrected sunglint–this is not surprising for an algorithm which is designed for atmospheric correction over land, taking aerosol optical thickness from dense dark vegetation (if present in scene) or from the fall-back external meteorological data (CAMS) and with no sunglint, or even skyglint, correction.

For the ACOLITE_DSF processor, without sunglint correction, results are improved somewhat compared to Sen2Cor with reduction of the positive bias (MD) at all bands, suggesting better estimation of aerosol reflectance, but with many positively biased outliers, most obvious at 865 nm, where the expected and *in situ* measured ρ_w is systematically low, especially at Acqua Alta.

For the ACOLITE_DSF_GC processor, with a sunglint correction, many of those positively biased outliers are now well-corrected at 865 nm, but little difference is found at 443 nm.

The spectral RMSD between Sentinel-2 (A&B) and PANTHYR measurements at Acqua Alta and Oostende for these matchups is shown in Figure 6. The general decrease of RMSD with increasing wavelength for the Sen2Cor and ACOLITE_DSF_GC processors is quite different from the "water-like" RMSD spectrum found in a validation study in the La Plata estuary - see Figure 4A of (Dogliotti et al., 2023). The RMSD spectrum of Figure 6 is typical of situations where the dominant error source is imperfect correction of atmospheric path reflectance (aerosols and/or Rayleigh)–see Figure 9 of (Vanhellemont and Ruddick, 2021) and associated discussion in that paper for similar experience with atmospheric correction of Sentinel-3/OLCI. This error is greater for Sen2Cor as discussed above. Interestingly, comparison of ACOLITE_DSF with ACOLITE_DSF_GC in Figure 6 shows that the sunglint correction has successfully reduced RMSD for 665–865 nm but not for 443–560 nm. This suggests that the remaining dominant error for ACOLITE_DSF_GC is related to atmospheric path reflectance but not sunglint. From the ACOLITE_DSF_GC 443 nm scatterplot in Figure 5 it seems that the atmospheric path reflectance error is positively biased for the Acqua Alta site but negatively biased for the Oostende site. The leading hypotheses for these biases are:

- ACOLITE_DSF_GC gives positively biased $\rho_w(443-560\,\text{nm})$ at the Acqua Alta site because of spatial variability of the atmosphere and/or air-water interface over the ROI. The fundamental DSF assumption is that the atmospheric composition (esp aerosols) and air-water interface are spatially invariant over the ROI, and can be estimated from the darkest pixel, where the water (or land surface) reflectance is negligible at least for a single wavelength. If the darkest pixel is "too dark", e.g., because of sensor noise, a darker than average wave facet, cloud shadowing of the atmosphere, etc., then the AOT will be underestimated, and ρ_w overestimated. If the validation pixel has a brighter atmosphere than the darkest pixel, e.g., because of patchy haze or undetected thin clouds, then a similar overestimation of ρ_w will occur. This is an inherent positive bias to the DSF assumption of spatial uniformity of atmosphere and air-water interface over the ROI. This bias could perhaps be reduced by reducing the ROI (while preserving the need for a sufficiently large ROI to find an appropriate dark pixel) or otherwise detecting situations where the assumption of spatial uniformity is violated.
- ACOLITE_DSF_GC gives negatively biased $\rho_w(443-865\,\text{nm})$ at the Oostende site because of images where the ROI does not contain a truly dark pixel-wavelength, when excluding the SWIR wavelengths. If there is a non-negligible ρ_w at the selected dark pixel-wavelength then AOT is overestimated, and ρ_w correspondingly underestimated. This bias could perhaps be reduced by including SWIR bands in the dark pixel-wavelength selection process, although such bands need careful treatment (averaging/filtering) because of the low signal-to-noise of the Sentinel-2/MSI sensor.

Full testing of these hypotheses is beyond the scope of the present paper, which serves to demonstrate the usefulness of WATERHYPERNET *in situ* measurements in general and specifically to provide clues to how Sentinel-2 data quality might be improved when using ACOLITE_DSF.

In addition to the abovementioned biases, the scatterplots of Figure 5 suggest an important number of outlier cases. Validation outliers are not always studied in detail, particularly when there are a large number of matchups. However, these outliers contain very important information on the real quality of satellite data that reach end-users as well as vital clues on how to improve processing. While some of the outliers for Sen2Cor and ACOLITE_DSF can be attributed to the lack of a sunglint correction, many outliers remain in the ACOLITE_DSF_GC processing.

We define here "outlier" as a matchup where the difference between satellite and *in situ* exceeds the RMSD difference over all matchups for that site, i.e., $|\Delta\rho_w(443\,\text{nm})| > \rho_w^{RMSD-site}(443\,\text{nm})$, where $\Delta\rho_w$ (443 nm) is the difference between in situ and satellite measurements of ρ_w (443 nm), $\rho_w^{RMSD-VEIT}(443\,\text{nm}) = 0.01894$ and $\rho_w^{RMSD-O1BE}(443\,\text{nm}) = 0.01380$. All outliers (40/124 for VEIT and 11/31 for O1BE) were analysed subjectively by two experts on the basis of "Validation Diagnostic sheets" (Supplementary Data Sheet S4–S7) showing the spectral plot for satellite ρ_w (all three processors) compared to the *in situ* measurement, both hyperspectral and Sentinel-2 bands together with imagettes of the ROI for:

- Surface reflectance, ρ_s, RGB composite (665 nm, 560 nm, 443 nm)
- Surface reflectance, ρ_s, single band greyscale (443 nm)
- Surface reflectance, ρ_s, single band greyscale (865 nm)
- Top Of Atmosphere (TOA) reflectance, ρ_t, single band greyscale (S2A:1373 nm, S2B: 1377 nm)
- Top Of Atmosphere (TOA) reflectance, ρ_t, single band greyscale (S2A: 2202 nm, S2B: 2186 nm)

All outliers were positively biased at $\rho_w(443\,\text{nm})$ for VEIT and negatively biased at $\rho_w(443\,\text{nm})$ for O1BE.

Figure 7 shows an example Validation Diagnostic sheet for the matchup with Sentinel-2/A acquisition over Acqua Alta (VEIT) on 2022-11-21T10:03:44. Inspection of the $\rho_s(865\,\text{nm})$ and $\rho_t(2202\,\text{nm})$ imagettes suggests that there are thin (undetected) patchy clouds in the pixels near the reference location, marked as a red cross in Figure 7. Furthermore cloud shadow at the dark pixel may add further low bias to the AOT estimate.

Figure 8 shows an example Validation Diagnostic sheet for the matchup with Sentinel-2/A acquisition over Oostende (O1BE) on 2022-06-12T10:59:33. Inspection of the $\rho_s(RGB)$ and $\rho_t(2202\,\text{nm})$ imagettes suggests that there is a cloud/contrail shadow over the reference location. Inspection of the full image (not shown) showed indeed a suitably shaped and positioned contrail just South of this ROI.

On the basis of this subjective expert analysis, the hypotheses for all outliers are:

- For VEIT, 37/40 outlier cases it is thought that the AOT used at the validation pixel is too low, although the underlying reason can be diverse, and is sometimes unclear. The dark pixel may be "too dark", e.g., because of sensor noise, a darker than average wave facet, cloud shadowing of the atmosphere, etc., or the validation pixel may have a brighter atmosphere/interface than the dark pixel, e.g., because of patchy haze or undetected thin clouds. In 3/40 outlier cases, the cause of the outlier is difficult to discern. In 38/40 outlier cases (and most non-outlier cases) the DSF approach uses the 865 nm band (8A) for the dark pixel.
- For O1BE, 2/11 cases with the validation pixel in a cloud shadow and 9/11 cases where it is suspected that the dark pixel is not black enough because of thin clouds (including cirrus) and/or glint and/or water reflectance (when the 443 nm is used for the DSF). In 8/11 cases the DSF approach uses the 865 nm band (8A) for the dark pixel, with the 443 nm band (1) used in the other 3/11 cases.

5.2 Validation of Sentinel-3/OLCI (A&B) by HYPSTAR® deployments at Acqua Alta, Lake Garda, Etang de Berre, Gironde, La Plata and Zeebrugge sites

Figure 9 shows the scatterplot of matchups between Sentinel-3_OLCI/A&B Level 2 Water Full Resolution (WFR) and the

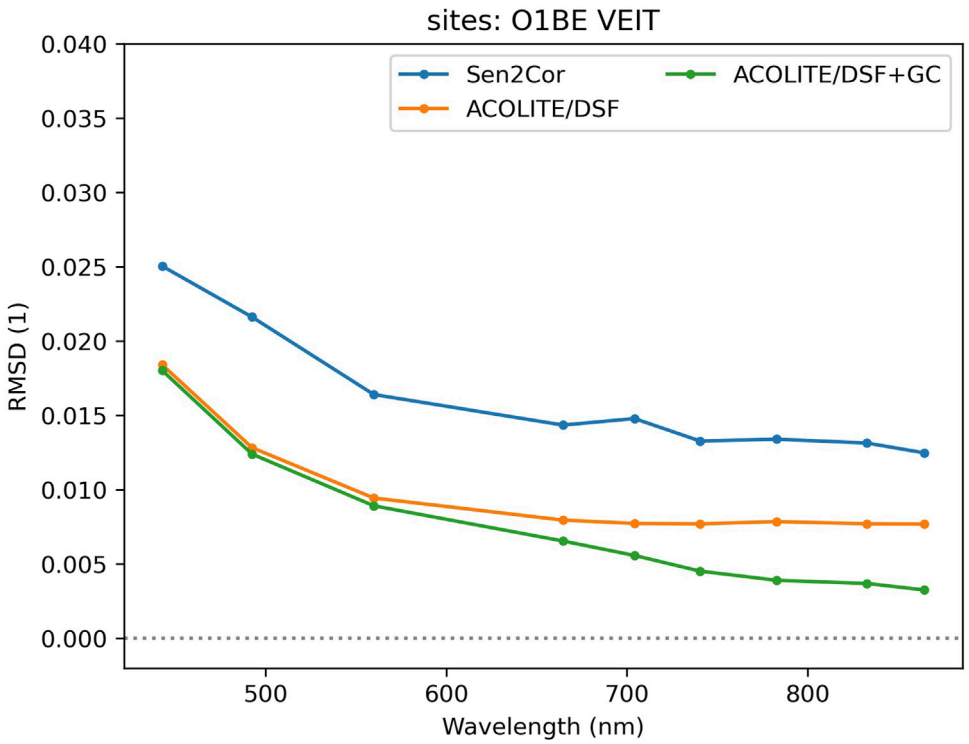


FIGURE 6
Root mean squared difference (RMSD) between Sentinel-2 (A&B) and WATERHYPERNET/PANTHYR measurements at Acqua Alta (VEIT) and Oostende (O1BE) as a function of wavelength for the 155 matchups shown in Figure 5.

HYPSTAR® deployments at six sites (VEIT, GAIT, BEFR, MAFR, LPAR and M1BE, see Section 4.2) for each individual band and grouped by satellite sensor.

Overall, better fits were achieved between 490 nm and 885 nm ($R^2 > 0.88$), whereas a higher dispersion and worse correlation were observed in the blue part of the spectrum (400 nm, 412.5 nm, 442.5 nm). A negative bias (MD) is observed in all the bands. While the regression slope is close to 1 (between 0.9 and 1.0) for bands 709–885 nm, the lower regression slope (between 0.79 and 0.89) for bands 442–681 nm suggests a systematic difference between satellite and *in situ* measurements that warrants further attention.

The spectral shape of the bias (MD) and RMSD (Figures 10B, C) for 442–885 nm is similar to a turbid water reflectance spectrum. While some atmospheric correction algorithms have uncertainty which can be proportional to water reflectance, this is not expected for the WFR algorithm, suggesting that this difference may be dominated in the range 442–885 nm either by a systematic *in situ* measurement error or by space (or, less likely, time or angular) differences between the satellite and the *in situ* measurement. Both satellite sensors show similar performance.

The global scatter plot of matchups of Sentinel-3_OLCI/A&B Level 2 and HYPSTAR® including all the bands is shown in Figure 10A. There is an overlap of data points from both sensors, with a good fit and high correlation ($R^2 = 0.93$).

The number of valid matchups (whole spectra) from both sensors was very similar (S3A: 295, S3B: 300), as well as the global metrics including all the bands (Table 3). Spectral variation metrics (Figures 10B–D) follow similar patterns for both S3A and S3B. In fact, RMSD and bias (MD) differences between both satellites are always lower than 0.0006 and 0.0002, respectively. The single satellite metric values are also close to those obtained combining both sensors (see R^2 and MD in Table 3).

This analysis is reassuring as to the interoperability of the A and B units of the Sentinel-3/OLCI constellation, achieved by good harmonisation of space hardware and ground processing elements, and for the satellite ρ_w in the NIR bands 709–885 nm. For the spectral range 442–681 nm a better understanding is needed of *in situ* measurement uncertainty before conclusions can be drawn on the atmospheric correction algorithm performance.

5.3 Phytoplankton monitoring from PANTHYR and HYPSTAR® measurements in Belgian coastal waters

Although designed for the launching application of satellite validation, the WATERHYPERNET data can be used without satellite data for single point monitoring of water quality parameters, including phytoplankton.

Figure 11 shows a time series of phytoplankton parameters derived from the PANTHYR data at Oostende (O1BE) in 2020, extended from the previous analysis of Figure 5 of (Lavigne et al., 2022) to include MALH per unit chlorophyll *a* as a biomass-independent indicator of species fraction of *P. globosa*. The

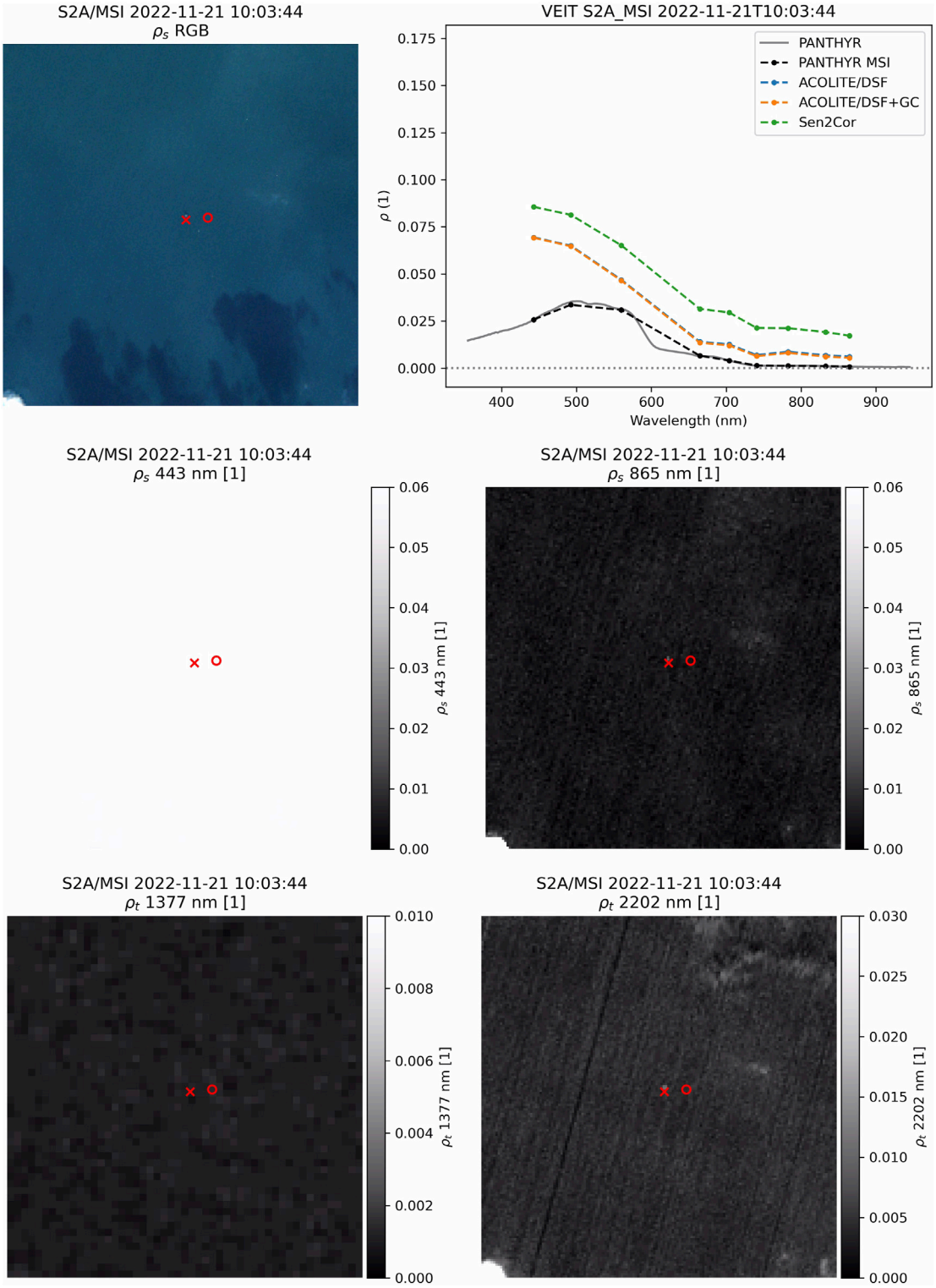


FIGURE 7
Validation Diagnostics sheet for the matchup with Sentinel-2/A acquisition over Acqua Alta (VEIT) on 2022-11-21T10:03:44, showing the 3 km*3 km ROI (top-left) Surface reflectance RGB composite (665 nm, 560 nm, 443 nm); (top-right) spectral plot comparing ρ_w from satellite (three processors, here ACOLITE_DSF and _DSF_GC coincide) with the *in situ* measurement, both hyperspectral (solid black) and Sentinel-2 bands (dashed black); (middle-left) surface reflectance at 443 nm; (middle-right) surface reflectance at 865 nm; (bottom-left) TOA reflectance at 1377 nm; (bottom-right) TOA reflectance at 2186 nm.

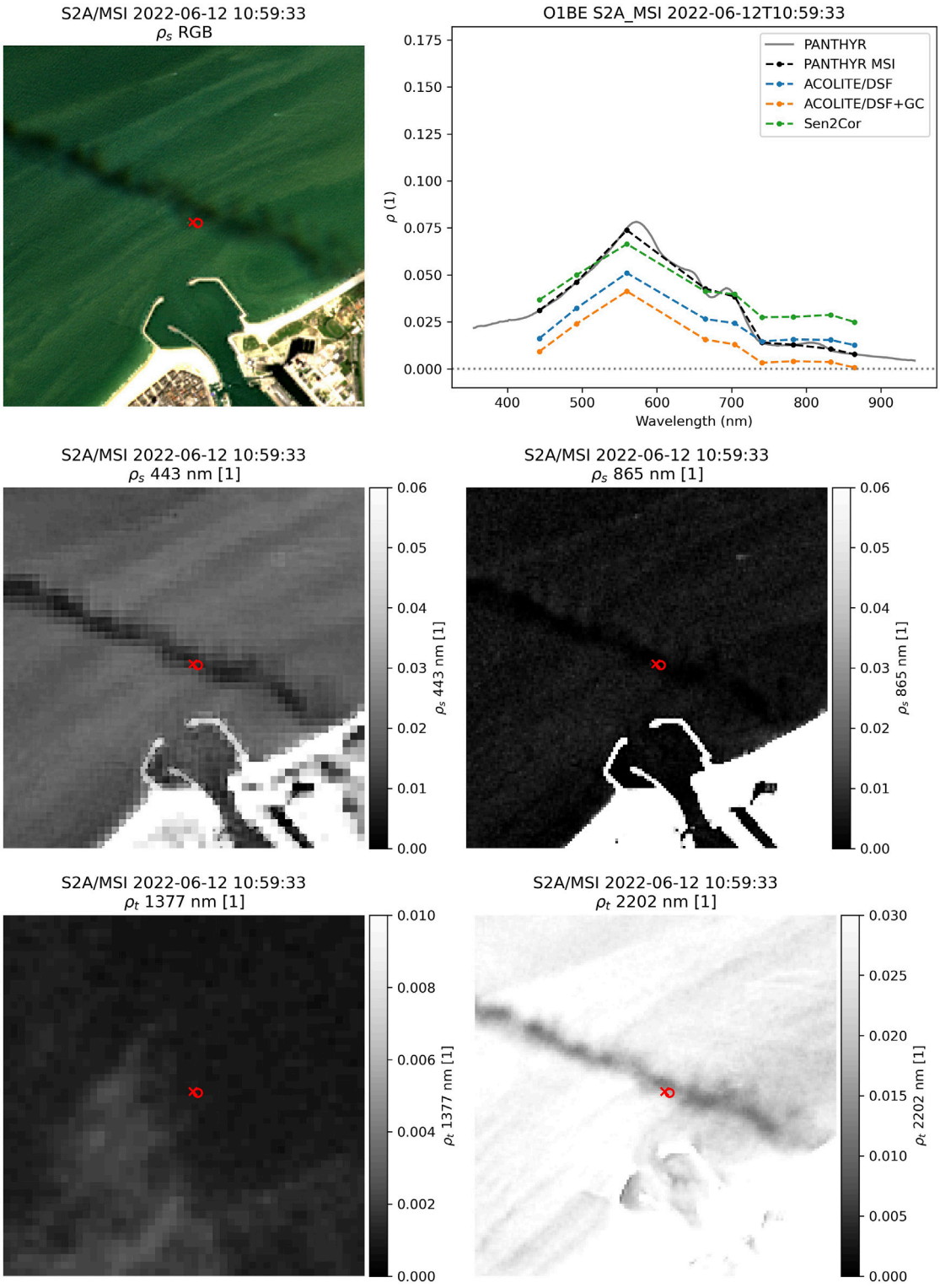


FIGURE 8
Validation Diagnostics sheet for the matchup with Sentinel-2/A acquisition over Oostende (O1BE) on 2022-06-12T10:59:33. Same plot content as in Figure 7.

striking difference in MALH between the end-April/beginning-May bloom (positive ⇒ dominated by *P. globosa*), and the end-June bloom (negative ⇒ not dominated by *P. globosa*) is matched by the LI flag, and can be traced back to subtle differences in curvature (second derivative) of the water-leaving radiance reflectance - see (Lavigne et al., 2022) for full details.

Figure 12 shows a similar time series of phytoplankton parameters, but now derived from the HYPSTAR® data at

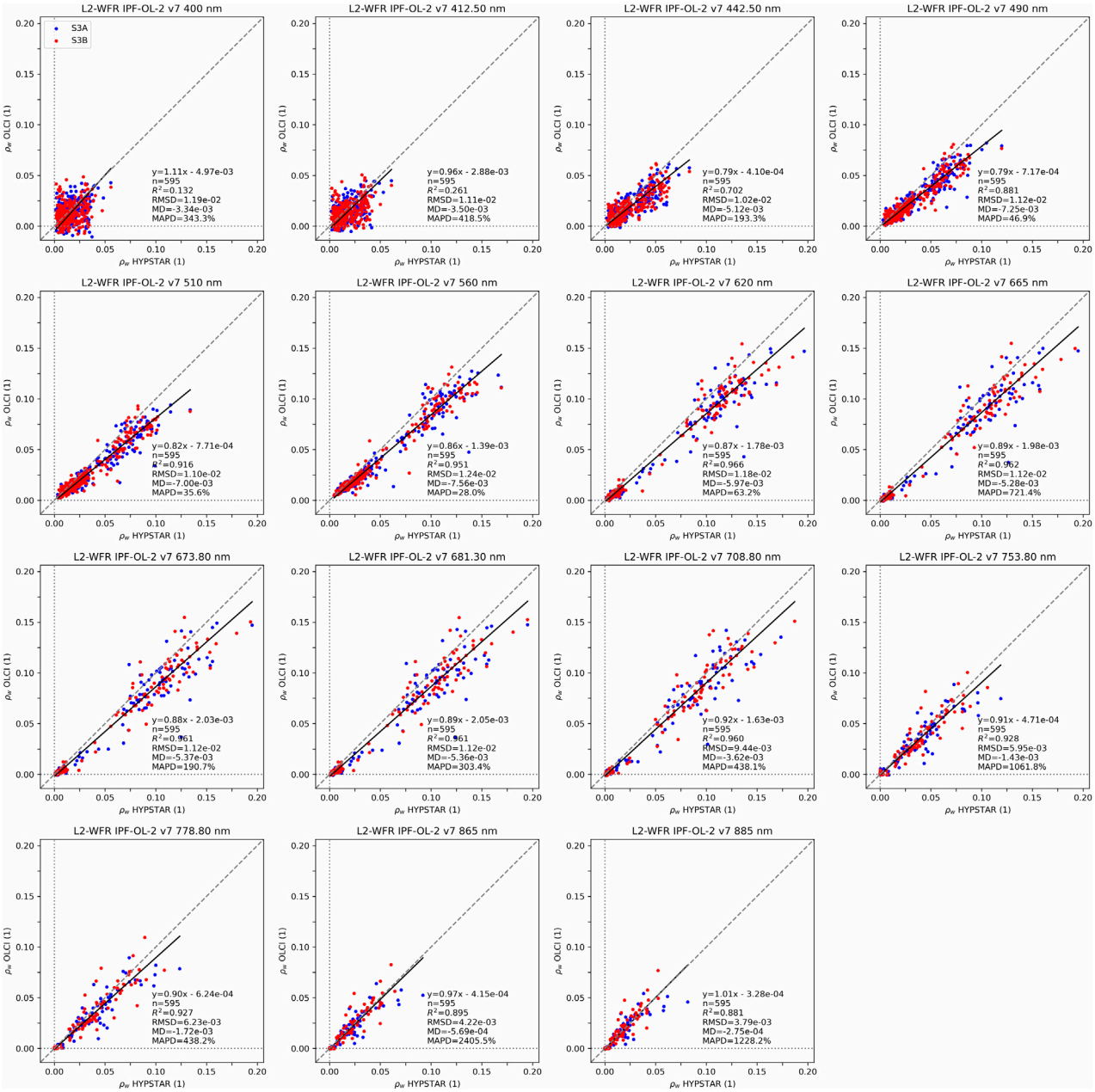


FIGURE 9
Scatterplots of matchups between OLCI sensor of Sentinel-3A (blue) and Sentinel-3B (red) for Acqua Alta (VEIT), Lake Garda (GAIT), Etang de Berre (BEFR), Gironde (MAFR), La Plata (LPAR) and Zeebrugge (M1BE) sites.

Zeebrugge (M1BE) in 2023. In this dataset, the phytoplankton blooms are less strong, and the MALH shows fewer positive values, although MALH, LI and MALH/Chl-a all indicate a phytoplankton bloom dominated by *P. globosa* in early/mid-Apr.

While the MALH algorithm was originally designed (Astoreca et al., 2009) and refined (Lavigne et al., 2022) for application to hyperspectral satellite data, and the WATERHYPERNET network was designed for validation of satellite data, these time series of *in situ* measurements both reinforce the expected potential of future hyperspectral satellite data, and raise the possibility of using standalone WATERHYPERNET data for single-point time series of water quality parameters. A similar study showed the potential for using HYPSTAR® data for detecting the presence of cyanobacteria in a drinking water reservoir (Goyens et al., 2022).

6 Discussion

6.1 Summary of demonstration cases

The results of Section 5.1 comparing PANTHYR data from Oostende and Acqua Alta with Sentinel-2 data show that:

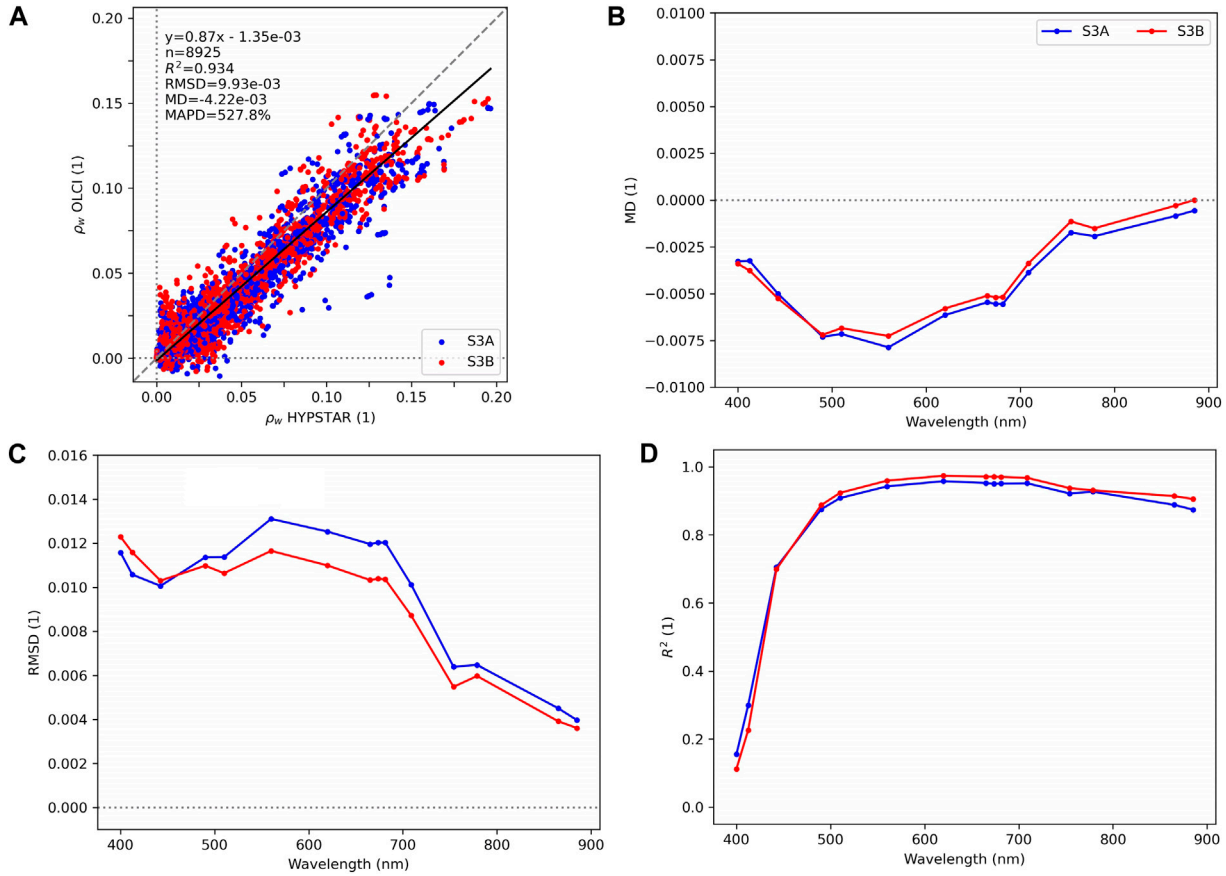


FIGURE 10
(A) Scatter plot of ρ_w matchups between satellite (Sentinel-3/OLCI WFR) and *in situ* (L2 HYPSTAR®) measurements including all the wavelengths. Data points are coloured by satellite. **(B–D)**: Spectral variation of validation metrics computed for each mission for the Sentinel-3 WFR matchups with HYPSTAR® L2 *in situ* data. **(B)** Mean Difference; **(C)** RMSD; **(D)** Determination coefficient (R^2).

TABLE 3 Validation statistics for matchups between OLCI sensor of Sentinel-3A and Sentinel-3B for Acqua Alta (VEIT), Lake Garda (GAIT), Etang de Berre (BEFR), Gironde (MAFR), La Plata (LPAR) and Zeebrugge (M1BE) sites.

	Global	Sentinel-3A	Sentinel-3B
# Match-ups	595	295	300
RMSD	$9.9*10^{-3}$	$10*10^{-3}$	$9.5*10^{-3}$
MD	$-4.2*10^{-3}$	$-4.3*10^{-3}$	$-4.0*10^{-3}$
R^2	0.93	0.93	0.94

- The ACOLITE_DSF atmospheric correction algorithm performs better than the Sen2Cor atmospheric correction (designed for land, but still the only standard Sentinel-2 product for coastal waters) for all spectral bands, for both clear and turbid waters (Figure 5; Figure 6).
- The ACOLITE_DSF_GC atmospheric correction with SWIR-based sunglint correction performs better than ACOLITE_DSF (with no sunglint correction), but only for red and near infrared wavelengths (665–865 nm) - see Figure 6. For shorter wavelengths (443–560 nm) the GC makes little difference to the RMSD over 155 matchups. This suggests that the dominant error source in satellite data processing when using ACOLITE_DSF_GC is not inadequate sunglint correction. The spectral shape of the RMSD between satellite and *in situ* reflectance suggests that the dominant error source is related to atmospheric path reflectance, probably associated with the aerosol correction, but the possibility of inaccurate Rayleigh or coupled Rayleigh-aerosol corrections (including air-water interface reflection) cannot be excluded.
- Detailed analysis of the biggest outliers for each site suggests quite different problems for the satellite data processing in clear *versus* turbid waters.
- For Oostende the negative bias of satellite data and the detailed inspection of the outlier matchups suggest in most cases that the ACOLITE_DSF(_GC) algorithm does not find a dark pixel-wavelength with sufficiently low surface reflectance, thus leading to an overestimation of aerosol reflectance and underestimation of ρ_w. Processing for this region could be improved by including SWIR wavelengths in the dark pixel-wavelength search algorithm, provided sufficient filtering is applied to reduce noise in those bands.
- For Acqua Alta, the positive bias of satellite data and the detailed inspection of the outlier matchups suggest that the

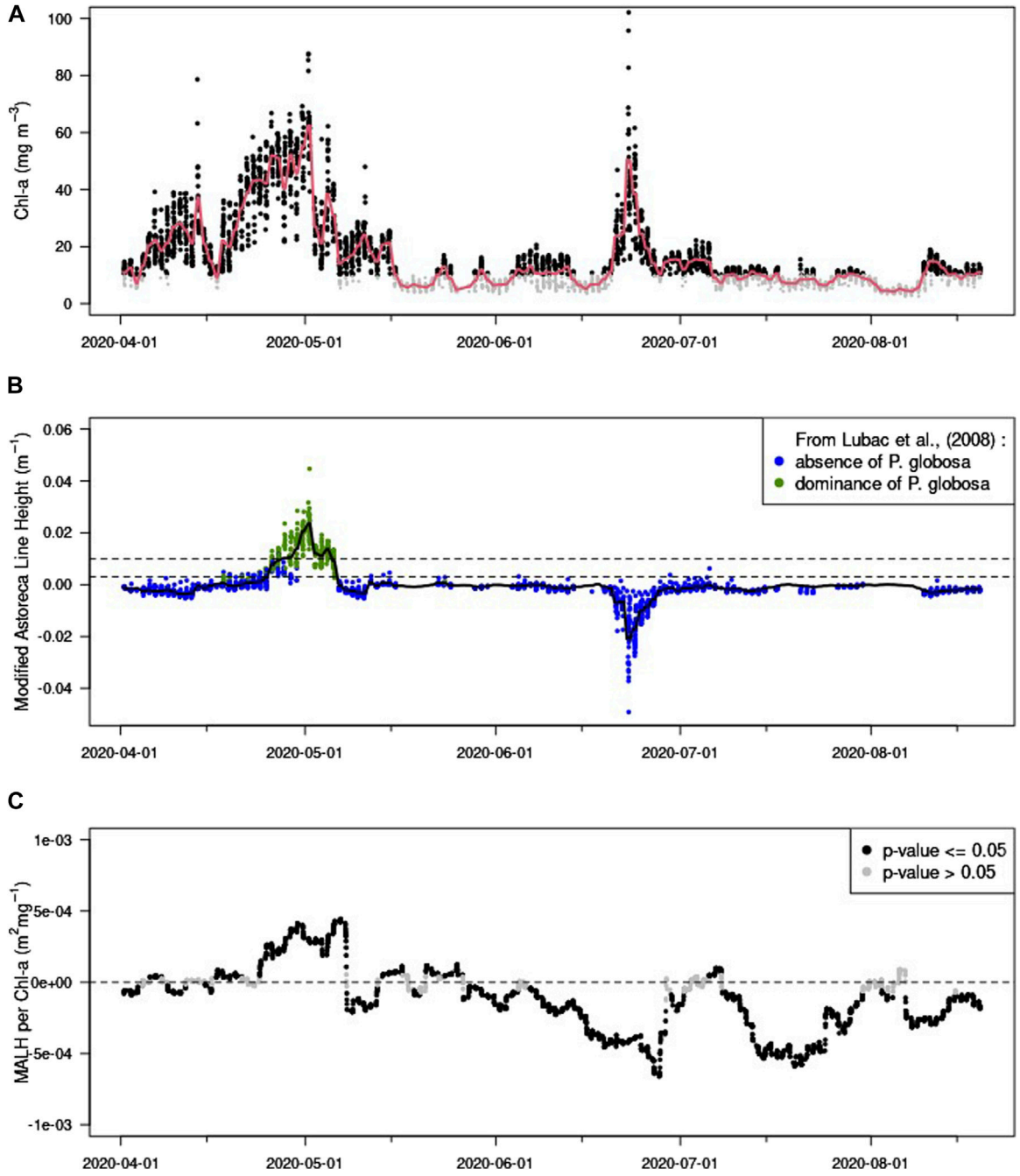


FIGURE 11
Time-series of phytoplankton parameters from the PANTHYR at Oostende (O1BE) for April-August 2020. **(A)** Chl-a concentration estimated from the CRAT algorithm (black dots, with concentrations <13.45 µg/L in grey) with daily mean (red line); **(B)** *Phaeocystis globosa* indicators: MALH on *y*-axis with suggested >0.01 threshold for presence and <0.003 for absence, together with point colouring from the LI flag and daily mean (solid black line); **(C)** MALH per unit Chl-a obtained by regression over a rolling 5-day window with point colouring according to significance of regression slope (*p*-value).

AOT used at the validation pixel is too low, although the underlying reason can be diverse, and is sometimes unclear. The dark pixel may be "too dark", darker than the average atmospheric path reflectance over the 3*3 km ROI, e.g. because of sensor noise, a darker than average wave facet, cloud shadowing of the atmosphere, etc. Alternatively, the validation pixel may have a brighter atmosphere/interface than the dark pixel, e.g. because of patchy haze or undetected thin clouds.

- For both sites some outliers are seen to result from thin unmasked clouds, especially cirrus with TOA reflectance at 1.3 µm just less than the masking threshold of 0.005, and/or from cloud edges. Occasional cloud shadows, including the shadows of clouds outside the ROI, can give negative

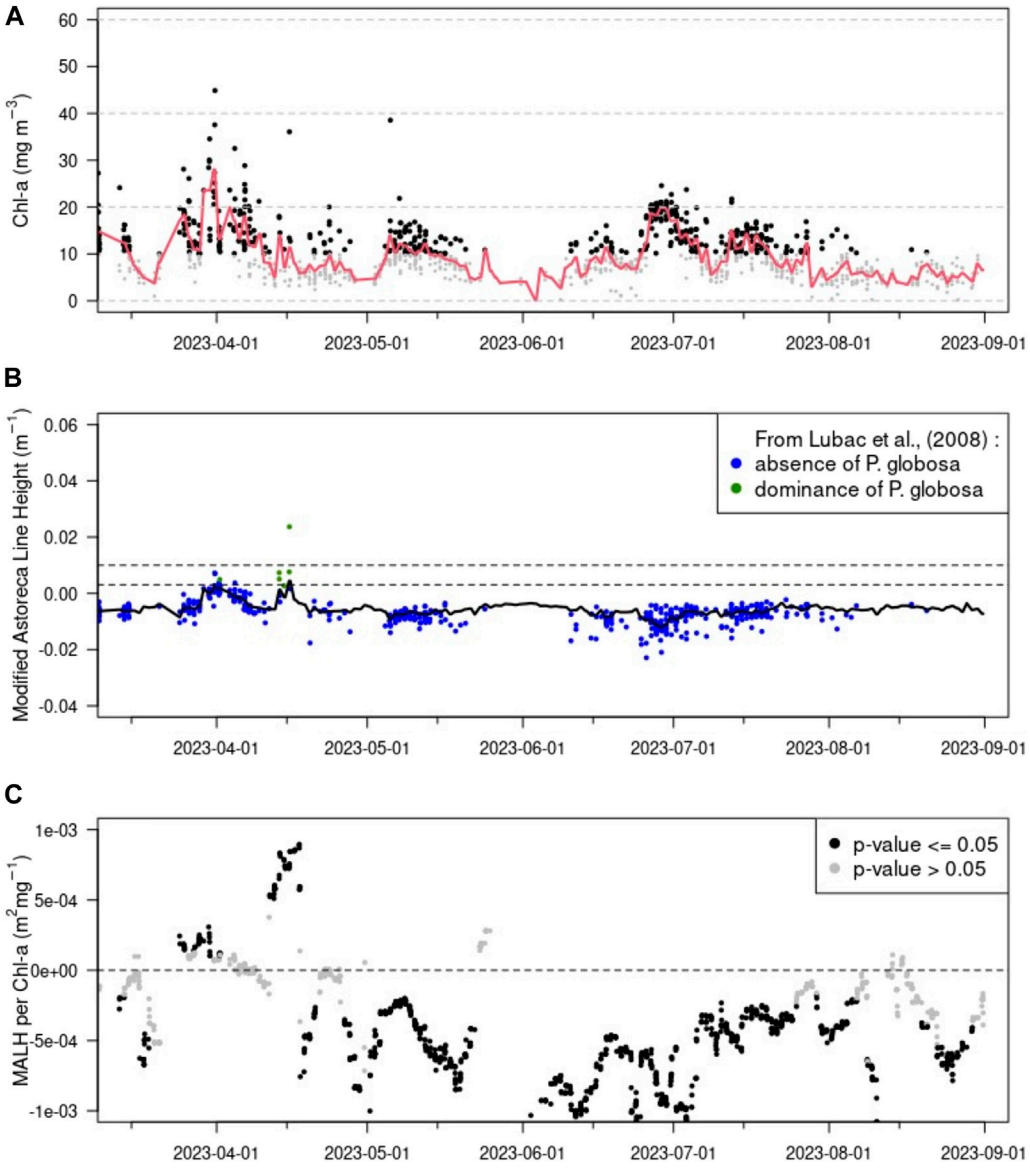


FIGURE 12
Time-series of phytoplankton parameters from the HYPSTAR® at Zeebrugge (M1BE) for Mar-August 2023. Details as for Figure 11.

outliers. For these situations, the atmospheric correction algorithm performance statistics could be improved by better cloud and cloud shadow masking algorithms (Lebreton et al., 2016) and stricter thresholds for cirrus and non-water pixels, although the latter will lead to a removal of data that may be of interest for some users/applications.

- For both sites, imagery of ρ_w shows in some cases surface wave effects, suggesting that these have not been perfectly removed by ACOLITE_DSF_GC, the best-performing satellite data processing algorithm of those tested here.
- The large number of matchups provided by WATERHYPERNET, and the automation of the validation analysis, including a standard Validation Diagnostic sheet per matchup, is clearly essential for validation of Sentinel-2 ρ_w, and consequently establishing confidence in downstream products for users, and providing recommendations for how to further improve the processing algorithm, here ACOLITE_DSF_GC.
- While the use of two contrasting validation sites provided very different and relevant information on satellite algorithm performance the analysis should be expanded to more validation sites in a future operational context.

The results of Section 5.2 comparing HYPSTAR® data from six validation sites with Sentinel-3 data show that:

- Reasonable results are achieved at all spectral bands (RMSD<0.014) with very similar performance for the A and B units of the Sentinel-3/OLCI, confirming that good

interoperability of the constellation has been achieved by harmonisation of space hardware and ground processing elements.
- While in situ and satellite measurements agree well for the range 709-885 nm (regression slope between 0.9 and 1.0, RMSD<0.01) a more systematic difference is found for the range 490-681 nm (R^2>0.88 but regression slope between 0.79 and 0.89) where the RMSD has the spectral shape of turbid water reflectance. An explanation of this difference requires further study of the in situ measurements themselves, the satellite processing algorithm (including intermediate parameters such as aerosol Angstrom exponent), and any space-time differences between the satellite and the *in situ* measurement.

The results of Section 5.3 using the PANTHYR and HYPSTAR® data in Belgian waters (without satellite data), as a follow-up of work by (Lavigne et al., 2022), show that:

- Phytoplankton biomass and some information on dominant species (here *Phaeocystis globosa*) can be monitored at high frequency from these hyperspectral data.

This finding is of interest both in its own right for pointwise monitoring of water quality, and as a precursor for information that might be retrieved from the new generation of hyperspectral satellite missions (Dierssen et al., 2020), provided that the treatment of sub-resolution scale spectral features such as absorbing atmospheric gases renders second derivative spectra of adequate quality (Ruddick et al., 2023).

6.2 Discussion of WATERHYPERNET status and future

This paper has described the WATERHYPERNET, a federated network of automated *in situ* measurements of hyperspectral water reflectance designed for satellite validation. The medium-term ambition is to provide a sufficient quantity of high quality water reflectance data over sufficiently diverse water, atmosphere and Sun conditions to satisfy the needs for radiometric validation of all VIS/NIR (380–900 nm) spectral bands of all current and future optical satellite missions used for aquatic applications. The list of satellite missions expected to use WATERHYPERNET data is long, and includes: dedicated "water colour" missions such as Sentinel-3A&B (&C&D), MODIS, VIIRS; "land" missions repurposed for coastal and inland water applications such as Sentinel-2A&B (&C&D) and Landsat 8&9; recent and future hyperspectral missions such as PRISMA, ENMAP PACE . . . CHIME, SBG and the geostationary GLIMR; and the emerging "Newspace" cubesat constellations pioneered by the PlanetScope Doves and Superdoves.

The network is currently at the stage of a proof-of-concept prototype, with two functioning hardware systems, PANTHYR and HYPSTAR®, automated data acquisition, transmission and processing of data and demonstration datasets. Although significant improvements are expected in the next 2 years with evolution of the *in situ* data processing, particularly regarding quality control and estimation of measurement uncertainties, the prototype datasets are already considered by satellite validation/performance team users to be relevant for showing some performance issues and by water quality managers for describing phytoplankton dynamics, including some indication of species composition.

6.3 Possibilities and limitations

The validation sites described here constitute a network with reasonable coverage of water and atmosphere conditions where satellite data need to be validated (i.e., everywhere where end-users use final products), including clear and turbid waters, coastal and inland waters, various phytoplankton species, low and moderate Coloured Dissolved Organic Matter (CDOM) absorption, various Sun zenith, cloud and wind conditions, etc. A very complete network could be achieved with 20 appropriately chosen validation sites, although the choice of site is clearly limited by availability of funding, dedicated local scientist(s) and stable mounting platforms. Moreover, the current sites can be affected by occasional and/or long-term downtime associated from diverse causes (hardware failures, recalibration of radiometers, platform and/or ship crew availability, funding, etc.).

If the network manager could choose where to locate additional validation sites it would be relevant to add: better coverage of the Southern hemisphere (for satellite commissioning phases occurring in the Northern hemisphere winter), one or two sites at very high latitude (e.g., >70° to validate for the difficult high zenith angles and high air masses but with increased acquisitions/week), one or two sites at low latitudes (e.g., <30° to validate for the difficult high sunglint conditions), one or more very nearshore/inland/high altitude sites for testing adjacency effect removal and atmospheric pressure (and hence Rayleigh scattering) differences, one or two sites with very high CDOM and better longitudinal coverage (e.g., over the West and East coasts of North or South America and over Western and Eastern Asia to provide validation data for geostationary satellites). However, it is likely that the siting of additional validation sites will be more opportunistic (related to national funding and individual motivated scientists) than strategic.

6.4 Challenges and opportunities

The main challenges in establishing and consolidating a network such as WATERHYPERNET are organizational (funding, governance/coordination) and hardware-related. The equipment used here consists of one system (PANTHYR) based on a mature/aging COTS radiometer and COTS pan-tilt with non-commercial assemblage of driving electronics and mechanics and one system (HYPSTAR®) with a newly-designed prototype radiometer and pre-commercial assembly of pan-tilt, host system PC and mechanics with some custom-designed elements (relay board, junction box/cabling). These systems can function autonomously for many months/years in the best cases, but are far from plug-n-play, requiring considerable expertise for preparation and installation and troubleshooting/repairs. The large number of components and the hostile environmental conditions combine to generate a wide range of low probability but high impact failure modes with difficult logistics (safety training and

equipment, availability of transfer boats and crew and seaworthy specialized technical/scientific staff) for maintenance visits to most offshore sites.

Abovewater radiometry, led by the AERONET-OC network (Zibordi et al., 2009; Zibordi et al., 2021), is now established as the main source of *in situ* data for radiometric validation of water colour missions, and there is a growing expertise in laboratory calibration and characterization of hyperspectral radiometers (Talone et al., 2016; Zibordi et al., 2017; Talone and Zibordi, 2018; Vabson et al., 2019; Kuusk et al., 2024), and how to propagate the related uncertainties (Białek et al., 2020; De Vis et al., 2024). However, there are still two elements of the measurement method where the quantification of measurement uncertainties for each individual measurement result can be improved:

- Removal of light reflected at the air-water interface is currently implemented in WATERHYPERNET using the wind speed formulation for effective Fresnel coefficient of (Mobley, 1999), which is a common approach and corresponds to the recommendations of the IOCCG protocols (Zibordi et al., 2019). However, there are many known problems with this model - see Section 4 and Section 6.2 of (Ruddick et al., 2019) and references therein - and no clear consensus on the bias/uncertainty associated with this correction at moderate and high wind speed (>5 m/s), especially for the shorter wavelengths.
- The measurement bias/uncertainty associated with optical perturbations of the water target from the radiometer mounting structure, generally termed "platform perturbations" are not quantified for the WATERHYPERNET sites. An experimental determination of platform perturbations has been made only for the Acqua Alta AERONET-OC site (Talone and Zibordi, 2019) to our knowledge, but is needed for all WATERHYPERNET sites (including Acqua Alta since the deployment there is not located at the same position on the platform as the AERONET-OC deployment).

In addition to these aspects of the measurement method, the uncertainties relating to space, time and viewing angle differences between the *in situ* measurement and the satellite measurement need to be included for a full validation uncertainty analysis, although these are beyond the scope of WATERHYPERNET, which aims to estimate first the uncertainty of the WATERHYPERNET measurement for its own space, time and viewing angle coverage. For comparison between satellite and *in situ* data:

- Spatial differences between satellite and *in situ* measurements can be quantified using higher resolution satellite data, potentially multispectral or even very broadband, which could provide a site-dependent estimate of spatial differences as a function of satellite pixel size. Some validation sites should only be used for metre or decametre scale satellite validation.
- Temporal differences between satellite and *in situ* measurements can generally be quantified from the bounding WATERHYPERNET measurements in time since these are continuous (notwithstanding QC) and are often small because of the 20 min sampling frequency.
- Angular differences between satellite and *in situ* measurements require the use of "BRDF-correction" models (Morel and Gentili, 1996; Park and Ruddick, 2005; Lee et al., 2011). Since the latter are not (yet) mature and generic for all water types, the WATERHYPERNET approach will be, at least initially, to provide data in the acquisition geometry, and point to external tools if angular extrapolation is required by users.

As regards data processing, archiving and distribution and user support:

- The increase in number of sites and data volume will necessitate efficient storage, increased computing power, especially for the time-consuming uncertainty calculations, and careful automation, including exception handling.
- The transformation from evolving R&D project to maturing pre-operational service implies rigorous traceability and versioning including: instrument firmware, data acquisition software, data processing software and calibration and characterization data.
- Extension of the network to new site Principal Investigators (PI) and opening up of the datasets to the scientific community will increase the need for site PI and user support, including documentation, FAQ, online forum and individual responses.

6.5 Future perspectives

In this paper we describe the prototype of the WATERHYPERNET network, and demonstrate its utility for massively multi-satellite radiometric validation. Future work (next 2 years) will focus on:

- Keeping the existing validation sites running as far as possible, and adding a few new sites within the current hardware and human resource limits (especially radiometer manufacturing, calibration and characterization).
- Increasing uptime of validation sites with improvements to critical system components, diagnostics and troubleshooting procedures.
- Incremental improvements in automated and generic quality control of data, especially using experience and time series from these first deployments.
- Including air-water interface correction uncertainty in the quantification and output of measurement uncertainties for each measurement result (i.e., for each time and wavelength).
- Quantification of platform perturbations for each validation site/viewing azimuth/Sun zenith.
- Estimation of aerosol properties (optical thickness, Angstrom exponent) from the E_d measurement to aid diagnosis of aerosol correction problems found in satellite data (Zibordi et al., 2018)
- Recommendations for reference location (away from platform and from land/mixed pixels) to be used for comparison with satellite imagery and quantification of spatial variability as a

function of length scale of satellite data pixel (Dogliotti et al., 2024).

- Near-real time public distribution of consolidated hyperspectral data from the whole network, with water reflectance data supplemented by radiance and irradiance data to facilitate spectral convolution of E_d, L_d and L_u separately (Burggraaff, 2020).

Data availability statement

The original contributions presented in the study are included in the article/Supplementary Material. Further inquiries can be directed to the corresponding author.

Author contributions

KR: Conceptualization, Formal Analysis, Funding acquisition, Methodology, Project administration, Supervision, Validation, Visualization, Writing–original draft, Writing–review and editing. VB: Conceptualization, Formal Analysis, Funding acquisition, Investigation, Methodology, Project administration, Resources, Supervision, Validation, Visualization, Writing–original draft, Writing–review and editing. AC: Conceptualization, Investigation, Methodology, Resources, Software, Writing–review and editing. AD: Conceptualization, Funding acquisition, Investigation, Methodology, Project administration, Resources, Supervision, Validation, Writing–review and editing. DD: Conceptualization, Funding acquisition, Investigation, Methodology, Project administration, Resources, Software, Supervision, Validation, Writing–review and editing. CG: Conceptualization, Data curation, Funding acquisition, Investigation, Methodology, Project administration, Resources, Software, Supervision, Validation, Writing–original draft, Writing–review and editing. JK: Conceptualization, Investigation, Methodology, Project administration, Resources, Software, Supervision, Validation, Writing–review and editing. QV: Conceptualization, Data curation, Formal Analysis, Investigation, Methodology, Resources, Software, Validation, Visualization, Writing–original draft, Writing–review and editing. DV: Investigation, Methodology, Resources, Software, Writing–review and editing. AB: Conceptualization, Funding acquisition, Methodology, Project administration, Supervision, Validation, Writing–review and editing. PD: Conceptualization, Data curation, Methodology, Resources, Software, Writing–review and editing. HL: Formal Analysis, Investigation, Visualization, Writing–original draft, Writing–review and editing. MB: Investigation, Methodology, Resources, Writing–review and editing. KF: Methodology, Resources, Writing–review and editing. AG: Investigation, Methodology, Resources, Writing–review and editing. LG: Formal Analysis, Investigation, Methodology, Visualization, Writing–original draft, Writing–review and editing. KL: Conceptualization, Methodology, Resources, Software, Writing–review and editing. FO: Investigation, Resources, Writing–review and editing. PP: Investigation, Methodology, Resources, Software, Writing–review and editing. EP: Investigation, Methodology, Resources, Writing–review and editing. LR: Investigation, Methodology, Resources, Writing–review and editing. MS: Investigation, Writing–review and editing. DV: Investigation, Writing–review and editing.

Funding

The author(s) declare that financial support was received for the research, authorship, and/or publication of this article. This work was carried out in the context of: the H2020/HYPERNETS project funded by the European Union's Horizon 2020 research and innovation programme (Grant agreement no. 775983), the HYPERNET-POP project funded by the European Space Agency (contract no. 4000139081/22/I-EF), and by the PICT-2020/2636 project funded by the ANPCyT.

Acknowledgments

The Copernicus programme of the European Union, the European Space Agency and EUMETSAT is acknowledged for the supply of Sentinel-2 and Sentinel-3 data.

The Escuela Naval Militar and Servicio de Hidrografía Naval (LPAR), POM West-Vlaanderen Blue Accelerator Platform (O1BE), C-POWER (TBBE), the Italian National Research Council (Acqua Alta Oceanographic Tower—VEIT) and het agentschap Maritieme Dienstverlening en Kust (M1BE) are thanked for hosting and supporting the WATERHYPERNET validation sites.

Over the last 6 years we have benefited from input, discussions and support from many colleagues from the H2020/HYPERNETS and FRM4SOC projects and related activities and we thank particularly: Giuseppe Zibordi, Nigel Fox, Sam Hunt, Ilmar Ansko, Viktor Vabson, Kim Duong, Riho Vendt, Claudia Giardino, Mariano Bresciani, Salvatore Mangano, Javier A. Concha, André Cattrijsse, Daniel Spengler, Edouard Leymarie, Christope Penkerc'h, Erwin Goor, Miroslaw Darecki, Craig Donlon, Tania Casal, Ewa Kwiatkowska, Juan Gossn, Philippe Goryl, Kevin Alonso Gonzalez and Fabrizio Niro. Acknowledgement of these individuals does not constitute endorsement of or responsibility for the content of this work but is merely an expression of thanks.

Two reviewers are thanked for their careful reading and constructive suggestions.

Conflict of interest

Co-authors from Tartu University and Sorbonne University may benefit from future commercialisation of the HYPSTAR® radiometer and system. All authors are likely to receive future research funding for WATERHYPERNET data acquisition and/or exploitation. The authors declare that these interests do not affect the statements and findings of this paper, which has been written according to the normal scientific ethics and values of the academic community. The authors declare that the research was conducted in the absence of any other commercial or financial relationships that could be construed as a potential conflict of interest.

The author(s) declared that they were an editorial board member of Frontiers, at the time of submission. This had no impact on the peer review process and the final decision.

Publisher's note

All claims expressed in this article are solely those of the authors and do not necessarily represent those of their affiliated organizations, or those of the publisher, the editors and the reviewers. Any product that may be evaluated in this article, or claim that may be made by its manufacturer, is not guaranteed or endorsed by the publisher.

Supplementary material

The Supplementary Material for this article can be found online at: https://www.frontiersin.org/articles/10.3389/frsen.2024.1347520/full#supplementary-material

References

Alonso, K., Bachmann, M., Burch, K., Carmona, E., Cerra, D., De los Reyes, R., et al. (2019). Data products, quality and validation of the DLR earth sensing imaging spectrometer (DESIS). *Sensors* 19 (20), 4471. doi:10.3390/s19204471

Arabi, B., Salama, M. S., Wernand, M. R., and Verhoef, W. (2018). Remote sensing of water constituent concentrations using time series of *in-situ* hyperspectral measurements in the wadden Sea. *Remote Sens. Environ.* 216 (October), 154–170. doi:10.1016/j.rse.2018.06.040

Astoreca, R., Rousseau, V., Ruddick, K., Knechciak, C., Van Mol, B., Parent, J.-Y., et al. (2009). Development and application of an algorithm for detecting Phaeocystis globosa blooms in the case 2 Southern North Sea waters. *J. Plankton Res.* 31 (3), 287–300. doi:10.1093/plankt/fbn116

Banks, A. C., Vendt, R., Alikas, K., Bialek, A., Kuusk, J., Lerebourg, C., et al. (2020). Fiducial reference measurements for satellite ocean colour (FRM4SOC). *Remote Sens.* 12 (8), 1322. doi:10.3390/rs12081322

Białek, A., Douglas, S., Kuusk, J., Ansko, I., Vabson, V., Vendt, R., et al. (2020). Example of Monte Carlo method uncertainty evaluation for above-water ocean colour radiometry. *Remote Sens.* 12 (5), 780. doi:10.3390/rs12050780

Braga, F., Fabbretto, A., Vanhellemont, Q., Bresciani, M., Giardino, C., Scarpa, G. M., et al. (2022). Assessment of PRISMA water reflectance using autonomous hyperspectral radiometry. *ISPRS J. Photogrammetry Remote Sens.* 192 (October), 99–114. doi:10.1016/j.isprsjprs.2022.08.009

Brando, V., Lovell, J., King, E., Boadle, D., Scott, R., and Schroeder, T. (2016). The potential of autonomous ship-borne hyperspectral radiometers for the validation of Ocean Color radiometry data. *Remote Sens.* 8 (2), 150. doi:10.3390/rs8020150

Brown, S. W., Flora, S. J., Feinholz, M. E., Yarbrough, M. A., Houlihan, T., Peters, D., et al. 2007. The marine optical buoy (MOBY) radiometric calibration and uncertainty budget for Ocean color satellite sensor vicarious calibration. *Proc. SPIE 6744, Sensors, Systems, and Next-Generation Satellites XI, 67441M*. doi:10.1117/12.737400

Burggraaff, O. (2020). Biases from incorrect reflectance convolution. *Opt. Express* 28 (9), 13801–13816. doi:10.1364/OE.391470

Carswell, T., Costa, M., Young, E., Komick, N., Gower, J., and Sweeting, R. (2017). Evaluation of MODIS-AQUA atmospheric correction and chlorophyll products of western North American coastal waters based on 13 Years of data. *Remote Sens.* 9 (10), 1063. doi:10.3390/rs9101063

Castagna, A., Johnson, B. C., Voss, K., Dierssen, H. M., Patrick, H., Germer, T., et al. (2019). Uncertainty in global downwelling plane irradiance estimates from sintered polytetrafluoroethylene plaque radiance measurements. *Appl. Opt.* 58 (16), 4497–4511. doi:10.1364/ao.58.004497

Concha, J. A., Bracaglia, M., and Brando, V. E. (2021). Assessing the influence of different validation protocols on ocean colour match-up analyses. *Remote Sens. Environ.* 259 (June), 112415. doi:10.1016/j.rse.2021.112415

De Vis, P., Goyens, C., Hunt, S., Vanhellemont, Q., Ruddick, K. G., and Bialek, A. (2024). Generating hyperspectral reference measurements for surface reflectance from the LANDHYPERNET and WATERHYPERNET networks. *Front. Remote Sens.* 5. doi:10.3389/frsen.2024.1347230

Dierssen, H., Bracher, A., Brando, V., Loisel, H., and Ruddick, K. (2020). Data needs for hyperspectral detection of algal diversity across the globe. *Oceanography* 33 (1), 74–79. doi:10.5670/oceanog.2020.111

Dogliotti, A. I., Gossn, J., Vanhellemont, Q., and Ruddick, K. G. 2015. Evaluation of Two Sites for Ocean Color Validation in the Turbid Waters of the Rio de La Plata (Argentina) (2015), In Proceedings of the Sentinel-3 for Science Workshop, Venice-Lido, Italy, June 2–5, 2015, ESA Special Publication SP-734.

Dogliotti, A. I., Merlo, R., Yema, L., and O'Farrell, I. (2023). Validation of Sentinel-2/MSI Water Reflectance and Water Quality Products in the Turbid Waters of Río de La Plata Estuary Using Fixed Automated Hyperspectral *in situ* Observations. *Remote Sens. Ocean, Sea Ice, Coast. Waters, Large Water Regions 2023* 12728, 1272802. doi:10.1117/12.2684141

Dogliotti, A. I., Piegari, E., Rubinstein, L., Perna, P., and Ruddick, K. G. (2024). Using the automated HYPERNETS hyperspectral system for multimission satellite ocean colour validation in the Río de La Plata, accounting for different spatial resolutions. *Front. Remote Sens.* 5, 1354662. doi:10.3389/frsen.2024.1354662

Dorji, P., and Fearns, P. (2018). Atmospheric correction of geostationary HIMAWARI-8 satellite data for total suspended sediment mapping: a case study in the coastal waters of western Australia. *ISPRS J. Photogrammetry Remote Sens.* 144 (October), 81–93. doi:10.1016/j.isprsjprs.2018.06.019

Doron, M., Bélanger, S., Doxaran, D., and Babin, M. (2011). Spectral variations in the near-infrared ocean reflectance. *Remote Sens. Environ.* 115, 1617–1631. doi:10.1016/j.rse.2011.01.015

EUMETSAT (2021). Sentinel-3 OLCI L2 report for baseline collection OL_L2M_003. Available from: https://user.eumetsat.int/s3/eup-strapi-media/Sentinel_3_OLCI_L2_report_for_baseline_collection_OL_L2_M_003_2_B_c8bbc6d986.pdf.

EUMETSAT (2022). Recommendations for Sentinel-3 OLCI Ocean colour product validations in comparison with *in situ* measurements – matchup protocols. *EUM/SEN3/DOC/19/1092968 v8b*. Available from: https://user.eumetsat.int/s3/eup-strapi-media/Recommendations_for_Sentinel_3_OLCI_Ocean_Colour_product_validations_in_comparison_with_in_situ_measurements_Matchup_Protocols_V8_B_e6c62ce677.pdf.

Franz, B. A., Werdell, P. J., Meister, G., Bailey, S. W., Eplee Jr, R. E., Feldman, G. C., et al. 2005. The continuity of Ocean Color measurements from SeaWiFS to MODIS. *Proc. SPIE 5882, Earth Observing Systems X, 58820 W*. doi:10.1117/12.620069

Garnesson, P., Mangin, A., Fanton d'Andon, O., Demaria, J., and Bretagnon, M. (2019). The CMEMS GlobColour chlorophyll *a* product based on satellite observation: multi-sensor merging and flagging strategies. *Ocean Sci.* 15 (3), 819–830. doi:10.5194/os-15-819-2019

Gonzalez Vilas, L., Brando, V. E., Concha, J. A., Goyens, C., Dogliotti, A. I., Doxaran, D., et al. (2024). Validation of satellite water products based on HYPERNETS *in situ* data using a Match-up Database (MDB) file structure. *Front. Remote Sens.* 5, 1330317. doi:10.3389/frsen.2024.1330317

Gorelick, N., Hancher, M., Dixon, M., Ilyushchenko, S., Thau, D., and Moore, R. (2017). Google Earth Engine: planetary-scale geospatial analysis for everyone. *Remote Sens. Environ.* 202 (December), 18–27. doi:10.1016/j.rse.2017.06.031

Gorman, E. T., Kubalak, D. A., Patel, D., Mott, D. B., Meister, G., and Werdell, P. J. (2019). The NASA Plankton, aerosol, cloud, ocean Ecosystem (PACE) mission: an emerging era of global, hyperspectral Earth system remote sensing. *Proc. SPIE 11151, Sensors, Systems, and Next-Generation Satellites XXIII, 111510G*. doi:10.1117/12.2537146

Goyens, C., Lavigne, H., Dille, A., and Vervaeren, H. (2022). Using hyperspectral remote sensing to monitor water quality in drinking water reservoirs. *Remote Sens.* 14 (21), 5607. doi:10.3390/rs14215607

Goyens, C., and Ruddick, K. (2023). Improving the standard protocol for above-water reflectance measurements: 1. Estimating effective wind speed from angular variation of sunglint. *Appl. Opt.* 62 (February), 2442. doi:10.1364/AO.481787

Gregg, W. W., and Carder, K. L. (1990). A simple spectral solar irradiance model for cloudless maritime atmospheres. *Limnol. Oceanogr.* 35 (8), 1657–1675.

Hedley, J. D., Roelfsema, C., Brando, V., Giardino, C., Kutser, T., Phinn, S., et al. (2018). Coral reef applications of Sentinel-2: coverage, characteristics, bathymetry and benthic mapping with comparison to Landsat 8. *Remote Sens. Environ.* 216 (October), 598–614. doi:10.1016/j.rse.2018.07.014

Hieronymi, M. (2019). Spectral band adaptation of Ocean Color sensors for applicability of the multi-water biogeo-optical algorithm ONNS. *Opt. Express* 27 (12), A707–A724. doi:10.1364/OE.27.00A707

Hooker, S. B., Bernhard, G., Morrow, J. H., Booth, C. R., Comer, T., Lind, R. N., et al. (2012). "Optical sensors for planetary radiant energy (OSPREY): calibration and validation of current and next-generation NASA missions," in *NASA technical memorandum 2012–215872* (Greenbelt, MD, USA: NASA).

Kaufmann, H., Segl, K., Chabrillat, S., Hofer, S., Stuffler, T., Mueller, A., et al. (2006). "EnMAP a hyperspectral sensor for environmental mapping and analysis," in *2006 IEEE international symposium on geoscience and remote sensing* (Germany: IEEE), 1617–1619.

Kou, L., Labrie, D., and Chylek, P. (1993). Refractive indices of water and ice in the 0.65 to 2.5 μm spectral range. *Appl. Opt.* 32, 3531–3540. doi:10.1364/ao.32.003531

Kuusk, J., Corizzi, A., Doxaran, D., Duong, K., Flight, K., Kivastik, J., et al. (2024). HYPSTAR: a hyperspectral pointable system for terrestrial and aquatic radiometry. *Front. Remote Sens* 5. doi:10.3389/frsen.2024.1347507

Kwiatkowska, E. J., Bonekamp, H. G., Ramon, D., Vanhellemont, Q., Brockmann, C., Lebreton, C., et al. (2016). Ocean colour opportunities from METEOSAT Second and Third Generation geostationary platforms. *Ocean Sci.* 12 (3), 703–713. doi:10.5194/os-12-703-2016

Lavigne, H., and Ruddick, K. (2018). The potential use of geostationary MTG/FCI to retrieve chlorophyll-a concentration at high temporal resolution for the open oceans. *Int. J. Remote Sens.* 39 (8), 2399–2420. doi:10.1080/01431161.2017.1420935

Lavigne, H., Ruddick, K., and Vanhellemont, Q. (2022). Monitoring of high biomass Phaeocystis globosa blooms in the Southern North Sea by *in situ* and future spaceborne hyperspectral radiometry. *Remote Sens. Environ.* 282 (December), 113270. doi:10.1016/j.rse.2022.113270

Lebreton, C., Stelzer, K., Brockmann, C., Bertels, L., Pringle, N., Paperin, M., et al. (2016). Cloud and cloud shadow masking of high and medium resolution optical sensors-an algorithm inter-comparison example for Landsat 8. *Living Planet Symp.* ESA Special Publication SP-740, 407.

Lee, Z. P., Du, K., Voss, K. J., Zibordi, G., Lubac, B., Arnone, R., et al. (2011). An inherent-optical-property-centered approach to correct the angular effects in water-leaving radiance. *Appl. Opt.* 50 (19), 3155–3167. doi:10.1364/ao.50.003155

Lubac, B., Loisel, H., Guiselin, N., Astoreca, R., Artigas, L. F., and Mériaux, X. (2008). Hyperspectral and Multispectral Ocean color Inversions to Detect Phaeocystis globosa blooms in coastal waters. *J. Geophys. Res.* 113 (C06026). doi:10.1029/2007jc004451

Luo, Y., Doxaran, D., and Vanhellemont, Q. (2020). Retrieval and validation of water turbidity at metre-scale using Pléiades satellite data: a case study in the Gironde estuary. *Remote Sens.* 12 (6), 946. doi:10.3390/rs12060946

Main-Knorn, M., Pflug, B., Louis, J., Debaecker, V., Müller-Wilm, U., and Gascon, F. (2017). Sen2Cor for Sentinel-2. *Image Signal Process. Remote Sens. XXIII* 10427, 37–48. doi:10.1117/12.2278218

Mélin, F., and Sclep, G. (2015). Band shifting for Ocean color multi-spectral reflectance data. *Opt. Express* 23 (3), 2262–2279. doi:10.1364/OE.23.002262

Meygret, A., Santer, R. P., and Berthelot, B. (2011). ROSAS: a Robotic Station for Atmosphere and Surface Characterization dedicated to on-orbit calibration. *Proc. SPIE 8153, Earth Observing Systems XVI, 815311*. doi:10.1117/12.892759

Mills, D. K., Laane, R. W. P. M., Rees, J. M., Loeff, M. R. V. d., Suylen, J. M., Pearce, D. J., et al. (2003). "Smartbuoy: a marine environmental monitoring buoy with a difference," in *Building the European capacity in operational oceanography, proc. Third international conference on EuroGOOS*. Editors H. Dahlin, N. C. Flemming, K. Nittis, and S. E. Peterson (Germany: Elsevier Oceanography Series Publication Series 19), 311–316.

Mobley, C. D. (1999). Estimation of the remote-sensing reflectance from above-surface measurements. *Appl. Opt.* 38, 7442–7455. doi:10.1364/ao.38.007442

Morel, A., and Gentili, B. (1996). Diffuse reflectance of oceanic waters III. Implication of bidirectionality for the remote-sensing problem. *Appl. Opt.* 35 (24), 4850–4862. doi:10.1364/ao.35.004850

Mueller, J. L., Davis, C., Arnone, R., Frouin, R., Carder, K., Lee, Z. P., et al. (2003). "Above-water radiance and remote sensing reflectance measurements and analysis protocols (chapter 3)," in *Ocean optics protocols for satellite Ocean color sensor validation revision* (Greenbelt, MD, USA: NASA), 4, 21–31.

Neukermans, G., Ruddick, K., Bernard, E., Ramon, D., Nechad, B., and Deschamps, P.-Y. (2009). Mapping total suspended matter from geostationary satellites: a feasibility study with SEVIRI in the Southern North Sea. *Opt. Express* 17 (16), 14029–14052. doi:10.1364/OE.17.014029

Neukermans, G., Ruddick, K. G., and Greenwood, N. (2012). Diurnal variability of turbidity and light attenuation in the Southern North Sea from the SEVIRI geostationary sensor. *Remote Sens. Environ.* 124 (September), 564–580. doi:10.1016/j.rse.2012.06.003

Pahlevan, N., Mangin, A., Balasubramanian, S. V., Smith, B., Alikas, K., Arai, K., et al. (2021). ACIX-Aqua: a global assessment of atmospheric correction methods for Landsat-8 and Sentinel-2 over lakes, rivers, and coastal waters. *Remote Sens. Environ.* 258 (June), 112366. doi:10.1016/j.rse.2021.112366

Pahlevan, N., and Schott, J. R. (2013). Leveraging EO-1 to evaluate capability of new generation of Landsat sensors for coastal/inland water studies. *IEEE J. Sel. Top. Appl. Earth Observations Remote Sens.* 6 (2), 360–374. doi:10.1109/JSTARS.2012.2235174

Pahlevan, N., Smith, B., Binding, C., and O'Donnell, D. M. (2017). Spectral band adjustments for remote sensing reflectance spectra in coastal/inland waters. *Opt. Express* 25 (23), 28650–28667. doi:10.1364/OE.25.028650

Park, Y., and Ruddick, K. (2005). Model of remote-sensing reflectance including bidirectional effects for case 1 and case 2 waters. *Appl. Opt.* 44 (7), 1236–1249. doi:10.1364/AO.44.001236

Peters, S., Laanen, M., Groetsch, P., Ghezehegn, S., Poser, K., Hommersom, A., et al. (2018). WISPstation: a new autonomous above water radiometer system. *Zenodo*. doi:10.5281/zenodo.2533079

Philippart, K., Blauw, A., Bolhuis, H., Brandenburg, K., Brussaard, C., Gerkema, T., et al. (2020). Quick scan zeeschuim. *NIOZ/Bureau Waardenbg. Statistics/CNR/KBIN/NIOO-KNAW/Rijkswaterstaat (RWS-WVL)/Technische Univ. Delft/Universiteit Amsterdam/Universiteit Utr. Groningen/Water Insight BV. NIOZ Open Respository*, 356236.

Reinersman, P. N., and Carder, K. L. (1995). Monte Carlo simulation of the atmospheric point-spread function with an application to correction for the adjacency effect. *Appl. Opt.* 34 (21), 4453–4471. doi:10.1364/ao.34.004453

Rousseau, V., Becquevort, S., Parent, J. Y., Gasparini, S., Daro, M. H., Tackx, M., et al. (2000). Trophic efficiency of the planktonic food web in a coastal Ecosystem dominated by Phaeocystis colonies. *J. Sea Res.* 43, 357–372. doi:10.1016/s1385-1101(00)00018-6

Ruddick, K., De Cauwer, V., and Van Mol, B. (2005). Use of the near infrared similarity spectrum for the quality control of remote sensing data. *Proc. SPIE 5885* (USA: SPIE), 5885. doi:10.1117/12.615152

Ruddick, K., De Cauwer, V., Park, Y., and Moore, G. (2006). Seaborne measurements of near infrared water-leaving reflectance: the similarity spectrum for turbid waters. *Limnol. Oceanogr.* 51 (2), 1167–1179. doi:10.4319/lo.2006.51.2.1167

Ruddick, K., Gons, H., Rijkeboer, M., and Tilstone, G. (2001). Optical remote sensing of chlorophyll a in case 2 waters by use of an adaptive two-band algorithm with optimal error properties. *Appl. Opt.* 40 (21), 3575–3585. doi:10.1364/AO.40.003575

Ruddick, K., Voss, K., Boss, E., Castagna, A., Frouin, R. J., Gilerson, A., et al. (2019). A review of protocols for fiducial reference measurements of water-leaving radiance for validation of satellite remote sensing data over water. *Remote Sens.* 11 (19), 2198. doi:10.3390/rs11192198

Ruddick, K. G., De Vis, P., Goyens, C., Kuusk, J., Lavigne, H., and Vanhellemont, Q. (2023). Second derivative water reflectance spectra for phytoplankton species detection – origin, impact and removal of spectral wiggles. *Proc. SPIE 12728, Remote Sensing of the Ocean, Sea Ice, Coastal Waters, and Large Water Regions 2023, 127280A*. doi:10.1117/12.2684336

Ryu, J.-H., Han, H.-J., Cho, S., Park, Y.-J., and Ahn, Y.-H. (2012). Overview of Geostationary Ocean color imager (GOCI) and GOCI data processing system (GDPS). *Ocean Sci. J.* 47 (3), 223–233. doi:10.1007/s12601-012-0024-4

Santer, R., and Schmechtig, C. (2000). Adjacency effects on water surfaces: primary scattering approximation and sensitivity study. *Appl. Opt.* 39 (3), 361–375. doi:10.1364/ao.39.000361

Simis, S. G. H., and Olsson, J. (2013). Unattended processing of shipborne hyperspectral reflectance measurements. *Remote Sens. Environ.* 135 (August), 202–212. doi:10.1016/j.rse.2013.04.001

Slivkoff, M. M. (2014). "Ocean colour remote sensing of the great barrier reef waters, ". PhD Thesis. *Curtin Univ.*

Talone, M., and Zibordi, G. (2019). Non-linear response of a class of hyper-spectral radiometers. *Metrologia* 55 (5), 747–758. doi:10.1088/1681-7575/aadd7f

Talone, M., and Zibordi, G. (2019). Spectral assessment of deployment platform perturbations in above-water radiometry. *Opt. Express* 27 (12), A878. doi:10.1364/OE.27.00A878

Talone, M., Zibordi, G., Ansko, I., Banks, A. C., and Kuusk, J. (2016). Stray light effects in above-water remote-sensing reflectance from hyperspectral radiometers. *Appl. Opt.* 55 (15), 3966. doi:10.1364/AO.55.003966

Thompson, D., Thompson, D. R., Green, R. O., Bradley, C., Brodrick, P. G., Dor, B., et al. (2023). On-orbit calibration and performance of the EMIT imaging spectrometer. *ESS Open Archive*. doi:10.22541/essoar.168988432.29040205/v1

Tilstone, G. H., Pardo, S., Dall'Olmo, G., Brewin, R. J. W., Nencioli, F., Dessailly, D., et al. (2021). Performance of ocean colour chlorophyll a algorithms for sentinel-3 OLCI, MODIS-aqua and suomi-VIIRS in open-ocean waters of the atlantic. *Remote Sens. Environ.* 260 (July), 112444. doi:10.1016/j.rse.2021.112444

Vabson, V., Kuusk, J., Ansko, I., Vendt, R., Alikas, K., Ruddick, K., et al. (2019). Laboratory intercomparison of radiometers used for satellite validation in the 400-900 nm range. *Remote Sens.* 11 (9), 1101. doi:10.3390/rs11091101

Vanhellemont, Q. (2019a). Adaptation of the dark spectrum fitting atmospheric correction for aquatic applications of the Landsat and Sentinel-2 archives. *Remote Sens. Environ.* 225, 175–192. doi:10.1016/j.rse.2019.03.010

Vanhellemont, Q. (2019b). Daily metre-scale mapping of water turbidity using CubeSat imagery. *Opt. Express* 27 (20), A1372–A1399. doi:10.1364/OE.27.0A1372

Vanhellemont, Q. (2020). Sensitivity analysis of the dark spectrum fitting atmospheric correction for metre- and decametre-scale satellite imagery using autonomous hyperspectral radiometry. *Opt. Express* 28 (20), 29948–29965. doi:10.1364/OE.397456

Vanhellemont, Q. (2023). Evaluation of eight band SuperDove imagery for aquatic applications. *Opt. Express* 31 (9), 13851–13874. doi:10.1364/OE.483418

Vanhellemont, Q., and Ruddick, K. (2014). Turbid wakes associated with offshore wind turbines observed with Landsat 8. *Remote Sens. Environ.* 145 (April), 105–115. doi:10.1016/j.rse.2014.01.009

Vanhellemont, Q., and Ruddick, K. (2015). Assessment of Sentinel-3/OLCI sub-pixel variability and platform impact using Landsat-8/OLI, In *Proceedings of the Sentinel-3 for Science Workshop, Venice-Lido, Italy*, June 2–5, 2015. ESA Special Publication SP-734.

Vanhellemont, Q., and Ruddick, K. (2021). Atmospheric correction of metre-scale optical satellite data for inland and coastal water applications. *Remote Sens. Environ.* 216, 586–597. doi:10.1016/j.rse.2018.07.015

Vanhellemont, Q., and Ruddick, K. (2021). Atmospheric correction of Sentinel-3/OLCI data for mapping of suspended particulate matter and chlorophyll-a concentration in Belgian turbid coastal waters. *Remote Sens. Environ.* 256, 112284. doi:10.1016/j.rse.2021.112284

Wang, M., Jiang, L., Liu, X., Son, S., Sun, J., Shi, W., et al. 2016. *VIIRS Ocean Color products: a progress update*. Beijing, China: IEEE International Geoscience and Remote Sensing Symposium (IGARSS), 5848–5851. doi:10.1109/IGARSS.2016.7730528

Werdell, P. J., Bailey, S., Fargion, G., Pietras, C., Knobelspiesse, K., Feldman, G., et al. (2003). Unique data repository facilitates Ocean Color satellite validation. *Eos, Trans. Am. Geophys. Union* 84 (38), 377–387. doi:10.1029/2003EO380001

Zibordi, G., Holben, B., Slutsker, I., Giles, D., D'Alimonte, D., Mélin, F., et al. (2009). AERONET-OC: a network for the validation of Ocean Color primary products. *J. Atmos. Ocean. Technol.* 26, 1634–1651. doi:10.1175/2009jtecho654.1

Zibordi, G., Holben, B. N., Talone, M., D'Alimonte, D., Slutsker, I., Giles, D. M., et al. (2021). Advances in the Ocean Color component of the aerosol robotic network (AERONET-OC). *J. Atmos. Ocean. Technol.* 38 (4), 725–746. doi:10.1175/JTECH-D-20-0085.1

Zibordi, G., Kwiatkowska, E., Mélin, F., Talone, M., Cazzaniga, I., Dessailly, D., et al. (2022). Assessment of OLCI-A and OLCI-B radiometric data products across European seas. *Remote Sens. Environ.* 272 (April), 112911. doi:10.1016/j.rse.2022.112911

Zibordi, G., Mélin, F., and Berthon, J.-F. (2018). A regional assessment of OLCI data products. *IEEE Geoscience Remote Sens. Lett.* 15 (10), 1490–1494. doi:10.1109/LGRS.2018.2849329

Zibordi, G., Mélin, F., Voss, K. J., Johnson, B. C., Franz, B. A., Kwiatkowska, E., et al. (2015). System vicarious calibration for Ocean color climate change applications: requirements for *in situ* data. *Remote Sens. Environ.* 159, 361–369. doi:10.1016/j.rse.2014.12.015

Zibordi, G., Talone, M., and Jankowski, L. (2017). Response to temperature of a class of *in situ* hyperspectral radiometers. *J. Atmos. Ocean. Technol.* 34 (8), 1795–1805. doi:10.1175/JTECH-D-17-0048.1

Zibordi, G., Voss, K., Johnson, B. C., and Mueller, J. L. (2019). Protocols for satellite Ocean Color data validation: *in situ* optical radiometry (v3.0). *IOCCG Protocols Document*.

frontiers | Frontiers in Remote Sensing

TYPE Original Research
PUBLISHED 26 August 2024
DOI 10.3389/frsen.2024.1323998

Check for updates

OPEN ACCESS

EDITED BY
Enner Alcântara,
São Paulo State University, Brazil

REVIEWED BY
Yonggang Qian,
Chinese Academy of Sciences (CAS), China
Changyong Cao,
National Oceanic and Atmospheric Administration (NOAA), United States

*CORRESPONDENCE
Pieter De Vis,
pieter.de.vis@npl.co.uk,
pieter.devis1@gmail.com

RECEIVED 18 October 2023
ACCEPTED 16 May 2024
PUBLISHED 26 August 2024

CITATION
De Vis P, Howes A, Vanhellemont Q, Bialek A, Morris H, Sinclair M and Ruddick K (2024), Feasibility of satellite vicarious calibration using HYPERNETS surface reflectances from Gobabeb and Princess Elisabeth Antarctica sites.
Front. Remote Sens. 5:1323998.
doi: 10.3389/frsen.2024.1323998

COPYRIGHT
© 2024 De Vis, Howes, Vanhellemont, Bialek, Morris, Sinclair and Ruddick. This is an open-access article distributed under the terms of the Creative Commons Attribution License (CC BY). The use, distribution or reproduction in other forums is permitted, provided the original author(s) and the copyright owner(s) are credited and that the original publication in this journal is cited, in accordance with accepted academic practice. No use, distribution or reproduction is permitted which does not comply with these terms.

Feasibility of satellite vicarious calibration using HYPERNETS surface reflectances from Gobabeb and Princess Elisabeth Antarctica sites

Pieter De Vis[1]*, Adam Howes[1], Quinten Vanhellemont[2], Agnieszka Bialek[1], Harry Morris[1], Morven Sinclair[1] and Kevin Ruddick[2]

[1]National Physical Laboratory, Teddington, United Kingdom, [2]Royal Belgian Institute of Natural Sciences (RBINS), Operational Directorate Natural Environment, Brussels, Belgium

The HYPERNETS project developed a new hyperspectral radiometer (HYPSTAR®) integrated in automated networks of water (WATERHYPERNET) and land (LANDHYPERNET) bidirectional reflectance measurements for satellite validation. In this paper, the feasibility of using LANDHYPERNET surface reflectance data for vicarious calibration of multispectral (Sentinel-2 and Landsat 8/9) and hyperspectral (PRISMA) satellites is studied. The pipeline to process bottom of atmosphere (BOA) surface reflectance HYPERNETS data to band-integrated top of atmosphere (TOA) reflectances and compare them to satellite observations is detailed. Two LANDHYPERNET sites are considered in this study: the Gobabeb HYPERNETS site in Namibia (GHNA) and Princess Elizabeth Base in Antarctica (PEAN). 36 near-simultaneous match-ups within 1 h are found where HYPERNETS and satellite data pass all quality checks. For the Gobabeb HYPERNETS site, agreement to within 5% is found with Sentinel-2 and Landsat 8/9. The differences with PRISMA are smaller than 10%. For the HYPERNETS Antarctica site, there are also a number of match-ups with good agreement to within 5% for Landsat 8/9. The majority show notable disagreement, i.e., HYPERNETS being over 10% different compared to satellite. This is due to small-scale irregularities in the wind-blown snow surface, and their shadows cast by the low Sun. A study comparing the HYPERNETS measurements against a bidirectional reflectance distribution function (BRDF) model is recommended. Overall, we confirm data from radiometrically stable HYPERNETS sites with sufficient spatial and angular homogeneity can successfully be used for vicarious calibration purposes.

KEYWORDS

HYPERNETS, hyperspectral, validation, surface reflectance, uncertainty, fiducial reference measurements, earth observation, vicarious calibration

1 Introduction

The HYPERNETS project (Ruddick et al., 2024b) has the overall aim to ensure that high quality *in situ* measurements are available to support the (VNIR/SWIR) optical Copernicus products. Therefore, a new autonomous hyperspectral spectroradiometer (HYPSTAR®) with instrument pointing capabilities, dedicated to land and water surface reflectance validation, was developed and deployed within the project (Kuusk et al., in prep). The

instrument is being deployed at 24 sites covering a range of water and land types and a range of climatic and logistic conditions, and spanning a range of atmosphere and Sun angle conditions as well as various surface types. At this stage of the project, many of the instruments have already been deployed and are acquiring data. These data are now publicly available as part of the WATERHYPERNET (Ruddick et al., 2024a) and LANDHYPERNET (Bialek et al., in prep) network respectively.

The primary goal of the HYPERNETS networks is the validation of satellite surface reflectance products. However, as an automated network of hyperspectral instruments covering various surface types, some HYPERNETS sites may also be ideally suited for the vicarious calibration of satellites. Vicarious calibration is defined by the Committee on Earth Observation Satellites (CEOS[1]) as 'techniques that make use of natural or artificial sites on the surface of the Earth for the post-launch calibration of sensors'. Similarly to surface validation techniques, this involves the near-coincident viewing of the same area of land/ocean and the comparison of observations from the ground-based sensor to the satellite sensor. However, in the case of vicarious calibration the comparison is made at the Top of Atmosphere (TOA) rather than at the bottom of atmosphere (BOA) and the surface reflectance acquired with the ground-based sensor must be propagated to TOA before comparisons can be made.

The RadCalNet network (Bouvet et al., 2019) has been successfully used for vicarious calibration (Zhao et al., 2021; Murakami et al., 2022) and radiometric assessments (Banks et al., 2017; Alhammoud et al., 2019; Jing et al., 2019) for years. RadCalNet is a Radiometric Calibration Network for Earth Observing Imagers Operating in the Visible to Shortwave Infrared Spectral Range which was set up by the RadCalNet Working Group under the umbrella of the CEOS Working Group on Calibration and Validation (WGCV) and the Infrared Visible Optical Sensors (IVOS). RadCalNet provides TOA reflectances, with associated uncertainties, at a 10 nm spectral sampling interval, in the spectral range from 380 nm to 2,500 nm and at 30 min intervals. There are five radiometric calibration instrumented sites located in the USA, France, China, and Namibia, which all have good spatial uniformity and typically stable atmospheric conditions in terms of aerosol and gas concentrations. RadCalNet is used systematically for vicarious calibration of many major satellites, including Sentinel-2 and Landsat 8/9, and could also become even more important for calibration of the NewSpace private space industry missions (either directly or indirectly due to improved calibration of, e.g., Sentinel-2).

Even though there are many similarities between the HYPERNETS and RadCalNet networks (they are both automated networks making uncertainty-quantified surface reflectance measurements), there are also some key differences. RadCalNet, being more tailored to TOA calibration, includes sky and direct Sun measurements, as well as ground instruments for the determination of the atmospheric properties that are used in the processing to TOA. HYPERNETS currently needs to rely on atmospheric data from external sources. On the other hand, the LANDHYPERNET data are provided at a number of different viewing geometries, whereas RadCalNet data are only publicly available at nadir. Additionally, even though RadCalNet provides hyperspectral data (sampled at 10 nm intervals), some sites are based on multispectral observations which are then spectrally interpolated. For HYPERNETS no spectral interpolation is necessary as the measurements themselves are hyperspectral. Finally, it is worth noting that one of the LANDHYPERNET sites used in this study (at Gobabeb, Namibia, described in Section 2.1.1) is planned to be added to the RadCalNet network in the near future.

This paper investigates the feasibility of using HYPERNETS data for vicarious calibration of satellites. Two LANDHYPERNET sites were chosen because of their temporal stability and spatial homogeneity at the scale of a satellite pixel footprint. Any near-simultaneous surface reflectance measurements to a Sentinel-2 A/B, Landsat 8/9 or PRISMA overpass were processed to TOA and compared to the satellite data. In addition to studying the potential for vicarious calibration, this also verifies the accuracy of these two HYPERNETS sites.

In Section 2, the different datasets that were used in this work are discussed, as well as how the data were downloaded and appropriate subsets selected. Section 3 details the methodology, including the processing to TOA (atmospheric propagation), the spectral integration with the spectral response function, and the uncertainty propagation. In Section 4, the results of the comparisons are shown for the three included sensors (Sentinel-2 MSI, Landsat 8/9 OLI and PRISMA HYC), and discussed in Section 5. Finally, the conclusions will be listed in Section 6.

2 Datasets used

2.1 HYPERNETS data

The two HYPERNETS sites used in this study are part of the LANDHYPERNET network. The HYPSTAR®-XR (eXtended Range) instruments deployed at each LANDHYPERNET site consist of a VNIR and a SWIR sensor which autonomously measure radiance and irradiance between 380 and 1680 nm at various viewing geometries. The field of view for the HYPSTAR®-XR instrument is 5° for radiance and 180° for irradiance. Data are collected on a central server for processing and quality control. The VNIR sensor spans 1,260 channels between 380 and 1,000 nm with a FWHM of 3 nm and the SWIR sensor has 220 channels between 1,000 and 1,680 nm with a FWHM of 10 nm. The LANDHYPERNET sequences include measurements at a range of different viewing zenith angles and viewing azimuth angles (see Bialek et al., in prep for further details). The HYPERNETS_PROCESSOR (De Vis et al., 2024) automatically processed all these data into various uncertainty-quantified products, including a L2A surface reflectance product. The surface reflectance ρ is the Hemispherical-Conical Reflectance Factor (HCRF) defined as in Eq. 1 below:

$$\rho = \pi \frac{L}{E} \tag{1}$$

where L is the directional upwelling radiance (with field of view of 5°) and E is the (hemispherical) downwelling irradiance. Further information on the details of the HYPERNETS processor and the associated uncertainty calculations can be found in De Vis et al.

1 http://calvalportal.ceos.org/cal/val-wiki/-/wiki/CalVal+Wiki/Vicarious+Calibration

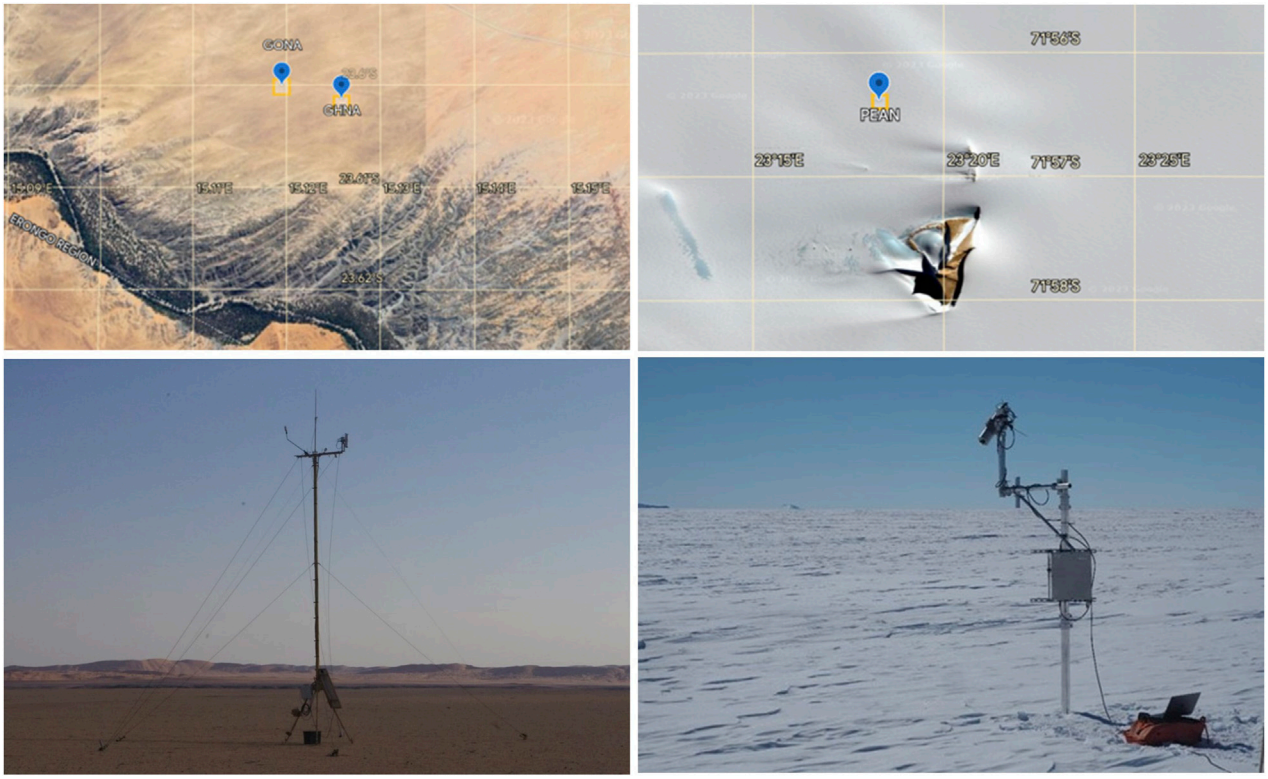


FIGURE 1
Left: Gobabeb HYPERNETS Namibia (GHNA) Site Location (top) and mast (bottom). Right: Princess Elisabeth Antarctica (PEAN) Site location (top) and mast during the second deployment (bottom).

(2024) or in the HYPERNETS_PROCESSOR documentation[2]. Further site-specific quality checks are performed, and the processed dataset for Gobabeb HYPERNETS Namibia has been made publicly available on Zenodo[3] (De Vis et al., 2023). Future processed data for all LANDHYPERNET sites will be made available on the LANDHYPERNET data portal (www.landhypernet.org.uk). In the following subsections, we will detail the two sites and how the HYPERNETS data were read in and quality screened.

2.1.1 GHNA

The Gobabeb HYPERNETS Namibia (GHNA) site has minimal daily variation in surface cover and weather conditions and is an ideal location for sustained, homogeneous measurements. The site is well characterised as it is very close to an instrument already recognised as a radiometric calibration site (GONA) as part of the RadCalNet network (Bialek et al., 2016).

The HYPERNETS site itself (23.60153° S, 15.12589° E) is 650 m from the RadCalNet site (Figure 1 top left), and is located on a gravel plain near a dry riverbed which separates it from the neighbouring dune sea. The daily average temperature is 27°C and there is low precipitation recorded at this location and atmospheric conditions are typically stable throughout the day. The HYPSTAR®-XR sensor was installed May 2022 at the top of a 9 m mast on an extended 1 m horizontal boom to minimise interruption of the field of view (Figure 1 bottom left). Data are collected every 30 min between 9a.m. and 6p.m. local time (UTC+02) between viewing zenith angles of 0 and 60°. No measurements were taken between 2p.m. and 3p.m. local time to avoid the hottest part of the day.

An example of the GHNA radiance, radiance uncertainty and reflectance is shown in Figure 2. In the bottom panel of this figure, we also show a time series plot showing the temporal stability of the GHNA surface. Only reflectances for one viewing geometry (vza = 5°, vaa = 98°) and wavelength (900 nm) are shown but results for other geometries and wavelengths are also stable. The colour coding shows that there are some differences between the reflectances at different times due to BRDF effects. We also note that the later sequences (14:00-16:00 UTC) show more variability due to the low zenith angle. The measurements used in this study are all in the 8:00-10:00 UTC time window, which are very stable. We also note that the shaded points in the plot show outliers which have effectively been removed by the HYPERNETS quality checks.

2.1.2 PEAN

The Belgian Scientific Polar Research Station at Princess Elizabeth Base in Antarctica (PEAN) hosted a HYPSTAR®-XR system between January and March 2022 and between December 2022 and February 2023. This instrument was installed on a mast approximately 2 m above the snow surface (bottom right panel of Figure 1) and operated 24 h per day in temperatures of −5°C to −10°C. The site is located at 71.94013° S, 23.30526° E (top right panel of Figure 1).

2 https://HYPERNETS-processor.readthedocs.io/en/latest/?badge=latest

3 https://doi.org/10.5281/zenodo.8039303

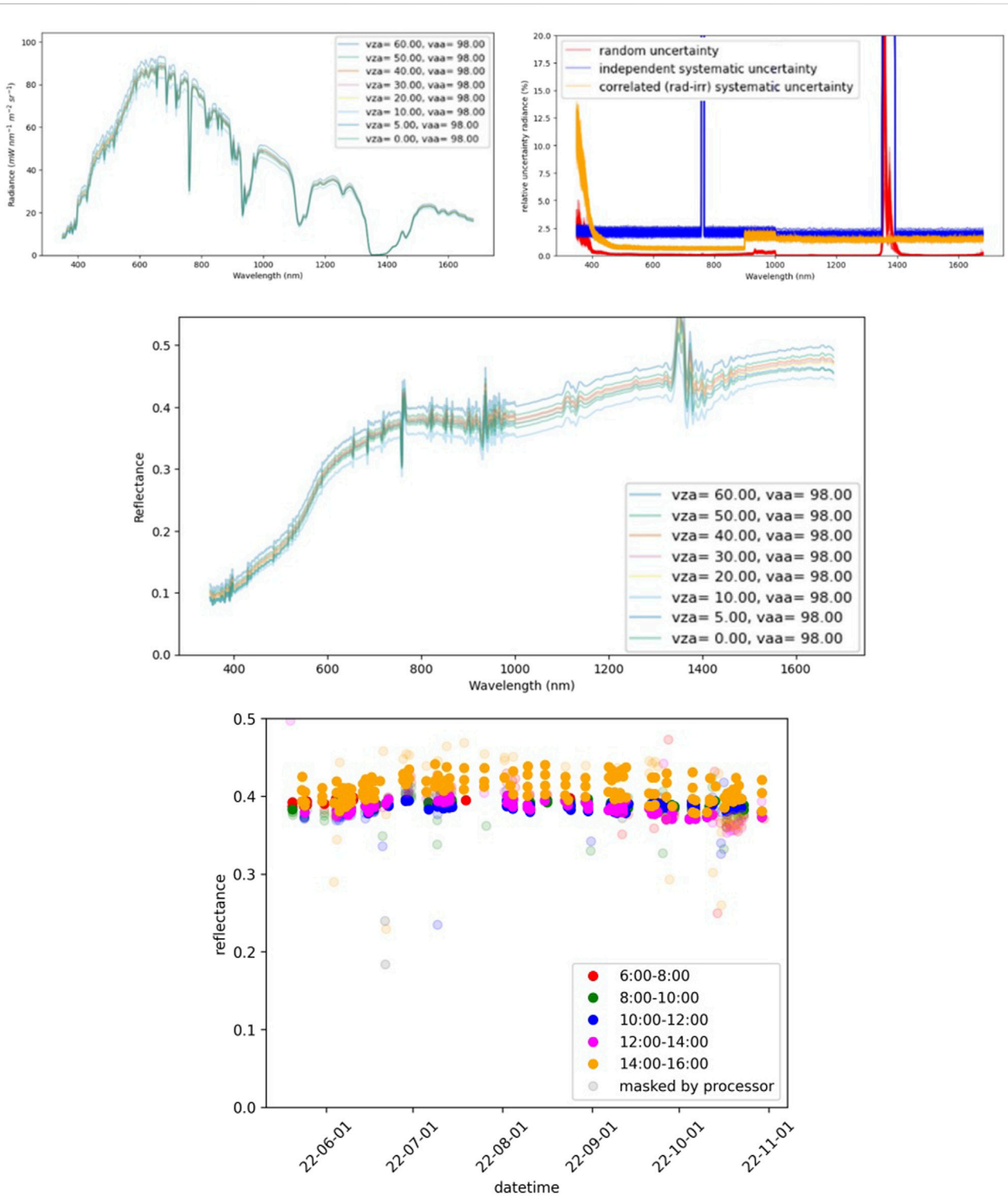


FIGURE 2
Plots produced by the HYPERNETS_PROCESSOR for the GHNA site. The radiances (top left), uncertainties (top right) and surface reflectances (centre) on the 2022-06-06 at 09:00 UTC all look sensible. Coloured lines show different viewing zenith (vza) and azimuth (vaa) angles. The bottom panel shows a time series of the 900 nm HYPERNETS measurement for vza = 5°, vaa = 98°, colour-coded by time of day (in UTC, shaded points have not passed the HYPERNETS quality checks). The GHNA site is very stable throughout the deployment.

The snow surface experiences some change throughout the deployment, mainly as a result of the accumulation of wind-blown snow, and the erosion of the snow surface by the wind. The surface was also affected by shadowing due to the low elevation of the Sun and uneven surface (bottom right panel of Figure 1). The deployment of the HYPSTAR instrument and mast also significantly disturbed the surface for the first deployment. To avoid the worst of the surface disturbance, we do not use the first 2 days after the deployment,

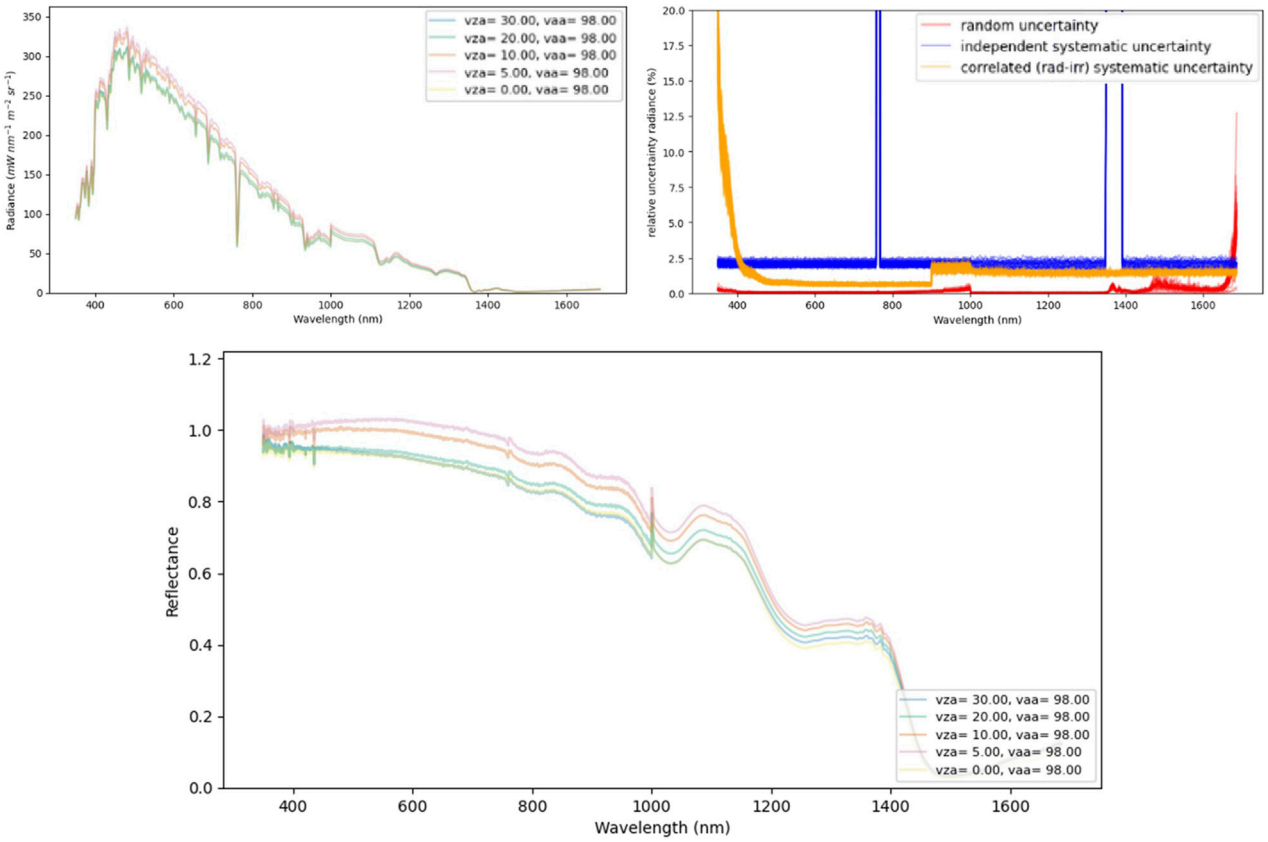


FIGURE 3
Plots produced by the HYPERNETS_PROCESSOR for the PEAN site on 2022-01-29 at 07:00 UTC. Coloured lines show different viewing zenith (vza) and azimuth (vaa) angles. The radiances (top left), uncertainties (top right) and surface reflectances (bottom) all look plausible.

to allow wind-blown snow to smooth the surface (which makes a notable difference). During the second deployment, the snow surface was undisturbed. The protocol does not measure in the direction of the access route (trodden snow - Figure 1).

2.1.3 Extracting surface reflectances

BOA surface reflectances at various geometries are available from the HYPERNETS L2A files. All surface reflectance products for GHNA and PEAN that are near simultaneous to a satellite overpass are first downloaded. Examples of the HYPERNETS products are shown in Figures 2, 3 for the GHNA and PEAN data respectively. Surface reflectance measured at the geometry best matching the satellite observation, as well as the associated random and systematic uncertainties, are extracted from the L2A HYPERNETS NetCDF files. For cases where the nearest viewing zenith angle is nadir, the HYPERNETS surface reflectances for the different azimuth angles are averaged.

2.2 Satellite data

2.2.1 Sentinel-2

The Sentinel-2 (S2) Copernicus mission acquires optical imagery at decametre spatial resolution (10 m–60 m) over land and coastal waters. It consists of two sun-synchronous (polar-orbiting) satellites (S2A and S2B), phased at 180° to each other. S2A and S2B launched in June 2015 and March 2017 respectively. The two satellites together have a revisit time of 5 days at the equator, with shorter revisit times towards the poles. The S2 satellites each carry a multispectral instrument (MSI), which has 13 bands in the visible, near infrared, and short wave infrared part of the spectrum. MSI is a pushbroom scanner with a swath width of 290 km. Radiometric uncertainties for the Sentinel-2 MSI L1C product are available from the Sentinel-2 Radiometric Uncertainty tool (Gorroño et al., 2017), which is part of the ESA SNAP toolbox. A detailed description of S2 together with an S2A performance review is available in (Gascon et al., 2017). A range of papers has investigated the absolute and relative calibration of S2A and S2B and found good radiometric performance to better than 3% for most bands (e.g., Lamquin et al., 2018; Revel et al., 2019).

2.2.2 Landsat 8/9

Landsat 8 (L8) and Landsat 9 (L9) are the two most recent (launched in February 2013 and September 2021 respectively) missions of the NASA/USGS Landsat program, which has been providing satellite imagery of the Earth for more than 50 years. L8 and L9 both have a payload comprised of two instruments, the Operational Land Imager (OLI) and the Thermal Infrared Sensor (TIRS). OLI provides decametre spatial resolution (15-30 m) imagery in the visible, near-infrared and shortwave infrared in

TABLE 1 Details of all the match-ups between the HYPERNETS data observations for GHNA with the three satellites, including time of measurements, and the viewing and solar zenith and azimuth (measured clockwise from north) angles from the satellite and HYPERNETS (separated by comma in same column).

Satellite	Site	HYPERNETS observation (UTC)	RadCalNet observation (UTC)	Satellite observation (UTC)	VZA satellite, HYP* (°)	VAA satellite, HYP* (°)	SZA satellite, HYP* (°)	SAA satellite, HYP* (°)
S2B	GHNA	2022-06-08 09:00:43	2022-06-08 09:00	2022-06-08 08:45:49	5.6, 5.0	268.5, 278.0	52.6, 53.9	29.8, 32.6
S2B	GHNA	2022-06-28 09:01:28	2022-06-28 09:00	2022-06-28 08:46:09	5.6, 5.0	268.7, 278.0	53.4, 54.7	30.5, 33.1
S2A	GHNA	2022-07-13 09:00:42	2022-07-13 09:00	2022-07-13 09:00:42	5.6, 5.0	269.7, 278.0	52.4, 53.8	32.1, 34.9
S2A	GHNA	2022-08-02 09:00:42		2022-08-02 08:46:11	5.5, 5.0	269.4, 278.0	49.1, 50.6	35.1, 38.1
S2A	GHNA	2022-09-11 09:01:28		2022-09-11 08:46:11	5.6, 5.0	269.6, 278.0	37.0, 38.8	43.8, 47.1
S2A	GHNA	2022-09-21 09:01:33		2022-09-21 08:46:41	5.5, 5.0	269.4, 278.0	33.5, 35.3	47.0, 50.4
S2B	GHNA	2022-09-26 09:01:31	2022-09-26 09:00	2022-09-26 08:47:19	5.5, 5.0	268.3, 278.0	31.8, 33.7	48.9, 52.4
S2B	GHNA	2022-10-06 09:09:27	2022-10-06 09:00	2022-10-06 08:48:29	5.5, 5.0	268.2, 278.0	28.5, 30.4	53.3, 56.6
S2A	GHNA	2022-10-11 09:02:59		2022-10-11 08:49:11	5.5, 5.0	269.4, 278.0	27.0, 28.7	55.8, 58.6
L9	GHNA	2022-06-06 09:00:44	2022-06-06 09:00	2022-06-06 08:56:41	0.7, 0.0	38.1, 83.0*	54.9, 53.7	34.8, 32.6
L9	GHNA	2022-06-22 09:00:40		2022-06-22 08:56:57	0.5, 0.0	−77.4, 83.0*	55.9, 54.8	34.9, 32.9
L8	GHNA	2022-06-30 09:01:28		2022-06-30 08:57:23	0.6, 0.0	26.7, 83.0*	55.8, 56.6	35.4, 33.3
L9	GHNA	2022-09-10 09:01:31	2022-09-10 09:00	2022-09-10 08:57:23	0.7, 0.0	44.4, 83.0*	40.7, 39.7	49.7, 46.7
L9	GHNA	2022-09-26 09:01:31	2022-09-26 09:00	2022-09-26 08:57:30	0.7, 0.0	37.8, 83.0*	35.4, 33.7	55.0, 52.3
L9	GHNA	2022-10-12 09:01:31		2022-10-12 08:57:33	0.7, 0.0	38.4, 83.0*	30.6, 28.6	62.5, 59.9
PRISMA	GHNA	2022-07-10 08:31:27	2022-07-10 08:30	2022-07-10 09:15:48	0.6, 0.0	125.2, 113.0*	52.9, 58.3	32.1, 40.8
PRISMA	GHNA	2022-08-02 09:00:42		2022-08-02 09:12:24	8.1, 10.0	101.2, 98.0	49.7, 50.8	36.3, 38.2
PRISMA	GHNA	2022-09-23 08:31:28		2022-09-23 09:09:04	16.2, 20.0	101.2, 98.0	33.6, 40.6	50.4, 59.6

[a]The different azimuths for this nadir observation are averaged.

nine multispectral bands and TIRS performs thermal imaging in two infrared bands. Both L8 and L9 are in a sun-synchronous orbit with a revisit time of 16 days (at the equator). OLI has a pushbroom scanner with a swath of 185 km. L8 and L9 have been shown to have good radiometric performance to within 3% in reflectance (Markham et al., 2014; Micijevic et al., 2022) and agreement to within 2.5% between L8 and S2 has been demonstrated (Barsi et al., 2018).

2.2.3 PRISMA

PRISMA is a hyperspectral mission by the Italian Space Agency which was launched in March 2019. PRISMA caries a payload of two sensors, the HYC (Hyperspectral Camera) module and the PAN (Panchromatic Camera) module. The HYC sensor is a prism spectrometer with two hyperspectral detectors. The visible/near infrared observed in 66 channels over the spectral interval of 400-1,010 nm, and the near-infrared/shortwave-infrared detector has 171 channels with a spectral interval of 920-2,505 nm. PRISMA is in a sun-synchronous orbit and the HYC has a spatial resolution of 30 m. It is a pushbroom scanner with a swath width of 30 km. The revisit time in nadir view is 29 days, but it is capable of off-nadir observations which can be targeted. The PRISMA radiometric calibration is not as good as S2 and L8, with typical deviations of 5%–7% up to 1800 nm, with a decrease in accuracy in the SWIR (Pignatti et al., 2022).

2.2.4 Identifying match-ups between HYPERNETS and satellite data

A Python tool was developed for identifying match-ups between the HYPERNETS and satellite data. The approach consisted of first downloading all satellite data that covered the GHNA and PEAN sites over the periods for which these sites were operational. The Sentinel-2 (S2) and Landsat 8/9 (L8/9) data were downloaded using the EODAG Python package[4], using the https://earthexplorer.usgs.gov/ repository for Landsat 8/9 and https://peps.cnes.fr/ for Sentinel-2. For PRISMA, data for the appropriate time periods have been manually downloaded from the PRISMA data portal in December 2022 (https://prisma.asi.it/js-cat-client-prisma-src/).

Once the satellite data are downloaded, the Python tool is used to identify the nearest data from the HYPERNETS database to each of the satellite images. Only cloud-free (as identified by HYPERNETS quality checks and/or the satellite masks) match-ups which are found within 1 h of a HYPERNETS measurement are included, with the nearest (in time) HYPERNETS measurement being chosen should there be greater than one HYPERNETS measurement in the time period. Once the match-up is identified, a 200 by 200 m cut-out is made from the satellite

4 https://eodag.readthedocs.io/en/stable/

10.3389/frsen.2024.1323998

TABLE 2 Details of all the match-ups between the HYPERNETS data observations for PEAN with Sentinel-2 and Landsat 8/9, including time of measurements, and the viewing and solar angles from the satellite and HYPERNETS (separated by comma in same column).

Satellite	Site	Hypernets observation (UTC)	Satellite observation (UTC)	VZA satellite, HYP* (°)	VAA satellite, HYP* (°)	SZA satellite, HYP* (°)	SAA satellite, HYP* (°)
S2B	PEAN	2022-12-26 07:29:51	2022-12-26 07:19:09	7.9, 10.0	298.0, 293.0	55.1, 53.7	54.6, 48.4
S2B	PEAN	2022-12-27 06:29:52	2022-12-27 06:49:39	9.9, 10.0	125.4, 128.0	57.2, 57.9	62.6, 65.4
S2B	PEAN	2022-12-30 06:59:57	2022-12-30 06:58:39	4.2, 5.0	112.8, 113.0	56.7, 54.2	60.4, 49.7
S2B	PEAN	2023-01-02 06:59:55	2023-01-02 07:09:19	1.8, 0.0	283.4, 278.0*	56.4, 56.2	58.0, 57.2
S2B	PEAN	2023-01-05 07:29:51	2023-01-05 07:18:59	7.8, 10.0	298.0, 293.0	56.1, 53.0	55.6, 41.1
L9	PEAN	2022-01-26 07:00:17	2022-01-26 07:01:37	4.4, 5.0	−55.6, −67.0	61.6, 61.4	61.2, 60.6
L9	PEAN	2022-01-28 07:00:18	2022-01-28 06:49:15	4.4, 5.0	−55.6, −67.0	56.5, 56.4	59.8, 59.7
L8	PEAN	2022-01-29 07:00:17	2022-01-29 06:42:56	8.0, 10.0	117.2, 113.0	63.7, 62.1	65.8, 60.1
L8	PEAN	2022-12-27 07:29:58	2022-12-27 07:07:55	8.5, 10.0	−68.0, −67.0	56.0, 54.0	58.1, 49.6
L9	PEAN	2022-12-30 07:29:57	2022-12-30 06:49:25	3.9, 5.0	127.1, 128.0	57.5, 55.8	63.2, 57.0
L8	PEAN	2023-01-05 06:59:45	2023-01-05 07:01:45	4.4, 5.0	−56.2, −52.0	57.3, 56.7	60.6, 58.2
L8	PEAN	2023-01-07 06:59:53	2023-01-07 06:49:23	3.9, 5.0	127.8, 128.0	58.5, 58.9	63.9, 65.7
L9	PEAN	2023-01-08 06:59:53	2023-01-08 06:43:15	7.9, 10.0	116.7, 113.0	59.0, 59.0	65.5, 65.6
L9	PEAN	2023-01-12 06:59:45	2023-01-12 07:07:29	8.5, 10.0	−68.0, −67.0	58.0, 58.0	59.4, 59.3
L9	PEAN	2023-01-13 06:59:51	2023-01-13 07:01:45	4.4, 5.0	−55.6, −52.0	58.6, 58.1	61.0, 58.9
L9	PEAN	2023-01-14 06:59:46	2023-01-14 06:55:29	0.6 0.0	−62.5, −67.0*	59.3, 58.3	62.7, 58.9
L9	PEAN	2023-01-16 06:29:43	2023-01-16 06:43:05	8.0, 10.0	117.2, 113.0	60.5 60.5	65.9, 66.1
L9	PEAN	2023-01-31 06:59:16	2023-01-31 06:49:26	3.9, 5.0	127.1, 128.0	63.7, 62.1	64.1, 58.3

[a]The different azimuths for this nadir observation are averaged.

image centred on the HYPERNETS site location and stored for further comparison (see Section 3.2).

Limiting the matchups to be within 1 h means that the surface and atmosphere will not vary much between the HYPERNETS and satellite observations. As discussed in Section 2.1.1, the GHNA surface is very temporally stable. This stability means that any uncertainty arising from temporal variation in the surface between the HYPERNETS and satellite measurement is negligible. The PEAN surface is less temporally stable than GHNA due to snow drift, but the temporal variability between the time of the HYPERNETS and the time of the satellite observation is still negligible. The atmospheric parameters are not known exactly (Section 2.3). The uncertainty we include on these parameters also covers any temporal variation they might undergo during 1 h (during clear sky conditions). Finally, the illumination conditions also change with time due to the changing solar zenith angle. We account for this by ensuring to use the solar geometry at the time of the satellite observation when propagating the HYPERNETS measurements to TOA (Section 3.1).

For the GHNA site, there are initially 10 match-ups found with S2 (over 4 months or so), that passed the automated quality checks of the HYPERNETS_PROCESSOR. Upon further manual quality checks, it was noticed in visual checks of the 'rgb' images of the HYPERNETS instrument that for one of the match-ups there was some low fog at the GHNA site. The clear sky quality checks also showed some evidence for this as the irradiance measurements were slightly reduced, but not enough to raise the HYPERNETS_PROCESSOR clear-sky quality flag. This S2 match-up was also an outlier in terms of the TOA reflectances. As such, this match-up has been manually identified as being of poor quality, and is removed from further analysis, reducing the total number of S2 match-ups over GHNA to 9. Additionally, there are six good quality match-ups with either L8 or L9 and three good quality match-ups with PRISMA within the 1-h match-up window. The total number of match-ups for the GHNA site in this study is thus 18.

For each of the GHNA match-ups, we also check whether RadCalNet data is available within 30 min from the GONA site (located 650 m away from GHNA). GONA data is available for five of the S2 match-ups, three of the L8/9 match-ups and one of the PRISMA match-ups. During the other match-ups, the RadCalNet instrument was not operational. For the nine match-ups with GONA data available, the GONA TOA reflectances are taken directly from the '.output' RadCalNet files. In Section 5.2, we discuss the differences in processing methods between RadCalNet and our own processing. In order to calculate biases between the RadCalNet and satellite data, a separate 200 m by 200 m cut-out is made from the satellite image centred on the GONA site location.

For PEAN, a total of 18 match-ups with valid HYPERNETS data are found in the 1 h window, five match-ups with S2, 13 with L8/9 (after removing outliers with cirrus clouds), and none for PRISMA. It is noted that there are two date (2022-12-27 and 2023-01-12) for which the PEAN site appears in two consecutive tiles for L8/9. In

these cases only the matchup where the tile start date is nearest to the HYPERNETS observation is used.

For the two sites combined, we are thus performing comparisons for 36 match-ups between HYPERNETS and the three satellites in this study. A full record of the match-ups is provided in Tables 1, 2 for GHNA and PEAN respectively, including time of observations and respective viewing and solar angles. Plots for each of the match-ups are given in Supplementary Material.

2.3 Atmospheric data

During the atmospheric propagation process (see Section 3.1), radiative transfer models will be run which take a number of atmospheric parameters as input (specifically aerosol optical depth at 550 nm τ_{AOD}, aerosol Angstrom component α, total column water vapour *TCWV*, ozone column density O_3 and pressure p).

For the 9 GHNA match-ups where GONA data is available, τ_{AOD}, α, *TCWV*, O_3, p and their uncertainties are all readily available from the RadCalNet GONA data. However, RadCalNet data are not available for all dates for which there are match-ups between GHNA and the satellites. Therefore, we also use ERA5 data (Hersbach et al., 2020) and AERONET (version 3) (Sinyuk et al., 2020) or CAMS (Inness et al., 2019) data. The ERA5 data are downloaded from the Climate Data Store[5] for *TCWV*, O_3 and p, with the parameter values taken from the ensemble mean and uncertainties from the ensemble spread. For τ_{AOD} and α, data for the AERONET Gobabeb site (23.562° S, 14.041° E) are downloaded from the AERONET website[6]. CAMS data are downloaded from the Atmospheric Data Hub[7] for dates in October 2022 when AERONET data are not available. Results for both types of atmospheric parameters (RadCalNet and ERA5+AERONET/CAMS) are available in Supplementary Figures S1, S2, S4, S5.

PEAN is not a RadCalNet site, and we instead use a combination of either AERONET or CAMS (when AERONET is not available) for τ_{AOD} and α and ERA5 for *TCWV*, O_3 and p data. The AERONET data are downloaded from the AERONET website for the Utsteinen site (71.950° S, 23.333° E), which is 1.6 km from the PEAN site. CAMS data are extracted when AERONET data are not available on a given day. For ERA5 (Hersbach et al., 2020), the reanalysis data for the appropriate days were downloaded from the Climate data store. We then extracted the data for the nearest grid point (72.00°S, 23.25° E) at the nearest time. The parameter values were taken from the ensemble mean and the uncertainties from the ensemble spread.

3 Methodology

3.1 Atmospheric propagation

Vicarious calibration of satellites relies on realistic atmospheric propagation of surface reflectances to TOA. In order to determine how much light reaches the TOA, it is necessary to solve the radiative transfer equation, taking into account all the interactions light has with all the atmospheric constituents and the surface (e.g., Rayleigh scattering, aerosol scattering, water vapour absorption, . . .). The best tools to solve this equation are numerical Radiative Transfer (RT) models. In this section we will provide details on how we performed the atmospheric propagation using the libRadtran RT software package (Emde et al., 2016). We use a metrological approach, where we start by defining a measurement function for the atmospheric propagation and then specify its input quantities in Section 3.1.2.

3.1.1 Atmospheric propagation measurement function

The libRadtran RT software package contains multiple solvers for the RT equation. For this work, we use the 1-dimensional pseudo-spherical DISORT solver, which has been shown to be fast and reliable (Emde et al., 2016). LibRadtran can be set up using a wide range of parameters to define the atmosphere, geometry and processing options. In order to automatically create input files and run the RT models, we have made a Python package, named FORTS, which among other things, is a wrapper for the libRadtran functionality.

One big advantage of this approach is that we can define a Python version of the measurement function for the atmospheric propagation:

$$L_{TOA} = f\left(\rho_{HYPERNETS}, \tau_{AOD}, \alpha, TCWV, O_3, p\right) + 0 \qquad (2)$$

Where L_{TOA} is the full-resolution TOA RT model for radiance, $\rho_{HYPERNETS}$ is the surface reflectance from the L2A HYPERNETS product, τ_{AOD} is the aerosol optical depth at 550 nm, α is the aerosol Angstrom component, *TCWV* is the total column water vapour, O_3 is the total column ozone and p is the surface pressure. The +0 term is added to indicate this measurement function is an approximation and that there will be errors associated with this approach (in line with the QA4EO guidelines[8]). There are many more parameters that need to be defined in order to fully describe the RT model. However, by defining the measurement function in this way, we can follow a metrological approach when propagating the uncertainties, and use $\rho_{HYPERNETS}$, τ_{AOD}, α, *TCWV*, O_3 and p as input quantities for which we have uncertainties. The input quantities listed in Eq. 2 are thus the only ones for which we intend to propagate uncertainties. All other inputs to the RT model are hidden within the measurement function f. A Python equivalent of this measurement function is implemented using the FORTS package, which enables numerical uncertainty propagation, as described in Section 3.3.

3.1.2 Atmospheric propagation parameters

In this section we describe the various inputs to the RT models. We will start with the input quantities for which we propagate uncertainties. $\rho_{HYPERNETS}$ is taken from the L2A HYPERNETS products for the viewing geometry that most closely matches the satellite geometry. The L2A products also give the random and systematic uncertainties as well as error-correlation matrices for

5 https://cds.climate.copernicus.eu/cdsapp\#!/dataset/reanalysis-era5-single-levels?tab=form

6 https://aeronet.gsfc.nasa.gov/

7 https://ads.atmosphere.copernicus.eu/cdsapp\#!/yourrequests?tab=form

8 https://qa4eo.org/

the surface reflectances. The atmospheric datasets used are described in Section 2.3, and also provide uncertainties, which are assumed to have a random error-correlation with respect to each-other.

The following parameters are also set up as part of the radiative transfer model:

- Standard atmosphere: As a starting point, the vertical profiles of all gasses are set to one of the standard atmospheres implemented in libRadtran (cut-off to the input pressure). We use "midlatitude_summer" as the standard atmosphere for our models.
- Solar spectrum: The TSIS solar spectrum at 1 nm resolution (0.1 nm sampling) from Coddington et al. (2021) is used as the extra-terrestrial irradiance. See end of Section 3.3 for a note on the TSIS uncertainties.
- Geometry: The solar zenith angle and solar azimuth angle are calculated for the time and date of the overpass using the PYSOLAR Python package. The viewing zenith and azimuth angle are known from the satellite files.
- Wavelength range: The wavelength range is chosen to be from 380–1,680 nm, based on the availability or HYPERNETS data.
- Wavelength resolution: The RT simulation is run at the resolution of the coarse REPTRAN (Gasteiger et al., 2014) molecular absorption parameterization, which corresponds to a bandwidth of 15 cm^{-1} when expressed in wavenumber. This corresponds to bandwidths of 0.23 nm in the UV part of the spectrum and increases up to 4 nm for the wavelength around 1700 nm. This is fine enough to get a good sampling of the spectral response function of the various satellites. The spectral sampling is set to 0.1 nm.
- Aerosol properties: Aerosol profiles and optical properties based on size distribution parameters and refractive indices are taken from the "desert" aerosols in the OPAC database (Hess et al., 1998).

The standard atmospheres and "desert" aerosols are thus set up first, and then modified by changing the total aerosol optical depth τ_{AOD}, aerosol Angstrom component α, total column water vapour $TCWV$, ozone column density, O_3 and surface pressure p. This allows us to fully define the atmosphere with only few parameters, although this does require assumptions/approximations (mainly that the vertical profiles are known and unchanging and that the aerosol type is represented by a desert aerosol).

3.2 Spectral integration

Before comparing the TOA radiances from the RT models to the satellite observations, they need to be spectrally integrated over the satellite Spectral Response Function (SRF). We use the MATHEO[9] Python package, which was developed at NPL for this type of spectral integration and other mathematical algorithms for EO. The Sentinel-2 and Landsat 8 SRFs are available through the PYSPECTRAL Python package[10]. The MATHEO package first interpolates the (ir)radiances from the RT model to the wavelengths of the SRF (if the SRF has the highest resolution) or interpolates the SRF to the RT wavelengths (if the RT has higher resolution). It then performs a numerical integration using the composite trapezoidal rule to get the band radiances.

Using MATHEO, it is possible to define an additional measurement function f_2:

$$L_{\text{band,HYPERNETS}} = f_2\left(L_{\text{TOA}}, \xi_{\text{SRF}}\right) + 0 \tag{3}$$

where $L_{\text{band, HYPERNETS}}$ are the band-integrated TOA radiances and L_{TOA} are the full resolution (0.1 nm sampling) TOA radiances from Eq. 2, and ξ_{SRF} is the spectral response function for the corresponding satellite band. We then also band-integrate the extra-terrestrial irradiance models E_{TOA} to the same bands:

$$E_{\text{band,HYPERNETS}} = f_2\left(cos\left(\theta_{sun}\right)E_{\text{TOA}}, \xi_{\text{SRF}}\right) + 0 \tag{4}$$

where $E_{\text{band, HYPERNETS}}$ are the band-integrated downwelling TOA irradiance, θ_{sun} is the solar zenith angle, E_{TOA} is the TSIS extraterrestrial irradiance (0.1 nm sampling) and ξ_{SRF} is the spectral response function for the corresponding satellite band.

The band-integrated radiances (from Eq. 3) and irradiances (from Eq. 4) can then be combined into reflectance (or rather the Hemispherical-directional Reflectance Factor):

$$\rho_{\text{band,HYPERNETS}} = \pi \frac{L_{\text{band,HYPERNETS}}}{E_{\text{band,HYPERNETS}}} \tag{5}$$

The resulting band reflectances can directly be compared to the satellite observations ρ_{sat}. The relative difference, also called bias, δ can be calculated as:

$$\delta = \frac{\rho_{\text{sat}}}{\rho_{\text{band,HYPERNETS}}} - 1 \tag{6}$$

where $\rho_{\text{band,HYPERNETS}}$ are the band-integrated TOA reflectances from Eq. 5 and ρ_{sat} are the observed TOA satellite reflectances.

3.3 Uncertainity propagation

To propagate uncertainties in this work, we use a Monte Carlo (MC) approach (see Supplement one to the "Guide to the expression of uncertainty in measurement", BIPM et al., 2008), implemented in the PUNPY Python package. The PUNPY module is part of the NPL-developed open-source CoMet toolkit (www.comet-toolkit.org). PUNPY is a Python software package to propagate random, structured and systematic uncertainties through a given measurement function. It has implementations for both the law of propagation of uncertainties and MC methods. For further info on PUNPY, we refer to De Vis & Hunt (in prep.) or the PUNPY ATBD[11]. By defining the atmospheric propagation as a measurement function which has an equivalent

9 https://matheo.readthedocs.io/en/latest/

10 https://pyspectral.readthedocs.io/en/master/installation.html\#the-spectral-response-data

11 https://punpy.readthedocs.io/en/latest/content/atbd.html

Python function, as done in Sections 3.1, 3.2, it is straightforward to propagate uncertainties through this measurement function. We use the MC approach here, because for a numerical measurement function such as ours, this requires much less computing power.

We use 100 MC steps to determine the uncertainties on the TOA band reflectances from the known uncertainties on the input quantities. The uncertainties are determined from the standard deviation in the spread between the 100 MC draws.

When propagating uncertainties in this way, we separate the uncertainties in three contributions:

- Random uncertainties on surface reflectance: These come directly from the L2A HYPERNETS file and are mainly due to noise in the measurements. The errors associated with these uncertainties are entirely uncorrelated. There is no correlation with respect to wavelength, nor with respect to different measurements.
- Systematic uncertainties on surface reflectance: These come directly from the L2A HYPERNETS file and are due to a range of different uncertainty contributions in the calibration of the HYPSTAR® instruments (such as uncertainties on the calibration distance, alignment, non-linearity, wavelength, lamp and panel). Within these L2A files, the errors associated with these uncertainties are entirely correlated between all different HYPERNETS measurements of that instrument (until the next calibration of that HYPSTAR® instrument). This means that the errors arising from this component will also be correlated between various match-ups for the same HYPERNETS site. This does not immediately affect the results in this report, but will become important when studying time-series of match-ups. With respect to wavelength, these systematic uncertainties on the surface reflectances have a custom error-correlation, provided as a separate error correlation matrix in the L2A files. This error-correlation will be propagated through the uncertainty propagation. The inclusion of this error-correlation information has a significant effect on the final band-integrated uncertainties, as we will show in Section 4.1.
- Atmospheric uncertainties: The uncertainties on the atmospheric parameters come from the RadCalNet, AERONET, ERA5 and CAMS datasets. RadCalNet has uncertainties available in all files, ERA5 has an ensemble that can be used to determine uncertainties, for AERONET an AOD uncertainty of 0.02 was used (Sinyuk et al., 2020), and for CAMS the AOD uncertainty was set to 10%. The atmospheric parameters are single values, and there is thus no error correlation with wavelength to define. The error-correlation between different match-ups will likely be random as the atmospheric parameters vary on much shorter timescales. We also assume the error-correlation between the different atmospheric parameters is random.

These three uncertainty components are propagated separately, and then combined in quadrature. It is important to propagate these uncertainties separately because for the systematic uncertainties, the covariance between the various wavelengths has to be taken into account. Taking into account the covariances will result in larger uncertainties on the band-integrated radiances compared to treating them as random (see Section 4.1).

For the SRF, no uncertainties are available from PYSPECTRAL and we thus neglect these uncertainties. The extra-terrestrial solar irradiances from Coddington et al. (2021) have (k = 1) uncertainties of 0.3% between 460 and 2,365 nm and 1.3% at wavelengths outside that range. However, any error in the irradiance will also affect the radiances in the same manner and will largely cancel out in the reflectances. We thus do not propagate these uncertainties to our TOA reflectances.

There are also uncertainties on the satellite data themselves. There are a range of random (e.g., noise), systematic (e.g., calibration errors) and structured (e.g., straylight) uncertainty components that affect the satellite data. However, a detailed analysis of these for each of the sensors under study is outside the scope of this work. Instead, we used a much simplified uncertainty budget with a random uncertainty component, defined as the standard deviation between the pixels in our cut-out, and a systematic uncertainty component. The errors for this systematic component are assumed to be fully correlated and the uncertainties are set to 3% for S2 and L8/9 and 6% for PRISMA (following radiometric performance assessments detailed in Section 2.2).

Finally, it is worth noting that there are a range of wavelength-dependent model errors (such as any errors present in the RT model itself, the aerosol model used, the vertical profiles assumed, . . .) for which we have not included an uncertainty contribution (as quantifying these is very difficult and outside the scope of the current study).

4 Results

4.1 Uncertainty budget

As shown in Figure 4, the GHNA and PEAN surfaces have quite different spectral shapes, and different proportions of the TOA reflectance originating in the atmosphere (light directly scattered by the atmosphere without ever interacting with the surface, i.e., the path reflectance). For each match-up, the random and systematic uncertainties on the HYPERNETS surface reflectances and the atmospheric uncertainty are propagated to the TOA HYPERNETS reflectances. These uncertainties are computed for both the full-resolution RT model for the HYPERNETS data as well as for the band integrated models, as is shown in Figure 4 for the GHNA Sentinel-2B match-up on 2022-06-08 and the PEAN Landsat 9 match-up on 2022-01-29. These results are representative for both Sentinel-2 and Landsat 8/9 match-ups. For both cases, the systematic uncertainties are the dominant source of uncertainty at most wavelengths, with smaller contributions for the random and atmospheric uncertainties. It is noted that in the absorption features, there is a greater contribution from the other uncertainties, notably the atmospheric uncertainties. These wavelengths are not suitable for vicarious calibration due to the low gas transmission, but are included here for completeness.

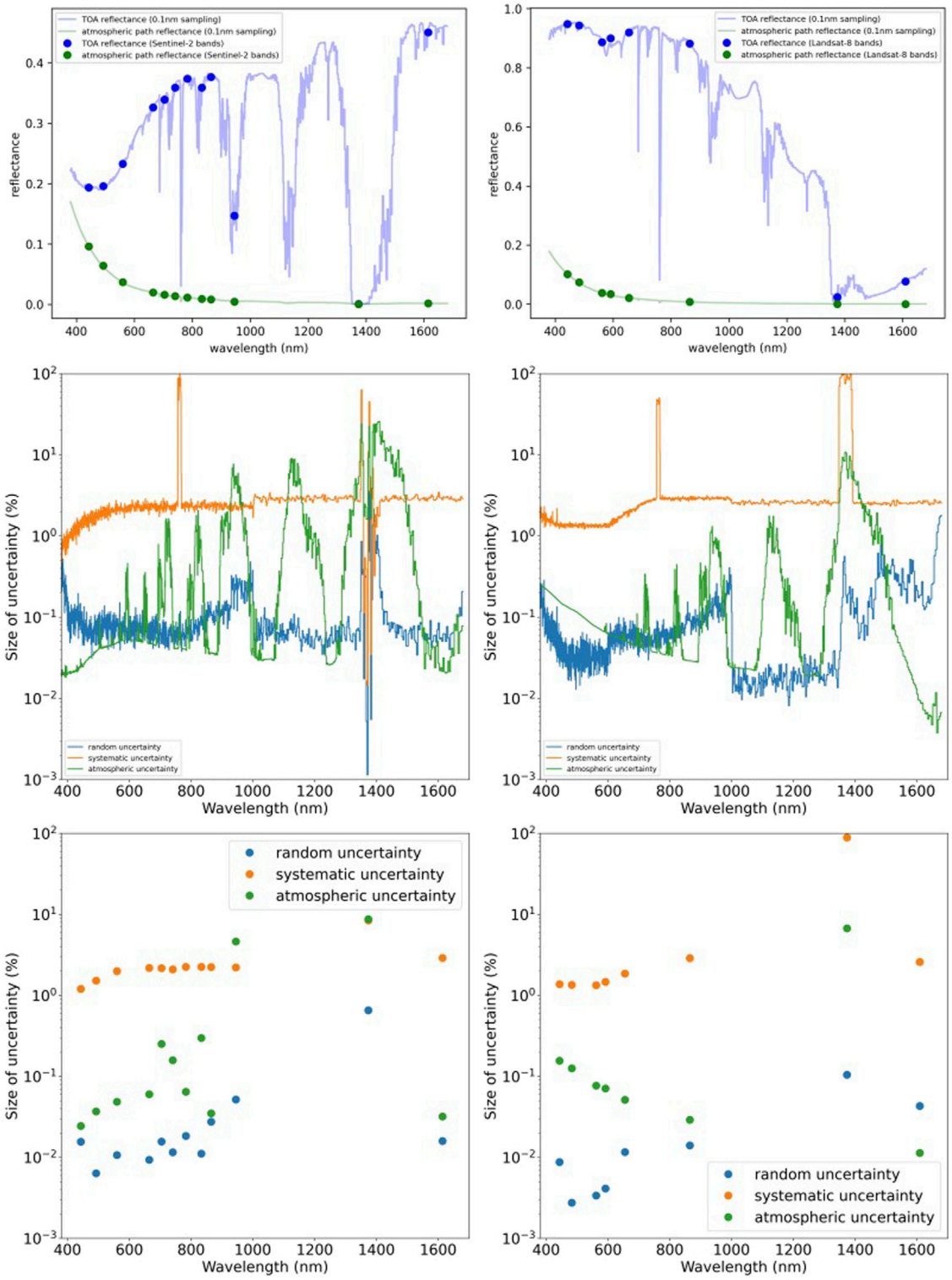


FIGURE 4
The top row shows the total TOA reflectance together with the atmospheric path reflectance for the GHNA Sentinel-2B match-up on 2022-06-08 (left) and the PEAN Landsat 9 match-up on 2022-01-29 (right). The different uncertainty components (in percent) of the full-resolution RT model are shown in the middle row and the band integrated TOA HYPERNETS uncertainties are shown in the bottom row. The systematic uncertainty dominates the uncertainty except in the atmospheric absorption features.

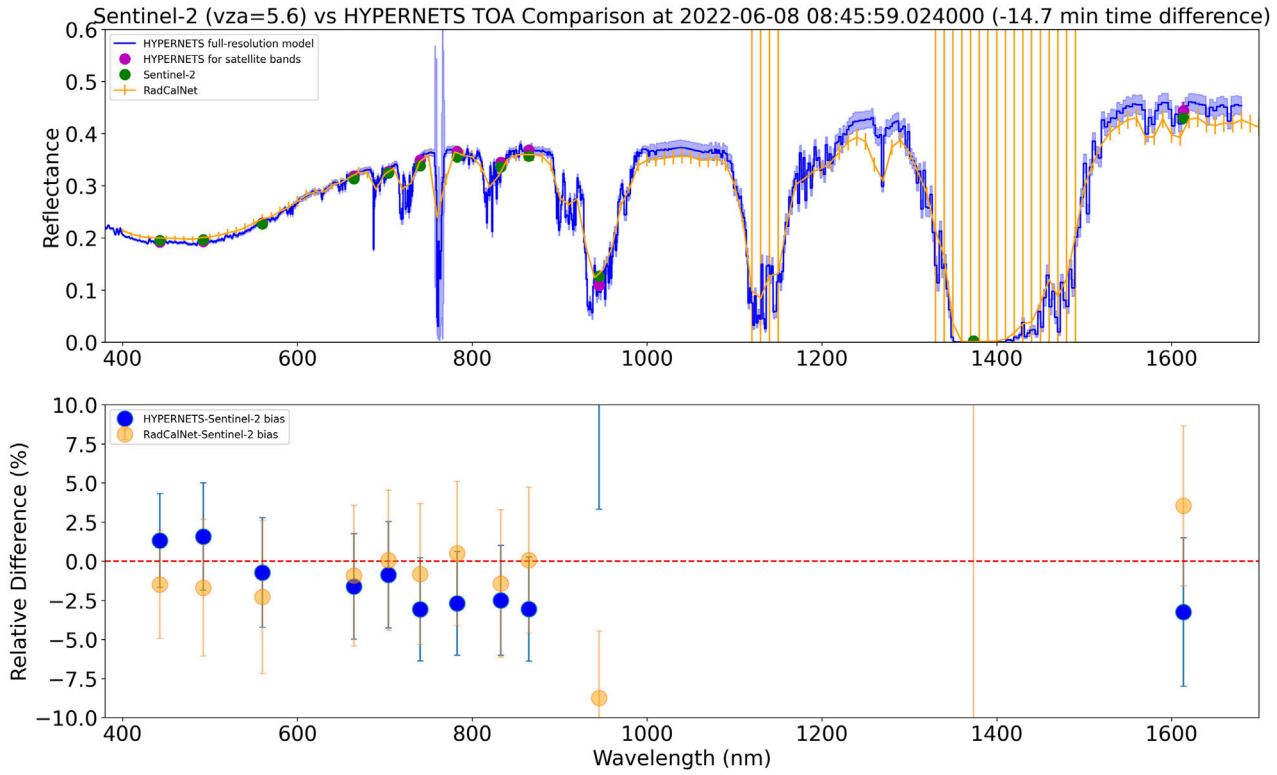


FIGURE 5
Top: The full-resolution and band-integrated HYPERNETS data compared to Sentinel-2 data and GONA RadCalNet data for the GHNA match-up on 2022-06-08. Shaded area represents uncertainties of HYPERNETS TOA reflectances. Bottom: The percentage difference bias δ between S2 data over GHNA and the band-integrated HYPERNETS data, and between the S2 data over GONA and the RadCalNet TOA reflectances. A few points are off the percentage graph due to the absolute values in reflectance being very small.

When the models are band integrated, it is seen for most bands that the systematic and atmospheric uncertainties stay more or less the same as for the full-resolution model. The random uncertainties are significantly reduced by the process of integrating over the spectral response function, following the expected behaviour of scaling with the inverse of the square root of the number of channels being integrated over. For both the Landsat 9 match-up and the Sentinel-2 match-up, the resulting band-integrated uncertainties are again dominated by the systematic uncertainty. For Landsat 9, the B9 band is dominated by the atmospheric uncertainty, as are the B09 and B10 bands for Sentinel-2, as these bands are found in absorption features. The systematic uncertainties (and thus the total uncertainties as well) on the TOA HYPERNETS reflectances are typically slightly larger than the systematic radiometric uncertainties of Sentinel-2 and Landsat 8/9, but smaller than the PRISMA uncertainties.

4.2 GHNA

4.2.1 Sentinel-2

Observations of the TOA reflectance from S2, and from the HYPERNETS data propagated to the TOA follow a similar pattern, which is nearly the same for each of the match-ups as the sites used are radiometrically stable. When RadCalNet data is available, the results between HYPERNETS and RadCalNet TOA reflectances also match well. An example for GHNA (match-up on 2022-06-08) is shown in Figure 5, and similar plots for the full record of match-ups are provided in Supplementary Figures S1–S3. GHNA has TOA reflectances of roughly 0.2 in the visible region, increasing to the region of 0.35–0.4 in the NIR and SWIR. Atmospheric absorption also affects both sets of reflectances, in particular in the 900 and 1,380 nm regions for both S2 and HYPERNETS (the B09 and B10 bands), in addition to the 1,100 nm region for HYPERNETS, as is seen in the top figure of Figure 5, for the 2022-06-08 match-up.

For each of the S2 bands, the bias δ (Eq. 6) between the Sentinel-2 and band integrated HYPERNETS data for each Sentinel-2 band is calculated and plotted in the figures as a percentage. For the 2022-06-08 match-up, shown in the bottom of Figure 5, this difference is less than 4% for much of the wavelength range, but is much greater for in the absorption features for bands B09 and B10, where the reflectances are lower due to the absorption. In absolute terms, the bias for B09 and B10 is fairly small. The uncertainties at $k = 1$ (68% confidence interval), are either consistent with zero (error bars cross zero), or fairly close to it for nearly all bands. For the absorption bands, our placeholder values for the uncertainties are likely underestimated. When inspecting the results for other match-ups in Supplementary Figures S1–S3, we find a similar pattern generally holds. Interestingly, a similar spectral pattern in the bias shows up

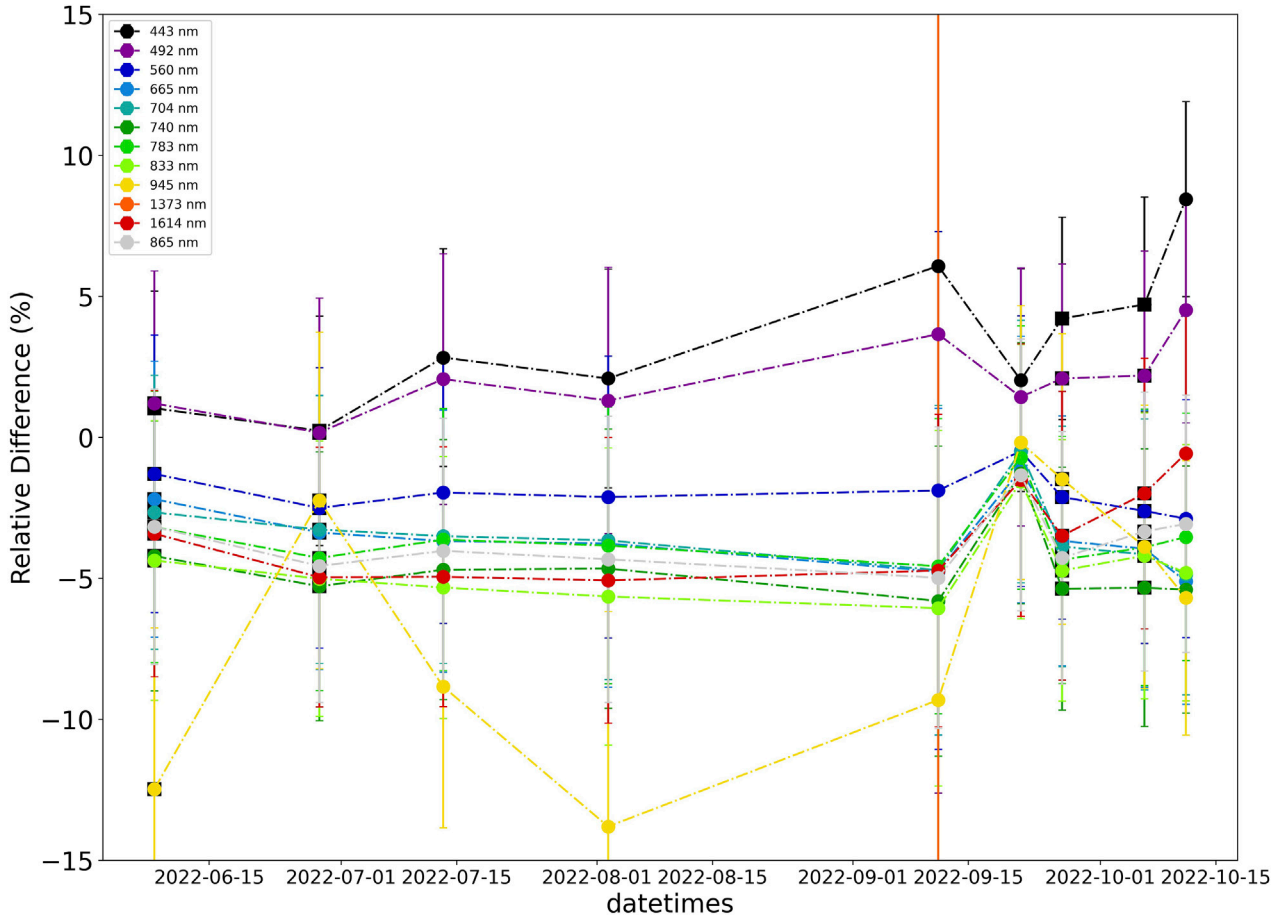


FIGURE 6
Time series of the percentage difference in S2 data and band-integrated HYPERNETS data for TOA reflectance for the 8 S2-HYPERNETS GHNA match-ups. To propagate the HYPERNETS data to TOA, atmospheric properties from ERA5 + AERONET/CAMS have been used for all match-ups for consistency. S2B results have a black square behind the circles, whereas S2A results are simply circles.

for most of the match-ups. We will further discuss these differences in Section 5.1.

When the HYPERNETS GHNA biases are compared to those for RadCalNet GONA, we find in some cases RadCalNet GONA has smaller biases, while in others HYPERNETS GHNA has smaller biases. More match-ups would be required to draw robust conclusions, but initial results indicate the GHNA site has similar performance to the GONA site. Further differences between GHNA and GONA are discussed in Section 5.2.

Next, we study whether there is any temporal variation within the nine match-ups between S2 and HYPERNETS. The percentage difference (bias) for all match-ups are plotted as a time series in Figure 6. For this plot, in the propagation of the HYPERNETS data to TOA we used atmospheric properties from ERA5 and AERONET/CAMS for all match-ups for consistency (as opposed to using RadCalNet atmospheric properties when available). For most dates for which there is a match-up between S2 and HYPERNETS at GHNA, each band has a similar bias, showing that the patterns between S2 and HYPERNETS are constant with time. This lack or trend means that during this short 4 month period, there is no notable degradation (which means there is no accumulation of dust, etc., on the HYPERNETS/HYPSTAR® instrument).

Longer time series would be required to draw any definitive conclusions or to infer anything about the degradation of the satellite. The constant offset also means that these differences are caused by an unchanging effect. This type of offset is likely caused by either a systematic difference in the atmospheric properties, in the calibration, or a systematic difference in how the measurements are made (e.g., misalignment). We note (see also Section 5.2) that the biases are smaller when the RadCalNet atmospheric properties are used.

4.2.2 Landsat 8/9

Landsat 8/9 observations of the TOA reflectances over GHNA, the propagated HYPERNETS data and the RadCalNet TOA data follow a similar pattern to the Sentinel-2 data in the previous section, as well as similar to each other. An example spectrum for the 2022-06-06 match-up and the associated biases are shown in Figure 7. For the 6 Landsat 8/9 match-ups, the percentage difference between them are generally less than 5%, for most of the Landsat 8/9 bands, as is seen in the bottom panel of Figure 7. The B9 band is the exception to this, as this is around the 1,380 nm absorption features, so the reflectances here are lower (resulting in larger percentage difference in spite of reasonable small absolute uncertainties), similar to band B09 and B10 for Sentinel-2. The results for the other match-ups,

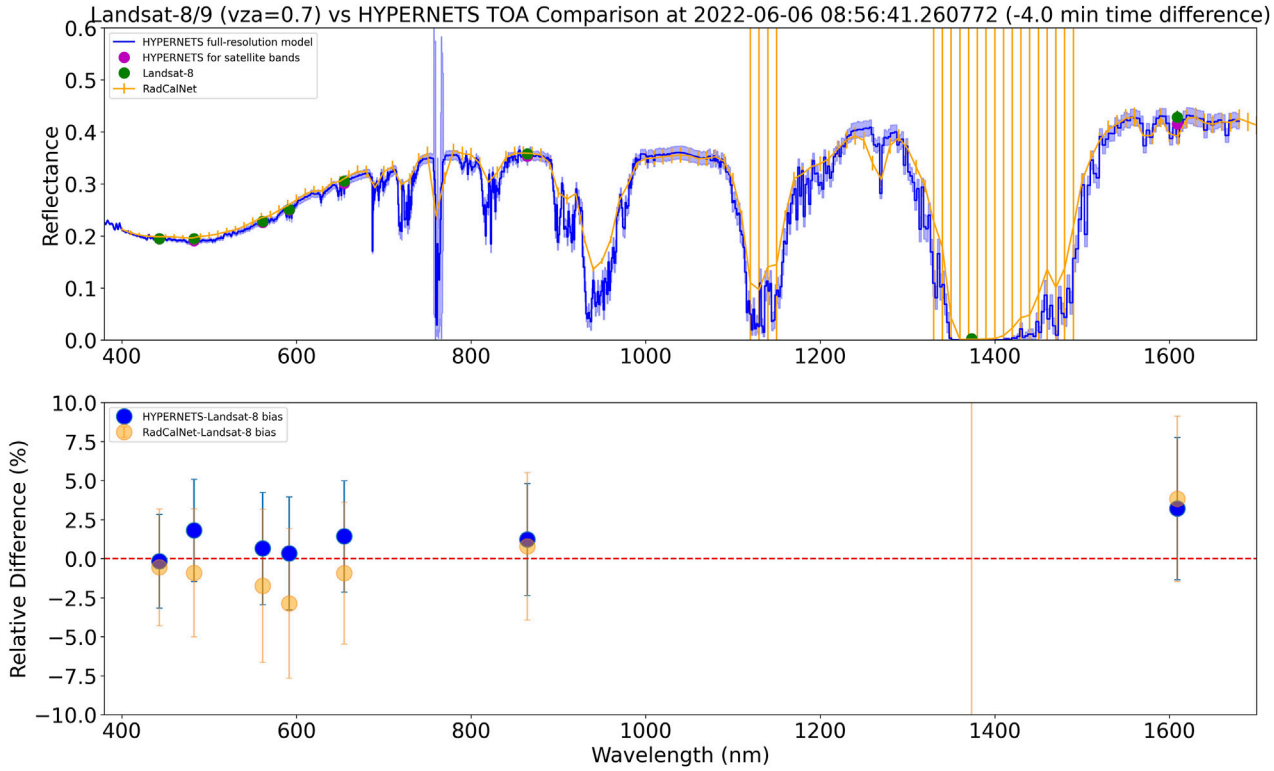


FIGURE 7
Top: TOA reflectances for the Landsat 9 data and the full-resolution and band-integrated HYPERNETS data, and RadCalNet data for the PEAN match-up on the 2022-06-06. Shaded area represents uncertainties of HYPERNETS TOA reflectances. Bottom: The bias δ (in percentage) between the Landsat 9 data over GHNA and the band-integrated HYPERNETS data, and between the Landsat 9 data over GONA and the RadCalNet TOA reflectances.

shown in Supplementary Figures S4–S6, are all quite similar, with biases below 5% for most bands, and consistent with zero within the uncertainties.

The timeseries for all six of the Landsat 8/9 observations is shown in Figure 8, and the differences for all bands apart from B9, mostly being below 5% for all dates. The exception to this is the October match-up is in the region of 8%-10% for B1 and B2. As for the Sentinel-2 match-ups, this increase in the size of the difference could be due to using CAMS data for the aerosol optical depth rather than AERONET data[12] (though this would not affect the larger wavelengths as much).

4.2.3 PRISMA

Finally, we compare the match-ups found between PRISMA and HYPERNETS TOA reflectances. We find good agreement for the GHNA site. Figure 9 shows an example of such a match-up, with differences smaller than 10% for most bands, consistent within the uncertainties. In the absorption features, the measurements still agree reasonably well, but the percentage differences are increased due to the low reflectances. Similar differences are found between RadCalNet and PRISMA. From inspecting the TOA reflectances in Figure 9, we see the RadCalNet GONA and HYPERNETS GHNA data agree better with each other than with PRISMA (when using the same atmospheric properties). The other two match-ups are shown in Supplementary Figure S7. Both these match-ups have somewhat smaller biases ($|\delta| < 7.5\%$) than the match-up in Figure 9.

4.3 PEAN

Next, we discuss the TOA reflectances and biases for the PEAN site. An example for the Landsat-8 match-up for 2022-01-29 is given is given in Figure 10 and figures for all other match-ups are provided in Supplementary Figures S8, S9. This particular match-up performs quite well with the visible and VNIR bands having biases below 5%, with all of them consistent with zero within their $k = 1$ uncertainties. The SWIR bands perform poorer, but still show small absolute biases.

Even though the example shown in Figure 10 shows that the PEAN site is promising for vicarious calibration, especially given how bright it is, when the other match-ups shown in Supplementary Figures S8, S9 are inspected we find the majority of them perform quite poorly. This is due to variability of the surface on the smaller scales sampled at the 20 cm footprint of the HYPSTAR instrument (due to the mast being only 2 m high). These differences will be further discussed in Section 5.3.

12 AERONET and CAMS were found to be consistent when both were available, though with larger uncertainties for CAMS.

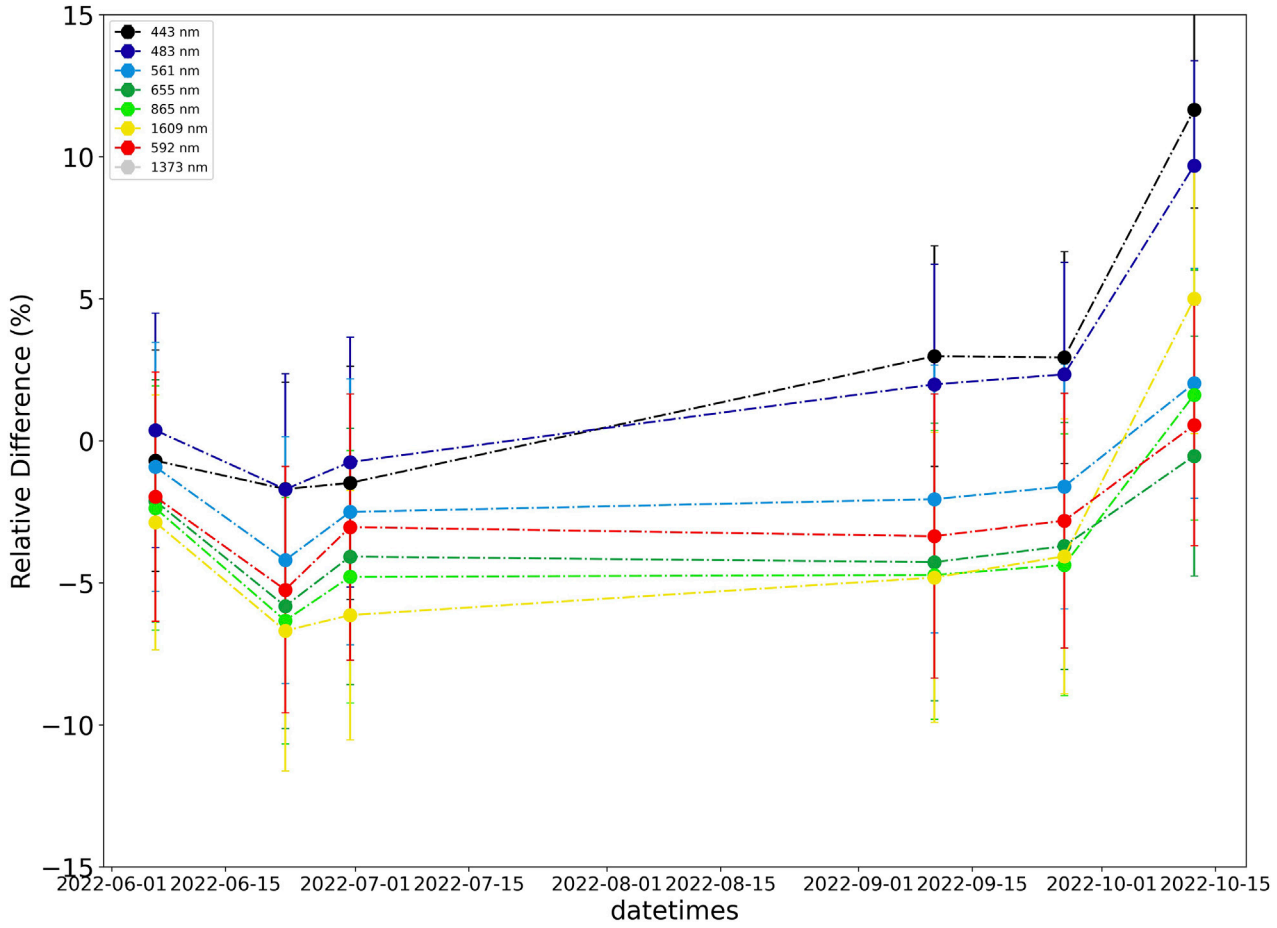


FIGURE 8
Timeseries of percentage difference for TOA reflectance for the band-integrated HYPERNETS data and Landsat 8/9 observations for the six match-ups at the GHNA sites. To propagate the HYPERNETS data to TOA, atmospheric properties from ERA5 + AERONET/CAMS have been used for all match-ups for consistency.

5 Discussions and caveats

5.1 GHNA caveats

The results for GHNA generally perform quite well for each of the different satellites. One potential issue that is revealed when comparing the biases for the different match-ups is that there is a similar spectral pattern, with positive biases (HYPERNETS reflectances smaller than satellite reflectances) in the blue part of the spectrum, but negative biases in the red-VNIR part of the spectrum. The observed biases are mostly within the propagated $k = 1$ uncertainties, so this is not problematic, but the systematic pattern could indicate an issue either with the calibration, or with the atmospheric correction (either uncertainties on atmospheric properties, or uncertainties in the RT model, see also the caveat about using HCRF in Section 5.4).

Another issue could be that some of the cables or feet holding up the mast, or the solar panel that is mounted on the west leg are in the field of view of the instrument (right panel of Figure 11). In principle the boom on top of the mast is long enough to avoid most of this, but there might be some contamination for certain viewing zenith geometries. In the left panel of Figure 11, we show a polar plot of the surface reflectances at 900 nm for each of the viewing geometries. There is reasonable smooth variability. In future work, we will fit BRDF models to these measurements and check if there are any outliers compared to these models due to contamination by the mast legs or solar panel. If any viewing geometries are affected, these will be masked and replaced by interpolated values. From inspecting the polar plots such as the one given in Figure 11 for each of the match-ups, there is no evidence that the viewing geometries used in the match-ups (indicated by magenta circle) are noticeably affected by this issue.

5.2 Differences between GHNA and GONA

Generally, as shown in Section 4, the agreement between the GHNA HYPERNETS results and GONA RadCalNet results is good ($|\delta| < 5\%$). In this section, we investigate the differences between the two sites in a bit more detail. In particular, we investigate variation between the GHNA and GONA surface, differences due to which atmospheric properties are used and differences due to the processing chains used. Each of these are explored for an

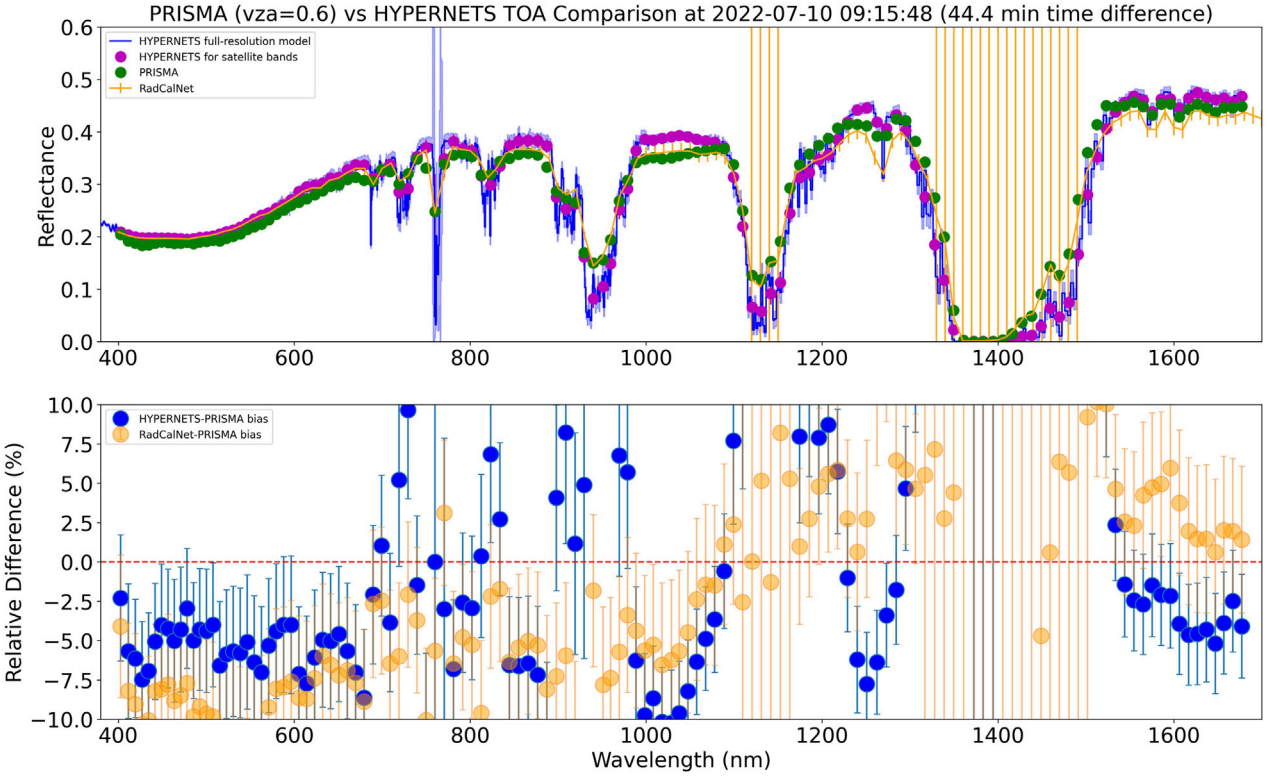


FIGURE 9
Top: PRISMA reflectances, together with the full-resolution RT model for GHNA, the band-integrated TOA HYPERNETS reflectances, and RadCalNet Reflectances on 2022-07-10. Bottom: The percentage differences between the PRISMA data over GHNA and the TOA HYPERNETS reflectances, and between the PRISMA data over GONA and the RadCalNet TOA reflectances.

example Sentinel-2 match-up on 2022-06-28, but similar differences apply for all match-ups.

In Figure 12, we show the percentage differences between the mean TOA reflectances in the GHNA 200 m by 200 m cutout and the GONA 200 m by 200 m cutout, as measured by Sentinel-2 on 2022-06-28. The differences are rather small ($<2\%$), indicating the surface at the two sites are consistent with each other.

Next we compare the differences due to either using RadCalNet atmospheric properties or those of ERA5 reanalysis data combined with AERONET. In Table 3, we show the extracted atmospheric properties for the Sentinel-2 overpass on 2022-06-28. In Figure 12 (bottom), we show the comparison results for processing the HYPERNETS data using the different sets of atmospheric properties. The results using RadCalNet atmospheric parameters show slightly smaller biases. In Supplementary Figures S1, S2, S4, S5, comparison plots for each Sentinel-2 and Landsat 8 matchup are available for both types of atmospheric parameters. Comparing these results for the different match-ups reveals that generally the performance is slightly better when using RadCalNet atmospheric parameters than when using ERA5+AERONET atmospheric parameters (with even more significant improvement when AERONET is not available and CAMS is used instead).

Finally, we also investigate differences due to the different processing chains. In order to do this, the RadCalNet processing chain has been applied to the GHNA hypernets data. This means that nadir data at GHNA was used, spectrally integrated to the RadCalNet SRF (triangular bands with a width of 10 nm) using MATHEO, and then processed to TOA by Brian Wenny at NASA (using same methodology as for other RadCalNet sites) using the RadCalNet atmospheric properties. In Figure 12, we show the differences due to these two processing chains for an example by the Sentinel-2 match-up on the 2022-06-28. For this specific example the HYPERNETS processed data results in the smallest biases, but there are other examples where the RadCalNet processing results in smaller biases.

5.3 PEAN variability

Whereas the example for PEAN discussed in Section 4.3 is promising, the additional results shown in the Supplementary Figures S8, S9 show a number of mismatches where the differences were larger than 10%. The differences are in many cases significantly larger than the uncertainties. This is likely because there is significant spatial variability in the PEAN surface reflectances at the scale of the footprint of the PEAN instrument, which is around 20 cm (field of view of 5° on top of 2 m mast). Even though at the spatial resolution observed by satellites ($\geq$10m) the PEAN surface is very homogeneous, there is significant small-scale variability causes by shadows, as can be seen in Figure 13 (see also

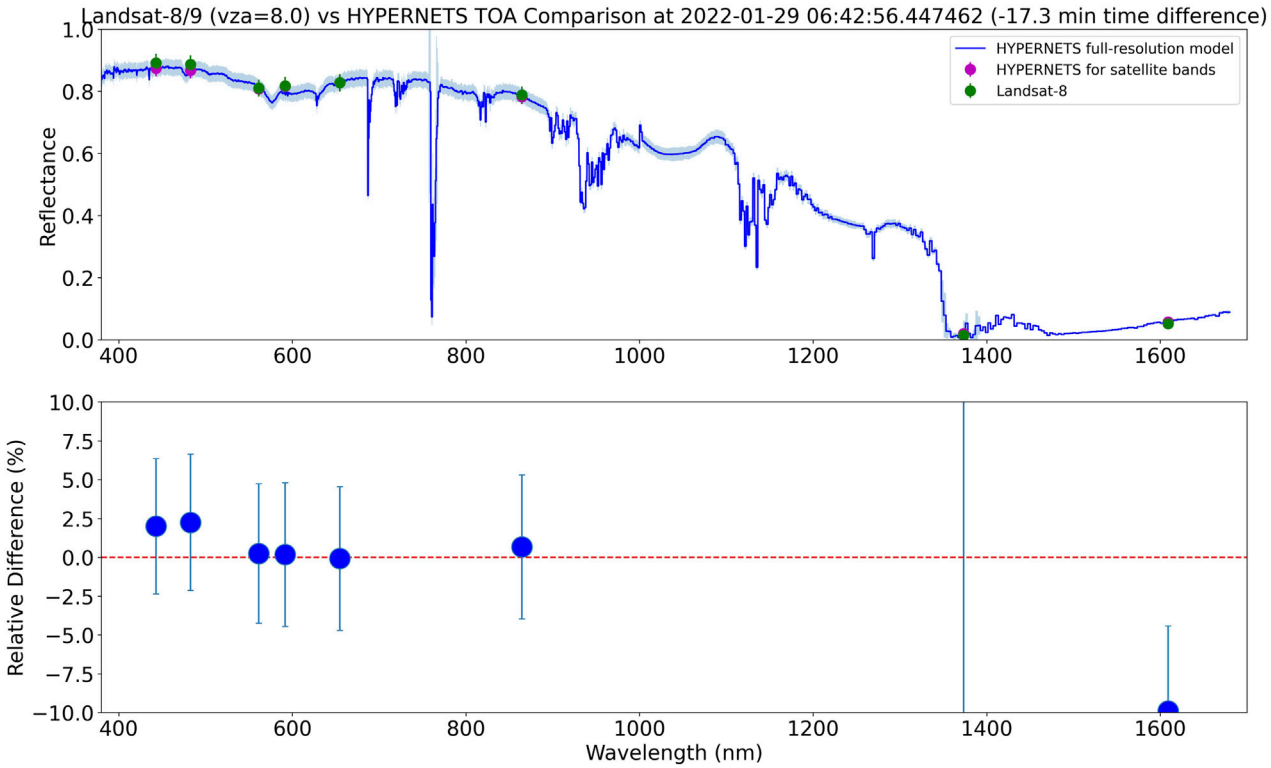


FIGURE 10
Top: TOA reflectances for the Landsat 8 data and the full-resolution and band-integrated HYPERNETS data for the PEAN match-up on 2022-01-29. Shaded area represents uncertainties of HYPERNETS TOA reflectances. Bottom: The bias δ (in percentage) between the Landsat 9 data and the band-integrated HYPERNETS data.

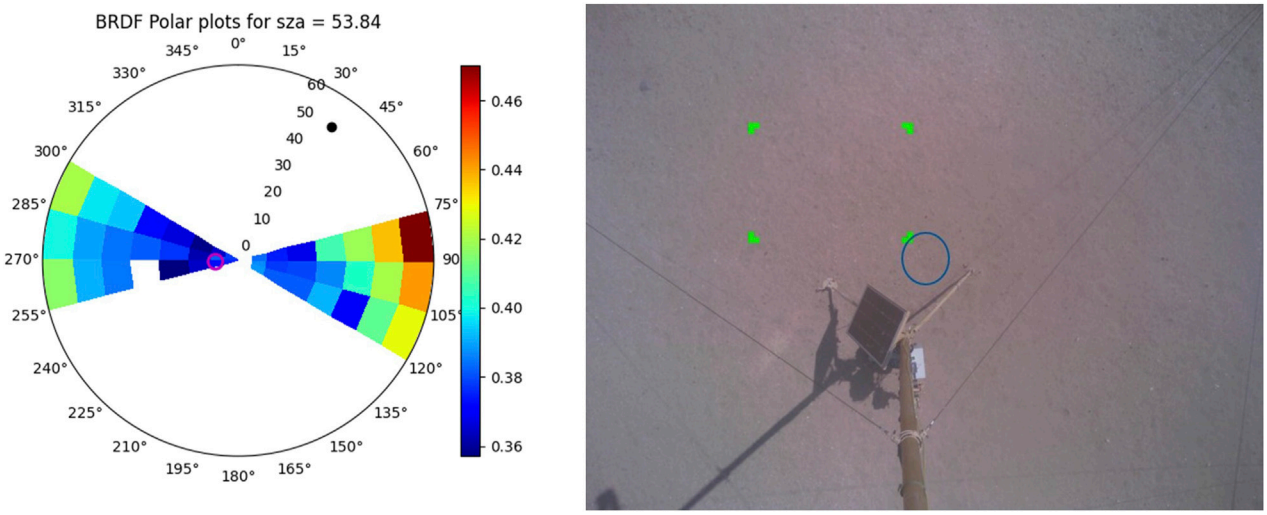


FIGURE 11
Left: Polar plot showing surface reflectances at 900 nm for different viewing geometries for the GHNA-S2 match-up on 2022-07-13. The solar position is shown as a black dot and satellite viewing geometry as a magenta circle. Right: RGB image taken by the instrument in nadir position. Green box shows the brightest area, which is used to calculate picture exposure. A rough approximation of the field of view is shown as a blue circle.

the PEAN surface in bottom right panel of Figure 1). This is the result of naturally occurring sastrugi, i.e., small-scale irregularities in the wind-blown snow surface, and their shadows cast by the low Sun.

The surface continuously changes due to deposition of wind-blown snow and the erosion of the snow surface. This results in an ever changing surface with different patches of shadow. This leads to many of the match-ups shown in Supplementary Figures S8,

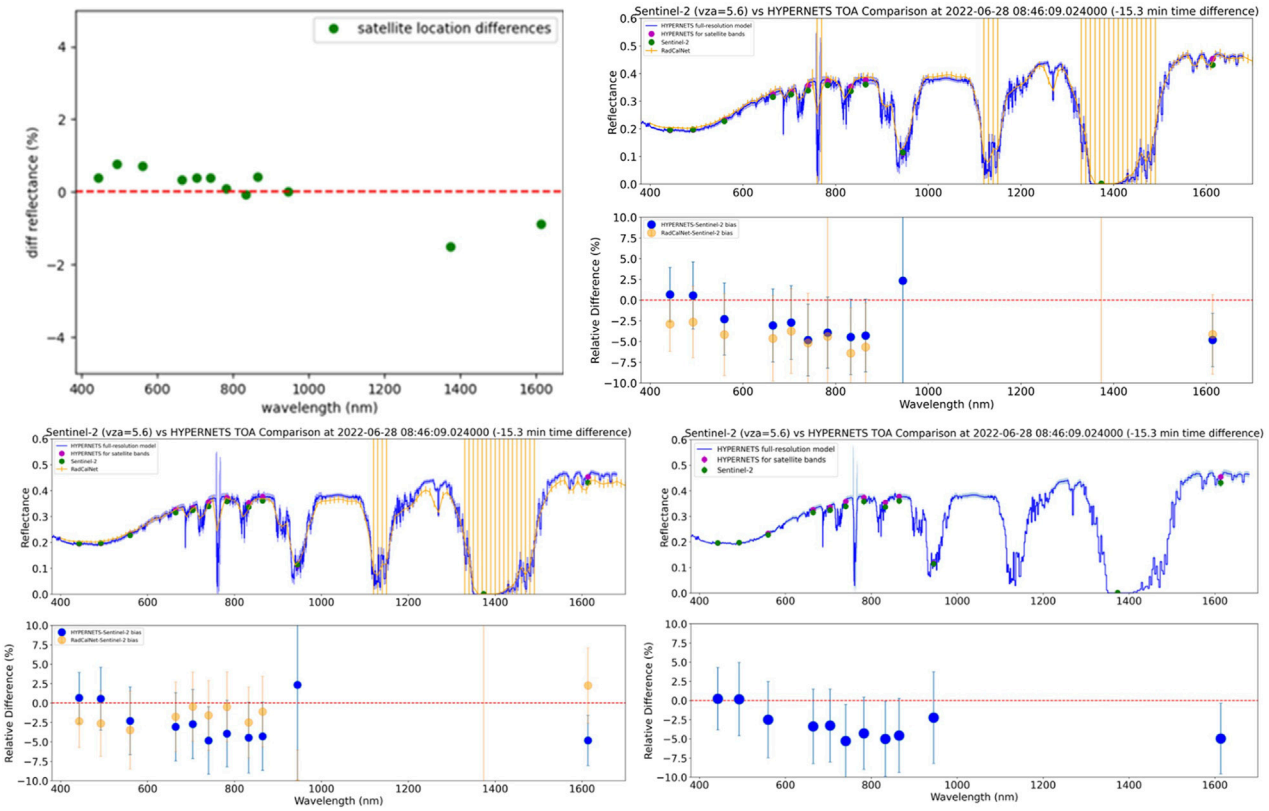


FIGURE 12
Top left: Differences between the mean Sentinel-2 reflectances on 2022-06-28 in the 200 m by 200 m cutout for GHNA and the cutout for GONA. Top right: Reflectance and bias results HYPERNETS GHNA data (blue), and GHNA (nadir) TOA reflectances processed using the RadCalNet processing chain (orange) for the match-up on 2022-06-28. Bottom: Plots showing the TOA reflecances and biases δ for the Sentinel-2 match-up on 2022-06-28 for the case where RadCalNet atmospheric data is used for the HYPERNETS processing (left) and the case where ERA5+AERONET atmospheric data is used for the HYPERNETS processing (right).

TABLE 3 Atmospheric properties from ERA5 reanalysis data combined with AERONET, compared to atmospheric properties from RadCalNet.

Parameter	ERA5 + AERONET	RadCalNet
AOD	0.045	0.062
Å	1.05	0.983
H2O (mm)	13.0	13.8
O3 (DU)	269	261
Pressure (hPa)	967	960

S9 being of poor quality, but some being good by coincidence. There are both match-ups where the HYPERNETS measurements are overestimated, as well as many where HYPERNETS is underestimated. It is worth pointing out that the small-scale shadowing is also present in the satellite images, yet it is not resolved as a result of the spatial resolution of the satellite sensors. One can thus not simply get rid of any shadow measurements and only use the brightest areas. A more correct approach would be to smooth the data. This cannot be done doing simple averaging over different viewing geometries, as significant BRDF effects are expected for this type of site (Ball et al., 2015). One solution could be to place the instrument significantly higher, though this is likely too challenging in the harsh Antarctic conditions. Another approach would be to fit BRDF models to understand the expected angular behaviour with respect to the observations, and using these BRDF models to smooth the data. Further investigation is required.

In Figure 14, some results are shown for PEAN during observations in cloudy conditions. In these diffuse illumination conditions, the surface variability is much smoother, indicating that the variability observed in Figure 13 indeed results from shadows, and is not caused by instrumental effects. We have discarded any match-ups with cloudy conditions, using the cloud masks of the satellite data to identify them and verifying the presence of clouds by manually inspecting the HYPERNETS sky images. We note that using the HYPERNETS irradiances only, it is hard to identify the cloudy conditions, as the surface is so bright (e.g., multiple surface-atmosphere scattering) and the solar zenith angle is so high (e.g., diffuse cloud scattering combined with cosine response) that the irradiance measurements are sometimes brighter than a clear sky model (Figure 14 right), and as a result the automated HYPERNETS quality checks do not mask these measurements.

One other problem is that due to the low Sun, the irradiance measurements are very sensitive to the allignment of the instrument.



FIGURE 13
Left: Polar plot showing surface reflectances at 900 nm for different viewing geometries for the PEAN-L8 match-up on 2023-01-07. The solar position is shown as a black dot and satellite viewing geometry as a magenta circle. Middle: RGB image taken by the instrument in nadir position during first deployment. Green box shows the brightest area, which is used to calculate picture exposure. Right: RGB image taken by the instrument in nadir position during second deployment.

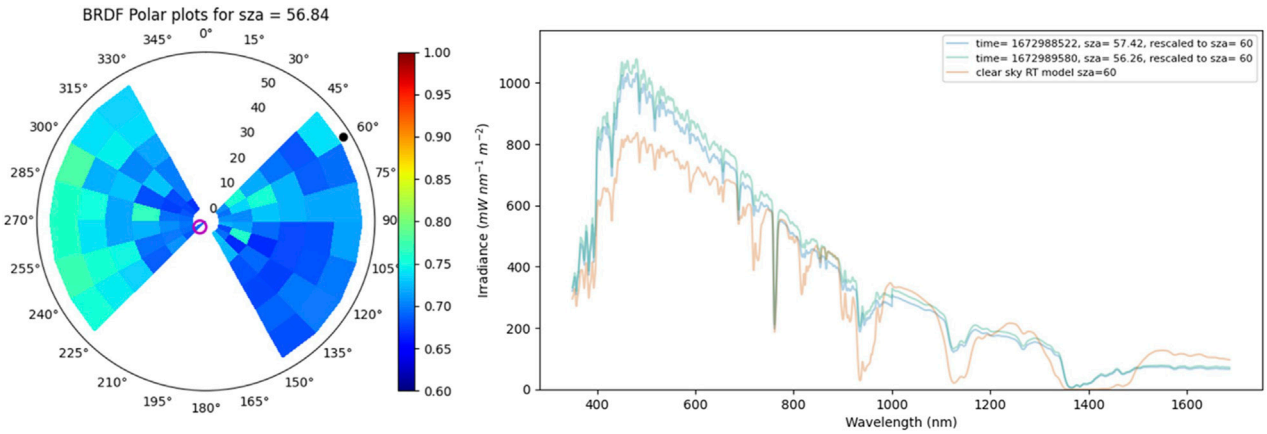


FIGURE 14
Left: Polar plot showing surface reflectances at 900 nm for different viewing geometries for the PEAN-L8 match-up on 2023-01-06. The solar position is shown as a black dot and satellite viewing geometry as a magenta circle. Right: plot produced by the HYPERNETS_PROCESSOR which shows its internal quality check comparing the HYPERNETS BOA irradiance measurements to a rudimentary clear sky model. Note that this match-up is not included in Table 2 as it was discarded based on the cloud mask.

Another caveat is that the current methodology for propagating the surface reflectances to TOA is somewhat limited when it comes to modelling PEAN. Due to its high reflectance and BRDF model, there are some combinations of angles that have a directional surface reflectances above 1. While this is not physically impossible, it is currently not possible to use surface reflectances above one in the RT models used in our method.

5.4 General caveats and future work

Even though the biases shown in the previous sections are generally within the uncertainties, there are some bands (especially in the additional examples in the Supplementary Material) for which the biases are significantly larger than the uncertainties. One caveat to this is that our uncertainty budgets are not complete, as we are not including uncertainties on some inputs like the aerosol type, vertical profiles, spatial heterogeneity (at the scale of ~ 1m footprint for GHNA and ~ 0.2m for PEAN) *etc.* The satellite uncertainties could also be improved beyond the simplified random and systematic components we use (e.g., from the S2 RUT tool). Additionally, the HYPERNETS uncertainties not yet include uncertainties accounting for temperature corrections, straylight (placeholder values are used instead) and instrument levelling, which should be added in the future.

As discussed in previous sections, fitting BRDF models would allow us to identify outliers due to contamination and to smooth over small-scale surface variability. More generally, this would also allow us to do a detailed interpolation between the various viewing angles (as opposed to taking the nearest set of angles available from the HYPERNETS measurements), and extend to angles not currently sampled within the measurement sequence. We thus

recommend the use of BRDF models in future efforts on vicarious calibration using HYPERNETS data.

In Section 5.2, we discussed the better performance of using RadCalNet GONA atmospheric properties for use in the GHNA processing (which is possible as the sites are only 650 m from each other) as opposed to using reanalysis data such as that from ERA5 and CAMS (AERONET is used for aerosol optical depth when available which is less different from RadCalNet properties). The RadCalNet atmospheric properties use a combination of *in situ* measurments using a weather station, combined with direct solar measurements to fit the absorption. When the GONA site is down for any reason, no GONA atmospheric data is available and this currently means that GHNA needs to use less reliable reanalysis atmospheric data. However the HYPERNETS measurement sequence does include irradiance measurements, which could also be used for fitting the atmospheric absorption (though both diffuse and direct solar irradiance contributions would need to be taken into account in the fitting). Future studies investigating the use of the HYPERNETS irradiance measurement in combination with weather station data are recommended to derive self-consistent atmospheric properties for GHNA. These atmospheric properties are expected to be of better quality then reanalysis data and will be of most benefit when RadCalNet GONA is not operational for any reason (and thus no GONA atmospheric properties are available). This will also be of significant benefit for the inclusion of the GHNA site into RadCalNet (as GHNA data cannot be included into RadCalNet at times when no reliable atmospheric data is available).

As discussed in Section 2.1, HYPERNETS provides reflectance as Hemispherical-Conical Reflectance Factor (HCRF) instead of the Bi-directional Reflectance Factor (BRF). The BRF is a purely theoretical quantity and cannot be measured directly in the field. However in the radiative transfer simulations, the reflectance is typically expected as BRF. This introduces a small error in the calculated TOA reflectances (few percent for blue wavelengths, reducing for higher wavelengths and negligible for SWIR). This could explain why in our results we typically see more positive biases in the blue bands than for higher wavelengths. In future work we will correct for the HCRF-BRF differences (see, e.g., Schunke et al., 2023).

In this work we have shown that the biases between the HYPERNETS data and Sentinel-2 and Landsat-8/9 are within 5%, and consistent with the uncertainties. Whereas that is a good result that shows the good performance of the HYPERNETS network, this is not a significant improvement (nor is it worse) with respect to previous studies using RadCalNet (Banks et al., 2017; Alhammoud et al., 2019; Jing et al., 2019; Zhao et al., 2021; Murakami et al., 2022). There are a number of areas where further improvement is possible. Some caveats were already discussed above. Another way to improve the study would be to use multiple years of data, over multiple calibration periods, and including various sites. This study is planned in a few years when more data is available. By including more data, it will be possible to average out over any random effects (including random effects that might result in different errors for each calibration period) and to reveal drifts in the calibration.

Another significant improvement would be to make the HYPERNETS data more representative of the satellite measurement. This would mean to better correct for any temporal, spatial and angular differences between the HYPERNETS measurements and the satellite. There are no temporal differences expected in the surface, and changes in illumination are already accounted for, but some improvement could be made from including atmospheric data sampled at higher temporal resolution. Obtaining high resolution imagery over the HYPERNETS sites (either UAV measurements or commercial metre-scale observations from space) would help quantify and correct any spatial differences. Fitting BRDF models would allows to address the angular differences.

6 Conclusion

We have compared a total of 36 satellite images (from Sentinel-2, Landsat 8/9 and PRISMA) to near-simultaneous TOA reflectances for which surface measurements were acquired as part of the HYPERNETS network and processed to TOA. For the GHNA HYPERNETS site, generally good agreement is found, with comparisons with Landsat 8/9 and Sentinel-2 performing well with typical differences smaller than 5%. This performance is similar to that of the RadCalNet GONA site. Comparisons with PRISMA show slightly bigger differences, with typical differences between 0% and 10%. A study comparing the GHNA measurements against a BRDF model and fitting HYPERNETS atmospheric properties is recommended.

The PEAN site also shows good potential for vicarious calibration, with a few match-ups with good agreement to within 5% for Landsat 8/9. However for the majority of match-ups for PEAN the agreement is notable less good (worse than 10%). This is likely due to small-scale variability caused by a wind-blown uneven surface affected by small-scale shadowing. Fitting BRDF models and using these to smooth the data is expected to improve the results.

On the basis on the results presented here the Gobabeb/HYPERNETS site is confirmed as of high interest for vicarious calibration within RadCalNet. The location is already known to be radiometrically stable with good spatial homogeneity and frequent clear sky conditions and there is already a RadCalNet site nearby based on a multispectral radiometer. The added value of HYPERNETS is that the use of a hyperspectral radiometer (with relatively fine spectral resolution, 3 nm FWHM) avoids the need for spectral interpolation/fitting for bands that are not well-covered by the multispectral instrument because wide and/or with wavelengths simply not measured multispectrally. This is particularly important for the new generation of hyperspectral instruments such as ENMAP, PRISMA, EMIT, PACE, SBG, CHIME and GLIMR.

The PEAN/HYPERNETS site, which was originally intended only for validation purposes is revealed here to be relevant also as a new vicarious calibration site, which may be included in RadCalNet. The added value of this site, compared to existing RadCalnet sites, is that: the site has very different surface reflectance from existing sites (very bright for most of the VNIR), ensures that the HYPSTAR instrument is tested in both very hot (Gobabeb) and very cold (Antarctica) conditions and has potentially a large number of match-ups due to the high latitude and long photoperiod in the Southern hemisphere summer. This site also has often a clear atmosphere and benefits from intensive atmospheric measurements, which may help improve the modelling to TOA reflectance. The challenges of this site include the modelling of atmospheric radiative transfer at high Sun zenith angle and the complicated BRDF effects associated with terrain shadowing at high

Sun zenith angle. The latter requires extra research, but the multi-angle high frequency HYPERNETS data are ideally suited for improving the understanding of BRDF of snow surfaces and hence potentially the remote sensing of snow properties.

Data availability statement

The raw data supporting the conclusion of this article will be made available by the authors, without undue reservation.

Author contributions

PD: Formal Analysis, Methodology, Writing–original draft, Conceptualization, Investigation, Software, Visualization. AH: Formal Analysis, Visualization, Writing–review and editing. QV: Investigation, Writing–review and editing. AB: Conceptualization, Funding acquisition, Investigation, Project administration, Writing–review and editing. HM: Software, Writing–review and editing. MS: Investigation, Writing–review and editing. KR: Funding acquisition, Project administration, Writing–review and editing.

Funding

The author(s) declare that financial support was received for the research, authorship, and/or publication of this article. The HYPERNETS project is funded by the European Union's Horizon 2020 research and innovation program under grant agreement No 775983 and by the HYPERNET-POP project funded by the European Space Agency (contract n° 4000139081/22/I-EF). This work (and the CoMet toolkit used within) has also received funding from the ESA-funded Instrument Data quality Evaluation and Assessment Service - Quality Assurance for Earth Observation (IDEAS-QA4EO) contract funded by ESA-ESRIN (n. 4000128960/19/I-NS) and the UK's Department for Business, Energy and Industrial Strategy's (BEIS) National Measurement System (NMS) programme.

Acknowledgments

We thank the Copernicus program, the U.S. Geological Survey, and the Italian Space Agency for the use of their data, as well as the EODAG team for making their tools available. We also gratefully acknowledge Maddie Stedman for her help with the PRISMA data, Mattea Goalen for help with the data readers, Brian Wenny for the GHNA RadCalNet processing and Mohammadmehdi Saberioon for interesting discussion. We gratefully acknowledge Gillian Maggs-Kolling, Eugene Marais, Martin Handjaba and the Gobabeb Research Center team for their support during deployment and servicing of the RadCalNet GONA and HYPERNETS GHNA instruments. We thank Michel Van Roozendal, Alexander Mangold and Alexis Merlaud for their effort in establishing and maintaining the Utsteinen AERONET site and Stuart Piketh and Gillian Maggs-Kolling for their effort in establishing and maintaining the Gobabeb AERONET site. The International Polar Foundation (IPF) and Clemence Goyens are warmly thanked for supporting the PEAN deployment. The HYPERNETS partners, especially Tartu University and Sorbonne University are thanked for technical support and development of the HYPSTAR® instrument and system. Paul Green is thanked for useful comments.

Conflict of interest

The authors declare that the research was conducted in the absence of any commercial or financial relationships that could be construed as a potential conflict of interest.

Publisher's note

All claims expressed in this article are solely those of the authors and do not necessarily represent those of their affiliated organizations, or those of the publisher, the editors and the reviewers. Any product that may be evaluated in this article, or claim that may be made by its manufacturer, is not guaranteed or endorsed by the publisher.

Supplementary Material

The Supplementary Material for this article can be found online at: https://www.frontiersin.org/articles/10.3389/frsen.2024.1323998/full#supplementary-material

References

Alhammoud, B., Jackson, J., Clerc, S., Arias, M., Bouzinac, C., Gascon, F., et al. (2019). Sentinel-2 level-1 radiometry assessment using vicarious methods from dimitri toolbox and field measurements from radcalnet database. *IEEE J. Sel. Top. Appl. Earth Observations Remote Sens.* 12, 3470–3479. doi:10.1109/JSTARS.2019.2936940

Ball, C. P., Marks, A. A., Green, P. D., MacArthur, A., Maturilli, M., Fox, N. P., et al. (2015). Hemispherical-directional reflectance (hdrf) of windblown snow-covered arctic tundra at large solar zenith angles. *IEEE Trans. Geoscience Remote Sens.* 53, 5377–5387. doi:10.1109/TGRS.2015.2421733

Banks, A. C., Hunt, S. E., Gorroño, J., Scanlon, T., Woolliams, E. R., and Fox, N. P. (2017). "A comparison of validation and vicarious calibration of high and medium resolution satellite-borne sensors using radcalnet," in *Sensors, systems, and next-generation satellites XXI*. Editors S. P. Neeck, J.-L. Bézy, and T. Kimura (United States: International Society for Optics and Photonics), 10423. doi:10.1117/12.2278528

Barsi, J., Alhammoud, B., Czapla-Myers, J., Gascon, F., Haque, M., Kaewmanee, M., et al. (2018). Sentinel-2A MSI and Landsat-8 OLI radiometric cross comparison over desert sites. *Italian J. Remote Sens./Rivista Italiana di Telerilevamento* 51, 822–837. doi:10.1080/22797254.2018.1507613

Bialek, A., Greenwell, C., Lamare, M., Meygret, A., Marcq, S., Lachérade, S., et al. (2016). "New radiometric calibration site located at gobabeb, namib desert," in 2016 IEEE International Geoscience and Remote Sensing Symposium (IGARSS), Beijing, China, July 10-15, 2016, 6094–6097.

Bipm, Iec, Ifcc, Ilac, Iso, and Iupac, (2008). Evaluation of measurement data — guide to the expression of uncertainty in measurement. Joint Committee for Guides in Metrology. *JCGM* 100, 2008.

Bouvet, M., Thome, K., Berthelot, B., Bialek, A., Czapla-Myers, J., Fox, N. P., et al. (2019). Radcalnet: a radiometric calibration network for earth observing imagers

operating in the visible to shortwave infrared spectral range. *Remote Sens.* 11, 2401. doi:10.3390/rs11202401

Coddington, O. M., Richard, E. C., Harber, D., Pilewskie, P., Woods, T. N., Chance, K., et al. (2021). The tsis-1 hybrid solar reference spectrum. *Geophys. Res. Lett.* 48, e2020GL091709. doi:10.1029/2020GL091709

De Vis, P., Bialek, A., and Sinclair, M. (2023). Initial sample of HYPERNETS hyperspectral surface reflectance measurements for satellite validation from the gobabeb site in Namibia. *Zendo*. doi:10.5281/zenodo.8039303

De Vis, P., Goyens, C., Hunt, S., Vanhellemont, Q., Ruddick, K., and Bialek, A. (2024). Generating hyperspectral reference measurements for surface reflectance from the LANDHYPERNET and WATERHYPERNET networks. *Front. Remote Sens.* 5 ISSN=2673-6187. doi:10.3389/frsen.2024.1347230

Emde, C., Buras-Schnell, R., Kylling, A., Mayer, B., Gasteiger, J., Hamann, U., et al. (2016). The libradtran software package for radiative transfer calculations (version 2.0.1). *Geosci. Model Dev.* 9, 1647–1672. doi:10.5194/gmd-9-1647-2016

Gascon, F., Bouzinac, C., Thépaut, O., Jung, M., Francesconi, B., Louis, J., et al. (2017). Copernicus sentinel-2a calibration and products validation status. *Remote Sens.* 9, 584. doi:10.3390/rs9060584

Gasteiger, J., Emde, C., Mayer, B., Buras, R., Buehler, S. A., and Lemke, O. (2014). Representative wavelengths absorption parameterization applied to satellite channels and spectral bands. *J. Quantitative Spectrosc. Radiat. Transf.* 148, 99–115. doi:10.1016/j.jqsrt.2014.06.024

Gorroño, J., Fomferra, N., Peters, M., Gascon, F., Underwood, C. I., Fox, N. P., et al. (2017). A radiometric uncertainty tool for the sentinel 2 mission. *Remote Sens.* 9, 178. doi:10.3390/rs9020178

Hersbach, H., Bell, B., Berrisford, P., Hirahara, S., Horányi, A., Muñoz-Sabater, J., et al. (2020). The era5 global reanalysis. *Q. J. R. Meteorological Soc.* 146, 1999–2049. doi:10.1002/qj.3803

Hess, M., Koepke, P., and Schult, I. (1998). Optical properties of aerosols and clouds: the software package opac. *Bull. Am. Meteorological Soc.* 79, 831–844. doi:10.1175/1520-0477(1998)079-0831:OPOAAC-2.0.CO;2

Inness, A., Ades, M., Agustí-Panareda, A., Barré, J., Benedictow, A., Blechschmidt, A.-M., et al. (2019). The cams reanalysis of atmospheric composition. *Atmos. Chem. Phys.* 19, 3515–3556. doi:10.5194/acp-19-3515-2019

Jing, X., Leigh, L., Teixeira Pinto, C., and Helder, D. (2019). Evaluation of radcalnet output data using landsat 7, landsat 8, sentinel 2a, and sentinel 2b sensors. *Remote Sens.* 11, 541. doi:10.3390/rs11050541

Lamquin, N., Bruniquel, V., and Gascon, F. (2018). Sentinel-2 l1c radiometric validation using deep convective clouds observations. *Eur. J. Remote Sens.* 51, 11–27. doi:10.1080/22797254.2017.1395713

Markham, B., Barsi, J., Kvaran, G., Ong, L., Kaita, E., Biggar, S., et al. (2014). Landsat-8 operational land imager radiometric calibration and stability. *Remote Sens.* 6, 12275–12308. doi:10.3390/rs61212275

Micijevic, E., Barsi, J., Haque, M., Levy, R., Anderson, C., Thome, K., et al. (2022). English (US)Radiometric performance of the landsat 9 operational land imager over the first 8 months on orbit. In *Earth Observing Systems XXVII. Proc. SPIE - Int. Soc. Opt. Eng.* doi:10.1117/12.2634301

Murakami, H., Antoine, D., Vellucci, V., and Frouin, R. (2022). System vicarious calibration of GCOM-C/SGLI visible and near-infrared channels. *J. Oceanogr.* 78, 245–261. doi:10.1007/s10872-022-00632-x

Pignatti, S., Amodeo, A., Carfora, M. F., Casa, R., Mona, L., Palombo, A., et al. (2022). Prisma l1 and l2 performances within the priscav project: the pignola test site in southern Italy. *Remote Sens.* 14, 1985. doi:10.3390/rs14091985

Revel, C., Lonjou, V., Marcq, S., Desjardins, C., Fougnie, B., Luche, C. C.-D., et al. (2019). Sentinel-2a and 2b absolute calibration monitoring. *Eur. J. Remote Sens.* 52, 122–137. doi:10.1080/22797254.2018.1562311

Ruddick, K., Brando, V. E., Corizzi, A., Dogliotti, A. I., Doxaran, D., Goyens, C., et al. (2024a). WATERHYPERNET: A prototype network of automated in situ measurements of hyperspectral water reflectance for satellite validation and water quality monitoring. *Front. Remote Sens.* 5. doi:10.3389/frsen.2024.1347520

Ruddick, K. G., Bialek, A., Brando, V. E., De Vis, P., Dogliotti, A. I., Doxaran, D., et al. (2024b). HYPERNETS: a network of automated hyperspectral radiometers to validate water and land surface reflectance (380–1680 nm) from all satellite missions. *Front. Remote Sens.* 5 ISSN=2673-6187. doi:10.3389/frsen.2024.1372085

Schunke, S., Leroy, V., and Govaerts, Y. (2023). Retrieving brdfs from uav-based radiometers for fiducial reference measurements: caveats and recommendations. *Front. Remote Sens.* 4. doi:10.3389/frsen.2023.1285800

Sinyuk, A., Holben, B. N., Eck, T. F., Giles, D. M., Slutsker, I., Korkin, S., et al. (2020). The aeronet version 3 aerosol retrieval algorithm, associated uncertainties and comparisons to version 2. *Atmos. Meas. Tech.* 13, 3375–3411. doi:10.5194/amt-13-3375-2020

Zhao, Y., Ma, L., Li, W., He, H., Long, X., Wang, N., et al. (2021). "Vicarious radiometric calibration of superview-1 sensor using radcalnet toa reflectance product," in 2021 IEEE International Geoscience and Remote Sensing Symposium IGARSS, Brussels, Belgium, July 11-16, 2021, 8130–8133.

Frontiers in
Remote Sensing

Highlights innovation in remote sensing science and its applications

An exciting journal which focuses on physical and quantitative approaches to remote sensing of the land, oceans, biosphere, atmosphere and space at local and global levels.

Discover the latest Research Topics

See more →



Frontiers

Avenue du Tribunal-Fédéral 34
1005 Lausanne, Switzerland
frontiersin.org

Contact us

+41 (0)21 510 17 00
frontiersin.org/about/contact